



**US Army Corps
of Engineers**

Construction Engineering
Research Laboratories

USACERL Technical Manuscript 98/120
September 1998

Investigation of the Use of Viscoelastic Damping Devices to Rehabilitate a Lightly Reinforced Concrete Slab-Column Structure

John R. Hayes, Jr.

The objective of this study was to develop improved understanding of the seismic behavior of a lightly reinforced concrete (LRC) slab-column structure seismically retrofitted with viscoelastic dampers (VEDs). The feasibility of using VEDs to rehabilitate existing LRC slab-column structures was explored, and implications for structural design were considered.

A model of a section of a 1950s-era three-story military barracks building was fabricated for testing. A rehabilitation scheme using VEDs was designed and implemented. This section model was subjected to a series of earthquake simulations on the shaking table at the U.S. Army Construction Engineering Research Laboratories (CERL). Experimental measurements included floor and VED displacements, floor accelerations, VED forces, and reinforcement strains. The earthquake simulations comprised a series of gradually increasing intensity replications of two commonly used earthquake records, first on the frame fitted with VEDs, then on the frame without VEDs.

Interpretations of the testing results are provided through the use of linear models of the type that might be used in the design office. These analytical models also were used to assess the applicability of the linear modeling procedures that have been recommended in Federal Emergency Management Agency document 273, "NEHRP Guidelines for the Seismic Rehabilitation of Buildings."

19990301052

DTIC QUALITY INSPECTED 1

Approved for public release; distribution is unlimited.

The contents of this report are not to be used for advertising, publication, or promotional purposes. Citation of trade names does not constitute an official endorsement or approval of the use of such commercial products. The findings of this report are not to be construed as an official Department of the Army position, unless so designated by other authorized documents.

DESTROY THIS REPORT WHEN IT IS NO LONGER NEEDED

DO NOT RETURN IT TO THE ORIGINATOR

INVESTIGATION OF THE USE OF VISCOELASTIC DAMPING DEVICES TO REHABILITATE
A LIGHTLY REINFORCED CONCRETE SLAB-COLUMN STRUCTURE

BY

JOHN RIVES HAYES, JR.

B.S., Virginia Military Institute, 1973

M.E., University of Virginia, 1975

THESIS

Submitted in partial fulfillment of the requirements
for the degree of Doctor of Philosophy in Civil Engineering
in the Graduate College of the
University of Illinois at Urbana-Champaign, 1998

Urbana, Illinois

UNIVERSITY OF ILLINOIS AT URBANA-CHAMPAIGN

THE GRADUATE COLLEGE

AUGUST 1998

WE HEREBY RECOMMEND THAT THE THESIS BY

JOHN RIVES HAYES, JR.

ENTITLED INVESTIGATION OF THE USE OF VISCOELASTIC DAMPING DEVICES TO
REHABILITATE A LIGHTLY-REINFORCED CONCRETE SLAB-COLUMN STRUCTURE

BE ACCEPTED IN PARTIAL FULFILLMENT OF THE REQUIREMENTS FOR

THE DEGREE OF DOCTOR OF PHILOSOPHY

Douglas A. Foutch

Director of Thesis Research

William J. Hall

Head of Department

Committee on Final Examination†

Douglas A. Foutch

Chairperson

William J. Hall

John L. Hoan

Nail M. Hawkins

† Required for doctor's degree but not for master's.

REPORT DOCUMENTATION PAGE

Form Approved
OMB No. 0704-0188

Public reporting burden for this collection of information is estimated to average 1 hour per response, including the time for reviewing instructions, searching existing data sources, gathering and maintaining the data needed, and completing and reviewing the collection of information. Send comments regarding this burden estimate or any other aspect of this collection of information, including suggestions for reducing this burden, to Washington Headquarters Services, Directorate for Information Operations and Reports, 1215 Jefferson Davis Highway, Suite 1204, Arlington, VA 22202-4302, and to the Office of Management and Budget, Paperwork Reduction Project (0704-0188), Washington, DC 20503.

| | | | | | |
|---|---|--|--|--|--|
| 1. AGENCY USE ONLY (Leave Blank) | | 2. REPORT DATE September 1998 | | 3. REPORT TYPE AND DATES COVERED Final | |
| 4. TITLE AND SUBTITLE Investigation of the Use of Viscoelastic Damping Devices to Rehabilitate a Lightly Reinforced Concrete Slab-Column Structure | | | | 5. FUNDING NUMBERS 4A161102 AT23 FL-EJ8 4A162784 AT41 FM-CW4 | |
| 6. AUTHOR(S) John R. Hayes, Jr. | | | | | |
| 7. PERFORMING ORGANIZATION NAME(S) AND ADDRESS(ES) U.S. Army Construction Engineering Research Laboratories (USACERL) P.O. Box 9005 Champaign, IL 61826-9005 | | | | 8. PERFORMING ORGANIZATION REPORT NUMBER TM 98/120 | |
| 9. SPONSORING / MONITORING AGENCY NAME(S) AND ADDRESS(ES) Headquarters, U.S. Army Corps of Engineers ATTN: CEMP-ET 20 Massachusetts Ave NW Washington, DC 20314-1000 | | | | 10. SPONSORING / MONITORING AGENCY REPORT NUMBER | |
| 11. SUPPLEMENTARY NOTES Copies are available from the National Technical Information Service, 5285 Port Royal Road, Springfield, VA 22161. | | | | | |
| 12a. DISTRIBUTION / AVAILABILITY STATEMENT Approved for public release; distribution is unlimited. | | | | 12b. DISTRIBUTION CODE | |
| 13. ABSTRACT (Maximum 200 words) <p>The objective of this study was to develop improved understanding of the seismic behavior of a lightly reinforced concrete (LRC) slab-column structure seismically retrofitted with viscoelastic dampers (VEDs). The feasibility of using VEDs to rehabilitate existing LRC slab-column structures was explored, and implications for structural design were considered.</p> <p>A model of a section of a 1950s-era three-story military barracks building was fabricated for testing. A rehabilitation scheme using VEDs was designed and implemented. This section model was subjected to a series of earthquake simulations on the shaking table at the U.S. Army Construction Engineering Research Laboratories (CERL). Experimental measurements included floor and VED displacements, floor accelerations, VED forces, and reinforcement strains. The earthquake simulations comprised a series of gradually increasing intensity replications of two commonly used earthquake records, first on the frame fitted with VEDs, then on the frame without VEDs.</p> <p>Interpretations of the testing results are provided through the use of linear models of the type that might be used in the design office. These analytical models also were used to assess the applicability of the linear modeling procedures that have been recommended in Federal Emergency Management Agency document 273, "NEHRP Guidelines for the Seismic Rehabilitation of Buildings."</p> | | | | | |
| 14. SUBJECT TERMS concrete testing viscoelastic dampers (VEDs) seismic vulnerability structural engineering lightly reinforced concrete (LRC) | | | | 15. NUMBER OF PAGES 958 | |
| | | | | 16. PRICE CODE | |
| 17. SECURITY CLASSIFICATION OF REPORT Unclassified | 18. SECURITY CLASSIFICATION OF THIS PAGE Unclassified | 19. SECURITY CLASSIFICATION OF ABSTRACT Unclassified | | 20. LIMITATION OF ABSTRACT SAR | |

Foreword

This document is a reprint of a doctoral dissertation, the research for which was funded in part by Headquarters, U.S. Army Corps of Engineers under Project 4A161102 AT23, "Basic Research/Military Construction"; and Project 4A162784 AT41, "Military Facilities Engineering Technology." The technical monitors were Charles Gutberlet, CEMP-ET; Dr. Douglas A. Foutch, Professor of Civil Engineering, University of Illinois at Urbana-Champaign; and Dr. Sharon L. Wood, Associate Professor of Civil Engineering, University of Texas, Austin.

The work was performed under the supervision of the Engineering Division (FL-E) of the Facilities Technology Laboratory, U.S. Army Construction Engineering Research Laboratories (CERL). The Principal Investigator was John R. Hayes, Jr. Larry M. Windingland is Chief, CECER-FL-E, and L. Michael Golish is Operations Chief, CECER-FL.

COL James A. Walter is the Commander of CERL, and Dr. Michael J. O'Connor is Director.

ABSTRACT

INVESTIGATION OF THE USE OF VISCOELASTIC DAMPING DEVICES TO REHABILITATE A LIGHTLY REINFORCED CONCRETE SLAB-COLUMN STRUCTURE

John Rives Hayes, Jr., Ph.D.
Department of Civil Engineering
University of Illinois at Urbana-Champaign, 1998
Douglas A. Foutch, Advisor

The objective of this study was to develop improved understanding of the seismic behavior of a lightly reinforced concrete (LRC) slab-column structure that was modified by the addition of viscoelastic dampers (VEDs). The study includes both experimental and analytical phases. The feasibility of using VEDs to rehabilitate existing LRC slab-column structures was explored, and implications for structural design were considered.

The experimental phase of the study involved the fabrication and testing of a model of a section of a three-story military barracks building that was constructed in the mid-1950's. The barracks is a two-bay LRC slab-column frame. The model was constructed as closely as possible to one-third of full-scale. Material properties in the model emulated those of the prototype, and model reinforcement details paralleled prototype details. With the presumption that the model possessed seismic vulnerabilities, a rehabilitation scheme using VEDs was designed and implemented. VEDs were mounted in diagonal braces that extended between column lines in the model.

The model was subjected to a series of earthquake simulations on the shaking table at the U.S. Army Construction Engineering Research Laboratories (USACERL). Experimental measurements included floor and VED displacements, floor accelerations, VED forces, and reinforcement strains. This report includes detailed descriptions of the design and construction of the model, the testing program, and the data obtained during the testing. Discussion and interpretation of the data that were collected follows the data descriptions.

The earthquake simulations while VEDs were installed on the model were a series of gradually increasing intensity replications of two commonly used earthquake records. Simulation intensities were increased until the displacement limits of the shaking table actuators were reached. After that, the VEDs

were removed, and a second series of simulations with the bare frame was conducted.

Interpretations of the testing results are provided through the use of linear models of the type that might be used in the design office. The analytical models were used to assess strength, stiffness, and serviceability of the structure. In addition, the analytical models were used to assess the applicability of the linear modeling procedures that have been recommended in Federal Emergency Management Agency document 273, NEHRP Guidelines for the Seismic Rehabilitation of Buildings.

ACKNOWLEDGEMENTS

The work described in this report was jointly sponsored by the U.S. Army Corps of Engineers (USACE) through the U.S. Army Construction Engineering Research Laboratories (USACERL), and the National Center for Earthquake Engineering Research (NCEER), through the University of Illinois at Urbana-Champaign. Research funding was provided by both USACE and NCEER. NCEER funding was provided through State University of New York grants 91513A, 925101, and 935110, under master National Science Foundation grant numbers ECE-86-07591 and BCS 90-25010. Multiyear USACE funding was provided under program elements 61101 and 62784. 3M Corporation, Minneapolis, MN, supported the project through the provision of viscoelastic dampers and supporting design services. Ivy Wire and Steel, Houston, TX, donated welded steel wire stock for use as model reinforcement. The project that is reported is the cumulative result of the support provided by all of these agencies and would not have been possible without that support. Opinions, findings, conclusions, and recommendations in this report do not necessarily represent those of any of the sponsoring or supporting agencies.

Appreciation is expressed to all who have helped in the project. Some of the more prominent supporters are mentioned below.

The author first wishes to thank God for His creation and grace, and for His imparting patience, wisdom, and perseverance, to all who have been involved.

The author is forever indebted to his devoted wife, Sally, who has provided patient and loving support, countless words of encouragement, and frequent assistance with typing and editing. He is further indebted to his son, Thomas, who often went without his father's attention at critical times but nevertheless showed his loving devotion.

Many personal friends provided encouragement and prayer for the author during the period of study. Most supportive were Pastor Gary Sinclair, Russ Taylor, Gary Eden, and Dale Smoes. These men are dear friends.

Gratitude is extended to key individuals in the organizations that supported this work. The

USACE project technical monitors, Charles Gutberlet, Andrew Constantaras, and Ray Navidi, provided general oversight and consideration for technology transfer. USACERL leadership, including Michael O'Connor, Paul Howdysell, Alan Moore, and Larry Windingland, made it possible for the author to perform this research as a sponsored project. Professor Larry Soong of the State University of New York at Buffalo was instrumental in garnering NCEER support for the project. 3M Corporation's Ed Nielsen and Ming-Lai Lai provided invaluable technical assistance during the model design and experimental testing. Dick Ramsey of Ivy Wire and Steel was an eager supporter, arranging for the donation of the steel wire for the model reinforcement.

At USACERL, the list of valued co-workers is extensive. Deep and abiding appreciation is extended to James Gambill for his priceless direction and assistance with instrumentation, test conduct, and data reduction. William Gordon and Ernest Westfield provided valuable assistance with model construction and test instrumentation. Other team members, including Ghassan Al-Chaar, Pamalee Brady, Steve Sweeney, and James Wilcoski, were constant and continuing supporters.

Special thanks are due to key student assistants. Elizabeth Dausman, Brian Umbright, and Antonio Arthay were intimately involved with model construction and test conduct. Elizabeth Dausman and Jon Sfura provided invaluable support in the large volume of data reduction that was required following the testing program.

Within the Civil Engineering Department of the University of Illinois at Urbana-Champaign, several key figures were involved. Carroll Swan and the members of his machine shop organization fabricated numerous components of the model with timeliness and precision. Professors William Gamble and Neil Hawkins served as research committee members.

Special gratitude is reserved for three faculty members. Professor Sharon Wood, who was actually at the Universities of Texas and Washington for much of the project duration, was a willing technical consultant and a caring friend. Professor William Hall has been a mentor for the author and in many ways has filled the role of "father figure" to the author during the course of study. Finally, Professor Douglas Foutch has been an incredibly patient counselor, directing the author's work and, most important, never giving up on the author during the extended period of study.

TABLE OF CONTENTS

| <u>Chapter</u> | <u>Title</u> | <u>Page</u> |
|----------------|---|-------------|
| 1. | INTRODUCTION | 1 |
| | 1.1 Objective | 1 |
| | 1.2 Background | 1 |
| | 1.3 Experimental Program | 2 |
| | 1.4 Scope of Study | 4 |
| | 1.5 Report References | 5 |
| 2. | DESIGN OF PROTOTYPE AND TEST STRUCTURES | 6 |
| | 2.1 Prototype Structure Description | 6 |
| | 2.2 Reinforced Concrete Model Design | 16 |
| | 2.3 Viscoelastic Damper (VED) Design | 19 |
| | 2.4 VED Brace Design | 26 |
| 3. | EXPERIMENTAL PROGRAM | 30 |
| | 3.1 Viscoelastic Damper Testing | 30 |
| | 3.2 Test Structure Fabrication | 31 |
| | 3.3 Experimental Setup | 33 |
| | 3.4 Testing Procedure | 34 |
| 4. | OBSERVED RESPONSE OF THE TEST STRUCTURE | 38 |
| | 4.1 Floor Accelerations | 39 |
| | 4.2 Relative Story Displacements | 41 |
| | 4.3 Interstory Displacements | 43 |
| | 4.4 Story Shears | 45 |
| | 4.5 Story Shear Vs. Displacement Relations | 48 |
| | 4.6 Overturning Moments | 48 |
| | 4.7 Viscoelastic Damper (VED) Performance | 49 |
| | 4.8 Column Shears | 53 |
| | 4.9 Comparisons of Story Shear, Column Shear, and Sums of Horizontal Components of Damper Forces | 54 |

| | | |
|------|---|-----|
| 4.10 | Relative Floor Velocities | 54 |
| 4.11 | Dynamic Characterizations of Model | 55 |
| 4.12 | Reinforcement Strains | 59 |
| 4.13 | Observed Condition of Structure | 62 |
| 5. | DISCUSSION OF OBSERVED RESPONSE | 65 |
| 5.1 | Floor Accelerations | 65 |
| 5.2 | Displacements | 66 |
| 5.3 | Story Shears | 69 |
| 5.4 | Story Shear Vs. Interstory Displacement: Hysteretic Behavior | 69 |
| 5.5 | Overturning Moments | 70 |
| 5.6 | Viscoelastic Damper (VED) Performance | 70 |
| 5.7 | Variation of Dynamic Properties | 76 |
| 5.8 | Energy Input and Dissipation | 83 |
| 5.9 | Reinforcement Strains | 85 |
| 5.10 | Summary of Observed Responses | 89 |
| 5.11 | Primary Observations from the Experimental Program | 93 |
| 6. | INTERPRETATIONS OF STRENGTH AND STIFFNESS RESPONSE | 96 |
| 6.1 | General Approach to Structural Modeling | 96 |
| 6.2 | Determination of Member Capacities | 97 |
| 6.3 | Determination of Member Stiffnesses | 106 |
| 6.4 | Viscoelastic Damper (VED) Modeling | 109 |
| 6.5 | ETABS Modeling Procedures | 110 |
| 6.6 | Structural Analyses | 111 |
| 6.7 | Assessment of FEMA 273/274 Procedures | 124 |
| 6.8 | Primary Observations from Interpretations of Strength and Stiffness Response | 134 |
| 7. | SUMMARY AND CONCLUSIONS | 137 |
| 7.1 | Objective and Scope | 137 |
| 7.2 | Experimental Program | 137 |
| 7.3 | Primary Observations from the Experimental Program | 140 |
| 7.4 | Primary Observations from Interpretations of Strength and Stiffness Response | 142 |
| 7.5 | Concluding Remarks | 145 |
| | LIST OF REFERENCES | 147 |

| | |
|---------------|-----|
| TABLES | 152 |
| FIGURES | 233 |

Appendix

| | | |
|---|--|-----|
| A | DESCRIPTION OF MODEL FABRICATION | 386 |
| B | SHAKING TABLE CHARACTERISTICS, INSTRUMENTATION, AND DATA DESCRIPTIONS | 416 |
| C | SEISMIC SIMULATION TEST DATA | 432 |
| D | VISCOELASTIC DAMPER CHARACTERIZATION | 893 |
| | VITA | 921 |

LIST OF TABLES

| <u>Number</u> | <u>Title</u> | <u>Page</u> |
|---------------|---|-------------|
| 2.1 | Distributed Floor Loads in Prototype | 152 |
| 2.2 | Scaling Similitude Requirements for 1/3-Scale Model | 153 |
| 2.3 | Comparison of Key Dimensions in Prototype and 1/3-Scale Model | 153 |
| 2.4 | Prototype and Model Longitudinal Slab Reinforcement | 154 |
| 2.5 | Prototype and Model Lateral Slab Reinforcement | 154 |
| 2.6 | Prototype and Model Column and Spandrel Reinforcement | 155 |
| 3.1 | List of Earthquake Simulations Performed on Model | 156 |
| 4.1 | Maximum Floor Accelerations in Earthquake Simulations | 157 |
| 4.2 | Maximum Relative Displacements and Total Drift Ratios in Earthquake Simulations | 158 |
| 4.3 | Maximum Interstory Displacements and Drift Ratios in Earthquake Simulations | 159 |
| 4.4 | Maximum Story Shears in Earthquake Simulations (Model Weight = 58.67 kips) | 160 |
| 4.5 | Maximum Overturning Moments in Earthquake Simulations | 161 |
| 4.6 | Maximum Sums of Horizontal Components of Damper Forces | 162 |
| 4.7 | Story Shear Vs. Damper Force at Time of "Negative" (As Plotted) Story Shear Maximum | 163 |
| 4.8 | Story Shear Vs. Damper Force at Time of "Positive" (As Plotted) Story Shear Maximum | 164 |
| 4.9 | Story Shear Vs. Maximum Damper Force Before "Negative" (As Plotted) Story Shear Maximum | 165 |
| 4.10 | Story Shear Vs. Maximum Damper Force Before "Positive" (As Plotted) Story Shear Maximum | 166 |
| 4.11 | Elapsed Times to "Negative" (As Plotted) Story Shear Maxima | 167 |
| 4.12 | Elapsed Times to "Positive" (As Plotted) Story Shear Maxima | 168 |
| 4.13 | Maximum Column Shears in Earthquake Simulations | 169 |
| 4.14 | Maximum Relative Floor Velocities in Earthquake Simulations | 170 |
| 4.15 | Modal Properties from Earthquake Simulations, Acceleration-Based Transfer Functions (FL 3) | 171 |

| | | |
|-------|---|-----|
| 4.16 | Modal Properties from White Noise Tests | 172 |
| 4.17 | First Mode Characteristics from Free Vibration Tests | 173 |
| 4.18 | First Mode Characteristics from Pullback Tests | 173 |
| 4.19 | Maximum and Residual Strains in Reinforcement: Gages SGZ1 and SGZ3 | 174 |
| 4.20 | Maximum and Residual Strains in Reinforcement: Gages SGZ4 and S1Z1 | 175 |
| 4.21 | Maximum and Residual Strains in Reinforcement: Gages S1Z5 and S1Z6 | 176 |
| 4.22 | Maximum and Residual Strains in Reinforcement: Gages S1Z3 and S1Z7 | 177 |
| 4.23 | Maximum and Residual Strains in Reinforcement: Gages S1Z8 and S2Z2 | 178 |
| 4.24 | Maximum and Residual Strains in Reinforcement: Gages S2Z3 and S1X5 | 179 |
| 4.25 | Maximum and Residual Strains in Reinforcement: Gages S1X11 and S1X12 .. | 180 |
| 4.26 | Maximum and Residual Strains in Reinforcement: Gages S1X13 and S1X14 .. | 181 |
| 4.27 | Maximum and Residual Strains in Reinforcement: Gages S1X15 and S1X16 .. | 182 |
| 5.1.a | Curve Fits for Damper Force Vs. Displacement "Backbone" Curves, Brace in Tension | 183 |
| 5.1.b | Curve Fits for Damper Force Vs. Displacement "Backbone" Curves, Brace in Tension | 184 |
| 5.1.c | Curve Fits for Damper Force Vs. Displacement "Backbone" Curves, Brace in Tension | 185 |
| 5.2.a | Curve Fits for Damper Force Vs. Displacement "Backbone" Curves, Brace in Compression | 186 |
| 5.2.b | Curve Fits for Damper Force Vs. Displacement "Backbone" Curves, Brace in Compression | 187 |
| 5.2.c | Curve Fits for Damper Force Vs. Displacement "Backbone" Curves, Brace in Compression | 188 |
| 5.3 | Average Damper Brace Stiffnesses Based on Linear Curve Fits to "Backbone" Curves | 189 |
| 5.4 | Damper Stiffnesses Based on Linear Regressions for Time-Histories | 190 |
| 5.5.a | Individual Damper Stiffnesses, 0.25 Dmax to 1.0 Dmax | 191 |
| 5.5.b | Individual Damper Stiffnesses, 0.25 Dmax to 1.0 Dmax | 192 |
| 5.5.c | Individual Damper Stiffnesses, 0.25 Dmax to 1.0 Dmax | 193 |
| 5.6.a | Individual Damper Stiffnesses, 0.50 Dmax to 1.0 Dmax | 194 |
| 5.6.b | Individual Damper Stiffnesses, 0.50 Dmax to 1.0 Dmax | 195 |
| 5.6.c | Individual Damper Stiffnesses, 0.50 Dmax to 1.0 Dmax | 196 |
| 5.7 | Curve Fits for Story Shear Vs. Interstory Displacement "Backbone" Relationships | 197 |
| 5.8 | Curve Fits for Column Shear Vs. Interstory Displacement "Backbone" Relationships | 198 |
| 5.9 | Interstory Stiffnesses Based on "Backbone" Curves | 199 |

| | | |
|------|---|-----|
| 5.10 | Interstory Stiffnesses Based on Linear Regression from Time-Histories | 200 |
| 5.11 | Energy Input and Dissipation Quantities for Earthquake Simulations | 201 |
| 6.1 | Reinforced Concrete Column Properties Used in BIAx Analyses | 202 |
| 6.2 | Interior (Centerline) Column Properties Used in ETABS Analyses | 203 |
| 6.3 | Exterior (Outside) Column Properties Used In ETABS Analyses | 204 |
| 6.4 | Proposed Effective Width Factors for Two-Beam Models | 205 |
| 6.5 | Equivalent Beam Widths Used in ETABS Analyses | 206 |
| 6.6 | Viscoelastic Damper and Rotational Spring Properties Used in EATBS Analyses of Response Maxima | 207 |
| 6.7 | Comparison of ETABS Analysis and Measured Top Floor Drift, Base Shear, and Input Energy | 208 |
| 6.8 | Comparison of ETABS Analysis and Measured Story Shear Stiffnesses and VED Forces | 209 |
| 6.9 | Comparison of Dynamic Properties Used in ETABS Analyses with Measured Modal Properties | 210 |
| 6.10 | Computed and Measured Mode Shapes | 211 |
| 6.11 | Maximum Column Forces: Interior Column, Floor 1 | 212 |
| 6.12 | Maximum Column Forces: Interior Column, Floor 2 | 213 |
| 6.13 | Maximum Column Forces: Interior Column, Floor 3 | 214 |
| 6.14 | Maximum Column Forces: Exterior Column, Floor 1 | 215 |
| 6.15 | Maximum Column Forces: Exterior Column, Floor 2 | 216 |
| 6.16 | Maximum Column Forces: Exterior Column, Floor 3 | 217 |
| 6.17 | Maximum Unbalanced Moments at Slab-Column Connections, Floor 1 | 218 |
| 6.18 | Maximum Unbalanced Moments at Slab-Column Connections, Floor 2 | 219 |
| 6.19 | Maximum Unbalanced Moments at Slab-Column Connections, Floor 3 | 220 |
| 6.20 | FEMA 273 Maximum Column Forces: Interior Column, Floor 1 | 221 |
| 6.21 | FEMA 273 Maximum Column Forces: Interior Column, Floor 2 | 222 |
| 6.22 | FEMA 273 Maximum Column Forces: Interior Column, Floor 3 | 223 |
| 6.23 | FEMA 273 Maximum Column Forces: Exterior Column, Floor 1 | 224 |
| 6.24 | FEMA 273 Maximum Column Forces: Exterior Column, Floor 2 | 225 |
| 6.25 | FEMA 273 Maximum Column Forces: Exterior Column, Floor 3 | 226 |
| 6.26 | FEMA 273 Maximum Unbalanced Moments at Slab-Column Connections, Floor 1 | 227 |
| 6.27 | FEMA 273 Maximum Unbalanced Moments at Slab-Column Connections, Floor 2 | 228 |
| 6.28 | FEMA 273 Maximum Unbalanced Moments at Slab-Column Connections, Floor 3 | 229 |
| 6.29 | FEMA 273 Acceptance Criteria Checks for Interior Columns | 230 |

| | | |
|------|---|-----|
| 6.30 | FEMA 273 Acceptance Criteria Checks for Exterior Columns | 231 |
| 6.31 | FEMA 273 Acceptance Criteria Checks for Slab-Column Connections | 232 |
| A.1 | Test Results, Deformed Steel Wire Used in Model Structure Reinforcement ... | 397 |
| A.2 | Test Results, 6" x 12" Concrete Compression Cylinders | 398 |
| A.3 | Flexural Test Results, 6" x 6" x 30" Concrete Beams | 399 |
| A.4 | Split Cylinder Test Results, 6" x 12" Concrete Cylinders | 399 |
| A.5 | Model Floor Weights and Centers of Gravity | 400 |
| B.1 | Instrumentation List for Model | 423 |
| D.1 | Damper Characterization Test Results, Dampers 65I and 65L @ 1 Hz | 900 |
| D.2 | Damper Characterization Test Results, Dampers 65I and 65L @ 2 and 3 Hz .. | 901 |
| D.3 | Damper Characterization Test Results, Dampers 66D and 66M @ 1 Hz | 902 |
| D.4 | Damper Characterization Test Results, Dampers 66D and 66M @ 2 and 3 Hz . | 903 |
| D.5 | Comparison of Damper Properties from Tests with Published Data | 904 |

LIST OF FIGURES

| <u>Number</u> | <u>Title</u> | <u>Page</u> |
|---------------|--|-------------|
| 2.1 | Prototype Barracks Building, Fort Lewis, WA | 233 |
| 2.2 | As-Built Drawing of Prototype Building, Ground Floor Plan | 234 |
| 2.3 | As-Built Drawing of Prototype Building, Second and Third Floor Plans | 235 |
| 2.4 | As-Built Drawing of Prototype Building, Exterior Wall Sections | 236 |
| 2.5 | As-Built Drawing of Prototype Building, Exterior Column Detail | 237 |
| 2.6 | As-Built Drawing of Prototype Building, Interior Column Shearhead Detail . . . | 237 |
| 2.7 | Post-Construction View of Model, East Side | 238 |
| 2.8 | Post-Construction View of Model, North Side | 238 |
| 2.9 | Bare Model Prior to Placement on Shaking Table | 239 |
| 2.10 | Model After Placement on Shaking Table (Safety Frame in Place) | 239 |
| 2.11 | Plan View of Model on Shaking Table Platform | 240 |
| 2.12 | Model Elevation, Section A-A | 240 |
| 2.13 | Model Elevation, Section B-B | 241 |
| 2.14 | Model Elevation, Dampers in Place | 241 |
| 2.15 | Longitudinal Reinforcement in Model Slabs, Top Bars | 242 |
| 2.16 | Longitudinal Reinforcement in Model Slabs, Bottom Bars | 242 |
| 2.17 | Longitudinal Reinforcement, Middle Strip | 243 |
| 2.18 | Longitudinal Reinforcement, Column Strip | 243 |
| 2.19 | Lateral Reinforcement in Model Slabs, Top Bars | 244 |
| 2.20 | Lateral Reinforcement in Model Slabs, Bottom Bars | 244 |
| 2.21 | Lateral Reinforcement, Middle Strip | 245 |
| 2.22 | Lateral Reinforcement, Column Strip | 245 |
| 2.23 | Exterior Column Details | 246 |
| 2.24 | Interior (Centerline) Column Details | 246 |
| 2.25 | Spandrel Beam Details | 247 |
| 2.26 | Elevation and Plan Views of Typical Viscoelastic Damper | 247 |
| 2.27 | 3M Viscoelastic Damper | 248 |
| 2.28 | Original 3M Damper Design Curve | 248 |
| 2.29 | Diagonal Brace Details | 249 |
| 2.30 | Typical Exterior Column Details | 250 |

| | | |
|------|--|-----|
| 2.31 | Typical Interior Column Details | 251 |
| 3.1 | Elastic Acceleration and Displacement Response Spectra, 100% El Centro, Compressed Time Scale | 252 |
| 3.2 | Time History and FFT of 100% El Centro, Compressed Time Scale | 253 |
| 3.3 | Time History and FFT of Base Girder Motion, Simulation E100DL | 253 |
| 3.4 | Time History and FFT of Base Girder Motion, Simulation E200DL | 254 |
| 3.5 | Time History and FFT of Base Girder Motion, Simulation E250DL | 254 |
| 3.6 | Time History and FFT of Base Girder Motion, Simulation E100N | 255 |
| 3.7 | Time History and FFT of Base Girder Motion, Simulation E200N | 255 |
| 3.8 | Elastic Acceleration and Displacement Response Spectra, 100% Taft, Compressed Time Scale | 256 |
| 3.9 | Time History and FFT of 100% Taft, Compressed Time Scale | 257 |
| 3.10 | Time History and FFT of Base Girder Motion, Simulation T105DL | 257 |
| 3.11 | Time History and FFT of Base Girder Motion, Simulation T420DL | 258 |
| 3.12 | Spectral Velocities (SV) and Spectrum Intensities (SI) for El Centro and Taft Records | 259 |
| 4.1 | Acceleration Vs. Elapsed Time: E050DL Vs. E150DL | 260 |
| 4.2 | Acceleration Vs. Elapsed Time: E050N Vs. E150N | 261 |
| 4.3 | Maximum Floor Acceleration Profiles for El Centro Simulations | 262 |
| 4.4 | Maximum Floor Acceleration Vs. Peak Ground Acceleration (PGA) | 263 |
| 4.5 | Relative Displacement Vs. Elapsed Time: E050DL Vs. E150DL | 264 |
| 4.6 | Relative Displacement Vs. Elapsed Time: E050N Vs. E150N | 265 |
| 4.7 | Maximum Relative Story Displacement Profiles for El Centro Simulations | 266 |
| 4.8 | Maximum Relative Displacement Vs. Peak Ground Acceleration (PGA) | 267 |
| 4.9 | Interstory Drift Vs. Elapsed Time: E050DL Vs. E150DL | 268 |
| 4.10 | Interstory Drift Vs. Elapsed Time: E050N Vs. E150N | 269 |
| 4.11 | Maximum Story Drift Profiles for El Centro Simulations | 270 |
| 4.12 | Maximum Story Drift Vs. Peak Ground Acceleration (PGA) | 271 |
| 4.13 | Story Shear Vs. Elapsed Time: E050DL Vs. E150DL | 272 |
| 4.14 | Story Shear Vs. Elapsed Time: E050N Vs. E150N | 273 |
| 4.15 | Maximum Story Shear Normalized by Total Model Weight: E050DL, E150DL, E050N | 274 |
| 4.16 | Maximum Story Shear Vs. Peak Ground Acceleration (PGA) | 275 |
| 4.17 | Story Shear Vs. Interstory Displacement: E050DL, E150DL | 276 |
| 4.18 | Story Shear Vs. Interstory Displacement: E050N, E150N | 277 |
| 4.19 | Maximum Overturning Moments: E050DL, E150DL, E050N, E150N | 278 |
| 4.20 | Maximum Overturning Moment Vs. PGA | 279 |

| | | |
|------|--|-----|
| 4.21 | Damper Force Vs. Displacement: E050DL, NW and NE | 280 |
| 4.22 | Damper Force Vs. Displacement: E050DL, SW and SE | 281 |
| 4.23 | Damper Force Vs. Displacement: E150DL, NW and NE | 282 |
| 4.24 | Damper Force Vs. Displacement: E150DL, SW and SE | 283 |
| 4.25 | Maximum Sums of Horizontal Components of Damper Forces and Maximum Column Shears Vs. Maximum Story Shears: E050DL, E150DL | 284 |
| 4.26 | Maximum Sum of Horizontal Components of Damper Forces Vs. PGA | 285 |
| 4.27 | Sums of Horizontal Components of Damper Forces/Maximum Story Shear Vs. PGA | 286 |
| 4.28 | Maximum Column Shear Vs. PGA | 287 |
| 4.29 | Story Shear, Column Shear, and Sum of Horizontal Components of Damper Forces: E050DL | 288 |
| 4.30 | Story Shear, Column Shear, and Sum of Horizontal Components of Damper Forces: E150DL | 289 |
| 4.31 | Relative Floor Velocities: E050DL, E150DL | 290 |
| 4.32 | Maximum Relative Floor Velocity Vs. PGA | 291 |
| 4.33 | Acceleration-Based Transfer Functions (TFs): E050DL, E150DL, E050N, E150N | 292 |
| 4.34 | Apparent First Mode Properties Based on Earthquake Simulation Transfer Functions | 293 |
| 4.35 | Fourier Amplitude Spectra of Interstory Displacements: E050DL, E150DL ... | 294 |
| 4.36 | Fourier Amplitude Spectra of Interstory Displacements: E050N, E150N | 295 |
| 4.37 | Acceleration-Based Transfer Functions, White Noise Tests: E050DL, E150DL, E050N, E150N | 296 |
| 4.38 | Crack Pattern, South Side of South Columns, Pre-Test | 297 |
| 4.39 | Crack Pattern, North Side of North Columns, Pre-Test | 298 |
| 4.40 | Crack Pattern, West Side of West Columns, Pre-Test | 299 |
| 4.41 | Crack Pattern, East Side of East Columns, Pre-Test | 300 |
| 4.42 | Crack Pattern, First Floor Slab, Bottom Side, Pre-Test | 301 |
| 4.43 | Crack Pattern, First Floor Slab, Top Side, Pre-Test | 302 |
| 4.44 | Crack Pattern, Second Floor Slab, Bottom Side, Pre-Test | 303 |
| 4.45 | Crack Pattern, Second Floor Slab, Top Side, Pre-Test | 304 |
| 4.46 | Crack Pattern, Third Floor Slab, Bottom Side, Pre-Test | 305 |
| 4.47 | Crack Pattern, Third Floor Slab, Top Side, Pre-Test | 306 |
| 4.48 | Crack Pattern, South Side of South Columns, Post-T420DL | 307 |
| 4.49 | Crack Pattern, North Side of North Columns, Post-T420DL | 308 |
| 4.50 | Crack Pattern, West Side of West Columns, Post-T420DL | 309 |
| 4.51 | Crack Pattern, East Side of East Columns, Post-T420DL | 310 |

| | | |
|------|--|-----|
| 4.52 | Crack Pattern, First Floor Slab, Bottom Side, Post-T420DL | 311 |
| 4.53 | Crack Pattern, First Floor Slab, Top Side, Post-T420DL | 312 |
| 4.54 | Crack Pattern, Second Floor Slab, Bottom Side, Post-T420DL | 313 |
| 4.55 | Crack Pattern, Second Floor Slab, Top Side, Post-T420DL | 314 |
| 4.56 | Crack Pattern, Third Floor Slab, Bottom Side, Post-T420DL | 315 |
| 4.57 | Crack Pattern, Third Floor Slab, Top Side, Post-T420DL | 316 |
| 4.58 | Crack Pattern, South Side of South Columns, Post-E200N | 317 |
| 4.59 | Crack Pattern, North Side of North Columns, Post-E200N | 318 |
| 4.60 | Crack Pattern, West Side of West Columns, Post-E200N | 319 |
| 4.61 | Crack Pattern, East Side of East Columns, Post-E200N | 320 |
| 4.62 | Crack Pattern, First Floor Slab, Bottom Side, Post-E200N | 321 |
| 4.63 | Crack Pattern, First Floor Slab, Top Side, Post-E200N | 322 |
| 4.64 | Crack Pattern, Second Floor Slab, Bottom Side, Post-E200N | 323 |
| 4.65 | Crack Pattern, Second Floor Slab, Top Side, Post-E200N | 324 |
| 4.66 | Crack Pattern, Third Floor Slab, Bottom Side, Post-E200N | 325 |
| 4.67 | Crack Pattern, Third Floor Slab, Top Side, Post-E200N | 326 |
| 4.68 | Top of Third Floor Slab at SW Column, Post-E200N | 327 |
| 4.69 | Third Floor at SW Column, Post-E200N | 328 |
| 4.70 | Bottom of Third Floor Slab at SW Column, Post-E200N | 328 |
| 4.71 | Third Floor at NE Column, Post-E200N | 329 |
| 4.72 | Bottom of Third Floor Slab at NE Column, Post-E200N | 329 |
| 4.73 | Second Floor at NW Column, Post-E200N | 330 |
| 4.74 | Spandrel, Second Floor, NW Column, East Side, Post-E200N | 330 |
| 4.75 | Second Floor, NW Column, Post-E200N | 331 |
| 4.76 | Second Floor at NE Column, Post-E200N | 331 |
| 4.77 | Bottom of Second Floor Slab and Spandrel, NE Column, Post-E200N | 332 |
| 4.78 | Second Floor at SW Column, Post-E200N | 332 |
| 4.79 | Bottom of Second Floor Slab and Spandrel, SW Column, Post-E200N | 333 |
| 4.80 | First Floor at NW Column, Post-E200N | 333 |
| 4.81 | Base of Second Story, SW Column, Post-E200N | 334 |
| 4.82 | Bottom of Third Floor Slab, East Center Column, Post-E200N | 334 |
| 4.83 | Bottom of Second Floor Slab, East Center Column, Post-E200N | 335 |
| 4.84 | Top of Second Floor Slab, East Center Column, Post-E200N | 335 |
| 4.85 | Top of Second Floor Slab, West Center Column, Post-E200N | 356 |
| 4.86 | Top of First Floor Slab, West Center Column, Post-E200N | 336 |
| 5.1 | Comparison of Story and Column Shears Vs. Interstory Displacement | 337 |
| 5.2 | Damper Force Vs. Displacement "Backbone" Curves, First Story, North Side | 338 |
| 5.3 | Damper Force Vs. Displacement "Backbone" Curves, First Story, South Side | 339 |

| | | |
|------|---|-----|
| 5.4 | Damper Force Vs. Displacement “Backbone” Curves, Second Story, North Side | 340 |
| 5.5 | Damper Force Vs. Displacement “Backbone” Curves, Second Story, South Side | 341 |
| 5.6 | Damper Force Vs. Displacement “Backbone” Curves, Third Story, North Side | 342 |
| 5.7 | Damper Force Vs. Displacement “Backbone” Curves, Third Story, South Side | 343 |
| 5.8 | Story Shear Vs. Interstory Displacement “Backbone” Curves, First and Second Stories | 344 |
| 5.9 | Story Shear Vs. Interstory Displacement “Backbone” Curves, Third Story | 345 |
| 5.10 | Column Shear Vs. Interstory Displacement “Backbone” Curves | 346 |
| 5.11 | Normalized Mode Shapes from White Noise Tests 3, 13, and 28 | 347 |
| 5.12 | Normalized Mode Shapes from White Noise Tests 2 and 29 | 348 |
| 5.13 | Normalized Mode Shapes from White Noise Tests 31 and 34 | 349 |
| 5.14 | Normalized Mode Shapes from White Noise Tests 35 and 1 | 350 |
| 5.15 | Input, Damper Dissipation, Kinetic, and Elastic Strain Energies: E050DL, E150DL | 351 |
| 5.16 | Input, Kinetic, and Elastic Strain Energies: E075N, E150N | 352 |
| 6.1 | Interior (Centerline) Column Properties, 4 – D9 Bars | 353 |
| 6.2 | Interior (Centerline) Column Properties, 4 – #3 Bars | 354 |
| 6.3 | Exterior (Edge) Column Properties, 6 – D7 Bars | 355 |
| 6.4 | Exterior (Edge) Column Properties, 6 – #3 Bars | 356 |
| 6.5 | Forces Acting on Luo-Durrani Interior Slab-Column Model | 357 |
| 6.6 | Forces Acting on Luo-Durrani Exterior Slab-Column Model | 357 |
| 6.7 | Equivalent Beam Widths Used in ETABS Analyses | 358 |
| 6.8 | Idealized Model Used for ETABS Analyses | 359 |
| 6.9 | ETABS Nonlinear Simulation of E050DL: Interstory Displacements | 360 |
| 6.10 | ETABS Nonlinear Simulation of E050DL: Story Shear | 361 |
| 6.11 | ETABS Nonlinear Simulation of E050DL: Story Shear Vs. Interstory Displacement | 362 |
| 6.12 | ETABS Nonlinear Simulation of E100DL: Interstory Displacements | 363 |
| 6.13 | ETABS Nonlinear Simulation of E100DL: Story Shear | 364 |
| 6.14 | ETABS Nonlinear Simulation of E100DL: Story Shear Vs. Interstory Displacement | 365 |
| 6.15 | ETABS Nonlinear Simulation of E150DL: Interstory Displacements | 366 |
| 6.16 | ETABS Nonlinear Simulation of E150DL: Story Shear | 367 |
| 6.17 | ETABS Nonlinear Simulation of E150DL: Story Shear Vs. Interstory Displacement | 368 |
| 6.18 | ETABS Nonlinear Simulation of E200DL: Interstory Displacements | 369 |
| 6.19 | ETABS Nonlinear Simulation of E200DL: Story Shear | 370 |
| 6.20 | ETABS Nonlinear Simulation of E200DL: Story Shear Vs. Interstory | |

| | | |
|------|---|-----|
| | Displacement | 371 |
| 6.21 | ETABS Nonlinear Simulation of E025N: Interstory Displacements | 372 |
| 6.22 | ETABS Nonlinear Simulation of E025N: Story Shear | 373 |
| 6.23 | ETABS Nonlinear Simulation of E050N: Interstory Displacements | 374 |
| 6.24 | ETABS Nonlinear Simulation of E050N: Story Shear | 375 |
| 6.25 | ETABS Nonlinear Simulation of E100N: Interstory Displacements | 376 |
| 6.26 | ETABS Nonlinear Simulation of E100N: Story Shear | 377 |
| 6.27 | ETABS Nonlinear Simulation of E125N: Interstory Displacements | 378 |
| 6.28 | ETABS Nonlinear Simulation of E125N: Story Shear | 379 |
| 6.29 | ETABS Nonlinear Simulation of E150N: Interstory Displacements, Run 1 | 380 |
| 6.30 | ETABS Nonlinear Simulation of E150N: Story Shear, Run 1 | 381 |
| 6.31 | ETABS Nonlinear Simulation of E150N: Interstory Displacements, Run 2 | 382 |
| 6.32 | ETABS Nonlinear Simulation of E150N: Story Shear, Run 2 | 383 |
| 6.33 | Comparison of Measured and Computed Response Maxima | 384 |
| 6.34 | Comparison of Measured and Predicted Stiffnesses with VEDs | 384 |
| 6.35 | Comparison of Measured and Predicted Stiffnesses without VEDs | 385 |
| | | |
| A.1 | Deformed Wire Used as Reinforcement | 401 |
| A.2 | Pre-Annealing Load-Strain Curve for D5 Bar | 401 |
| A.3 | Post-Annealing Load-Strain Curve for D5 Bar | 401 |
| A.4 | Plan View of Base Girder | 402 |
| A.5 | Cross-Sections of Primary Base Girder Members | 403 |
| A.6 | Cross-Section of Lateral Base Girder Members | 403 |
| A.7 | Casting of Base Girder | 404 |
| A.8 | Slab Formwork and Reinforcement | 404 |
| A.9 | Interior Column and Slab Joint Reinforcement | 405 |
| A.10 | Exterior Column Reinforcement | 405 |
| A.11 | Slab-Spandrel-Exterior Column Joint Reinforcement | 406 |
| A.12 | Casting of Third Story of Model, Upper View | 406 |
| A.13 | Casting of Third Story of Model, Lower View | 407 |
| A.14 | Diagonal Brace Details | 407 |
| A.15 | Typical Exterior Column Collar Details | 408 |
| A.16 | Typical Interior Column Collar Details | 409 |
| A.17 | Collar on First Floor Exterior Column | 410 |
| A.18 | Collar on Second Floor Exterior Column | 410 |
| A.19 | Side View of Collar on Second Floor Exterior Column | 411 |
| A.20 | Side View of Collar on Second Floor Interior Column | 411 |
| A.21 | Typical Spot-Weld of Brace to Collar | 412 |
| A.22 | Typical Lead Weight Arrangement | 412 |

| | | |
|--------|---|-----|
| A.23 | Lead Weight Locations, First and Second Floor Slabs | 413 |
| A.24 | Lead Weight Locations, Third Floor (Roof) Slab | 413 |
| A.25 | Lead Weight Configuration, Floors 2 and 3 | 414 |
| A.26 | Lead Weight Configuration, Floors 1 and 2 (Shoring in Place) | 414 |
| A.27 | Typical Lead Weight Stacks, Side View | 415 |
| A.28 | Typical Lead Weight Stacks, End View | 415 |
| | | |
| B.1 | Plan View of USACERL Shaking Table | 425 |
| B.2 | Shaking Table Acceleration Transducer | 425 |
| B.3 | Base Girder Displacement and Acceleration Transducers | 426 |
| B.4 | First Floor Displacement and Acceleration Transducers | 426 |
| B.5 | Second Floor Displacement and Acceleration Transducers | 427 |
| B.6 | Third Floor Displacement and Acceleration Transducers | 427 |
| B.7 | Displacement Frame Transducers | 428 |
| B.8 | Damper Displacement and Load Transducers | 428 |
| B.9 | Active Reinforcement Strain Gages in First Floor Slab | 429 |
| B.10 | Slab Reinforcement Strain Gage Locations, Exterior Column | 429 |
| B.11 | Slab Reinforcement Strain Gage Locations, Interior Column | 430 |
| B.12 | Active Column and Slab Reinforcement Strain Gages | 430 |
| B.13 | Block Diagram Showing Shake Table Controls and Data Acquisition Systems | 431 |
| | | |
| C.1.1 | Acceleration Vs. Elapsed Time: E010DL, E025DL | 442 |
| C.1.2 | Acceleration Vs. Elapsed Time: E050DL, E075DL | 443 |
| C.1.3 | Acceleration Vs. Elapsed Time: E100DL, E125DL | 444 |
| C.1.4 | Acceleration Vs. Elapsed Time: E150DL, E200DL | 445 |
| C.1.5 | Acceleration Vs. Elapsed Time: E250DL | 446 |
| C.1.6 | Acceleration Vs. Elapsed Time: T021DL, T052DL | 447 |
| C.1.7 | Acceleration Vs. Elapsed Time: T105DL, T157DL | 448 |
| C.1.8 | Acceleration Vs. Elapsed Time: T210DL, T262DL | 449 |
| C.1.9 | Acceleration Vs. Elapsed Time: T315DL, T420DL | 450 |
| C.1.10 | Acceleration Vs. Elapsed Time: E010DS, E025DS | 451 |
| C.1.11 | Acceleration Vs. Elapsed Time: E025DM | 452 |
| C.1.12 | Acceleration Vs. Elapsed Time: T021DS, T052DS | 453 |
| C.1.13 | Acceleration Vs. Elapsed Time: T052DM | 454 |
| C.1.14 | Acceleration Vs. Elapsed Time: E025N, E050N | 455 |
| C.1.15 | Acceleration Vs. Elapsed Time: E075N, E100N | 456 |
| C.1.16 | Acceleration Vs. Elapsed Time: E125N, E150N | 457 |
| C.1.17 | Acceleration Vs. Elapsed Time: E200N | 458 |

| | | |
|--------|---|-----|
| C.1.18 | Maximum Floor Acceleration Profiles: E0101DL – E125DL | 459 |
| C.1.19 | Maximum Floor Acceleration Profiles: E150DL – E250DL | 460 |
| C.1.20 | Maximum Floor Acceleration Profiles: T021DL – T262DL | 461 |
| C.1.21 | Maximum Floor Acceleration Profiles: T315DL – T420DL | 462 |
| C.1.22 | Maximum Floor Acceleration Profiles: E010DS – T052DS | 463 |
| C.1.23 | Maximum Floor Acceleration Profiles: E025N – E150N | 464 |
| C.1.24 | Maximum Floor Acceleration Profile: E200N | 465 |
| C.2.1 | Relative Displacement Vs. Elapsed Time: E010DL, E025DL | 466 |
| C.2.2 | Relative Displacement Vs. Elapsed Time: E050DL, E075DL | 467 |
| C.2.3 | Relative Displacement Vs. Elapsed Time: E100DL, E125DL | 468 |
| C.2.4 | Relative Displacement Vs. Elapsed Time: E150DL, E200DL | 469 |
| C.2.5 | Relative Displacement Vs. Elapsed Time: E250DL | 470 |
| C.2.6 | Relative Displacement Vs. Elapsed Time: T021DL, T052DL | 471 |
| C.2.7 | Relative Displacement Vs. Elapsed Time: T105DL, T157DL | 472 |
| C.2.8 | Relative Displacement Vs. Elapsed Time: T210DL, T262DL | 473 |
| C.2.9 | Relative Displacement Vs. Elapsed Time: T315DL, T420DL | 474 |
| C.2.10 | Relative Displacement Vs. Elapsed Time: E010DS, E025DS | 475 |
| C.2.11 | Relative Displacement Vs. Elapsed Time: E025DM | 476 |
| C.2.12 | Relative Displacement Vs. Elapsed Time: T021DS, T052DS | 477 |
| C.2.13 | Relative Displacement Vs. Elapsed Time: T052DM | 478 |
| C.2.14 | Relative Displacement Vs. Elapsed Time: E025N, E050N | 479 |
| C.2.15 | Relative Displacement Vs. Elapsed Time: E075N, E100N | 480 |
| C.2.16 | Relative Displacement Vs. Elapsed Time: E125N, E150N | 481 |
| C.2.17 | Relative Displacement Vs. Elapsed Time: E200N | 482 |
| C.2.18 | Maximum Relative Story Displacement Profiles: E010DL – E125DL | 483 |
| C.2.19 | Maximum Relative Story Displacement Profiles: E150DL – E250DL | 484 |
| C.2.20 | Maximum Relative Story Displacement Profiles: T021DL – T262DL | 485 |
| C.2.21 | Maximum Relative Story Displacement Profiles: T315DL – T420DL | 486 |
| C.2.22 | Maximum Relative Story Displacement Profiles: E010DS – T052DS | 487 |
| C.2.23 | Maximum Relative Story Displacement Profiles: E025N – E150N | 488 |
| C.2.24 | Maximum Relative Story Displacement Profile: E200N | 489 |
| C.3.1 | Interstory Displacement Vs. Elapsed Time: E010DL, E025DL | 490 |
| C.3.2 | Interstory Displacement Vs. Elapsed Time: E050DL, E075DL | 491 |
| C.3.3 | Interstory Displacement Vs. Elapsed Time: E100DL, E125DL | 492 |
| C.3.4 | Interstory Displacement Vs. Elapsed Time: E150DL, E200DL | 493 |
| C.3.5 | Interstory Displacement Vs. Elapsed Time: E250DL | 494 |
| C.3.6 | Interstory Displacement Vs. Elapsed Time: T021DL, T052DL | 495 |
| C.3.7 | Interstory Displacement Vs. Elapsed Time: T105DL, T157DL | 496 |
| C.3.8 | Interstory Displacement Vs. Elapsed Time: T210DL, T262DL | 497 |

| | | |
|--------|--|-----|
| C.3.9 | Interstory Displacement Vs. Elapsed Time: T315DL, T420DL | 498 |
| C.3.10 | Interstory Displacement Vs. Elapsed Time: E010DS, E025DS | 499 |
| C.3.11 | Interstory Displacement Vs. Elapsed Time: E025DM | 500 |
| C.3.12 | Interstory Displacement Vs. Elapsed Time: T021DS, T052DS | 501 |
| C.3.13 | Interstory Displacement Vs. Elapsed Time: T052DM | 502 |
| C.3.14 | Interstory Displacement Vs. Elapsed Time: E025N, E050N | 503 |
| C.3.15 | Interstory Displacement Vs. Elapsed Time: E075N, E100N | 504 |
| C.3.16 | Interstory Displacement Vs. Elapsed Time: E125N, E150N | 505 |
| C.3.17 | Interstory Displacement Vs. Elapsed Time: E200N | 506 |
| C.3.18 | Interstory Drift Vs. Elapsed Time: E010DL, E025DL | 507 |
| C.3.19 | Interstory Drift Vs. Elapsed Time: E050DL, E075DL | 508 |
| C.3.20 | Interstory Drift Vs. Elapsed Time: E100DL, E125DL | 509 |
| C.3.21 | Interstory Drift Vs. Elapsed Time: E150DL, E200DL | 510 |
| C.3.22 | Interstory Drift Vs. Elapsed Time: E250DL | 511 |
| C.3.23 | Interstory Drift Vs. Elapsed Time: T021DL, T052DL | 512 |
| C.3.24 | Interstory Drift Vs. Elapsed Time: T105DL, T157DL | 513 |
| C.3.25 | Interstory Drift Vs. Elapsed Time: T210DL, T262DL | 514 |
| C.3.26 | Interstory Drift Vs. Elapsed Time: T315DL, T420DL | 515 |
| C.3.27 | Interstory Drift Vs. Elapsed Time: E025N, E050N | 516 |
| C.3.28 | Interstory Drift Vs. Elapsed Time: E075N, E100N | 517 |
| C.3.29 | Interstory Drift Vs. Elapsed Time: E125N, E150N | 518 |
| C.3.30 | Interstory Drift Vs. Elapsed Time: E200N | 519 |
| C.3.31 | Maximum Interstory Drift Ratios: E010DL – E125DL | 520 |
| C.3.32 | Maximum Interstory Drift Ratios: E150DL – E250DL | 521 |
| C.3.33 | Maximum Interstory Drift Ratios: T021DL – T420DL | 522 |
| C.3.34 | Maximum Interstory Drift Ratios: E010DS – T052DS | 523 |
| C.3.35 | Maximum Interstory Drift Ratios: E025N – E200N | 524 |
| C.4.1 | Story Shear Vs. Elapsed Time: E010DL, E025DL | 525 |
| C.4.2 | Story Shear Vs. Elapsed Time: E050DL, E075DL | 526 |
| C.4.3 | Story Shear Vs. Elapsed Time: E100DL, E125DL | 527 |
| C.4.4 | Story Shear Vs. Elapsed Time: E150DL, E200DL | 528 |
| C.4.5 | Story Shear Vs. Elapsed Time: E200DL | 529 |
| C.4.6 | Story Shear Vs. Elapsed Time: T021DL, T052DL | 530 |
| C.4.7 | Story Shear Vs. Elapsed Time: T105DL, T157DL | 531 |
| C.4.8 | Story Shear Vs. Elapsed Time: T210DL, T262DL | 532 |
| C.4.9 | Story Shear Vs. Elapsed Time: T315DL, T420DL | 533 |
| C.4.10 | Story Shear Vs. Elapsed Time: E010DS, E025DS | 534 |
| C.4.11 | Story Shear Vs. Elapsed Time: E025DM | 535 |
| C.4.12 | Story Shear Vs. Elapsed Time: T021DS, T052DS | 536 |

| | | |
|--------|---|-----|
| C.4.13 | Story Shear Vs. Elapsed Time: T052DM | 537 |
| C.4.14 | Story Shear Vs. Elapsed Time: E025N, E050N | 538 |
| C.4.15 | Story Shear Vs. Elapsed Time: E075N, E100N | 539 |
| C.4.16 | Story Shear Vs. Elapsed Time: E125N, E150N | 540 |
| C.4.17 | Story Shear Vs. Elapsed Time: E200N | 541 |
| C.4.18 | Maximum Measured Story Shears: E010DL – E125DL | 542 |
| C.4.19 | Maximum Measured Story Shears: E150DL – E250DL | 543 |
| C.4.20 | Maximum Measured Story Shears: T021DL – T262DL | 544 |
| C.4.21 | Maximum Measured Story Shears: T315DL – T420DL | 545 |
| C.4.22 | Maximum Measured Story Shears: E010DS – T052DM | 546 |
| C.4.23 | Maximum Measured Story Shears: E025N – E150N | 547 |
| C.4.24 | Maximum Measured Story Shears: E200N | 548 |
| C.4.25 | Maximum Story Shear Normalized by Total Model Weight: E010DL – E125DL | 549 |
| C.4.26 | Maximum Story Shear Normalized by Total Model Weight: E150DL – E250DL | 550 |
| C.4.27 | Maximum Story Shear Normalized by Total Model Weight: T021DL – T262DL | 551 |
| C.4.28 | Maximum Story Shear Normalized by Total Model Weight: T315DL – T420DL | 552 |
| C.4.29 | Maximum Story Shear Normalized by Total Model Weight: E010DS – T052DS | 553 |
| C.4.30 | Maximum Story Shear Normalized by Total Model Weight: E025N – E150N | 554 |
| C.4.31 | Maximum Story Shear Normalized by Total Model Weight: E200N | 555 |
| C.5.1 | Story Shear Vs. Interstory Displacement: E010DL, E025DL | 556 |
| C.5.2 | Story Shear Vs. Interstory Displacement: E050DL, E075DL | 557 |
| C.5.3 | Story Shear Vs. Interstory Displacement: E100DL, E125DL | 558 |
| C.5.4 | Story Shear Vs. Interstory Displacement: E150DL, E200DL | 559 |
| C.5.5 | Story Shear Vs. Interstory Displacement: E250DL | 560 |
| C.5.6 | Story Shear Vs. Interstory Displacement: T021DL, T052DL | 561 |
| C.5.7 | Story Shear Vs. Interstory Displacement: T105DL, T157DL | 562 |
| C.5.8 | Story Shear Vs. Interstory Displacement: T210DL, T262DL | 563 |
| C.5.9 | Story Shear Vs. Interstory Displacement: T315DL, T420DL | 564 |
| C.5.10 | CStory Shear Vs. Interstory Displacement: E010DS, E025DS | 565 |
| C.5.11 | Story Shear Vs. Interstory Displacement: E025DM | 566 |
| C.5.12 | Story Shear Vs. Interstory Displacement: T021DS, T052DS | 567 |
| C.5.13 | Story Shear Vs. Interstory Displacement: T052DM | 568 |
| C.5.14 | Story Shear Vs. Interstory Displacement: E025N, E050N | 569 |
| C.5.15 | Story Shear Vs. Interstory Displacement: E075N, E100N | 570 |
| C.5.16 | Story Shear Vs. Interstory Displacement: E125N, E150N | 571 |
| C.5.17 | Story Shear Vs. Interstory Displacement: E200N | 572 |
| C.6.1 | Base Shear Vs. Third Floor Relative Displacement: E010DL, E025DL | 573 |
| C.6.2 | Base Shear Vs. Third Floor Relative Displacement: E150DL – E250DL | 574 |
| C.6.3 | Base Shear Vs. Third Floor Relative Displacement: T021DL – T420DL | 575 |

| | | |
|--------|---|-----|
| C.16.4 | Base Shear Vs. Third Floor Relative Displacement: E010DS – T052DM | 576 |
| C.6.5 | Base Shear Vs. Third Floor Relative Displacement: E025N – E150N | 577 |
| C.7.1 | Maximum Overturning Moments: E010DL – E125DL | 578 |
| C.7.2 | Maximum Overturning Moments: E150DL – E250DL | 579 |
| C.7.3 | Maximum Overturning Moments: T021DL – T262DL | 580 |
| C.7.4 | Maximum Overturning Moments: T315DL – T420DL | 581 |
| C.7.5 | Maximum Overturning Moments: E010DS – T052DS | 582 |
| C.7.6 | Maximum Overturning Moments: E025N – E150N | 583 |
| C.7.7 | Maximum Overturning Moments: E200N | 584 |
| C.8.1 | Damper Force Vs. Elapsed Time: E010DL, NW and NE | 585 |
| C.8.2 | Damper Force Vs. Elapsed Time: E010DL, SW and SE | 586 |
| C.8.3 | Damper Force Vs. Elapsed Time: E025DL, NW and NE | 587 |
| C.8.4 | Damper Force Vs. Elapsed Time: E025DL, SW and SE | 588 |
| C.8.5 | Damper Force Vs. Elapsed Time: E050DL, NW and NE | 589 |
| C.8.6 | Damper Force Vs. Elapsed Time: E050DL, SW and SE | 590 |
| C.8.7 | Damper Force Vs. Elapsed Time: E075DL, NW and NE | 591 |
| C.8.8 | Damper Force Vs. Elapsed Time: E075DL, SW and SE | 592 |
| C.8.9 | Damper Force Vs. Elapsed Time: E100DL, NW and NE | 593 |
| C.8.10 | Damper Force Vs. Elapsed Time: E100DL, SW and SE | 594 |
| C.8.11 | Damper Force Vs. Elapsed Time: E125DL, NW and NE | 595 |
| C.8.12 | Damper Force Vs. Elapsed Time: E125DL, SW and SE | 596 |
| C.8.13 | Damper Force Vs. Elapsed Time: E150DL, NW and NE | 597 |
| C.8.14 | Damper Force Vs. Elapsed Time: E150DL, SW and SE | 598 |
| C.8.15 | Damper Force Vs. Elapsed Time: E200DL, NW and NE | 599 |
| C.8.16 | Damper Force Vs. Elapsed Time: E200DL, SW and SE | 600 |
| C.8.17 | Damper Force Vs. Elapsed Time: E250DL, NW and NE | 601 |
| C.8.18 | Damper Force Vs. Elapsed Time: E250DL, SW and SE | 602 |
| C.8.19 | Damper Force Vs. Elapsed Time: T021DL, NW and NE | 603 |
| C.8.20 | Damper Force Vs. Elapsed Time: T021DL, SW and SE | 604 |
| C.8.21 | Damper Force Vs. Elapsed Time: T052DL, NW and NE | 605 |
| C.8.22 | Damper Force Vs. Elapsed Time: T052DL, SW and SE | 606 |
| C.8.23 | Damper Force Vs. Elapsed Time: T105DL, NW and NE | 607 |
| C.8.24 | Damper Force Vs. Elapsed Time: T105DL, SW and SE | 608 |
| C.8.25 | Damper Force Vs. Elapsed Time: T157DL, NW and NE | 609 |
| C.8.26 | Damper Force Vs. Elapsed Time: T157DL, SW and SE | 610 |
| C.8.27 | Damper Force Vs. Elapsed Time: T210DL, NW and NE | 611 |
| C.8.28 | Damper Force Vs. Elapsed Time: T210DL, SW and SE | 612 |
| C.8.29 | Damper Force Vs. Elapsed Time: T262DL, NW and NE | 613 |
| C.8.30 | Damper Force Vs. Elapsed Time: T262DL, SW and SE | 614 |

| | | |
|--------|---|-----|
| C.8.31 | Damper Force Vs. Elapsed Time: T315DL, NW and NE | 615 |
| C.8.32 | Damper Force Vs. Elapsed Time: T315DL, SW and SE | 616 |
| C.8.33 | Damper Force Vs. Elapsed Time: T420DL, NW and NE | 617 |
| C.8.34 | Damper Force Vs. Elapsed Time: T420DL, SW and SE | 618 |
| C.8.35 | Damper Force Vs. Elapsed Time: E010DS, NW and NE | 619 |
| C.8.36 | Damper Force Vs. Elapsed Time: E010DS, SW and SE | 620 |
| C.8.37 | Damper Force Vs. Elapsed Time: E025DS, NW and NE | 621 |
| C.8.38 | Damper Force Vs. Elapsed Time: E025DS, SW and SE | 622 |
| C.8.39 | Damper Force Vs. Elapsed Time: E025DM, NW and NE | 623 |
| C.8.40 | Damper Force Vs. Elapsed Time: E025DM, SW and SE | 624 |
| C.8.41 | Damper Force Vs. Elapsed Time: T021DS, NW and NE | 625 |
| C.8.42 | Damper Force Vs. Elapsed Time: T021DS, SW and SE | 626 |
| C.8.43 | Damper Force Vs. Elapsed Time: T052DS, NW and NE | 627 |
| C.8.44 | Damper Force Vs. Elapsed Time: T052DS, SW and SE | 628 |
| C.8.45 | Damper Force Vs. Elapsed Time: T052DM, NW and NE | 629 |
| C.8.46 | Damper Force Vs. Elapsed Time: T052DM, SW and SE | 630 |
| C.9.1 | Damper Displacement Vs. Elapsed Time: E010DL, NW and NE | 631 |
| C.9.2 | Damper Displacement Vs. Elapsed Time: E010DL, SW and SE | 632 |
| C.9.3 | Damper Displacement Vs. Elapsed Time: E025DL, NW and NE | 633 |
| C.9.4 | Damper Displacement Vs. Elapsed Time: E025DL, SW and SE | 634 |
| C.9.5 | Damper Displacement Vs. Elapsed Time: E050DL, NW and NE | 635 |
| C.9.6 | Damper Displacement Vs. Elapsed Time: E050DL, SW and SE | 636 |
| C.9.7 | Damper Displacement Vs. Elapsed Time: E075DL, NW and NE | 637 |
| C.9.8 | Damper Displacement Vs. Elapsed Time: E075DL, SW and SE | 638 |
| C.9.9 | Damper Displacement Vs. Elapsed Time: E100DL, NW and NE | 639 |
| C.9.10 | Damper Displacement Vs. Elapsed Time: E100DL, SW and SE | 640 |
| C.9.11 | Damper Displacement Vs. Elapsed Time: E125DL, NW and NE | 641 |
| C.9.12 | Damper Displacement Vs. Elapsed Time: E125DL, SW and SE | 642 |
| C.9.13 | Damper Displacement Vs. Elapsed Time: E150DL, NW and NE | 643 |
| C.9.14 | Damper Displacement Vs. Elapsed Time: E150DL, SW and SE | 644 |
| C.9.15 | Damper Displacement Vs. Elapsed Time: E200DL, NW and NE | 645 |
| C.9.16 | Damper Displacement Vs. Elapsed Time: E200DL, SW and SE | 646 |
| C.9.17 | Damper Displacement Vs. Elapsed Time: E250DL, NW and NE | 647 |
| C.9.18 | Damper Displacement Vs. Elapsed Time: E250DL, SW and SE | 648 |
| C.9.19 | Damper Displacement Vs. Elapsed Time: T021DL, NW and NE | 649 |
| C.9.20 | Damper Displacement Vs. Elapsed Time: T021DL, SW and SE | 650 |
| C.9.21 | Damper Displacement Vs. Elapsed Time: T052DL, NW and NE | 651 |
| C.9.22 | Damper Displacement Vs. Elapsed Time: T052DL, SW and SE | 652 |
| C.9.23 | Damper Displacement Vs. Elapsed Time: T105DL, NW and NE | 653 |

| | | |
|---------|---|-----|
| C.9.24 | Damper Displacement Vs. Elapsed Time: T105DL, SW and SE | 654 |
| C.9.25 | Damper Displacement Vs. Elapsed Time: T157DL, NW and NE | 655 |
| C.9.26 | Damper Displacement Vs. Elapsed Time: T157DL, SW and SE | 656 |
| C.9.27 | Damper Displacement Vs. Elapsed Time: T210DL, NW and NE | 657 |
| C.9.28 | Damper Displacement Vs. Elapsed Time: T210DL, SW and SE | 658 |
| C.9.29 | Damper Displacement Vs. Elapsed Time: T262DL, NW and NE | 659 |
| C.9.30 | Damper Displacement Vs. Elapsed Time: T262DL, SW and SE | 660 |
| C.9.31 | Damper Displacement Vs. Elapsed Time: T315DL, NW and NE | 661 |
| C.9.32 | Damper Displacement Vs. Elapsed Time: T315DL, SW and SE | 662 |
| C.9.33 | Damper Displacement Vs. Elapsed Time: T420DL, NW and NE | 663 |
| C.9.34 | Damper Displacement Vs. Elapsed Time: T420DL, SW and SE | 664 |
| C.9.35 | Damper Displacement Vs. Elapsed Time: E010DS, NW and NE | 665 |
| C.9.36 | Damper Displacement Vs. Elapsed Time: E010DS, SW and SE | 666 |
| C.9.37 | Damper Displacement Vs. Elapsed Time: E025DS, NW and NE | 667 |
| C.9.38 | Damper Displacement Vs. Elapsed Time: E025DS, SW and SE | 668 |
| C.9.39 | Damper Displacement Vs. Elapsed Time: E025DM, NW and NE | 669 |
| C.9.40 | Damper Displacement Vs. Elapsed Time: E025DM, SW and SE | 670 |
| C.9.41 | Damper Displacement Vs. Elapsed Time: T021DS, NW and NE | 671 |
| C.9.42 | Damper Displacement Vs. Elapsed Time: T021DS, SW and SE | 672 |
| C.9.43 | Damper Displacement Vs. Elapsed Time: T052DS, NW and NE | 673 |
| C.9.44 | Damper Displacement Vs. Elapsed Time: T052DS, SW and SE | 674 |
| C.9.45 | Damper Displacement Vs. Elapsed Time: T052DM, NW and NE | 675 |
| C.9.46 | Damper Displacement Vs. Elapsed Time: T052DM, SW and SE | 676 |
| C.10.1 | Damper Force Vs. Displacement: E010DL, NW and NE | 677 |
| C.10.2 | Damper Force Vs. Displacement: E010DL, SW and SE | 678 |
| C.10.3 | Damper Force Vs. Displacement: E025DL, NW and NE | 679 |
| C.10.4 | Damper Force Vs. Displacement: E025DL, SW and SE | 680 |
| C.10.5 | Damper Force Vs. Displacement: E050DL, NW and NE | 681 |
| C.10.6 | Damper Force Vs. Displacement: E050DL, SW and SE | 682 |
| C.10.7 | Damper Force Vs. Displacement: E075DL, NW and NE | 683 |
| C.10.8 | Damper Force Vs. Displacement: E075DL, SW and SE | 684 |
| C.10.9 | Damper Force Vs. Displacement: E100DL, NW and NE | 685 |
| C.10.10 | Damper Force Vs. Displacement: E100DL, SW and SE | 686 |
| C.10.11 | Damper Force Vs. Displacement: E125DL, NW and NE | 687 |
| C.10.12 | Damper Force Vs. Displacement: E125DL, SW and SE | 688 |
| C.10.13 | Damper Force Vs. Displacement: E150DL, NW and NE | 689 |
| C.10.14 | Damper Force Vs. Displacement: E150DL, SW and SE | 690 |
| C.10.15 | Damper Force Vs. Displacement: E200DL, NW and NE | 691 |

| | | |
|---------|---|-----|
| C.10.16 | Damper Force Vs. Displacement: E200DL, SW and SE | 692 |
| C.10.17 | Damper Force Vs. Displacement: E250DL, NW and NE | 693 |
| C.10.18 | Damper Force Vs. Displacement: E250DL, SW and SE | 694 |
| C.10.19 | Damper Force Vs. Displacement: T021DL, NW and NE | 695 |
| C.10.20 | Damper Force Vs. Displacement: T021DL, SW and SE | 696 |
| C.10.21 | Damper Force Vs. Displacement: T052DL, NW and NE | 697 |
| C.10.22 | Damper Force Vs. Displacement: T052DL, SW and SE | 698 |
| C.10.23 | Damper Force Vs. Displacement: T105DL, NW and NE | 699 |
| C.10.24 | Damper Force Vs. Displacement: T105DL, SW and SE | 700 |
| C.10.25 | Damper Force Vs. Displacement: T157DL, NW and NE | 701 |
| C.10.26 | Damper Force Vs. Displacement: T157DL, SW and SE | 702 |
| C.10.27 | Damper Force Vs. Displacement: T210DL, NW and NE | 703 |
| C.10.28 | Damper Force Vs. Displacement: T210DL, SW and SE | 704 |
| C.10.29 | Damper Force Vs. Displacement: T262DL, NW and NE | 705 |
| C.10.30 | Damper Force Vs. Displacement: T262DL, SW and SE | 706 |
| C.10.31 | Damper Force Vs. Displacement: T315DL, NW and NE | 707 |
| C.10.32 | Damper Force Vs. Displacement: T315DL, SW and SE | 708 |
| C.10.33 | Damper Force Vs. Displacement: T420DL, NW and NE | 709 |
| C.10.34 | Damper Force Vs. Displacement: T420DL, SW and SE | 710 |
| C.10.35 | Damper Force Vs. Displacement: E010DS, NW and NE | 711 |
| C.10.36 | Damper Force Vs. Displacement: E010DS, SW and SE | 712 |
| C.10.37 | Damper Force Vs. Displacement: E025DS, NW and NE | 713 |
| C.10.38 | Damper Force Vs. Displacement: E025DS, SW and SE | 714 |
| C.10.39 | Damper Force Vs. Displacement: E025DM, NW and NE | 715 |
| C.10.40 | Damper Force Vs. Displacement: E025DM, SW and SE | 716 |
| C.10.41 | Damper Force Vs. Displacement: T021DS, NW and NE | 717 |
| C.10.42 | Damper Force Vs. Displacement: T021DS, SW and SE | 718 |
| C.10.43 | Damper Force Vs. Displacement: T052DS, NW and NE | 719 |
| C.10.44 | Damper Force Vs. Displacement: T052DS, SW and SE | 720 |
| C.10.45 | Damper Force Vs. Displacement: T052DM, NW and NE | 721 |
| C.10.46 | Damper Force Vs. Displacement: T052DM, SW and SE | 722 |
| C.11.1 | Maximum Sum of Horizontal Components of Damper Forces Vs. Maximum Story Shear: E010DL – E125DL | 723 |
| C.11.2 | Maximum Sum of Horizontal Components of Damper Forces Vs. Maximum Story Shear: E150DL – E250DL | 724 |
| C.11.3 | Maximum Sum of Horizontal Components of Damper Forces Vs. Maximum Story Shear: T021DL – T262DL | 725 |
| C.11.4 | Maximum Sum of Horizontal Components of Damper Forces Vs. Maximum Story Shear: T315DL – T420DL | 726 |

| | | |
|---------|--|-----|
| C.11.5 | Maximum Sum of Horizontal Components of Damper Forces Vs. Maximum Story Shear: E010DS – T052DM | 727 |
| C.12.1 | Column Shear Vs. Elapsed Time: E010DL, E025DL | 728 |
| C.12.2 | Column Shear Vs. Elapsed Time: E050DL, E075DL | 729 |
| C.12.3 | Column Shear Vs. Elapsed Time: E100DL, E125DL | 730 |
| C.12.4 | Column Shear Vs. Elapsed Time: E150DL, E200DL | 731 |
| C.12.5 | Column Shear Vs. Elapsed Time: E250DL | 732 |
| C.12.6 | Column Shear Vs. Elapsed Time: T021DL, T052DL | 733 |
| C.12.7 | Column Shear Vs. Elapsed Time: T105DL, T157DL | 734 |
| C.12.8 | Column Shear Vs. Elapsed Time: T210DL, T262DL | 735 |
| C.12.9 | Column Shear Vs. Elapsed Time: T315DL, T420DL | 736 |
| C.12.10 | Column Shear Vs. Elapsed Time: E010DS, E025DS | 737 |
| C.12.11 | Column Shear Vs. Elapsed Time: E025DM | 738 |
| C.12.12 | Column Shear Vs. Elapsed Time: T021DS, T052DS | 739 |
| C.12.13 | Column Shear Vs. Elapsed Time: T052DM | 740 |
| C.13.1 | Column Shear Vs. Interstory Displacement: E010DL, E025DL | 741 |
| C.13.2 | Column Shear Vs. Interstory Displacement: E050DL, E075DL | 742 |
| C.13.3 | Column Shear Vs. Interstory Displacement: E100DL, E125DL | 733 |
| C.13.4 | Column Shear Vs. Interstory Displacement: E150DL, E200DL | 744 |
| C.13.5 | Column Shear Vs. Interstory Displacement: E250DL | 745 |
| C.13.6 | Column Shear Vs. Interstory Displacement : T021DL, T052DL | 746 |
| C.13.7 | Column Shear Vs. Interstory Displacement: T105DL, T157DL | 747 |
| C.13.8 | Column Shear Vs. Interstory Displacement: T210DL, T262DL | 748 |
| C.13.9 | Column Shear Vs. Interstory Displacement: T315DL, T420DL | 749 |
| C.13.10 | Column Shear Vs. Interstory Displacement: E010DS, E025DS | 750 |
| C.13.11 | Column Shear Vs. Interstory Displacement: E025DM | 751 |
| C.13.12 | Column Shear Vs. Interstory Displacement: T021DS, T052DS | 752 |
| C.13.13 | Column Shear Vs. Interstory Displacement: T052DM | 753 |
| C.13.14 | Maximum Column Shear Vs. Maximum Story Shear: E010DL – E125DL | 754 |
| C.13.15 | Maximum Column Shear Vs. Maximum Story Shear: E150DL – E205DL | 755 |
| C.13.16 | Maximum Column Shear Vs. Maximum Story Shear: T021DL – T262DL | 756 |
| C.13.17 | Maximum Column Shear Vs. Maximum Story Shear: T315DL – T420DL | 757 |
| C.13.18 | Maximum Column Shear Vs. Maximum Story Shear: E010DS – T052DM ... | 758 |
| C.14.1 | Story Shear, Column Shear, and Sum of Horizontal Component of Damper Forces: E010DL | 759 |
| C.14.2 | Story Shear, Column Shear, and Sum of Horizontal Component of Damper Forces: E025DL | 760 |
| C.14.3 | Story Shear, Column Shear, and Sum of Horizontal Component of Damper Forces: E050DL | 761 |

| | | |
|---------|--|-----|
| C.14.4 | Story Shear, Column Shear, and Sum of Horizontal Component of Damper Forces: E075DL | 762 |
| C.14.5 | Story Shear, Column Shear, and Sum of Horizontal Component of Damper Forces: E100DL | 763 |
| C.14.6 | Story Shear, Column Shear, and Sum of Horizontal Component of Damper Forces: E125DL | 764 |
| C.14.7 | Story Shear, Column Shear, and Sum of Horizontal Component of Damper Forces: E150DL | 765 |
| C.14.8 | Story Shear, Column Shear, and Sum of Horizontal Component of Damper Forces: E200DL | 766 |
| C.14.9 | Story Shear, Column Shear, and Sum of Horizontal Component of Damper Forces: E250DL | 767 |
| C.14.10 | Story Shear, Column Shear, and Sum of Horizontal Component of Damper Forces: T021DL | 768 |
| C.14.11 | Story Shear, Column Shear, and Sum of Horizontal Component of Damper Forces: T052DL | 769 |
| C.14.12 | Story Shear, Column Shear, and Sum of Horizontal Component of Damper Forces: T105DL | 770 |
| C.14.13 | Story Shear, Column Shear, and Sum of Horizontal Component of Damper Forces: T157DL | 771 |
| C.14.14 | Story Shear, Column Shear, and Sum of Horizontal Component of Damper Forces: T210DL | 772 |
| C.14.15 | Story Shear, Column Shear, and Sum of Horizontal Component of Damper Forces: T262DL | 773 |
| C.14.16 | Story Shear, Column Shear, and Sum of Horizontal Component of Damper Forces: T315DL | 774 |
| C.14.17 | Story Shear, Column Shear, and Sum of Horizontal Component of Damper Forces: T420DL | 775 |
| C.15.1 | Relative Floor Velocities: E010DL, E025DL | 776 |
| C.15.2 | Relative Floor Velocities: E050DL, E075DL | 777 |
| C.15.3 | Relative Floor Velocities: E100DL, E125DL | 778 |
| C.15.4 | Relative Floor Velocities: E150DL, E200DL | 779 |
| C.15.5 | Relative Floor Velocities: E250DL | 780 |
| C.15.6 | Relative Floor Velocities: T021DL, T052DL | 781 |
| C.15.7 | Relative Floor Velocities: T105DL, T157DL | 782 |
| C.15.8 | Relative Floor Velocities: T210DL, T262DL | 783 |
| C.15.9 | Relative Floor Velocities: T315DL, T420DL | 784 |
| C.16.1 | Acceleration-Based Transfer Functions: E010DL – E075DL | 785 |
| C.16.2 | Acceleration-Based Transfer Functions: E100DL – E200DL | 786 |

| | | |
|---------|--|-----|
| C.16.3 | Acceleration-Based Transfer Functions: T021DL – T157DL | 787 |
| C.16.4 | Acceleration-Based Transfer Functions: T210DL – T420DL | 788 |
| C.16.5 | Acceleration-Based Transfer Functions: E025N – E100N | 789 |
| C.16.6 | Acceleration-Based Transfer Functions: E125N – E200N | 790 |
| C.16.7 | Fourier Amplitude Spectra of Interstory Displacements: E010DL and E025DL | 791 |
| C.16.8 | Fourier Amplitude Spectra of Interstory Displacements: E050DL and E075DL | 792 |
| C.16.9 | Fourier Amplitude Spectra of Interstory Displacements: E100DL and E125DL | 793 |
| C.16.10 | Fourier Amplitude Spectra of Interstory Displacements: E150DL and E200DL | 794 |
| C.16.11 | Fourier Amplitude Spectra of Interstory Displacements: E250DL | 795 |
| C.16.12 | Fourier Amplitude Spectra of Interstory Displacements: T021DL and T052DL | 796 |
| C.16.13 | Fourier Amplitude Spectra of Interstory Displacements: T105DL and T157DL | 797 |
| C.16.14 | Fourier Amplitude Spectra of Interstory Displacements: T210DL and T262DL | 798 |
| C.16.15 | Fourier Amplitude Spectra of Interstory Displacements: T315DL and T420DL | 799 |
| C.16.16 | Fourier Amplitude Spectra of Interstory Displacements: E025N and E050N ... | 800 |
| C.16.17 | Fourier Amplitude Spectra of Interstory Displacements: E075N and E100N ... | 801 |
| C.16.18 | Fourier Amplitude Spectra of Interstory Displacements: E125N and E150N ... | 802 |
| C.16.19 | Fourier Amplitude Spectra of Interstory Displacements: E200N | 803 |
| C.16.20 | Acceleration-Based Transfer Functions, White Noise Tests: Initial Conditions | 804 |
| C.16.21 | Acceleration-Based Transfer Functions, White Noise Tests: E050DL – E100DL | 805 |
| C.16.22 | Acceleration-Based Transfer Functions, White Noise Tests: T210DL – E150DL | 806 |
| C.16.23 | Acceleration-Based Transfer Functions, White Noise Tests: T315DL – T420DL | 807 |
| C.6.24 | Acceleration-Based Transfer Functions, White Noise Tests: E250DL – E050N | 808 |
| C.16.25 | Acceleration-Based Transfer Functions, White Noise Tests: E075N – E150N | 809 |
| C.16.26 | Free Vibration Tests | 810 |
| C.16.27 | Pullback Test Results | 811 |
| C.17.1 | Input, Damper Dissipation, Kinetic, and Elastic Strain Energies: E050DL and E075DL | 812 |
| C.17.2 | Input, Damper Dissipation, Kinetic, and Elastic Strain Energies: E100DL and E125DL | 813 |
| C.17.3 | Input, Damper Dissipation, Kinetic, and Elastic Strain Energies: E150DL and E200DL | 814 |
| C.17.4 | Input, Damper Dissipation, Kinetic, and Elastic Strain Energies: E250DL and T105DL | 815 |
| C.17.5 | Input, Damper Dissipation, Kinetic, and Elastic Strain Energies: T157DL and T210DL | 816 |
| C.17.6 | Input, Damper Dissipation, Kinetic, and Elastic Strain Energies: T262DL and T315DL | 817 |
| C.17.7 | Input, Damper Dissipation, Kinetic, and Elastic Strain Energies: T420DL and E075N | 818 |

| | | |
|---------|--|-----|
| C.17.8 | Input, Kinetic, and Elastic Strain Energies: E100N and E125N | 819 |
| C.17.9 | Input, Kinetic, and Elastic Strain Energies: E150N and E200N | 820 |
| C.18.1 | Reinforcement Strain Vs. Elapsed Time, Gages SGZ1, SGZ3, SGZ4: E010DL, E025DL | 821 |
| C.18.2 | Reinforcement Strain Vs. Elapsed Time, Gages SGZ1, SGZ3, SGZ4: E050DL, E075DL | 822 |
| C.18.3 | Reinforcement Strain Vs. Elapsed Time, Gages SGZ1, SGZ3, SGZ4: E100DL, E125DL | 823 |
| C.18.4 | Reinforcement Strain Vs. Elapsed Time, Gages SGZ1, SGZ3, SGZ4: E150DL, E200DL | 824 |
| C.18.5 | Reinforcement Strain Vs. Elapsed Time, Gages SGZ1, SGZ3, SGZ4: T021DL, T052DL | 825 |
| C.18.6 | Reinforcement Strain Vs. Elapsed Time, Gages SGZ1, SGZ3, SGZ4: T105DL, T157DL | 826 |
| C.18.7 | Reinforcement Strain Vs. Elapsed Time, Gages SGZ1, SGZ3, SGZ4: T210DL, T262DL | 827 |
| C.18.8 | Reinforcement Strain Vs. Elapsed Time, Gages SGZ1, SGZ3, SGZ4: T315DL, T420DL | 828 |
| C.18.9 | Reinforcement Strain Vs. Elapsed Time, Gages SGZ1, SGZ3, SGZ4: E025N, E050N | 829 |
| C.18.10 | Reinforcement Strain Vs. Elapsed Time, Gages SGZ1, SGZ3, SGZ4: E075N, E100N | 830 |
| C.18.11 | Reinforcement Strain Vs. Elapsed Time, Gages SGZ1, SGZ3, SGZ4: E125N, E150N | 831 |
| C.18.12 | Reinforcement Strain Vs. Elapsed Time, Gages SGZ1, SGZ3, SGZ4: E200N | 832 |
| C.19.1 | Reinforcement Strain Vs. Elapsed Time, Gages S1Z1, S1Z5, S1Z6: E010DL, E025DL | 833 |
| C.19.2 | Reinforcement Strain Vs. Elapsed Time, Gages S1Z1, S1Z5, S1Z6: E050DL, E075DL | 834 |
| C.19.3 | Reinforcement Strain Vs. Elapsed Time, Gages S1Z1, S1Z5, S1Z6: E100DL, E125DL | 835 |
| C.19.4 | Reinforcement Strain Vs. Elapsed Time, Gages S1Z1, S1Z5, S1Z6: E150DL, E200DL | 836 |
| C.19.5 | Reinforcement Strain Vs. Elapsed Time, Gages S1Z1, S1Z5, S1Z6: T021DL, T052DL | 837 |
| C.19.6 | Reinforcement Strain Vs. Elapsed Time, Gages S1Z1, S1Z5, S1Z6: T105DL, T157DL | 838 |
| C.19.7 | Reinforcement Strain Vs. Elapsed Time, Gages S1Z1, S1Z5, S1Z6: T210DL, T262DL | 839 |

| | | |
|---------|---|-----|
| C.19.8 | Reinforcement Strain Vs. Elapsed Time, Gages S1Z1, S1Z5, S1Z6: T315DL, T420DL | 840 |
| C.19.9 | Reinforcement Strain Vs. Elapsed Time, Gages S1Z1, S1Z5, S1Z6: E025N, E050N | 841 |
| C.19.10 | Reinforcement Strain Vs. Elapsed Time, Gages S1Z1, S1Z5, S1Z6: E075N, E100N | 842 |
| C.19.11 | Reinforcement Strain Vs. Elapsed Time, Gages S1Z1, S1Z5, S1Z6: E125N, E150N | 843 |
| C.19.12 | Reinforcement Strain Vs. Elapsed Time, Gages S1Z1, S1Z5, S1Z6: E200N ... | 844 |
| C.20.1 | Reinforcement Strain Vs. Elapsed Time, Gages S1Z3, S1Z7, S1Z8: E010DL, E025DL | 845 |
| C.20.2 | Reinforcement Strain Vs. Elapsed Time, Gages S1Z3, S1Z7, S1Z8: E050DL, E075DL | 846 |
| C.20.3 | Reinforcement Strain Vs. Elapsed Time, Gages S1Z3, S1Z7, S1Z8: E100DL, E125DL | 847 |
| C.20.4 | Reinforcement Strain Vs. Elapsed Time, Gages S1Z3, S1Z7, S1Z8: E150DL, E200DL | 848 |
| C.20.5 | Reinforcement Strain Vs. Elapsed Time, Gages S1Z3, S1Z7, S1Z8: T021DL, T052DL | 849 |
| C.20.6 | Reinforcement Strain Vs. Elapsed Time, Gages S1Z3, S1Z7, S1Z8: T105DL, T157DL | 850 |
| C.20.7 | Reinforcement Strain Vs. Elapsed Time, Gages S1Z3, S1Z7, S1Z8: T210DL, T262DL | 851 |
| C.20.8 | Reinforcement Strain Vs. Elapsed Time, Gages S1Z3, S1Z7, S1Z8: T315DL, T420DL | 852 |
| C.20.9 | Reinforcement Strain Vs. Elapsed Time, Gages S1Z3, S1Z7, S1Z8: E025N, E050N | 853 |
| C.20.10 | Reinforcement Strain Vs. Elapsed Time, Gages S1Z3, S1Z7, S1Z8: E075N, E100N | 854 |
| C.20.11 | Reinforcement Strain Vs. Elapsed Time, Gages S1Z3, S1Z7, S1Z8: E125N, E150N | 855 |
| C.20.12 | Reinforcement Strain Vs. Elapsed Time, Gages S1Z3, S1Z7, S1Z8: E200N | 856 |
| C.21.1 | Reinforcement Strain Vs. Elapsed Time, Gages S1X5, S1X14, S1X15: E010DL, E025DL | 857 |
| C.21.2 | Reinforcement Strain Vs. Elapsed Time, Gages S1X5, S1X14, S1X15: E050DL, E075DL | 858 |
| C.21.3 | Reinforcement Strain Vs. Elapsed Time, Gages S1X5, S1X14, S1X15: E100DL, E125DL | 859 |
| C.21.4 | Reinforcement Strain Vs. Elapsed Time, Gages S1X5, S1X14, S1X15: | |

| | | |
|---------|---|-----|
| | E150DL, E200DL | 860 |
| C.21.5 | Reinforcement Strain Vs. Elapsed Time, Gages S1X5, S1XZ14, S1X15: T021DL, T052DL | 861 |
| C.21.6 | Reinforcement Strain Vs. Elapsed Time, Gages S1X5, S1X14, S1X15: T105DL, T157DL | 862 |
| C.21.7 | Reinforcement Strain Vs. Elapsed Time, Gages S1X5, S1X14, S1X15: T210DL, T262DL | 863 |
| C.21.8 | Reinforcement Strain Vs. Elapsed Time, Gages S1X5, S1X14, S1X15: T315DL, T420DL | 864 |
| C.21.9 | Reinforcement Strain Vs. Elapsed Time, Gages S1X5, S1X14, S1X15: E025N, E050N | 865 |
| C.21.10 | Reinforcement Strain Vs. Elapsed Time, Gages S1X5, S1X14, S1X15: E075N, E100N | 866 |
| C.21.11 | Reinforcement Strain Vs. Elapsed Time, Gages S1X5, S1X14, S1X15: E125N, E150N | 867 |
| C.21.12 | Reinforcement Strain Vs. Elapsed Time, Gages S1X5, S1X14, S1X15: E200N | 868 |
| C.22.1 | Reinforcement Strain Vs. Elapsed Time, Gages S1X11, S1X12, S1X13: E010DL, E025DL | 869 |
| C.22.2 | Reinforcement Strain Vs. Elapsed Time, Gages S1X11, S1X12, S1X13: E050DL, E075DL | 870 |
| C.22.3 | Reinforcement Strain Vs. Elapsed Time, Gages S1X11, S1X12, S1X13: E100DL, E125DL | 871 |
| C.22.4 | Reinforcement Strain Vs. Elapsed Time, Gages S1X11, S1X12, S1X13: E150DL, E200DL | 872 |
| C.22.5 | Reinforcement Strain Vs. Elapsed Time, Gages S1X11, S1X12, S1X13: T021DL, T052DL | 873 |
| C.22.6 | Reinforcement Strain Vs. Elapsed Time, Gages S1X11, S1X12, S1X13: T105DL, T157DL | 874 |
| C.22.7 | Reinforcement Strain Vs. Elapsed Time, Gages S1X11, S1X12, S1X13: T210DL, T262DL | 875 |
| C.22.8 | Reinforcement Strain Vs. Elapsed Time, Gages S1X11, S1X12, S1X13: T315DL, T420DL | 876 |
| C.22.9 | Reinforcement Strain Vs. Elapsed Time, Gages S1X11, S1X12, S1X13: E025N, E050N | 877 |
| C.22.10 | Reinforcement Strain Vs. Elapsed Time, Gages S1X11, S1X12, S1X13: E075N, E100N | 878 |
| C.22.11 | Reinforcement Strain Vs. Elapsed Time, Gages S1X11, S1X12, S1X13: E125N, E150N | 879 |
| C.22.12 | Reinforcement Strain Vs. Elapsed Time, Gages S1X11, S1X12, S1X13: E200N | 880 |

| | | |
|---------|--|-----|
| C.23.1 | Reinforcement Strain Vs. Elapsed Time, Gages S1X16, S2Z2, S2Z3: E010DL, E025DL | 881 |
| C.23.2 | Reinforcement Strain Vs. Elapsed Time, Gages S1X16, S2Z2, S2Z3: E050DL, E075DL | 882 |
| C.23.3 | Reinforcement Strain Vs. Elapsed Time, Gages S1X16, S2Z2, S2Z3: E100DL, E125DL | 883 |
| C.23.4 | Reinforcement Strain Vs. Elapsed Time, Gages S1X16, S2Z2, S2Z3: E150DL, E200DL | 884 |
| C.23.5 | Reinforcement Strain Vs. Elapsed Time, Gages S1X16, S2Z2, S2Z3: T021DL, T052DL | 885 |
| C.23.6 | Reinforcement Strain Vs. Elapsed Time, Gages S1X16, S2Z2, S2Z3: T105DL, T157DL | 886 |
| C.23.7 | Reinforcement Strain Vs. Elapsed Time, Gages S1X16, S2Z2, S2Z3: T210DL, T262DL | 887 |
| C.23.8 | Reinforcement Strain Vs. Elapsed Time, Gages S1X16, S2Z2, S2Z3: T315DL, T420DL | 888 |
| C.23.9 | Reinforcement Strain Vs. Elapsed Time, Gages S1X16, S2Z2, S2Z3: E025N, E050N | 889 |
| C.23.10 | Reinforcement Strain Vs. Elapsed Time, Gages S1X16, S2Z2, S2Z3: E075N, E100N | 890 |
| C.23.11 | Reinforcement Strain Vs. Elapsed Time, Gages S1X16, S2Z2, S2Z3: E125N, E150N | 891 |
| C.23.12 | Reinforcement Strain Vs. Elapsed Time, Gages S1X16, S2Z2, S2Z3: E200N | 892 |
| D.1 | Viscoelastic Damper Response to Sinusoidal Loading (1) | 905 |
| D.2 | Damper Characterization Testing | 905 |
| D.3 | Damper Test Results, Dampers 65I and 65L, 1 Hz, 0.250" | 906 |
| D.4 | Damper Test Results, Dampers 65I and 65L, 1 Hz, 0.500" | 907 |
| D.5 | Damper Test Results, Dampers 65I and 65L, 1 Hz, 0.625" | 908 |
| D.6 | Damper Test Results, Dampers 65I and 65L, 2 Hz, 0.250" | 909 |
| D.7 | Damper Test Results, Dampers 65I and 65L, 2 Hz, 0.500" | 910 |
| D.8 | Damper Test Results, Dampers 65I and 65L, 3 Hz, 0.250" | 911 |
| D.9 | Damper Test Results, Dampers 65I and 65L, 3 Hz, 0.500" | 912 |
| D.10 | Damper Test Results, Dampers 66D and 66M, 1 Hz, 0.500" | 913 |
| D.11 | Damper Test Results, Dampers 66D and 66M, 1 Hz, 0.625" | 914 |
| D.12 | Damper Test Results, Dampers 66D and 66M, 2 Hz, 0.250" | 915 |
| D.13 | Damper Test Results, Dampers 66D and 66M, 2 Hz, 0.500" | 916 |
| D.14 | Damper Test Results, Dampers 66D and 66M, 3 Hz, 0.250" | 917 |
| D.15 | Damper Test Results, Dampers 66D and 66M, 3 Hz, 0.500" | 918 |

| | | |
|------|---|-----|
| D.16 | Damper Test Results, Damper 66B, Quasi-Static Loading, 0.250" | 919 |
| D.17 | Average Damper Properties from Tests | 920 |

CHAPTER 1

INTRODUCTION

1.1 Objective

The objective of this study was to investigate the dynamic behavior of a lightly reinforced concrete (LRC) slab-column structure that was modified by adding viscoelastic dampers (VEDs) to it. Through the investigation, simplified analytical methods to facilitate the use of VEDs in seismic retrofit and rehabilitation of LRC slab-column structures were sought.

1.2 Background

Older LRC frame buildings have performed poorly in moderate to high intensity earthquakes. Such structures were designed using building codes that emphasize gravity loading, without providing sufficient deformation ductility to withstand cyclic lateral motions. LRC structures include a number of inadequate reinforcement details. Among them are insufficient column reinforcement ties to provide adequate shear capacity and confinement of column longitudinal reinforcement, location of column reinforcement lap splices in zones of maximum bending moment, and insufficient column reinforcement lap splice length.

In addition to the low ductility of LRC construction, slab-column structures provide poor seismic resistance. They often lack sufficient joint capacities for adequate transfer of earthquake-induced shears and moments, leading to slab punching shear failures. Older slab-column structures often lack continuity of positive moment (bottom) slab reinforcement in joint regions, further lowering their punching shear capacities. The low stiffness of slab-column structures can also lead to large earthquake-induced motions in buildings, which can damage critical equipment and architectural elements.

Conventional means of rehabilitating these structures (E.G. adding shear walls) can be costly and functionally disruptive to building occupants. Supplemental passive energy dissipation devices may

provide cost-effective alternatives to the conventional technologies. One supplemental energy dissipation technique involves adding VEDs to a structure. VEDs are typically mounted in braces that extend between the column lines in a structure. Earthquake-induced tensile and compressive forces that develop in the braces are carried in direct shear by the VEDs. The VEDs both stiffen the structure and enhance its energy dissipation capacity. The viscoelastic material possesses the unique property of a phase angle between shear stress and shear strain when it is loaded dynamically, leading to the energy dissipation mechanism. The energy dissipation, or damping, reduces structural response to ground motion.

While the use of supplemental VEDs is conceptually effective, most prior research has focused on their use in steel structures. There has been concern that VEDs have limitations that might preclude their use in reinforced concrete structures. Foremost is the possibility that, for a VED to deform sufficiently to utilize its energy dissipation characteristics, the parent reinforced concrete structure will have deformed enough to undergo significant cracking. In addition, the high flexibility of slab-column construction has not been studied in previous research.

1.3 Experimental Program

To achieve the research objective, a one-third scale replica of an LRC slab-column structure was fabricated and subjected to simulated earthquake motions on the shaking table at the U.S. Army Construction Engineering Research Laboratories (USACERL).

(a) Model Structure

The prototype for this study is a three wing "H-shaped" complex of three story structures, one wing of which was modeled in the study. The wing is rectangular in plan, with dimensions of approximately 40 feet by 117 feet. The structural framing system is predominately an LRC slab-column moment frame system. Cast-in-place shear walls at the ends of the long dimension provide lateral force resistance for transverse ground motions. In the longitudinal dimension, spandrel beams run the length of the building on both exterior walls, at the top of each story. The spandrel beams are cast monolithically with the floor slabs and support exterior wall and window systems. They stiffen the framing system in the longitudinal direction, and aid in shear and moment transfer from the slab to the exterior columns. Columns are founded on individual spread footings. The prototype was constructed in the mid-1950's.

As-built structural drawings show that the characteristic weaknesses of LRC frames and slab-column systems are present. Details of the building are provided in Chapter 2.

A transverse section near the center of the prototype was modeled. This region was considered the most vulnerable area in the structure, because of its long distance from the transverse shear walls and its potential for pounding into the adjoining wing of the building during earthquakes.

The model was constructed at one-third of full scale. Insofar as possible, reinforcement was scaled to one-third of the prototype. Deformed steel wire was used to model the reinforcement. Wire used for longitudinal reinforcement was annealed to lower its yield strength to match the prototype. First-story columns in the model were cast over longitudinal reinforcement that extended out of a monolithic reinforced concrete base girder. To simulate gravity load stresses in the model and maintain its proper dynamic response characteristics, lead ingots were placed on the floor slabs. The resulting total floor load in the model was approximately 100 psf.

VEDs were added in the column lines of the test structure by using diagonal braces that contained the devices as links in the braces. The braces were attached to the columns by means of steel collars that were placed on the columns. The only other significant strengthening measure was to increase column flexural strength at the connection to the base girder by using No. 3 bars of Grade 60 steel, instead of the annealed wire reinforcement.

(b) Testing Procedures

Prior to the earthquake simulation testing, representative samples of the VEDs were subjected to static and dynamic tests in a universal testing machine, to characterize them and ensure they were fabricated soundly.

Following its construction, the model was placed on the shaking table for earthquake simulation tests. Approximately 75 channels of data were recorded in each test. Instrumentation included longitudinal and lateral accelerations and displacements of the shaking table, base girder, and each floor; damper displacements; damper brace force; damper temperature change (in selected dampers); and reinforcement strains in selected column and slab locations.

Before beginning the earthquake simulations, researchers determined the natural frequencies and equivalent viscous damping properties of the undamaged structure in four different configurations: with no VEDs or braces installed, with solid steel braces installed, with small VEDs installed, and with large VEDs

installed. Two different sized VEDs were available for use.

All earthquake simulations with VEDs installed were conducted before any earthquake simulations without VEDs were performed. For the simulations with VEDs installed, two characteristic earthquake records were used. The first was the El Centro site record from the May 18, 1940, Imperial Valley, CA, earthquake. The second was the Taft site record from the July 21, 1952, Kern County, CA, earthquake. Time scales for both records were compressed; elapsed times were $1/\sqrt{3}$ times the full-scale records. Peak motion amplitudes and frequency contents of the two records differ. The Taft record motion amplitude was multiplied by a factor of 2.1 to equilibrate its spectrum intensity with that of the El Centro record.

Researchers conducted a series of low level ($\text{PGA} < 0.2 \text{ g}$) earthquake simulations with the small VEDs installed, using both the El Centro and Taft acceleration records. The structure was then tested using the same records with large VEDs installed. After each earthquake simulation, modal characteristics of the model were determined, and the model was checked visually for cracking or other deterioration.

After the low level tests, further simulations were conducted using only the large VEDs. A series of simulations of increasing input motion intensity was conducted, with PGAs ranging from 0.05 g to almost 0.90 g. The sequence of tests involved running an El Centro simulation followed by a Taft simulation of approximately the same spectrum intensity, then repeating the sequence at a higher intensity. These simulations were conducted until the displacement limits of the shaking table horizontal actuators were reached, without inducing significant damage in the model.

Earthquake simulations were then conducted on the structure with the VEDs and their braces removed. The collars that were used to attach the VEDs to the columns were left in place, so that the only test variable that was changed was the effects of the dampers and braces. These simulations used only the El Centro record as input, with PGAs ranging from 0.10 g to almost 1.00 g. Testing was concluded after 1.00 g El Centro simulation, when failure of the second and third story exterior slab-column joints occurred.

1.4 Scope of Study

Chapter 2 outlines the designs of the prototype and model structures. The as-built details of the prototype slab-column structure are presented, and the details are compared with currently recommended design procedures. This comparison illuminates the shortcomings of older construction practices that lead to “non-ductile” behavior. The design of the scaled-model is also presented, showing areas of both

similarity and difference between the prototype and it. Chapter 2 also outlines the basic procedures that are used to design VED systems for buildings, and presents an overview of the procedures used to design the VED system that was implemented for this study.

Chapter 3 outlines the preliminary testing of the VEDs that was used to characterize their stiffness and damping properties, discusses the actual fabrication of the test structure, and details the earthquake simulation sequence. The information in this chapter is supplemented by three appendices that are provided at the end of this report. Appendix A provides a more detailed discussion of the model fabrication procedures. Appendix B summarizes key operating characteristics of the USACERL shaking table and the data acquisition systems used in the study. Appendix D provides more detail on the dynamic testing of the VEDs.

Chapter 4 presents general observations that were made during the earthquake simulations, without extensive interpretation. Recorded data and visual observations of the condition of the model are provided. Because of the large quantity of data, only significant and representative samples of data are provided in Chapter 4. Appendix C provides a complete compilation of all recorded data.

Chapter 5 presents an interpretation of the recorded data and visual observations, keying on the representative data samples of Chapter 4. A synthesis of the recorded data and visual observations provides an overview of the condition of the structure and the performance of the various structural elements, particularly the VEDs.

In Chapter 6, linear dynamic analysis techniques are employed as a further means of data interpretation, and as a means of examining potential approaches for modeling VED-equipped slab-column structures in the retrofit design process. In addition, techniques for modeling and analyzing these structures that are emerging through the auspices of the Federal Emergency Management Agency and the National Earthquake Hazards Reduction Program are examined.

Chapter 7 summarizes the study, draws conclusions from the analyses and interpretations of Chapters 2-6, and makes recommendations for future activities.

1.5 Report References

References used in this report are listed alphabetically in the List of References, which is placed immediately after Chapter 7. References are listed alphabetically and numbered. In the body of each chapter and appendix, reference numbers are provided in brackets ([]).

CHAPTER 2

DESIGN OF PROTOTYPE AND TEST STRUCTURES

This chapter describes major features of the prototype structure, the design of the scaled test structure, and the design of the viscoelastic damper (VED) system that was installed as a rehabilitation measure on the test structure. In Section 2.1, detailed descriptions of the prototype structure are provided. Key details are shown. Relevant provisions of the design basis building codes are listed, and those provisions are compared with current building code requirements. In this manner, some of the prominent shortcomings in the seismic resistance of the original structural system are highlighted, pointing out the need for developing effective seismic rehabilitation schemes for it. In Section 2.2, the design of the scaled model structure is discussed, showing primary similarities and differences between it and the prototype. Emphasizing the *Modal Strain Energy Method*, the design procedure for VEDs is discussed in Section 2.3. The basic design procedure for lightly damped structures, as with structural steel, is outlined, and modifications to the procedure that account for the higher inherent damping found in reinforced concrete structures are introduced. Finally, in Section 2.4 the interaction of VEDs with adjoining brace elements is discussed, to provide background for the later consideration of the brace effects in modeling the structure analytically.

2.1 Prototype Structure Description

The model that was tested on the USACERL shaking table replicates a section of a barracks building that was constructed by the U.S. Army Corps of Engineers at Fort Lewis, Washington, near Seattle, in the mid-1950's. The barracks' original design analysis was not available, but as-built drawings for it, dated June 1956, were. The drawings provided construction details, and key statements concerning the basis for the design.

(a) As-Built Drawings

The prototype barracks building is a structural system that combines three adjoining wings, two of which are mirror images of each other and are connected by the third wing. Several of these systems were built at Fort Lewis. One of the two nearly-identical wings was the focus of this study. Figure 2.1 shows the exterior of this structure as it appears today; the door shown was apparently added after the initial construction. The structure is 39' 8" wide and 117' 0" long. Figures 2.2 and 2.3 are copies of its as-built floor plans. The building is three stories tall, with both lower floors and the roof having a flat slab construction. The roof slab is sloped upward ($\frac{3}{8}$ " per foot) to the center of the structure and is topped with a built-up roofing system. All columns in the structure are founded on individual spread footings.

In its longitudinal dimension, the structure is a reinforced concrete moment frame, two bays wide and six bays long. The two exterior column lines have continuous spandrel beams at all levels. The left section shown in Figure 2.4 shows the exterior column line-wall system. The spandrels support the exterior wall and window systems, provide flexural and shear capacity in the longitudinal direction, and transmit loads from the floor slabs to the columns in the exterior column line.

In the transverse dimension, the structure has 8" reinforced concrete shear walls at each end of the structure (right side of Figure 2.4). Between the two shear walls, the structure is an open-bay flat slab system that is two bays wide. At the first floor level, there are numerous 4" concrete masonry walls. They are not typically placed within column lines. One bay in each of two of the five transverse column lines contains such a wall. On each of the second and third floors, there is a 4" concrete masonry wall in the middle transverse column line (of five). The masonry wall is lightly reinforced, with single #3 reinforcing bars placed at 4' 0" intervals, horizontally and vertically, in grouted cells. There is no evidence that the walls were designed to resist lateral force. For the purposes of this study, these walls were assumed not to contribute to the lateral force-resisting system.

All slabs are 7" thick. The first and second floor slabs are conventional flat slabs; the roof slab differs slightly, in that it has the previously mentioned slope. The slabs were designed as two-way elements, with "column" and "middle" strip reinforcement designs. The slab reinforcing schedules for the first and second floor slabs are identical, while the third floor, or roof, slab is more lightly reinforced. The positive moment (bottom) steel is discontinuous over the interior column. While there is no capital at the interior column, there is a "shearhead" (term used on as-built drawings) composed of bent steel reinforcement. Figure 2.6 is an as-built detail of this shearhead. The shearhead is composed of two upper

and two lower #3 ties that extend around the column perimeter, and a series of V-shaped #3 “prongs” (term used on as-built drawings) that are placed around the column perimeter and oriented at an approximate 45° angle to the slab surfaces. Each leg of each prong is 9-½" long. Approximately 50% of the negative moment (top) reinforcement in the column strip zone in each direction at the interior column is concentrated over the width of the shearhead. At the exterior column lines, the slabs are cast monolithically with the spandrel beams for the exterior walls. The negative moment reinforcement is bent 90° downward into the spandrels.

The exterior column dimensions are typically 12" x 23-¾" for all three stories (Figure 2.5), although dimensions vary in the area where the adjacent building wings adjoin. Longitudinal reinforcement is eight #6 bars for the entire building height. Confinement of the longitudinal reinforcement is provided by double #3 closed loop ties spaced 12" center-to-center (c-c).

The interior column dimensions are all 14" x 14" for all stories. Longitudinal reinforcement for each upper story interior column is four #7 bars. First story longitudinal reinforcement varies from four #8 bars (two columns), to four #9 bars (two columns), to four #10 bars (one column). Confinement is provided by single #3 closed loop ties spaced 12" c-c.

The spandrel beam cross-sections are somewhat irregularly shaped, because of their use in external architecture. The roof spandrel approximates a rectangular section that is 1' 0" wide x 1' 6-½" deep, while the lower floor spandrels approximate rectangular sections that are 10" wide x 1' 3-⅝" deep. Positive moment reinforcement varies from two #6 bars in the roof spandrel to three #6 bars in the lower floors; this reinforcement is discontinuous in the spandrel-column joint regions. Maximum negative moment reinforcement varies from two #6 and one #5 in the roof spandrel to two #6 and two #7 in the lower floors. At least two #6 bars are placed in the top of each spandrel beam for its entire length. Specified minimum splice length is 1' 6" for the top bars. Confinement is provided by single #3 closed loop ties spaced 12" c-c.

Minimum concrete cover is specified as ¾" in the slabs and 1-½" in the columns.

(b) Design Basis Building Codes

The as-built drawings indicate that the Pacific Coast Uniform Building Code (PCUBC) and the ACI Building Code were used in design calculations. Code dates were not given. Based on the drawing dates and the codes that were available to the author, the requirements of the 1955 edition of the Pacific Coast Uniform Building Code [33] and ACI 318-51 [5] were assumed to be the design basis codes.

Reference 33 provided designers with the following basis for an "equivalent" static lateral seismic loading:

$$F_i = C_i W \quad (2.1)$$

$$C_i = \frac{0.15Z}{N_i + 4.5} \quad (2.2)$$

In these equations, " F_i " represents the lateral force that is to be applied at story level i ; " Z " is a seismic zonation factor; " N_i " is the number of stories above the story level i ; and " W_i " is the total dead load of story i . The as-built drawings indicate that the structure was designed for PCUBC Zone 3; Reference 33 specifies a value of 4 for Z in this case. Using these equations results in the following lateral load distributions for the structure:

$$\begin{aligned} F_3 &= 0.133 W_3 \\ F_2 &= 0.109 W_2 \\ F_1 &= 0.092 W_1 \end{aligned} \quad (2.3)$$

Using the approximate dead load distributions of 108 psf for floor 3 and 115 psf for floors 1 and 2 (see Table 2.1), and an approximate area of 4,641 square feet per floor, the lateral forces computed using Equations 2.3 are 67 kips, 58 kips, and 49 kips, for floors 3, 2, and 1, respectively. The resulting base shear is 174 kips, which is approximately 11% of the total dead load weight of the building.

Reference 5 (ACI 318-51) outlines the basis for the reinforced concrete design for the structure.

Working stress procedures were followed (standard practice for the day). The as-built drawings indicate that the required 28 day compressive strength (f'_c) for the structural concrete was 3,000 psi, while all reinforcement was specified as "intermediate grade" deformed bars, with $f_s = 20,000$ psi.

The as-built drawings provide slab reinforcement details (i.e. column and middle strip requirements for both the lateral and longitudinal slab directions) that indicate two-way slab design procedures were followed.

Key design detail requirements from ACI 318-51 include:

- (1) *Minimum slab thickness* = $\frac{L}{36}$, where L is the c-c distance between columns. In this structure, the minimum thickness is therefore 6.44" (vs the 7" provided).
- (2) *Minimum slab reinforcement in the primary direction* = $0.0025 bd$. The prototype

slab reinforcement configurations exceeded this minimum.

(3) *Minimum slab reinforcement in the transverse direction = $0.002 bd$ ($0.0025 bd$ for the roof slab).* The prototype slab reinforcement configurations exceeded this minimum.

(4) *Maximum slab reinforcement spacing $\leq 3t$, in the primary direction, \leq the smaller of $5t$ or $18"$ in the transverse direction.* Since the slab is $7"$ thick, a logical interpretation of this requirement ($3t = 21"$) would require a maximum spacing of $18"$ in either the primary or transverse directions.

Examination of the prototype slab reinforcement schedules showed one area in which this requirement is violated. The negative moment zone of the middle strip ($116"$ wide) in the transverse direction has 7 bars, for an average spacing of $19.33"$. Otherwise, all specified slab reinforcement meets this requirement.

(5) *Where a column capital is present, at least 50% of the slab's negative moment (top) steel must pass through the capital width.* While no capital is present, the designers concentrated the negative moment steel in the "shearhead" region, with the apparent intent of complying with this requirement. The exact width of the shearhead is not given, but scaling from the as-built drawings indicates that this zone is approximately $38"$ wide. Of the total of 7.06 square inches (in^2) of column strip top reinforcement (nine #6 and ten #5) in the primary direction for a typical interior column, 3.96 in^2 (nine #6) is concentrated in the shearhead zone. Of the total of 5.12 in^2 of column strip top reinforcement (six #6 and eight #5) in the transverse direction for a typical interior column, 2.64 in^2 (six #6) is concentrated in the shearhead zone. In both instances, slightly more than 50% of the reinforcement has been concentrated in the shearhead zone.

(6) *In exterior panels, positive moment (bottom) slab steel must be embedded at least $6"$ in spandrel beams. Negative moment (top) slab steel must be bent into spandrel beams.* The as-built drawings are not clear but seem to indicate that the reinforcement was placed in accordance with these requirements. The drawings specify that the top bars are "hooked" at the spandrel beams.

(7) *A "hook" may be a 90° bend, with a minimum radius of four bar diameters and a minimum extension of 12 bar diameters.* In the typical first floor column strip, #6 bars were used in the exterior panels, which would require an extension of $9"$ beyond the bar bend. In the typical first floor middle strip, #4 and #5 bars were used in the exterior panels, which would require extensions of $6"$ and $7\frac{1}{2}"$ beyond the bar bends, respectively. This specific information is not provided by the as-built drawings, but is assumed to have been followed.

(8) *In tied columns, the minimum splice length is 20 bar diameters (d_b).* The as-built drawings added the requirement that the minimum splice length could not be less than $18"$. They do not

delineate the actual splice lengths, or their locations. The author assumed that all column reinforcement splices were made immediately above the floor slab level in each story. For the typical column reinforcement of #6 bars in the exterior first floor columns, and the typical column reinforcement of #8 bars in the interior first floor columns, the required minimum splice length would be 18".

(9) *In tied columns, ties must have a minimum diameter (d_t) of $1/4$ ". The maximum tie spacing is the lesser of $16 d_b$, $48 d_t$, or the smaller cross-sectional dimension of the column. All ties were specified as #3 bars ($3/8$ " diameter). For the typical interior (14" x 14") column with #8 bars, the required maximum tie spacing is therefore 14". For the typical exterior column with #6 bars, the required maximum tie spacing is therefore 12". Tie spacings are shown on the drawings to be a uniform 12" c-c for all columns, complying with the code requirements.*

(10) *When there are more than four vertical bars in a tied column, ties must be furnished to hold every longitudinal bar in position and provide lateral support that is equivalent to a 90° tie corner. Figure 2.5, which is excerpted from the as-built drawings, indicates that this requirement is met by the design.*

(c) Comparison of Design with Current Building Code Requirements

No attempt has been made to establish the ultimate lateral load capacity of the prototype structure, because, as will be discussed in the model design narrative, several generalizations were made in developing the model design that result in the model's not being an exact replica of the prototype. However, a comparison of the 1950's design with current building code requirements is helpful in establishing the general need for seismically upgrading a structure like the prototype.

A direct comparison of design-basis equivalent static lateral loading is difficult, because the 1950's procedure was based on working stress principles, while current procedures are based on a combination of the ultimate strength of the structure and a number of working stress principles. In addition, the actual strength and ductility of the structure are more important than the original design procedure. However, it is instructive to examine the vertical distribution of the inertial loads that are applied in the equivalent static lateral load procedures because all design forces and displacements depend on it. Using the distributed loads found on the as-built drawings, the approximate distributed dead load on the first and second floors is 115 psf, while the distributed dead load on the third floor, or roof, is 108 psf (Table 2.1). Using these distributed loads, the design lateral loads in Equation 2.3 can be normalized with respect to the top floor

load:

$$\begin{aligned}F_3 &= 1.00F \\F_2 &= 0.87F \\F_1 &= 0.74F\end{aligned}\tag{2.4}$$

In Equation 2.4, the term “ F ” represents the lateral force for the third floor, F_3 , from Equation 2.3.

Using the procedures outlined in Section 2.3 of Reference 32, for an ordinary reinforced concrete moment frame system and an effective peak velocity-related acceleration (A_v) of 0.20 (applicable for Fort Lewis), the normalized lateral force distribution is:

$$\begin{aligned}F_3 &= 1.00F \\F_2 &= 0.71F \\F_1 &= 0.35F\end{aligned}\tag{2.5}$$

In Equation 2.5, the term “ F ” represents the lateral force for the third floor, F_3 , that is computed using the NEHRP [32] requirements.

Using the approximate dead load distributions of 108 psf for floor 3 and 115 psf for floors 1 and 2 (Table 2.1), and an approximate area of 4,641 square feet per floor, the lateral forces computed using Equations 2.5 are 184 kips, 131 kips, and 65 kips, for floors 3, 2, and 1, respectively. The resulting base shear is 380 kips, which is approximately 24% of the total dead load weight of the building.

Current design procedures provide a load distribution that places over twice the total lateral force on the structure and significantly higher relative force on the upper sections of the structure than the 1950's procedures did. Both calculated member forces and resulting member displacements will be much higher using the current procedures. Because of the different vertical distribution of lateral forces, the implications are more severe for upper floors than for lower floors. It will be instructive to reflect on these design load distributions when examining the test data that were collected, both in terms of the inertial forces and displacements that occur at each floor level, and in terms of observed structural damage mechanisms.

As mentioned in Chapter 1, the flat slab system is not viewed as an effective lateral load-resisting system. The inherent flexibility of the system permits very large lateral displacements to occur, and the low

shear and flexural capacities of the slab-column connection increase the likelihood of catastrophic failure. Neither of the 1950's codes [5, 33] addressed the use of the flat slab system for seismic applications. By contrast, present-day codes discourage the use of this system in areas of moderate to high seismicity. Reference 32 ("NEHRP") does not specifically address flat slab structures. But, granting the inclusion of this system in the NEHRP classification of Ordinary (concrete) Moment Frames (frames that conform to the provisions of Reference 7, exclusive of its Chapter 21), or the classification of Intermediate (concrete) Moment Frames (frames that conform to the provisions Section 21.8 of Reference 7) this construction would not be permitted at Fort Lewis today, based on NEHRP Table 2.2.2, which lists basic structural systems and limitations on their use. This conclusion is based on the building's classification in NEHRP Seismic Hazard Exposure Group II (buildings that have a substantial public hazard due to occupancy or use), and thus into NEHRP Seismic Performance Category D, for an A_v value of 0.20 (A_v for Fort Lewis). In Section 21.8 of Reference 7 (ACI 318-95), design detailing requirements for flat slab construction in zones of "moderate" seismic risk are given. The area in which Fort Lewis is located is classified as an area of higher seismicity, leading to the conclusion that ACI 318-95 discourages the use of the flat slab system in this higher seismicity region, regardless of occupancy.

Older (pre-1970's) reinforced concrete building construction has become known as "nonductile" or "lightly reinforced." This terminology is related to the lesser degree of core confinement in flexural members, shorter reinforcement development and lap splice lengths, and more lightly reinforced joint regions in the older structures, as compared to current requirements. Following is a brief comparison of some of the key reinforcement requirements of ACI 318-95 with the design of the prototype structure. The comparison focuses on the seismic provisions of Section 21.8 of ACI 318-95, which presupposes siting in an area of low to moderate seismicity. Comparison with the more stringent provisions of Sections 21.2 - 21.7 of ACI 318-95 would be inconsistent with the use of the flat slab system.

(1) ACI 318-95 requires the same minimum slab thickness of $L/36$ that was required by ACI 318-51.

(2) Minimum slab reinforcement quantities and maximum slab reinforcement spacings, *for temperature reinforcement*, remain largely unchanged. But, ACI 318-95 Section 13.3.2 requires a maximum reinforcement spacing $\leq 2t$ in critical sections (for flexure calculations). This provision is intended to enhance structural integrity and reduce slab cracking. Several of the middle strip regions of each floor would violate this requirement.

(3) ACI 318-95 does not carry the same specific requirement for concentrating 50% of

the slab's negative moment steel in the capital width that is found in ACI 318-51. Rather, ACI 318-95 Section 13.5.3 requires that an effective slab width 1.5 slab thicknesses on either side of the column or capital be designed to transfer a fraction of the unbalanced slab moment at the joint in flexure, and that sufficient slab reinforcement be concentrated in the effective width to accommodate the unbalanced moment. Similar to the ACI 318-51 provision, Section 21.8.6.3 requires that, in areas of moderate seismicity, at least 50% of the column strip steel be placed in the effective width zone.

(4) The ACI 318-51 requirements for embedding both the top and bottom slab steel in the spandrel beam zone, and the requirements for "hooked" bars, remain largely unchanged in ACI 318-95. However, Section 12.5.2 of ACI 318-95 adds basic development lengths for hooked bars. For the #6 bars found bent into the spandrels from the prototype slabs, ACI 318-95 requires a minimum development length of 7.7" from the hook to the critical section for flexure. The prototype spandrel widths of 10" - 12" (varies) permit less than the full development length for the slab reinforcement. Since it is likely that the 90° hook is placed at the mid-width of the spandrel beam, a length of only 5" - 6" to the spandrel-slab interface is available for development. Bar slippage can prevent the full tensile capacity of the reinforcement from developing at the interface and limit the energy dissipation capacity of the system.

(5) Section 13.3.8.5 of ACI 318-95 requires that all bottom bars in the slab column strips in each direction be continuous (splices are permitted), with at least two bars passing through the column core. This provision is intended to help prevent a catastrophic collapse of the slab if a punching shear failure of the slab occurs. In areas of moderate seismicity, Section 21.8.6.5 of ACI 318-95 specifies that the continuous bottom reinforcement quantity be not less than $\frac{1}{3}$ the quantity of the top reinforcement in the column strip. Section 21.8.6.6 of ACI 318-95 further specifies that the continuous bottom reinforcement quantity not be less than $\frac{1}{2}$ the required bottom reinforcement quantity at midspan. The prototype has discontinuous bottom bars. In addition to posing a safety problem, the discontinuity at the column centerline can lead to bar slippage under load reversals, reducing energy dissipation capacity.

(6) Section 21.8.6.4 of ACI 318-95 requires that not less than $\frac{1}{4}$ of the top reinforcement in the column strip at the support be continuous throughout the span, in areas of moderate seismicity. This requirement again helps prevent catastrophic collapse. The top bars in the prototype are all discontinuous.

(7) Sections 12.2.2, 12.15.1, 12.15.2, and 12.17.2 require column reinforcement splice lengths of 43" for #6 bars and 72" for #8 bars, for Class B splices. These splice lengths exceed the 18" specified for the prototype, indicating potential development length, and accompanying bar slip, problems in the column reinforcement. In addition, the author assumed that column reinforcement lap splices were

placed directly above each floor slab level; no information on splice locations was provided on the as-built drawings. Because of its convenience for construction, this practice has been common, but the location is poor because of high flexural force magnitude and load transfer. While Section 21.8 of ACI 318-95, which addresses seismic design for areas of moderate seismicity, does not specifically treat this practice, Section 21.4.3.2 states "Lap splices shall be permitted only within the center half of the member length ..." The potential bar slip mechanism limits the energy dissipation capacity of the system.

(8) Section 21.8.5 of ACI 318-95 requires ties for the entire height of each column. For a length, l_o , extending from each joint face, the maximum tie spacing cannot exceed s_o . The spacing s_o is the lesser of $8 d_b$, $24 d_t$, or $\frac{1}{2}$ the smaller cross-sectional dimension of the column. The length l_o is the larger of $1/6$ the clear span, the larger cross-section dimension of the column, or 18". In the column mid-height length, the tie spacing cannot exceed twice s_o . For the exterior columns, this requires a maximum tie spacing not exceeding 6.00" for a length of 24.00" from each end of each column, and a maximum tie spacing not exceeding 12.00" in the column mid-height region. For the interior columns, this requires a maximum tie spacing not exceeding 7.00" for a length of 18.00" from each end of each column, and a maximum tie spacing not exceeding 14.00" in the column mid-height region. The prototype design complies with the mid-height region requirements, but not the joint region requirements. This lack of longitudinal reinforcement confinement in the joint regions can lead to buckling of the longitudinal reinforcement under moderate to severe earthquake-induced shaking.

(9) Section 21.8.4 of ACI 318-95 also requires stirrups in all beams. For a length at each end of each beam of twice the member depth ($2d$), measured from the joint face toward midspan, stirrup spacing, s , cannot exceed the smaller of $d/4$, $8 d_b$ (for smallest bar present), $24 d_t$, or 12". Stirrup spacing through the rest of the member length cannot exceed $d/2$. Using the average gross spandrel beam depth of 15.00", this results in a stirrup spacing of approximately $3\frac{3}{4}$ " over a distance of 30" from each column face, and a stirrup spacing of approximately $7\frac{1}{2}$ " over the remaining beam midspan length. The prototype stirrup spacing of 12" violates these requirements. This lack of longitudinal reinforcement confinement in the joint regions can lead to buckling and twisting of the longitudinal reinforcement under moderate to severe earthquake-induced shaking. Moreover, the lack of stirrups decreases the torsional capacity of the spandrel, creating potential moment transfer problems at the spandrel-column interface zone.

Without analyzing the ultimate capacity of the prototype system, this comparison provides an overview of some of its major shortcomings in terms of its ability to withstand moderate to severe ground shaking. The system is therefore a good candidate for seismic upgrade. The primary purpose of this study

is to analyze the behavior of the older slab-column structure that has been retrofitted with a viscoelastic damper (VED) system. To accomplish this, a scaled model was “designed” and built for seismic simulation testing on the USACERL shaking table.

2.2 Reinforced Concrete Model Design

There are two primary purposes for earthquake simulation in the laboratory: to test an actual prototype, and to test a theoretical concept represented by a physical model [44]. In this instance, the goal was to test the concept of using VEDs to retrofit an existing lightly reinforced concrete structure. It was not essential to reproduce the prototype precisely to fulfill this goal. The author adopted an approach that balanced realism for the structural model with practical application of the USACERL shaking table.

Even though shear walls are the dominant lateral force-resisting elements in the transverse, or lateral, dimension of the prototype building, this dimension was chosen for modeling. This decision was largely driven by the size of the shaking table platform (12' x 12'). A 1/3-scale model of the prototype could be fabricated and placed on the table with the aid of a stiff base girder. At 1/3-scale, the length of the model was 13' 4"; the base girder could accommodate the small “overhang” of 8" on either end of the table platform. Appendix A describes the base girder construction. A larger scale would have necessitated a significantly larger base girder and more severely taxed the force capabilities of the shaking table actuators (because of larger model mass). A significantly smaller scale would have made modeling the reinforcement and the concrete aggregate more problematic, and it would have created potentially significant strain rate scaling effects on material properties. Had the longitudinal dimension of the prototype been chosen for modeling, either a very small scale would have been needed, or a small section of the structure would have been tested. Again, smaller scale was not desirable. To test a section in the longitudinal direction would have necessitated great care, and expense, in modeling slab boundary conditions properly.

In a practical sense, the study of the transverse dimension of the prototype is also relevant because the relatively flexible and weak nature of the flat slab system is likely not to be effective in a dual-system combination with the end shear walls. Moreover, the abutting of this building directly against another at its mid-length poses serious potential seismic pounding potential, so reducing displacements is important. For the stability of the model, two column lines were included in the model. The model slabs extend laterally to the point that would be the mid-spans between column lines in the longitudinal dimension. No supports were provided along the free edges of the extensions, so the transverse slab action in these overhanging

regions does not exactly model the prototype.

A geometric scale of $\frac{1}{3}$ was therefore chosen for the model. Table 2.2 lists the relevant scaling similitude requirements for $\frac{1}{3}$ scale. All major structural elements were sized to be $\frac{1}{3}$ the corresponding prototype dimensions. Table 2.3 summarizes all major dimensions in the prototype, exact (ideal) $\frac{1}{3}$ -scale model dimensions, and the actual model dimensions. Ratios of the actual dimensions to the exact dimensions are also given, as a means of checking the accuracy of the model.

Several explanatory notes are required for Table 2.3. The prototype exterior columns on the column line that abuts the adjoining building (see Figure 2.2) vary in gross dimensions; no two adjacent columns in that line are alike. The dimensions chosen that were modeled ($12" \times 23\frac{3}{4}"$) are found in the columns in this line and all but the two corner columns in the opposite exterior column line. Using these dimensions for all exterior columns provided symmetry in the model. The prototype spandrel beams were irregularly shaped and varied in size from floor to floor. The "core" rectangle of this spandrel was used and was made the same for all three floors in the model, to simplify formwork. For the model dimensions, problems encountered in the fabrication of the model formwork necessitated a small ($\frac{1}{4}"$) increase in the width and thickness of each column over the original design. The spandrel beam width was likewise increased. This seemingly small increase resulted in significant moment of inertia, and thus stiffness, increases for the columns. These increases are particularly significant for uncracked section properties. Since the slab dimensions are more faithfully reproduced, there is more of a relative difference in the column and slab stiffnesses in the model than in the prototype.

Figures 2.7 - 2.10 are photographs of the constructed model. Figures 2.7 and 2.8 show the model immediately after all formwork was removed. Figure 2.9 shows the model after the VED collars and braces were installed, but before it was placed on the shaking table. Figure 2.10 shows the model in place and ready for testing on the shaking table. In Figure 2.10, the reader can see the lead weights that were required for modeling the mass properties of the prototype and the supplemental steel safety frame that was placed before testing began. Appendix A describes both of these features. Figures 2.11 - 2.14 show the model structure layout and all gross dimensions for the model. Note that the roof, or third floor, in the model is flat, instead of sloped as in the prototype.

To model the reinforcement in the slabs and columns, the reinforcement quantities and spacing were modeled as faithfully as possible, consistent with the similitude requirements listed in Table 2.2 and the availability of deformed wire reinforcement. Tables 2.4 - 2.5 list the reinforcement quantities in both the prototype and the model and compare the reinforcement ratios in the two. Figures 2.15 - 2.25 show

details for all reinforcement use in the model.

Several explanatory notes are required for these tables. In the prototype, the slab reinforcement volume was somewhat smaller in the roof slab than in the lower two floors. To simplify the preparation of the model slab reinforcement (which required annealing), the same reinforcing layout was used on all three floor levels. The reported prototype quantities are therefore based on the floor slabs found on the lower floors. The exterior prototype column reinforcement for the 12" x 23- $\frac{3}{4}$ " columns was uniform for the entire building height. The interior column reinforcement varied, both on a given floor level and from floor to floor, though all interior columns had the same dimensions. On the first floor level, interior column reinforcement quantities varied from 4-#8 to 4-#10 bars; the configuration with 4-#8 bars is reported here for comparison. On the upper two floors, the interior column was generally reinforced with 4-#7 bars. Similarly, the reinforcement quantities in the prototype spandrel beams varied by floor level. The prototype quantities shown are dominant for the spandrels on the first and second floors. As shown in Table 2.5, the model columns were more significantly reinforced at the base level connection with the base girder, where #3 Grade 60 bars were stubbed up from the girder. This action was driven by project schedule constraints. Conventional #3 reinforcement was readily available locally. The deformed wire that was used elsewhere in the model required annealing before its use in the structure. It was necessary to construct the base girder before the wire was available. It was also assumed that any actual retrofit would likely involve strengthening the first story columns, so that the use of the #3 reinforcement did not seem unrealistic.

The interior slab-column joint "shearhead" design found in the prototype was not used in the model structure. The V-shaped "prongs" found in the shearhead design would have legs that are approximately 3" long in the model. This extremely short length would prohibit effective development of the reinforcement strength and likely result in rapid pullout in a shear-related failure. The addition of this shear reinforcement would also congest the slab-column joint region and make concrete placement more difficult and possibly induce aggregate segregation in the region.

Detailed discussion of the concrete and steel reinforcement properties is provided in Appendix A. Since the as-built drawings indicated a design 28-day concrete compression strength of 3,000 psi, a strength of 3,600 psi was targeted for the mix design. The 20% strength increase was included to compensate for age-related strength increases in the prototype. The quantities of concrete that were required for each floor of the model exceeded the in-house ability to mix concrete manually, so ready-mix concrete was ordered. As described in Appendix A, the strength of the concrete that was provided greatly exceeded the 3,600 psi target. The three floor average was close to 5,900 psi. The concrete that was

provided had the smallest commercially available coarse aggregate, a $\frac{3}{8}$ " river gravel.

As supplied, the deformed steel wire used for the model flexural reinforcement had yield strengths significantly above the nominal 40 ksi (based on $f_y = 20$ ksi) of the prototype reinforcement. The wire was annealed to lower yield strengths to approximately 40 ksi. This process is described and the post-annealing strengths are listed in Appendix A.

The plain wire that was used for column ties and spandrel stirrups was not annealed and thus had significantly higher yield strength, approximately 100 ksi, than the 40 ksi of the prototype. As shown above, the prototype stirrup and tie spacings were significantly larger than current seismic code provisions permit. The poor core concrete and flexural reinforcement confinement that was provided by the wide spacings was deemed to be a more significant problem than the individual tie strength. For economic reasons, the plain wire was therefore not annealed.

The prototype structure had its column founded on individual spread footings, so that some rotational flexibility is present at the prototype column bases. In the model, the columns were cast directly against the base girder. Since there is a cold concrete joint at the column-base girder interface, there is some rotational flexibility present, but the degree of flexibility is probably less than in the prototype. This will result in a higher first story stiffness in the model than in the prototype. The rotational stiffnesses of the model column bases will be discussed in Chapter 5.

2.3 Viscoelastic Damper (VED) Design

The VEDs used in the test structure were designed, fabricated, and donated to the project by 3M Corporation. Two different VED sizes were provided. Figures 2.26 and 2.27 detail the larger of the two VED sizes. The larger VEDs had four 3" x 6" x $\frac{1}{2}$ " pads of 3M ISD 110 material. The smaller VEDs were identical to the larger ones, except that they had four 3" x 3" x $\frac{1}{2}$ " pads. The VEDs are described in detail in Appendix D.

3M engineers employed the *Modal Strain Energy Method* (MSEM) to design the VEDs. The MSEM is summarized here. It is based on idealizing a structural system as a series of elastic spring elements, with added viscous damping that provides the appropriate modal damping ratios for global motions.

The *strain energy* characteristic of the MSEM involves examining a proportionally damped system, in which all damping is provided by VEDs [9]:

$$\xi_i = \frac{E_d^i}{4\pi E_s^i} \quad (2.6)$$

Here, ξ_i represents the structural damping ratio for the i th vibration mode; E_d^i is the energy dissipated in one cycle of motion by the VEDs, for the i th vibration mode; and E_s^i is the structural strain energy in one cycle of motion, for the i th vibration mode.

The *modal* attribute of the MSEM involves characterizing the damped structure in terms of the real natural modes of an associated undamped system, with damping terms inserted into the uncoupled equations of motion [9]:

$$\ddot{Z}_i(t) + \eta_i \omega_i \dot{Z}_i(t) + \omega_i^2 Z_i(t) = p_i(t) \quad (2.7)$$

$$u(t) = \sum_{i=1}^N \phi_i Z_i(t), \quad i = 1, 2, 3, \dots, N \quad (2.8)$$

In Equations 2.7 and 2.8, Z_i is the i th modal coordinate; ω_i is the i th natural frequency; ϕ_i is the i th mode shape vector of the associated undamped system; η_i is the modal loss factor of the i th natural frequency, and is equal to $2\xi_i$; and $u(t)$ is the generalized coordinate. These equations imply that the damping matrix expressed in these generalized coordinates can be uncoupled using the natural vibration modes of the system, leading to the ability to calculate the modal damping of the structure using the mode shapes and the VED loss factor [9]. This is accomplished through examining the free vibration characteristics of an undamped system:

$$M\ddot{u} + Ku = 0 \quad (2.9)$$

M and K represent the structural mass and stiffness matrices. The stiffness matrix, K , is constant, but complex, because of the influence of the VED. Assume a displacement of the form [9]:

$$u = \phi_i^* e^{i\omega_i^* t} \quad (2.10)$$

In Equation 2.10 and later in this chapter, the asterisk (*) denotes complex terms. The complete solution for the natural frequencies may be found in Reference 9 and others, but, after derivation, the complex

natural frequencies of the system are found to be of the form:

$$(\omega_i^*)^2 = \omega_i^2(1 + i\eta_i) = \frac{\phi_i^{*T} K_R \phi_i^*}{\phi_i^{*T} M_R \phi_i^*} + i \frac{\phi_i^{*T} K_I \phi_i^*}{\phi_i^{*T} M_I \phi_i^*} \quad (2.11)$$

In Equation 2.11, the “R” subscript denotes the real coefficients of the stiffness or mass matrix, both of which are complex, while the “I” subscript denotes imaginary coefficients. From this formulation, the MSEM approximates the complex mode shape vector, ϕ_i^* , as its real counterpart, ϕ_i , which then enables the following approximations to be made [9]:

$$\omega_i^2 \approx \frac{\phi_i^T K_R \phi_i}{\phi_i^T M \phi_i} \quad (2.12)$$

$$\omega_i^2 \eta_i \approx \frac{\phi_i^T K_I \phi_i}{\phi_i^T M \phi_i} \quad (2.13)$$

$$\therefore \eta_i \approx \frac{\phi_i^T K_I \phi_i}{\phi_i^T K_R \phi_i} \quad (2.14)$$

The structural stiffness matrix, K , is viewed as the sum of two parts, that of the original structure, K_o , whose coefficients are all real, and that of the dampers, K_d , which has both real and imaginary coefficients, K_{dR} and iK_{dI} :

$$K = K_o + K_d = K_o + K_{dR} + iK_{dI} = K_o + K_{dR} + i\eta_v K_{dR} \quad (2.15)$$

In Equation 2.15, η_v is the loss factor of the VED (see Appendix D). Equation 2.14 can then be rewritten:

$$\eta_i \approx \eta_v \frac{\phi_i^T K_{dR} \phi_i}{\phi_i^T K_R \phi_i} = \eta_v \frac{\phi_i^T (K_R - K_o) \phi_i}{\phi_i^T K_R \phi_i} = \eta_v \left(1 - \frac{\phi_i^T K_o \phi_i}{\phi_i^T K_R \phi_i} \right) \quad (2.16)$$

In Equation 2.16, $K_R = K_o + K_{dR}$. Equation 2.16 facilitates calculating the modal damping ratio:

$$\xi_i = \frac{\eta_i}{2} = \frac{\eta_v}{2} \left(1 - \frac{\phi_i^T K_o \phi_i}{\phi_i^T K_R \phi_i} \right) \quad (2.17)$$

A further approximation is often made by assuming that the vibration mode shapes do not change when VEDs are added to a structure [9]. With this assumption,

$$\xi_i = \frac{\eta_v}{2} \left(1 - \frac{\omega_{oi}^2}{\omega_{di}^2} \right) \quad (2.18)$$

In Equation 2.18, the subscript “oi” denotes the i th natural frequency of the structure without VEDs, and the subscript “di” denotes the i th natural frequency of the structure with VEDs. References 9 and 11 compare the results of first mode damping ratios calculated using Equations 2.17 and 2.18 with experimentally determined first mode damping ratios in a five story steel model for several different distributions of VEDs throughout its height. The damping ratio that was calculated using Equation 2.18 was consistently higher than that calculated using Equation 2.17, but the absolute differences in the two damping ratios was always less than 1%. The absolute differences between the calculated first mode damping ratios using either Equation 2.17 or 2.18 and the measured first mode damping ratios were consistently less than 1% in the study. In the study, vertical distributions of VEDs in the structure that more closely resembled the vertical distribution of story stiffnesses in the undamped structure resulted in smaller differences in first mode damping ratios calculated using Equations 2.17 and 2.18 than did vertical distributions of VEDs that significantly differed from the vertical distribution of story stiffnesses in the undamped structure. Reference 42 confirms this observation independently. In low to mid-rise structures with uniform vertical distributions of VEDs, the approximation of Equation 2.18 should not result in large errors in the calculated first mode damping ratios.

The above discussion is predicated upon the structure’s being undamped prior to the addition of VEDs. In some cases, the inherent energy dissipation in a structure, particularly so long as it is responding elastically, is low enough to accommodate this assumption. However, the effects of inherent damping, which can be very complicated, may be approximated if the damping can be assumed to be distributed evenly throughout the structure. In this case, Equation 2.15 may be modified as follows [9]:

$$K = K_o + K_{dR} + i(2\xi_o K_o + \eta_v K_{dR}) \quad (2.19)$$

In Equation 2.19, ξ_o represents the inherent damping ratio in the structure. Inserting the imaginary coefficients into Equation 2.14 results in:

$$\xi_i = \xi_{oi} + \left(\frac{(\eta_v - 2\xi_{oi})}{2} \right) \left(1 - \frac{\phi_i^T K_o \phi_i}{\phi_i^T K_R \phi_i} \right) \approx \xi_{oi} + \left(\frac{(\eta_v - 2\xi_{oi})}{2} \right) \left(1 - \frac{\omega_{oi}^2}{\omega_{di}^2} \right) \quad (2.20)$$

Equation 2.20 is a more generalized form of Equations 2.17 and 2.18. If $\xi_{oi} = 0$, then Equation 2.20 reduces to Equations 2.17 and 2.18. One further simplification that is often made is to assume that all natural modes higher than the first mode contribute only negligibly to the structural response, so they are ignored in designing the VED system.

Equation 2.20 forms the basis of using the MSEM to design a VED system for a structure. The pre-VED-equipped structure is analyzed for response maxima and yielding mechanisms. If a reduced response is desired, an appropriate modal damping ratio is selected, usually based on the examination of response spectra. VED locations are selected and VEDs are sized. The individual VED storage stiffness (k_d) and loss factor (η_v) are the primary parameters used in sizing the VEDs:

$$k_d = \frac{G'A}{t} \quad (2.21)$$

$$c_d = \frac{G''A}{\omega t} = \frac{\eta_v k_d}{\omega} = \frac{\eta_v k_d}{2\pi f} \quad (2.22)$$

In Equations 2.21 and 2.22, G' , G'' , η_v and are material properties that are fully explained in Appendix D. The term c_d represents the equivalent viscous damping coefficient of the individual VED. The terms A and t represent the area of viscoelastic material that is placed in shear and viscoelastic layer thickness, respectively. The terms ω and f represent the circular and cyclic frequencies of the VED excitation, respectively.

The total added stiffness or damping at a given story level will be the sum of the horizontal components for all VEDs in the story, using Equations 2.21 and 2.22. The design process can be a trial and error procedure, but different authors have proposed various techniques to organize the procedure. Reference 1 presents a number of these approaches. Two of the primary techniques are summarized here.

The required added stiffness at a given story level may be designed in proportion to the stiffness of the original structure, in which case the MSEM may be applied at the story level. Modifying Equation 2.20 for this purpose yields [43]:

$$k_{dj} = \frac{2(\xi_1 - \xi_{ol})}{\eta_v - 2\xi_1} k_{oj} \quad (2.23)$$

In Equation 2.23, k_{dj} is the required added stiffness at the j th story level that will be contributed by VEDs; it is the sum of the horizontal components of the storage stiffnesses of all VEDs in the story. The term k_{oj} is the original story stiffness for the j th story, before adding VEDs. The damping terms, ξ_1 and ξ_{ol} , represent the desired new total (with VEDs) viscous damping ratio and the original viscous damping ratio for the first mode, respectively, assuming a response dominated by the first mode. Using Equation 2.21 and incorporating the appropriate geometric considerations to account for the horizontal component of the VED stiffness, the engineer can then design the VEDs.

Following VED design, the new modal damping ratio can be estimated using Equation 2.20, and a new dynamic analysis of the structure can be performed, or the stiffness and damping contributions of the individual VED can be modeled discretely using Equations 2.21 and 2.22.

Alternatively, the VED can be designed by developing a “damper design curve” that plots the “normalized loss factor” as a function of the VED storage stiffness and then using the curve and Equation 2.21 to design the VEDs. The “normalized loss factor” is defined as the left side of the following equation [9]:

$$\frac{2(\xi_1 - \xi_{ol})}{(\eta_v - 2\xi_{ol})} = 1 - \frac{\phi_1^T K_o \phi_1}{\phi_1^T K_R \phi_1} = \frac{\phi_1^T K_{dR} \phi_1}{\phi_1^T K_R \phi_1} = 1 - \frac{\omega_{ol}^2}{\omega_{dl}^2} \quad (2.24)$$

With known damping and stiffness properties for the original structure, a known first mode shape, a desired modal damping ratio, and a known VED loss factor (η_v), Equation 2.24 permits solving for the required VED storage stiffness. By changing the desired total viscous damping ratio and solving repeatedly for the required VED storage stiffness, the “design curve” may be constructed; it plots the normalized loss factor as a function of VED storage stiffness. In addition, Equation 2.24 may be used to determine the new (with VEDs added) first mode frequency of the structure as a function of normalized loss factor, which allows the new first mode to be plotted as a function of VED storage stiffness. Figure 2.28 exemplifies this technique using the original 3M design curve for this project (described in the following paragraphs). In this plot, the normalized structural loss factor represents the left side of Equation 2.24, while the damper

storage stiffness represents Equation 2.21. Equation 2.21 is used to derive the far right side of Equation 2.24.

In Equations 2.21 - 2.24, two basic properties of the viscoelastic material are required, the loss factor, η , and the storage modulus, G' . These are temperature, frequency, and peak shear strain-dependent. Both the natural frequency and the peak strain may be determined from the equations that have been presented here. This determination will be an iterative process that involves sizing and locating candidate VEDs, and analyzing the structure. The engineer must determine if the natural frequency of the modified structure matches that which was assumed for the material properties. Likewise, the engineer must check the actual VED shear strains against the initial assumption. Because of the variability of the viscoelastic material properties with strain amplitude, a number of suggestions have been made in the literature concerning the target shear strain amplitude. The authors of Reference 9 recommend using the material properties at a strain amplitude of 20%; they further recommend that the maximum strain amplitude not be allowed to exceed 60%. On the other hand, the authors of Reference 1 recommend designing the VED for shear strain amplitudes of 100% - 150%. These variables will be studied later in this report. The temperature of the viscoelastic material also has a significant effect on the material properties. The authors of Reference 1 recommend a target temperature of the ambient, plus 10° F, which allows for temperature increase due to structural motion.

In the design of a VED system for an actual building, other design criteria (E.G. maximum allowable story drift) may also be included.

In the design of the VED system for use in this research, Dr. M-L Lai of 3M and the author developed a structural model based on the assumed dimensions and properties of the model, which was still under construction at the time of the VED design. The columns were assumed to be uncracked, and gross cross-sectional dimensions of 5" x 5" for the interior columns and 4-1/4" x 8-1/4" for the exterior columns were used. The effective slab width to develop a "beam" model was assumed to be 14.3 inches (17.8% of the centerline distance between columns); full slab depth (2-3/8") was assumed to be effective. The concrete modulus of elasticity was assumed to be 3,420 ksi ($f'_c = 3,600$ psi). The floor weights were assumed to be 18,343 lb on each of the first and second floors, and 17,142 lb for the third floor. The column bases were assumed to be fixed.

Dr. M-L Lai used the MSEM and Equation 2.24 to design the VEDs, based on the chevron pattern that was adopted by the author. Dr. Lai assumed that the baseline structure was undamped. He targeted an ambient temperature of 24° C (75° F), and did not assume any damper temperature increase during the

simulations. VED thickness was adjusted to ensure that shear strain was $\leq 75\%$. Damper properties were based on 20% shear strain. The targeted damping ratio was 20%. The axial stiffness of the VED brace was assumed to be 10 times the VED storage stiffness; the significance of this assumption is discussed in Section 2.4. The required VED storage stiffness, k_d , was 11.86 kips/inch, based on $G' = 356$ psi and $\eta_v = 1$. This VED design resulted in a requirement for VED pads with 16.64 sq in of area in each of two 1" thick layers. With the uncracked section properties, the first mode frequency of the analytical model of the damped structure was 2.84 Hz. 3M engineers actually supplied VED with 3" x 6" pads, for a total pad area of 36 sq in for the two pads. These initial design parameters will be analyzed in Chapter 6.

2.4 VED Brace Design

Figure 2.29 details the brace elements used to link the VEDs to the structure. Figures 2.30 and 2.31 show the connections of the braces to the "collars" that were used to attach the braces to the columns. The original design, as illustrated by those figures, used a single $\frac{3}{4}$ " diameter B7 (A490) bolt as a "pinned" connection, at either end of each brace. After initial low-level seismic simulations were conducted, each brace was fixed to the adjoining gusset plate with a small spot-weld at each end, as shown in Figure A.21. The author's original intent was to permit the member to act simply as a "truss" element, with axial loading, without flexure. The initial low-level seismic simulations showed that the stiffness of the viscoelastic material in the VEDs was low enough to permit damper rotation under brace compression, so that the VEDs were largely ineffective when their linked braces were in compression. In addition, the viscoelastic material actually deformed under self-weight over time, permitting the braces to sag downward slightly. Each brace-to-gusset plate connection was therefore lightly welded. Since the VED-brace assemblies still had low flexural stiffness, all analyses were still performed using the assumption that the braces transmitted axial force only. An "insert" fabricated of the same double-angle section and the same length as the VED was also available for each brace. The inserts were used in conjunction with the braces to provide stiffness and stability during the operations to place the model on the shaking table, and, later, to remove it. Also, low-level white noise tests on the model were run with the inserts in place, to contrast the stiffness and damping characteristics of solid braces with the VED-brace assemblies.

In designing the braces, the author's intent was to remove the VED-brace interaction from consideration as a significant variable in the overall system performance. Much of the analytical research that has been performed on VED-brace systems has assumed that the stiffness of the VED-brace assembly

is identical to the stiffness of the VED alone. If the brace is not significantly stiffer than the VED, this assumption may not be valid.

The initial analysis for VED-brace interaction was based on a simplified approach. Recall the equation for the effective stiffness of two springs that are connected in series:

$$\begin{aligned} \frac{1}{k_b} + \frac{1}{k_d} &= \frac{1}{k_{bd}} \\ \therefore k_{bd} &= \frac{k_b k_d}{k_b + k_d} \end{aligned} \quad (2.25)$$

In Equation 2.25, k_b is the brace axial stiffness (AE/L), k_d is the damper storage stiffness ($G'A/t$), and k_{bd} is the effective stiffness of the two-spring system (see Appendix D for complete definitions of VED properties). The effective stiffness, k_{bd} , will be less than k_d . More significantly, if k_b is not significantly greater than k_d , assuming that all of the VED-brace deformation occurs in the VED will significantly overestimate VED deformation and consequently overestimate the VED energy dissipation, or "damping" capacity [1].

Equation 2.25 was used for the initial analysis of the VED-brace assembly. A double L 3-1/2" x 2-1/2" x 5/16" steel section was selected for the brace assembly. With a length of 57-1/4" (total pin-to-pin length, less the VED length), $k_b \approx 1800$ kips/inch (k/in). With an initially assumed k_d of 12 k/in, $k_{bd} \approx 11.92$ k/in, which is 99.3% of the initial assumption.

It is also possible to perform a more rigorous analysis to compare the VED-brace assembly damping ratio and stiffness to those of the VED alone, using the following relationships adapted from Reference 29. These equations also assume that the VED and brace are connected in series, but they include the effects of the complex stiffness modulus, G^* , which is described in Appendix D:

$$\xi = \left(\frac{\eta_v}{2} \right) \left(\frac{k_d}{\left(1 + \left(\frac{k_d}{k_b} \right) \right) (\Gamma k_d)} \right) \quad (2.26)$$

$$\Gamma = 1 + \frac{\eta_v^2 \left(\frac{k_d}{k_b} \right)}{1 + \left(\frac{k_d}{k_b} \right)} \quad (2.27)$$

The damping coefficient, ξ , and the loss factor, η_v , for the VED are described in Appendix D. If η_v is assumed to be 1.15, which is in the range of the VED test data reported in Appendix D, then $\xi = 56.6\%$ of critical damping. If the VED-brace interaction were ignored, then $\xi = 57.5\%$, using Equation D.9. The damping coefficient computed with consideration for the VED-brace interaction is 98.4% of that computed by ignoring the interaction. These calculations assume zero damping in the brace assembly.

An adaptation from Reference 29 also provides a more precise calculation for the VED-brace stiffness that accounts for the complex stiffness modulus of the viscoelastic material:

$$k_{bd} = \frac{\Gamma k_d}{1 + \left(\frac{\Gamma k_d}{k_b} \right)} \quad (2.28)$$

Using Equation 2.28 to calculate k_{bd} yields a value of 12.03 k/in.

Both the stiffness and damping properties of the VED-brace assembly are within 2% of the corresponding properties for the VED alone. These values are within the level of accuracy that can be expected for engineering analysis, so the basic VED properties without modification for VED-brace interaction were used to characterize the VED-brace assemblies.

In addition to characterizing the behavior of the VED-brace assembly for use in structural modeling, brief checks were made on the tensile and compressive strengths of the various elements of the assembly. Allowable shear stresses on the bolts at the VED-brace connection and at the “pinned” connection were checked, as were the bearing stresses on both the bolts (A490) and the connection steel (specified as A36). The limiting allowable load was that based on the bearing stress in the gusset plate at the pinned connection, which was approximately 12 kips, for an assumed yield stress of 36 ksi. If the strength of the small tack weld that was added there were also included, this load would increase. For the entire VED-brace assembly, the seismic simulations showed that the behavior of the assembly in compression was problematic. The rotational stiffness of the VEDs is not defined, so it was not possible to predict accurately a buckling load for the assembly. The buckling load for a solid length of steel brace was much higher and did not offer a practical means of comparison. The compression behavior for the VED-brace assemblies thus was a major object of test observation. The tensile capacities of the braces were limited by the shear strain behavior of the VEDs and were assumed to be approximately 12 kips, based on the limiting shear strain of 75% that was used in the design, which exceeded the predicted peak shear strain

of 62.5%.

The exact dimensions of each column and each bay were used to fabricate both the braces and the column "collars." The dimensions shown in Figures 2.29 - 2.31 are the nominal dimensions for typical members.

The collars at the brace-column connections were used to attach the braces to the columns, provide concrete confinement in the column reinforcement lap splice regions, and transmit VED brace forces into and across the columns. To ensure that concrete confinement was provided, the side plates in each column collar assembly were fabricated approximately 1/16" shorter than the measured thickness of the column. This accommodated a tight collar fit when the two 1/2" diameter A490 bolts that connected the "clip angle" on each side plate to the respective L 7 x 4 x 3/8 or 3/8" backing plate were tightened. In addition, a non-shrink grout was applied between the collar elements and the column at each connection, prior to tightening the collar bolts.

The collar assembly design was not completely balanced. The two 1/2" diameter bolts at each "clip angle" had a combined tensile capacity in excess of 20 kips, compared to the approximately 6 kips that would be carried by them due to their 50% of the total load that would be carried by the VED-brace assembly. In addition, if the outstanding "clip angle" leg is viewed as a cantilever with a concentrated load applied at the center of the bolt hole, then, with a specified yield stress of 36 ksi, the yield force for the angle leg is about 6.75 kips. No "allowable stress" or "safety" factor was applied here, because the peak VED-brace load was established at approximately 12 kips. Since it is likely that the structural steel had an actual yield stress higher than 36 ksi, the yield load for the "clip angle" is probably higher than the assumed 6.75 kips. In any case, when such a collar assembly is "scaled up" to full-scale and applied in the field, economy would dictate the use of a more balanced design. In full-scale, the selection of structural sections and associated hardware will facilitate this.

As mentioned in the description of the model in Appendix A, at each collar location, a 1/2" diameter A490 steel "all-thread" rod was cast into the model column. The side plates for each collar fit over this bolt, to prevent the assembly from slipping up (or down) along the column. Because the columns were only 4-1/4" or 5" thick, cast-in-place was chosen over drilling after casting. With two planes in shear at each column, the all-thread rods provided resistance against collar movement of over 11 kips, exceeding the vertical components of any anticipated VED-brace forces.

CHAPTER 3

EXPERIMENTAL PROGRAM

This chapter provides an overview of the viscoelastic damper (VED) testing, test structure fabrication, experimental setup and instrumentation, earthquake simulations, dynamic characterization procedures used with the simulations, and data recorded. Additional details may be found in Appendices A - D. Section 3.1 briefly describes the sinusoidal tests that were conducted on the VEDs, to determine their fundamental properties; more detailed information on the testing is provided in Appendix D. Section 3.2 briefly describes the construction of the scaled test structure; more detailed information is provided in Appendix A. This section amplifies the information found in Chapter 2 concerning the design of the model and provides a further means of comparison between the model and the prototype. In Section 3.3, the pretest setup procedure is outlined. The setup included the installation of all transducers and the supplemental lead weights. More comprehensive information is provided in Appendices A and B. Section 3.4 outlines the test procedures, keying on the earthquake simulations and the pretest and post-test dynamic characterizations that were conducted on the model. Basic characteristics of the two earthquake waveforms that were used in the simulations are presented and discussed.

3.1 Viscoelastic Damper Testing

The energy dissipation devices used in this research contain viscoelastic polymeric materials. They have properties of both *viscous* liquids and *elastic* solids when they undergo shear deformations [1]. A viscoelastic material that is placed in a sinusoidal shear loading exhibits hysteretic behavior that is described in detail in Appendix D. This behavior may be characterized in terms of stiffness and energy dissipation properties that depend on temperature, excitation frequency, and shear strain magnitude. The energy dissipation mechanism results in heating the polymer.

Considerable testing of various viscoelastic materials has been conducted and reported. The 3M *ISD 110* polymer used for the VEDs in this project has been tested extensively, and a substantial data base

on its behavior exists. Two VEDs of each size used in the earthquake simulations were tested in Newmark Civil Engineering Laboratory to validate the applicability of the data base to these VEDs. The testing consisted of deforming the VEDs sinusoidally at several different combinations of excitation frequency and peak displacement in a standard load frame. The validation testing was conducted at approximately the same ambient temperature that was expected for the seismic simulations.

Excitation frequencies of 1, 2, and 3 Hz were used in the tests to bracket the structural response frequencies that were expected in the earthquake simulations. Peak displacements corresponding to 25%, 50%, and 62.5% shear strains were attained. A waiting period of approximately 30 minutes followed each test, to permit the polymer to cool before retesting.

Figures D.3 - D.16 plot the results of these tests. Tables D.1 - D.4 summarize the test results and present calculated values for the material properties for each cycle, as well as for the average of four cycles. Table D.5 compares test data averages with published 3M data [1] that were interpolated to match the conditions under which the test data were recorded.

3.2 Test Structure Fabrication

The test model was fabricated in accordance with the requirements outlined in Chapter 2. The model was constructed at approximately one-third scale. Figures. 2.7 - 2.10 provide overall views of the structure. Its nominal dimensions are shown in Figures. 2.11 - 2.14. Details of the fabrication process may be found in Appendix A.

Most of the steel reinforcement used in the model was deformed steel wire, which is used in fabricating welded wire fabric. The wire is cold-drawn from hot-rolled low carbon steel rod. It exhibits higher yield strengths than the nominal 40 ksi of the prototype reinforcement. Prior to its placement in the model, the wire used in the slab, column, and spandrel reinforcement was annealed to lower its tensile yield stress characteristics to approximate that of the steel reinforcement in the prototype. Appendix A details the annealing procedures that were used. Following the annealing, all reinforcement was cut to length. Locally-fabricated jigs were used to bend the wire.

Model fabrication was begun by constructing a reinforced concrete base girder. The base girder was constructed on the floor of the test facility, directly adjacent to the shaking table. Figures A.4 - A.6 present key base girder dimensions. Figure A.7 shows casting of the base girder. The model was constructed atop the base girder, and the model was lifted on and off the shaking table using the base girder

for support. The base girder served as the “foundation” for the test model during the earthquake simulations. The girder was rigidly bolted to the shaking table during the earthquake simulations.

Reinforcement for the first story column bases was stubbed up from the base girder. This reinforcement may be seen in Figure A.7; its design is discussed in Chapter 2. Because the base girder was a monolithic unit and the columns were cast directly on top of it, the foundation behavior of the test structure differs from the independent behavior of the individual column spread footings found in the prototype. Concrete for the base girder and other structural elements was provided by a commercial supplier. The target 28 day compressive strength for the mix was 3,600 psi (Chapter 2). Compression cylinder strength tests showed an average unconfined compression strength of 4,990 psi at 28 days after casting.

Above the base girder, the structure was comprised of cast-in-place columns, flat slabs, and spandrel beams. Each of the three story levels was formed and cast as a monolithic unit of flat slab, spandrels, and supporting columns. For each floor level, starting with the first story columns, slab, and spandrels, a floor was formed; formwork was oiled; reinforcement was placed (Figures A.8 - A.11); and concrete was cast and finished. Longitudinal (north-south) reinforcement was placed closest to the slab surfaces in both the top and bottom reinforcement layers. Reinforcement details are provided in Figures 2.15 - 2.25.

Prior to slab concrete placement, capped brass tube lengths were placed at the intended locations for the bolts that would be used to secure lead weights on the test structure. One-half inch diameter steel all-thread bolts were extended through the columns, to secure the damper collars that would be attached externally on the columns.

Concrete was purchased from a commercial supplier and placed and finished by in-house personnel. Formwork for each floor was removed seven days after casting. A light shoring system was installed under each floor before work proceeded on the floor above. Once the shoring was in place, the formwork was re-erected for the next higher story, and the process was repeated. Following completion of all casting and removal of all formwork, each floor was shored as described above. The entire structure was painted with a thinned white latex paint, to facilitate observing crack formation and propagation.

The concrete mix design was specified as a 3,600 psi “pea gravel” mix, with superplasticizer added to enhance workability. Time-of-test compression strengths averaged approximately 5,900 psi for the three stories. Detailed material test data are provided in Appendix A.

The VED bracing system was designed for simplicity and symmetry. Since the model was two

column lines wide, bracing was used in both column lines, minimizing torsion. And, since the model was two bays deep in the direction of shaking, structural symmetry favored adding bracing in both bays. Load paths and deformation patterns were uniform. A chevron pattern was adopted, in which opposing braces would be subjected to approximately equal but opposite loadings. This configuration ensured that any differences in structural response between brace compression and brace tension would be averaged out by the opposing members. The configuration may be seen in Figures 2.9 and 2.14. The brace elements were fabricated as double-angle sections, with the angles placed back to back (Figure A.14). The braces were fabricated such that the VEDs could be inserted in the brace line and bolted in place using four bolts at each end of each VED. The brace cross-section (Figure A.14) was selected to provide an axial stiffness that was significantly larger than the shear stiffness of the VED. As detailed in Chapter 2, the bracing and the VED must be viewed as a system of structural elements in series when designing the VED, and the relative shear stiffness of the VED with respect to the brace axial stiffness must be considered.

To attach the braces to the columns, close-fitting A36 steel "collars" were fabricated to clamp tightly around the columns. See Figures A.15 - A.20. Details of the collar design are given in Chapter 2 and in Appendix A.

The original design for the collars and braces included a single $\frac{3}{4}$ " diameter bolt acting as a pin to connect each collar and brace (Figures A.15 and A.16). During the initial low-level seismic simulations, it was seen that the VED rotational stiffnesses were so low that the braces would bend substantially off the brace centerline under compressive loading, necessitating adding small tack welds between the brace ends and the collars, to prevent brace rotation.

Supplemental anchorages to the base girder were provided for the exterior columns to increase the shear capacities of those columns (Figure A.17). One-half inch diameter A490 (B7) all-thread bolts were secured in drilled holes using a commercial epoxy mix. Similar anchorage was provided for the second story exterior columns. This anchorage involved drilling into the spandrel beam, inserting a $\frac{1}{2}$ " diameter all-thread bolt, and epoxying the bolt into place (Figures A.18 and A.19).

3.3 Experimental Setup

Following the curing period for the third story concrete, the model was braced using the VED braces, with steel inserts replacing the VEDs, and the model was lifted onto the USACERL shaking table. The model was clamped to the shaking table using high strength bolts. Sufficient clamping force was

provided to develop the friction required to prevent slippage during seismic simulations. The base girder would therefore undergo the same motions that the shaking table experienced. Displacement transducers and accelerometers mounted on both the base girder and the shaking table were used to verify that no slippage occurred.

Supplemental lead weights were added to the floor slabs at each level to model gravity and inertial loads during seismic simulations. The lead weights and the weights of the slabs and columns in the model approximated the evenly distributed gravity loads of the prototype structure. Imposed live loads and other structural loads (e.g. walls) were not simulated. The total structural loading in the first and second floors of the prototype, excluding live loads, was approximately 115 psf. On the third floor, or roof, of the prototype, the loading, excluding live loads, was approximately 108 psf. In the model, the average distributed loading from the lead weights and the concrete structure was approximately 104 psf on the first and second floors, and 99 psf on the third floor. The weights were located in four rows, stacked two deep, paralleling the north-south column lines. Within those lines, the weights were distributed as uniformly as possible. Their layouts may be seen in Figures A.23 through A.28. The two-deep configuration of the weights raised the effective center of gravity for each floor slightly above the point that would result from scaling directly from the prototype. The weights were secured to the floor slabs by means of a system that ensured the weights did not move on the slab and did not stiffen or strengthen the slab. This layout is discussed in detail in Appendix A.

To protect those who worked around the model, a structural steel “safety frame” was erected to catch the model if it collapsed. The frame may be seen in Figure 2.10. It was fabricated from built-up and single structural steel members. Beam elements of the frame were inserted beneath each of the floor slabs and bolted to steel towers that rested on the shaking table reaction mass. The safety frame did not touch the model.

Test structure instrumentation was installed to record absolute accelerations, relative floor displacements, VED brace forces, VED deformations, and reinforcement strains. Details of the data acquisition system and test instrumentation are provided in Appendix B. Table B.1 lists all data acquisition channels. Figures B.2 - B.12 show the locations of all transducers.

3.4 Testing Procedure

Prior to conducting any earthquake simulations, a series of initial system characterization studies

was conducted. The structure was characterized in several different states: equipped with large dampers in each of the six braces, equipped with small dampers in the braces, equipped with steel angle inserts in the braces, and equipped with no dampers or inserts in the braces. System characterization consisted of measuring responses to low-amplitude white noise, responses to low amplitude sinusoidal motion input at first mode frequency, and responses following the release of a statically applied lateral load.

The primary testing for the model structure was a series of earthquake simulations of gradually increasing intensity. All earthquake motions were in a single horizontal direction (north-south); no vertical motions and no horizontal motions in the direction orthogonal to the direction of primary motion (east-west) were input. Following each earthquake simulation, system characterization studies and visual checks for significant structural damage were conducted. Following several of the simulations, extensive mapping of structural cracking was conducted.

Base accelerations for the earthquake simulations were modeled after the S00E component of the El Centro site accelerations of the Imperial Valley earthquake of 18 May 1940 (hereafter called "El Centro") and the S69E component of the Taft site accelerations of the Kern County earthquake of 21 July 1952 (hereafter called "Taft"). Time scales for all simulations were compressed by a factor of $\sqrt{3}$, in keeping with similitude requirements. The shaking table was operated in the displacement control mode; the acceleration records were integrated twice to generate base displacement records. With each integration, the records were corrected for drift from a zero mean. Base motion intensity was varied by changing the amplitude of the input displacements.

The El Centro and Taft records possess somewhat different frequency contents and thus permit characterization of the structure under different loading conditions.

Figures 3.1 - 3.7 demonstrate key characteristics of the compressed El Centro record. The elastic acceleration response spectrum is broad-banded, with peak responses in the period range of 0.15 sec - 0.5 sec (2 Hz - 6 Hz). The elastic displacement response spectrum is also broad-banded, with a relevant peak response in the period range of 0.5 sec - 0.6 sec (1.7 Hz - 2 Hz). Figure 3.2 shows peak Fourier amplitude spectra in the frequency range of 2 Hz - 4 Hz. While Figure 3.2 shows the characteristics of the El Centro record that was used for shaking table input, Figures 3.3 - 3.7 show the characteristics of recorded motions of the table during actual earthquake simulations using the El Centro input adjusted to various intensities. The records shown in Figures 3.4 and 3.7 (E200DL, E200N) are based on input motions that were subjected to a 0.2 Hz hi-pass filter. The record shown in Figure 3.5 (E250DL) is based on input motions that were subjected to a 0.5 Hz hi-pass filter. These filters were required to remove large displacement,

low frequency motions that exceeded the peak displacement capabilities of the shaking table. The fidelity of the measured motions as compared to the input record is high.

Figures 3.8 - 3.11 demonstrate key characteristics of the compressed Taft record. The elastic acceleration response spectrum is more narrowly banded than the El Centro spectrum, with peak responses in the period range of 0.1sec - 0.3 sec (3 Hz - 10 Hz). The elastic displacement response spectrum is also more narrowly banded than the El Centro spectrum, with relevant peak responses in the period ranges of 0.5 sec (2 Hz) and 1.0 sec (1 Hz). Figure 3.9 shows peak Fourier amplitude spectra in the frequency range of 2 Hz - 5 Hz. While Figure 3.9 shows the characteristics of the Taft record that was used for shaking table input, Figures 3.10 - 3.11 show the characteristics of recorded motions of the table during actual earthquake simulations using the Taft input adjusted to various intensities. No filtering of the Taft record was required. The fidelity of the measured motions as compared to the input record is high.

The earthquake simulation sequence for testing the structure with VEDs installed involved running a given El Centro input, followed by running a Taft input that had approximately the same ground motion intensity. To equilibrate the El Centro and Taft inputs, the intensity of the Taft record was scaled upward by the ratio of the Housner spectrum intensities [20] of the two compressed records, at a 7% viscous damping ratio, over the structural period range of 0.058 sec - 1.44 sec (Figure 3.12). The structural period range is compressed from that recommended by Housner, in keeping with the time scale compression for the records.

Thirty-six earthquake simulations of generally increasing intensity were conducted. They are listed in Table 3.1. In this table, the "span" refers to the scaling of the intensity of the compressed input record. Thus, a "100% span" for the El Centro record is the actual El Centro record, with time compression, while a "200% span" for the El Centro record indicates the acceleration amplitudes are double the original record, with time compression. Simulations E200DL and T420DL reached the peak attainable shaking table displacements without seriously damaging the model. Higher-intensity simulations would have required such heavy filtering that the similarity to the original records would have been reduced. Note that simulation E250DL resulted in a lower peak ground acceleration (PGA) than that of simulation E200DL. Following test E250DL, the VEDs were removed, and El Centro simulations were conducted again. For these simulations, the VED brace collars were left on the model, so that the only variables that were changed were the structural stiffness and damping effects of the added VEDs.

Following each simulation, a series of structural characterization tests was conducted. Initially, each series included a "pullback" test, in which a 550 lb weight was attached via a cable and pulley to the

third floor and the model was displaced laterally. Sudden release of the weight ostensibly permitted a first mode response of the model. While this worked for tests in which no VEDs were installed, the VEDs so heavily damped the motion that no motion oscillations occurred during pullback tests that included VED effects. This procedure was therefore abandoned. System characterization then consisted of measuring responses to band-limited (0 - 50 Hz), low-amplitude ($\leq 0.025g$) white noise that was input with the shaking table, and responses to low amplitude ($\leq 0.025g$) sinusoidal motion input at first mode frequency. Transfer functions of the Fourier amplitude spectra of the base and floor accelerations in the white noise tests were used for structural response frequency (maximum of three modes) and damping characterization. For the sinusoidal inputs, the first mode frequency observed in the white noise testing served as a starting point, with adjustments made in the input frequency to match the apparent resonant frequency for the model. Using logarithmic decrement calculations, the sinusoidal tests could also be used to determine the first mode damping ratio.

CHAPTER 4

OBSERVED RESPONSE OF THE TEST STRUCTURE

This chapter summarizes data on the responses of the test structure during the earthquake simulations and dynamic characterization tests that are described in Chapter 3. A detailed summary of the responses in earthquake simulations E010DL - E250DL, and E025N - E200N, is provided. Summaries of structural accelerations, displacements, shears, and overturning moments; viscoelastic damper (VED) forces and displacements; dynamic characterizations; reinforcement strains; and physical observations are provided. Chapter 5 presents a more detailed discussion of the observed responses.

Simulations T021DL - T420DL will be summarized more briefly, because the responses observed in those simulations were found to resemble closely those of simulations E010DL - E200DL, for approximately equal input motion intensities. Simulations E010DS, E025DM, E025DS, T021DS, T052DM, and T052DS will not be discussed. Those simulations were conducted while the VED braces were still pinned; the VEDs were not fully coupled into the structure and tended to deflect out of plane when their braces were in compression.

Complete response history and hysteresis plots for the recorded and derived measurements in all simulations are provided in Appendix C. In a number of instances, representative response history or hysteresis plots from Appendix C have been reprinted in this chapter to provide the reader with easily accessed illustrations. In those instances, the responses from simulations E050DL, E150DL, E050N, and E150N are shown. They contrast low and high level response for the simulations with and without VEDs, respectively. Since the El Centro and Taft responses with VEDs installed were generally quite similar, no Taft response histories are presented in this chapter.

The sequence of earthquake simulations while VEDs were installed involved an El Centro simulation followed by a Taft simulation of approximately the same input motion intensity. For example, simulations E100DL and T210DL were run sequentially. This process was repeated over the range of input motion intensities, from simulations E010DL and T021DL to simulations E200DL and T420DL. Table 3.1 lists the simulations sequentially. In the simulation titles, the first letter (*E* or *T*) designates the

source earthquake record, El Centro or Taft. The three numbers represent the magnitude of the simulation PGA, referenced as a percentage of the source record. The last letter (*DL*, *DM*, *DS*, or *N*) indicates the VED configuration. *DL* represents all large VEDs; *DM* represents mixed VEDs; *DS* represents all small VEDs; and *N* represents no dampers.

The reported maximum responses in this chapter are for the respective complete response histories. For all simulations with VEDs installed, both acceleration-related and displacement-related maxima in the El Centro and Taft simulations occurred at essentially the same elapsed times in each record. Confirmation of this may be seen in Tables 4.11 and 4.12, which will be discussed later. With VEDs removed, the maxima again occurred at essentially the same (within 0.01 sec) elapsed time in each record, through simulation E100N. In simulations E125N and E150N, the acceleration-based maxima occurred at a different elapsed time (3.50 sec) than in simulations E025N - E100N (1.84 sec). Displacement-based maxima occurred within 0.02 sec of the same elapsed time in all simulations with VEDs removed. The absence of significant changes in the times of maxima occurrence until later simulations with VEDs removed indicates a high degree of linearity in the overall response of the model.

Several of the summaries provided in this chapter use response maxima that have been normalized using the peak ground acceleration (PGA) for the relevant earthquake simulation. The author selected this portrayal as a means of examining the degree of nonlinearity that was present in the responses. Ideally, the responses of a linear structure to input motions would vary directly with their magnitudes. Variations in response that differ from variations in input motion magnitude are indications of potential nonlinearity in the system. The measured PGA is an imperfect yardstick, because of its instantaneous and measured nature. In the end, one should not overstate the accuracy of the use of PGA as means of normalization, but accept it as an indication of general trends.

The reader is reminded that the input motion was hi-pass filtered in simulation E250DL, resulting in lower PGA and correspondingly lower response measurements than those of simulation E200DL. Section 3.4 describes the filtering process.

4.1 Floor Accelerations

Floor acceleration histories for all simulations are provided in Figures C.1.1 - C.1.17, while maximum floor acceleration profiles for all simulations are provided in Figures C.1.18 - C.1.24. Figure 4.1 shows representative acceleration histories for simulations E050DL and E150DL, for the initial ten

seconds (sec) of each record, while Figure 4.2 shows the same for simulations E050N and E150N. Figure 4.3 presents maximum floor acceleration profiles for simulations E025DL - E200DL and E025N - E200N. Figure 4.4 plots maximum recorded floor accelerations vs. peak ground acceleration (PGA) for the three series of earthquake simulations; both maxima and maxima normalized by PGA are presented. Table 4.1 lists the maximum recorded and normalized (by PGA) floor accelerations.

In Figure 4.1, the overlay of the floor acceleration records for simulations E050DL and E150DL shows virtually identical responses for the two simulations, with respect to the time scale. The input record overlay also shows almost identical input acceleration characteristics with respect to the time scale. The ratios of the floor accelerations in simulation E150DL to those in E050DL are 5% - 15% higher than the ratios of the respective PGAs, with the difference increasing with floor height above the base girder. The similarities of the time scales in the records implies there is good repeatability in the inputs, and that only limited structural degradation occurred at the lower input motion intensities. The plots also show that the response is dominated by the first mode of the structure. Higher frequency base accelerations are progressively filtered out by the system with increasing floor height above the base girder.

In Figure 4.2, the overlay of the acceleration records for simulations E050N and E150N shows very similar responses for the two simulations, with respect to the time scale, until approximately 4.5 sec elapsed time, when the E150N record shows a shift to a response that has a slightly longer first mode period and more influence from the second mode. Prior to that shift, the ratios of the floor accelerations in simulation E150N to those in E050N are 15% - 20% higher than the ratios of the respective PGAs. After the shift, the relationship of the two different records is more erratic.

In Figure 4.3, the maximum acceleration profiles for the simulations with VEDs installed (E025DL - E200DL) show almost linear acceleration amplification from floor one up to floor three, which is consistent with first mode response. In simulation E025DL, the third floor acceleration is 116% of the base acceleration. By simulation E150DL, the third floor acceleration is 157% of the base acceleration. In general, for the simulations with VEDs installed, amplification from the base to the first floor is less than 3%. Some first floor acceleration deamplification occurs in simulation E200DL. The maximum acceleration profiles for simulations with VEDs removed (E025N - E200N) do not reflect amplification with height that would be consistent with first mode response. At low to mid-range input motion intensities (\leq E100N), slight amplification occurs from floor one to floor two, while deamplification occurs from floor 2 to floor 3, indicating likely occurrence of higher mode response. This trend disappears in the profiles for simulations E150N and E200N, where deamplification occurs with height. Deamplification is most

pronounced in simulation E200N, when spandrel failure occurred.

Several trends may be seen in the simulations that included VEDs. Figure 4.4, which plots the floor acceleration maxima, provides an overview. For simulations E010DL - E250DL, the following trends are noted. The maximum normalized (by PGA) first floor accelerations at the lower input motion intensities are approximately 1.0. Maximum normalized second floor accelerations at the lower input motion intensities average about 1.15. Maximum normalized third floor accelerations at the lower input motion intensities average about 1.25. Maximum normalized accelerations in the mid-range of input motion intensities ($0.25 \text{ g} < \text{PGA} < 0.65 \text{ g}$) remain relatively constant. In this range, maximum normalized first floor accelerations are about 1.0; maximum normalized second floor accelerations are about 1.2; and maximum normalized third floor accelerations are about 1.5. At the higher input motion intensities ($\text{PGA} > 0.65 \text{ g}$), maximum normalized floor accelerations reduce somewhat ($\approx 10\%$) on all three floors. For the lower intensity simulations ($\text{PGA} < 0.25 \text{ g}$) maximum Taft series responses on all floors are generally comparable to the El Centro series maxima (both are erratic). For the simulations with $\text{PGA} > 0.25 \text{ g}$, Taft maxima on all floors are consistently lower than El Centro maxima. Differences increase with floor height.

Figure 4.4 also characterizes the response of the structure in simulations E025N - E200N, when VEDs were removed. Increasing from a low input motion intensity ($\text{PGA} = 0.11 \text{ g}$) to a moderate input motion intensity ($\text{PGA} = 0.56 \text{ g}$), the maximum normalized first floor accelerations increase from approximately 1.00 to 1.14. The maximum normalized second floor accelerations increase from approximately 1.05 for the low input motion intensity to 1.2 for moderate input intensities, $\text{PGA} = 0.41 \text{ g} - 0.48 \text{ g}$. At higher input motion intensities, the maximum normalized second floor accelerations reduce to 1.07 ($\text{PGA} = 0.56 \text{ g}$). The third floor level maximum normalized accelerations parallel those of the second floor, increasing from 0.84 at the low input intensity, $\text{PGA} = 0.11 \text{ g}$, to 1.05 at a moderate input intensity ($\text{PGA} = 0.48 \text{ g}$). At higher intensities, the maximum normalized third floor accelerations reduce to 1.01 ($\text{PGA} = 0.56 \text{ g}$). In simulation E200N, when spandrel failure occurred, the maximum normalized first floor acceleration falls to approximately 0.88. The maximum normalized second and third floor accelerations reduce to 0.81 and 0.69, respectively.

4.2 Relative Story Displacements

The *relative displacement* is obtained by subtracting the measured base girder displacement from the measured floor displacement. Both measurements are made with respect to a fixed reference point.

Relative floor displacement histories for all simulations are provided in Figures C.2.1 - C.2.17, while maximum relative story displacement profiles for all simulations are provided in Figures C.2.18 - C.2.24. Figure 4.5 shows representative relative displacement histories for simulations E050DL and E150DL, for the initial 10 sec of each record, while Figure 4.6 shows the same for simulations E050N and E150N. Figure 4.7 presents maximum relative story displacement profiles for all floors for simulations E025DL - E200DL and E025N - E200N. Figure 4.8 plots maximum recorded relative displacement vs. PGA for all three complete series of earthquake simulations; both maxima and maxima normalized by PGA are presented. Table 4.2 lists the maximum recorded and normalized (by PGA) relative displacements.

In Figure 4.5, the overlay of the relative displacement records for simulations E050DL and E150DL shows virtually identical responses for the two simulations, with respect to the time scale. At the instants of maximum relative displacement, the ratios of the displacements in simulation E150DL to those in E050DL are larger than the ratios of the respective PGAs (330%, vs. 240%). The similarities of the time scales in the records implies that only limited structural degradation occurred at the lower input motion intensities. These plots also show that the response is dominated by the first mode of the structure.

In Figure 4.6, the overlay of the relative displacement records for simulations E050N and E150N shows very similar responses for the two simulations, with respect to the time scale, until approximately 4.5 sec elapsed time, when the E150N record shows a shift to a response that has a slightly longer period and lower displacement because of the period shift. Prior to the shift, the ratios of the maximum displacements in simulation E150N to those in E050N are larger than the ratios of the respective PGAs (approximately 320%, vs. 265%).

The maximum relative story displacement profiles for simulations E025DL - E200DL (Figure 4.7) show consistently increasing relative displacements with increasing PGA. For example, the PGA in simulation E200DL is 610% of that in simulation E025DL, while the third floor relative displacement for simulation E200DL is 1,147% that of simulation E025DL. The profiles reflect the same general relative displacement relationships among the three stories. The same is generally true for simulations E025N - E200N, except that, in simulation E200N, the spandrel failures cause significant displacement increases in the second and third stories. Maximum relative displacements in simulations E025N - E200N are approximately twice the relative displacements in simulation E025DL - E200DL for corresponding PGA.

In the simulations with VEDs installed, maximum normalized displacements generally become larger with higher input motion intensity. Table 4.2 and Figure 4.8 show that, at the first floor level, the maximum normalized relative displacement rises from 0.5 inches/g to 0.7 inches/g, over the sequence of

simulations. Similarly, at the second floor level, the maximum normalized relative displacement rises from 1.1 inches/g to 1.65 inches/g, and, at the third floor level, the maximum normalized relative displacement rises from 1.45 inches/g to 2.15 inches/g. For $PGA \leq 0.25$ g, the maximum normalized Taft displacements are marginally larger than the El Centro displacements for corresponding input motion intensities. Above this PGA, the maximum normalized El Centro displacements are larger than the corresponding Taft values. However, differences between the El Centro and Taft responses are minor.

Figure 4.8 characterizes the response of the structure in simulations E025N - E200N, when the VEDs were removed. At the first floor level, the maximum normalized relative displacement rises from 0.96 inches/g to 1.20 inches/g, from simulation E025N to simulation E125N. Over the same range and at the second floor level, the maximum normalized relative displacement rises from 2.48 inches/g to 3.27 inches/g, while, at the third floor level, the maximum normalized relative displacement rises from 3.48 inches/g to 4.60 inches/g. In simulation E200N, the maximum normalized displacement falls to 0.86 inches/g at the first floor, increases to 3.94 inches/g at the second floor, and increases markedly to 6.91 inches/g at the third floor. In that simulation, the upper story spandrel beam failures occurred, probably shifting the structural response enough to reduce the first story displacement. The large increases in the maximum normalized relative second and third story displacements in simulations E150N and E200N indicate substantial stiffness degradation occurred.

4.3 Interstory Displacements

The *interstory displacement* is calculated as the difference between the measured displacement of the target floor level and the measured displacement of the next lower floor level. The *interstory drift* represents, in percent, the interstory displacement divided by the story height, measured to the center of the relevant floor slabs. Respective story heights are 38.81" for the first story, and 40.00" for each of the second and third stories. While maximum relative story displacements provide helpful information on the global response of the model, interstory displacements provide more detailed insight into its response. Interstory displacement histories for all simulations are plotted in Figures C.3.1 - C.3.17, while interstory drift histories for all major simulations are provided in Figures C.3.18 - C.3.41. Maximum interstory drift profiles for all simulations are provided in Figures C.3.42 - C.3.46. Figure 4.9 shows representative interstory drift histories for simulations E050DL and E150DL, for the initial 10 sec of each record, while Figure 4.10 shows the same for simulations E050N and E150N. Figure 4.11 presents story drift profiles

for simulations E025DL - E200DL and E025N - E200N. Figure 4.12 plots maximum recorded interstory drift vs. PGA for the three series of earthquake simulations; both maxima and maxima normalized by PGA are presented. Table 4.3 lists the maximum and normalized (by PGA) interstory displacements and drift ratios.

In Figure 4.9, the overlay of the interstory drift records for simulations E050DL and E150DL shows virtually identical responses for the two simulations with respect to the time scale. At the instants of maximum interstory displacement, the ratios of the drifts in simulation E150DL to those in E050DL are larger than the ratios of the respective PGAs. Whereas the PGA ratio is 242%, the first, second, and third story ratios are 333%, 354%, and 333%, respectively. The similarities of the time scales in the records implies that only limited structural degradation occurred at the lower input motion intensities. These plots also show that the response is dominated by the first mode of the structure.

In Figure 4.10, the overlay of the interstory drift records for simulations E050N and E150N shows very similar responses for the two simulations, with respect to the time scale, until approximately 4.5 sec elapsed time, when the E150N record shows a shift to a response that has a slightly longer period and reduced amplification. Prior to that shift, and at the instants of maximum interstory displacement, the ratios of the drifts in simulation E150N to those in E050N are larger than the ratios of the respective PGAs. Whereas the PGA ratio is 265%, the first, second, and third story ratios are 309%, 334%, and 376%, respectively. More complete examination of the interstory displacement records in Appendix C shows that significant changes in response also occurred in two other simulations. At approximately 7.0 sec into simulation E125N, a slight period shift occurs. At approximately 3.25 sec into simulation E200N, a significant period shift occurs (this marked the “failure” of the model). The displacement records also show some higher mode influence; this is most obvious in the third story response. This is seen in the range of 0.5 sec - 3.5 sec of Figure 4.10.

In Figure 4.11, the story drift profiles for simulations E025DL - E200DL show larger drift increases with increased PGA at the second story level than the first story level, with drift increases with larger PGA in the third story being smallest. The story drift profiles for simulations E025N - E200N show the same general trends. Because the second and third story drift ratios were so large ($> 7\%$) in simulation E200N, those values are not plotted in Figure 4.11.

In Figure 4.12, normalized drift ratios for all simulations with VEDs installed generally increase with increasing PGA on all floors. There is no significant difference between corresponding Taft and El Centro simulation drifts. Second story displacements are consistently largest, followed in decreasing order

by first story displacements and third story displacements. At the first story level, the maximum normalized interstory displacement increases from approximately 0.45 inches/g to 0.73 inches/g, over the range of simulations. Similarly, at the second story level, the maximum normalized interstory displacement increases from approximately 0.65 inches/g to 0.95 inches/g, and, at the third story level, the maximum normalized interstory displacement increases from approximately 0.40 inches/g to 0.55 inches/g.

Following removal of the VEDs, simulations E025N - E200N were conducted. Second story displacements are again the largest, but third story displacements are larger than first story displacements. The normalized displacements generally increase with increasing PGA on all three floors. At the first story level, the maximum normalized interstory displacement increases from approximately 0.96 inches/g to 1.20 inches/g, over the range of simulations E025N - E150N. Similarly, at the second story level, the maximum normalized interstory displacement increases from approximately 1.71 inches/g to 2.08 inches/g, and, at the third story level, the maximum normalized interstory displacement increases from approximately 1.19 inches/g to 1.66 inches/g. In simulation E200N, the interstory displacements change markedly, reflecting the spandrel failures on the second and third floor levels. Interstory displacements for stories two and three increase, while those in the first story decrease.

The serviceability of the structure is significantly improved by the addition of the VEDs. Reference 31 recommends a 2% story drift limit to maintain life safety in the rehabilitation of a concrete frame, while Reference 32 recommends a 1.5% story drift limit in new construction. With VEDs installed, the structure sustained the E150DL simulation (PGA = 0.55 g) without crossing either threshold. In simulation E200DL (PGA = 0.86 g), the second story had a 2.2% drift and the first story had a 1.6% drift, slightly exceeding the recommended limits. With VEDs removed, the second story had a 1.8% drift in simulation E100N (PGA = 0.41g) and a 2.2% drift in simulation E125N (PGA = 0.41 g).

4.4 Story Shears

Inertial forces for each floor were calculated as the product of floor acceleration and floor mass. *Story shear* is defined as the sum of target floor inertial force and the inertial forces of all floors above the target floor level, at any instant. The first story shear, or *base shear*, is therefore the sum of all floor inertial forces at any instant. Because of the direct dependence of story shear on floor accelerations, trends in the story shears reflect trends in the floor accelerations, particularly in first mode-dominated response. Story shear histories for all simulations are provided in Figures C.4.1 - C.4.17, while maximum story shear

profiles for all simulations are provided in Figures C.4.18 - C.4.24. In Figures C.4.25 - C.4.31, the maximum story shear profiles are replotted, normalized by the total model weight (58.7 kips). Figure 4.13 shows representative story shear histories for simulations E050DL and E150DL, for the initial 10 sec of each record, while Figure 4.14 shows the same for simulations E050N and E150N. Figure 4.15 presents maximum story shear profiles, normalized by the total model weight, for simulations E050DL, E150DL, E050N, and E150N. Figure 4.16 plots maximum story shear vs. PGA for the three series of earthquake simulations; both maxima and maxima normalized by PGA are presented. Table 4.4 lists the maximum recorded and normalized (by PGA) story shears.

In Figure 4.13, the overlay of the story shear records for simulations E050DL and E150DL shows virtually identical responses for the two simulations, with respect to the time scale. At the instants of maximum story shear, the ratios of the story shears in simulation E150DL to those in E050DL are larger than the ratios of the respective PGAs. Whereas the PGA ratio is 242%, the first, second, and third story ratios are 263%, 275%, and 287%, respectively; amplification increases with height. The similarities of the time scales in the records implies that only limited structural degradation occurred at the lower input motion intensities. These plots also show that the response is dominated by the first mode of the structure, although some higher mode influence is visible.

In Figure 4.14, the overlay of the story shear time histories for simulations E050N and E150N shows very similar responses for the two simulations, with respect to the time scale, until approximately 4.5 sec elapsed time, when the E150N record shows a distinct shift to a response that has a slightly longer period and reduced amplification. Prior to that shift, and at the instants of maximum story shear, the ratios of the shears in simulation E150N to those in E050N are larger than the ratios of the respective PGAs. Whereas the PGA ratio is 265%, the first, second, and third story ratios are 309%, 345%, and 309%, respectively.

The story shear profiles in Figure 4.15 show that the relative distributions of story shears do not change significantly from simulation E050DL to E150DL, or from simulation E050N to E150N. Figure 4.16 shows that, for the El Centro simulations with VEDs installed, the maximum base shear rises from 5% of total model weight in simulation E010DL to 80% of total model weight in simulation E200DL. For the parallel Taft simulations, the maximum base shear rises from 5% of total model weight in simulation T021DL to 70% of total model weight in simulation T420DL. For comparable PGAs, the Taft base shears are consistently lower than the El Centro base shears. The maximum base shears for simulations with VEDs removed are substantially lower than those for simulations with VEDs installed at approximately the

same PGAs. For example, the maximum base shear in simulation E100DL is 43% of total model weight, while the maximum base shear in simulation E100N is 20% of total model weight.

The maximum normalized (by PGA) story shears in Figure 4.16 provide a summary of trends in the story shears.

The third story shear is directly related to third floor acceleration, since it is simply the product of the acceleration and the story mass. In simulations E010DL - E250DL, the normalized third story shear is approximately 40%/g for $PGA \leq 0.25$ g. In the mid-range, $0.25 \text{ g} < PGA < 0.65$ g, the normalized third story shear increases to a level of slightly over 50%/g. At $PGA > 0.65$ g, the normalized third story shear decreases to a level of about 45%/g for simulation E200DL ($PGA = 0.86$ g). Normalized Taft values are consistently lower than El Centro values for corresponding input motion intensities.

In simulations E010DL - E250DL, the normalized second story shear is approximately 80%/g for $PGA \leq 0.25$ g. The normalized second story shear rises to approximately 85%/g for the mid-range, $0.25 \text{ g} < PGA < 0.65$ g, before falling again to approximately 75%/g at $PGA > 0.65$ g. Except for the lower input motion intensities, the normalized Taft values are consistently lower than the El Centro values, for corresponding input motion intensities.

In simulations E010DL - E250DL, the normalized first story (base) shear is approximately 105%/g for $PGA \leq 0.25$ g. The normalized base shear rises to approximately 115%/g at the mid-range, $0.30 \text{ g} < PGA < 0.60$ g, before falling to approximately 90%/g at $PGA > 0.60$ g. Except for the lower input motion intensities, the normalized Taft values are consistently lower than the El Centro values for corresponding input motion intensities.

In both the second story and the base levels, the normalized shears for simulation E250DL ($PGA = 0.74$ g) are somewhat lower than for simulation E200DL ($PGA = 0.86$ g).

In simulations E025N - E200N, the story shears are consistently lower at floor levels one and two than for simulations E025DL - E200DL, even though their maximum floor accelerations are comparable. This is an indication that higher mode response is significant in the simulations without VEDs installed, so that the three maximum floor accelerations do not occur simultaneously. At the third story level, the normalized story shear rises from 25%/g to 35%/g until simulation E150N ($PGA = 0.55$ g), where it falls slightly. At the second story level, the normalized story shear rises from 40%/g to 45%/g over the range of simulations up to simulation E150N. At the first story (base) level, the normalized base shear rises from 45%/g to 55%/g over the range of simulations up to simulation E150N. In simulation E200N, the story shears at all levels fall significantly below a linear extension of the results of the lower intensity

simulations, E025N - E150N. For example, the normalized base shear reduces from 55%/g in simulation E150N to 38%/g in simulation E200N.

4.5 Story Shear Vs. Displacement Relations

Plots of the story shear vs interstory displacement for all earthquake simulations may be found in Figures C.5.1 - C.5.17. These plots provide indications of the energy dissipation, or hysteresis, and stiffness characteristics in each story. Plots of the base shear vs third story displacement for all earthquake simulations may be found in Figures C.6.1 - C.6.5. These plots provide indications of the global hysteresis characteristics of the three stories acting as a system. Figure 4.17 plots story shear vs. interstory displacement for simulations E050DL and E150DL, and Figure 4.18 shows the same for simulations E050N and E150N.

For the simulations E010DL - E250DL and T021DL - T420DL, the hysteresis loops are broad, indicating good energy dissipation, and smooth, indicating only minimal stiffness changes occurred in each simulation. Moreover, within each series, sequential events appear to be almost linearly larger than previous ones, indicating that structural response remains very close to linearly elastic. This is illustrated in the story shear vs. interstory displacement plots for simulations E050DL and E150DL (Figure 4.17). By contrast, the results for simulations E025N - E200N show very tight, pinched hysteresis loops, indicating low energy dissipation. This is illustrated in the story shear vs. interstory displacement plots for simulations E050N and E150N (Figure 4.18). In addition, the higher stiffness of the structure with VEDs installed may be seen in the higher slopes of the hysteresis plots of the simulations that included VEDs. This will be studied further in Chapters 5 and 6.

4.6 Overturning Moments

Overturning moments (OTMs) for each floor level were calculated as the sum of the products of the floor accelerations, floor masses, and the distances from floor centers of mass to the reference location for calculating OTM, for each floor above the reference location. The reference locations were the top of the base girder, for base moment; the top of the first floor slab, for first floor moment; and the top of the second floor slab, for second floor moment. Floor masses and distances from the top of the base girder to the floor centers of mass are listed in Table A.5. Plots of the maximum OTM profiles for all earthquake

simulations may be found in Figures C.7.1 - C.7.7. Figure 4.19 plots the OTM profiles for simulations E050DL, E150DL, E050N, and E150N. Figure 4.20 plots maximum OTM vs. PGA for all three series of earthquake simulations; both maxima and maxima normalized by PGA are presented. Table 4.5 lists maximum OTMs, and maximum OTMs normalized by PGA, for each floor and each simulation.

The OTM profiles in Figure 4.19 show that the relative distributions of OTMs change little from simulation E050DL to E150DL, and from simulation E050N to E150N. The OTMs on all floors in simulation E150DL are about 275% of those in simulation E050DL. The base and floor 1 OTMs in simulation E150N are about 345% of those in simulation E050N, while the floor 2 OTM in simulation E150N is about 315% of the OTM in simulation E050N.

Figure 4.20 summarizes OTM trends for all of the earthquake simulations.

For both the El Centro and Taft simulations with VEDs installed, maximum normalized base and first floor OTMs are inconsistent when the $PGA < 0.25$ g, while the maximum normalized second floor OTMs are relatively constant at approximately 1,000 inch-kips/g (in-k/g). For the mid-range simulations, $0.25 \text{ g} < PGA < 0.65 \text{ g}$, the maximum normalized OTMs for all simulations with VEDs installed are relatively constant. The normalized maximum El Centro simulation OTMs are approximately 5,500 in-k/g, 3,300 in-k/g, and 1,100 in-k/g, for the base, first floor, and second floor, respectively. Corresponding normalized maximum Taft OTMs are somewhat lower. For simulations with the $PGA > 0.65 \text{ g}$, the maximum OTMs for both the El Centro and the Taft simulations reduce about 12% - 15% at the base and first floor levels, and about 6% for the second floor level.

For the simulations with VEDs removed, the maximum normalized OTMs increase about 33% at the base and first floor levels, and about 24% at the second floor level, over the series of simulations, through simulation E125N ($PGA = 0.48 \text{ g}$). At the base level, the increase is from 2,100 in-k/g to 2,800 in-k/g. At the first floor level, the increase is from 1,400 in-k/g to 1,900 in-k/g. At the second floor level, the increase is from 640 in-k/g to 800 in-k/g. In simulation E150N ($PGA = 0.56 \text{ g}$), normalized OTM magnitudes level off at about the same magnitudes as those of simulation E125N. In simulation E200N, when spandrel failure occurred, OTMs reduce about 40%.

4.7 Viscoelastic Damper (VED) Performance

There were four large VEDs installed at each floor level during simulations E010DL - E250DL and T021DL - T420DL. The structural configuration ensured that, at each floor level, shear deformations

of the two VEDs on the north side of the model opposed those of the two VEDs on the south side of the model. Both force and shear deformation were recorded for each VED in each simulation. VED force was measured via a strain gage bridge on one leg of each VED brace (Section B.2.(d)). VED shear deformation was measured by a linear variable displacement transducer (LVDT) that was bridged across each VED (Section B.2.(c)). For all simulations with VEDs installed, Figures C.8.1 - C.8.46 plot VED force histories, Figures C.9.1 - C.9.46 plot VED shear deformation histories, and Figures C.10.1 - C.10.46 plot VED force-deformation hystereses. Figures 4.21 - 4.24 plot the VED hystereses for simulations E050DL and E150DL, illustrating the trends found in the testing. The plots show the variation of the VED responses at the various locations in the model; the different VEDs tend to show individual damping and stiffness characteristics.

To analyze the general performance of the VEDs as they acted as a system at each story level, the maximum sums of the horizontal components of the VED forces (using the undeformed geometry of the structure at each level) were calculated and are presented. The horizontal component of the VED force corresponds closely to the story shear, and thus provides a means to compare the VED force with total inertial force in the structure. Figures C.11.1 - C.11.5 provide profiles of maximum story shears vs. the maximum sums of the horizontal components of the VED forces for all simulations with VEDs installed. Figure 4.25 provides profiles of maximum story shears and the maximum sums of the horizontal components of VED forces, for simulations E050DL and E150DL. Figure 4.26 plots the maximum sums of the horizontal components of VED forces vs. PGA; both maxima and maxima normalized by PGA are presented. Figure 4.27 plots the sums of the horizontal components of VED forces, as a fraction of the corresponding maximum story shears, vs. PGA, both at the time of maximum story shear and at the time of maximum damper force sum. Table 4.6 lists the maximum recorded and normalized (by PGA) sums of horizontal components of VED forces. Table 4.7 lists the maximum recorded story shears and corresponding sums of the horizontal components of VED forces, at the time of maximum *negative* story shear, as plotted in the story shear histories (Figures C.4.1 - C.4.9). Table 4.8 lists the maximum recorded story shears and corresponding sums of the horizontal components of VED forces, at the time of maximum *positive* story shear, as plotted in Figures C.4.1 - C.4.9. Table 4.9 lists the maximum recorded story shears and corresponding maximum sums of the horizontal components of VED forces that occur immediately before the maximum *negative* story shear occurs. Table 4.10 lists the maximum recorded story shears and corresponding maximum sums of the horizontal components of VED forces that occur immediately before the maximum *positive* story shear occurs. Tables 4.11 and 4.12 list elapsed times for

the story shear, VED force sum, and interstory displacement maxima.

In Figures 4.21 - 4.24, the VED hysteresses show general repeatability in scaling the responses up from simulation E050DL to simulation E150DL. There is variation in the behaviors of the four different VEDs at each story level. For example, in Figure 4.21, comparing the plots for the NW and NE VEDs on the first story shows a higher slope, or stiffness, for the NE VED than for the NW VED. In general, the VEDs on the south side of the model exhibit lower stiffness than the VEDs on the north side of the model, as evidenced by the slopes of the plots. The third story VEDs exhibit almost zero net slope, indicating that they have low stiffness. Energy dissipation characteristics, as evidenced by the areas enclosed by the loops, appear more uniform at each story level than the stiffness characteristics. More energy is dissipated in the first and second stories than in the third story. Figures 4.21 and 4.23 also show an anomaly at the second story level that appears throughout the data: the displacements measured in the NE VED are consistently 15% - 20% larger than those measured in the NW VED. The variations in VED characteristics will be explored more fully in Chapter 5.

The plots of the distributions of the maximum sums of the horizontal components of the VED forces by story level (Figure 4.25, Table 4.6) show that the second story VEDs carry about 4% higher total force than those of the first story in the El Centro simulations. This differential increases to 7% in the Taft simulations.

Figure 4.26 and Table 4.6 show that, for the El Centro simulations, the maximum sums of the horizontal components of the VED forces normalized by PGA increase significantly for all floors for successive simulations through $PGA = 0.55$ g (E150DL). For example the normalized sums increase by 21%, 28%, and 38% for the first, second, and third stories, respectively, from simulation E050DL to simulation E150DL. For simulations E200DL and E250DL, the third story normalized VED force sum remains elevated, while the corresponding normalized first and second story sums reduce about 8%. As the reinforced concrete structure accrues damage and softens, the VEDs attract higher percentages of total story shear. By contrast, for the Taft simulations, the maximum sums of the horizontal components of the VED forces normalized by PGA remain relatively constant on all story levels for all simulations. With increasing PGA, normalized El Centro sums become correspondingly larger than the Taft sums.

The plots of the ratios of sums of the horizontal components of the VED forces to the story shear at the instants of the positive and negative story shear maxima vs. PGA (left column of Figure 4.27, Tables 4.7 and 4.8) show high variability in the ratios; data are scattered.

More consistency is seen in the plots of the ratios of the maximum sums of the horizontal

components of the VED forces at the instants of maximum VED force sum vs. PGA (right column of Figure 4.27, Tables 4.9 and 4.10). In both the El Centro and Taft simulations, the VEDs assume a larger percentage of the story shear with increasing PGA, for the times of both reported story shear maxima, for all stories. In the Taft simulations, there is less consistency, and the increase is less pronounced. In the El Centro simulations, the percentage of the story shear assumed by the VEDs is about 15% higher at the time of the positive story shear maximum than at the time of the negative story shear maximum, for the first story. On the second story, the percentage of the story shear assumed by the VEDs is about the same for the two story shear maxima. For the third story, the percentage of the story shear assumed by the VEDs is about 15% higher at the time of the negative story shear maximum than at the time of the positive story shear maximum. In the Taft simulations, the percentage of the story shear assumed by the VEDs is consistently higher at the time of the positive story shear maximum than at the time of the negative story shear maximum, for all three stories; the differential averages about 15% on the first two stories and under 5% on the third story level.

In the El Centro simulations, both reported story shear maxima occur very early, at approximately 1.1 and 1.3 sec elapsed time, and in the same oscillatory cycle of structural motion. These maxima occur without significant prior oscillations. In the Taft simulations, both reported story shear maxima occur somewhat later and further apart in elapsed time, at approximately 4.6 and 6.3 sec elapsed time, respectively. The maximum that occurs at approximately 6.3 sec elapsed time, is preceded by at least two complete significant force - displacement cycles. The relative magnitudes of VED forces may be partially explained by the tendency for both VED stiffness and damping properties to degrade with sustained excitation. This will be explored in Chapter 5.

The El Centro story shear maximum that occurs at 1.3 sec elapsed time is 30% - 40% larger than the story shear maximum that occurs at 1.1 sec elapsed time, with correspondingly higher interstory displacements. The Taft story shear maximum that occurs at 6.3 sec elapsed time is 5% - 15% larger than the story shear maximum that occurs at 4.6 sec elapsed time. The relative magnitudes of VED forces may also be partially explained by the shear strain dependency of the VED stiffness and damping properties. This too will be explored in Chapter 5.

Tables 4.11 and 4.12 show that times of maximum VED force sums consistently precede maximum story shear times by 0.02 - 0.04 sec, and times of maximum interstory displacement by 0.04 - 0.06 sec, showing the phase angle between force and deformation that is characteristic of viscoelastic materials. Examination of the times at which individual floor maxima are reached also typically shows a

small time lag (0.02 - 0.04 sec) between the first floor maxima and the third floor maxima, with second floor maxima times occurring between the other two.

4.8 Column Shears

In simulations with VEDs installed in the model, for any given story, the total story shear above the exterior column collars in a story is carried by a combination of the horizontal components of the VED brace forces and the sum of the column shears in the model above the collars. The total *column shear* was estimated by subtracting the sum of the horizontal components of the VED forces from the total story shear, in each story. There was no direct measurement of column shear. Figures C.12.1 - C.12.13 plot column shear histories for all simulations with VEDs installed. Figures C.13.1 - C.13.13 plot column shear vs. interstory displacement hysteresses for all simulations with VEDs installed. Figures C.13.14 - C.13.18 plot maximum column shear and maximum story shear profiles for all simulations with VEDs installed.

Figure 4.25 (already reported above) provides profiles of maximum story shears and maximum column shears, for simulations E050DL and E150DL. Figure 4.28 plots the maximum column shear vs. PGA; both maxima and maxima normalized by PGA are presented. Table 4.13 lists the maximum column shears, and maximum column shears normalized by PGA, for each floor and each simulation. In the series E025N - E200N, the column shear is the same as the story shear, since no braces were used, so those maxima are not repeated.

Figure 4.25 indicates that, with higher PGA, the maximum column shear decreases slightly as a portion of the maximum story shear, at all three floor levels. For example, in simulation E050DL, the maximum first story column shear is 67% of the maximum base shear, while, in simulation E150DL, the maximum first story column shear is 64% of the maximum base shear. *The reader is reminded that, because of the phase angle between VED force and deformation, the maximum column shear and the maximum sum of the horizontal components of the VED forces do not occur simultaneously.*

The maximum normalized (by PGA) column shears in Figure 4.28 and Table 4.13 are inconsistent at all story levels for simulations with $PGA < 0.25$ g. For the mid-range, $0.25 \text{ g} < PGA < 0.60 \text{ g}$, normalized column shears are almost constant: the normalized first story column shear is about 40 kips/g for both series; the normalized second story column shear averages about 28 kips/g for the El Centro simulations; and, the normalized third story column shears average about 25 kips/g for the El Centro

simulations. Taft simulation column shears are somewhat lower than corresponding El Centro column shears. For $PGA > 0.60$ g, the normalized column shears drop significantly on all story levels. For example, the normalized first story column shear drops from 42 kips/g in simulation E150DL to 32 kips/g in simulation E200DL; reductions in the Taft simulations are similar.

4.9 Comparisons of Story Shear, Column Shear, and Sums of Horizontal Components of Damper Forces

Figures C.14.1 - C.14.17 overlay the story shear, column shear, and the sum of the horizontal components of VED forces, for simulations E010DL - E250DL and T021DL - T420DL. The overlays cover the 4 sec periods of elapsed time during which maximum system forces occur. Figures 4.29 and 4.30 replot the overlays for simulations E050DL and E150DL. They illustrate the repeatability of successively higher intensity simulations and the relationship among VED forces, column forces, and story shears. The portion of total story shear that is borne by the VEDs is constantly changing. The phase angle that exists between VED force and shear deformation causes VED force to peak before story shear peaks. Column shear peaks after story shear peaks. There are instants when the sum of the horizontal components of VED forces is algebraically opposite in sign to the story shear.

4.10 Relative Floor Velocities

Viscous damping is often modeled using a linear viscous damper, or “dashpot,” in which damper force is the product of a viscous damping coefficient, c_d , and damper excitation velocity. One approach to analyzing the contribution of a VED to structural response involves substituting a dashpot and spring for the VED in the mathematical model of a structure (Section 2.3). It is therefore helpful to examine VED deformation velocities. Since the VEDs are mounted in diagonal braces in the structure, their deformation velocities are directly related to the relative velocities of the adjacent floor levels through the geometry of the structure at each story level. *Relative floor velocities* were derived by integrating the acceleration records for the base and each floor, to calculate base and floor velocities, and then subtracting the velocities for the floor level immediately below the floor being analyzed from the velocities for that floor. For example, to derive the relative velocity of floor 3 with respect to floor 2, the velocity of floor 2 was subtracted from the velocity of floor 3. To eliminate the tendency for the integrated velocity values to drift from zero at the end of a simulation, tenth order curve fits of the acceleration histories were subtracted

from them before the integration was performed. This procedure in effect subtracted the “average” of each acceleration record from itself, removing the tendency for the integrated velocity to drift from a zero baseline.

Relative floor velocity histories for all simulations are provided in Figures C.15.1 - C.15.17. Figure 4.31 replots the relative floor velocities for simulations E050DL and E150DL, to illustrate the trends found in the testing. Figure 4.32 plots the maximum relative floor velocities vs. PGA for simulations E010DL - E250DL and T021DL - T420DL; both maxima and maxima normalized by PGA are presented. Table 4.14 lists the maximum relative floor velocities, and maximum relative floor velocities normalized by PGA, for each floor and each simulation.

Figure 4.31 shows good repeatability from simulation E050DL to simulation E150DL, reaffirming the dominance of linearity in the response; the figures also show the dominance of the first mode of the structure, as the relative velocities for all floors are largely mirror images of one another in any given test. The figure also shows that there are significant periods of low relative velocity.

Figure 4.32 and Table 4.14 show that the normalized relative velocities are 15% - 25% higher in the El Centro simulations than in the Taft simulations. There is also a general tendency for the normalized relative velocities to increase with increasing PGA in both series. This is more pronounced for the El Centro simulations than for the Taft simulations. The relative velocity of floor 2 with respect to floor 1 is 20% - 50% higher than the relative velocity of floor 1 with respect to the base, with the differential generally increasing with PGA. The relative velocity of floor 3 with respect to floor 2 is smaller than the other two relative velocities.

4.11 Dynamic Characterizations of Model

Several types of low-level dynamic characterizations were performed on the model. These tests were used to determine modal frequencies and damping ratios, which could be used to assess structural deterioration and assist with analytical modeling. Several specific dynamic characterization tests were performed, including low-level white noise testing and pullback testing of the model (see Section 3.4). White noise tests (WNTs) were conducted often during the research program, including before any earthquake simulations were begun, and after each major earthquake simulation. For the WNTs, acceleration-based *transfer functions* were calculated, from which modal frequencies and damping ratios could be calculated. Section C.2.(k) provides background on the derivation and use of these transfer

functions (TFs), including application of the half-power bandwidth method for determining the modal damping ratios. Following each WNT, from which the model's first mode frequency was determined, the shaking table was used to excite the model at the observed first mode frequency, at a low acceleration amplitude. After an approximately resonant condition was reached, the shaking table actuators would be stopped. The structure's decreasing oscillations could then be used to calculate the first mode damping ratio using the logarithmic decrement method. The final dynamic characterization method that was used was a "pullback" test. A 550 lb static lateral force was applied at the top floor level, forcing the model to displace laterally. The displaced shape was assumed to approximate the first mode shape of the structure. The weight was suddenly released. The resulting oscillating motions, and their decay, could be used to measure the first mode frequency and its viscous damping coefficient using the logarithmic decrement method. The sinusoidal and pullback tests were relatively ineffective, because the large amount of damping imparted by the VEDs so quickly damped out the low-level free oscillations. Because of their relative ineffectiveness, those tests were abandoned early in the program. While summary data on those methods are provided here, they are not discussed.

In addition to specific dynamic characterization tests, TFs for the acceleration records and Fourier Amplitude Spectra (FAS) for the interstory displacement records were calculated for selected earthquake simulations.

Second and third floor TFs for all major earthquake simulation acceleration histories are shown in Figures C.16.1 - C.16.6. FAS of the interstory displacement records for all major earthquake simulations are shown in Figures C.16.7 - C.16.19. Second and third floor TFs for all WNTs are shown in Figures C.16.20 - C.16.25. Free vibration test results are shown in Figure C.16.26, and pullback test results are shown in Figure C.16.27. To illustrate the trends found in modal characterizations, Figure 4.33 plots the third floor TFs for simulations E050DL, E150DL, E050N, and E150N; Figure 4.34 plots first mode frequency, period, and damping ratio, as a function of PGA, for all major earthquake simulations; Figures 4.35 and 4.36 plot the FAS from the interstory displacement records for simulations E050DL, E150DL, E050N, and E150N; and, Figure 4.37 plots the third floor TFs for WNTs that were conducted in conjunction with simulations E050DL, E150DL, E050N, and E150N. Table 4.15 lists the calculated modal properties based on the third floor TFs from the earthquake simulations. Table 4.16 lists the calculated modal properties based on the second and third floor TFs from the WNTs. Tables 4.17 and 4.18 list free vibration and pullback test results.

(a) Earthquake Simulation-Based Transfer Functions

For the simulations with VEDs installed, only the first mode is clearly discernable in the TF plots (Figure 4.33). The dynamic amplification from the base to the third floor for the first mode is approximately two. Figure 4.33 shows a lowering of the first mode frequency from simulation E050DL to simulation E150DL. Figure 4.34 summarizes the trends found over the series of simulations. For $PGA \leq 0.25$ g, the structure responds at a first mode frequency of approximately 2.9 Hz. The TFs for these simulations are quite noisy, as the measured acceleration signals are very small and on the same order as the electronic noise that is present. For the mid-range of $0.25 \text{ g} < PGA < 0.65 \text{ g}$, the first mode frequency exhibits a gradual reduction from about 2.6 Hz to 2.4 Hz. At $PGA > 0.85 \text{ g}$, the first mode frequency reduces to approximately 1.9 Hz. El Centro and Taft frequencies are very similar.

The approximate nature of the half-power bandwidth method using the TFs derived from the data smoothing process inhibit detailed observations about the first mode equivalent viscous damping ratios. There is scatter in the calculated first mode damping ratios, but they average about 38% of critical damping, with no distinct trend with respect to increasing PGA. El Centro and Taft damping ratios are very similar.

For the simulations with VEDs removed, Figure 4.33 shows clearly the first two response modes, while a third mode also appears to be discernable. Figure 4.33 shows clear peaks for modes one and two in simulation E050N. In simulation E150N, both of the first two mode frequencies reduce somewhat, and their dynamic amplifications have also reduced. In the second mode, the TF bandwidth broadens and becomes irregular, with lower dynamic amplification, indicating that damage has occurred.

Figure 4.34 and Table 4.15 show that, for simulations E025N - E150N, the first mode frequency lowers from 1.29 Hz to 1.09 Hz, indicating stiffness degradation occurs. For simulation E200N ($PGA \approx 0.98 \text{ g}$), there is a more substantial reduction, to 0.76 Hz. During simulations E025N - E150N, the apparent first mode viscous damping ratio lowers slightly, from approximately 8% to approximately 5% of critical damping. The damping ratio was higher for simulation E200N, approximately 17%, paralleling the large amount of inelastic behavior that occurred in that simulation.

The fidelity of the TF in the second mode bandwidth after simulation E075N is poor, inhibiting accurate measurements. The measured second mode frequency in simulations E025N - E075N reduces from 4.96 Hz to 4.59 Hz; after simulation E075N, precise measurement is difficult. In simulation E200N, there is a substantial reduction, to 3.48 Hz. Damping ratios are likewise imprecise, but the data indicate

that second mode damping is on the order of 1- 4 % of critical damping.

Third mode frequency changes parallel those of the first mode. From simulation E025N to simulation E150N, the measured third mode frequency reduces from 9.30 Hz to 7.83 Hz. In simulation E200N, the third mode frequency drops substantially, to 5.04 Hz. Third mode damping is approximately 1 - 2 % of critical damping. The TF bandwidth is broad, and dynamic amplification is small, making damping measurements imprecise.

(b) Interstory Displacement-Based Fourier Amplitude Spectra

Fourier amplitude spectra (FAS) of the interstory displacements in each earthquake simulation were calculated, corroborating the acceleration-based TF calculations.

FAS for simulations with VEDs installed indicate that most of the energy in the structure is banded over the frequency range of 1 - 4 Hz (Figure 4.35). In simulations E200DL, E250DL, and T420DL, the banding narrows to a range of 1 - 3 Hz. Peak Fourier amplitudes occur at frequencies of 2.0 - 2.5 Hz in simulations E010DL - E150DL and 2.0 - 2.75 Hz in simulations T021DL - T315DL. In simulations E200DL, E250DL, and T420DL, the 2.0 Hz peak becomes more pronounced, indicating some softening of the structure occurs.

FAS of simulations E025N - E200N (Figure 4.36) clearly delineated first mode peaks. The peak occurs at approximately 1.50 Hz in simulation E025N, 1.10 Hz in simulations E050N - E100N, 1.05 Hz in simulations E125N and E150N, and 0.80 Hz in simulation E200N. The lowering of the first modal frequency indicates deterioration of the model occurs.

(c) White Noise Test-Based Transfer Functions

An initial WNT evaluated the model with steel inserts replacing the VEDs in all braces. The inserts were fabricated of the same double-angle sections used for the braces. While the steel inserts were not used for the earthquake simulations, the dynamic characteristics of the model in this configuration could be used to develop an analytical model of the structure with braces added for stiffening, but with no increased damping in the structure (one alternative to adding supplemental damping in an actual application is such stiffening). This WNT indicated that the first mode dominated the structural response, with a modal frequency of 8.38 Hz. First mode damping was calculated as 3.9% of critical damping.

For the simulations with VEDs installed, the response is dominated by the first mode of the model. There is no clear evidence of the second or third modes. The WNTs show a generally decreasing first mode frequency with successively higher input motion intensities. First mode damping ratios are inconsistent, but they are typically under 30%. Since all of the WNTs were conducted at low input acceleration amplitudes, the TFs from the WNTs with the VEDs installed, with their relatively small dynamic amplification of about two at the third floor level, were often dominated by electronic noise, making detailed interpretation difficult. Figure 4.37 shows the WNT-based third floor TFs for simulations E050N and E150N. Table 4.16 lists the modal properties that were determined in the WNTs.

Prior to commencing seismic simulations, with no VEDs or steel braces installed on the model, WNTs showed a first mode frequency of 1.88 Hz. Following completion of all simulations with VEDs installed and removal of the VEDs, the first mode frequency as measured by the WNTs dropped to 1.63 Hz. Since frequency is a function of the square root of the stiffness, this drop indicates a stiffness reduction of approximately 23%. Damping measured by the WNTs had increased from 6.7% of critical to 7.7% of critical damping. The increased damping and reduced first mode frequency indicate some damage had occurred in the model during the tests with VEDs installed. The observed second and third mode frequencies as measured by the WNTs also decreased somewhat from the baseline condition to the condition found immediately before simulation E025N. During simulations E025N - E150N, WNTs show a general reduction in first mode frequency, from 1.63 Hz to 1.41 Hz. The second and third mode frequencies also decrease, from 5.63 Hz to 5.03 Hz and 9.88 Hz to 9.25 Hz, respectively. The first mode damping ratio measured at the third story level remains relatively stable, at approximately 7% - 9% of critical damping, through the WNT following simulation E125N. The half-power bandwidth method for calculating damping is less sensitive to bandwidth and amplification precision for higher frequencies, so the damping ratios for the second and third modes do not change significantly. Dynamic amplification for the first mode frequency decreases in successive tests, until the test following simulation E150N. The decrease is more pronounced on the second floor level than it is on the first floor level.

4.12 Reinforcement Strains

Several reinforcing bars in the model were instrumented with strain gages. Column bar gages were located in bar lap splice and potential yield regions in the first two stories. First floor slab reinforcement gages were placed near the column lines to assist in determining the effective slab width for flexural

calculations. Figures B.9 - B.12 show active gage locations. Figures C.18.1 - C.23.12 plot strains for active gages. Tables 4.19 - 4.27 list maximum and residual reinforcement strains for each simulation. In each table, the approximate yield strains (f_y/E) for the reinforcing bars are also listed, and strains above yield are highlighted in bold font. Gravity load-based strains have been subtracted from each record. Each strain gage channel was set to zero strain before each simulation, so accumulated residual strains are not included in the dynamic strains. This section summarizes significant observations from the strain gage data.

(a) Column Reinforcement

Two gages, *SGZ1* and *SGZ4*, were located on reinforcing bars at the base of the model. *SGZ1* was in the NW column, and *SGZ4* was located in the west centerline column. In the NW column gage, tensile yielding occurs in simulations E125DL - E200DL, T315DL, and E150N - E200N. In the centerline column, the gage shows elastic behavior for all simulations but E200N. The strain records also indicate that bar slip occurs in the column bases.

Two gages, *S1Z1* and *S1Z3*, were located on reinforcing bars directly below the first floor slab. *S1Z1* was located in the NW column. *S1Z3* was located in the west centerline column. In the NW column gage, tensile strains remain below yield, but compressive strains increase significantly in simulations T315DL, E200DL, and T420DL, reaching yield in simulation E200DL. In the centerline column gage, tensile strains are below yield, while compressive yield strain is exceeded in simulations E200DL, T420DL, and E050N and higher.

Four gages, *S1Z5*, *S1Z6*, *S1Z7*, and *S1Z8*, were located at the bases of the second story columns. *S1Z5* was on the outside middle reinforcing bar in the NW column. *S1Z6* was located on the inside middle reinforcing bar in the NW column. *S1Z7* was located on one of the north face reinforcing bars in the west centerline column. *S1Z8* was located on one of the south face reinforcing bars in the west centerline column. Compressive strains in gage *S1Z5* grow faster than input motion intensity, and compressive yield strain is reached in simulations E150N and E200N. Peak tensile strains remain below yield. In gage *S1Z6*, compressive yield strains are reached in simulations E125N - E200N. Tensile strains measured by both *S1Z5* and *S1Z6* indicate that slip occurred with higher input motion intensities. At the centerline, gage *S1Z7* registers no yielding. In simulations E100N - E200N, tensile slip increasingly occurs, and the strain histories become increasingly dominated by compression. Maximum strains drop from simulation

E150DL to E200DL and from simulation T315DL to T420DL. Strains measured by gage S1Z8 are on the same order as those measured by gage S1Z7, except that compressive yield is slightly exceeded in simulation E200N. Higher frequency signals indicate that bar slip occurred.

Two gages, S2Z2 and S2Z3, were located directly below the second floor slab. S2Z2 was located on an inside middle reinforcing bar in the NW column. Strains measured by gage S2Z2 exceeded yield in simulations E075DL - T420DL and E050N - E100N. The gage did not function for simulations E125N - E200N. S2Z3 was located on one of the north face reinforcing bars in the west centerline column. Strains measured by S2Z3 exceeded yield in simulations E200DL and E125N - E200N.

(b) Slab Reinforcement

All slab reinforcement gages were located on bars in the top layer of longitudinal reinforcement. Gages S1X5, S1X14, and S1X16 are on first floor slab reinforcing bars on the north side of the west centerline column (Figures B.9 and B.11). S1X5 is in the slab "column strip." Measured strains do not exceed yield. In simulations E075DL - T315DL and E025N - E200N, maximum strains are constant. In simulations E200DL and T420DL, strains reduce markedly from previous maxima. S1X14 is approximately 4-½" east of gage S1X5, but still in the slab "column strip." Commencing in simulations E100DL and T210DL, peak tensile strains significantly exceed those of gage S1X5. In simulations E025N - E125N, strains are dominated by tension. Tensile strains are ten times those found in gage S1X5. Tensile yield strain is exceeded in simulations E200DL, T420DL, and E075N - E200N. S1X16 is approximately 24-¼" east of gage S1X5, in the slab "middle strip." Measured strains remained below yield in all simulations and were significantly lower than the strains measured at gages S1X14 and S1X15. In simulations E200DL and T420DL, compressive strains increase significantly, while tensile strains are approximately the same as those of simulations E150DL and T315DL.

Gages S1X11, S1X12, and S1X13 are on reinforcing bars in the first floor slab adjacent to the NW column (Figures B.9 and B.10). S1X11 is located within the spandrel beam width, in the slab "column strip." Measured strains remained below yield. S1X12 is located approximately 7-½" east of gage S1X11, at the interface of the slab and the spandrel beam, still in the slab "column strip." Measured strains increasingly exceeded yield in simulations E075DL - T420DL and E050N - E200N. S1X13 is approximately 17-¼" east of gage S1X11, at the interface of the slab and the spandrel beam, and in the slab "middle strip." Tensile strains are consistently small, while compressive strains are significantly

larger. Measured strains remained below yield.

4.13 Observed Condition of Structure

Researchers mapped surface cracking of the model several times during the testing series. The surface condition of the concrete supplements the acquired data in assessing the performance of the structure. Figures 4.38 - 4.67 map the progression of cracks and spalled areas at three different times: prior to testing, following simulation T420DL, and following simulation E200N. Figures 4.68 - 4.86 are photographs of key locations on the model following simulation E200N. Permanent ink markers were used to mark the cracks, so the crack widths in the photographs are not as large as they appear.

Figures 4.38 - 4.47 map the crack patterns on the model prior to any earthquake simulations. These figures document damage that accrued when a spurious horizontal actuator motion occurred during initial system checkout, causing a brief yawing oscillation of the shaking table. No data acquisition channels were operating at the time, so the observed pretest crack patterns in the figures offer the only definitive information that is available concerning the effects of the yawing motions on the model. The columns sustained hairline flexural cracking in many locations. Cracks largely seemed to overlay locations of reinforcing ties, where concrete cover is thinnest. Exterior slab-column joints sustained numerous hairline cracks on all floor levels. Those cracks appear to be extensions of "X-shaped" torsional cracks that occurred in the spandrel beams at their interfaces with the columns. The torsional crack pattern in the spandrels closely paralleled their stirrup spacing. All three floor slabs sustained hairline cracks. The cracking was most severe on the first floor slab, followed in severity by the second and third floor slabs, respectively. The cracks were more severe on slab bottom surfaces than on slab top surfaces. Numerous flexural (east-west) cracks were present from midspan to the outside column line, in each span. On each floor, particularly floors one and two, the yawing motions created almost circular cracks in each corner of the floor slab. On the slab top surfaces, a small number of longitudinal (north-south) hairline cracks extended along varying lengths of the slab surfaces. These cracks fell in planes of weakness that were created by the lines of holes in the slabs that were used to secure the lead weights to the model. On floors one and two, hairline cracks extended radially in the slab top surfaces from the centerline columns.

Figures 4.48 - 4.57 map the crack patterns on the model following the completion of simulation T420DL. These figures document the extension of damage during the entire sequence of simulations with VEDs installed on the model. Comparing these figures with Figures 4.38 - 4.47 shows that very little

added surface damage occurred during the sequence. The various cracking mechanisms extended only slightly. The most notable change occurred during simulations E200DL and T420DL, when the torsional cracks in the spandrel beams opened up and extended slightly.

During simulations E025N - E200N, several significant changes in the damage state were noted. In simulation E075N, a number of hairline flexural cracks appeared at the base of the first floor west centerline column. In simulations E100N and following, torsional cracking in the spandrel beams on floor one continued extending and opening. In simulations E125N and following, torsional cracking in the spandrel beams on floor two continued extending and opening. Commencing in simulation E150N, large joint rotations in the model forced the centerline column collars to strike the bottom surface of the slab, causing spalling of the slab concrete. Throughout the series of simulations, slab flexural cracking continued to extend. Figures 4.58 - 4.67 map the crack patterns on the model following the completion of simulation E200N. These figures document the final condition of the model.

Figures 4.68 - 4.86 are photographs of various locations on the model following simulation E200N. The most severe damage occurred in the exterior slab-column joint regions on floors two and three. The torsional cracks in the spandrel-column interfaces opened substantially. On the third floor, the torsional cracking in all four exterior slab-column joints caused spalling of the concrete cover. This is sketched in Figures 4.58 - 4.67 and shown in photographs in Figures 4.68 - 4.72. Second floor joint damage was almost as severe, as illustrated in Figures 4.73 - 4.79. At the first floor level, torsional cracks in the spandrels also opened substantially, although the damage was not as severe as on the upper two floors (Figure 4.80). Figure 4.81 shows the damage that occurred in one of the first floor slab-column joints. A crack initiated at the hole that was drilled into the spandrel beam to assist in load transfer from the VED brace collar. This damage was seen at all four exterior first floor slab-column joints (the detail was not used on the upper two floors). Figure 4.81 illustrates the spalling that occurred on the bottom of the third floor slab in the centerline slab-column joints. Figures 4.83 - 4.86 show some of the slab damage that occurred, particularly the extension of radial cracks from the centerline columns. On all three floors, slab cracking was much more substantial by the end of the testing. Flexural cracks that had occurred on the bottoms of the first and second floor slabs earlier had extended further; some had extended the full slab width. On the first and second floors, numerous new flexural cracks on the bottoms of the slabs appeared, and some flexural cracks appeared on the bottom of the third floor slab. On the first and third floors, cracking on the bottoms of the slabs was largely located in the regions from mid-span to the exterior column lines. On the second floor slab, cracking of the slab bottom was more extensive and included

cracks in the centerline column region. Also on the bottom of the second floor slab, some radial cracking extended outward from the centerline columns. On the tops of the slabs, existing radial cracks extending from the first and second floor centerline columns grew, and others formed. Flexural cracks along the center east-west column line appeared on the tops of the first and second floor slabs, with more extensive cracking occurring on the second floor. Longitudinal cracks ran the entire length of the top of each floor slab, on each side of each column line. As mentioned earlier, these cracks tended to follow the bolt holes in the slab that were used to attach the weights for the model.

CHAPTER 5

DISCUSSION OF OBSERVED RESPONSE

This chapter discusses the behavior of the model during the testing program. Discussions follow the sequence used in Chapter 4. The response of the structure during the earthquake simulations is reviewed in terms of floor accelerations, relative and interstory displacements, story shears, load-displacement hysteretic behavior, overturning moments (OTMs), viscoelastic damper (VED) performance, relative floor velocities, and energy input and dissipation. Variations in the dynamic properties of the model are examined, emphasizing changes in vibration periods, structural stiffnesses, equivalent viscous damping, mode shapes. Next, reinforcement strains are examined. Finally, a general summary of the response of the model is provided, combining visual observations about the surface cracking patterns with the major trends noted in the test data. This chapter provides a basis for analytical modeling assumptions for both the slab-column structure and the supplemental VEDs. In addition, some practical observations concerning the application of VEDs in seismic retrofit for existing concrete buildings are made.

5.1 Floor Accelerations

Section 4.1 presents floor acceleration data. Maximum floor accelerations on the lower two floors of the test model are similar for both simulations with VEDs installed and simulations with VEDs removed, for similar PGAs (Figure 4.4). On the third floor level, maximum floor accelerations in simulations with VEDs removed fall below those of simulations with VEDs installed.

For the two series of simulations with VEDs installed, El Centro responses are generally higher than Taft responses for the same PGAs. Maximum floor accelerations of the three floor levels generally increase with height above the base. On all three floors, the maximum normalized acceleration varies inconsistently ($\pm 15\%$) in simulations E010DL - T315DL, and then reduces significantly in simulations E200DL and T420DL.

While the structural system is somewhat nonlinear, the high degree of damping that is induced by

the VEDs is sufficiently influential in the structural response to permit the use of elastic response spectra to make general observations about its behavior. The earthquake simulation-based transfer functions (TFs), described in Section 4.11.(a), show a strong first mode dominance in the tests with VEDs installed, with three ranges of first mode periods for the model: 0.35 sec (E010DL - T105DL), 0.40 sec (E100DL - T315DL), and 0.50 sec (E200DL - E250DL). For a viscous damping ratio of 30%, approximately that which was observed, the compressed El Centro ground acceleration record has peak spectral accelerations (PSAs) of approximately 0.39 g, 0.32 g, and 0.20 g for the three period ranges (Figure 3.1). For the compressed Taft record, corresponding 30% damped PSAs are approximately 0.34 g, 0.30 g, and 0.26 g (Figure 3.8) when its PSAs are multiplied by 2.1 to equilibrate Housner intensities. The relative magnitudes of the El Centro and Taft PSAs reverse in the long period region. Both records have reduced PSAs with increasing structural period. Normalized maximum floor accelerations do not reduce as sharply with increased PGA as the corresponding PSAs.

This apparent discrepancy is believed to be largely due to the VED properties. Equations 2.21 and 2.22 show that, for a constant excitation frequency, stiffness and damping properties of the VEDs are approximately proportional to the shear storage modulus, G' , which varies inversely with the shear strain of the VED (Appendix D). The effective stiffness and damping contributions of the VEDs will both reduce at the larger strains that accompany higher PGAs. A lower damping ratio for the model, which would result from lower damping contributions from the VEDs, will increase the PSA. A lower model stiffness, which would result from lower VED stiffness as well as structural degradation, will decrease PSAs. The lower damping and lower stiffness will therefore have offsetting effects on PSA. The net result is that PSA does not reduce as much as it would if the stiffness lowered while the damping remained constant.

The floor acceleration records (E.G. Figure 4.2) show that floor accelerations in simulations E025N - E200N are influenced by the model's second mode period of about 0.2 sec. The participation of the second mode in the response with VEDs removed increases maximum accelerations to higher levels than would occur with strictly first mode response.

5.2 Displacements

Section 4.2 presents trends that were observed in the relative story displacements, while Section 4.3 presents trends that were observed in the interstory displacement data. Since relative displacements are aggregations of the interstory displacements, examination of the interstory displacements provides a more

meaningful perspective and will be used here.

Maximum displacements provide important indications concerning serviceability for a structural system. As noted in Section 4.3, current model building code provisions restrict maximum interstory drifts to 1.5% - 2.0%, for life safety. Reference 30 indicates structural damage is likely with drift ratios as low as 0.7%. With VEDs installed, the model sustained simulations E075DL and T157DL ($PGA \approx 0.31$ g), with interstory drifts of less than 0.6% (Table 4.3). The model also sustained simulations E150DL ($PGA = 0.55$ g) and T315DL ($PGA = 0.63$ g) with interstory drifts under 1.3%. Following removal of the VEDs, the model reached 0.87% interstory drift in the second story in event E050N ($PGA = 0.21$ g), and it reached 1.76% interstory drift in the second story in event E100N ($PGA = 0.41$ g). The VEDs reduced displacements, significantly improving serviceability.

The interstory displacement histories (E.G. Figure 4.9) and the earthquake simulation-based TFs show first mode dominance for all simulations with VEDs installed. This provides evidence that, for low-rise structures, design efforts for VEDs may focus on first mode response.

For the simulations with VEDs installed, only minor differences between the El Centro and Taft responses exist. The interstory displacements of the stories differ, with the largest interstory displacements occurring in the second story. Normalized interstory displacements for simulations E010DL - T420DL increase by 70% - 90% over the series, in all stories.

To interpret the observed displacement increase with higher PGA, it is again instructive to examine the elastic response spectra (Figures 3.1 and 3.8). The earthquake simulation-based transfer functions (TFs), described in Section 4.11.(a), show strong first mode dominance in the tests with VEDs installed, with three ranges of first mode periods for the model: 0.35 sec (E010DL - T105DL), 0.40 sec (E100DL - T315DL), and 0.50 sec (E200DL - E250DL). If the stiffness, mass, and damping properties of the structure remained exactly the same, one would expect the normalized displacements to remain constant at each floor level with increasing PGA. However, the gradually lengthening period indicates that stiffness lowered, given that the mass of the model is constant. With $T \propto 1/\sqrt{K}$, the stiffness of the model in simulations E150DL and T315DL is about 73% of the stiffness in simulations E010DL and T021DL. The spectral displacements in the linear response spectra for the two earthquakes indicate an increase of 10% - 20% in normalized displacements for linear systems for this increase in first mode period is expected, for a constant viscous damping ratio of 30% (approximately what was measured in the model). An increase in spectral displacement of the magnitude that was actually measured (70% - 90%) corresponds to an increase in first mode period to approximately 0.80 sec, which would indicate a 90% stiffness decrease occurred.

While the observed behavior is nonlinear, so that elastic response spectra cannot be strictly applied, the high damping again allows them to be used for general observation. The difference between the observed growth in normalized maximum displacements and the growth in elastic spectral displacements is believed largely due to the strain sensitivity of the VEDs. The observed first mode periods are based on TFs for the complete acceleration histories, so they represent “average” values. The displacement (and resulting VED strain) histories associated with those averages are dominated by small displacements. The maximum displacements of the model occur only during very small segments of each simulation. The structural properties of the model during the times of maximum displacement, and not the average properties, must be considered to explain the observed increased normalized displacements.

The stiffness and damping properties of the VEDs are both approximately proportional to the shear storage modulus, which is inversely proportional to the VED shear strain. Using unpublished 3M data on the properties of its *ISD 110* polymer, a displacement increase of approximately 25 times (roughly that observed over the series of simulations) will result in about a 60% reduction in both the stiffness and damping properties of the VEDs. Stiffness and damping reductions will both contribute to increased normalized displacement. The observed normalized displacement increases are therefore not solely due to spectral shifts.

In the series of simulations with VEDs removed, the interstory displacements of the three floor levels differ, but normalized displacements increase with increased PGA at all levels. As noted in Section 4.3, the interstory displacement histories indicate discernable changes occurred during simulations E125N, E150N, and E200N. The significantly higher increase in the third story displacement in simulation E150N is likely due to damage in the spandrel beams on the second and third floor levels.

The interstory displacement histories (E.G. Figure 4.10) and the earthquake simulation-based TFs for simulations E025N - E200N indicate second mode influence is present in the response. While the first mode dominates, there are smaller cyclic oscillations that are most obvious in the first and third story responses. This behavior has a frequency of approximately 5.0 Hz, corresponding to the measured second mode frequency. The higher mode first and third floor oscillations also appear to be of opposite phase, which would be expected for the second mode response. The second mode influence on displacement is not as significant as it is on acceleration.

5.3 Story Shears

Normalized maximum story shears (Figure 4.16) for simulations E010DL - T420DL follow the same relative trends as noted above for the maximum normalized floor accelerations. Normalized story shears are almost level through simulation T315DL, before falling 10% - 20% in simulations E200DL and T420DL. With response heavily dominated by the first mode, maximum story shears in the simulations with VEDs are essentially summations of the products of the maximum floor accelerations and their respective story masses.

In simulations E025N - E200N, the second mode affects floor accelerations. Maximum story shears for stories one and two are not equal to summations of the products of maximum floor accelerations and respective story masses, because the maximum floor accelerations at the three floor levels do not occur simultaneously. While maximum third story shears in simulations E025N - E200N are approximately equal to third story shears in simulations E010DL - T420DL, the first and second story shears are approximately half those in corresponding simulations with VEDs installed. Consistent with the floor accelerations in simulations E025N - E150N, maximum normalized story shears increase slightly with increased input motion intensity, before falling substantially in simulation E200N (Figure 4.16).

5.4 Story Shear vs. Interstory Displacement: Hysteretic Behavior

For simulations E010DL - T420DL, the story shear vs. interstory displacement plots reveal good energy dissipation in each story, with only minor stiffness degradation (e.g. Figure 4.17). Hysteresis loops are broad and of relatively uniform slope. In each simulation, there are three or four significant excursions, corresponding to maximum displacements, with other loops being closely spaced and considerably smaller.

Reinforced concrete (RC) structures behave inelastically under large displacement cyclic loading. With increased displacement, an RC structure's stiffness lowers and its response period lengthens. Under cyclic loading, RC structure load-displacement hystereses commonly pass through or very near the origin during load reversals, with little energy dissipation. The opening and closing of cracks, and reinforcing bar slip, often lead to "pinching" of the hysteresis loops, in which the slope of the load-displacement curve is low as it passes near the origin but becomes higher as displacements reach new maxima. The increased slope, or stiffness, is due to re-engagement of reinforcement and uncracked surfaces as displacement reaches a magnitude that has not previously occurred.

Comparing the story and column shears vs. interstory displacement (Figure 5.1) for simulation E100DL provides some insight into the RC behavior in the model while VEDs were installed. As evidenced by the column shear hystereses, only minimal energy dissipation occurs in the RC. The areas of the column shear hysteresis loops are small, with cyclic reversals passing through or very close to the origin. In each story, a single displacement cycle encompasses a single, larger loop. Such behavior is followed by lower stiffness, as evidenced by the overall slope of the plot, in the following displacement cycles and on the subsequent simulation. Evidence of stiffening effects that are associated with pinching is notable in the single large loop. Most of the input energy is dissipated by the VEDs.

With VEDs removed, the model behavior typifies the RC behavior described above. In Figure 4.18, story shear vs. interstory displacement for simulations E050N and E150N, energy dissipation, evidenced by the relative size of the hysteresis loops, is low. Story stiffness is lower than for the simulations with VEDs installed. Pinching is evident, with increased stiffness for new displacement maxima that occur in each simulation. Wider hysteresis loops result when new displacement maxima occur, but narrower loops occur for lower magnitude responses.

5.5 Overtuning Moments

The same general relationship for simulations E010DL - T420DL exists for OTM as for floor acceleration and story shear (Figures 4.19 and 4.20). Maximum normalized OTMs for simulations E025N - E200N are significantly lower than those of simulations E025DL - E200DL, reflecting both the overall lower maximum accelerations at each floor level and the occurrence of maximum floor accelerations at different times, because of higher mode effects.

5.6 Viscoelastic Damper (VED) Performance

(a) General Trends

Figure 4.26 plots the maximum sums of the horizontal components of all VED forces in each story, normalized by PGA, for all simulations. Figure 4.27 plots the maximum sums of the horizontal components of the VED forces, normalized by maximum story shear, *at the time of maximum story shear and at the time of maximum VED force summation*. The phase angle between shear stress and strain in

the VEDs (force leads deformation) results in the different sums at the two different times. The plots are erratic, but several trends are present.

Maximum second story VED forces exceed maximum first story VED forces. Because of the relative fixity of the base, the first story columns are stiffer than the second story columns. This results in attracting a higher percentage of total story shear to the first story columns than to the second story columns. Therefore, a lower percentage of the total story shear is attracted to the first story VED braces than to the second story VED braces.

Normalized El Centro simulation sums are higher than corresponding Taft sums, paralleling previous observations concerning maximum story shears; the sums increase slightly with increasing PGA. The slightly higher frequency content of the El Centro responses leads the VEDs to act somewhat more stiffly, attracting relatively higher force levels. Material property changes associated with elapsed times to reach the maximum responses likely contribute more significantly to this trend (Tables 4.11 and 4.12). Taft maxima occur after longer excitation times (4.6 sec and 6.3 sec) than those of the corresponding El Centro maxima (1.15 sec and 1.30 sec). See Section 4.7 for definitions of these maxima. As the viscoelastic material is cyclically deformed, it dissipates energy through heating, causing both its stiffness and damping properties to decrease (Appendix D). The lower VED stiffness resulting from the longer excitation time of the Taft simulation before its maxima occur results in attracting relatively less force than is attracted for the El Centro simulation.

The elapsed times between the two maxima in each simulation also seem linked to material property changes. In the El Centro simulations, there is only a half cycle, 0.15 sec elapsed time, between the two maxima. The relative amounts of story shear borne by the VEDs in the two maxima are not significantly different. No distinct dependence on relative floor velocity, VED strain, or displacement frequency emerges. However, in the Taft simulations, the positive story shear maximum occurs 1.7 sec before the negative story shear maximum. The percentage of the story shear assumed by the VEDs is higher for all stories at the time of the positive story shear maximum than at the time of the negative story shear maximum. Differences in the third story are small, but differences in the first two stories are significant. The longer interval between the two maxima permits several excitation cycles to occur. The energy dissipation that occurs during this time would lead to lower stiffness at the time of the negative story shear maximum than at the time of the positive story shear maximum, resulting in the attraction of relatively lower amounts of the story shear. Again, no distinct dependence on relative floor velocity, VED strain, or displacement frequency emerges.

In both series of simulations, the relative amount of the story shear transmitted by the VEDs increases with increasing PGA on all story levels. VED stiffness reduces with increased strains, lowering force attraction. Offsetting this is the relatively higher force attraction that would occur with higher deformation velocity. Finally, the column stiffnesses would reduce with increased inelastic deformation.

Figures 4.29 and 4.30 plot the 4.0 sec elapsed times of maximum story shears for simulations E050DL and E150DL, with the corresponding sums of the horizontal components of the VED forces, and the calculated column shears. The phase angle between VED force and displacement results in a lag between maximum VED forces and maximum story shear. The angle differs slightly from story to story. VED forces peak before story shear in each major motion cycle, and there are times that column shears and sums of the horizontal components of the VED forces are opposite in sign. Figure 4.31 shows relative floor velocities that correspond to Figures 4.29 and 4.30. Even in simulations with higher PGAs, there are times of low relative floor velocity, indicating that very little interstory displacement occurs then. During these times, the VED deformations are extremely small, significantly raising their effective stiffness and damping properties.

(b) VED Stiffness Properties

VED force-deformation relationships were examined to assess VED stiffnesses. Within each series of simulations, and for each VED, each successive VED displacement history was processed to record only those displacements that exceeded maximum displacements from the previous displacement history. These displacements and the corresponding VED forces are plotted as “backbone” curves in Figures 5.2 - 5.7. Separate plots of the conditions for VED braces in compression and tension are provided. The reader will note that the “backbone” plots do not closely resemble such plots from undamped structures. The outline of the largest hysteresis loop in each simulation can be seen in each plot.

Tables 5.1 and 5.2 provide linear and quadratic regressions for each plot in Figures 5.2 - 5.7. Table 5.3 lists average VED stiffnesses based on the slopes of the linear regressions in Tables 5.1 and 5.2. Correlation coefficients for the quadratic regressions show essentially the same accuracy as those of the linear regressions, so analysis focused on the linear regressions.

The data plots and the corresponding linear regressions (Table 5.3) show wide scatter in the data. Since the NE and NW, and SE and SW, pairs of VEDs move in phase at each story level, the closest comparisons can be made within each pair. Figures 5.2 - 5.7 show that maximum force and displacement

levels in the VEDs are variable. If the VED braces behaved identically, maximum displacements would be identical for the NE and NW VEDs in each story, and for the SE and SW VEDs in each story, but they are not. For example, Figure 5.4 shows that the NE VED in the second story has 20% - 30% higher maximum displacement in each simulation than the counterpart NW VED.

The four VEDs in each story also have significant average stiffness variations. Variations are larger for the VED brace in compression condition than for the VED brace in tension condition. It is probable that the VED braces experienced lateral "bowing" displacements under compressive loading. This behavior would be the aggregate result of misalignment of the VED braces, rotational flexibility of the VEDs, and rotational flexibility of the slab-column joints. Such deflections would increase measured VED strains for given compressive forces, lowering the computed stiffness. The reader may see this by comparing the tensile "backbone" curve of the NE (or NW) VED with the corresponding compressive curve for the SE (or SW) VED, and vice versa (Figures 5.2 - 5.7). Assuming that the floor diaphragms forced lateral displacement compatibility in all columns at each floor level, maximum displacements for opposing braces should be equal. The brace that is in compression often shows slightly larger displacement. Confirmation of this hypothesis may be seen on the first floor, where the computed SW VED stiffness is almost the same in both compression and tension (Table 5.6). When this VED is in compression, its deformation almost exactly matches the corresponding tensile deformation of the NW VED (Figures 5.2 and 5.3). By contrast, the NW VED stiffness is lower in compression than in tension. When this VED is in compression, its deformation is larger than the tensile deformation of the SW VED, indicating bowing may have occurred.

Neither maximum VED strains nor maximum VED forces vary as widely as the computed stiffnesses, indicating VED performance at maximum force and deformation levels is more consistent than the computed stiffness values indicate. In addition, model displacements and accelerations showed no inclination toward torsion, so the differing VED brace properties did not seem to induce detrimental motions.

Table 5.6 shows that the "backbone" curve stiffness is 5% - 8% higher for the El Centro simulations than for the Taft simulations. This table also shows that backbone stiffness decreases with increased story height. The average stiffness of the first story VEDs is slightly higher than that of the second story VEDs (10.75 kips/inch vs. 9.39 kips/inch). The interstory displacements in the first story are approximately 80% of those on the second story, so the first story VED stiffnesses are expected to be higher than those in the second story. Both average stiffnesses are below those measured during VED

characterization testing (Appendix D), in which the VED displacements were carefully controlled. In that testing, an average stiffness of 13.3 kips/inch was observed for an excitation frequency of 3.0 Hz and a shear strain of 25%, and an average stiffness of 9.7 kips/inch was observed for an excitation frequency of 2.0 Hz and a shear strain of 50%, for four displacement cycles.

The observed average third story stiffness of 4.99 kips/inch is significantly lower than either of the lower story stiffnesses. Third story interstory displacements are smaller than those of either of the lower stories, which implies that VED stiffness should be higher than it is on either of the lower stories. The third story VED force-displacement hystereses, Figures C.10.1 - C.10.46, in simulations E010DL - T420DL resemble those of the simulations that were conducted before the VED braces were fixed by welding them to the column collars (E.G. simulation E025DS). The third story VED force-displacement hystereses show significant energy dissipation with little stiffness contribution. In the simulations that were conducted before fixing the braces, rotations of the VED brace elements that were permitted by their pinned end conditions significantly reduced their axial stiffness, because lateral displacements occurred with very small axial forces. In simulations E010DL - T420DL, although the VED brace ends were welded to their respective column collars, the third floor slab-column connections were more flexible than those at the first and second floor levels, allowing larger joint rotations to occur than in the lower stories. The larger joint rotations would be transferred to the VEDs through movement of the VED brace ends. This would effectively lower the axial stiffness of the VEDs, since their shear strains would increase without corresponding increases in the axial forces in the braces. While this condition is most exaggerated in the third story, it may also partially explain the lower stiffness of the second story VEDs with respect to the first story VEDs, since the base fixity of the columns would permit no joint rotation at the bases of the first story columns.

Examination of the VED force-displacement behavior from other perspectives is also helpful in analyzing VED behavior. Table 5.4 lists average stiffnesses for the El Centro VED force-deformation hystereses for the first 20 sec of each simulation, and for the 3.5 sec of maximum interstory displacement. While not shown here, trends for the Taft simulations are similar. These stiffnesses are based on linear regressions of the hystereses for all data points that fall within the respective elapsed times. Several observations may be made about these data. First, in comparison with linear regression data from the backbone curves (Table 5.3), computed stiffnesses are much lower. The linear regressions summarized in Table 5.3 are separate for tensile and compressive brace loading, so the stiffness values are not directly comparable. Table 5.4 confirms the large variability in stiffnesses for the various VEDs in the various

tests. It also shows the same reduced VED stiffnesses with increased story height as the Table 5.3 data show. The regressions for the third story actually average negative values, as a consequence of the extremely low stiffness at that level. Finally, the stiffness values are higher for the 3.5 sec of maximum displacement than for the longer elapsed time. This supports the observation that VED stiffness properties lower with elapsed excitation time, because the material softens due to heating that results from energy dissipation.

Other authors [3] have recommended using those VED hysteresis data points that fall within a specified VED deformation range, specifically $0.50 D_{max}$ to $1.00 D_{max}$, to perform a linear regression that determines the effective VED stiffness. Table 5.5 lists the results of linear regressions for the VED force-deformation hysteresses for each simulation, for all deformations from 25% of the maximum deformation ($0.25 D_{max}$) to $1.00 D_{max}$, while Table 5.6 lists the results of linear regressions for the VED force-deformation hysteresses for each simulation, for all deformations from $0.50 D_{max}$ to $1.00 D_{max}$. Tables 5.5 and 5.6 provide separate regressions for the conditions of VED braces in tension and VED braces in compression. Data are given only for the El Centro simulations. The tables also provide the maximum shear strains and brace axial forces, and the numbers of data points in each regression analysis. Tables 5.5 and 5.6 show the same general trends that are reported above. There is large scatter in the data. As with the third story VED regressions in Table 5.4, there are several instances of negative regression slopes in these tables. In those instances, the hysteresis plots show such extremely low, or nonexistent, stiffness that the groups of selected data points result in negative slope computations.

In Tables 5.5 and 5.6, brace compression stiffness is generally lower than brace tensile stiffness. Brace stiffness generally decreases with higher PGA. The reported stiffnesses for the range of $0.50 D_{max}$ to $1.00 D_{max}$ are generally higher than those for the range $0.25 D_{max}$ to $1.00 D_{max}$. As has been discussed, VED stiffness lowers with increased shear strain, making the reported data seem contradictory. However, for the El Centro simulations, the maximum displacements occur very early in the elapsed time. A cursory check of the VED deformation histories shows that displacements for the range of $0.50 D_{max}$ to $1.00 D_{max}$ occur during the first six seconds (sec) of the record, while displacements for the range $0.25 D_{max}$ to $1.00 D_{max}$ occur during the first 15 sec of the record. It would therefore be expected that the heat-induced softening that occurs during the longer excitation time would be responsible for the apparent contradiction.

The dependence of viscoelastic stiffness and damping properties on excitation frequency and maximum strain is well documented [1, 9]. From that research, shear storage and loss moduli (G' , G'') for viscoelastic materials have been found to be approximately proportional to the square root of the excitation

frequency and inversely proportional to the fifth root of the maximum shear strain (Appendix D). The moduli are more sensitive to excitation frequency than to maximum strain. Equation 2.21 shows the VED stiffness to be proportional to G' , so the VED stiffness (k_d) is also proportional to the square root of the excitation frequency and inversely proportional to the fifth root of the maximum shear strain. Equation 2.22 shows VED damping to be proportional to G'' divided by the excitation frequency, so the VED damping coefficient (c_d) is inversely proportional to the square root of the excitation frequency and the fifth root of the maximum shear strain. These approximate relationships may be expressed as:

$$k_d \propto G' \propto (\omega^{(0.5)}, \gamma^{(-0.2)}) \quad (5.1)$$

$$c_d \propto \frac{G''}{\omega} \propto (\omega^{(-0.5)}, \gamma^{(-0.2)}) \quad (5.2)$$

Focusing on the VED stiffness, the first mode frequency of the model lowered through the test sequence, and displacements, with resulting VED strains, increased. Both of these trends would contribute to lowered VED stiffness. Stiffnesses calculated from the test data are inconsistent, although the backbone curves corroborate the tendency for the VED stiffness to be lower with increased PGA.

5.7 Variation of Dynamic Properties

This section examines stiffness and equivalent viscous damping properties of the model during the earthquake simulations, providing insight into the global response of the model and its general condition.

Stiffness variations in the structure were monitored during the simulations by measuring resonant modal frequencies and corresponding periods. Table 4.15 lists modal frequencies that were computed from base to third floor acceleration-based transfer functions (TFs) during the various simulations. Table 4.16 lists the modal frequencies that were computed from base to third floor, and base to second floor, acceleration-based TFs from the white noise tests (WNTs) that were conducted before and after the simulations. The same trends are seen in both tables. Observed modal frequency decreases with each new simulation, and observed first mode frequencies are higher for the model equipped with VEDs than they are when the model is not.

The data in the two tables are based on responses to different input motions, leading to differences in the observed stiffness properties. The modal frequencies in Table 4.15 are derived from the simulations,

where PGAs ranged from 0.05 g to almost 1.00 g. The modal frequencies in Table 4.16 are derived from WNTs, in which the PGA \approx 0.025 g for all tests.

Some minimum level of excitation will be required to open cracks and initiate reinforcement slippage in the RC, even following a previous event in which such cracking and slippage has been initiated. Because of this, the stiffness of the RC structure, excluding VEDs, is expected to be higher at very low excitation levels than at higher excitation levels. Also, VED stiffness decreases with larger strain. It therefore would be expected that the frequencies and associated structural stiffnesses determined from the WNTs (Table 4.16) would be higher than those determined in the earthquake simulations (Table 4.15).

Modal frequencies reported in Tables 4.15 and 4.16 are resonant peaks in the TF plots. Modal periods are computed as the inverses of the modal frequencies. Modal damping ratios were computed from the TFs using the half-power bandwidth method. Both the modal frequencies and damping ratios are approximate. The resonant frequency (ω_r) and the natural frequency (ω_n) of the system are not identical, with the difference between the two becoming larger with increased viscous damping. Using procedures outlined by Chopra [reference 12, pp 83-89] for evaluating transmissibility, $\omega_r/\omega_n \approx 0.99$ for a damping ratio (ξ) of 10%; $\omega_r/\omega_n \approx 0.96$ for $\xi = 20\%$; $\omega_r/\omega_n \approx 0.93$ for $\xi = 30\%$; and $\omega_r/\omega_n \approx 0.89$ for $\xi = 40\%$. So, the reported resonant frequencies are somewhat lower than the natural frequencies of the model. In computing the modal damping ratio using the half-power bandwidth method, the TF magnitude at its peak is critical. As exhibited in Figure C.16.20, the smoothing process lowered the peak TF magnitude, effectively increasing the half-power bandwidth, which increases the computed damping ratio.

These discussions concentrate on the measured resonant frequencies. In Chapter 6, when analytical models are developed, it will be necessary to account for the difference when comparing observed response to calculated response. The smaller damping ratios of the model with VEDs removed result in no significant difference between the observed resonant frequencies and the natural frequencies for those simulations.

(a) Vibration Periods and Stiffnesses: Simulations E010DL - T420DL

In simulations E010DL - T420DL, only the first mode was discernable in the TFs. Table 4.15 shows a gradual lengthening of the first mode period from 0.35 sec to 0.41 sec from simulation E010DL to T315 DL, for the average response of the model over the entire simulation. The period increase indicates the stiffness decreased to approximately 73% of its initial value during this sequence. In simulation

E250DL, the first mode period increased to 0.51 sec, indicating that the stiffness decreased to approximately 47% of its initial value. First mode periods obtained by measuring the elapsed time between zero crossings of the interstory displacement vs. time plots at the times of maximum displacement corroborated the values based on the TFs.

Table 4.16 shows TF maxima from the WNTs. From the WNT prior to simulation E010DL through the WNT following simulation T420DL, the first mode period based on WNTs was approximately constant, averaging 0.35 sec. Following simulation E250DL, the first mode period based on WNT was approximately 0.42 sec. The WNT-based periods connote higher stiffnesses than those which were observed in the simulations. With increased PGAs, differences between the natural periods observed in the simulations and those of the WNTs widened, with the WNTs consistently yielding shorter periods. It is reasonable to conclude that the observed stiffness properties in the WNTs may be used as general indicators of the condition of the structure but cannot be used as absolute indicators of the structural condition during the actual tests.

The stiffness properties of the model were also examined from other perspectives. Since structural properties at maximum displacement are critical for design purposes, “backbone” curves of the story shear and column shear vs. interstory displacement for simulations E010DL - E200DL and T021DL - T420DL were constructed in the same manner that was previously described for the VEDs. The plots are again affected by the hysteretic loop behavior of the VEDs.

The backbone curves are plotted in Figures 5.8 - 5.10 (only “positive” maximum displacements are presented). Both linear and quadratic curve fits to the plotted data were calculated. They are reported in Tables 5.7 - 5.8, and the computed interstory “tangent stiffness” values (slopes of the curve fits at maximum displacement levels for each simulation) are presented in Table 5.9. Curve fits for the El Centro data and the Taft data are very similar, indicating very similar response to the different input signals. The regression correlation coefficients for the quadratic regressions are only slightly higher than for the linear regressions, which may make the simpler stiffness relationship found with the linear regression appealing for use in structural analysis. However, the linear regressions generally have “y-intercepts” much larger than those of the quadratic regressions. A y-intercept that passes through the origin would be expected for the ideal curve fit. Except for simulations E200DL and T420DL, which are at the limits of the recorded data, the quadratic regressions provide a better fit and show the stiffness decrease that occurs.

Table 5.8 presents curve fits for the column shear vs. interstory displacement backbone curves. These data are more scattered than the corresponding story shear data. Regression correlation coefficients

are lower. The regressions indicate that the column shear stiffnesses of the Taft simulations are somewhat higher than those of the El Centro simulations.

Using Table 5.9 and simulations E010DL and T315DL to compare the stiffnesses computed using the TFs, the first, second, and third story tangent stiffnesses (quadratic regression) at the instant of maximum displacement in simulation T315DL are 43%, 43%, and 60%, respectively, of those in simulation E010DL. The tangent stiffnesses are significantly below the 73% estimate from the TF analysis and indicate that stiffness decrease at maximum displacement is more severe than is indicated by the TFs of the time histories. The TF analysis represents an average condition for the entire simulation, while the backbone tangent stiffness characterizes conditions at the time of maximum displacement.

In Table 5.10, the results of linear regressions of the story shear vs. interstory displacement records for the first 20 sec of each record and for the 3.5 sec of maximum interstory displacement are given. The regressions provide average stiffnesses for those elapsed times. The stiffnesses are very nearly the same for the two different regressions. Stiffness again decreases with increasing PGA, but the decrease is not as pronounced as it is with the tangent stiffnesses. These stiffnesses are generally lower than the backbone tangent stiffnesses for the lower PGA simulations and higher than the backbone tangent stiffnesses for the higher PGA simulations. At lower PGAs and correspondingly smaller strains, the softening of the viscoelastic material with increased excitation time probably leads the stiffness averages over time to be lower than the stiffness at maximum displacement. At higher PGAs, the very large VED strains that occur at times of maximum displacement probably result in instantaneous stiffnesses that are smaller than the average stiffnesses over time that are dominated by smaller strains, outweighing the stiffness decrease that occurs with excitation time.

(b) Vibration Periods and Stiffnesses: Simulations E025N - E200N

In simulations E025N - E200N, the first three modes are discernable in the TFs. Table 4.15 shows a lengthening of the first mode period from 0.78 sec to 0.83 sec from simulation E025N to E050N, where it remained through simulation E100N. The first mode period lengthened to 0.85 sec in simulation E125N, 0.92 sec in simulation E150N, and 1.32 sec in simulation E200N, matching observed changes in the condition of the model. Using simulation E025N as a baseline, the stiffness decreased to approximately 88% of its baseline stiffness in simulation E050N and remained constant through simulation E100N. The stiffness decreased to approximately 84% of its baseline value in simulation E125N, 72% of its baseline

value in simulation E150N, and 35% of its baseline value in simulation E200N. First mode periods obtained by measuring the elapsed time between zero crossings of the interstory displacement vs. time plots at the times of maximum displacement again corroborated the values based on the TFs.

Table 4.16 shows that, during the series E025N - E200N, the first mode period based on WNTs was almost constant, at 0.67 sec - 0.71 sec. The WNTs project significantly higher stiffnesses than those which were observed in the simulations. There is a threshold excitation level that is required to open cracks and induce reinforcement slip that is not reached in the WNTs. This confirms the earlier observation that the stiffness properties obtained from the WNTs may be only used as general indicators of the condition of the structure. WNTs of the model were also performed before any simulations were conducted and again before simulation E025N. Between those tests, the first mode period lengthened from 0.53 sec to 0.65 sec, confirming that stiffness degradation of the model occurred during the series of simulations that included VEDs.

Backbone curves of the story shear vs. interstory displacement for simulations E025N - E200N are plotted in Figures 5.8 - 5.9. Linear and quadratic curve fits to the plotted data were calculated. They are reported in Table 5.7, and the apparent interstory tangent stiffness values for each simulation are presented in Table 5.9. Linear and quadratic regressions for the first story show almost linear behavior for maximum displacements through the range of simulations, and they result in the same first story stiffness over the entire sequence. The second story regressions indicate that maximum second story displacement behavior was almost linear through a maximum interstory displacement of 1.20", while the third story regressions indicate that maximum third story displacement behavior was almost linear through a maximum interstory displacement of 0.75". Quadratic regressions for the second and third stories show the deviations from linear response, with the third story's softening first and more substantially, followed by the second story.

Table 5.10 presents linear regression slopes of the hysteretic response for the first 20 sec elapsed time of each simulation and for the 3.5 sec of maximum interstory displacement. The stiffnesses computed for 20 sec are generally somewhat lower than those computed for the 3.5 sec of maximum interstory displacement. These stiffnesses are also generally lower than the quadratic regression stiffnesses that were computed from the backbone curves. This trend may be due to pinching effects in the RC model, whereby observed stiffness is lower for lower amplitude displacements and higher for larger displacements that have not been previously reached.

The TFs in both the WNTs and the earthquake simulations detected second and third modes for simulations E025N - E200N. The smaller dynamic amplification associated with those frequencies made

discernment of the frequencies more difficult and less precise. Because the WNT input frequencies were more broadly banded than the earthquake simulation input frequencies, the dynamic amplification of the second and third modes was higher in the WNTs, making them more distinct. The second mode frequencies determined in WNTs were slightly higher than those determined during the simulations, but the two sets of results were very comparable. During simulations E025N - E150N, the second mode period was approximately 0.20 sec, while the corresponding third mode period was 0.11 sec - 0.13 sec.

(c) Equivalent Viscous Damping

Tables 4.15 and 4.16 list equivalent viscous damping ratios for the various simulations, as determined using the half-power bandwidth method.

For simulations with VEDs installed, E010DL - T420DL, the computed first mode damping ratio averaged approximately 38% of critical damping, randomly ranging from 36% to 45%, except for simulation E010DL. In the corresponding WNTs with VEDs installed, the first mode damping ratio ranged widely, from under 10% to approximately 30% of critical damping. As discussed above, the low amplitude of the excitation in the WNTs, coupled with the small dynamic amplification that occurred with VEDs installed and the consequences of the TF smoothing process, made these measurements very imprecise. The damping ratios from the WNTs were consistently lower than those from the simulations. Even with increasing PGA, the damping ratios in the earthquake simulations were consistent. Recalling that the VED damping contribution decreases with increasing strain deformation, but increases with decreasing natural frequency, it is plausible that the equivalent viscous damping ratio of the VED-equipped model would remain relatively constant.

The computed average damping ratios in simulations E010DL - T420DL are likely to be somewhat higher than the actual damping ratios, because of the effective increase in half-power bandwidth that results from the TF smoothing process. Comparison of the original and smoothed TFs indicates that the damping ratio may be closer to 30% than the calculated 38%. This will be examined further in Chapter 6.

In simulations E025N - E200N, measured first mode damping ratios are erratic in both the earthquake simulations and the WNTs. Measurements are more erratic and somewhat lower in the simulations than they are in the WNTs. For the first mode, the average damping ratios from both the simulations and the WNTs are comparable at approximately 7.0% of critical damping. For the second and third modes, the damping ratios from the WNTs are consistently higher than those from the simulations.

Because the WNT input frequencies were more broadly banded and the resulting TFs were clearer, those damping ratios would seem to be more accurate, yielding ratios of approximately 4.0% for both the second and third modes.

(d) Mode Shapes from White Noise Tests

For several of the WNTs, TFs of all three floors were computed, from which the mode shapes of the structure could be plotted. Figures 5.11 - 5.14 plot the mode shapes at several different instances during the total testing sequence. Each plot is normalized so that the maximum modal displacement equals one.

In Figure 5.11, the mode shapes of the model with VEDs installed are plotted for three different WNTs. Only the first mode is shown. As mentioned previously, dynamic amplification was very small in the WNTs with VEDs installed, so that TFs were very noisy, making higher modes virtually impossible to detect. The first and second plots in the figure are taken at the beginning and end of the initial dynamic characterization tests. The plots are very similar, though the displacements of the first and second stories are somewhat higher in the latter plot. In the third plot, which was taken after the last simulation with VEDs installed, the plot is quite different, with displacements of the lower two stories having become significantly larger after significant repeated strong motion shaking. With the dominance of the first mode, the low level WNTs indicate that assuming a linear mode shape for design of VED systems for use in low-rise construction using the modal strain energy method (Chapter 2) is valid.

Figures 5.12 - 5.14 plot the mode shapes of the model with VEDs removed. All three primary modes are plotted. From WNT 2, which was performed prior to any earthquake simulations, until WNT 29 the first simulation with VED removal, the first mode shape shows increased modal displacements in the second floor. The second and third mode shapes change very little. Subsequent WNTs show only minor changes in the first mode shape, and the third mode shape never changes significantly. As damage accrues, the second mode shape varies with respect to the modal displacements of the first and second floors. Comparison of the first mode shapes for the model with and without VEDs installed, and before damage accrued, shows that they are very similar, supporting the assumption used in Equations 2.18 and 2.20 that the mode shape when VEDs are installed is the same as it is without VEDs installed.

Figure 5.14 also shows the mode shapes for the model with solid steel braces installed. This WNT was performed during the initial dynamic characterization testing. The TFs gave clear results for the first

mode. Dynamic amplifications for the second mode were small, so the second mode is an estimate.

(e) Comparison of Earthquake Simulations and White Noise Tests

Modal properties from the WNTs differ in two significant ways from the modal properties from the earthquake simulation time-histories, even though the properties were calculated in the same manner. First, the WNT data are based on low level inputs, $PGA \leq 0.025$ g, while the earthquake simulations have increasing PGAs, from 0.05 g to 0.75 g. The input motion magnitude will affect several primary variables that will in turn influence the observed modal properties. The properties of the VEDs are strain-dependent. The stiffness of reinforced concrete is strain rate-dependent [36]. And, concrete cracks that develop will likely remain closed at lower excitation levels and open at higher excitation levels, resulting in relatively lower effective stiffness with higher excitation levels. Second, by definition, the input signals in the WNTs have a broader frequency content than the earthquake signals. The WNTs are better suited to provide insight into the higher modes of the structure, which may not be significantly excited by the earthquake records. This is especially true for the model with VEDs removed.

Comparison of Tables 4.15 and 4.16 shows that, for corresponding characterizations, observed modal frequencies are higher in the WNTs than in the earthquake simulations. With VEDs installed, the decrease in first mode frequency (approximately 1 Hz) is more pronounced over the entire test program based on the earthquake simulation data than the decrease in first mode frequency (approximately 0.7 Hz) that is based on the WNT data. With VEDs removed, the first mode frequency decrease during the program is approximately 0.2 Hz based on both the earthquake simulation data and the WNTs. For the simulations with VEDs installed, first mode damping ratios are typically about 10% higher based on the earthquake simulations than they are based on the WNTs.

5.8 Energy Input and Dissipation

Table 5.11 lists the total input energy, the maximum kinetic energy, the maximum elastic strain energy, and the energy dissipated by the VEDs, for all simulations. Procedures used for computing these quantities are described in Section C.2.(I). Figures C.17.1 - C.17.9 plot the energy input and dissipation relationships for simulations E050DL - E250DL, T105DL - T420DL, and E075N - E200N. Figure 5.15 reproduces the plots for simulations E050DL and E150DL. Figure 5.16 reproduces the plots for

simulations E075N and E150N. Simulation E075N was plotted instead of simulation E050N because the energy quantities in simulation E050N were small. In all plots, input energy is based on the base girder velocities that were derived from the integrated accelerations.

The data in Table 5.11 show the VEDs dissipate over 90% of the input energy in all simulations where they were used, showing a high degree of effectiveness in reducing structural damage. In Figure 5.15, the plots for simulations E050DL and E150DL are virtually identical, except for scale.

For simulations E250DL and T420DL (Table 5.11), the energy dissipated by the VEDs is calculated to be larger than the input energy, using the acceleration-based velocities. This is not possible, so error is present. Two sources of inaccuracy seem most likely. First, the assumed weight of the model may have been lower than was actually the case. The base shear, which is based on story masses, is used in calculating the input energy. One source of error in calculating story mass is in the assumed mass of the lead weights that were used. Over half of the total model mass is contributed by the weights. Approximately half of the weights were weighed to establish the average mass. The unit weight of the reinforced concrete may have also been somewhat higher than the 150 pcf that was assumed. More likely, error may have accrued from the above-mentioned measured VED displacement increase that could have resulted from lateral bowing of the VED braces when they were in compression. An increase in measured VED displacement would increase the areas of the VED hysteresis loops, increasing the computed dissipated energy. This indicates that the energy dissipated by the VEDs may be somewhat lower than the calculated values for all simulations with VEDs installed.

For the simulations with VEDs removed, a significant percentage of the input energy in each simulation was dissipated by hysteretic damping (Table 5.11, Figure 5.16). No significant changes in the energy dissipation mechanisms occurred in simulations E025N - E100N. In simulation E125N, a noticeable reduction in the sum of kinetic and elastic strain energies occurred in the range of 5 - 10 sec elapsed time. Exemplifying this, the plot for E150N (Figure 5.15) shows significantly lower combined kinetic and elastic strain energy, as a percentage of the input energy, after about 5.0 sec elapsed time than the plot for E075N (Figure 5.15). Table 5.11 also indicates that the maximum kinetic energy became a larger percentage of the input energy (34%) than the maximum elastic strain energy (25%) during simulation E150N. In simulation E200N, both the kinetic and elastic strain energies significantly reduced as percentages of the total input energy.

5.9 Reinforcement Strains

This section presents general observations about the measurements of the active reinforcement strain gages in the simulations. Reinforcement strain data is presented in Section 4.11.

(a) Column Reinforcement

Gages *SGZ1* and *SGZ4*, were located on reinforcing bars at the base of the model. *SGZ1* was in the NW column, and *SGZ4* was located in the west centerline column. The observed reinforcement yield and bar slip in the NW column reduces the rotational stiffness of the joint in simulations E125DL - E200DL, T315DL, and E150N - E200N. Strains in simulations E025N - E200N show high frequency content, indicating that localized response, perhaps concrete cracking, occurred, which would also lower rotational stiffness in the joint.

Gages *S1Z1* and *S1Z3* were located on reinforcing bars directly below the first floor slab. *S1Z1* was located in the NW column. Gage *S1Z1* was within the depth of the spandrel beam that frames into the column. In simulations E010DL - T262DL, strains were significantly below yield and only about 10% of the strains measured by gage *SGZ1*. For conventional frame flexure, the strains at the top of the first story columns would be expected to about 50% of the strains measured at the base. The increased section properties that result from the spandrel presence may have acted to lower the strains that were measured. In the west centerline column gage (*S1Z3*), impacts of the collar face plates as the VED braces are loaded may lead to the addition of the higher frequency signals. These signals disappear in the records for simulations when the VED braces were disconnected. Measured compressive strains exceed the crushing strains for unconfined concrete in simulations E125N - E200N, though no signs of concrete crushing were noted in post-test inspections. This indicates the collars effectively confined the concrete.

Gages *S1Z5*, *S1Z6*, *S1Z7*, and *S1Z8*, were located at the bases of the second story columns.

Gages *S1Z5* and *S1Z6* were located in the lap splice zone for the column reinforcement. *S1Z5* was on the outside middle reinforcing bar in the NW column. Compressive strains are consistently and significantly higher than tensile strains, but no bar slip is observed. Because the gage is in the lap splice region, it is possible that the full tensile force may not be on the bar at the gage location. In simulations E050N - E150N, erratic strains are measured during the first 10 sec of each record that are higher in frequency content than the first mode of the structure, indicating that damage accrued, which would soften

the joint. Gage S1Z6 was located on the inside middle reinforcing bar in the NW column. In simulations E025N - E200N, erratic strains were again measured during the first 10 sec of each record that are higher in frequency content than the first mode of the structure, indicating that damage accrued. In simulations E075N - E200N, increasing degrees of bar slip appear.

Gage S1Z7 was located on one of the north face reinforcing bars in the west centerline column. The gage was within the region that is confined by the column collar at the base of the second story column. Strains do not increase in direct proportion to PGA, and maximum tensile strains peak in simulations E075DL and T157DL at slightly less than $\frac{1}{3}$ of yield. Maximum tensile strains do not exceed this level in subsequent simulations with VEDs installed. No indication of tensile slip is present. Low amplitude high frequency signals in simulations E125N - E200N indicate local cracking and slipping occur, softening the joint.

Gage S1Z8 was located on one of the south face reinforcing bars in the west centerline column. The gage was also within the region that is enclosed by the concrete confinement collar at the base of the second story column. In simulations E125DL - E200DL, compressive shifts occur at elapsed times of approximately 3.0 sec, though behavior continues to be linear. The offsets indicate damage occurred. Compressive yield strain is reached in simulation E200N, at the time of structural failure.

Gages S2Z2 and S2Z3 were located directly below the second floor slab. Gage S2Z2 was located on an inside middle reinforcing bar in the NW column. The gage is in a region of the model that suffered severe surface cracking during the simulations. Torsional cracking of the spandrel beam on both sides of the column, and flexural cracking of the column at the bottom edge of the spandrel beam, progressed during these simulations. Post-test surveys revealed a small ($\frac{1}{16}$ ") offset along the flexural crack line adjacent to the gage. The gage probably registered strains that were caused by the localized effects of the spandrel damage. Its failure following simulation E100N may have been caused by the spandrel failure.

Gage S2Z3 was located on one of the north face reinforcing bars in the west centerline column, within the region that is confined by the column collar for the second story VED braces. At approximately 11 sec into simulation E125N, there is a brief drop in the measured strain that parallels similar drops in other gage measurements, indicating a time of damage accrual in the structure.

(b) Slab Reinforcement

Gages *S1X5*, *S1X14*, and *S1X16* were on first floor slab reinforcing bars on the north side of the

west centerline column. Gages S1X5, S1X14, and S1X15 were located in the "column strip," while gage S1X16 was located in the "middle strip," of the slab longitudinal reinforcement. The column strip is a 40 in wide zone, centered on the column centerline, and the middle strip is a 40 in wide zone between adjacent column strips (Figure 2.15). Half of the slab top reinforcement was concentrated in the 14 in center width of the column strip. Gage locations were chosen to provide insight into the "effective slab width" for flexural response.

In gage S1X5, tensile and compressive strains in simulations E010DL - T210DL remain well below yield. Tensile strains drop, while compressive strains continue to increase, in simulations E150DL and T315DL. In simulations E200DL and T420DL, strains reduce significantly. In simulations E025N - E200N, measured strains are less than 15% of yield. Bar slip appears to occur increasingly, commencing in simulation E075N. Cracking occurred on the top of the slab near this gage very early in the testing. With only 1/4" concrete cover, it seems likely that the closely spaced top bars lost concrete bond, reducing their effectiveness.

Gage S1X14 was east of gage S1X5, but still in the slab "column strip" and within the region of concentrated top reinforcement. In simulations E010DL - T420DL, compressive strains are extremely small. Tensile strains during those simulations are dominated by a small number of large "spikes," with otherwise very small magnitudes. The spikes occur simultaneously with significant structural displacements and correspond to the instants of peak tensile strains in the other slab bars. The spikes are initially smaller than the corresponding strains in gage S1X5; by simulation E075DL, they roughly equal the corresponding strains in gage S1X5. In simulations E100DL - T420DL, the spikes exceed the corresponding strains in gage S1X5. Tensile yield is reached in simulations E200DL and T420DL, and in simulations E075N - E200N. In simulation E150N, peak tensile strains drop, and significant high frequency signals are recorded, commencing at approximately 6 sec into the simulation. In simulations E025N - E200N, strains measured by gage S1X14 are much larger than those measured by gage S1X5. This gage is also in the area that visibly cracked on top of the slab. It is likely that the cracking affected bond in the local area, reducing the effectiveness of the bar. Above some "triggering" lateral displacement level in the structure, the bar was probably engaged through bond in adjacent uncracked areas. As bond deterioration lessened the effectiveness of the bars closer to the center of the column strip, the bar monitored by gage S1X14 attracted more force. The strain fluctuations that occurred during simulation E150N were paralleled by similar high frequency strains in gage S1Z8. Localized concrete cracking apparently affected the joint behavior. First mode frequency data registered a clear frequency reduction in

this simulation.

Gage S1X16 was in the slab "middle strip." With increasing PGA, maximum strains in gage S1X16 increase more rapidly than the strains in gages S1X5 and S1X14. In simulations E200DL and T420DL, maximum tensile strains are constant but compressive strains increase. In simulations E125N - E200N, the rate of increase in tensile strains decrease, while the rate of increase in compressive strains accelerates. In simulations E025N - E200N, maximum tensile strains exceed those measured in gage S1X5. The increasing strains in gage S1X16, with increased lateral displacement, indicate more of the slab width participates in the lateral load resistance mechanism.

Gages S1X11, S1X12, and S1X13 were on reinforcing bars in the first floor slab adjacent to the NW column. These bars were bent 90° down into the spandrel beam, at approximately the middle of the spandrel beam width (Figure 2.15). Gages S1X11 and S1X12 were located in the column strip zone of the slab, while gage S1X13 was located in the middle strip of the slab.

Gage S1X11 was located within the spandrel beam width and in the slab "column strip," approximately $\frac{3}{4}$ " into the spandrel beam width, measured from the inside face of the spandrel beam. The location inside the spandrel beam width was inadvertent and limited the usefulness of the data recorded. By its being inside the spandrel beam width, the longitudinal flexural moments and associated reinforcement strains were below the maxima measured in the slab. In addition, the larger depth of the spandrel beam, relative to the slab depth will reduce flexural strains for a given applied moment. In simulation E125N, there is a brief inconsistency at approximately 11 sec into the simulation. In simulation E150N, maximum strains do not exceed those of simulation E125N, and all strains reduce significantly at approximately 7 sec into the simulation.

Gage S1X12 was located east of gage S1X11 and in the slab "column strip," approximately $\frac{3}{4}$ " into the slab span from the inside (south) face of the spandrel beam. In simulation E125N, there is a brief inconsistency at approximately 11 sec into the simulation. In simulation E150N, maximum tensile strains increase significantly; there is a significant permanent tensile offset, at approximately 3.5 sec into the simulation, with a residual strain of twice the yield strain. This gage recorded larger strains than at any other location, exceeding unconfined concrete crushing strains in several simulations. This region is very close to the zone of significant cracking that resulted from torsional failure of the spandrel beam. The large permanent offset in simulation E150N indicates that significant damage occurred and parallels significant reduction in observed first mode frequency.

Gage S1X13 was east of gage S1X11 and in the slab "middle strip," approximately 1" into the slab span from the inside face of the spandrel beam. Strains are dominated by compressive strain spikes that are similar to the tensile spikes observed in the records for gage S1X14; magnitudes of these spikes increase more rapidly than the PGA. A small compressive offset remains following simulation E200DL. In simulations E075N - E200N, maximum tensile strains gradually decrease, and, by simulation E100N, net compressive strain offsets remained after each simulation. Once net compressive strains occur, there is also evidence of bar slip. The small tensile strains indicate that the effective slab width for negative moment lies within the slab column strip. The high compressive strains and the observed permanent compressive offsets likely reflect a wider required slab width to develop positive moment strength. While the positive moment (bottom) steel ratio almost equals the negative moment (top) steel ratio in the column strip (Table 2.4), the bottom steel is not bent into the spandrel beam, so the full tensile capacity of any given bar is not as likely to develop as it is for the top steel.

5.10 Summary of Observed Responses

This section provides a qualitative overview of the model's condition as the testing progressed. Observed surface conditions of the model and interpretations of the recorded data are combined to characterize the condition of the model. The conditions of the model prior to the earthquake simulations, during the simulations with VEDs installed, and during the simulations following removal of the VEDs are discussed.

(a) Pretest Condition of the Structure

Prior to the beginning of the testing and before the data acquisition system had been activated, the shaking table system "self-initiated" a yawing motion when its hydraulic system was being energized. The shaking table's SE horizontal actuator began pulsing, and the other horizontal actuators activated to offset its motions. The shaking table operator manually shut down the system, but yawing oscillations of the table and model damaged the model. Surface crack examination revealed the patterns seen in Figures 4.38 - 4.47. Hairline cracks were found in all outside columns, spandrel beams, and floor slabs. Column cracks appeared to be minor, largely centered on areas of thin concrete cover over ties. The spandrels, on all floors experienced torsional cracks on either side of each outside column. Significant hairline cracking

occurred in the northern and southern ends of the bottoms of the floor slabs, particularly on floors one and two. In addition, circular cracks in the corners of the floor slabs developed. Some cracking developed on the tops of the floor slabs around the perimeters of the center columns on floors one and two. These mechanisms reduced the stiffness properties of the model below those that would be expected based on “uncracked” section properties.

Before the earthquake simulations, low-level WNTs were conducted. Without any VED bracing, the first modal period was 0.53 sec. The first mode equivalent viscous damping ratio was 6.7%. With large VEDs installed, the first mode period was about 0.30 sec, with a corresponding equivalent viscous damping ratio of about 30%. An additional WNT was conducted, in which the VEDs were replaced by steel braces. In this case, the first mode period was 0.12 sec, with an equivalent viscous damping ratio of 3.9%.

(b) Simulations with VEDs Installed

Initial dynamic characterizations consisted of low acceleration WNTs. At the outset of the simulations with VEDs installed, surface inspections showed that previous cracks in the joints, slabs, and spandrel beams had extended only slightly. Additional WNTs showed essentially no change in modal frequency characteristics.

In simulations E010DL - E250DL, global response of the structure was heavily dominated by the VEDs. Response was dominated by the first mode. Story shear vs. interstory displacement hystereses were broad and consistent, showing good energy dissipation. The slopes of the hysteresis plots show only minor changes from simulation to simulation, indicating that major damage did not occur. Measured stiffness properties gradually decreased in simulations E010DL - T315DL, as the first mode period lengthened from 0.35 sec to 0.41 sec. During this sequence, the normalized (by PGA) interstory displacements increase by approximately 50%; normalized floor accelerations remain fairly stable. Normalized story shears parallel floor accelerations. Equivalent viscous damping in the system was constant at approximately 40%.

The strain dependence of the VEDs is evidenced by their decreasing stiffness over the sequence. However, the relative portion of the story shear transmitted by the VEDs increased by about 50%. Both the VEDs and the baseline structure exhibited stiffness reduction. The VED stiffness reduction is due to the recoverable properties of the viscoelastic material, while the RC structure degraded through minor

damage. Reinforcement strain gages indicate yielding of outside column reinforcement at the second story level occurred by simulation E075DL. Yielding of outside column reinforcement at the base level occurred by simulation E125DL. Evidence of bar slip and concrete cracking appeared in the centerline column reinforcement at the first floor slab level by simulation E075DL. Slab reinforcement adjacent to the spandrel beams began yielding in simulation E075DL. Structural deterioration was not severe enough at that point to affect significantly the behavior of the model. Damage mechanisms continue in subsequent simulations after first appearing, gradually increasing the degradation.

In simulations E150DL and T315DL, maximum normalized accelerations and story shears show significant reductions, indicating more distinct stiffness degradation occurred. Slab reinforcement strains near the first floor centerline columns indicate that reinforcement bond near the columns deteriorated, shifting flexural strains out into the slab width. Reduced tensile strain capacity occurred in the outside column reinforcement in the first floor joint region.

In simulations E200DL and T420DL, maximum normalized accelerations and story shears again reduced. The first mode period lengthened significantly, to 0.51 sec. Previously noted reinforcement strain trends continued. In addition, slab reinforcement strains near the first floor centerline columns indicate that reinforcement bond near the columns deteriorated further; tensile yield occurred in bars away from the center of the column strip; and middle strip reinforcement strains rose. All of these mechanisms indicate more of the slab width contributed to resistance with increasing PGA. Yielding of outside column reinforcement at the second story level was accompanied by bar slip. The centerline column reinforcement at the second floor slab level reaches yield strain. While the data indicate that significant degradation occurred, observed surface cracking changed only slightly from initial observations. Hairline flexural cracking in the slab extended somewhat, while torsional cracks in the spandrel beams also extended further. No cracks show significant widening.

(c) Simulations with VEDs Removed

Following removal of the VEDs, the model stiffness was reduced, as evidenced by lower natural frequencies, and the inherent equivalent viscous damping was slightly higher, compared to the initial dynamic characterizations. As measured by low level WNTs, the first mode period lengthened from 0.53 sec before simulation E010DL to 0.65 sec following simulation E250DL. The measured equivalent viscous damping was approximately 7%.

The high flexibility of the slab-column structure resulted in significant second mode response. The second mode frequency, approximately 5.0 Hz, influences the floor accelerations. Maximum normalized accelerations on floors one and two are comparable to those with VEDs installed, while those on floor three are lower. Maximum normalized first floor accelerations increased through simulation E150N before falling. Maximum normalized second floor accelerations increased through simulation E100N before falling. Maximum normalized third floor accelerations increased through simulation E125N before falling. The decreased acceleration maxima are indicators of the onset of damage mechanisms. Story shears were affected by first and second mode responses and were lower than story shears for comparable PGAs with VEDs installed. Maximum normalized story shears increased slightly with higher PGA through simulation E150N, before falling in simulation E200N. Interstory displacements were dominated by the first mode but second mode influence was present. In simulations E025N - E100N, there was a gradual increase in the maximum normalized interstory displacements with increased PGA. In simulations E125N - E200N, distinct changes occurred in the displacement records, reflecting damage occurrence in the model. Hysteresis plots showed low energy dissipation and pinching.

Whereas the simulations with VEDs installed resulted in a gradual softening of the model with few instances of specific damage, the simulations without VEDs showed several distinct periods of damage.

In simulations E025N and E050N, minor damage accrued. Reinforcement slip occurred in the base of the NW first story column. High frequency signals in the strain histories of the column reinforcement in the NW first floor slab-column joint indicated that concrete cracking occurred in the region. Reinforcement yielding occurred in the column reinforcement at the west centerline first floor slab-column connection. Flexural cracking in the floor slabs gradually lengthened and deepened. The first mode period measured during the simulation lengthened from 0.78 sec in simulation E025N to 0.83 sec in simulation E050N.

In simulations E075N and E100N, slip was detected in the column reinforcement at the west centerline first floor slab-column connection. Reinforcement slip and reduced tensile capacity were found in the floor slab adjacent to that column, and in the floor slab adjacent to the NW first floor slab-column joint. In simulation E075N, hairline flexural cracks appeared at the base of the first story of the west centerline column. In simulation E100N, the first floor spandrel torsional cracks extended. With these minor damage mechanisms, the first mode period remained at 0.83 sec.

In simulation E125N, column reinforcement yielded in the NW first floor slab-column joint. At the west centerline first floor slab-column joint, the column reinforcement experienced strains that were large

enough to cause concrete crushing in unconfined sections. At approximately 11 sec into the simulation, irregularities in the strain histories of the first floor slab reinforcement and of the west centerline column reinforcement at the second floor slab level were recorded. Torsional cracking in the first and second floor spandrel beams extended. The first mode period lengthened to 0.85 sec.

In simulation E150N, deterioration continued. Large strain increases occurred in the first floor slab reinforcement at the NW slab-column joint, and in the west centerline column reinforcement at the second floor slab level at approximately 3 sec into the simulation. Large strain decreases occurred in the first floor slab reinforcement near the west centerline column at approximately 6 sec into the simulation. Spandrel torsional cracking extended on three floor levels. Centerline slab-column joint rotations became large enough for impacts of the column collars to cause spalling of the lower surfaces of the slab concrete on the second and third floor levels. The first mode period lengthened to 0.92 sec.

In simulation E200N, all active reinforcement strain gages registered significant irregularities. At the conclusion of this simulation, the second and third floor spandrel beams had severe torsional cracks. Concrete cover in the spandrel-column joints was spalled. Numerous flexural cracks in the floor slabs extended full width and full depth. The first mode period lengthened significantly to 1.32 sec.

5.11 Primary Observations from the Experimental Program

The testing program was based on an RC slab-column structure that was constructed in the 1950's. The structure possessed inherently low lateral strength and stiffness properties. The construction detailing practices of the 1950's also lead it to be highly nonductile. The testing program examined the use of VEDs placed in diagonal braces in the structure as a means of seismically retrofitting it. A series of seismic simulations was run on the retrofitted model using the USACERL shaking table. The input motion intensities of the simulations were increased with each successive simulation, until the displacement limits of the table actuators were reached. The VEDs were then removed, and the model was again subjected to a series of seismic simulations with increasing input motion intensities. While some damage accrued in the model over the series of simulations, useful comparisons can be made of its behavior with and without VEDs.

Most importantly, the VEDs significantly reduced lateral displacements in the structure, enhancing its serviceability. For example, in simulations E100DL and E100N, the 0.41g El Centro simulations with and without VEDs, maximum interstory drifts in the second story, which sustained the largest interstory

drifts, were 0.76% and 1.76%, respectively. For comparable input motion intensities, interstory drifts in all stories were higher in the simulations without VEDs. In both the simulations with VEDs and those without, lateral displacements normalized by PGA increased slightly with increasing PGA. In the instances of simulations with VEDs present, the increasing normalized displacements primarily result from reductions in the stiffness and damping contributions of the VEDs as VED strains increase. In the simulations with no VEDs present, the increasing normalized displacements resulted from inelastic behavior in the RC structure.

Inertial behavior in the model differed from its displacement response. On the first and second floor levels, maximum accelerations in the simulations with VEDs present and those with VEDs removed were comparable, while, on the third floor level, maximum accelerations in simulations with VEDs present were higher than in those with VEDs removed. In the simulations with VEDs present, the response was dominated by the first mode, while, in the simulations with VEDs removed, second and third mode responses were present. The second mode was influential in the acceleration response when VEDs were not present. For example, in dynamic analyses that were conducted for Chapter 6, isolation of the first mode base shears from the total base shears showed that base shears were 50% - 75% higher in the 1 - 3 sec portion of the El Centro simulations when all modes were considered than when only the first mode was considered. Because of the higher mode effects, floor acceleration maxima in the simulations without VEDs did not occur simultaneously. Story shears that were derived from the floor accelerations and masses showed consistently higher first (base) and second story shears in the simulations with VEDs installed than in simulations without VEDs for equal input motion intensities. Third story shears were lower in the simulations without VEDs than in comparable simulations with VEDs. With VEDs installed, story shears normalized by PGA remain essentially unchanged with increasing PGA, before dropping substantially in the simulations with $PGA > 0.6$ g. In simulations without VEDs, normalized story shears increased slightly with increasing PGA, until significant structural failure occurred in simulation E200N. In the simulations with VEDs installed, both the stiffness and damping contributions of the VEDs decreased with increasing PGA. Lower stiffness lowers acceleration response, while lower damping increases acceleration response. These offsetting factors combined to hold the normalized accelerations almost constant in the simulations with VEDs installed.

The hysteretic behavior of the model was enhanced by the addition of the VEDs. Story shear vs. interstory displacement plots show broad, relatively smooth hysteresis loops in simulations with VEDs installed. In contrast, comparable plots for simulations with VEDs removed show the highly pinched and

irregular behavior that is characteristic of RC structures that do not have ductile reinforcing details. As evidenced by the hysteresis loops, energy dissipation is excellent in the simulations with VEDs installed. Over 90% of the input energy in those simulations is dissipated by the VEDs. By contrast, in the simulations without VEDs, recoverable energy dissipation is poor, and most energy is dissipated through inelastic damage to the model.

While the VEDs greatly improved the behavior of the model in the seismic simulations, the configuration used for the VEDs was found to be inefficient. The VEDs were mounted in a simple chevron bracing scheme, attached to the primary structure via steel column collars that were outfitted for the model. The high rotational flexibilities of the joints in the slab-column structure, coupled with the rotational flexibilities of the VEDs, permitted the VED braces to rotate out of line and induced P-Delta effects in the braces. This lowered their effective axial stiffnesses. This problem was most severe in the third story, where the VED braces had almost zero stiffness. These rotations prohibited full coupling of the VED stiffness and damping contributions into the model, so that currently recognized VED design techniques would not have been accurate. A manufacturer-related overdesign of the VEDs probably kept this problem from being worse than it was, because the overdesign increased VED rotational stiffness. A VED configuration that prevents lateral displacement of the VED would greatly enhance VED effectiveness.

The 1950's-era construction details were significant factors in the structural response. The columns had insufficient lap splice lengths by ACI 318-95 requirements and vulnerable locations right above the floor levels. Bar slip or pullout was a likelihood in severe shaking. The column collars that were installed successfully confined the column concrete, which raised the effective confined strength of the concrete and thus prevented significant bar slip from occurring. At the centerline column locations, the floor slab bottom steel was discontinuous, in violation of ACI 318-95 requirements. Those locations were therefore sources of concern for combined shear and moment transfer failure, which could be catastrophic. No serious failures occurred in those regions. On the other hand, the wide tie spacing in the spandrel beams contributed to their torsional failure, ultimately leading to significant structural deterioration.

CHAPTER 6

INTERPRETATIONS OF STRENGTH AND STIFFNESS RESPONSE

In keeping with the general approach of Chapters 4 and 5, this chapter examines the response of the model during the El Centro seismic simulations. The discussion includes a brief review of the prevalent modeling techniques for slab-column structural systems; describes recommended techniques for determining column and slab capacities and stiffnesses; summarizes the techniques presented in Chapter 2 and Appendix D for modeling viscoelastic dampers (VEDs); and briefly describes the use of the ETABS structural analysis program [17]. Next, using the ETABS software, several of the El Centro simulations are interpreted. A review of the FEMA 273/274 [31] requirements for analyzing and retrofitting existing reinforced concrete slab-column buildings is presented. Finally, a summary of the major observations of this chapter is provided.

The ETABS program is primarily a linear model. The modeling performed for the following interpretations did include the use of a nonlinear damper element, so the time-histories that are discussed include limited nonlinear behavior properties. This approach provides the practical advantage of being quickly transferred to the design community, because of its widespread use of ETABS and similar models.

6.1 General Approach to Structural Modeling

Two-dimensional analyses of one column line of the two-bay, three-story structure were performed. Analysis of the single column line was possible because of symmetry in the structure. As with the experimental portion of the study, input motions were unidirectional, parallel to the longitudinal axis of the structure.

Section 13.7 of ACI 318-95 continues the recommended use of the ACI Equivalent Frame Method (ACI-EFM), which was originally developed by Corley and Jirsa [13]. The ACI-EFM develops substitute column stiffness properties that combine the effects of direct moment transfer from the slab to the column over the column width and indirect moment transfer from the slab to the column through transverse

torsional members. The flexibilities of the columns above and below a joint and the transverse torsional elements are summed and inverted, yielding the equivalent column stiffness. The slab is modeled as a conventional beam element. Variations of this procedure have been devised in terms of “extended” equivalent column and “extended” equivalent beam methods [8]. Computing the torsional element models and the equivalent column stiffnesses is tedious and not intuitive, and the method is strictly applicable to single-story models only, so the ACI-EFM and its variants are not ideal approaches.

An alternative to the ACI-EFM is the *effective slab width method*, in which conventional frame analysis is performed on a modified structural model, in which “beams” are substituted for the slabs in planar analysis of frames comprised of flat slab elements. The beams are typically the same depth as the actual slab, and beam widths are adjusted to provide a conventional rectangular beam whose uniform rotational properties in the joint regions permits the same amount of column rotation as the actual slab, which has non-uniform rotation properties across its width. This approach was initially proposed for static load analysis based on elastic finite element modeling, by Pecknold [37] and others, using the elastic stiffnesses of interior slab-column joints. In recent years, this procedure has been refined to account for the observed behavior of both interior and exterior slab-column joints in laboratory experiments. The technique is simpler and more intuitive to employ than the variants of the ACI-EFM, so it is more appealing to the designer. For that reason, the analyses in this report are based on the effective slab width method.

Sections 6.2 and 6.3 review techniques that have been proposed for determining the strengths and stiffnesses of the column and equivalent beam elements in slab-column structures. Section 6.4 briefly reviews the VED modeling procedures that are presented elsewhere in this report. Section 6.5 describes the fabrication of the analytical model used in this study, and Section 6.6 presents the results of the analyses that were conducted.

6.2 Determination of Member Capacities

This section summarizes the procedures that were used to determine the flexural and shear capacities of the column and slab elements in the test structure, and, where appropriate, lists calculated capacities. No design-related strength reduction (“ ϕ ”) factors were applied to member capacities, and no code-specified load factors were applied to member forces.

(a) Column Capacities

Conventional axial load-moment interaction diagrams were constructed using the “BIAX” computer program [48]. Concrete tensile strength and tension stiffening (contribution of concrete strength between cracks) of the concrete were considered. Material properties used in the BIAx models were chosen to represent the observed properties of the reinforcement and concrete in the model. Four different interaction diagrams were developed for both the exterior columns and the interior (centerline) columns. Two interaction diagrams represent the column capacities incorporating the #3 bars that were stubbed up from the base girder, while two represent the column capacities incorporating the annealed wire that was used above the first story level. For each reinforcement configuration, there is one interaction diagram based on the average concrete unconfined compressive strength (f'_c) of 5.9 ksi and one interaction diagram based on a higher, confined compressive strength for the column lengths that were covered by the VED brace collars. As explained in Chapter 2 and Appendix A, the collars were installed in a manner that effectively confined the concrete. The confined concrete compressive strength in the columns was estimated as 15.8 ksi, at a corresponding strain of 1.9% [36]:

$$f'_{kx} = K_s \rho_x f_y, \quad f'_{ky} = K_s \rho_y f_x \quad (6.1)$$

$$f'_{cc} = f'_c \left(-1.254 - 2.254 \sqrt{1 + \frac{7.94 f'_l}{f'_c}} - \frac{2 f'_l}{f'_c} \right) \quad (6.2)$$

$$\epsilon_{cc} = 0.002 \left[1 + 5 \left(\frac{f'_{cc}}{f'_c} - 1 \right) \right] \quad (6.3)$$

In Equation 6.1, f'_{kx} and f'_{ky} represent the effective confining stresses in the orthogonal x and y dimensions of the column cross-section, ρ_x and ρ_y are the section area ratios of the confining steel to core concrete, and K_s is a confinement stress coefficient. For rectangular sections, K_s is 0.75. If the confining stresses are unequal, Reference 36 provides a graphical means of deriving f'_{kx} and f'_{ky} . They were assumed equal here. In Equation 6.2, f'_{cc} represents the confined concrete compressive strength. In Equation 6.3, ϵ_{cc} represents the concrete strain at peak stress, f'_{cc} .

Table 6.1 lists the material properties used in the BIAx models, and Figures 6.1 - 6.4 plot the appropriate material stress-strain curves and column interaction diagrams. Material properties were not adjusted for strain rate effects (which tend to increase observed strengths) or cyclic loading effects (which

tend to decrease observed strengths).

Tension splice lengths for the column longitudinal reinforcement were 6" for the D7 bars in the exterior columns and 6-¾" for the D9 bars in the interior columns (Figures 2.23 and 2.24). The splice zones were confined by the column collars, so, in computing tension splice lengths required to satisfy current American Concrete Institute (ACI) requirements, the concrete compressive strength was assumed to be 15.8 ksi. Application of Sections 12.2.2, 12.2.3, and 21.5.4 of ACI 318-95 [7] results in required minimum tension splice lengths of 4.24" and 4.41", for the D7 and D9 bars, respectively. Because these required lengths are less than the provided lengths, no reduction in the flexural capacities of the columns was applied to account for anticipated bar slip in the splice zone. While the reinforcement strain gage data indicates some slip may have occurred, the lack of significant observed concrete cracking in the splice zones indicates slip was minimal. For the unconfined concrete compressive strength of 5.9 ksi, the splice lengths provided would have been insufficient, resulting in reduced column flexural capacity.

Column shear strengths were determined by summing Equations 11-3 and 11-15 of ACI 318-95, which are repeated here:

$$V_c = 2 \sqrt{f'_c} b_w d \quad (6.4)$$

$$V_s = \frac{A_v f_y d}{s} \quad (6.5)$$

In Equation 6.4, V_c is the concrete diagonal tension (shear) strength, b_w is the column width, and d is the effective flexural depth of the column. In Equation 6.5, V_s is the shear strength provided by column ties or stirrups, A_v is the area of shear reinforcement at a spacing of s , and f_y is stirrup steel yield stress. This approach conservatively ignores the benefit of the column compressive loads on the concrete diagonal tension strength. Column ties were spaced at 4" (Figures 2.23 and 2.24) and had a yield strength of 100 ksi (which exceeds that allowed by ACI 318-95). The exterior column shear strengths were 9.9 kips and 12.4 kips in the unconfined and confined zones, respectively. The interior column shear strengths were 6.5 kips and 8.5 kips in the unconfined and confined zones, respectively. These column strengths also conservatively ignore the abilities of the column collar assemblies to transmit lateral shear forces. If the column tie strength were 40 ksi instead of 100 ksi, the exterior column shear strengths would be about 3 kips lower, and the interior column shear strengths would be about 2 kips lower.

(b) Slab Flexural Capacities: Interior Column Connections

While the determination of column capacity is straightforward and standardized through the provisions of ACI 318-95, analysis of the flexural capacities of flat slabs is more complex and still the subject of considerable research effort. The moment transfer mechanism in a slab-column connection is quite different from that of a beam-column connection, with loads transferred through a combination of slab flexure, shear, and torsion. The procedure used in ACI 318-95 is the *eccentric shear stress model*, which is based on the Di Stasio and Van Buren research reported in Reference 14. In this model, the vertical shear and a portion of the unbalanced moment at the slab-column connection are assumed to be carried by a linear variation of the shear stress in the slab at a critical perimeter around the column, while the remaining portion of the unbalanced moment is assumed to be carried in flexure by a specified effective slab width. Other researchers have developed various "beam analogies" to determine slab-column connection strengths. The Park and Islam beam analogy [21, 35] models the connection as a series of beams that frame into all four column faces, at a distance of $\frac{1}{2}d$ (effective depth of slab in flexure) from the column face. Unbalanced moment transfer capacity is computed as the sum of the appropriate flexural, shear, and torsional strengths of the beams that frame into the column. Hawkins refined the Park and Islam model, adding slab reinforcement contributions to the beam torsional strength [18, 19].

More recently, modifications of the basic ACI approach have been studied and proposed by a number of researchers [E.G. 15, 25, and 41]. The most recently published study [25], by Luo and Durrani, examines the data base of previous experimental research. The study finds that the eccentric shear stress model is not very accurate and develops new unbalanced moment models that also consider the flexural reinforcement ratio of the slab top steel and the gravity shear ratio at the connection. Briefly, Luo and Durrani suggest that, as the gravity shear ratio ($V_g/4A_c\sqrt{f'_c}$) increases, the mode of connection failure changes from flexure-dominated to punching shear-dominated; and, that, as the slab top steel ratio increases, the fraction of the unbalanced moment transferred by shear decreases. Because the procedures proposed by Luo and Durrani represent an alternative to the recognized ACI procedure, both approaches will be examined.

Section 13.5.3.2 of ACI 318-95 requires that a fraction of the unbalanced moment at the joint be transferred in flexure by a width of slab that extends $1\frac{1}{2}$ slab thicknesses on either side of the column. In the connection under study, this effective width is $12\frac{1}{8}$ inches. The fraction is specified by:

$$\gamma_f = \frac{1}{1 + \frac{2}{3} \sqrt{\frac{b_1}{b_2}}} \quad (6.6)$$

In this instance, b_1 and b_2 are the column dimensions, both equaling five inches, so γ_f is 0.6. Therefore:

$$M_{unb} \leq \frac{M_{n-sw}}{0.6} = 1.67 M_{n-sw} \quad (6.7)$$

In this equation, M_{unb} is the unbalanced moment capacity of the connection, and M_{n-sw} is the moment transfer capacity of the effective slab width (sum of positive and negative moment strengths).

Section 11.12.6.2 of ACI 318-95 requires that M_{unb} satisfy the eccentric shear stress model:

$$M_{unb} \leq \left(v_c - \frac{V_u}{A_c} \right) \left(\frac{2J_c}{\gamma_v (c_1 + d)} \right) \quad (6.8)$$

In Equation 6.8, v_c is the allowable concrete shear strength ($\approx 4\sqrt{f'_c}$), V_u is the applied shear force at the joint, A_c is the area of the critical section, J_c is a property of the critical section that is analogous to its polar moment of inertia, c_1 is the column dimension in the direction of bending, d is the effective depth of the slab, and γ_v is the quantity $(1-\gamma_f)$, which here is 0.4. The smaller of Equations 6.7 and 6.8 would represent the maximum permissible unbalanced moment using the ACI procedure. Equation 6.7 signifies slab flexural yielding, while Equation 6.8 signifies a slab punching shear failure. The yielding predicted by Equation 6.7 would be more ductile than yielding based on Equation 6.8. Using Equation 6.7, M_{unb} is found to be 50 inch-kips. In that instance, the negative moment capacity is computed using the negative moment reinforcement in the effective slab width, and the positive moment is computed using the cracking moment of the effective slab width, since the bottom steel is discontinuous through the column zone. Using Equation 6.8 and the gravity load shears found in the ETABS analyses for Floors 1, 2, and 3, M_{unb} is found to be 75 inch-kips, 74 inch-kips, and 77 inch-kips, respectively. Yielding of the slab flexural reinforcement in the ACI-specified slab width should be accompanied by engagement of more of the total slab width, so catastrophic failure should not occur until the punching shear limit is reached. A check of the negative moment capacity of the total slab width shows a capacity of 83 inch-kips, which slightly exceeds the predicted unbalanced moment capacity using Equation 6.8.

In References 15 and 16, Durrani, et al, suggest reducing v_c by $0.25\sqrt{f'_c}$ for every one percent

increase in lateral drift that occurs to account for the reduced area of slab that is available for shear resistance as the slab cracks under cyclic load reversals. Reference 25 portrays this relationship between drift and capacity graphically.

In Reference 25, Luo and Durrani first propose a refinement of the ACI 318-95 procedure that recalculates γ_v as a function of the top slab reinforcement steel ratio in the joint region:

$$\gamma_v = 1.1 - 18\rho_{ic} - \frac{1}{1 + \frac{2}{3} \sqrt{\frac{b_1}{b_2}}} \quad (6.9)$$

In Equation 6.9, ρ_{ic} represents the steel ratio of the top slab reinforcement in the direction of bending. In this instance, γ_v is 0.32. This modified γ_v results in a larger permissible M_{unb} (93-95 inch-kips) using Equation 6.8, indicating a higher M_{unb} that is governed by punching shear capacity than is predicted by the current ACI procedure.

Luo and Durrani also propose a completely different approach to determining M_{unb} . This approach first calculates an effective beam width that considers both gravity load and the approximate slab width that, with uniform rotation across its width, yields the same column displacement as the full slab width with the actual non-uniform rotation distribution across its width:

$$b_{eff} = \chi \alpha_i l_2 \quad (6.10)$$

In Equation 6.10, l_2 is the full width of the slab transverse to bending (from column center to column center), χ is a width reduction factor that accounts for gravity load influence, and α_i is the effective width factor. The factors are derived as follows:

$$\chi_i = 1 - 0.4 \frac{V_g}{4A_c \sqrt{f'_c}} \quad (6.11)$$

$$\alpha_i = \frac{1.02 \left(\frac{c_1}{l_2} \right)}{0.05 + 0.002 \left(\frac{l_1}{l_2} \right)^4 - 2.0 \left(\frac{c_1}{l_1} \right)^3 - 2.8 \left(\frac{c_1}{l_1} \right)^2 + 1.1 \left(\frac{c_1}{l_1} \right)} \quad (6.12)$$

Previously undefined terms in Equations 6.11 and 6.12 are V_g , the gravity load shear, and l_1 , which is the center to center column spacing in the span. The right-hand term in Equation 6.11 ($V_g/4A_c\sqrt{f_c}$) is the gravity shear ratio, which here is 0.275, indicating that punching shear of the slab is the likely failure mode [27]. Equation 6.12 is a simplification of earlier elastic finite element analysis work that was performed by Pecknold [37].

In this instance, the factor α_i is 0.583, and the factor χ is 0.891, 0.888, and 0.901, for Floors 1, 2, and 3, respectively, leading to an average effective beam width (b_{eff}) of 41.7" for the three floors. Using this effective width, the nominal flexural capacity of the equivalent rectangular section can be calculated in the usual manner. Luo and Durrani suggest that M_{unb} may be determined by considering force equilibrium in the joint region (Figure 6.5):

$$M_{unb} = M_{ut} + \min(M_{ub}, M_{smin}) + 0.5c_1(V_{smax} - V_{smin}) \quad (6.13)$$

Previously undefined terms in Equation 6.13 are M_{ut} , the nominal flexural capacity of b_{eff} in negative bending; M_{ub} , the nominal flexural capacity of b_{eff} in positive bending; M_{smin} , the minimum negative or maximum positive moment produced at the connection by combined gravity and lateral loads; V_{smax} , the maximum shear force acting on the column face; and V_{smin} , the minimum shear force acting on the column face. The nominal flexural capacity of b_{eff} in negative bending, M_{ut} , is 61 inch-kips. Since the slab bottom steel is discontinuous in the joint region, M_{ub} is estimated as the cracking moment (M_{cr}) of the full slab width of 80 inches, which here is 50 inch-kips. This approach is consistent with observations made in Reference 16. Because using Equation 6.13 requires the applied moment, it is a less straightforward approach to determining capacity than the ACI 318-95 approach or the modified ACI approach that uses Equation 6.9, so it will likely not be as readily accepted in the professional design community.

(c) Slab Flexural Capacities: Exterior Column Connection

In Reference 24, Luo and Durrani review the techniques that have been proposed for determining the strength of exterior slab-column connections. Testing of laboratory models [27, 40] has shown that the ACI eccentric shear stress model does not accurately predict the strength of exterior slab-column connections, particularly when spandrel beams are also present (as is the case here). Moehle [27] and Robertson, et al [40], suggest modifications to the effective moment transfer width in the slab as a means of

more accurately predicting moment transfer capacity. ACI Committee 352 [2] suggests predicting the moment transfer capacity when spandrel beams are present as the smaller of the slab column strip flexural capacity or the sum of the torsional capacities ($2T_n$) of the spandrel beams that frame into the column and the flexural capacity of a slab width centered on the column that equals the column width (M_{c2}). This approach may be expressed as:

$$M_{unb} = M_{c2} + 2T_n \quad (6.14)$$

Luo and Durrani note that this approach does not satisfy equilibrium, as the moment that is created by shear forces at the column faces is ignored. It also fails to specify a procedure for determining the spandrel torsional capacity.

Luo and Durrani propose a refinement of the ACI 352 approach:

$$M_{unb} = M_{c1+c2} + 2(\kappa T_c + T_s) \leq M_{l2} \quad (6.15)$$

In Equation 6.15, M_{c1+c2} is the flexural capacity of a slab width that equals the sum of the two column dimensions, T_c is the torsional capacity of the concrete in the spandrel, T_s is the contribution of spandrel stirrups to spandrel torsional capacity, and κ ($= 2.0$) is a multiplier that accounts for spandrel torsional strength increase that is due to the confining effects of the slab. The inequality that includes M_{l2} indicates that the unbalanced moment capacity cannot exceed the flexural capacity of the entire slab width.

Luo and Durrani consider the force equilibrium at the exterior connection to determine M_{unb} (Figure 6.6):

$$\begin{aligned} V_u &= V_{c1+c2} + 2V_{slab} + 2V_{spand} \\ V_{c1+c2} &= V_u \frac{A_{c1+c2}}{\Sigma A} \\ V_{slab} &= V_u \frac{A_{slab}}{\Sigma A} \\ V_{spand} &= V_u \frac{A_{spand}}{\Sigma A} \end{aligned} \quad (6.16)$$

In Equation 6.16, the area terms are defined as follows:

$$\begin{aligned}
 A_{c1+c2} &= (c_1 + c_2)h \\
 A_{slab} &= (c_1 - B)h \\
 A_{spand} &= BH \\
 \sum A &= A_{c1+c2} + A_{slab} + A_{spand}
 \end{aligned} \tag{6.17}$$

Using the definitions of Equations 6.16 and 6.17:

$$M_{unb} = M_{c1+c2} + 2(\kappa T_c + T_s) + 0.5c_1 V_{c1+c2} + B V_{slab} + (B - c_1) V_{spand} \tag{6.18}$$

In Equations 6.15 and 6.18, the torsional strengths are determined as:

$$\begin{aligned}
 T_c &= \left(\frac{x^2 y}{3} \right) 6 \sqrt{f'_c} \\
 T_s &= \frac{\alpha_t A_t x_1 y_1 f_y}{s}
 \end{aligned} \tag{6.19}$$

Terms in Equation 6.19 correspond to those found in Sections 11.6.5 and 11.6.9 of ACI 318-89 [6]. The calculation of T_c using Equation 6.19 yields a larger torque than the torsional cracking moment in the absence of beam shear, as defined in Section 11.6.1 of ACI 318-95 (14 inch-kips vs 11 inch-kips). These values are comparable to those computed using a truss analogy procedure suggested by Zee and Moehle [49], if beam shear is neglected.

Equation 6.18 requires knowledge of the applied shear. The equation yields slightly higher allowable unbalanced moments than Equation 6.15. Unless Equation 6.18 yields a lower estimate, full slab width moments will govern. The procedure of Equation 6.15 is likely to be favored by designers because it does not require knowledge of the applied shear to determine M_{unb} . Applying Equation 6.15 yields $M_{unb} = 84$ inch-kips ($M_{c1+c2} = 14$ inch-kips, $T_c = 14$ inch-kips, and $T_s = 7$ inch-kips). T_c and T_s are defined in Equation 6.19. However, M_{12} is 67 inch-kips for negative bending and 50 inch-kips (M_{cr}) for positive bending. Those lower values govern the allowable value for M_{unb} .

6.3 Determination of Member Stiffnesses

This section summarizes the procedures that were used to determine flexural stiffnesses of the column and slab elements in the test structure. These quantities are required for characterizing the structure in any analyses that are conducted. Published guidelines were used for initial estimates of member stiffness properties and then adjusted so that the properties of the analytical models closely resembled the observed properties of the test model.

(a) Column Stiffnesses

Reference 36 suggests using an effective moment of inertia (I_{eff}) of $0.5 I_g - 0.7 I_g$ for columns loaded axially with $P = 0.2 f'_c A_g$. The reduction from gross section properties reflects the consequences of concrete cracking in the columns. Column properties used in the analyses reported here are listed in Tables 6.2 and 6.3. For portions of the column heights that were not covered by column collars, I_{eff} fell in the general range of the recommended values. In the regions covered by column collars, I_{eff} was increased to values at or near I_g . This increase was made to account for the higher stiffness that would be expected in the concrete because of the confining effects of the collars. It would have been more strictly accurate to adjust the modulus of elasticity in those regions, but, since other stiffness adjustments were made via adjusting moments of inertia, the same approach was employed here.

(b) Slab Stiffnesses

As with strength definition, there has been, and continues to be, substantial research conducted concerning the effective flexural stiffness of flat slabs. As the approach used here employs the *effective beam width method*, the discussion focuses on developing appropriate widths of the slab, centered on the column line, that result in plausible stiffness properties. In general, some fraction of the l_2 (span length between column centerlines, transverse to major bending direction) and the full slab depth are used in computing the “beam” section properties. Two reduction factors, α and β , are normally applied to l_2 . The factor α is applied to reduce the beam stiffness to that of the initial uncracked slab, and β is applied to account for the stiffness reduction that is due to cracking:

$$b_{eff} = \alpha \beta l_2 \quad (6.20)$$

Vanderbilt and Corley [47] were among the earliest researchers to propose this approach (1983). In addition, Reference 47 summarizes the results of research from 1960 through 1978 that led to those authors' conclusions. Moehle and Diebold [28] analyzed a two-story shaking table model using this approach in 1984. Pan and Moehle [34] analyzed beam-column subassemblages using this approach, and Cano and Klingner [8] analyzed small-scale models using the same approach in 1988. In those works, an α coefficient of approximately 0.5 was typically used for geometric conditions that were similar to those of this study, and a β coefficient of 0.33 was used, so that b_{eff} would be about $0.165 l_2$. In Reference 25, Luo and Durrani note that this approach tends to underestimate the slab stiffness at low drift levels and overestimate the slab stiffness at high drift levels.

Luo and Durrani [25] propose using Equation 6.10 to derive b_{eff} to compute *uncracked* stiffness properties at interior connections, effectively making the effective width for the interior connection in this study $0.52 l_2$. They recommend using Equation 9-7 of ACI 318-95 to vary the moment of inertia from this uncracked condition to a fully cracked condition, requiring knowledge of the fully cracked section properties (I_{cr}) and cracking moment (M_{cr}):

$$I_e = \left(\frac{M_{cr}}{M_a} \right)^3 I_g + \left[1 - \left(\frac{M_{cr}}{M_a} \right)^3 \right] I_{cr} \quad (6.21)$$

If one assumes that the b_{eff} determined by Equation 6.10 represents the uncracked gross section, then an effective width of b_{eff} could be used to calculate M_{cr} , and an effective width of about $0.33 b_{eff}$ could be used to approximate I_{cr} . Using this approximation results in a fully cracked effective width of $0.17 l_2$.

In Reference 26, Luo and Durrani calculate α_e for exterior connections as:

$$\alpha_e = \frac{K_t \chi}{K_t + K_s} \quad (6.22)$$

In Equation 6.22, K_t is calculated using Section R13.7.5 of ACI 318-95:

$$K_t = \sum \frac{9E_{cs}C}{l_2 \left(1 - \frac{c_2}{l_2} \right)^3} \quad (6.23)$$

K_t is the torsional stiffness of the torsional member, which includes the spandrel beam and a portion of the

adjoining slab. The term C is a cross-sectional constant defined as:

$$C = \sum \left(1 - 0.63 \frac{x}{y} \right) \frac{x^3 y}{3} \quad (6.24)$$

In calculating C , the cross-section of the torsional member is broken into rectangular areas of dimensions x and y , with $x < y$.

In Equation 6.22, K_s is the flexural stiffness of the slab that frames into the exterior connection ($K_s = 4E_s I_s / l_1$ for the full slab width), and χ is defined by Equation 6.11. This procedure results in an uncracked effective width for the exterior connection in this study of $0.73 l_2$, and a fully cracked effective width of $0.24 l_2$.

For an end span, Luo and Durrani recommend averaging the two effective widths for the interior and exterior connections for the member properties. This procedure would result in an uncracked effective width of $0.62 l_2$ and a cracked effective width of $0.21 l_2$ for the end span, which would be the case in this study.

More recently, Robertson [38, 39] has proposed equivalent beam width procedures that consider the different levels of cracking that typically exist in different locations in the slab. There is usually significantly more cracking in negative moment regions of the slab than in positive moment regions. In addition, the concentration of top slab steel in the column regions usually results in a smaller width of slab resisting negative moment than the width that resists positive moment. This results in lower effective stiffness in negative moment regions than in positive moment regions. Robertson proposes a procedure for monotonic lateral force analysis that breaks each slab span into two regions, one of positive moment influence and one of negative moment influence, broken at the approximate point of contraflexure. In Reference 38, this point is about 35% of the span length from the negative moment end of the span. In Reference 39, this point is about 20% of the span length from the negative moment end of the span. In Reference 38, he assigns α and β factors for each of the regions, for drifts of 0.5% and 1.5%. In Reference 39, he assigns α and β factors for each of the regions, for drifts of 0.5% and 1.0%. These factors are listed in Table 6.4.

The data in Reference 38 are based on tests of a two span single story model, while the data in Reference 39 are based on tests of a three span single story model. In Table 6.4, the cracked effective width properties proposed in References 38 and 39 for 0.5% drift are consistent, except for a significant difference at the interior negative moment region. In the experiments conducted in the current study, the

structure reached 0.5% interstory drift in simulations E075DL and T157DL, 1.0% interstory drift in simulations E125DL and T262DL, and 1.5% interstory drift in simulations E200DL and T420DL.

Reference 38 shows the slab cracking patterns that were observed in the experimental tests upon which the factors in it are based. Those cracking patterns show flexural cracks in the top of the slab that were not observed in the current study; they also show less cracking in the slab bottom at mid-span than was observed here. The different observed cracking conditions suggest differences may exist between the effective stiffnesses observed herein and those from the Robertson work.

These effective width factors will be compared to the effective widths used in the analyses in the current study. It is noted that the majority of the analysis in the current study is time-history analysis, so the joint regions undergo moment reversal. The factors proposed by Robertson will thus not be directly applicable. Figure 6.7 shows the segments of the slab spans that were used in the analyses of the present study. Table 6.5 lists the effective widths for the various segments that were used in the time history analyses that were conducted. At each end of each span, there is an 8.20" zone of narrower effective width. This zone roughly reflects the areas of most severe cracking degradation that were observed, but the exact distance was selected because it matched the location of the attachment points for the viscoelastic damper (VED) braces, so it accommodated the required model geometry well. Each end zone is divided into two segments. The division point approximately marks a distance of $d_{slab}/2$ from the respective column face. This dimension was selected because the ACI-specified shear stress checks use this location.

6.4 Viscoelastic Damper (VED) Modeling

VEDs were modeled using procedures outlined in Chapter 2 and Appendix D of this report. Detailed discussion of those procedures is not repeated here.

Recalling that the VEDs were mounted in diagonal braces within each story, they were modeled by including a linear truss element and a viscous damping dashpot element in parallel in the appropriate locations in the structural model. The linear truss element was given an axial stiffness (AE/L) that was equal to the damper stiffness as computed by Equation 2.21. The damping coefficient of the dashpot was computed using Equation 2.22. Damping force was assumed to be linearly dependent on deformation velocity ($F=CV$). Equations 2.21 and 2.22 require the use of viscoelastic material properties that are ambient temperature, strain, and frequency dependent. Unpublished 3M data that was supplied for use on the project was used for determining the material properties.

In employing Equations 2.21 and 2.22 to define the stiffness and the damping coefficient of the VED, some degree of inaccuracy is built into the modeling procedure because the material properties vary with frequency and with strain magnitude. Absent a more sophisticated damping model, the analyst is required to study the modal frequencies and anticipated maximum displacements to select the appropriate material properties. In the design process, this procedure would be iterative. Here, with known responses in the experiments, anticipated and actual VED characteristics are compared.

Equations 2.18 - 2.24 were used to analyze the results of the stiffness and damping changes that were made to the structure with the addition of the VEDs to it.

6.5 ETABS Modeling Procedures

Observation of the model response during the earthquake simulations and analysis of the test data led the author to believe that most of its nonlinear behavior was due to the VED behavior, deterioration of the spandrel beam stiffness, and cracking of the joint regions. None of these mechanisms is well modeled by available nonlinear analysis programs, so a primarily linear model, ETABS, was selected for use in analysis. It has the advantage of being widely used in the design community. If its use in the present study were found to be practical, it would have good implications for field application.

ETABS version 6.22 [17] was used for both static and dynamic analyses. Because of the lack of observed out-of-plane motion in the shaking table tests, a two-dimensional model of one column line of the test structure was used. Calculated story shears were doubled to account for the complete structure. Figure 6.8 shows the idealized ETABS model. Following is a brief description of the key features of the idealized model and a discussion of some of the features of ETABS that are significant to this application.

Columns were modeled conventionally using the procedures outlined in Sections 6.2.(a) and 6.3. The slabs were modeled as equivalent-width beams using the procedures outlined in Sections 6.2.(b) and 6.3. Both columns and slab-beams were divided into segments that permitted the use of varying moments of inertia along the member lengths. VED braces were modeled with two separate elements in each VED location. One was a linear truss element, and the other was a linear axial damper element, as described in Section 6.4.

The truss and damper elements were connected to the frame via pinned connections. Although the connections in the actual model were welded to prevent rotation, the low rotational stiffness of the VEDs was estimated to allow relatively little moment to be transmitted via the VED braces. Because the

geometry of the VED braces is very influential in governing the VED deformations, and thus their contribution to total structure stiffness and damping, it was important to orient the braces properly. Steel elements that had high flexural stiffness were used to link the structural columns to the braces.

A rotational spring was located at the base of each column. In calibrating the structural analysis models, it was found that total fixity of the column bases resulted in the first story's columns being too stiff before significant column cracking was noted. The rotational springs were therefore added to calibrate the analytical models.

The three floor diaphragms were modeled as rigid translational elements, so all columns at each floor level had the same lateral displacements.

Column P-Delta effects were included in the analyses. ETABS permits the use of rigid zones at beam-column connections. The rigid zone can be sized from 0% to 100% of the member dimensions in 25% increments. In these analyses, 50% of the connection dimensions were considered rigid.

ETABS version 6.22 includes a nonlinear uniaxial damper element, with $F = CV^\alpha$. As described in Section 6.4, this element was employed to model the VEDs. For linear time history analysis, the program converts the damping coefficient, C , to modal damping, assuming that damping is proportional and $\alpha = 1$. This feature was useful for determining equivalent modal damping ratios that could be compared to observed damping from the experiments.

The author discovered through communications with ETABS technical support personnel that the current version of ETABS does not include vertical dynamics. This is not clearly documented in the software literature. Because the VED elements are mounted in a diagonal configuration, they induce some vertical components in the actual structural motions that are therefore not considered. In discussing this issue with the technical support personnel, the author concluded that global responses should not be seriously affected by the exclusion of vertical dynamics, but the calculation of column forces in the structure were definitely affected. As a result, a separate linear time history analysis with damping converted to equivalent modal damping was used for calculating column forces. This approximation does not capture the hysteretic behavior of the damping elements in the reported column forces.

Both the linear time history analyses and the static analyses that were conducted excluded the hysteretic behavior of the VEDs, though the truss elements that were used modeled their storage stiffness.

6.6 Structural Analyses

This Section summarizes the results of the dynamic and static analyses that were conducted.

(a) Initial 3M Design Calculations

The original 3M VED design relied upon Equation 2.24 to develop a damper design curve that assumed a uniform distribution of VED elements (I.E., all VEDs the same size) in the model and focused on the first mode damping and frequency characteristics of the structure. It is helpful to review briefly the assumptions that were used to develop the analytical model that was used in defining the curve. The analyses that supported the VED design were based on assumed conditions before model construction was completed.

Because the 3M design was completed before final construction details for the model were developed, the actual configuration of the lead floor weights was unknown. Total floor weights were assumed to be 18.34 kips on each of the first and second floors, while the third floor weight was assumed to be 17.14 kips. Actual floor weight totals were 20.11 kips on the first floor, 20.07 kips on the second floor, and 18.49 kips on the third floor. The effect of assuming lower floor weights than the actual floor weights is that the initially assumed structural frequency would have been somewhat higher than the actual frequency.

Columns were considered to be uncracked, so gross section properties were used. A uniform equivalent slab width of $0.18 l_2$ was used, approximately consistent with older guidance discussed in Section 6.3. Column bases were considered to be fixed. The concrete E_c was assumed to be 3,420 ksi, lower than the 4,400 ksi that was observed. While assumptions concerning the other stiffness-related parameters generally increased the assumed natural frequency of the model, this assumption lowered it.

3M engineers assumed 0% inherent damping in the baseline model, whereas dynamic testing showed 4% - 5% inherent equivalent viscous damping. 3M had a target of 20% first mode equivalent viscous damping with VEDs installed.

With the assumptions mentioned, the first mode period of the baseline (without VEDs) 3M model was 0.52 sec. Story shear stiffnesses were 48.3 kips/inch, 27.8 kips/inch, and 19.9 kips/inch, for the first, second, and third stories, respectively, in the baseline structure.

The 3M design specified a uniform VED k_d of 11.86 kips/inch, which required a total VED pad

area of 33.28 sq in (Equation 2.21, with $G' = 0.356$ ksi and $\eta_v = 1.0$, and $t = 1.0$ in). 3M fabricated pads of 18 sq in, for total pad areas of 36 sq in, in each VED.

Without changing any of the assumptions concerning the stiffness and damping properties of the structure, but employing the procedure of Equation 2.23, required VED pad areas were found to be 28.8 sq in, 16.6 sq in, and 11.9 sq in, for the first, second, and third story VEDs, respectively. If the inherent equivalent first mode viscous damping ratio were assumed to be 4%, then required VED pad areas dropped to 23.0 sq in, 13.2 sq in, and 9.5 sq in, respectively. All of these quantities were significantly below the 36.0 sq in provided in each VED. This preliminary check of the VEDs used indicates that they were probably oversized for cost-effective response reduction of the structure.

Equation 2.23 shows that the required VED stiffness (and hence size) is proportional to the baseline shear stiffness of the story being considered. As mentioned above, a number of key differences existed between the assumptions used in developing the 3M model and the final model configuration. By using the structural model developed for the ETABS dynamic analysis of simulation E050DL in Section 6.6.(b), and removing the VED braces that were used in that model, a more accurate depiction of the model can be gained. With those properties, the first mode period of the baseline (without VEDs) model was 0.45 sec. Story shear stiffnesses were 61.8 kips/inch, 40.6 kips/inch, and 33.8 kips/inch, for the first, second, and third stories, respectively, in the baseline structure. At an excitation frequency of 2.5 Hz and maximum shear strain of 35%, and for an ambient temperature of 75° F, $G' \approx 0.289$ ksi and $\eta_v \approx 1.38$. These properties differ from the properties targeted in the 3M design. Assuming an inherent 4% equivalent viscous damping ratio and targeting a total first mode damping ratio of 20%, the required VED pad areas were found to be 22.2 sq in, 14.6 sq in, and 12.2 sq in, for the first, second, and third story VEDs, respectively. Increasing the damping ratio from 20% to 25% raised the corresponding required VED pad areas to 32.5 sq in, 21.3 sq in, and 17.8 sq in. All of these areas are substantially below that which was provided.

(b) Time-History Analyses of Response Maxima: VEDs Installed

Time-history analyses of simulations E050DL, E100DL, E150DL, and E200DL were conducted to trace the change in structural properties with increased input motion intensity. For each simulation, the ETABS analysis parameters were adjusted to "back-calculate" the maximum responses that were observed in the simulations. These back-calculations balanced maximum story shears and relative displacements,

maximum sums of horizontal components of VED forces (both absolute and as a percentage of the total story shears), and observed surface cracking patterns. By considering all of these variables, the ETABS analyses provided good “snapshots” of the maximum responses. However, with no load cells on either the columns or the slabs, there was no means of directly calibrating their relative stiffness characteristics, which could lead to inaccuracies.

Column properties (Tables 6.2 and 6.3) were generally consistent with recommended values. In the slab-column joint regions, gross section properties were used, reflecting the observed integrity of the concrete in those regions. Similarly, in the column collar regions, section properties at or near the gross section properties were used, reflecting the stiffening effects of the collars. In other regions, section properties that fell within the guidelines of Section 6.3.(a) were employed. The initial section properties reflected the relatively lower level of damage that was observed in the third story. The gradual softening of the structure is reflected in the decreased section properties with increasing input motion intensity.

The equivalent beam width models (Table 6.5) reflect the significantly higher level of observed cracking in the joint regions, particularly in the spandrel beams. The effective beam widths differ from those proposed by earlier studies [2, 8, 28, 34]. For the lower input motion intensities, the model is stiffer than would have been predicted by their recommendations for fully cracked sections, but more flexible than their recommended uncracked properties. The effective beam widths that were used parallel those recommended by Robertson (Table 6.4). It is important to recall that the pretest damage that was caused by the spurious actuator motion cracked the model, so that comparison with recommended section properties must be measured. Based on the observed slab and spandrel cracking, the third floor slab was assumed to be the stiffest, while the second floor slab was assumed to be the most flexible. The stiffnesses of the lower two floors were also seen to deteriorate more rapidly than that of the third floor.

Table 6.6 lists the VED and column base rotational spring properties that were used. The rotational spring properties reflect a general softening of the column to base girder connections with increased motion intensity. These properties were selected to match the ETABS analyses more closely with the observed responses. For example, in simulation E100DL, the observed base shear was 25.2 kips. With rotational springs, the computed base shear was 25.3 kips. With a fixed base, the computed base shear was 26.1 kips. The VED stiffnesses and damping coefficients for each story are listed, as are the stiffness and damping coefficients that would be calculated using Equations 2.21 and 2.22. There are significant differences between the ideal values and those that were required for back-calculation. The VED properties will be discussed in the following paragraphs that address the analysis results.

Figures 6.9 - 6.20 present interstory displacement and story shear vs. elapsed time plots, and story shear vs. interstory displacement plots, for the first ten seconds of simulations E050DL, E100DL, E150DL, and E200DL. The plots compare computed and measured quantities. The computed responses show excellent agreement with the measured responses.

In all four analyses with VEDs installed, *maximum* story shears and displacements are calculated accurately using the ETABS models (Table 6.7, Figure 6.33). The calculated input energy (Table 6.7) is a progressively smaller percentage of the measured input with increased input motion intensity. Review of the story shear vs. interstory displacement hystereses (Figures 6.11, 6.14, 6.17, and 6.20) shows the calculated hysteretic behavior, while matching well at the points of response maxima, increasingly deviates from the measured behavior with increased input motion intensity (I.E., the calculated hysteresis loops are smaller than the measured loops). Table 6.8 shows story shear stiffnesses for stories 1 and 2 are consistently higher for the ETABS analyses than for the measured quantities, while they are about equal for story 3. As a percent of total story shear, the maximum sum of the horizontal components of the VED forces in the ETABS analyses are approximately equal to the corresponding measured quantities (although there is wide variation among individual VEDs in each story in the measured data). Table 6.9 shows calculated and measured modal periods to be consistent until simulation E200DL, when the computed first mode period (0.44 sec) is substantially lower than the measured first mode period (0.53 sec). Table 6.9 also shows the calculated first mode equivalent viscous damping ratios to be essentially equal to the measured damping ratio for simulation E050DL, but to become increasingly less than the measured damping ratio with increased motion intensity. With the majority of the input energy being related to the damping mechanisms in the structure, the downward trends in the relative magnitudes of input energy and the various damping measures are directly related.

Table 6.10 presents calculated mode shape ordinates for the analyses and corresponding mode shape ordinates from test data. There is good general agreement between the first mode ordinates in the analytical models and those from test data, while the second and third mode ordinates do not compare as well. Overall for all three modes, the ordinates for the first floor are relatively lower in the analytical models than the test data. One of the basic assumptions in applying the modal strain energy method is that the first mode shape ordinates do not vary significantly from the structure with no added braces or VEDs to the damped structure (Section 2.3). Comparison of the mode shape ordinates for the analytical models shows close agreement for this structure, validating this assumption.

Several significant observations can be made from these analyses.

First, in reviewing the overall response characteristics of the model, it appears that the equivalent beam width approach can adequately characterize the structure. This will be explored further in examining the time-histories after the VEDs were removed.

Second, the VED effectiveness in the upper stories, particularly the third story, was limited. As can be seen for the data in Table 6.6, in simulation E050DL, a relatively low input motion intensity simulation, only the VED characteristics for the first story closely replicated the ideal VED characteristics. As speculated in Chapters 4 and 5, it is believed that the relatively flexible joints of the slab-column structure permitted rotations of the VEDs. While their energy dissipation characteristics were lowered somewhat, their stiffness characteristics were drastically lowered. This is probably because they still dissipated energy in the shearing actions that occurred when they rotated, but the rotations greatly reduced the VED brace axial stiffnesses. This lack of added stiffness is actually an indirect attribute, since it lowered story shear because of less period shift. However, the rotations prohibit accurate modeling based on the ideal VED characteristics. As mentioned above, the large VED pad sizes theoretically resulted in an “overdamped” (as compared to the design) structure. Because the pads were as large as they were, however, they probably rotated less than they would have at the nominally designed sizes for each story level.

Third, the erratic changes in VED properties that were required to match the measured response maxima are inconsistent with the published idealized behavior, hampering accurate predictions of behavior. Table 6.6 shows a need to decrease the VED damping coefficients for the first and second stories significantly more than the idealized values would be for the anticipated maximum shear strains. Table 6.6 also shows changes for the VED stiffnesses that are inconsistent with the corresponding changes in damping coefficients. Examination of the hysteresis plots (Figures 6.11, 6.14, 6.17, and 6.20) provides insight into the modeling problem. In simulation E050DL (Figure 6.11), measured stiffness for each story is approximately uniform from the smaller hysteresis loops to the one large loop. In the ETABS model, the stiffness is exactly uniform because brace properties are fixed. Also in simulation E050DL, the measured larger and smaller hysteresis loops are relatively uniform, except that in the larger loop, the area of the loop in the region of maximum displacement is pinched as compared to the area of the larger loop in the ETABS analytical model.

Data from simulations E100DL - E200DL show there is a tendency for the larger hysteresis loops to exhibit somewhat higher stiffness characteristics than the smaller loops. The higher observed stiffness may be partially due to the stiffening of the concrete structure as it reaches larger displacements, for which

it exhibits uncracked properties. The measured hysteresis loops show more pronounced pinching (reduction in force) in the larger displacement region. The smaller measured hysteresis loops do not exhibit the pinching effects at their displacement maximum that the larger loops do. The constant material properties in the ETABS model do not permit modeling this variation.

To match the measured pinching of the hysteresis loops near the points of maximum force and displacement, the single-valued damping coefficient in the ETABS model must be reduced to a value that is below that which is needed to match the average value for the measured responses in each simulation. This also reduces the associated energy dissipation characteristics of each analysis below the average values for each simulation. The relative reductions in damping coefficients required to match the measured conditions at maximum displacement become larger as the input motion intensity increases.

(c) Time-History Analyses of Response Maxima: VEDs Removed

Time-history analyses of simulations E025N, E050N, E100N, E125N, and E150N were conducted to trace the change in structural properties with increased input motion intensity following removal of the VEDs. No attempt to model simulation E200N was made, because of the unique failure mechanism that developed. The ETABS analysis parameters were again adjusted to "back-calculate" the maximum responses that were observed in the simulations. These back-calculations targeted maximum story shears and relative displacements and observed surface cracking patterns. Two analyses of simulation E150N were conducted. They are designated E150N R1 and E150N R2. A significant change in the model response was measured at about three seconds into this simulation, when the model significantly softened. The two analyses were run to bound the conditions of the structure before and after this occurred. Figures 6.21 - 6.32 plot the computed and measured story shear and interstory displacements vs. elapsed time for the first ten seconds of each of these simulations.

Column stiffness properties (Tables 6.2 and 6.3) were lowered following simulation E200DL, reflecting additional cracking that occurred in the model. Because the columns did not noticeably deteriorate during the simulations with VEDs removed, their stiffness properties were held constant for all of these time-history analyses.

The equivalent beam widths (Table 6.5) were significantly lowered following simulation E200DL, reflecting the significant cracking that occurred, especially in the joint regions. The equivalent beam widths for the first and second floor slabs were again lowered following the analysis of simulation E025N,

accounting for crack opening that was observed. For the analyses of simulations E050N - E150N R1, the equivalent beam widths were held constant. In analysis E150N R2, the joint region beam widths were lowered to reflect added cracking that occurred during the simulation. Throughout these analyses, the equivalent beam widths in the joint regions were very small, reflecting the significant deterioration that occurred there. In the exterior joints, most of the softening was caused by opening and extension of the spandrel cracks. At the interior joint, the floor slab was cracking around the column.

The column base rotational spring properties (Table 6.6) were also lowered following the analysis of simulation E200DL. The spring stiffness was held constant until the analysis of simulation E150N R2.

Particularly in the story shear plots, second and third mode responses are clearly shown in both the measured data and the ETABS analyses. Second mode responses are reflected on floors one and three, while the third mode response is evident on floor two. The ETABS analyses for simulations E025N and E050N show very close agreement with the measured responses. In simulation E100N, the ETABS analysis differs from the measured data in some of the regions of peak displacement and/or acceleration. Until approximately five seconds into simulation E125N, the ETABS analysis replicates the measured responses with about the same fidelity as that of simulation E100N. At that time, the measured response shifts to a slightly longer period, which also reduces the measured responses somewhat. The linear ETABS model does not reflect this shift. In simulation E150N, the measured responses show a significant period lengthening, with corresponding significantly reduced spectral response that becomes very significant in the elapsed time of three to five seconds. Analyses E150N R1 and E150N R2 reflect the approximate “before” and “after” conditions. The major changes between the analyses were to decrease the joint stiffness properties and to increase the modal damping ratios from analysis E150N R1 to analysis E150N R2. The base shear and top floor displacement maxima of Table 6.7 summarize the time-history results.

The story shear stiffnesses (Table 6.8) of the ETABS analyses very closely reflect the measured story shear stiffnesses from the simulations, on the first and second stories. The ETABS third story shear stiffness is somewhat lower than the measured story shear stiffness, in the lower input intensity simulations.

Two significant factors stand out in the ETABS analyses of the simulations with VEDs removed. First, though the overall stiffness of the structure was left largely unchanged from simulation E025N through simulation E150N R1, the modal damping ratios were decreased progressively and significantly, to match the ETABS models with the maximum measured responses. The first modal damping ratio was lowered from 6% in simulation E025N to 1% in simulation E150N R1. It is likely that, as the existing cracks in the model widened with each successively higher intensity simulation, pinching became more

severe, lowering hysteretic energy dissipation. The second significant factor is that, while the ETABS models did very well in predicting maximum displacement responses, they did less well in predicting maximum story shears. As the input motion intensity increased, the ETABS models increasingly underpredicted the maximum story shears. Here, it is likely that, as the ETABS models were adjusted to reflect the average condition of the structure during each simulation, the relatively higher strength that would result from loading uncracked sections at times of maximum displacement would result in momentary higher strength characteristics.

(d) Evaluation of Demand Vs. Capacity

For each of the ETABS dynamic analyses, reviews were made of the column axial forces, shears, and moments. Reviews were also made of the slab moments, considering combined shear and moment transfer. Axial forces, shears, and moments were checked at element joints. Gravity loads were superimposed on corresponding time-history loads. Gravity forces were computed once before any of the dynamic analyses with VEDs installed were performed, and then again following the stiffness degradation that was applied during the dynamic analyses with VEDs installed. For the dynamic analyses, slab stiffness characteristics in the two slab spans were mirror images. Without the use of nonlinear models, this results in reasonable representation of global behavior, but may result in less accurate local behavior. As described in Section 6.3, slab stiffnesses in other research have been observed to vary from instants of net positive moment to instants of net negative moment.

(1) Columns

Tables 6.11 - 6.16 present the estimated column capacities and demands.

In analyses E050DL and E100DL, column moments were below yield, based on the interaction diagrams of Figures 6.1 - 6.4. Column shears were below capacity. Column axial forces were in net compression.

In analyses E150DL and E200DL, yield moment is exceeded at the tops of the third story interior columns. In analysis E200DL, yield moment is equaled or slightly exceeded at the bases of the interior first story columns, the bases of the exterior first story columns, and the tops of the third story exterior columns. The zone of calculated yielding of the exterior third story columns is in the length of column that is

effectively widened by the spandrel beam, which may serve to increase the column flexural capacity. No significant flexural cracking was noted in this area during the experiments, indicating little degradation occurred. Shear capacities were exceeded at the tops of the first and second story interior columns. In those locations, column shear is increased by VED brace forces. Since the column collars added approximately twelve kips to the column shear capacity (see Chapter 2), total shear capacity is sufficient.

Net uplift was noted at the bases of the exterior first and second story columns in analyses E150DL and E200DL. The uplift is due to the higher inertial forces that were generated by the stiffness added by the VEDs and the vertical forces added by the VED braces to the columns at the collar connections. The momentary uplift forces were satisfactorily carried by the model. Uplift would be a major concern for the prototype building. Its columns were founded on spread footings.

Also noteworthy in the four analyses of the model with VEDs installed are the significant force redistributions that occurred as the model was adjusted to account for concrete cracking and for VED property changes. For example, some of the maximum column moments in analysis E150DL are lower than those noted for analysis E100DL. This indicates that the modeling assumptions are very critical. While the member stiffness reductions that were applied in the analyses were based largely on the observed crack propagation in the experiments, they are generally consistent with the computed flexural yielding.

In analyses E125N and E150N, yield moment is equaled or exceeded at the bases of the interior first story columns. In analysis E150N, yield moment is exceeded at the tops of the third story interior columns. The same observations as those made for analyses E150DL and E200DL concerning member strength apply.

If the zones of column yielding are characterized as “hinges,” there would be an insufficient number of them in the columns alone to create a theoretical collapse mechanism.

(2) Slabs

Tables 6.17 - 6.19 present the estimated slab capacities and demands.

At the interior connections, the flexural capacities (Equation 6.7) of the critical slab widths are exceeded in almost all of the analyses on all three floors. However, there is significant reserve flexural capacity. This is because the critical slab width is a small portion of the total slab width, thus accommodating added moment. While currently recommended design procedures were not followed, the tests indicate that sufficient reserve flexural capacity existed in the interior connections.

The ACI 318-95 procedure (Equation 6.8) indicates that combined shear and moment transfer failures occur in the first floor slab in analyses E100DL and E200DL, and in the third floor slab in analyses E200DL and E150N. The magnitudes of the unbalanced moments that were computed for analysis E150N imply that, using Equation 6.8, it is likely that a combined shear and moment transfer failure would also have occurred in the first and third floor slabs in simulation E200N. "Modified" Equation 6.8 that implements the Luo-Durrani capacity increase for the effects of top reinforcement in the slab, and the procedure using Equation 6.13, indicate that the first floor slab capacity is sufficient, but the third floor slab capacity would still be insufficient in analysis E200DL.

Added insight on the interior connection strength may be gained by examining the maximum drift ratios that were reached in the seismic simulations. Reference 25 plots the available drift capacity of interior connections as a function of the gravity shear ratio, which was determined in Section 6.2.(b) to be 0.275. For this ratio, Reference 25 projects the lateral drift capacity of the interior connections to be about 2.25%. This drift ratio was met or exceeded on the second floor level in simulations E125N - E200N, and was almost met on the second floor level in simulation E200DL. At the third floor level, it was exceeded in simulations E150N and E200N. At the first floor level, it was almost met in simulation E200N.

While minor slab cracking around the interior columns was observed on all three floors in the higher input motion intensity simulations, the catastrophic mechanism of a shear failure did not occur, even with repeated attainment of conditions that would imply pending failure. The interior connections appear to be stronger than current prediction techniques would indicate. An intangible factor in the simulations may have been the effect that the column collars under the slabs had. Each collar included the four inch leg of an L 7 x 4 x $\frac{3}{8}$ under the slab, on each side of the column in the direction of bending (Figure A.16). Simply by supporting the slab, a collar angle leg could act to increase its effective shear strength.

At the exterior connections, applying Equation 6.15 indicates that flexural yielding of the top steel in the third floor slab would occur in analyses E150DL and E200DL, but other simulations would have no yield. In addition, the analyses imply that the cracking moment of the slab would not be reached during times of positive moment occurrence. The observed damage in the exterior connection contradicts the recommended capacity analyses. This damage also lowered the moments transmitted by the exterior joints, because of their low stiffness. Both positive moment flexural cracks in the slab and significant torsional cracks in the spandrel beams were observed in the tests. This cracking was initiated prior to the first seismic simulations (Section 4.12), and it propagated during the simulation sequence.

The spandrel torsional cracking is particularly significant in strength evaluation. The torsional

cracks on each side of each exterior column formed almost perfectly in the four inch space between the first and second stirrups on each side of each column. This four inch spacing significantly exceeds that which would be required by Section 11.6.6.1 of ACI 318-95 ($\approx 1\text{--}7/8$ "). It is therefore plausible that the stirrups were so widely spaced that they were ineffective, in which case T_s in Equations 6.15 and 6.18 would be zero. In addition, the slab restraint factor of 2.0 in Equations 6.15 and 6.18 may be unconservative. The result is that the moment transfer capacity of the exterior connections may have been significantly below the predicted capacities, with the limitation driven by the torsional capacities of the spandrel beams. Additional study of the unbalanced moment capacities of exterior connections with spandrel beam is merited.

(3) Strength of Structural System

Because of the nature of the anticipated failure mechanism of the interior (centerline) columns in combined shear and moment transfer, conventional limit analysis, which assumes flexural behavior, is difficult to implement. A failure of the interior slab-column connection can result in immediate collapse via the formation of a punching shear mechanism of the slab at the column perimeter. Analysis here is complicated by the apparent severe deterioration of the exterior slab-column joints because of the torsional deterioration of the spandrel beams.

The above-described predictions of interior slab-column joint strength imply that centerline joint failure was imminent at all floor levels. Such failure would have led quickly to a collapse mechanism in the structure. The structure appears to be stronger than would have been predicted. Several factors are likely to be involved. It is possible that the prediction techniques require further refinement; the assumed relative member stiffnesses are incorrect (which would yield a different distribution of moments); strain rate effects may yield higher material strengths (which would increase capacities); or that, even with the localized mechanism, some membrane action occurs in the model. In the only other known shaking table experiment involving a flat slab model, Moehle and Diebold made similar observations [28].

It is also significant that, over the series of seismic simulations, the slab-column joints progressively softened through cracking of the slabs and the spandrel beams. As a result, the joints acted increasingly like pinned connections, with low moments in the joint regions and higher positive moments in the slab mid-span regions. Comparing the mid-span crack patterns of the slab bottoms before the seismic simulations (Figures 4.36, 4.38, and 4.40) with corresponding crack patterns following simulation E200N

(Figures 4.56, 4.58, and 4.60) shows substantial flexural crack propagation in the slab mid-spans, which are positive moment regions.

In addition to the moment redistribution that occurred, the stiffness degradations that developed over the series of simulations shifted the structure to a longer period, lowering member demands, particularly in the simulations with VEDs removed. As a simple illustration of the combined effects of the moment redistribution and reduced demand for the same motion input, analysis E100N was rerun with all of the member properties that were found to be effective in analysis E050DL. Section properties in analysis E050DL, with VED braces removed, were all significantly higher than those of E100N. This analysis assumed all members remained elastic. The maximum base shear computed using this model was 63% of the model weight, compared to the 16% - 20% of the model weight in analysis and simulation E100N. All joints in the analysis had moments that exceeded predicted moment transfer capacities, and all columns at the first and second story levels showed yield moments at their tops and bases that exceeded yield moments. At the third story, the moments at the tops of the columns exceeded yield. Moments in the first story slab-column connections and the bases and tops of the first story columns were two to three times predicted yield. Such high overstressing in all of the joints of the first story indicates that a collapse mechanism would have formed, because there were no joint regions available to assume redistributed moments.

(e) Evaluation of System Stiffness Characteristics

Using maximum base shear and third floor drift, Figure 6.33 reviews the computed and actual stiffness characteristics of the model during the series of simulations. As discussed above, the maximum responses reflect the combined effects of stiffness and damping changes in the model.

In the series of simulations with VEDs installed, the model stiffness decreases over the series of simulations. There are three ranges of approximately constant stiffness, each successively lower than the previous. In Figure 6.34, the curve of measured and computed response maxima is compared to four predictions of response based upon the procedures recommended by Robertson and Ambrose in Reference 39, and by Robertson in Reference 38. In Figure 6.34, curve 1 is that predicted by the Robertson and Ambrose model for 0.5% maximum drift and curve 2 is that predicted by the Robertson and Ambrose model for 1.0% maximum drift. Curve 3 is that predicted by the Robertson model for 0.5% maximum drift, while curve 4 is that predicted by the Robertson model for 1.5% maximum drift. Table 6.4 lists the

effective beam width factors for each of the models. Other models mentioned in Section 6.3.(b) are not shown but, in general, the models represented by curves 1 and 3 emulate uncracked section properties, while those represented by curves 2 and 4 emulate fully cracked section properties of those earlier models. These plots are based on applied static lateral forces at each story level that were derived by modal analysis for the first three modes and then summed using the Square Root Sum of the Squares (SRSS) method. *Column, VED brace, and spring stiffnesses were held constant at the same level as those used for ETABS analysis E050DL.* Figure 6.34 shows that the four models provide reasonable accuracy in predicting the stiffness of the structure at all drift levels. As should be expected, the models based on higher drifts reflect lower stiffness than the models based on lower drifts.

In the series of simulations with VEDs removed, the model stiffness remains fairly constant over the series of simulations. In Figure 6.35, the curve of measured and computed response maxima is compared to four predictions of response based upon the procedures recommended by Robertson and Ambrose in Reference 139, and by Robertson in Reference 38. In Figure 6.35, curves 1 - 4 are based on the same effective beam width models as curves 1 - 4 in Figure 6.34. Table 6.4 lists the effective beam width factors for each of the models. Other models mentioned in Section 6.3.(b) would again correspond as described above. These plots are based on applied static lateral forces at each story level that were derived by modal analysis for the first three modes and then summed using the SRSS method. *Column stiffnesses were again held constant at the same level as those used for ETABS analysis E050DL,* so the damage that occurred in the simulations with VEDs installed is not reflected. Figure 6.35 shows that the Robertson and Robertson and Ambrose models both reflect significantly higher stiffnesses than those observed in the actual testing, because of the prior damage that had accrued during the tests.

6.7 Assessment of FEMA 273/274 Procedures

In recognition of the likelihood that FEMA 273/274 [31] would be used by designers in any future seismic retrofit of the prototype for the model studied here, a brief examination of its provisions with respect to the model was undertaken.

While FEMA 273/274 also outlines approaches for nonlinear static and dynamic procedures, the approach adopted here is to use the FEMA 273/274 Linear Static Procedure (LSP) and Linear Dynamic Procedure (LDP). FEMA 273/274 Paragraph 2.9.1.1 outlines a method to determine whether the linear procedures are applicable. Briefly, FEMA 273/274 requires that the demand-capacity ratio (DCR) be

computed for all building components:

$$DCR = \frac{Q_{UD}}{Q_{CE}} \quad (6.25)$$

In Equation 6.25, Q_{UD} represents force (“demand” due to combined earthquake and gravity loads), and Q_{CE} represents the expected strength (“capacity”) of the component or element. If the $DCR \geq 1.0$ for any element, then inelastic behavior is expected. If the $DCR \leq 2.0$ for all controlling components, then the LSP and LDP may be used without qualification. If the $DCR \geq 2.0$ for any controlling components, then the use of LSP and LDP are subject to various qualifications concerning stiffness, strength, or mass irregularities in the structure. While the calculations that are reported in this section show $DCRs$ that exceed two (Tables 6.20 - 6.28), the structure does not possess any of the irregularities stipulated in FEMA 273/274, so the LSP and LDP may be employed.

(a) Selection of Design Earthquake Forces

Section 3.3 of FEMA 273/274 outlines procedures for determining the design-level base shear for the LSP and the design-level time-histories for the LDP. The procedures consider the soil conditions of the site for the structure. Since this report has not focused on soil conditions, the 150% time-compressed El Centro record ($PGA \approx 0.55$ g) was selected as the “design” earthquake. The maximum base shear that was computed in the LDP was used as the design-level base shear in the LSP, to facilitate comparison of the two procedures. Two cases were considered, with VEDs and without VEDs.

In the LSP, once the total base shear (V) is known, the shear is distributed vertically in accordance with provisions of Section 3.3.1.3.B of FEMA 273/274:

$$F_x = C_{vx} V \quad (6.26)$$

$$C_{vx} = \frac{w_x h_x^k}{\sum_{i=1}^n w_i h_i^k} \quad (6.27)$$

In Equation 6.26, F_x is the lateral load applied at floor level x . Equation 6.27 computes the vertical distribution factor, C_{vx} for each floor level. This equation considers higher mode effects through the

exponents that are employed. The variables in Equation 6.27 are:

w_i = Weight of floor level i

w_x = Weight of floor level x

h_i = Height from base to floor level i (ft)

h_x = Height from base to floor level x (ft)

$k = 1.0$ for $T_1 \leq 0.5$ sec

$k = 2.0$ for $T_1 \geq 2.5$ sec

k is to be interpolated linearly for intermediate values of T_1

Using the full-scale dimensions of the prototype structure and the structural stiffness models described in the following section, the following lateral force distributions, normalized to unity at the third floor level, were calculated. With VEDs, the force distributions are:

$$\begin{aligned} F_3 &= 1.00F \\ F_2 &= 0.73F \\ F_1 &= 0.35F \end{aligned} \tag{6.28}$$

Without VEDs, the force distributions are:

$$\begin{aligned} F_3 &= 1.00F \\ F_2 &= 0.68F \\ F_1 &= 0.32F \end{aligned} \tag{6.29}$$

Equations 6.28 and 6.29 reflect the slightly larger influence of higher mode effects in the more flexible structure without VEDs. In contrast with these lateral force distributions, modal analysis of the model structure, considering its first three modes (summed using SRSS) shows a lateral force distribution of:

$$\begin{aligned} F_3 &= 1.00F \\ F_2 &= 0.78F \\ F_1 &= 0.48F \end{aligned} \tag{6.30}$$

Comparing Equations 6.28 - 6.30 indicates that the FEMA 273/274 lateral force distributions may tend to assign relatively higher inertial forces to the upper stories than were present in the dynamic response.

While this study avoids the calculation of response spectrum-based base shears, it is instructive to examine the procedures of Section 3.3.1.2 of FEMA 273/274 that are used to calculate the fundamental period (T_1), which is required for base shear computation. FEMA 273/274 specifies:

$$T_1 = C_t h_n^{3/4} \quad (6.31)$$

Using the prototype structure height and $C_t = 0.03$ for concrete moment frames results in a fundamental period of 0.38 sec for the prototype. When scaled, this translates to a fundamental period of 0.22 sec for the model in this study. This period is significantly lower than any of the measured or calculated fundamental periods for the model. In the following sections, T_1 for the model without VEDs is found to be 0.48 sec, and T_1 for the model with VEDs is found to be 0.37 sec. This indicates that Equation 6.31 in its current form does not amply account for the low stiffness of slab-column structures, potentially increasing demand forces that are used in design calculations above those which might actually be expected.

(b) Stiffness Parameters for Use in Structural Modeling

Chapter 6 of FEMA 273/274 presents procedures for modeling reinforced concrete structures. The chapter generally recommends that joint regions be modeled as completely rigid. FEMA 273/274 Table 6-4 recommends that column moments of inertia be modeled as $0.7 I_g$ for sections in net compression and $0.5 I_g$ for sections in net tension. Because limited uplift (net tension) was expected in the analyses, an intermediate stiffness of $0.6 I_g$ was used, except in the column collar regions, where the same properties used in all previous analyses were used. This approach is suggested in Section C6.4.1.2 of FEMA 273/274. See Tables 6.2 and 6.3. The column properties are similar to those used in the previous analyses.

FEMA 273/274 Section 6.5.4 covers slab-column moment frames. It permits the use of the effective beam width model that was used in the previously described analyses. The Section stipulates that effective component stiffnesses shall be adjusted on the basis of experimental evidence. While this provision would permit the use of the knowledge gained in the experimental portions of this study, the knowledge would not have been available to a designer working with the prototype. FEMA 273/274 Section C6.5.4.2 recommends that, in the absence of experimental evidence, the effective width may be computed as:

$$b_{eff} = \beta (5c_1 + 0.25l_1) \quad (6.32)$$

Terms in Equation 6.32 were presented previously in Equations 6.8, 6.10, 6.12, and 6.20 of this report. The cracking factor, β , varies between 0.33 and 0.50, depending on the degree of cracking present. Applied to the model structure, with $\beta = 0.33$, b_{eff} is 15 in, or 0.188 l_2 . A review of Table 6.5 shows that this effective width is comparable the effective widths employed in the midspan sections of the model in the previous analyses, but it is wider than the effective widths employed in the connection regions. The larger width will result in larger moment transfer into the slab-beams in the FEMA 273/274 model.

Section 9.3.3.2 of FEMA 273/274 presents modeling procedures for VEDs. The FEMA 273/274 procedures are the same as those presented in this report, so Equations 2.21 and 2.22 may be used to model both the stiffness and damping properties of the VEDs. Since the 150% El Centro record was used as input, the ideal VED properties for simulation E150DL ($k_d = 8.9$ kips/in, $c_d = 0.75$ kip-sec/in) were initially selected.

(c) Strength Parameters for Use in Structural Modeling

In general, FEMA 273/274 follows ACI 318-95 [7] requirements for reinforced concrete member strength determination. FEMA 273/274 makes no special recommendations concerning column strength, so the analyses reported here use the same load-moment interaction diagrams for nominal capacity that were used previously (Figures 6.1 - 6.4). Section 6.4.5 of FEMA 273/274 recommends a reduced reinforcement stress capacity for sections that have insufficient reinforcement development length, compared to ACI 318-95 development length requirements. The reduced capacity is simply the steel yield stress multiplied by the ratio of the provided splice or development length to the length now required by ACI 318-95. Since the column collars in this model provide sufficient confinement (Section 6.2) to develop the reinforcement yield stress, no reduction in column strength in the reinforcement lap splice zones was made. The reader should note that, if the collars were absent, column flexural capacities at the base of each story would be smaller. Column flexure and shear capacities for the FEMA 273/274 analyses are listed in Tables 6.20 - 6.25.

Section 6.5.4.3 of FEMA 273/274 essentially prescribes the use of ACI 318-95 procedures (Equations 6.7 and 6.8) to determine flexural capacities of slab-column connections. The only specific guidance given covers interior column connection strength. FEMA 273/274 permits the use of a slightly

larger effective beam width for strength, column width + 2-½ slab thicknesses from each column face, vs column width + 1-½ slab thicknesses from each column face in ACI 318-95. Because of the lack of guidance for the exterior column connection that includes the spandrel beam, this study assumes the use of the same exterior connection strength model that was used in Equation 6.15. Slab-column connection capacities for the FEMA 273/274 analyses are listed in Tables 6.26 - 6.28.

(d) Additional Structural Modeling Considerations

Because the previous analyses that have been reported showed that the column connections to the base girder were modeled more accurately with rotational springs than with fixed bases, the same rotational springs used in the analysis of simulation E050DL, 25,000 in-kips/rad, were used in the FEMA 273/274 analyses.

The FEMA 273/274 analyses with VEDs in the model required some added considerations. The previously reported analyses showed that the stiffness and damping properties of the VEDs did not couple into the structure equally on all floor levels, and that the stiffness and damping properties were in general not exactly equal to the ideal properties based on prevailing material modeling techniques. It was assumed for the sake of the FEMA 273/274 analyses that the VED stiffness and damping properties were uniform and could be expected to be coupled in the structure adequately. It is likely that a designer would make this assumption.

Section 9.3.4 of FEMA 273/274 stipulates that the effective damping in a structure with supplemental energy dissipation devices cannot exceed 30% of critical damping, including an estimated 5% of critical damping in the baseline structural frame. FEMA 273/274 provides an approach for determining the effective first mode damping, β_{eff} :

$$\beta_{eff} = \beta + \frac{\sum_j W_j}{4\pi W_k}, \beta = 0.05 \quad (6.33)$$

$$W_j = \frac{2\pi^2}{T} C_j \delta_j^2 \quad (6.34)$$

$$W_k = \frac{1}{2} \sum_i F_i \delta_i \quad (6.35)$$

Equation 6.33 estimates the first mode damping as a percent of critical. Equation 6.34 computes the work done by each of “j” viscous devices, for known first mode period, T , damping coefficient, C_j , and relative displacements between the ends of the viscous devices, δ_j . Equation 6.35 computes the maximum strain energy in the structure for “i” floor levels, using the inertial force at each floor level, F_i , and the maximum lateral displacement of each floor level, δ_i . Equations 6.33 - 6.35 examine an idealized single cycle of sinusoidal motion. Applying both these equations and the algorithms that are internal to the ETABS software showed that, with the assumed VED properties, the first mode damping was about 36% of critical. Therefore, the VED properties were reduced to $k_d = 7.6$ kips/in and $c_d = 0.64$ kip-sec/in. The reduction was driven by the need to reduce the damping in the structure to the maximum permitted. Since the stiffness and damping properties are linked, both VED stiffness and damping were reduced by the same percentage, resulting in a first mode damping ratio of 30% of critical.

FEMA 273/274 Section 9.3.4.1 prescribes application of the LSP to structures with velocity-dependent damping devices. Three different design actions must be considered. The first (LSP-1) requires the calculation of lateral forces at the stage of maximum drift. This is simply the application of the static lateral force distribution and computation of forces and displacement in the structure that result when the stiffness components of the VEDs are applied. The second design action (LSP-2) is that which occurs at the stage of maximum velocity and zero drift, which considers the viscous damping force components of the VEDs. Maximum viscous damping force for each VED is estimated by approximating maximum VED deformation velocity as:

$$F_j = C_j \dot{\Delta}_{\max} \approx C_j \frac{2\pi}{T_1} \delta_{nj(\max)} \quad (6.36)$$

The forces generated by the VEDs are applied to the structure in the locations of VED attachment to it, and lateral displacements of the floors are prevented. The resulting force distribution forms design action LSP-2. Since VED stiffness and damping properties are proportional for a fixed excitation frequency, and the maximum velocities and displacements are linked algebraically by equation 6.36, a separate analysis was not required. Maximum viscous forces in each VED were found to be 143% of the maximum forces that were generated by drift. The third design action (LSP-3) is to be computed at the stage of maximum floor acceleration. FEMA 273/274 prescribes that LSP-3 forces for each component are computed as:

$$F_{LSP-3} = F_{LSP-1} \left\{ \cos \left[\tan^{-1} (2\beta_{eff}) \right] \right\} + F_{LSP-2} \left\{ \sin \left[\tan^{-1} (2\beta_{eff}) \right] \right\} \quad (6.37)$$

(e) Evaluation of Demand Vs. Capacity

Six analyses were performed. For the model with VEDs, the LDP, LSP-1, LSP-2, and LSP-3 were performed. For the model without VEDs, the LDP and the LSP were performed. For the LDP, the same procedures that are described in Section 6.6.(d) were used. For the LSP, the models were constructed as described above and then loaded laterally with the force distributions described in Section 6.7.(a). Critical column forces determined in the analyses are found in Tables 6.20 - 6.25. Critical slab forces are found in Tables 6.26 - 6.28.

In the analysis with VEDs installed (FEMA 273-D), the LDP shows yield moments are exceeded in the bases of all first story columns and at the tops of the interior (centerline) second story columns. The analysis also shows shear (diagonal tension) failure at the tops of the second story interior columns, using the unconfined compressive strength of the concrete. As retrofitted on the model, this failure would be unlikely, because column collars were placed at these locations. A small net uplift force occurs in the outside exterior column bases in the first story. While the column collar configuration could accommodate this uplift in the model, the uplift might cause failure in the prototype's spread footings. Combined shear and moment transfer failures occur on the interior slab-column connections on floors 1 and 2. Flexural failures occur in the exterior slab-column connections on floors 1 and 2.

Since LSP-3 is the most severe static loading analysis with VEDs installed, it is reviewed here. Because the static lateral force distribution (Equation 6.28) assigns higher percentages of the total lateral force to the upper stories than does the dynamic analysis (Equation 6.30) for equal base shears, moments are higher in the LSP. The LSP-3 shows yield moments are exceeded in the bases of all first story columns, the bases of the second story interior columns, and at the tops of the interior second and third story columns. The analysis also shows shear (diagonal tension) failures at the tops of the interior columns in all three stories, using the unconfined compressive strength of the concrete. This failure would again be unlikely, because column collars were placed at these locations. Net uplift force occurs in the outside exterior columns. The uplift would again be problematic in the prototype's spread footings. Combined shear and moment transfer failures occur on the interior slab-column connections on all floors. Flexural failures occur in the exterior slab-column connections on all floors.

In both the LDP and the LSP for model FEMA 273-D, forces are higher than those of analysis E150DL. The most significant overall differences between the FEMA 273-D models and the E150DL model are in the smaller connection stiffnesses and smaller VED stiffnesses and damping contributions in

the E150DL model.

In the model without VEDs (FEMA 273-N) the LDP shows yield moments are exceeded in the bases of all first and second story columns, and at the tops of all columns in all stories. The analysis also shows shear (diagonal tension) failure at the bottoms of the interior columns in stories 1 and 2, when using the unconfined compressive strength of the concrete. Net uplift force occurs in the outside exterior columns. The uplift would again be problematic in the prototype's spread footings. Combined shear and moment transfer failures occur on the interior slab-column connections on all floors. Flexural failures occur in the exterior slab-column connections on all floors. While force magnitudes differ slightly, the same failures are noted in the LSP.

In both the LDP and the LSP for model FEMA 273-N, forces are much higher than those of analysis E150N. By simulation E150N, the model had deteriorated significantly. Its stiffness was much lower than for model FEMA 273-N, resulting in much lower force demands.

(f) Evaluation of System Stiffness and Damping Characteristics

In analysis FEMA 273-D, the first mode period is 0.37 sec, compared to a first mode period of 0.39 sec in analysis E150DL (Table 6.9). Story shear stiffnesses in analysis FEMA 273-D are 51.3 kips/in, 60.4 kips/in, and 88.3 kips/in, for the third, second, and first stories, respectively (Table 6.8). Corresponding story shear stiffnesses in analysis E150DL are 36.0 kips/in, 51.8 kips/in, and 91.1 kips/in, respectively. First mode damping is 30% in analysis FEMA 273-D, vs. 24% in analysis E150DL. Maximum base shears in the two analyses are comparable, 61.4% of model weight in analysis FEMA 273-D, vs. 61.8% in analysis E150DL. The slightly higher system stiffness characteristics of the FEMA 273-D model are offset by the lower damping characteristics of the E150DL model in the comparison of base shears. Maximum total top floor drift is significantly larger in analysis E150DL, 0.94%, vs. 0.77% in analysis FEMA 273-D. The higher system stiffness and higher damping characteristics of the FEMA 273-D model combine to reduce its drifts when compared to the E150DL model.

In analysis FEMA 273-N, the first mode period is 0.48 sec, compared to a first mode period of 0.83 sec in analysis E150N (Table 6.9). This is a significant difference. Story shear stiffnesses in analysis FEMA 273-N are 28.1 kips/in, 35.7 kips/in, and 57.0 kips/in, for the third, second, and first stories, respectively (Table 6.8). Corresponding story shear stiffnesses in analysis E150N are 7.9 kips/in, 11.2 kips/in, and 21.5 kips/in, respectively. First mode damping is 5% in analysis FEMA 273-N, vs. 1% in

analysis E150N. Maximum base shears in the two analyses are very different: 80.6% of model weight in analysis FEMA 273-N, vs. 24.5% in analysis E150. Maximum total top floor drift is comparable in the analyses, 1.94% in analysis E150N, vs. 1.98% in analysis FEMA 273-N.

(g) FEMA 273/274 Acceptance Criteria

FEMA 273/273 Section 6.5.4.4 carries two general acceptance criteria for evaluating the “design actions” in deformation-controlled members.

First, the DCRs of the primary components must be checked (Equation 6.25). If the average DCRs of columns in a story level exceed the average values of the slab DCRs in that level, and certain other criteria are met, then that story must be treated as a weak story, which triggers the application of special measures. DCRs for column and slab flexure are presented in Tables 6.29 - 6.31. Because of the use of the column collars in the model structure, column shear DCRs are not presented. The column DCRs are seen to be below the slab DCRs.

Second, for structural elements controlled by deformation actions, each element must be assessed:

$$\frac{DCR}{m\kappa} = \frac{\frac{Q_{UD}}{Q_{CE}}}{m\kappa} \leq 1.0 \quad (6.38)$$

In Equation 6.38, the term m is an element demand modifier that accounts for the expected element ductility for the performance level that is selected for the design. The term κ represents a “knowledge factor” that accounts for the designer’s knowledge of the structure. In this case, with comprehensive knowledge of the structure at hand, κ is 1.0.

In this analysis, the “Life Safety” (LS) performance level as defined by FEMA 273/274 was selected. Table 6-11 of FEMA 273 lists the LS m factor for the column conditions found here as 2.0. Table 6-14 of FEMA 273 lists the LS m factor for the slab conditions found here as 1.625.

Evaluation of Equation 6.38 is shown in Tables 6.29 - 6.31, in the table columns labeled as “Eq. 6.38.” Where a value in those columns exceeds 1.0, FEMA 273 recommends the member capacity as insufficient.

For the analyses with VEDs installed, both the LDP and LSP-3 indicate that column capacities are satisfactory. The slab-column connections on floors 1 and 2 are unsatisfactory, while the slab-column

connections on floor 3 are satisfactory.

For the analyses without VEDs, both the LDP and LSP indicate that column capacities are unsatisfactory at numerous locations. The interior slab-column connections on all floors unsatisfactory, while the exterior slab-column connections on floors 1 and 2 are satisfactory.

6.8 Primary Observations from Interpretations of Strength and Stiffness Response

The effective beam width modeling procedure provides accurate predictions of global maximum response of the slab-column structure, both with and without VEDs. For the cases where VED brace forces in the experimental simulations were measured, the corresponding analyses indicate that maximum member force distributions in the planar column line of the analysis were also reasonably accurately predicted. The procedure is seen to be very sensitive to variations of member properties, particularly equivalent beam widths for slab elements and effective stiffness and damping properties of the VEDs. This high sensitivity dictates that very careful attention be paid to assessing the condition of the structure and the way in which the VEDs will behave when attached to it. The effective beam width procedure is planar in nature and does not provide any information about lateral force distributions in the slabs, spandrel beams, or connections. The analyst is required to apply lessons learned from the results of other experimental work to assess the lateral load distribution.

The use of linear elastic models of the structural stiffness properties was seen to be practical and accurate, so long as thorough assessment of the structural condition could be made for use in establishing those properties and the objective was to assess maximum response. Because the inelastic energy dissipation capability of slab-column construction is more limited than in well-detailed beam-column construction, the elastic modeling approach is more effectively employed. In addition, the complexity of modeling lateral force and strain distributions in slab-column construction would likely negate any gain in accuracy that would arise from the use of currently available 2-D analysis software that models inelastic behavior. Such an approach limits accurate assessment of force redistributions that occur because of inelastic behavior.

Comparing the analytical results with corresponding measured experimental results indicates that the most recently available effective beam width models can be used accurately to predict response of a previously undamaged structure. In the tests with VEDs installed, the experimentally observed tangent stiffnesses closely paralleled the secant stiffnesses of the Robertson models. In tests with VEDs removed,

which occurred after a number of damaging events with VEDs installed, the experimentally observed stiffnesses were well below those derived using the current models. In those tests, the stiffness of the structure remained substantially constant until after a number of additional damaging simulations, with maximum drift exceeding 1.5%.

Comparison of the test results with prevailing methods of computing slab, spandrel, and slab-column strengths indicates that the current methods are conservative (which is desirable). The model structure sustained repeated earthquake simulations, with PGAs approaching 0.9 g in the highest intensity simulations, without catastrophic failure.

Two overarching factors are likely to be at the root of the observed conservatism in both stiffness and strength. First, almost all of the experimental work that has been conducted on slab-column structures has been on subassemblages. Most of the previous work has been performed on single connection subassemblages, though some of it has examined single story models consisting of several columns. Only one previous experimental study [28] has examined a multistory shaking table model. Current analytical models for both strength and stiffness rely largely on subassemblage data. Echoing the observations reported in Reference 28, the structural system here seems to be both stiffer and stronger than is predicted by the available models. The force redistributions that are accommodated in the system are not available in the majority of the subassemblage tests. Second, with enough reinforcement present to maintain structural integrity, the cracking mechanisms that occurred in the slab and spandrels reduced moment transfers in the slabs, lowering demands on critical zones in the structure. These observations indicated that the "Life Safety" goal in older buildings may be more easily attained than previously thought, although serviceability is still an issue.

The analyses of VED behavior show clearly that such devices can lower displacement demands, which is critical for serviceability and structural integrity. Four primary issues arise from the analyses. First, the VEDs must be mounted in the structure in a manner that ensures coupling their stiffness and damping characteristics into it. In all reported previous experiments, VEDs were employed in beam-column models that possessed sufficient connection stiffness to accommodate such coupling. The highly flexible slab-column connections apparently permitted rotations to occur that prohibited full coupling. Second, comparing the analyses with the experimental data shows that VED properties are highly variable. This simply confirmed the published literature on VEDs. Without the inclusion of strain and frequency-dependent VED models, the analyst will need to work carefully to select VED properties that are based on anticipated response frequencies and maximum strains. It is likely that an iterative process will be required

to realize a final configuration of VEDs. The VEDs in this study were oversized for their intended application. Third, the analyses refute the use of an equivalent modal damping ratio without modeling individual VEDs. While the use of an equivalent modal damping ratio can give good general global response, individual member actions are heavily influenced by local behavior. The use of individual VED elements for both stiffness and viscous damping force provides more accurate representation of element behavior. With the inclusion of such elements in commercially available software, use of individual VED elements is prudent. While not explored in this study, it seems intuitively obvious that other supplemental energy dissipation devices, such as viscous dampers, would also be better modeled in this manner.

It is also reassuring and helpful to note that the high degree of damping that can be added to a structure with supplemental energy dissipation devices makes both displacement and inertia response less sensitive to variations in stiffness in the baseline structure, reducing somewhat the need for highly accurate modeling of stiffness properties.

The FEMA 273/274 analyses showed that the current FEMA 273/274 approach for analyzing slab-column construction is very similar to the other analyses that were performed and is thus subject to the same general strengths and limitations. Two noteworthy shortcomings of the FEMA 273/274 approach relate to the low stiffness of slab-column construction. The empirical methods for computing the natural period and for determining the vertical distribution of lateral forces for use in the FEMA 273/274 Linear Static Procedure are inaccurate. With VEDs included, the Linear Static Procedure is cumbersome to apply. The availability of commercial software that includes the ability to model both the stiffness and viscous damping characteristics of VEDs makes the Linear Dynamic Procedure more appealing.

CHAPTER 7

SUMMARY AND CONCLUSIONS

7.1 Objective and Scope

The objective of this study was to investigate the dynamic behavior of a lightly reinforced concrete (LRC) slab-column structure that was modified by adding viscoelastic dampers (VEDs) to it. The investigation was dual-focused. An experimental program involved subjecting an LRC slab-column model to earthquake simulations on the USACERL shaking table. A complementary analytical program used the commercially available ETABS [17] structural analysis software to analyze the response of the model during the earthquake simulations. Through the investigation, simplified analytical methods to facilitate the use of VEDs in seismic retrofit and rehabilitation of LRC slab-column structures were sought.

7.2 Experimental Program

To achieve the research objective, a replica of an existing LRC slab-column structure was fabricated and subjected to simulated earthquake motions on the USACERL shaking table.

(a) Model Structure

The prototype for this study is a three wing "H-shaped" complex of three story structures that was constructed in the mid-1950's near Seattle, WA. One wing of the complex was modeled. The wing is rectangular in plan, with dimensions of approximately 40 feet by 117 feet (Figures 2.1 and 2.2).

The structural framing system is predominately an LRC slab-column moment frame, which contains a number of key reinforcement detailing inadequacies. Column longitudinal reinforcement splices are located immediately above the floor levels. Longitudinal reinforcement splice lengths are inadequate to meet ACI 318-95 [7] requirements, indicating potential inadequate development for full load transfer.

Column reinforcement tie spacing in joint regions is about twice that required by ACI 318-95. Slab bottom reinforcement is discontinuous in the interior column region, violating ACI 318-95 requirements for reinforcement continuity. Spandrel beam stirrups are too widely spaced to meet ACI 318-95 requirements.

In addition to the inadequate reinforcement details, the original total design lateral load was about half that now required by NEHRP [32] in the Seattle area. The vertical distribution of the total design lateral force was also more uniform than required by NEHRP [32], which requires concentrating higher percentages of total load in the upper stories.

A transverse section near the center of the prototype length was modeled. The model was constructed at one-third of full scale (Figures 2.7 and 2.8). Insofar as possible, reinforcement was scaled to one-third of the prototype. Deformed steel wire was used to model the reinforcement. Slab reinforcement consisted of D3 and D5 wire, while column reinforcement consisted of D7 and D9 wire. Wire used for column and slab primary reinforcement was annealed to lower its yield strength to approximately 40 ksi. Unconfined compressive strength of the concrete in the model averaged about 5.9 ksi. First-story columns in the model were cast over longitudinal reinforcement that extended out of a monolithic reinforced concrete base girder. Each floor slab and its six supporting columns were cast monolithically.

To simulate gravity load stresses in the model and provide mass similitude, lead ingots were placed on the floor slabs. The ingots were placed on elastomeric pads, minimizing their interactions with the slabs, and then bolted to the slabs. The resulting floor load in the model was approximately 100 psf on each floor.

VEDs were added in the column lines of the test structure by using diagonal braces that contained them as links in the braces (Figures 2.9 and 2.10). The braces were attached to the columns by means of steel collars that were placed on the columns. The collars confined the column concrete in the lap splice zones, improving flexural capacity. Column flexural strength was increased at the connections to the base girder by substituting No. 3 bars of Grade 60 steel for the D7 and D9 annealed wire reinforcement.

(b) Testing Procedures

Two different sized VEDs were supplied by 3M Corporation. The primary VED configuration consisted of 3" x 6" x 1" pads of 3M ISD 110 polymer (Figure 2.26). The one inch pad thickness was provided by two ½" thick bonded layers. A secondary configuration consisted of 3" x 3" x 1" polymer

pads. Prior to earthquake simulation testing, representative samples of the VEDs were subjected to static and dynamic tests in a universal testing machine. These tests enabled calibration of VED stiffness and damping properties with unpublished manufacturer's data. They also served to point out problems with adhesive bonding of the viscoelastic material and the steel plates in the VEDs.

Following its construction, the model was placed on the shaking table and subjected to earthquake simulations. Approximately 75 channels of data were recorded in each test. The acquired data included longitudinal and lateral accelerations and displacements of the shaking table, base girder, and each floor; VED shear deformations and brace forces, and reinforcement strains in selected column and slab locations.

During the initial checkout of the shaking table hydraulic system following the placement of the model on the table, a spurious horizontal actuator motion excited the model and cracked the columns, spandrels, and slabs. The structure thus had some damage and associated stiffness degradation at the outset of testing. The damage was most consequential in the spandrel beams adjacent to the exterior column faces and in the slabs near the spandrels on the first and second story levels.

Before the start of the earthquake simulations, natural frequencies and equivalent viscous damping properties of the baseline structure in four different configurations were determined: with no VEDs or braces installed, with solid steel braces installed, with small VEDs installed, and with large VEDs installed.

All earthquake simulations with VEDs installed were completed before any earthquake simulations without VEDs were performed. For the simulations with VEDs installed, two characteristic earthquake records were used. The first was the El Centro site record from the May 18, 1940, Imperial Valley, CA, earthquake. The second was the Taft site record from the July 21, 1952, Kern County, CA, earthquake. Time scales for both records were compressed by $\sqrt{3}$. Peak motion amplitudes and frequency contents of the two records differ, allowing some comparison of VED performance under different loading conditions. The Taft record motion amplitude was multiplied by a factor of 2.1 to equilibrate its Housner intensity [20] with that of the El Centro record.

After each earthquake simulation, modal characteristics of the model were determined, and the model was checked visually for cracking or other deterioration. The primary means of assessing modal characteristics was through analyzing acceleration-based transfer functions of the model. Transfer functions were generated from Fast Fourier Transforms (FFTs) of both the simulation time-histories and from low-level white noise tests (WNTs).

Researchers conducted a series of low level ($\text{PGA} < 0.2 \text{ g}$) earthquake simulations with the small VEDs installed, using both the El Centro and Taft acceleration records. The structure was then tested

using the same records with large VEDs installed.

After the low level simulations, further simulations were conducted using only the large VEDs. A series of simulations of increasing input motion intensity was conducted, with PGAs ranging from 0.05 g to almost 0.90 g. The sequence of tests involved running an El Centro simulation followed by a Taft simulation of approximately the same Housner intensity, then repeating the sequence at a higher intensity. These simulations were conducted until the displacement limits of the shaking table horizontal actuators were reached. At this point, significant damage in the model had not occurred.

Earthquake simulations were then conducted on the structure with the VEDs and their braces removed. The collars that were used to attach the VEDs to the columns were left in place, so that the only test variable that was changed was the effects of the dampers and braces. These simulations used only the El Centro record as input, with PGAs ranging from 0.10 g to almost 1.00 g. Testing was concluded after 1.00 g El Centro simulation, when failure of the second and third story exterior slab-column joints occurred.

7.3 Primary Observations from the Experimental Program

Experimental results are summarized in Chapter 4 and discussed in Chapter 5. Appendix D provides a complete listing of data recorded in the earthquake simulations. A number of key observations concerning the addition of VEDs to the slab-column structure resulted from the experimental program.

Most importantly, the VEDs significantly reduced lateral displacements in the structure, enhancing its serviceability. For example, in simulations E100DL and E100N, the 0.41g El Centro simulations with and without VEDs, maximum interstory drifts in the second story, which sustained the largest interstory drifts, were 0.76% and 1.76%, respectively. For comparable input motion intensities, interstory drifts for all stories were higher in the simulations without VEDs. In both the simulations with VEDs and those without, lateral displacements normalized by PGA increased slightly with increasing PGA. In the simulations with VEDs present, the increasing normalized displacements primarily result from reductions in the stiffness and damping contributions of the VEDs as their strains increase. In the simulations with no VEDs present, the increasing normalized displacements resulted from inelastic behavior in the LRC structure.

The hysteretic behavior of the model was greatly enhanced by the addition of the VEDs. Story shear vs. interstory displacement plots show broad, smooth hysteresis loops in simulations with VEDs

installed. In contrast, comparable plots for simulations with VEDs removed show the highly pinched and irregular behavior that is characteristic of RC structures that do not have ductile reinforcing details. As evidenced by the hysteresis loops, energy dissipation is excellent in the simulations with VEDs installed. Over 90% of the input energy in those simulations is dissipated by the VEDs. By contrast, in the simulations without VEDs, recoverable energy dissipation is poor, and most energy is dissipated through inelastic damage to the model.

Inertial behavior of the model differed from its displacement response. On the first and second floor levels, maximum accelerations in the simulations with VEDs present and those with VEDs removed were very comparable, while, on the third floor level, maximum accelerations in simulations with VEDs present were higher than in those with VEDs removed. In the simulations with VEDs present, the response was dominated by the first mode. In the simulations with VEDs removed, second and third mode responses were significant. The second mode was most influential in the acceleration response when VEDs were not present. For example, in dynamic analyses that were conducted for Chapter 6, isolation of the first mode base shears from the total base shears showed that base shears were 50% - 75% higher in the 1 - 3 sec portion of the El Centro simulations when all modes were considered than when only the first mode was considered.

Because of the higher modes, floor acceleration maxima in the simulations without VEDs did not occur simultaneously. Story shears that were derived from the floor accelerations and masses showed consistently higher first story (base) and second story shears in the simulations with VEDs installed than in simulations without VEDs, for equal input motion intensities. Third story shears were lower in the simulations without VEDs than in comparable simulations with VEDs. Story shears normalized by PGA remain essentially unchanged with increasing PGA, before dropping substantially in the simulations with $PGA > 0.6 g$, with VEDs installed. In simulations without VEDs, normalized story shears increased slightly with increasing PGA, until structural failure occurred in simulation E200N. In the simulations with VEDs installed, both the stiffness and damping contributions of the VEDs decreased with increasing PGA. Lower stiffness lowers acceleration response, while lower damping increases acceleration response. These offsetting factors combined to hold the normalized accelerations almost constant in the simulations with VEDs installed.

While the VEDs greatly improved the behavior of the model in the seismic simulations, the configuration used for the VEDs was found to be inefficient. The VEDs were mounted in a relatively simple chevron bracing scheme, attached to the primary structure via steel column collars. The high

rotational flexibility of the joints in the slab-column structure, coupled with the rotational flexibility of the VEDs themselves, permitted the VED braces to rotate out of plane, inducing P-Delta effects in the braces and lowering their effective axial stiffnesses. This problem was particularly severe in the third story, where the VED braces had almost zero stiffness. These rotations prohibited full coupling of the VED stiffness and damping contributions into the model, so that currently recognized VED design techniques would not have been accurate. A manufacturer-related overdesign of the VEDs probably kept this problem from being worse than it was, because the overdesign increased VED rotational stiffness.

The 1950's-era construction details were significant factors to be considered in the response. The columns had insufficient lap splice lengths by ACI 318-95 requirements. The splices were located in vulnerable locations immediately above the floor levels. Bar slip or pullout was a likelihood in the baseline structure if no remedial measures had been taken. The column collars confined the column concrete, raising the effective compressive strength of the concrete and thus preventing significant bar slip from occurring. At the centerline column locations, the floor slab bottom steel was discontinuous, in violation of ACI 318-95 requirements. Those locations were sources of concern for combined shear and moment transfer failure, which could be catastrophic. However, no serious degradation occurred in those regions. On the other hand, the wide tie spacing in the spandrel beams contributed to their torsional failure, ultimately leading to significant structural deterioration.

7.4 Primary Observations from Interpretations of Strength and Stiffness Response

The analyses that were undertaken confirmed the applicability of current modeling procedures, showed areas for improving the accuracy of the procedures, and assisted in the general evaluation of the experimental data. All analyses were performed using the ETABS structural analysis software [17]. Detailed analytical results are reported in Chapter 6.

The effective beam width modeling procedure provides accurate predictions of global maximum response of the slab-column structure, both with and without VEDs. For the cases where VED brace forces in the experimental simulations were measured, the corresponding analyses indicate that maximum member force distributions in the planar column line of the analysis could also be reasonably accurately predicted. The procedure is very sensitive to variations of member properties, particularly equivalent beam widths for slab elements and effective stiffness and damping properties of the VEDs. This high sensitivity dictates that very careful attention be paid to assessing the condition of the structure and the way in which

the VEDs will behave when attached to it. The effective beam width procedure is planar in nature and does not provide any information about lateral force distributions in the slabs, spandrel beams, or connections. The analyst is required to apply lessons learned from the results of other experimental work to assess the lateral load distribution.

The use of linear elastic models of the structural stiffness properties was seen to be practical and accurate for predicting global behavior, so long as thorough assessment of the structural condition could be made for use in establishing those properties and the objective was to assess maximum response. Because the inelastic energy dissipation capability of slab-column construction is more limited than in well-detailed beam-column construction, the elastic modeling approach is more effectively employed. In addition, the complexity of modeling lateral force and strain distributions in slab-column construction would likely negate any gain in accuracy that would arise from the use of currently available 2-D analysis software that models inelastic behavior. Such an approach limits accurate assessment of force redistributions that occur because of inelastic behavior.

Comparing the analytical results with corresponding measured experimental results indicates that the newly available effective beam width models can be used accurately to predict the response of a previously undamaged structure. In the tests with VEDs installed, the experimentally observed tangent stiffnesses closely paralleled the secant stiffnesses that were predicted by current models. At drifts below 1%, the experimentally observed stiffnesses were significantly higher than predicted. In the tests with VEDs removed, which occurred after a number of damaging events with VEDs installed, the experimentally observed stiffnesses were well below those derived using the current models. In the tests with VEDs removed, the stiffness of the structure remained substantially constant until after a number of additional damaging simulations had occurred, with maximum drift exceeding 1.5%.

Comparing the test results with prevailing methods of computing slab, spandrel, and slab-column strengths indicates that the current methods are conservative (which is desirable). The model structure sustained repeated earthquake simulations, with PGAs approaching 0.9 g in the highest intensity simulations, without catastrophic failure.

Two overarching factors are likely to be at the root of the observed conservatism in both stiffness and strength. First, almost all of the experimental work that has been conducted on slab-column structures has been on subassemblages. Most of the previous work has been performed on single connection subassemblages, though some of it has examined single story models consisting of several columns. Only one previous experimental study [28] has examined a multistory shaking table model. Current analytical

models for both strength and stiffness rely largely on the subassembly data. Echoing the observations reported in Reference 28, the structural system here seems to be both stiffer and stronger than is predicted by the available models. The force redistributions that are accommodated in the system are not available in the majority of the subassembly tests. Second, with enough reinforcement present to maintain structural integrity, the cracking mechanisms that occurred in the slab and spandrels reduced moment transfers in the slabs, lowering demands on critical zones in the structure. These observations indicated that the NEHRP [31] “Life Safety” goal in older buildings may be more easily attained than previously thought, although serviceability is still an issue.

The analyses of VED behavior confirm that such devices can lower displacement demands, which is critical for improved serviceability and structural integrity. Four primary issues arise from the analyses. First, the VEDs must be mounted in the structure in a manner that ensures coupling their stiffness and damping characteristics into it. In all reported previous experiments, VEDs were employed in beam-column models that possessed sufficient connection stiffness to accommodate such coupling. The highly flexible slab-column connections apparently permitted rotations to occur that prohibited full coupling. Second, comparing the analyses with the experimental data shows that VED properties are highly variable. Without the use of strain and frequency-dependent VED models, the analyst must work carefully to select VED properties that are based on anticipated response frequencies and maximum strains. It is likely that an iterative process will be required to realize a final configuration of VEDs. The VEDs in this study were oversized for their intended application. Third, the analyses refute the use of an equivalent modal damping ratio without modeling individual VEDs. While the use of an equivalent modal damping ratio can give good general global response, individual member actions are heavily influenced by local behavior. The use of individual VED elements for both stiffness and viscous damping force provides more accurate representation of element behavior. With the inclusion of such elements in commercially available software, use of individual VED elements is prudent. While not explored in this study, it is obvious that other supplemental energy dissipation devices, such as viscous dampers, would also be better modeled in this manner.

It is also reassuring and helpful to note that the high degree of damping that can be added to a structure with supplemental energy dissipation devices makes both displacement and inertia response less sensitive to variations in stiffness in the baseline structure, reducing somewhat the need for highly accurate modeling of stiffness properties.

The FEMA 273/274 [31] analyses showed that the current FEMA 273/274 approach for analyzing

slab-column construction is very similar to the other analyses that were performed and is thus subject to the same general strengths and limitations. Two noteworthy shortcomings of the FEMA 273/274 approach relate to the low stiffness of slab-column construction. The empirical methods for computing the natural period and determining the vertical distribution of lateral forces for use in the FEMA 273/274 Linear Static Procedure [LSP] are inaccurate. With VEDs included, the LSP is cumbersome to apply. The availability of commercial software that includes the ability to model both the stiffness and viscous damping characteristics of VEDs makes the Linear Dynamic Procedure more appealing.

7.5 Concluding Remarks

This experimental program has shown that supplemental energy dissipation devices, such as VEDs, can successfully be employed to reduce earthquake-induced displacements in existing flexible slab-column structures. In this study, the VED-equipped model was able to withstand substantial lateral motions, with PGAs approaching 0.90 g, without serious structural degradation and with good displacement serviceability. With a substantial number of slab-column structures found in areas of moderate seismicity, the use of such devices may be a valuable alternative to the addition of shear walls or the strengthening of critical structural members.

The research showed the need for care in developing the structural configuration that is used to incorporate VEDs in building rehabilitation or retrofit schemes. The use of the VEDs in diagonal braces in the model resulted in poor coupling of the VED stiffness and damping properties into the structure. The VED effectiveness was most limited in the top story, where slab-column connections were most flexible. The diagonal brace configuration could also result in a related serviceability problem in field application, as diagonal braces could leave VEDs under long-term self-weight loading. Without proper support to prevent this, VEDs could creep downward and introduce the possibility of inducing secondary moments during earthquakes. A more appropriate approach is to attach the VEDs to the parent structure in a manner that avoids long-term self-weight loads and minimizes the possibility of the VED rotations that apparently occurred in this research.

The effective beam width modeling approach is capable of providing accurate predictions of dynamic behavior, when member properties are precisely characterized. In addition, elastic structural modeling procedures are adequate for analyzing global behavior in the retrofit design process. Without employing computationally intensive 3-D nonlinear finite element analysis, and given the complexity of

modeling the strength and stiffness characteristics of slab-column frames, this approach, combined with thorough study of the available literature, is more justified than employing currently available nonlinear 2-D structural modeling techniques.

In employing the effective beam width method, structural condition assessment and subsequent determination of member properties are critical. Current techniques can accurately predict structural stiffness, when structural conditions are considered. The FEMA 273/274 [31] approach accurately predicted the stiffness properties of the model in its condition at the very beginning of testing (at simulation E050DL). Available literature is consistent on establishing column stiffness properties, but is somewhat inconsistent on establishing effective slab width properties. The slab widths used in analysis will significantly affect structural stiffness. This in turn would affect the determination of VED properties, as they are both frequency and strain dependent.

The results of this research indicate that slab-column systems are somewhat stronger than ACI 318-95 [7] and FEMA 273/274 [31] reflect. This is particularly true for the structure that has had the relatively simple addition of column collars that would minimize reinforcement slippage in splice zones.

The use of single-valued VED stiffness and damping properties was seen to be accurate in defining maximum responses. However, those properties must be based on conditions that accurately reflect the maximum displacements in the structure and the structural stiffness at the times of maximum displacement.

LIST OF REFERENCES

1. Abbas, H, and Kelly, JM, "A Methodology for Design of Viscoelastic Dampers in Earthquake-Resistant Structures," Earthquake Engineering Research Center, Report Number UCB/EERC-93/09, November 1993.
2. ACI Committee 352, "Recommendations for Design of Slab-Column Connections in Monolithic Reinforced Concrete Structures," ACI Structural Journal, American Concrete Institute, Volume 85, Number 6, November-December 1988, pp 675-696.
3. Aiken, ID, and Kelly, JM, "Earthquake Simulator Testing and Analytical Studies of Two Energy-Absorbing Systems for Multistory Structures," Earthquake Engineering Research Center, Report Number UCB/EERC-90/03, October 1990.
4. Bergman, DM, and Hanson, RD, "Viscoelastic Mechanical Damping Devices Tested at Real Earthquake Displacements," Earthquake Spectra, Earthquake Engineering Research Institute, Volume 9, Number 3, August 1993, pp 389-417.
5. "Building Code Requirements for Reinforced Concrete," ACI 318-51, American Concrete Institute.
6. "Building Code Requirements for Structural Concrete," ACI 318-89, American Concrete Institute.
7. "Building Code Requirements for Structural Concrete," ACI 318-95, American Concrete Institute.
8. Cano, MT, and Klingner, RE, "Comparison of Analysis Procedures for Two-Way Slabs," ACI Structural Journal, American Concrete Institute, Volume 85, Number 6, November-December 1988, pp 597-608.
9. Chang, KC, Lai, ML, Soong, TT, Hao, DS, and Yeh, YC, "Seismic Behavior and Design Guidelines for Steel Frame Structures with Added Viscoelastic Dampers," Technical Report NCEER-93-0009, National Center for Earthquake Engineering Research, May 1, 1993.
10. Chang, KC, Soong, TT, Lai, ML, and Nielsen, EJ, "Viscoelastic Dampers as Energy Dissipation Devices for Seismic Applications," Earthquake Spectra, Earthquake Engineering Research Institute, Volume 9, Number 3, August 1993, pp 371-387.

11. Chang, KC, Soong, TT, Oh, S-T, and Lai, ML, "Seismic Behavior of Steel Frame with Added Viscoelastic Dampers," Journal of Structural Engineering, American Society of Civil Engineers, Volume 121, Number 10, October 1995, pp 1418-1426.
12. Chopra, AK, Dynamics of Structures: Theory and Applications to Earthquake Engineering, Prentice-Hall, 1995.
13. Corley, WG, and Jirsa, JO, "Equivalent Frame Analysis for Lateral Loads," Journal of Structural Division, American Society of Civil Engineers, Volume 105, Number ST10, October 1979, pp 1981-1998.
14. Di Stasio, J, and Van Buren, MR, "Transfer of Bending Moment between Flat Plate Floor and Column," ACI Journal, Proceedings, Volume 57, Number 3, September 1960, pp 299-314.
15. Durrani, AJ, and Du, Y, "Seismic Resistance of Slab-Column Connections in Existing Non-Ductile Flat-Plate Buildings," Technical Report NCEER-92-0010, National Center for Earthquake Engineering Research, 18 May 1992.
16. Durrani, AJ, Du, Y, and Luo, YH, "Seismic Resistance of Nonductile Slab-Column Connections in Existing Flat Slab Buildings," ACI Structural Journal, American Concrete Institute, Volume 92, Number 4, July-August 1995, pp 479-487.
17. ETABS: Three Dimensional Analysis of Building Systems, Version 6.22, Computers and Structures, Incorporated.
18. Hawkins, NM, "Shear Strength of Slabs with Moments Transferred to Columns," Shear in Reinforced Concrete, ACI Special Publication SP-42, American Concrete Institute, 1973, pp 817-846.
19. Hawkins, NM, Bao, A, and Yamazaki, J, "Moment Transfer from Concrete Slabs to Columns," ACI Structural Journal, American Concrete Institute, Volume 86, Number 6, November-December 1989, pp 705-716.
20. Housner, GW, "Behavior of Structures During Earthquakes," Journal of the Engineering Mechanics Division, American Society of Civil Engineers, Volume 85, Number EM4, October 1959, pp 109-129.
21. Islam, S, and Park, R, "Tests on Slab-Column Connections with Shear and Unbalanced Flexure," Journal of the Structural Division, American Society of Civil Engineers, Volume 102, Number ST3, March 1976, pp 549-568.
22. Kasai, K, Munshi, JA, Lai, M-L, Maison, BF, "Viscoelastic Damper Hysteretic Model: Theory, Experiment, and Application," Proceedings of Seminar on Seismic Isolation, Passive Energy Dissipation, and Active Control, ATC 17-1, Applied Technology Council, 11-12 March 1993, pp 521-532.

23. Lobo, RF, Bracci, JM, Shen, KL, Reinhorn, AM, and Soong, TT, "Inelastic Response of R/C Structures with Viscoelastic Braces," Technical Report NCEER-93-0006, National Center for Earthquake Engineering Research, April 5, 1993.
24. Luo, YH, Durrani, AJ, and Conte, JP, "Equivalent Frame Analysis of Flat Plate Buildings for Seismic Loading," Journal of Structural Engineering, American Society of Civil Engineers, Volume 120, Number 7, July 1994, pp 2137-2155.
25. Luo, YH, and Durrani, AJ, "Equivalent Beam Model for Flat-Slab Buildings-Part 1: Interior Connections," ACI Structural Journal, American Concrete Institute, Volume 92, Number 1, January-February 1995, pp 115-124.
26. Luo, YH, and Durrani, AJ, "Equivalent Beam Model for Flat-Slab Buildings-Part II: Exterior Connections," ACI Structural Journal, American Concrete Institute, Volume 92, Number 2, March-April 1995, pp 250-257.
27. Moehle, JP, "Strength of Slab-Column Edge Connections," ACI Structural Journal, American Concrete Institute, Volume 85, Number 1, January-February 1988, pp 89-98.
28. Moehle, JP, and Diebold, JW, "Experimental Study of the Seismic Response of a Two-Story Flat-Plate Structure," Earthquake Engineering Research Center, Report Number UCB/EERC-84/08, August 1984.
29. Munshi, JA, and Kasai, K, "Modal Analysis Procedures for Viscoelastic Frames," Proceedings of Fifth U.S. National Conference on Earthquake Engineering, Earthquake Engineering Research Institute, 10-14 July 1994, pp 1055-1064.
30. Naeim, F, The Seismic Design Handbook, Van Nostrand Reinhold, 1989.
31. NEHRP Guidelines for the Seismic Rehabilitation of Buildings, and NEHRP Commentary on Guidelines for the Seismic Rehabilitation of Buildings, FEMA 273/274, Federal Emergency Management Agency, October 1997.
32. NEHRP Recommendations for Seismic Regulations for New Buildings, 1994 Edition, FEMA 222A, Federal Emergency Management Agency, May 1995.
33. Pacific Coast Uniform Building Code, 1955 Edition, pp 90-95, pp 313-316.
34. Pan, AA, and Moehle, JP, "Reinforced Concrete Flat Plates Under Lateral Loading: An Experimental Study Including Biaxial Effects," Earthquake Engineering Research Center, Report Number UCB/EERC-88/16, October 1988.
35. Park, R, and Islam, S, "Strength of Slab-Column Connections with Shear and Unbalanced

Flexure," Journal of the Structural Division, American Society of Civil Engineers, Volume 102, Number ST9, September 1976, pp 1879-1901.

36. Paulay, T, and Priestley, MJN, Seismic Design of Reinforced Concrete and Masonry Buildings, John Wiley & Sons.

37. Pecknold, DA, "Slab Effective Width for Equivalent Frame Analysis," ACI Journal, Proceedings, American Concrete Institute, Volume 72, Number 4, April 1975. pp 135-137.

38. Robertson, IN, "Analysis of Flat Slab Structures Subjected to Combined Lateral and Gravity Loads," ACI Structural Journal, American Concrete Institute, Volume 94, Number 6, November-December 1997, pp 723-729.

39. Robertson, IN, and Ambrose, CJ, "Analytical Representation of Flat Plate Structures Under Vertical and Lateral Loads," Recent Developments in Deflection Evaluation of Concrete, ACI Special Publication SP-161, American Concrete Institute, 1996, pp 51-74.

40. Robertson, IN, and Durrani, AJ, "Gravity Load Effect on Seismic Behavior of Exterior Slab-Column Connections," ACI Structural Journal, American Concrete Institute, Volume 88, Number 3, May-June 1991, pp 255-267.

41. Robertson, IN, and Durrani, AJ, "Gravity Load Effect on Seismic Behavior of Interior Slab-Column Connections," ACI Structural Journal, American Concrete Institute, Volume 89, Number 1, January-February 1992, pp 37-45.

42. Sause, R, Hemingway, G, and Kasai, K, "Simplified Seismic Response Analysis of Viscoelastic-Damped Frame Structures," Proceedings of Fifth U.S. National Conference on Earthquake Engineering, Earthquake Engineering Research Institute, 10-14 July 1994, pp 839-848.

43. Shen, KL, and Soong, TT, "Design of Energy Dissipation Devices Based on Concept of Damage Control," Journal of Structural Engineering, American Society of Civil Engineers, Volume 122, Number 1, January 1996, pp 76-82.

44. Sozen, MA, "Uses of an Earthquake Simulator," Eleventh Water Reactor Safety Research Meeting, 1983.

45. Uang, CM, and Bertero, VV, "Use of Energy as a Design Criterion in Earthquake-Resistant Design," Earthquake Engineering Research Center, Report Number UCB/EERC-88/18, November 1988.

46. Uniform Building Code, 1991 Edition, International Conference of Building Officials, pp 156-195.

47. Vanderbilt, MD, and Corley, WG, "Frame Analysis of Concrete Buildings," Concrete International, American Concrete Institute, December 1983, pp 33-43.

48. Wallace, JW, "BIAX: Revision 1, A Computer Program for the Analysis of Reinforced Concrete and Reinforced Masonry Sections," Department of Civil Engineering, Clarkson University, Report CU/CEE-92/4, February 1992.

49. Zee, HL, and Moehle, JP, "Behavior of Interior and Exterior Flat Plate Connections Subjected to Inelastic Load Reversals," Earthquake Engineering Research Center, Report Number UCB/EERC-84/07, August 1984.

| Location | Item | Load (PSF) |
|--|-------------------------------|------------|
| Roof Level (Third Floor) | | |
| | Slab (7") | 87.5 |
| | Roofing/Insulation | 8.0 |
| | Ceiling | 2.0 |
| | Parapet, Misc. | 10.0 |
| | Snow | 20.0 |
| | Live Load (As-Built Drawings) | 20.0 |
| | Total | 147.5 |
| 1 ST & 2 ND Floors | | |
| | Slab (7") | 87.5 |
| | Ceiling | 2.0 |
| | Partitions, etc. | 25.0 |
| | Live Load (As-Built Drawings) | 40.0 |
| | Total | 154.5 |

Table 2.1 Distributed Floor Loads in Prototype

| Parameter | Scaling Relationship | Prototype ÷ 1/3-Scale |
|-------------------|----------------------|--------------------------|
| Length | L | 3 |
| Time | \sqrt{L} | $\sqrt{3} \approx 1.732$ |
| Mass | L^2 | 9 |
| Displacement | L | 3 |
| Velocity | \sqrt{L} | $\sqrt{3} \approx 1.732$ |
| Acceleration | 1 | 1 |
| Stress | 1 | 1 |
| Strain | 1 | 1 |
| Force | L^2 | 9 |
| Shear | L^2 | 9 |
| Bending Moment | L^3 | 27 |
| Area | L^2 | 9 |
| Moment of Inertia | L^4 | 81 |

Table 2.2 Scaling Similitude Requirements for 1/3-Scale Model

| Quantity | Prototype | Exact 1/8-Scale Model | Actual Model | Actual/Exact |
|----------------------------------|------------------------|-----------------------|-----------------------|--------------|
| Lateral Column Spacing, C-C | 19' 4" | 77.33" | 77.88" | 1.01 |
| Longitudinal Column Spacing, C-C | 19' 4" | 77.33" | 79.75" | 1.03 |
| Story Height | 10 '0" | 40" | 40" | 1.00 |
| Slab Thickness | 7" | 2.33" | 2.375" | 1.02 |
| Slab Steel Cover | 0.75" | 0.25" | 0.25" | 1.00 |
| Exterior Column Width | 23.75" | 7.92" | 8.25" | 1.04 |
| Exterior Column Gross Depth | 12" | 4" | 4.25" | 1.06 |
| Exterior Column Gross Area | 285 in ² | 31.67 in ² | 35.06 in ² | 1.11 |
| Exterior Column Gross Moment of | 3,420 in ⁴ | 42.22 in ⁴ | 52.78 in ⁴ | 1.25 |
| Interior Column Width | 14" | 4.67" | 5.00" | 1.07 |
| Interior Column Gross Depth | 14" | 4.67" | 5.00" | 1.07 |
| Interior Column Gross Area | 196 in ² | 21.78 in ² | 25.00 in ² | 1.15 |
| Interior Column Gross Moment of | 3,201 in ⁴ | 39.52 in ⁴ | 52.01 in ⁴ | 1.32 |
| Column Steel Cover | 0.75" | 0.25" | 0.375" | 1.50 |
| Spandrel Beam Width | 10" | 3.33" | 4.25" | 1.28 |
| Spandrel Beam Gross Depth | 15.625" | 5.21" | 5.00" | 0.96 |
| Spandrel Beam Gross Area | 156.25 in ² | 17.36 in ² | 21.25 in ² | 1.22 |
| Spandrel Beam Gross Moment of | 3,179 in ⁴ | 39.25 in ⁴ | 44.27 in ⁴ | 1.13 |
| Spandrel Steel Cover | 0.75" | 0.25" | 0.375" | 1.50 |

Table 2.3 Comparison of Key Dimensions in Prototype and 1/8-Scale Model

| Location | Prototype | | Model | | ρ_m / ρ_p |
|---|---------------------------|--------------------|---------------------------|----------------|-------------------|
| | Steel Ratio (ρ_p)* | Number of Bars | Steel Ratio (ρ_m)* | Number of Bars | |
| <i>Column Strip</i> | | | | | |
| Edge (-M) | 0.0065 | 12 - # 6 | 0.0063 | 12 - D5 | 0.97 |
| Midspan (+M) | 0.0060 | 11 - # 6 | 0.0058 | 11 - D5 | 0.97 |
| Interior (-M) | 0.0087 | 9 - # 6 + 10 - # 5 | 0.0084 | 16 - D5 | 0.96 |
| <i>Middle Strip</i> | | | | | |
| Edge (-M) | 0.0020 | 8 - # 4 | 0.0022 | 7 - D3 | 1.10 |
| Midspan (+M) | 0.0031 | 8 - # 5 | 0.0028 | 9 - D3 | 0.90 |
| Interior (-M) | 0.0027 | 11 - # 4 | 0.0032 | 6 - D5 | 1.19 |
| * Reinforcement ratios are based on gross slab depth. | | | | | |

Table 2.4 Prototype and Model Longitudinal Slab Reinforcement

| Location | Prototype | | Model | | ρ_m / ρ_p |
|---|---------------------------|-------------------|---------------------------|----------------|-------------------|
| | Steel Ratio (ρ_p)* | Number of Bars | Steel Ratio (ρ_m)* | Number of Bars | |
| <i>Column Strip</i> | | | | | |
| Midspan (+M) | 0.0038 | 10 - # 5 | 0.0037 | 7 - D5 | 0.97 |
| Interior (-M) | 0.0063 | 6 - # 6 + 8 - # 5 | 0.0063 | 12 - D5 | 1.00 |
| <i>Middle Strip</i> | | | | | |
| Midspan (+M) | 0.0022 | 9 - # 4 | 0.0025 | 8 - D3 | 1.14 |
| Interior (-M) | 0.0027 | 7 - # 5 | 0.0022 | 7 - D3 | 0.81 |
| <i>Edge Strip (½ width)</i> | | | | | |
| Midspan (+M) | 0.0020 | 4 - # 4 | 0.0025 | 4 - D3 | 1.25 |
| Interior (-M) | 0.0025 | 5 - # 4 | 0.0025 | 4 - D3 | 1.00 |
| * Reinforcement ratios are based on gross slab depth. | | | | | |

Table 2.5 Prototype and Model Lateral Slab Reinforcement

| Location | Prototype | | | | Model | | | | ρ_m / ρ_p |
|-------------------------------------|--|--------------------|--------------|---------|--|----------------|--------------|---------|-------------------|
| | Steel Ratio (ρ_p) ¹ | Number of Bars | Tie/Stirrup | | Steel Ratio (ρ_p) ¹ | Number of Bars | Tie/Stirrup | | |
| | | | Bar Diameter | Spacing | | | Bar Diameter | Spacing | |
| Exterior Column | 0.0124 | 8 - # 6 | 0.375" | 12" | 0.0120 | 6 - D7 | 0.147" | 4" | 0.97 |
| Exterior Column @ Base ² | 0.0124 | 8 - # 6 | 0.375" | 12" | 0.0188 | 6 - #3 | 0.147" | 4" | 1.49 |
| Interior Column | 0.0161 | 4 - # 8 | 0.375" | 12" | 0.0144 | 4 - D9 | 0.147" | 4" | 0.89 |
| Interior Column @ Base ² | 0.0161 | 4 - # 8 | 0.375" | 12" | 0.0176 | 4 - # 3 | 0.147" | 4" | 1.09 |
| Spandrel Beam (-M) | 0.0132 | 2 - # 6 2 - # 7 | 0.375" | 12" | 0.0113 | 2 - D12 | 0.147" | 4" | 0.85 |
| Spandrel Beam (+M) | 0.0084 | 3 - # 6 | | | 0.0075 | 2 - D8 | | | 0.89 |

¹ Reinforcement ratios are based on gross member dimensions.

² Reinforcement in first story columns at connections with base girder.

Table 2.6 Prototype and Model Column and Spandrel Reinforcement

| Test Sequence No. | Test Designation | Source Record | Shake Table Span (%) | PGA (g) | Dampers | Notes |
|--|------------------|---------------|----------------------|---------|---------|--|
| 1 | E001DS | El Centro | 1 | N/A | Small | Braces Pinned, Calibration Run |
| 2 | E010DST | El Centro | 10 | N/A | Small | Braces Pinned, Calibration Run |
| 3 | T021DST | Taft | 21 | N/A | Small | Braces Pinned, Calibration Run |
| 4 | E010DST | El Centro | 10 | N/A | Small | Braces Pinned, Calibration Run |
| 5 | E025DS | El Centro | 25 | 0.140 | Small | Braces Pinned |
| 6 | T052DS | Taft | 52.5 | 0.159 | Small | Braces Pinned |
| 7 | E010DS | El Centro | 10 | 0.073 | Small | Braces Pinned |
| 8 | T021DS | Taft | 21 | 0.048 | Small | Braces Pinned |
| 9 | E025DMX | El Centro | 25 | N/A | Mixed | Braces Pinned, Not Recorded |
| 10 | E025DM | El Centro | 25 | 0.125 | Mixed | Braces Pinned |
| 11 | T052DM | Taft | 52.5 | 0.093 | Mixed | Braces Pinned |
| 12 | E010DL | El Centro | 10 | 0.050 | Large | Braces Fixed |
| 13 | T021DL | Taft | 21 | 0.046 | Large | Braces Fixed |
| 14 | E025DL | El Centro | 25 | 0.141 | Large | Braces Fixed |
| 15 | T052DL | Taft | 52.5 | 0.099 | Large | Braces Fixed |
| 16 | E050DL | El Centro | 50 | 0.228 | Large | Braces Fixed |
| 17 | T105DL | Taft | 105 | 0.175 | Large | Braces Fixed |
| 18 | E075DL | El Centro | 76 | 0.312 | Large | Braces Fixed |
| 19 | T157DL | Taft | 157.5 | 0.309 | Large | Braces Fixed |
| 20 | E100DL | El Centro | 100 | 0.408 | Large | Braces Fixed |
| 21 | T210DL | Taft | 210 | 0.414 | Large | Braces Fixed |
| 22 | E125DL | El Centro | 125 | 0.467 | Large | Braces Fixed |
| 23 | T262DL | Taft | 262.5 | 0.522 | Large | Braces Fixed |
| 24 | E150DL | El Centro | 150 | 0.553 | Large | Braces Fixed |
| 25 | T315DL | Taft | 315 | 0.628 | Large | Braces Fixed |
| 26 | E200DLX | El Centro | 200 | N/A | Large | Braces Fixed, Not Recorded |
| 27 | E200DL | El Centro | 200 | 0.858 | Large | Braces Fixed, 0.2 Hz Hi-Pass Filter |
| 28 | T420DL | Taft | 420 | 0.888 | Large | Braces Fixed |
| 29 | E250DL | El Centro | 250 | 0.736 | Large | Braces Fixed, 0.5 Hz Hi-Pass Filter |
| 30 | E025N | Taft | 25 | 0.108 | None | No Braces, Collars in Place |
| 31 | E050N | El Centro | 50 | 0.212 | None | No Braces, Collars in Place |
| 32 | E075N | El Centro | 75 | 0.305 | None | No Braces, Collars in Place |
| 33 | E100N | El Centro | 100 | 0.408 | None | No Braces, Collars in Place |
| 34 | E125N | El Centro | 125 | 0.467 | None | No Braces, Collars in Place |
| 35 | E150N | El Centro | 150 | 0.553 | None | No Braces, Collars in Place |
| 36 | E200N | El Centro | 200 | 0.983 | None | No Braces, Collars in Place, 0.2 Hz Hi-Pass Filter |
| Source Records: El Centro S00E, 18 May 1940, and Taft S69E, 21 July 1952 | | | | | | |

Table 3.1 List of Earthquake Simulations Performed on Model

| Test Designation | PGA (g) | Maximum Floor Acceleration, g | | | Maximum Floor Acceleration/PGA | | |
|------------------|---------|-------------------------------|-------|-------|--------------------------------|-------|-------|
| | | FL 1 | FL 2 | FL 3 | FL 1 | FL 2 | FL 3 |
| E010DS | 0.073 | 0.061 | 0.031 | 0.071 | 0.828 | 0.424 | 0.965 |
| E025DM | 0.125 | 0.090 | 0.115 | 0.138 | 0.720 | 0.918 | 1.106 |
| E025DS | 0.140 | 0.114 | 0.120 | 0.155 | 0.814 | 0.862 | 1.113 |
| T021DS | 0.048 | 0.042 | 0.043 | 0.055 | 0.879 | 0.891 | 1.151 |
| T052DM | 0.093 | 0.082 | 0.090 | 0.116 | 0.879 | 0.961 | 1.238 |
| T052DS | 0.159 | 0.120 | 0.094 | 0.129 | 0.758 | 0.596 | 0.812 |
| E010DL | 0.050 | 0.043 | 0.062 | 0.065 | 0.872 | 1.249 | 1.306 |
| E025DL | 0.141 | 0.138 | 0.151 | 0.164 | 0.978 | 1.072 | 1.161 |
| E050DL | 0.228 | 0.224 | 0.261 | 0.306 | 0.985 | 1.144 | 1.341 |
| E075DL | 0.312 | 0.311 | 0.384 | 0.479 | 0.994 | 1.230 | 1.535 |
| E100DL | 0.408 | 0.397 | 0.475 | 0.598 | 0.973 | 1.162 | 1.464 |
| E125DL | 0.467 | 0.471 | 0.564 | 0.739 | 1.009 | 1.208 | 1.584 |
| E150DL | 0.553 | 0.567 | 0.690 | 0.866 | 1.026 | 1.249 | 1.568 |
| E200DL | 0.858 | 0.779 | 0.960 | 1.247 | 0.909 | 1.119 | 1.454 |
| E250DL | 0.736 | 0.667 | 0.764 | 1.081 | 0.907 | 1.039 | 1.469 |
| T021DL | 0.046 | 0.046 | 0.062 | 0.051 | 1.019 | 1.361 | 1.124 |
| T052DL | 0.099 | 0.096 | 0.108 | 0.128 | 0.972 | 1.095 | 1.298 |
| T105DL | 0.175 | 0.166 | 0.203 | 0.233 | 0.947 | 1.157 | 1.331 |
| T157DL | 0.309 | 0.254 | 0.305 | 0.357 | 0.820 | 0.985 | 1.155 |
| T210DL | 0.414 | 0.348 | 0.425 | 0.489 | 0.839 | 1.026 | 1.179 |
| T262DL | 0.522 | 0.436 | 0.524 | 0.643 | 0.836 | 1.004 | 1.232 |
| T315DL | 0.628 | 0.530 | 0.562 | 0.722 | 0.843 | 0.895 | 1.149 |
| T420DL | 0.888 | 0.695 | 0.770 | 1.072 | 0.783 | 0.867 | 1.207 |
| E025N | 0.108 | 0.108 | 0.114 | 0.091 | 1.000 | 1.054 | 0.840 |
| E050N | 0.212 | 0.213 | 0.229 | 0.179 | 1.006 | 1.083 | 0.844 |
| E075N | 0.305 | 0.326 | 0.350 | 0.286 | 1.071 | 1.149 | 0.941 |
| E100N | 0.407 | 0.424 | 0.493 | 0.402 | 1.041 | 1.211 | 0.989 |
| E125N | 0.482 | 0.539 | 0.579 | 0.505 | 1.118 | 1.200 | 1.048 |
| E150N | 0.563 | 0.640 | 0.602 | 0.567 | 1.137 | 1.070 | 1.008 |
| E200N | 0.983 | 0.862 | 0.798 | 0.675 | 0.877 | 0.812 | 0.687 |

Table 4.1 Maximum Floor Accelerations in Earthquake Simulations

| Test Designation | PGA (g) | Relative Displacement, Inches | | | Relative Displacement/PGA, Inches/g | | | Total Drift Ratio, % | | |
|------------------|---------|-------------------------------|------|------|-------------------------------------|------|------|----------------------|------|------|
| | | FL 1 | FL 2 | FL 3 | FL 1 | FL 2 | FL 3 | FL 1 | FL 2 | FL 3 |
| E010DS | 0.073 | 0.02 | 0.07 | 0.09 | 0.31 | 0.95 | 1.28 | 0.06 | 0.09 | 0.08 |
| E025DM | 0.125 | 0.07 | 0.16 | 0.21 | 0.55 | 1.29 | 1.66 | 0.18 | 0.20 | 0.17 |
| E025DS | 0.140 | 0.08 | 0.17 | 0.22 | 0.55 | 1.20 | 1.57 | 0.20 | 0.21 | 0.19 |
| T021DS | 0.048 | 0.03 | 0.06 | 0.09 | 0.53 | 1.35 | 1.80 | 0.06 | 0.08 | 0.07 |
| T052DM | 0.093 | 0.06 | 0.15 | 0.19 | 0.64 | 1.57 | 2.04 | 0.15 | 0.19 | 0.16 |
| T052DS | 0.159 | 0.08 | 0.17 | 0.23 | 0.49 | 1.09 | 1.44 | 0.20 | 0.22 | 0.19 |
| E010DL | 0.050 | 0.02 | 0.06 | 0.07 | 0.49 | 1.11 | 1.32 | 0.06 | 0.07 | 0.06 |
| E025DL | 0.141 | 0.06 | 0.13 | 0.17 | 0.42 | 0.92 | 1.19 | 0.15 | 0.16 | 0.14 |
| E050DL | 0.228 | 0.12 | 0.25 | 0.34 | 0.55 | 1.10 | 1.47 | 0.32 | 0.32 | 0.28 |
| E075DL | 0.312 | 0.19 | 0.40 | 0.56 | 0.62 | 1.28 | 1.79 | 0.50 | 0.51 | 0.47 |
| E100DL | 0.408 | 0.26 | 0.56 | 0.76 | 0.64 | 1.37 | 1.87 | 0.67 | 0.71 | 0.64 |
| E125DL | 0.467 | 0.32 | 0.72 | 0.98 | 0.69 | 1.53 | 2.09 | 0.83 | 0.91 | 0.82 |
| E150DL | 0.553 | 0.40 | 0.84 | 1.12 | 0.73 | 1.53 | 2.03 | 1.03 | 1.07 | 0.95 |
| E200DL | 0.858 | 0.63 | 1.45 | 1.95 | 0.73 | 1.70 | 2.27 | 1.62 | 1.84 | 1.64 |
| E250DL | 0.736 | 0.52 | 1.18 | 1.62 | 0.70 | 1.61 | 2.20 | 1.34 | 1.50 | 1.36 |
| T021DL | 0.046 | 0.02 | 0.05 | 0.06 | 0.44 | 1.06 | 1.39 | 0.05 | 0.06 | 0.05 |
| T052DL | 0.099 | 0.06 | 0.12 | 0.16 | 0.57 | 1.19 | 1.61 | 0.14 | 0.15 | 0.13 |
| T105DL | 0.175 | 0.11 | 0.24 | 0.32 | 0.64 | 1.37 | 1.80 | 0.29 | 0.30 | 0.27 |
| T157DL | 0.309 | 0.19 | 0.39 | 0.52 | 0.62 | 1.27 | 1.69 | 0.49 | 0.50 | 0.44 |
| T210DL | 0.414 | 0.25 | 0.56 | 0.75 | 0.61 | 1.36 | 1.82 | 0.65 | 0.72 | 0.63 |
| T262DL | 0.522 | 0.33 | 0.75 | 1.00 | 0.64 | 1.43 | 1.91 | 0.86 | 0.95 | 0.84 |
| T315DL | 0.628 | 0.41 | 0.89 | 1.17 | 0.65 | 1.42 | 1.86 | 1.05 | 1.13 | 0.98 |
| T420DL | 0.888 | 0.65 | 1.41 | 1.84 | 0.73 | 1.59 | 2.07 | 1.67 | 1.79 | 1.55 |
| E025N | 0.108 | 0.10 | 0.27 | 0.38 | 0.96 | 2.48 | 3.48 | 0.27 | 0.34 | 0.32 |
| E050N | 0.212 | 0.22 | 0.56 | 0.81 | 1.02 | 2.64 | 3.83 | 0.55 | 0.71 | 0.68 |
| E075N | 0.305 | 0.33 | 0.86 | 1.23 | 1.09 | 2.82 | 4.03 | 0.86 | 1.09 | 1.03 |
| E100N | 0.407 | 0.42 | 1.12 | 1.59 | 1.04 | 2.75 | 3.92 | 1.09 | 1.42 | 1.34 |
| E125N | 0.482 | 0.53 | 1.43 | 2.01 | 1.10 | 2.96 | 4.18 | 1.37 | 1.81 | 1.69 |
| E150N | 0.563 | 0.68 | 1.84 | 2.59 | 1.20 | 3.27 | 4.59 | 1.75 | 2.34 | 2.18 |
| E200N | 0.983 | 0.84 | 3.87 | 6.79 | 0.86 | 3.94 | 6.91 | 2.17 | 4.91 | 5.72 |

Table 4.2 Maximum Relative Displacements and Total Drift Ratios in Earthquake Simulations

| Test Designation | PGA (g) | Interstory Displacement, Inches | | | Interstory Displacement/PGA, Inches/g | | | Interstory Drift Ratio, % | | |
|------------------|---------|---------------------------------|------|------|---------------------------------------|------|------|---------------------------|------|------|
| | | FL 1 | FL 2 | FL 3 | FL 1 | FL 2 | FL 3 | FL 1 | FL 2 | FL 3 |
| E010DS | 0.073 | 0.02 | 0.05 | 0.03 | 0.31 | 0.68 | 0.37 | 0.06 | 0.13 | 0.07 |
| E025DM | 0.125 | 0.07 | 0.10 | 0.05 | 0.56 | 0.78 | 0.40 | 0.18 | 0.24 | 0.13 |
| E025DS | 0.140 | 0.08 | 0.11 | 0.06 | 0.55 | 0.80 | 0.44 | 0.20 | 0.28 | 0.15 |
| T021DS | 0.048 | 0.03 | 0.04 | 0.03 | 0.53 | 0.94 | 0.66 | 0.06 | 0.11 | 0.08 |
| T052DM | 0.093 | 0.06 | 0.09 | 0.05 | 0.63 | 0.95 | 0.53 | 0.15 | 0.22 | 0.12 |
| T052DS | 0.159 | 0.08 | 0.10 | 0.06 | 0.49 | 0.61 | 0.37 | 0.20 | 0.24 | 0.15 |
| E010DL | 0.050 | 0.02 | 0.03 | 0.02 | 0.50 | 0.66 | 0.37 | 0.06 | 0.08 | 0.05 |
| E025DL | 0.141 | 0.06 | 0.07 | 0.05 | 0.42 | 0.52 | 0.33 | 0.15 | 0.18 | 0.11 |
| E050DL | 0.228 | 0.12 | 0.13 | 0.09 | 0.55 | 0.59 | 0.41 | 0.32 | 0.33 | 0.23 |
| E075DL | 0.312 | 0.19 | 0.22 | 0.16 | 0.62 | 0.71 | 0.50 | 0.50 | 0.55 | 0.39 |
| E100DL | 0.408 | 0.26 | 0.31 | 0.21 | 0.64 | 0.75 | 0.53 | 0.67 | 0.76 | 0.54 |
| E125DL | 0.467 | 0.32 | 0.41 | 0.28 | 0.69 | 0.88 | 0.59 | 0.83 | 1.02 | 0.69 |
| E150DL | 0.553 | 0.40 | 0.46 | 0.30 | 0.73 | 0.83 | 0.54 | 1.03 | 1.14 | 0.74 |
| E200DL | 0.858 | 0.63 | 0.87 | 0.51 | 0.73 | 1.01 | 0.60 | 1.62 | 2.17 | 1.29 |
| E250DL | 0.736 | 0.52 | 0.71 | 0.45 | 0.70 | 0.96 | 0.61 | 1.34 | 1.76 | 1.12 |
| T021DL | 0.046 | 0.02 | 0.03 | 0.02 | 0.44 | 0.64 | 0.43 | 0.05 | 0.07 | 0.05 |
| T052DL | 0.099 | 0.06 | 0.07 | 0.04 | 0.57 | 0.67 | 0.44 | 0.14 | 0.16 | 0.11 |
| T105DL | 0.175 | 0.11 | 0.13 | 0.08 | 0.64 | 0.72 | 0.46 | 0.29 | 0.32 | 0.20 |
| T157DL | 0.309 | 0.19 | 0.21 | 0.13 | 0.62 | 0.66 | 0.43 | 0.49 | 0.51 | 0.34 |
| T210DL | 0.414 | 0.25 | 0.32 | 0.19 | 0.61 | 0.76 | 0.47 | 0.65 | 0.79 | 0.48 |
| T262DL | 0.522 | 0.33 | 0.42 | 0.25 | 0.64 | 0.81 | 0.48 | 0.86 | 1.06 | 0.63 |
| T315DL | 0.628 | 0.41 | 0.49 | 0.28 | 0.65 | 0.78 | 0.45 | 1.05 | 1.23 | 0.71 |
| T420DL | 0.888 | 0.65 | 0.81 | 0.45 | 0.73 | 0.91 | 0.50 | 1.67 | 2.01 | 1.11 |
| E025N | 0.108 | 0.10 | 0.18 | 0.13 | 0.96 | 1.71 | 1.19 | 0.27 | 0.46 | 0.32 |
| E050N | 0.212 | 0.22 | 0.35 | 0.25 | 1.02 | 1.65 | 1.19 | 0.55 | 0.87 | 0.63 |
| E075N | 0.305 | 0.33 | 0.53 | 0.39 | 1.09 | 1.74 | 1.29 | 0.86 | 1.32 | 0.99 |
| E100N | 0.407 | 0.42 | 0.71 | 0.54 | 1.04 | 1.73 | 1.32 | 1.09 | 1.76 | 1.34 |
| E125N | 0.482 | 0.53 | 0.90 | 0.70 | 1.10 | 1.86 | 1.46 | 1.37 | 2.25 | 1.76 |
| E150N | 0.563 | 0.68 | 1.17 | 0.94 | 1.20 | 2.08 | 1.66 | 1.75 | 2.92 | 2.34 |
| E200N | 0.983 | 0.84 | 3.05 | 2.97 | 0.86 | 3.10 | 3.02 | 2.17 | 7.62 | 7.42 |

Table 4.3 Maximum Interstory Displacements and Drift Ratios in Earthquake Simulations

| Test Designation | PGA (g) | Story Shear, Kips | | | Story Shear/PGA, Kips/g | | | Story Shear/Model Weight, % | | |
|------------------|---------|-------------------|------|------|-------------------------|------|------|-----------------------------|------|------|
| | | FL 1 | FL 2 | FL 3 | FL 1 | FL 2 | FL 3 | FL 1 | FL 2 | FL 3 |
| E010DS | 0.073 | 2.1 | 1.9 | 1.3 | 29.0 | 26.3 | 17.9 | 3.6 | 3.3 | 2.2 |
| E025DM | 0.125 | 5.3 | 4.4 | 2.6 | 42.5 | 35.3 | 20.4 | 9.0 | 7.5 | 4.3 |
| E025DS | 0.140 | 5.9 | 5.0 | 2.9 | 42.2 | 35.5 | 20.5 | 10.1 | 8.5 | 4.9 |
| T021DS | 0.048 | 2.2 | 1.7 | 1.0 | 46.0 | 36.4 | 21.3 | 3.8 | 3.0 | 1.7 |
| T052DM | 0.093 | 5.1 | 4.1 | 2.2 | 54.8 | 43.7 | 23.7 | 8.7 | 6.9 | 3.8 |
| T052DS | 0.159 | 4.6 | 3.9 | 2.4 | 28.8 | 24.7 | 15.0 | 7.8 | 6.7 | 4.1 |
| E010DL | 0.050 | 3.1 | 2.4 | 1.2 | 62.4 | 48.6 | 24.0 | 5.3 | 4.1 | 2.0 |
| E025DL | 0.141 | 7.9 | 5.4 | 3.0 | 55.9 | 38.5 | 21.5 | 13.4 | 9.2 | 5.2 |
| E050DL | 0.228 | 13.9 | 10.3 | 5.5 | 61.1 | 45.0 | 24.1 | 23.8 | 17.5 | 9.4 |
| E075DL | 0.312 | 19.6 | 15.6 | 8.8 | 62.6 | 49.8 | 28.1 | 33.3 | 26.5 | 15.0 |
| E100DL | 0.408 | 25.2 | 19.7 | 11.0 | 61.8 | 48.3 | 26.9 | 43.0 | 33.6 | 18.7 |
| E125DL | 0.467 | 29.6 | 23.8 | 13.5 | 63.4 | 50.9 | 29.0 | 50.4 | 40.5 | 23.1 |
| E150DL | 0.553 | 36.6 | 28.3 | 15.8 | 66.3 | 51.3 | 28.7 | 62.4 | 48.3 | 27.0 |
| E200DL | 0.858 | 47.1 | 39.3 | 22.9 | 54.9 | 45.9 | 26.7 | 80.2 | 67.1 | 39.1 |
| E250DL | 0.736 | 37.7 | 32.2 | 20.0 | 51.3 | 43.7 | 27.2 | 64.3 | 54.8 | 34.1 |
| T021DL | 0.046 | 2.9 | 2.1 | 0.9 | 62.8 | 47.0 | 20.9 | 4.9 | 3.6 | 1.6 |
| T052DL | 0.099 | 6.0 | 4.4 | 2.3 | 61.1 | 44.1 | 23.6 | 10.3 | 7.4 | 4.0 |
| T105DL | 0.175 | 11.0 | 8.3 | 4.3 | 63.0 | 47.4 | 24.7 | 18.8 | 14.2 | 7.4 |
| T157DL | 0.309 | 16.2 | 12.6 | 6.6 | 52.4 | 40.6 | 21.4 | 27.6 | 21.4 | 11.3 |
| T210DL | 0.414 | 21.0 | 16.9 | 9.0 | 50.8 | 40.9 | 21.8 | 35.8 | 28.9 | 15.4 |
| T262DL | 0.522 | 26.8 | 21.8 | 11.9 | 51.4 | 41.8 | 22.7 | 45.7 | 37.1 | 20.2 |
| T315DL | 0.628 | 30.5 | 23.9 | 13.3 | 48.6 | 38.1 | 21.1 | 52.0 | 40.8 | 22.6 |
| T420DL | 0.888 | 40.9 | 34.0 | 19.5 | 46.0 | 38.3 | 22.0 | 69.7 | 58.0 | 33.3 |
| E025N | 0.108 | 3.0 | 2.4 | 1.7 | 28.1 | 22.1 | 15.7 | 5.2 | 4.1 | 2.9 |
| E050N | 0.212 | 5.8 | 4.4 | 3.4 | 27.2 | 20.9 | 15.8 | 9.8 | 7.5 | 5.7 |
| E075N | 0.305 | 8.6 | 7.4 | 5.3 | 28.3 | 24.1 | 17.3 | 14.7 | 12.5 | 9.0 |
| E100N | 0.407 | 11.9 | 10.0 | 7.5 | 29.4 | 24.6 | 18.4 | 20.4 | 17.0 | 12.8 |
| E125N | 0.482 | 15.0 | 12.7 | 9.4 | 31.1 | 26.3 | 19.5 | 25.5 | 21.6 | 16.1 |
| E150N | 0.563 | 17.9 | 15.2 | 10.5 | 31.9 | 27.1 | 18.7 | 30.6 | 26.0 | 18.0 |
| E200N | 0.983 | 21.9 | 17.4 | 12.4 | 22.2 | 17.7 | 12.6 | 37.3 | 29.6 | 21.2 |

Table 4.4 Maximum Story Shears in Earthquake Simulations (Model Weight = 58.67 kips)

| Test Designation | PGA (g) | Maximum Overturning Moment, Inch-Kips | | | Maximum Overturning Moment/PGA, Inch-Kips/g | | |
|------------------|---------|--|-------|------|--|-------|-------|
| | | Base | FL 1 | FL 2 | Base | FL 1 | FL 2 |
| E010DS | 0.073 | 201 | 132 | 54 | 2,735 | 1,796 | 736 |
| E025DM | 0.125 | 460 | 275 | 105 | 3,688 | 2,205 | 842 |
| E025DS | 0.140 | 479 | 313 | 118 | 3,432 | 2,243 | 848 |
| T021DS | 0.048 | 195 | 111 | 42 | 4,073 | 2,319 | 877 |
| T052DM | 0.093 | 445 | 251 | 91 | 4,764 | 2,687 | 972 |
| T052DS | 0.159 | 430 | 248 | 98 | 2,713 | 1,564 | 619 |
| E010DL | 0.050 | 268 | 148 | 49 | 5,399 | 2,981 | 995 |
| E025DL | 0.141 | 639 | 329 | 125 | 4,538 | 2,337 | 885 |
| E050DL | 0.228 | 1,158 | 645 | 227 | 5,081 | 2,830 | 996 |
| E075DL | 0.312 | 1,747 | 959 | 363 | 5,592 | 3,070 | 1,162 |
| E100DL | 0.408 | 2,179 | 1,237 | 453 | 5,335 | 3,029 | 1,109 |
| E125DL | 0.467 | 2,591 | 1,493 | 557 | 5,552 | 3,199 | 1,193 |
| E150DL | 0.553 | 3,163 | 1,796 | 653 | 5,725 | 3,251 | 1,182 |
| E200DL | 0.858 | 4,195 | 2,521 | 945 | 4,892 | 2,940 | 1,102 |
| E250DL | 0.736 | 3,387 | 2,091 | 823 | 4,603 | 2,842 | 1,118 |
| T021DL | 0.046 | 234 | 124 | 39 | 5,138 | 2,723 | 857 |
| T052DL | 0.099 | 510 | 272 | 96 | 5,172 | 2,759 | 974 |
| T105DL | 0.175 | 949 | 516 | 178 | 5,420 | 2,947 | 1,014 |
| T157DL | 0.309 | 1,413 | 782 | 273 | 4,568 | 2,528 | 883 |
| T210DL | 0.414 | 1,897 | 1,062 | 372 | 4,579 | 2,563 | 898 |
| T262DL | 0.522 | 2,457 | 1,376 | 489 | 4,709 | 2,637 | 937 |
| T315DL | 0.628 | 2,698 | 1,498 | 547 | 4,293 | 2,384 | 870 |
| T420DL | 0.888 | 3,658 | 2,191 | 806 | 4,118 | 2,466 | 907 |
| E025N | 0.108 | 225 | 150 | 70 | 2,085 | 1,390 | 649 |
| E050N | 0.212 | 460 | 303 | 138 | 2,174 | 1,432 | 652 |
| E075N | 0.305 | 778 | 498 | 218 | 2,555 | 1,635 | 717 |
| E100N | 0.407 | 1,085 | 713 | 309 | 2,667 | 1,752 | 759 |
| E125N | 0.482 | 1,366 | 887 | 388 | 2,833 | 1,840 | 805 |
| E150N | 0.563 | 1,571 | 1,052 | 435 | 2,792 | 1,870 | 773 |
| E200N | 0.983 | 1,639 | 1,170 | 512 | 1,668 | 1,191 | 521 |

Table 4.5 Maximum Overturning Moments in Earthquake Simulations

| Test Designation | PGA (g) | Sum of Horizontal Components of All Damper Forces, Kips | | | Sum of Horizontal Component of All Damper Forces/PGA, Kips/g | | |
|------------------|---------|--|------|------|---|------|------|
| | | FL 1 | FL 2 | FL 3 | FL 1 | FL 2 | FL 3 |
| E010DS | 0.073 | 1.4 | 0.8 | 0.5 | 18.9 | 11.3 | 7.1 |
| E025DM | 0.125 | 2.1 | 2.1 | 1.2 | 17.2 | 17.1 | 9.9 |
| E025DS | 0.140 | 2.5 | 3.2 | 1.5 | 17.7 | 22.8 | 10.4 |
| T021DS | 0.048 | 1.0 | 0.8 | 0.6 | 20.3 | 17.0 | 12.0 |
| T052DM | 0.093 | 2.2 | 1.6 | 1.0 | 23.6 | 17.4 | 10.7 |
| T052DS | 0.159 | 1.8 | 2.6 | 1.2 | 11.4 | 16.1 | 7.7 |
| E010DL | 0.050 | 1.3 | 1.3 | 0.7 | 25.9 | 25.6 | 15.0 |
| E025DL | 0.141 | 3.8 | 3.3 | 1.5 | 26.9 | 23.7 | 10.9 |
| E050DL | 0.228 | 7.1 | 7.0 | 2.9 | 31.1 | 30.7 | 12.7 |
| E075DL | 0.312 | 10.3 | 10.8 | 4.1 | 32.9 | 34.7 | 13.2 |
| E100DL | 0.408 | 13.2 | 13.8 | 5.5 | 32.2 | 33.7 | 13.4 |
| E125DL | 0.467 | 15.8 | 16.6 | 6.7 | 33.9 | 35.5 | 14.4 |
| E150DL | 0.553 | 20.8 | 21.7 | 9.7 | 37.7 | 39.2 | 17.5 |
| E200DL | 0.858 | 29.7 | 30.9 | 16.1 | 34.6 | 36.0 | 18.7 |
| E250DL | 0.736 | 25.5 | 26.5 | 13.9 | 34.7 | 36.1 | 18.9 |
| T021DL | 0.046 | 1.1 | 1.1 | 0.7 | 23.9 | 24.7 | 15.9 |
| T052DL | 0.099 | 2.6 | 2.6 | 1.4 | 25.9 | 26.6 | 13.9 |
| T105DL | 0.175 | 4.8 | 5.0 | 2.5 | 27.3 | 28.3 | 14.1 |
| T157DL | 0.309 | 7.2 | 7.9 | 3.5 | 23.2 | 25.7 | 11.2 |
| T210DL | 0.414 | 9.8 | 10.8 | 4.2 | 23.7 | 26.0 | 10.1 |
| T262DL | 0.522 | 12.4 | 13.3 | 5.2 | 23.8 | 25.5 | 9.9 |
| T315DL | 0.628 | 16.8 | 18.0 | 7.7 | 26.7 | 28.6 | 12.2 |
| T420DL | 0.888 | 22.2 | 23.8 | 11.9 | 25.0 | 26.8 | 13.4 |

Table 4.6 Maximum Sums of Horizontal Components of Damper Forces

| Test | Story Shear, Kips | | | Sum of Horizontal Components of All Damper Forces, Kips | | | Sum of Horizontal Components of All Damper Forces/Story Shear | | |
|--------|-------------------|------|------|---|------|------|---|------|------|
| | FL 1 | FL 2 | FL 3 | FL 1 | FL 2 | FL 3 | FL 1 | FL 2 | FL 3 |
| E010DL | 1.7 | 1.4 | 0.7 | 0.9 | 0.5 | 0.2 | 0.49 | 0.37 | 0.32 |
| E025DL | 5.3 | 3.7 | 1.8 | 2.0 | 1.9 | 1.0 | 0.37 | 0.52 | 0.52 |
| E050DL | 10.1 | 7.5 | 4.3 | 4.1 | 4.4 | 1.7 | 0.40 | 0.59 | 0.39 |
| E075DL | 13.5 | 10.1 | 5.2 | 5.0 | 5.6 | 1.3 | 0.37 | 0.55 | 0.25 |
| E100DL | 17.6 | 13.3 | 6.9 | 5.3 | 6.6 | 1.0 | 0.30 | 0.50 | 0.15 |
| E125DL | 21.1 | 16.2 | 8.6 | 6.8 | 8.8 | 1.5 | 0.32 | 0.55 | 0.17 |
| E150DL | 25.8 | 19.8 | 10.3 | 9.6 | 12.3 | 3.3 | 0.37 | 0.62 | 0.32 |
| E200DL | 36.6 | 29.5 | 15.8 | 12.6 | 16.5 | 5.7 | 0.35 | 0.56 | 0.36 |
| E250DL | 29.6 | 23.9 | 13.1 | 13.5 | 15.2 | 4.3 | 0.46 | 0.64 | 0.33 |
| T021DL | 2.9 | 2.1 | 0.9 | 0.7 | 0.6 | 0.1 | 0.26 | 0.29 | 0.11 |
| T052DL | 6.0 | 4.4 | 2.3 | 1.9 | 2.1 | 0.5 | 0.32 | 0.47 | 0.20 |
| T105DL | 11.0 | 8.3 | 4.3 | 3.4 | 4.0 | 0.9 | 0.31 | 0.48 | 0.21 |
| T157DL | 16.2 | 12.6 | 6.6 | 4.8 | 6.4 | 1.3 | 0.30 | 0.51 | 0.19 |
| T210DL | 21.0 | 16.9 | 9.0 | 4.1 | 6.9 | 1.8 | 0.20 | 0.41 | 0.19 |
| T262DL | 26.8 | 21.8 | 11.9 | 7.5 | 11.0 | 3.4 | 0.28 | 0.50 | 0.29 |
| T315DL | 30.5 | 23.9 | 12.9 | 10.7 | 15.0 | 4.1 | 0.35 | 0.63 | 0.32 |
| T420DL | 40.9 | 34.1 | 19.6 | 18.8 | 19.1 | 9.4 | 0.46 | 0.56 | 0.48 |

Table 4.7 Story Shear Vs. Damper Force at Time of "Negative" (As Plotted) Story Shear Maximum

| Test | Story Shear, Kips | | | Sum of Horizontal Components of All Damper Forces, Kips | | | Sum of Horizontal Components of All Damper Forces/Story Shear | | |
|--------|-------------------|------|------|---|------|------|---|------|------|
| | FL 1 | FL 2 | FL 3 | FL 1 | FL 2 | FL 3 | FL 1 | FL 2 | FL 3 |
| E010DL | 3.1 | 2.4 | 1.2 | 1.1 | 0.9 | 0.2 | 0.34 | 0.38 | 0.18 |
| E025DL | 7.9 | 5.4 | 3.0 | 3.2 | 3.3 | 0.5 | 0.41 | 0.62 | 0.16 |
| E050DL | 13.9 | 10.3 | 5.5 | 6.4 | 4.8 | 2.0 | 0.46 | 0.46 | 0.36 |
| E075DL | 19.6 | 15.6 | 8.8 | 7.5 | 10.1 | 3.1 | 0.38 | 0.65 | 0.35 |
| E100DL | 25.2 | 19.7 | 11.0 | 10.4 | 11.6 | 2.6 | 0.41 | 0.59 | 0.24 |
| E125DL | 29.6 | 23.8 | 13.5 | 13.3 | 15.0 | 4.0 | 0.45 | 0.63 | 0.29 |
| E150DL | 36.6 | 28.3 | 15.9 | 18.1 | 20.1 | 6.8 | 0.49 | 0.71 | 0.43 |
| E200DL | 47.1 | 39.4 | 22.9 | 23.6 | 27.8 | 12.9 | 0.50 | 0.71 | 0.56 |
| E250DL | 37.7 | 32.2 | 20.0 | 19.7 | 24.4 | 8.0 | 0.52 | 0.76 | 0.40 |
| T021DL | 2.0 | 1.6 | 1.0 | 0.5 | 0.6 | 0.4 | 0.25 | 0.40 | 0.38 |
| T052DL | 5.2 | 4.0 | 2.1 | 1.8 | 2.3 | 0.5 | 0.34 | 0.59 | 0.22 |
| T105DL | 9.7 | 7.4 | 4.0 | 3.6 | 3.9 | 1.6 | 0.38 | 0.52 | 0.40 |
| T157DL | 15.3 | 11.7 | 6.5 | 6.1 | 6.9 | 1.8 | 0.40 | 0.59 | 0.27 |
| T210DL | 20.1 | 15.6 | 8.9 | 8.2 | 9.7 | 2.5 | 0.41 | 0.62 | 0.28 |
| T262DL | 24.2 | 19.3 | 11.0 | 10.7 | 10.1 | 1.8 | 0.44 | 0.53 | 0.17 |
| T315DL | 29.6 | 23.2 | 13.3 | 14.5 | 16.9 | 5.9 | 0.49 | 0.73 | 0.45 |
| T420DL | 34.6 | 28.9 | 17.0 | 20.3 | 22.0 | 9.5 | 0.59 | 0.76 | 0.56 |

Table 4.8 Story Shear Vs. Damper Force at Time of "Positive" (As Plotted) Story Shear Maximum

| Test | Story Shear, Kips | | | Sum of Horizontal Components of All Damper Forces, Kips | | | Sum of Horizontal Components of All Damper Forces/Story Shear | | |
|--------|-------------------|------|------|---|------|------|---|------|------|
| | FL 1 | FL 2 | FL 3 | FL 1 | FL 2 | FL 3 | FL 1 | FL 2 | FL 3 |
| E010DL | 1.7 | 1.4 | 0.7 | 1.0 | 1.0 | 0.4 | 0.55 | 0.74 | 0.58 |
| E025DL | 5.3 | 3.7 | 1.8 | 2.5 | 2.5 | 1.2 | 0.47 | 0.68 | 0.67 |
| E050DL | 10.1 | 7.5 | 4.3 | 4.3 | 4.8 | 2.3 | 0.42 | 0.64 | 0.55 |
| E075DL | 13.5 | 10.1 | 5.2 | 6.0 | 6.9 | 3.2 | 0.45 | 0.68 | 0.62 |
| E100DL | 17.6 | 13.3 | 6.9 | 7.6 | 8.9 | 4.0 | 0.43 | 0.67 | 0.59 |
| E125DL | 21.1 | 16.2 | 8.6 | 9.1 | 11.0 | 5.0 | 0.43 | 0.68 | 0.58 |
| E150DL | 25.8 | 19.8 | 10.3 | 12.9 | 15.1 | 7.0 | 0.50 | 0.77 | 0.68 |
| E200DL | 36.6 | 29.5 | 15.8 | 18.9 | 22.9 | 10.9 | 0.52 | 0.78 | 0.69 |
| E250DL | 29.6 | 23.9 | 13.1 | 16.8 | 19.7 | 9.1 | 0.57 | 0.82 | 0.69 |
| T021DL | 2.9 | 2.1 | 0.9 | 0.9 | 1.0 | 0.5 | 0.32 | 0.44 | 0.49 |
| T052DL | 6.0 | 4.4 | 2.3 | 2.5 | 2.6 | 1.1 | 0.42 | 0.60 | 0.45 |
| T105DL | 11.0 | 8.3 | 4.3 | 4.4 | 5.0 | 2.0 | 0.40 | 0.60 | 0.46 |
| T157DL | 16.2 | 12.6 | 6.6 | 6.4 | 7.7 | 3.1 | 0.39 | 0.61 | 0.47 |
| T210DL | 21.0 | 16.9 | 9.0 | 7.7 | 9.8 | 4.1 | 0.37 | 0.58 | 0.45 |
| T262DL | 26.8 | 21.8 | 11.9 | 9.4 | 12.3 | 5.0 | 0.35 | 0.56 | 0.42 |
| T315DL | 30.5 | 23.9 | 12.9 | 13.0 | 16.3 | 7.3 | 0.43 | 0.68 | 0.57 |
| T420DL | 40.9 | 34.1 | 19.6 | 19.4 | 23.7 | 11.8 | 0.47 | 0.70 | 0.60 |

Table 4.9 Story Shear Vs. Maximum Damper Force Before "Negative" (As Plotted) Story Shear Maximum

| Test | Story Shear, Kips | | | Sum of Horizontal Components of All Damper Forces, Kips | | | Sum of Horizontal Components of All Damper Forces/Story Shear | | |
|--------|-------------------|------|------|---|------|------|---|------|------|
| | FL 1 | FL 2 | FL 3 | FL 1 | FL 2 | FL 3 | FL 1 | FL 2 | FL 3 |
| E010DL | 3.1 | 2.4 | 1.2 | 1.3 | 1.3 | 0.6 | 0.42 | 0.53 | 0.47 |
| E025DL | 7.9 | 5.4 | 3.0 | 3.8 | 3.3 | 1.4 | 0.48 | 0.62 | 0.45 |
| E050DL | 13.9 | 10.3 | 5.5 | 7.1 | 7.0 | 2.9 | 0.51 | 0.68 | 0.53 |
| E075DL | 19.6 | 15.6 | 8.8 | 10.3 | 10.8 | 4.1 | 0.53 | 0.70 | 0.47 |
| E100DL | 25.2 | 19.7 | 11.0 | 13.2 | 13.8 | 5.5 | 0.52 | 0.70 | 0.50 |
| E125DL | 29.6 | 23.8 | 13.5 | 15.8 | 16.6 | 6.7 | 0.54 | 0.70 | 0.50 |
| E150DL | 36.6 | 28.3 | 15.9 | 20.8 | 21.7 | 9.7 | 0.57 | 0.76 | 0.61 |
| E200DL | 47.1 | 39.4 | 22.9 | 29.7 | 30.9 | 16.1 | 0.63 | 0.78 | 0.70 |
| E250DL | 37.7 | 32.2 | 20.0 | 25.5 | 26.5 | 13.9 | 0.68 | 0.83 | 0.70 |
| T021DL | 2.0 | 1.6 | 1.0 | 0.9 | 1.0 | 0.4 | 0.46 | 0.61 | 0.46 |
| T052DL | 5.2 | 4.0 | 2.1 | 2.3 | 2.4 | 1.0 | 0.45 | 0.60 | 0.50 |
| T105DL | 9.7 | 7.4 | 4.0 | 4.5 | 4.8 | 2.0 | 0.46 | 0.65 | 0.50 |
| T157DL | 15.3 | 11.7 | 6.5 | 7.2 | 8.0 | 3.1 | 0.47 | 0.68 | 0.48 |
| T210DL | 20.1 | 15.6 | 8.9 | 9.8 | 10.8 | 4.2 | 0.49 | 0.69 | 0.46 |
| T262DL | 24.2 | 19.3 | 11.0 | 12.4 | 13.3 | 5.2 | 0.51 | 0.69 | 0.47 |
| T315DL | 29.6 | 23.2 | 13.3 | 16.8 | 18.0 | 7.7 | 0.57 | 0.77 | 0.58 |
| T420DL | 34.6 | 28.9 | 17.0 | 22.2 | 23.8 | 11.9 | 0.64 | 0.82 | 0.70 |

Table 4.10 Story Shear Vs. Maximum Damper Force Before "Positive" (As Plotted) Story Shear Maximum

| Test | Elapsed Time to Maximum Story Shear, Seconds | | | Elapsed Time to Maximum Damper Force, Seconds | | | Elapsed Time to Maximum Interstory Displacement, Seconds | | |
|--------|--|------|------|---|------|------|--|------|------|
| | FL 1 | FL 2 | FL 3 | FL 1 | FL 2 | FL 3 | FL 1 | FL 2 | FL 3 |
| E010DL | 1.10 | 1.14 | 1.13 | 1.06 | 1.09 | 1.09 | 1.15 | 1.15 | 1.15 |
| E025DL | 1.13 | 1.13 | 1.10 | 1.05 | 1.08 | 1.08 | 1.14 | 1.16 | 1.18 |
| E050DL | 1.11 | 1.11 | 1.11 | 1.10 | 1.09 | 1.08 | 1.15 | 1.16 | 1.18 |
| E075DL | 1.13 | 1.14 | 1.15 | 1.10 | 1.10 | 1.08 | 1.15 | 1.18 | 1.18 |
| E100DL | 1.14 | 1.15 | 1.16 | 1.10 | 1.10 | 1.09 | 1.16 | 1.18 | 1.18 |
| E125DL | 1.14 | 1.15 | 1.16 | 1.10 | 1.11 | 1.09 | 1.16 | 1.18 | 1.18 |
| E150DL | 1.14 | 1.15 | 1.16 | 1.11 | 1.11 | 1.09 | 1.16 | 1.18 | 1.18 |
| E200DL | 1.16 | 1.18 | 1.18 | 1.12 | 1.14 | 1.11 | 1.18 | 1.20 | 1.20 |
| E250DL | 1.15 | 1.18 | 1.19 | 1.11 | 1.14 | 1.11 | 1.18 | 1.20 | 1.20 |
| T021DL | 6.30 | 6.31 | 6.33 | 6.29 | 6.25 | 6.24 | 6.31 | 6.34 | 6.35 |
| T052DL | 6.29 | 6.30 | 6.31 | 6.26 | 6.28 | 6.24 | 6.30 | 6.32 | 6.32 |
| T105DL | 6.29 | 6.30 | 6.31 | 6.26 | 6.28 | 6.25 | 6.31 | 6.31 | 6.32 |
| T157DL | 6.29 | 6.30 | 6.31 | 6.26 | 6.28 | 6.25 | 6.31 | 6.31 | 6.32 |
| T210DL | 6.30 | 6.31 | 6.31 | 6.26 | 6.28 | 6.25 | 6.31 | 6.32 | 6.34 |
| T262DL | 6.30 | 6.30 | 6.30 | 6.26 | 6.28 | 6.26 | 6.31 | 6.32 | 6.34 |
| T315DL | 6.29 | 6.30 | 6.31 | 6.26 | 6.28 | 6.26 | 6.31 | 6.32 | 6.34 |
| T420DL | 6.29 | 6.31 | 6.31 | 6.28 | 6.29 | 6.28 | 6.31 | 6.34 | 6.34 |

Table 4.11 Elapsed Times to "Negative" (As Plotted) Story Shear Maxima

| Test | Elapsed Time to Maximum Story Shear, Seconds | | | Elapsed Time to Maximum Dampener Force, Seconds | | | Elapsed Time to Maximum Interstory Displacement, Seconds | | |
|--------|---|------|------|--|------|------|---|------|------|
| | FL 1 | FL 2 | FL 3 | FL 1 | FL 2 | FL 3 | FL 1 | FL 2 | FL 3 |
| E010DL | 1.31 | 1.33 | 1.34 | 1.28 | 1.29 | 1.28 | 1.31 | 1.34 | 1.36 |
| E025DL | 1.30 | 1.30 | 1.34 | 1.29 | 1.30 | 1.26 | 1.31 | 1.32 | 1.35 |
| E050DL | 1.30 | 1.33 | 1.33 | 1.29 | 1.30 | 1.29 | 1.31 | 1.34 | 1.34 |
| E075DL | 1.31 | 1.31 | 1.33 | 1.29 | 1.30 | 1.29 | 1.32 | 1.34 | 1.34 |
| E100DL | 1.31 | 1.33 | 1.34 | 1.29 | 1.30 | 1.29 | 1.32 | 1.35 | 1.35 |
| E125DL | 1.31 | 1.33 | 1.34 | 1.29 | 1.30 | 1.30 | 1.32 | 1.35 | 1.35 |
| E150DL | 1.31 | 1.33 | 1.34 | 1.29 | 1.31 | 1.30 | 1.32 | 1.35 | 1.35 |
| E200DL | 1.33 | 1.34 | 1.35 | 1.30 | 1.31 | 1.32 | 1.34 | 1.36 | 1.36 |
| E250DL | 1.33 | 1.34 | 1.36 | 1.30 | 1.31 | 1.32 | 1.34 | 1.36 | 1.38 |
| T021DL | 4.61 | 4.61 | 4.60 | 4.56 | 4.58 | 4.58 | 4.62 | 4.64 | 4.64 |
| T052DL | 4.60 | 4.60 | 4.63 | 4.58 | 4.59 | 4.59 | 4.62 | 4.65 | 4.66 |
| T105DL | 4.60 | 4.61 | 4.61 | 4.58 | 4.59 | 4.59 | 4.62 | 4.64 | 4.65 |
| T157DL | 4.60 | 4.61 | 4.63 | 4.58 | 4.59 | 4.59 | 4.61 | 4.64 | 4.65 |
| T210DL | 4.60 | 4.61 | 4.63 | 4.58 | 4.59 | 4.59 | 4.62 | 4.65 | 4.65 |
| T262DL | 4.60 | 4.63 | 4.64 | 4.58 | 4.60 | 4.59 | 4.62 | 4.65 | 4.66 |
| T315DL | 4.60 | 4.61 | 4.63 | 4.58 | 4.60 | 4.60 | 4.62 | 4.65 | 4.65 |
| T420DL | 4.60 | 4.63 | 4.64 | 4.58 | 4.61 | 4.61 | 4.62 | 4.66 | 4.66 |

Table 4.12 Elapsed Times to "Positive" (As Plotted) Story Shear Maxima

| Test Designation | PGA (g) | Column Shear, Kips | | | Column Shear/PGA, Kips/g | | |
|------------------|---------|--------------------|------|------|--------------------------|------|------|
| | | FL 1 | FL 2 | FL 3 | FL 1 | FL 2 | FL 3 |
| E010DS | 0.073 | 1.3 | 1.8 | 1.2 | 18.0 | 24.5 | 16.5 |
| E025DM | 0.125 | 3.6 | 3.1 | 2.2 | 28.9 | 24.6 | 17.3 |
| E025DS | 0.140 | 3.8 | 2.8 | 2.4 | 27.0 | 19.8 | 17.5 |
| T021DS | 0.048 | 1.5 | 1.6 | 1.1 | 30.5 | 33.2 | 23.2 |
| T052DM | 0.093 | 3.3 | 3.0 | 2.0 | 35.0 | 32.3 | 21.2 |
| T052DS | 0.159 | 3.4 | 2.2 | 1.9 | 21.1 | 13.9 | 11.7 |
| E010DL | 0.050 | 2.4 | 1.8 | 1.1 | 47.7 | 35.5 | 22.9 |
| E025DL | 0.141 | 4.7 | 3.3 | 2.6 | 33.0 | 23.6 | 18.7 |
| E050DL | 0.228 | 9.3 | 6.5 | 4.8 | 40.6 | 28.3 | 21.0 |
| E075DL | 0.312 | 12.1 | 8.9 | 7.5 | 38.7 | 28.5 | 24.1 |
| E100DL | 0.408 | 16.9 | 12.1 | 10.2 | 41.4 | 29.7 | 25.0 |
| E125DL | 0.467 | 18.5 | 13.1 | 11.9 | 39.6 | 28.2 | 25.6 |
| E150DL | 0.553 | 23.3 | 15.7 | 13.1 | 42.2 | 28.4 | 23.7 |
| E200DL | 0.858 | 27.6 | 19.7 | 16.5 | 32.2 | 22.9 | 19.3 |
| E250DL | 0.736 | 21.4 | 15.6 | 14.0 | 29.0 | 21.2 | 19.0 |
| T021DL | 0.046 | 2.2 | 1.5 | 1.0 | 49.0 | 33.6 | 21.6 |
| T052DL | 0.099 | 4.2 | 2.9 | 2.1 | 42.6 | 29.1 | 21.3 |
| T105DL | 0.175 | 8.0 | 5.4 | 3.8 | 45.7 | 30.6 | 21.8 |
| T157DL | 0.309 | 12.2 | 7.9 | 5.9 | 39.3 | 25.5 | 19.2 |
| T210DL | 0.414 | 17.3 | 10.6 | 8.1 | 41.8 | 25.7 | 19.4 |
| T262DL | 0.522 | 21.6 | 12.6 | 10.5 | 41.4 | 24.1 | 20.2 |
| T315DL | 0.628 | 22.0 | 13.5 | 10.8 | 35.0 | 21.6 | 17.2 |
| T420DL | 0.888 | 25.8 | 16.6 | 12.5 | 29.1 | 18.7 | 14.1 |

Table 4.13 Maximum Column Shears in Earthquake Simulations

| Test Designation | PGA (g) | Maximum Relative Floor Velocity, in/sec | | | Maximum Relative Floor Velocity/PGA, in/sec-g | | |
|------------------|---------|---|-----------|-----------|---|-----------|-----------|
| | | FL 1-Base | FL 2-FL 1 | FL 3-FL 2 | FL 1-Base | FL 2-FL 1 | FL 3-FL 2 |
| E010DL | 0.050 | 0.4 | 0.5 | 0.5 | 7.3 | 10.5 | 10.1 |
| E025DL | 0.141 | 0.8 | 1.0 | 0.9 | 5.8 | 7.0 | 6.3 |
| E050DL | 0.228 | 1.9 | 1.9 | 1.4 | 8.2 | 8.4 | 6.1 |
| E075DL | 0.312 | 2.7 | 3.3 | 2.4 | 8.6 | 10.6 | 7.8 |
| E100DL | 0.408 | 4.0 | 5.0 | 3.1 | 9.9 | 12.2 | 7.5 |
| E125DL | 0.467 | 5.0 | 6.6 | 4.1 | 10.8 | 14.2 | 8.8 |
| E150DL | 0.553 | 5.9 | 7.6 | 4.4 | 10.6 | 13.8 | 8.0 |
| E200DL | 0.858 | 10.8 | 14.7 | 8.5 | 12.6 | 17.1 | 9.9 |
| E250DL | 0.736 | 9.6 | 12.3 | 7.8 | 13.1 | 16.7 | 10.5 |
| T021DL | 0.046 | 0.3 | 0.4 | 0.5 | 7.0 | 9.2 | 11.0 |
| T052DL | 0.099 | 0.7 | 0.8 | 0.7 | 7.0 | 8.3 | 7.1 |
| T105DL | 0.175 | 1.6 | 1.7 | 1.3 | 9.3 | 9.6 | 7.7 |
| T157DL | 0.309 | 2.1 | 2.7 | 2.0 | 6.8 | 8.7 | 6.6 |
| T210DL | 0.414 | 3.0 | 3.9 | 3.0 | 7.2 | 9.5 | 7.3 |
| T262DL | 0.522 | 4.3 | 5.2 | 3.6 | 8.2 | 10.0 | 6.9 |
| T315DL | 0.628 | 5.2 | 6.6 | 4.2 | 8.3 | 10.6 | 6.7 |
| T420DL | 0.888 | 7.5 | 10.6 | 6.5 | 8.5 | 12.0 | 7.3 |

Table 4.14 Maximum Relative Floor Velocities in Earthquake Simulations

| Test Designation | Frequency, Hz | | | Period, Sec | | | Damping, % | | |
|------------------|---------------|--------|--------|-------------|--------|--------|------------|--------|--------|
| | Mode 1 | Mode 2 | Mode 3 | Mode 1 | Mode 2 | Mode 3 | Mode 1 | Mode 2 | Mode 3 |
| E010DL | 2.89 | | | 0.35 | | | 18.2 | | |
| E025DL | 2.91 | | | 0.34 | | | 36.5 | | |
| E050DL | 2.97 | | | 0.34 | | | 36.6 | | |
| E075DL | 2.77 | | | 0.36 | | | 38.5 | | |
| E100DL | 2.60 | | | 0.38 | | | 35.8 | | |
| E125DL | 2.56 | | | 0.39 | | | 36.5 | | |
| E150DL | 2.38 | | | 0.42 | | | 36.8 | | |
| E200DL | 1.95 | | | 0.51 | | | 39.7 | | |
| E250DL | 1.97 | | | 0.51 | | | 38.0 | | |
| T021DL | 2.93 | | | 0.34 | | | 39.8 | | |
| T052DL | 2.89 | | | 0.35 | | | 41.3 | | |
| T105DL | 2.89 | | | 0.35 | | | 37.7 | | |
| T157DL | 2.48 | | | 0.40 | | | 43.7 | | |
| T210DL | 2.42 | | | 0.41 | | | 36.2 | | |
| T262DL | 2.44 | | | 0.41 | | | 36.9 | | |
| T315DL | 2.44 | | | 0.41 | | | 37.7 | | |
| T420DL | 1.93 | | | 0.52 | | | 44.9 | | |
| E025N | 1.29 | 4.96 | 9.30 | 0.78 | 0.20 | 0.11 | 7.2 | 1.1 | 0.6 |
| E050N | 1.21 | 4.73 | 8.77 | 0.83 | 0.21 | 0.11 | 9.6 | 3.0 | 1.2 |
| E075N | 1.21 | 4.59 | 8.77 | 0.83 | 0.22 | 0.11 | 5.7 | 4.3 | 1.0 |
| E100N | 1.21 | 4.77 | 8.22 | 0.83 | 0.21 | 0.12 | 5.1 | 3.9 | 2.7 |
| E125N | 1.17 | 5.00 | 8.38 | 0.85 | 0.20 | 0.12 | 6.3 | 2.1 | 2.5 |
| E150N | 1.09 | 5.00 | 7.83 | 0.92 | 0.20 | 0.13 | 5.3 | 1.0 | 1.3 |
| E200N | 0.76 | 3.48 | 5.04 | 1.32 | 0.29 | 0.20 | 17.3 | 1.6 | 1.1 |

Table 4.15 Modal Properties from Earthquake Simulations, Acceleration-Based Transfer Functions (FL 3)

| Conditions | Floor | Frequency, Hz | | | Period, Sec | | | Damping, % | | |
|----------------|-------|---------------|--------|--------|-------------|--------|--------|------------|--------|--------|
| | | Mode 1 | Mode 2 | Mode 3 | Mode 1 | Mode 2 | Mode 3 | Mode 1 | Mode 2 | Mode 3 |
| Steel Braces | 3 | 8.38 | | | 0.12 | | | 3.9 | | |
| Unbraced Frame | 3 | 1.88 | 6.25 | 10.50 | 0.53 | 0.16 | 0.10 | 6.7 | 3.9 | 4.6 |
| Pre-E010DL | 3 | 2.75 | | | 0.36 | | | 32.8 | | |
| Pre-E010DL | 2 | 3.13 | | | 0.32 | | | 26.2 | | |
| Post-T052DL | 2 | 3.19 | | | 0.31 | | | 27.9 | | |
| Post-E050DL | 2 | 3.13 | | | 0.32 | | | 23.4 | | |
| Post-E075DL | 3 | 2.75 | | | 0.36 | | | 26.7 | | |
| Post-T157DL | 3 | 2.56 | | | 0.39 | | | 18.5 | | |
| Post-T157DL | 2 | 2.88 | | | 0.35 | | | 20.2 | | |
| Post-E100DL | 3 | 3.19 | | | 0.31 | | | 14.1 | | |
| Post-T210DL | 3 | 2.88 | | | 0.35 | | | 32.0 | | |
| Post-E125DL | 2 | 3.00 | | | 0.33 | | | 8.5 | | |
| Post-T262DL | 2 | 3.00 | | | 0.33 | | | 29.3 | | |
| Post-E150DL | 3 | 3.13 | | | 0.32 | | | 29.6 | | |
| Post-T315DL | 3 | 2.94 | | | 0.34 | | | 10.2 | | |
| Post-T315DL | 2 | 3.13 | | | 0.32 | | | 16.8 | | |
| Post-E200DL | 3 | 2.63 | | | 0.38 | | | 13.5 | | |
| Post-E200DL | 2 | 2.94 | | | 0.34 | | | 12.8 | | |
| Post-T420DL | 3 | 2.88 | | | 0.35 | | | 7.5 | | |
| Post-T420DL | 2 | 2.63 | | | 0.38 | | | 7.1 | | |
| Post-E250DL | 2 | 2.38 | | | 0.42 | | | 17.4 | | |
| Pre-E025N | 3 | 1.63 | 5.63 | 9.88 | 0.62 | 0.18 | 0.10 | 7.7 | 3.6 | 4.0 |
| Pre-E025N | 2 | 1.50 | 5.63 | 9.94 | 0.67 | 0.18 | 0.10 | 7.3 | 3.9 | 3.1 |
| Post-E025N | 3 | 1.50 | 5.50 | 9.75 | 0.67 | 0.18 | 0.10 | 7.7 | 5.0 | 2.2 |
| Post-E050N | 3 | 1.50 | 5.50 | 9.75 | 0.67 | 0.18 | 0.10 | 7.7 | 5.0 | 2.2 |
| Post-E075N | 3 | 1.50 | 5.44 | 9.75 | 0.67 | 0.18 | 0.10 | 7.5 | 4.4 | 4.2 |
| Post-E100N | 3 | 1.50 | 5.44 | 9.69 | 0.67 | 0.18 | 0.10 | 8.0 | 3.2 | 3.5 |
| Post-E100N | 2 | 1.44 | 5.44 | 9.75 | 0.70 | 0.18 | 0.10 | 11.1 | 4.4 | 3.4 |
| Post-E125N | 3 | 1.56 | 5.31 | 9.56 | 0.64 | 0.19 | 0.10 | 8.5 | 3.5 | 3.3 |
| Post-E125N | 2 | 1.44 | 5.31 | 9.63 | 0.70 | 0.19 | 0.10 | 22.4 | 3.8 | 2.9 |
| Post-E150N | 3 | 1.41 | 5.00 | 9.22 | 0.71 | 0.20 | 0.11 | 6.0 | 4.1 | 5.2 |
| Post-E150N | 2 | 1.41 | 5.03 | 9.25 | 0.71 | 0.20 | 0.11 | 4.6 | 4.0 | 2.6 |

Table 4.16 Modal Properties from White Noise Tests

| Description | First Mode Calculations | | | | | Logarithmic Decrement Calculations | | | |
|-------------------------------|-------------------------|---------|--------|---------------|----------------|------------------------------------|--------------|--------|------------|
| | Time #1 | Time #2 | No. of | First Mode | Natural Period | Acceleration | Acceleration | No. of | First Mode |
| | Sec | Sec | Cycles | Frequency, Hz | Sec | #1, g | #2, g | Cycles | Damping, % |
| Steel Braces w/o Dampers | 2.946 | 4.020 | 9 | 8.38 | 0.12 | 0.0522 | 0.0122 | 9 | 2.4 |
| No Braces, Initial Conditions | 2.416 | 4.086 | 3 | 1.80 | 0.56 | 0.0087 | 0.0039 | 4 | 3.2 |
| Large Dampers, Pre-E010DL | 1.274 | 2.988 | 6 | 3.50 | 0.29 | 0.0062 | 0.0009 | 1 | 31.1 |
| No Braces, Pre-E025N | 0.280 | 3.480 | 5 | 1.56 | 0.64 | 0.0059 | 0.0022 | 3 | 5.1 |

Table 4.17 First Mode Characteristics from Free Vibration Tests

| Description | First Mode Calculations | | | | | Logarithmic Decrement Calculations | | | |
|-------------------------------|-------------------------|----------------|------------------|-----------------------------|-----------------------|------------------------------------|-----------------------|------------------|--------------------------|
| | Time #1 Sec | Time #2 Sec | No. of Cycles | First Mode Frequency, Hz | Natural Period Sec | Acceleration #1, g | Acceleration #2, g | No. of Cycles | First Mode Damping, % |
| Steel Braces w/o Dampers | 0.398 | 1.374 | 8 | 8.20 | 0.12 | 0.0094 | 0.0036 | 8 | 1.9 |
| No Braces, Initial Conditions | 1.606 | 4.840 | 6 | 1.86 | 0.54 | 0.0086 | 0.0034 | 6 | 2.4 |

Table 4.18 First Mode Characteristics from Pullback Tests

| Test | Gage SGZ1 (Yield Strain = 0.00152) | | | | Gage SGZ3 (Yield Strain = 0.00141) | | | |
|--------|------------------------------------|-------------|------------------------|--|------------------------------------|-------------|------------------------|--|
| | Maximum Strain, In/In | | Residual Strain, In/In | | Maximum Strain, In/In | | Residual Strain, In/In | |
| | Tension | Compression | | | Tension | Compression | | |
| E010DL | 0.000070 | -0.000034 | 0.000000 | | 0.000107 | -0.000015 | 0.000000 | |
| E025DL | 0.000197 | -0.000090 | -0.000002 | | 0.000667 | -0.000016 | 0.000033 | |
| E050DL | 0.000485 | -0.000170 | -0.000003 | | 0.003065 | -0.000270 | 0.000022 | |
| E075DL | 0.000863 | -0.000260 | 0.000004 | | 0.002620 | -0.000430 | 0.000093 | |
| E100DL | 0.001291 | -0.000350 | -0.000001 | | 0.010304 | -0.000570 | 0.000287 | |
| E125DL | 0.001711 | -0.000430 | -0.000003 | | 0.010486 | -0.000820 | 0.001154 | |
| E150DL | 0.002218 | -0.000500 | 0.000008 | | 0.010351 | -0.001020 | 0.000867 | |
| E200DL | 0.002431 | -0.000550 | -0.000270 | | Gage Non-Functional | | | |
| T021DL | 0.000046 | -0.000050 | -0.000002 | | 0.000235 | -0.000013 | 0.000003 | |
| T052DL | 0.000138 | -0.000120 | -0.000010 | | 0.000877 | -0.000044 | -0.000010 | |
| T105DL | 0.000340 | -0.000220 | -0.000012 | | 0.002642 | -0.000061 | 0.000103 | |
| T157DL | 0.000660 | -0.000330 | -0.000020 | | 0.010224 | -0.000340 | 0.000378 | |
| T210DL | 0.001028 | -0.000430 | 0.000034 | | 0.010397 | -0.000550 | 0.000478 | |
| T262DL | 0.001417 | -0.000520 | 0.000057 | | 0.010346 | -0.000890 | 0.000293 | |
| T315DL | 0.001774 | -0.000620 | 0.000076 | | 0.105400 | -0.000960 | 0.000796 | |
| T420DL | 0.001099 | 0.000780 | -0.000480 | | Gage Non-Functional | | | |
| E025N | 0.000153 | -0.000140 | 0.000026 | | Gage Non-Functional | | | |
| E050N | 0.000169 | -0.000250 | -0.000027 | | Gage Non-Functional | | | |
| E075N | 0.000345 | 0.000350 | -0.000023 | | Gage Non-Functional | | | |
| E100N | 0.000650 | -0.000430 | -0.000009 | | Gage Non-Functional | | | |
| E125N | 0.001203 | -0.000520 | -0.000013 | | Gage Non-Functional | | | |
| E150N | 0.002443 | -0.000640 | -0.000010 | | Gage Non-Functional | | | |
| E200N | 0.004934 | -0.000690 | -0.000110 | | Gage Non-Functional | | | |

Shaded cells with bold print indicate strain maxima above approximate yield strain.

Table 4.19 Maximum and Residual Strains in Reinforcement: Gages SGZ1 and SGZ3

| Test | Gage SGZ4 (Yield Strain = 0.00141) | | | | Gage S1Z1 (Yield Strain = 0.00152) | | | |
|--------|------------------------------------|-------------|------------------------|--|------------------------------------|-------------|------------------------|---------------------|
| | Maximum Strain, In/In | | Residual Strain, In/In | | Maximum Strain, In/In | | Residual Strain, In/In | |
| | Tension | Compression | | | Tension | Compression | | |
| | | | | | | | | Gage Non-Functional |
| E010DL | 0.000250 | -0.000023 | 0.000000 | | 0.000019 | -0.000013 | 0.000000 | |
| E025DL | 0.000079 | -0.000043 | 0.000000 | | 0.000048 | -0.000036 | 0.000000 | |
| E050DL | 0.000156 | -0.000075 | 0.000001 | | 0.000078 | -0.000051 | 0.000000 | |
| E075DL | 0.000252 | -0.000130 | 0.000005 | | 0.000110 | -0.000065 | 0.000000 | |
| E100DL | 0.000333 | -0.000190 | 0.000002 | | 0.000150 | -0.000084 | 0.000000 | |
| E125DL | 0.000411 | -0.000250 | 0.000007 | | 0.000170 | -0.000327 | -0.000038 | |
| E150DL | 0.000481 | -0.000300 | 0.000005 | | 0.000360 | -0.002653 | 0.000000 | |
| E200DL | 0.000751 | -0.000330 | -0.000007 | | 0.000014 | -0.000007 | -0.000001 | |
| T021DL | 0.000037 | -0.000020 | 0.000005 | | 0.000020 | -0.000011 | -0.000005 | |
| T052DL | 0.000092 | -0.000038 | 0.000004 | | 0.000047 | -0.000029 | 0.000000 | |
| T105DL | 0.000194 | -0.000066 | 0.000013 | | 0.000094 | -0.000061 | 0.000000 | |
| T157DL | 0.000311 | -0.000110 | 0.000015 | | 0.000160 | -0.000079 | -0.000005 | |
| T210DL | 0.000419 | -0.000160 | -0.000022 | | 0.000230 | -0.000100 | -0.000005 | |
| T262DL | 0.000499 | -0.000220 | -0.000024 | | 0.000260 | -0.000210 | -0.000010 | |
| T315DL | 0.000580 | -0.000250 | -0.000034 | | 0.000390 | -0.001467 | -0.000045 | |
| T420DL | 0.000841 | -0.000290 | -0.000049 | | 0.000130 | -0.000114 | 0.000000 | |
| E025N | 0.000134 | -0.000085 | -0.000004 | | 0.000220 | -0.000210 | 0.000000 | |
| E050N | 0.000337 | -0.000180 | -0.000005 | | 0.000300 | -0.000372 | 0.000001 | |
| E075N | 0.000556 | -0.000280 | -0.000006 | | 0.000390 | -0.000619 | 0.000000 | |
| E100N | 0.000748 | -0.000350 | -0.000006 | | 0.000480 | -0.000912 | -0.000003 | |
| E125N | 0.000994 | -0.000420 | 0.000005 | | 0.000580 | -0.001172 | 0.000005 | |
| E150N | 0.001204 | -0.000510 | 0.000034 | | 0.001080 | -0.001599 | -0.000004 | |
| E200N | 0.002572 | -0.000810 | 0.000151 | | | | | |

Shaded cells with bold print indicate strain maxima above approximate yield strain.

Table 4.20 Maximum and Residual Strains in Reinforcement: Gages SGZ4 and S1Z1

| Test | Gage S1Z5 (Yield Strain = 0.00141) | | | | Gage S1Z6 (Yield Strain = 0.00141) | | | |
|--------|------------------------------------|------------------|------------------------|-----------------------|------------------------------------|------------------|------------------------|-----------------------|
| | Maximum Strain, In/In | | Residual Strain, In/In | Maximum Strain, In/In | Maximum Strain, In/In | | Residual Strain, In/In | Maximum Strain, In/In |
| | Tension | Compression | | | Tension | Compression | | |
| E010DL | 0.000011 | -0.000010 | -0.000005 | -0.000005 | 0.000058 | -0.000042 | 0.000005 | 0.000005 |
| E025DL | 0.000023 | -0.000019 | -0.000001 | -0.000001 | 0.000107 | -0.000055 | 0.000002 | 0.000002 |
| E050DL | 0.000036 | -0.000034 | -0.000001 | -0.000001 | 0.000125 | -0.000078 | 0.000000 | 0.000000 |
| E075DL | 0.000044 | -0.000073 | 0.000000 | 0.000000 | 0.000154 | 0.000160 | 0.000002 | 0.000002 |
| E100DL | 0.000061 | -0.000180 | 0.000004 | 0.000004 | 0.000167 | -0.000280 | -0.000010 | -0.000010 |
| E125DL | 0.000072 | -0.000390 | -0.000002 | -0.000002 | 0.000196 | -0.000390 | 0.000003 | 0.000003 |
| E150DL | 0.000072 | -0.000480 | -0.000001 | -0.000001 | 0.000194 | -0.000460 | -0.000010 | -0.000010 |
| E200DL | 0.000109 | -0.001330 | -0.000014 | -0.000014 | 0.000282 | -0.000820 | -0.000018 | -0.000018 |
| T021DL | 0.000011 | -0.000008 | 0.000004 | 0.000004 | 0.000074 | -0.000045 | -0.000007 | -0.000007 |
| T052DL | 0.000018 | -0.000026 | -0.000001 | -0.000001 | 0.000118 | -0.000050 | -0.000010 | -0.000010 |
| T105DL | 0.000029 | -0.000059 | 0.000004 | 0.000004 | 0.000122 | -0.000071 | -0.000010 | -0.000010 |
| T157DL | 0.000053 | -0.000100 | 0.000003 | 0.000003 | 0.000162 | -0.000110 | 0.000000 | 0.000000 |
| T210DL | 0.000064 | -0.000160 | 0.000002 | 0.000002 | 0.000203 | -0.000200 | -0.000029 | -0.000029 |
| T262DL | 0.000071 | -0.000270 | 0.000001 | 0.000001 | 0.000245 | -0.000310 | -0.000057 | -0.000057 |
| T315DL | 0.000074 | -0.000320 | -0.000005 | -0.000005 | 0.000246 | -0.000410 | -0.000050 | -0.000050 |
| T420DL | 0.000096 | -0.000880 | -0.000004 | -0.000004 | 0.000391 | -0.001050 | -0.000110 | -0.000110 |
| E025N | 0.000047 | -0.000085 | -0.000004 | -0.000004 | 0.000252 | -0.000210 | -0.000001 | -0.000001 |
| E050N | 0.000082 | -0.000280 | -0.000004 | -0.000004 | 0.000261 | -0.000290 | -0.000008 | -0.000008 |
| E075N | 0.000109 | -0.000750 | -0.000009 | -0.000009 | 0.000263 | -0.000640 | -0.000001 | -0.000001 |
| E100N | 0.000171 | -0.001060 | -0.000008 | -0.000008 | 0.000251 | -0.001030 | 0.000012 | 0.000012 |
| E125N | 0.000229 | -0.001370 | -0.000010 | -0.000010 | 0.000203 | -0.001710 | -0.000002 | -0.000002 |
| E150N | 0.000247 | -0.001600 | 0.000000 | 0.000000 | 0.000716 | -0.002650 | -0.000003 | -0.000003 |
| E200N | 0.000332 | -0.002310 | -0.000005 | -0.000005 | 0.005185 | -0.004340 | -0.000002 | -0.000002 |

Shaded cells with bold print indicate strain maxima above approximate yield strain.

Table 4.21 Maximum and Residual Strains in Reinforcement: Gages S1Z5 and S1Z6

| Test | Gage S1Z3 (Yield Strain = 0.00141) | | | | Gage S1Z7 (Yield Strain = 0.00141) | | | |
|--------|------------------------------------|------------------|------------------------|------------------|------------------------------------|-------------|------------------------|-------------|
| | Maximum Strain, In/In | | Residual Strain, In/In | | Maximum Strain, In/In | | Residual Strain, In/In | |
| | Tension | Compression | Tension | Compression | Tension | Compression | Tension | Compression |
| E010DL | 0.000015 | -0.000030 | -0.000001 | -0.000001 | 0.000050 | -0.000040 | 0.000001 | 0.000001 |
| E025DL | 0.000017 | -0.000065 | -0.000002 | -0.000002 | 0.000203 | -0.000097 | 0.000000 | 0.000000 |
| E050DL | 0.000025 | -0.000106 | -0.000003 | -0.000003 | 0.000343 | -0.000150 | 0.000001 | 0.000001 |
| E075DL | 0.000042 | -0.000250 | -0.000012 | -0.000012 | 0.000369 | -0.000190 | 0.000000 | 0.000000 |
| E100DL | 0.000061 | -0.000465 | -0.000008 | -0.000008 | 0.000368 | -0.000220 | -0.000007 | -0.000007 |
| E125DL | 0.000079 | -0.000808 | -0.000014 | -0.000014 | 0.000355 | -0.000240 | -0.000005 | -0.000005 |
| E150DL | 0.000088 | -0.000990 | -0.000010 | -0.000010 | 0.000389 | -0.000320 | 0.000000 | 0.000000 |
| E200DL | 0.000340 | -0.003856 | -0.000098 | -0.000098 | 0.000287 | -0.000500 | 0.000001 | 0.000001 |
| T021DL | 0.000018 | -0.000020 | -0.000001 | -0.000001 | 0.000042 | -0.000055 | -0.000004 | -0.000004 |
| T052DL | 0.000022 | -0.000047 | 0.000000 | 0.000000 | 0.000111 | -0.000120 | 0.000000 | 0.000000 |
| T105DL | 0.000042 | -0.000097 | 0.000009 | 0.000009 | 0.000323 | -0.000150 | 0.000010 | 0.000010 |
| T157DL | 0.000060 | -0.000190 | -0.000001 | -0.000001 | 0.000394 | -0.000190 | 0.000013 | 0.000013 |
| T210DL | 0.000093 | -0.000312 | 0.000010 | 0.000010 | 0.000420 | -0.000220 | 0.000007 | 0.000007 |
| T262DL | 0.000120 | -0.000526 | -0.000003 | -0.000003 | 0.000397 | -0.000320 | 0.000003 | 0.000003 |
| T315DL | 0.000140 | -0.000651 | 0.000008 | 0.000008 | 0.000437 | -0.000400 | 0.000009 | 0.000009 |
| T420DL | 0.000390 | -0.002417 | -0.000089 | -0.000089 | 0.000382 | -0.000430 | 0.000055 | 0.000055 |
| E025N | 0.000230 | -0.000621 | -0.000007 | -0.000007 | 0.000208 | -0.000190 | 0.000002 | 0.000002 |
| E050N | 0.000370 | -0.001503 | 0.000013 | 0.000013 | 0.000219 | -0.000320 | -0.000024 | -0.000024 |
| E075N | 0.000450 | -0.002561 | -0.000011 | -0.000011 | 0.000215 | -0.000440 | -0.000016 | -0.000016 |
| E100N | 0.000540 | -0.003729 | -0.000050 | -0.000050 | 0.000216 | -0.000510 | -0.000003 | -0.000003 |
| E125N | 0.000580 | -0.005670 | -0.000198 | -0.000198 | 0.000211 | -0.000560 | -0.000023 | -0.000023 |
| E150N | 0.000450 | -0.008876 | -0.001196 | -0.001196 | 0.000267 | -0.000590 | 0.000031 | 0.000031 |
| E200N | 0.000630 | -0.009993 | -0.009990 | -0.009990 | 0.000504 | -0.000610 | -0.000001 | -0.000001 |

Shaded cells with bold print indicate strain maxima above approximate yield strain.

Table 4.22 Maximum and Residual Strains in Reinforcement: Gages S1Z3 and S1Z7

| Test | Gage S1Z8 (Yield Strain = 0.00141) | | | | Gage S2Z2 (Yield Strain = 0.00152) | | | |
|--------|------------------------------------|-------------|------------------------|--|------------------------------------|-------------|------------------------|--|
| | Maximum Strain, In/In | | Residual Strain, In/In | | Maximum Strain, In/In | | Residual Strain, In/In | |
| | Tension | Compression | | | Tension | Compression | | |
| E010DL | 0.000021 | -0.000007 | 0.000001 | | 0.000210 | -0.000109 | -0.000001 | |
| E025DL | 0.000007 | -0.000019 | 0.000000 | | 0.000670 | -0.000302 | 0.000000 | |
| E050DL | 0.000095 | -0.000050 | 0.000001 | | 0.001220 | -0.000546 | -0.000001 | |
| E075DL | 0.000119 | -0.000083 | 0.000000 | | 0.001880 | -0.000868 | 0.000000 | |
| E100DL | 0.000139 | -0.000110 | -0.000002 | | 0.002320 | -0.001207 | 0.000002 | |
| E125DL | 0.000174 | -0.000150 | -0.000012 | | 0.002260 | -0.001537 | 0.000012 | |
| E150DL | 0.000191 | -0.000180 | -0.000032 | | 0.002120 | -0.001637 | 0.000032 | |
| E200DL | 0.000358 | -0.000710 | -0.000150 | | 0.001990 | -0.002785 | 0.000150 | |
| T021DL | 0.000015 | -0.000010 | 0.000000 | | 0.000150 | -0.000151 | 0.000000 | |
| T052DL | 0.000050 | -0.000031 | 0.000000 | | 0.000460 | -0.000394 | 0.000000 | |
| T105DL | 0.000091 | -0.000061 | 0.000000 | | 0.000990 | -0.000730 | 0.000000 | |
| T157DL | 0.000107 | -0.000090 | 0.000000 | | 0.001630 | -0.001133 | 0.000000 | |
| T210DL | 0.000122 | -0.000140 | 0.000010 | | 0.002150 | -0.001564 | -0.000010 | |
| T262DL | 0.000162 | -0.000270 | 0.000005 | | 0.002180 | -0.002049 | -0.000005 | |
| T315DL | 0.000194 | -0.000290 | -0.000021 | | 0.002040 | -0.002372 | 0.000021 | |
| T420DL | 0.000363 | -0.000710 | -0.000088 | | 0.002090 | -0.002677 | 0.000088 | |
| E025N | 0.000161 | -0.000145 | -0.000001 | | 0.001350 | -0.001076 | 0.000001 | |
| E050N | 0.000207 | -0.000270 | 0.000035 | | 0.002260 | -0.002089 | -0.000035 | |
| E075N | 0.000237 | -0.000340 | 0.000021 | | 0.002280 | -0.002485 | -0.000021 | |
| E100N | 0.000281 | -0.000440 | 0.000002 | | 0.002310 | -0.002454 | -0.000002 | |
| E125N | 0.000306 | -0.000650 | -0.000016 | | Gage Non-Functional | | | |
| E150N | 0.000317 | -0.000750 | 0.000008 | | Gage Non-Functional | | | |
| E200N | 0.000287 | -0.001480 | -0.000010 | | Gage Non-Functional | | | |

Shaded cells with bold print indicate strain maxima above approximate yield strain.

Table 4.23 Maximum and Residual Strains in Reinforcement: Gages S1Z8 and S2Z2

| Test | Gage S2Z3 (Yield Strain = 0.00141) | | | | Gage S1X5 (Yield Strain = 0.00134) | | | |
|--------|------------------------------------|------------------|------------------------|--|------------------------------------|-------------|------------------------|--|
| | Maximum Strain, In/In | | Residual Strain, In/In | | Maximum Strain, In/In | | Residual Strain, In/In | |
| | Tension | Compression | | | Tension | Compression | | |
| E010DL | 0.000038 | -0.000066 | -0.000001 | | 0.000092 | -0.000045 | 0.000010 | |
| E025DL | 0.000068 | -0.000152 | -0.000003 | | 0.000210 | -0.000124 | 0.000005 | |
| E050DL | 0.000115 | -0.000285 | -0.000015 | | 0.000330 | -0.000211 | -0.000005 | |
| E075DL | 0.000190 | -0.000443 | 0.000007 | | 0.000350 | -0.000256 | -0.000001 | |
| E100DL | 0.000280 | -0.000593 | 0.000000 | | 0.000330 | -0.000301 | -0.000011 | |
| E125DL | 0.000390 | -0.000770 | -0.000004 | | 0.000270 | -0.000350 | -0.000009 | |
| E150DL | 0.000430 | -0.000874 | -0.000011 | | 0.000290 | -0.000356 | 0.000006 | |
| E200DL | 0.000860 | -0.001461 | 0.000100 | | 0.000052 | -0.000199 | 0.000003 | |
| T021DL | 0.000044 | -0.000047 | -0.000002 | | 0.000063 | -0.000067 | 0.000006 | |
| T052DL | 0.000084 | -0.000115 | -0.000016 | | 0.000160 | -0.000150 | 0.000004 | |
| T105DL | 0.000170 | -0.000223 | -0.000014 | | 0.000290 | -0.000230 | 0.000018 | |
| T157DL | 0.000280 | -0.000373 | -0.000022 | | 0.000330 | -0.000294 | 0.000029 | |
| T210DL | 0.000420 | -0.000509 | -0.000035 | | 0.000310 | -0.000347 | 0.000031 | |
| T262DL | 0.000560 | -0.000657 | -0.000053 | | 0.000240 | -0.000367 | 0.000024 | |
| T315DL | 0.000630 | -0.000752 | -0.000050 | | 0.000230 | -0.000389 | 0.000031 | |
| T420DL | 0.000890 | -0.001199 | -0.000081 | | 0.000170 | -0.000223 | 0.000060 | |
| E025N | 0.000240 | -0.000349 | -0.000004 | | 0.000085 | -0.000151 | 0.000001 | |
| E050N | 0.000540 | -0.000695 | 0.000028 | | 0.000093 | -0.000171 | -0.000018 | |
| E075N | 0.000770 | -0.001010 | 0.000006 | | 0.000087 | -0.000152 | -0.000017 | |
| E100N | 0.000910 | -0.001266 | -0.000004 | | 0.000095 | -0.000135 | -0.000012 | |
| E125N | 0.000910 | -0.001453 | 0.000014 | | 0.000099 | -0.000125 | -0.000009 | |
| E150N | 0.000980 | -0.002710 | 0.000220 | | 0.000120 | -0.000133 | -0.000009 | |
| E200N | 0.000850 | -0.002963 | -0.000559 | | 0.000210 | -0.000390 | 0.000064 | |

Shaded cells with bold print indicate strain maxima above approximate yield strain.

Table 4.24 Maximum and Residual Strains in Reinforcement: Gages S2Z3 and S1X5

| Test | Gage SIX11 (Yield Strain = 0.00134) | | | Gage SIX12 (Yield Strain = 0.00134) | | |
|--------|-------------------------------------|-------------|------------------------|-------------------------------------|-------------|------------------------|
| | Maximum Strain, In/In | | Residual Strain, In/In | Maximum Strain, In/In | | Residual Strain, In/In |
| | Tension | Compression | Strain, In/In | Tension | Compression | Strain, In/In |
| E010DL | 0.000010 | -0.000010 | 0.000005 | 0.000190 | -0.000239 | -0.000004 |
| E025DL | 0.000021 | -0.000020 | 0.000000 | 0.000480 | -0.000541 | -0.000006 |
| E050DL | 0.000044 | -0.000036 | 0.000000 | 0.000950 | -0.000985 | 0.000001 |
| E075DL | 0.000072 | -0.000063 | 0.000000 | 0.001390 | -0.001436 | 0.000030 |
| E100DL | 0.000104 | -0.000093 | 0.000001 | 0.001800 | -0.001677 | 0.000076 |
| E125DL | 0.000139 | -0.000120 | -0.000001 | 0.002120 | -0.001829 | 0.000120 |
| E150DL | 0.000163 | -0.000150 | 0.000000 | 0.002210 | -0.001898 | 0.000170 |
| E200DL | 0.000298 | -0.000200 | 0.000000 | 0.002670 | -0.002514 | -0.000009 |
| T021DL | 0.000012 | -0.000007 | 0.000000 | 0.000270 | -0.000180 | -0.000011 |
| T052DL | 0.000024 | -0.000017 | -0.000001 | 0.000650 | -0.000426 | -0.000002 |
| T105DL | 0.000054 | -0.000030 | -0.000001 | 0.001160 | -0.000822 | -0.000103 |
| T157DL | 0.000096 | -0.000052 | -0.000005 | 0.001730 | -0.001229 | -0.000070 |
| T210DL | 0.000138 | -0.000074 | -0.000009 | 0.002180 | -0.001485 | -0.000122 |
| T262DL | 0.000182 | -0.000099 | -0.000010 | 0.002450 | -0.001682 | -0.000157 |
| T315DL | 0.000219 | -0.000120 | -0.000015 | 0.002480 | -0.001736 | -0.000136 |
| T420DL | 0.000343 | -0.000150 | -0.000018 | 0.002990 | -0.002086 | -0.000168 |
| E025N | 0.000041 | -0.000030 | 0.000001 | 0.000860 | -0.000594 | 0.000007 |
| E050N | 0.000085 | -0.000061 | 0.000007 | 0.001580 | -0.001199 | 0.000033 |
| E075N | 0.000140 | -0.000110 | 0.000000 | 0.002140 | -0.002002 | -0.000008 |
| E100N | 0.000201 | -0.000150 | 0.000002 | 0.002670 | -0.002756 | 0.000050 |
| E125N | 0.000248 | -0.000180 | -0.000004 | 0.003260 | -0.003382 | 0.000220 |
| E150N | 0.000287 | -0.000180 | 0.000020 | 0.006730 | -0.004222 | 0.003150 |
| E200N | 0.000706 | -0.000140 | -0.000002 | 0.005200 | -0.004271 | 0.000640 |

Shaded cells with bold print indicate strain maxima above approximate yield strain.

Table 4.25 Maximum and Residual Strains in Reinforcement: Gages SIX11 and SIX12

| Test | Gage S1X13 (Yield Strain = 0.00203) | | | | Gage S1X14 (Yield Strain = 0.00134) | | | |
|--------|-------------------------------------|-------------|------------------------|--|-------------------------------------|-------------|------------------------|--|
| | Maximum Strain, In/In | | Residual Strain, In/In | | Maximum Strain, In/In | | Residual Strain, In/In | |
| | Tension | Compression | | | Tension | Compression | | |
| E010DL | 0.000038 | -0.000034 | 0.000000 | | 0.000011 | -0.000006 | 0.000004 | |
| E025DL | 0.000042 | -0.000114 | -0.000011 | | 0.000023 | 0.000014 | 0.000010 | |
| E050DL | 0.000039 | -0.000109 | -0.000019 | | 0.000084 | -0.000015 | 0.000012 | |
| E075DL | 0.000051 | -0.000191 | 0.000021 | | 0.000321 | -0.000025 | 0.000012 | |
| E100DL | 0.000058 | -0.000264 | 0.000024 | | 0.000681 | -0.000030 | 0.000019 | |
| E125DL | 0.000044 | -0.000388 | -0.000024 | | 0.001055 | -0.000052 | 0.000009 | |
| E150DL | 0.000064 | -0.000493 | -0.000035 | | 0.001289 | -0.000069 | 0.000001 | |
| E200DL | 0.000048 | -0.000967 | -0.000079 | | 0.002357 | -0.000130 | 0.000018 | |
| T021DL | 0.000039 | -0.000035 | 0.000001 | | 0.000011 | -0.000007 | 0.000005 | |
| T052DL | 0.000035 | -0.000053 | -0.000019 | | 0.000019 | -0.000011 | -0.000003 | |
| T105DL | 0.000041 | -0.000074 | 0.000004 | | 0.000040 | -0.000021 | 0.000006 | |
| T157DL | 0.000053 | -0.000132 | -0.000005 | | 0.000168 | -0.000019 | 0.000001 | |
| T210DL | 0.000054 | -0.000223 | -0.000005 | | 0.000427 | -0.000031 | -0.000001 | |
| T262DL | 0.000051 | -0.000327 | -0.000009 | | 0.000774 | -0.000042 | 0.000016 | |
| T315DL | 0.000076 | -0.000377 | -0.000023 | | 0.000958 | -0.000054 | 0.000010 | |
| T420DL | 0.000091 | -0.000638 | -0.000049 | | 0.001781 | -0.000230 | 0.000031 | |
| E025N | 0.000023 | -0.000112 | -0.000012 | | 0.000242 | -0.000085 | 0.000005 | |
| E050N | 0.000041 | -0.000289 | 0.000011 | | 0.000815 | -0.000180 | -0.000007 | |
| E075N | 0.000046 | -0.000500 | -0.000005 | | 0.001348 | -0.000270 | -0.000012 | |
| E100N | 0.000042 | -0.000716 | -0.000045 | | 0.001874 | -0.000320 | -0.000023 | |
| E125N | 0.000054 | -0.000969 | -0.000055 | | 0.002358 | -0.000340 | 0.000025 | |
| E150N | 0.000045 | -0.001342 | -0.000152 | | 0.001994 | -0.000720 | -0.000090 | |
| E200N | 0.000028 | -0.001462 | 0.000450 | | 0.002453 | -0.001000 | 0.000072 | |

Shaded cells with bold print indicate strain maxima above approximate yield strain.

Table 4.26 Maximum and Residual Strains in Reinforcement: Gages S1X13 and S1X14

| Test | Gage SIX15 (Yield Strain = 0.00134) | | | Gage SIX16 (Yield Strain = 0.00203) | | |
|--------|-------------------------------------|------------------|------------------------|-------------------------------------|-------------|------------------------|
| | Maximum Strain, In/In | | Residual Strain, In/In | Maximum Strain, In/In | | Residual Strain, In/In |
| | Tension | Compression | Strain, In/In | Tension | Compression | Strain, In/In |
| E010DL | 0.000098 | -0.000126 | -0.000003 | 0.000025 | -0.000012 | 0.000000 |
| E025DL | 0.000120 | -0.000125 | 0.000000 | 0.000053 | -0.000031 | -0.000001 |
| E050DL | 0.000240 | -0.000113 | 0.000008 | 0.000091 | -0.000055 | -0.000005 |
| E075DL | 0.000440 | -0.000248 | -0.000071 | 0.000140 | -0.000091 | 0.000000 |
| E100DL | 0.000660 | -0.000298 | -0.000025 | 0.000180 | -0.000141 | 0.000000 |
| E125DL | 0.000860 | -0.000388 | -0.000018 | 0.000220 | -0.000196 | 0.000001 |
| E150DL | 0.000880 | -0.000503 | -0.000008 | 0.000240 | -0.000239 | -0.000005 |
| E200DL | 0.002570 | -0.001059 | 0.000400 | 0.000250 | -0.000486 | -0.000003 |
| T021DL | 0.000120 | -0.000132 | 0.000014 | 0.000019 | -0.000015 | 0.000000 |
| T052DL | 0.000075 | -0.000161 | -0.000036 | 0.000039 | -0.000037 | 0.000001 |
| T105DL | 0.000150 | -0.000138 | -0.000017 | 0.000070 | -0.000071 | 0.000006 |
| T157DL | 0.000350 | -0.000243 | 0.000010 | 0.000120 | -0.000127 | 0.000010 |
| T210DL | 0.000570 | -0.000330 | 0.000024 | 0.000160 | -0.000197 | 0.000010 |
| T262DL | 0.000770 | -0.000451 | -0.000033 | 0.000190 | -0.000274 | 0.000017 |
| T315DL | 0.000800 | -0.000724 | -0.000366 | 0.000210 | -0.000336 | 0.000015 |
| T420DL | 0.002190 | -0.001663 | -0.000092 | 0.000210 | -0.000510 | 0.000029 |
| E025N | Gage Non-Functional | | | 0.000059 | -0.000077 | -0.000005 |
| E050N | Gage Non-Functional | | | 0.000100 | -0.000157 | -0.000013 |
| E075N | Gage Non-Functional | | | 0.000150 | -0.000256 | -0.000006 |
| E100N | Gage Non-Functional | | | 0.000190 | -0.000359 | 0.000006 |
| E125N | Gage Non-Functional | | | 0.000210 | -0.000450 | 0.000007 |
| E150N | Gage Non-Functional | | | 0.000220 | -0.000515 | 0.000005 |
| E200N | Gage Non-Functional | | | 0.000230 | -0.000824 | -0.000003 |

Shaded cells with bold print indicate strain maxima above approximate yield strain.

Table 4.27 Maximum and Residual Strains in Reinforcement: Gages SIX15 and SIX16

| Story 1: Brace in Tension | | | | |
|--|----------|------------|---------------------------------|-------------------------|
| Test Series | Location | Curve Type | Equation ¹ | Correlation Coefficient |
| E010DL-E200DL | NE | Linear | $y = 0.22 + 17.17x$ | 0.92 |
| E010DL-E200DL | NE | Quadratic | $y = 0.08 + 21.44x - 12.25x^2$ | 0.92 |
| T021DL-T420DL | NE | Linear | $y = 0.17 + 14.36x$ | 0.89 |
| T021DL-T420DL | NE | Quadratic | $y = -0.05 + 22.01x - 27.36x^2$ | 0.90 |
| E010DL-E200DL | NW | Linear | $y = -0.09 + 16.37x$ | 0.93 |
| E010DL-E200DL | NW | Quadratic | $y = -0.07 + 15.72x - 1.84x^2$ | 0.93 |
| T021DL-T420DL | NW | Linear | $y = -0.14 + 14.58x$ | 0.90 |
| T021DL-T420DL | NW | Quadratic | $y = -0.05 + 11.05x + 12.67x^2$ | 0.90 |
| E010DL-E200DL | SE | Linear | $y = 0.23 + 9.92x$ | 0.81 |
| E010DL-E200DL | SE | Quadratic | $y = 0.02 + 15.21x - 14.60x^2$ | 0.81 |
| T021DL-T420DL | SE | Linear | $y = -0.03 + 10.70x$ | 0.81 |
| T021DL-T420DL | SE | Quadratic | $y = 0.35 + 8.91x + 5.03x^2$ | 0.81 |
| E010DL-E200DL | SW | Linear | $y = 0.04 + 11.90x$ | 0.79 |
| E010DL-E200DL | SW | Quadratic | $y = -0.04 + 14.07x - 6.55x^2$ | 0.79 |
| T021DL-T420DL | SW | Linear | $y = 0.07 + 10.00x$ | 0.81 |
| T021DL-T420DL | SW | Quadratic | $y = -0.10 + 15.51x - 15.33x^2$ | 0.82 |
| ¹ x = Damper Displacement (inches), y = Damper Force (kips) | | | | |

Table 5.1.a Curve Fits for Damper Force Vs. Displacement “Backbone” Curves, Brace in Tension

| Story 2: Brace in Tension | | | | |
|---|----------|------------------------|---------------------------------|-------------------------|
| Test Series | Location | Curve Type | Equation ¹ | Correlation Coefficient |
| E010DL-E200DL | NE | Linear | $y = 0.10 + 12.60x$ | 0.91 |
| E010DL-E200DL | NE | Quadratic | $y = 0.01 + 14.67x - 3.80x^2$ | 0.91 |
| T021DL-T420DL | NE | Linear | $y = 0.11 + 10.95x$ | 0.89 |
| T021DL-T420DL | NE | Quadratic | $y = -0.02 + 15.26x - 11.12x^2$ | 0.89 |
| E010DL-E200DL | NW | Linear | $y = 0.05 + 15.00x$ | 0.91 |
| E010DL-E200DL | NW | Quadratic | $y = -0.20 + 21.13x - 13.07x^2$ | 0.92 |
| T021DL-T420DL | NW | Linear | $y = 0.09 + 13.08x$ | 0.82 |
| T021DL-T420DL | NW | Quadratic | $y = -0.15 + 18.94x - 15.67x^2$ | 0.82 |
| E010DL-E200DL | SE | Linear ² | $y = 0.16 + 9.47x$ | 0.72 |
| E010DL-E200DL | SE | Quadratic ² | $y = -0.24 + 18.82x - 23.77x^2$ | 0.76 |
| T021DL-T420DL | SE | Linear | $y = 0.06 + 8.69x$ | 0.69 |
| T021DL-T420DL | SE | Quadratic | $y = -0.06 + 11.28x - 5.89x^2$ | 0.69 |
| E010DL-E200DL | SW | Linear | $y = 0.13 + 14.39x$ | 0.85 |
| E010DL-E200DL | SW | Quadratic | $y = -0.02 + 17.92x - 8.98x^2$ | 0.85 |
| T021DL-T420DL | SW | Linear | $y = 0.18 + 12.17x$ | 0.89 |
| T021DL-T420DL | SW | Quadratic | $y = -0.05 + 17.03x - 10.51x^2$ | 0.90 |
| ¹ x = Damper Displacement (inches), y = Damper Force (kips) | | | | |
| ² Curve fit performed through peak damper displacement of 0.35". | | | | |

Table 5.1.b Curve Fits for Damper Force Vs. Displacement "Backbone" Curves, Brace in Tension

| Story 3: Brace in Tension | | | | |
|---|----------|------------------------|---------------------------------|-------------------------|
| Test Series | Location | Curve Type | Equation ¹ | Correlation Coefficient |
| E010DL-E200DL | NE | Linear | $y = -0.15 + 6.63x$ | 0.73 |
| E010DL-E200DL | NE | Quadratic | $y = 0.05 + 0.72x + 16.73x^2$ | 0.77 |
| T021DL-T420DL | NE | Linear | $y = -0.12 + 5.00x$ | 0.67 |
| T021DL-T420DL | NE | Quadratic | $y = 0.09 - 1.89x + 27.17x^2$ | 0.73 |
| E010DL-E200DL | NW | Linear | $y = -0.02 + 8.24x$ | 0.70 |
| E010DL-E200DL | NW | Quadratic | $y = 0.08 + 7.33x + 2.65x^2$ | 0.70 |
| T021DL-T420DL | NW | Linear | $y = -0.09 + 8.72x$ | 0.73 |
| T021DL-T420DL | NW | Quadratic | $y = -0.02 + 6.36x + 9.16x^2$ | 0.73 |
| E010DL-E200DL | SE | Linear ² | $y = -0.05 + 5.65x$ | 0.65 |
| E010DL-E200DL | SE | Quadratic ² | $y = 0.09 - 0.17x + 25.13x^2$ | 0.65 |
| T021DL-T420DL | SE | Linear | $y = -0.06 + 4.30x$ | 0.52 |
| T021DL-T420DL | SE | Quadratic | $y = 0.01 + 1.34x + 9.06x^2$ | 0.54 |
| E010DL-E200DL | SW | Linear | $y = 0.03 + 9.18x$ | 0.83 |
| E010DL-E200DL | SW | Quadratic | $y = -0.08 + 13.85x - 19.84x^2$ | 0.85 |
| T021DL-T420DL | SW | Linear | $y = -0.01 + 9.28x$ | 0.81 |
| T021DL-T420DL | SW | Quadratic | $y = -0.02 + 9.50x - 0.80x^2$ | 0.82 |
| ¹ x = Damper Displacement (inches), y = Damper Force (kips) ² Curve fit performed through peak damper displacement of 0.30". | | | | |

Table 5.1.c Curve Fits for Damper Force Vs. Displacement "Backbone" Curves, Brace in Tension

| Story 1: Brace in Compression | | | | |
|--|----------|------------|---------------------------------|-------------------------|
| Test Series | Location | Curve Type | Equation ¹ | Correlation Coefficient |
| E010DL-E200DL | NE | Linear | $y = 0.53 + 7.75x$ | 0.81 |
| E010DL-E200DL | NE | Quadratic | $y = -0.03 + 18.16x - 23.78x^2$ | 0.87 |
| T021DL-T420DL | NE | Linear | $y = 0.25 + 9.16x$ | 0.85 |
| T021DL-T420DL | NE | Quadratic | $y = -0.08 + 19.99x - 39.11x^2$ | 0.90 |
| E010DL-E200DL | NW | Linear | $y = 0.10 + 4.40x$ | 0.63 |
| E010DL-E200DL | NW | Quadratic | $y = 0.07 + 5.25x - 2.41x^2$ | 0.63 |
| T021DL-T420DL | NW | Linear | $y = 0.13 + 2.92x$ | 0.49 |
| T021DL-T420DL | NW | Quadratic | $y = 0.06 + 4.24x - 3.28x^2$ | 0.50 |
| E010DL-E200DL | SE | Linear | $y = 0.31 + 9.12x$ | 0.78 |
| E010DL-E200DL | SE | Quadratic | $y = -0.05 + 17.94x - 20.84x^2$ | 0.82 |
| T021DL-T420DL | SE | Linear | $y = 0.14 + 9.55x$ | 0.84 |
| T021DL-T420DL | SE | Quadratic | $y = 0.04 + 12.57x - 10.39x^2$ | 0.85 |
| E010DL-E200DL | SW | Linear | $y = 0.33 + 12.34x$ | 0.87 |
| E010DL-E200DL | SW | Quadratic | $y = 0.00 + 20.78x - 21.65x^2$ | 0.90 |
| T021DL-T420DL | SW | Linear | $y = 0.09 + 11.81x$ | 0.86 |
| T021DL-T420DL | SW | Quadratic | $y = 0.04 + 13.44x - 5.57x^2$ | 0.86 |
| ¹ x = Damper Displacement (inches), y = Damper Force (kips) | | | | |

Table 5.2.a Curve Fits for Damper Force Vs. Displacement “Backbone” Curves, Brace in Compression

| Story 2: Brace in Compression | | | | |
|--|----------|------------|---------------------------------|-------------------------|
| Test Series | Location | Curve Type | Equation ¹ | Correlation Coefficient |
| E010DL-E200DL | NE | Linear | $y = 0.23 + 8.30x$ | 0.90 |
| E010DL-E200DL | NE | Quadratic | $y = -0.03 + 13.52x - 9.63x^2$ | 0.91 |
| T021DL-T420DL | NE | Linear | $y = 0.15 + 8.33x$ | 0.89 |
| T021DL-T420DL | NE | Quadratic | $y = -0.07 + 11.40x - 4.84x^2$ | 0.89 |
| E010DL-E200DL | NW | Linear | $y = 0.23 + 5.39x$ | 0.65 |
| E010DL-E200DL | NW | Quadratic | $y = 0.06 + 8.71x - 7.55x^2$ | 0.66 |
| T021DL-T420DL | NW | Linear | $y = 0.13 + 4.27x$ | 0.70 |
| T021DL-T420DL | NW | Quadratic | $y = -0.01 + 7.30x - 6.24x^2$ | 0.71 |
| E010DL-E200DL | SE | Linear | $y = 0.44 + 4.13x$ | 0.58 |
| E010DL-E200DL | SE | Quadratic | $y = 0.00 + 13.65x - 20.69x^2$ | 0.71 |
| T021DL-T420DL | SE | Linear | $y = 0.13 + 5.25x$ | 0.67 |
| T021DL-T420DL | SE | Quadratic | $y = -0.01 + 9.30x - 12.27x^2$ | 0.69 |
| E010DL-E200DL | SW | Linear | $y = 0.46 + 8.78x$ | 0.71 |
| E010DL-E200DL | SW | Quadratic | $y = -0.20 + 22.58x - 27.71x^2$ | 0.79 |
| T021DL-T420DL | SW | Linear | $y = 0.34 + 9.47x$ | 0.71 |
| T021DL-T420DL | SW | Quadratic | $y = -0.11 + 20.44x - 28.63x^2$ | 0.75 |
| ¹ x = Damper Displacement (inches), y = Damper Force (kips) | | | | |

Table 5.2.b Curve Fits for Damper Force Vs. Displacement “Backbone” Curves, Brace in Compression

| Story 3: Brace in Compression | | | | |
|--|----------|------------|--------------------------------|-------------------------|
| Test Series | Location | Curve Type | Equation ¹ | Correlation Coefficient |
| E010DL-E200DL | NE | Linear | $y = 0.05 + 1.22x$ | 0.32 |
| E010DL-E200DL | NE | Quadratic | $y = 0.04 + 1.62x - 1.40x^2$ | 0.32 |
| T021DL-T420DL | NE | Linear | $y = -0.06 + 2.40x$ | 0.50 |
| T021DL-T420DL | NE | Quadratic | $y = 0.02 - 0.17x + 7.54x^2$ | 0.54 |
| E010DL-E200DL | NW | Linear | $y = 0.08 + 0.71x$ | 0.12 |
| E010DL-E200DL | NW | Quadratic | $y = 0.06 + 1.40x - 2.73x^2$ | 0.12 |
| T021DL-T420DL | NW | Linear | $y = 0.06 - 0.36x$ | 0.07 |
| T021DL-T420DL | NW | Quadratic | $y = 0.08 - 1.50x + 4.17x^2$ | 0.11 |
| E010DL-E200DL | SE | Linear | $y = 0.06 + 1.40x$ | 0.27 |
| E010DL-E200DL | SE | Quadratic | $y = 0.09 + 0.22x + 3.59x^2$ | 0.28 |
| T021DL-T420DL | SE | Linear | $y = 0.01 + 0.85x$ | 0.19 |
| T021DL-T420DL | SE | Quadratic | $y = 0.07 - 2.98x + 18.40x^2$ | 0.37 |
| E010DL-E200DL | SW | Linear | $y = 0.14 + 7.88x$ | 0.77 |
| E010DL-E200DL | SW | Quadratic | $y = 0.05 + 10.71x - 8.78x^2$ | 0.78 |
| T021DL-T420DL | SW | Linear | $y = 0.06 + 8.70x$ | 0.83 |
| T021DL-T420DL | SW | Quadratic | $y = 0.00 + 11.16x - 10.38x^2$ | 0.84 |
| ¹ x = Damper Displacement (inches), y = Damper Force (kips) | | | | |

Table 5.2.c Curve Fits for Damper Force Vs. Displacement “Backbone” Curves, Brace in Compression

| | | | Stiffness, Brace in: | | Story Average Kips/Inch |
|-------------------------------|----------|--------------------------|--------------------------|----------------------|-------------------------------|
| Test Series | Story | Location | Compression Kips/Inch | Tension Kips/Inch | |
| E010DL-E200DL | 1 | NE | 7.75 | 17.17 | 12.46 |
| | | NW | 4.40 | 16.37 | 10.39 |
| | | SE | 9.12 | 9.92 | 9.52 |
| | | SW | 12.34 | 11.90 | 12.12 |
| | | <i>All (Avg.)</i> | <i>8.40</i> | <i>13.84</i> | <i>11.12</i> |
| T021DL-T420DL | 1 | NE | 9.16 | 14.36 | 11.76 |
| | | NW | 2.92 | 14.58 | 8.75 |
| | | SE | 9.55 | 10.70 | 10.13 |
| | | SW | 11.81 | 10.00 | 10.91 |
| | | <i>All (Avg.)</i> | <i>8.36</i> | <i>12.41</i> | <i>10.39</i> |
| <i>All Simulations</i> | 1 | <i>All (Avg.)</i> | <i>8.38</i> | <i>13.13</i> | <i>10.75</i> |
| E010DL-E200DL | 2 | NE | 8.30 | 12.60 | 10.45 |
| | | NW | 5.39 | 15.00 | 10.20 |
| | | SE | 4.13 | 9.47 | 6.80 |
| | | SW | 8.78 | 14.39 | 11.59 |
| | | <i>All (Avg.)</i> | <i>6.65</i> | <i>12.87</i> | <i>9.76</i> |
| T021DL-T420DL | 2 | NE | 8.33 | 10.95 | 9.64 |
| | | NW | 4.27 | 13.08 | 8.68 |
| | | SE | 5.25 | 8.69 | 6.97 |
| | | SW | 9.47 | 12.17 | 10.82 |
| | | <i>All (Avg.)</i> | <i>6.83</i> | <i>11.22</i> | <i>9.03</i> |
| <i>All Simulations</i> | 2 | <i>All (Avg.)</i> | <i>6.74</i> | <i>12.04</i> | <i>9.39</i> |
| E010DL-E200DL | 3 | NE | 1.22 | 6.63 | 3.93 |
| | | NW | 0.71 | 8.24 | 4.48 |
| | | SE | 1.40 | 5.65 | 3.53 |
| | | SW | 7.88 | 9.18 | 8.53 |
| | | <i>All (Avg.)</i> | <i>2.80</i> | <i>7.43</i> | <i>5.11</i> |
| T021DL-T420DL | 3 | NE | 2.40 | 5.00 | 3.70 |
| | | NW | -0.36 | 8.72 | 4.18 |
| | | SE | 0.85 | 4.30 | 2.58 |
| | | SW | 8.70 | 9.28 | 8.99 |
| | | <i>All (Avg.)</i> | <i>2.90</i> | <i>6.83</i> | <i>4.86</i> |
| <i>All Simulations</i> | 3 | <i>All (Avg.)</i> | <i>2.85</i> | <i>7.13</i> | <i>4.99</i> |

Table 5.3 Average Damper Brace Stiffnesses Based on Linear Curve Fits to "Backbone" Curves

| Test | Average Damper Stiffness (Kips/Inch) | | | | | |
|---|--------------------------------------|------------|-------------|-------------------------------------|------------|-------------|
| | First 20 Seconds' Elapsed Time | | | 3.5 Seconds of Maximum Displacement | | |
| | Story 1 | Story 2 | Story 3 | Story 1 | Story 2 | Story 3 |
| NE Damper | | | | | | |
| E010DL | 6.8 | 5.2 | 3.2 | 9.8 | 6.1 | -1.9 |
| E025DL | 10.9 | 6.4 | -1.2 | 11.7 | 6.5 | -1.3 |
| E050DL | 10.4 | 6.5 | -1.3 | 10.6 | 6.6 | -1.3 |
| E075DL | 8.0 | 5.2 | -2.4 | 8.2 | 5.2 | -2.4 |
| E100DL | 6.3 | 4.3 | -3.0 | 6.6 | 4.4 | -2.9 |
| E125DL | 5.5 | 3.5 | -3.1 | 5.7 | 3.7 | -3.1 |
| E150DL | 6.8 | 5.1 | -1.4 | 7.1 | 5.3 | -1.2 |
| E200DL | 4.4 | 4.0 | -0.1 | 4.9 | 4.6 | 0.4 |
| <i>Average</i> | <i>7.4</i> | <i>5.0</i> | <i>-1.2</i> | <i>8.1</i> | <i>5.3</i> | <i>-1.7</i> |
| NW Damper | | | | | | |
| E010DL | 0.9 | 1.5 | -2.7 | 0.7 | 1.4 | -3.5 |
| E025DL | 1.3 | 2.1 | -3.1 | 1.4 | 2.8 | -3.0 |
| E050DL | 2.0 | 4.1 | -1.7 | 2.1 | 5.1 | -1.3 |
| E075DL | 1.1 | 2.8 | -2.5 | 1.2 | 3.2 | -2.2 |
| E100DL | 1.0 | 2.1 | -2.7 | 1.1 | 2.4 | -2.6 |
| E125DL | 1.1 | 1.7 | -2.7 | 1.1 | 2.0 | -2.5 |
| E150DL | 3.2 | 4.0 | -0.4 | 3.0 | 4.1 | -0.1 |
| E200DL | 1.6 | 1.8 | 0.0 | 1.7 | 2.3 | 0.3 |
| <i>Average</i> | <i>1.5</i> | <i>2.5</i> | <i>-2.0</i> | <i>1.5</i> | <i>2.9</i> | <i>-1.9</i> |
| SE Damper | | | | | | |
| E010DL | 2.5 | -1.2 | -2.9 | 4.6 | -1.8 | -2.9 |
| E025DL | 5.3 | -1.1 | -2.4 | 6.1 | -0.9 | -2.3 |
| E050DL | 0.4 | 0.1 | -1.7 | 6.7 | 0.3 | -1.6 |
| E075DL | 4.2 | 0.5 | -2.6 | 4.2 | 0.8 | -2.6 |
| E100DL | 2.8 | 0.9 | -3.2 | 3.1 | 1.1 | -3.1 |
| E125DL | 2.4 | 1.3 | -3.3 | 2.8 | 1.5 | -3.2 |
| E150DL | 4.2 | 2.6 | -1.4 | 4.8 | 4.8 | -1.2 |
| E200DL | 3.5 | 1.5 | -0.8 | 4.0 | 1.7 | -0.6 |
| <i>Average</i> | <i>3.2</i> | <i>0.6</i> | <i>-2.3</i> | <i>4.5</i> | <i>0.9</i> | <i>-2.2</i> |
| SW Damper | | | | | | |
| E010DL | 3.2 | 3.8 | 2.3 | 4.3 | 5.2 | 3.9 |
| E025DL | 4.0 | 5.2 | 4.7 | 4.3 | 5.8 | 5.3 |
| E050DL | 4.4 | 5.7 | 6.1 | 4.4 | 5.6 | 6.1 |
| E075DL | 2.9 | 4.5 | 4.2 | 3.1 | 4.7 | 4.2 |
| E100DL | 2.1 | 3.4 | 3.3 | 2.5 | 3.7 | 3.3 |
| E125DL | 1.7 | 2.9 | 2.7 | 2.3 | 3.4 | 2.8 |
| E150DL | 3.5 | 5.0 | 4.7 | 4.3 | 5.6 | 4.8 |
| E200DL | 1.9 | 3.7 | 2.9 | 2.9 | 4.5 | 3.0 |
| <i>Average</i> | <i>3.0</i> | <i>4.3</i> | <i>3.9</i> | <i>3.5</i> | <i>4.8</i> | <i>4.2</i> |
| Average for All Dampers and All Simulations | | | | | | |
| <i>Average</i> | <i>3.8</i> | <i>3.1</i> | <i>-0.4</i> | <i>4.4</i> | <i>3.5</i> | <i>-0.4</i> |

Table 5.4 Damper Stiffnesses Based on Linear Regressions for Time-Histories

| First Story Damper Stiffnesses | | | | | | | | | |
|--------------------------------|-------|------------------------|---------------------------|--------------------------|----------------------------|------------------------|---------------------------|--------------------------|----------------------------|
| Test | Strut | Brace in Tension | | | | Brace in Compression | | | |
| | | Stiffness Kips/Inch | No. of Data Points (+) | Max. Shear Strain (%) | Max. Strut Force (Kips) | Stiffness Kips/Inch | No. of Data Points (-) | Max. Shear Strain (%) | Max. Strut Force (Kips) |
| E010DL | NE | 4.8 | 126 | 2.2 | 0.46 | 3.9 | 112 | 1.9 | 0.32 |
| | NW | 4.5 | 77 | 1.7 | 0.29 | 2.6 | 418 | 1.5 | 0.30 |
| | SE | 4.2 | 79 | 1.1 | 0.32 | 0.6 | 474 | 2.5 | 0.36 |
| | SW | 6.8 | 153 | 1.2 | 0.31 | 8.8 | 142 | 1.7 | 0.37 |
| | Avg. | 3.0 | | | | 4.0 | | | |
| E025DL | NE | 18.5 | 67 | 4.5 | 1.29 | 15.9 | 150 | 3.7 | 0.77 |
| | NW | 6.1 | 77 | 4.7 | 0.85 | 1.6 | 108 | 3.7 | 0.62 |
| | SE | 6.5 | 271 | 3.3 | 0.73 | 9.5 | 53 | 4.2 | 1.05 |
| | SW | 5.9 | 92 | 3.7 | 0.70 | 9.2 | 84 | 4.0 | 1.04 |
| | Avg. | 9.3 | | | | 9.1 | | | |
| E050DL | NE | 17.1 | 84 | 9.2 | 2.33 | 10.1 | 99 | 7.1 | 1.39 |
| | NW | 7.4 | 69 | 9.0 | 1.68 | 2.2 | 115 | 7.1 | 1.14 |
| | SE | 7.1 | 112 | 5.8 | 1.31 | 9.4 | 87 | 9.5 | 1.98 |
| | SW | 4.6 | 109 | 6.4 | 1.39 | 10.7 | 66 | 8.7 | 2.02 |
| | Avg. | 9.1 | | | | 8.1 | | | |
| E075DL | NE | 13.8 | 87 | 14.3 | 3.33 | 10.0 | 109 | 11.1 | 1.96 |
| | NW | 8.6 | 79 | 15.0 | 2.59 | -1.8 | 112 | 10.6 | 1.57 |
| | SE | 5.1 | 112 | 10.5 | 1.74 | 8.9 | 74 | 15.1 | 2.67 |
| | SW | 3.4 | 104 | 10.4 | 1.96 | 6.9 | 101 | 14.2 | 2.91 |
| | Avg. | 7.7 | | | | 6.0 | | | |
| E100DL | NE | 11.1 | 91 | 19.3 | 4.14 | 7.4 | 119 | 15.3 | 2.41 |
| | NW | 8.8 | 82 | 19.7 | 3.50 | -2.4 | 120 | 15.1 | 1.99 |
| | SE | 2.9 | 115 | 14.7 | 2.14 | 5.7 | 87 | 19.9 | 3.31 |
| | SW | 2.3 | 117 | 14.6 | 2.44 | 7.6 | 94 | 19.1 | 3.78 |
| | Avg. | 6.3 | | | | 4.6 | | | |
| E125DL | NE | 11.0 | 102 | 23.7 | 4.98 | 6.4 | 120 | 19.9 | 2.88 |
| | NW | 8.4 | 90 | 25.1 | 4.42 | -2.9 | 122 | 19.5 | 2.41 |
| | SE | 2.7 | 120 | 18.8 | 2.58 | 4.3 | 100 | 24.6 | 3.91 |
| | SW | 3.3 | 122 | 18.4 | 2.94 | 5.5 | 100 | 24.0 | 4.50 |
| | Avg. | 6.4 | | | | 3.3 | | | |
| E150DL | NE | 13.4 | 99 | 29.4 | 6.46 | 7.2 | 119 | 23.3 | 3.90 |
| | NW | 10.9 | 99 | 28.8 | 6.14 | -0.8 | 119 | 23.1 | 3.19 |
| | SE | 5.7 | 128 | 21.4 | 3.75 | 6.1 | 99 | 29.7 | 5.22 |
| | SW | 7.9 | 119 | 21.2 | 4.30 | 7.0 | 106 | 28.9 | 5.74 |
| | Avg. | 9.5 | | | | 4.9 | | | |
| E200DL | NE | 7.2 | 125 | 43.3 | 8.91 | 5.5 | 153 | 45.5 | 5.19 |
| | NW | 5.8 | 143 | 44.4 | 9.02 | -1.3 | 152 | 41.6 | 5.28 |
| | SE | 6.0 | 150 | 39.9 | 5.91 | 3.9 | 127 | 48.1 | 7.40 |
| | SW | 6.3 | 159 | 38.0 | 6.46 | 3.5 | 131 | 47.0 | 7.96 |
| | Avg. | 6.3 | | | | 2.9 | | | |

Table 5.5.a Individual Damper Stiffnesses, 0.25 Dmax to 1.0 Dmax

| Second Story Damper Stiffnesses | | | | | | | | | |
|---------------------------------|-------|------------------------|---------------------------|--------------------------|----------------------------|------------------------|---------------------------|--------------------------|----------------------------|
| Test | Strut | Brace in Tension | | | | Brace in Compression | | | |
| | | Stiffness Kips/Inch | No. of Data Points (+) | Max. Shear Strain (%) | Max. Strut Force (Kips) | Stiffness Kips/Inch | No. of Data Points (-) | Max. Shear Strain (%) | Max. Strut Force (Kips) |
| E010DL | NE | 9.8 | 102 | 2.5 | 0.38 | 7.9 | 95 | 2.0 | 0.34 |
| | NW | 3.3 | 996 | 1.9 | 0.33 | 6.5 | 175 | 1.5 | 0.34 |
| | SE | -0.7 | 175 | 1.5 | 0.35 | -2.0 | 191 | 2.3 | 0.35 |
| | SW | 4.6 | 152 | 1.4 | 0.36 | 8.9 | 113 | 1.9 | 0.43 |
| | Avg. | 4.3 | | | | 5.3 | | | |
| E025DL | NE | 11.3 | 68 | 5.5 | 1.04 | 8.6 | 107 | 4.0 | 0.68 |
| | NW | 6.2 | 522 | 6.0 | 1.02 | 1.9 | 51 | 2.8 | 0.72 |
| | SE | 0.0 | 442 | 4.1 | 0.70 | 1.3 | 34 | 4.7 | 0.86 |
| | SW | 10.3 | 112 | 3.1 | 0.94 | 6.2 | 89 | 4.9 | 0.93 |
| | Avg. | 7.0 | | | | 4.5 | | | |
| E050DL | NE | 10.0 | 83 | 10.9 | 1.98 | 7.6 | 104 | 7.7 | 1.27 |
| | NW | 14.7 | 104 | 9.7 | 2.05 | 7.1 | 114 | 6.1 | 1.36 |
| | SE | 3.4 | 128 | 6.7 | 1.41 | 0.5 | 78 | 9.7 | 1.86 |
| | SW | 7.6 | 120 | 6.5 | 1.55 | 7.4 | 72 | 9.5 | 2.10 |
| | Avg. | 8.9 | | | | 5.7 | | | |
| E075DL | NE | 8.3 | 89 | 18.0 | 2.99 | 4.5 | 108 | 12.7 | 1.79 |
| | NW | 11.3 | 100 | 16.0 | 3.17 | 3.2 | 109 | 11.1 | 1.81 |
| | SE | 1.8 | 128 | 11.8 | 2.10 | 2.4 | 71 | 16.7 | 2.90 |
| | SW | 7.5 | 116 | 11.0 | 2.31 | 6.9 | 81 | 15.7 | 3.08 |
| | Avg. | 7.2 | | | | 4.3 | | | |
| E100DL | NE | 8.1 | 79 | 25.0 | 3.79 | 4.1 | 120 | 18.6 | 2.29 |
| | NW | 9.9 | 102 | 22.6 | 4.20 | 1.6 | 115 | 16.1 | 2.22 |
| | SE | 1.6 | 124 | 15.9 | 2.80 | 2.1 | 86 | 20.0 | 3.56 |
| | SW | 6.9 | 120 | 15.6 | 2.95 | 6.9 | 92 | 22.3 | 3.96 |
| | Avg. | 6.6 | | | | 3.7 | | | |
| E125DL | NE | 6.6 | 97 | 33.0 | 4.55 | 3.7 | 14 | 24.8 | 2.77 |
| | NW | 8.2 | 104 | 29.0 | 5.21 | 0.0 | 114 | 22.5 | 2.65 |
| | SE | 1.4 | 132 | 20.6 | 3.57 | 2.4 | 93 | 30.2 | 4.29 |
| | SW | 5.5 | 127 | 21.3 | 3.73 | 5.3 | 98 | 28.7 | 4.77 |
| | Avg. | 5.4 | | | | 2.9 | | | |
| E150DL | NE | 8.5 | 89 | 38.0 | 5.89 | 6.2 | 111 | 28.7 | 3.80 |
| | NW | 11.5 | 90 | 31.9 | 6.77 | 2.6 | 126 | 25.7 | 3.64 |
| | SE | 2.8 | 135 | 23.2 | 4.70 | 2.6 | 93 | 33.5 | 5.70 |
| | SW | 9.3 | 120 | 23.1 | 5.11 | 6.8 | 107 | 33.0 | 6.25 |
| | Avg. | 8.0 | | | | 4.6 | | | |
| E200DL | NE | 6.1 | 136 | 62.0 | 9.59 | 6.6 | 127 | 65.3 | 6.18 |
| | NW | 6.7 | 131 | 58.1 | 9.91 | 1.1 | 152 | 48.3 | 5.57 |
| | SE | 2.6 | 157 | 51.2 | 6.72 | 1.7 | 122 | 53.1 | 7.63 |
| | SW | 7.4 | 164 | 46.0 | 7.87 | 2.9 | 155 | 55.9 | 8.66 |
| | Avg. | 5.7 | | | | 3.1 | | | |

Table 5.5.b Individual Damper Stiffnesses, 0.25 Dmax to 1.0 Dmax

| Third Story Damper Stiffnesses | | | | | | | | | |
|--------------------------------|-------|------------------------|---------------------------|--------------------------|----------------------------|------------------------|---------------------------|--------------------------|----------------------------|
| Test | Strut | Brace in Tension | | | | Brace in Compression | | | |
| | | Stiffness Kips/Inch | No. of Data Points (+) | Max. Shear Strain (%) | Max. Strut Force (Kips) | Stiffness Kips/Inch | No. of Data Points (-) | Max. Shear Strain (%) | Max. Strut Force (Kips) |
| E010DL | NE | 0.5 | 94 | 1.3 | 0.14 | -2.6 | 134 | 1.0 | 0.24 |
| | NW | -0.1 | 107 | 1.2 | 0.17 | -2.9 | 128 | 1.0 | 0.20 |
| | SE | -2.4 | 110 | 0.7 | 0.27 | -3.4 | 91 | 1.4 | 0.18 |
| | SW | -0.1 | 124 | 1.4 | 0.16 | 3.9 | 105 | 1.3 | 0.17 |
| | Avg. | -0.5 | | | | -1.3 | | | |
| E025DL | NE | -0.6 | 76 | 3.4 | 0.34 | -0.8 | 124 | 2.0 | 0.41 |
| | NW | -2.0 | 71 | 3.0 | 0.45 | -2.2 | 126 | 2.0 | 0.49 |
| | SE | 0.1 | 129 | 2.5 | 0.45 | -2.8 | 40 | 3.4 | 0.40 |
| | SW | 6.0 | 105 | 2.6 | 0.39 | 7.5 | 74 | 3.2 | 0.44 |
| | Avg. | 0.9 | | | | 0.4 | | | |
| E050DL | NE | -0.3 | 75 | 6.7 | 0.59 | -0.8 | 104 | 3.9 | 0.77 |
| | NW | 0.7 | 85 | -0.9 | 1.02 | -0.9 | 107 | 5.9 | 0.87 |
| | SE | -0.1 | 108 | 4.4 | 0.84 | -0.8 | 71 | 6.6 | 0.77 |
| | SW | 7.5 | 118 | 3.9 | 0.73 | 8.8 | 62 | 5.7 | 0.93 |
| | Avg. | 2.0 | | | | 1.6 | | | |
| E075DL | NE | -1.1 | 65 | 11.2 | 0.86 | -1.0 | 107 | 7.0 | 1.06 |
| | NW | -0.7 | 69 | 10.0 | 1.47 | -2.1 | 110 | 6.7 | 1.18 |
| | SE | -0.7 | 108 | 7.7 | 1.10 | -1.9 | 68 | 11.2 | 1.10 |
| | SW | 6.6 | 111 | 7.2 | 1.02 | 5.1 | 67 | 9.6 | 1.32 |
| | Avg. | 1.0 | | | | 0.0 | | | |
| E100DL | NE | -0.8 | 66 | 16.0 | 1.15 | -2.8 | 109 | 10.4 | 1.31 |
| | NW | 0.2 | 66 | 14.4 | 2.03 | -5.1 | 112 | 10.0 | 1.33 |
| | SE | -2.8 | 115 | 11.2 | 1.38 | -2.6 | 76 | 15.4 | 1.42 |
| | SW | 3.1 | 111 | 9.6 | 1.30 | 4.5 | 74 | 14.1 | 1.71 |
| | Avg. | -0.1 | | | | -1.5 | | | |
| E125DL | NE | -0.9 | 74 | 21.1 | 1.42 | -2.7 | 107 | 14.0 | 1.44 |
| | NW | 1.8 | 59 | 19.3 | 2.54 | -4.1 | 121 | 14.2 | 1.57 |
| | SE | -1.6 | 111 | 14.9 | 1.59 | -3.2 | 79 | 20.6 | 1.72 |
| | SW | 4.5 | 113 | 13.2 | 1.57 | 3.7 | 79 | 18.3 | 2.08 |
| | Avg. | 1.0 | | | | -1.6 | | | |
| E150DL | NE | 2.4 | 78 | 22.8 | 2.17 | -0.1 | 103 | 14.9 | 1.15 |
| | NW | 3.2 | 70 | 21.0 | 3.65 | -0.6 | 109 | 14.5 | 2.20 |
| | SE | 0.2 | 110 | 15.5 | 2.14 | -1.0 | 78 | 22.2 | 2.43 |
| | SW | 7.7 | 111 | 14.0 | 2.17 | 6.4 | 76 | 19.8 | 2.85 |
| | Avg. | 3.4 | | | | 1.2 | | | |
| E200DL | NE | 6.2 | 92 | 42.4 | 4.28 | -1.2 | 120 | 32.0 | 2.58 |
| | NW | 5.2 | 89 | 40.0 | 6.28 | -2.5 | 133 | 28.0 | 3.44 |
| | SE | 0.2 | 125 | 33.5 | 3.50 | -0.9 | 94 | 40.1 | 3.87 |
| | SW | 5.1 | 139 | 26.7 | 3.38 | 3.9 | 98 | 46.0 | 4.36 |
| | Avg. | 4.2 | | | | -0.2 | | | |

Table 5.5.c Individual Damper Stiffnesses, 0.25 Dmax to 1.0 Dmax

| First Story Damper Stiffnesses | | | | | | | | | |
|--------------------------------|-------|------------------------|---------------------------|--------------------------|----------------------------|------------------------|---------------------------|--------------------------|----------------------------|
| Test | Strut | Brace in Tension | | | | Brace in Compression | | | |
| | | Stiffness Kips/Inch | No. of Data Points (+) | Max. Shear Strain (%) | Max. Strut Force (Kips) | Stiffness Kips/Inch | No. of Data Points (-) | Max. Shear Strain (%) | Max. Strut Force (Kips) |
| E010DL | NE | 13.4 | 27 | 2.2 | 0.46 | 3.1 | 21 | 1.9 | 0.32 |
| | NW | 5.4 | 17 | 1.7 | 0.29 | 7.9 | 88 | 1.5 | 0.30 |
| | SE | 9.4 | 19 | 1.1 | 0.32 | -4.9 | 32 | 2.5 | 0.36 |
| | SW | -1.2 | 46 | 1.2 | 0.31 | 15.0 | 14 | 1.7 | 0.37 |
| | Avg. | 6.8 | | | | 5.3 | | | |
| E025DL | NE | 25.3 | 8 | 4.5 | 1.29 | 12.6 | 33 | 3.7 | 0.77 |
| | NW | 22.2 | 8 | 4.7 | 0.85 | 4.1 | 30 | 3.7 | 0.62 |
| | SE | 14.3 | 50 | 3.3 | 0.73 | -5.8 | 8 | 4.2 | 1.05 |
| | SW | 19.6 | 20 | 3.7 | 0.70 | 4.0 | 12 | 4.0 | 1.04 |
| | Avg. | 20.4 | | | | 3.7 | | | |
| E050DL | NE | 26.0 | 13 | 9.2 | 2.33 | 1.3 | 25 | 7.1 | 1.39 |
| | NW | 4.0 | 10 | 9.0 | 1.68 | 1.6 | 35 | 7.1 | 1.14 |
| | SE | 5.2 | 30 | 5.8 | 1.31 | 13.6 | 13 | 9.5 | 1.98 |
| | SW | 5.7 | 35 | 6.4 | 1.39 | 10.0 | 11 | 8.7 | 2.02 |
| | Avg. | 10.2 | | | | 6.6 | | | |
| E075DL | NE | 14.3 | 15 | 14.3 | 3.33 | 12.9 | 42 | 11.1 | 1.96 |
| | NW | 18.5 | 12 | 15.0 | 2.59 | 0.9 | 42 | 10.6 | 1.57 |
| | SE | 5.2 | 44 | 10.5 | 1.74 | 11.3 | 12 | 15.1 | 2.67 |
| | SW | 6.7 | 39 | 10.4 | 1.96 | 11.7 | 18 | 14.2 | 2.91 |
| | Avg. | 11.2 | | | | 9.2 | | | |
| E100DL | NE | 16.2 | 15 | 19.3 | 4.14 | 5.0 | 49 | 15.3 | 2.41 |
| | NW | 13.8 | 15 | 19.7 | 3.50 | -6.7 | 47 | 15.1 | 1.99 |
| | SE | 2.9 | 44 | 14.7 | 2.14 | 6.7 | 13 | 19.9 | 3.31 |
| | SW | 2.4 | 46 | 14.6 | 2.44 | 13.6 | 16 | 19.1 | 3.78 |
| | Avg. | 8.8 | | | | 4.7 | | | |
| E125DL | NE | 16.5 | 25 | 23.7 | 4.98 | 13.0 | 49 | 19.9 | 2.88 |
| | NW | 13.6 | 19 | 25.1 | 4.42 | -2.3 | 51 | 19.5 | 2.41 |
| | SE | 6.9 | 47 | 18.8 | 2.58 | 6.0 | 23 | 24.6 | 3.91 |
| | SW | 6.6 | 50 | 18.4 | 2.94 | 9.9 | 23 | 24.0 | 4.50 |
| | Avg. | 10.9 | | | | 6.7 | | | |
| E150DL | NE | 20.4 | 18 | 29.4 | 6.46 | 6.6 | 47 | 23.3 | 3.90 |
| | NW | 18.5 | 19 | 28.8 | 6.14 | -1.1 | 47 | 23.1 | 3.19 |
| | SE | 6.9 | 49 | 21.4 | 3.75 | 10.2 | 17 | 29.7 | 5.22 |
| | SW | 11.5 | 46 | 21.2 | 4.30 | 13.6 | 19 | 28.9 | 5.74 |
| | Avg. | 14.3 | | | | 7.3 | | | |
| E200DL | NE | 13.0 | 47 | 43.3 | 8.91 | 6.4 | 59 | 45.5 | 5.19 |
| | NW | 9.7 | 53 | 44.4 | 9.02 | -1.8 | 63 | 41.6 | 5.28 |
| | SE | 7.1 | 58 | 39.9 | 5.91 | 6.2 | 45 | 48.1 | 7.40 |
| | SW | 8.4 | 67 | 38.0 | 6.46 | 7.3 | 49 | 47.0 | 7.96 |
| | Avg. | 9.6 | | | | 4.5 | | | |

Table 5.6.a Individual Damper Stiffnesses, 0.50 Dmax to 1.0 Dmax

| Second Story Damper Stiffnesses | | | | | | | | | |
|---------------------------------|-------|------------------------|---------------------------|--------------------------|----------------------------|------------------------|---------------------------|--------------------------|----------------------------|
| Test | Strut | Brace in Tension | | | | Brace in Compression | | | |
| | | Stiffness Kips/Inch | No. of Data Points (+) | Max. Shear Strain (%) | Max. Strut Force (Kips) | Stiffness Kips/Inch | No. of Data Points (-) | Max. Shear Strain (%) | Max. Strut Force (Kips) |
| E010DL | NE | 2.6 | 13 | 2.5 | 0.38 | 11.3 | 19 | 2.0 | 0.34 |
| | NW | 2.6 | 113 | 1.9 | 0.33 | 16.8 | 35 | 1.5 | 0.34 |
| | SE | -0.8 | 50 | 1.5 | 0.35 | -3.3 | 48 | 2.3 | 0.35 |
| | SW | -10.6 | 46 | 1.4 | 0.36 | 5.9 | 30 | 1.9 | 0.43 |
| | Avg. | -1.6 | | | | 7.7 | | | |
| E025DL | NE | 19.5 | 8 | 5.5 | 1.04 | -2.7 | 24 | 4.0 | 0.68 |
| | NW | 16.3 | 21 | 6.0 | 1.02 | 1.0 | 23 | 2.8 | 0.72 |
| | SE | 3.4 | 65 | 4.1 | 0.70 | -3.5 | 7 | 4.7 | 0.86 |
| | SW | 12.9 | 34 | 3.1 | 0.94 | 18.2 | 14 | 4.9 | 0.93 |
| | Avg. | 13.0 | | | | 3.3 | | | |
| E050DL | NE | 15.8 | 13 | 10.9 | 1.98 | -0.2 | 33 | 7.7 | 1.27 |
| | NW | 12.0 | 15 | 9.7 | 2.05 | 9.9 | 41 | 6.1 | 1.36 |
| | SE | 9.2 | 43 | 6.7 | 1.41 | 0.1 | 15 | 9.7 | 1.86 |
| | SW | 15.3 | 42 | 6.5 | 1.55 | 14.7 | 15 | 9.5 | 2.10 |
| | Avg. | 13.1 | | | | 6.1 | | | |
| E075DL | NE | 8.5 | 12 | 18.0 | 2.99 | 5.4 | 42 | 12.7 | 1.79 |
| | NW | 20.0 | 17 | 16.0 | 3.17 | 6.4 | 42 | 11.1 | 1.81 |
| | SE | 13.1 | 45 | 11.8 | 2.10 | -6.2 | 10 | 16.7 | 2.90 |
| | SW | 8.1 | 42 | 11.0 | 2.31 | 11.8 | 15 | 15.7 | 3.08 |
| | Avg. | 12.4 | | | | 4.4 | | | |
| E100DL | NE | 4.6 | 13 | 25.0 | 3.79 | 3.3 | 48 | 18.6 | 2.29 |
| | NW | 15.6 | 18 | 22.6 | 4.20 | -1.3 | 46 | 16.1 | 2.22 |
| | SE | 3.2 | 47 | 15.9 | 2.80 | 3.0 | 13 | 20.0 | 3.56 |
| | SW | 10.0 | 47 | 15.6 | 2.95 | 5.1 | 16 | 22.3 | 3.96 |
| | Avg. | 8.4 | | | | 2.5 | | | |
| E125DL | NE | 10.4 | 15 | 33.0 | 4.55 | 5.8 | 45 | 24.8 | 2.77 |
| | NW | 18.6 | 19 | 29.0 | 5.21 | 2.2 | 47 | 22.5 | 2.65 |
| | SE | 1.1 | 50 | 20.6 | 3.57 | 3.8 | 16 | 30.2 | 4.29 |
| | SW | 10.4 | 49 | 21.3 | 3.73 | 9.8 | 19 | 28.7 | 4.77 |
| | Avg. | 10.1 | | | | 5.4 | | | |
| E150DL | NE | 14.9 | 14 | 38.0 | 5.89 | 8.4 | 47 | 28.7 | 3.80 |
| | NW | 15.6 | 17 | 31.9 | 6.77 | 2.4 | 49 | 25.7 | 3.64 |
| | SE | 0.6 | 50 | 23.2 | 4.70 | 4.2 | 17 | 33.5 | 5.70 |
| | SW | 4.0 | 46 | 23.1 | 5.11 | 12.4 | 19 | 33.0 | 6.25 |
| | Avg. | 8.8 | | | | 6.9 | | | |
| E200DL | NE | 6.7 | 56 | 62.0 | 9.59 | 13.6 | 42 | 65.3 | 6.18 |
| | NW | 16.7 | 38 | 58.1 | 9.91 | 1.7 | 67 | 48.3 | 5.57 |
| | SE | 0.6 | 55 | 51.2 | 6.72 | 2.4 | 44 | 53.1 | 7.63 |
| | SW | 4.7 | 77 | 46.0 | 7.87 | 6.6 | 49 | 55.9 | 8.66 |
| | Avg. | 7.2 | | | | 6.1 | | | |

Table 5.6.b Individual Damper Stiffnesses, 0.50 Dmax to 1.0 Dmax

| Third Story Damper Stiffnesses | | | | | | | | | |
|--------------------------------|-------|------------------------|---------------------------|--------------------------|----------------------------|------------------------|---------------------------|--------------------------|----------------------------|
| Test | Strut | Brace in Tension | | | | Brace in Compression | | | |
| | | Stiffness Kips/Inch | No. of Data Points (+) | Max. Shear Strain (%) | Max. Strut Force (Kips) | Stiffness Kips/Inch | No. of Data Points (-) | Max. Shear Strain (%) | Max. Strut Force (Kips) |
| E010DL | NE | -3.0 | 25 | 1.3 | 0.14 | -0.1 | 34 | 1.0 | 0.24 |
| | NW | -1.0 | 33 | 1.2 | 0.17 | 3.8 | 128 | 1.0 | 0.20 |
| | SE | -3.1 | 46 | 0.7 | 0.27 | -2.6 | 14 | 1.4 | 0.18 |
| | SW | -0.7 | 38 | 1.4 | 0.16 | 9.4 | 27 | 1.3 | 0.17 |
| | Avg. | -2.0 | | | | 2.6 | | | |
| E025DL | NE | -3.2 | 10 | 3.4 | 0.34 | 1.6 | 34 | 2.0 | 0.41 |
| | NW | -4.3 | 9 | 3.0 | 0.45 | -1.9 | 126 | 2.0 | 0.49 |
| | SE | -3.6 | 35 | 2.5 | 0.45 | 2.2 | 7 | 3.4 | 0.40 |
| | SW | 11.7 | 17 | 2.6 | 0.39 | -4.7 | 8 | 3.2 | 0.44 |
| | Avg. | 0.1 | | | | -0.7 | | | |
| E050DL | NE | 1.4 | 11 | 6.7 | 0.59 | -3.1 | 31 | 3.9 | 0.77 |
| | NW | 1.2 | 11 | -0.9 | 1.02 | -2.0 | 35 | 5.9 | 0.87 |
| | SE | -4.5 | 33 | 4.4 | 0.84 | -10.3 | 8 | 6.6 | 0.77 |
| | SW | 7.4 | 38 | 3.9 | 0.73 | 9.2 | 11 | 5.7 | 0.93 |
| | Avg. | 1.4 | | | | -1.6 | | | |
| E075DL | NE | -2.4 | 8 | 11.2 | 0.86 | -1.7 | 43 | 7.0 | 1.06 |
| | NW | 0.4 | 9 | 10.0 | 1.47 | -3.3 | 42 | 6.7 | 1.18 |
| | SE | 0.9 | 41 | 7.7 | 1.10 | -0.7 | 8 | 11.2 | 1.10 |
| | SW | 2.9 | 36 | 7.2 | 1.02 | 6.8 | 10 | 9.6 | 1.32 |
| | Avg. | 0.5 | | | | 0.3 | | | |
| E100DL | NE | -0.3 | 11 | 16.0 | 1.15 | -2.0 | 47 | 10.4 | 1.31 |
| | NW | -1.5 | 11 | 14.4 | 2.03 | -6.6 | 45 | 10.0 | 1.33 |
| | SE | -2.9 | 49 | 11.2 | 1.38 | -2.2 | 12 | 15.4 | 1.42 |
| | SW | 3.7 | 50 | 9.6 | 1.30 | 4.1 | 12 | 14.1 | 1.71 |
| | Avg. | -0.3 | | | | -1.7 | | | |
| E125DL | NE | 2.5 | 12 | 21.1 | 1.42 | -4.7 | 47 | 14.0 | 1.44 |
| | NW | 1.8 | 10 | 19.3 | 2.54 | -4.3 | 49 | 14.2 | 1.57 |
| | SE | -4.4 | 47 | 14.9 | 1.59 | -7.0 | 12 | 20.6 | 1.72 |
| | SW | 1.9 | 48 | 13.2 | 1.57 | 4.4 | 14 | 18.3 | 2.08 |
| | Avg. | 0.4 | | | | -2.9 | | | |
| E150DL | NE | 0.0 | 11 | 22.8 | 2.17 | -1.9 | 44 | 14.9 | 1.15 |
| | NW | 2.1 | 12 | 21.0 | 3.65 | -4.1 | 43 | 14.5 | 2.20 |
| | SE | -1.4 | 45 | 15.5 | 2.14 | -4.1 | 12 | 22.2 | 2.43 |
| | SW | 6.4 | 43 | 14.0 | 2.17 | 5.4 | 12 | 19.8 | 2.85 |
| | Avg. | 1.8 | | | | -1.2 | | | |
| E200DL | NE | 11.2 | 25 | 42.4 | 4.28 | -3.0 | 47 | 32.0 | 2.58 |
| | NW | 8.0 | 26 | 40.0 | 6.28 | -5.0 | 62 | 28.0 | 3.44 |
| | SE | -1.1 | 47 | 33.5 | 3.50 | 3.0 | 24 | 40.1 | 3.87 |
| | SW | 6.6 | 61 | 26.7 | 3.38 | 8.5 | 26 | 46.0 | 4.36 |
| | Avg. | 6.2 | | | | 0.9 | | | |

Table 5.6.c Individual Damper Stiffnesses, 0.50 Dmax to 1.0 Dmax

| Test Series | Story | Curve Type | Equation ¹ | Correlation Coefficient |
|---|-------|------------------------|-----------------------------------|-------------------------|
| E010DL-E200DL | 1 | Linear | $y = 1.86 + 81.24x$ | 0.98 |
| E010DL-E200DL | 1 | Quadratic | $y = -0.22 + 121.66x - 76.85x^2$ | 0.99 |
| T021DL-T420DL | 1 | Linear | $y = 1.30 + 81.70x$ | 0.97 |
| T021DL-T420DL | 1 | Quadratic | $y = -0.04 + 122.30x - 109.09x^2$ | 0.99 |
| E010DL-E200DL | 2 | Linear | $y = 2.33 + 48.24x$ | 0.97 |
| E010DL-E200DL | 2 | Quadratic | $y = 0.12 + 77.31x - 38.81x^2$ | 0.99 |
| T021DL-T420DL | 2 | Linear | $y = 1.16 + 47.70x$ | 0.95 |
| T021DL-T420DL | 2 | Quadratic | $y = -0.10 + 79.92x - 63.35x^2$ | 0.97 |
| E010DL-E200DL | 3 | Linear | $y = 0.49 + 49.75x$ | 0.99 |
| E010DL-E200DL | 3 | Quadratic | $y = 0.08 + 63.99x - 35.36x^2$ | 0.99 |
| T021DL-T420DL | 3 | Linear | $y = 0.44 + 45.22x$ | 0.98 |
| T021DL-T420DL | 3 | Quadratic | $y = -0.07 + 58.22x - 41.73x^2$ | 0.98 |
| E010N-E200N | 1 | Linear | $y = -0.34 + 27.83x$ | 1.00 |
| E010N-E200N | 1 | Quadratic | $y = -0.34 + 27.91x - 0.12x^2$ | 1.00 |
| E010N-E200N | 2 | Linear ² | $y = 0.05 + 12.62x$ | 0.99 |
| E010N-E200N | 2 | Quadratic ² | $y = -0.16 + 14.63x - 1.94x^2$ | 0.99 |
| E010N-E200N | 3 | Linear ³ | $y = 0.15 + 11.21x$ | 0.96 |
| E010N-E200N | 3 | Quadratic ³ | $y = -0.24 + 15.54x - 6.05x^2$ | 0.96 |
| ¹ x = Interstory Displacement (inches), y = Story Shear (kips) ² Curve fit performed through 1.18" interstory displacement. ³ Curve fit performed through 0.88" interstory displacement. | | | | |

Table 5.7 Curve Fits for Story Shear Vs. Interstory Displacement "Backbone" Relationships

| Test Series | Story | Curve Type | Equation ^{1,4} | Correlation Coefficient |
|---------------|-------|------------------------|---------------------------------|-------------------------|
| E010DL-E200DL | 1 | Linear | $y = 1.18 + 40.23x$ | 0.94 |
| E010DL-E200DL | 1 | Quadratic | $y = 0.01 + 63.16x - 43.02x^2$ | 0.96 |
| T021DL-T420DL | 1 | Linear | $y = 0.92 + 47.17x$ | 0.97 |
| T021DL-T420DL | 1 | Quadratic | $y = -0.24 + 82.39x - 94.62x^2$ | 1.00 |
| E010DL-E200DL | 2 | Linear | $y = 1.34 + 19.36x$ | 0.90 |
| E010DL-E200DL | 2 | Quadratic | $y = 0.20 + 34.25x - 19.87x^2$ | 0.93 |
| T021DL-T420DL | 2 | Linear | $y = 0.88 + 20.25x$ | 0.89 |
| T021DL-T420DL | 2 | Quadratic | $y = -0.07 + 44.34x - 47.37x^2$ | 0.95 |
| E010DL-E200DL | 3 | Linear | $y = 0.60 + 28.06x$ | 0.93 |
| E010DL-E200DL | 3 | Quadratic | $y = 0.00 + 49.30x - 52.73x^2$ | 0.96 |
| T021DL-T420DL | 3 | Linear | $y = 0.51 + 30.77x$ | 0.94 |
| T021DL-T420DL | 3 | Quadratic | $y = -0.17 + 54.96x - 77.62x^2$ | 0.97 |
| E010N-E200N | 1 | Linear | $y = -0.34 + 27.83x$ | 1.00 |
| E010N-E200N | 1 | Quadratic | $y = -0.34 + 27.91x - 0.12x^2$ | 1.00 |
| E010N-E200N | 2 | Linear ² | $y = 0.05 + 12.62x$ | 0.99 |
| E010N-E200N | 2 | Quadratic ² | $y = -0.16 + 14.63x - 1.94x^2$ | 0.99 |
| E010N-E200N | 3 | Linear ³ | $y = 0.15 + 11.21x$ | 0.96 |
| E010N-E200N | 3 | Quadratic ³ | $y = -0.24 + 15.54x - 6.05x^2$ | 0.96 |

¹ x = Interstory Displacement (inches), y = Story Shear (kips)
² Curve fit performed through 1.18" interstory displacement.
³ Curve fit performed through 0.88" interstory displacement.
⁴ Column shear for E010DL-E200DL and T021DL-T420DL derived as difference between story shear and sum of horizontal component of all damper forces in story level.

Table 5.8 Curve Fits for Column Shear Vs. Interstory Displacement "Backbone" Relationships

| Test | Computed Story Stiffness at Maximum Displacement (Kips/Inch) | | | | | |
|--------|--|---------|---------|----------------------|---------|---------|
| | Linear Regression | | | Quadratic Regression | | |
| | Story 1 | Story 2 | Story 3 | Story 1 | Story 2 | Story 3 |
| E010DL | 81.2 | 48.2 | 49.8 | 117.9 | 74.8 | 62.7 |
| E025DL | 81.2 | 48.2 | 49.8 | 112.7 | 71.6 | 60.8 |
| E050DL | 81.2 | 48.2 | 49.8 | 102.6 | 67.0 | 57.4 |
| E075DL | 81.2 | 48.2 | 49.8 | 92.1 | 60.1 | 52.9 |
| E100DL | 81.2 | 48.2 | 49.8 | 81.6 | 53.6 | 48.8 |
| E125DL | 81.2 | 48.2 | 49.8 | 72.2 | 45.5 | 44.5 |
| E150DL | 81.2 | 48.2 | 49.8 | 60.0 | 41.9 | 43.0 |
| E200DL | 81.2 | 48.2 | 49.8 | 25.2 | 9.8 | 27.6 |
| E250DL | 81.2 | 48.2 | 49.8 | 42.0 | 22.6 | 32.3 |
| T021DL | 81.7 | 47.7 | 45.2 | 118.0 | 77.4 | 57.4 |
| T052DL | 81.7 | 47.7 | 45.2 | 113.6 | 73.6 | 55.7 |
| T105DL | 81.7 | 47.7 | 45.2 | 102.7 | 67.3 | 52.4 |
| T157DL | 81.7 | 47.7 | 45.2 | 89.6 | 57.1 | 48.2 |
| T210DL | 81.7 | 47.7 | 45.2 | 76.5 | 48.2 | 43.2 |
| T262DL | 81.7 | 47.7 | 45.2 | 61.2 | 38.1 | 39.0 |
| T315DL | 81.7 | 47.7 | 45.2 | 50.3 | 31.8 | 37.4 |
| T420DL | 81.7 | 47.7 | 45.2 | 21.9 | 2.6 | 26.5 |
| E025N | 27.8 | 12.6 | 11.2 | 27.9 | 14.0 | 14.0 |
| E050N | 27.8 | 12.6 | 11.2 | 27.9 | 13.3 | 12.5 |
| E075N | 27.8 | 12.6 | 11.2 | 27.8 | 12.6 | 10.9 |
| E100N | 27.8 | 12.6 | 11.2 | 27.8 | 11.9 | 9.6 |
| E125N | 27.8 | 12.6 | 11.2 | 27.8 | 11.1 | 7.9 |
| E150N | 27.8 | 12.6 | 11.2 | 27.7 | 10.1 | 6.5 |
| E200N | 27.8 | 12.6 | 11.2 | 27.7 | 6.1 | -1.3 |

Table 5.9 Interstory Stiffnesses Based on "Backbone" Curves

| Test | Average Story Stiffness (Kips/Inch) | | | | | |
|--------|-------------------------------------|---------|---------|-------------------------------------|---------|---------|
| | First 20 Seconds' Elapsed Time | | | 3.5 Seconds of Maximum Displacement | | |
| | Story 1 | Story 2 | Story 3 | Story 1 | Story 2 | Story 3 |
| E010DL | 87.3 | 26.6 | 9.2 | 104.5 | 44.7 | 23.5 |
| E025DL | 93.3 | 41.7 | 34.2 | 99.3 | 51.5 | 44.9 |
| E050DL | 90.4 | 51.9 | 41.1 | 93.5 | 57.9 | 48.2 |
| E075DL | 81.8 | 48.1 | 40.0 | 81.3 | 50.2 | 43.8 |
| E100DL | 76.8 | 46.4 | 39.4 | 76.3 | 47.6 | 41.7 |
| E125DL | 70.1 | 41.1 | 36.1 | 69.8 | 41.9 | 38.1 |
| E150DL | 72.5 | 44.9 | 40.9 | 72.3 | 45.8 | 42.9 |
| E200DL | 51.9 | 30.7 | 30.6 | 53.1 | 31.6 | 31.5 |
| E250DL | 51.6 | 30.8 | 30.1 | 52.3 | 31.1 | 30.5 |
| T021DL | 84.4 | 18.4 | 13.6 | 98.4 | 35.9 | 26.3 |
| T052DL | 88.4 | 40.8 | 35.0 | 91.5 | 48.7 | 46.1 |
| T105DL | 83.9 | 45.9 | 44.9 | 85.1 | 50.7 | 47.9 |
| T157DL | 74.4 | 44.2 | 40.7 | 75.4 | 46.8 | 42.6 |
| T210DL | 67.8 | 40.9 | 37.9 | 68.6 | 42.5 | 39.0 |
| T262DL | 63.5 | 38.1 | 35.8 | 64.8 | 39.5 | 36.6 |
| T315DL | 61.9 | 38.8 | 37.4 | 63.8 | 40.4 | 38.7 |
| T420DL | 46.9 | 29.0 | 28.7 | 49.1 | 30.2 | 29.9 |
| E025N | 23.6 | 12.1 | 10.8 | 23.1 | 11.6 | 10.4 |
| E050N | 22.2 | 11.2 | 10.0 | 22.5 | 11.2 | 9.9 |
| E075N | 22.8 | 11.2 | 10.1 | 23.3 | 11.4 | 10.3 |
| E100N | 23.3 | 11.3 | 10.1 | 24.2 | 11.6 | 10.4 |
| E125N | 23.1 | 10.8 | 9.5 | 24.3 | 11.4 | 9.9 |
| E150N | 22.3 | 9.5 | 8.1 | 23.5 | 10.0 | 8.3 |
| E200N | 18.8 | 4.5 | 3.4 | 18.6 | 5.0 | 3.5 |

Table 5.10 Interstory Stiffnesses Based on Linear Regressions from Time-Histories

| Test Number | Total Input Energy, Inch-Kips | | | Maximum Energy, Inch-Kips | | Total Energy Dissipated by VED, Inch Kips | Energy Dissipation Ratio* |
|-------------|-------------------------------|------------------------------|----------------------|---------------------------|-----------------------|---|---------------------------|
| | Integrated Accelerations | Differentiated Displacements | Direct Displacements | Kinetic Energy | Elastic Strain Energy | | |
| E025DS | 4.7 | 3.9 | 4.0 | 0.4 | 3.8 | 4.1 | 0.88 |
| E010DS | 0.6 | 0.5 | 0.5 | 0.1 | 1.0 | 0.6 | 0.99 |
| E025DM | 3.7 | 3.5 | 3.4 | 0.4 | 3.5 | 3.2 | 0.86 |
| T052DS | 5.0 | 4.2 | 4.0 | 0.5 | 3.0 | 4.5 | 0.91 |
| T021DS | 0.7 | 0.5 | 0.5 | 0.1 | 0.6 | 0.6 | 0.94 |
| T052DM | 3.9 | 3.3 | 3.3 | 0.5 | 3.2 | 3.5 | 0.90 |
| E010DL | 0.6 | 0.3 | 0.4 | 0.1 | 0.1 | 0.6 | 0.98 |
| E025DL | 3.3 | 3.1 | 3.0 | 0.4 | 0.5 | 3.2 | 0.97 |
| E050DL | 14 | 15 | 14 | 2 | 2 | 13 | 0.95 |
| E075DL | 32 | 33 | 32 | 4 | 6 | 30 | 0.94 |
| E100DL | 59 | 61 | 62 | 7 | 9 | 55 | 0.93 |
| E125DL | 94 | 95 | 94 | 11 | 12 | 87 | 0.93 |
| E150DL | 133 | 139 | 139 | 16 | 18 | 129 | 0.97 |
| E200DL | 368 | 376 | 375 | 38 | 32 | 362 | 0.98 |
| E250DL | 253 | 260 | 260 | 24 | 21 | 258 | 1.02 |
| T021DL | 1 | 1 | 1 | 0 | 0 | 1 | 0.97 |
| T052DL | 4 | 3 | 3 | 0 | 0 | 4 | 0.98 |
| T105DL | 15 | 13 | 13 | 2 | 2 | 14 | 0.97 |
| T157DL | 37 | 34 | 34 | 4 | 4 | 35 | 0.94 |
| T210DL | 66 | 63 | 63 | 7 | 6 | 63 | 0.95 |
| T262DL | 105 | 98 | 100 | 12 | 11 | 98 | 0.93 |
| T315DL | 151 | 145 | 146 | 16 | 13 | 148 | 0.98 |
| T420DL | 266 | 263 | 263 | 30 | 24 | 276 | 1.04 |
| E025N | 1.9 | 1.6 | 1.7 | 0.4 | 0.3 | | |
| E050N | 7.0 | 6.2 | 6.6 | 1.8 | 1.3 | | |
| E075N | 15 | 15 | 15 | 4 | 4 | | |
| E100N | 27 | 25 | 26 | 8 | 7 | | |
| E125N | 43 | 42 | 42 | 13 | 12 | | |
| E150N | 61 | 62 | 60 | 21 | 15 | | |
| E200N | 214 | 213 | 215 | 31 | 18 | | |

* Energy Dissipation Ratio = Energy Dissipated by Dampers / Input Energy Based on Integrated Accelerations Used for Velocity Calculations

Table 5.11 Energy Input and Dissipation Quantities for Earthquake Simulations

| Location | Reinforcement | Confined by Collar | Steel Properties | | | | | | | | Concrete Properties | | | |
|-----------------|---------------|-----------------------|------------------|----------------|----------------|----------------|----------------|----------------|--------|----------------|---------------------|----------------|-----------------|----------------|
| | | | f _y | e _l | f _u | e _u | f _f | e _f | E | E _T | f _c | e _c | e ₅₀ | f _r |
| Center Column | 4 - D9 | No | 41 | 0.004 | 61 | 0.060 | 55 | 0.100 | 29,000 | 1,500 | 5.0 | 0.004 | 0.010 | 0.670 |
| Center Column | 4 - D9 | Yes | 41 | 0.004 | 61 | 0.060 | 55 | 0.100 | 29,000 | 1,500 | 13.5 | 0.019 | 0.038 | 0.670 |
| Center Column | 4 - #3 | No | 60 | 0.004 | 85 | 0.080 | 75 | 0.120 | 29,000 | 1,500 | 5.0 | 0.004 | 0.010 | 0.670 |
| Center Column | 4 - #3 | Yes | 60 | 0.004 | 85 | 0.080 | 75 | 0.120 | 29,000 | 1,500 | 13.5 | 0.019 | 0.038 | 0.670 |
| Exterior Column | 6 - D7 | No | 44 | 0.004 | 64 | 0.060 | 55 | 0.100 | 29,000 | 1,500 | 5.0 | 0.004 | 0.010 | 0.670 |
| Exterior Column | 6 - D7 | Yes | 44 | 0.004 | 64 | 0.060 | 55 | 0.100 | 29,000 | 1,500 | 13.5 | 0.019 | 0.038 | 0.670 |
| Exterior Column | 6 - #3 | No | 60 | 0.004 | 85 | 0.080 | 75 | 0.120 | 29,000 | 1,500 | 5.0 | 0.004 | 0.010 | 0.670 |
| Exterior Column | 6 - #3 | Yes | 60 | 0.004 | 85 | 0.080 | 75 | 0.120 | 29,000 | 1,500 | 13.5 | 0.019 | 0.038 | 0.670 |

f_y = Steel yield stress, KSI
 e_1 = Steel strain at onset of strain hardening, In/In
 f_u = Steel ultimate stress, KSI
 e_u = Steel strain at ultimate stress, In/In
 f_f = Steel rupture stress, KSI
 e_f = Steel strain at rupture stress, In/In
E = Steel modulus of elasticity, KSI
 E_T = Steel modulus of elasticity at onset of strain hardening, KSI
 f_c = Peak concrete compressive stress ($0.85f_c$), KSI
 e_c = Concrete strain at f_c , In/In
 e_{50} = Specified strain for Modified Kent-Park Method, In/In
 f_r = Concrete tensile rupture stress, KSI

Table 6.1 Reinforced Concrete Column Properties Used in BIAx Analyses

| Analysis | Centerline Column Properties | | | | | | | | | | |
|----------|------------------------------|---------------------|---------------------|--|----------------|---------------------|---------------------|---------------------|----------------|---------------------|---------------------|
| | Story 3 | | | | Story 2 | | | | Story 1 | | |
| | Joint | Collar | Lower Story | | Joint | Collar | Lower Story | Lower Collar | Joint | Collar | Lower Story |
| E050DL | I _g | I _g | 0.65 I _g | | I _g | 0.90 I _g | 0.60 I _g | 0.90 I _g | I _g | 0.9 I _g | 0.60 I _g |
| E100DL | I _g | I _g | 0.60 I _g | | I _g | 0.80 I _g | 0.56 I _g | 0.56 I _g | I _g | 0.8 I _g | 0.56 I _g |
| E150DL | I _g | I _g | 0.50 I _g | | I _g | 0.80 I _g | 0.50 I _g | 0.50 I _g | I _g | 0.8 I _g | 0.50 I _g |
| E200DL | I _g | I _g | 0.50 I _g | | I _g | 0.72 I _g | 0.45 I _g | 0.45 I _g | I _g | 0.72 I _g | 0.45 I _g |
| E025N | I _g | 0.72 I _g | 0.47 I _g | | I _g | 0.72 I _g | 0.45 I _g | 0.45 I _g | I _g | 0.72 I _g | 0.45 I _g |
| E050N | I _g | 0.72 I _g | 0.47 I _g | | I _g | 0.72 I _g | 0.45 I _g | 0.45 I _g | I _g | 0.72 I _g | 0.45 I _g |
| E100N | I _g | 0.72 I _g | 0.47 I _g | | I _g | 0.72 I _g | 0.45 I _g | 0.45 I _g | I _g | 0.72 I _g | 0.45 I _g |
| E125N | I _g | 0.72 I _g | 0.47 I _g | | I _g | 0.72 I _g | 0.45 I _g | 0.45 I _g | I _g | 0.72 I _g | 0.45 I _g |
| E150N R1 | I _g | 0.72 I _g | 0.47 I _g | | I _g | 0.72 I _g | 0.45 I _g | 0.45 I _g | I _g | 0.72 I _g | 0.45 I _g |
| E150N R2 | I _g | 0.72 I _g | 0.47 I _g | | I _g | 0.72 I _g | 0.45 I _g | 0.45 I _g | I _g | 0.72 I _g | 0.45 I _g |
| FEMA 273 | I _g | I _g | 0.60 I _g | | I _g | I _g | 0.60 I _g | I _g | I _g | I _g | 0.60 I _g |

Table 6.2 Interior (Centerline) Column Properties Used in ETABS Analyses

| Analysis | Outside Column Properties | | | | | | | | | |
|----------|---------------------------|---------------------|---------------------|----------------|---------------------|---------------------|----------------|---------------------|---------------------|--|
| | Story 3 | | | Story 2 | | | Story 1 | | | |
| | Joint | Upper Story | Collar | Joint | Upper Story | Collar | Joint | Upper Story | Collar | |
| E050DL | I _g | 0.64 I _g | I _g | I _g | 0.64 I _g | I _g | I _g | 0.64 I _g | I _g | |
| E100DL | I _g | 0.60 I _g | I _g | I _g | 0.55 I _g | 0.80 I _g | I _g | 0.55 I _g | 0.80 I _g | |
| E150DL | I _g | 0.50 I _g | I _g | I _g | 0.52 I _g | 0.80 I _g | I _g | 0.52 I _g | 0.80 I _g | |
| E200DL | I _g | 0.50 I _g | I _g | I _g | 0.45 I _g | 0.80 I _g | I _g | 0.45 I _g | 0.80 I _g | |
| E025N | I _g | 0.45 I _g | 0.61 I _g | I _g | 0.45 I _g | 0.61 I _g | I _g | 0.45 I _g | 0.61 I _g | |
| E050N | I _g | 0.45 I _g | 0.61 I _g | I _g | 0.45 I _g | 0.61 I _g | I _g | 0.45 I _g | 0.61 I _g | |
| E100N | I _g | 0.45 I _g | 0.61 I _g | I _g | 0.45 I _g | 0.61 I _g | I _g | 0.45 I _g | 0.61 I _g | |
| E125N | I _g | 0.45 I _g | 0.61 I _g | I _g | 0.45 I _g | 0.61 I _g | I _g | 0.45 I _g | 0.61 I _g | |
| E150N R1 | I _g | 0.45 I _g | 0.61 I _g | I _g | 0.45 I _g | 0.61 I _g | I _g | 0.45 I _g | 0.61 I _g | |
| E150N R2 | I _g | 0.45 I _g | 0.61 I _g | I _g | 0.45 I _g | 0.61 I _g | I _g | 0.45 I _g | 0.61 I _g | |
| FEMA 273 | I _g | 0.60 I _g | I _g | I _g | 0.60 I _g | I _g | I _g | 0.60 I _g | I _g | |

Table 6.3 Exterior (Outside) Column Properties Used in ETABS Analyses

| Connection Location | Recommended Effective Width Factors | | | | | | | | | | | |
|--------------------------------|---|---------|---------------|------------|---------|---------------|---------------------------------|---------|---------------|------------|---------|---------------|
| | Robertson-Ambrose Model Reference 39 (Span/Depth Ratio = 30) | | | | | | Robertson Model Reference 38 | | | | | |
| | 0.5% Drift | | | 1.0% Drift | | | 0.5% Drift | | | 1.5% Drift | | |
| | α | β | $\alpha\beta$ | α | β | $\alpha\beta$ | α | β | $\alpha\beta$ | α | β | $\alpha\beta$ |
| Exterior Negative Moment | 0.20 | 0.60 | 0.12 | 0.20 | 0.46 | 0.09 | 0.40 | 0.25 | 0.10 | 0.40 | 0.20 | 0.08 |
| Exterior Positive Moment | 0.40 | 1.00 | 0.40 | 0.40 | 0.70 | 0.28 | 0.40 | 1.00 | 0.40 | 0.40 | 0.50 | 0.20 |
| First Interior Negative Moment | 0.40 | 1.00 | 0.40 | 0.40 | 0.70 | 0.28 | 0.40 | | | 0.40 | | |
| Interior Negative Moment | 0.40 | 1.00 | 0.40 | 0.40 | 0.70 | 0.28 | 0.40 | 0.10 | 0.04 | 0.40 | 0.10 | 0.04 |
| Interior Positive Moment | 0.40 | 1.00 | 0.40 | 0.40 | 0.70 | 0.28 | 0.40 | 1.00 | 0.40 | 0.40 | 0.50 | 0.20 |

Table 6.4 Proposed Effective Width Factors for Two-Beam Models

| Analysis | Equivalent Beam Widths for Floor Slabs | | | | | | | | | | | | | | |
|----------|--|----------------------|----------------------|----------------------|----------------------|----------------------|----------------------|----------------------|----------------------|----------------------|----------------------|----------------------|----------------------|----------------------|----------------------|
| | Floor 3 | | | | | Floor 2 | | | | | Floor 1 | | | | |
| | Section* | | | | | Section* | | | | | Section* | | | | |
| | A | B | C | D | E | A | B | C | D | E | A | B | C | D | E |
| E050DL | 0.200 b _w | 0.250 b _w | 0.400 b _w | 0.200 b _w | 0.200 b _w | 0.150 b _w | 0.200 b _w | 0.325 b _w | 0.200 b _w | 0.200 b _w | 0.150 b _w | 0.200 b _w | 0.375 b _w | 0.200 b _w | 0.200 b _w |
| E100DL | 0.200 b _w | 0.250 b _w | 0.400 b _w | 0.200 b _w | 0.125 b _w | 0.075 b _w | 0.100 b _w | 0.225 b _w | 0.100 b _w | 0.100 b _w | 0.075 b _w | 0.100 b _w | 0.275 b _w | 0.100 b _w | 0.100 b _w |
| E150DL | 0.175 b _w | 0.200 b _w | 0.375 b _w | 0.188 b _w | 0.112 b _w | 0.031 b _w | 0.038 b _w | 0.150 b _w | 0.088 b _w | 0.038 b _w | 0.031 b _w | 0.038 b _w | 0.200 b _w | 0.088 b _w | 0.038 b _w |
| E200DL | 0.125 b _w | 0.150 b _w | 0.325 b _w | 0.150 b _w | 0.075 b _w | 0.018 b _w | 0.025 b _w | 0.100 b _w | 0.050 b _w | 0.025 b _w | 0.018 b _w | 0.025 b _w | 0.150 b _w | 0.050 b _w | 0.025 b _w |
| E025N | 0.031 b _w | 0.050 b _w | 0.200 b _w | 0.075 b _w | 0.038 b _w | 0.016 b _w | 0.025 b _w | 0.100 b _w | 0.050 b _w | 0.025 b _w | 0.016 b _w | 0.022 b _w | 0.150 b _w | 0.050 b _w | 0.025 b _w |
| E050N | 0.031 b _w | 0.050 b _w | 0.200 b _w | 0.075 b _w | 0.038 b _w | 0.014 b _w | 0.016 b _w | 0.081 b _w | 0.038 b _w | 0.016 b _w | 0.014 b _w | 0.022 b _w | 0.144 b _w | 0.044 b _w | 0.022 b _w |
| E100N | 0.031 b _w | 0.050 b _w | 0.200 b _w | 0.075 b _w | 0.038 b _w | 0.014 b _w | 0.016 b _w | 0.081 b _w | 0.038 b _w | 0.016 b _w | 0.014 b _w | 0.022 b _w | 0.144 b _w | 0.044 b _w | 0.022 b _w |
| E125N | 0.031 b _w | 0.050 b _w | 0.200 b _w | 0.075 b _w | 0.038 b _w | 0.014 b _w | 0.016 b _w | 0.081 b _w | 0.038 b _w | 0.016 b _w | 0.014 b _w | 0.022 b _w | 0.144 b _w | 0.044 b _w | 0.022 b _w |
| E150N R1 | 0.031 b _w | 0.050 b _w | 0.200 b _w | 0.075 b _w | 0.038 b _w | 0.014 b _w | 0.016 b _w | 0.081 b _w | 0.038 b _w | 0.016 b _w | 0.014 b _w | 0.022 b _w | 0.144 b _w | 0.044 b _w | 0.022 b _w |
| E150N R2 | 0.019 b _w | 0.031 b _w | 0.200 b _w | 0.050 b _w | 0.031 b _w | 0.012 b _w | 0.014 b _w | 0.081 b _w | 0.025 b _w | 0.014 b _w | 0.012 b _w | 0.016 b _w | 0.144 b _w | 0.031 b _w | 0.016 b _w |
| FEMA 273 | 0.188 b _w | 0.188 b _w | 0.188 b _w | 0.188 b _w | 0.188 b _w | 0.188 b _w | 0.188 b _w | 0.188 b _w | 0.188 b _w | 0.188 b _w | 0.188 b _w | 0.188 b _w | 0.188 b _w | 0.188 b _w | 0.188 b _w |

*See Figure 6.7 for section locations.

Table 6.5 Equivalent Beam Widths Used in ETABS Analyses

| Analysis | Viscoelastic Damper Properties | | | | | | | | | | Base Rotational Spring Stiffness In-Kips/Rad | |
|--|--------------------------------|-------------------------------------|--|------------------------|-------------------------------------|--|------------------------|-------------------------------------|------------------------|-------------------------------------|---|--------|
| | Story 3 | | | Story 2 | | | Story 1 | | Ideal for 3M ISD 110* | | | |
| | Stiffness Kips/Inch | Damping Coefficient Kip-Sec/Inch | | Stiffness Kips/Inch | Damping Coefficient Kip-Sec/Inch | | Stiffness Kips/Inch | Damping Coefficient Kip-Sec/Inch | Stiffness Kips/Inch | Damping Coefficient Kip-Sec/Inch | | |
| | | | | | | | | | | | | |
| E050DL | 1.4 | 0.65 | | 10.1 | 0.85 | | 12.2 | 0.90 | | 12.8 | 1.07 | 25,000 |
| E100DL | 1.4 | 0.46 | | 10.1 | 0.54 | | 12.2 | 0.46 | | 10.9 | 0.95 | 25,000 |
| E150DL | 3.4 | 0.50 | | 12.6 | 0.48 | | 15.8 | 0.30 | | 8.9 | 0.75 | 25,000 |
| E200DL | 3.1 | 0.44 | | 10.1 | 0.28 | | 14.4 | 0.20 | | 6.7 | 0.61 | 23,000 |
| E025N | | | | | | | | | | | | 15,000 |
| E050N | | | | | | | | | | | | 15,000 |
| E100N | | | | | | | | | | | | 15,000 |
| E125N | | | | | | | | | | | | 15,000 |
| E150N R1 | | | | | | | | | | | | 15,000 |
| E150N R2 | | | | | | | | | | | | 12,500 |
| FEMA 273 | 8.9 | 0.75 | | 8.9 | 0.75 | | 8.9 | 0.75 | | 8.9 | 0.75 | 25,000 |
| *Based on published 3M data and assuming f = 2.5 Hz, T = 24° C (75° F), and maximum strain in simulation. Values interpolated from data. | | | | | | | | | | | | |

Table 6.6 Viscoelastic Damper and Rotational Spring Properties Used in ETABS Analyses of Response Maxima

| Simulation | Top Floor Drift, % | | ETABS/Measured | | Base Shear/Weight, % | | ETABS/Measured | | Input Energy, Inch-Kips | | ETABS/Measured | |
|------------|--------------------|----------|----------------|----------|----------------------|----------|----------------|----------|-------------------------|----------|----------------|----------|
| | ETABS | Measured | ETABS | Measured | ETABS | Measured | ETABS | Measured | ETABS | Measured | ETABS | Measured |
| E050DL | 0.27 | 0.28 | | 0.95 | 24.7 | 23.8 | | 1.04 | 15 | 14 | | 1.06 |
| E100DL | 0.64 | 0.64 | | 1.00 | 43.0 | 43.0 | | 1.00 | 55 | 60 | | 0.92 |
| E150DL | 0.94 | 0.94 | | 1.00 | 61.8 | 62.4 | | 0.99 | 107 | 135 | | 0.79 |
| E200DL | 1.66 | 1.64 | | 1.01 | 81.6 | 80.2 | | 1.02 | 274 | 372 | | 0.74 |
| E025N | 0.34 | 0.32 | | 1.07 | 4.9 | 5.2 | | 0.95 | 2 | 2 | | 1.22 |
| E050N | 0.68 | 0.68 | | 1.00 | 8.4 | 9.8 | | 0.86 | 7 | 7 | | 1.11 |
| E100N | 1.30 | 1.34 | | 0.97 | 16.7 | 20.4 | | 0.82 | 26 | 26 | | 1.00 |
| E125N | 1.73 | 1.69 | | 1.02 | 22.1 | 25.5 | | 0.87 | 34 | 42 | | 0.81 |
| E150N R1 | 1.94 | 2.18 | | 0.89 | 24.5 | 30.6 | | 0.80 | 47 | 61 | | 0.77 |
| FEMA 273-D | 0.77 | 0.94 | | 0.82 | 61.4 | 62.4 | | 0.98 | 147 | 135 | | 1.09 |
| FEMA 273-N | 1.98 | 2.18 | | 0.91 | 80.6 | 30.6 | | 2.64 | 143 | 61 | | 2.34 |

Table 6.7 Comparison of ETABS Analysis and Measured Top Floor Drift, Base Shear, and Input Energy

| Simulation | Story Shear Stiffness, Kips/Inch | | | | | | | Maximum Sum of Horizontal Components of VED Forces/Story Shear | | | | | | |
|------------|----------------------------------|---------|---------|---------|--------------------------|---------|---------|--|---------|---------|-------------------------|---------|---------|---------|
| | ETABS Analysis | | | | Measured in Simulations* | | | ETABS Analysis | | | Measured in Simulations | | | |
| | Story 3 | Story 2 | Story 1 | Story 3 | Story 2 | Story 1 | Story 1 | Story 3 | Story 2 | Story 1 | Story 3 | Story 2 | Story 1 | Story 1 |
| E050DL | 45.6 | 67.7 | 103.8 | 48.2 | 57.9 | 93.5 | 93.5 | 55% | 69% | 53% | 53% | 68% | 51% | 51% |
| E100DL | 37.5 | 53.6 | 89.3 | 41.7 | 47.6 | 76.3 | 76.3 | 52% | 71% | 52% | 50% | 70% | 52% | 52% |
| E150DL | 36.0 | 51.8 | 91.1 | 42.9 | 45.8 | 72.3 | 72.3 | 66% | 80% | 54% | 61% | 76% | 57% | 57% |
| E200DL | 28.9 | 41.3 | 77.0 | 31.5 | 31.6 | 53.1 | 53.1 | 74% | 73% | 57% | 70% | 78% | 63% | 63% |
| E025N | 8.8 | 12.3 | 22.9 | 10.4 | 11.6 | 23.1 | 23.1 | | | | | | | |
| E050N | 7.9 | 11.2 | 21.5 | 9.9 | 11.2 | 22.5 | 22.5 | | | | | | | |
| E100N | 7.9 | 11.2 | 21.5 | 10.4 | 11.6 | 24.2 | 24.2 | | | | | | | |
| E125N | 7.9 | 11.2 | 21.5 | 9.9 | 11.4 | 24.3 | 24.3 | | | | | | | |
| E150N R1 | 7.9 | 11.2 | 21.5 | 8.3 | 10.0 | 23.5 | 23.5 | | | | | | | |
| FEMA 273-D | 51.3 | 60.4 | 88.3 | 42.9 | 45.8 | 72.3 | 72.3 | | | | | | | |
| FEMA 273-N | 28.1 | 35.7 | 57.0 | 8.3 | 10.0 | 23.5 | 23.5 | | | | | | | |

*Based on 3.5 sec of maximum displacement-see Table 5.10

Table 6.8 Comparison of ETABS Analysis and Measured Story Shear Stiffnesses and VED Forces

| Test Designation | ETABS Natural Period, Sec | | | Measured Resonant Period, Sec | | | Measured Natural Period, Sec* | | | ETABS Damping, % | | | Measured Damping, % | | |
|------------------|---------------------------|--------|--------|-------------------------------|--------|--------|-------------------------------|--------|--------|------------------|--------|--------|---------------------|--------|--------|
| | Mode 1 | Mode 2 | Mode 3 | Mode 1 | Mode 2 | Mode 3 | Mode 1 | Mode 2 | Mode 3 | Mode 1 | Mode 2 | Mode 3 | Mode 1 | Mode 2 | Mode 3 |
| E050DL | 0.35 | 0.12 | 0.06 | 0.34 | | | 0.36 | | | 36 | 72 | 82 | 37 | | |
| E100DL | 0.39 | 0.12 | 0.06 | 0.38 | | | 0.41 | | | 26 | 44 | 57 | 36 | | |
| E150DL | 0.39 | 0.13 | 0.06 | 0.42 | | | 0.44 | | | 24 | 51 | 50 | 37 | | |
| E200DL | 0.44 | 0.14 | 0.07 | 0.51 | | | 0.53 | | | 20 | 45 | 36 | 40 | | |
| E025N | 0.80 | 0.19 | 0.08 | 0.78 | 0.20 | 0.11 | 0.78 | 0.20 | 0.11 | 6 | 6 | 6 | 7 | 1 | 1 |
| E050N | 0.83 | 0.19 | 0.08 | 0.83 | 0.21 | 0.11 | 0.83 | 0.21 | 0.11 | 5 | 6 | 6 | 10 | 3 | 1 |
| E100N | 0.83 | 0.19 | 0.08 | 0.83 | 0.21 | 0.12 | 0.83 | 0.21 | 0.12 | 4 | 5 | 5 | 5 | 4 | 3 |
| E125N | 0.83 | 0.19 | 0.08 | 0.85 | 0.20 | 0.12 | 0.85 | 0.20 | 0.12 | 3 | 4 | 4 | 6 | 2 | 3 |
| E150N R1 | 0.83 | 0.19 | 0.08 | 0.92 | 0.20 | 0.13 | 0.92 | 0.20 | 0.13 | 1 | 4 | 4 | 5 | 1 | 1 |
| E150N R2 | 0.91 | 0.20 | 0.08 | 0.92 | 0.20 | 0.13 | 0.92 | 0.20 | 0.13 | 3 | 6 | 6 | 5 | 1 | 1 |
| FEMA 273-D | 0.37 | 0.11 | 0.06 | 0.42 | | | 0.44 | | | 30 | | | 37 | | |
| FEMA 273-N | 0.48 | 0.13 | 0.06 | 0.92 | 0.20 | 0.13 | 0.92 | 0.20 | 0.13 | 5 | 5 | 5 | 5 | 1 | 1 |

* Natural period estimated using procedures of Section 5.8 and ETABS modal damping ratios.

Table 6.9 Comparison of Dynamic Properties Used in ETABS Analyses with Measured Modal Properties

| Normalized Mode Shape Ordinate | Computed Analysis E050DL | | | Computed Analysis E150DL | | | Computed Analysis E200DL | | | Measured Pre-E010DL | | | Measured Post-E250DL | | |
|--------------------------------------|-----------------------------|--------|--------|-----------------------------|--------|--------|-----------------------------|--------|--------|------------------------|--------|--------|-------------------------|--------|--------|
| | Mode 1 | Mode 2 | Mode 3 | Mode 1 | Mode 2 | Mode 3 | Mode 1 | Mode 2 | Mode 3 | Mode 1 | Mode 2 | Mode 3 | Mode 1 | Mode 2 | Mode 3 |
| FL 3 | 1.000 | -0.915 | 0.343 | 1.000 | -0.894 | 0.353 | 1.000 | -0.874 | 0.356 | 1.000 | | | 0.770 | | |
| FL 2 | 0.685 | 0.785 | -0.908 | 0.680 | 0.798 | -0.895 | 0.669 | 0.808 | -0.887 | 0.700 | | | 1.000 | | |
| FL 1 | 0.305 | 1.000 | 1.000 | 0.282 | 1.000 | 1.000 | 0.265 | 1.000 | 1.000 | 0.397 | | | 0.663 | | |

| Normalized Mode Shape Ordinate | Computed Analysis E025N | | | Computed Analysis E50N | | | Computed Analyses E100N & E125N | | | Computed Analysis E150N R1 | | | Computed Analysis E150N R2 | | |
|--------------------------------------|----------------------------|--------|--------|---------------------------|--------|--------|------------------------------------|--------|--------|-------------------------------|--------|--------|-------------------------------|--------|--------|
| | Mode 1 | Mode 2 | Mode 3 | Mode 1 | Mode 2 | Mode 3 | Mode 1 | Mode 2 | Mode 3 | Mode 1 | Mode 2 | Mode 3 | Mode 1 | Mode 2 | Mode 3 |
| FL 3 | 1.000 | -0.871 | 0.367 | 1.000 | -0.859 | 0.371 | 1.000 | -0.859 | 0.371 | 1.000 | -0.859 | 0.371 | 1.000 | -0.862 | 0.352 |
| FL 2 | 0.677 | 0.785 | -0.902 | 0.672 | 0.785 | -0.904 | 0.672 | 0.785 | -0.904 | 0.672 | 0.785 | -0.904 | 0.658 | 0.813 | -0.888 |
| FL 1 | 0.271 | 1.000 | 1.000 | 0.264 | 1.000 | 1.000 | 0.264 | 1.000 | 1.000 | 0.264 | 1.000 | 1.000 | 0.259 | 1.000 | 1.000 |

| Normalized Mode Shape Ordinate | Measured No Braces-Initial Cond. | | | Measured Pre-E025N | | | Measured Post-E050N | | | Measured Post-E125N | | | Measured Post-E150N | | |
|--------------------------------------|-------------------------------------|--------|--------|-----------------------|--------|--------|------------------------|--------|--------|------------------------|--------|--------|------------------------|--------|--------|
| | Mode 1 | Mode 2 | Mode 3 | Mode 1 | Mode 2 | Mode 3 | Mode 1 | Mode 2 | Mode 3 | Mode 1 | Mode 2 | Mode 3 | Mode 1 | Mode 2 | Mode 3 |
| FL 3 | 1.000 | 1.000 | 0.369 | 1.000 | 1.000 | 0.362 | 1.000 | 0.782 | 0.349 | 1.000 | 0.862 | 0.298 | 1.000 | 1.000 | 0.282 |
| FL 2 | 0.612 | -0.906 | -0.681 | 0.704 | -0.921 | -0.780 | 0.633 | -0.636 | -0.793 | 0.645 | -1.000 | -0.847 | 0.759 | -0.839 | -0.716 |
| FL 1 | 0.374 | -0.942 | 1.000 | 0.358 | -0.997 | 1.000 | 0.288 | -1.000 | 1.000 | 0.301 | -0.735 | 1.000 | 0.386 | -0.940 | 1.000 |

Table 6.10 Computed and Measured Mode Shapes

| Maximum Column Forces: Interior Column, Floor 1 | | | | | | | | | | | |
|---|----------------------------------|----------------------------|--|--------------------------------------|---------------------|----------------------------|----------------------------------|----------------------------|--------------------------------------|----------------------------------|---------------|
| Analysis | Top of Column | | | | | | Bottom of Column | | | | |
| | Capacities | | | Calculated in ETABS Dynamic Analysis | | | Capacities | | Calculated in ETABS Dynamic Analysis | | |
| | Moment ¹ Inch-kips | Shear ² Kips | | Axial Force ³ Kips | Moment Inch-kips | Shear ⁴ Kips | Moment ¹ Inch-kips | Shear ² Kips | Axial Force ³ Kips | Moment ⁴ Inch-kips | Shear Kips |
| E050DL | 75 | 8.5 | | -14.7 | 20 | 4.3 | 80 | 6.5 | -14.7 | 34 | 1.6 |
| E100DL | 75 | 8.5 | | -14.7 | 23 | 7.9 | 80 | 6.5 | -14.7 | 62 | 2.4 |
| E150DL | 75 | 8.5 | | -14.7 | 14 | 12.6 | 80 | 6.5 | -14.7 | 75 | 2.6 |
| E200DL | 75 | 8.5 | | -14.7 | 19 | 16.5 | 80 | 6.5 | -14.7 | 106 | 3.5 |
| E025N | 77 | 8.5 | | -15.2 | 6 | 0.5 | 82 | 6.5 | -15.2 | 15 | 0.5 |
| E050N | 77 | 8.5 | | -15.2 | 13 | 0.8 | 82 | 6.5 | -15.2 | 30 | 0.8 |
| E100N | 77 | 8.5 | | -15.2 | 29 | 1.7 | 82 | 6.5 | -15.2 | 60 | 1.7 |
| E125N | 77 | 8.5 | | -15.2 | 36 | 2.3 | 82 | 6.5 | -15.2 | 82 | 2.3 |
| E150N R1 | 77 | 8.5 | | -15.2 | 42 | 2.4 | 82 | 6.5 | -15.2 | 84 | 2.4 |

1. Computed using interaction diagrams of Figures 6.1 - 6.4 and calculated axial forces.

2. See section 6.2.(a).

3. At *approximate* time of most severe combination of moment & axial force, (+) indicates net tension, (-) indicates net compression.

4. Italicized quantities indicate calculated demand exceeds calculated capacity.

Table 6.11 Maximum Column Forces: Interior Column, Floor 1

| Maximum Column Forces: Interior Column, Floor 2 | | | | | | | | | | | |
|---|----------------------------------|----------------------------|--|--------------------------------------|---------------------|----------------------------|----------------------------------|----------------------------|--------------------------------------|---------------------|---------------|
| Analysis | Top of Column | | | | | | Bottom of Column | | | | |
| | Capacities | | | Calculated in ETABS Dynamic Analysis | | | Capacities | | Calculated in ETABS Dynamic Analysis | | |
| | Moment ¹ Inch-kips | Shear ² Kips | | Axial Force ³ Kips | Moment Inch-kips | Shear ⁴ Kips | Moment ¹ Inch-kips | Shear ² Kips | Axial Force ³ Kips | Moment Inch-kips | Shear Kips |
| E050DL | 75 | 8.5 | | -9.7 | 24 | 4.0 | 75 | 6.5 | -9.7 | 24 | 1.4 |
| E100DL | 75 | 8.5 | | -9.7 | 32 | 8.1 | 75 | 6.5 | -9.7 | 35 | 2.0 |
| E150DL | 75 | 8.5 | | -9.7 | 22 | 13.5 | 75 | 6.5 | -9.7 | 35 | 1.9 |
| E200DL | 75 | 8.5 | | -9.7 | 36 | 18.6 | 75 | 6.5 | -9.7 | 49 | 2.8 |
| E025N | 75 | 8.5 | | -9.9 | 10 | 0.4 | 75 | 6.5 | -9.9 | 10 | 0.4 |
| E050N | 75 | 8.5 | | -9.9 | 16 | 0.8 | 75 | 6.5 | -9.9 | 17 | 0.8 |
| E100N | 75 | 8.5 | | -9.9 | 34 | 1.6 | 75 | 6.5 | -9.9 | 36 | 1.6 |
| E125N | 75 | 8.5 | | -9.9 | 48 | 2.2 | 75 | 6.5 | -9.9 | 45 | 2.2 |
| E150N R1 | 75 | 8.5 | | -9.9 | 48 | 2.4 | 75 | 6.5 | -9.9 | 56 | 2.4 |

1. Computed using interaction diagrams of Figures 6.1 - 6.4 and calculated axial forces.
2. See section 6.2.(a).
3. At *approximate* time of most severe combination of moment & axial force, (+) indicates net tension, (-) indicates net compression.
4. Italicized quantities indicate calculated demand exceeds calculated capacity.

Table 6.12 Maximum Column Forces: Interior Column, Floor 2

| Maximum Column Forces: Interior Column, Floor 3 | | | | | | | | | | | |
|---|----------------------------------|----------------------------|--|--------------------------------------|----------------------------------|----------------------------|----------------------------------|----------------------------|--------------------------------------|---------------------|---------------|
| Analysis | Top of Column | | | | | | Bottom of Column | | | | |
| | Capacities | | | Calculated in ETABS Dynamic Analysis | | | Capacities | | Calculated in ETABS Dynamic Analysis | | |
| | Moment ¹ Inch-kips | Shear ² Kips | | Axial Force ³ Kips | Moment ⁴ Inch-kips | Shear ⁴ Kips | Moment ¹ Inch-kips | Shear ² Kips | Axial Force ³ Kips | Moment Inch-kips | Shear Kips |
| E050DL | 65 | 8.5 | | -4.6 | 28 | 1.5 | 55 | 6.5 | -4.6 | 15 | 1.2 |
| E100DL | 65 | 8.5 | | -4.6 | 63 | 3.1 | 55 | 6.5 | -4.6 | 26 | 2.4 |
| E150DL | 65 | 8.5 | | -4.6 | 84 | 5.7 | 55 | 6.5 | -4.6 | 28 | 3.1 |
| E200DL | 65 | 8.5 | | -4.6 | 111 | 9.5 | 55 | 6.5 | -4.6 | 29 | 3.9 |
| E025N | 65 | 8.5 | | -4.7 | 13 | 0.4 | 55 | 6.5 | -4.7 | 6 | 0.4 |
| E050N | 65 | 8.5 | | -4.7 | 23 | 0.8 | 55 | 6.5 | -4.7 | 11 | 0.8 |
| E100N | 65 | 8.5 | | -4.7 | 47 | 1.7 | 55 | 6.5 | -4.7 | 22 | 1.7 |
| E125N | 65 | 8.5 | | -4.7 | 63 | 2.1 | 55 | 6.5 | -4.7 | 27 | 2.1 |
| E150N R1 | 65 | 8.5 | | -4.7 | 70 | 2.6 | 55 | 6.5 | -4.7 | 31 | 2.6 |

1. Computed using interaction diagrams of Figures 6.1 - 6.4 and calculated axial forces.

2. See section 6.2.(a).

3. At *approximate* time of most severe combination of moment & axial force, (+) indicates net tension, (-) indicates net compression.

4. Italicized quantities indicate calculated demand exceeds calculated capacity.

Table 6.13 Maximum Column Forces: Interior Column, Floor 3

| Maximum Column Forces: Exterior Column, Floor 1 | | | | | | | | | | | |
|---|----------------------------------|----------------------------|--|--------------------------------------|---------------------|---------------|----------------------------------|----------------------------|--------------------------------------|----------------------------------|---------------|
| Analysis | Top of Column | | | | | | Bottom of Column | | | | |
| | Capacities | | | Calculated in ETABS Dynamic Analysis | | | Capacities | | Calculated in ETABS Dynamic Analysis | | |
| | Moment ¹ Inch-kips | Shear ² Kips | | Axial Force ³ Kips | Moment Inch-kips | Shear Kips | Moment ¹ Inch-kips | Shear ² Kips | Axial Force ³ Kips | Moment ⁴ Inch-kips | Shear Kips |
| E050DL | 62 | 9.9 | | -10.0 | 21 | 1.7 | 110 | 12.4 | -10.7 | 40 | 3.1 |
| E100DL | 63 | 9.9 | | -12.1 | 26 | 2.6 | 105 | 12.4 | -1.3 | 66 | 5.4 |
| E150DL | 64 | 9.9 | | -14.1 | 23 | 3.1 | 95 | 12.4 | 1.9 | 85 | 8.1 |
| E200DL | 48 | 9.9 | | 2.0 | 20 | 4.0 | 90 | 12.4 | 5.3 | 118 | 10.6 |
| E025N | 59 | 9.9 | | -6.7 | 8 | 0.6 | 108 | 12.4 | -7.5 | 18 | 0.6 |
| E050N | 60 | 9.9 | | -7.9 | 14 | 1.0 | 108 | 12.4 | -7.9 | 36 | 1.0 |
| E100N | 61 | 9.9 | | -8.7 | 28 | 1.9 | 109 | 12.4 | -8.6 | 69 | 1.9 |
| E125N | 62 | 9.9 | | -9.4 | 34 | 2.6 | 109 | 12.4 | -9.4 | 95 | 2.6 |
| E150N R1 | 62 | 9.9 | | -9.5 | 39 | 2.6 | 105 | 12.4 | -5.0 | 98 | 2.6 |

1. Computed using interaction diagrams of Figures 6.1 - 6.4 and calculated axial forces.

2. See section 6.2.(a).

3. At *approximate* time of most severe combination of moment & axial force, (+) indicates net tension, (-) indicates net compression.

4. Italicized quantities indicate calculated demand exceeds calculated capacity.

Table 6.14 Maximum Column Forces: Exterior Column, Floor 1

| Maximum Column Forces: Exterior Column, Floor 2 | | | | | | | | | | | |
|---|----------------------------------|----------------------------|--|--------------------------------------|---------------------|---------------|----------------------------------|----------------------------|--------------------------------------|---------------------|---------------|
| Analysis | Top of Column | | | | | | Bottom of Column | | | | |
| | Capacities | | | Calculated in ETABS Dynamic Analysis | | | Capacities | | Calculated in ETABS Dynamic Analysis | | |
| | Moment ¹ Inch-kips | Shear ² Kips | | Axial Force ³ Kips | Moment Inch-kips | Shear Kips | Moment ¹ Inch-kips | Shear ² Kips | Axial Force ³ Kips | Moment Inch-kips | Shear Kips |
| E050DL | 60 | 9.9 | | -6.0 | 22 | 1.2 | 65 | 12.4 | -6.7 | 23 | 2.6 |
| E100DL | 61 | 9.9 | | -7.0 | 30 | 1.8 | 67 | 12.4 | -8.6 | -33 | 4.9 |
| E150DL | 62 | 9.9 | | -7.7 | 27 | 1.7 | 48 | 12.4 | 1.1 | 18 | 7.6 |
| E200DL | 64 | 9.9 | | -9.1 | 41 | 2.3 | 45 | 12.4 | 3.6 | 27 | 10.3 |
| E025N | 59 | 9.9 | | -5.0 | 11 | 0.6 | 60 | 12.4 | -5.0 | -14 | 0.6 |
| E050N | 58 | 9.9 | | -4.1 | 16 | 0.9 | 58 | 12.4 | -4.1 | 23 | 0.9 |
| E100N | 57 | 9.9 | | -3.5 | 28 | 1.5 | 56 | 12.4 | -3.5 | 44 | 1.5 |
| E125N | 60 | 9.9 | | -6.2 | 39 | 2.0 | 66 | 12.4 | -6.2 | 51 | 2.0 |
| E150N R1 | 60 | 9.9 | | -6.3 | 40 | 2.1 | 66 | 12.4 | -6.3 | 66 | 2.1 |

1. Computed using interaction diagrams of Figures 6.1 - 6.4 and calculated axial forces.

2. See section 6.2.(a).

3. At *approximate* time of most severe combination of moment & axial force, (+) indicates net tension, (-) indicates net compression.

4. Italicized quantities indicate calculated demand exceeds calculated capacity.

Table 6.15 Maximum Column Forces: Exterior Column, Floor 2

| Maximum Column Forces: Exterior Column, Floor 3 | | | | | | | | | | | |
|---|----------------------------------|----------------------------|--|--------------------------------------|----------------------------------|---------------|----------------------------------|----------------------------|--------------------------------------|---------------------|---------------|
| Analysis | Top of Column | | | | | | Bottom of Column | | | | |
| | Capacities | | | Calculated in ETABS Dynamic Analysis | | | Capacities | | Calculated in ETABS Dynamic Analysis | | |
| | Moment ¹ Inch-kips | Shear ² Kips | | Axial Force ³ Kips | Moment ⁴ Inch-kips | Shear Kips | Moment ¹ Inch-kips | Shear ² Kips | Axial Force ³ Kips | Moment Inch-kips | Shear Kips |
| E050DL | 60 | 9.9 | | -2.8 | 25 | 1.1 | 65 | 12.4 | -2.9 | 17 | 1.3 |
| E100DL | 62 | 9.9 | | -3.3 | 49 | 2.0 | 67 | 12.4 | -3.5 | 24 | 2.4 |
| E150DL | 63 | 9.9 | | -3.7 | 62 | 2.2 | 69 | 12.4 | -4.4 | 22 | 3.6 |
| E200DL | 50 | 9.9 | | -0.6 | 69 | 2.6 | 52 | 12.4 | 0.9 | 19 | 5.4 |
| E025N | 60 | 9.9 | | -2.5 | 13 | 0.5 | 64 | 12.4 | -2.4 | 10 | 0.5 |
| E050N | 60 | 9.9 | | -2.6 | 19 | 0.7 | 65 | 12.4 | -2.6 | 16 | 0.8 |
| E100N | 62 | 9.9 | | -3.0 | 35 | 1.4 | 65 | 12.4 | -2.9 | 28 | 1.4 |
| E125N | 62 | 9.9 | | -3.2 | 45 | 1.5 | 66 | 12.4 | -3.2 | 33 | 1.7 |
| E150N R1 | 63 | 9.9 | | -3.3 | 50 | 1.8 | 66 | 12.4 | -3.3 | 38 | 2.0 |

1. Computed using interaction diagrams of Figures 6.1 - 6.4 and calculated axial forces.

2. See section 6.2.(a).

3. At *approximate* time of most severe combination of moment & axial force, (+) indicates net tension, (-) indicates net compression.

4. Italicized quantities indicate calculated demand exceeds calculated capacity.

Table 6.16 Maximum Column Forces: Exterior Column, Floor 3

| Maximum Unbalanced Moments (Inch-Kips): Floor 1 | | | | | | | | |
|---|-----------------------|----------------|---------|------------------|----------|--|-----------------------|---|
| Analysis | Interior Connections | | | | | Exterior Connections | | |
| | Connection Capacities | | | | | Calculated ETABS Dynamic Analysis* | Capacities Eq 6.15 | Calculated ETABS Dynamic Analysis |
| | Flexure | Punching Shear | | | | | | |
| | | Eq. 6.7 | Eq. 6.8 | Eq. 6.8 Modified | Eq. 6.13 | | | |
| | | | | | | | | |
| E050DL | 50 | 75 | 94 | 94 | 69 | 55 | -67 | -53 |
| E100DL | 50 | 75 | 94 | 94 | 80 | 76 | -67 | -63 |
| E150DL | 50 | 75 | 94 | 94 | 77 | 71 | -67 | -54 |
| E200DL | 50 | 75 | 94 | 94 | 87 | 89 | -67 | -58 |
| E025N | 50 | 75 | 94 | 94 | 76 | 13 | -67 | -20 |
| E050N | 50 | 75 | 94 | 94 | 71 | 23 | -67 | -23 |
| E100N | 50 | 75 | 94 | 94 | 64 | 47 | -67 | -32 |
| E125N | 50 | 75 | 94 | 94 | 72 | 63 | -67 | -38 |
| E150N R1 | 50 | 75 | 94 | 94 | 74 | 67 | -67 | -40 |
| * Italics indicate calculated demand exceeds calculated ACI capacity. | | | | | | | | |

Table 6.17 Maximum Unbalanced Moments at Slab-Column Connections, Floor 1

| Maximum Unbalanced Moments (Inch-Kips): Floor 2 | | | | | | | |
|---|-----------------------|----------------|------------------|--|-----------------------|---|----------|
| Analysis | Interior Connections | | | | | Exterior Connections | |
| | Connection Capacities | | | Calculated ETABS Dynamic Analysis* | Capacities Eq 6.15 | Calculated ETABS Dynamic Analysis | |
| | Flexure Eq. 6.7 | Punching Shear | | | | | |
| | | Eq. 6.8 | Eq. 6.8 Modified | | | | Eq. 6.13 |
| | | | | | | | |
| E050DL | 50 | 74 | 93 | 66 | 48 | -67 | -45 |
| E100DL | 50 | 74 | 93 | 77 | 72 | -67 | -57 |
| E150DL | 50 | 74 | 93 | 74 | 69 | -67 | -49 |
| E200DL | 50 | 74 | 93 | 84 | 71 | -67 | -53 |
| E025N | 50 | 74 | 93 | 80 | 11 | -67 | -22 |
| E050N | 50 | 74 | 93 | 77 | 17 | -67 | -24 |
| E100N | 50 | 74 | 93 | 70 | 34 | -67 | -31 |
| E125N | 50 | 74 | 93 | 65 | 49 | -67 | -36 |
| E150N R1 | 50 | 74 | 93 | 65 | 48 | -67 | -38 |
| * Italics indicate calculated demand exceeds calculated ACI capacity. | | | | | | | |

Table 6.18 Maximum Unbalanced Moments at Slab-Column Connections, Floor 2

| Maximum Unbalanced Moments (Inch-Kips): Floor 3 | | | | | | | | | |
|---|-----------------------|----------------|------------------|----------|------------|--|-----------------------|---|--|
| Analysis | Interior Connections | | | | | | Exterior Connections | | |
| | Connection Capacities | | | | | Calculated ETABS Dynamic Analysis* | Capacities Eq 6.15 | Calculated ETABS Dynamic Analysis | |
| | Flexure Eq. 6.7 | Punching Shear | | | Eq. 6.13 | | | | |
| | | Eq. 6.8 | Eq. 6.8 Modified | Eq. 6.13 | | | | | |
| | | | | | | | | | |
| E050DL | 50 | 77 | 96 | 70 | 32 | -67 | -40 | | |
| E100DL | 50 | 77 | 96 | 81 | 69 | -67 | -62 | | |
| E150DL | 50 | 77 | 96 | 94 | 93 | -67 | -74 | | |
| E200DL | 50 | 77 | 96 | 112 | 124 | -67 | -91 | | |
| E025N | 50 | 77 | 96 | 74 | 13 | -67 | -23 | | |
| E050N | 50 | 77 | 96 | 68 | 25 | -67 | -28 | | |
| E100N | 50 | 77 | 96 | 73 | 56 | -67 | -41 | | |
| E125N | 50 | 77 | 96 | 83 | 74 | -67 | -49 | | |
| E150N R1 | 50 | 77 | 96 | 83 | 78 | -67 | -53 | | |
| * Italics indicate calculated demand exceeds calculated ACI capacity. | | | | | | | | | |

Table 6.19 Maximum Unbalanced Moments at Slab-Column Connections, Floor 3

| Analysis | FEMA 273 Procedure | Maximum Column Forces: Interior Column, Floor 1 | | | | | | | | | | | |
|------------|--------------------------|---|----------------------------|----------------------------------|----------------------------------|----------------------------|--|----------------------------------|----------------------------|----------------------------------|----------------------------------|----------------------------|--|
| | | Top of Column | | | | | | Bottom of Column | | | | | |
| | | Capacities | | | Calculated | | | Capacities | | | Calculated | | |
| | | Moment ¹ Inch-kips | Shear ² Kips | Axial Force ³ Kips | Moment ⁴ Inch-kips | Shear ⁴ Kips | | Moment ¹ Inch-kips | Shear ² Kips | Axial Force ³ Kips | Moment ⁴ Inch-kips | Shear ⁴ Kips | |
| FEMA 273-D | LDP | 80 | 8.5 | -14.7 | 52 | 9.2 | | 80 | 6.5 | -14.7 | 95 | 4.1 | |
| FEMA 273-D | LSP-1 | 80 | 8.5 | -14.8 | 49 | 9.5 | | 80 | 6.5 | -14.7 | 97 | 4.1 | |
| FEMA 273-D | LSP-2 | 80 | 8.5 | -14.8 | 70 | 13.6 | | 80 | 6.5 | -14.7 | 139 | 5.9 | |
| FEMA 273-D | LSP-3 | 80 | 8.5 | -14.8 | 78 | 15.1 | | 80 | 6.5 | -14.7 | 154 | 6.5 | |
| FEMA 273-N | LDP | 80 | 8.5 | -14.7 | 103 | 7.8 | | 80 | 6.5 | -14.7 | 190 | 7.8 | |
| FEMA 273-N | LSP | 80 | 8.5 | -14.8 | 95 | 7.5 | | 80 | 6.5 | -14.8 | 186 | 7.5 | |

1. Computed using interaction diagrams of Figures 6.1 - 6.4 and calculated axial forces.

2. See section 6.2.(a).

3. At *approximate* time of most severe combination of moment & axial force, (+) indicates net tension, (-) indicates net compression.

4. Italicized quantities indicate calculated demand exceeds calculated capacity.

Table 6.20 FEMA 273 Maximum Column Forces: Interior Column, Floor 1

| | | Maximum Column Forces: Interior Column, Floor 2 | | | | | | | | | | | |
|------------|--------------------|---|----------------------------|----------------------------------|----------------------------------|----------------------------|--|----------------------------------|----------------------------|----------------------------------|----------------------------------|----------------------------|--|
| Analysis | FEMA 273 Procedure | Top of Column | | | | | | Bottom of Column | | | | | |
| | | Capacities | | | Calculated | | | Capacities | | | Calculated | | |
| | | Moment ¹ Inch-kips | Shear ² Kips | Axial Force ³ Kips | Moment ⁴ Inch-kips | Shear ⁴ Kips | | Moment ¹ Inch-kips | Shear ² Kips | Axial Force ³ Kips | Moment ⁴ Inch-kips | Shear ⁴ Kips | |
| FEMA 273-D | LDP | 70 | 8.5 | -9.7 | 77 | 9.7 | | 70 | 6.5 | -9.7 | 59 | 3.8 | |
| FEMA 273-D | LSP-1 | 70 | 8.5 | -9.7 | 78 | 10.2 | | 70 | 6.5 | -9.7 | 60 | 3.9 | |
| FEMA 273-D | LSP-2 | 70 | 8.5 | -9.7 | 111 | 14.5 | | 70 | 6.5 | -9.7 | 86 | 5.6 | |
| FEMA 273-D | LSP-3 | 70 | 8.5 | -9.7 | 123.7 | 16.2 | | 70 | 6.5 | -9.7 | 95.5 | 6.2 | |
| FEMA 273-N | LDP | 70 | 8.5 | -9.7 | 164 | 7.4 | | 70 | 6.5 | -9.7 | 118 | 7.4 | |
| FEMA 273-N | LSP | 70 | 8.5 | -9.7 | 178 | 8.5 | | 70 | 6.5 | -9.7 | 142 | 8.5 | |

1. Computed using interaction diagrams of Figures 6.1 - 6.4 and calculated axial forces.

2. See section 6.2.(a).

3. At *approximate* time of most severe combination of moment & axial force, (+) indicates net tension, (-) indicates net compression.

4. Italicized quantities indicate calculated demand exceeds calculated capacity.

Table 6.21 FEMA 273 Maximum Column Forces: Interior Column, Floor 2

| Maximum Column Forces: Interior Column, Floor 3 | | | | | | | | | | | | | |
|---|--------------------|----------------------------------|----------------------------|----------------------------------|----------------------------------|----------------------------|--|----------------------------------|----------------------------|----------------------------------|----------------------------------|----------------------------|--|
| Analysis | FEMA 273 Procedure | Top of Column | | | | | | Bottom of Column | | | | | |
| | | Capacities | | | Calculated | | | Capacities | | | Calculated | | |
| | | Moment ¹ Inch-kips | Shear ² Kips | Axial Force ³ Kips | Moment ⁴ Inch-kips | Shear ⁴ Kips | | Moment ¹ Inch-kips | Shear ² Kips | Axial Force ³ Kips | Moment ⁴ Inch-kips | Shear ⁴ Kips | |
| FEMA 273-D | LDP | 60 | 8.5 | -4.6 | 49 | 5.7 | | 60 | 6.5 | -4.6 | 17 | 1.9 | |
| FEMA 273-D | LSP-1 | 60 | 8.5 | -4.7 | 53 | 6.3 | | 60 | 6.5 | -4.6 | 19 | 2.1 | |
| FEMA 273-D | LSP-2 | 60 | 8.5 | -4.7 | 75 | 9.0 | | 60 | 6.5 | -4.6 | 27 | 3.0 | |
| FEMA 273-D | LSP-3 | 60 | 8.5 | -4.7 | 84 | 10.0 | | 60 | 6.5 | -4.7 | 30 | 3.3 | |
| FEMA 273-N | LDP | 60 | 8.5 | -4.6 | 120 | 4.6 | | 60 | 6.5 | -4.6 | 54 | 4.6 | |
| FEMA 273-N | LSP | 60 | 8.5 | -4.7 | 139 | 5.1 | | 60 | 6.5 | -4.7 | 54 | 5.1 | |

1. Computed using interaction diagrams of Figures 6.1 - 6.4 and calculated axial forces.

2. See section 6.2.(a).

3. At approximate time of most severe combination of moment & axial force, (+) indicates net tension, (-) indicates net compression.

4. Italicized quantities indicate calculated demand exceeds calculated capacity.

Table 6.22 FEMA 273 Maximum Column Forces: Interior Column, Floor 3

| | | Maximum Column Forces: Exterior Column, Floor 1 | | | | | | | | | |
|------------|--------------------|---|----------------------------|----------------------------------|----------------------------------|---------------|----------------------------------|----------------------------|----------------------------------|----------------------------------|---------------|
| Analysis | FEMA 273 Procedure | Top of Column | | | | | Bottom of Column | | | | |
| | | Capacities | | Calculated | | | Capacities | | Calculated | | |
| | | Moment ¹ Inch-kips | Shear ² Kips | Axial Force ³ Kips | Moment ⁴ Inch-kips | Shear Kips | Moment ¹ Inch-kips | Shear ² Kips | Axial Force ³ Kips | Moment ⁴ Inch-kips | Shear Kips |
| FEMA 273-D | LDP | 50 | 9.9 | -0.8 | 38 | 4.4 | 95 | 12.4 | 0.5 | 111 | 7.0 |
| FEMA 273-D | LSP-1 | 50 | 9.9 | -0.2 | 35 | 4.4 | 95 | 12.4 | 1.2 | 114 | 7.2 |
| FEMA 273-D | LSP-2 | 48 | 9.9 | 2.9 | 52 | 6.3 | 90 | 12.4 | 4.9 | 164 | 10.1 |
| FEMA 273-D | LSP-3 | 49 | 9.9 | 1.3 | 57 | 7.0 | 92 | 12.4 | 3.5 | 182 | 11.3 |
| FEMA 273-N | LDP | 49 | 9.9 | 0.6 | 68 | 8.0 | 95 | 12.4 | 0.6 | 223 | 8.0 |
| FEMA 273-N | LSP | 48 | 9.9 | 2.4 | 60 | 7.9 | 93 | 12.4 | 2.4 | 226 | 7.6 |

1. Computed using interaction diagrams of Figures 6.1 - 6.4 and calculated axial forces.
2. See section 6.2.(a).
3. At *approximate* time of most severe combination of moment & axial force, (+) indicates net tension, (-) indicates net compression.
4. Italicized quantities indicate calculated demand exceeds calculated capacity.

Table 6.23 FEMA 273 Maximum Column Forces: Exterior Column, Floor 1

| | | Maximum Column Forces: Exterior Column, Floor 2 | | | | | | | | | | | |
|------------|--------------------|---|----------------------------|----------------------------------|----------------------------------|---------------|--|----------------------------------|----------------------------|----------------------------------|----------------------------------|---------------|--|
| Analysis | FEMA 273 Procedure | Top of Column | | | | | | Bottom of Column | | | | | |
| | | Capacities | | | Calculated | | | Capacities | | | Calculated | | |
| | | Moment ¹ Inch-kips | Shear ² Kips | Axial Force ³ Kips | Moment ⁴ Inch-kips | Shear Kips | | Moment ¹ Inch-kips | Shear ² Kips | Axial Force ³ Kips | Moment ⁴ Inch-kips | Shear Kips | |
| FEMA 273-D | LDP | 55 | 9.9 | -1.8 | 46 | 2.7 | | 50 | 12.4 | -0.1 | 31 | 5.7 | |
| FEMA 273-D | LSP-1 | 54 | 9.9 | -1.2 | 42 | 2.8 | | 48 | 12.4 | 0.4 | 27 | 6.0 | |
| FEMA 273-D | LSP-2 | 48 | 9.9 | 0.3 | 63 | 3.9 | | 46 | 12.4 | 2.6 | 42 | 6.4 | |
| FEMA 273-D | LSP-3 | 54 | 9.9 | -0.9 | 68 | 4.4 | | 47 | 12.4 | 1.7 | 45 | 8.4 | |
| FEMA 273-N | LDP | 55 | 9.9 | -0.1 | 97 | 5.2 | | 50 | 12.4 | -0.1 | 80 | 5.2 | |
| FEMA 273-N | LSP | 47 | 9.9 | 0.9 | 95 | 5.0 | | 47 | 12.4 | 0.9 | 91 | 5.0 | |

1. Computed using interaction diagrams of Figures 6.1 - 6.4 and calculated axial forces.

2. See section 6.2.(a).

3. At *approximate* time of most severe combination of moment & axial force, (+) indicates net tension, (-) indicates net compression.

4. Italicized quantities indicate calculated demand exceeds calculated capacity.

Table 6.24 FEMA 273 Maximum Column Forces: Exterior Column, Floor 2

| Analysis | FEMA 273 Procedure | Maximum Column Forces: Exterior Column, Floor 3 | | | | | | | | | | | |
|------------|--------------------|---|----------------------------|----------------------------------|---------------------|---------------|--|----------------------------------|----------------------------|----------------------------------|----------------------------------|---------------|--|
| | | Top of Column | | | | | | Bottom of Column | | | | | |
| | | Capacities | | | Calculated | | | Capacities | | | Calculated | | |
| | | Moment ¹ Inch-kips | Shear ² Kips | Axial Force ³ Kips | Moment Inch-kips | Shear Kips | | Moment ¹ Inch-kips | Shear ² Kips | Axial Force ³ Kips | Moment ⁴ Inch-kips | Shear Kips | |
| FEMA 273-D | LDP | 54 | 9.9 | -1.6 | 26 | 1.4 | | 55 | 12.4 | -0.6 | 2 | 3.3 | |
| FEMA 273-D | LSP-1 | 54 | 9.9 | -1.4 | 26 | 1.6 | | 54 | 12.4 | -0.3 | 3 | 3.8 | |
| FEMA 273-D | LSP-2 | 53 | 9.9 | -1.0 | 41 | 2.1 | | 50 | 12.4 | 0.6 | 1 | 5.1 | |
| FEMA 273-D | LSP-3 | 54 | 9.9 | -1.7 | 43 | 2.4 | | 50 | 12.4 | 0.0 | 3 | 5.9 | |
| FEMA 273-N | LDP | 52 | 9.9 | -0.5 | 69 | 3.3 | | 55 | 12.4 | -0.5 | 44 | 3.3 | |
| FEMA 273-N | LSP | 56 | 9.9 | -4.4 | 92 | 3.6 | | 58 | 12.4 | -4.4 | 42 | 3.6 | |

1. Computed using interaction diagrams of Figures 6.1 - 6.4 and calculated axial forces.
2. See section 6.2.(a).
3. At *approximate* time of most severe combination of moment & axial force, (+) indicates net tension, (-) indicates net compression.
4. Italicized quantities indicate calculated demand exceeds calculated capacity.

Table 6.25 FEMA 273 Maximum Column Forces: Exterior Column, Floor 3

| Analysis | FEMA 273 Procedure | Maximum Unbalanced Moments (Inch-Kips): Floor 1 | | | | | |
|------------|--------------------------|---|-----------------------|---------------------|-----------------------|---------------------|--|
| | | Interior Connections | | | Exterior Connections | | |
| | | Connection Capacities | | Calculated ETABS | Capacities Eq 6.15 | Calculated ETABS | |
| | | <i>Flexure</i> | <i>Punching Shear</i> | | | | |
| | | Eq. 6.7 ¹ | Eq. 6.8 | | | | |
| FEMA 273-D | LDP | 70 | 75 | 134 | -67 | -94 | |
| FEMA 273-D | LSP-1 | 70 | 75 | 114 | -67 | -86 | |
| FEMA 273-D | LSP-2 | 70 | 75 | 201 | -67 | -131 | |
| FEMA 273-D | LSP-3 | 70 | 75 | 201 | -67 | -141 | |
| FEMA 273-N | LDP | 70 | 75 | 259 | -67 | -156 | |
| FEMA 273-N | LSP | 70 | 75 | 288 | -67 | -176 | |

1. Equation 6.7 is modified here use wider effective slab width of FEMA 273, 6.5.4.3.

2. Italicized quantities indicate calculated demand exceeds calculated capacity.

Table 6.26 FEMA 273 Maximum Unbalanced Moments at Slab-Column Connections, Floor 1

| Analysis | FEMA 273 Procedure | Maximum Unbalanced Moments (Inch-Kips): Floor 2 | | | | | |
|------------|--------------------------|---|----------------------------------|---------------------|-----------------------|---------------------|--|
| | | Interior Connections | | | Exterior Connections | | |
| | | Connection Capacities | | Calculated ETABS | Capacities Eq 6.15 | Calculated ETABS | |
| | | <i>Flexure</i> Eq. 6.7 ¹ | <i>Punching Shear</i> Eq. 6.8 | | | | |
| FEMA 273-D | LDP | 70 | 75 | 103 | -67 | -73 | |
| FEMA 273-D | LSP-1 | 70 | 75 | 92 | -67 | -60 | |
| FEMA 273-D | LSP-2 | 70 | 75 | 162 | -67 | -110 | |
| FEMA 273-D | LSP-3 | 70 | 75 | 162 | -67 | -108 | |
| FEMA 273-N | LDP | 70 | 75 | 210 | -67 | -129 | |
| FEMA 273-N | LSP | 70 | 75 | 256 | -67 | -158 | |

1. Equation 6.7 is modified here use wider effective slab width of FEMA 273, 6.5.4.3.
2. Italicized quantities indicate calculated demand exceeds calculated capacity.

Table 6.27 FEMA 273 Maximum Unbalanced Moments at Slab-Column Connections, Floor 2

| Analysis | FEMA 273 Procedure | Maximum Unbalanced Moments (Inch-Kips): Floor 3 | | | | | |
|------------|--------------------------|---|----------------------------------|---------------------|-----------------------|---------------------|--|
| | | Interior Connections | | | Exterior Connections | | |
| | | Connection Capacities | | Calculated ETABS | Capacities Eq 6.15 | Calculated ETABS | |
| | | <i>Flexure</i> Eq. 6.7 ¹ | <i>Punching Shear</i> Eq. 6.8 | | | | |
| FEMA 273-D | LDP | 70 | 75 | 57 | -67 | -52 | |
| FEMA 273-D | LSP-1 | 70 | 75 | 66 | -67 | -59 | |
| FEMA 273-D | LSP-2 | 70 | 75 | 94 | -67 | -74 | |
| FEMA 273-D | LSP-3 | 70 | 75 | 105 | -67 | -88 | |
| FEMA 273-N | LDP | 70 | 75 | 132 | -67 | -90 | |
| FEMA 273-N | LSP | 70 | 75 | 156 | -67 | -105 | |

1. Equation 6.7 is modified here use wider effective slab width of FEMA 273, 6.5.4.3.
2. Italicized quantities indicate calculated demand exceeds calculated capacity.

Table 6.28 FEMA 273 Maximum Unbalanced Moments at Slab-Column Connections, Floor 3

| Analysis | FEMA 273 Procedure | Column Tops | | | | Column Bases | | | |
|------------|--------------------------|---|--------|------|----------|---|--------|------|----------|
| | | Moment, Inch-Kips | | DCR | Eq. 6.38 | Moment, Inch-Kips | | DCR | Eq. 6.38 |
| | | Capacity Based on Flexure at Applied Axial Load | Demand | | | Capacity Based on Flexure at Applied Axial Load | Demand | | |
| | | | | | | | | | |
| Floor 1 | | | | | | | | | |
| FEMA 273-D | LDP | 80 | 52 | 0.65 | 0.33 | 80 | 95 | 1.19 | 0.59 |
| FEMA 273-D | LSP-3 | 80 | 78 | 0.98 | 0.49 | 80 | 154 | 1.93 | 0.96 |
| FEMA 273-N | LDP | 80 | 103 | 1.29 | 0.64 | 80 | 190 | 2.38 | 1.19 |
| FEMA 273-N | LSP | 80 | 95 | 1.19 | 0.59 | 80 | 186 | 2.33 | 1.16 |
| Floor 2 | | | | | | | | | |
| FEMA 273-D | LDP | 70 | 77 | 1.10 | 0.55 | 70 | 59 | 0.84 | 0.42 |
| FEMA 273-D | LSP-3 | 70 | 124 | 1.77 | 0.89 | 70 | 96 | 1.37 | 0.69 |
| FEMA 273-N | LDP | 70 | 164 | 2.34 | 1.17 | 70 | 118 | 1.69 | 0.84 |
| FEMA 273-N | LSP | 70 | 178 | 2.54 | 1.27 | 70 | 142 | 2.03 | 1.01 |
| Floor 3 | | | | | | | | | |
| FEMA 273-D | LDP | 60 | 49 | 0.82 | 0.41 | 60 | 17 | 0.28 | 0.14 |
| FEMA 273-D | LSP-3 | 60 | 84 | 1.40 | 0.70 | 60 | 30 | 0.50 | 0.25 |
| FEMA 273-N | LDP | 60 | 120 | 2.00 | 1.00 | 60 | 54 | 0.90 | 0.45 |
| FEMA 273-N | LSP | 60 | 139 | 2.32 | 1.16 | 60 | 54 | 0.90 | 0.45 |

Table 6.29 FEMA 273 Acceptance Criteria Checks for Interior Columns

| Analysis | FEMA 273 Procedure | Column Tops | | | | Column Bases | | | |
|------------|--------------------------|---|--------|------|----------|---|--------|------|----------|
| | | Moment, Inch-Kips | | DCR | Eq. 6.38 | Moment, Inch-Kips | | DCR | Eq. 6.38 |
| | | Capacity Based on Flexure at Applied Axial Load | Demand | | | Capacity Based on Flexure at Applied Axial Load | Demand | | |
| | | | | | | | | | |
| | | Floor 1 | | | | | | | |
| FEMA 273-D | LDP | 50 | 38 | 0.76 | 0.38 | 95 | 111 | 1.17 | 0.58 |
| FEMA 273-D | LSP-3 | 49 | 57 | 1.16 | 0.58 | 92 | 182 | 1.98 | 0.99 |
| FEMA 273-N | LDP | 49 | 68 | 1.39 | 0.69 | 95 | 223 | 2.35 | 1.17 |
| FEMA 273-N | LSP | 48 | 60 | 1.25 | 0.63 | 93 | 226 | 2.43 | 1.22 |
| | | Floor 2 | | | | | | | |
| FEMA 273-D | LDP | 55 | 46 | 0.84 | 0.42 | 50 | 31 | 0.62 | 0.31 |
| FEMA 273-D | LSP-3 | 54 | 68 | 1.26 | 0.63 | 47 | 45 | 0.96 | 0.48 |
| FEMA 273-N | LDP | 55 | 97 | 1.76 | 0.88 | 50 | 80 | 1.60 | 0.80 |
| FEMA 273-N | LSP | 47 | 95 | 2.02 | 1.01 | 47 | 91 | 1.94 | 0.97 |
| | | Floor 3 | | | | | | | |
| FEMA 273-D | LDP | 54 | 26 | 0.48 | 0.24 | 55 | 2 | 0.04 | 0.02 |
| FEMA 273-D | LSP-3 | 54 | 43 | 0.80 | 0.40 | 50 | 3 | 0.06 | 0.03 |
| FEMA 273-N | LDP | 52 | 69 | 1.33 | 0.66 | 55 | 44 | 0.80 | 0.40 |
| FEMA 273-N | LSP | 56 | 92 | 1.64 | 0.82 | 58 | 42 | 0.72 | 0.36 |

Table 6.30 FEMA 273 Acceptance Criteria Checks for Exterior Columns

| Analysis | FEMA 273 Procedure | Interior Connections | | | | Exterior Connections | | | |
|------------|--------------------------|--|--------|------|----------|---------------------------------|--------|------|----------|
| | | Moment, Inch-Kips | | DCR | Eq. 6.38 | Moment, Inch-Kips | | DCR | Eq. 6.38 |
| | | Capacity Based on Combined Shear-Moment Transfer | Demand | | | Capacity Based on Flexure | Demand | | |
| | | | | | | | | | |
| Floor 1 | | | | | | | | | |
| FEMA 273-D | LDP | 75 | 134 | 1.79 | 1.10 | -67 | -94 | 1.40 | 0.86 |
| FEMA 273-D | LSP-3 | 75 | 201 | 2.67 | 1.65 | -67 | -141 | 2.10 | 1.29 |
| FEMA 273-N | LDP | 75 | 259 | 3.45 | 2.13 | -67 | -156 | 2.33 | 1.43 |
| FEMA 273-N | LSP | 75 | 288 | 3.84 | 2.36 | -67 | -176 | 2.63 | 1.62 |
| Floor 2 | | | | | | | | | |
| FEMA 273-D | LDP | 75 | 103 | 1.37 | 0.85 | -67 | -73 | 1.09 | 0.67 |
| FEMA 273-D | LSP-3 | 75 | 162 | 2.16 | 1.33 | -67 | -108 | 1.61 | 0.99 |
| FEMA 273-N | LDP | 75 | 210 | 2.80 | 1.72 | -67 | -129 | 1.93 | 1.18 |
| FEMA 273-N | LSP | 75 | 256 | 3.41 | 2.10 | -67 | -158 | 2.36 | 1.45 |
| Floor 3 | | | | | | | | | |
| FEMA 273-D | LDP | 75 | 57 | 0.76 | 0.47 | -67 | -52 | 0.78 | 0.48 |
| FEMA 273-D | LSP-3 | 75 | 105 | 1.40 | 0.86 | -67 | -88 | 1.32 | 0.81 |
| FEMA 273-N | LDP | 75 | 132 | 1.76 | 1.08 | -67 | -90 | 1.34 | 0.83 |
| FEMA 273-N | LSP | 75 | 156 | 2.08 | 1.28 | -67 | -105 | 1.57 | 0.96 |

Table 6.31 FEMA 273 Acceptance Criteria Checks for Slab-Column Connections



Figure 2.1 Prototype Barracks Building, Fort Lewis, WA

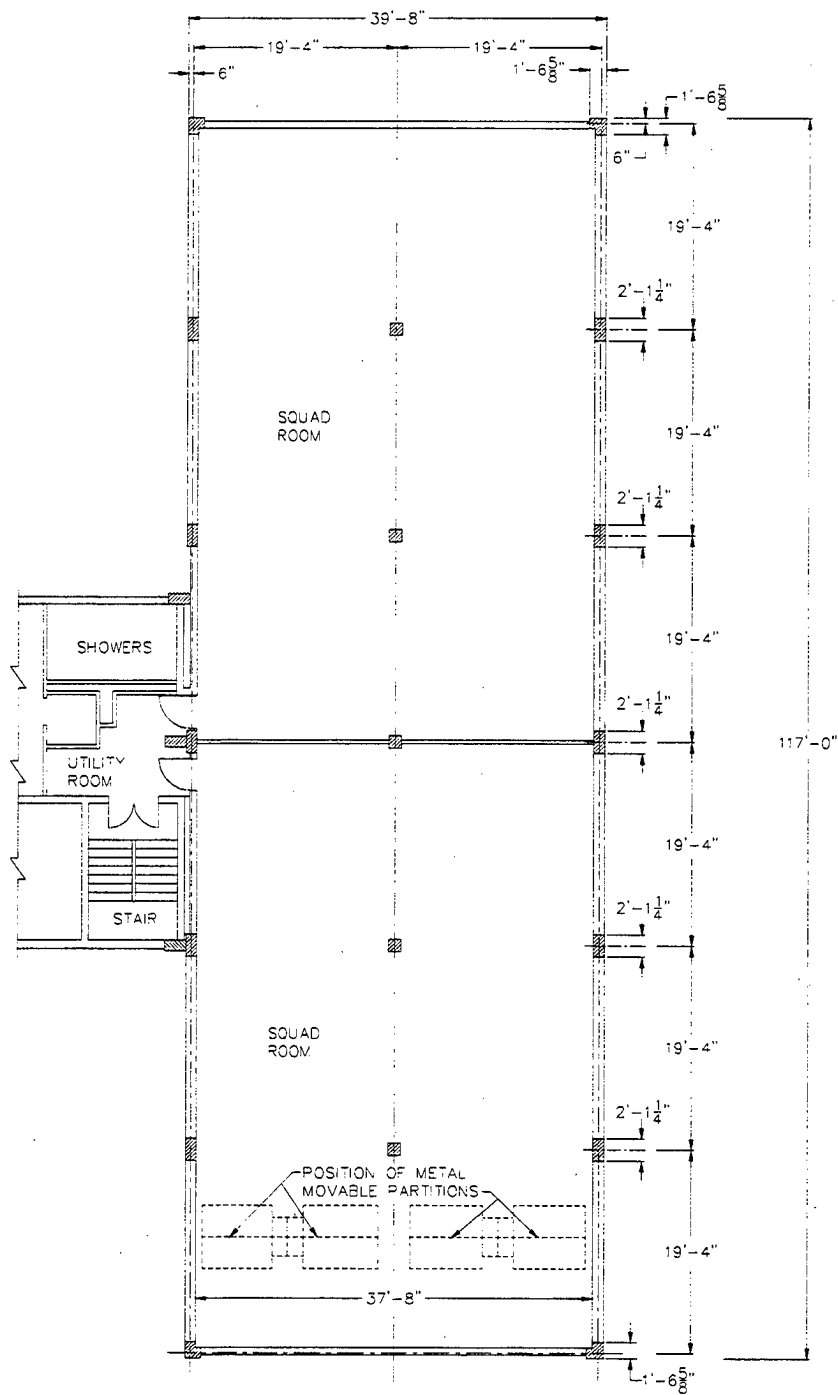


Figure 2.3 As-Built Drawings of Prototype Building, Second and Third Floor Plans

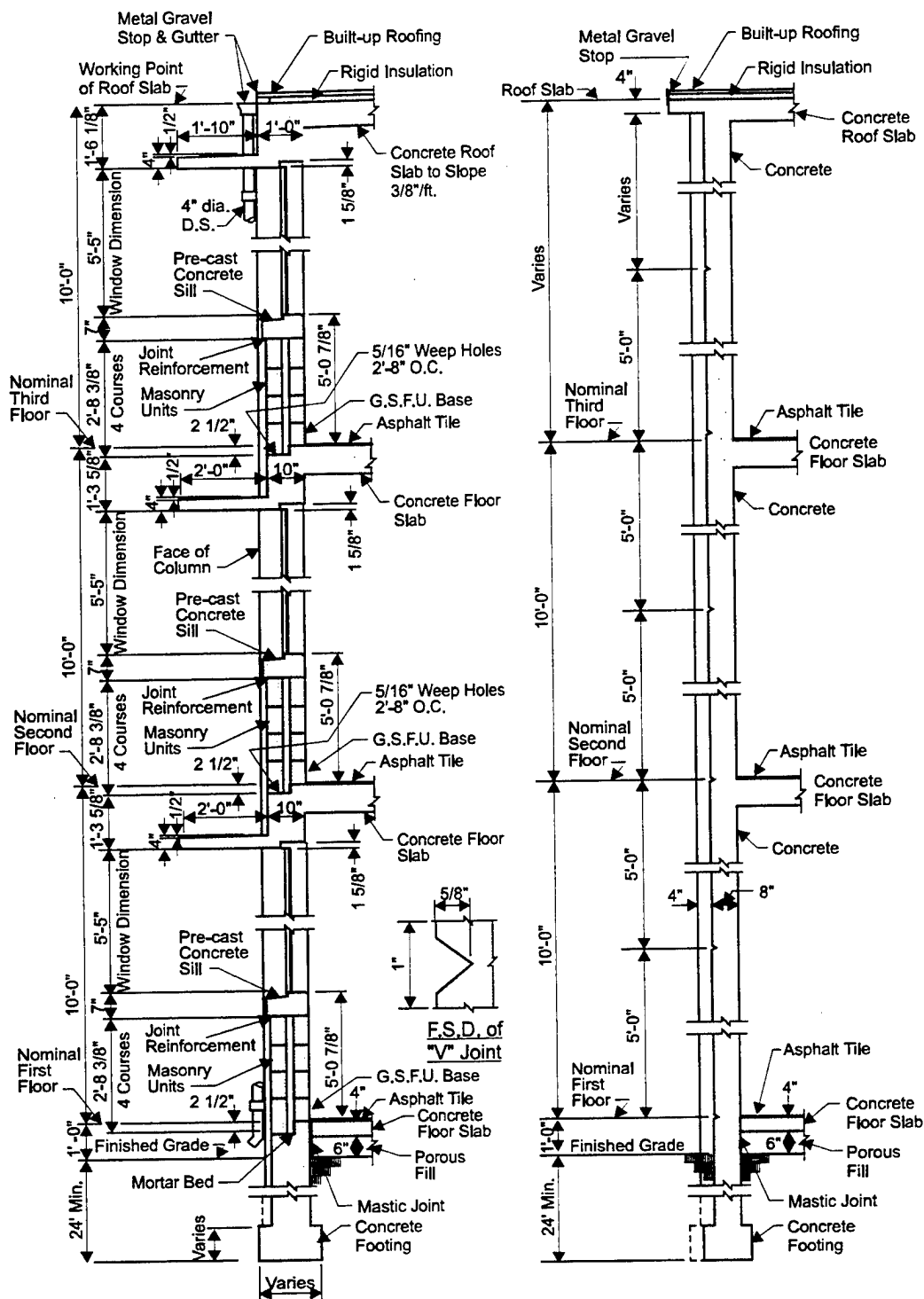


Figure 2.4 As-Built Drawing of Prototype Building, Exterior Wall Sections

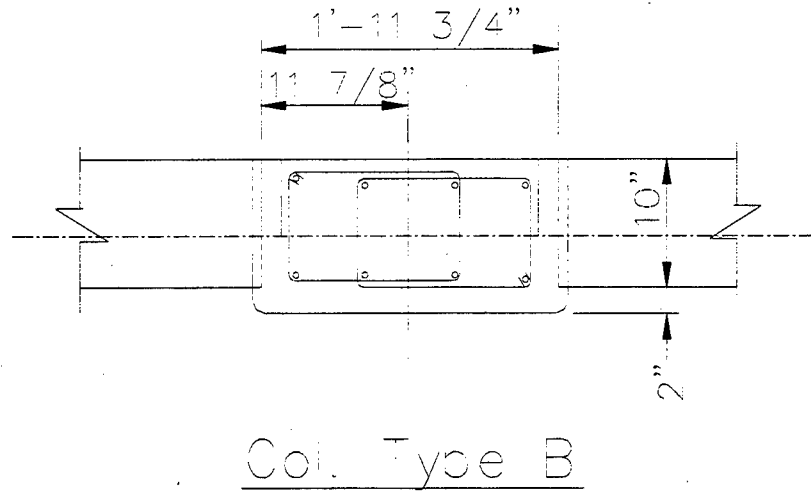


Figure 2.5 As-Built Drawing of Prototype Building, Exterior Column Detail

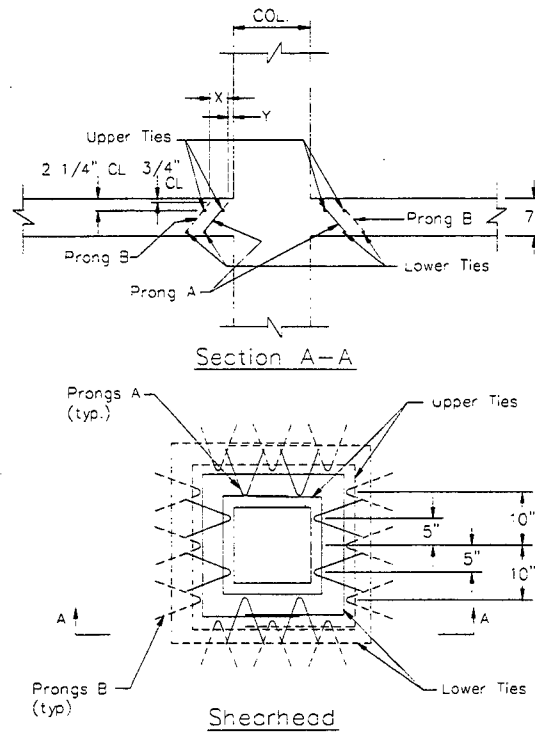


Figure 2.6 As-Built Drawing of Prototype Building,
Interior Column Shearhead Detail

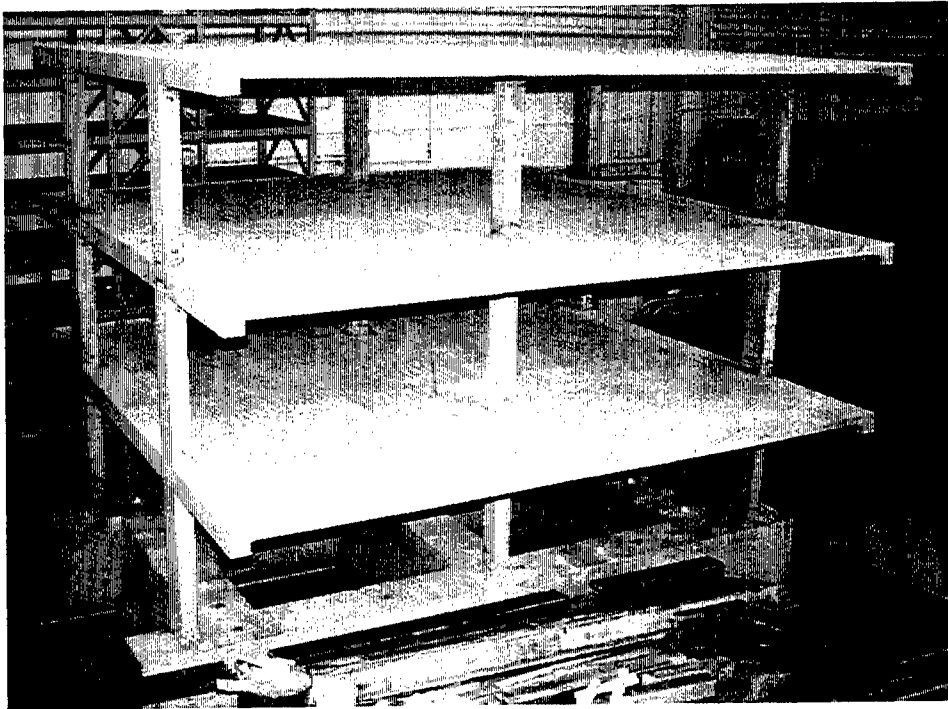


Figure 2.7 Post-Construction View of Model, East Side

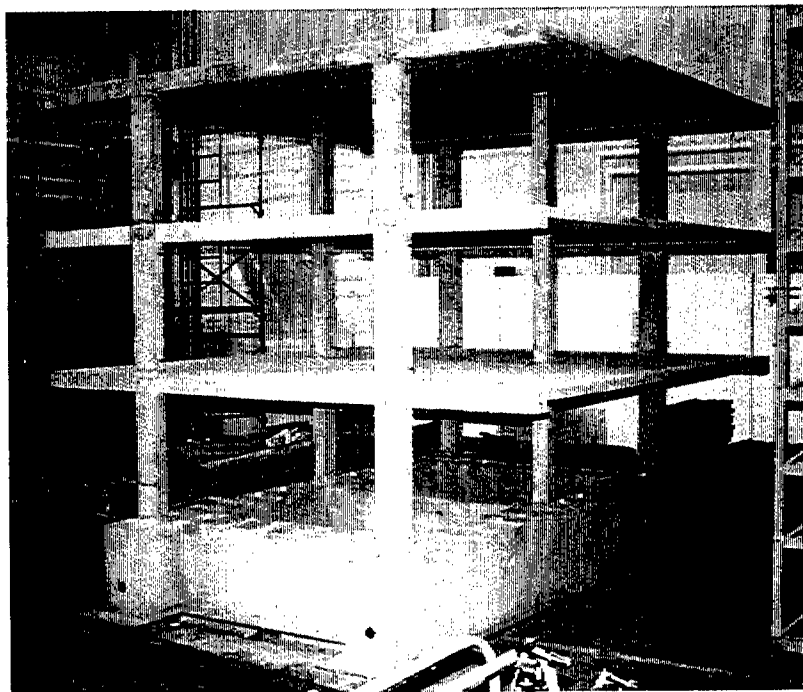


Figure 2.8 Post-Construction View of Model, North Side

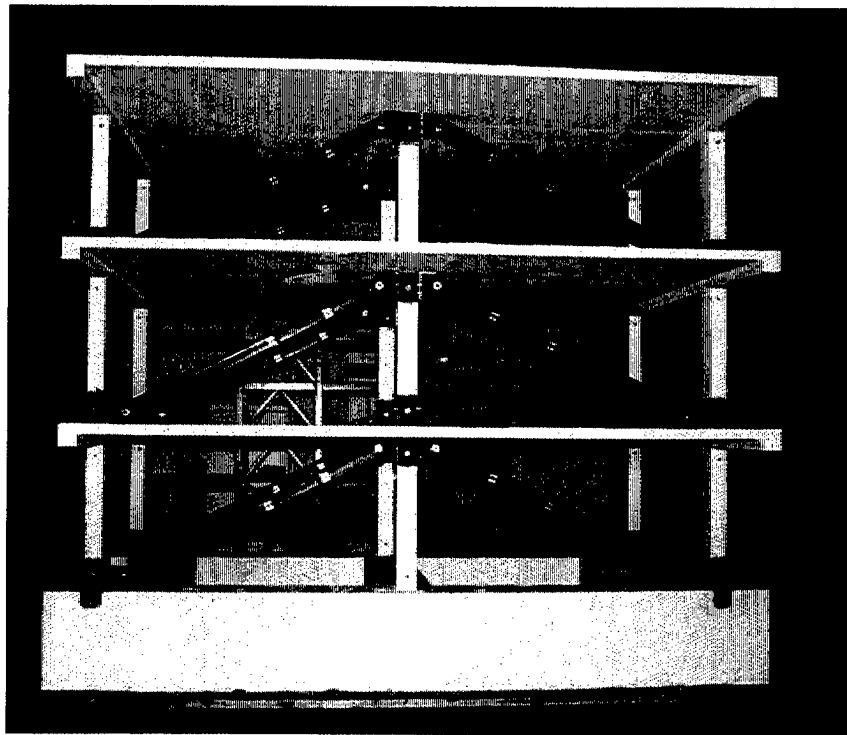


Figure 2.9 Bare Model Prior to Placement on Shaking Table

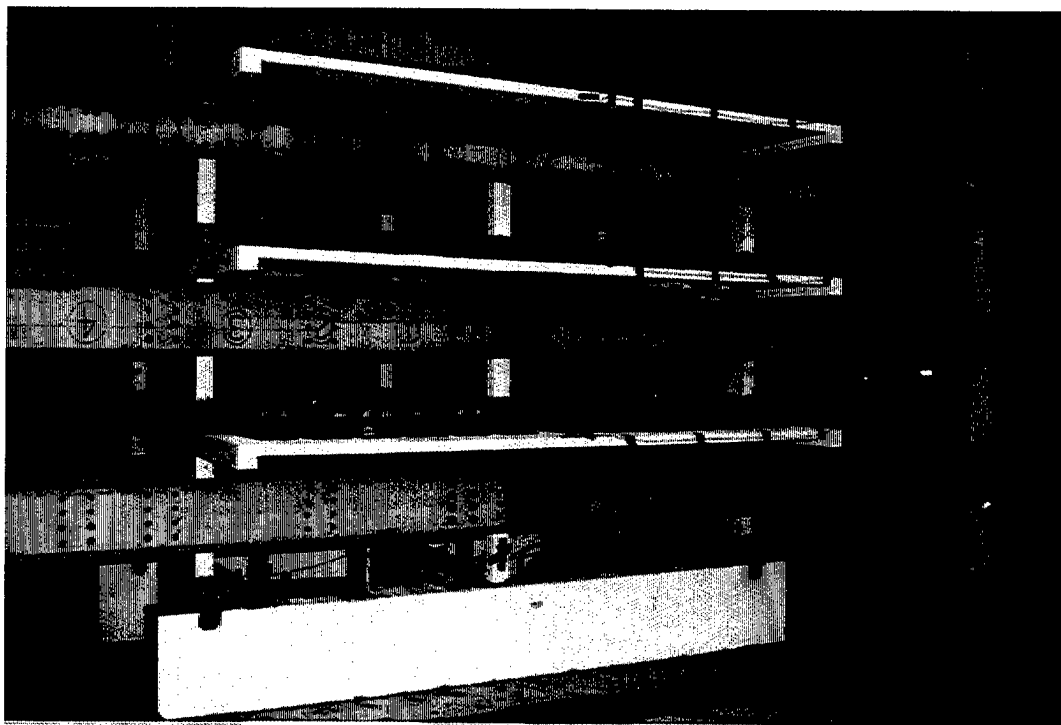


Figure 2.10 Model After Placement on Shaking Table (Safety Frame in Place)

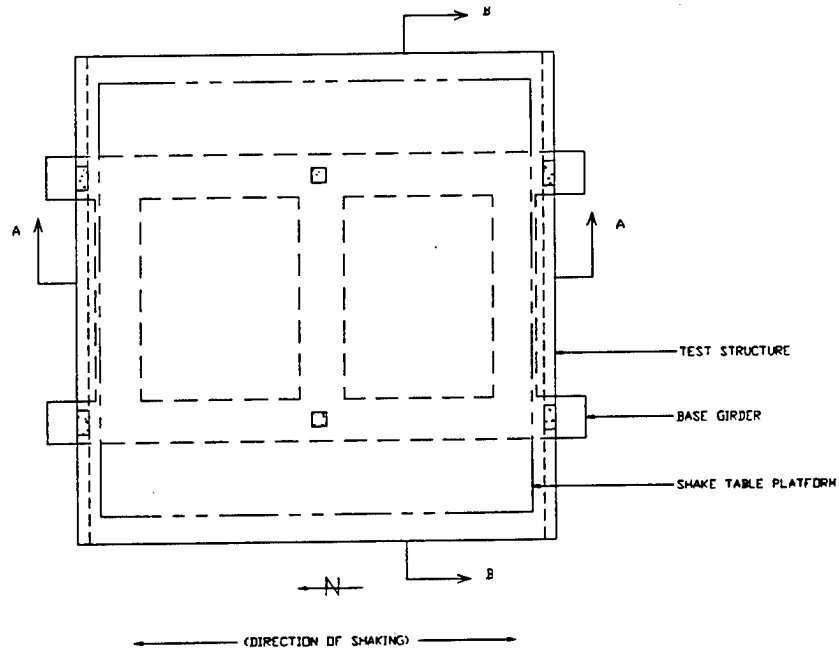


Figure 2.11 Plan View of Model on Shaking Table Platform

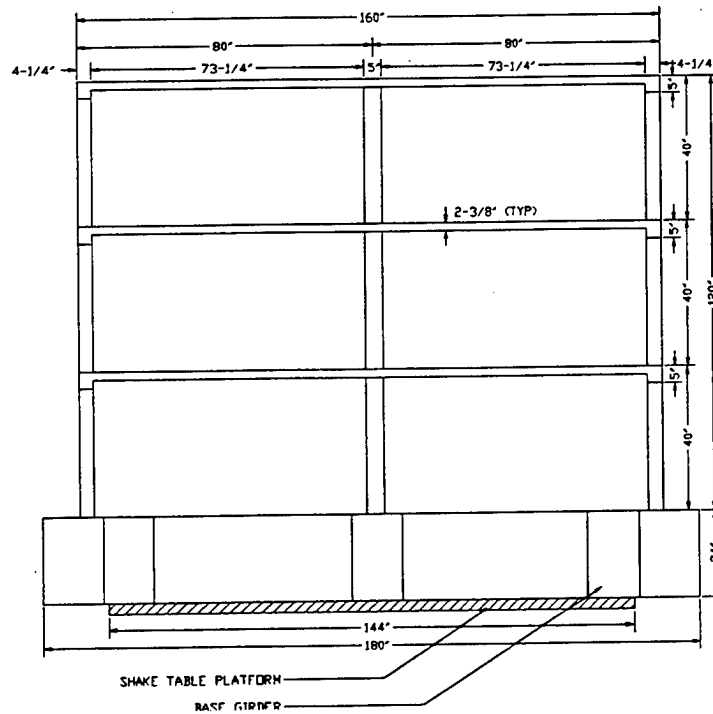


Figure 2.12 Model Elevation, Section A-A

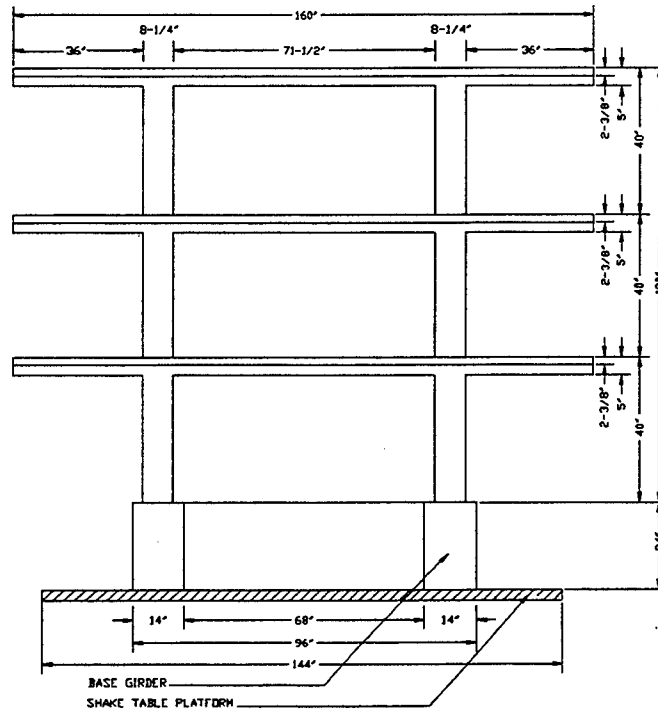


Figure 2.13 Model Elevation, Section B-B

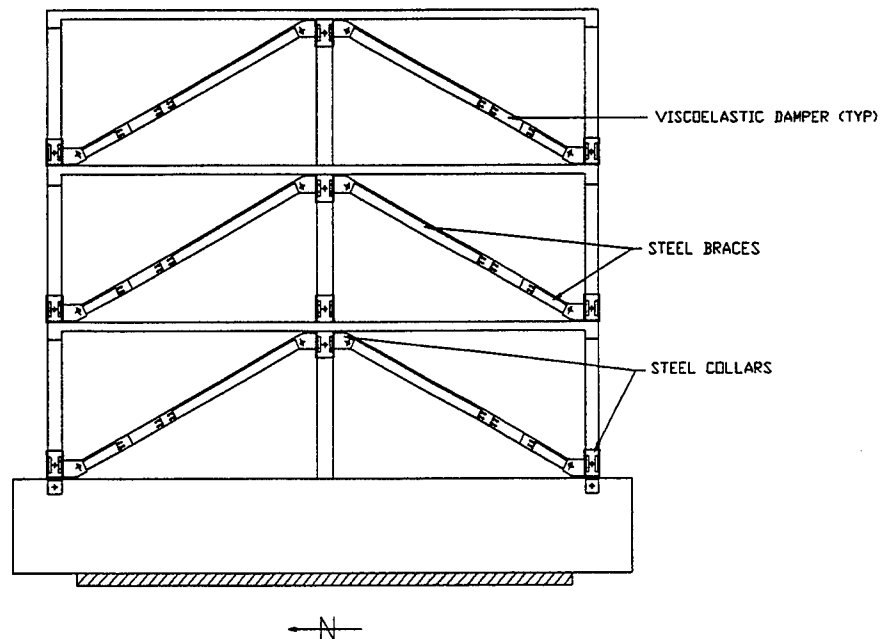
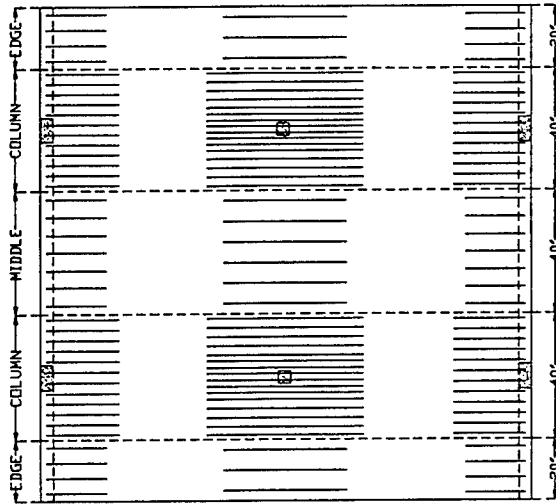
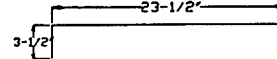


Figure 2.14 Model Elevation, Dampers in Place

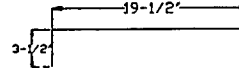


NOTES :
=====

- ① EACH COLUMN STRIP, CENTERLINE COLUMN: 16 D5 @ 50', STRAIGHT, WITH 8 D5 CONCENTRATED IN MIDDLE 14'.
- ② MIDDLE STRIP, CENTERLINE COLUMN: 6 D5 @ 39', STRAIGHT.
- ③ EACH EDGE STRIP, CENTERLINE COLUMN: 3 D5 @ 39', STRAIGHT.
- ④ EACH COLUMN STRIP, OUTSIDE COLUMNS: 24 D5, BENT:

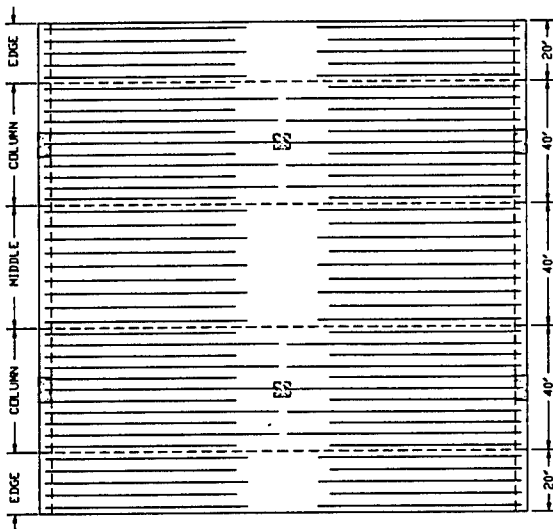


- ⑤ MIDDLE STRIP, OUTSIDE COLUMNS: 14 D3, BENT:



- ⑥ EACH EDGE STRIP, OUTSIDE COLUMNS: 8 D3, BENT, SAME AS MIDDLE STRIP.

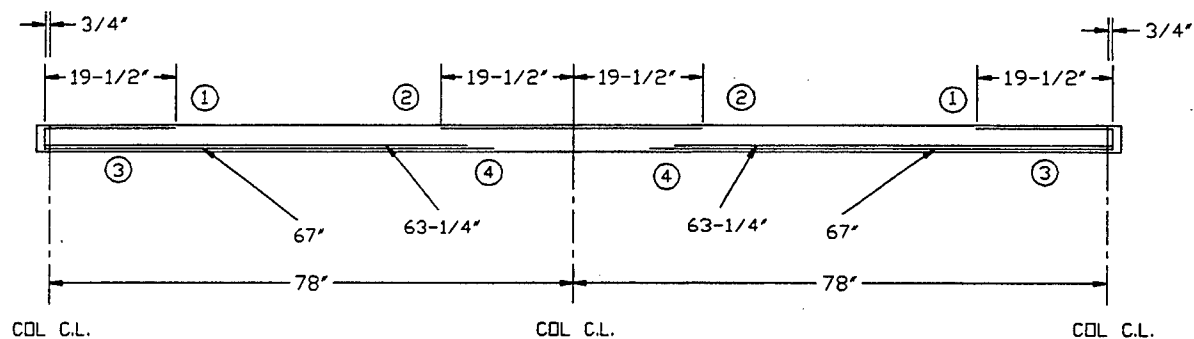
Figure 2.15 Longitudinal Reinforcement in Model Slabs, Top Bars



NOTES :
=====

- ① ALL BARS STRAIGHT.
- ② EACH COLUMN STRIP: 10 D5 @ 76-3/4', 12 D5 @ 63-1/4'
- ③ MIDDLE STRIP: 10 D3 @ 67', 8 D3 @ 63-1/4'
- ④ EACH EDGE STRIP: 6 D3 @ 67', 4 D3 @ 63-1/4'

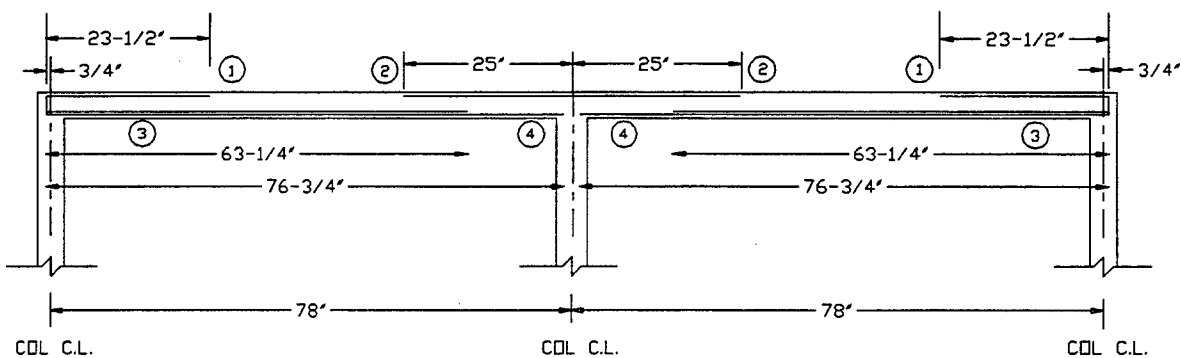
Figure 2.16 Longitudinal Reinforcement in Model Slabs, Bottom Bars



NOTES:

- ① $0.25L = 0.25(78) = 19-1/2'$
- ② $0.25L = 19-1/2'$
- ③ $L - (0.25L - 4') + (1/3)(2') = 0.75(78) + 4' + (2/3') = 63.17' \rightarrow 63-1/4'$
- ④ $L - 0.15L - (1/3)(2') = 0.85(78) + 0.67' = 66.97' \rightarrow 67'$
- ⑤ BOTTOM BARS ARE ACTUALLY PLACED ON SAME LEVEL. THEY ARE SEPARATED HERE TO ILLUSTRATE DIFFERENT BAR LENGTHS.

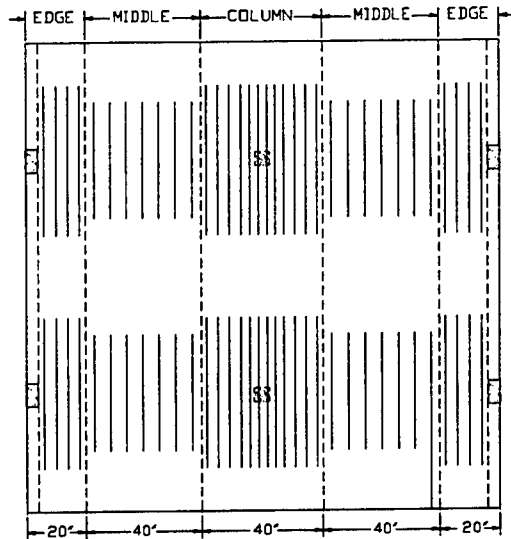
Figure 2.17 Longitudinal Reinforcement, Middle Strip



NOTES :

- ① $0.30L = 0.30(78) = 23.4' \Rightarrow 23-1/2'$
- ② $0.32L = 0.32(78) = 24.96' \Rightarrow 25'$
- ③ $L - (0.25L - 4') + 1/3(2') = 78 - 0.25(78) + 4 + 0.67 = 63.17' \Rightarrow 63-1/4'$
- ④ $L - (6'/3) + (2'/3) = 78 - (4'/3) = 76.67' \Rightarrow 76-3/4'$

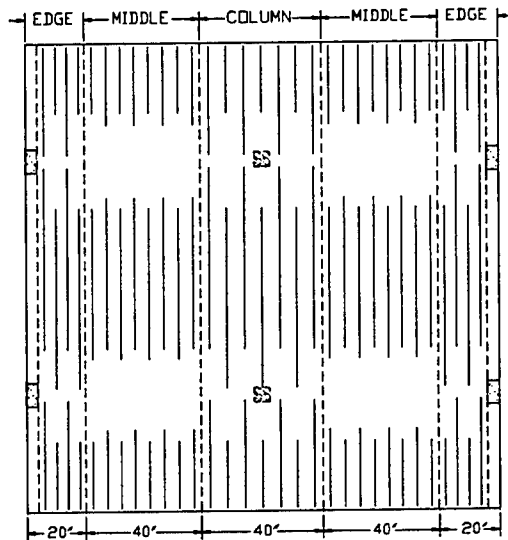
Figure 2.18 Longitudinal Reinforcement, Column Strip



NOTES:

- ① ALL BARS ARE STRAIGHT
- ② EACH EDGE STRIP: 8 D3 @ 51-1/4"
- ③ EACH MIDDLE STRIP: 14 D3 @ 40"
- ④ COLUMN STRIP: 24 D5 @ 51-1/4", WITH 12 D5 CONCENTRATED IN MIDDLE 14"

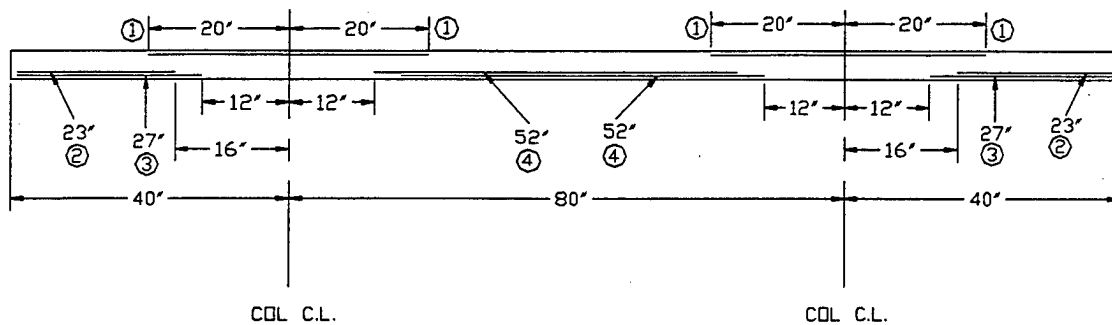
Figure 2.19 Lateral Reinforcement in Model Slabs, Top Bars



NOTES:

- ① ALL BARS ARE STRAIGHT.
- ② EACH EDGE STRIP: 4 D3 @ 37", 4 D3 @ 23", 4 D3 @ 62"
- ③ EACH MIDDLE STRIP: 8 D3 @ 27", 8 D3 @ 23", 8 D3 @ 52"
- ④ EACH COLUMN STRIP: 8 D5 @ 37", 6 D5 @ 23", 7 D5 @ 62"

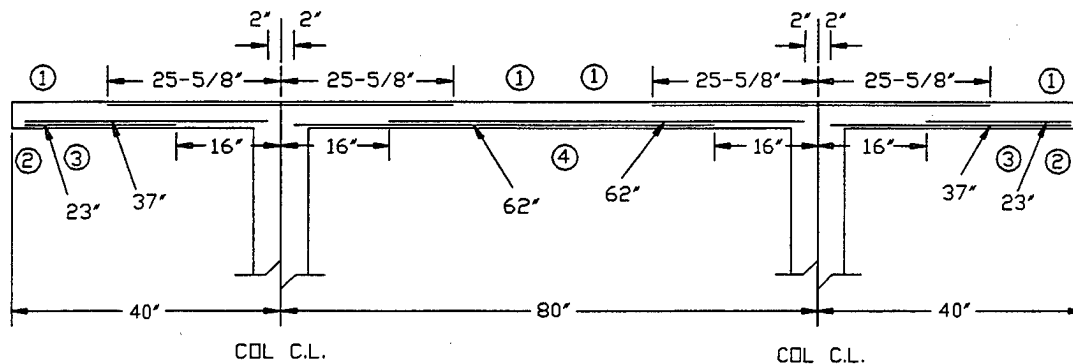
Figure 2.20 Lateral Reinforcement in Model Slabs, Bottom Bars



NOTES:

- ① $0.25L = 0.25(80) = 20'$
- ② $40 - (0.25L - 4) = 40 - 20 + 4 = 24' \rightarrow 23'$ (FOR END CLEARANCE)
- ③ $40 - 0.15L = 40 - 0.15(80) = 28' \rightarrow 27'$ (FOR END CLEARANCE)
- ④ $80 - 0.15L - (0.25L - 4) = 80 - 0.4(80) + 4 = 80 - 32 + 4 = 52'$
- ⑤ BOTTOM BARS ARE ACTUALLY PLACED ON SAME LEVEL. THEY ARE SEPARATED HERE TO ILLUSTRATE DIFFERENT BAR LENGTHS.

Figure 2.21 Lateral Reinforcement, Middle Strip



NOTES:

- ① $0.32L = 0.32(80) = 25.6' \rightarrow 25-5/8'$
- ② $40 - (0.25L - 4) = 40 - 20 + 4 = 24' \rightarrow 23'$ (FOR END CLEARANCE)
- ③ $40 - 2 = 38' \rightarrow 37'$ (FOR END CLEARANCE)
- ④ $80 - (0.25L - 4) - (6/3') = 80 - 20 + 4 - 2 = 62'$
- ⑤ BOTTOM BARS ARE ACTUALLY PLACED ON SAME LEVEL. THEY ARE SEPARATED TO ILLUSTRATE DIFFERENT BAR LENGTHS.

Figure 2.22 Lateral Reinforcement, Column Strip

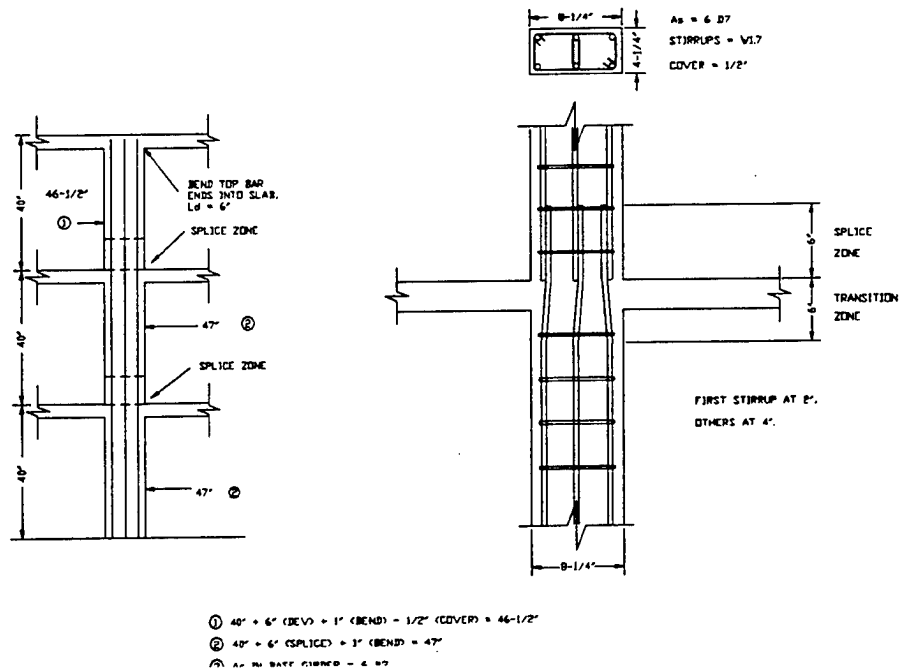


Figure 2.23 Exterior Column Details

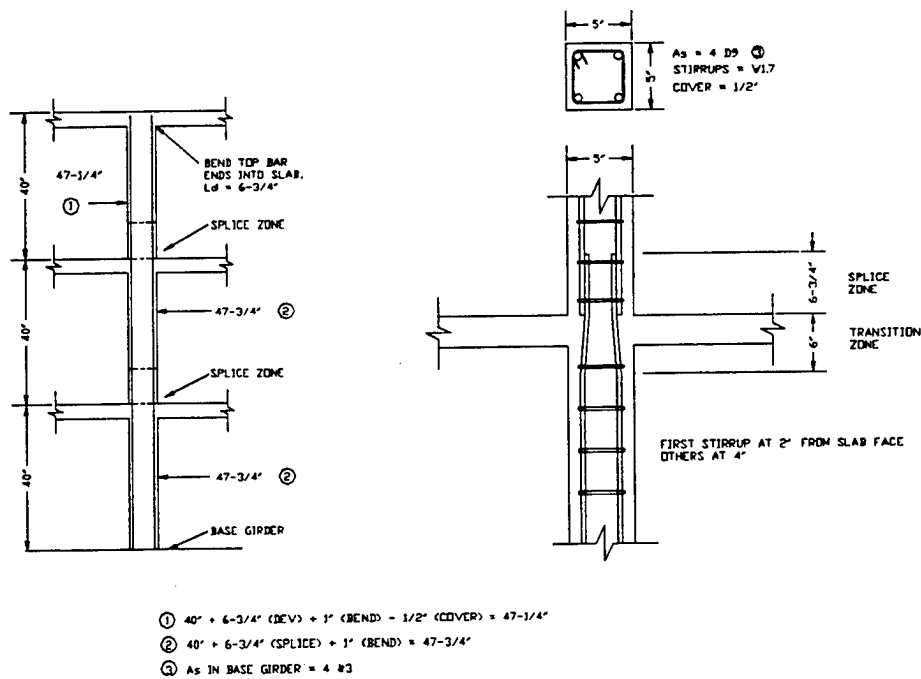


Figure 2.24 Interior (Centerline) Column Details

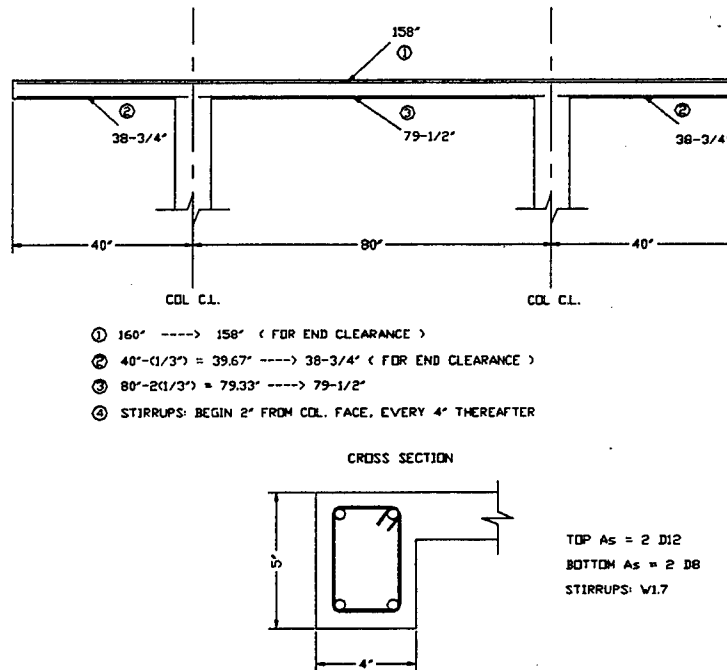


Figure 2.25 Spandrel Beam Details

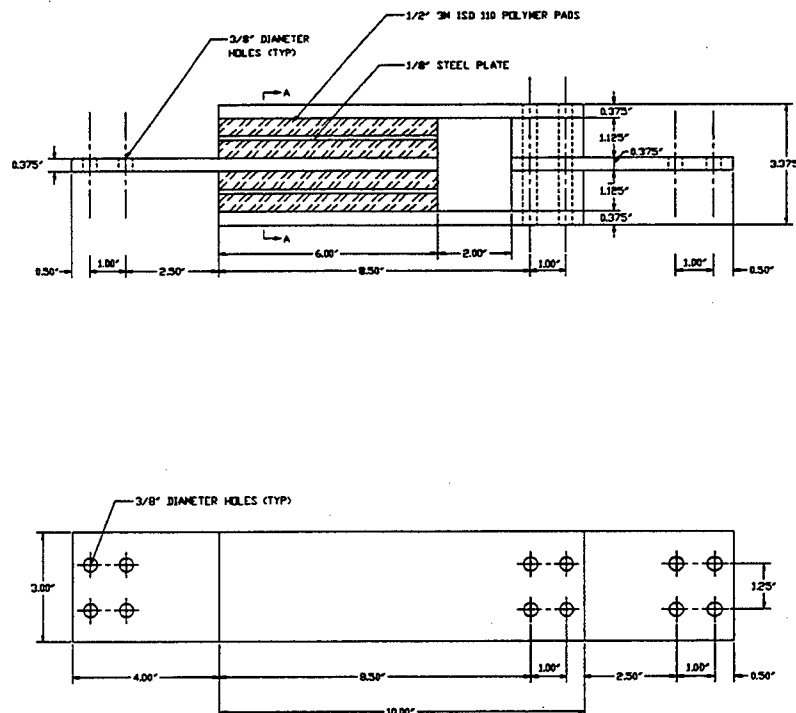


Figure 2.26 Elevation and Plan Views of Typical Viscoelastic Damper

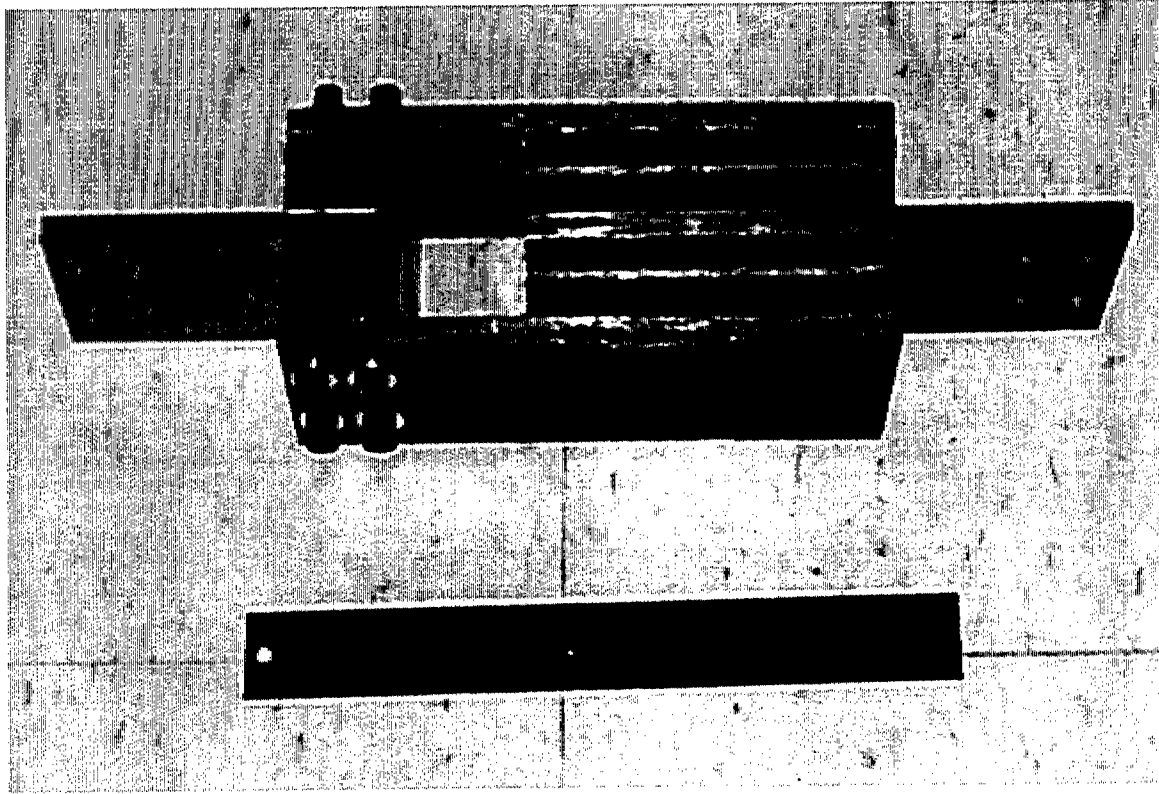


Figure 2.27 3M Viscoelastic Damper

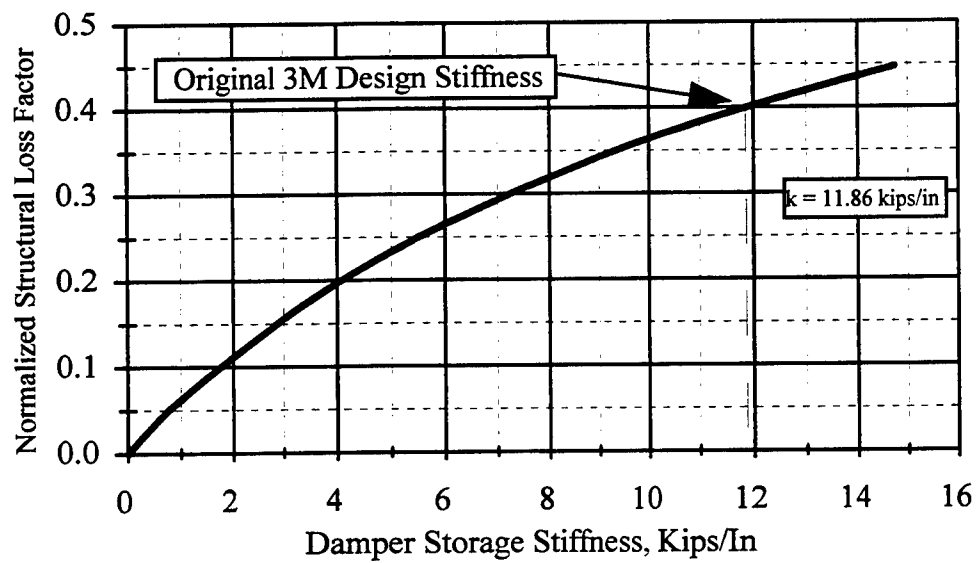


Figure 2.28 Original 3M Damper Design Curve

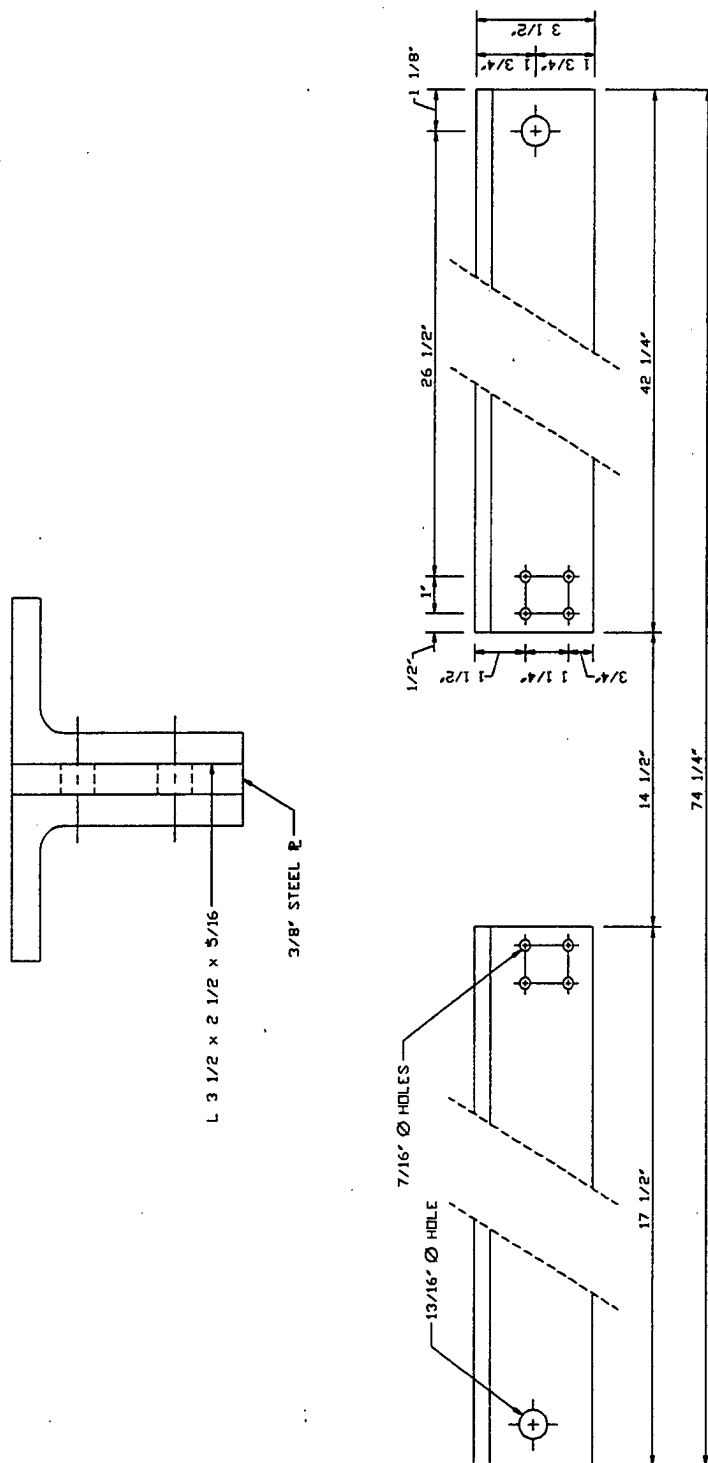


Figure 2.29 Diagonal Brace Details

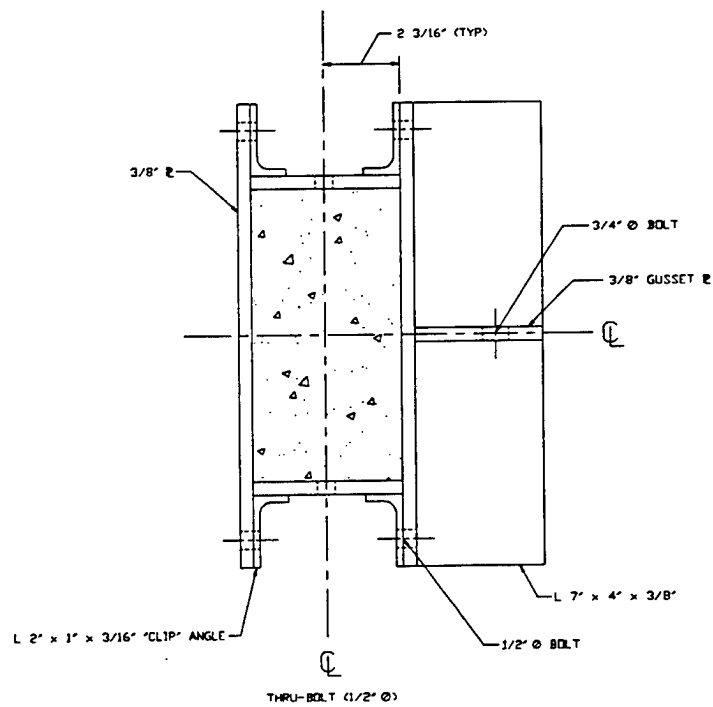
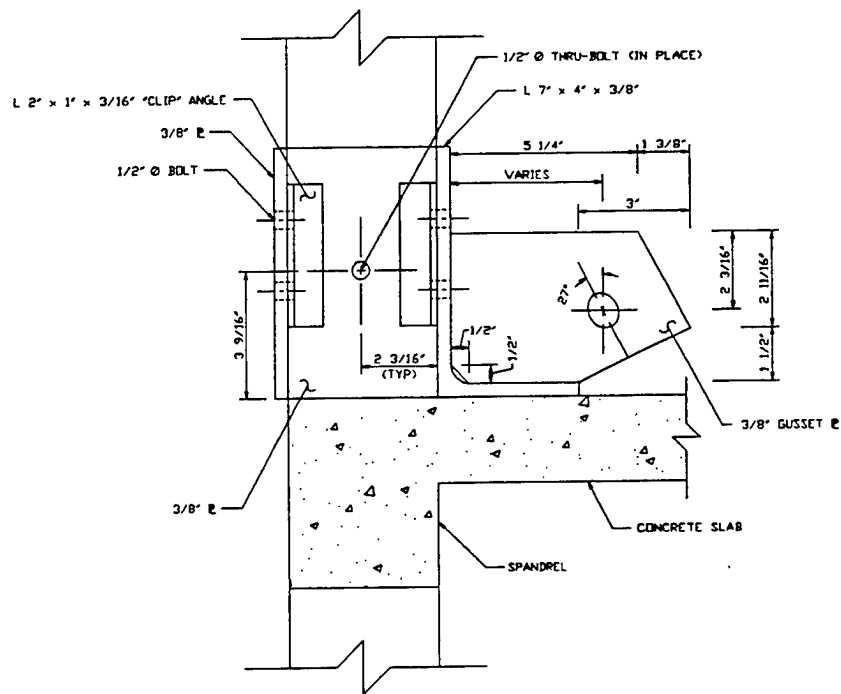


Figure 2.30 Typical Exterior Column Collar Details

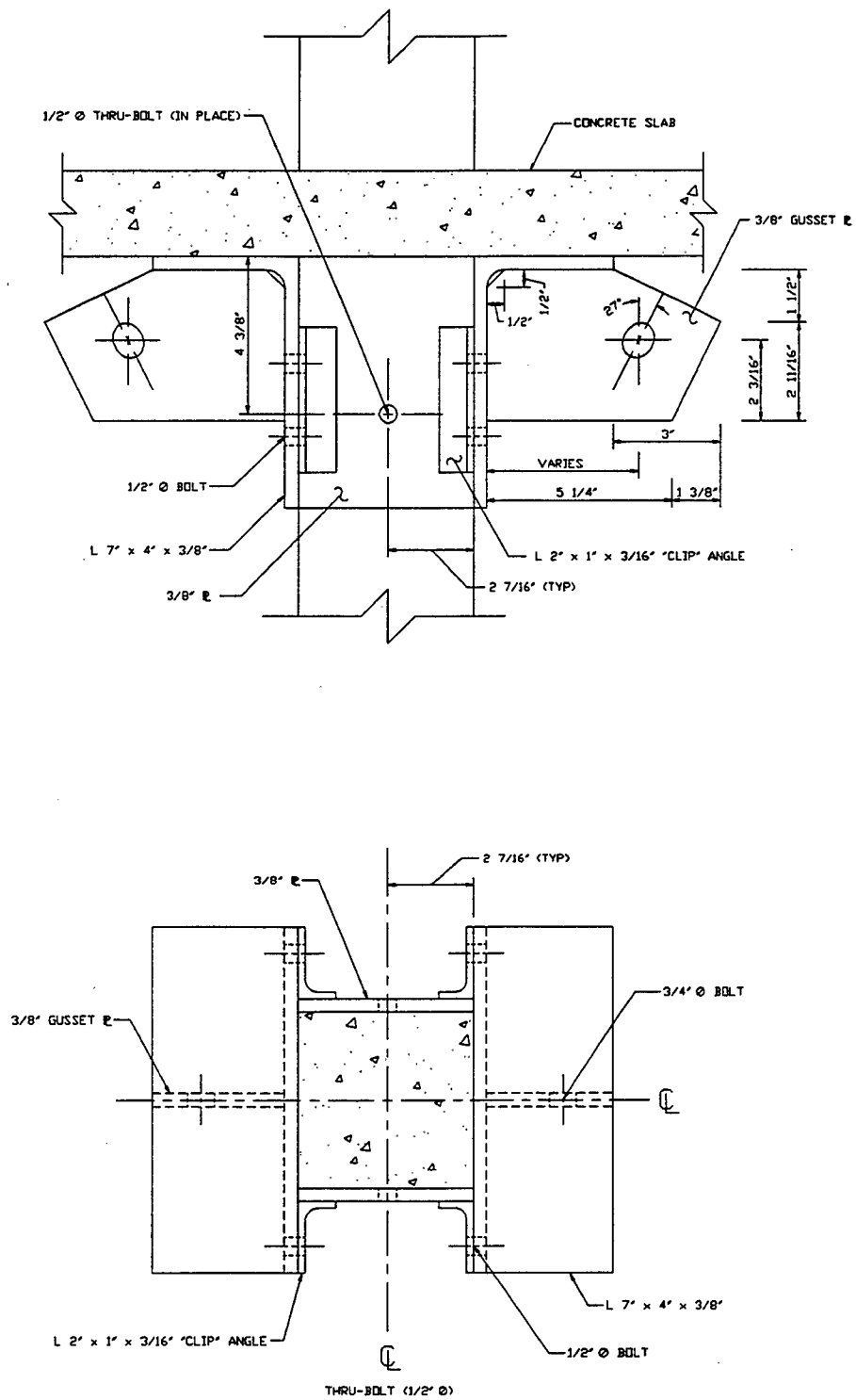


Figure 2.31 Typical Interior Column Collar Details

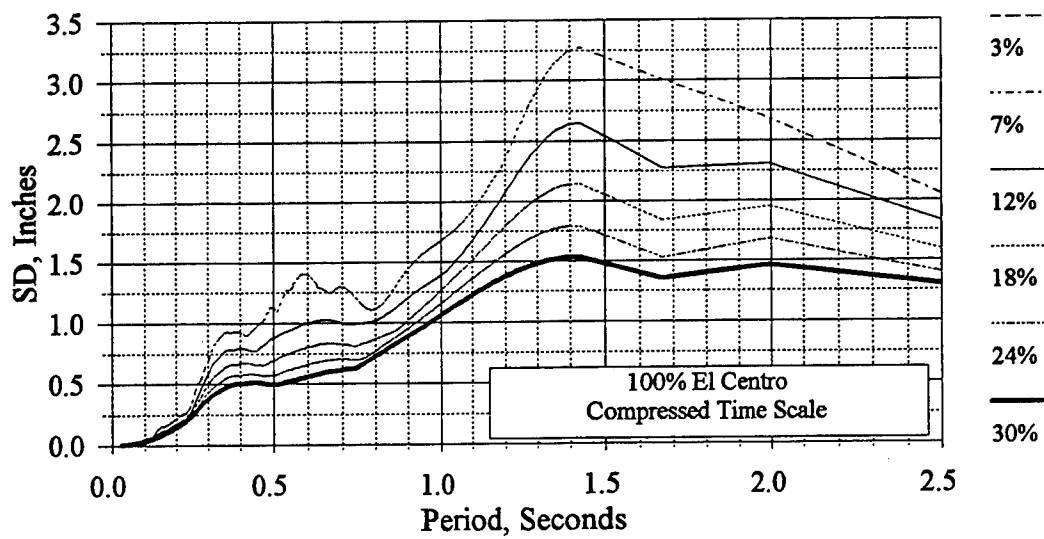
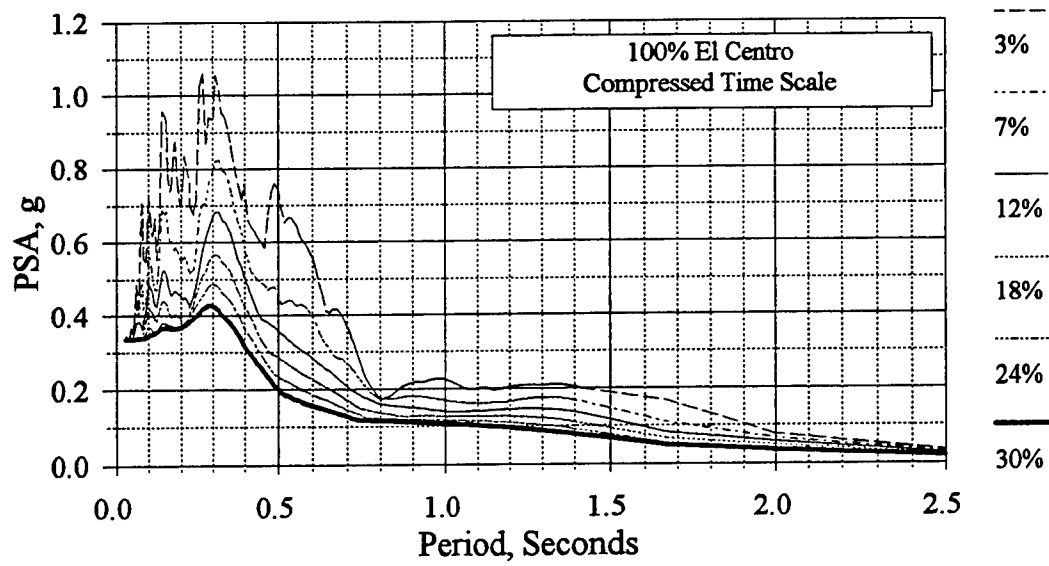


Figure 3.1 Elastic Acceleration and Displacement Response Spectra, 100% El Centro, Compressed Time Scale

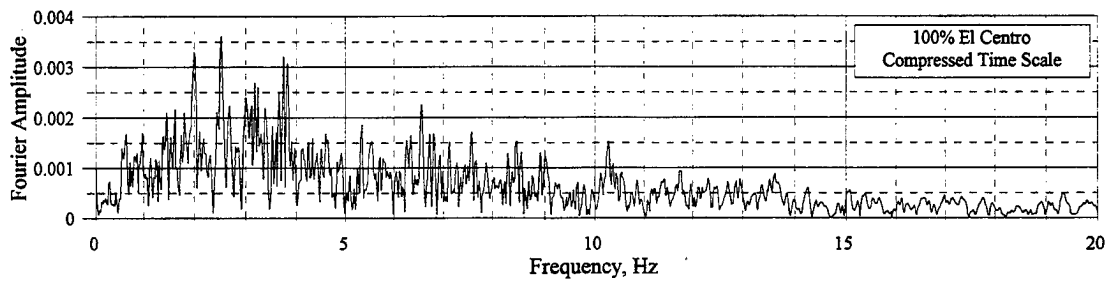
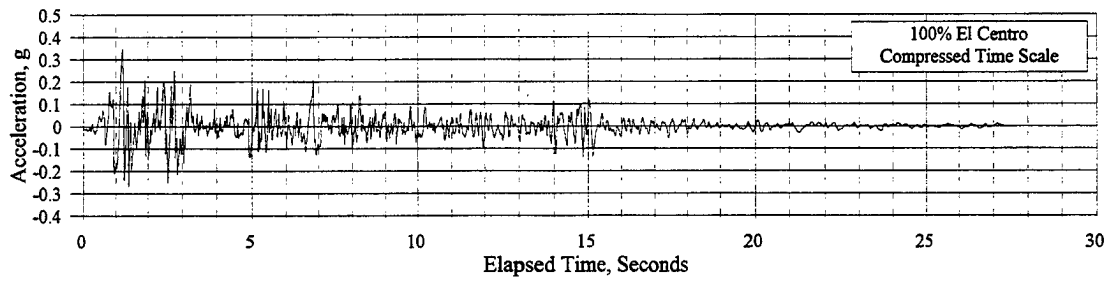


Figure 3.2 Time History and FFT of 100% El Centro, Compressed Time Scale

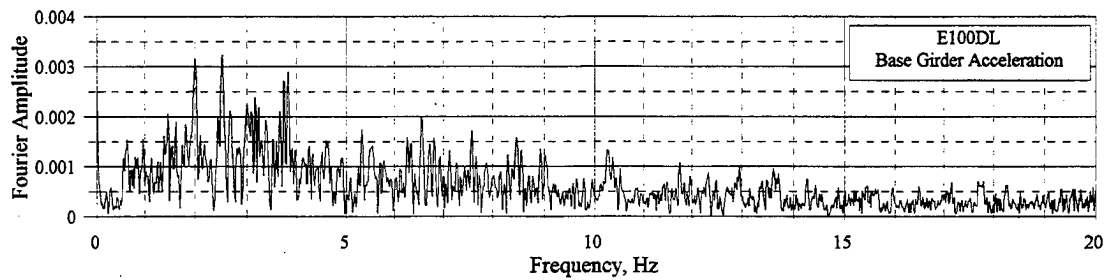
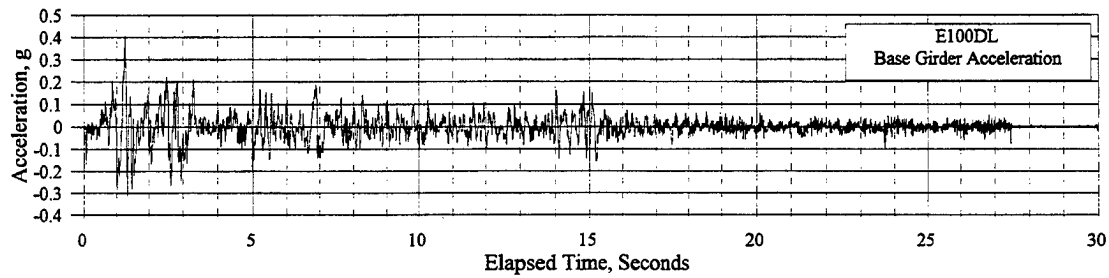


Figure 3.3 Time History and FFT of Base Girder Motion, Simulation E100DL

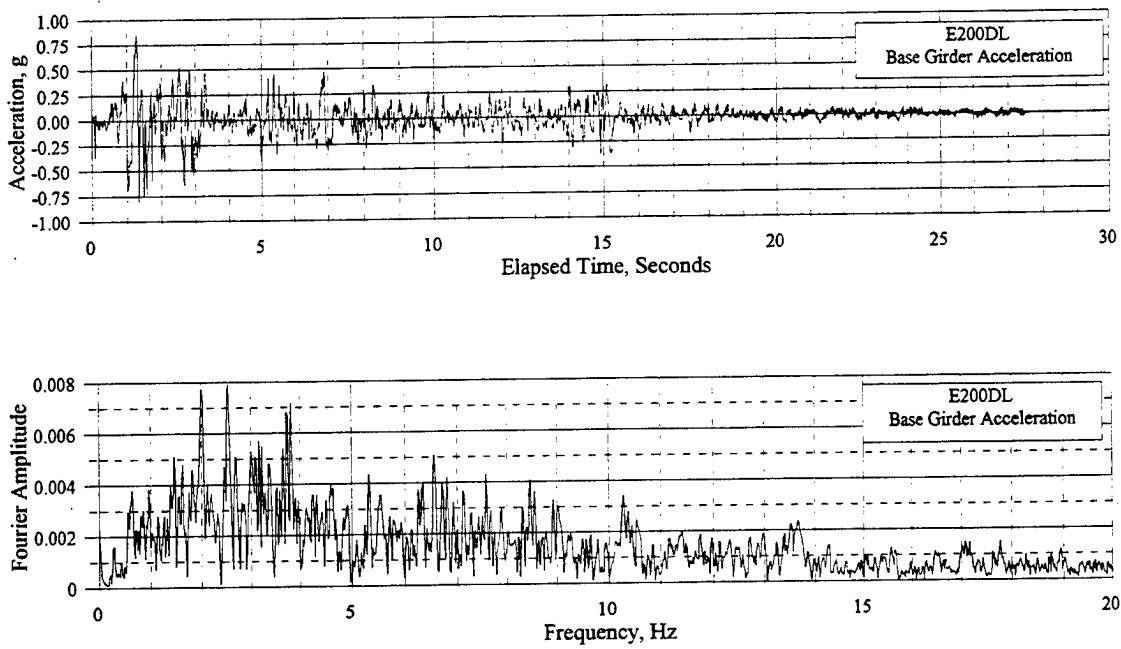


Figure 3.4 Time History and FFT of Base Girder Motion, Simulation E200DL

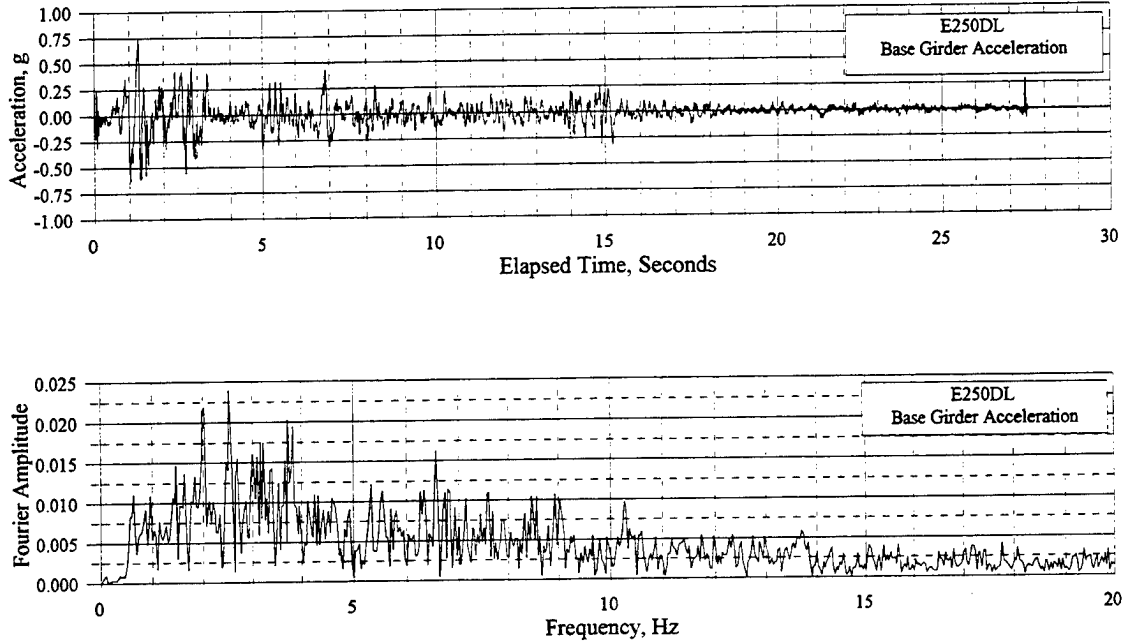


Figure 3.5 Time History and FFT of Base Girder Motion, Simulation E250DL

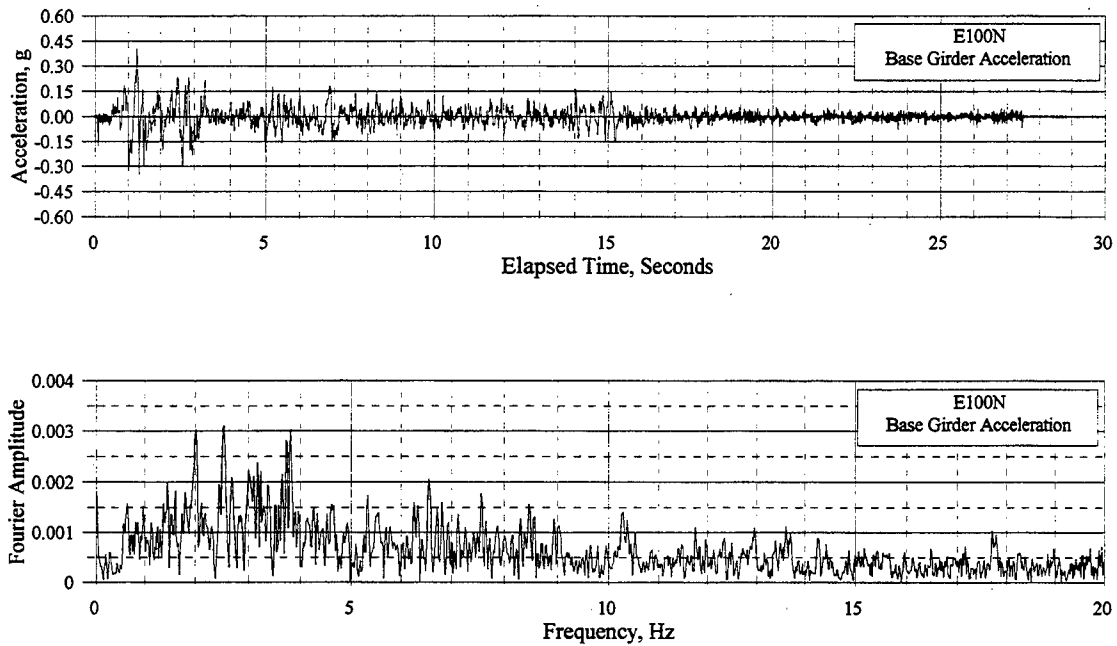


Figure 3.6 Time History and FFT of Base Girder Motion, Simulation E100N

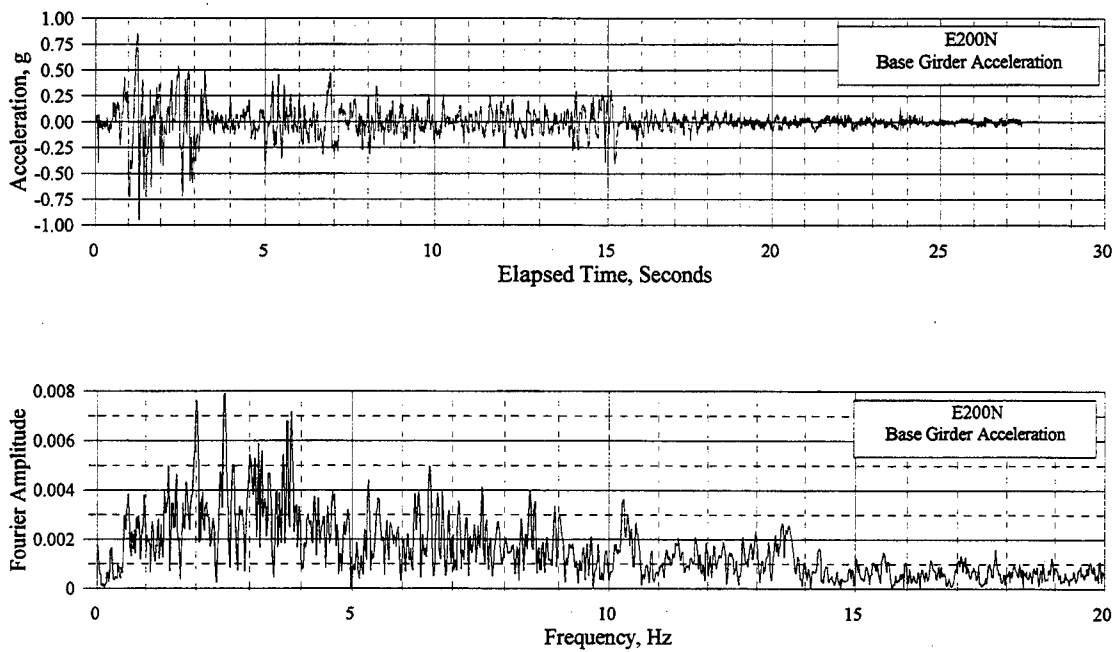


Figure 3.7 Time History and FFT of Base Girder Motion, Simulation E200N

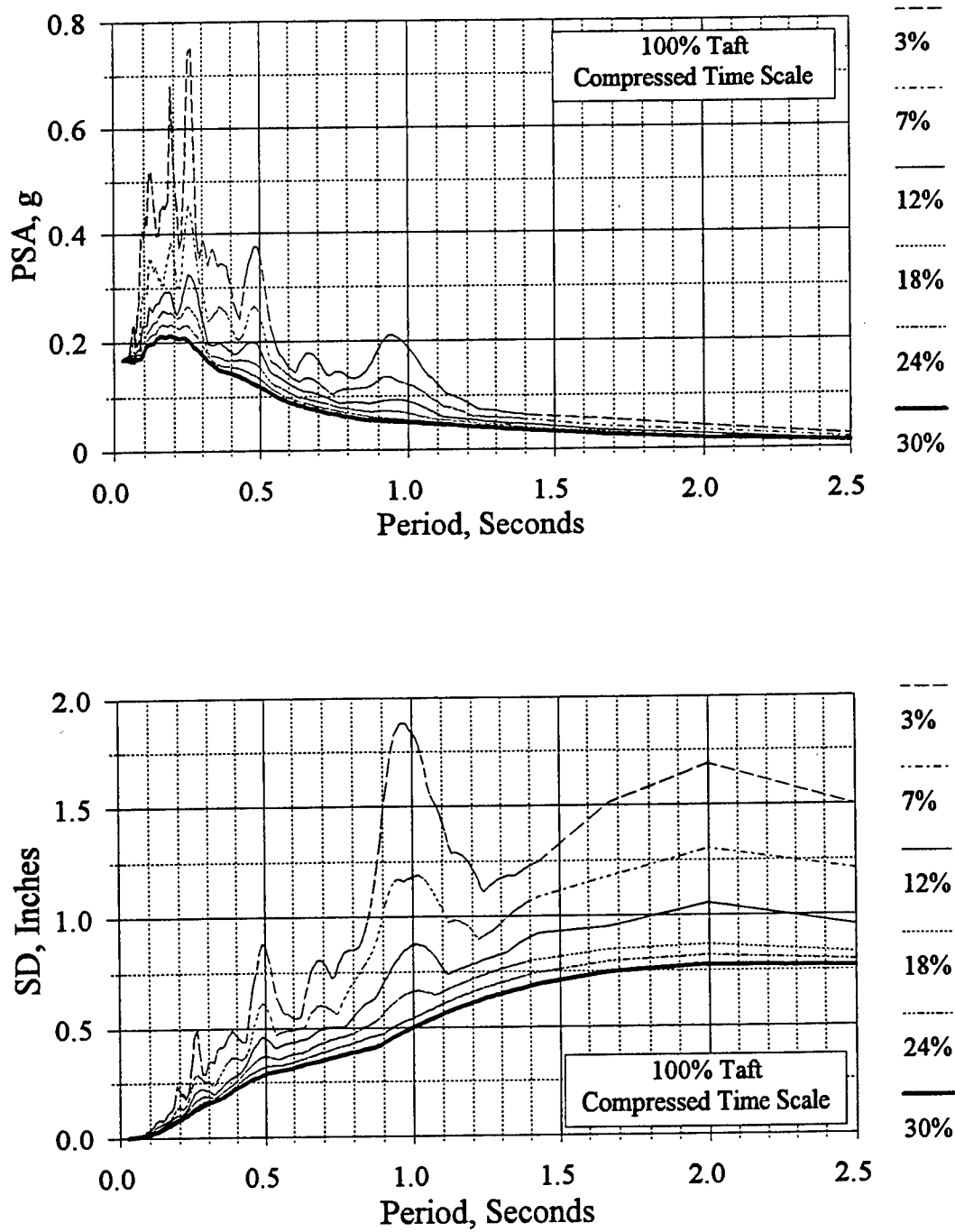


Figure 3.8 Elastic Acceleration and Displacement Response Spectra, 100% Taft, Compressed Time Scale

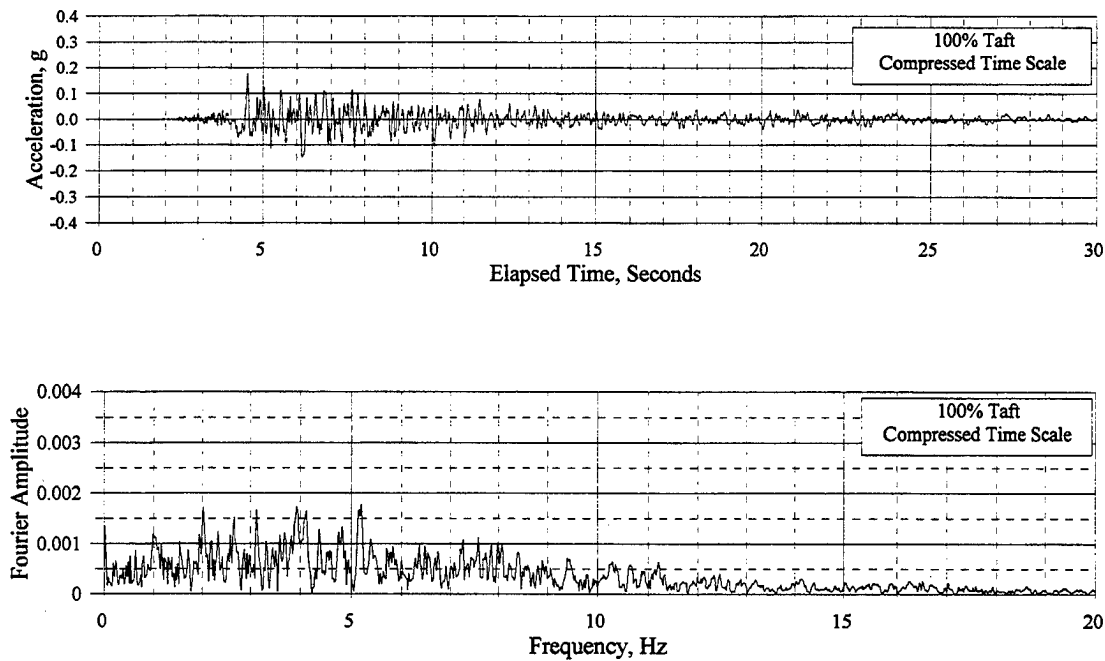


Figure 3.9 Time History and FFT of 100% Taft, Compressed Time Scale

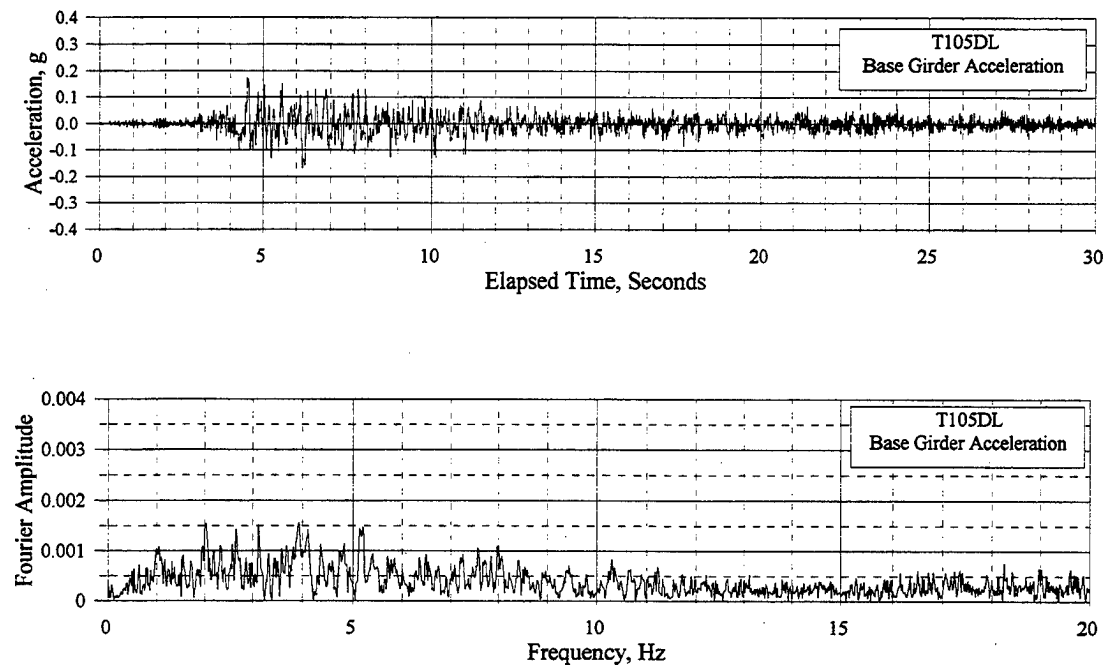


Figure 3.10 Time History and FFT of Base Girder Motion, Simulation T105DL

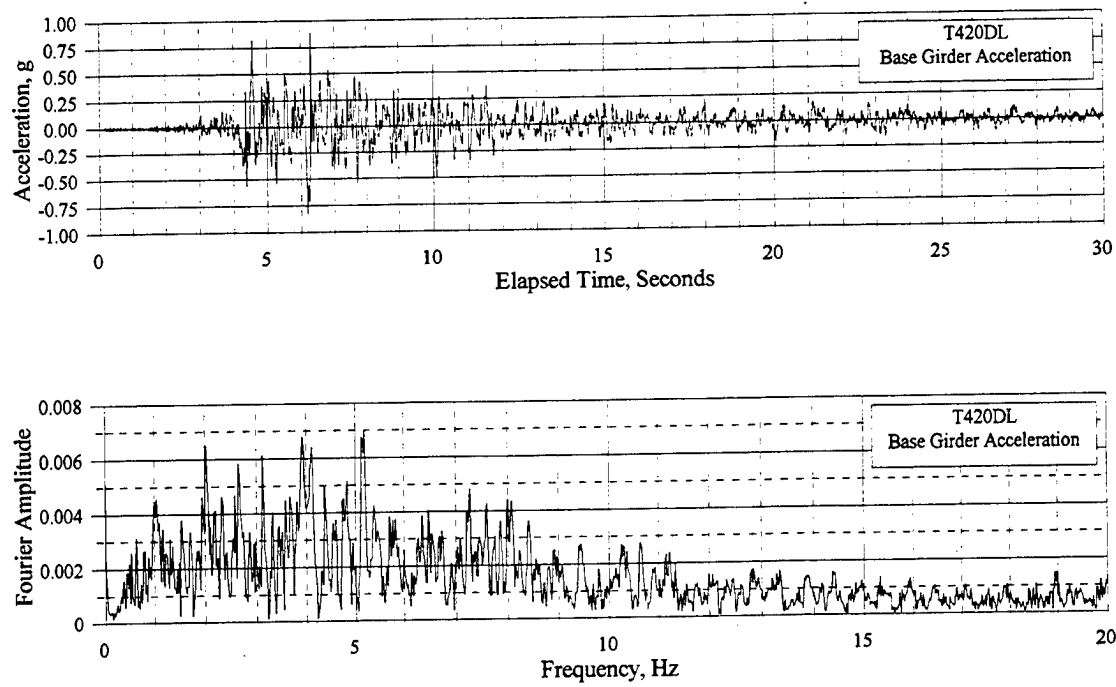


Figure 3.11 Time History and FFT of Base Girder Motion, Simulation T420DL

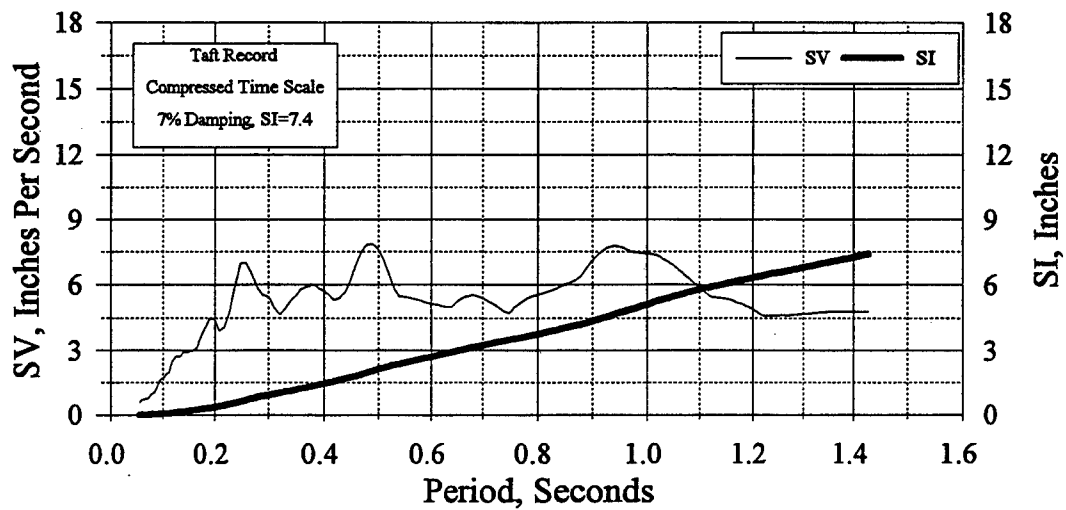
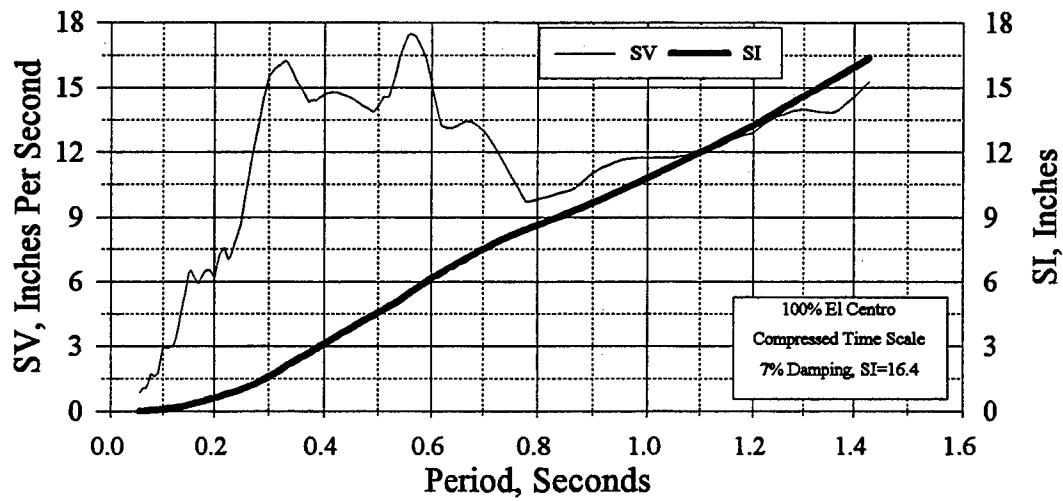


Figure 3.12 Spectral Velocities (SV) and Spectrum Intensities (SI) for El Centro and Taft Records

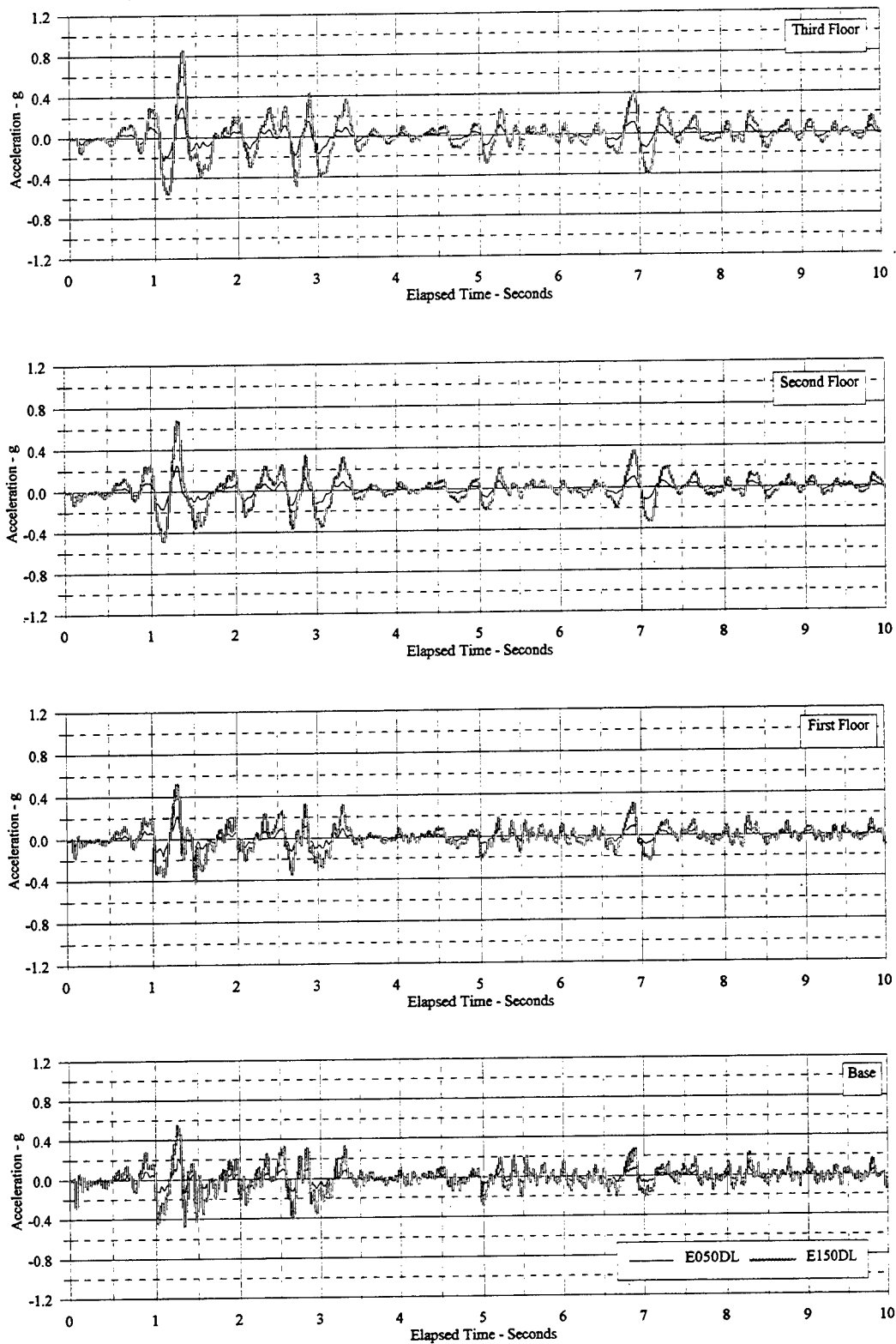


Figure 4.1 Acceleration Vs. Elapsed Time: E050DL Vs. E150DL

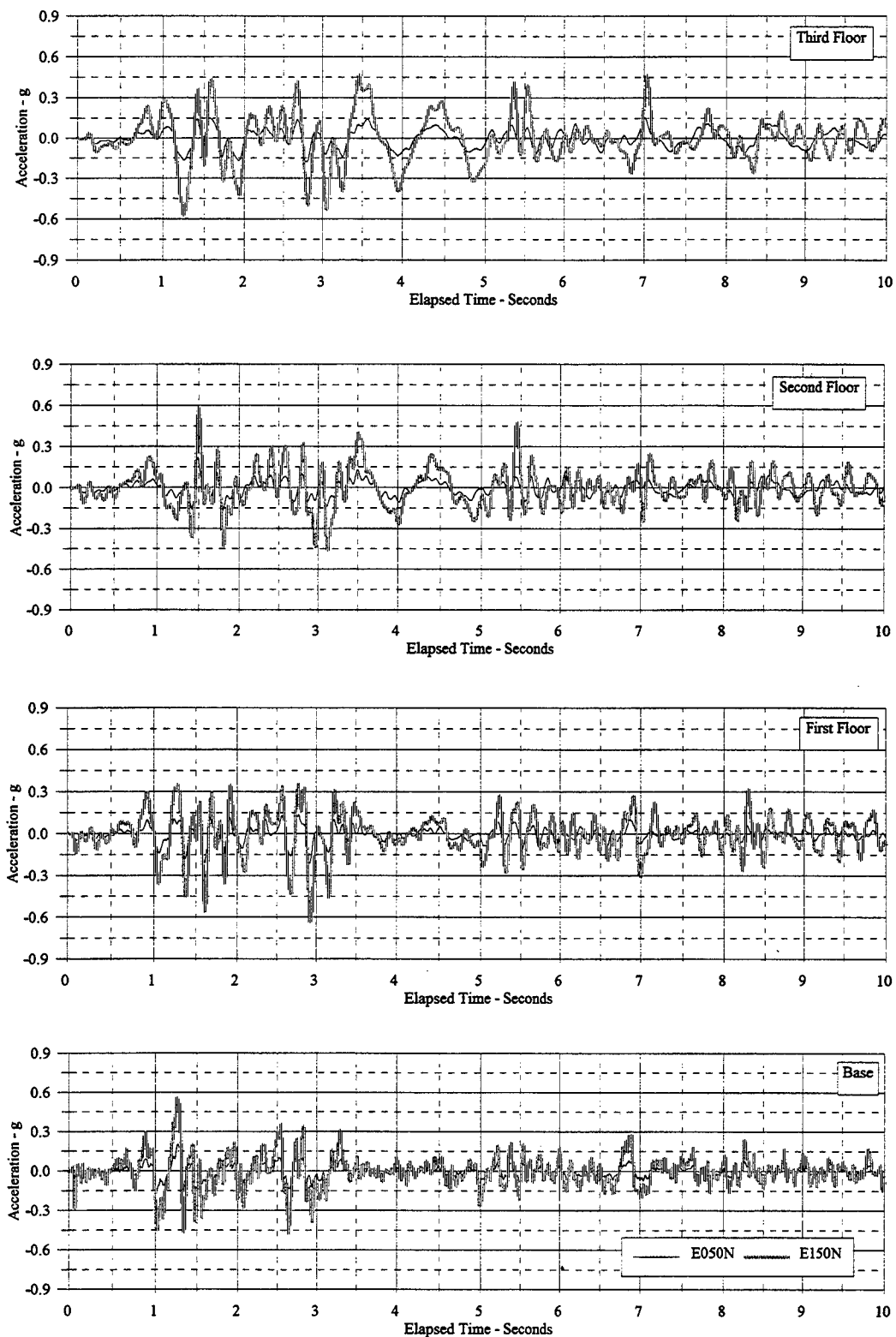


Figure 4.2 Acceleration Vs. Elapsed Time: E050N Vs. E150N

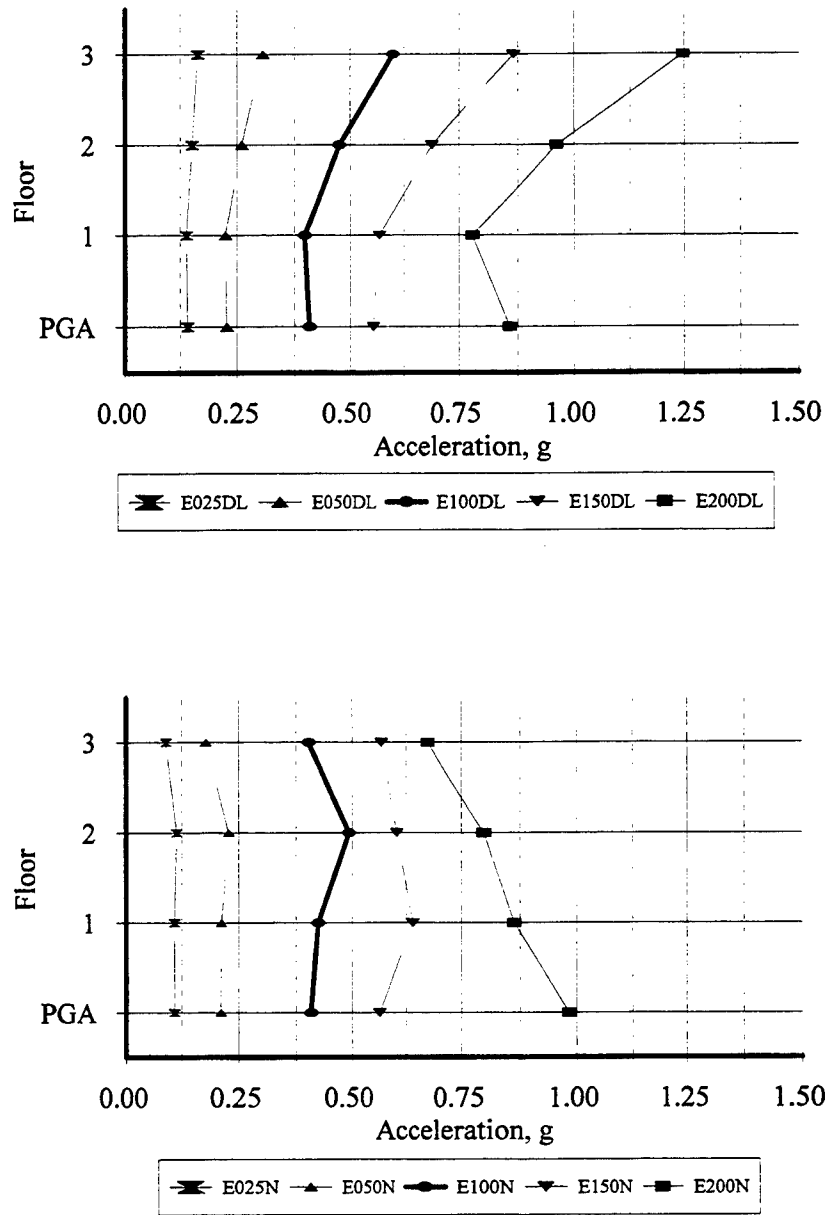


Figure 4.3 Maximum Floor Acceleration Profiles for El Centro Simulations

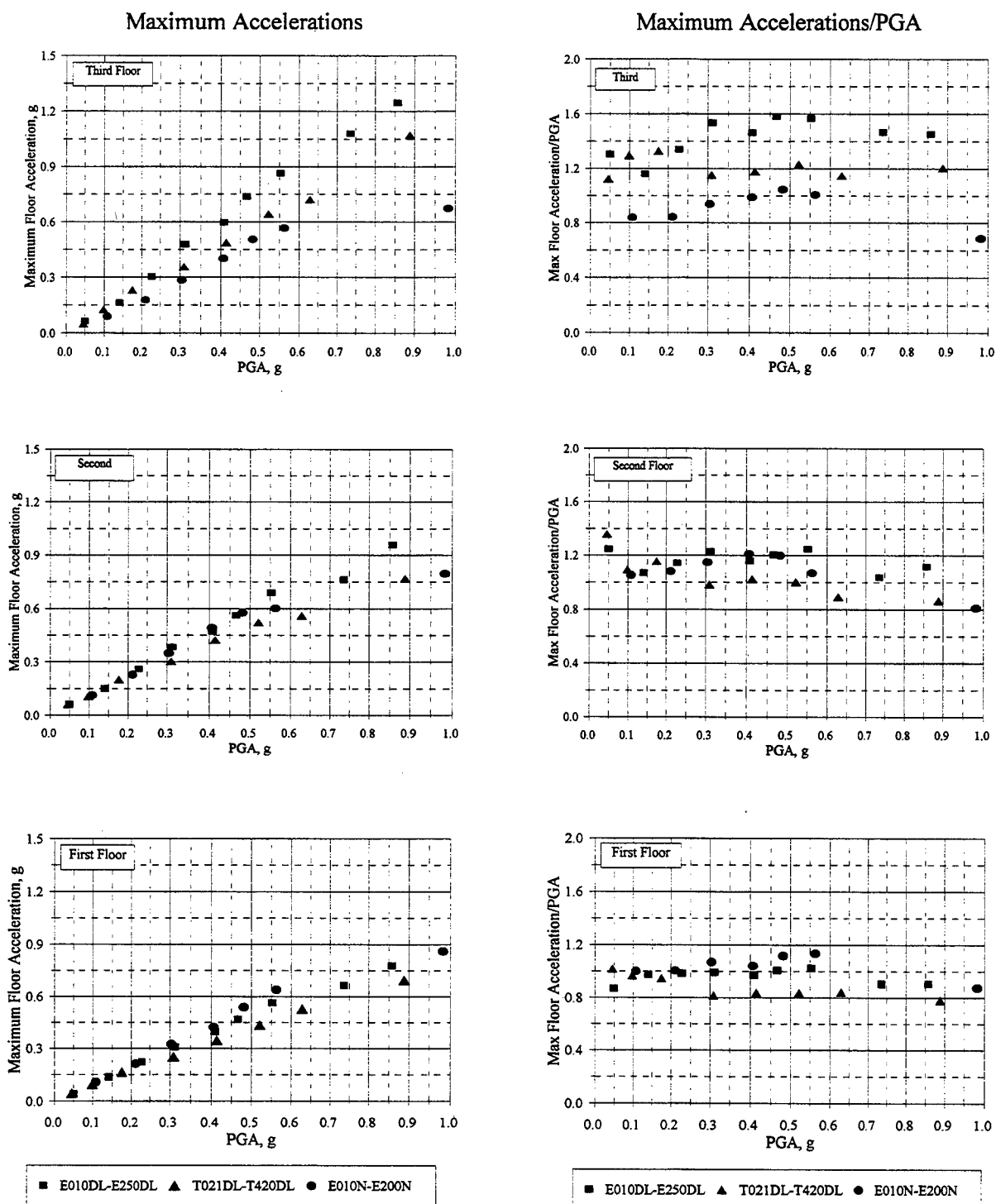


Figure 4.4 Maximum Floor Acceleration Vs. Peak Ground Acceleration (PGA)

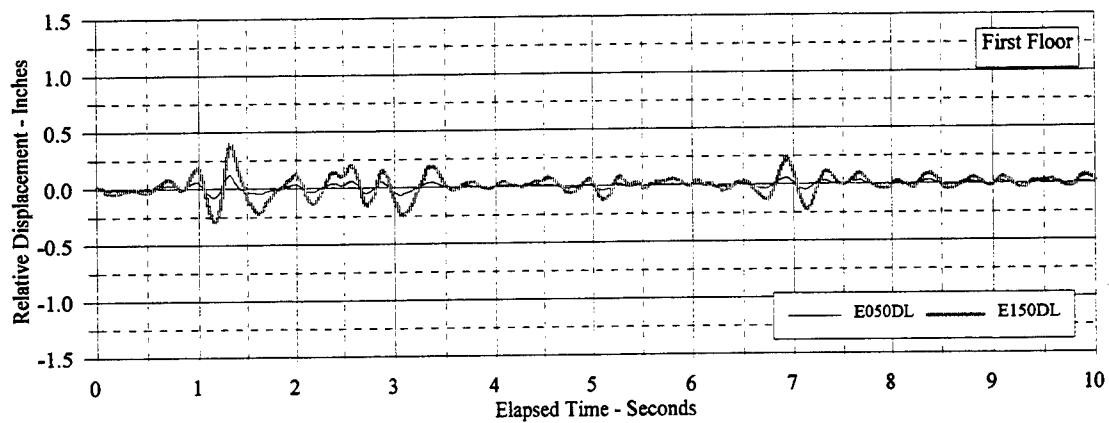
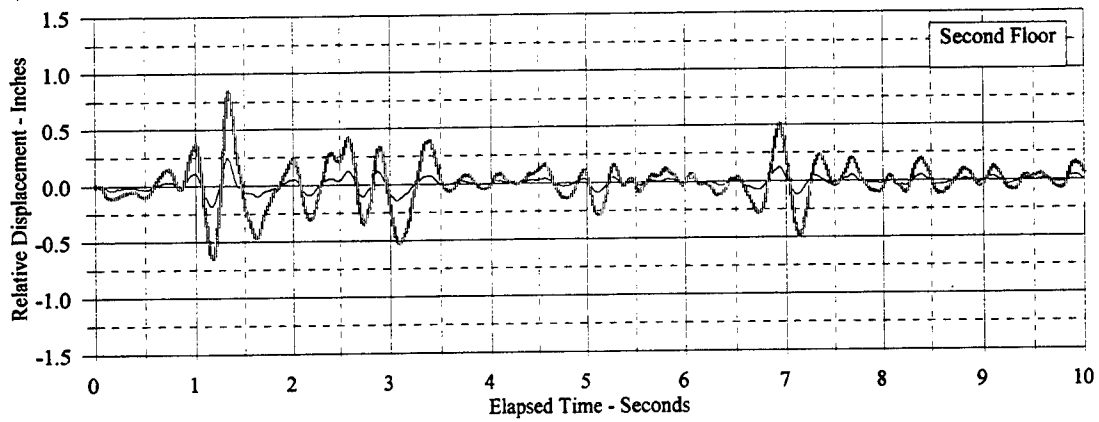
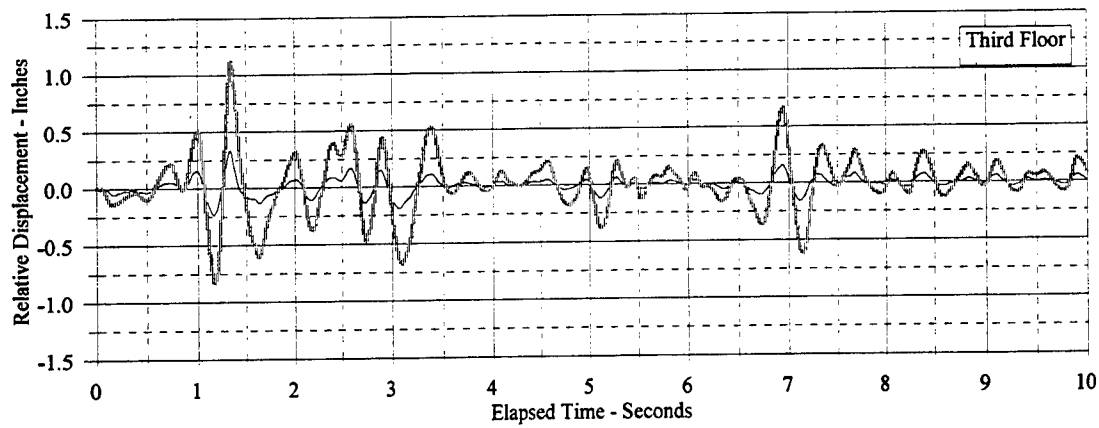


Figure 4.5 Relative Displacement Vs. Elapsed Time: E050DL Vs. E150DL

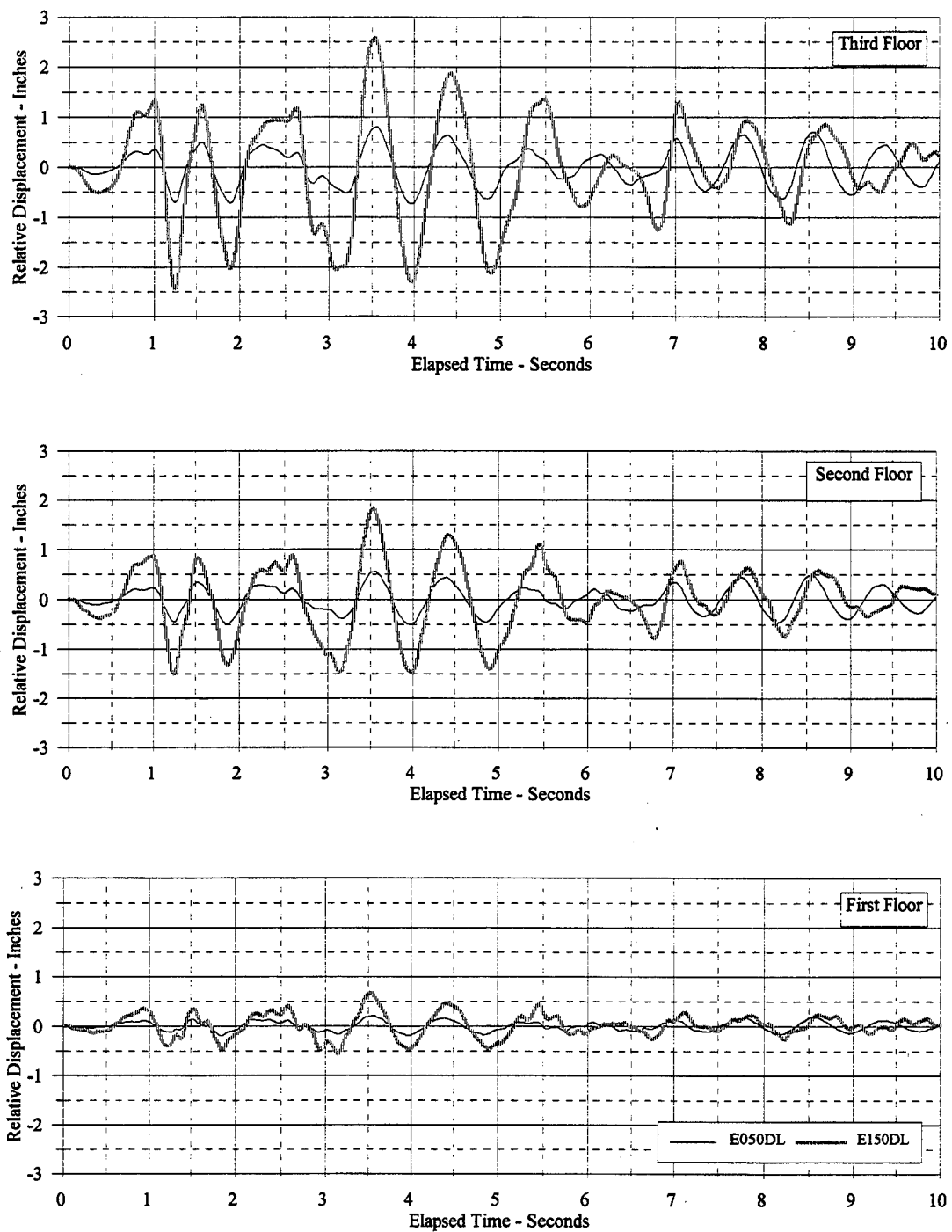


Figure 4.6 Relative Displacement Vs. Elapsed Time: E050N Vs. E150N

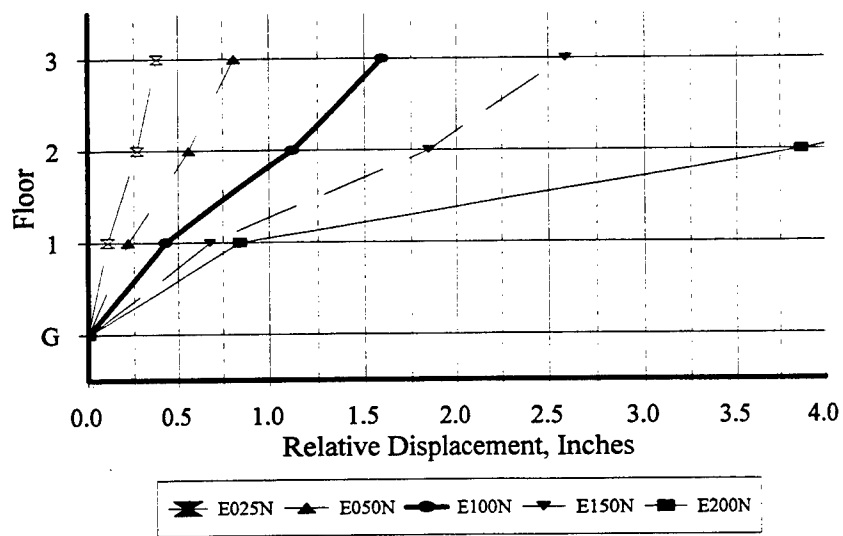
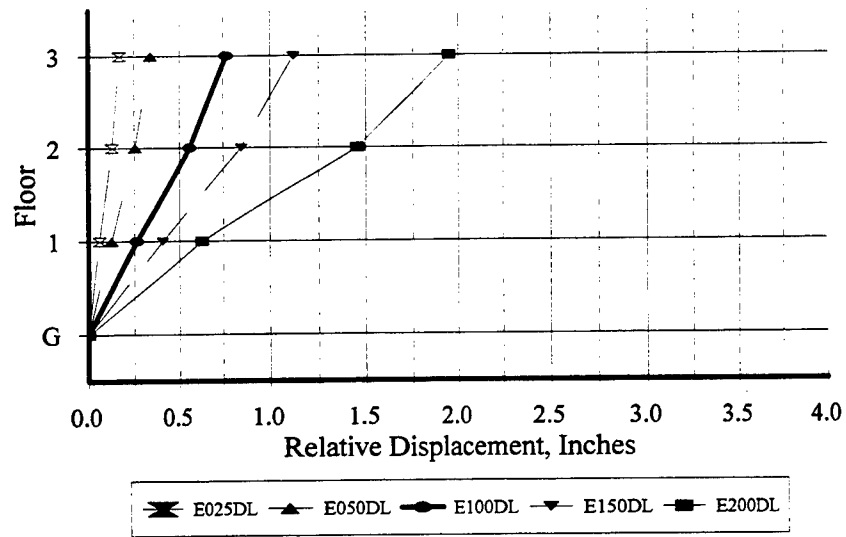


Figure 4.7 Maximum Relative Story Displacement Profiles for El Centro Simulations

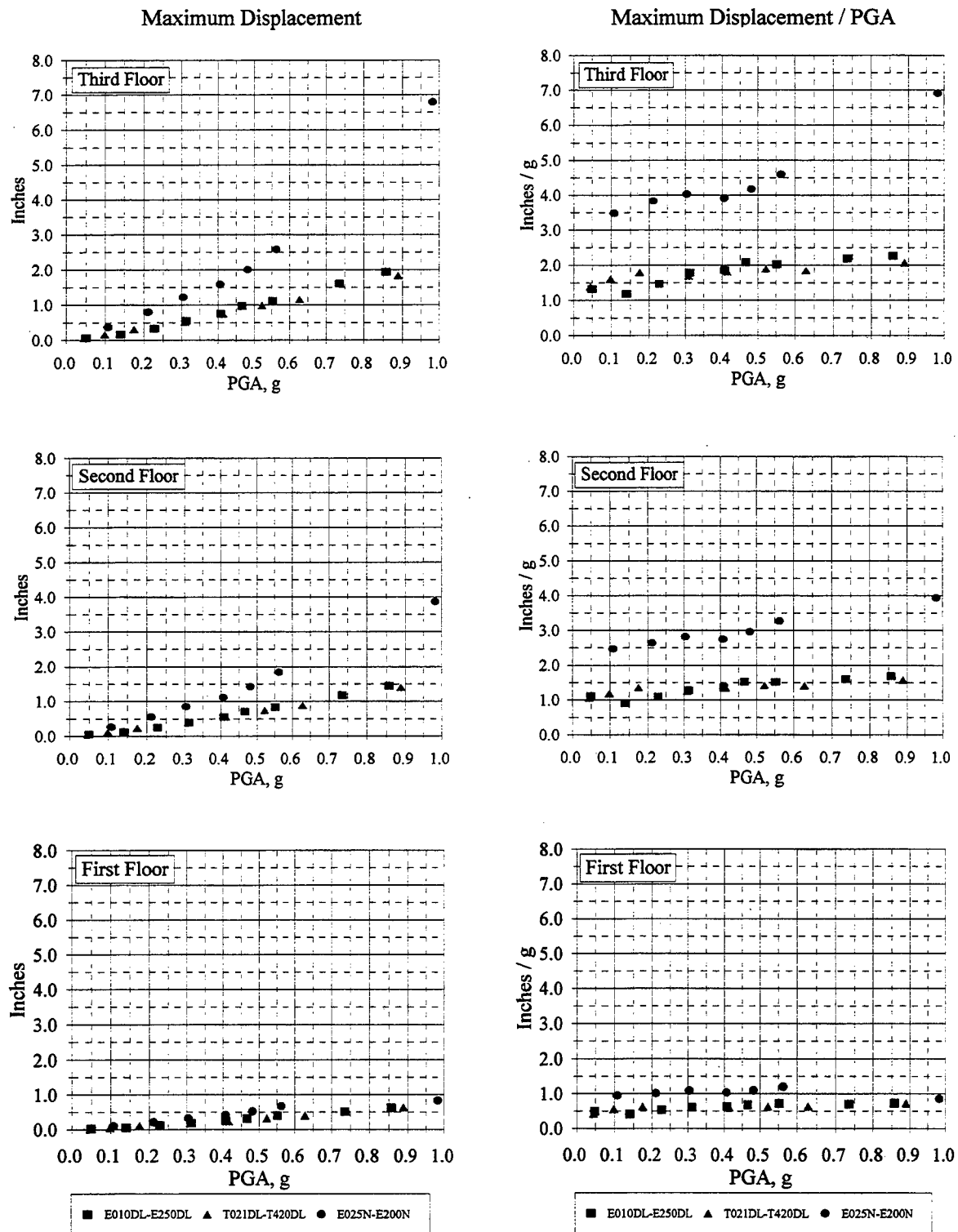


Figure 4.8 Maximum Relative Displacement Vs. Peak Ground Acceleration (PGA)

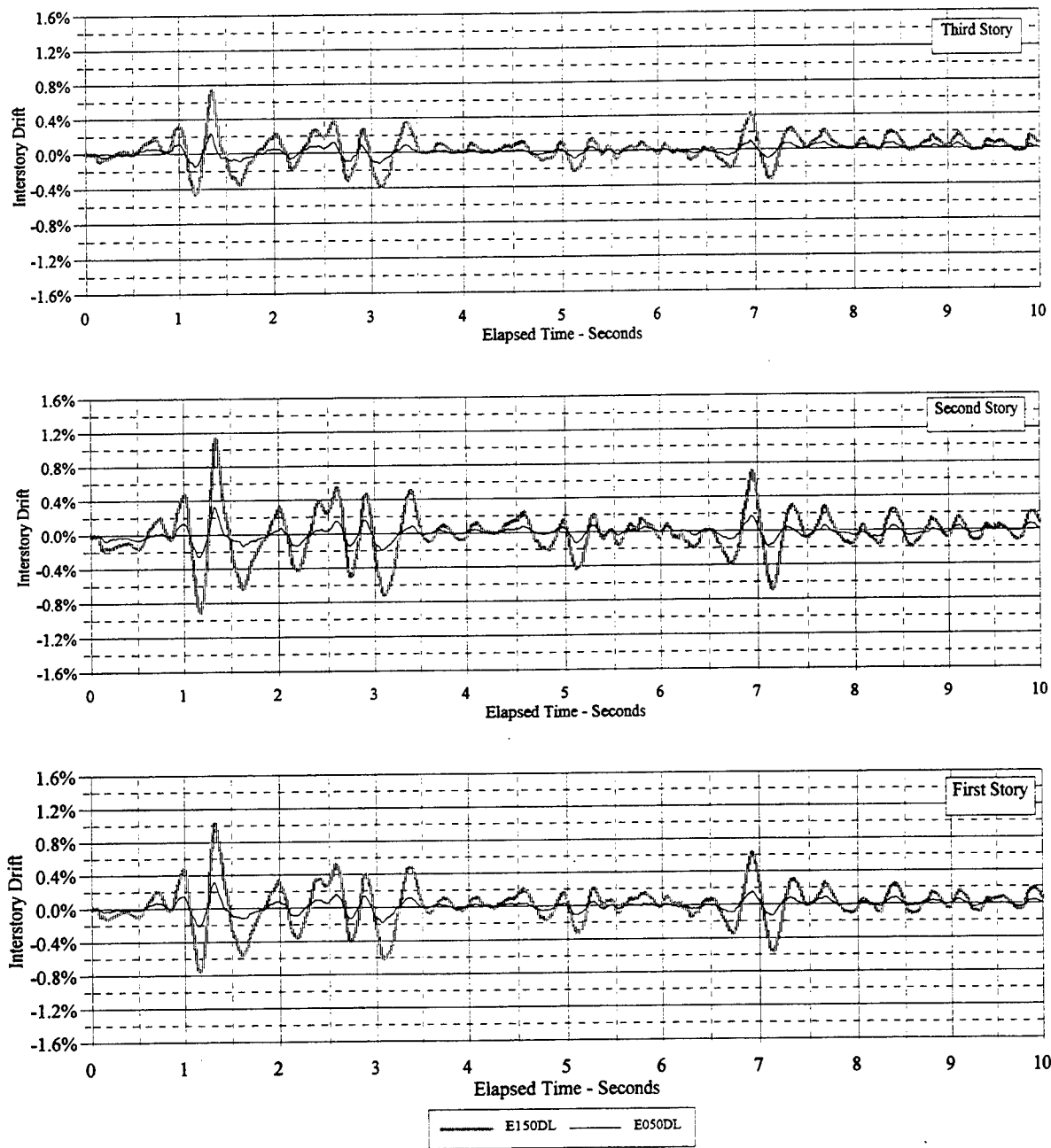


Figure 4.9 Interstory Drift Vs. Elapsed Time: E050DL Vs. E150DL

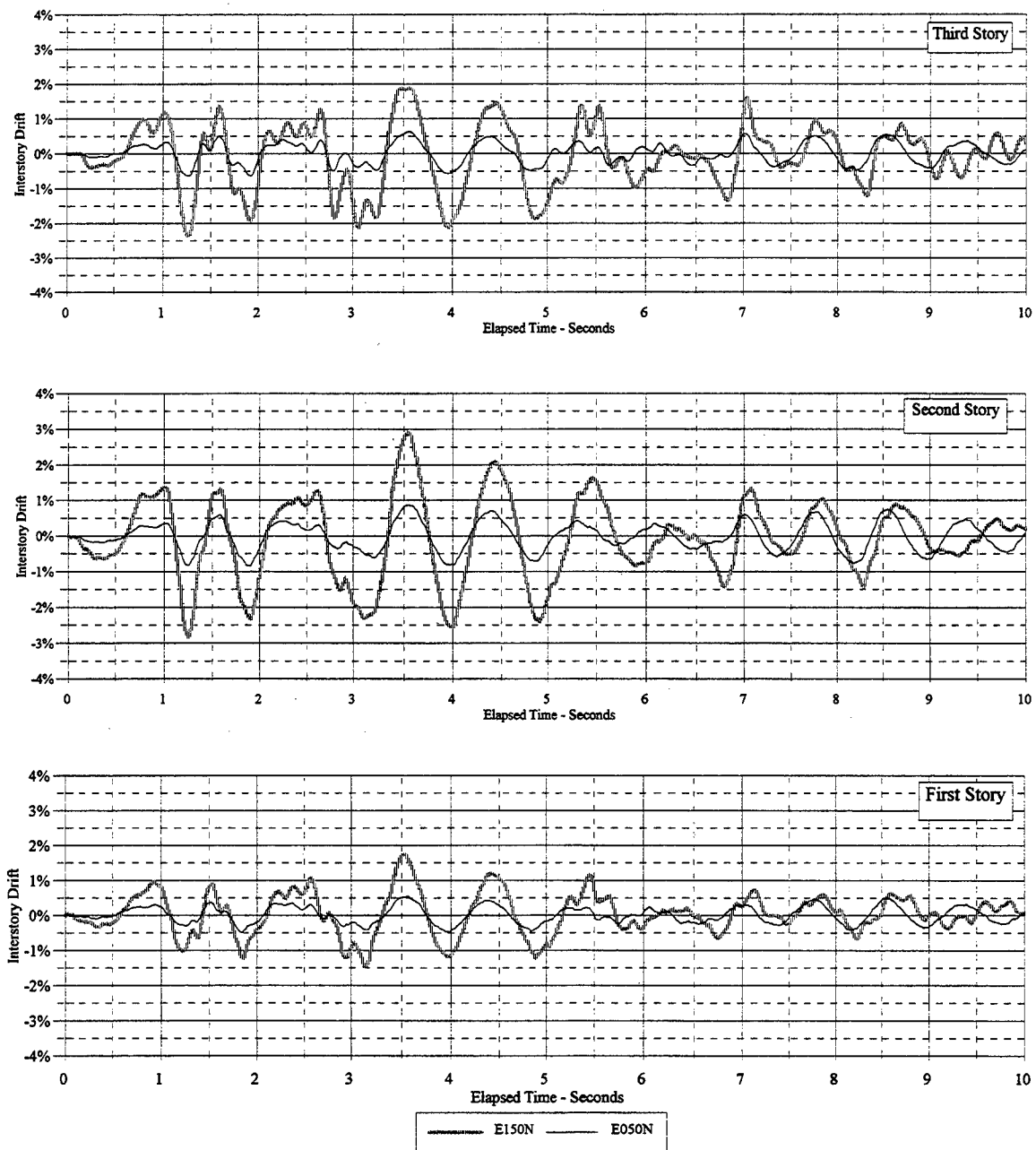


Figure 4.10 Interstory Drift Vs. Elapsed Time: E050N Vs. E150N

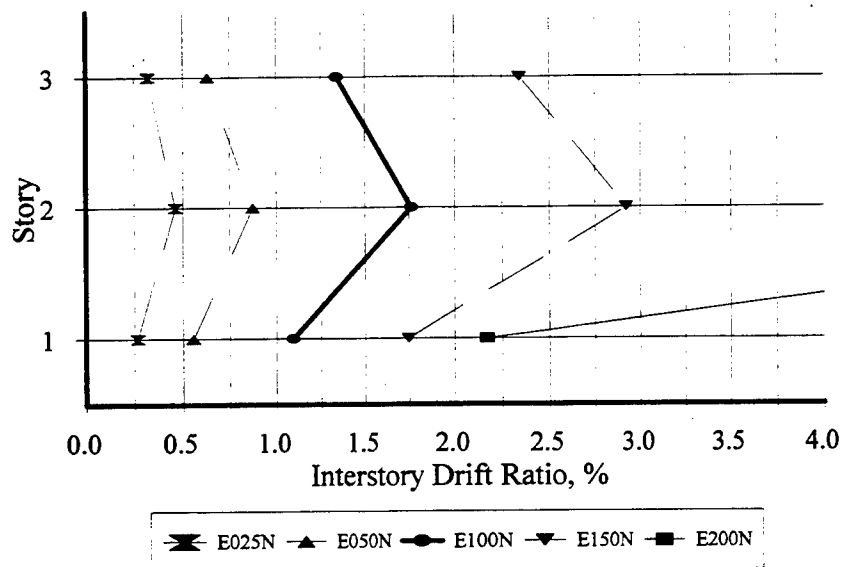
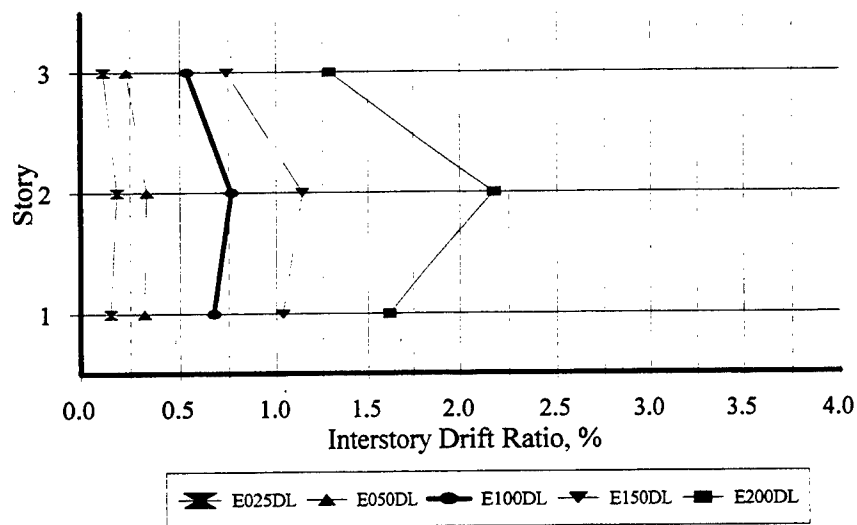


Figure 4.11 Maximum Story Drift Profiles for El Centro Simulations

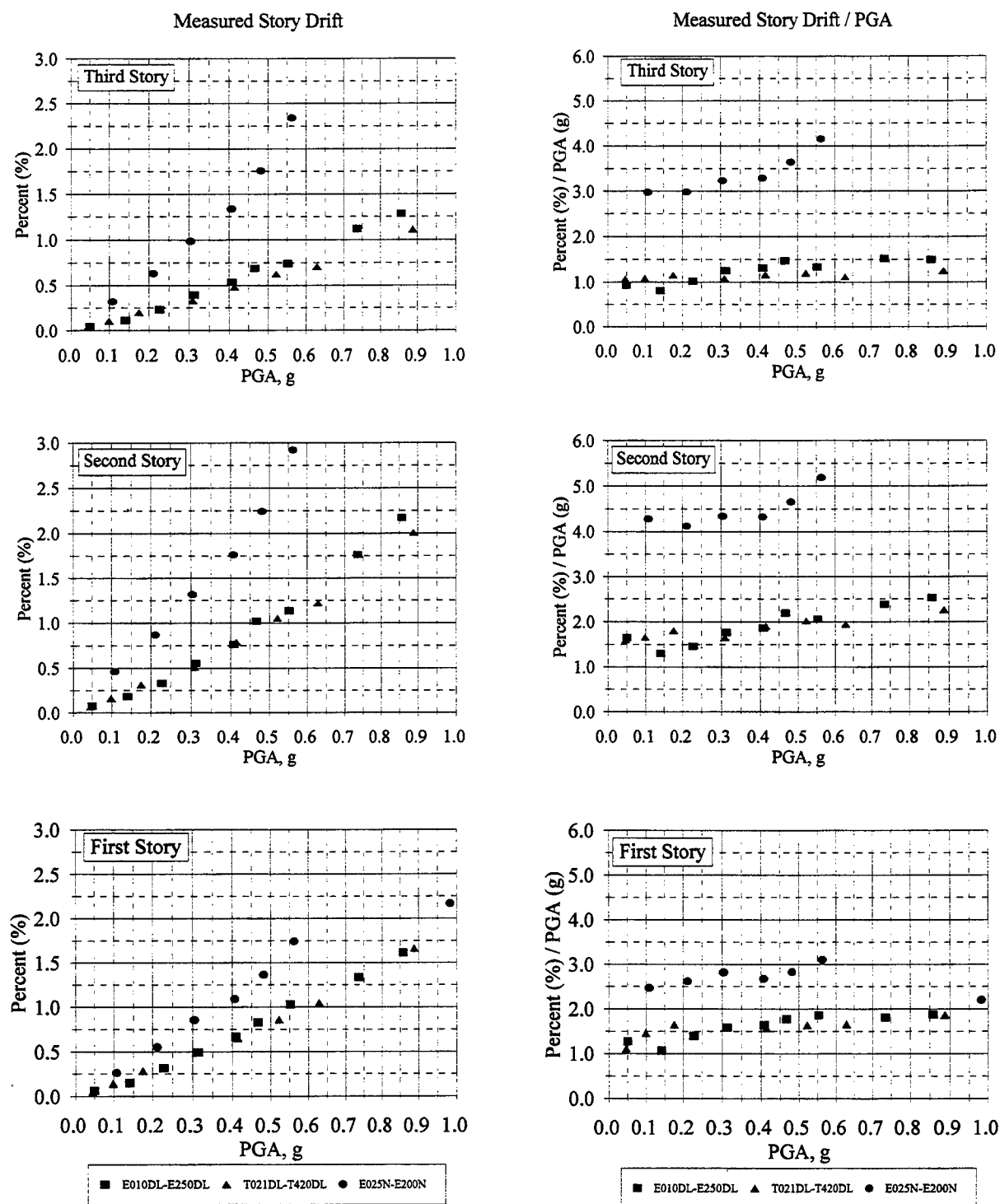


Figure 4.12 Maximum Story Drift Vs. Peak Ground Acceleration (PGA)

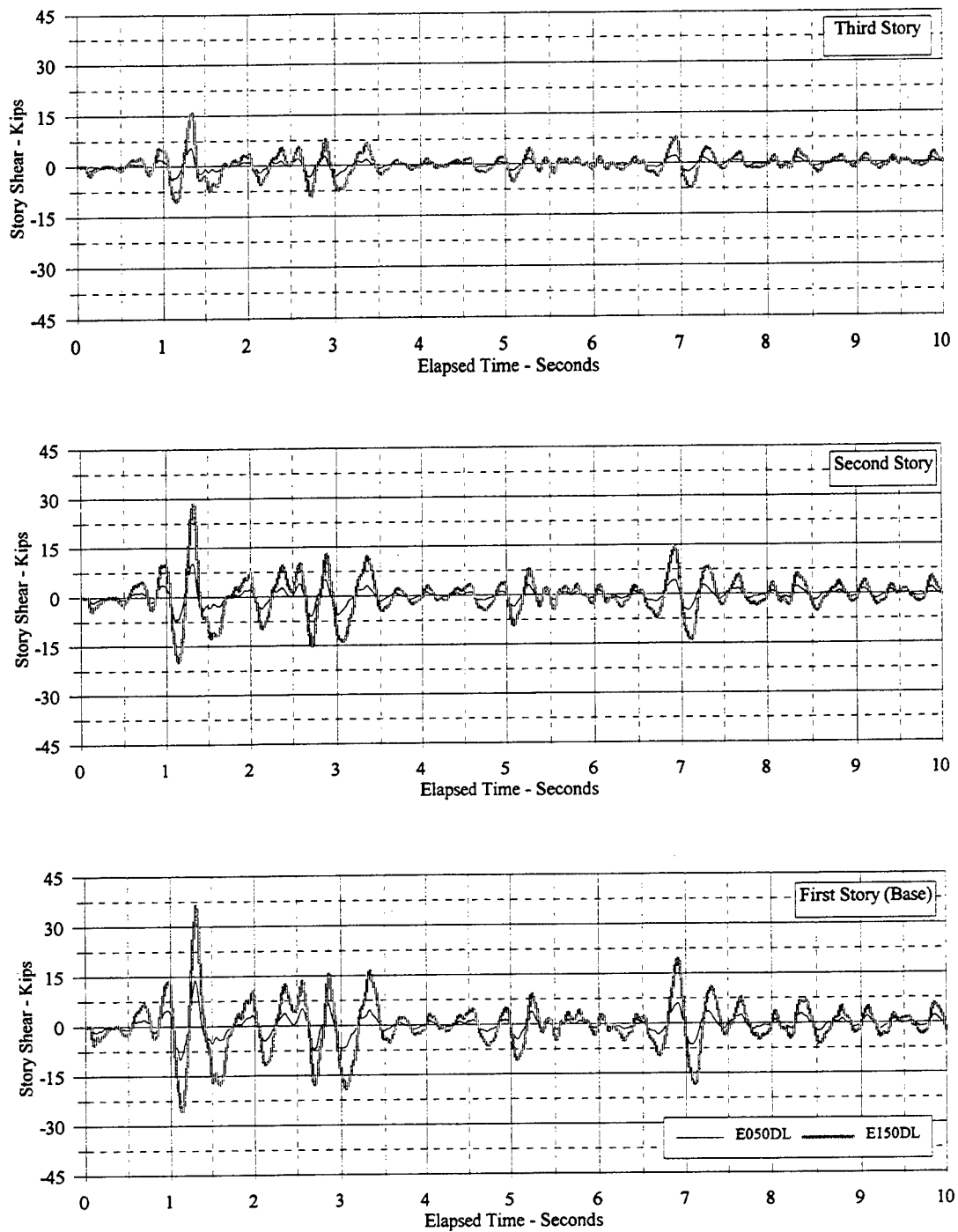


Figure 4.13 Story Shear Vs. Elapsed Time: E050DL Vs. E150DL

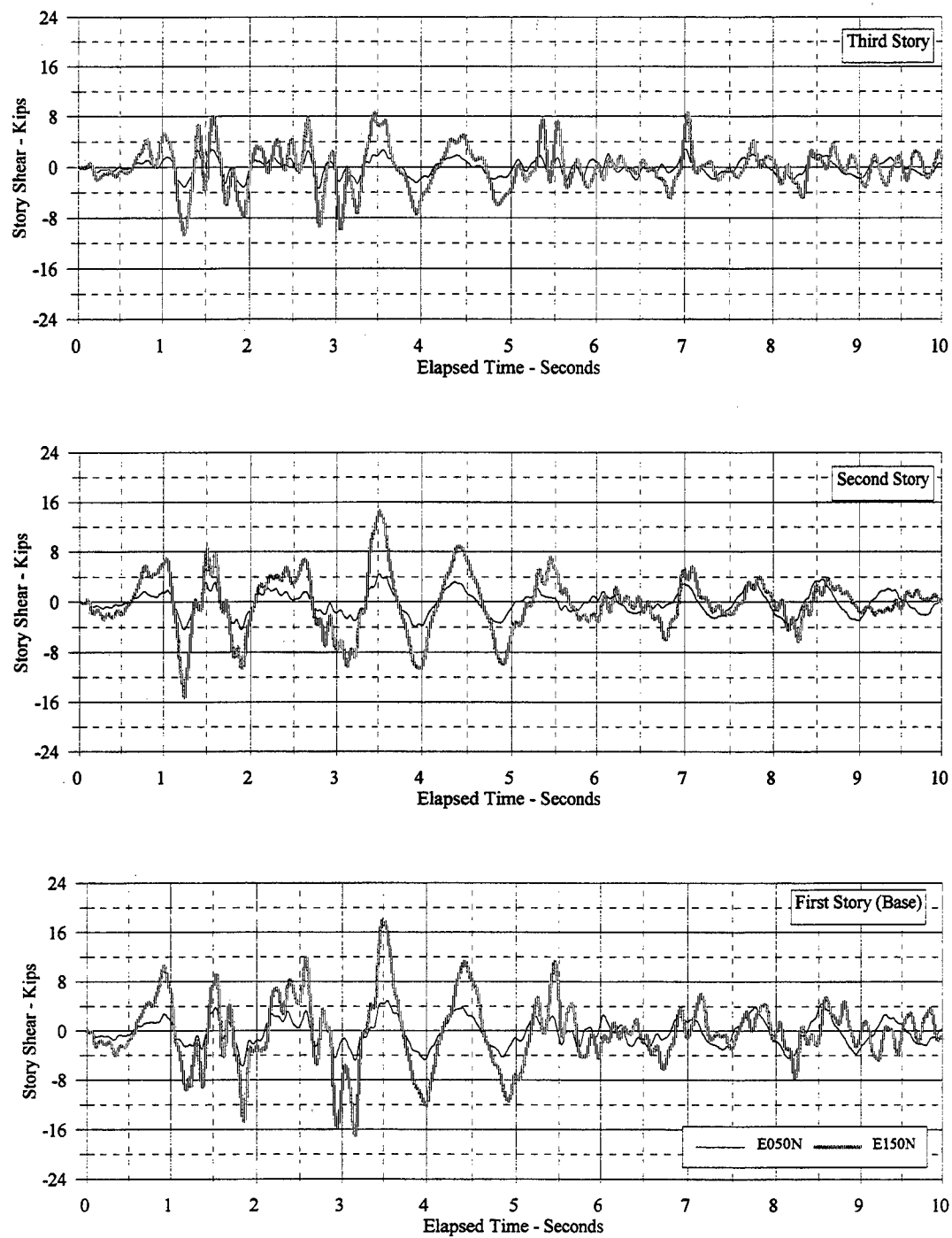


Figure 4.14 Story Shear Vs. Elapsed Time: E050N Vs. E150N

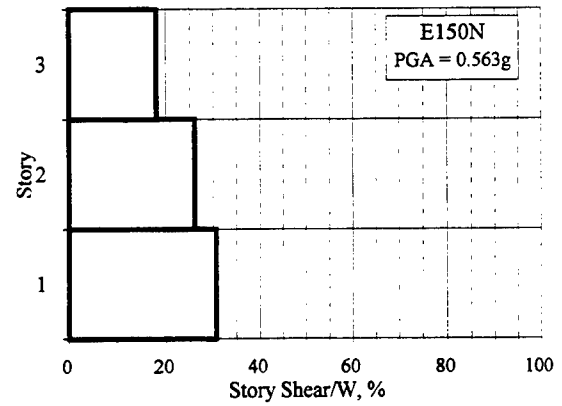
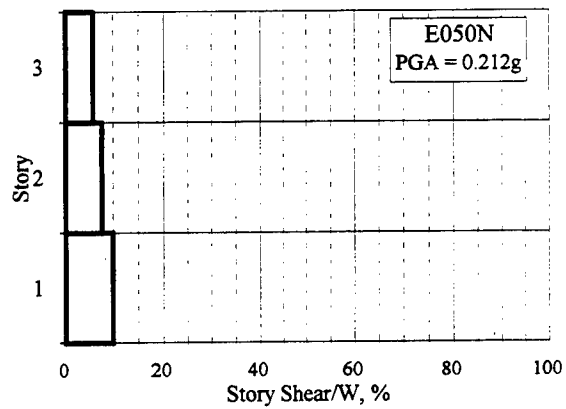
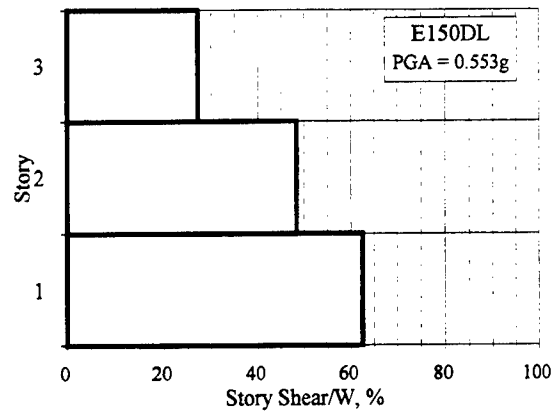
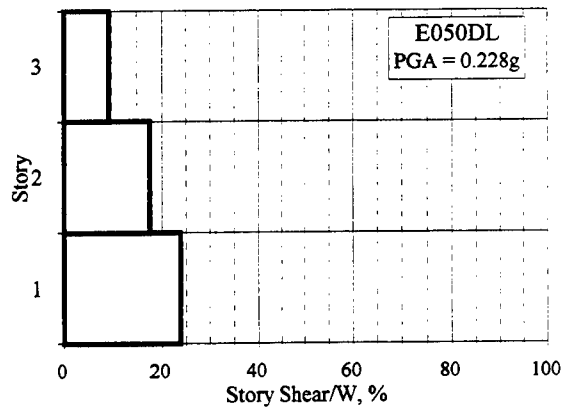


Figure 4.15 Maximum Story Shear Normalized by Total Model Weight: E050DL, E150DL, E050N, E150N

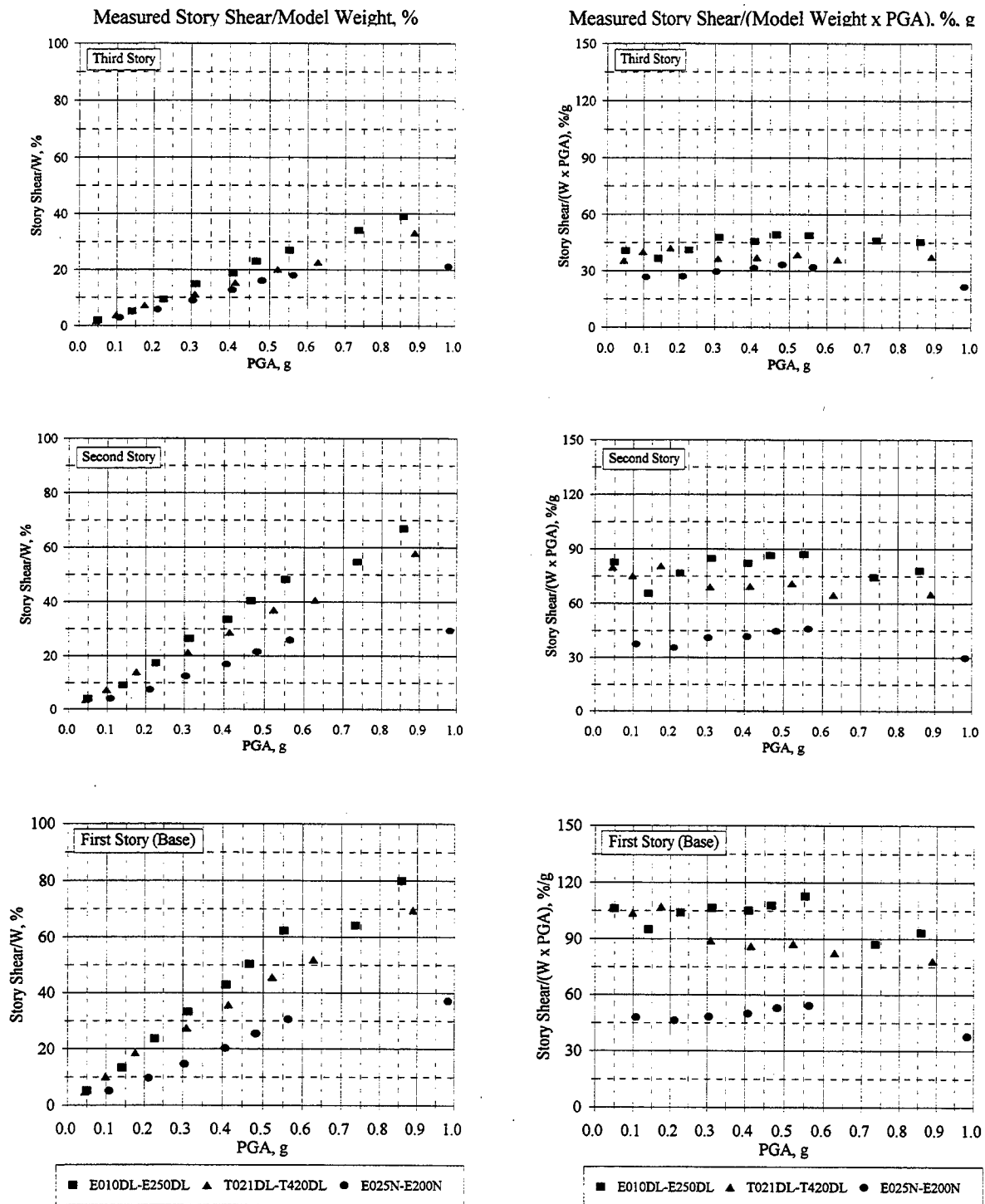


Figure 4.16 Maximum Story Shear Vs. Peak Ground Acceleration (PGA)

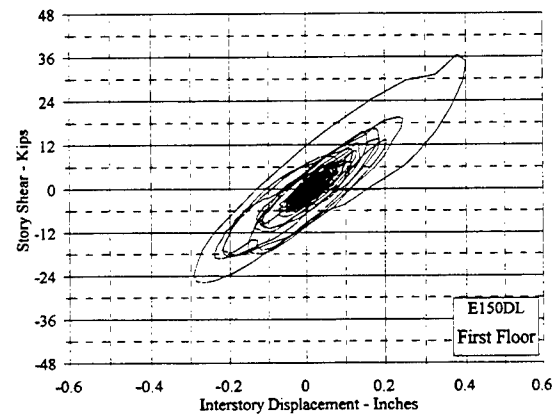
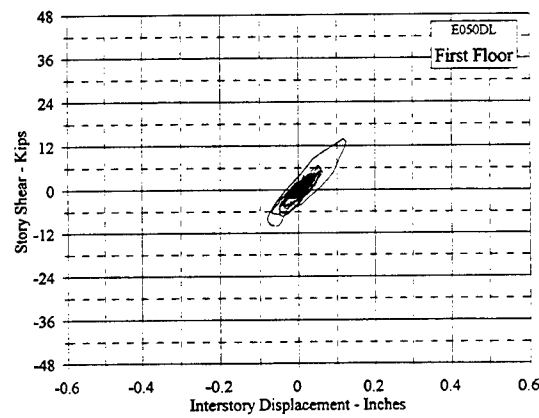
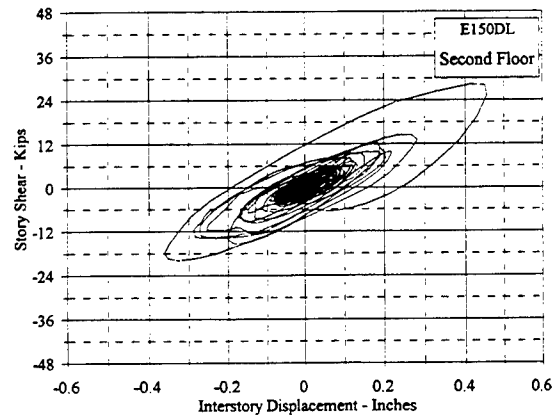
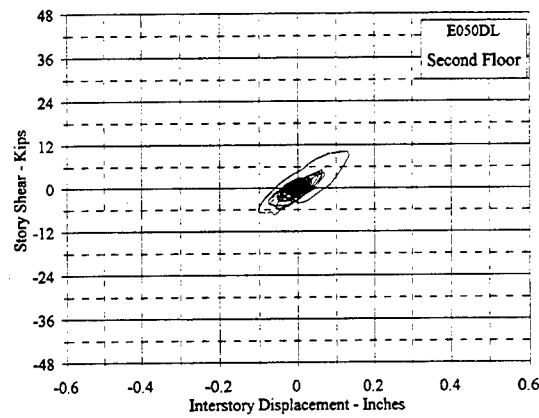
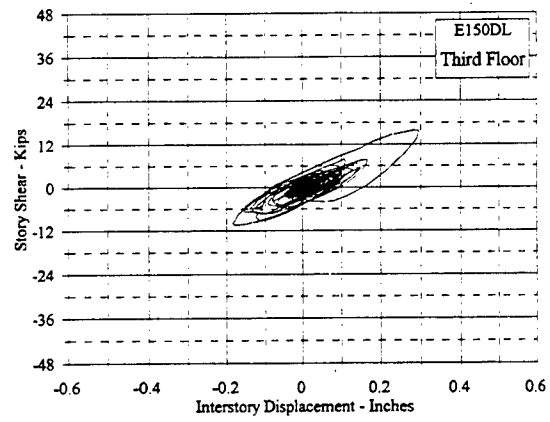
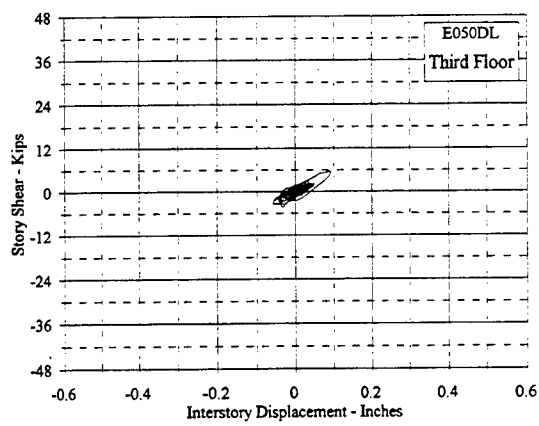


Figure 4.17 Story Shear Vs. Interstory Displacement : E050DL, E150DL

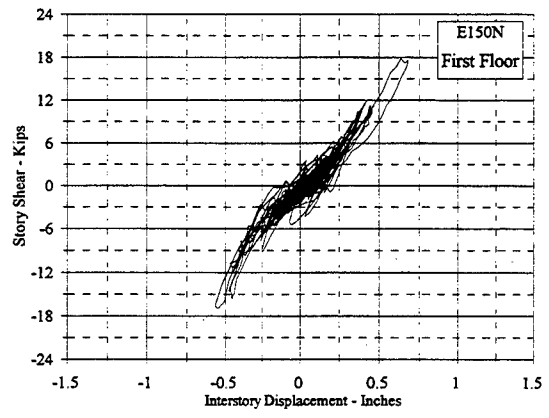
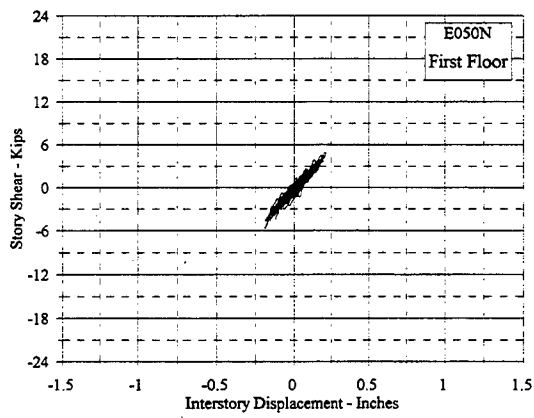
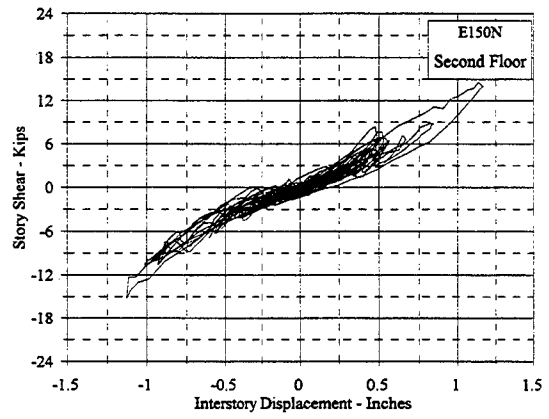
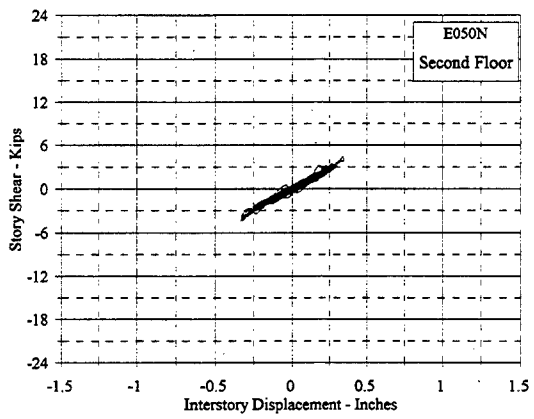
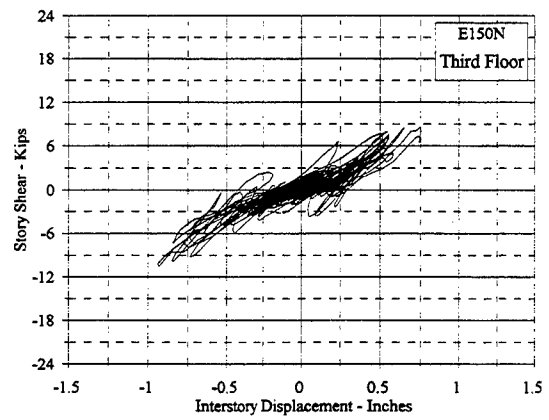
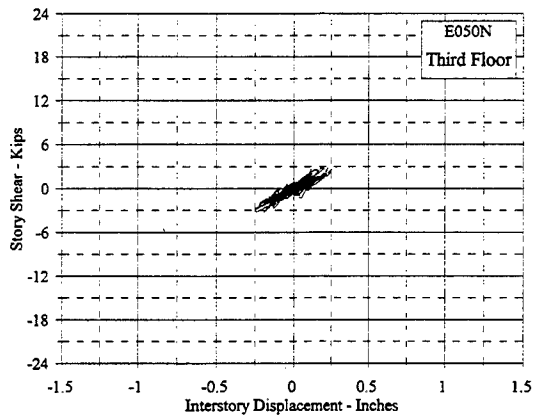


Figure 4.18 Story Shear Vs. Interstory Displacement: E050N, E150N

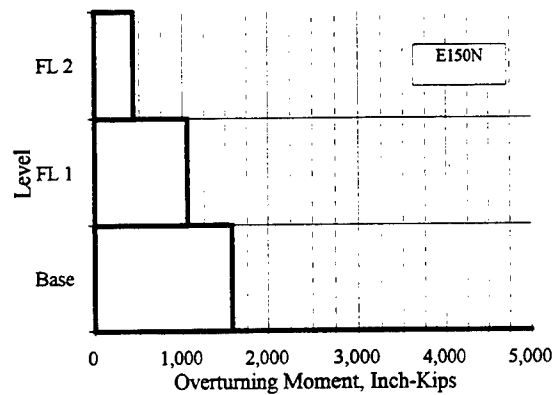
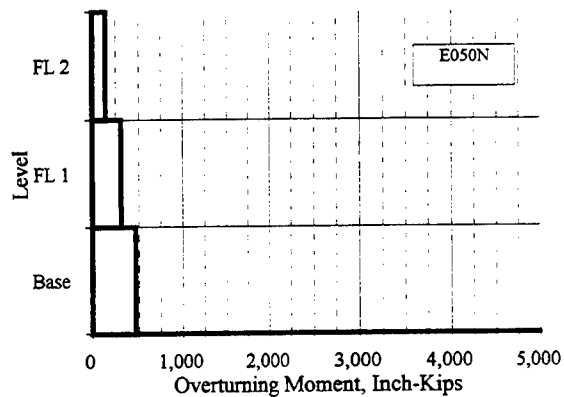
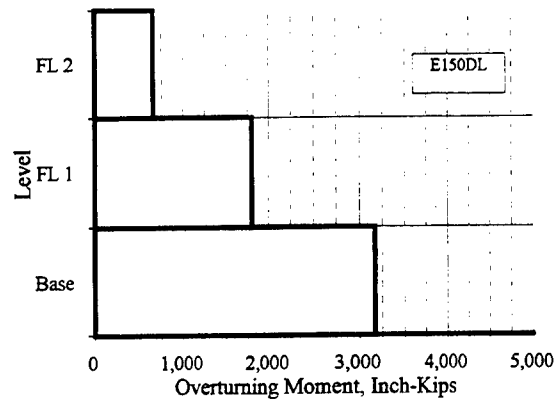
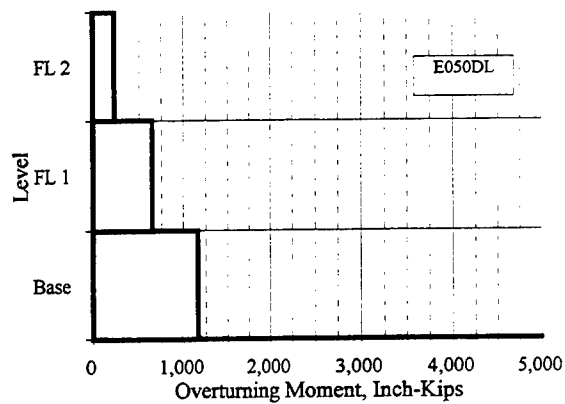


Figure 4.19 Maximum Overturning Moments: E050DL, E150DL, E050N, E150N

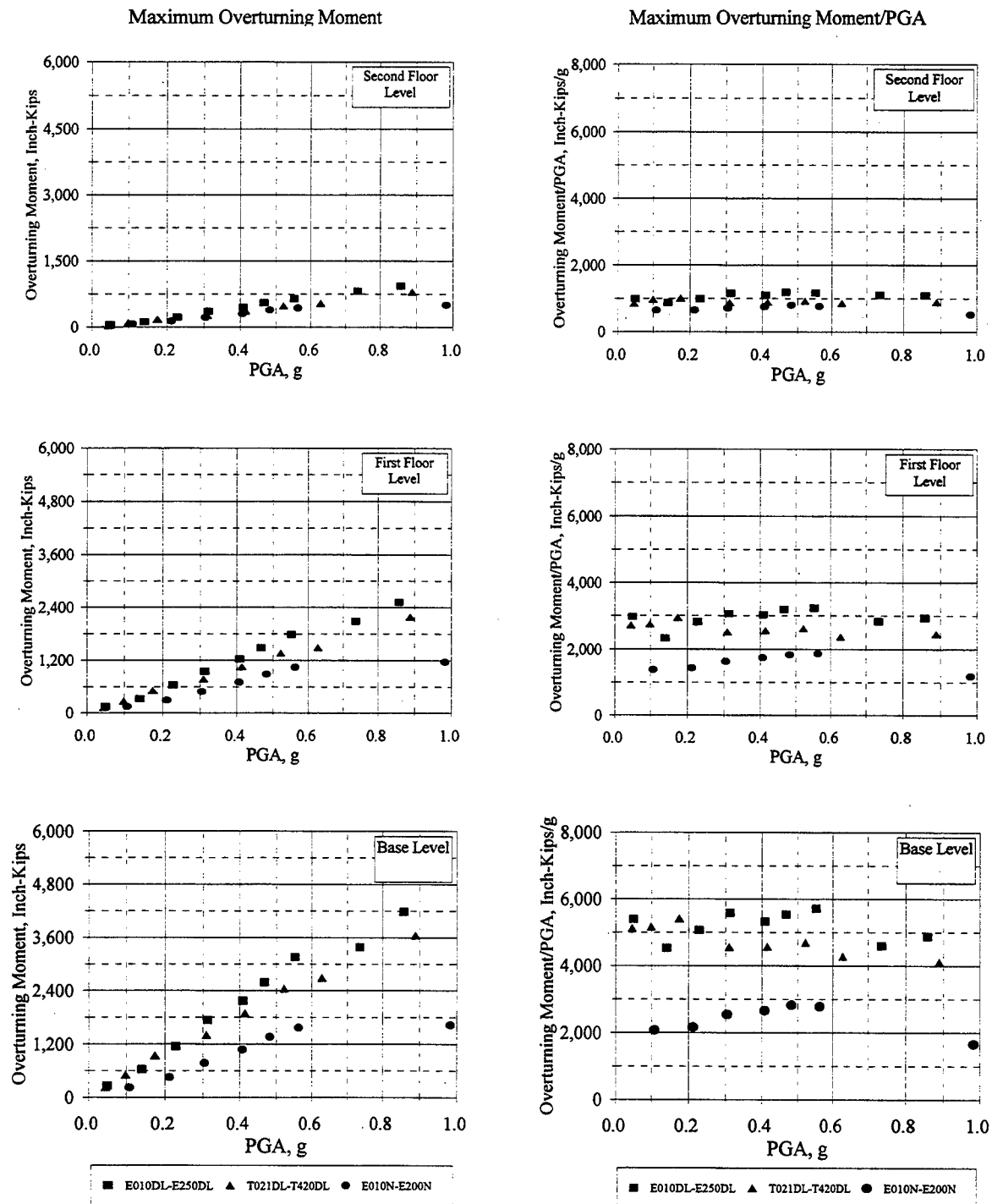


Figure 4.20 Maximum Overturning Moment Vs. PGA

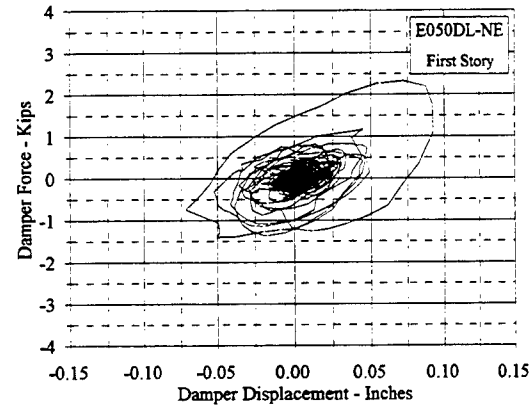
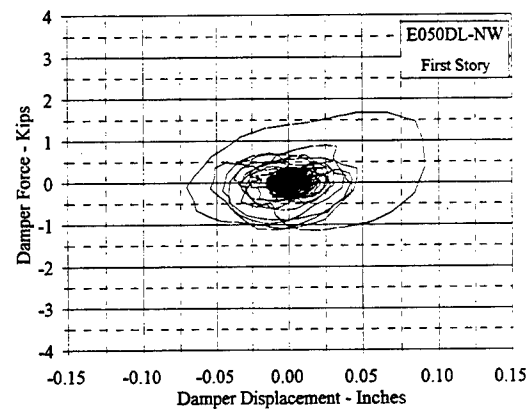
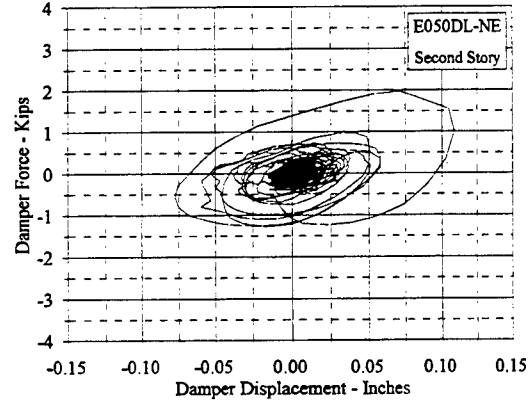
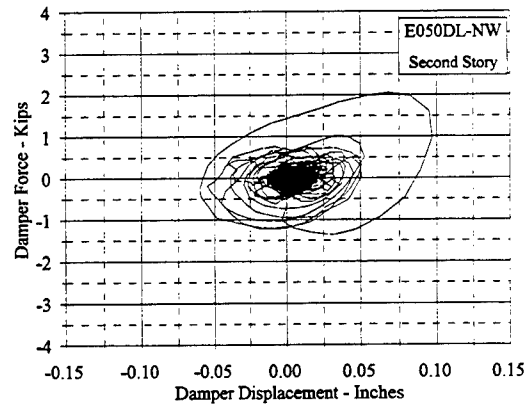
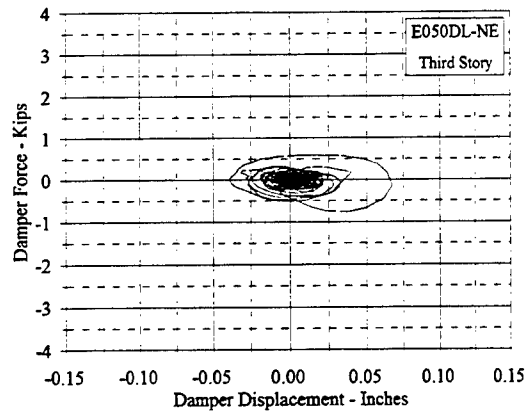
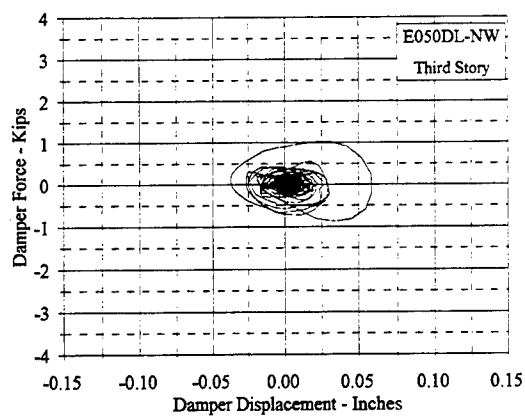


Figure 4.21 Damper Force Vs. Displacement: E050DL, NW and NE

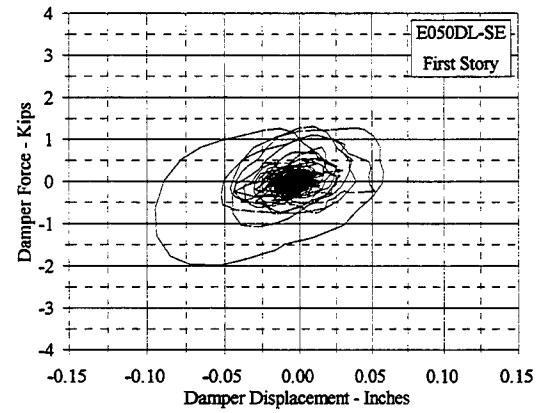
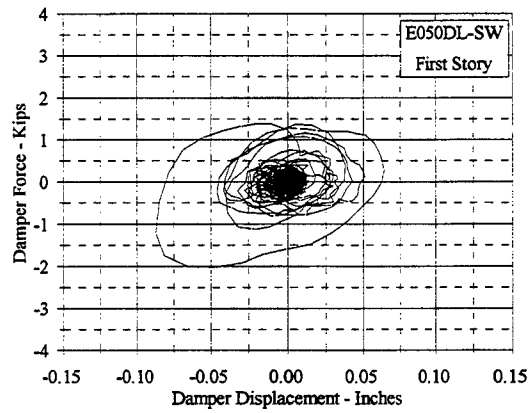
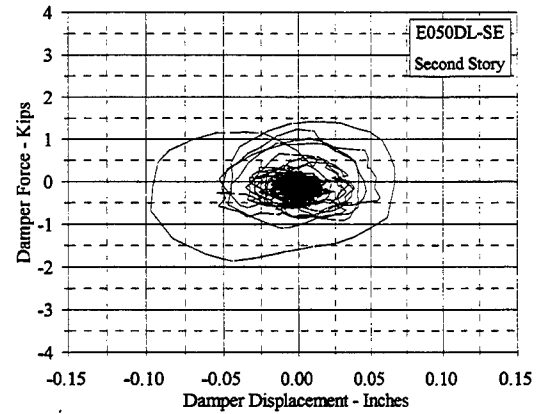
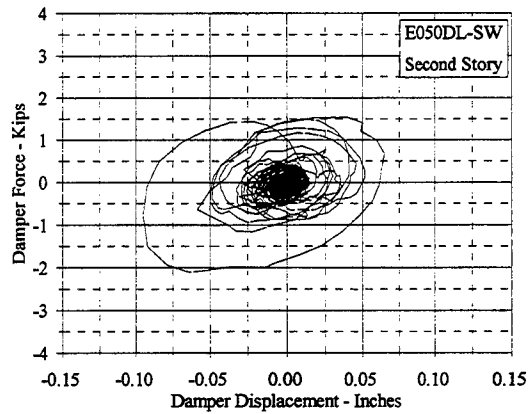
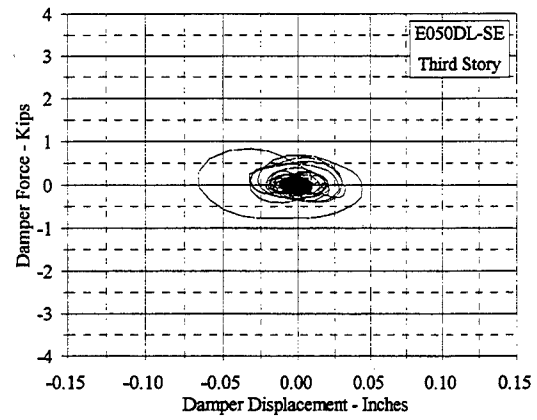
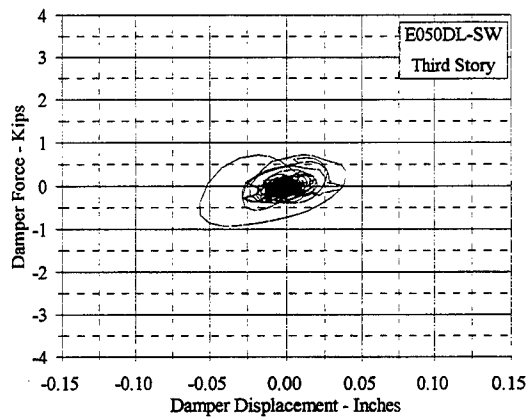


Figure 4.22 Damper Force Vs. Displacement: E050DL, SW and SE

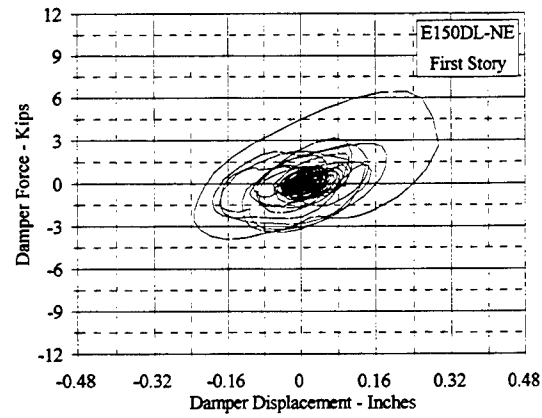
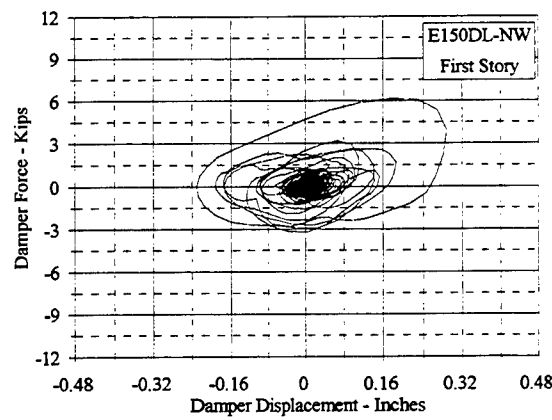
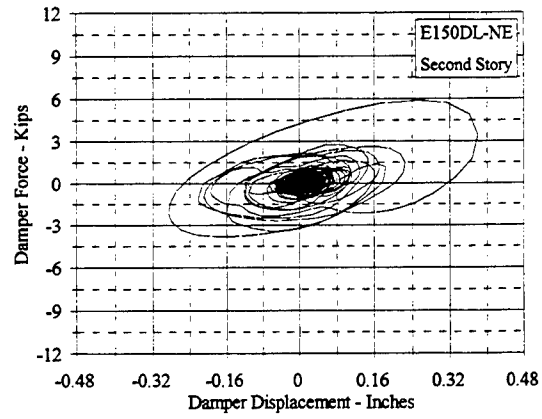
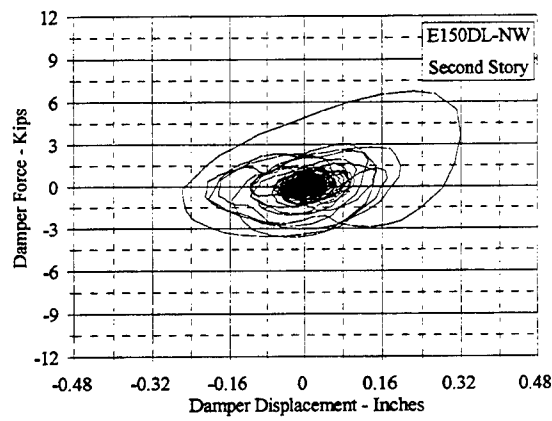
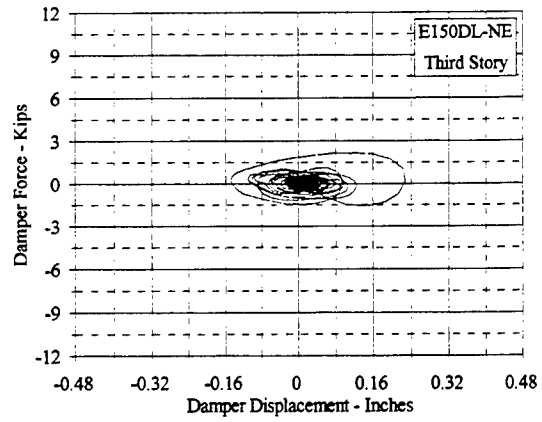
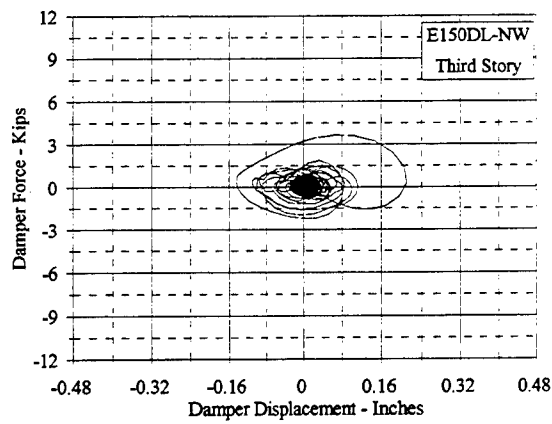


Figure 4.23 Damper Force Vs. Displacement: E150DL, NW and NE

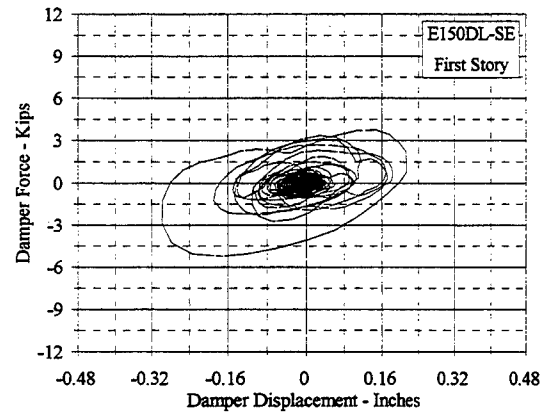
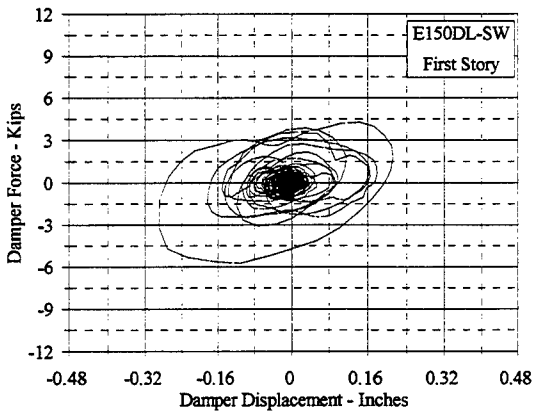
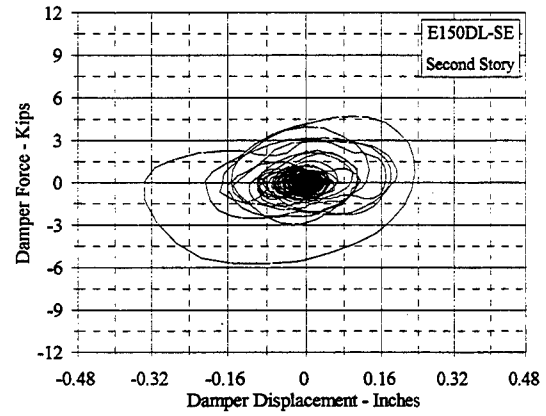
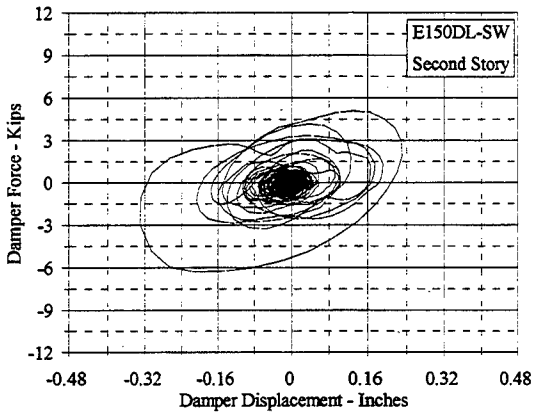
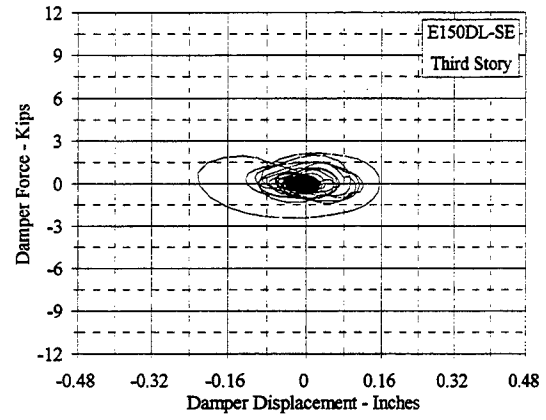
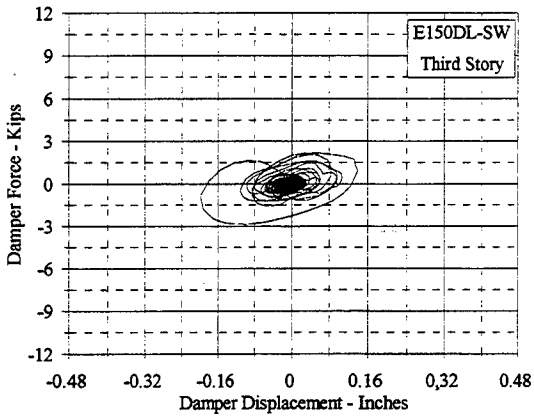


Figure 4.24 Damper Force Vs. Displacement: E150DL, SW and SE

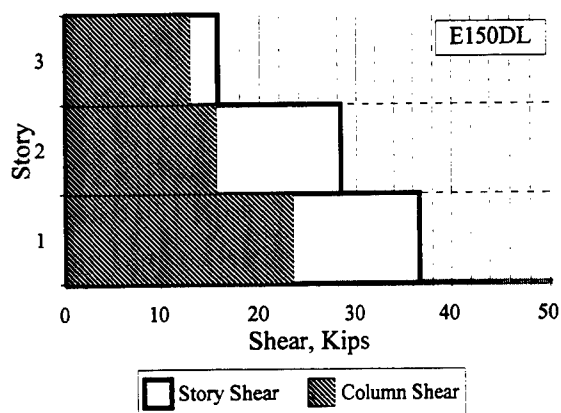
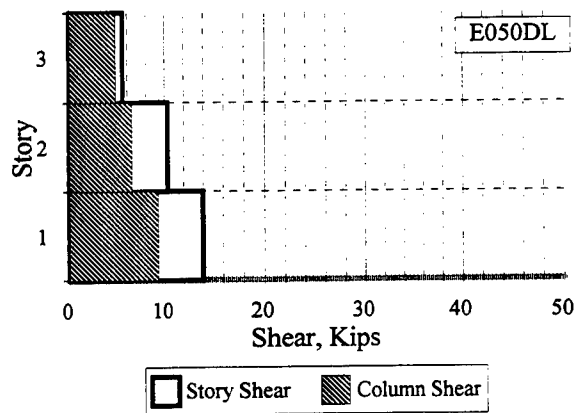
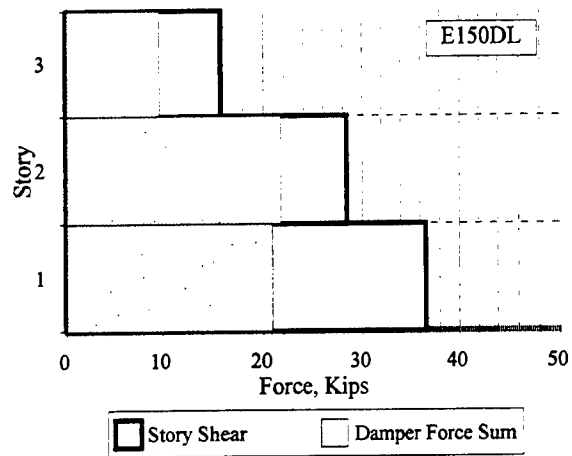
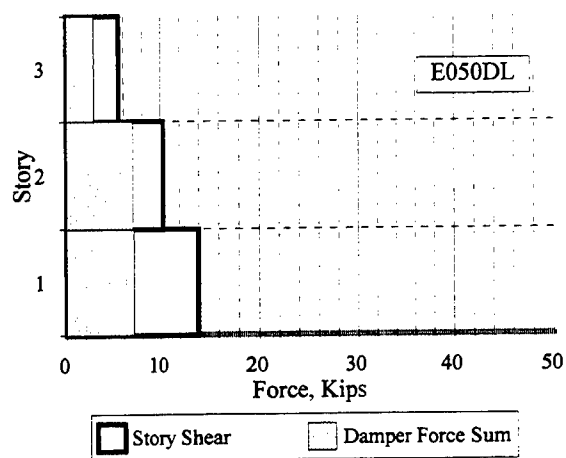


Figure 4.25 Maximum Sums of Horizontal Components of Damper Forces and Maximum Column Shears Vs. Maximum Story Shears: E050DL, E150DL

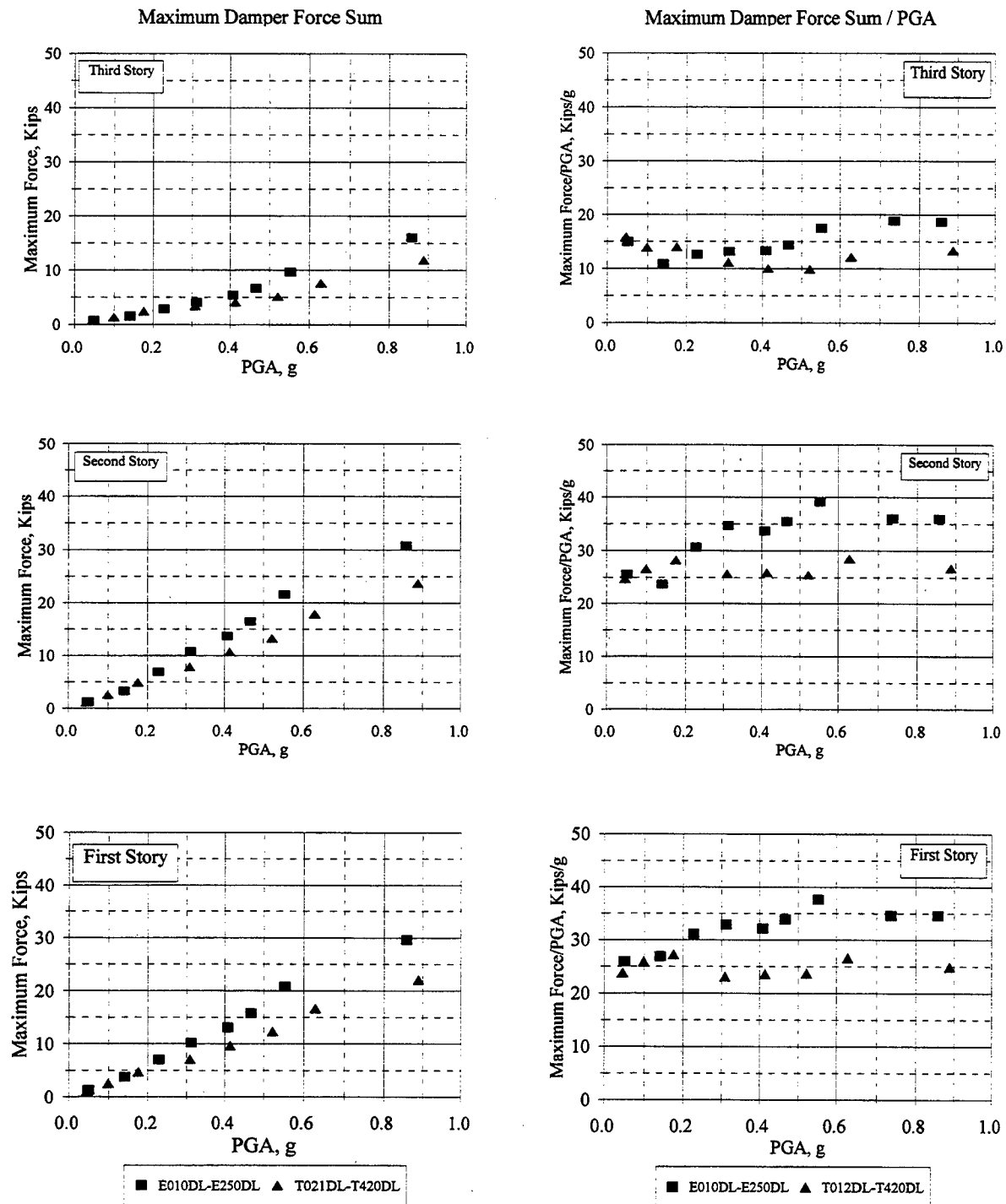


Figure 4.26 Maximum Sum of Horizontal Components of Damper Forces Vs. PGA

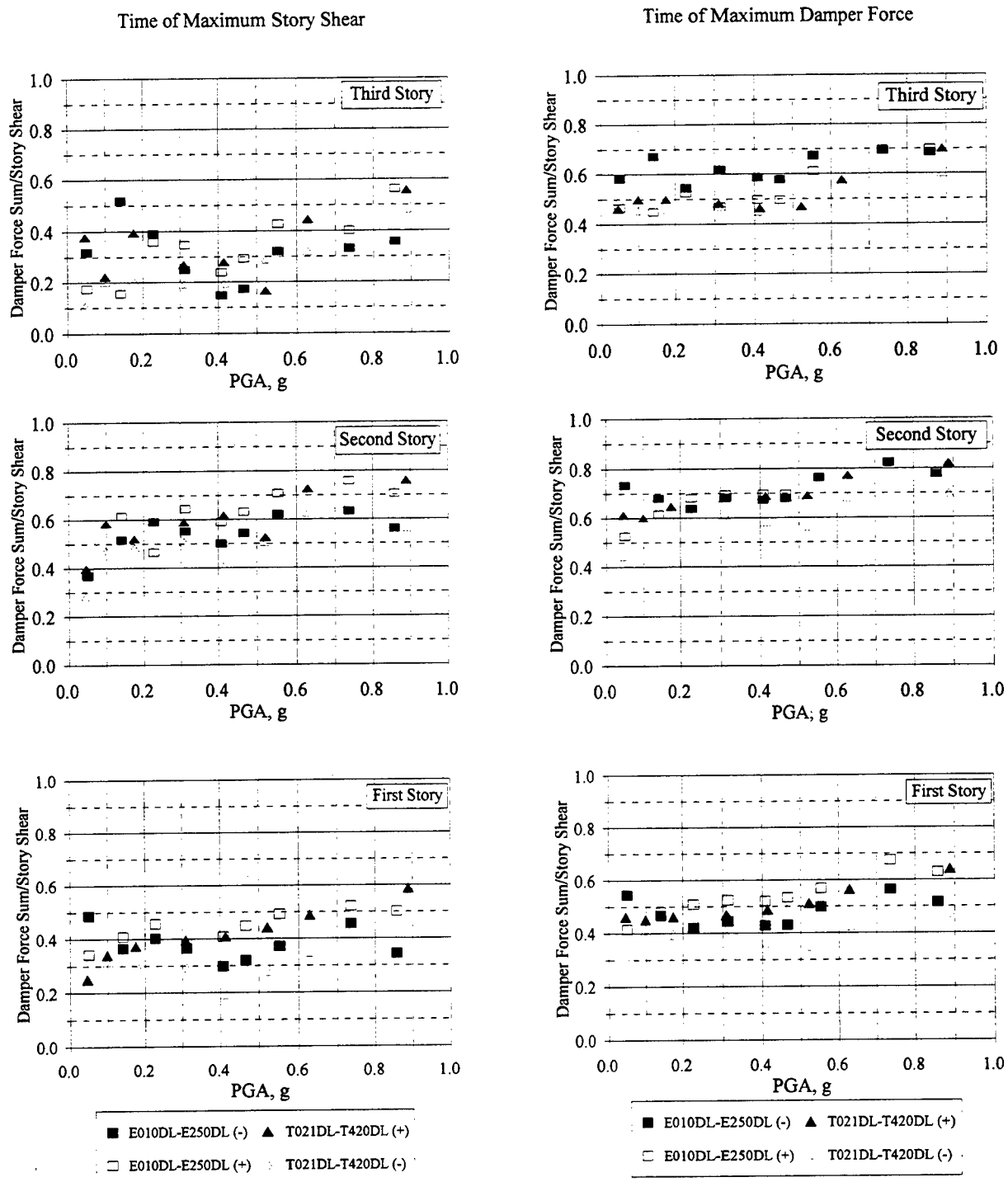


Figure 4.27 Sums of Horizontal Components of Damper Forces/Maximum Story Shear Vs. PGA

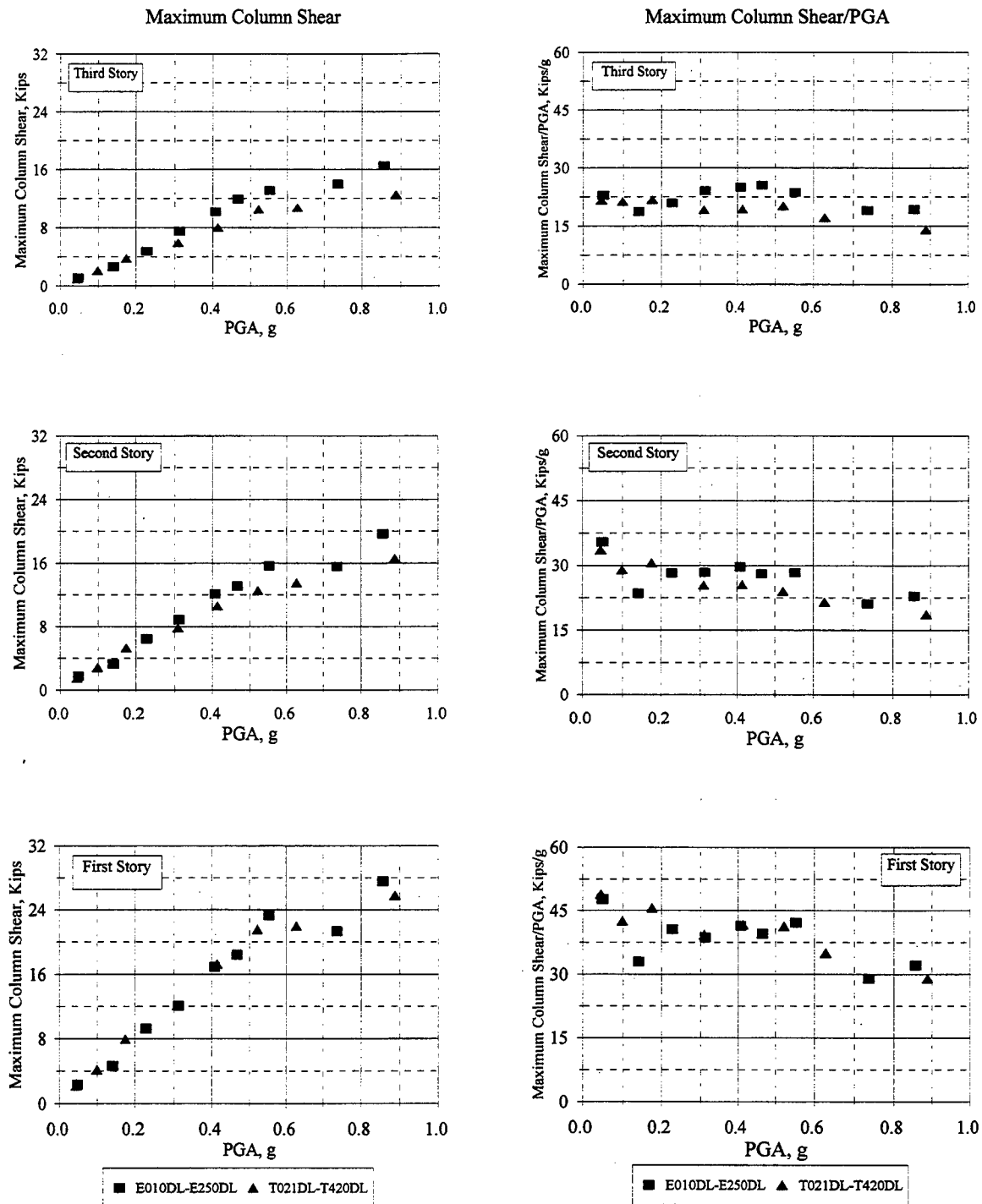


Figure 4.28 Maximum Column Shear Vs. PGA

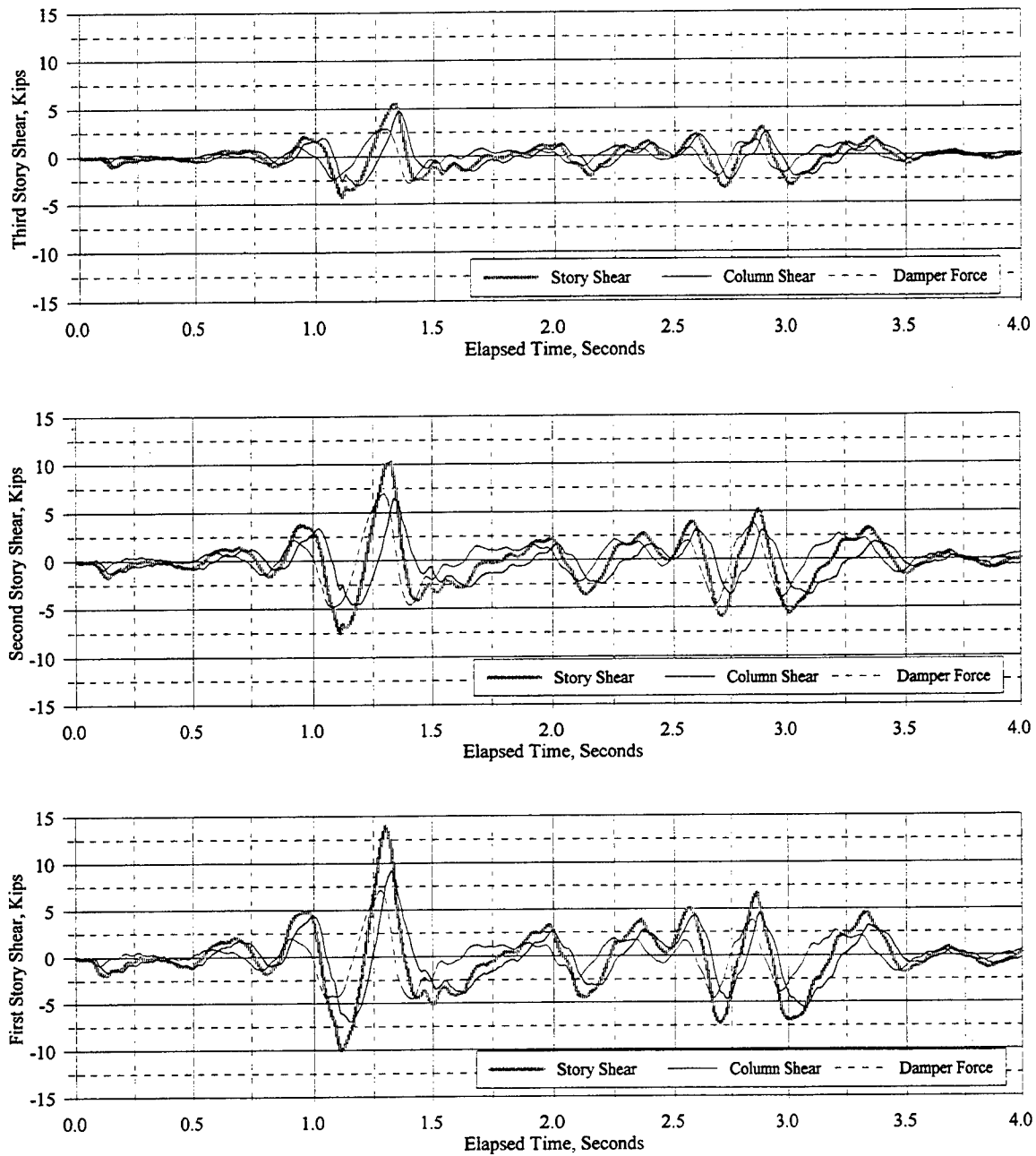


Figure 4.29 Story Shear, Column Shear, and Sum of Horizontal Components of Damper Forces: E050DL

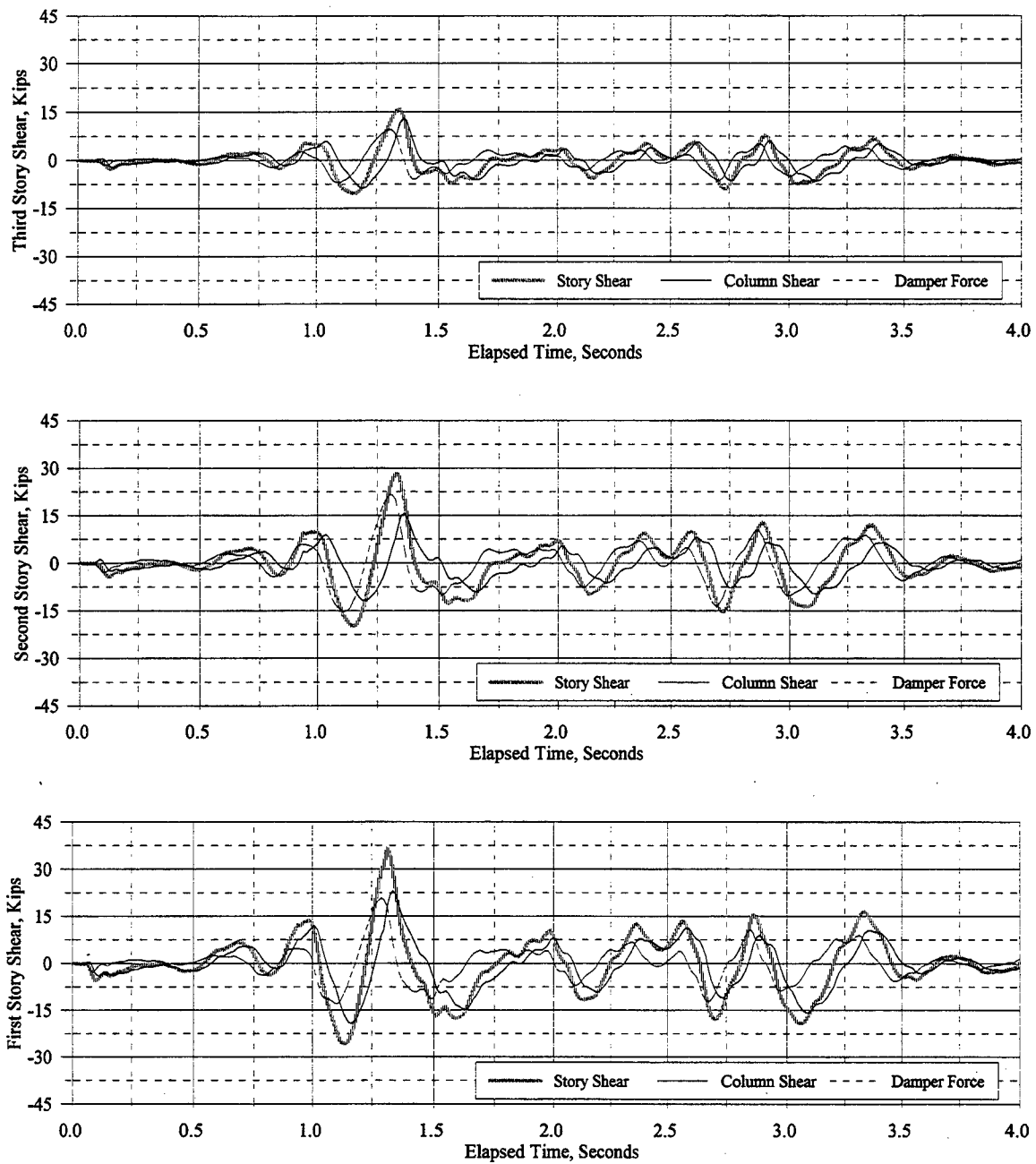


Figure 4.30 Story Shear, Column Shear, and Sum of Horizontal Components of Damper Forces: E150DL

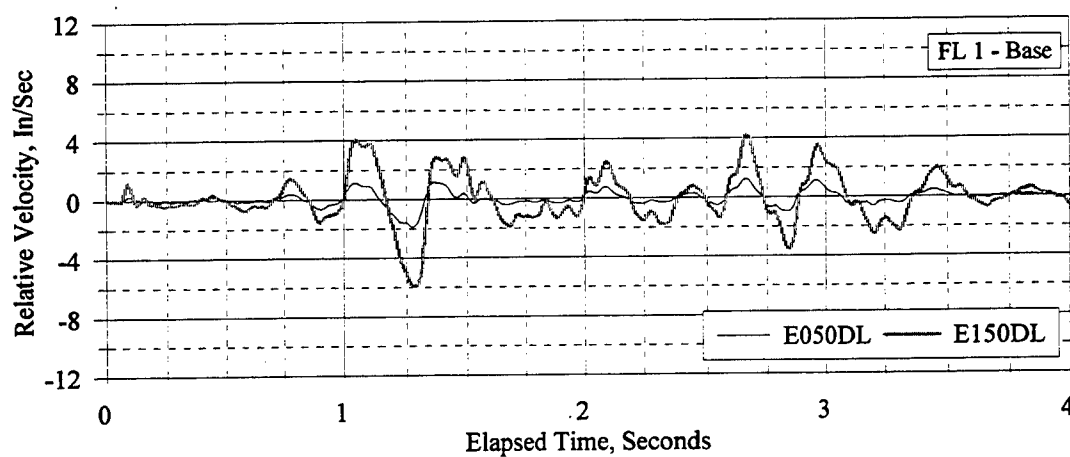
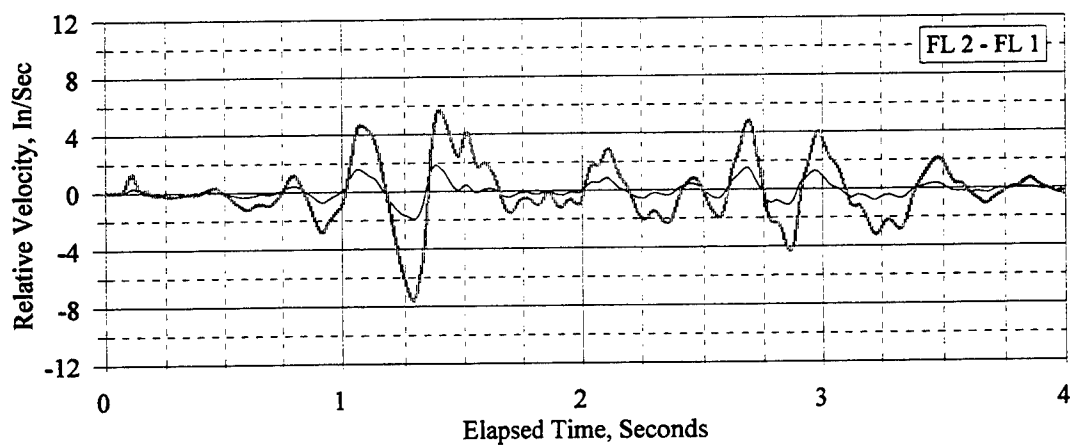
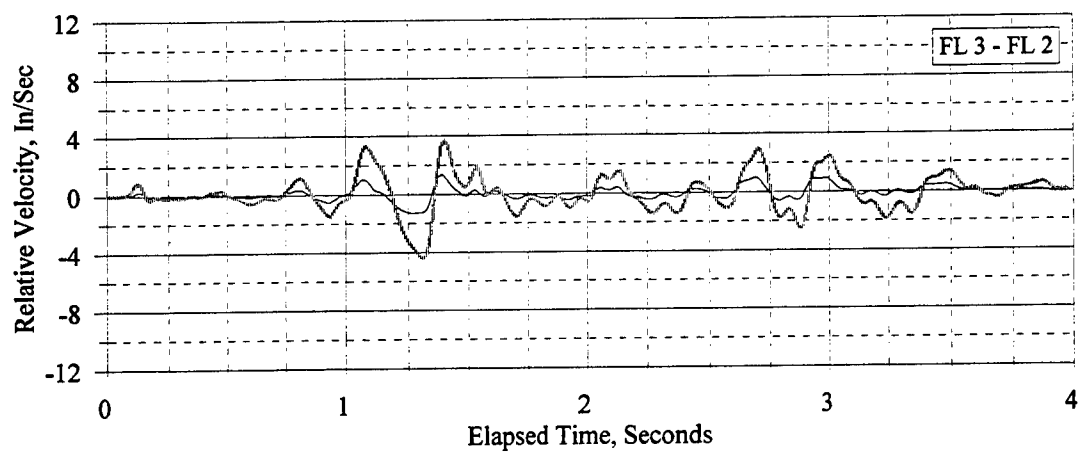


Figure 4.31 Relative Floor Velocities: E050DL, E150DL

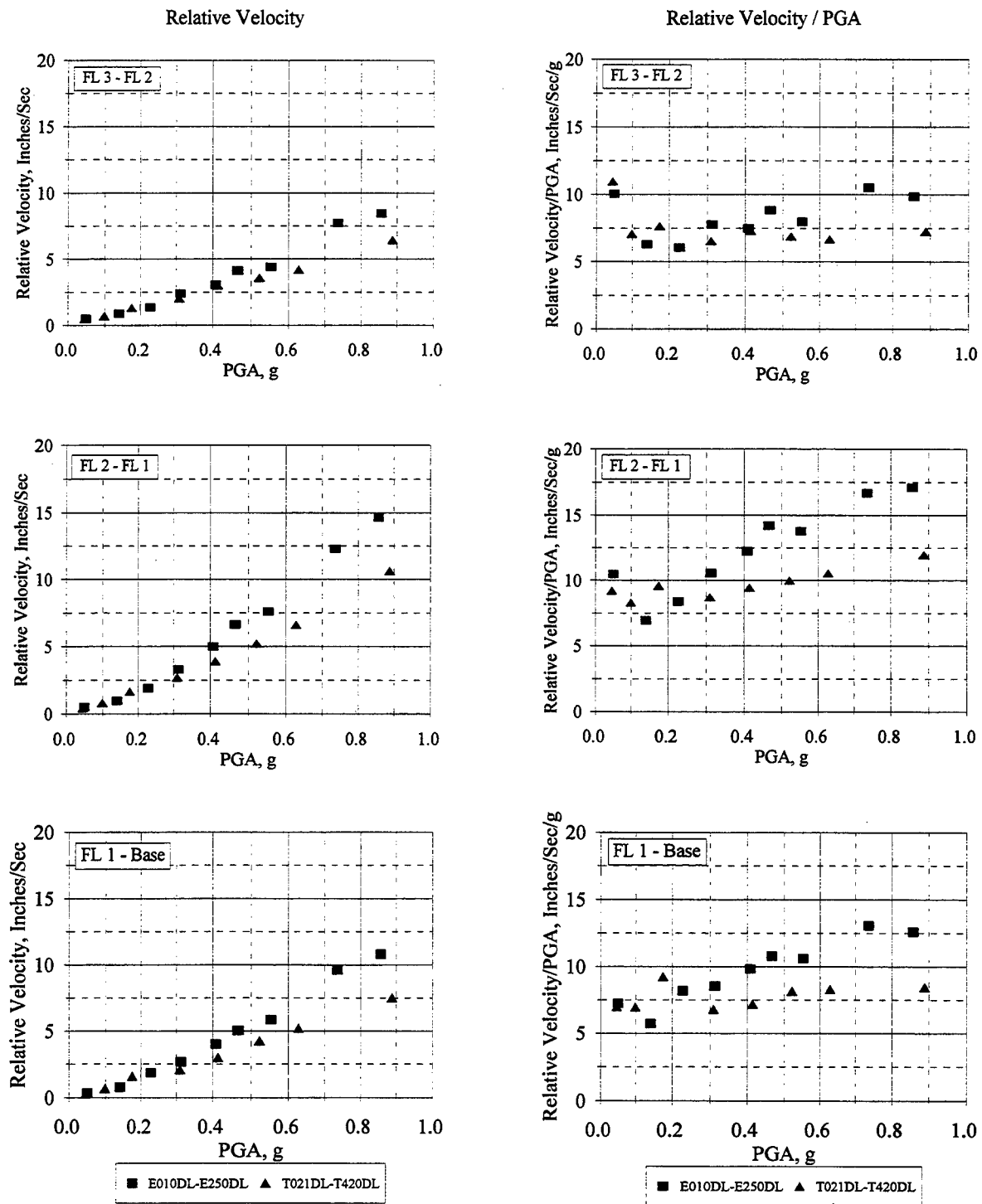


Figure 4.32 Maximum Relative Floor Velocity Vs. PGA

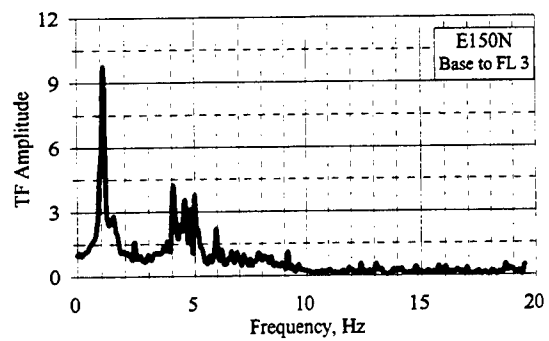
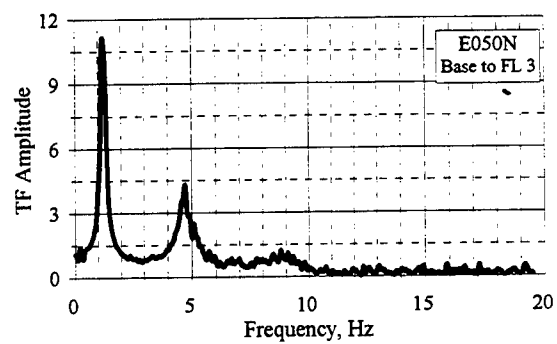
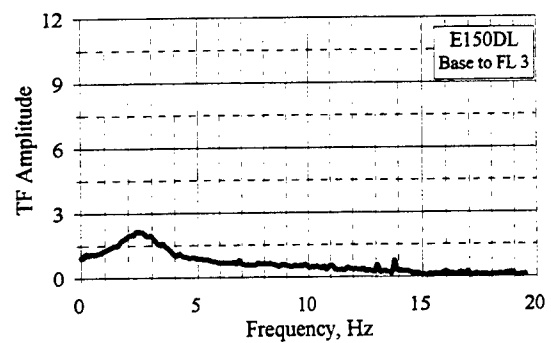
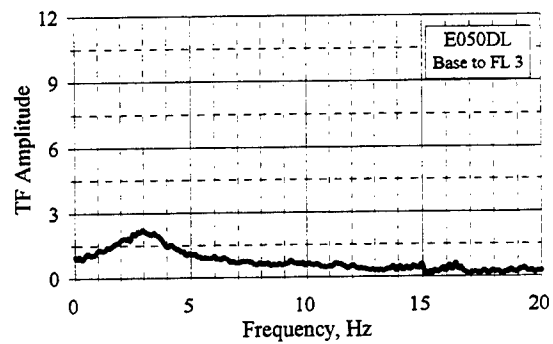


Figure 4.33 Acceleration-Based Transfer Functions (TFs): E050DL, E150DL, E050N, E150N

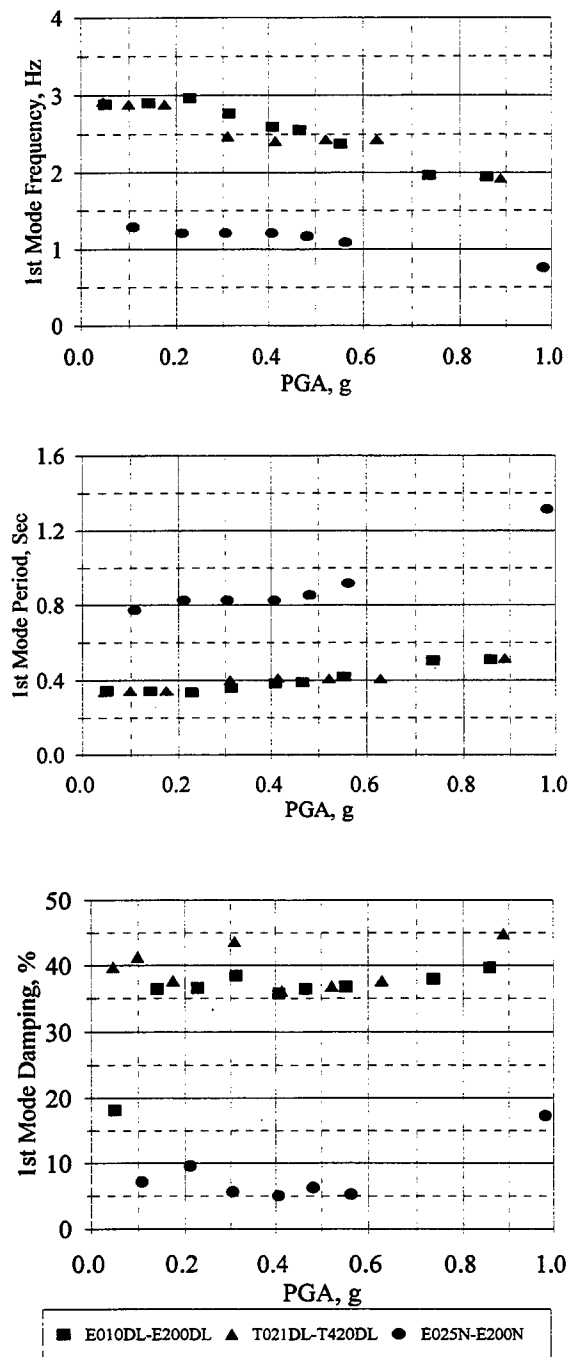


Figure 4.34 Apparent First Mode Properties Based on Earthquake Simulation Transfer Functions

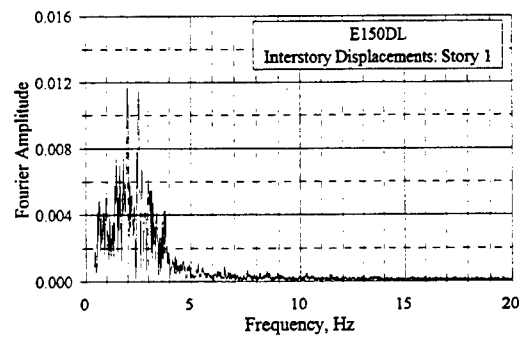
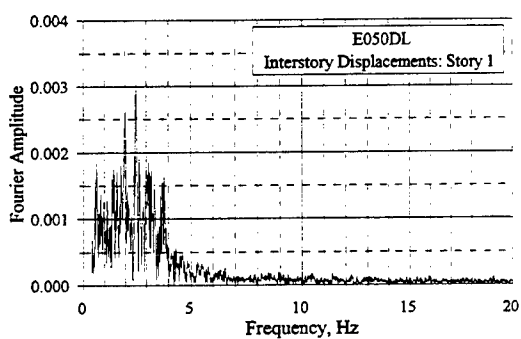
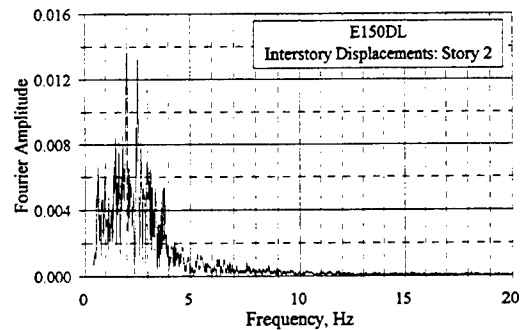
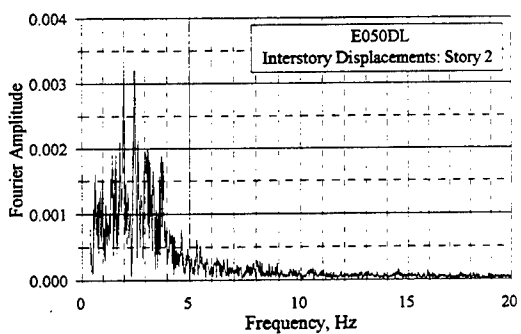
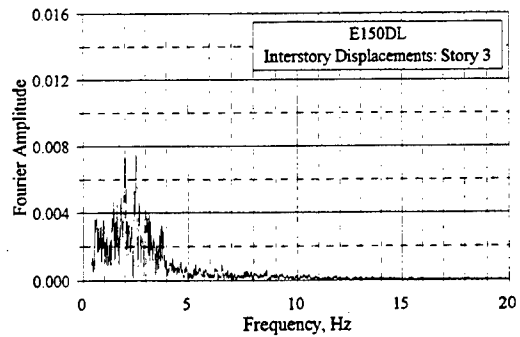
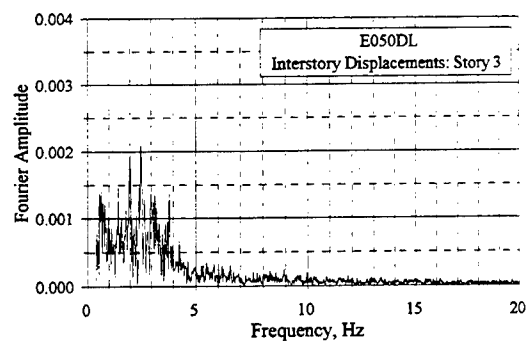


Figure 4.35 Fourier Amplitude Spectra of Interstory Displacements: E050DL, E150DL

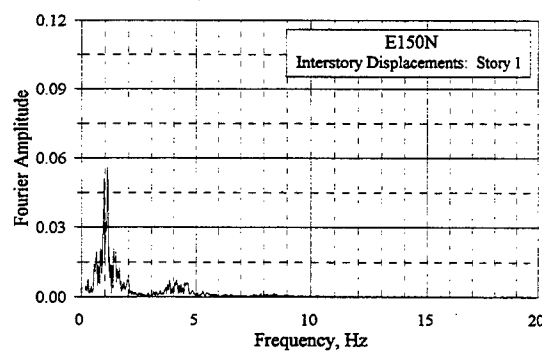
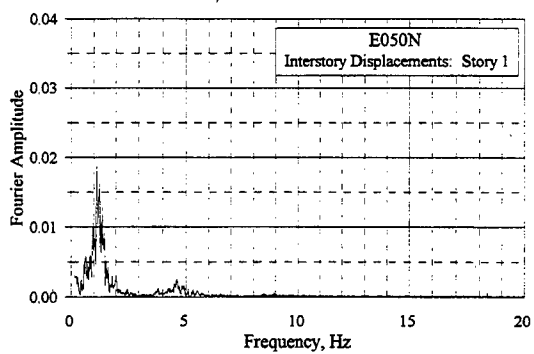
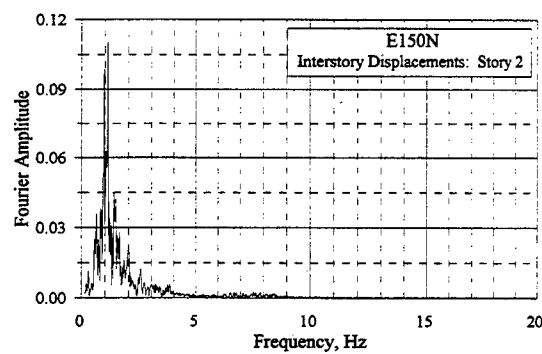
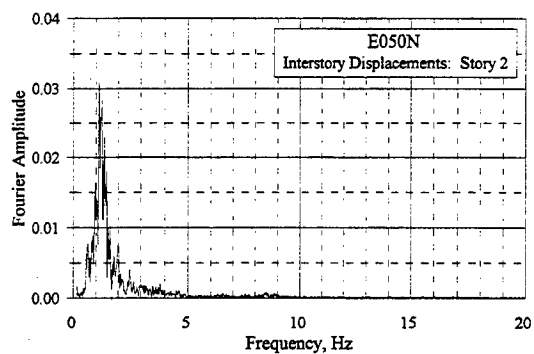
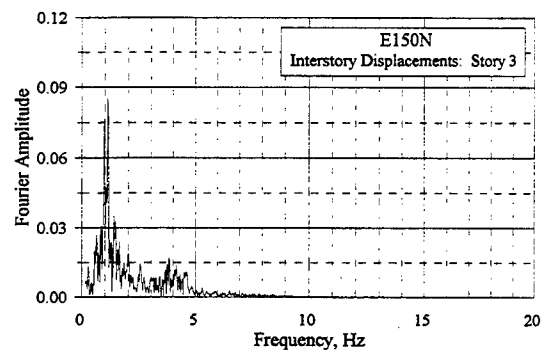
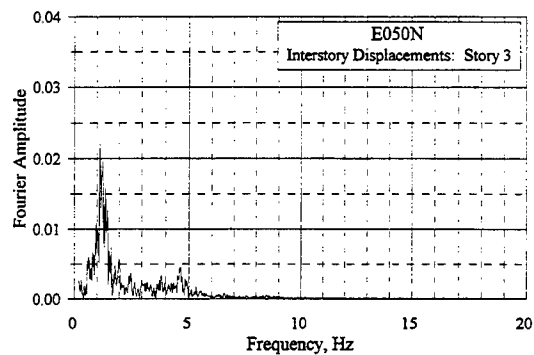


Figure 4.36 Fourier Amplitude Spectra of Interstory Displacements: E050N, E150N

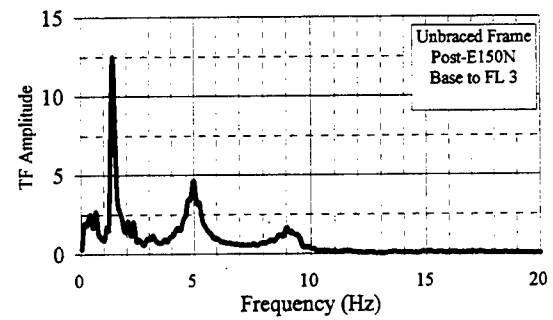
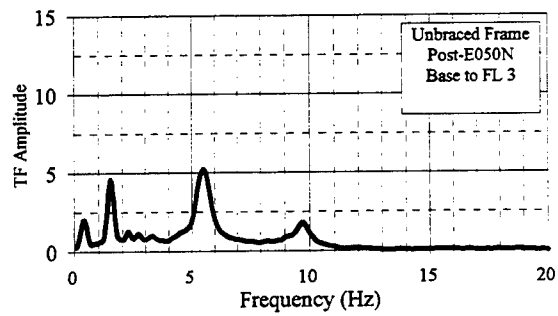
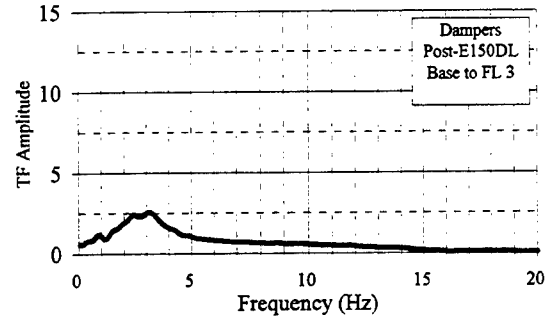
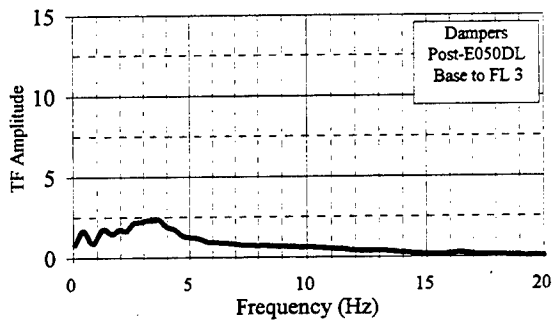


Figure 4.37 Acceleration-Based Transfer Functions, White Noise Tests: E050DL, E150DL, E050N, E150N

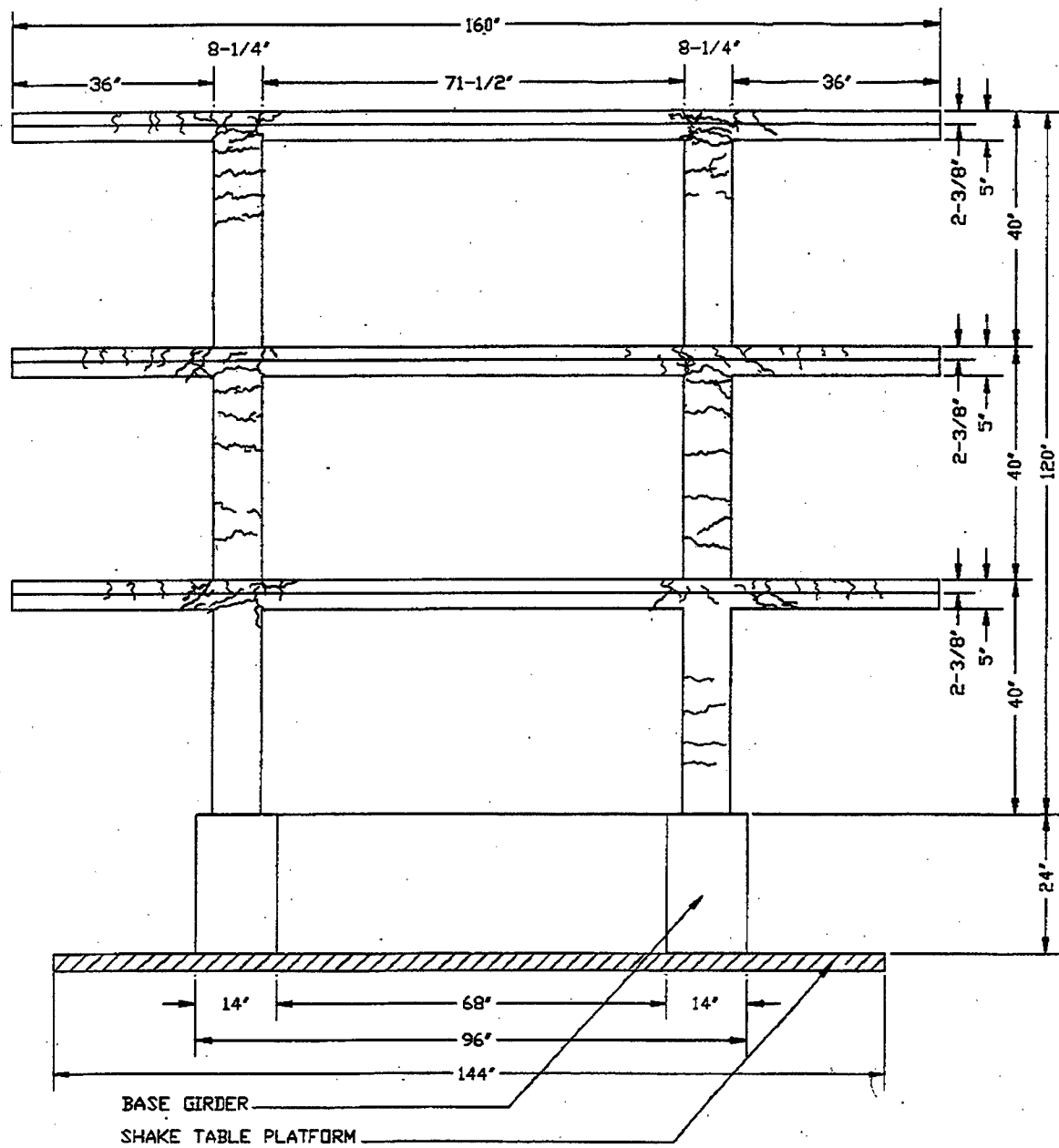


Figure 4.38 Crack Pattern, South Side of South Columns, Pre-Test

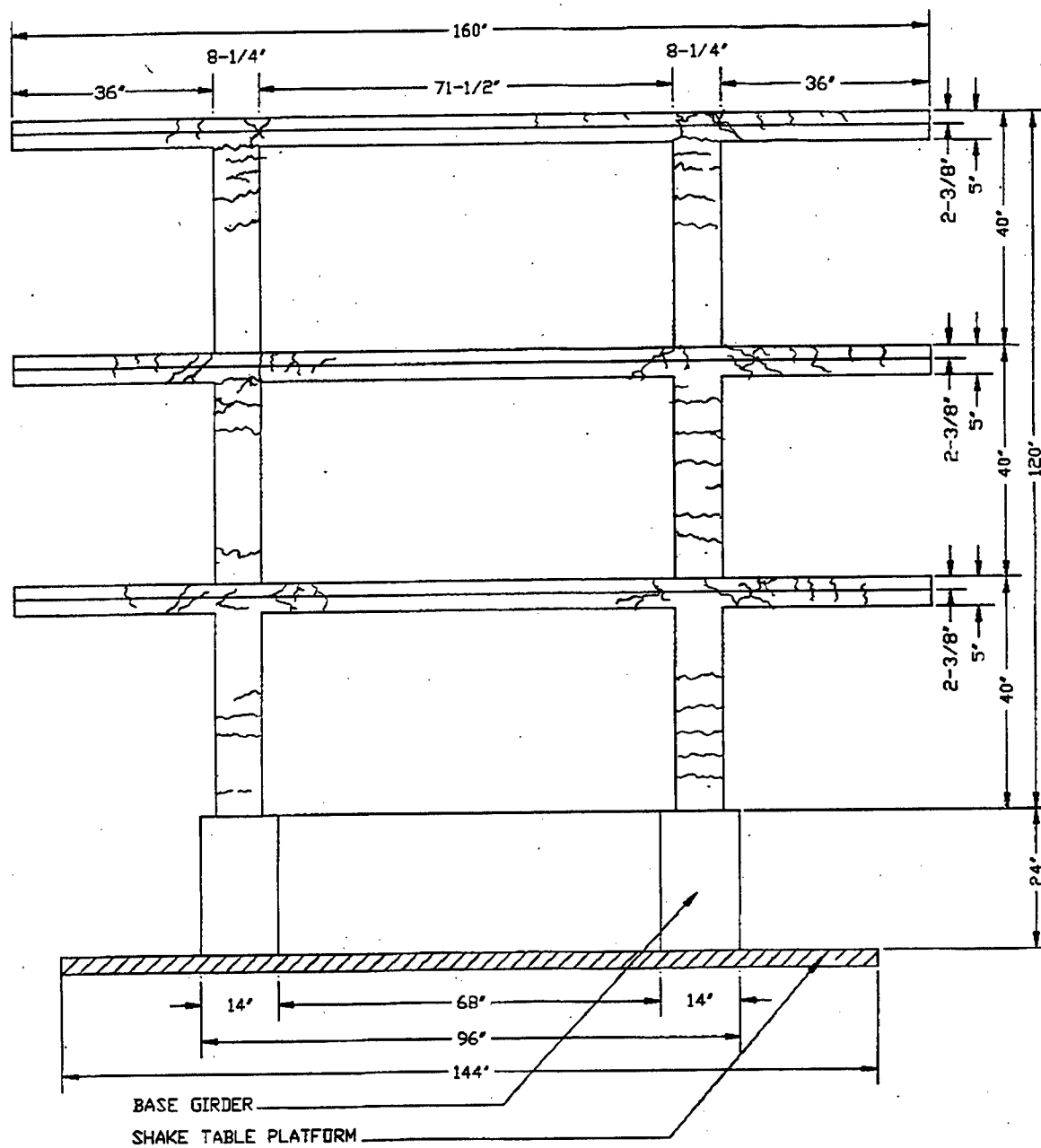


Figure 4.39 Crack Pattern, North Side of North Columns, Pre-Test

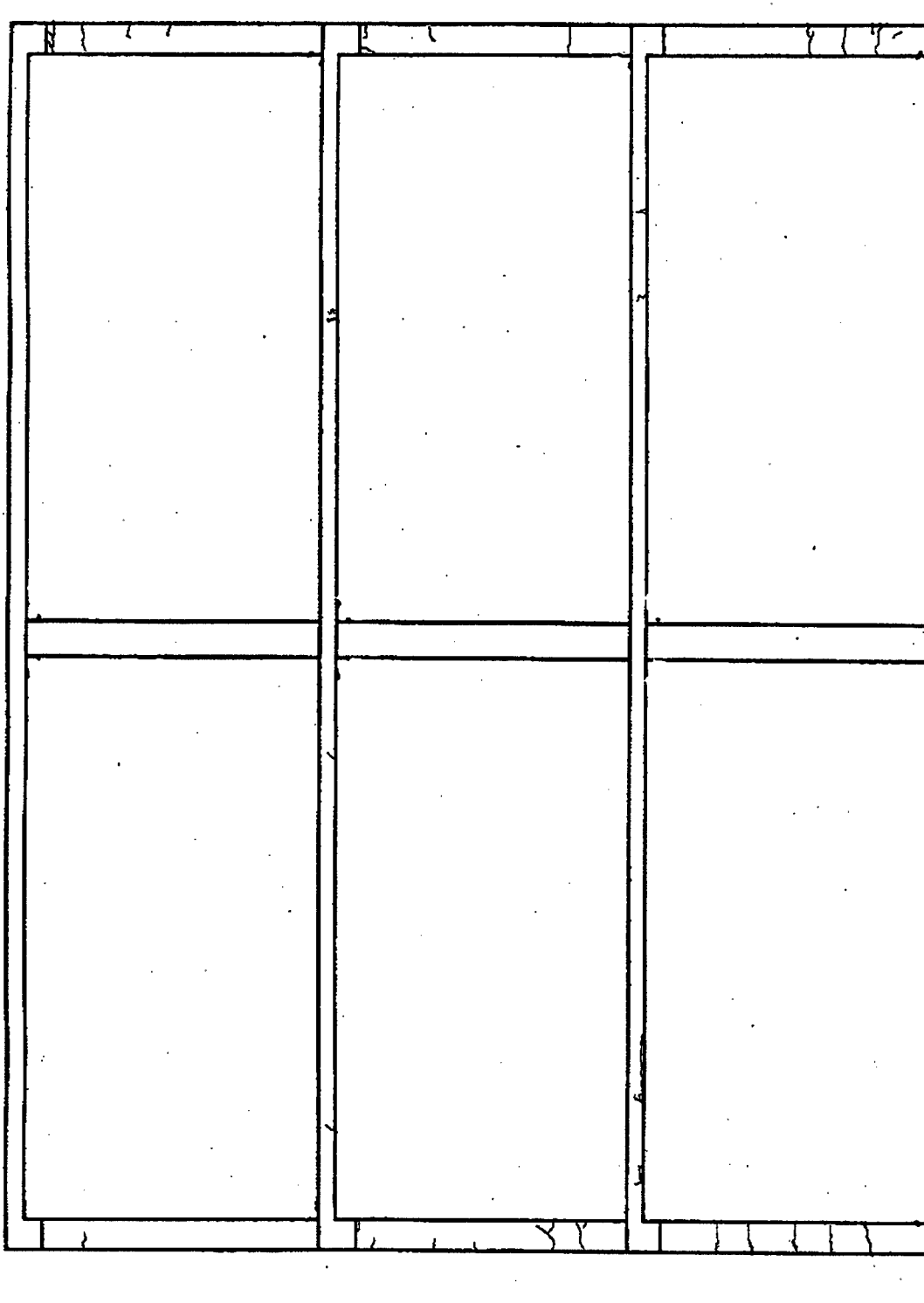


Figure 4.40 Crack Pattern, West Side of West Columns, Pre-Test

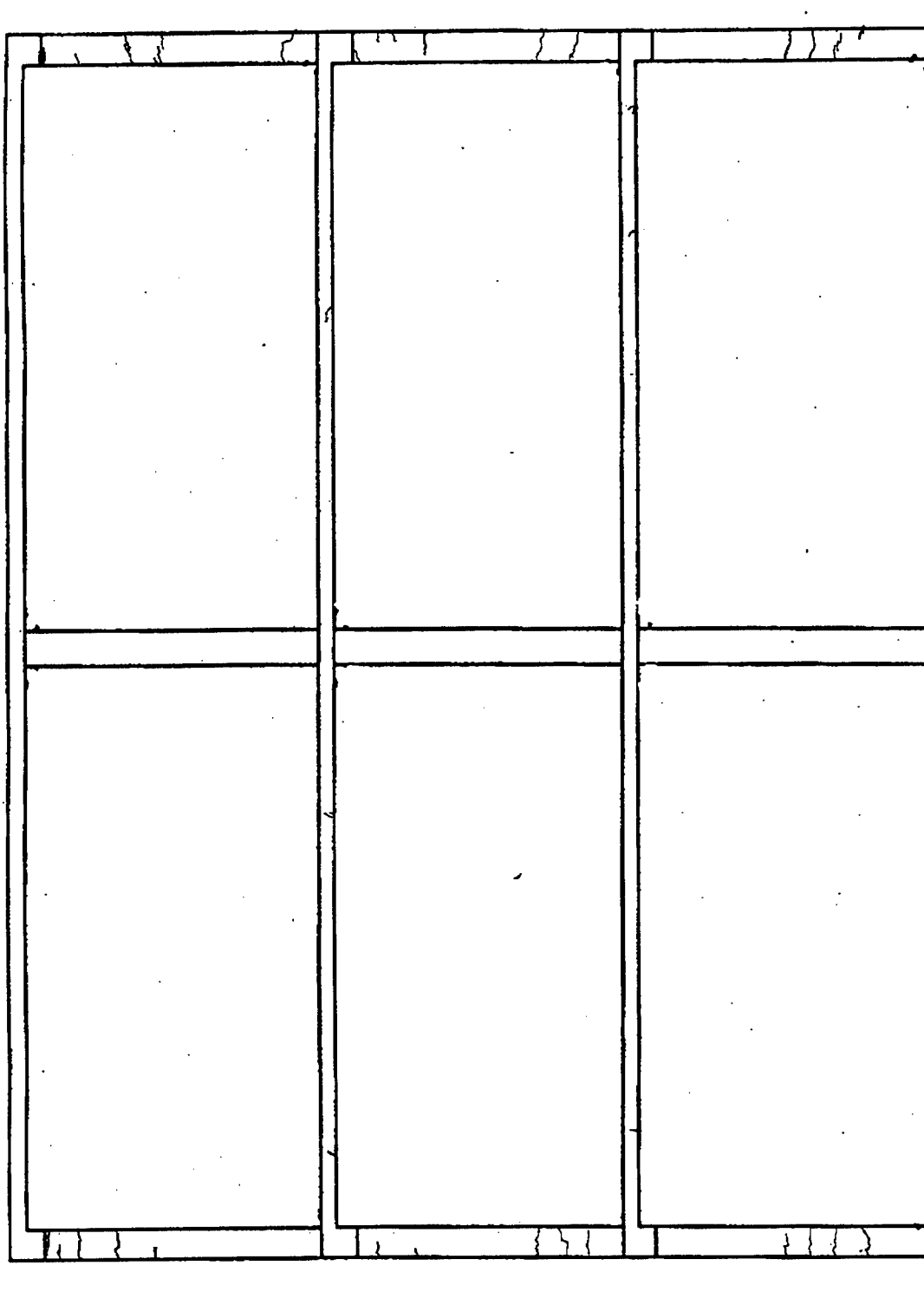


Figure 4.41 Crack Pattern, East Side of East Columns, Pre-Test

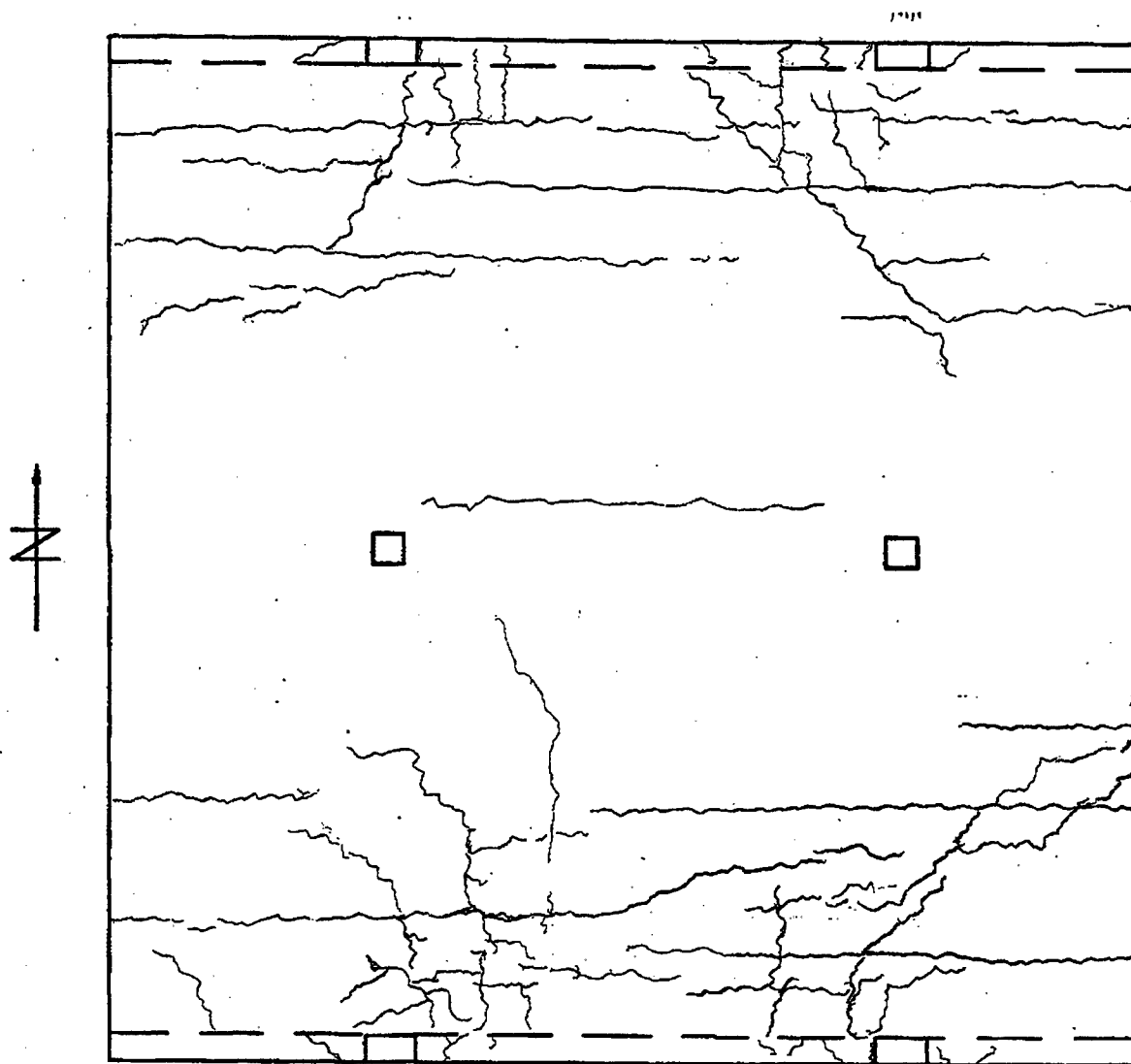


Figure 4.42 Crack Pattern, First Floor Slab, Bottom Side, Pre-Test

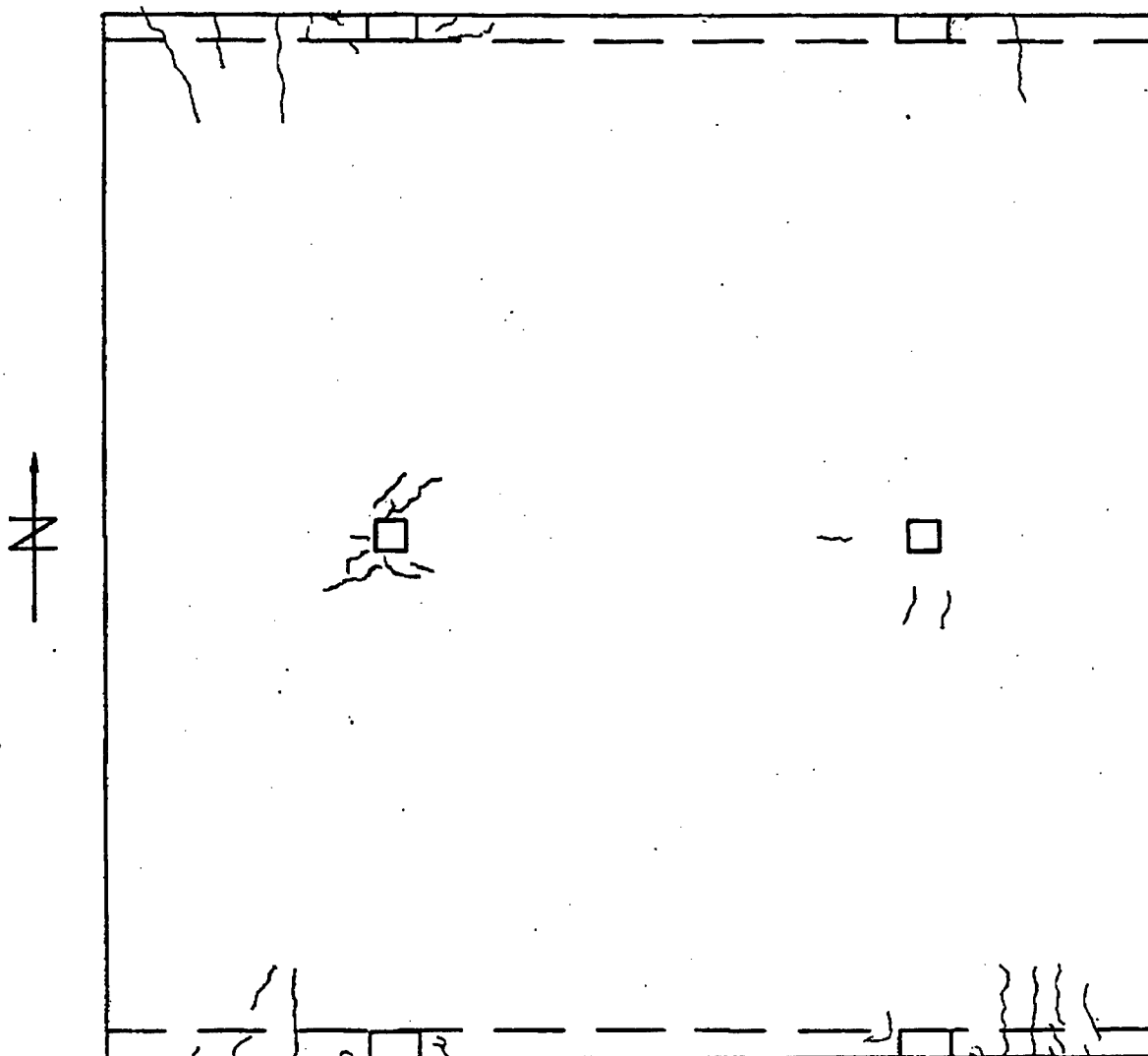


Figure 4.43 Crack Pattern, First Floor Slab, Top Side, Pre-Test

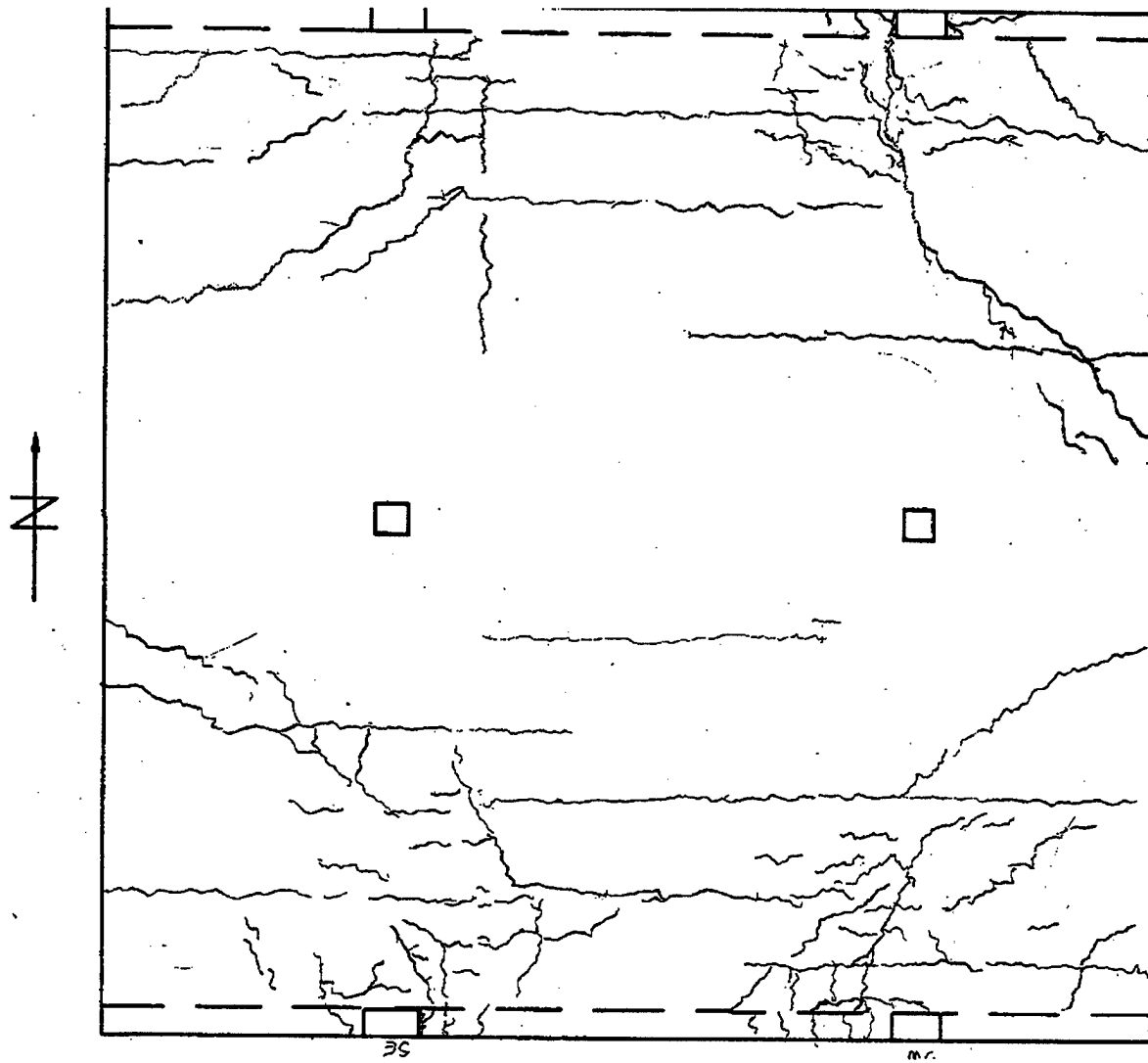


Figure 4.44 Crack Pattern, Second Floor Slab, Bottom Side, Pre-Test

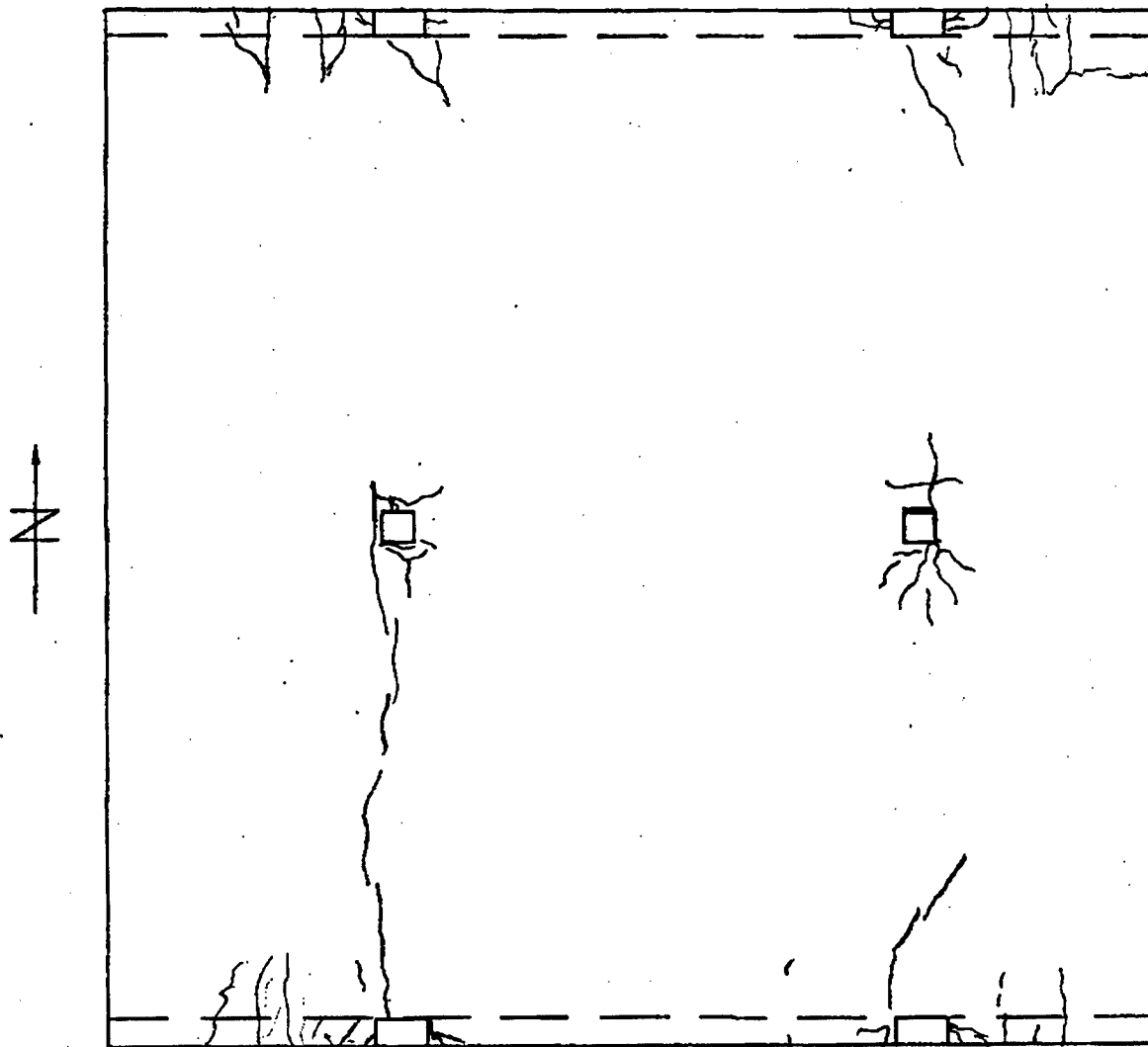


Figure 4.45 Crack Pattern, Second Floor Slab, Top Side, Pre-Test

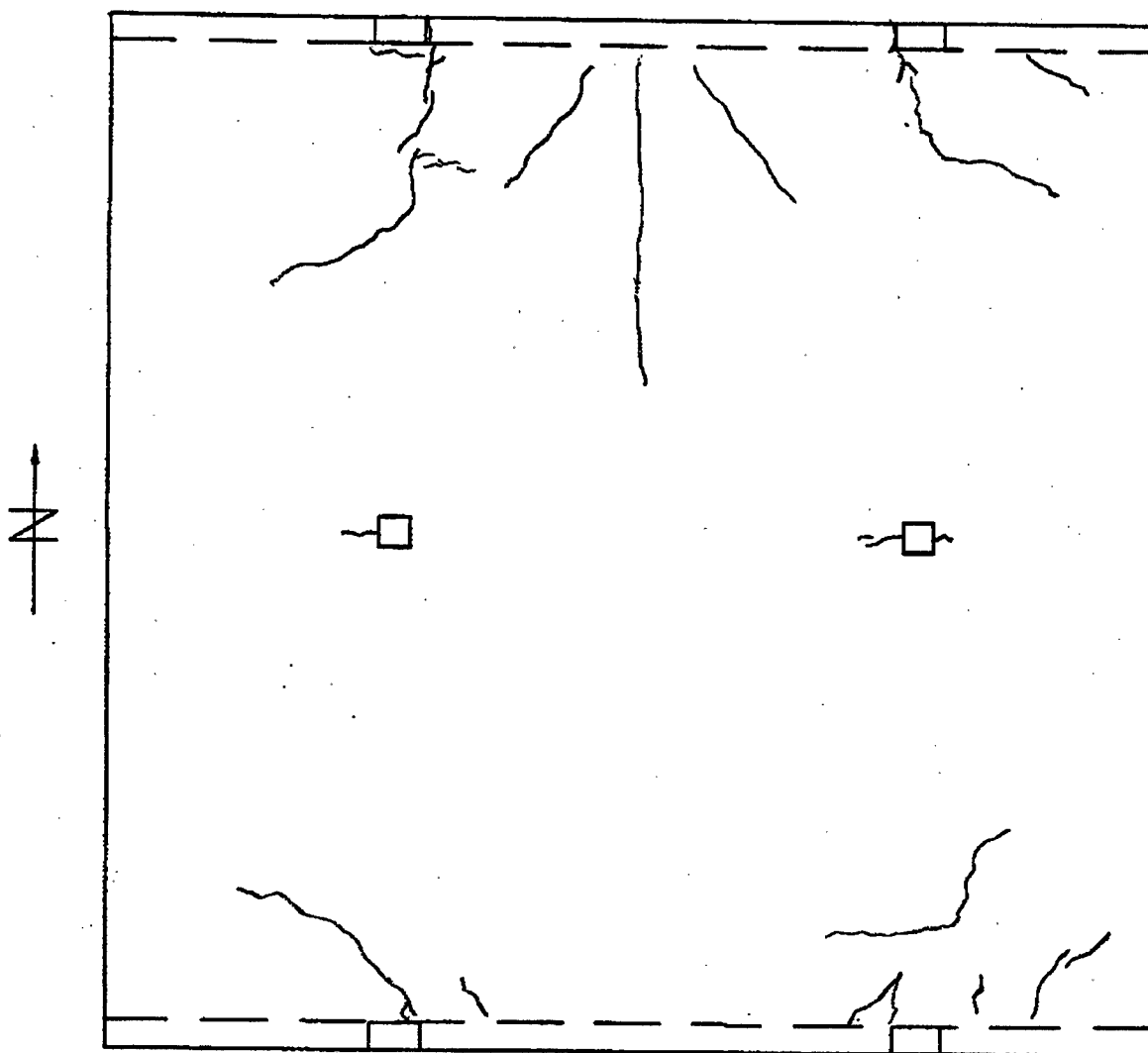


Figure 4.46 Crack Pattern, Third Floor Slab, Bottom Side, Pre-Test

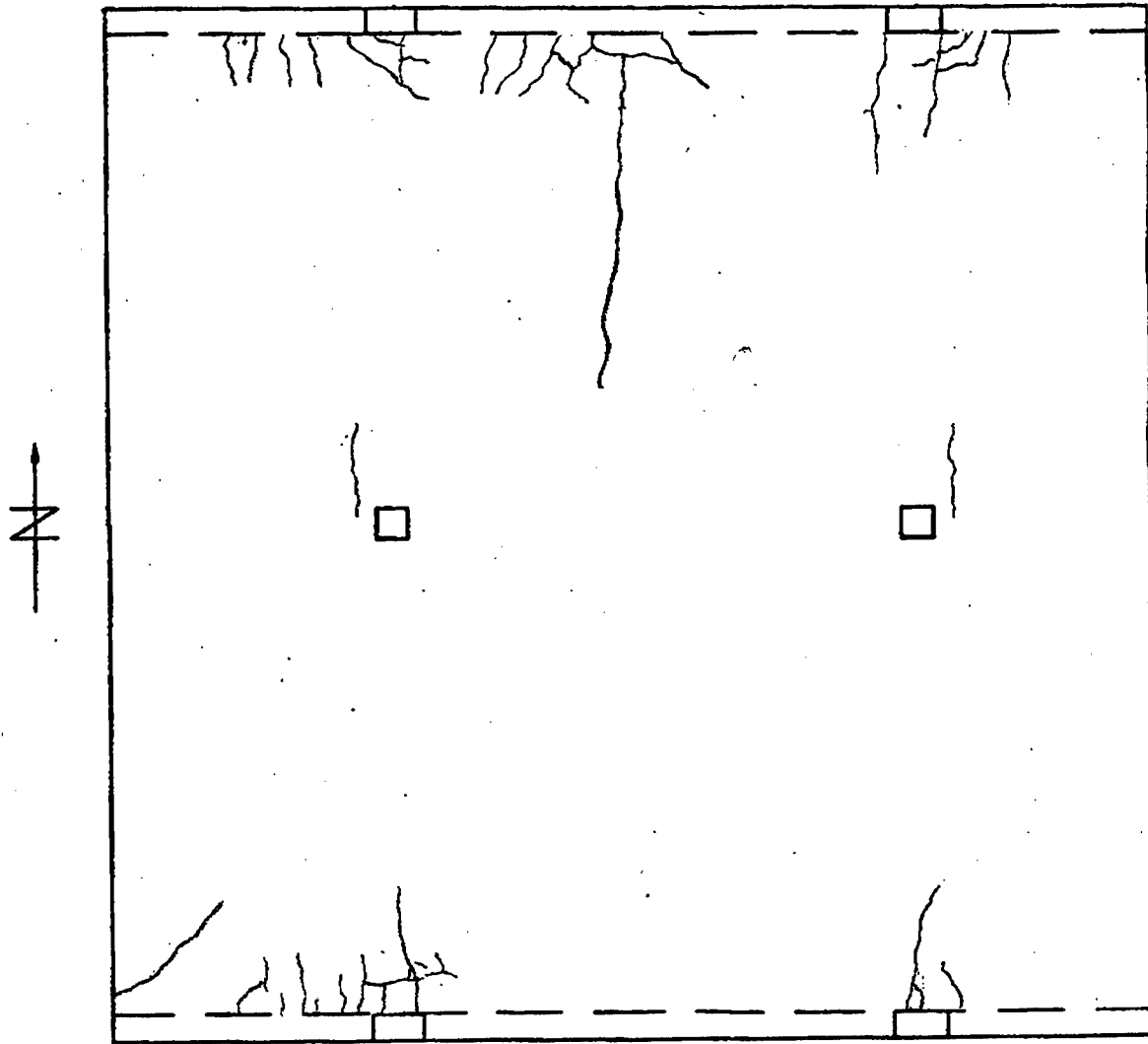


Figure 4.47 Crack Pattern, Third Floor Slab, Top Side, Pre-Test

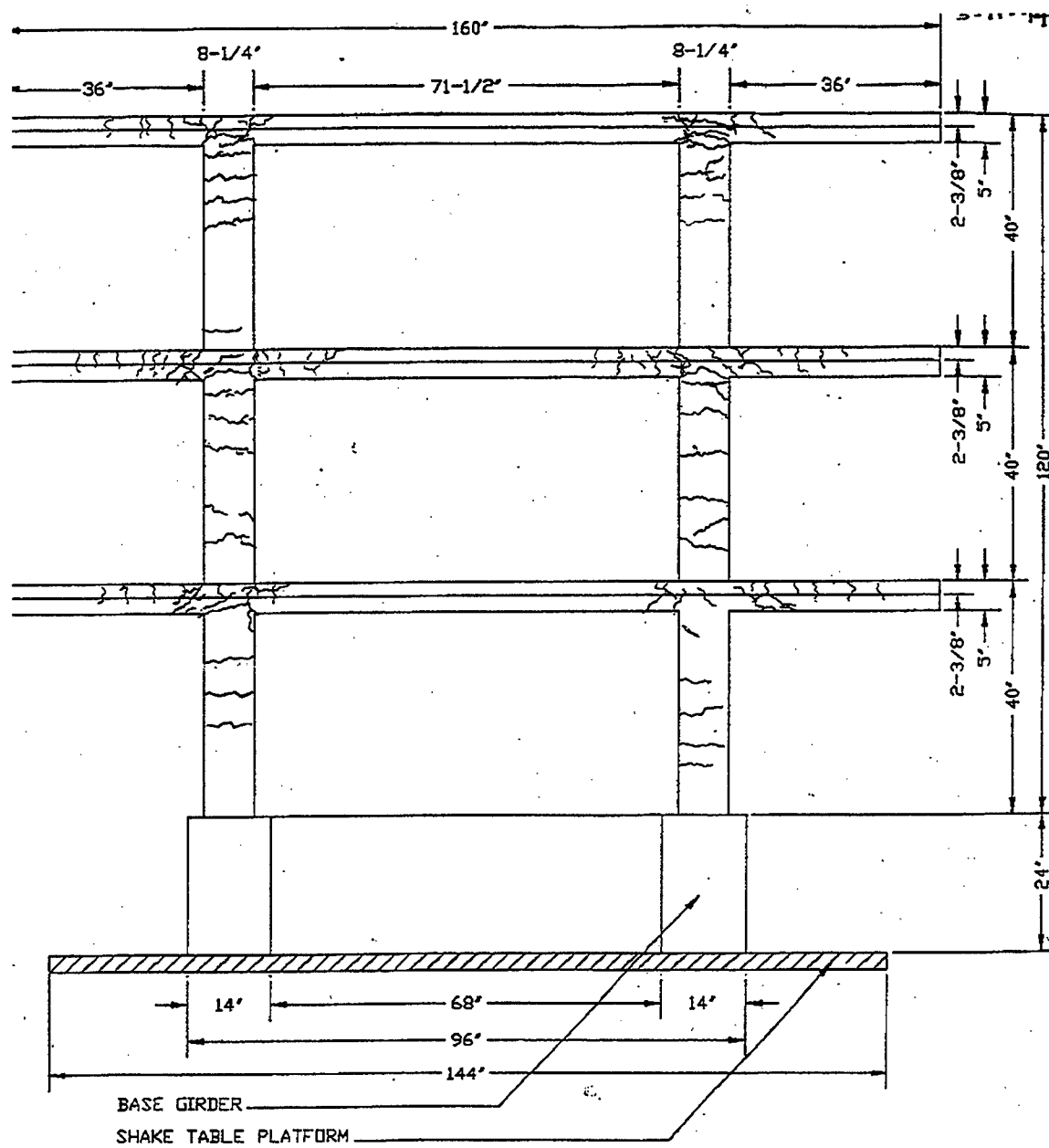


Figure 4.48 Crack Pattern, South Side of South Columns, Post-T420DL

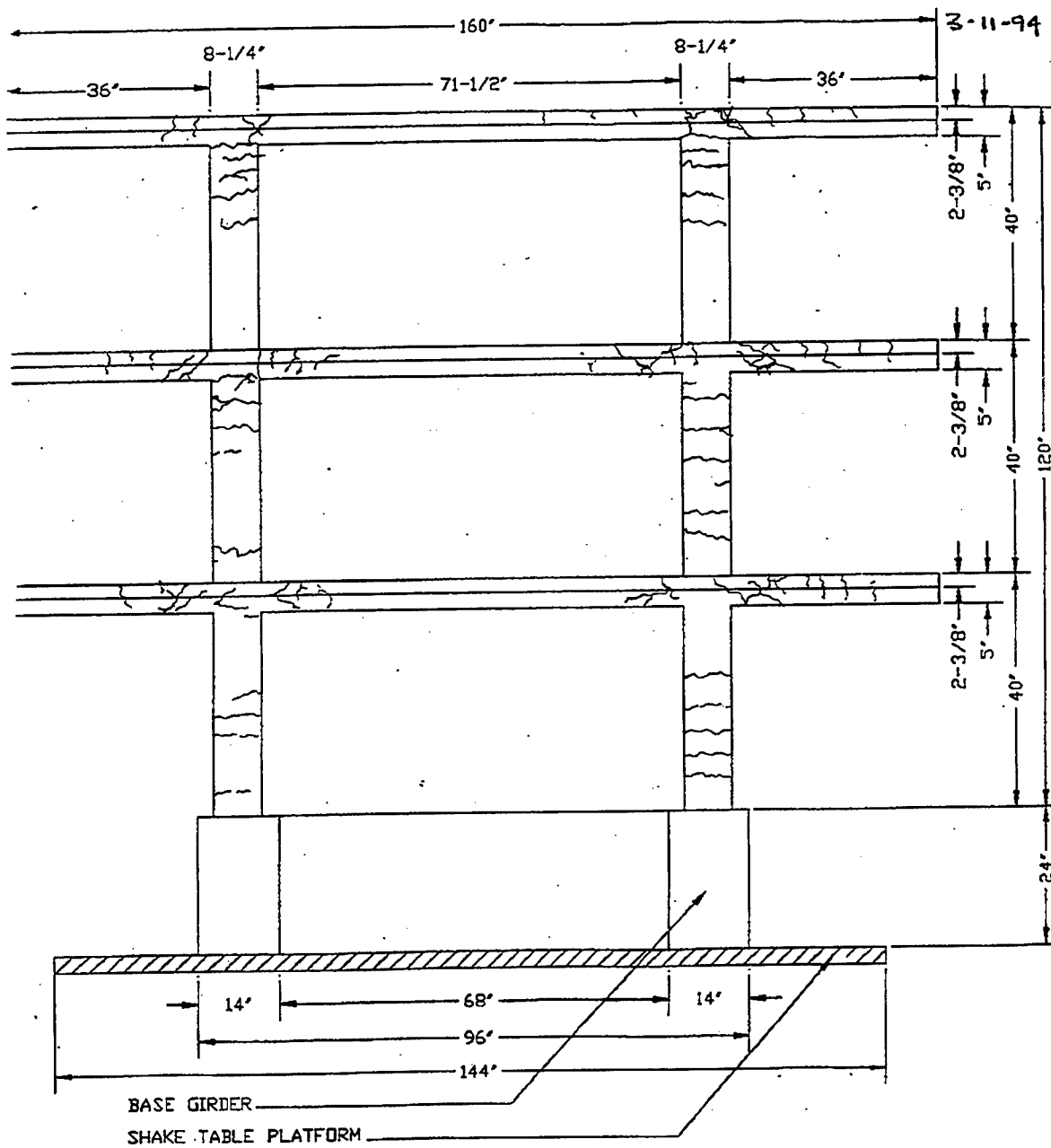


Figure 4.49 Crack Pattern, North Side of North Columns, Post-T420DL

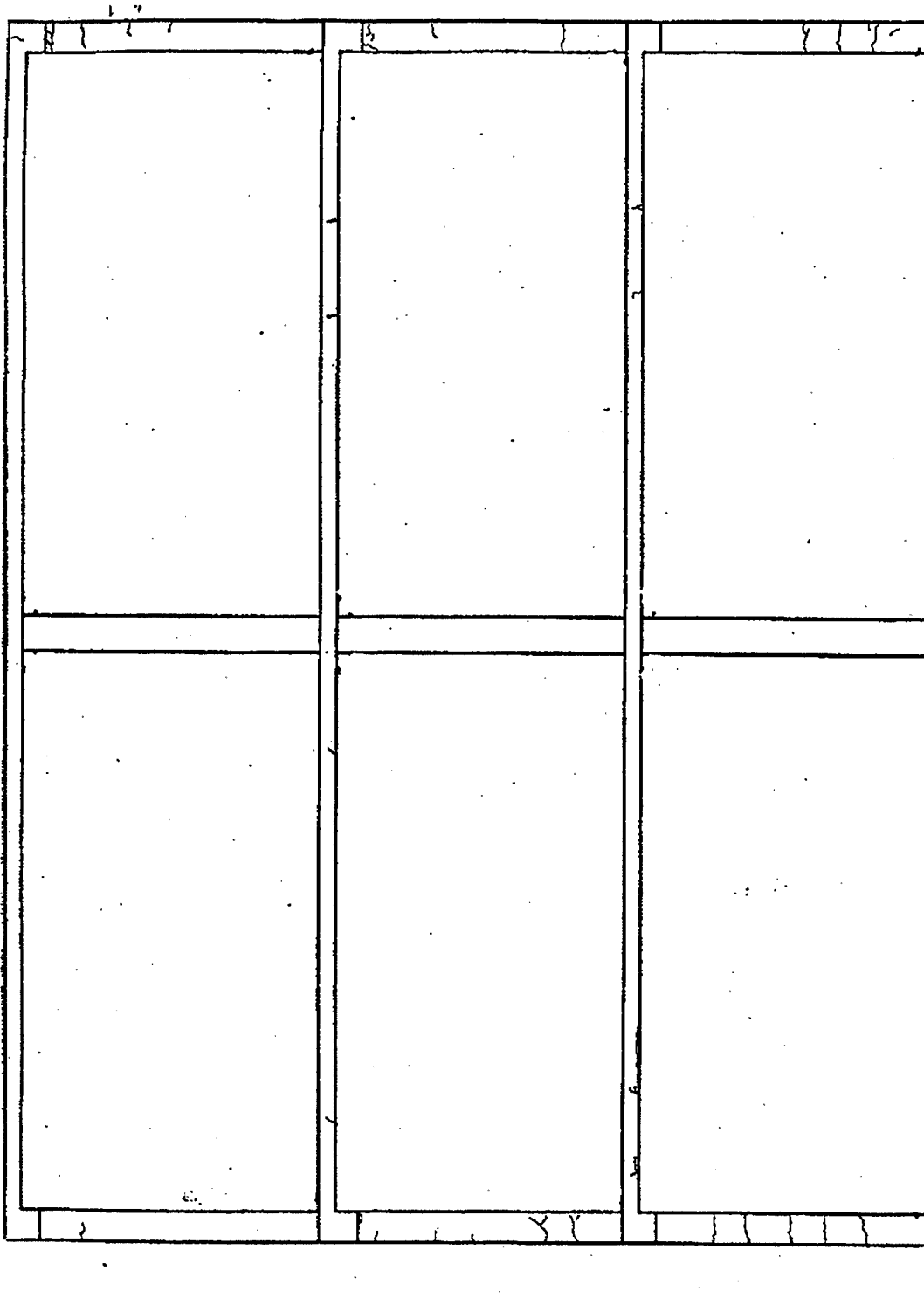


Figure 4.50 Crack Pattern, West Side of West Columns, Post-T420DL

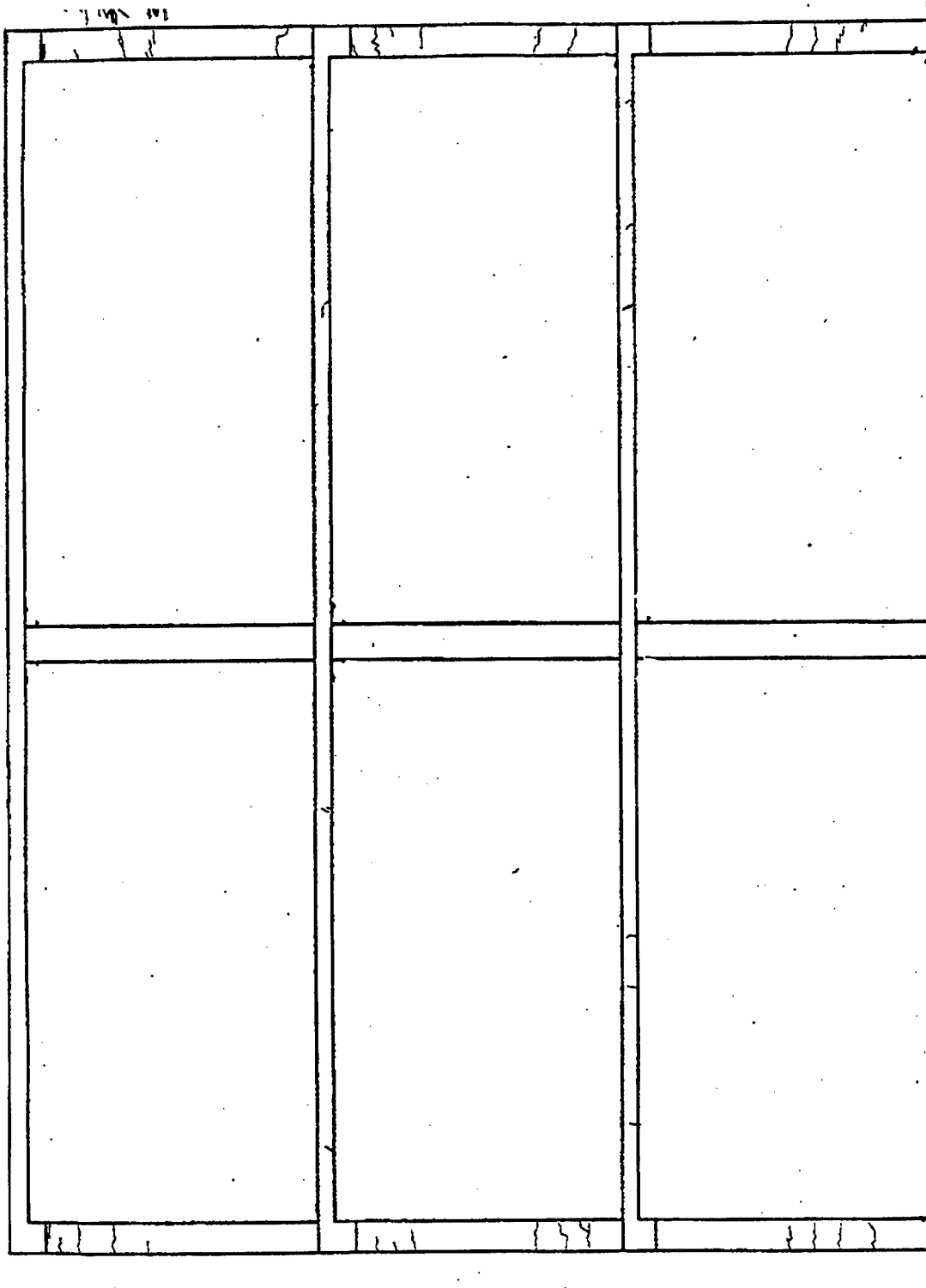


Figure 4.51 Crack Pattern, East Side of East Columns, Post-T420DL

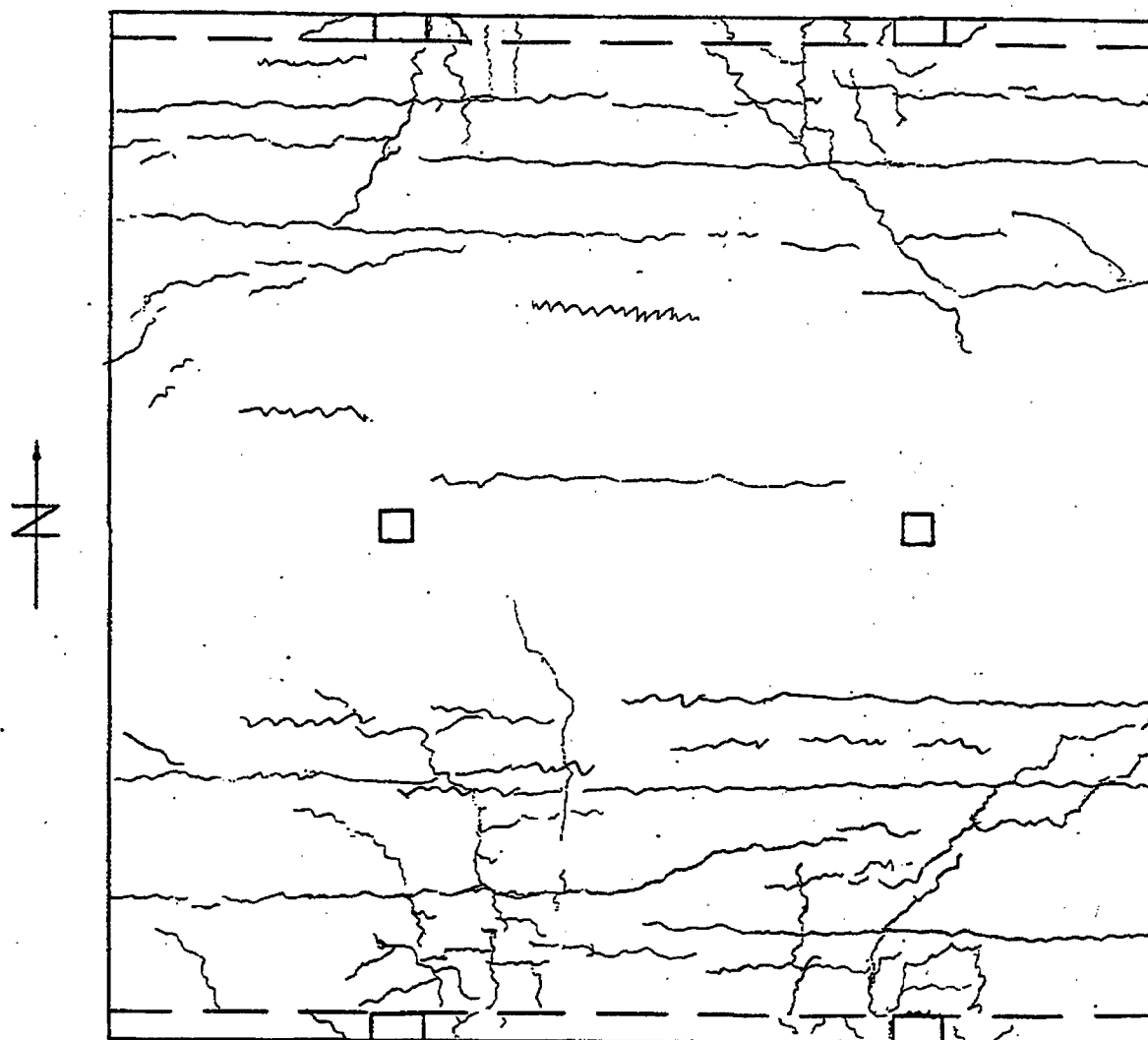


Figure 4.52 Crack Pattern, First Floor Slab, Bottom Side, Post-T420DL

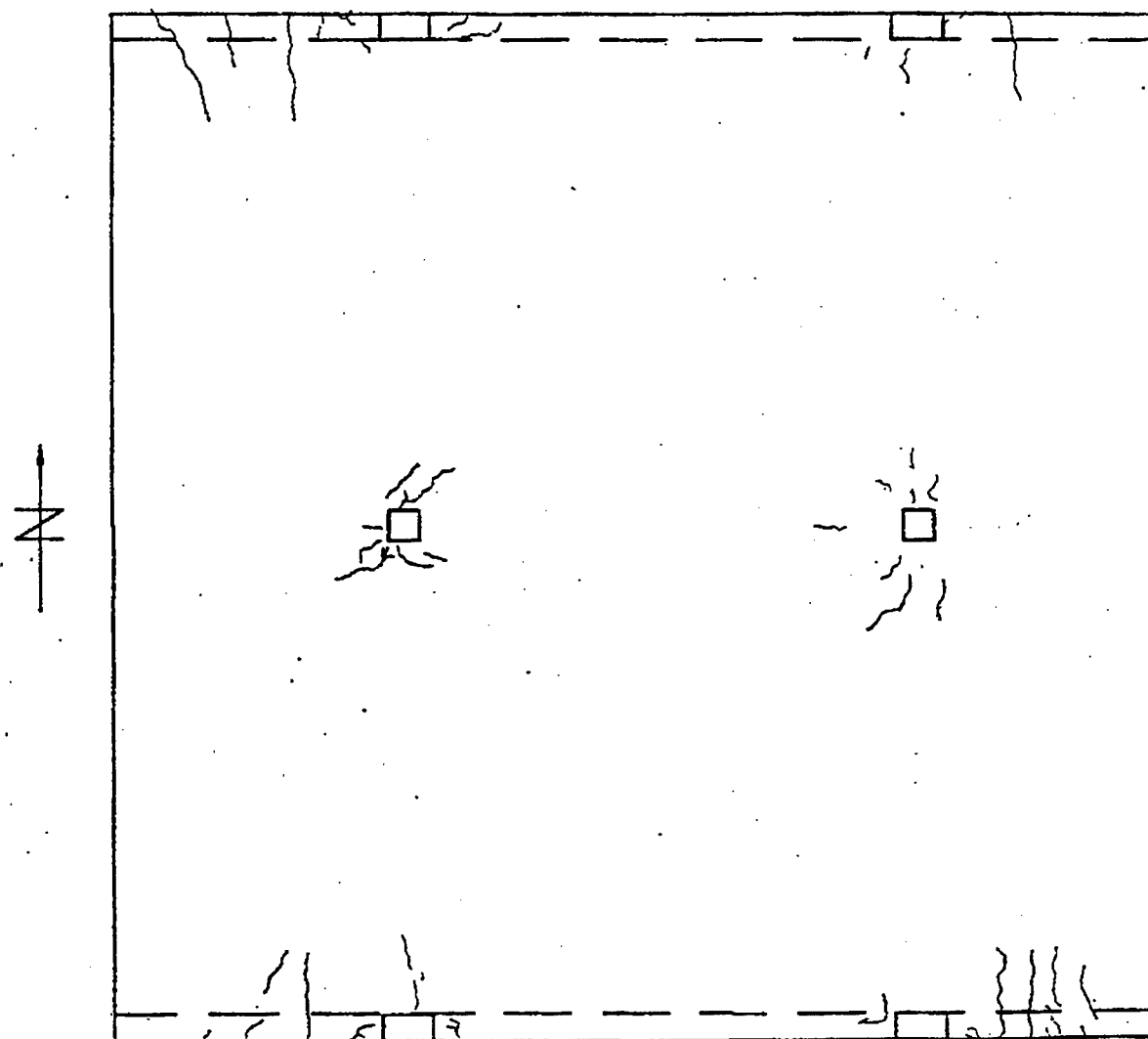


Figure 4.53 Crack Pattern, First Floor Slab, Top Side, Post-T420DL

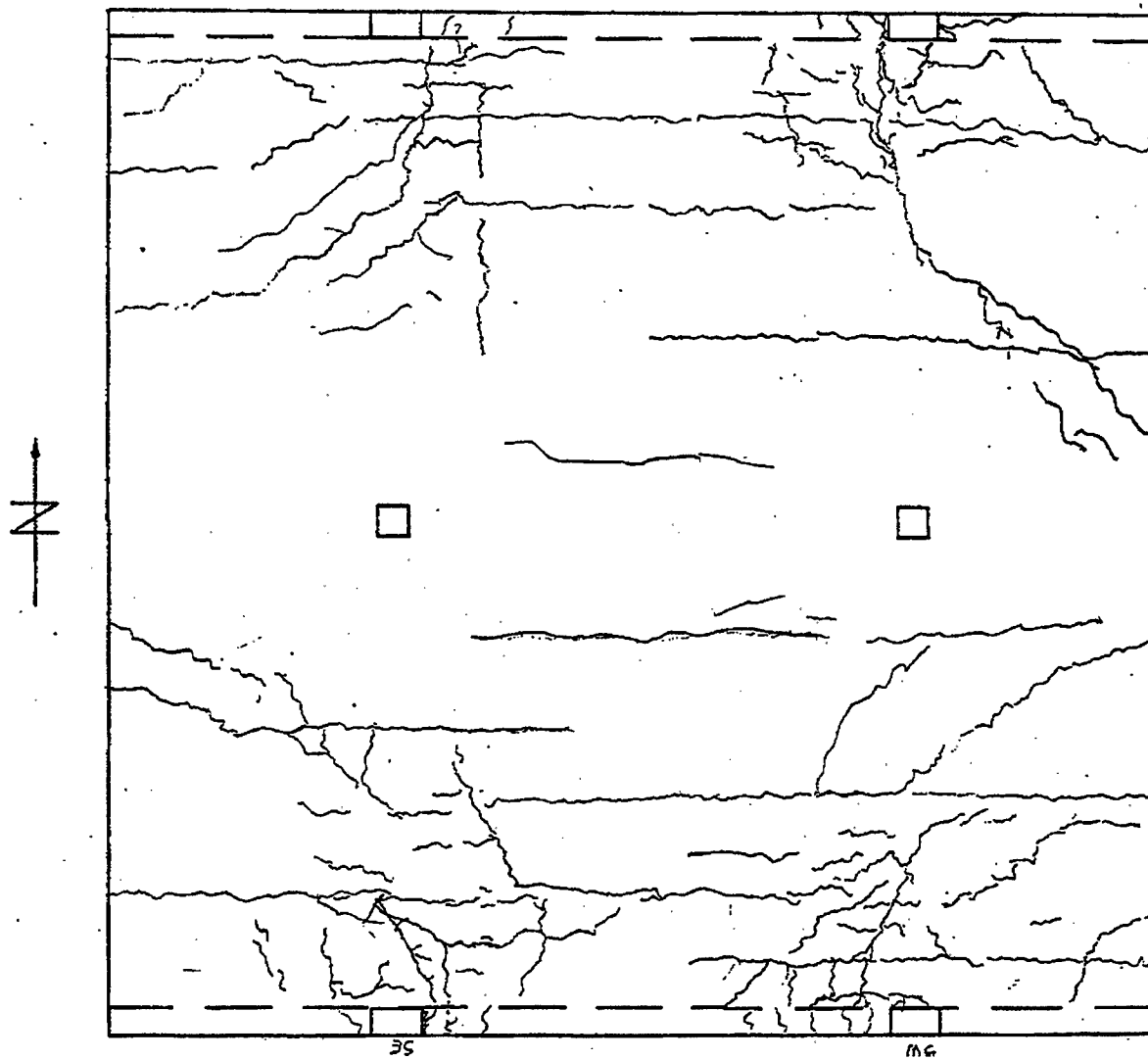


Figure 4.54 Crack Pattern, Second Floor Slab, Bottom Side, Post-T420DL

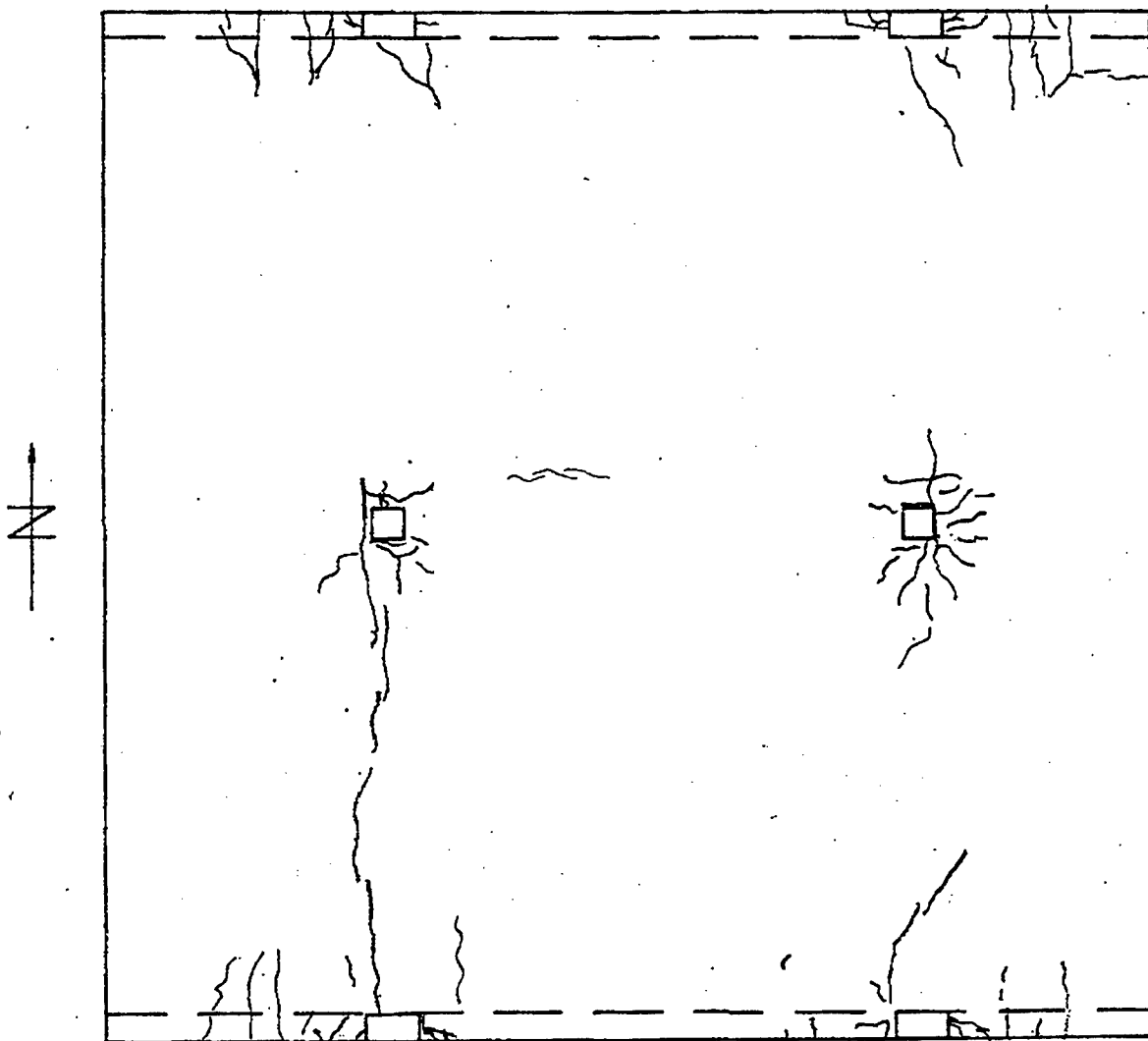


Figure 4.55 Crack Pattern, Second Floor Slab, Top Side, Post-T420DL

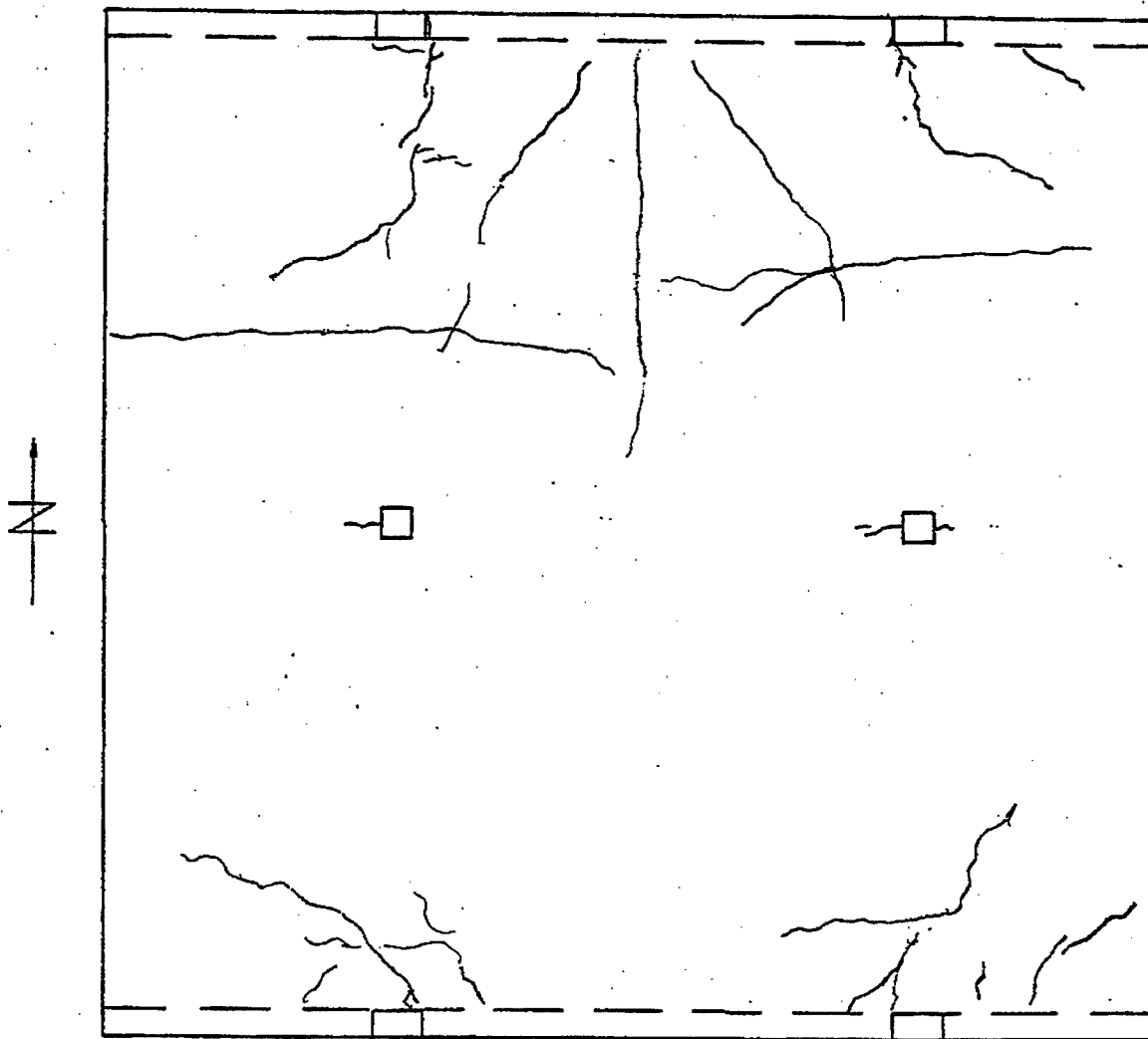


Figure 4.56 Crack Pattern, Third Floor Slab, Bottom Side, Post-T420DL

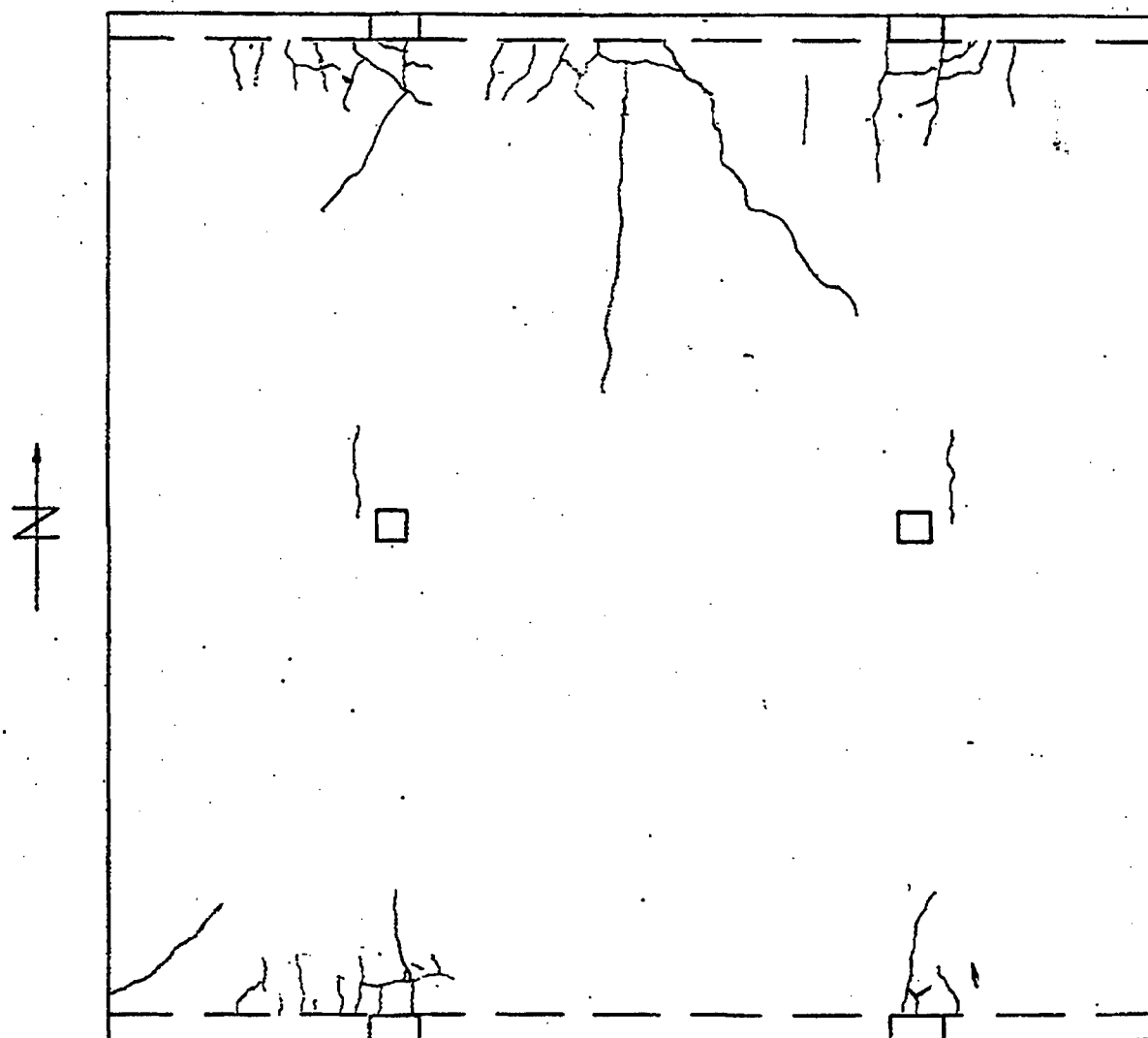


Figure 4.57 Crack Pattern, Third Floor Slab, Top Side, Post-T420DL

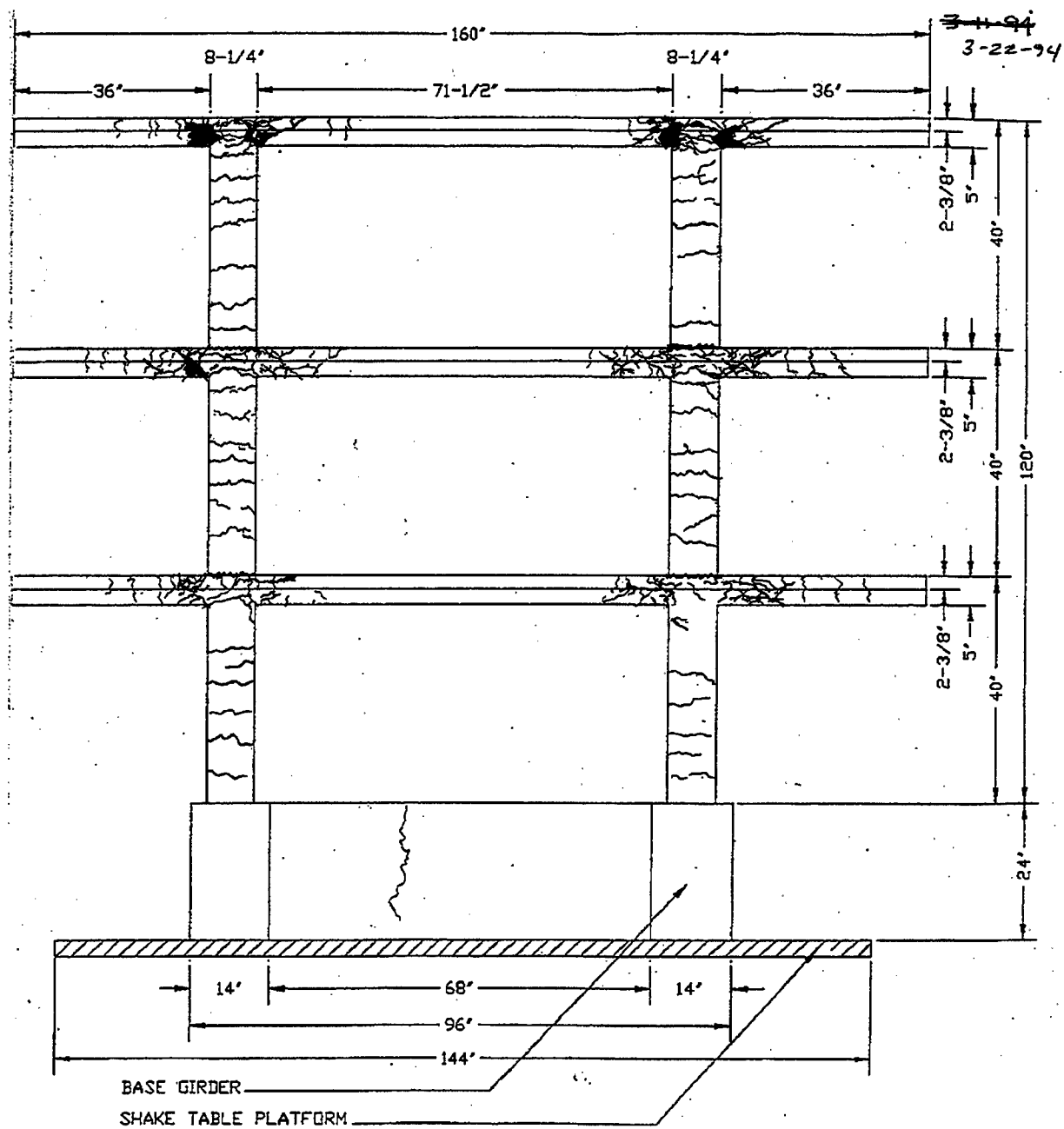


Figure 4.58 Crack Pattern, South Side of South Columns, Post-E200N

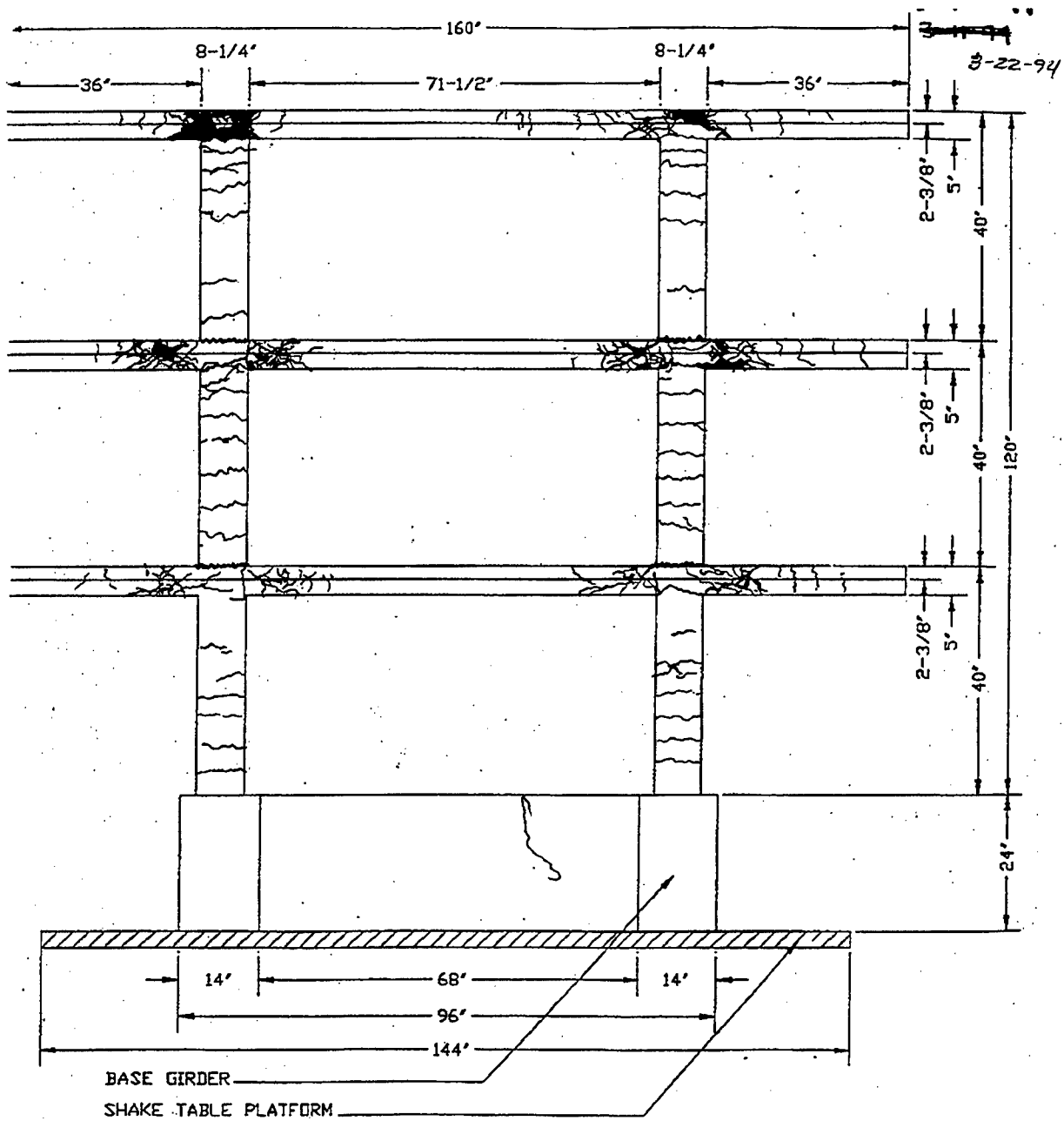


Figure 4.59 Crack Pattern, North Side of North Columns, Post-E200N

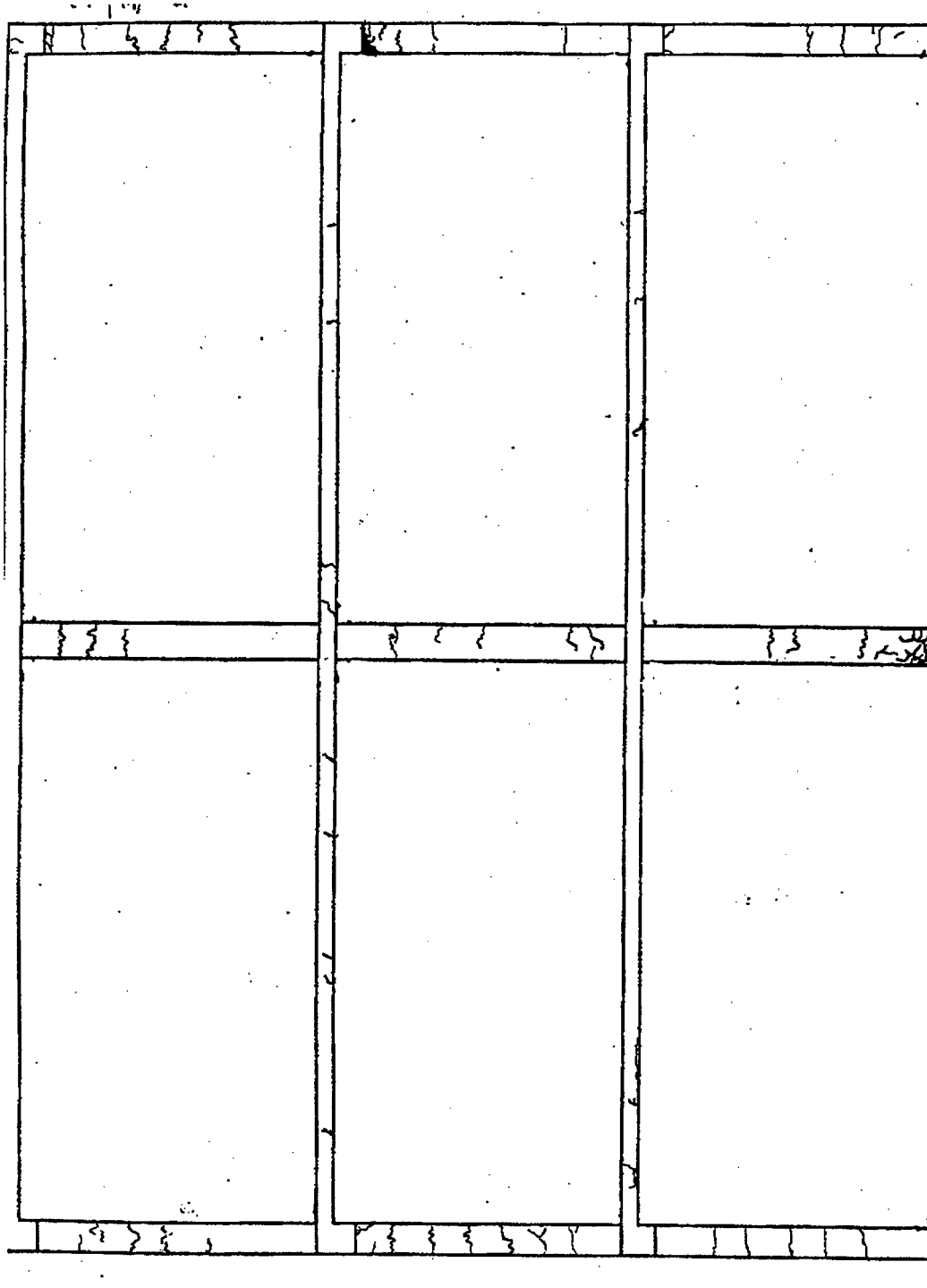


Figure 4.60 Crack Pattern, West Side of West Columns, Post-E200N

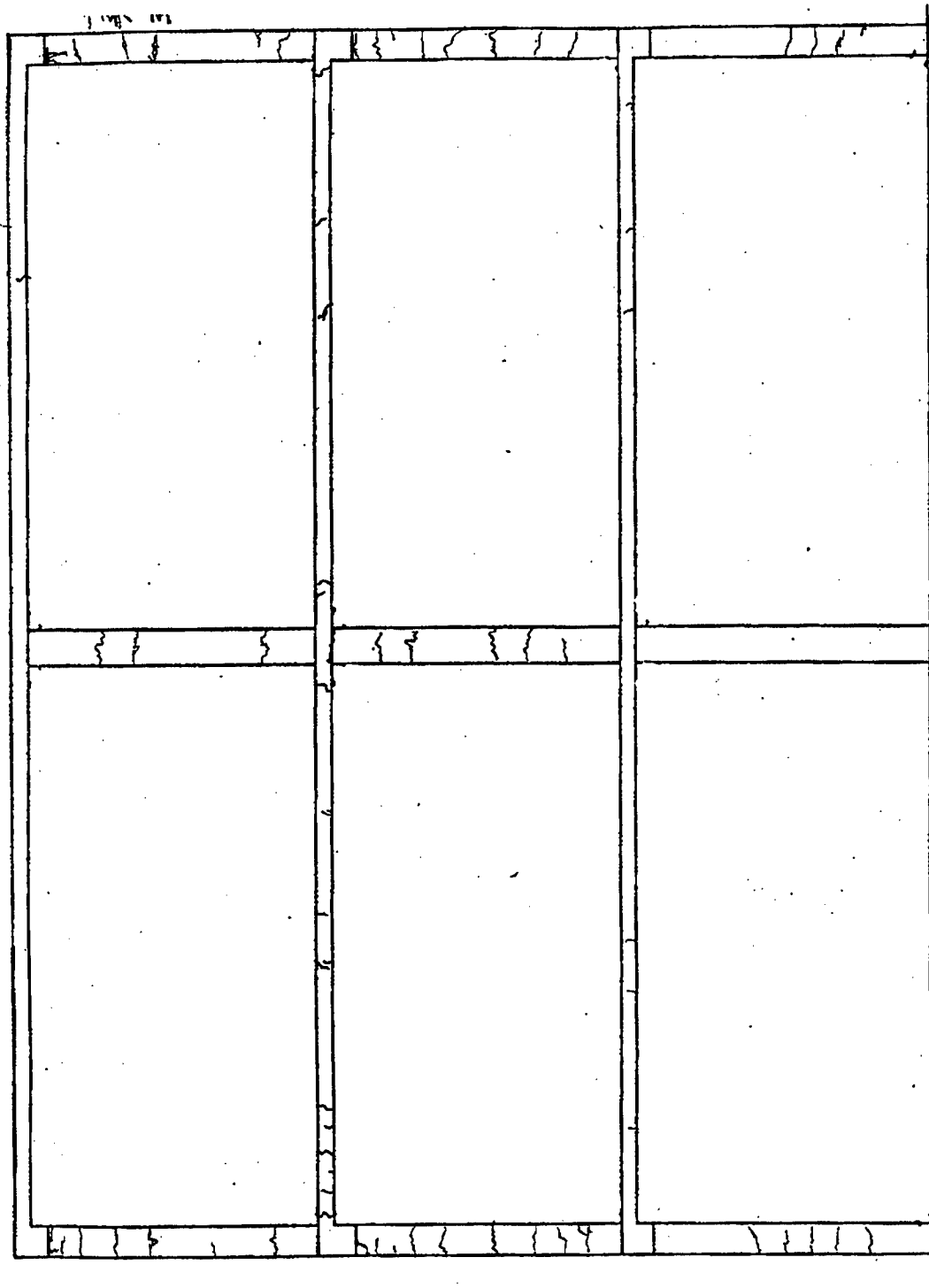


Figure 4.61 Crack Pattern, East Side of East Columns, Post-E200N

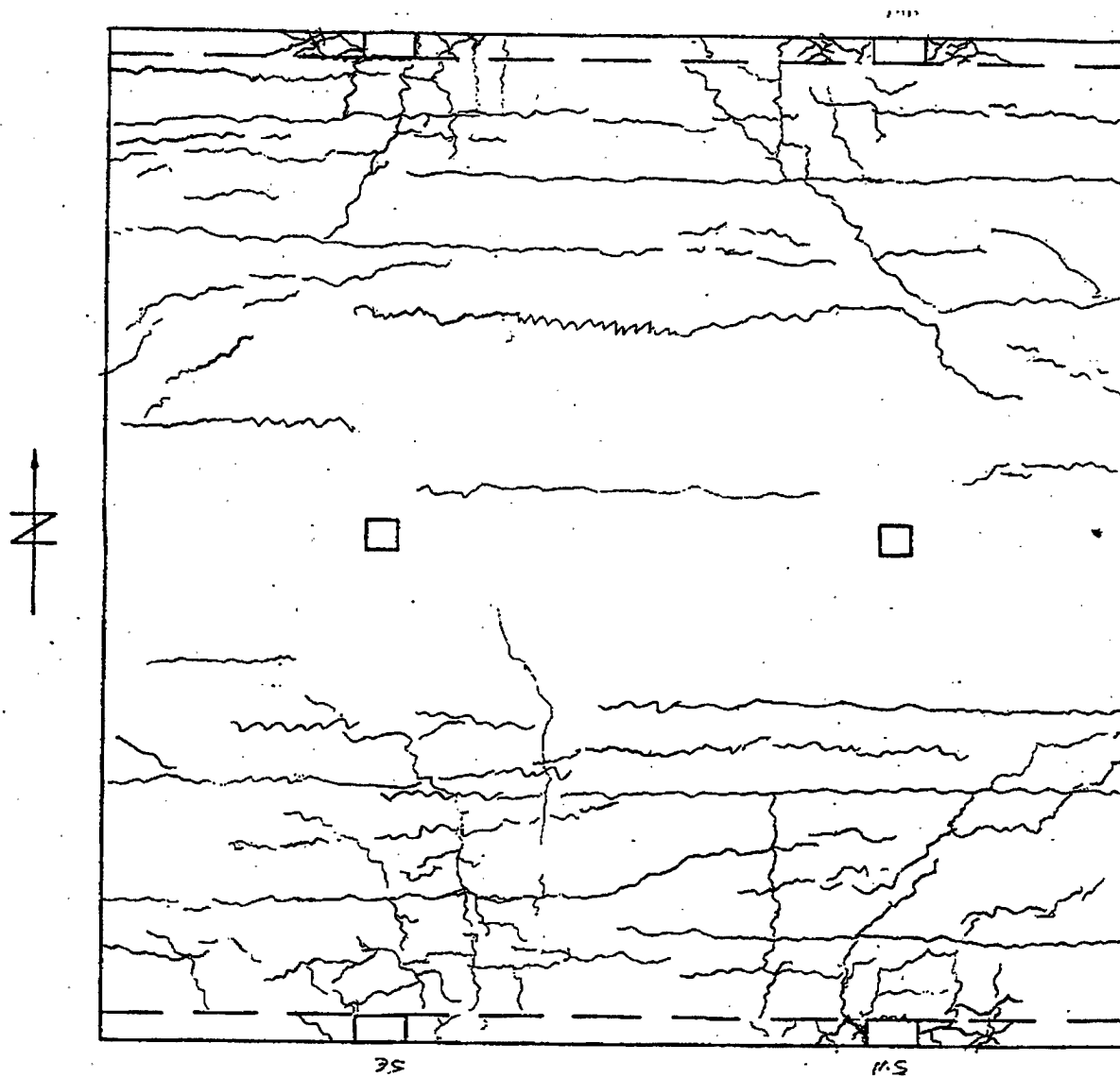


Figure 4.62 Crack Pattern, First Floor Slab, Bottom Side, Post-E200N

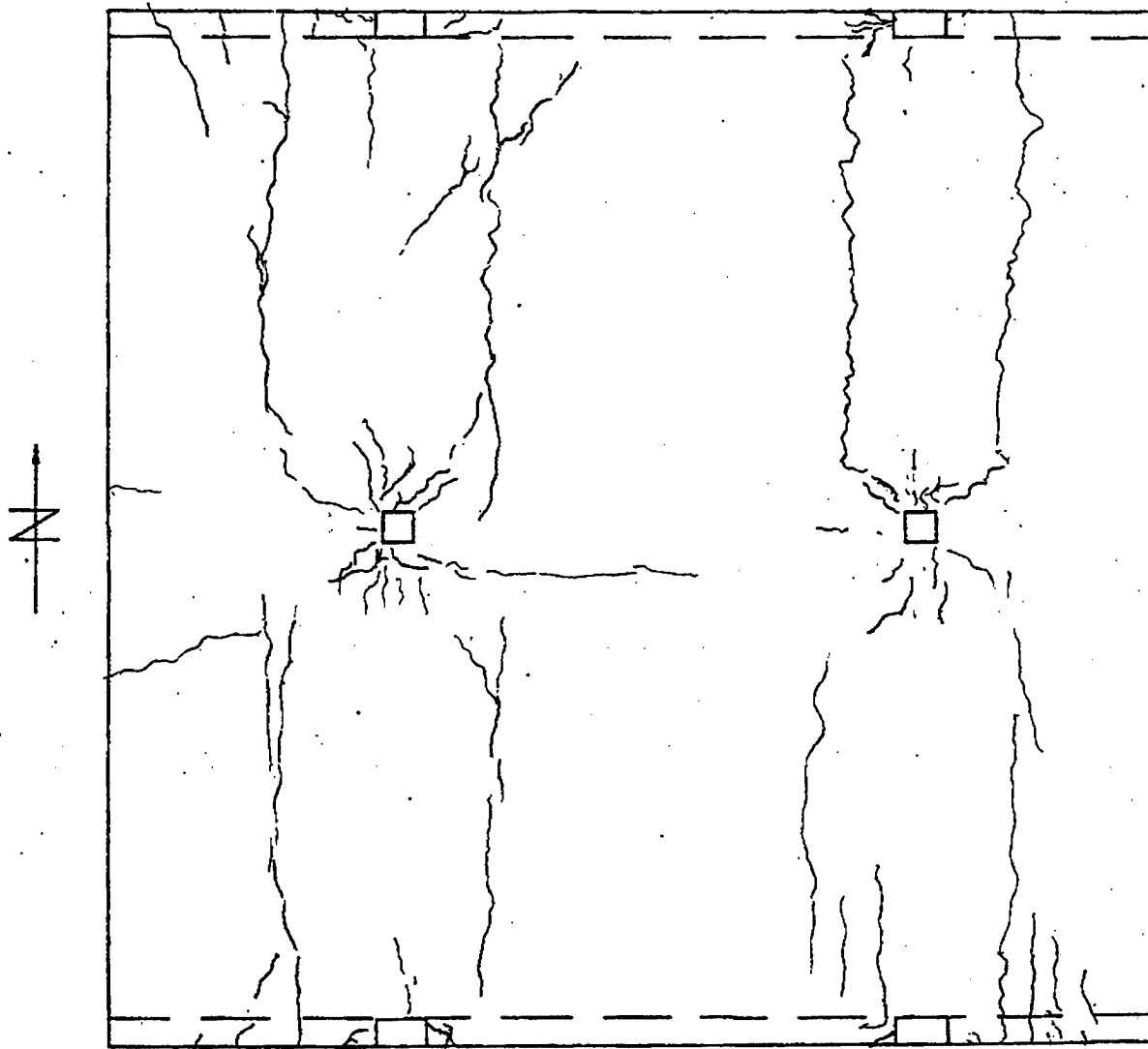


Figure 4.63 Crack Pattern, First Floor Slab, Top Side, Post-E200N

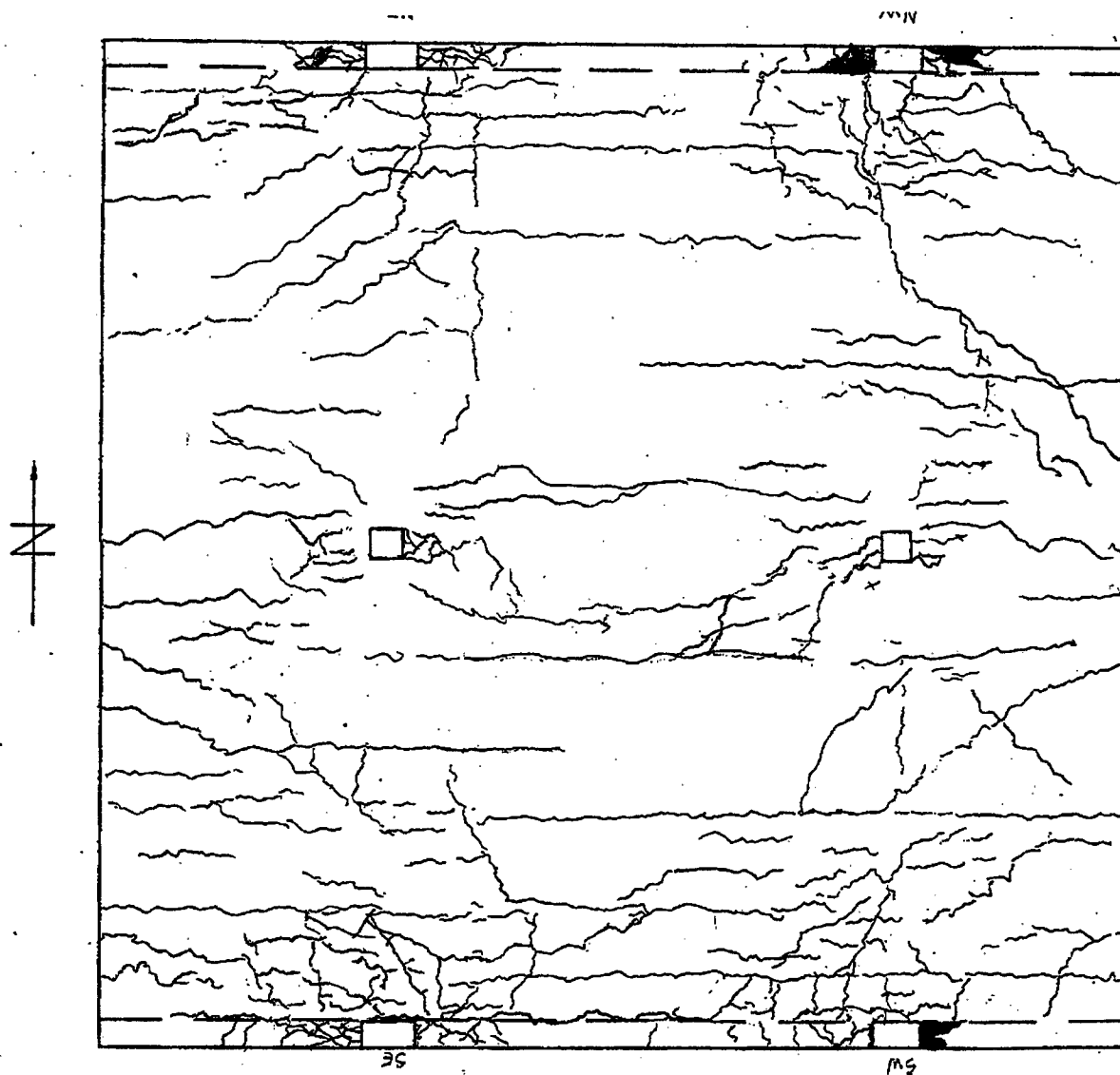


Figure 4.64 Crack Pattern, Second Floor Slab, Bottom Side, Post-E200N

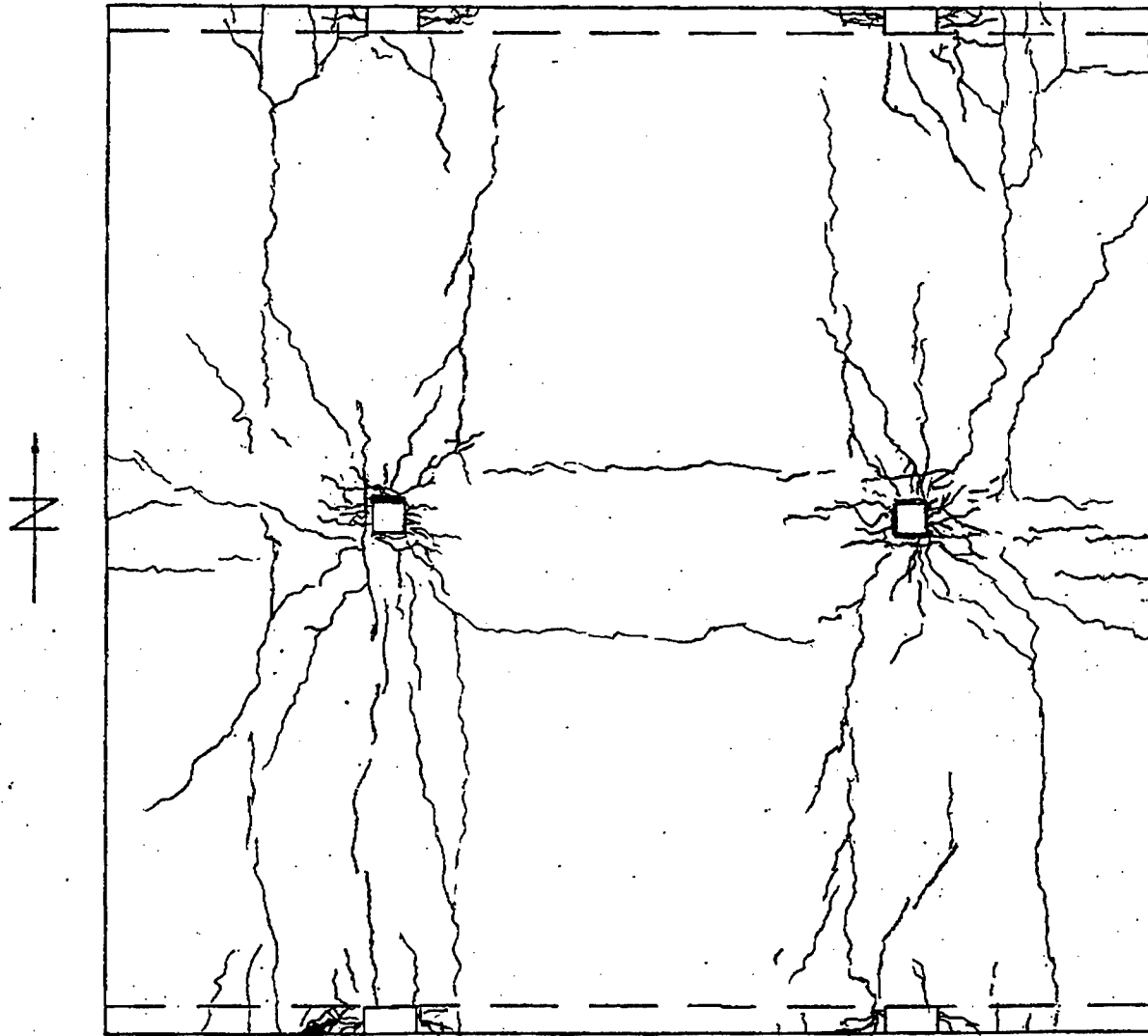


Figure 4.65 Crack Pattern, Second Floor Slab, Top Side, Post-E200N

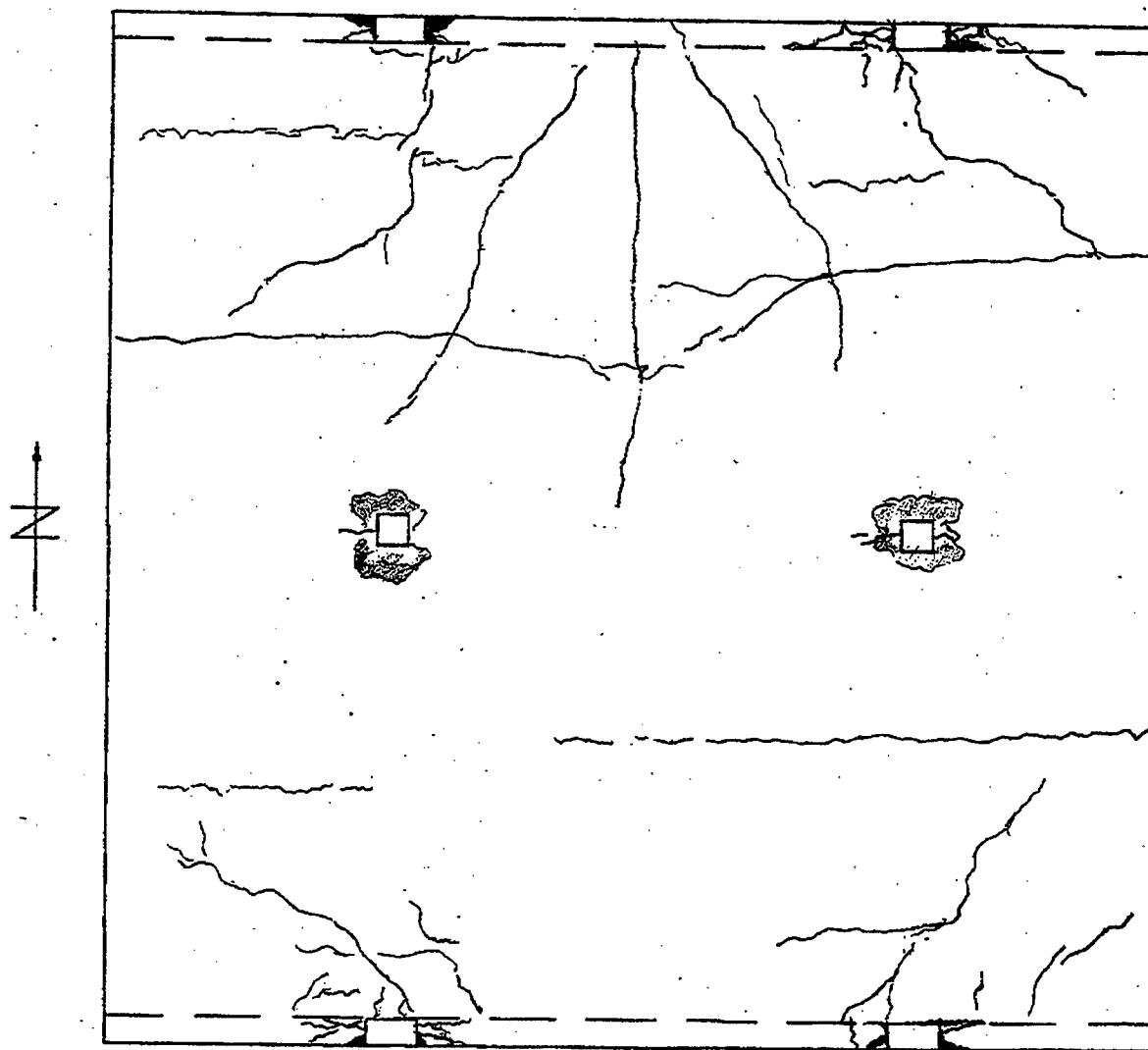


Figure 4.66 Crack Pattern, Third Floor Slab, Bottom Side, Post-E200N

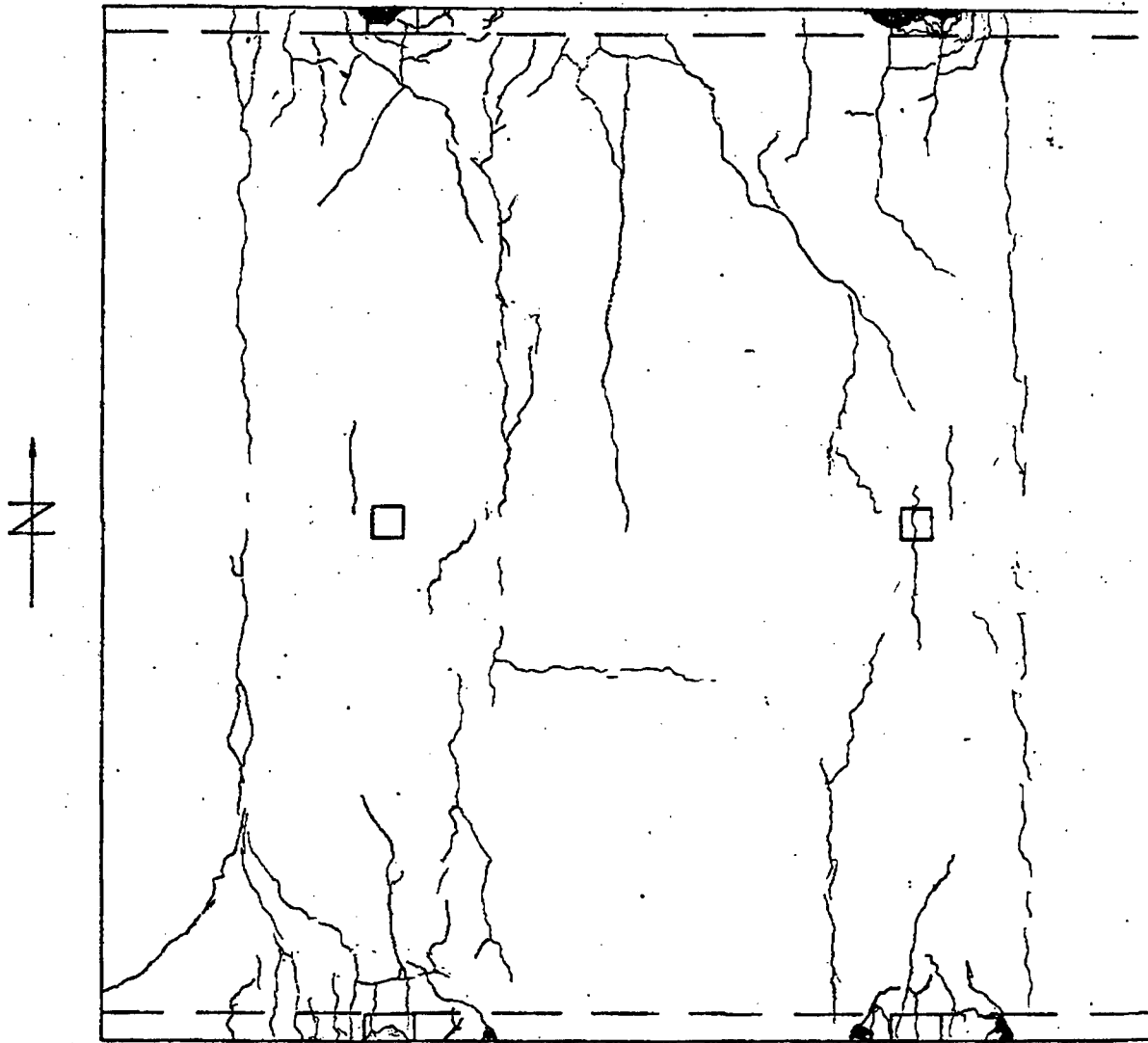


Figure 4.67 Crack Pattern, Third Floor Slab, Top Side, Post-E200N



Figure 4.68 Top of Third Floor Slab at SW Column, Post-E200N



Figure 4.69 Third Floor at SW Column, Post-E200N

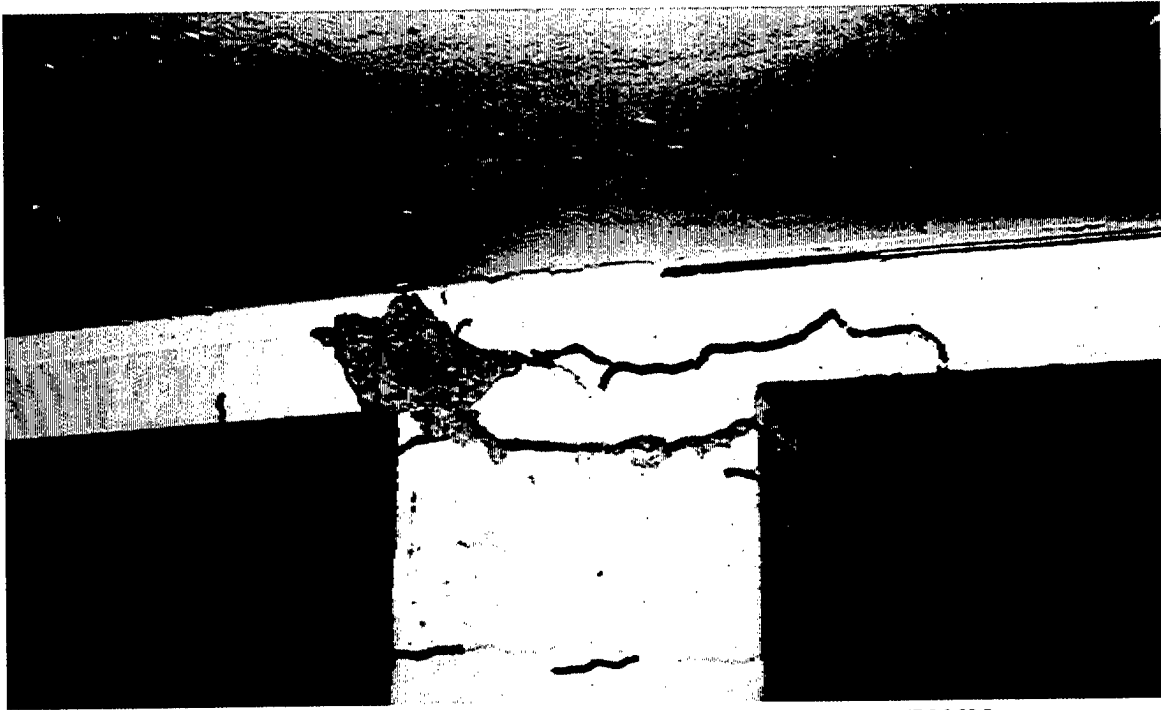


Figure 4.70 Bottom of Third Floor Slab at SW Column, Post-E200N

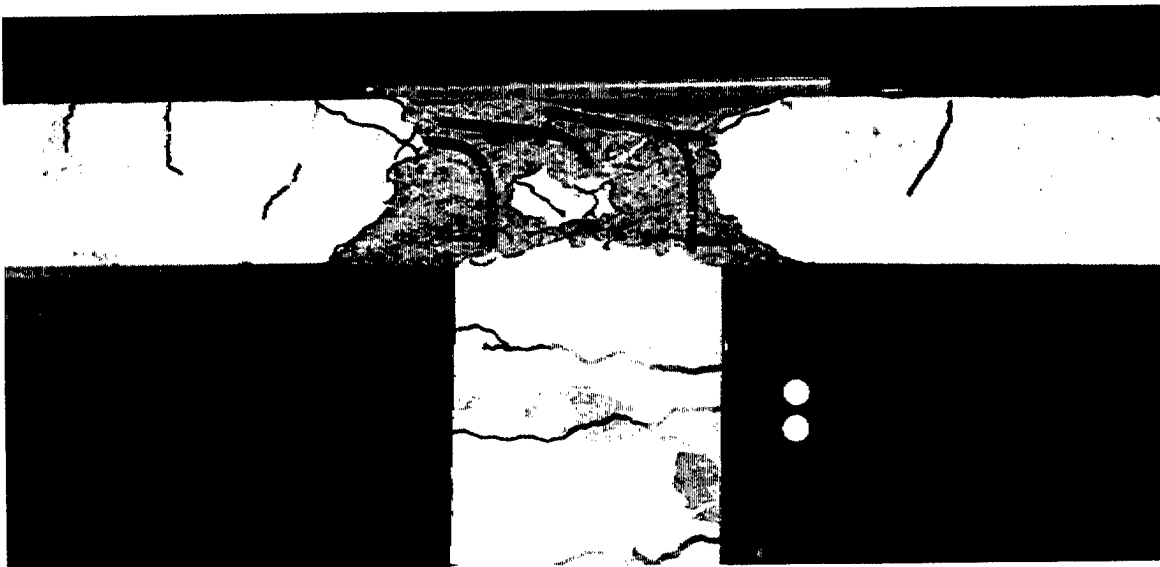


Figure 4.71 Third Floor at NE Column, Post-E200N

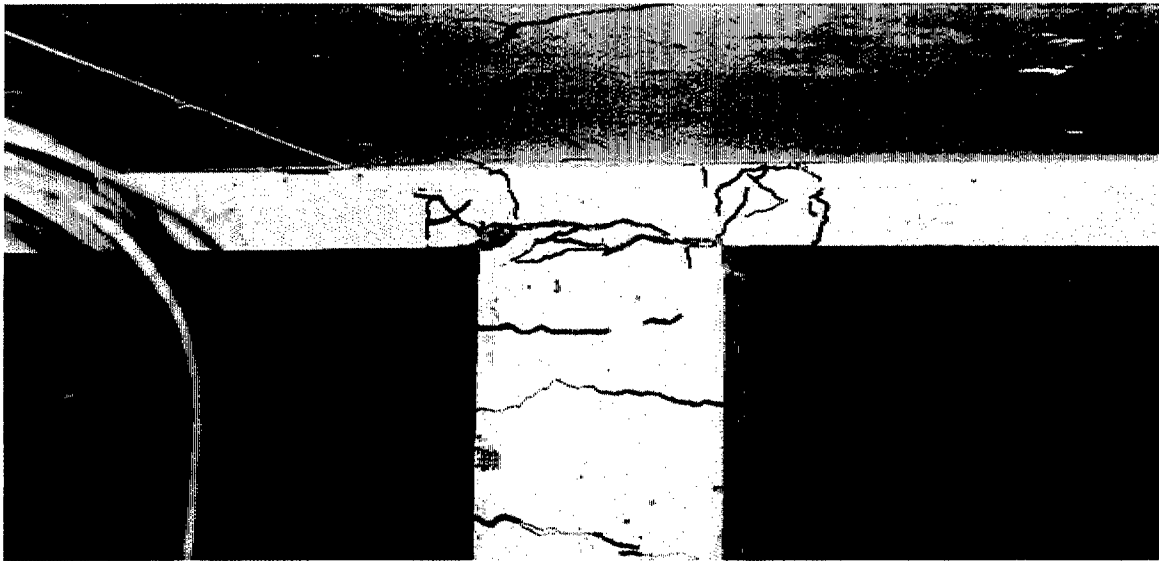


Figure 4.72 Bottom of Third Floor Slab at NE Column, Post-E200N

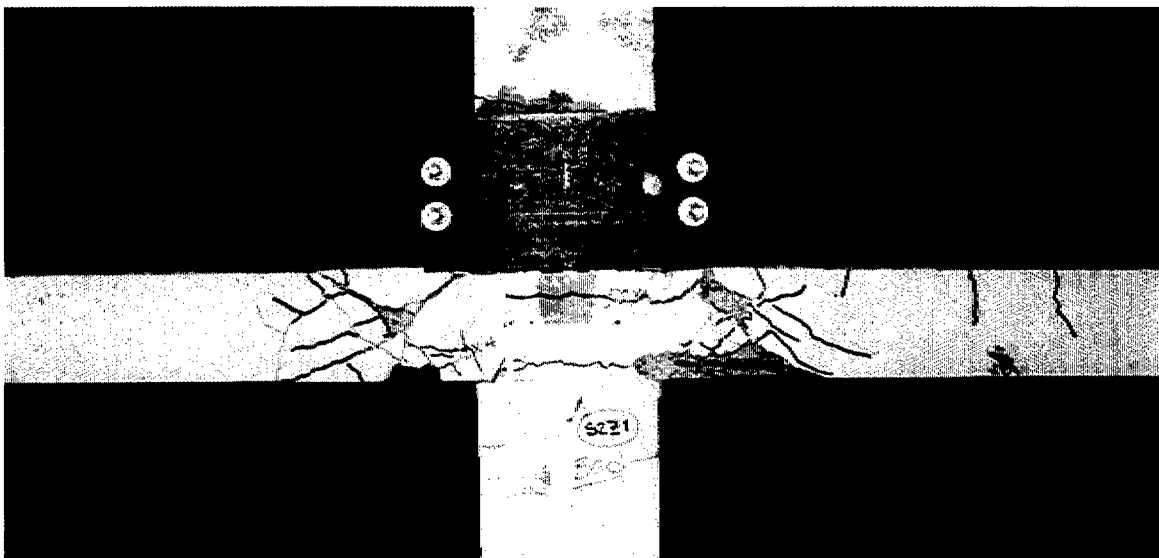


Figure 4.73 Second Floor at NW Column, Post-E200N

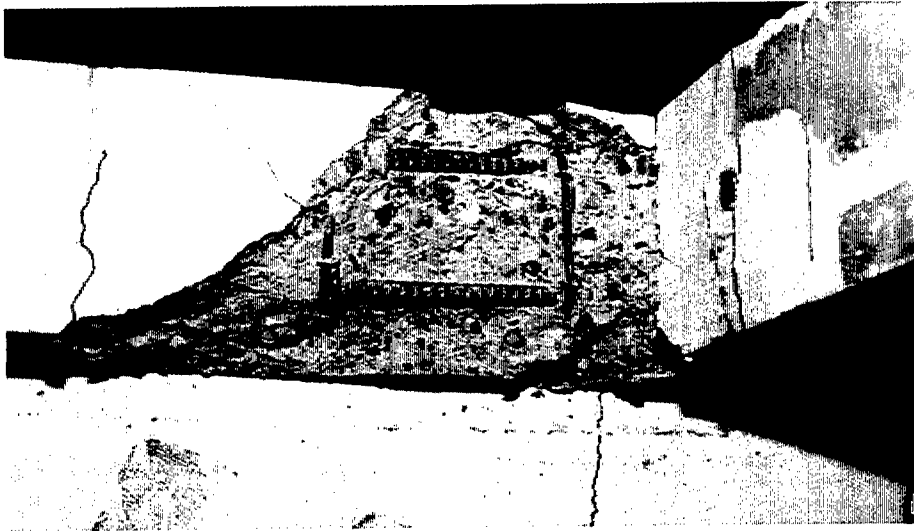


Figure 4.74 Spandrel, Second Floor, NW Column, East Side, Post-E200N

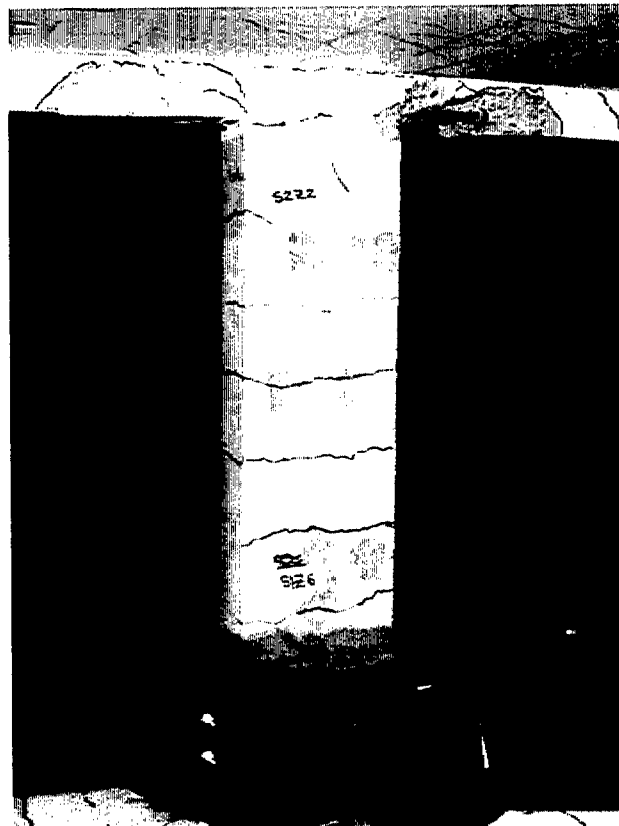


Figure 4.75 Second Floor, NW Column, Post-E200N



Figure 4.76 Second Floor at NE Column, Post-E200N



Figure 4.77 Bottom of Second Floor Slab and Spandrel, NE Column, Post-E200N

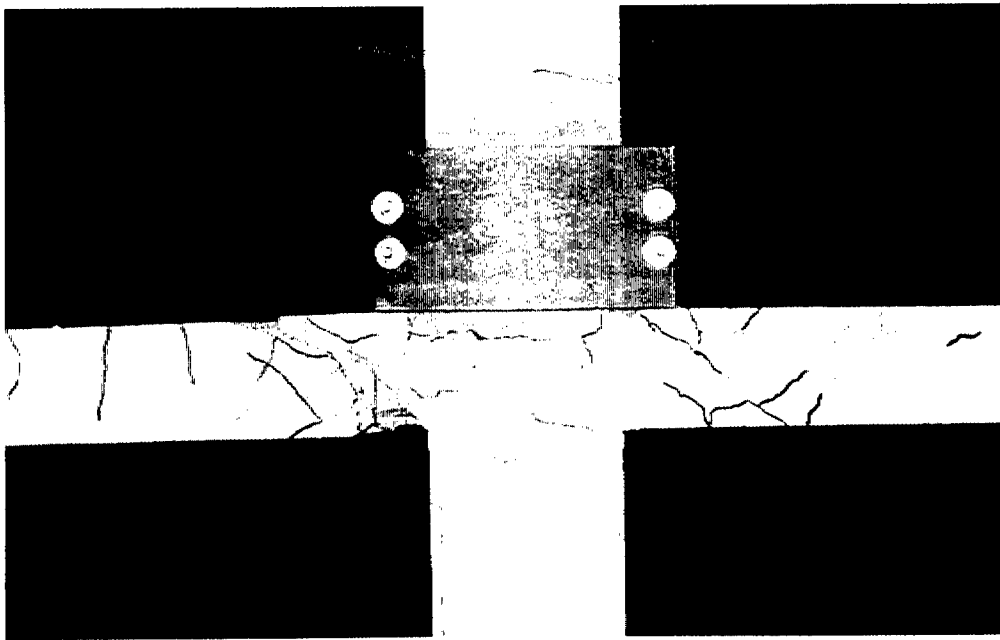


Figure 4.78 Second Floor at SW Column, Post-E200N

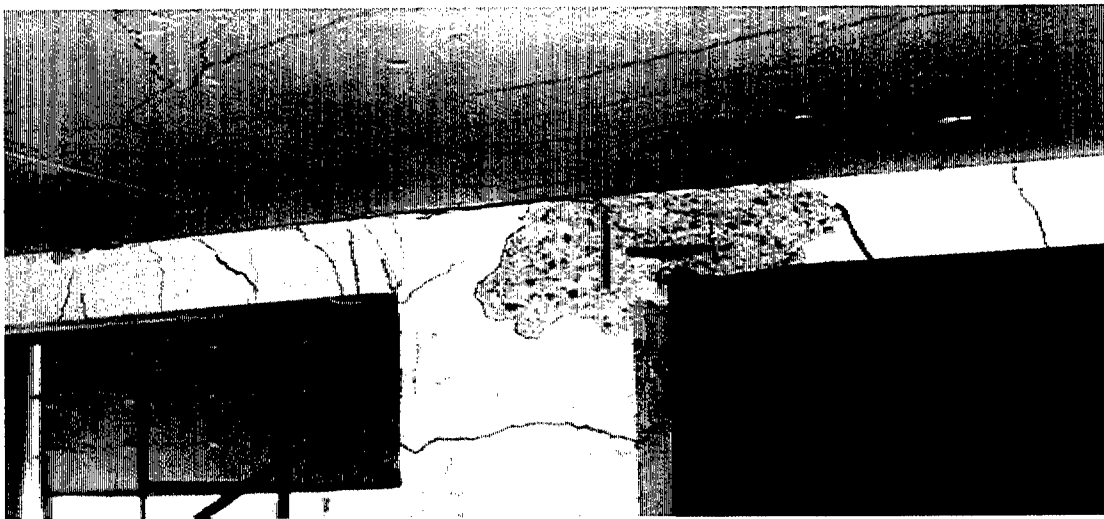


Figure 4.79 Bottom of Second Floor Slab and Spandrel, SW Column, Post-E200N

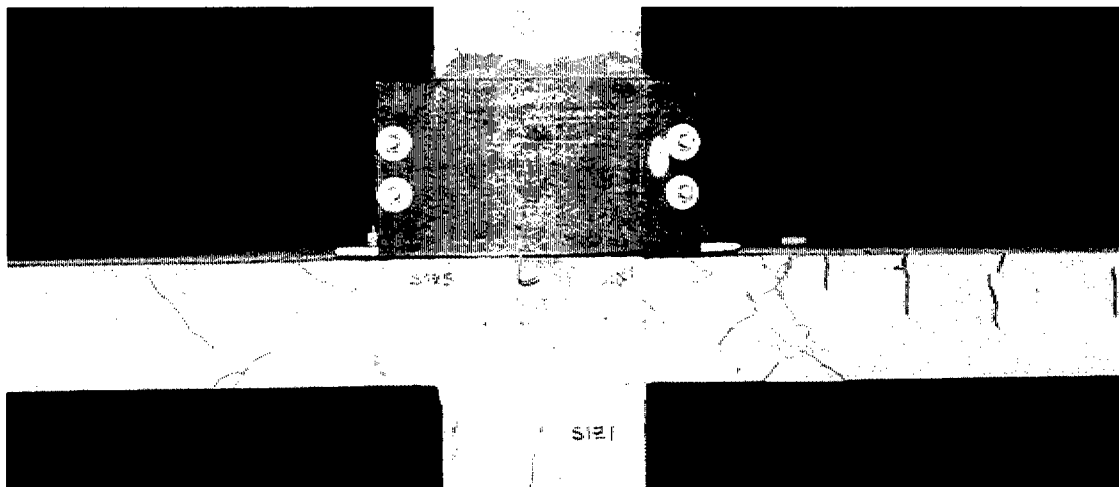


Figure 4.80 First Floor at NW Column, Post-E200N

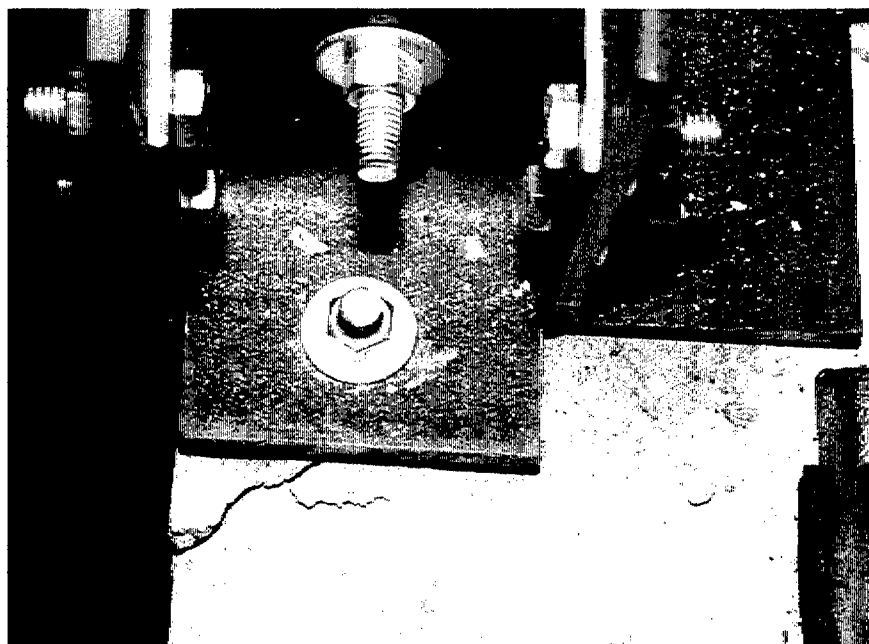


Figure 4.81 Base of Second Story, SW Column, Post-E200N

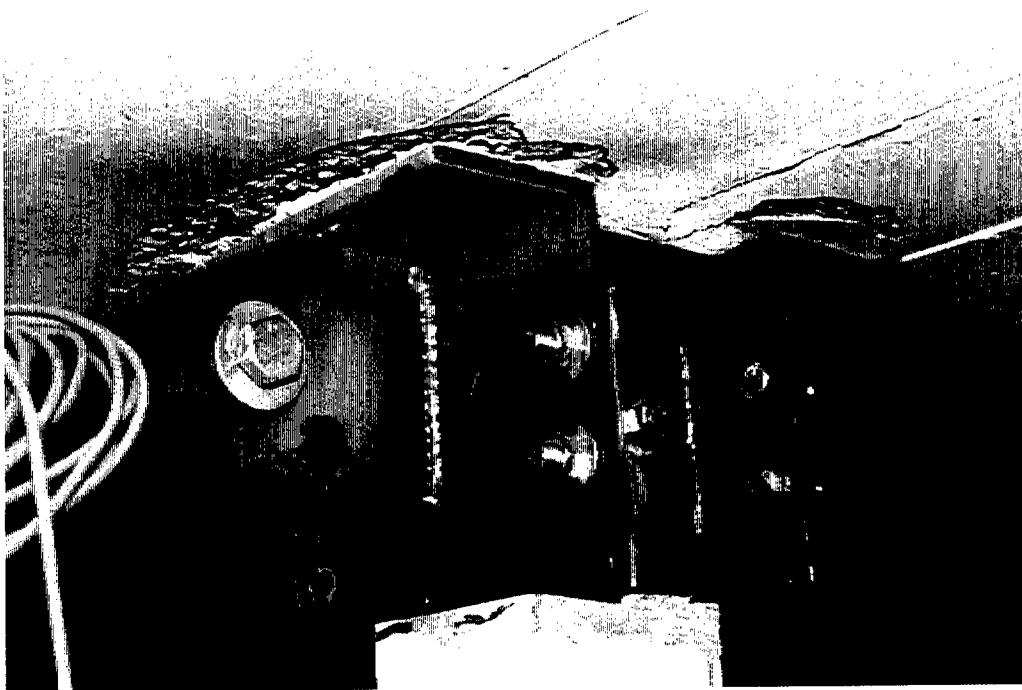


Figure 4.82 Bottom of Third Floor Slab, East Center Column, Post-E200N



Figure 4.83 Bottom of Second Floor Slab, East Center Column, Post-E200N



Figure 4.84 Top of Second Floor Slab, East Center Column, Post-E200N



Figure 4.85 Top of Second Floor Slab, West Center Column, Post-E200N



Figure 4.86 Top of First Floor Slab, West Center Column, Post-E200N

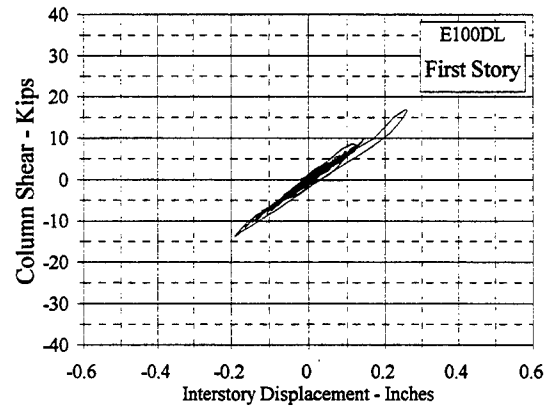
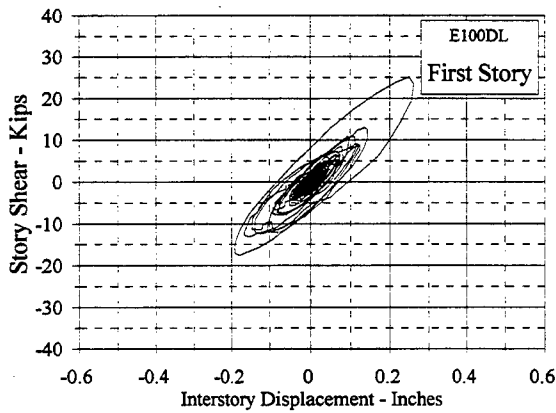
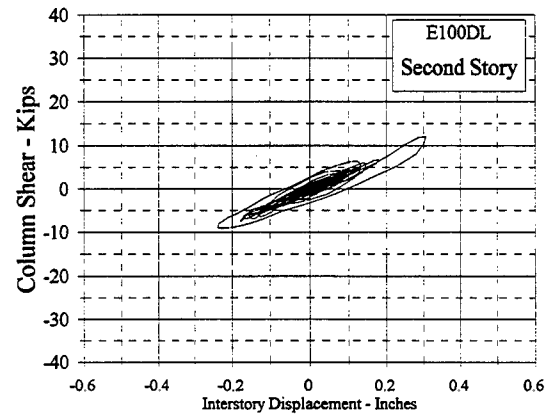
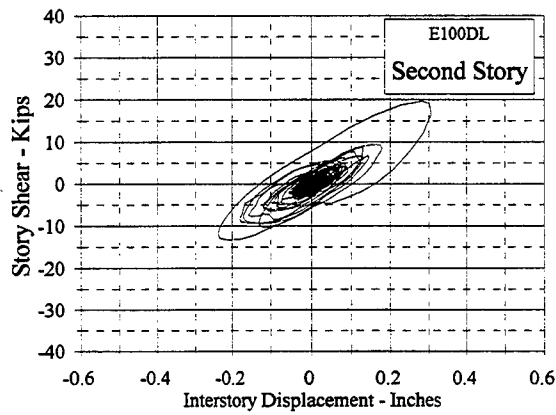
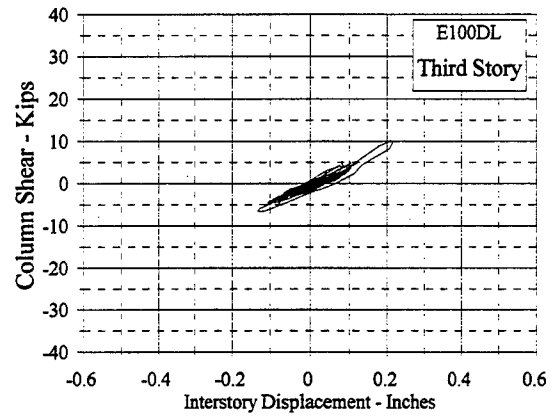
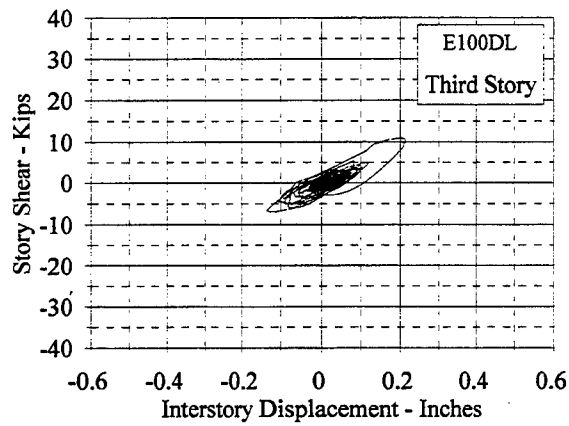


Figure 5.1 Comparison of Story and Column Shears Vs. Interstory Displacement, E100DL

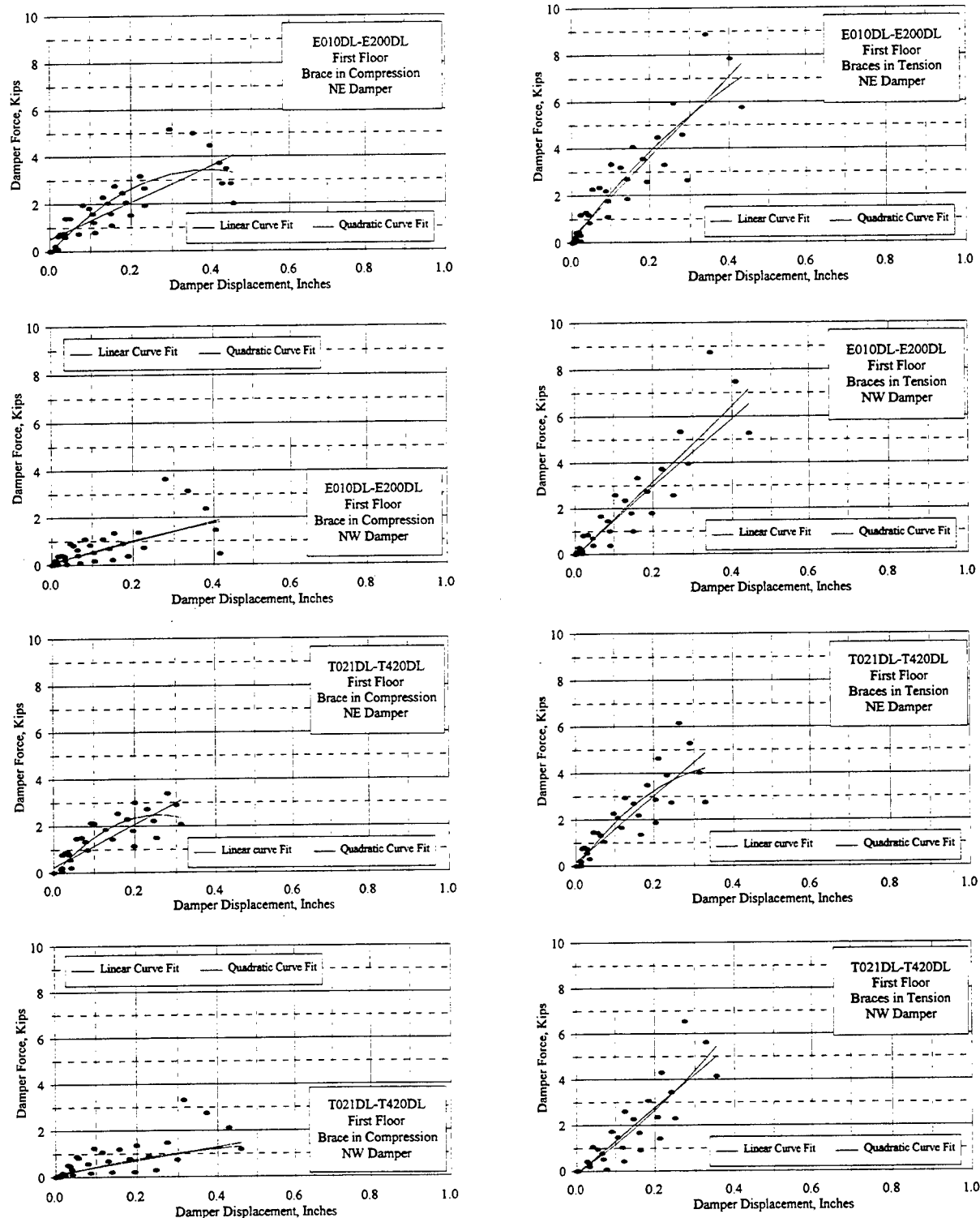


Figure 5.2 Damper Force Vs. Displacement "Backbone" Curves, First Story, North Side

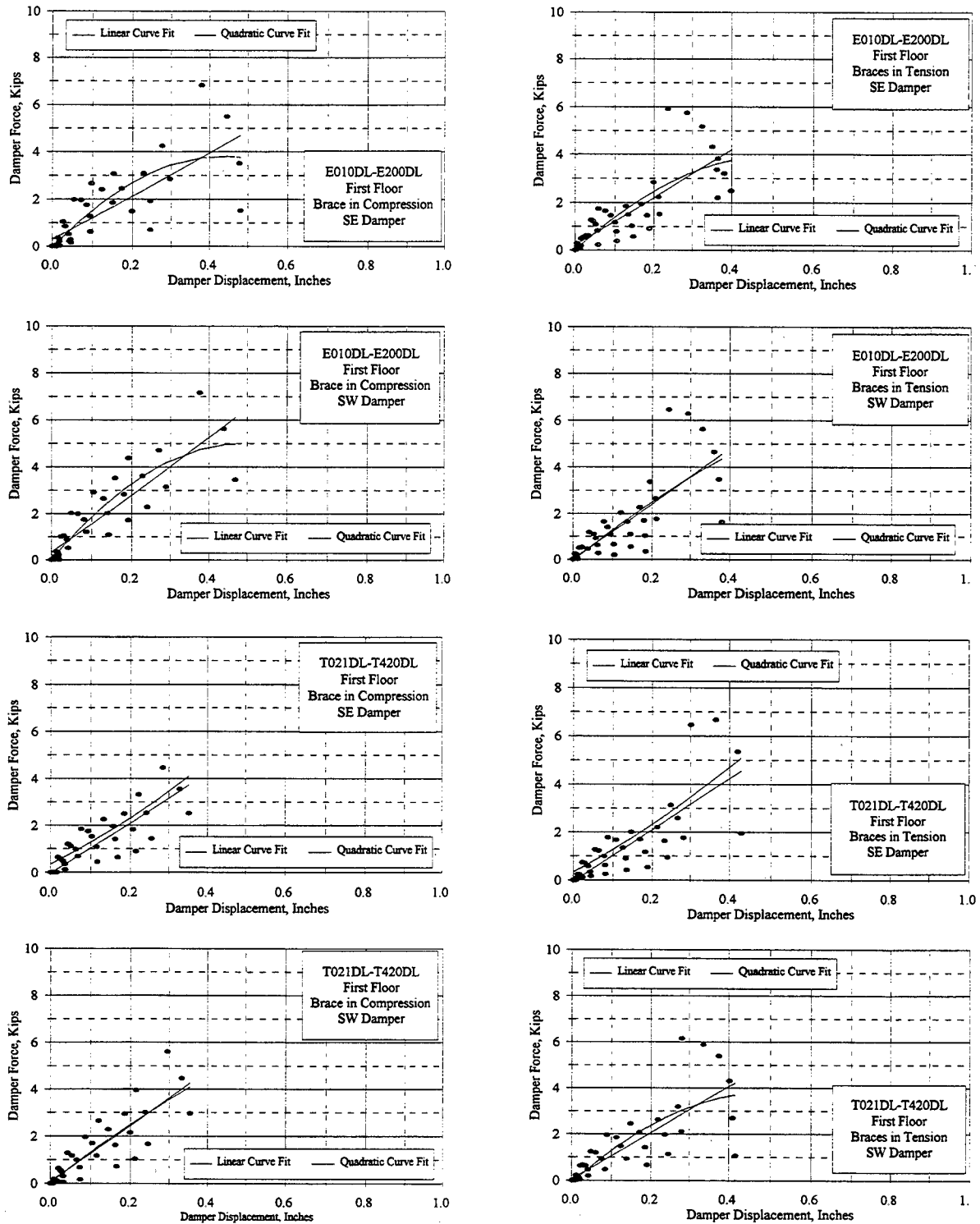


Figure 5.3 Damper Force Vs. Displacement "Backbone" Curves, First Story, South Side

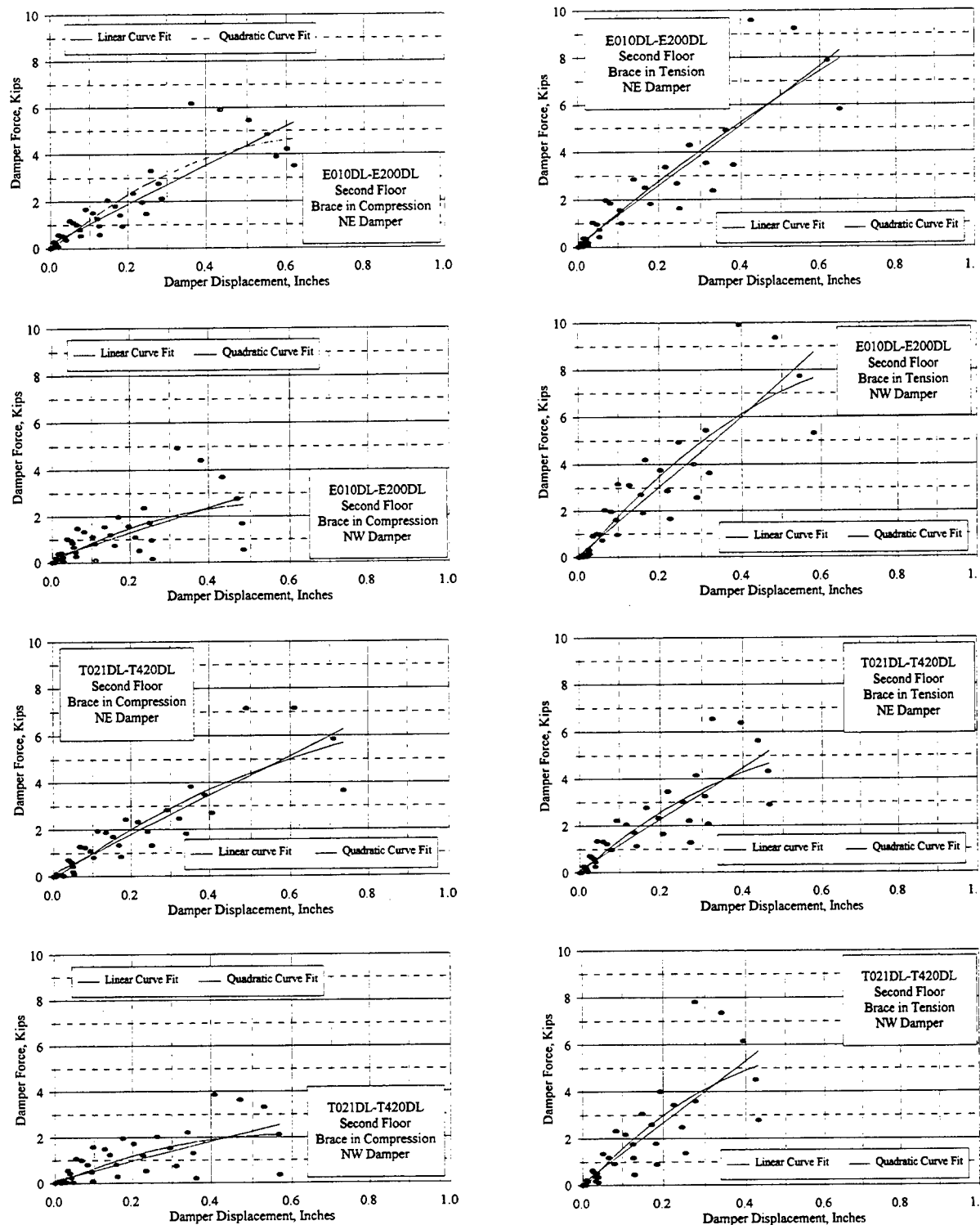


Figure 5.4 Damper Force Vs. Displacement "Backbone" Curves, Second Story, North Side

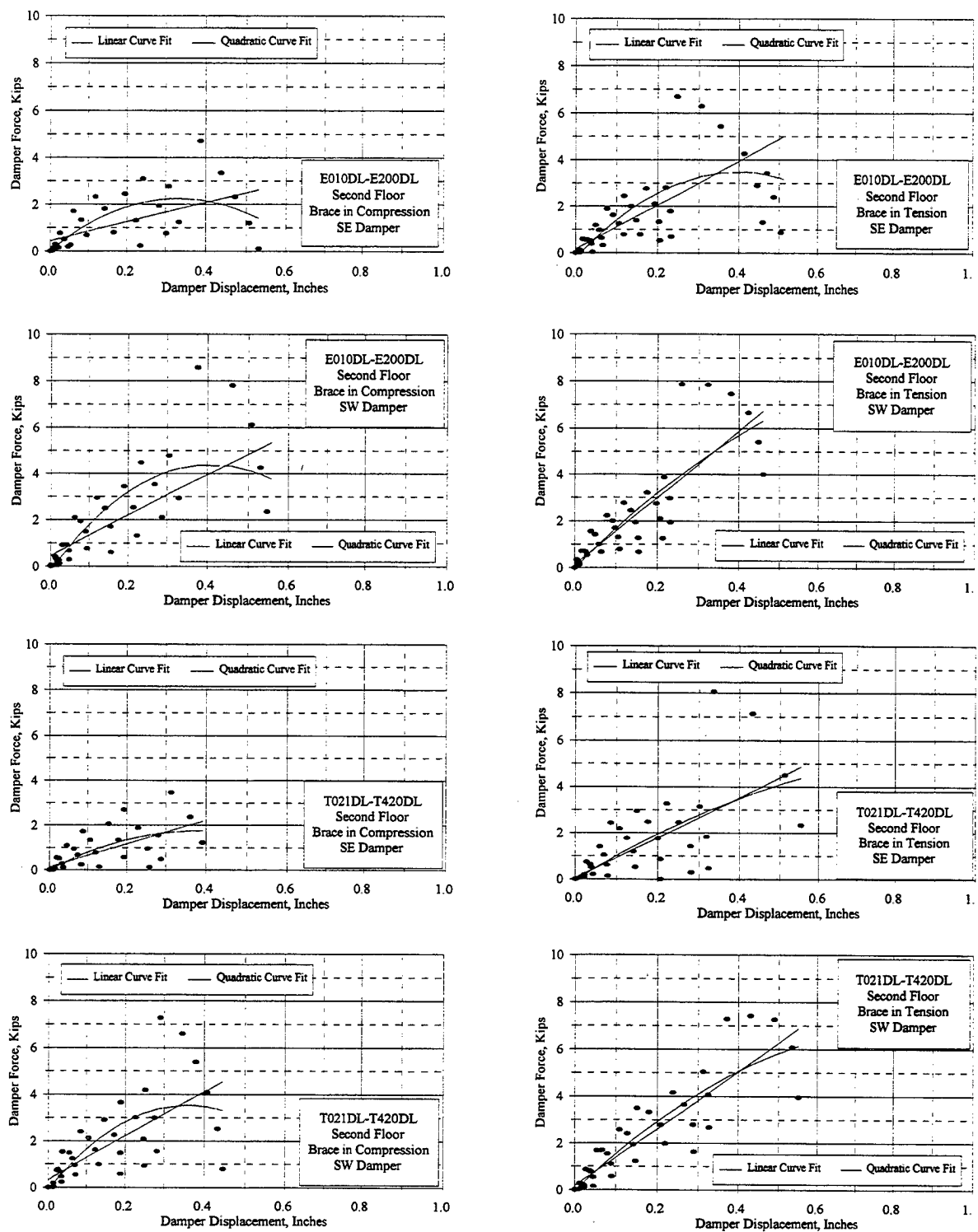


Figure 5.5 Damper Force Vs. Displacement "Backbone" Curves, Second Story, South Side

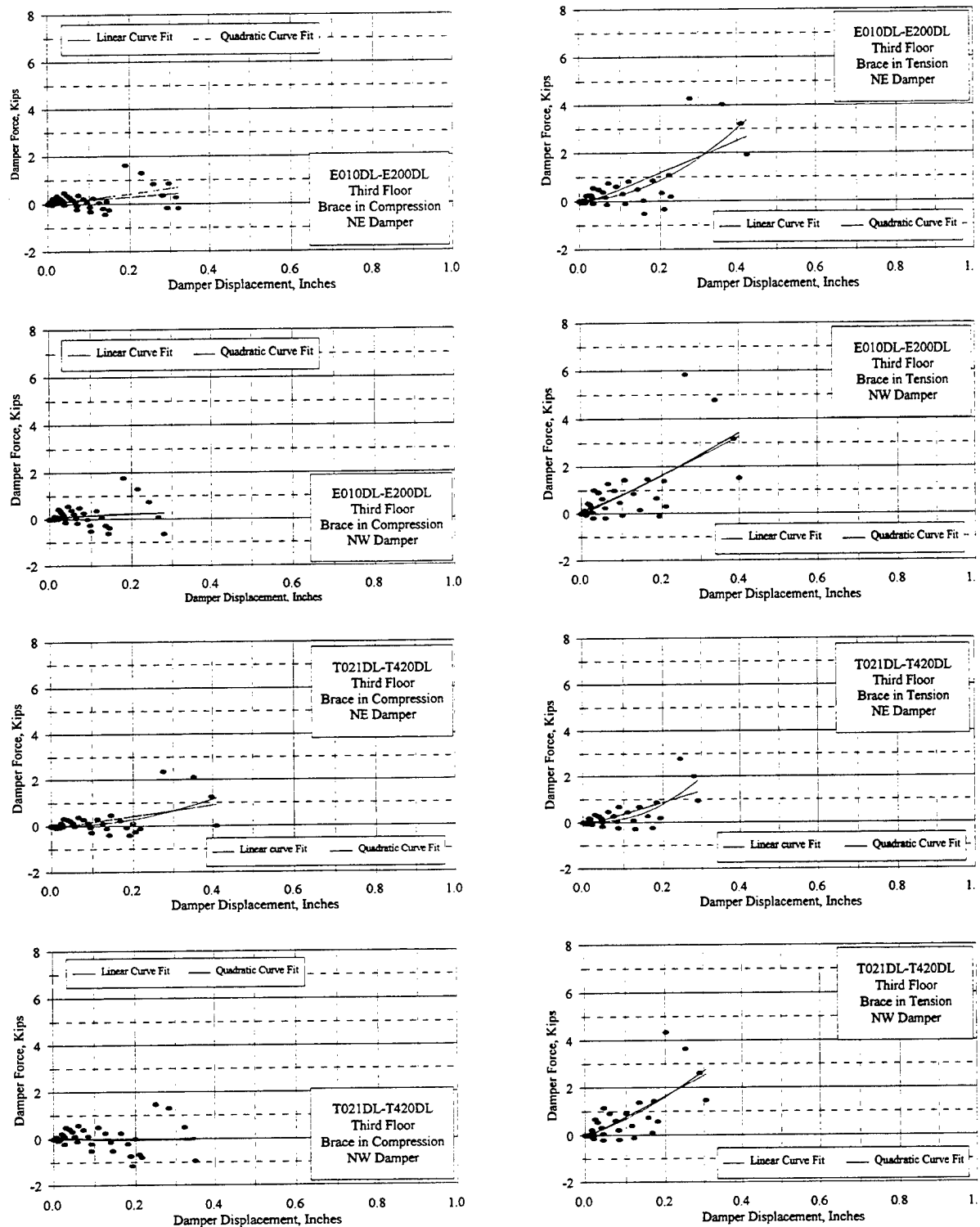


Figure 5.6 Damper Force Vs. Displacement "Backbone" Curves, Third Story, North Side

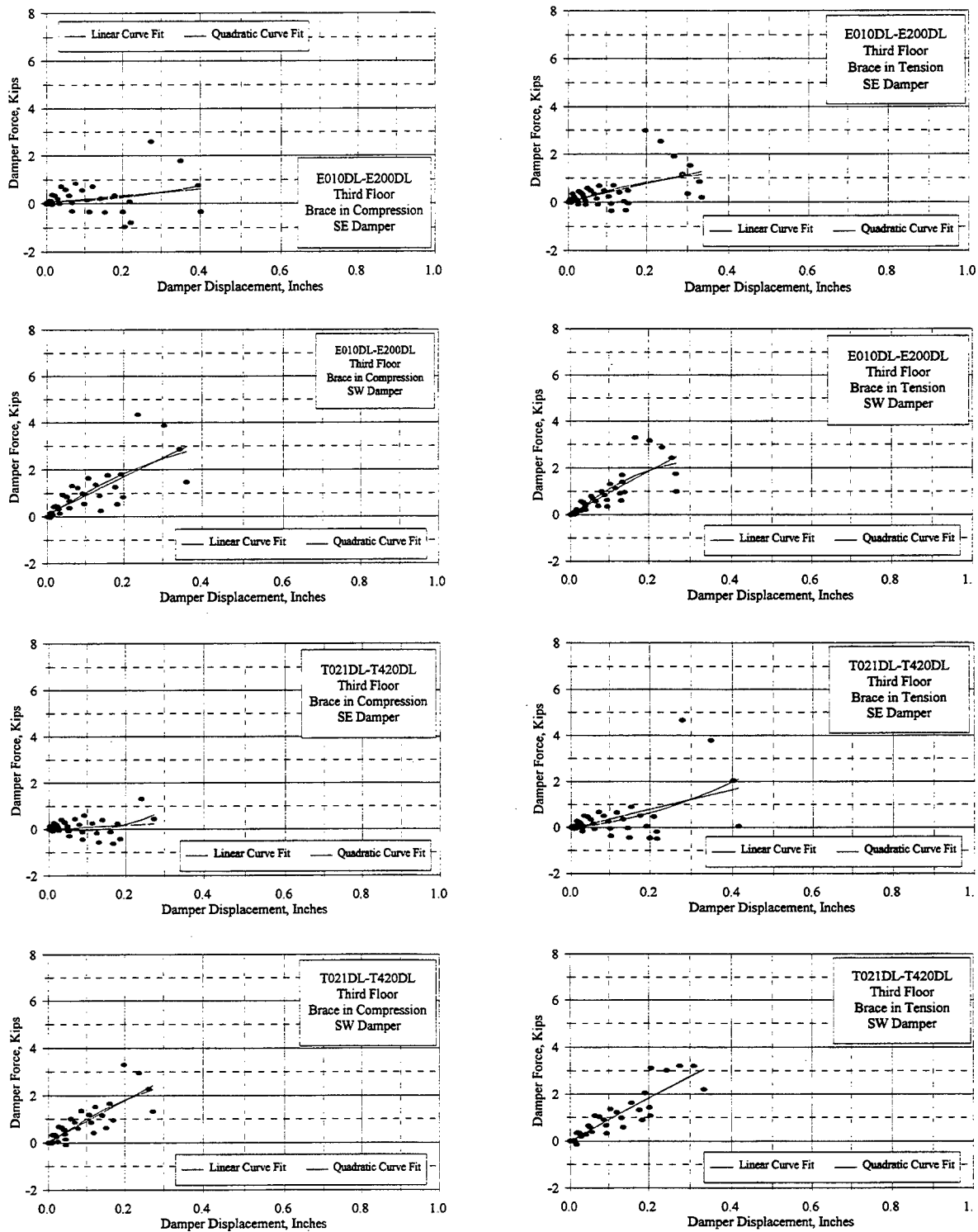


Figure 5.7 Damper Force Vs. Displacement "Backbone Curves," Third Story, South Side

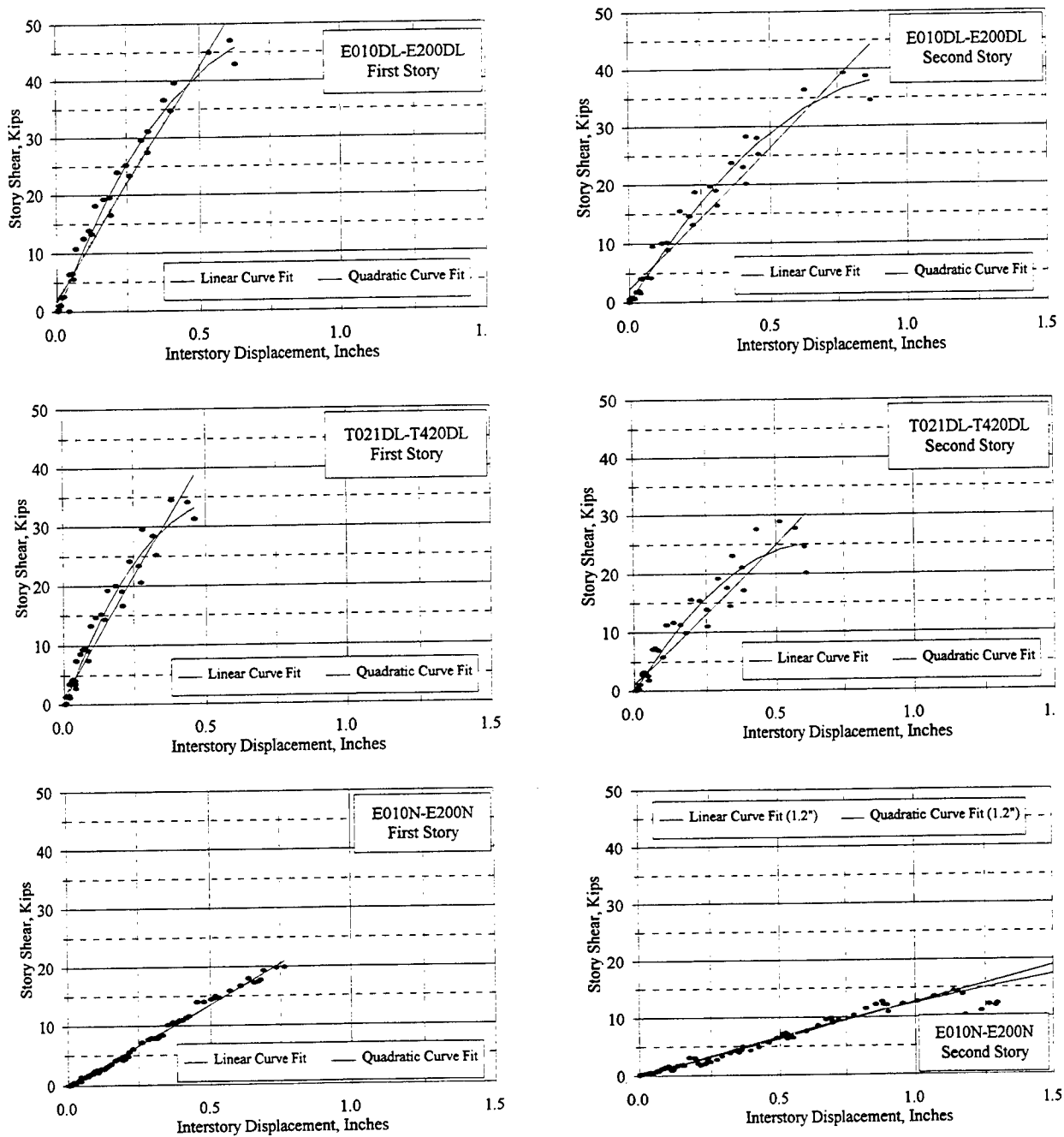


Figure 5.8 Story Shear Vs. Interstory Displacement "Backbone" Curves, First and Second Stories

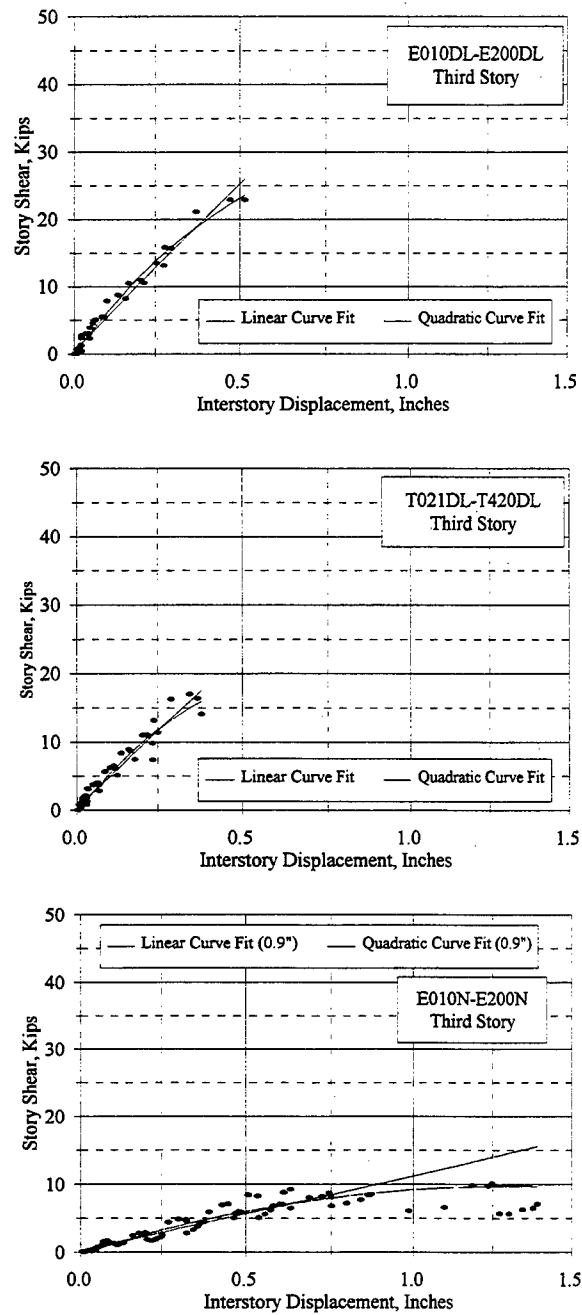


Figure 5.9 Story Shear Vs. Interstory Displacement "Backbone" Curves, Third Story

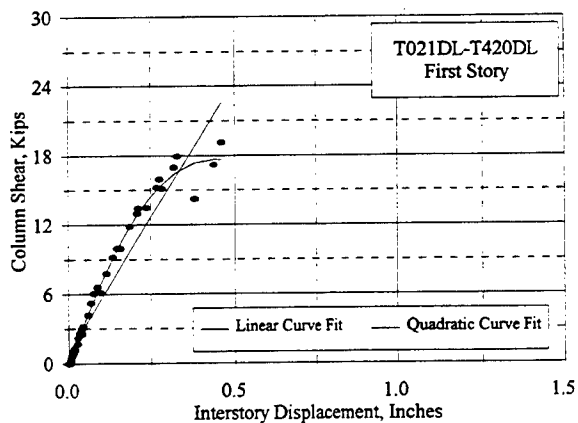
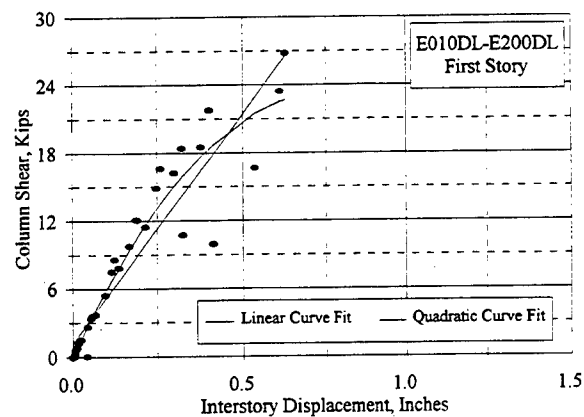
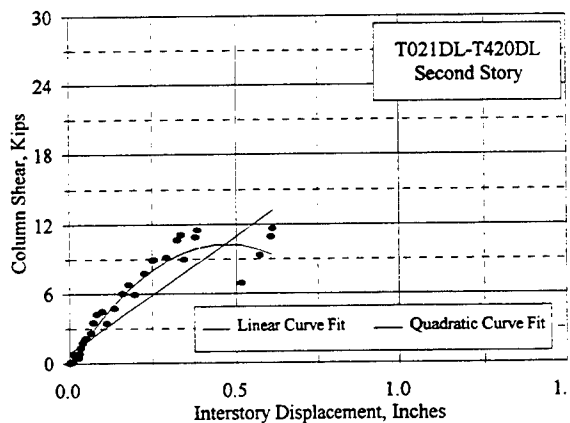
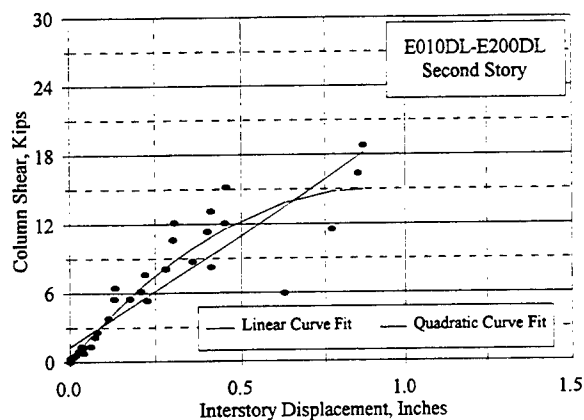
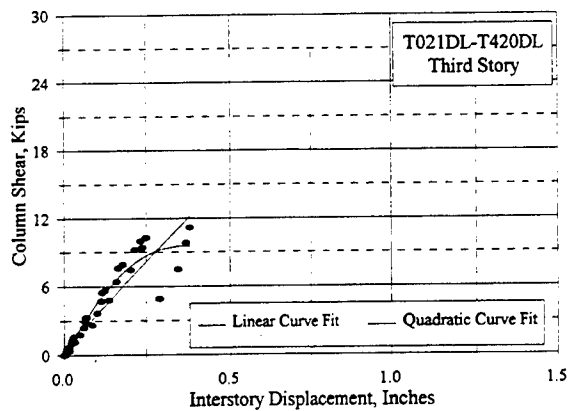
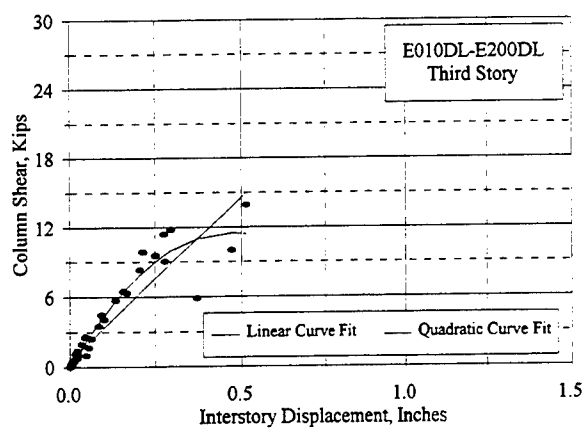


Figure 5.10 Column Shear Vs. Interstory Displacement "Backbone" Curves

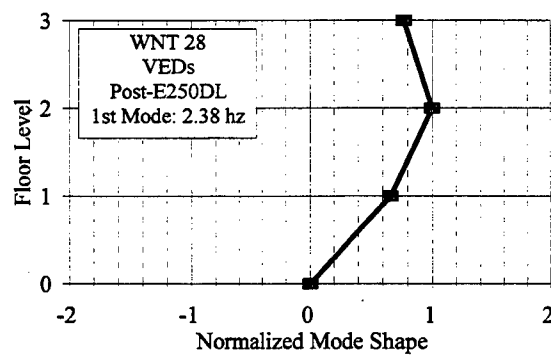
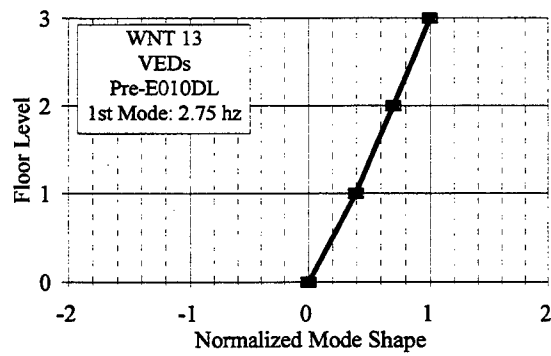
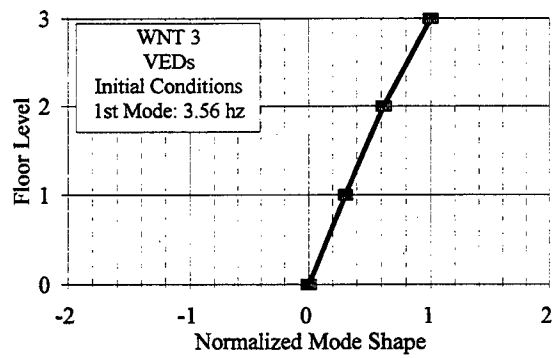


Figure 5.11 Normalized Mode Shapes from White Noise Tests 3, 13, and 28

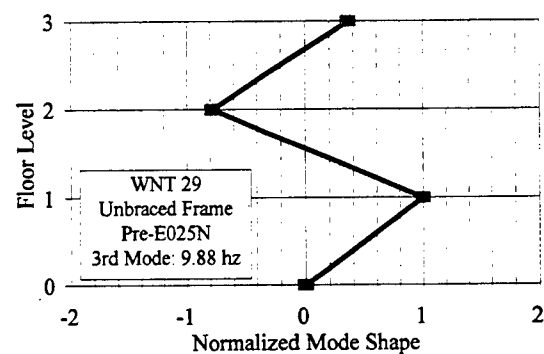
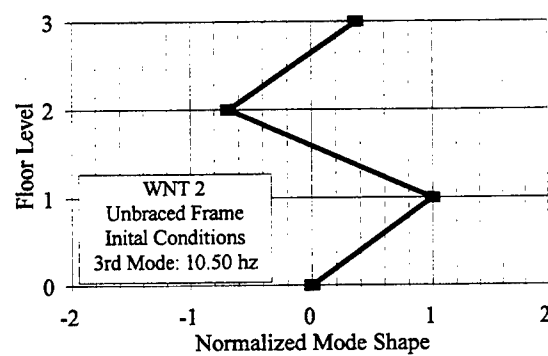
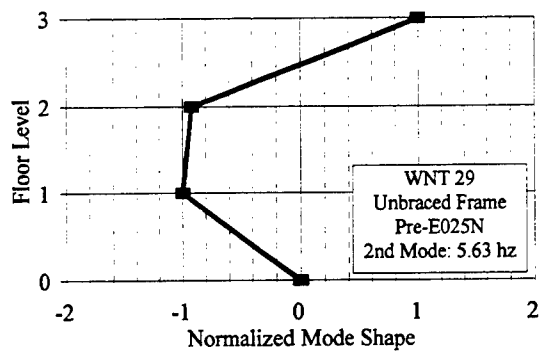
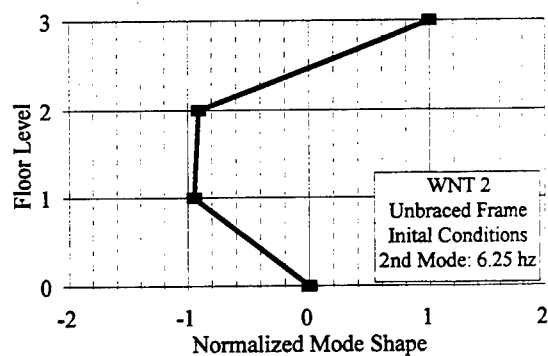
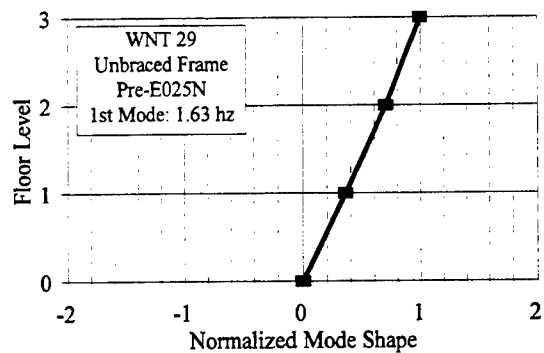
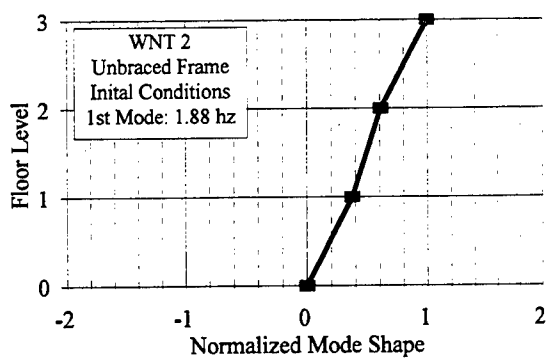


Figure 5.12 Normalized Mode Shapes from White Noise Tests 2 and 29

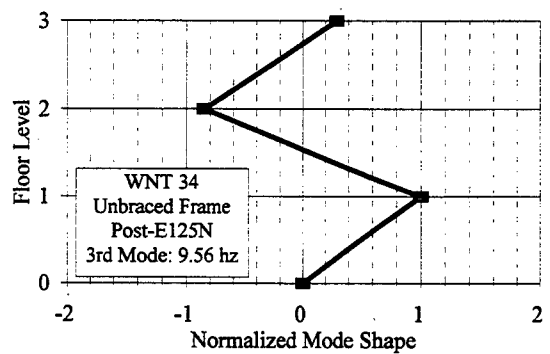
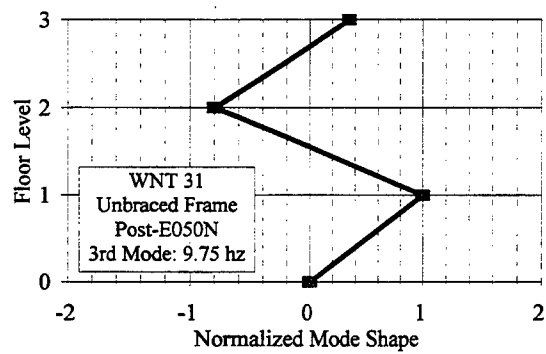
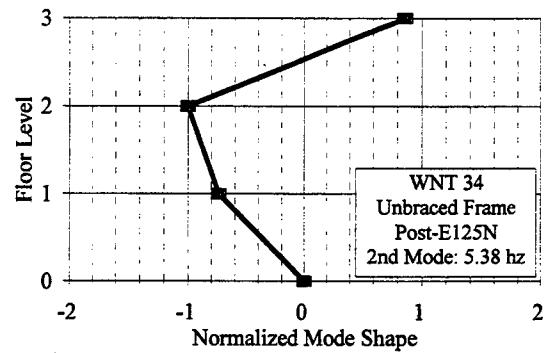
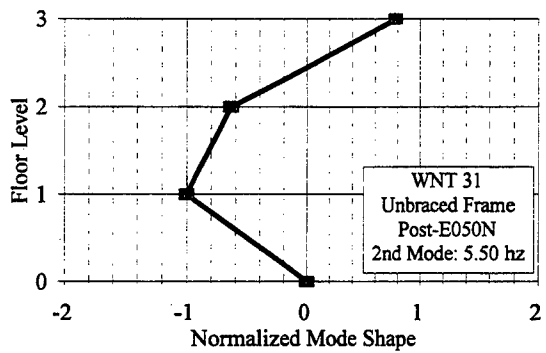
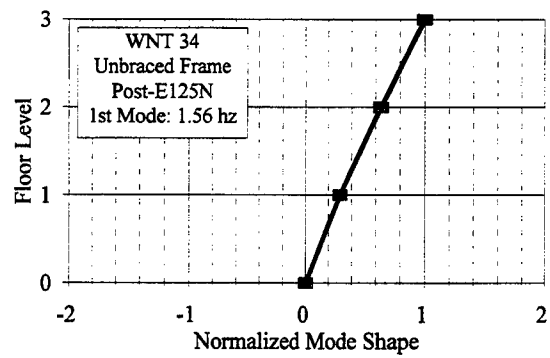
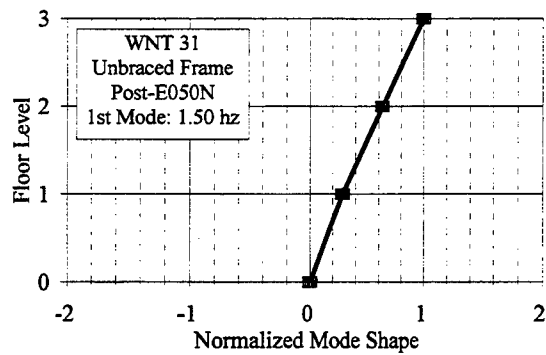


Figure 5.13 Normalized Mode Shapes from White Noise Tests 31 and 34

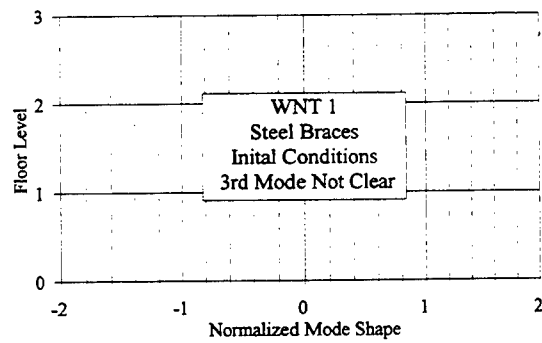
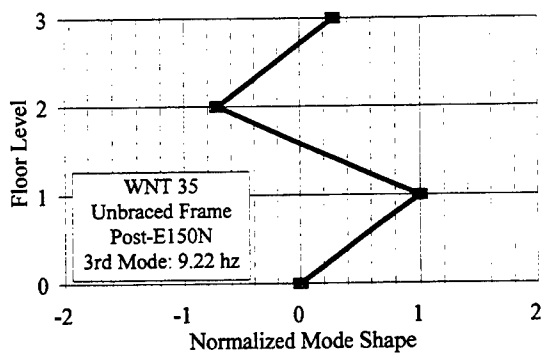
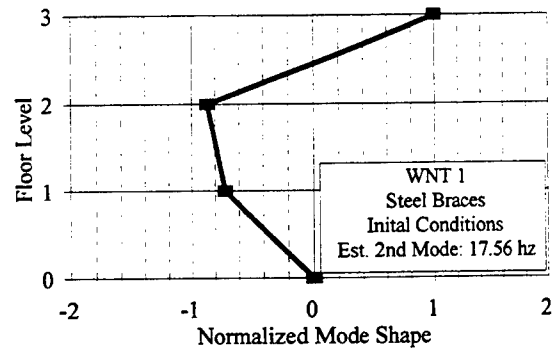
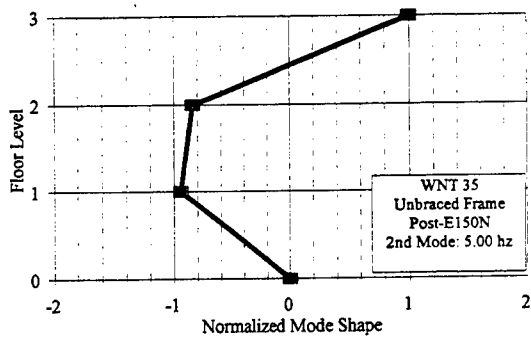
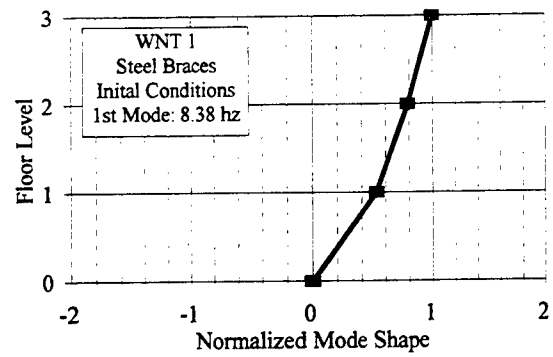
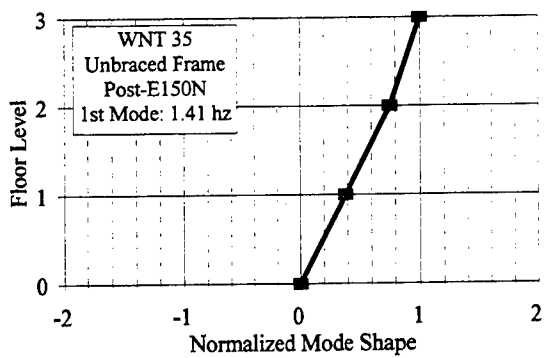


Figure 5.14 Normalized Mode Shapes from White Noise Tests 35 and 1

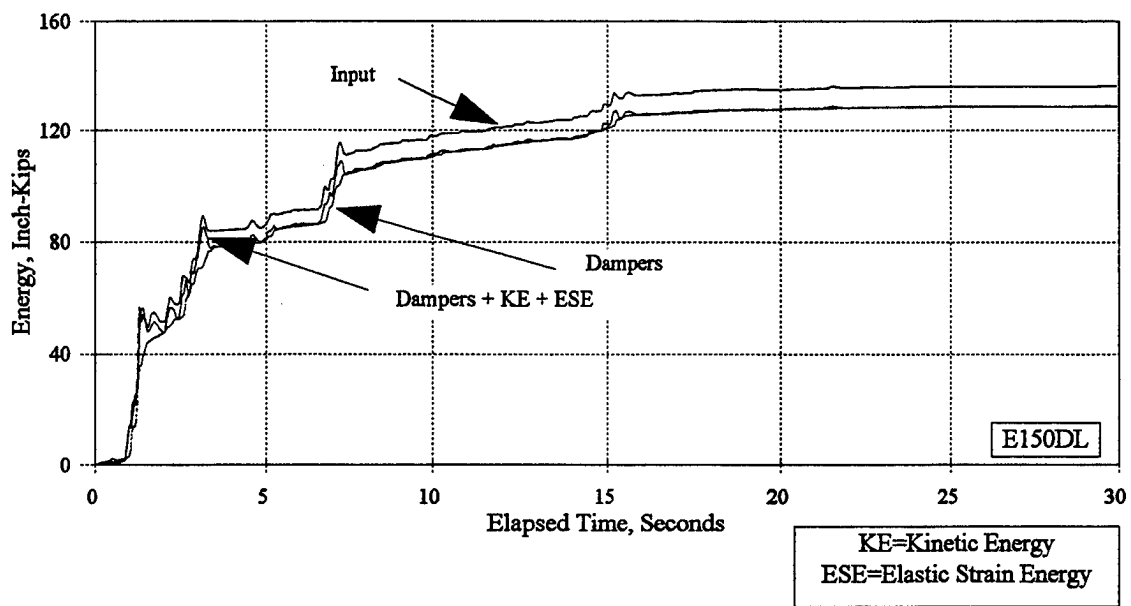
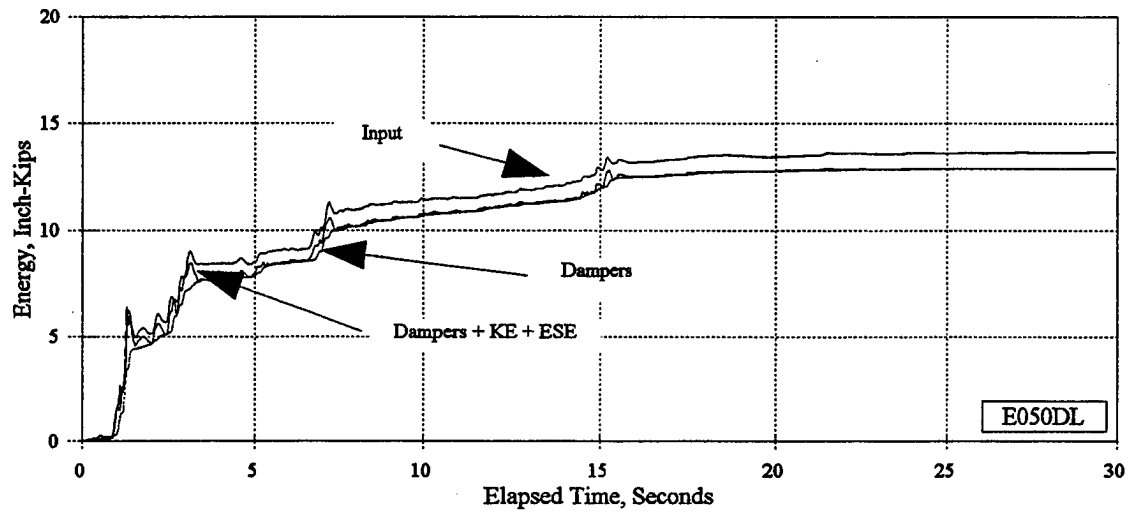


Figure 5.15 Input, Damper Dissipation, Kinetic, and Elastic Strain Energies: E050DL, E150DL

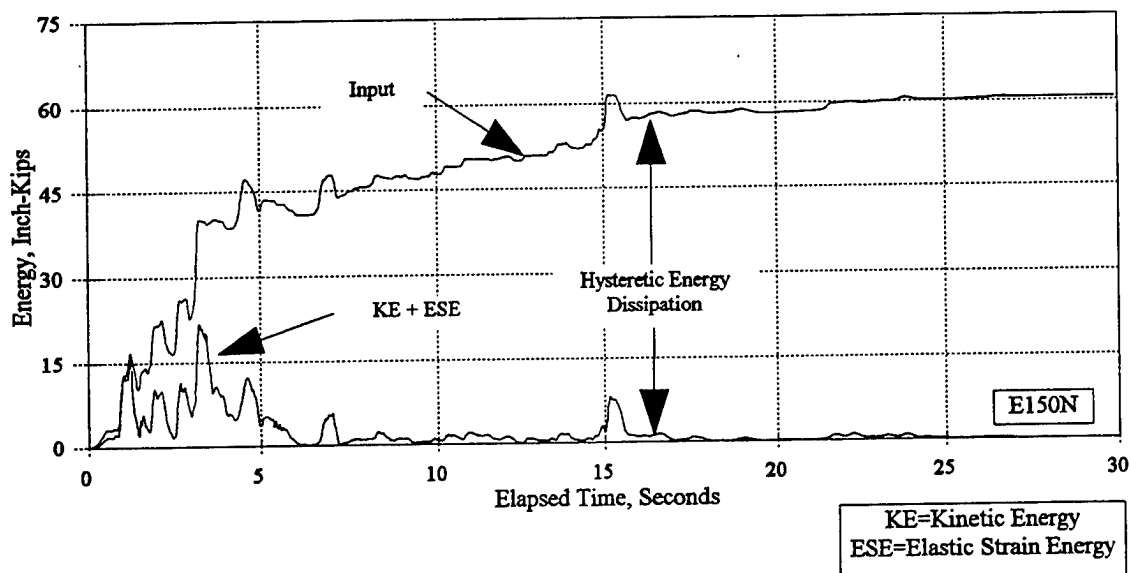
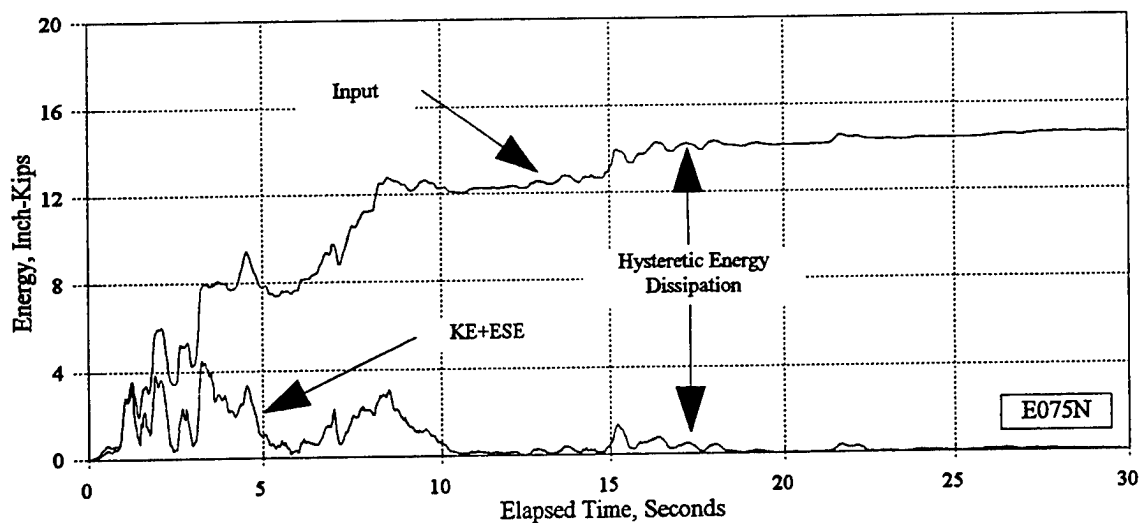


Figure 5.16 Input, Kinetic, and Elastic Strain Energies: E075N, E150N

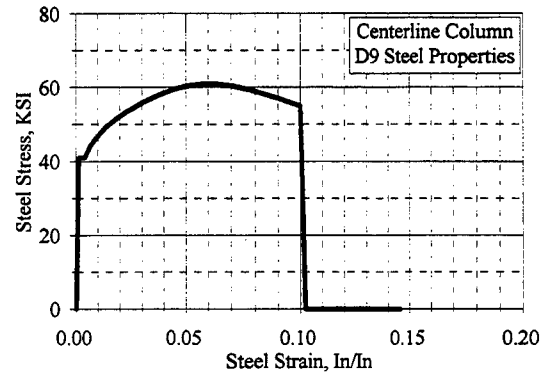
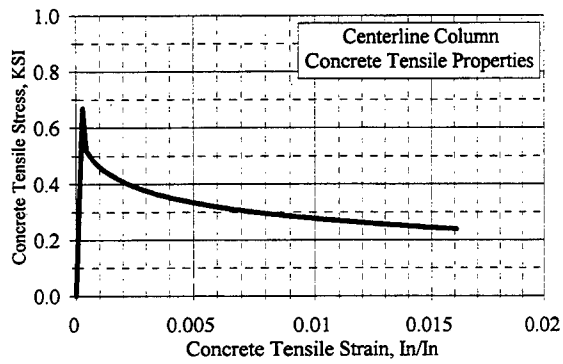
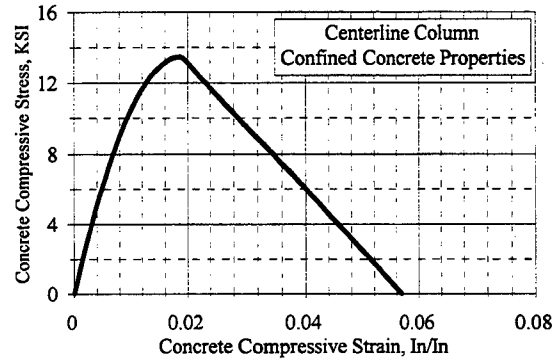
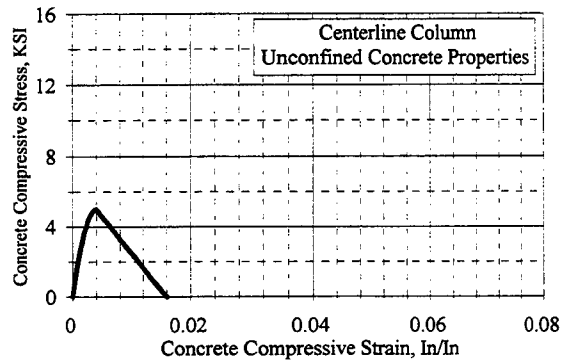
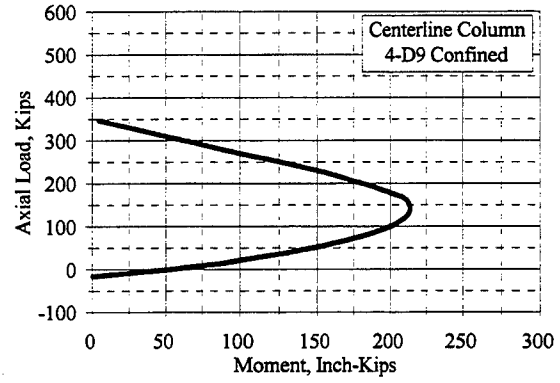
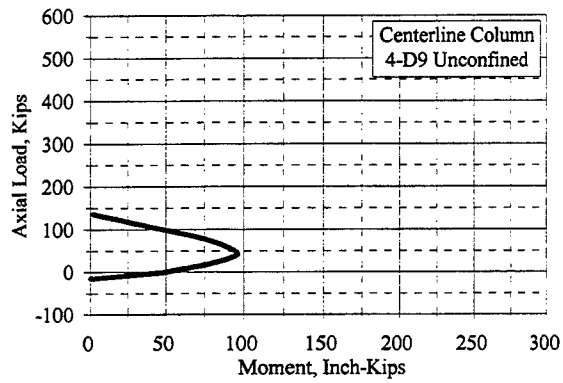


Figure 6.1 Interior (Centerline) Column Properties, 4 - D9 Bars

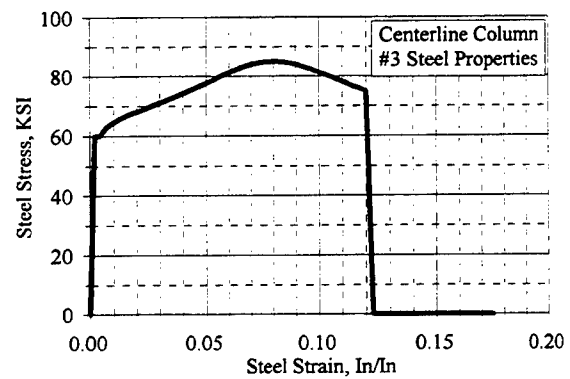
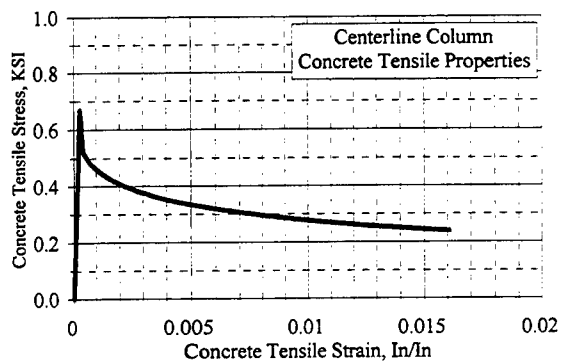
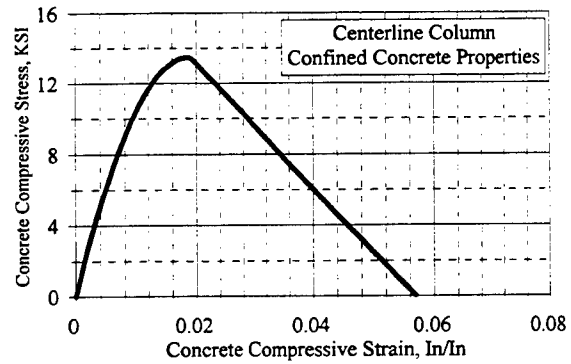
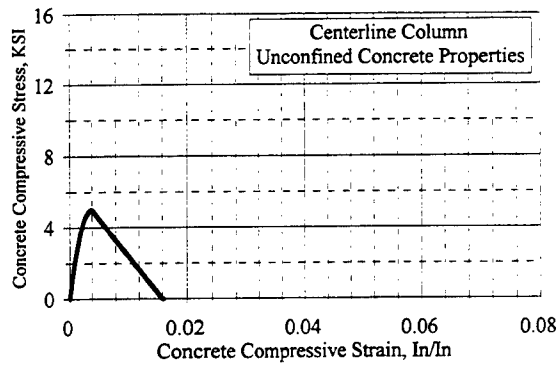
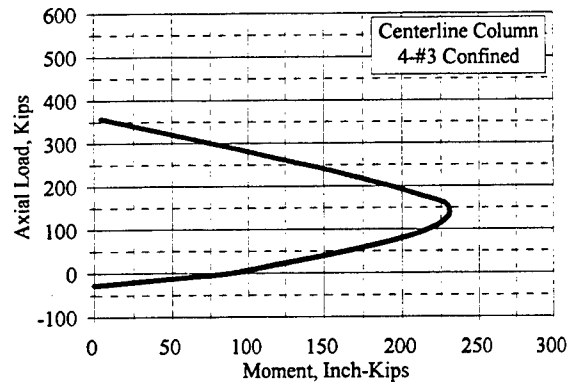
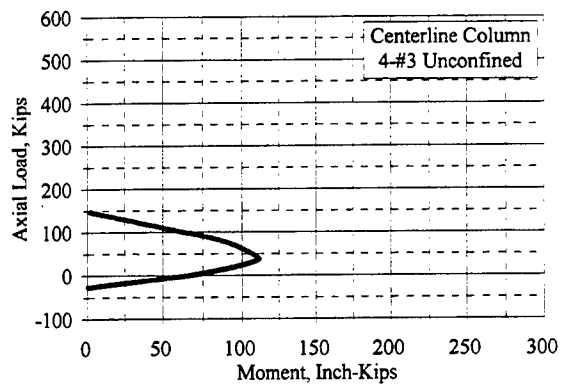


Figure 6.2 Interior (Centerline) Column Properties, 4 - #3 Bars

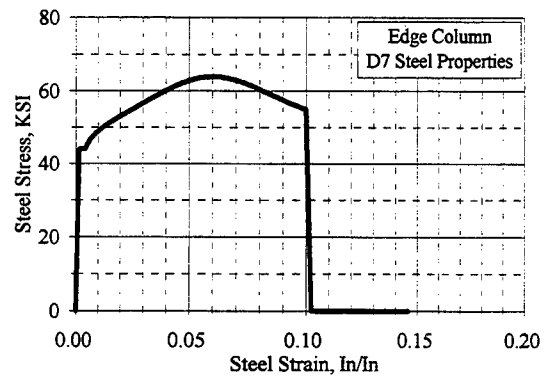
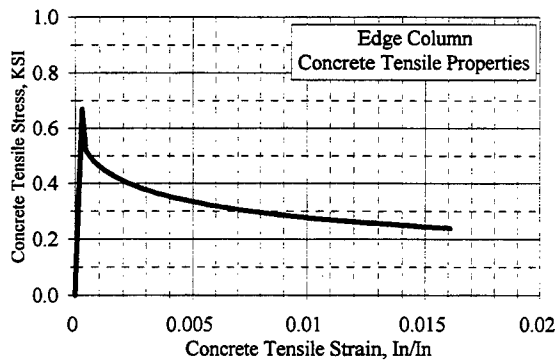
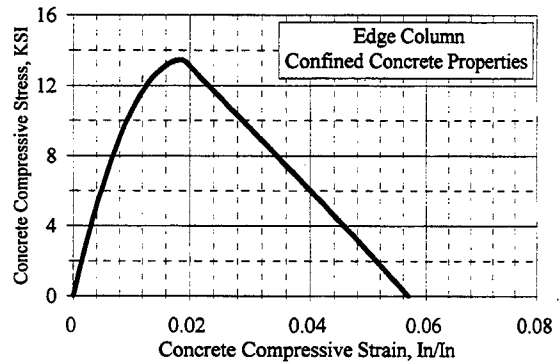
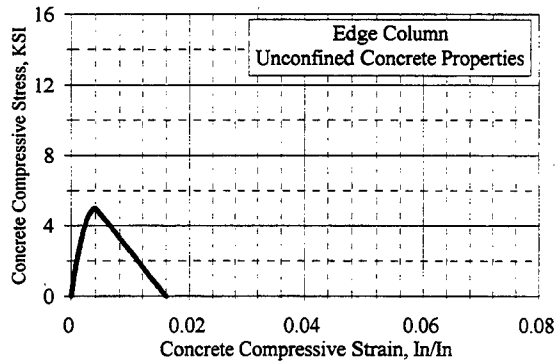
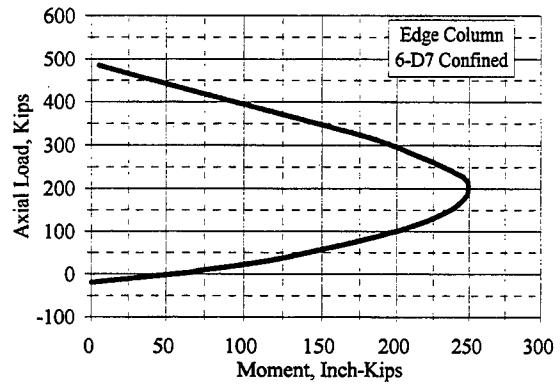
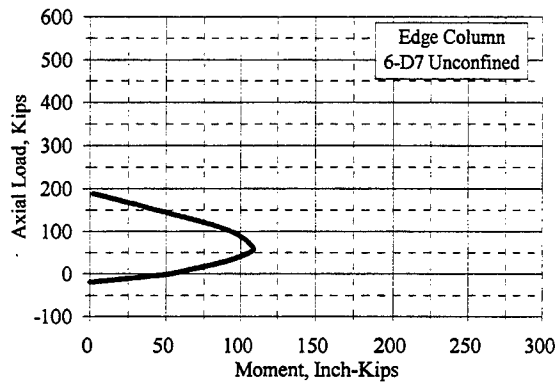


Figure 6.3 Exterior (Edge) Column Properties, 6 - D7 Bars

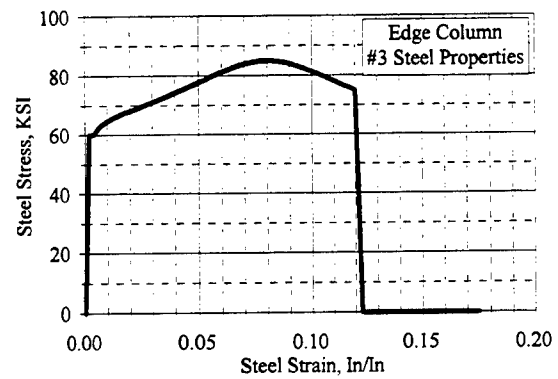
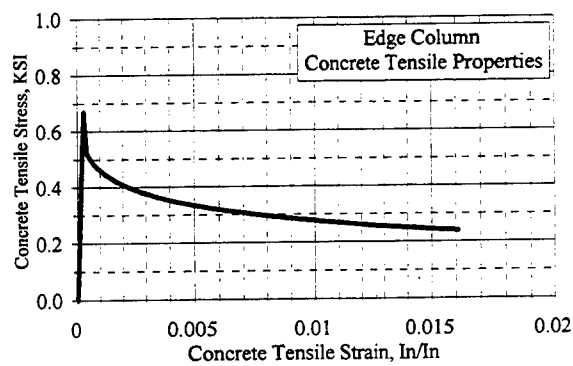
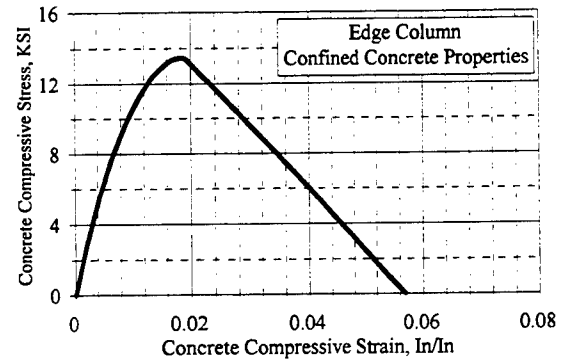
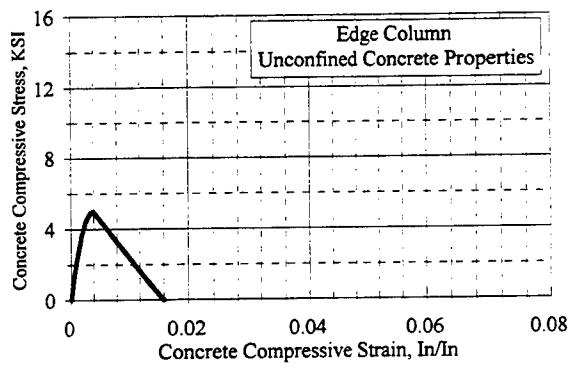
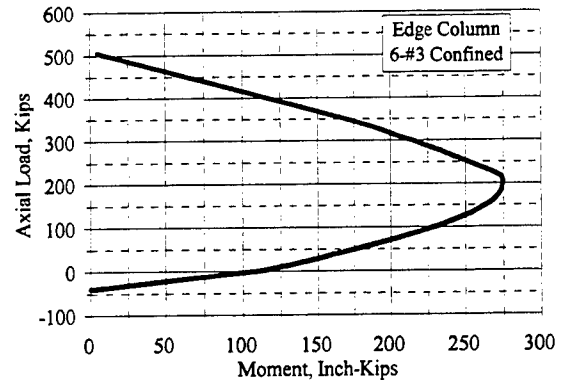
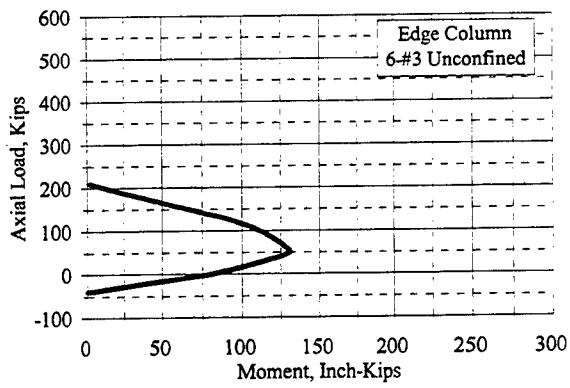


Figure 6.4 Exterior (Edge) Column Properties, 6 - #3 Bars

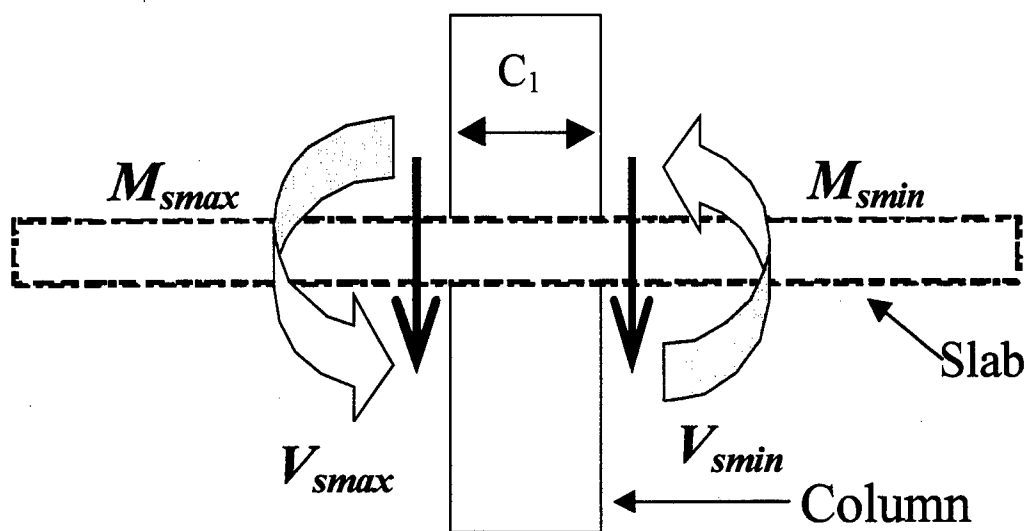


Figure 6.5 Forces Acting on Luo-Durrani Interior Slab-Column Model (Reference 27)

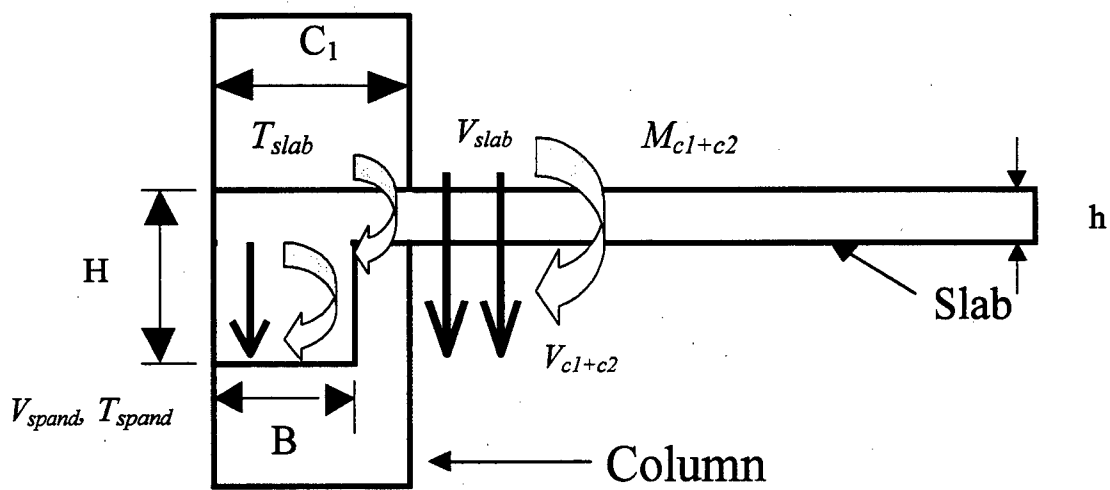
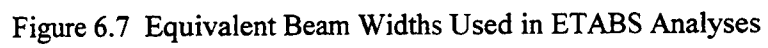


Figure 6.6 Forces Acting on Luo-Durrani Exterior Slab-Column Model (Reference 28)



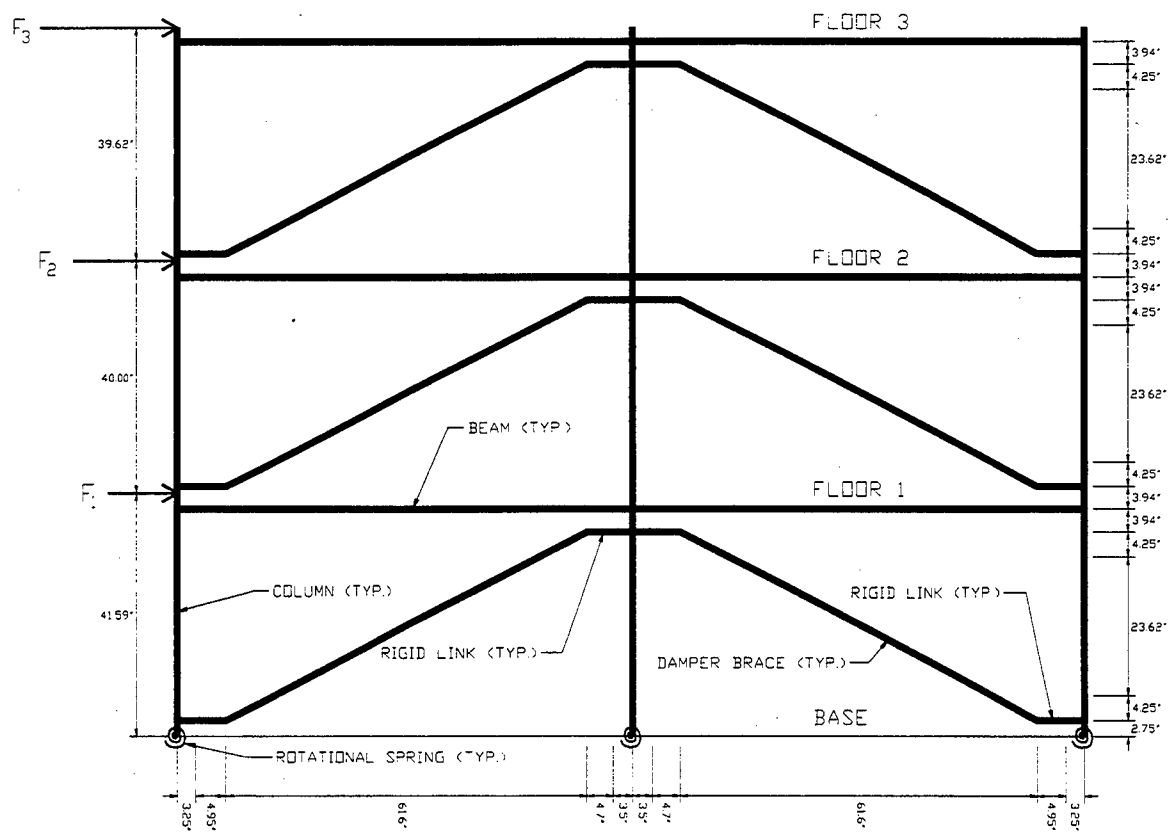


Figure 6.8. Idealized Model Used for ETABS Analyses

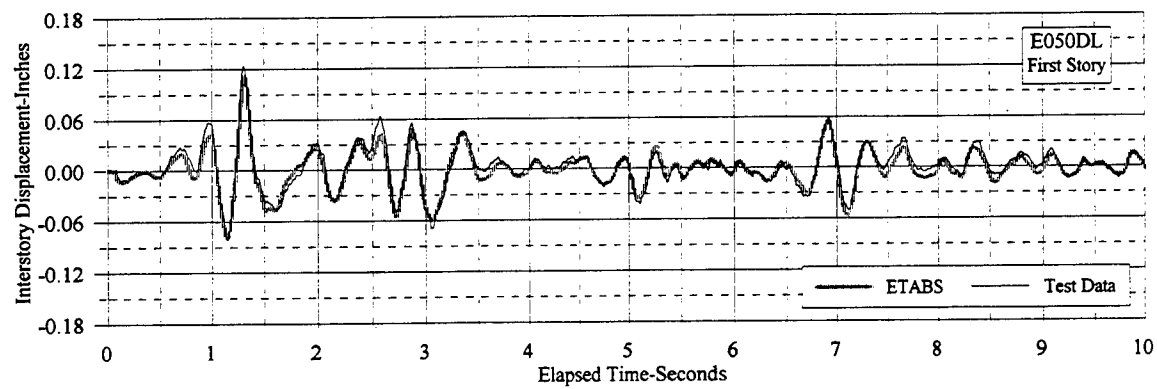
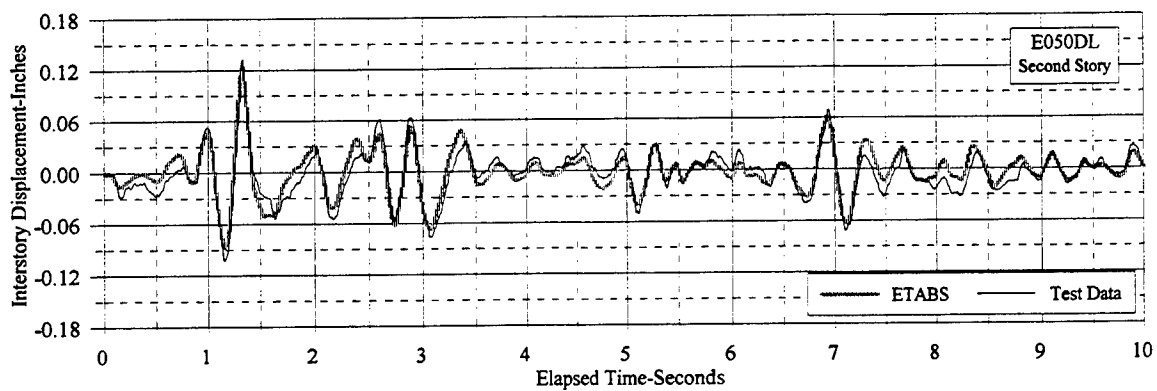
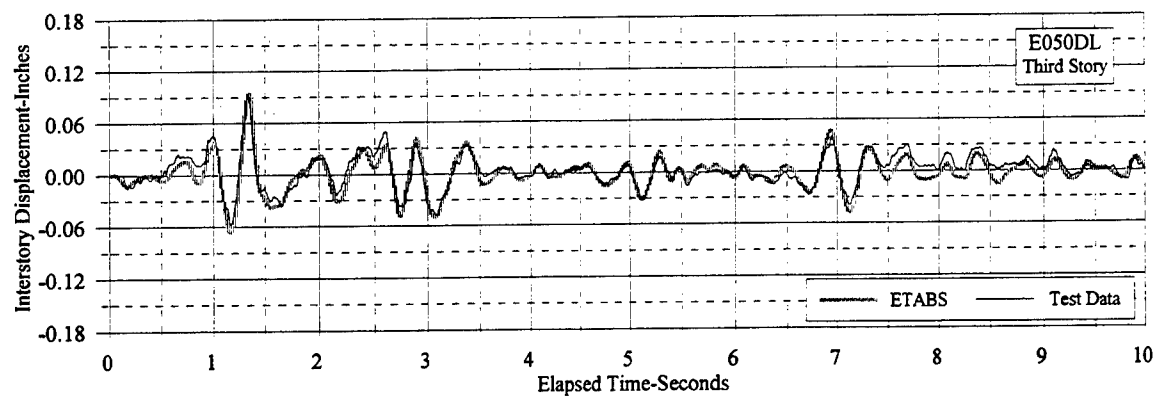


Figure 6.9 ETABS Nonlinear Simulation of E050DL: Interstory Displacements

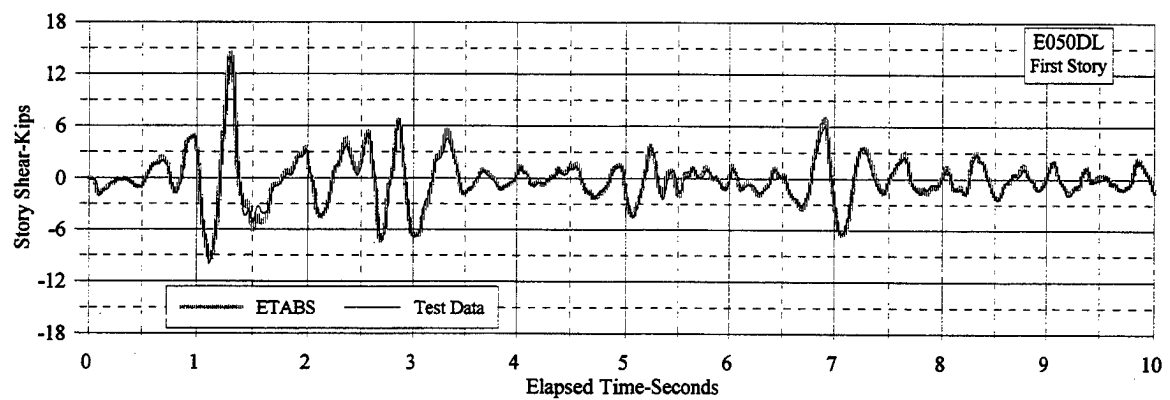
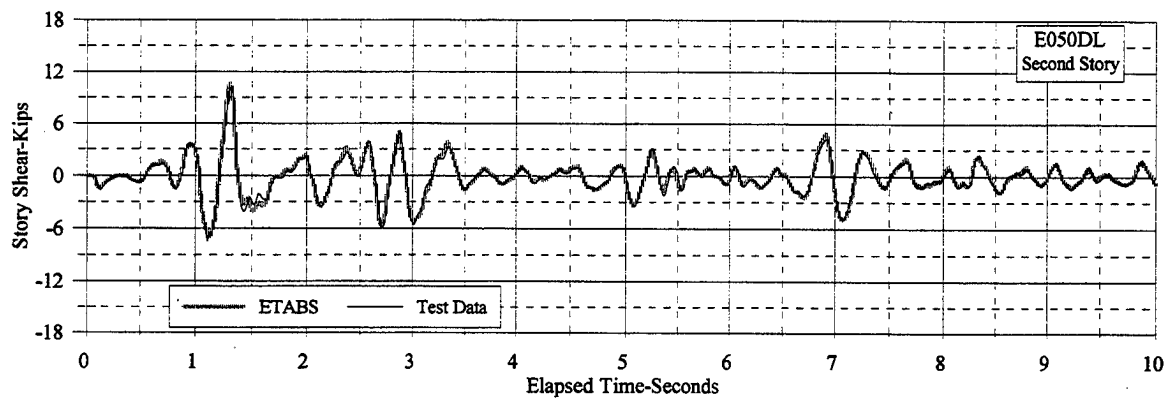
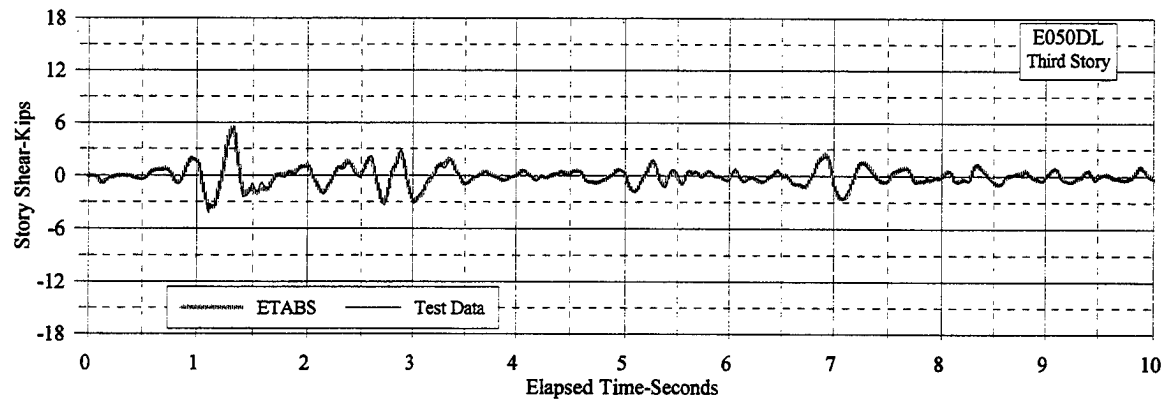


Figure 6.10 ETABS Nonlinear Simulation of E050DL: Story Shear

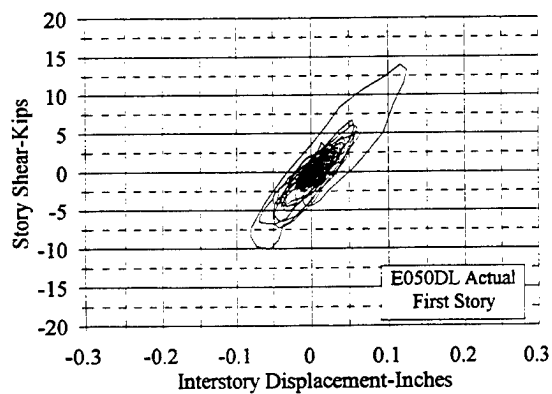
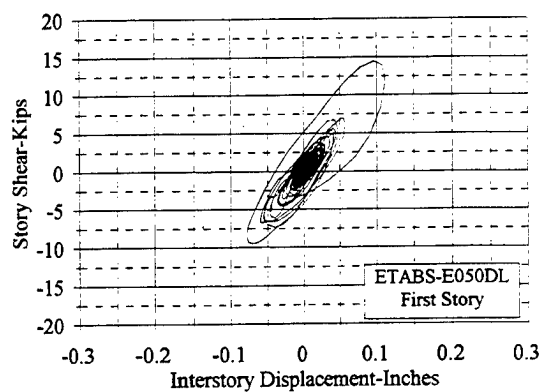
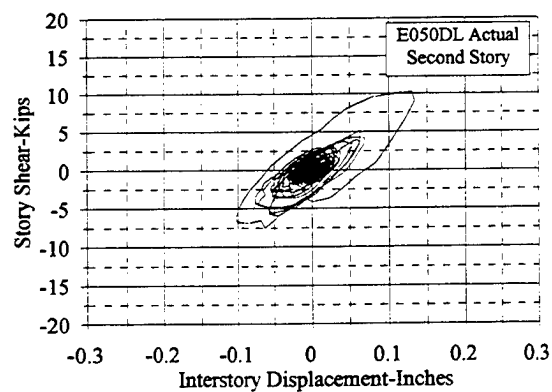
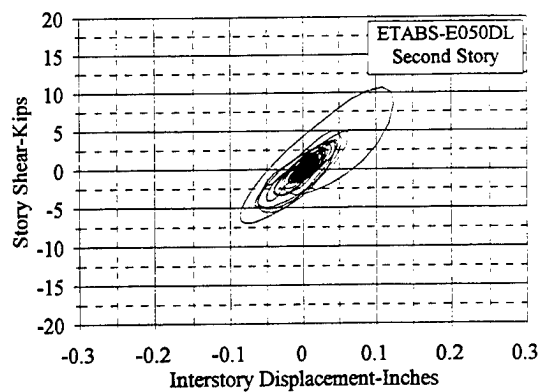
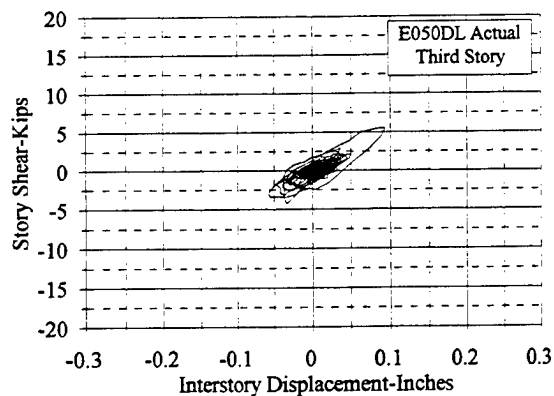
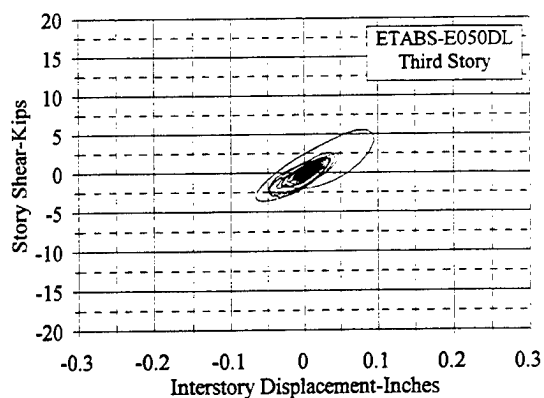


Figure 6.11 ETABS Nonlinear Simulation of E050DL: Story Shear Vs. Interstory Displacement

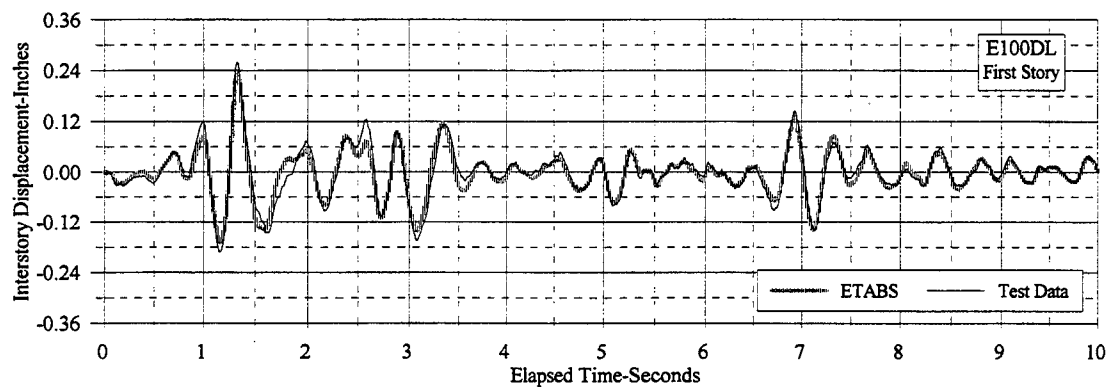
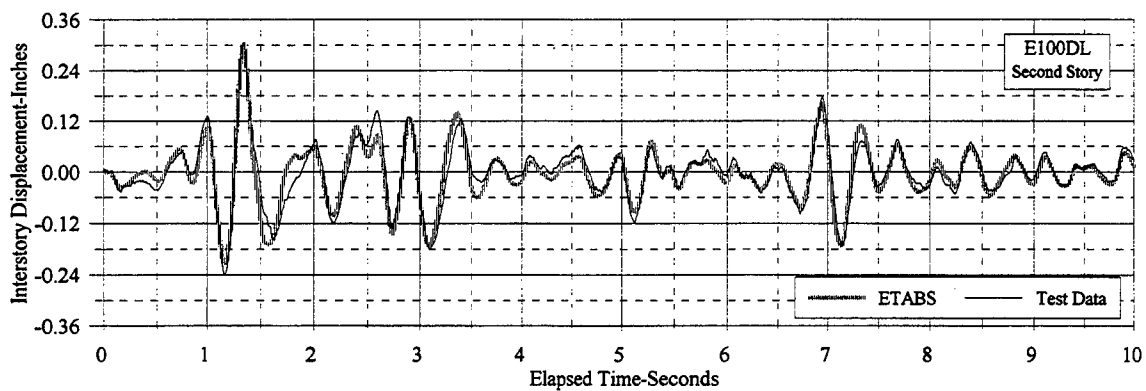
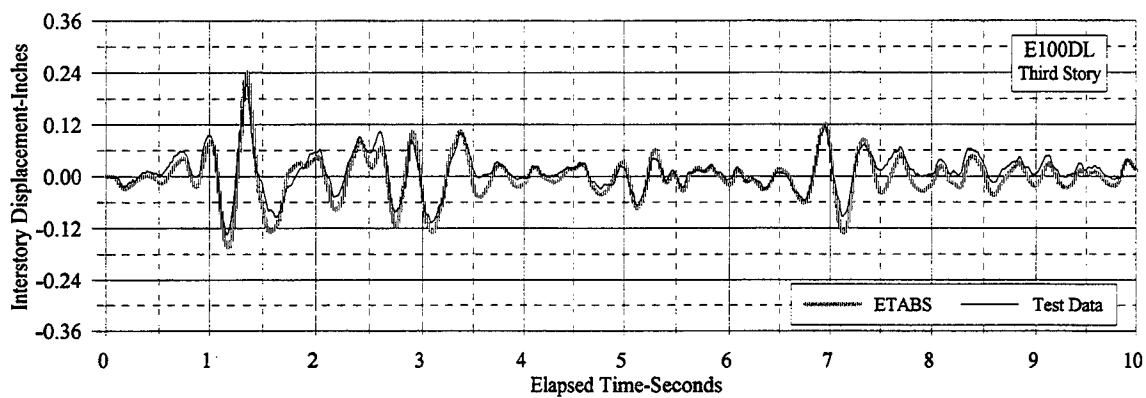


Figure 6.12 ETABS Nonlinear Simulation of E100DL: Interstory Displacements

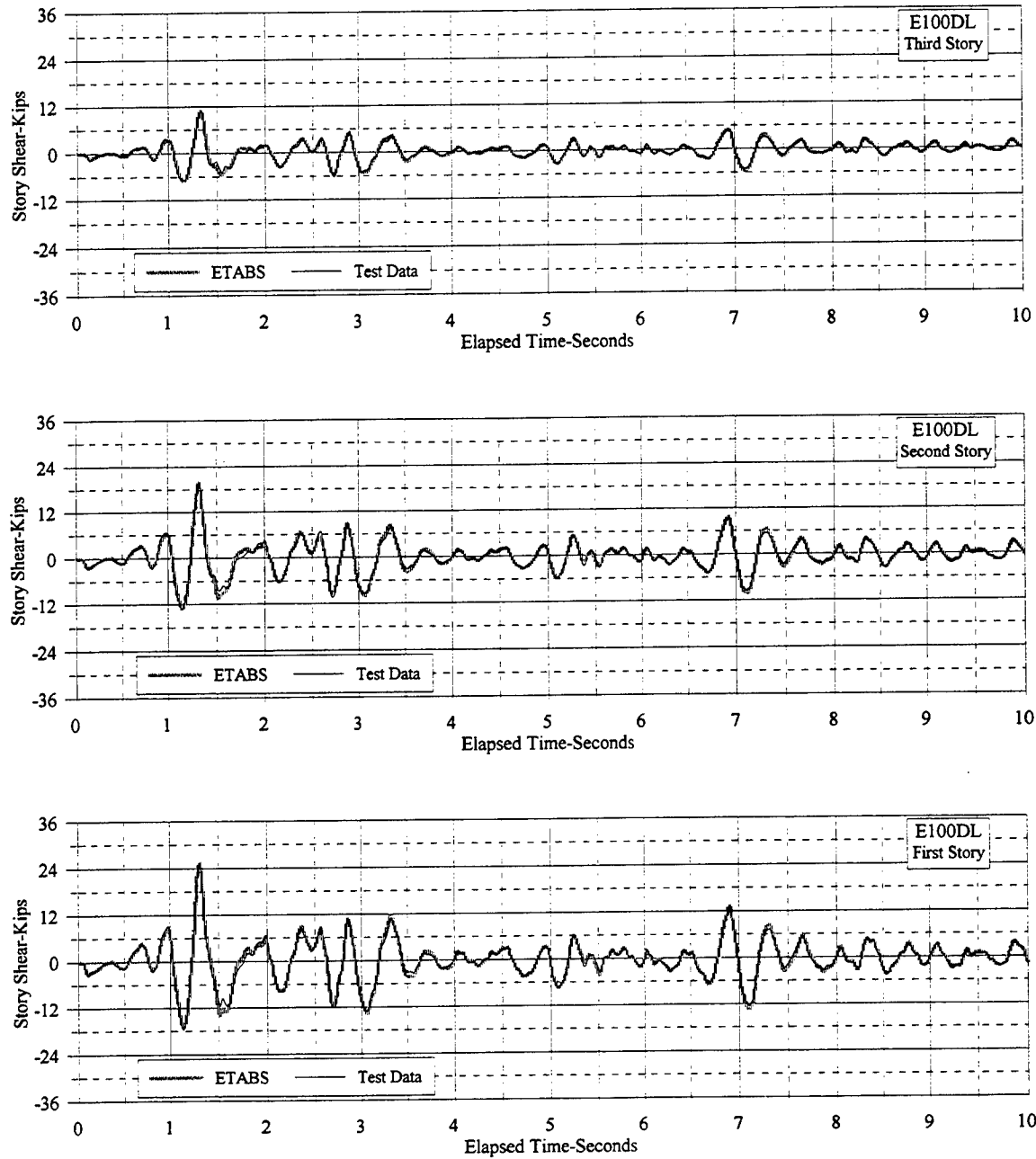


Figure 6.13 ETABS Nonlinear Simulation of E100DL: Story Shear

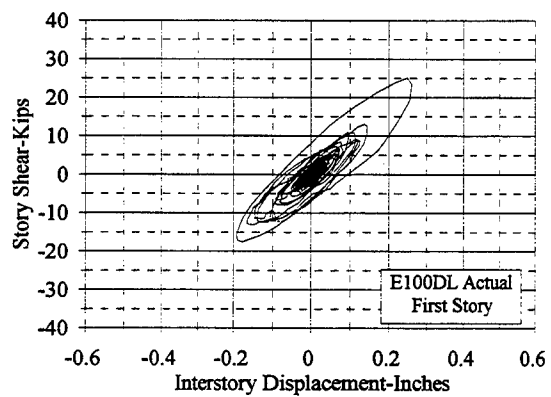
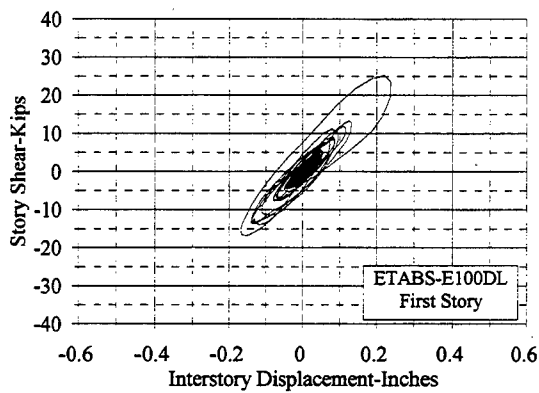
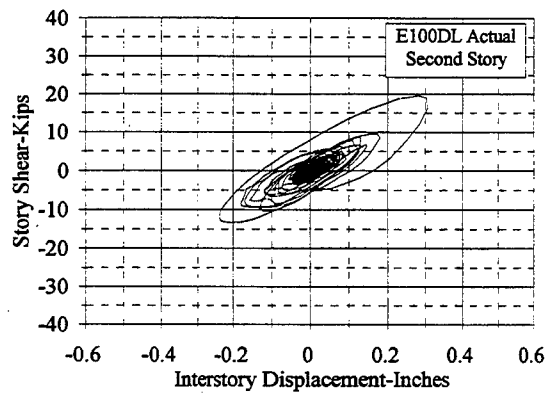
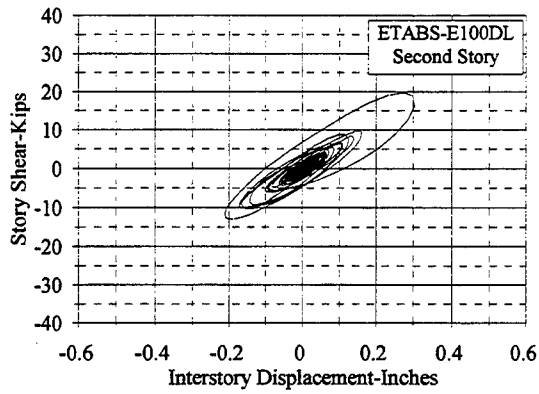
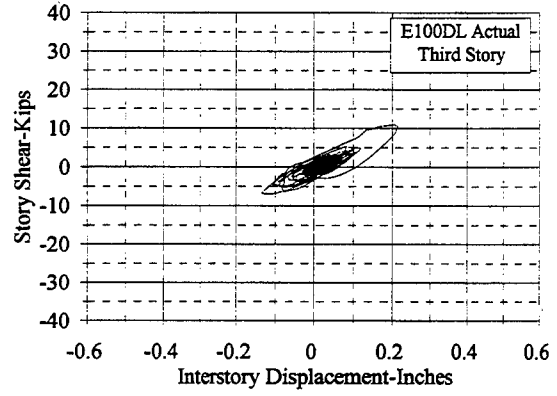
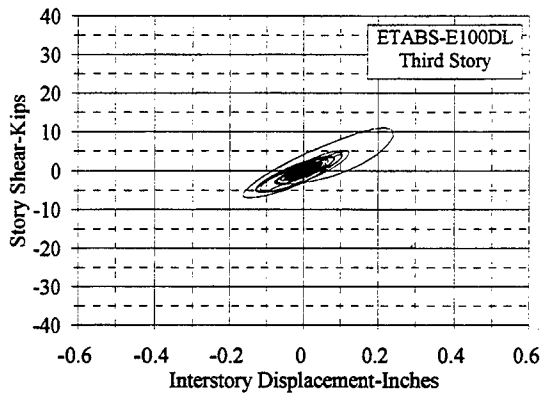


Figure 6.14 ETABS Nonlinear Simulation of E100DL: Story Shear Vs. Interstory Displacement

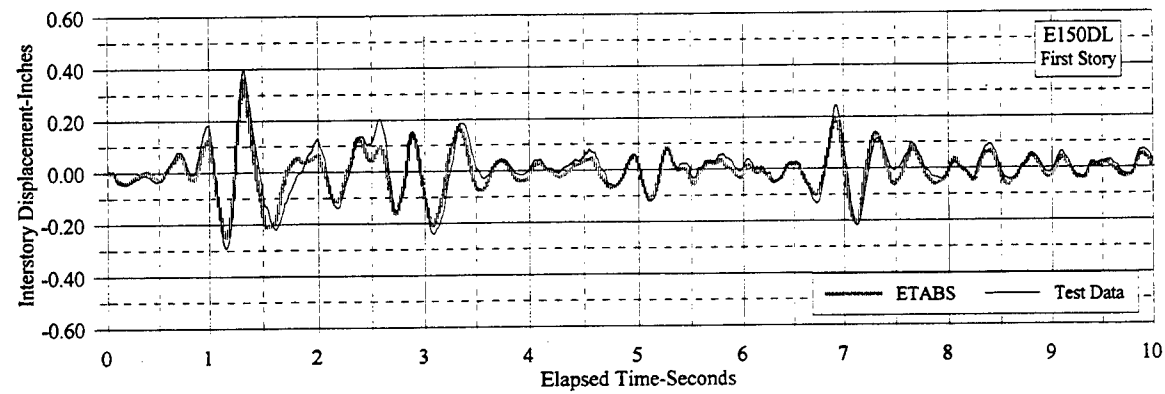
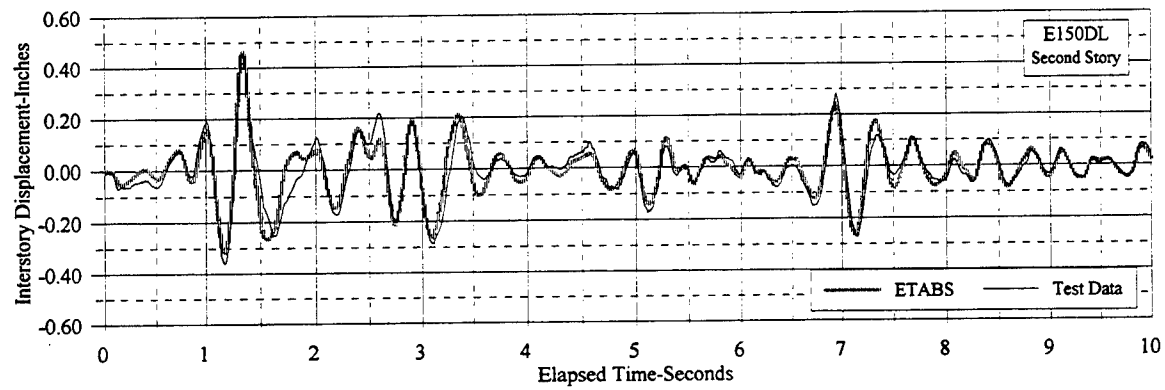
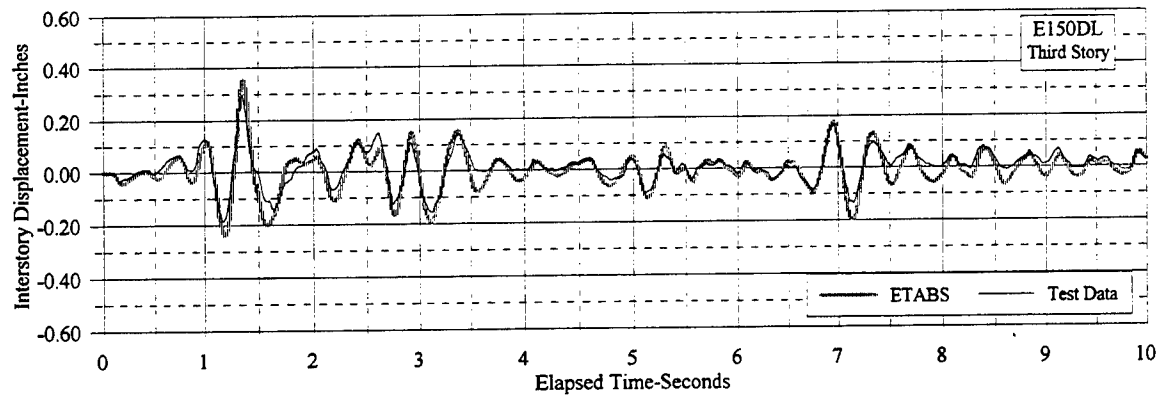


Figure 6.15 ETABS Nonlinear Simulation of E150DL: Interstory Displacements

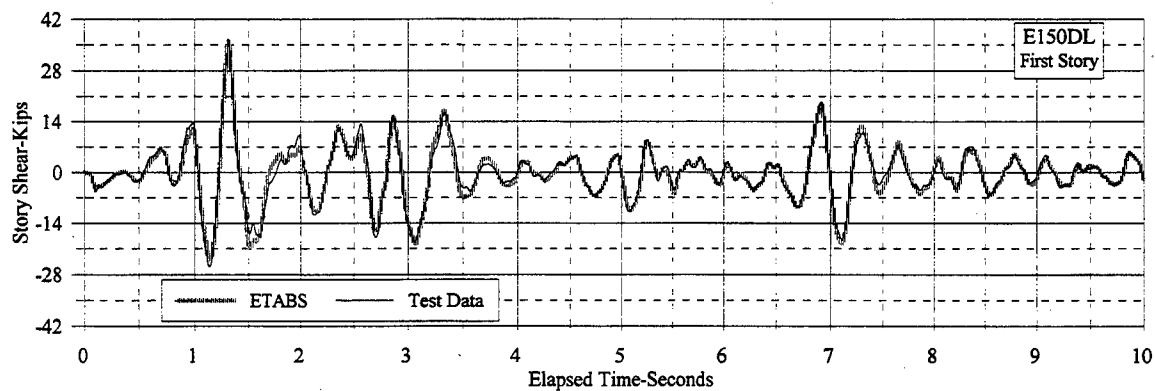
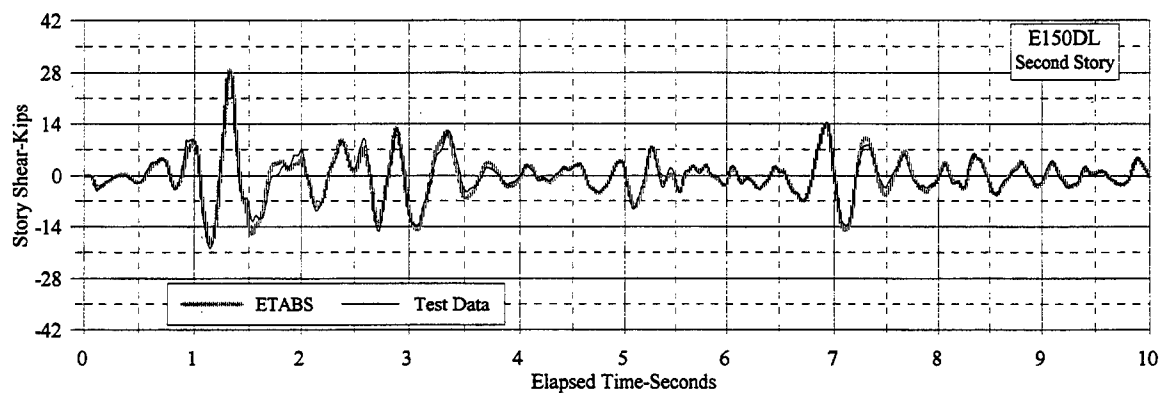
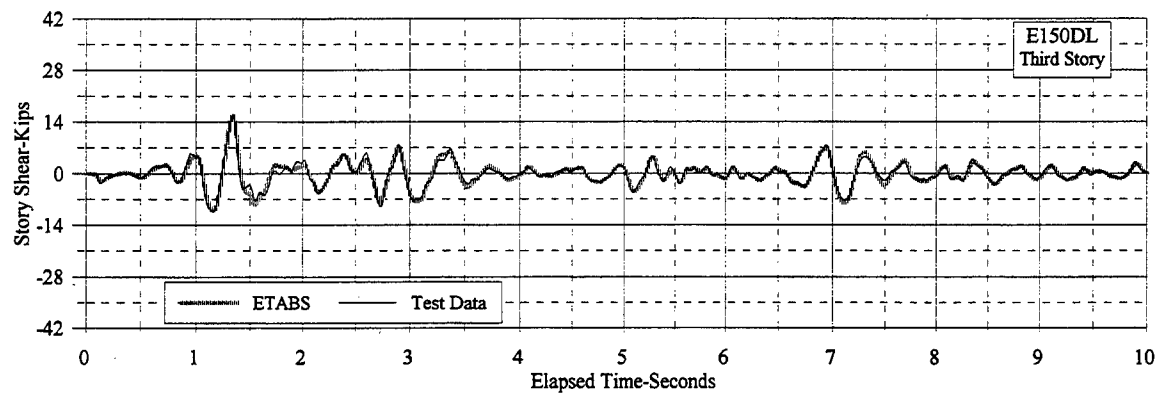


Figure 6.16 ETABS Nonlinear Simulation of E150DL: Story Shear

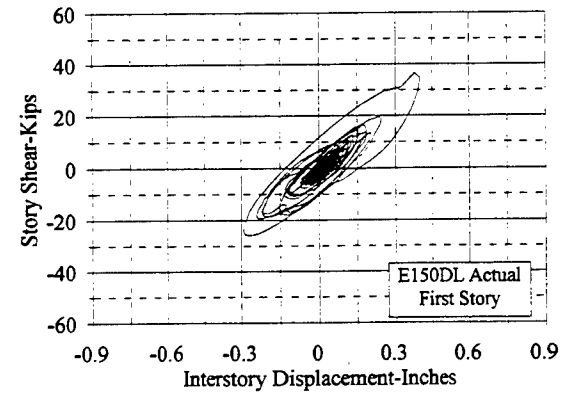
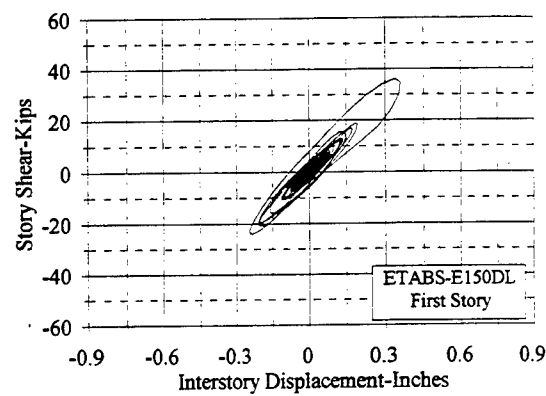
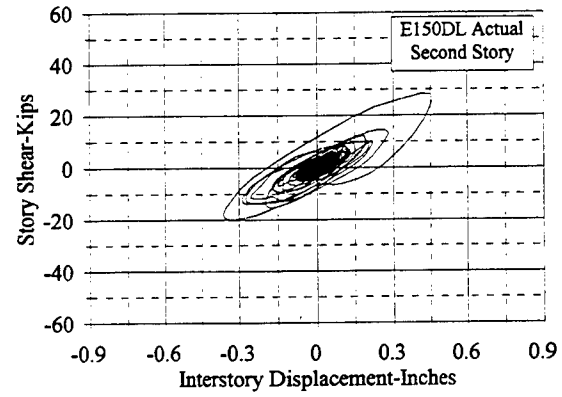
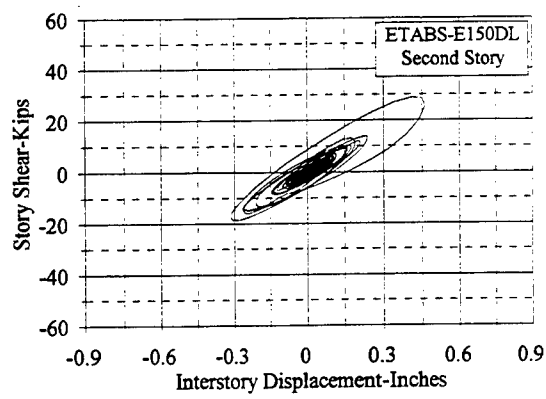
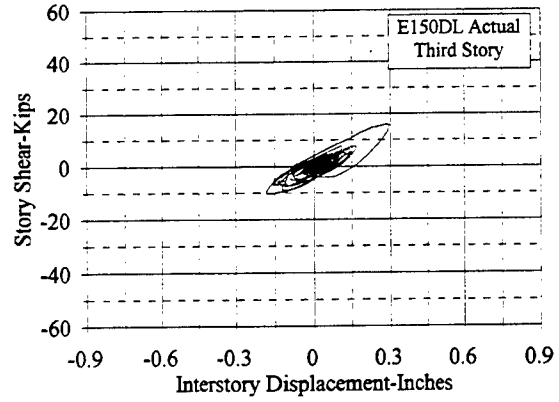
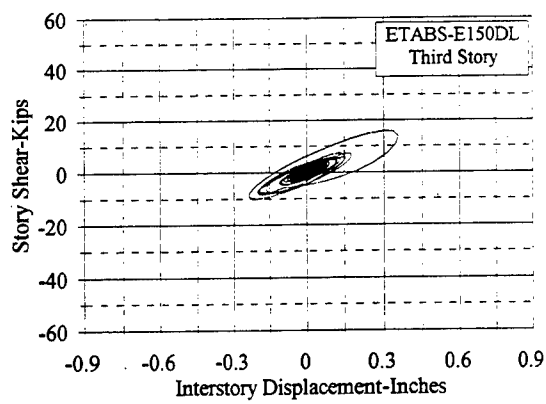


Figure 6.17 ETABS Nonlinear Simulation of E150DL: Story Shear Vs. Interstory Displacement

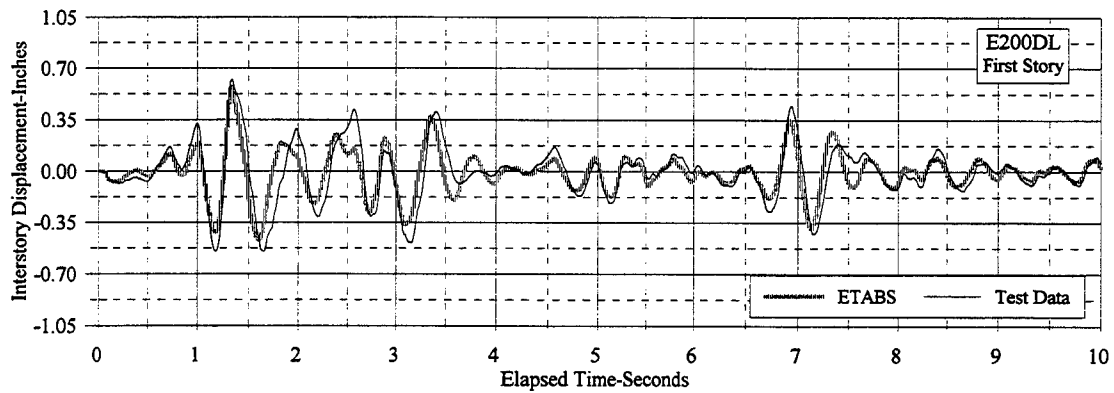
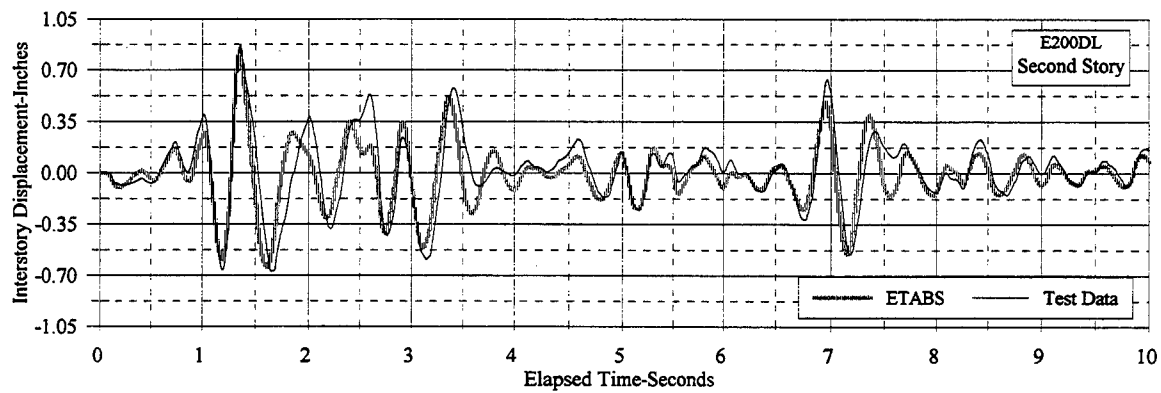
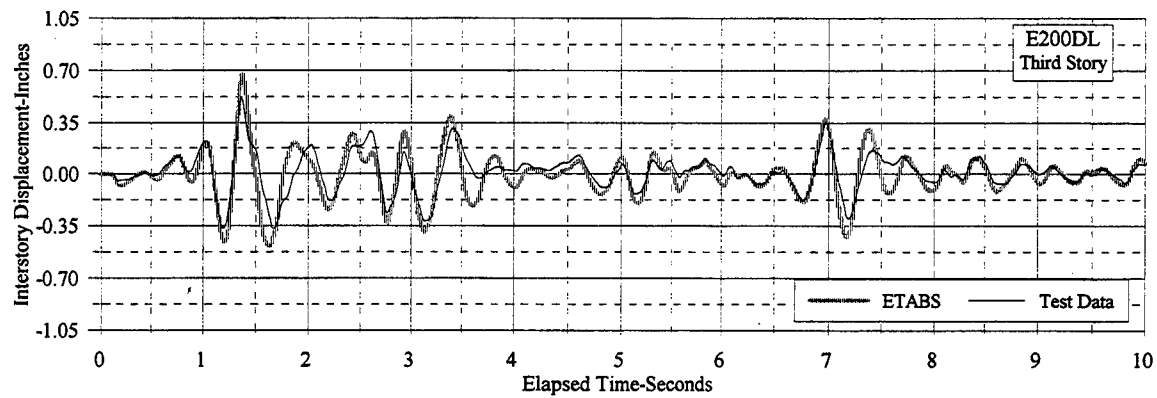


Figure 6.18 ETABS Nonlinear Simulation of E200DL: Interstory Displacements

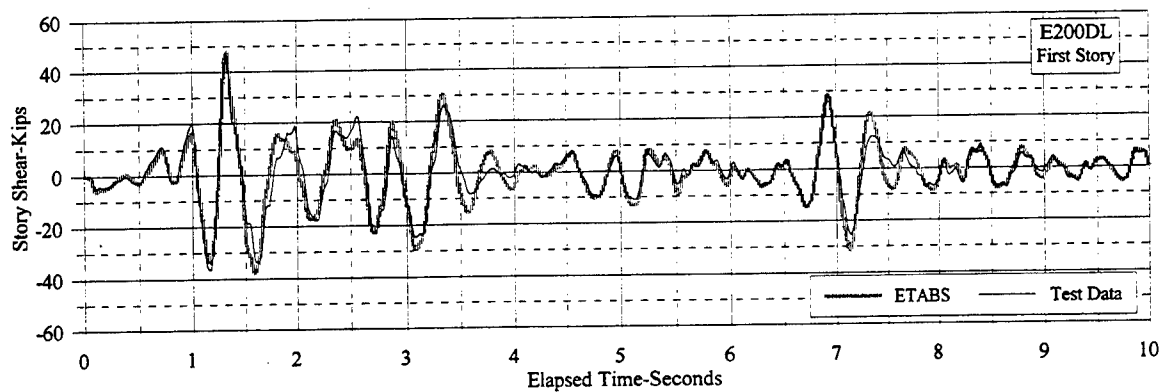
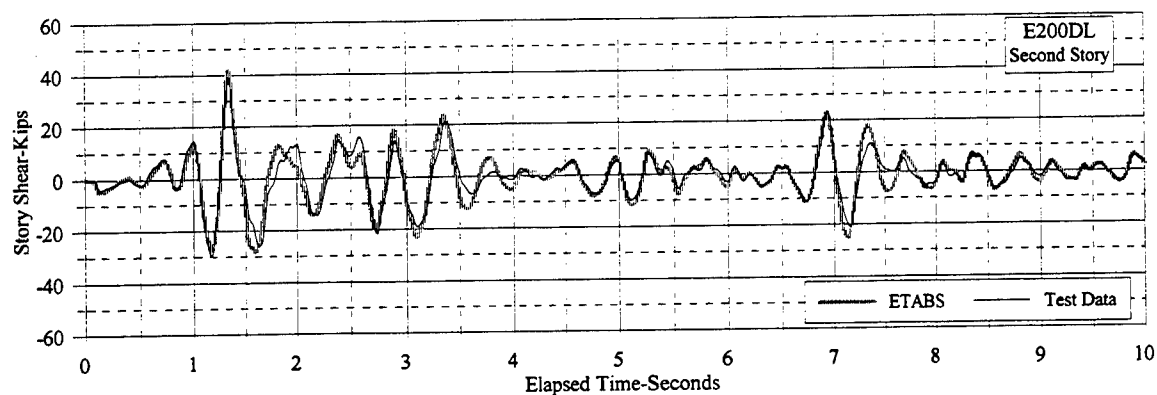
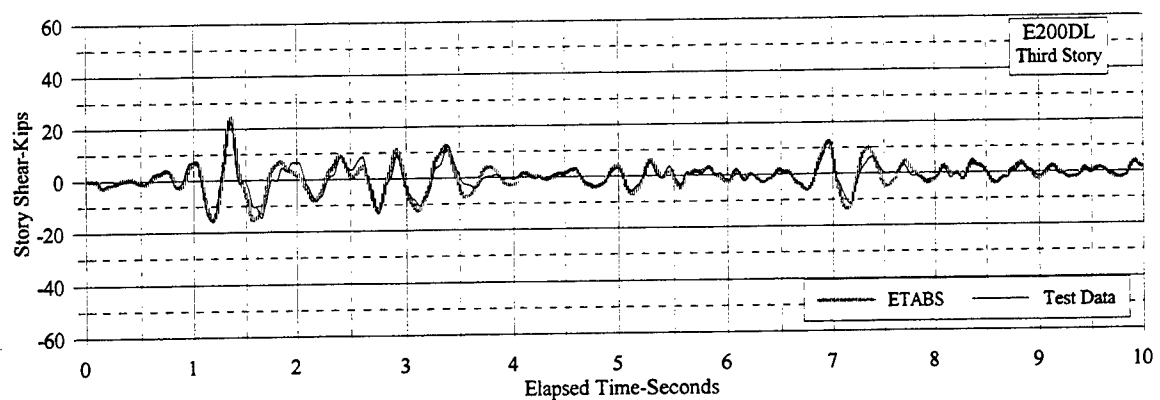


Figure 6.19 ETABS Nonlinear Simulation of E200DL: Story Shear

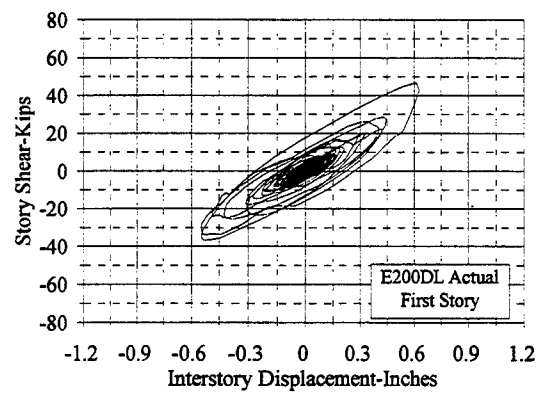
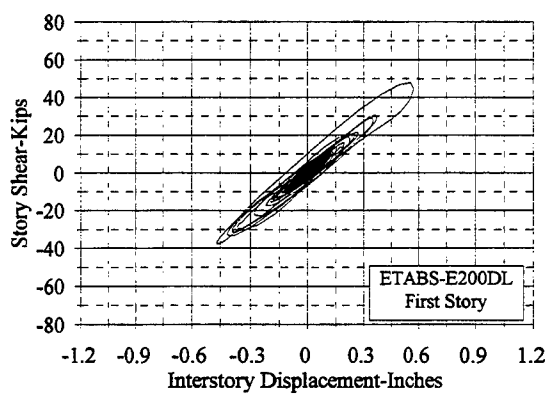
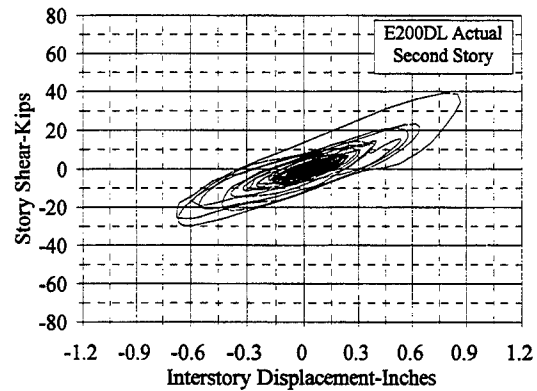
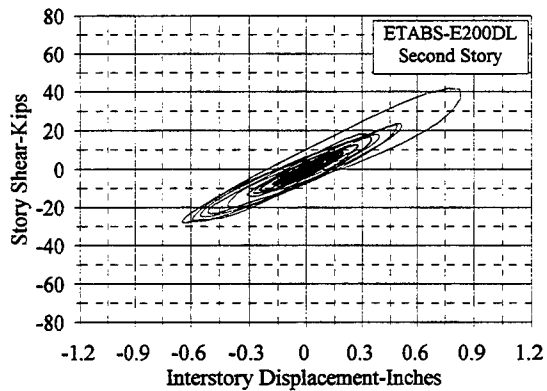
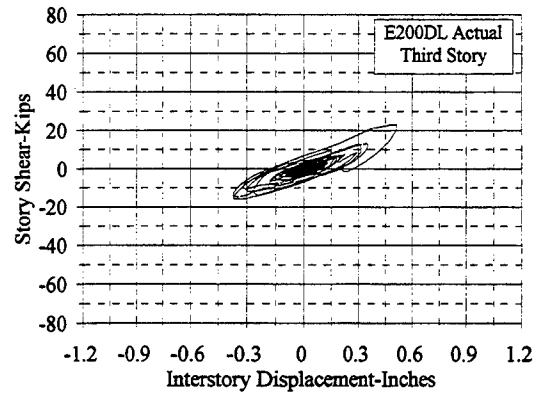
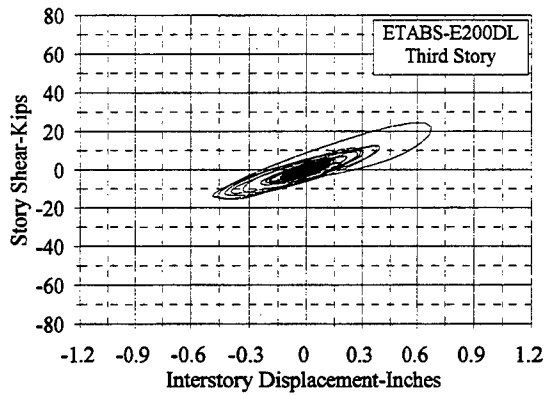


Figure 6.20 ETABS Nonlinear Simulation of E200DL: Story Shear Vs. Interstory Displacement

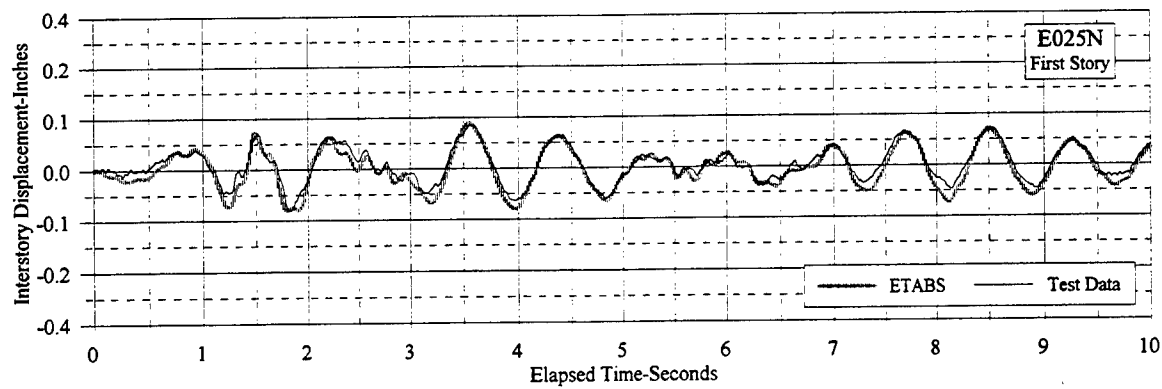
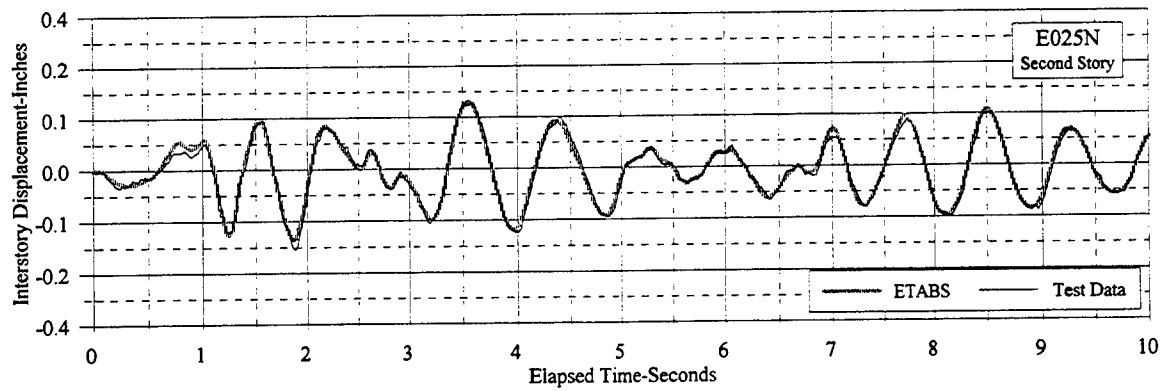
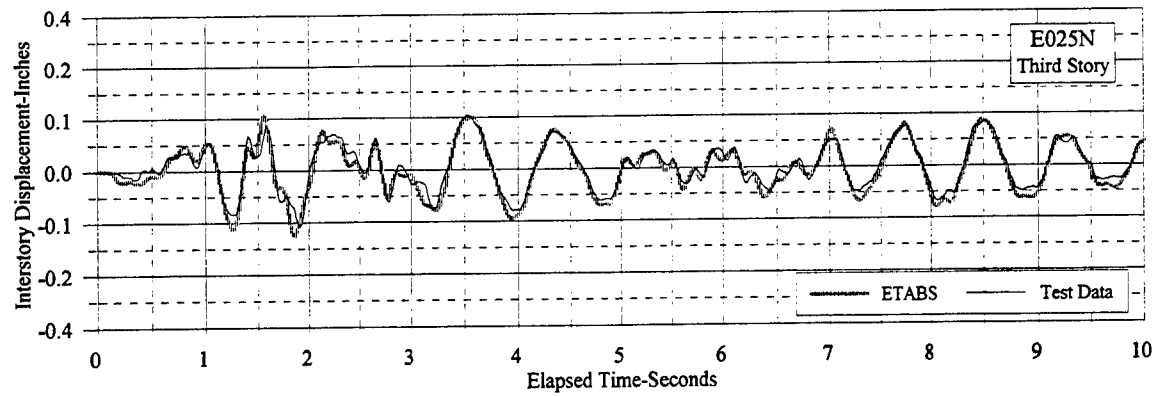


Figure 6.21 ETABS Simulation of E025N: Interstory Displacements

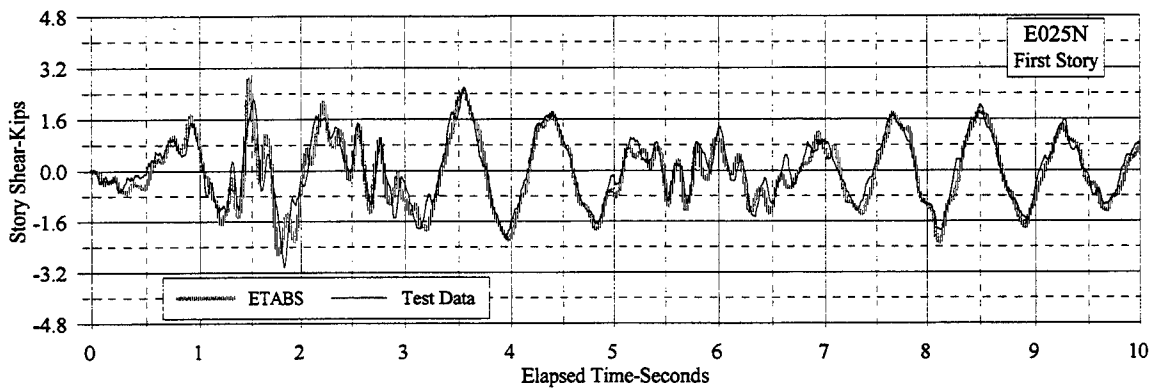
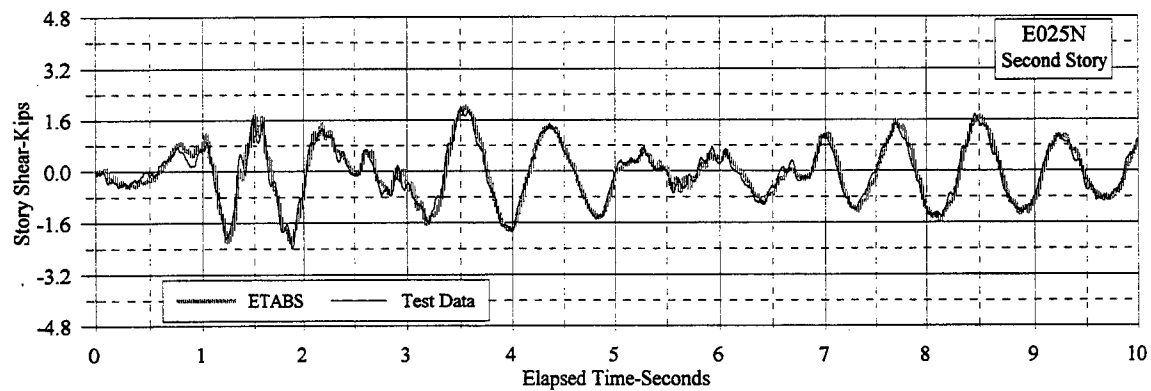
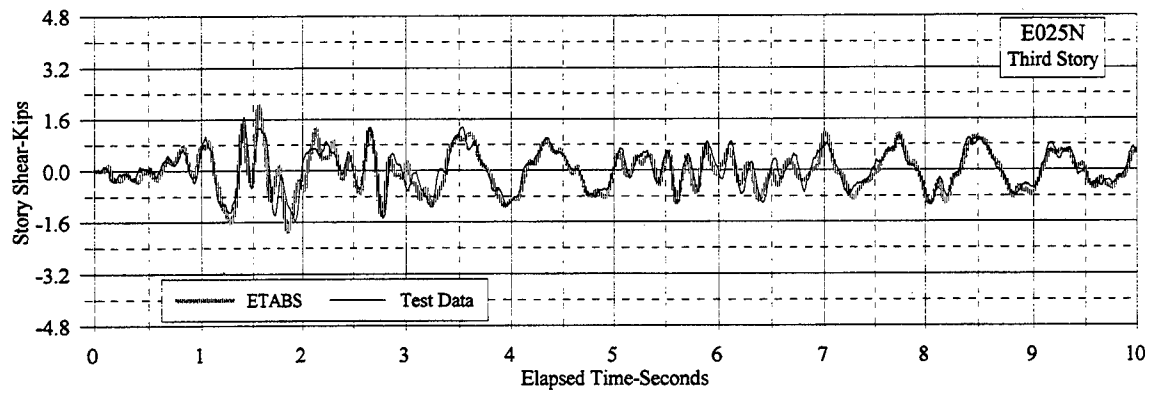


Figure 6.22 ETABS Simulation of E025N: Story Shear

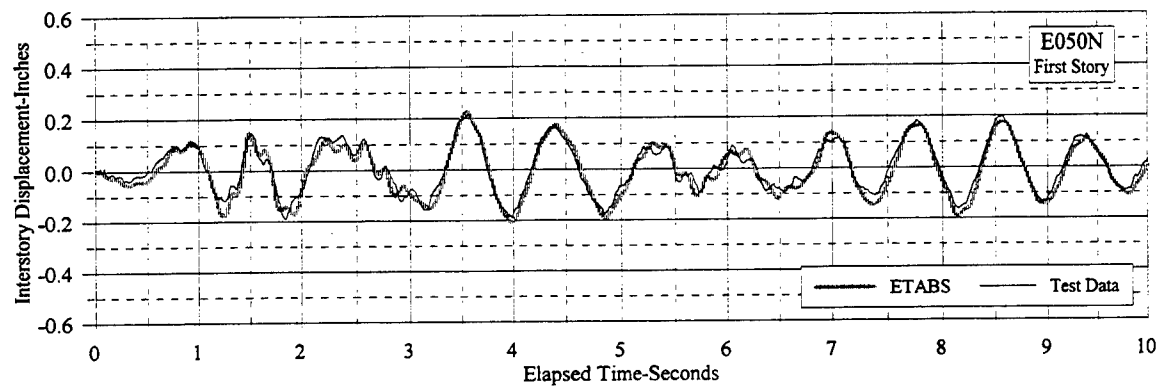
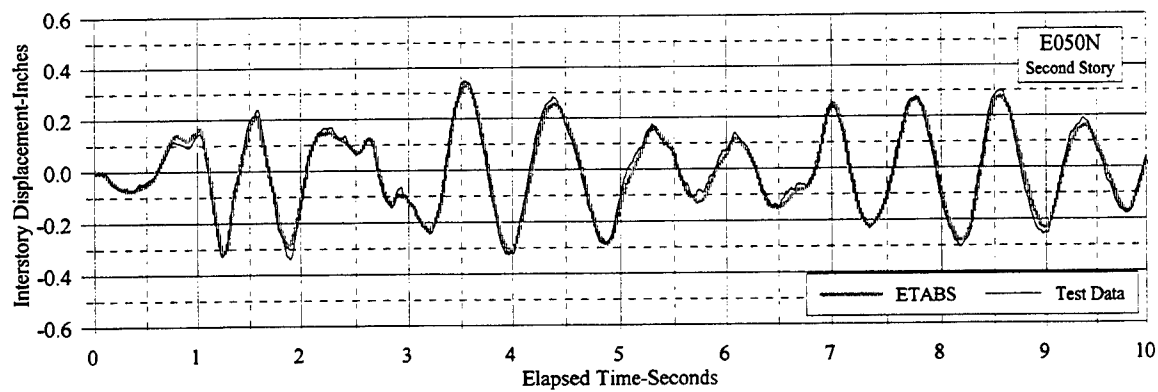
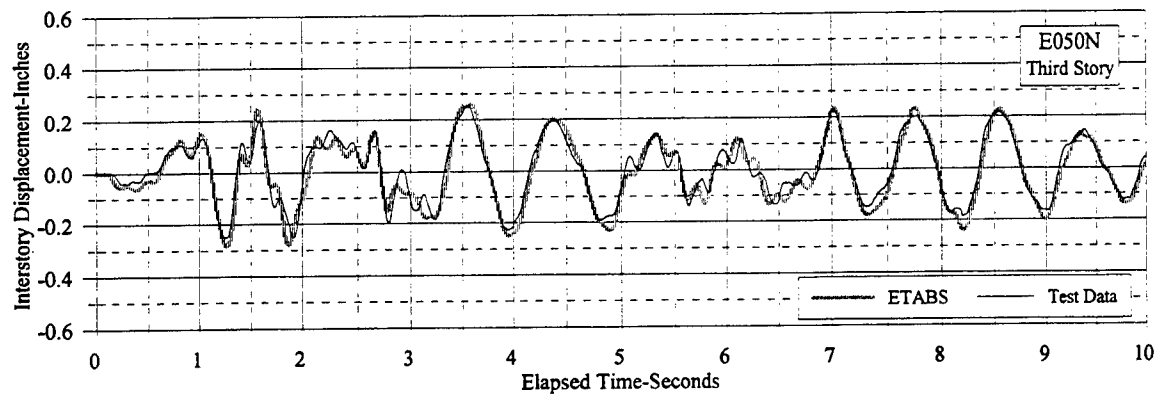


Figure 6.23 ETABS Simulation of E050N: Interstory Displacements

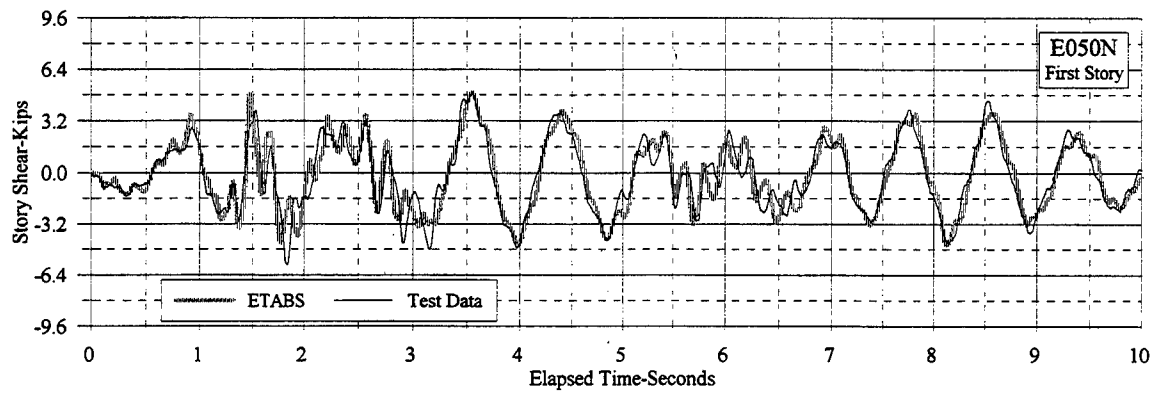
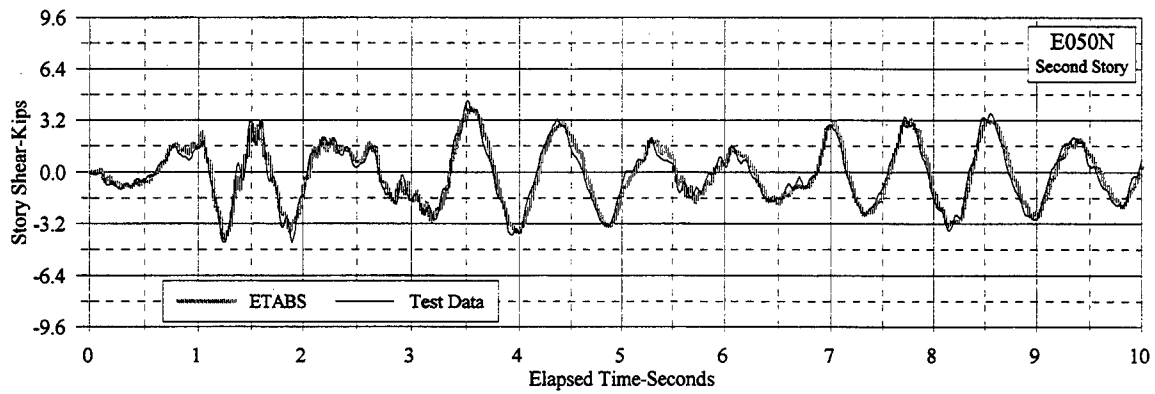
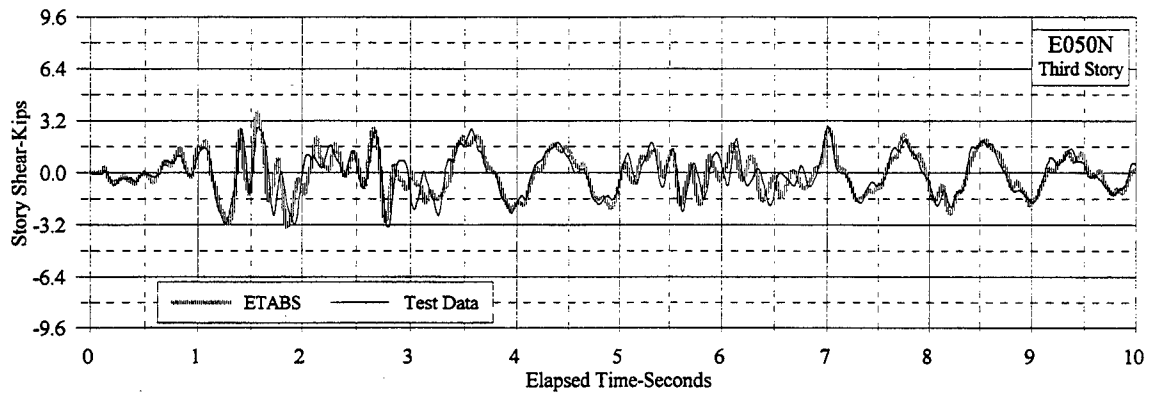


Figure 6.24 ETABS Simulation of E050N: Story Shear

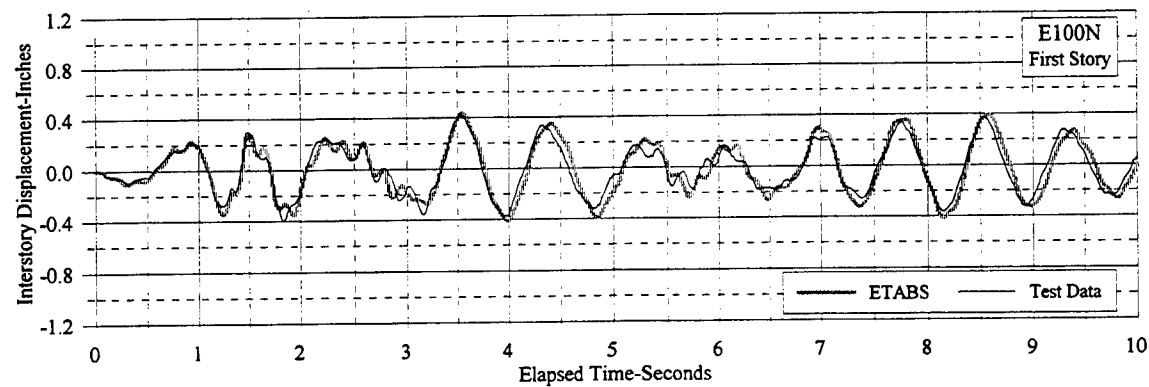
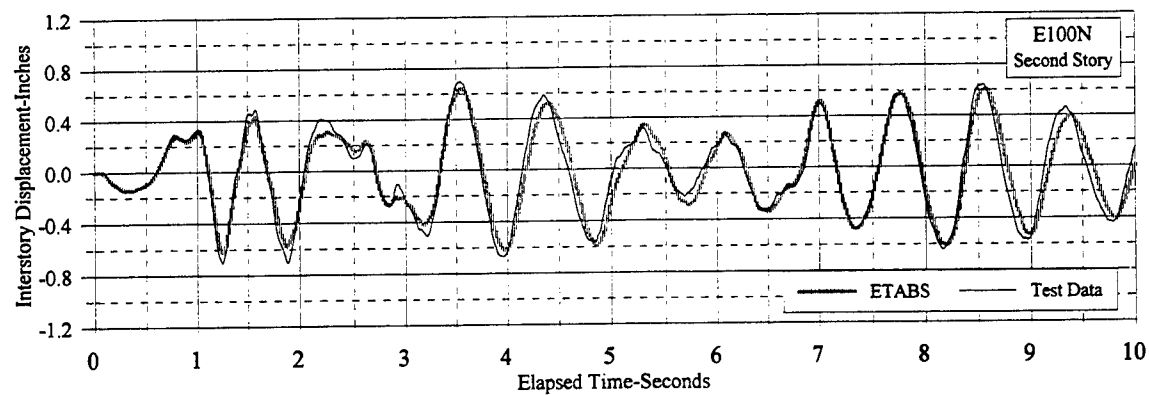
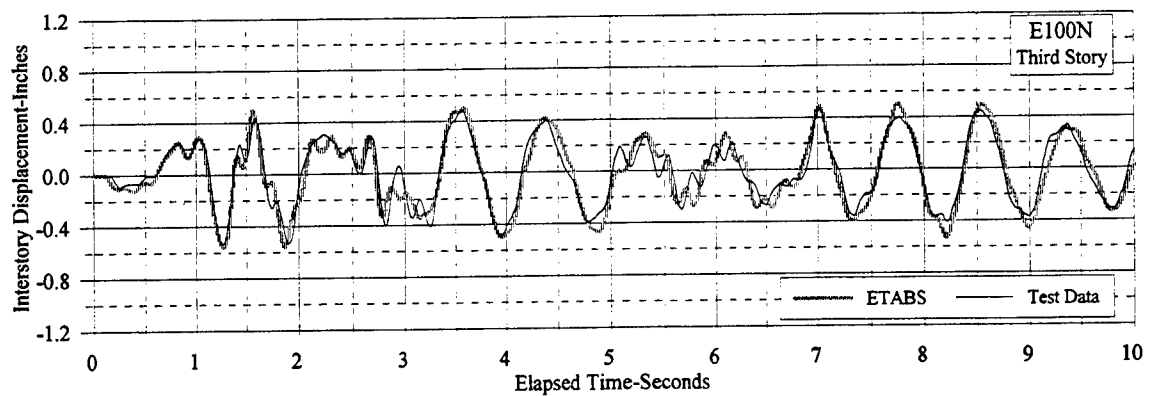


Figure 6.25 ETABS Simulation of E100N: Interstory Displacements

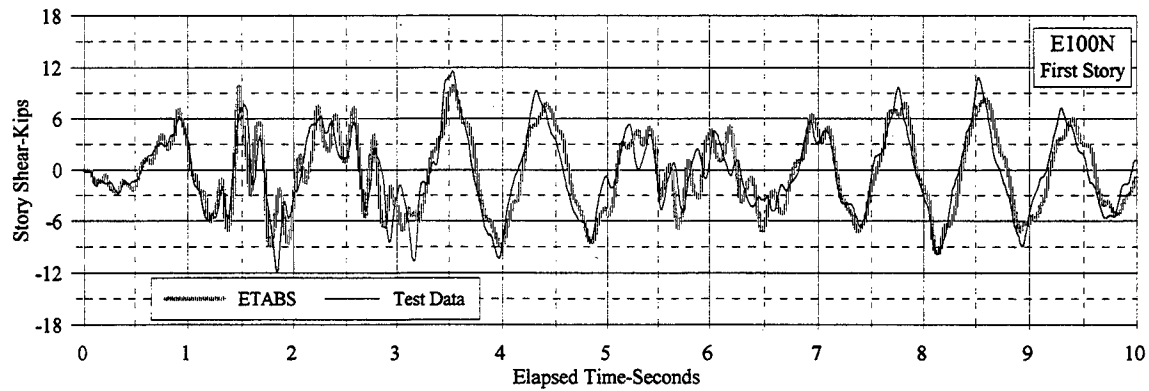
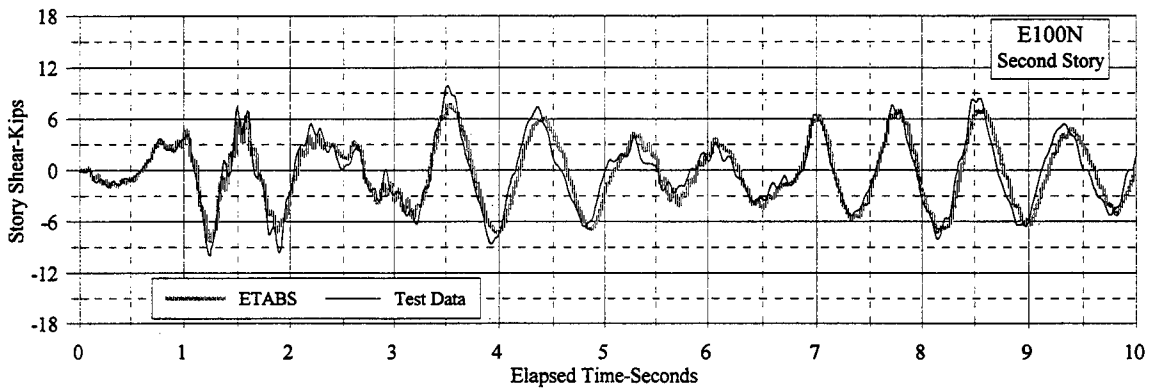
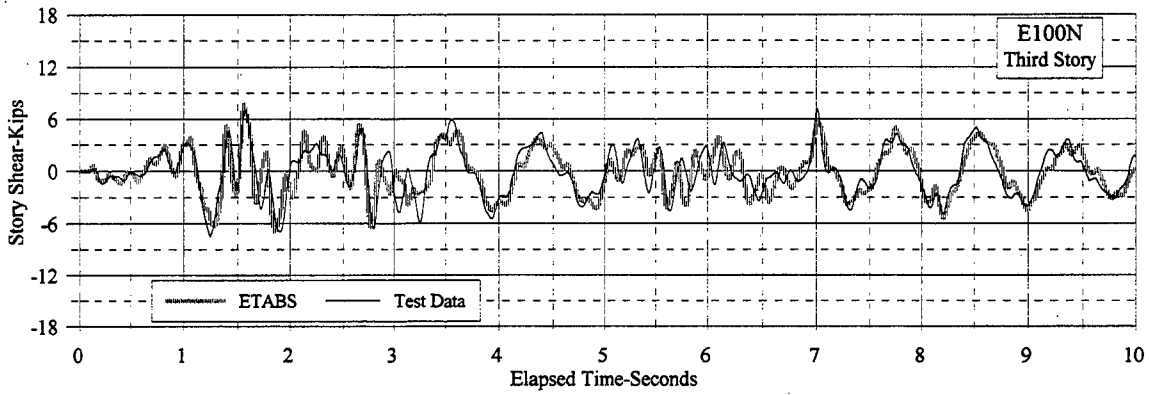


Figure 6.26 ETABS Simulation of E100N, Story Shear

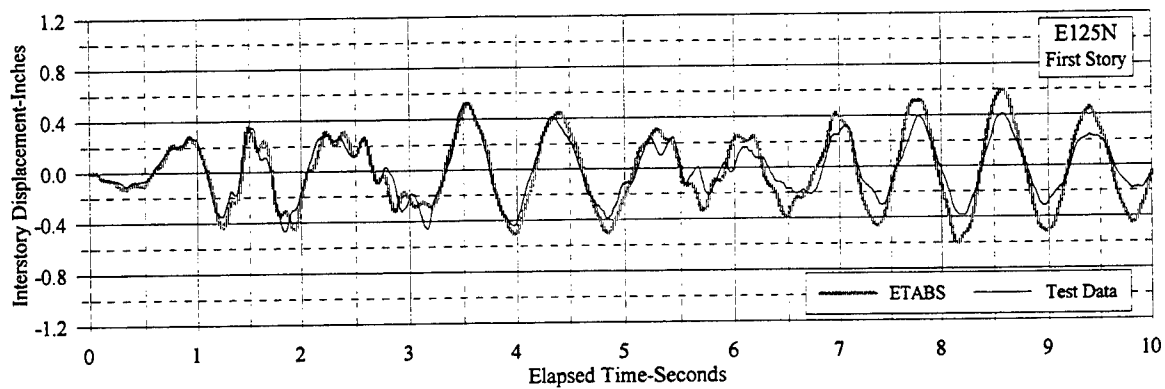
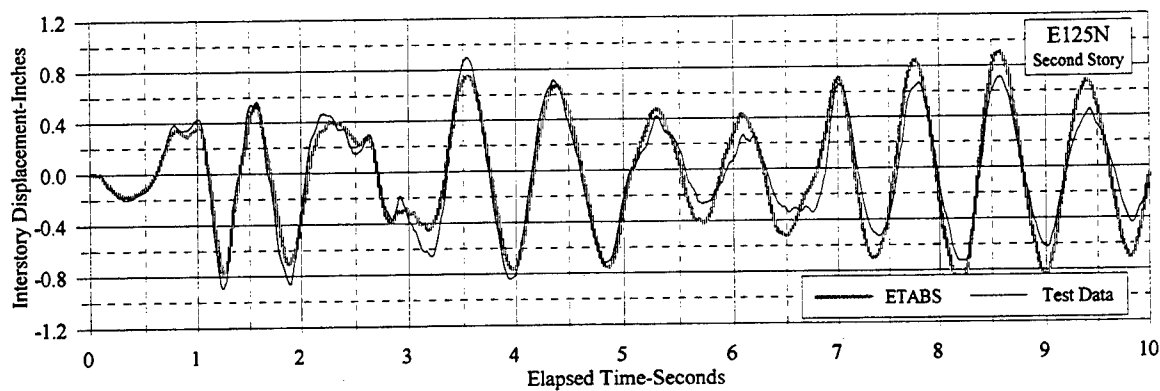
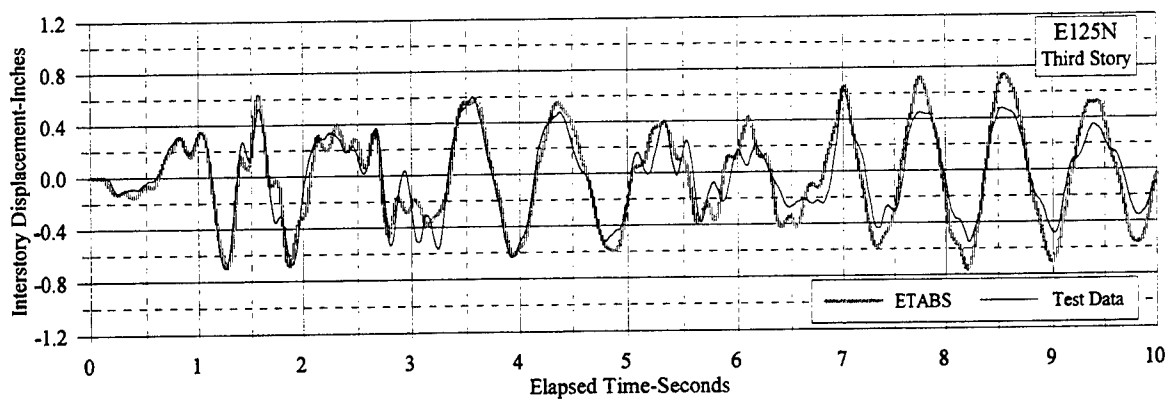


Figure 6.27 ETABS Simulation of E125N: Interstory Displacements

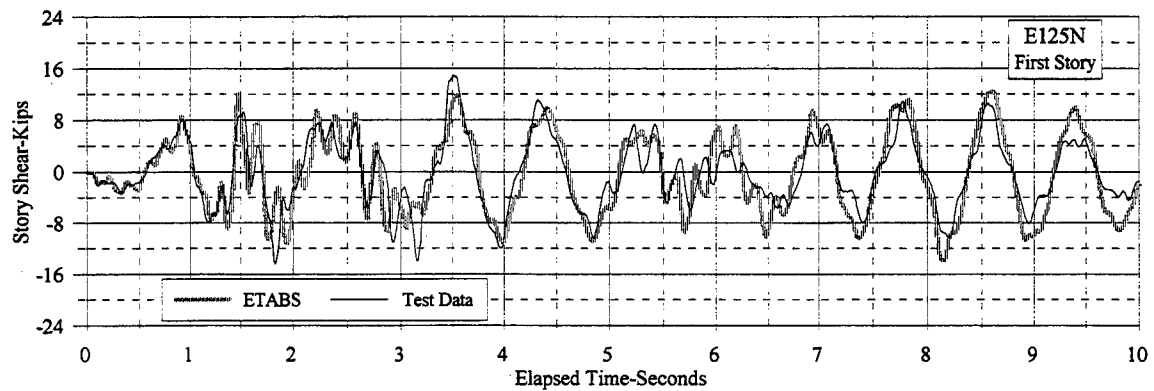
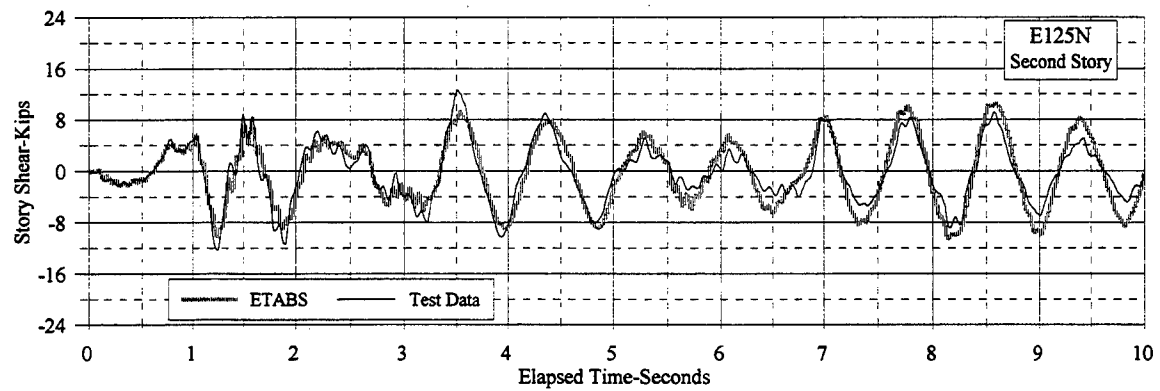
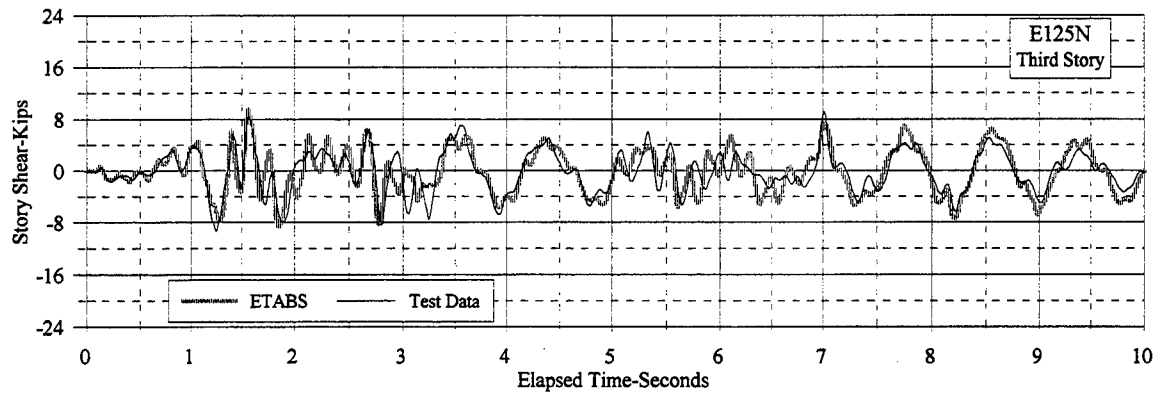


Figure 6.28 ETABS Simulation of E125N: Story Shear

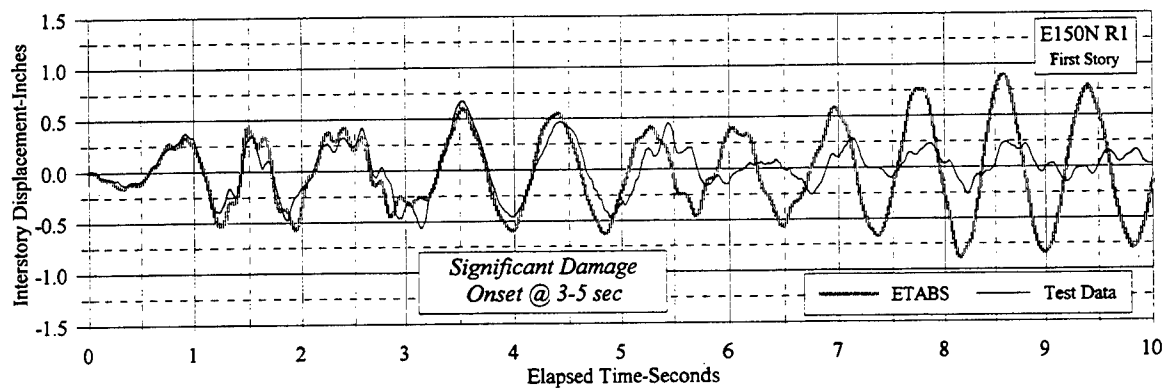
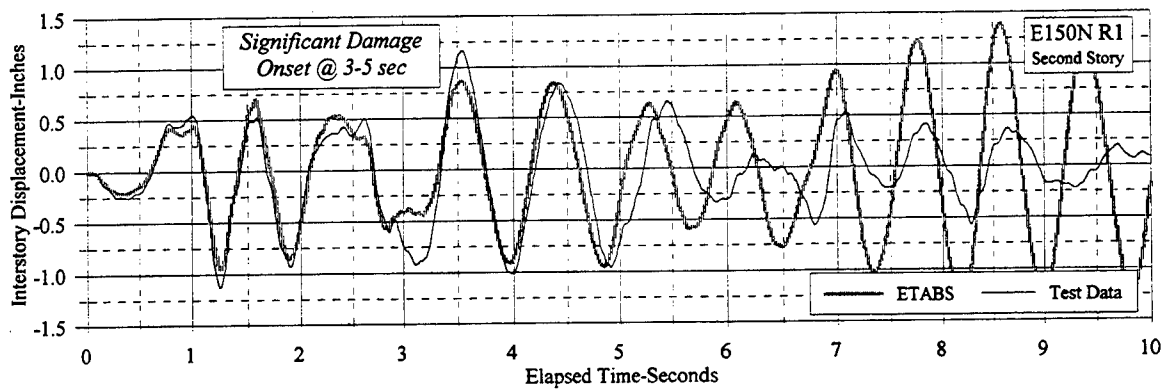
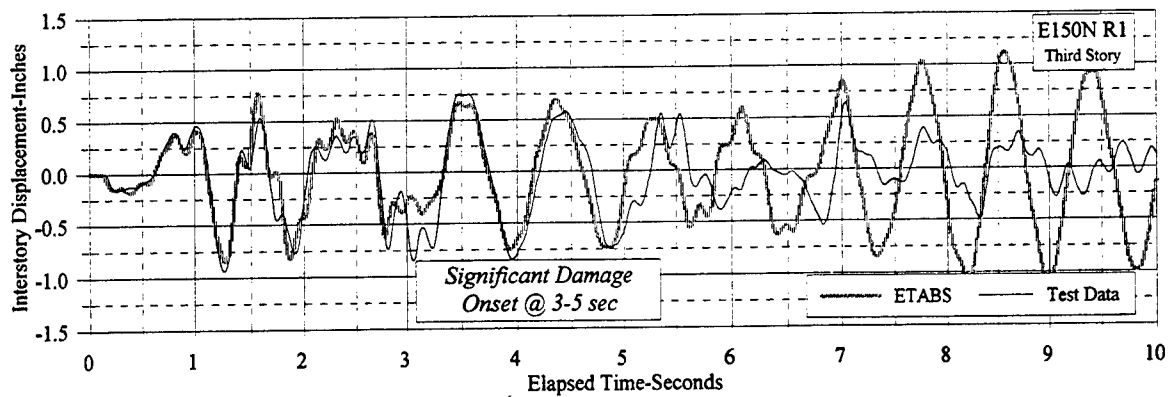


Figure 6.29 ETABS Simulation of E150N: Interstory Displacements, Run 1

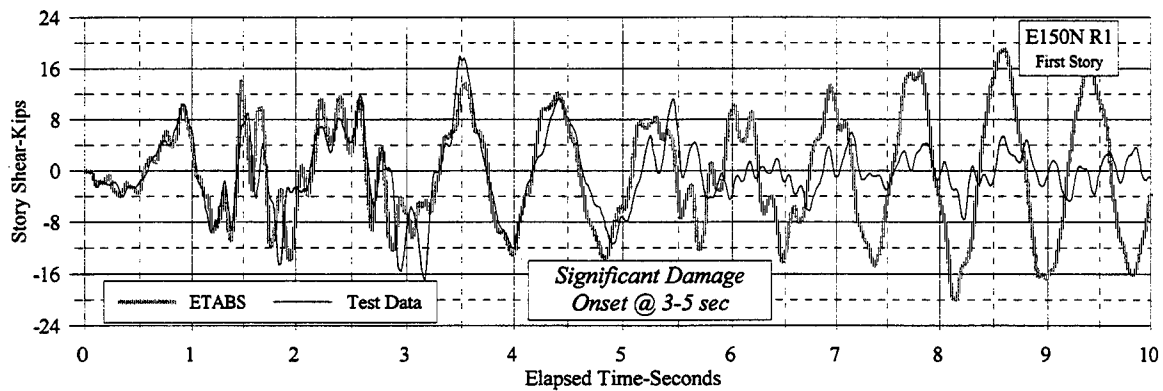
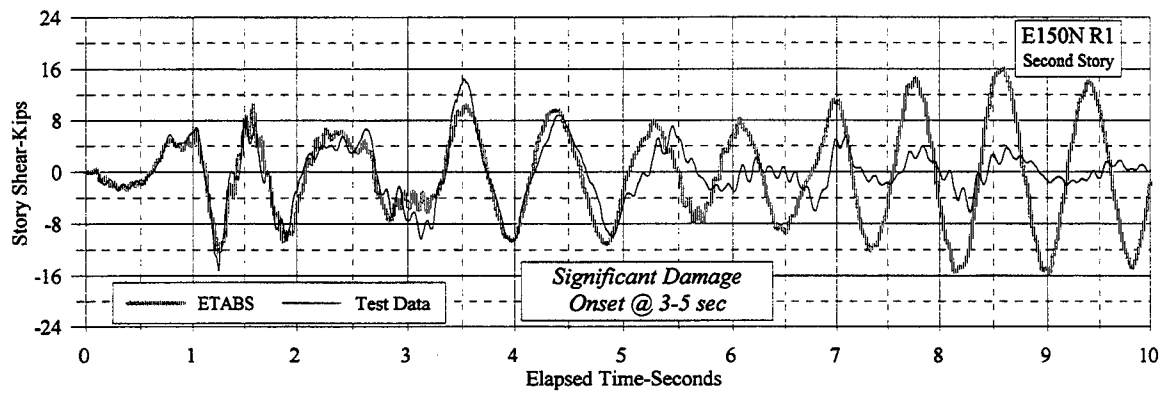
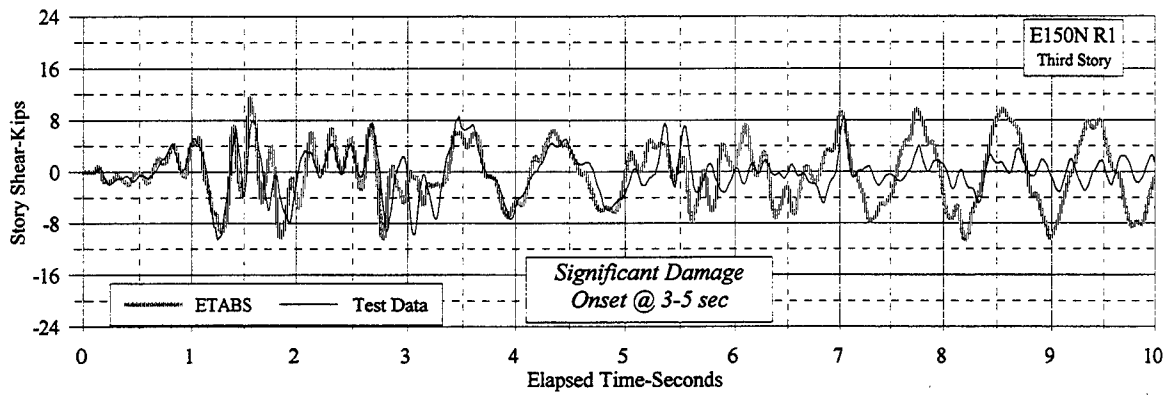


Figure 6.30 ETABS Simulation of E150N: Story Shear, Run 1

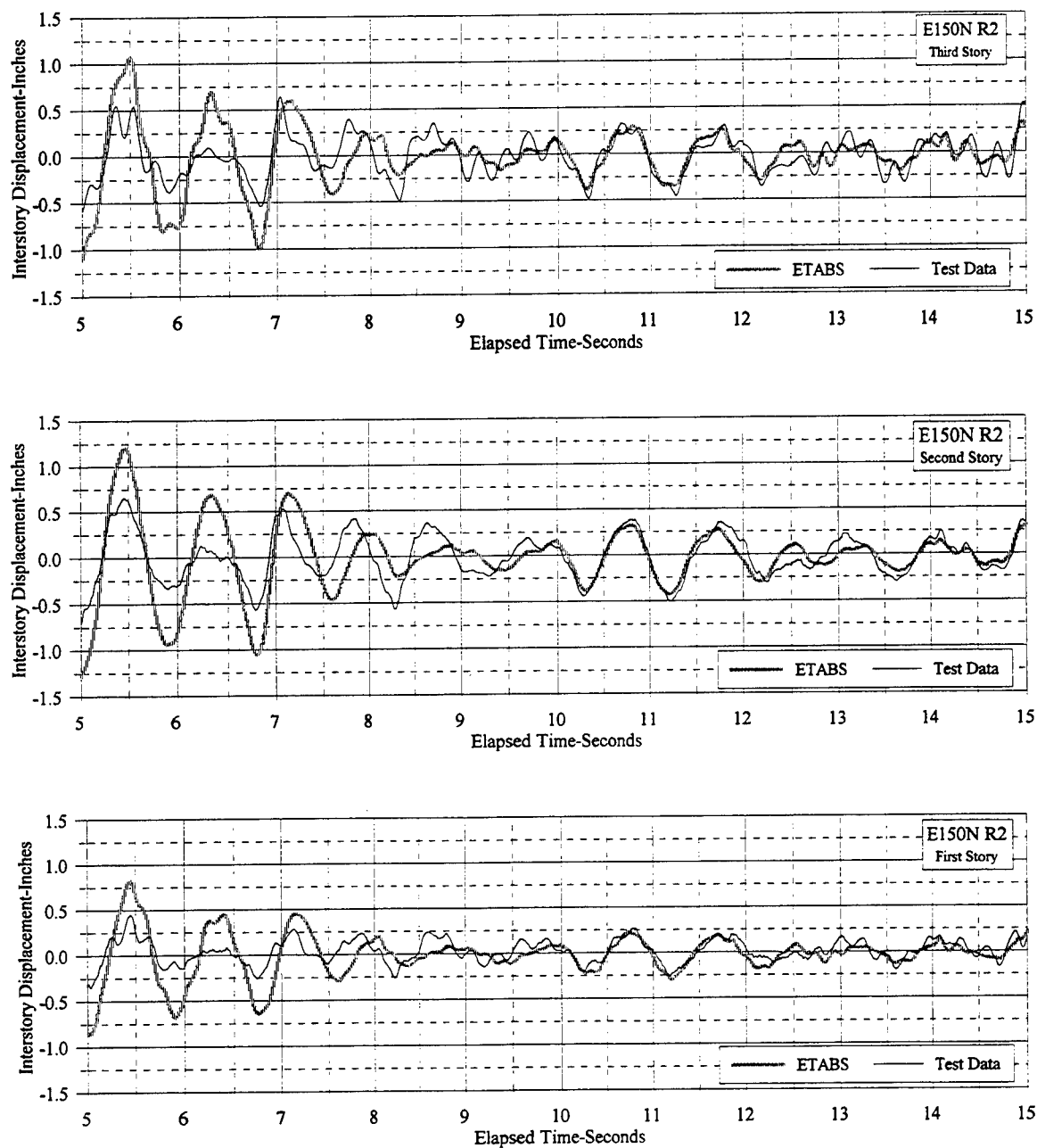


Figure 6.31 ETABS Simulation of E150N: Interstory Displacements, Run 2

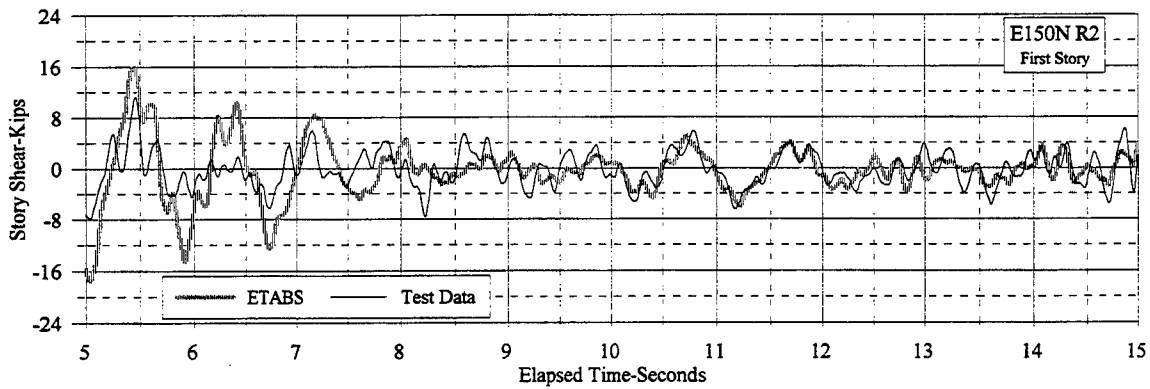
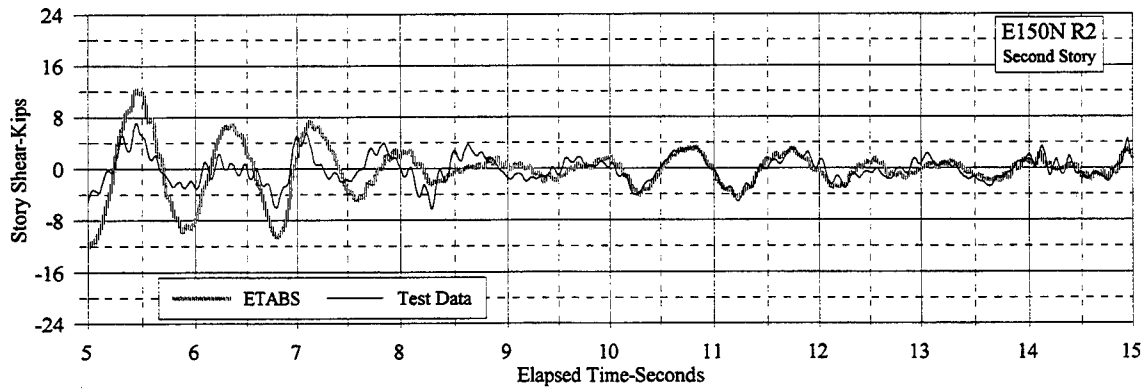
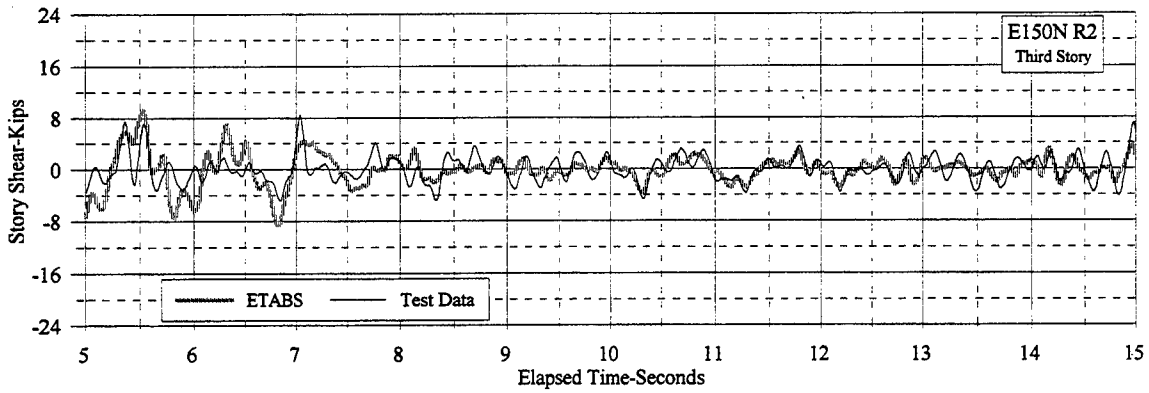


Figure 6.32 ETABS Simulation of E150N: Story Shear, Run 2

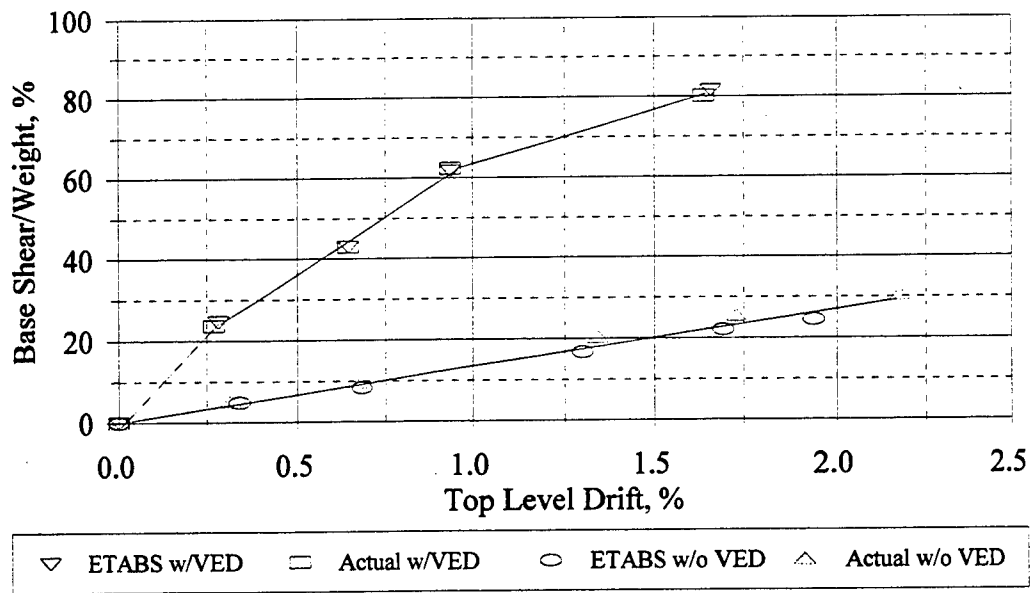


Figure 6.33 Comparison of Measured and Computed Response Maxima

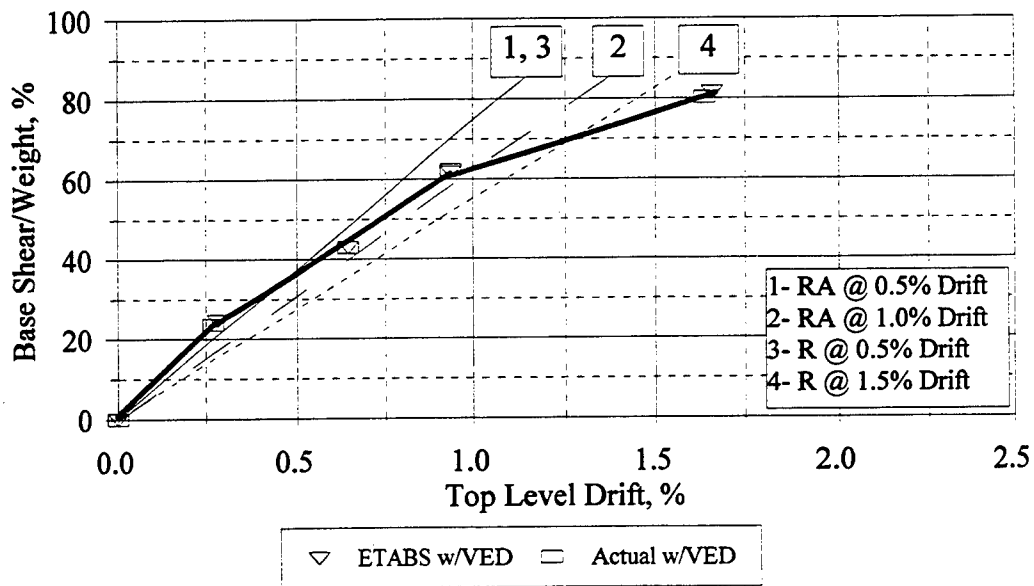


Figure 6.34 Comparison of Measured and Predicted Stiffnesses with VEDs

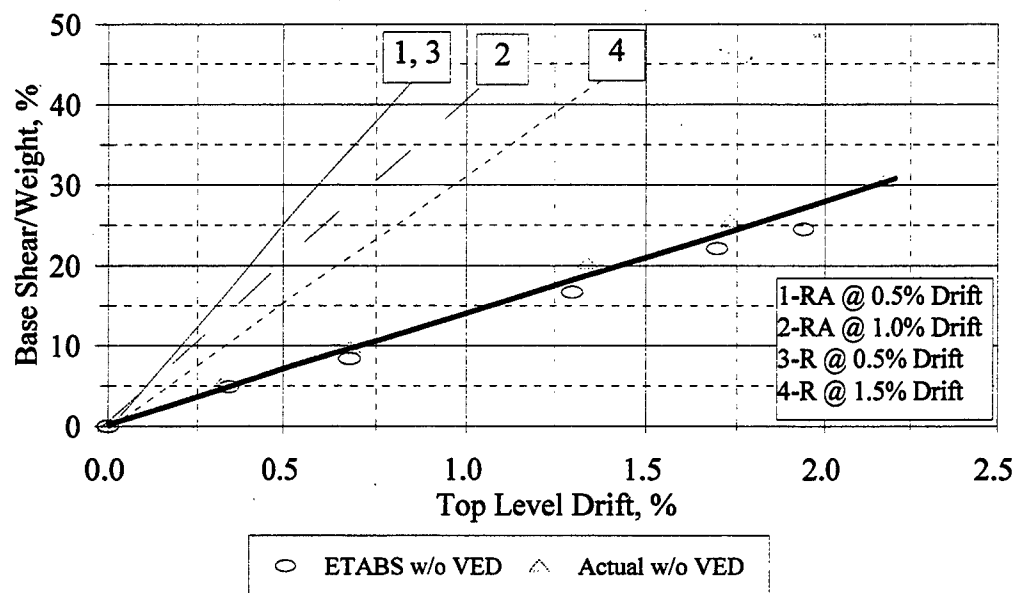


Figure 6.35 Comparison of Measured and Predicted Stiffnesses without VEDs

APPENDIX A

DESCRIPTION OF MODEL FABRICATION

This appendix provides a more detailed description of the construction of the test structure than is presented in Chapter 2. Detailed descriptions of the dimensions of the model structure are provided. The steel reinforcement for the model was based on high strength steel wire. The wire required annealing to adjust its yield strength characteristics to emulate those of the prototype reinforcement; the annealing process is described in section A.2. In section A.3, the construction of the model is described in detail. The construction of the three main structural system components, the base girder, the primary model structure, and the VED bracing, is outlined. In addition, the installation of lead weights on each floor of the structure, which were required for modeling prototype gravity loads, is described. Finally, in section A.4, the provision of a separate steel “safety frame” is described. This frame was added to prevent a total collapse of the model, if a severe structural failure had occurred during testing.

A.1 Dimensions

The design of the test structure is described in Chapter 2 of this report. Figures 2.7 - 2.10 provide overall views of the structure. The structure’s nominal dimensions are shown in Figures 2.11 - 2.14. All gross dimensions in the structure were scaled to be approximately $\frac{1}{3}$ of the prototype dimensions.

A.2. Preparation of Steel Reinforcement

Ivy Steel and Wire Company, Inc., of Houston, TX, provided the deformed steel wire for the project. It is typically used in fabricating welded wire fabric. Figure A.1 illustrates the deformation pattern for this wire. The supplier’s literature indicates that the wire deformation patterns comply with the minimum requirements of ANSI/ASTM A 496, Deformed Steel Wire for Concrete Reinforcement. The wire is cold-drawn from hot-rolled low carbon steel rod. It exhibited significantly higher yield strengths

than the nominal 40 ksi of the prototype structure reinforcement. Prior to its placement in the model, the wire used in the slab, column, and spandrel reinforcement was annealed to lower its tensile yield stress characteristics to resemble more nearly that of the steel reinforcement in the prototype. Before annealing, three specimens of each wire diameter were tension tested in accordance with the provisions of ANSI/ASTM A 496. Using nominal wire cross-section areas, a gage length of 4", and an elongation rate of 0.16" per minute, the tests showed average tensile yield strengths (stress at 0.5% tensile strain) of 99.9 ksi for D3, 98.1 ksi for D5, 95.1 ksi for D7, 83.5 ksi for D8, 81.7 ksi for D9, and 89.2 ksi for D12.

Several references [117, 118, 121, 126] present the results of different annealing processes for various grades of steel. Using those reported results, two-foot lengths of each wire diameter were annealed to several combinations of sustained elevated temperature and time in a small annealing oven in the Department of Theoretical and Applied Mechanics (TAM) at the University of Illinois at Urbana-Champaign (UIUC). ASTM A 496 tensile tests of these samples showed that an approximate average tensile strength of 40 ksi for all wire diameters could be obtained by a heating the wire to a sustained 1,200° F for one hour, followed by air-cooling. Average post-annealing yield stresses were 42.4 ksi for D3, 40.5 ksi for D5, 45.3 ksi for D7, 36.9 ksi for D8, 40.0 ksi for D9, and 39.6 ksi for D12.

Because no oven large enough to handle the wire lengths of 7'6" was available locally, all wire for the tests was shipped to a commercial annealing company in Chicago. The commercial process necessitated using a single annealing specification: while slightly more consistent average strengths could have been obtained by using different combinations of temperature and time, the difficulty of ensuring that the different specifications for different wire diameters were met outweighed the likelihood of greatly improved yield strength accuracy. All deformed wire used for primary slab, column, and spandrel reinforcement was annealed.

Samples of the commercially annealed wire were tested in accordance with ANSI/ASTM A 496. The annealing process results in a tensile behavior that is essentially bilinear up to an ultimate tensile strain of at least 2.0%. The initial slope of the curve follows a conventional elastic modulus of 29,000 ksi, while the post-yield modulus is almost zero. Comparisons of pre and post-annealing behavior of D5 wire samples may be seen in Figures A.2 and A.3. The results for all wire diameters are summarized in Table A.1. All wire diameters except the D3 wire had post-annealing yield strengths very close to the desired 40 ksi. Because the D3 wire would be used in slab "middle strip" regions, which are significantly less likely to reach yield strain than in "column strip" regions, it was decided to use the D3 bars in their as-annealed condition, with a yield strength of 59 ksi.

The stirrups in the columns and spandrel beams were formed from W1.7 smooth steel wire. Tensile tests of samples of this wire indicated that its tensile yield strength was approximately 100 ksi. Although its strength exceeded the nominal 40 ksi of the prototype reinforcement, this wire was not annealed. Stirrup spacing was deemed to be a more critical quantity in the earthquake simulations than stirrup strength, because the prototype stirrup spacing significantly exceeds current code requirements and raises questions about the adequacy of the confinement of the primary column and spandrel reinforcement.

Following the annealing procedure, all reinforcement for the slabs, columns, and spandrels was cut to length. Locally-fabricated jigs were used to bend the wire that required bending.

A.3 Fabrication

(a) Base Girder

Fabrication was begun by constructing a reinforced concrete base girder for the model. The base girder was constructed on the floor of the test facility, directly adjacent to the shaking table. Because of the length of time involved in constructing the model, it was necessary to perform all construction off of the shaking table, to permit other testing to continue. Figures A.4 - A.6 present key base girder dimensions, while Figure A.7 shows casting of the base girder.

There were three primary requirements for the base girder. First, it had to be rigid during seismic simulations and attached rigidly to the shaking table platform. During the simulations, the girder was expected to function essentially as an extension of the shaking table, with its motions matching those of the table. Second, because the $\frac{1}{3}$ scale chosen for the model resulted in dimensions that slightly exceeded the length of the shaking table platform (12 feet), the ends of the base girder extended beyond the edge of the shaking table platform. Figure A.4 shows how the girder extended off the platform. The girder "overhangs" could not undergo any measurable vertical deflection under full anticipated loading, necessitating high stiffness in the overhanging regions. Third, since the entire model structure would be lifted onto the shaking table using the facility's overhead crane (20 ton capacity) following construction, the base girder had to carry the weight of the bare model and itself during lifting, without damaging deflection.

The stiffness of the girder that rested on the table surface was believed to be less critical than the stiffness of the overhangs or the stiffness of the entire structure during lifting, so no specific stiffness calculations were undertaken for the condition wherein the model was on the table. Rigid attachment of the

girder to the table was deemed to be the most critical aspect of this part of the design. Friction forces between the bottom surface of the base girder and the table surface were used to ensure that the model would not move during earthquake simulations. With an assumed test weight of 80 kips and coefficient of friction of 0.2, approximately 16 kips of weight-induced friction force will develop at the girder-table interface. Since developing a base shear of 50 kips appeared to be a realistic expectation for the earthquake simulations, an added 34 kips of friction force was required, which necessitated an additional 170 kips of vertical force. The added vertical force was provided by tie down bolts that clamped the girder to the shaking table. With an planned 10 tie down bolts, the required vertical force per bolt was 17 kips. The 1-¼ inch diameter high strength steel tie down bolts have a manufacturer's recommended working load of 58 kips, so the required force per bolt was well below the working load. Because the base girder thickness (24 inches) and reinforcement quantities precluded drilling for tie down bolt holes after construction, the bolt holes had to be located precisely. Hole templates were used in both the bottom and the top of the base girder forms to hold capped 1-½ inch diameter capped PVC pipe sections in place during casting. The center-to-center spacing for tie down bolts on the shaking table platform is $12 - \frac{1}{16}$ " in both its length and width dimensions. Because of a concern about possible shrinkage-induced dimension changes in the base girder, pipe sections were placed at every potential tie down point in the footprint of the base girder as it would rest on the table surface. This resulted in a total of 36 possible tie down points for the girder, well in excess of the required 10 points. See Figure A.4. In practice, shrinkage proved not to be a problem, and all holes lined up well with the table holes.

Because a uniform cross-section was used, to simplify forming and casting, the critical deflection condition was associated with lifting the entire structure onto the shaking table. The model was lifted by means of a steel lifting frame (see Figure 2.9) that had one lifting point at each of the four end sections of the base girder. The critical deflection was that of the girder mid-span, directly under the interior (centerline) columns, during the lifting operation. To avoid damaging the model slabs, a maximum downward mid-span deflection of 0.1" was targeted in the design, conservatively assuming that the girder cross-section alone provided flexural stiffness. A final design cross-section of 14" wide by 24" high, which was required to ensure that girder cracking moment was not reached during the lifting, resulted in an anticipated mid-span deflection of less than 0.04". The entire structure was monitored visually during the lifting operation, and no cracking of the model slabs or columns was observed. Stiffness requirements governed the girder design. Minimum tensile flexural reinforcement was required in accordance with ACI 318-89; six #5 deformed 60 ksi bars were used to reinforce the positive moment section at mid-span and

the negative moment sections in the overhang regions, with two #5 bars used on the respective opposite face of the cross-section. While preliminary calculations indicated that no shear reinforcement was required in the legs of the base girder, #3 deformed 60 ksi bar stirrups were placed at 12" c-c spacings in all sections of the base girder, except in the overhang regions between the exterior columns and the lifting points, where the spacing was reduced to 4" c-c. Figure A.4 shows the base girder in plan, while Figures A.5 and A.6 show cross-sections of the base girder.

Reinforcement for the first story column bases was stubbed up from the base girder. This reinforcement may be seen in Figure A.7; its design is discussed in Chapter 2. Each interior column stub consisted of four #3 deformed 60 ksi bars, while each exterior column stub consisted of six #3 deformed 60 ksi bars.

The base girder was cast on May 19, 1993 (Figure A.7). At casting time, which began at 09:00 AM, the air temperature was 55° F, with cloudy, humid conditions. As with the rest of the structure, the concrete used in the casting was purchased from a local ready-mix plant. The concrete mix specification for the base girder served as a trial run for the main structure. The target 28 day compressive strength for the mix was 3,600 psi; Chapter 2 discusses the rationale for this strength. Coarse aggregate for the mix was a rounded, plant-described "pea gravel," with maximum aggregate size of $\frac{3}{8}$ ". This was the smallest available coarse aggregate and was specified to minimize size scaling effects on the concrete material properties. A superplasticizer admixture, "*Daracem 100*," which is manufactured by Grace Concrete Products, was used to extend slump life and workability. The supplier recommended a range of 5-20 ounces of the admixture per 100 lb of cement; a quantity of 8.5 ounces per 100 lb of cement was added to the mix, for a target of 6" slump for an extended time. Initial slump at delivery was only 3" and water was added, increasing the slump to almost 6". Twelve 6" diameter x 12" high cylinders were cast for use in compression strength testing. Subsequent compression strength tests showed a three cylinder average of 3,490 psi at seven days after casting, 4,480 psi at fourteen days after casting, and 4,990 psi at 28 days after casting. Immediately after completion of concrete finishing, the exposed top surface of the concrete was covered with wet burlap and plastic sheeting. The burlap was moistened again on May 20. The forms were stripped on May 21.

(b) Primary Structure

Above the base girder, the structure was comprised of cast-in-place columns, flat slabs, and

spandrel beams. Each of the three story levels was formed and cast as a monolithic unit of flat slab, spandrels, and supporting columns.

A single set of wooden forms was designed and fabricated so that it could be broken down, removed, and re-erected repeatedly. The plywood formwork had a compressed, oiled paper surface that facilitated removal without its bonding to the concrete. In addition, form oil was used to reduce further the likelihood that the formwork would bond to the concrete.

For each floor level, starting with the first story columns, slab, and spandrels, a floor was formed; formwork was oiled; reinforcement was placed (Figures A.8 - A.11); and concrete was cast and finished. Commercially available plastic reinforcement chairs were shortened and used to support both the top and bottom reinforcement layers. The chairs may be seen in Figures A.9 and A.11. Longitudinal (north-south) reinforcement was placed closest to the slab surfaces in both the top and bottom reinforcement layers.

In addition, capped brass tube lengths were placed at the intended locations for the bolts that would be used to secure lead weights in place on the test structure. As discussed in Chapter 2, 1/2" diameter steel all-thread bolts were extended through the columns, to secure the damper collars that would be attached externally on the columns. Concrete placement from a ready-mix truck was facilitated by the use of a small concrete bucket that was lifted using the overhead crane in the high bay. Figures A.12 and A.13, which show casting of the third floor slab, illustrate both the basic process used in casting and the configuration of the formwork that was used to support each of the three floors. Primary concrete finishing was accomplished with an aluminum screed beam that was slightly longer than the slab span. Final finishing for the slab was accomplished by brushing with a coarse broom. Following completion of finishing, wet burlap was placed on the exposed slab surface and topped with plastic sheeting. The burlap was moistened daily such that it stayed damp for seven days following casting.

Formwork for each floor was removed seven days after casting. A light shoring system was installed under each floor before work proceeded on the floor above. For the first floor slab, 4" x 4" shores were placed roughly under the two primary north-south column lines, topped by 2" x 4" lumber that was in contact with the bottom side of the slab. The shores extended to the base girder. A tight fit was ensured by the use of small screw jacks under each shore. For the upper two floors, a similar shoring system was used, with the shores placed directly over the shores for the respective next lower floor. Once the shoring was in place, the formwork would be re-erected for the next floor up, and the process was repeated.

In the construction of the formwork at the first story level, difficulty in aligning the column forms with the base girder necessitated slightly increasing the column dimensions from those which were

originally designed for the $\frac{1}{3}$ scale model. Thus, the interior columns, which had been designed as a $4\frac{3}{4}$ " x $4\frac{3}{4}$ " cross-section, became 5" x 5" in section; the exterior columns, which had been designed as a 4" x 8" cross-section, became a $4\frac{1}{4}$ " x $8\frac{1}{4}$ " section. Spandrel width likewise was enlarged from 4" to $4\frac{1}{4}$ ", to match the exterior column dimension and simplify formwork.

Concrete was again obtained from a local ready-mix company. The basic mix was specified in the same manner as it had been for the base girder: a 3,600 psi "pea gravel" mix, with superplasticizer added to extend workability. The first story elements were cast beginning at approximately 09:00 AM on July 2, 1993. The ambient temperature was 75° F, with overcast, humid conditions. As had been the case with the base girder concrete, the concrete was initially very stiff, with a slump of less than 3", and water was added. Second story elements were cast beginning at approximately 01:30 PM on July 20, 1993. The ambient temperature was 85° F, with sunny, humid conditions. The initial slump was again very low, $1\frac{1}{4}$ ", and water was again added. Third story elements were cast beginning at approximately 07:15 AM on September 8, 1993. The ambient temperature was 60° F, with overcast, humid conditions. The initial slump was 6".

For each story placement, 6" x 12" cylinders were cast for both compression and split cylinder testing, and 6" x 6" x 30" rectangular prisms were cast for modulus of rupture testing. Compression cylinders were tested in accordance with the provisions of ASTM C 39, Standard Test Method for Compressive Strength of Cylindrical Concrete Specimens. Split cylinder tensile tests were accomplished in accordance with the provisions of ASTM C 496, Standard Test Method for Splitting Tensile Strength of Cylindrical Concrete Specimens. Modulus of rupture tests were performed in accordance with ASTM C 78, Standard Test Method for Flexural Strength of Concrete (Using Simple Beam with third Point Loading). Concrete properties on the first day of earthquake simulation testing are presented in Tables A.2 - A.4. The reported compression strengths indicate that, in all castings, the in-place strengths greatly exceeded the specified strength. It is likely that, despite repeated discussions concerning the need for complying with the specified strengths, the supplier adopted a conservative approach to the strength provided, which is consistent with general practice. This experience illustrates a problem that is apparently common to research projects that rely on commercial sources for concrete; other researchers have related similar experiences to the author.

Following completion of all casting and removal of all formwork, all floors were shored as described above. The entire structure, including the base girder, was painted with a thinned white latex paint, to facilitate observing crack formation and propagation during the earthquake simulations.

(c) Damper Bracing System

The primary focus of the research was to study how the addition of viscoelastic dampers (VEDs) modified the response of the lightly reinforced concrete (LRC) slab-column model to simulated seismic motions. A conservative, simplified approach to the design of the VED bracing system was adopted. No effort was made to explore extensively a large number of options on the bracing system configuration.

Since the model was two bays deep in the direction of shaking motions, structural symmetry favored adding bracing in both bays. Load paths and deformation patterns were thus uniform at all times before localized failures occurred. Similarly, since the model was two column lines wide, bracing was used in both column lines, minimizing torsion. In bracing both bays, a chevron pattern was adopted, in which, on any floor level and column line, opposing braces would essentially be subjected to equal but opposite loadings at any given instant. This configuration ensured that any differences in structural response between brace compression and brace tension would be averaged out by the opposing members. This overall configuration may be seen clearly in Figures 2.9 and 2.14.

The brace elements were fabricated as double-angle sections, with the angles placed back to back (Figure A.14). The angle material was A36 steel. The braces were fabricated such that the VED could be inserted in the brace line and bolted in place using four $\frac{3}{8}$ " diameter bolts at each end of the VED. The point of insertion was chosen to be at the approximate $\frac{1}{3}$ point in the brace length. This location was chosen for two main reasons. First, it would permit smaller out of plane lateral VED displacements than those which would occur if the VED were placed at brace mid-length, if any were to occur. Second, in-test visibility of the VED would be somewhat better there than at a mid-length location; a separate steel safety frame (see discussion below) blocked the view of the VED, less at the $\frac{1}{3}$ point than at mid-length.

The brace cross-section (Figure A.14) was selected to provide an axial stiffness that was significantly larger than the shear stiffness of the VED. As reported in Reference 84, the bracing and the VED must be viewed as a system of structural elements in series when designing the VED. If the bracing is assumed to be "rigid" with respect to the VED, then the VED is assumed to undergo the total displacement that occurs in the brace-VED system. If the brace is actually not rigid, this assumption results in overestimating the VED displacement and therefore overestimating the degree of damping it provides. In this instance, with a total length of approximately 58.25 inches, a damper brace has an axial stiffness of 1,800 kips/inch, while a VED has a shear stiffness of slightly less than 12 kips/inch. Joining the brace and VED in series results in an effective system stiffness of 11.92 kips/inch, over 99% of the

stiffness of the VED alone. Within the accuracy that can be achieved experimentally and analytically, this difference is insignificant.

To attach the braces to the columns, close-fitting A36 steel "collars" were fabricated to clamp around the columns (Figures A.15 - A.20). Each column was measured, and the collar for it was fabricated to provide a precise fit to its dimensions. In addition, when the collars were attached to the columns, a non-shrink bedding grout was placed between the collar components and the columns to ensure as tight a fit as possible. The collars were also utilized to provide confinement for the concrete in the lap splice regions of the exterior columns, increasing the need for a tight fit. To minimize fabrication costs, L 7" x 4" x $\frac{3}{8}$ " sections were used (Figures A.14 and A.15). The 7" leg was chosen to cover the lap splice region of the external columns. The $\frac{3}{8}$ " thickness was the minimum available for the 7" leg length, but the thickness had the added advantage of providing sufficient strength and stiffness to prevent collar deformation. To provide uniformity, $\frac{3}{8}$ " plate stock was used in fabricating the side faces in the collars.

The gusset plate in each connection was welded using $\frac{3}{16}$ " fillet welds (E70 electrodes) over the entire length of contact between the plate and the adjoining L 7" x 4" x $\frac{3}{8}$ " section, on both sides of the plate. The L 2" x 1" x $\frac{3}{16}$ " clip angle used to connect the collar side faces to the L 7" x 4" x $\frac{3}{8}$ " or the $\frac{3}{8}$ " back plate was connected to the side face using a continuous $\frac{3}{16}$ " fillet weld (E70 electrodes) along the exposed perimeter of the clip angle, resulting in a weld length of approximately 5- $\frac{1}{2}$ " on each clip angle. These welds are not shown in figures A.15 and A.16, to minimize clutter in them.

To avoid the possibility that the collars might slip along the column heights during seismic simulations, a $\frac{1}{2}$ " diameter "all-thread" bolt was cast into each column in the collar region and used as a means of positive attachment for each collar. In a full-scale rehabilitation, such a measure would require drilling into an existing column and inserting dowels to provide positive attachment. Concern for damage to the relatively small model column dimensions by drilling dictated that the bolts be precast into the model.

The original design for the collars and braces included a single $\frac{1}{2}$ " diameter bolt acting as a pin to connect each collar and brace (Figures A.15 and A.16). Conceptually, such a pinned joint would permit the braces to act as true pinned members, with no frame-induced flexure. In practice, during the initial low-level seismic simulations, it was seen that the VED rotational stiffnesses were so low that the braces would bend substantially out of plane under compressive loading. This necessitated adding small tack welds between the brace ends and the collars, to prevent brace rotation; see Figure A.21.

Pre-test predictions of responses to the earthquake simulations indicated that the shear capacities of the bases of the first story exterior columns might be exceeded. Therefore, supplemental anchorages to the base girder were provided, to increase the shear capacities of those columns. These anchorages could transmit forces from the braces directly to the "foundation," or base girder. See Figure A.17. One-half inch diameter all-thread bolts were secured in drilled holes using a commercial epoxy mix with a shear strength of 2,250 psi. Because pre-test analyses showed that column shears at the bases of the second story exterior columns would be similar to those at the first story, similar anchorage was provided for the second story exterior columns. This anchorage involved drilling into the spandrel beam, inserting a ½" diameter A490 (B7) all-thread bolt, and epoxying the bolt into place (Figures A.18 & A.19). In both the base girder and the first floor slab, the two all-thread bolts added 8.6 kips of shear transfer capacity (allowable stress, friction-type connection) to each column. This was a higher added capacity than pretest analyses indicated was needed, but the bolts were used because of their local availability. Two bolts per column were used to ensure that force distributions were uniform around each column. The design of these elements is discussed in Chapter 2.

(d) Supplemental Weights

Supplemental lead weights were added to the floor slabs at each level to model more accurately gravity loads at all times and inertial loads during seismic simulations. Because its density is the highest of any commonly available material, lead was chosen for the supplemental weight material. The lead weights and the weights of the slabs and columns in the model resulted in simulating approximately the evenly distributed gravity loads of the prototype structure. Imposed live loads and other structural loads (e.g. walls) were not simulated. Space limitations on and around the model structure prohibited the addition of more weights than were used.

Exact similitude modeling would require the same distributed loads in the scaled model as in the full-scale prototype. From the original design drawings for the prototype, the total structural loading in the first and second floors of the prototype, excluding live loads, was approximately 115 psf. On the third floor, or roof, of the prototype, the loading, excluding live loads, was approximately 108 psf. In the model, the average distributed loading from the lead weights and the concrete structure was approximately 104 psf on the first and second floors, and 99 psf on the third floor.

Floors 1 and 2 each had 192 lead weights ("pigs") that weighed approximately 66 lb each, while

floor 3 had 208 pigs that weighed approximately 56 lb each. The two different sizes of pigs were purchased at different times. Their shapes were essentially identical, but their dimensions varied slightly. Within each size, the pigs varied slightly in their individual weights. A random sampling of six pallets (25 pigs per pallet) of each size pig was used to establish the average weights. Since the primary area of study was the north-south response of the structure, the pigs were located in four lines paralleling the north-south column lines. Within those lines, the weights were distributed as uniformly as possible. Their layouts may be seen in Figures A.23 and A.24. The weights were stacked two-deep (Figures A.25 - A.28). This configuration resulted in a less uniform distribution of total loading in the transverse, or east-west, direction than would be observed in the prototype, but the layout was necessitated by working space limitations in and around the model. Since the model had free ends on its east and west sides, its transverse load distribution did not precisely replicate those of the prototype anyway.

The two-deep stacks were secured to the structure by means of $\frac{1}{2}$ " diameter all-thread bolts that passed through brass tubes that were cast in the floor slab (Figure A.22). An elastomeric pad under each pig stack allowed the slab underneath to move and deform, reducing the direct influence of the pigs on structural stiffnesses. The two-deep configuration raised the effective center of gravity for each floor slightly above the point that would result from scaling directly from the prototype. Summaries of the vertical distribution of weight in the model are shown in Table A.5. The vertical centers of gravity shown there were used in all overturning moment calculations.

A.4 Safety Frame

The possibility of a complete structural collapse during the earthquake simulations was a concern. Of particular note was the possibility of a "pancake" collapse of the slabs if a shear failure of the slab occurred around the interior columns. The slab bottom reinforcement did not continue through the column connection regions, so the interior column joints were vulnerable. To protect those who worked around the model and the shaking table equipment, a structural steel "safety frame" was erected to catch the model if it should collapse. The frame is shown in Figure 2.10. It was fabricated from built-up and single structural steel members that were readily available. Beam elements of the frame were carefully inserted beneath each of the floor slabs and bolted to steel towers that rested on the shaking table reaction mass. The elements of the frame did not contact the model, so the frame did not influence the model response. The structure did not collapse. The frame hampered model access and visibility.

| Wire Size | Sample | Diameter Inches | Area Sq. Inches | Yield Force, Kips | Ultimate Force, Kips | Yield Strength, KSI | Ultimate Strength, KSI |
|-----------|----------------|--------------------|--------------------|----------------------|-------------------------|------------------------|---------------------------|
| D3 | A-FA-1 | 0.195 | 0.03 | 2.00 | 2.15 | 67 | 72 |
| D3 | A-FA-2 | 0.195 | 0.03 | 1.03 | 1.75 | 34 | 58 |
| D3 | A-FA-3 | 0.195 | 0.03 | 1.55 | 1.95 | 52 | 65 |
| D3 | A-FA-4 | 0.195 | 0.03 | 2.22 | 2.40 | 74 | 80 |
| D3 | A-FA-5 | 0.195 | 0.03 | 2.31 | 2.25 | 77 | 75 |
| D3 | A-FA-6 | 0.195 | 0.03 | 2.20 | 2.40 | 73 | 80 |
| D3 | A-FA-7 | 0.195 | 0.03 | 1.30 | 1.73 | 43 | 58 |
| D3 | A-FA-8 | 0.195 | 0.03 | 1.17 | 1.70 | 39 | 57 |
| D3 | A-FA-9 | 0.195 | 0.03 | 2.10 | | 70 | |
| D3 | A-FA-10 | 0.195 | 0.03 | 2.15 | 2.33 | 72 | 78 |
| D3 | A-FA-11 | 0.195 | 0.03 | 1.55 | 1.95 | 52 | 65 |
| D3 | <i>Average</i> | 0.195 | 0.03 | 1.78 | 2.06 | 59 | 69 |
| D5 | A-FA-1 | 0.252 | 0.05 | 1.95 | 2.95 | 39 | 59 |
| D5 | A-FA-2 | 0.252 | 0.05 | 1.97 | 2.96 | 39 | 59 |
| D5 | A-FA-3 | 0.252 | 0.05 | 1.95 | 2.90 | 39 | 58 |
| D5 | <i>Average</i> | 0.252 | 0.05 | 1.96 | 2.94 | 39 | 59 |
| D7 | A-FA-1 | 0.298 | 0.07 | 3.03 | 4.55 | 43 | 65 |
| D7 | A-FA-2 | 0.298 | 0.07 | 3.12 | 4.57 | 45 | 65 |
| D7 | A-FA-3 | 0.298 | 0.07 | 3.08 | 4.40 | 44 | 63 |
| D7 | <i>Average</i> | 0.298 | 0.07 | 3.08 | 4.51 | 44 | 64 |
| D8 | A-FA-1 | 0.319 | 0.08 | 2.70 | 3.95 | 34 | 49 |
| D8 | A-FA-2 | 0.319 | 0.08 | 2.88 | 4.30 | 36 | 54 |
| D8 | A-FA-3 | 0.319 | 0.08 | 2.85 | 4.30 | 36 | 54 |
| D8 | <i>Average</i> | 0.319 | 0.08 | 2.81 | 4.18 | 35 | 52 |
| D9 | A-FA-1 | 0.338 | 0.09 | 3.67 | 5.57 | 41 | 62 |
| D9 | A-FA-2 | 0.338 | 0.09 | 3.70 | 5.44 | 41 | 60 |
| D9 | A-FA-3 | 0.338 | 0.09 | 3.70 | 5.57 | 41 | 62 |
| D9 | <i>Average</i> | 0.338 | 0.09 | 3.69 | 5.53 | 41 | 61 |
| D12 | A-FA-1 | 0.39 | 0.12 | 4.42 | 6.70 | 37 | 56 |
| D12 | A-FA-2 | 0.39 | 0.12 | 4.42 | 6.78 | 37 | 57 |
| D12 | A-FA-3 | 0.39 | 0.12 | 4.52 | 6.82 | 38 | 57 |
| D12 | <i>Average</i> | 0.39 | 0.12 | 4.45 | 6.77 | 37 | 56 |

Table A.1 Test Results, Deformed Steel Wire Used in Model Structure Reinforcement

| | | | Age | Compressive | Average Compressive | Modulus of Elasticity, |
|------------------------|-----------|-----------|--------|---------------|---------------------|------------------------|
| Location | Cast Date | Test Date | (Days) | Strength, PSI | Strength, PSI | ACI 8.5.1, KSI |
| Floor 1 | 02-Jul-93 | 03-Mar-94 | 244 | 5,857 | | |
| Floor 1 | 02-Jul-93 | 03-Mar-94 | 244 | 5,522 | | |
| Floor 1 | 02-Jul-93 | 03-Mar-94 | 244 | 5,638 | | |
| Floor 1 | 02-Jul-93 | 03-Mar-94 | 244 | 6,005 | | |
| Floor 1 | 02-Jul-93 | 03-Mar-94 | 244 | 5,904 | | |
| Floor 1 | 02-Jul-93 | 03-Mar-94 | 244 | 5,921 | | |
| Floor 1 Average | | | | | 5,808 | 4,344 |
| Floor 2 | 20-Jul-93 | 03-Mar-94 | 226 | 5,474 | | |
| Floor 2 | 20-Jul-93 | 03-Mar-94 | 226 | 5,410 | | |
| Floor 2 | 20-Jul-93 | 03-Mar-94 | 226 | 5,599 | | |
| Floor 2 | 20-Jul-93 | 03-Mar-94 | 226 | 5,633 | | |
| Floor 2 | 20-Jul-93 | 03-Mar-94 | 226 | 5,547 | | |
| Floor 2 | 20-Jul-93 | 03-Mar-94 | 226 | 5,566 | | |
| Floor 2 Average | | | | | 5,538 | 4,242 |
| Floor 3 | 08-Sep-93 | 03-Mar-94 | 176 | 6,554 | | |
| Floor 3 | 08-Sep-93 | 03-Mar-94 | 176 | 6,327 | | |
| Floor 3 | 08-Sep-93 | 03-Mar-94 | 176 | 6,442 | | |
| Floor 3 Average | | | | | 6,441 | 4,575 |
| Total Structure | | | | | 5,929 | 4,389 |

Table A.2 Test Results, 6" x 12" Concrete Compression Cylinders

| Location | Cast Date | Test Date | Age (Days) | Modulus of Rupture, PSI | Average Modulus of Rupture, PSI | ACI EQ. 9-9 PSI |
|------------------------|-----------|-----------|---------------|----------------------------|------------------------------------|--------------------|
| Floor 1 | 02-Jul-93 | 03-Mar-94 | 244 | 592 | | |
| Floor 1 | 02-Jul-93 | 03-Mar-94 | 244 | 642 | | |
| Floor 1 | 02-Jul-93 | 03-Mar-94 | 244 | 675 | | |
| Floor 1 | 02-Jul-93 | 03-Mar-94 | 244 | 708 | | |
| Floor 1 Average | | | | | 654 | 572 |
| Floor 2 | 20-Jul-93 | 03-Mar-94 | 226 | 758 | | |
| Floor 2 | 20-Jul-93 | 03-Mar-94 | 226 | 667 | | |
| Floor 2 | 20-Jul-93 | 03-Mar-94 | 226 | 617 | | |
| Floor 2 Average | | | | | 681 | 558 |
| Floor 3 | 08-Sep-93 | 03-Mar-94 | 176 | 625 | | |
| Floor 3 | 08-Sep-93 | 03-Mar-94 | 176 | 704 | | |
| Floor 3 | 08-Sep-93 | 03-Mar-94 | 176 | 683 | | |
| Floor 3 | 08-Sep-93 | 03-Mar-94 | 176 | 658 | | |
| Floor 3 Average | | | | | 668 | 602 |

Table A.3 Flexural Test Results, 6" x 6" x 30" Concrete Beams

| Location | Cast Date | Test Date | Age (Days) | Split Cylinder Strength, PSI | Average Split Cylinder Strength, PSI | ACI 11.2.1.1 PSI |
|------------------------|-----------|-----------|---------------|---------------------------------|---|---------------------|
| Floor 1 | 02-Jul-93 | 03-Mar-94 | 244 | 367 | | |
| Floor 1 | 02-Jul-93 | 03-Mar-94 | 244 | 458 | | |
| Floor 1 | 02-Jul-93 | 03-Mar-94 | 244 | 508 | | |
| Floor 1 | 02-Jul-93 | 03-Mar-94 | 244 | 517 | | |
| Floor 1 | 02-Jul-93 | 03-Mar-94 | 244 | 570 | | |
| Floor 1 | 02-Jul-93 | 03-Mar-94 | 244 | 464 | | |
| Floor 1 Average | | | | | 481 | 511 |
| Floor 2 | 20-Jul-93 | 03-Mar-94 | 226 | 493 | | |
| Floor 2 | 20-Jul-93 | 03-Mar-94 | 226 | 528 | | |
| Floor 2 | 20-Jul-93 | 03-Mar-94 | 226 | 523 | | |
| Floor 2 | 20-Jul-93 | 03-Mar-94 | 226 | 601 | | |
| Floor 2 | 20-Jul-93 | 03-Mar-94 | 226 | 462 | | |
| Floor 2 | 20-Jul-93 | 03-Mar-94 | 226 | 581 | | |
| Floor 2 Average | | | | | 531 | 499 |
| Floor 3 | 08-Sep-93 | 03-Mar-94 | 176 | 539 | | |
| Floor 3 | 08-Sep-93 | 03-Mar-94 | 176 | 508 | | |
| Floor 3 | 08-Sep-93 | 03-Mar-94 | 176 | 518 | | |
| Floor 3 Average | | | | | 522 | 538 |

Table A.4 Split Cylinder Test Results, 6" x 12" Concrete Cylinders

| Third Floor | Dimensions (In) | | | Number | Unit Weight* | Total Weight (Kips) | Center of Gravity (In) | Moment (In-Kips) |
|------------------------------|-----------------|--------|-------|--------|--------------|---------------------|------------------------|------------------|
| Item | X | Y | Z | | | | | |
| Slab | 160.00 | 160.00 | 2.38 | 1 | 0.0868 | 5.28 | 118.81 | 627.05 |
| Edge Columns | 8.25 | 4.25 | 18.81 | 4 | 0.0868 | 0.23 | 108.22 | 24.79 |
| Center Columns | 5.00 | 5.00 | 18.81 | 2 | 0.0868 | 0.08 | 108.22 | 8.84 |
| Spandrels | 143.50 | 4.25 | 2.63 | 2 | 0.0868 | 0.28 | 116.31 | 32.33 |
| Braces/Collars/Dampers | | | | 4 | 75.4 | 0.30 | 108.22 | 32.64 |
| Lead Ingots | | | | 208 | 56 | 11.65 | 123.00 | 1432.70 |
| Pads/Mounts for Ingots | | | | 52 | 12.9 | 0.67 | 123.00 | 82.51 |
| | | | | | | | | |
| Total Story Weight | | | | | | 18.49 | | 2240.85 |
| Story Center of Gravity | | | | | | | 121.21 | |
| | | | | | | | | |
| Distributed Floor Load (PSF) | | | | | 99 | | | |

| Second Floor | Dimensions (In) | | | Number | Unit Weight* | Total Weight (Kips) | Center of Gravity (In) | Moment (In-Kips) |
|------------------------------|-----------------|--------|-------|--------|--------------|---------------------|------------------------|------------------|
| Item | X | Y | Z | | | | | |
| Slab | 160.00 | 160.00 | 2.38 | 1 | 0.0868 | 5.28 | 78.81 | 415.94 |
| Edge Columns | 8.25 | 4.25 | 37.63 | 4 | 0.0868 | 0.46 | 80.00 | 36.65 |
| Center Columns | 5.00 | 5.00 | 37.63 | 2 | 0.0868 | 0.16 | 80.00 | 13.06 |
| Spandrels | 143.50 | 4.25 | 2.63 | 2 | 0.0868 | 0.28 | 76.31 | 21.21 |
| Braces/Collars/Dampers | | | | 4 | 150.8 | 0.60 | 78.81 | 47.54 |
| Lead Ingots | | | | 192 | 66 | 12.67 | 83.00 | 1051.78 |
| Pads/Mounts for Ingots | | | | 48 | 12.9 | 0.62 | 83.00 | 51.39 |
| | | | | | | | | |
| Total Story Weight | | | | | | 20.07 | | 1637.57 |
| Story Center of Gravity | | | | | | | 81.59 | |
| | | | | | | | | |
| Distributed Floor Load (PSF) | | | | | 104 | | | |

| First Floor | Dimensions (In) | | | Number | Unit Weight* | Total Weight (Kips) | Center of Gravity (In) | Moment (In-Kips) |
|------------------------------|-----------------|--------|-------|--------|--------------|---------------------|------------------------|------------------|
| Item | X | Y | Z | | | | | |
| Slab | 160.00 | 160.00 | 2.38 | 1 | 0.0868 | 5.28 | 38.81 | 204.83 |
| Edge Columns | 8.25 | 4.25 | 37.63 | 4 | 0.0868 | 0.46 | 40.00 | 18.32 |
| Center Columns | 5.00 | 5.00 | 37.63 | 2 | 0.0868 | 0.16 | 40.00 | 6.53 |
| Spandrels | 143.50 | 4.25 | 2.63 | 2 | 0.0868 | 0.28 | 36.31 | 10.09 |
| Braces/Collars/Dampers | | | | 4 | 150.8 | 0.60 | 38.81 | 23.41 |
| Added Centerline Collars | | | | 2 | 20 | 0.04 | 43.50 | 1.74 |
| Lead Ingots | | | | 192 | 66 | 12.67 | 43.00 | 544.90 |
| Pads/Mounts for Ingots | | | | 48 | 12.9 | 0.62 | 43.00 | 26.63 |
| | | | | | | | | |
| Total Story Weight | | | | | | 20.11 | | 836.45 |
| Story Center of Gravity | | | | | | | 41.59 | |
| | | | | | | | | |
| Distributed Floor Load (PSF) | | | | | 104 | | | |

*Concrete Unit Weight in PCI. Lead Ingot Weight in Pounds per Ingot. Distributed Floor Load Comprised of Slab and Lead Ingot Weights.

Table A.5 Model Floor Weights and Centers of Gravity.

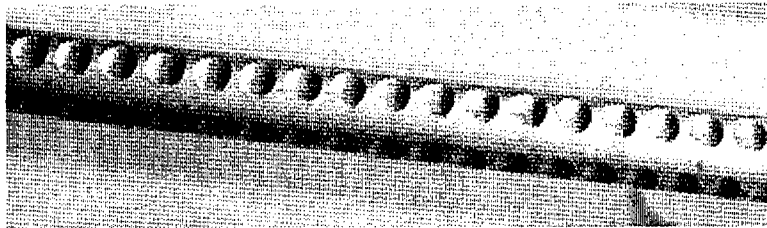


Figure A.1 Deformed Wire Used as Reinforcement

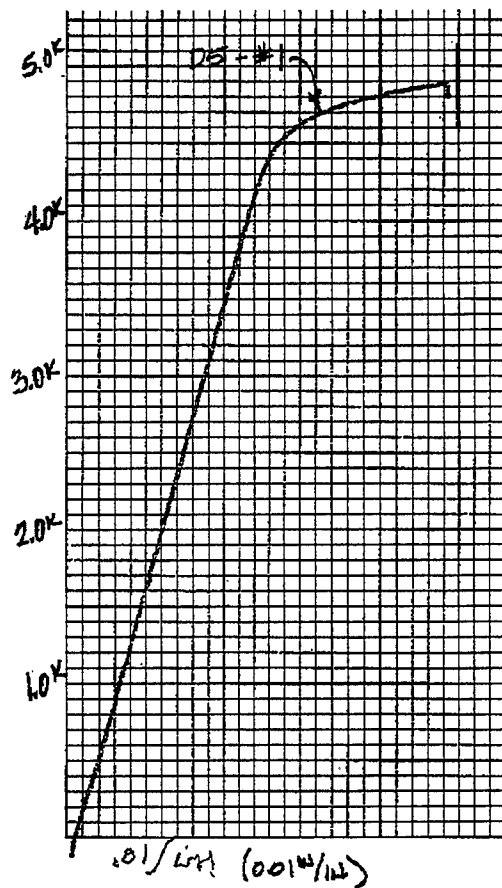


Figure A.2 Pre-Annealing Load-Strain Curve for D5 Bar

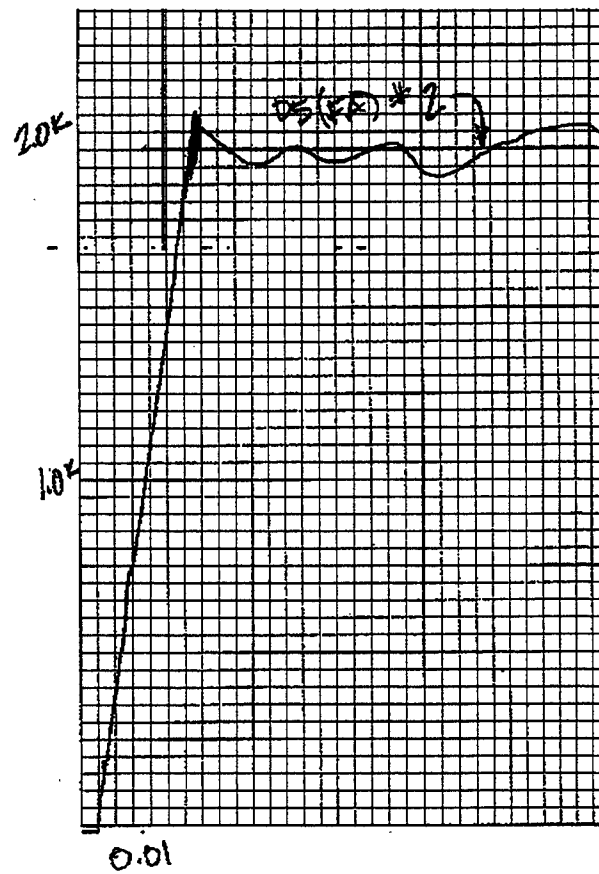


Figure A.3 Post-Annealing Load-Strain Curve for D5 Bar

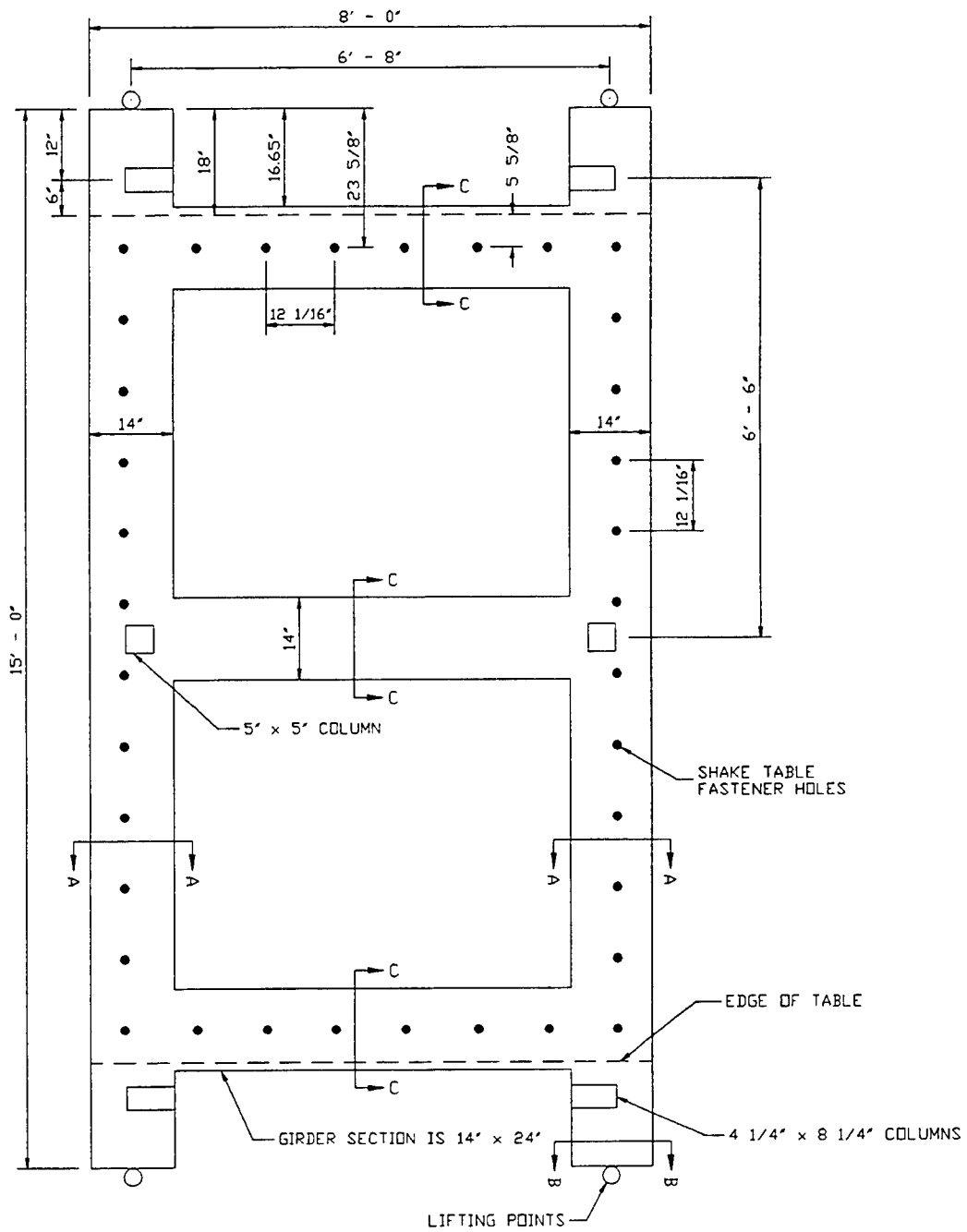


Figure A.4 Plan View of Base Girder

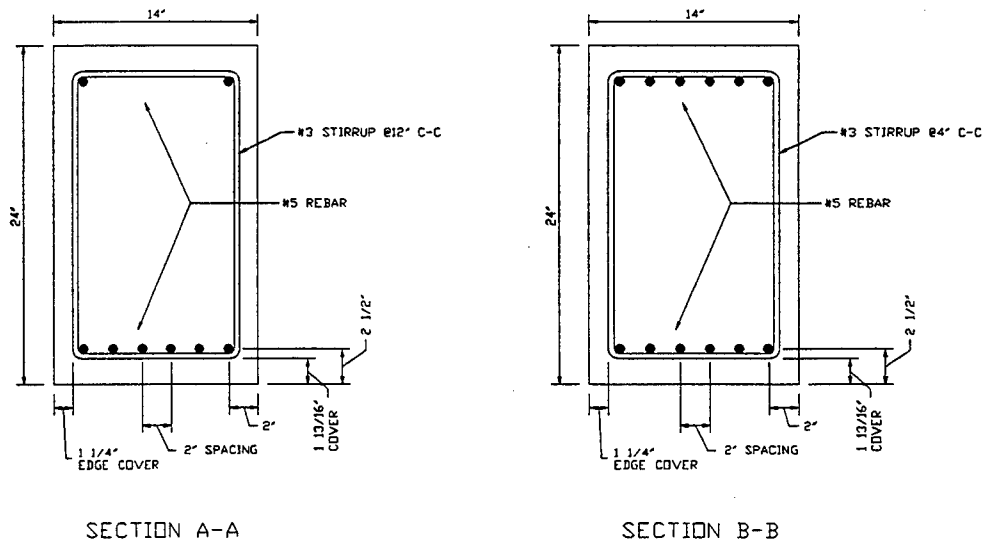


Figure A.5 Cross-Sections of Primary Base Girder Members

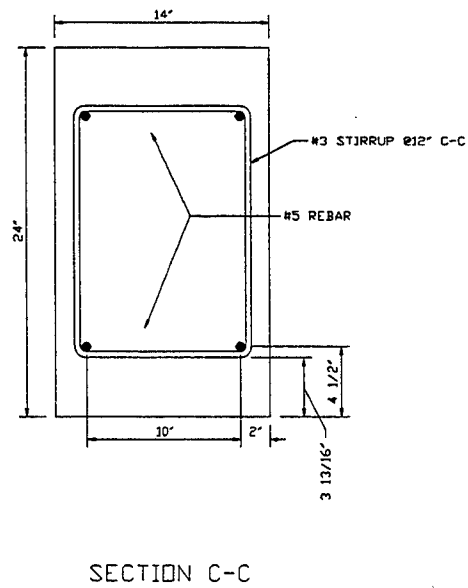


Figure A.6 Cross-Section of Lateral Base Girder Members

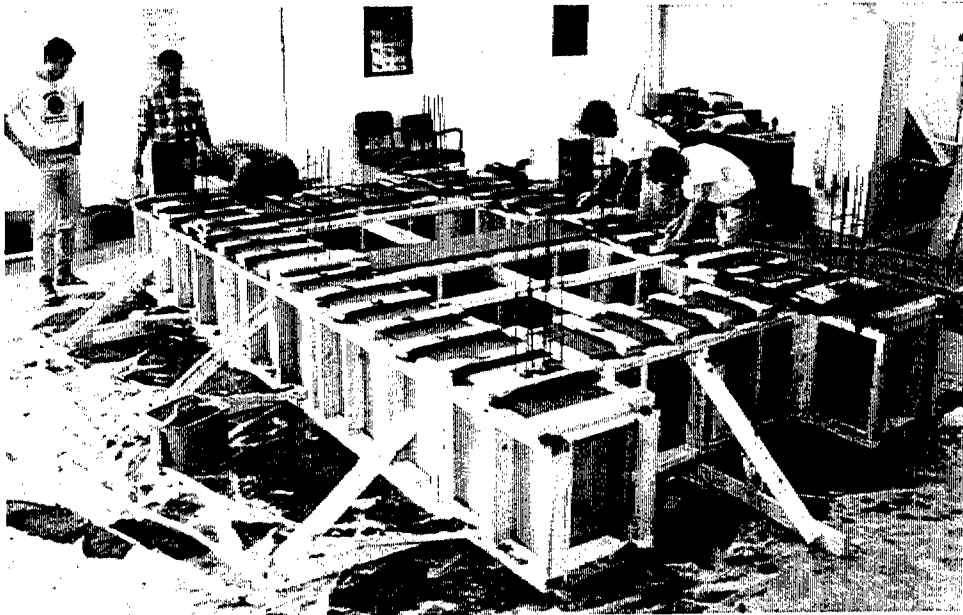


Figure A.7 Casting of Base Girder

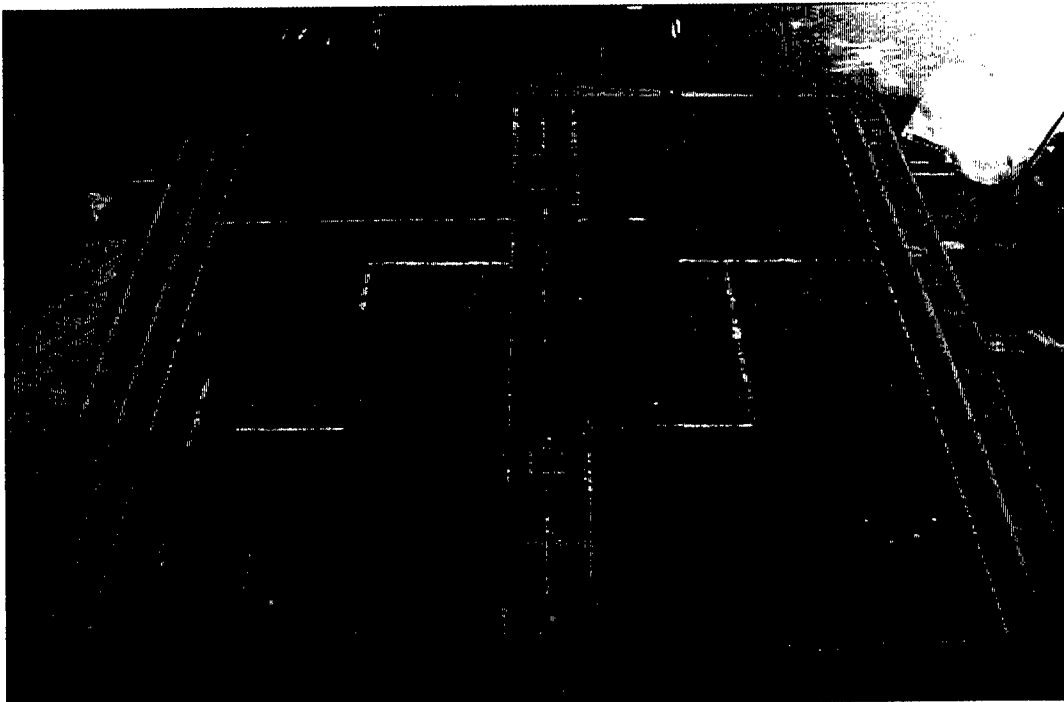


Figure A.8 Slab Formwork and Reinforcement

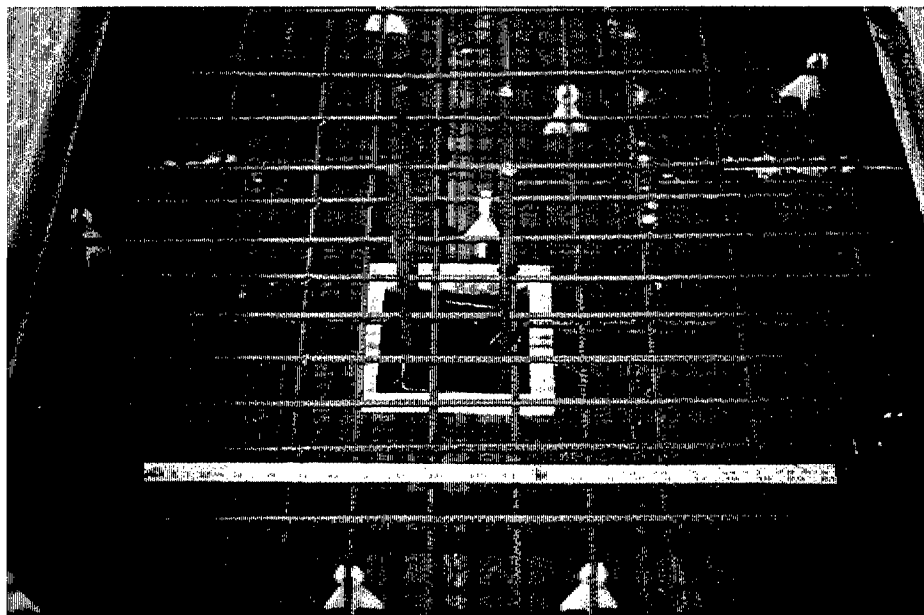


Figure A.9 Interior Column and Slab Joint Reinforcement

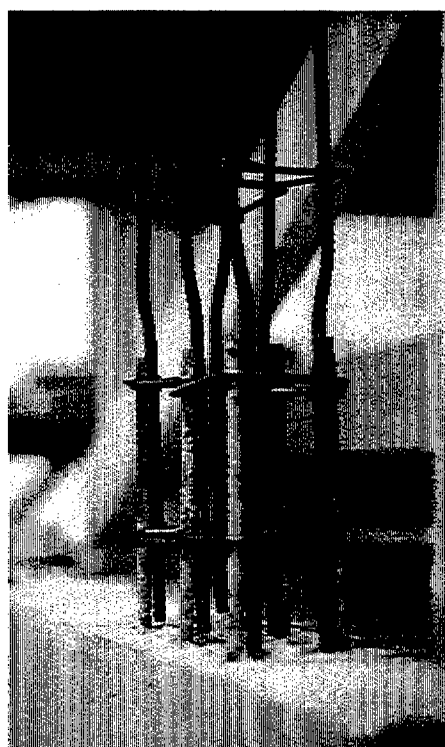


Figure A.10 Exterior Column Reinforcement

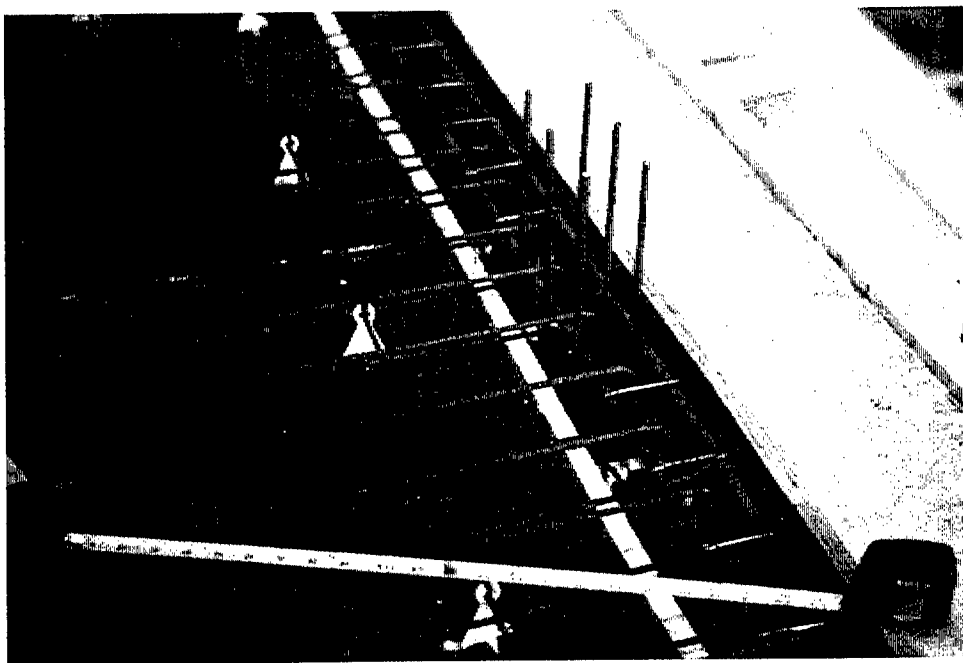


Figure A.11 Slab-Spandrel-Exterior Column Joint Reinforcement

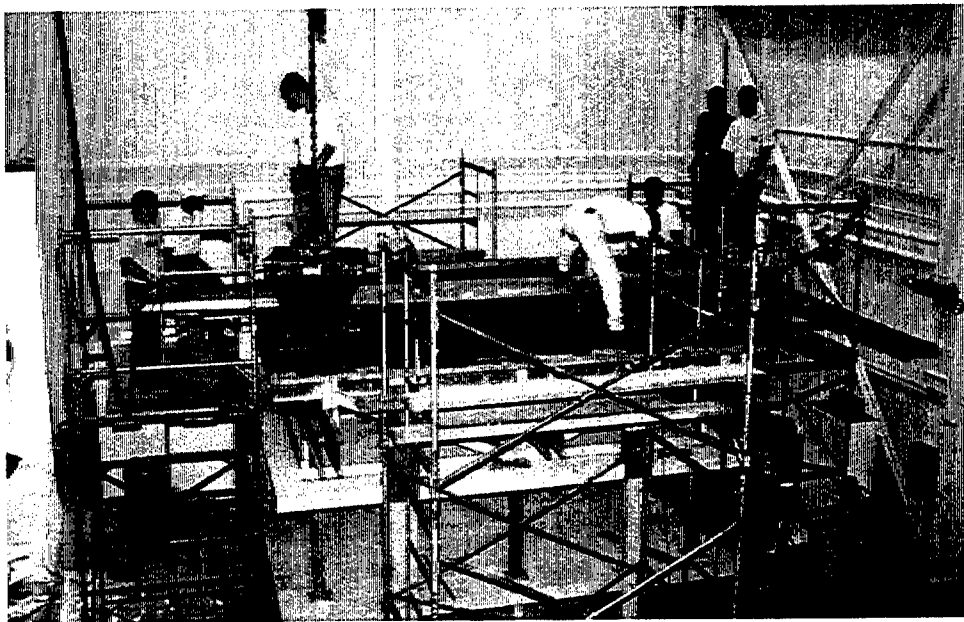


Figure A.12 Casting of Third Story of Model, Upper View

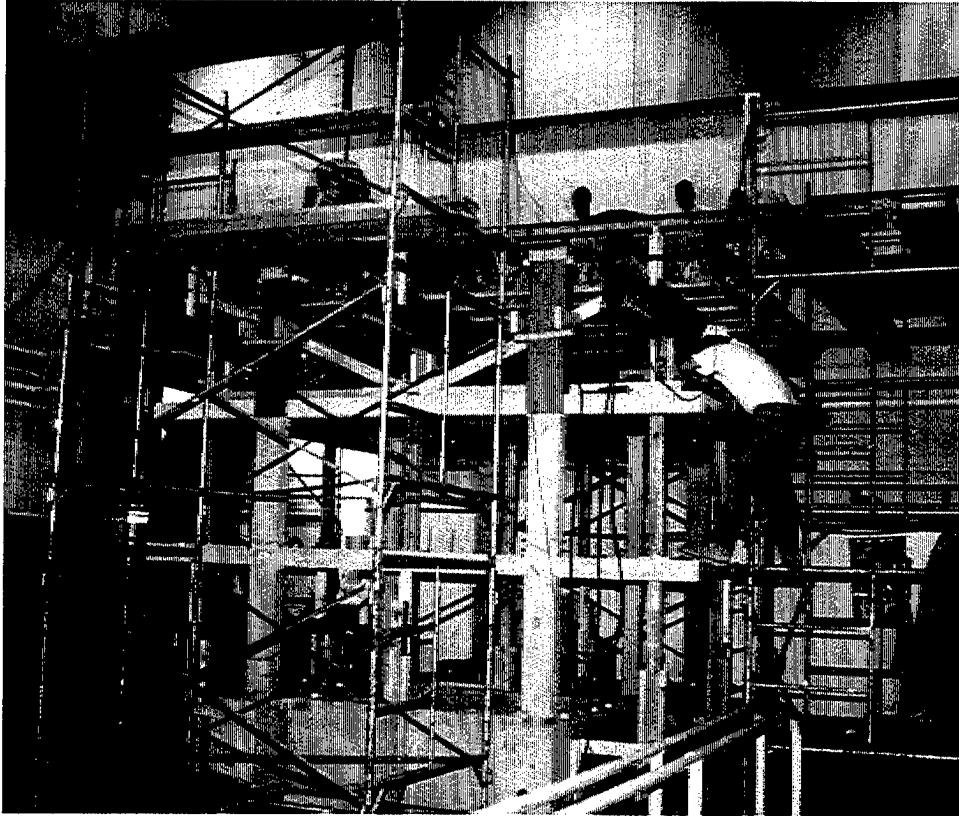


Figure A.13 Casting of Third Story of Model, Lower View

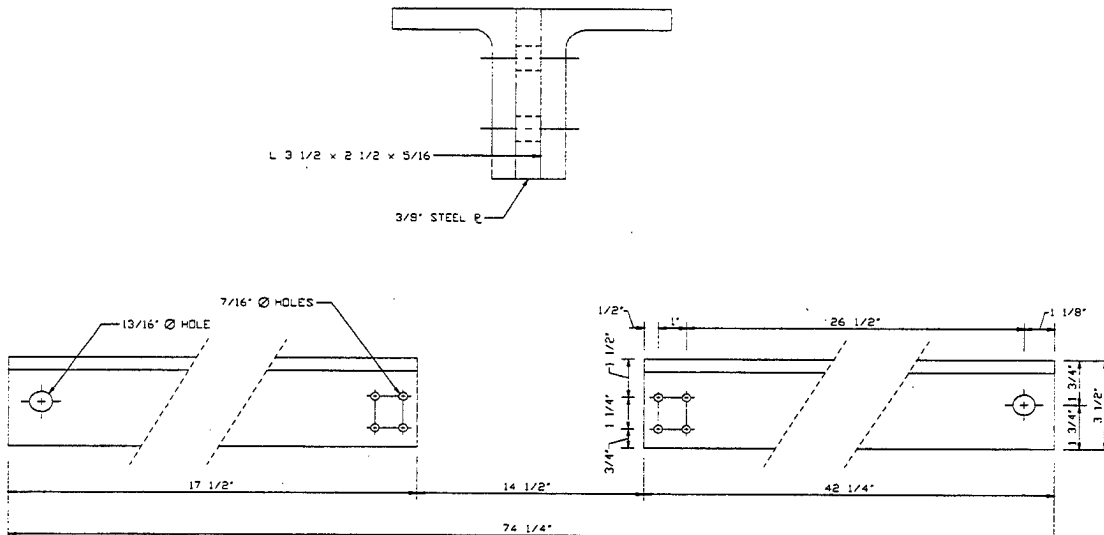


Figure A.14 Diagonal Brace Details

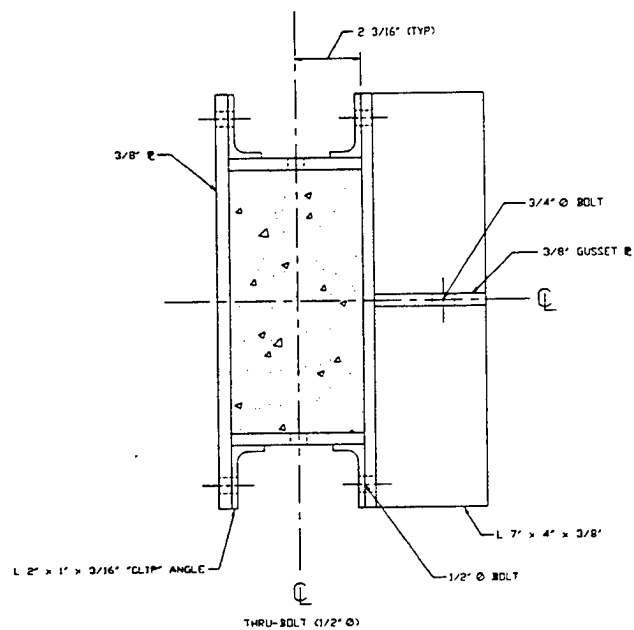
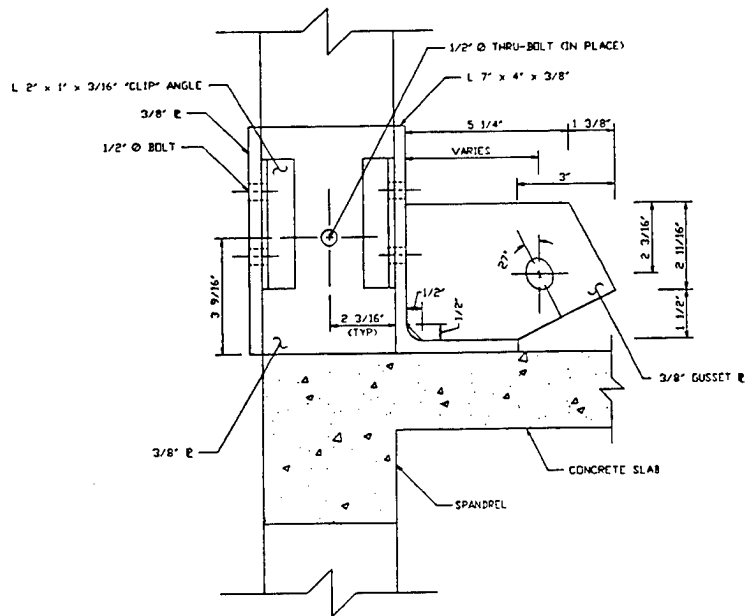


Figure A.15 Typical Exterior Column Collar Details

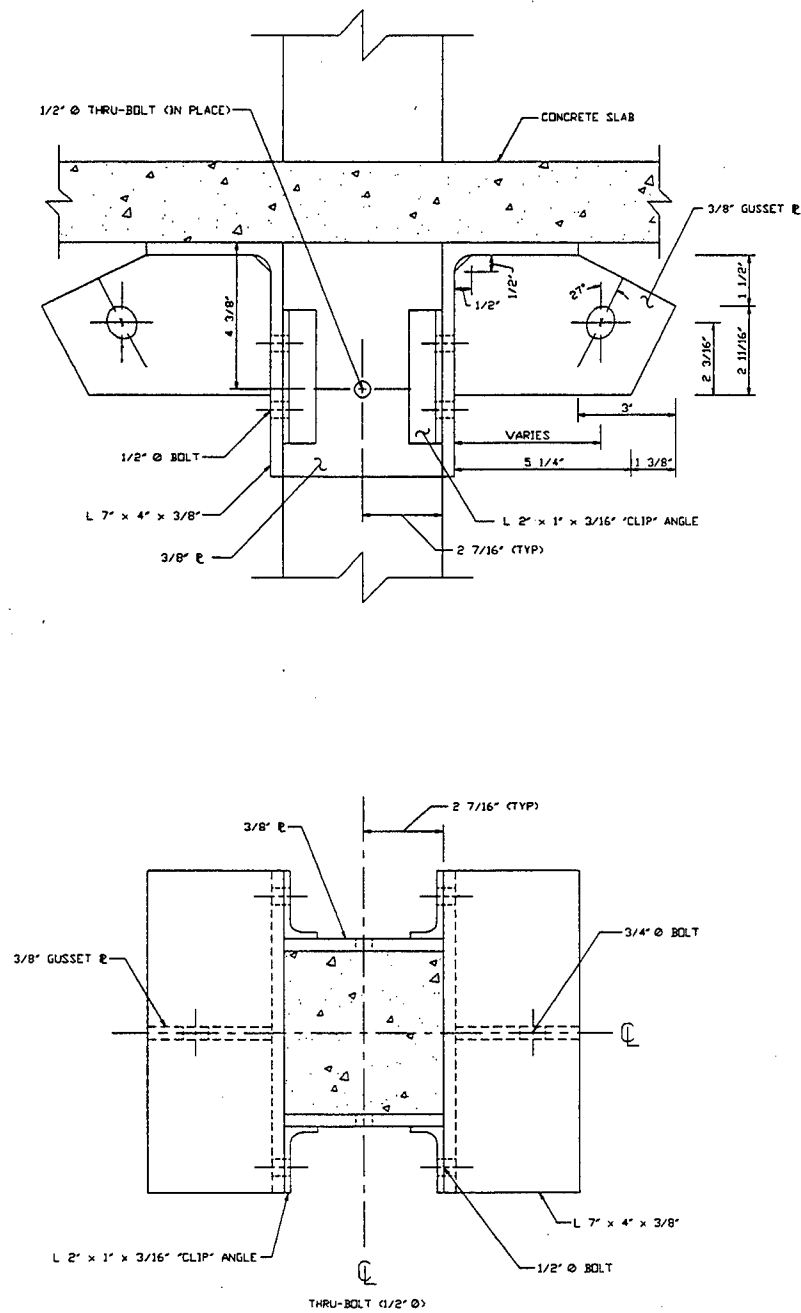


Figure A.16 Typical Interior Column Collar Details

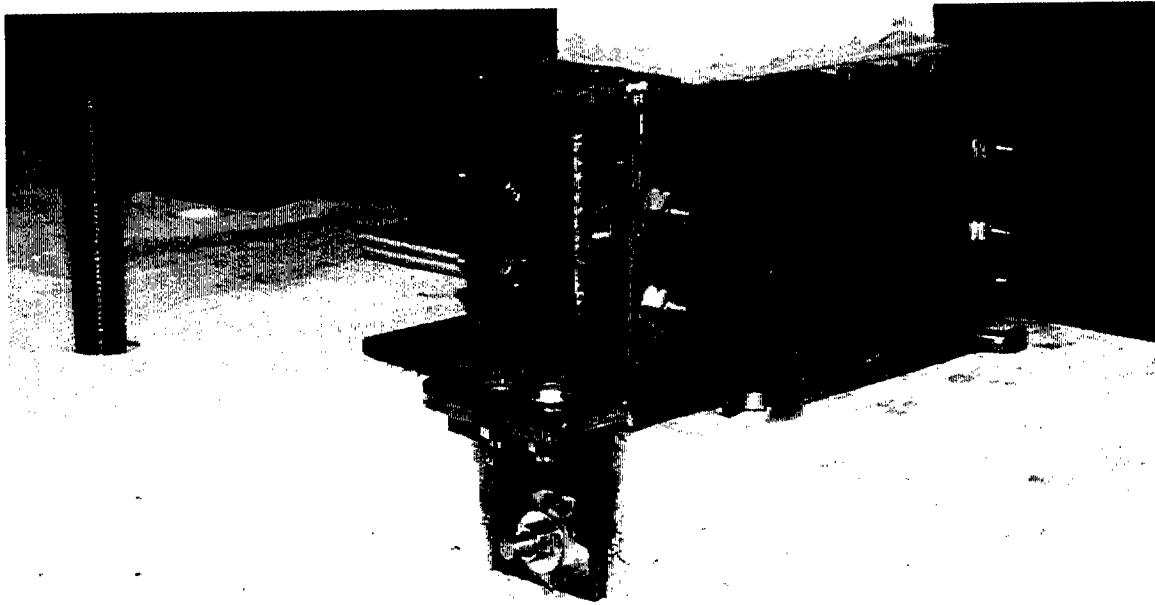


Figure A.17 Collar on First Floor Exterior Column

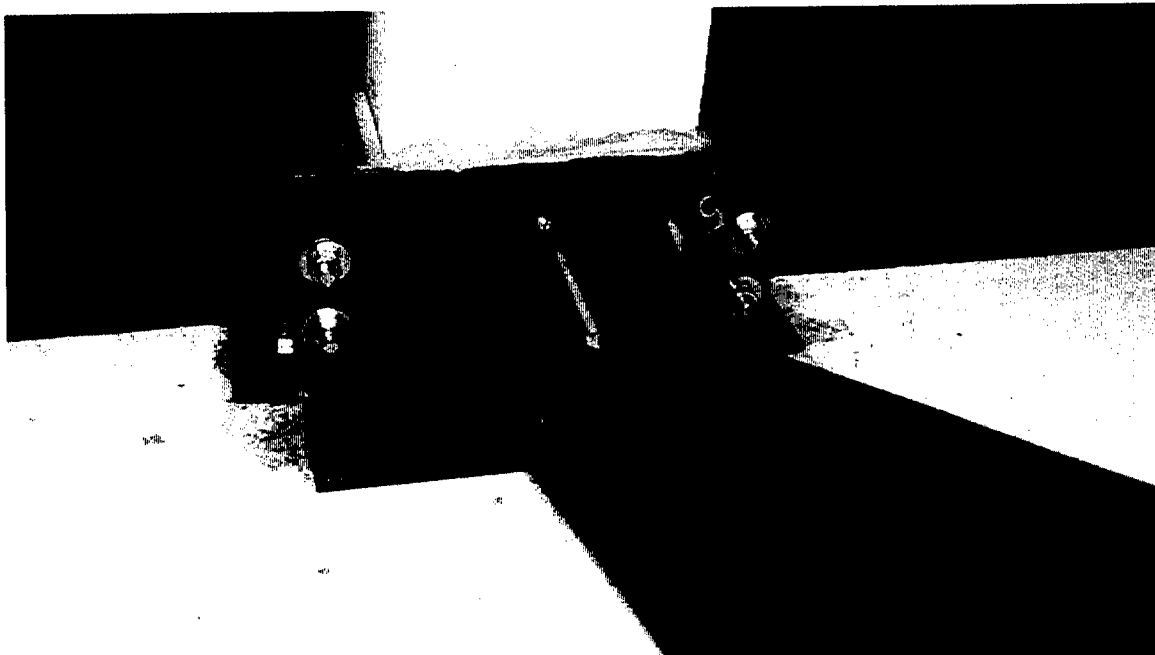


Figure A.18 Collar on Second Floor Exterior Column

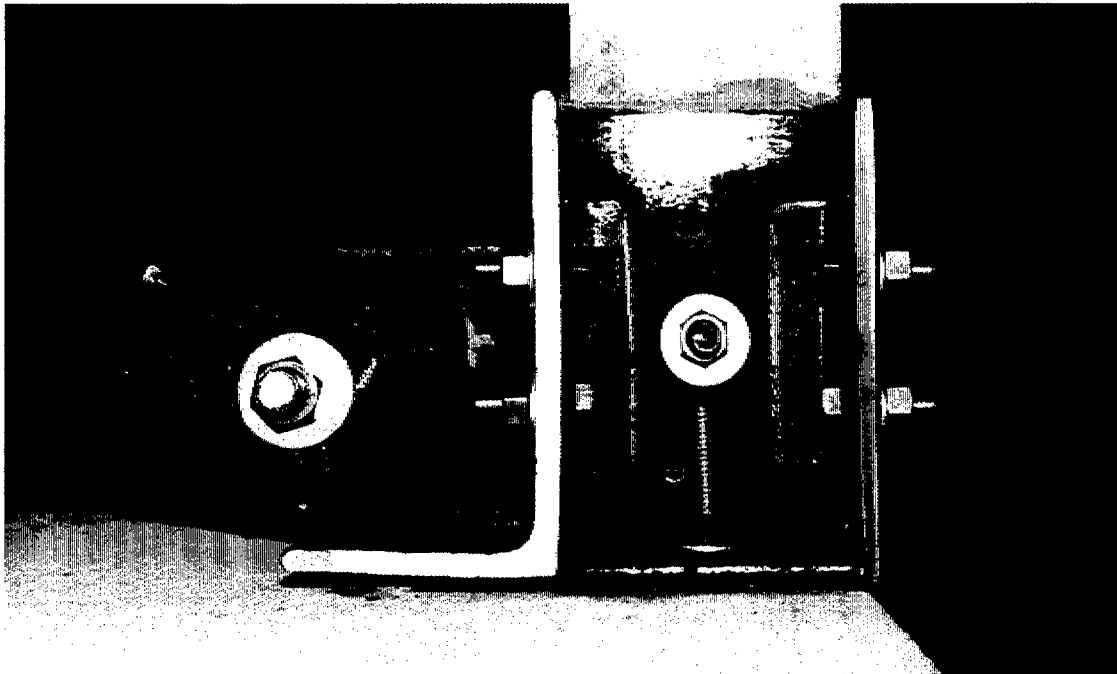


Figure A.19 Side View of Collar on Second Floor Exterior Column

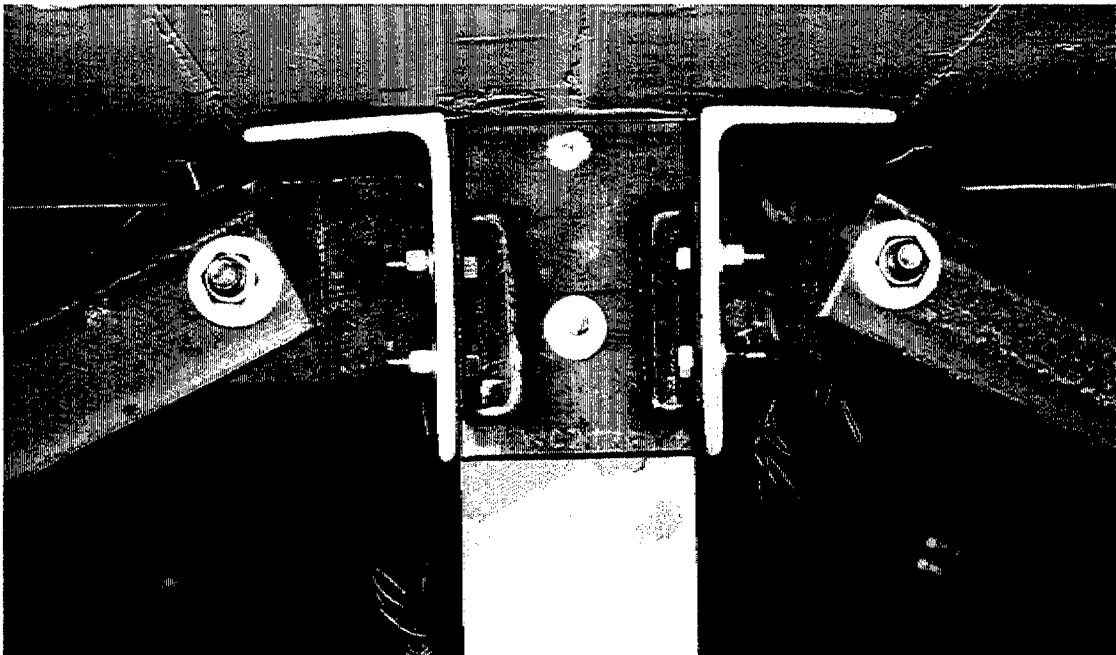


Figure A.20 Side View of Collar on Second Floor Interior Column

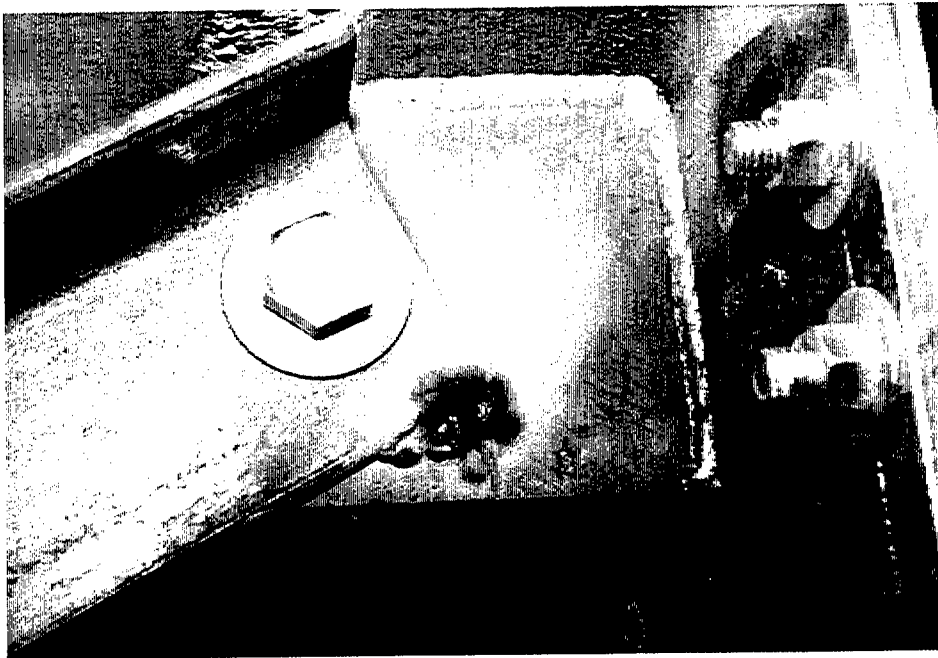


Figure A.21 Typical Spot-Weld of Brace to Collar

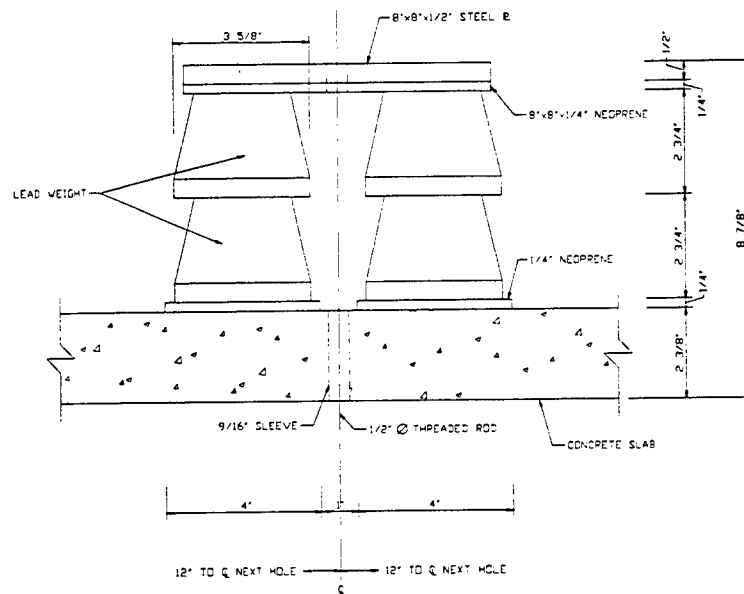


Figure A.22 Typical Lead Weight Arrangement

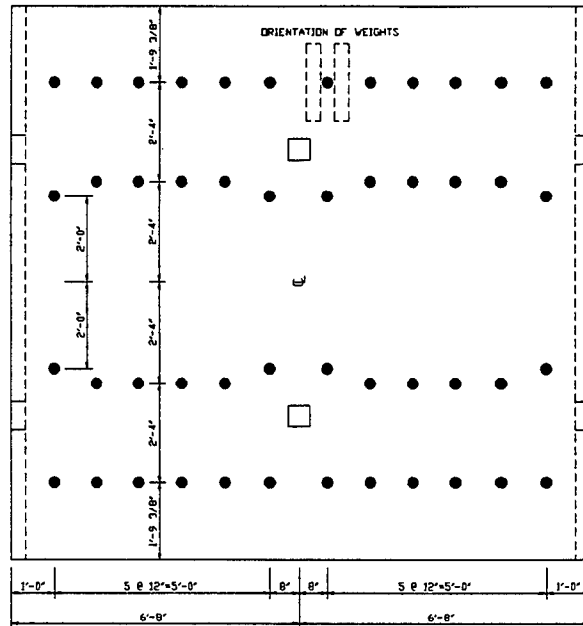


Figure A.23 Lead Weight Locations, First and Second Floor Slabs

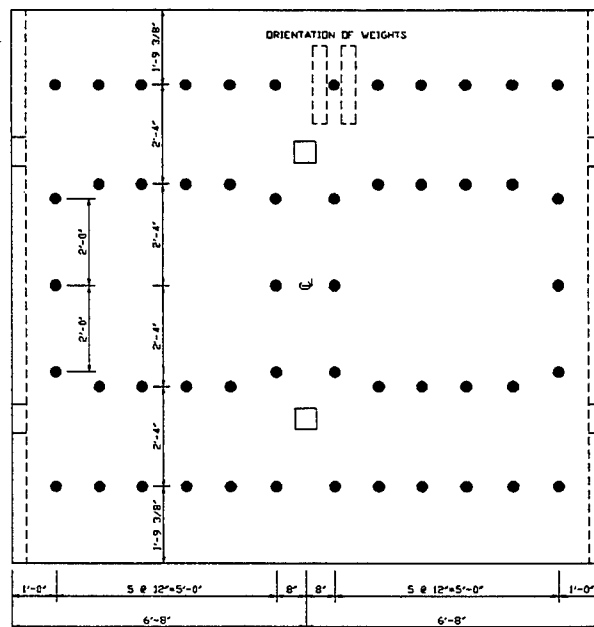


Figure A.24 Lead Weight Locations, Third Floor (Roof) Slab

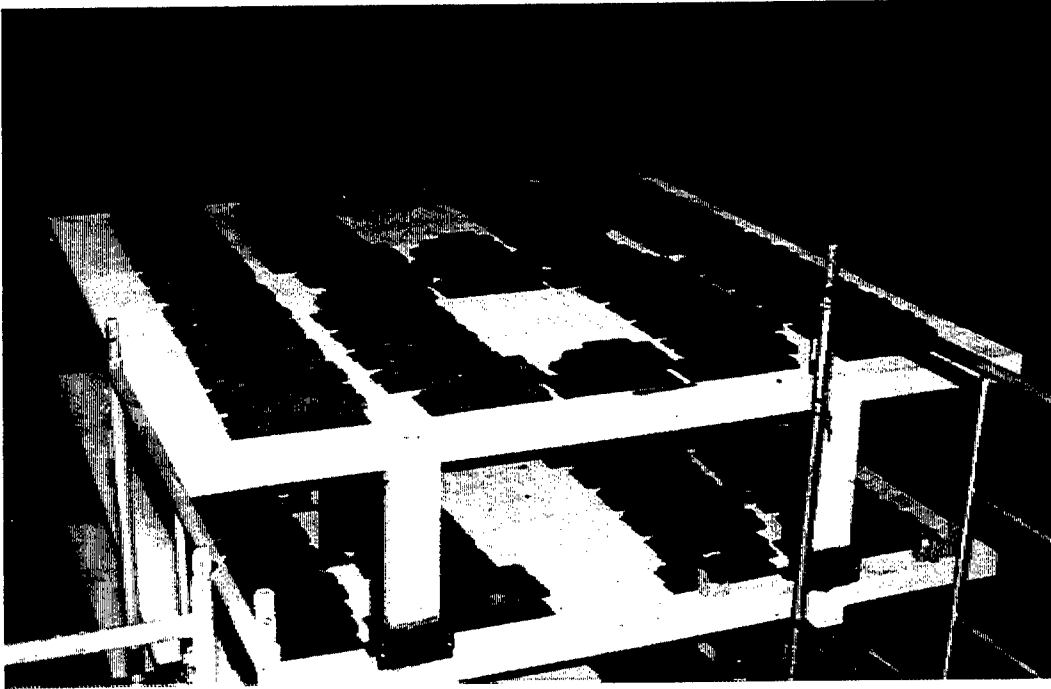


Figure A.25 Lead Weight Configuration, Floors 2 and 3

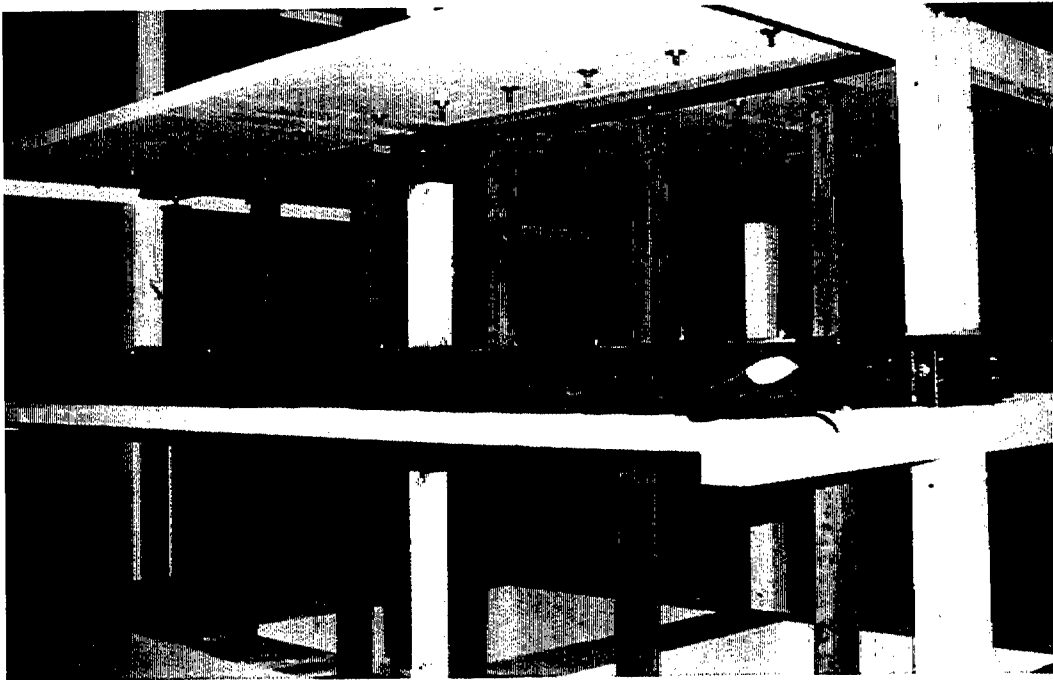


Figure A.26 Lead Weight Configuration, Floors 1 and 2 (Shoring in Place)



Figure A.27 Typical Lead Weight Stacks, Side View

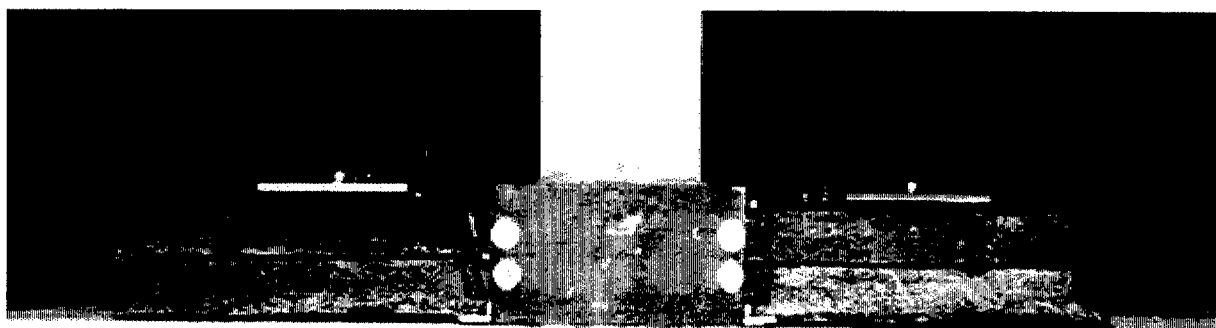


Figure A.28 Typical Lead Weight Stacks, End View

APPENDIX B

SHAKING TABLE CHARACTERISTICS, INSTRUMENTATION, AND DATA DESCRIPTIONS

This appendix briefly details the physical characteristics of the U.S. Army Construction Engineering Research Laboratories' (USACERL) shaking table, presents the instrumentation plan for the earthquake simulation testing, and describes the instrumentation systems used in the tests. Section B.1 describes the shaking table's physical characteristics, basic performance envelope, and electronic control systems. Section B.2 outlines the instrumentation used in the project. Accelerometers, variable resistance displacement transducers, linear variable displacement transducers, strain gages, and thermocouples were used to record information on the performance of the model. These transducers are described, and their locations on the models are shown.

B.1. USACERL Shaking Table

(a) General Description

The USACERL shaking table, or Biaxial Shock Test Machine (BSTM), was constructed by the U.S. Army in 1971 to support research for the SAFEGUARD antiballistic missile system development. This research required the unique operating characteristics of high frequency and high acceleration for payloads weighing up to 12,000 lb. In 1996, a complete "triaxial" upgrade of the BSTM was completed. In its new configuration, the shaking table system has been improved in a number of major areas. This description summarizes the capabilities of the original BSTM configuration, which was used in this project.

A plan view of the BSTM is shown in Figure B.1. The BSTM had controlled motion capability for its vertical axis and one horizontal axis. The biaxial motion control required that five degrees of freedom (DOFs) be controlled: translations for each of the two axes of motion, roll, pitch, and yaw. The sixth DOF, lateral translation, was controlled passively by spherical hydraulic bearings mounted between

the platform and the sidewalls of the pit for the platform. For the testing in this project, no vertical motions were input. All earthquake simulations were uniaxial.

The BSTM platform is a welded cellular aluminum structure measuring 12 ft x 12 ft in plan (Figure B.1). Its relatively light weight of 12,000 lb and its inherent structural stiffness, combined with large actuator capacities, accommodate controlled frequencies of 0-200 hertz (Hz) with its "rated" payload of 12,000 lb. At this rated payload, peak controlled accelerations of 30.0 g, vertical, and 20.0 g, horizontal, are attainable. For test payloads weighing more than the rated 12,000 lb, peak attainable accelerations are commensurately smaller. Peak attainable actuator velocities exceed 30 inches per second (ips). Previous testing experience indicated that motions with peak accelerations exceeding 2.0 g for a 60,000 payload were attainable, indicating that no problems in generating the required seismic simulations would be encountered.

Peak-to-peak displacement capabilities are 2-¾", vertical, and 5-½", horizontal. The nine BSTM vertical actuators can develop a total maximum thrust of 810 kips, while the six horizontal actuators can develop a total maximum thrust of 450 kips. Hydraulic power was provided by a hydraulic power supply operating at 3,000 psi. An 1,800 gallon accumulator system provided a 10-12 second surge capacity for maximum excitation levels.

Separate reinforced concrete vertical and horizontal foundations accommodate all reactions. Their combined weight is approximately 4,000 kips. The separate foundations minimize cross-coupling between vertical and horizontal reaction forces.

(b) BSTM Control System

The BSTM control system is a hybrid digital-analog system. The analog hardware directly controlled the hydraulic system, while the digital hardware acted as a user interface. Analog-to-digital and digital-to-analog converter systems linked the two.

The analog system directly controlled each actuator separately with separate closed-loop control circuits consisting of three integrated feedback loops per actuator. The control loops for all 15 actuators were interconnected, permitting active control of the five table DOF. Roll, pitch, and yaw compensations were added algebraically to the average horizontal and vertical commands to ensure biaxial performance. Several compensation functions were also provided: actuator force balancing, actuator overshoot and ringing, oil column spring-mass characteristics stabilization, test specimen center of gravity overturning

compensation, and horizontal-vertical displacement cross-coupling compensation.

A Data Translation model DT2831-G 16-channel digital data acquisition board, installed in an 80386-based microcomputer and operated in the digital-to-analog mode, was used to provide the analog drive signal to the BSTM for table control.

B.2 Instrumentation

Instrumentation was provided to measure displacements and accelerations of the shaking table platform, base girder, and each of the floor slabs; all viscoelastic damper (VED) displacements and forces; temperature in two VEDs; and key slab and column reinforcement strains.

A total of 76 channels of data was acquired for each seismic simulation in which the VED were installed on the model. Table B.1 lists the individual data channels. Channels 1-15 recorded accelerations of the shaking table platform, base girder, and floor slabs; channels 16-27 recorded their displacements. Channels 28-39 recorded VED displacements; channels 40-51 recorded VED loads. Channels 52-74 recorded reinforcement strains. Channels 75 and 76 recorded temperatures in two VEDs. When seismic simulations for the structure without VEDs installed were conducted, channels 28-51 and 75-76 were inactive.

Figures B.2 - B.8 show the locations and, where appropriate, the directions of measured displacement or acceleration, for all transducers.

(a) Accelerometers

Endevco model 7290-10 and 7290-30 accelerometers were used to measure accelerations. These accelerometers employ variable capacitance microsensors with a frequency response of 0- 500Hz. The accelerometers were connected to Endevco model 4476.2 and 4476.2A signal conditioners, which provided power, balancing, and signal amplification. Acceleration measurement ranges for the various sensors differed. Their acceleration measurement ranges varied, but checks of all data recorded indicated the ranges were satisfactory. All accelerometers were mounted on aluminum blocks that had been epoxied to the model or the shaking table. Sensors were typically mounted on the top horizontal surface of the elements for which accelerations were being measured.

One accelerometer, ATX1, was mounted on the north-south centerline of the shaking table

platform (Figure B.2). This sensor served two primary purposes. First, it confirmed the accuracy of the accelerometer array inside the shaking table platform that was used to control the BSTM. Second, in conjunction with accelerometers AGX1 and AGX2 (Figure B.3), it confirmed that the base girder did not slip on the shaking table platform. Checks of data recorded with these gages confirmed both the accuracy of the internal accelerometer array and the lack of base girder slippage.

Accelerometers AGX1 and AGX2 were also used to confirm that all input motions were purely translational, with no directly-induced torsion at the base. Accelerometers AGZ1 and AGZ2 (Figure B.3) measured vertical accelerations at the base girder level, to confirm that input motions did not include vertical components due to any rocking of the shaking table platform.

As shown in Figures B.4 - B.6, two accelerometers on each of the three floor slab levels measured north-south accelerations; the dual sensors on each floor provided redundancy and a means of checking possible torsional motions in the model. One accelerometer was also mounted at the top of each of the two stationary reaction frames to measure reaction frame accelerations (Figure B.7). The information from these sensors was used to determine whether the reaction frames were moving sufficiently to negate the assumption that they were "stationary." The assumption allowed the use of the reaction frames as fixed points from which absolute displacements of the model could be measured.

(b) Absolute Displacement Transducers

Celesco model PT101-10 and PT101-60A variable resistance displacement transducers were used to measure the absolute displacement of the shaking table and various locations on the model that were referenced to the shaking table foundation floor. The Celesco unit employs a spring-loaded precision rotary potentiometer with flexible steel wire cable wrapped around the potentiometer shaft. The other end of the cable is attached to the point where displacement is to be measured. When displacement occurs, the cable motion rotates the shaft of the potentiometer, causing a change in electrical resistance that is proportional to displacement. Transducers were connected to Endevco model 4471.3 signal conditioners, which provided DC power and electrical balancing, but no signal amplification.

The transducers were mounted on large steel reference frames that were placed on the shaking table foundation; transducer mounts were bolted to the reaction frame members. Transducer sensing elements were attached to the model and the shaking table using stranded steel extension wires; the wires were typically connected to rigid hooks that were epoxied on the model. Measurement locations are shown in

Figures B.3- B.6.

For each slab displacement gage, the mount was located at slab mid-depth. At the base girder level, three displacements were measured: the north-south displacements of each of its legs, and its east-west displacement near its northwest corner. These displacement measurements provided another check on the degree of torsional motion that was input at the base level. For each of the floor slabs, three displacements were measured: the north-south displacements of each of the floor slab at the main column lines, and the east-west displacement at the northwest corner of the slab. These displacement measurements provided checks on the degree of torsional motion that occurred in each of the floor slabs, in addition to providing redundancy on the measurement of north-south displacements.

Because of damage to some of the transducers that was caused by workers becoming entangled in the gage wires, several adjustments to the gage scheme were required during the test series. The gage at DGX2 was damaged following simulation T021DS. The gage at DGY1 was moved to the DGX2 location, so no further DGY1 measurements were possible. Following simulation E250DL, the gage at DGX2 was again damaged. The gage at D1Y1 was moved to the DGX2 location, so no further D1Y1 measurements were possible. Following simulation E125N, the gage at D1X2 was damaged. At that time, it was decided to rely solely on gage D1X1 for north-south translation measurements. From that point, there were no averaged first floor translations, and checks on torsion were based more heavily on upper floor measurements.

(c) Linear Variable Displacement Transducers (LVDTs)

Trans-Tek model 0245-0000D90 LVDTs and Hewlett Packard model 7DCDT-3000 DC LVDTs were used to measure relative displacements across all VEDs. These transducers are DC powered units that provided electrically isolated output signals. The LVDTs were connected to Endevco model 4471.1A signal conditioners, which provide DC power but no signal amplification or electrical balancing. The LVDTs were electrically balanced by adjusting the physical position of their sensing cores to produce zero output signal as the transducers were installed on the diagonal braces.

Mounts for the LVDTs were epoxied to the braces that contained the VEDs. The mounts were located 2-1/2" from each end of each VED, so that displacement measurements were effectively entirely composed of VED displacements, with no measurable brace strain added.

(d) Strain Gages

Electrical resistance strain gages were installed on all of the diagonal VED braces and at several locations on the steel reinforcement that was embedded in the concrete columns and floor slabs.

For measuring VED loads, each VED brace had a four strain gage bridge consisting of Measurements Group type CEA-06-250U-350 strain gages. These gages have a constantan alloy sensing grid with complete polyamide encapsulation that is temperature compensated for steel. The gage sensing grid is 0.25" long by 0.18" wide.

Each brace was composed of two angle sections placed back to back (Figure 2.26). On the back face of each angle, one gage was mounted parallel to the longitudinal axis of the brace, while another gage was mounted perpendicular to the longitudinal axis of the brace. The four gages on the two angle sections were connected to form a single Wheatstone bridge circuit. Each bridge circuit was connected to a Vishay model 2120 signal conditioner to provide power, balancing, and signal amplification. Prior to being placed in the model, each double-angle brace was calibrated as a load transducer in a 50 kip load frame. As loads were applied to the brace, the output of the bridge circuit was used to derive a brace load calibration factor in pounds/volt.

Selected steel reinforcing bars were instrumented with Measurements Group type CEA-06-125UN-350 strain gages with constantan alloy sensing grids, with complete polyamide encapsulation that is temperature compensated for steel. The gage sensing grid is 0.125" long by 0.100" wide. Each gage was connected to a Vishay model 2120 signal conditioner to provide power, balancing, and signal amplification. In this configuration, the strain gage formed one arm of a Wheatstone bridge, with the remaining three arms consisting of precision resistors in the signal conditioner equipment.

The reinforcement strain gages were mounted on a number of slab and column reinforcement bars. The locations of the slab reinforcement strain gages were selected to provide information concerning the variation of slab flexural strain with transverse distance from the longitudinal column lines; this variation can assist in the determination of the "effective width" of the slab in flexural calculations. Locations of slab reinforcement gages are shown in Figures B.9 - B.11. The gages were all located on top longitudinal bars. The locations of column reinforcement strain gages were selected for the dual purpose of tracking flexural strains and reinforcement slippage in bar lap splice zones. Gages on the column reinforcement were mounted at locations of 1" above the top slab (or base girder) surfaces and 1" below the bottom slab surfaces. Locations of these gages are shown in Figure B.12. Only those gages that actively recorded data

are shown in the figures.

Each reinforcing bar that was gaged was ground to remove cold-rolled deformations and, to the extent possible, flatten the curvature of the round wire circumference. Following gage attachment, an epoxy coating was applied to protect each gage from later concrete casting activity. As will be observed in the test results, many of the strain gages were ineffective during the testing. Several gages apparently did not bond well to the reinforcement. It is speculated that the small wire diameters and accompanying sharp wire circumference curvatures, combined with the gage backing stiffness, prevented adequate bond. In at least two instances, researchers accidentally broke off the gage lead wires when they were stripping the concrete forms; it was not possible to clear enough concrete away from the broken leads to accommodate reattachment efforts.

(e) Thermocouples

Two thermocouples were mounted by 3M Corporation in two of the VEDs. These thermocouples were intended to measure temperature changes in the viscoelastic material. The stiffness and damping properties of the material are temperature-dependent, and the energy dissipation that occurs during shearing of the material causes it to get warmer. The thermocouples were inoperative and never provided any data.

(f) Data Acquisition and Shaking Table Control

Figure B.13 is a schematic block diagram of the instrumentation, data acquisition, and test control systems. The 76 transducer channels were recorded using a digital data acquisition system. Transducer output signals were connected to Data Translation model DT2831-G 16 channel digital data acquisition boards installed in 80386-base microcomputers. The data acquisition boards were all programmed for the same digital sampling rate (300 Hz) and number of sampling points. A common external trigger signal was used to initiate data recording on all of the data acquisition boards simultaneously, so that a common time reference was established for all test data. A separate DT2831-G board operated in the digital-to-analog mode was used to provide the analog drive signal to the BSTM for test control during the seismic tests.

| Channel Number | Gage Number | Quantity | Direction | Gage Location |
|----------------|-------------|--------------|-----------|---|
| 1 | AFM1 | Acceleration | N-S Axis | 1st Floor, North Reference Frame |
| 2 | AFM2 | Acceleration | E-W Axis | 1st Floor, West Reference Frame |
| 3 | ATX1 | Acceleration | N-S Axis | Table Surface, Center Line |
| 4 | AGX1 | Acceleration | N-S Axis | Base Girder, West Column Line |
| 5 | AGX2 | Acceleration | N-S Axis | Base Girder, East Column Line |
| 6 | AGZ1 | Acceleration | Vertical | Base Girder, North Center |
| 7 | AGZ2 | Acceleration | Vertical | Base Girder, South Center |
| 8 | A1X1 | Acceleration | N-S Axis | 1st Floor, West Side |
| 9 | A1X2 | Acceleration | N-S Axis | 1st Floor, East Side |
| 10 | A2X1 | Acceleration | N-S Axis | 2nd Floor, West Side |
| 11 | A2X2 | Acceleration | N-S Axis | 2nd Floor, East Side |
| 12 | A3X1 | Acceleration | N-S Axis | 3rd Floor, West Side |
| 13 | A3X2 | Acceleration | N-S Axis | 3rd Floor, East Side |
| 14 | AFM3 | Acceleration | N-S Axis | 3rd Floor, North Reference Frame |
| 15 | AFM4 | Acceleration | E-W Axis | 3rd Floor, West Reference Frame |
| 16 | DGX1 | Displacement | N-S Axis | Base Girder-North Reference Frame, West Column Line |
| 17 | DGX2 | Displacement | N-S Axis | Base Girder-North Reference Frame, East Column Line |
| 18 | DGY1 | Displacement | E-W Axis | Base Girder-West Reference Frame |
| 19 | D1X1 | Displacement | N-S Axis | 1st Floor-North Reference Frame, West Column Line |
| 20 | D1X2 | Displacement | N-S Axis | 1st Floor-North Reference Frame, East Column Line |
| 21 | D1Y1 | Displacement | E-W Axis | 1st Floor-West Reference Frame |
| 22 | D2X1 | Displacement | N-S Axis | 2nd Floor-North Reference Frame, West Column Line |
| 23 | D2X2 | Displacement | N-S Axis | 2nd Floor-North Reference Frame, East Column Line |
| 24 | D2Y1 | Displacement | E-W Axis | 2nd Floor-West Reference Frame |
| 25 | D3X1 | Displacement | N-S Axis | 3rd Floor-North Reference Frame, West Column Line |
| 26 | D3X2 | Displacement | N-S Axis | 3rd Floor-North Reference Frame, East Column Line |
| 27 | D3Y1 | Displacement | E-W Axis | 3rd Floor-West Reference Frame |
| 28 | DSNW1 | Displacement | Damper | 1st Floor, Northwest Damper |
| 29 | DSNE1 | Displacement | Damper | 1st Floor, Northeast Damper |
| 30 | DSSW1 | Displacement | Damper | 1st Floor, Southwest Damper |
| 31 | DSSE1 | Displacement | Damper | 1st Floor, Southeast Damper |
| 32 | DSNW2 | Displacement | Damper | 2nd Floor, Northwest Damper |
| 33 | DSNE2 | Displacement | Damper | 2nd Floor, Northeast Damper |
| 34 | DSSW2 | Displacement | Damper | 2nd Floor, Southwest Damper |
| 35 | DSSE2 | Displacement | Damper | 2nd Floor, Southeast Damper |
| 36 | DSNW3 | Displacement | Damper | 3rd Floor, Northwest Damper |
| 37 | DSNE3 | Displacement | Damper | 3rd Floor, Northeast Damper |
| 38 | DSSW3 | Displacement | Damper | 3rd Floor, Southwest Damper |
| 39 | DSSE3 | Displacement | Damper | 3rd Floor, Southeast Damper |

Table B.1.a Instrumentation List for Model

| Channel Number | Gage Number | Quantity | Direction | Gage Location |
|----------------|-------------|---------------|-----------|---|
| 40 | SSNW1 | Strain (Load) | Strut | 1st Floor, Northwest Damper |
| 41 | SSNE1 | Strain (Load) | Strut | 1st Floor, Northeast Damper |
| 42 | SSNW2 | Strain (Load) | Strut | 1st Floor, Southwest Damper |
| 43 | SSNE2 | Strain (Load) | Strut | 1st Floor, Southeast Damper |
| 44 | SSSW3 | Strain (Load) | Strut | 2nd Floor, Northwest Damper |
| 45 | SSNE3 | Strain (Load) | Strut | 2nd Floor, Northeast Damper |
| 46 | SSSW1 | Strain (Load) | Strut | 2nd Floor, Southwest Damper |
| 47 | SSSE1 | Strain (Load) | Strut | 2nd Floor, Southeast Damper |
| 48 | SSSW2 | Strain (Load) | Strut | 3rd Floor, Northwest Damper |
| 49 | SSSE2 | Strain (Load) | Strut | 3rd Floor, Northeast Damper |
| 50 | SSNW3 | Strain (Load) | Strut | 3rd Floor, Southwest Damper |
| 51 | SSSE3 | Strain (Load) | Strut | 3rd Floor, Southeast Damper |
| 52 | SGZ1 | Rebar Strain | Column | 1st Floor, Northwest Column, Base, North Side |
| 53 | SGZ3 | Rebar Strain | Column | 1st Floor, Centerline Column, Base, North Side |
| 54 | SGZ4 | Rebar Strain | Column | 1st Floor, Centerline Column, Base, South Side |
| 55 | S1Z1 | Rebar Strain | Column | 1st Floor, Northwest Column, Top, North Side |
| 56 | S1Z2 | Rebar Strain | Column | 1st Floor, Northwest Column, Top, South Side |
| 57 | S1Z3 | Rebar Strain | Column | 1st Floor, Centerline Column, Top, North Side |
| 58 | S1Z5 | Rebar Strain | Column | 2nd Floor, Northwest Column, Base, North Side |
| 59 | S1Z6 | Rebar Strain | Column | 2nd Floor, Northwest Column, Base, South Side |
| 60 | S1Z7 | Rebar Strain | Column | 2nd Floor, Centerline Column, Base, North Side |
| 61 | S1Z8 | Rebar Strain | Column | 2nd Floor, Centerline Column, Base, South Side |
| 62 | S1X4 | Rebar Strain | Slab | 1st Floor, Northwest Column, Column Strip, Top Bar |
| 63 | S1X5 | Rebar Strain | Slab | 1st Floor, Centerline Column, Column Strip, Top Bar |
| 64 | S1X16 | Rebar Strain | Slab | 1st Floor, Centerline Column, Middle Strip, Top Bar |
| 65 | S1X11 | Rebar Strain | Slab | 1st Floor, Northwest Column, Column Strip, Top Bar |
| 66 | S1X12 | Rebar Strain | Slab | 1st Floor, Northwest Column, Column Strip, Top Bar |
| 67 | S1X13 | Rebar Strain | Slab | 1st Floor, Northwest Column, Middle Strip, Top Bar |
| 68 | S1X14 | Rebar Strain | Slab | 1st Floor, Centerline Column, Column Strip, Top Bar |
| 69 | S1X15 | Rebar Strain | Slab | 1st Floor, Centerline Column, Column Strip, Top Bar |
| 70 | S2Z2 | Rebar Strain | Column | 2nd Floor, Northwest Column, Top, South Side |
| 71 | S2Z3 | Rebar Strain | Column | 2nd Floor, Centerline Column, Top, North Side |
| 72 | S2X4 | Rebar Strain | Slab | 2nd Floor, Northwest Column, Column Strip, Top Bar |
| 73 | S2X5 | Rebar Strain | Slab | 2nd Floor, Centerline Column, Column Strip, Top Bar |
| 74 | S2X6 | Rebar Strain | Slab | 2nd Floor, Centerline Column, Column Strip, Top Bar |
| 75 | ThSW1 | Thermocouple | Damper | 1st Floor, Northwest Damper |
| 76 | ThSW2 | Thermocouple | Damper | 2nd Floor, Northwest Damper |

Table B.1.b Instrumentation List for Model, Continued

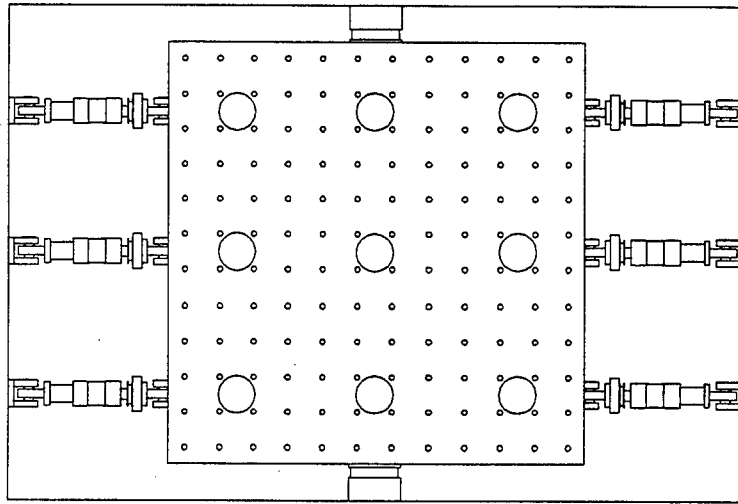


Figure B.1 Plan View of USACERL Shaking Table

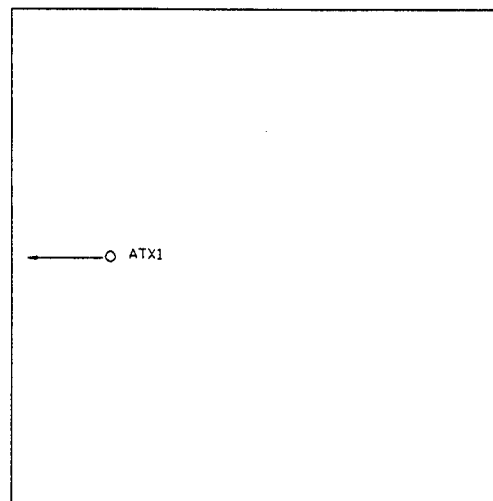


Figure B.2 Shaking Table Acceleration Transducer

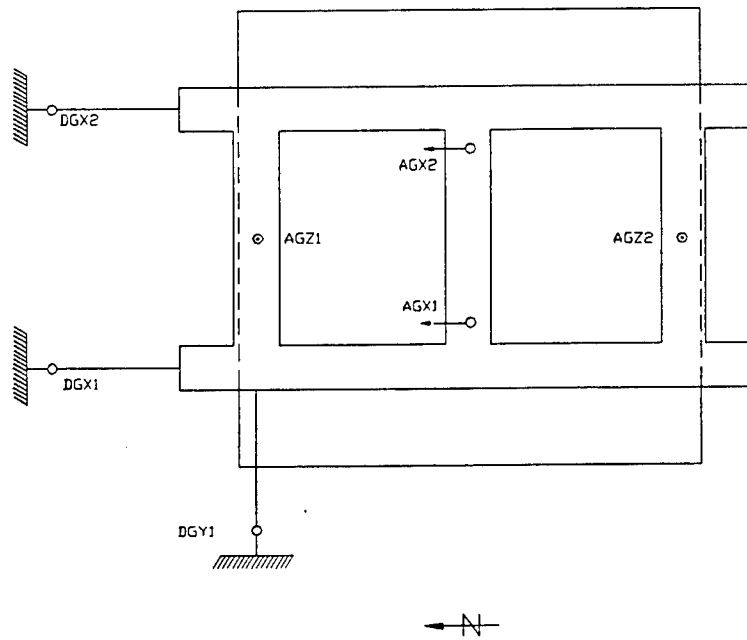


Figure B.3 Base Girder Displacement and Acceleration Transducers

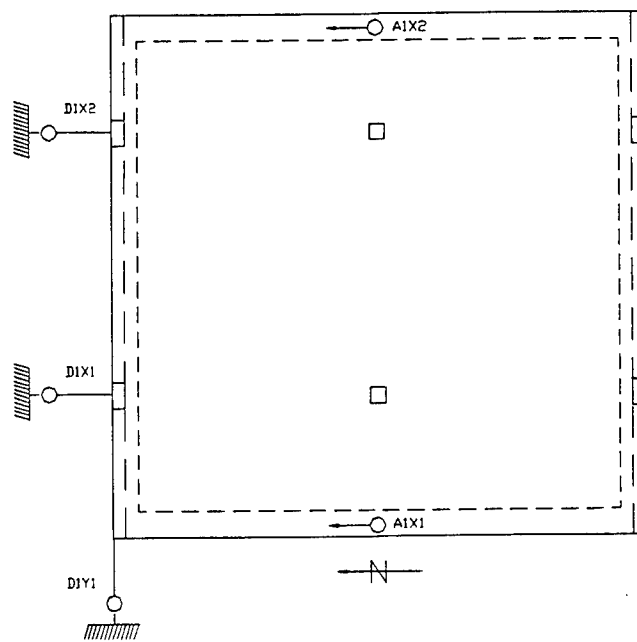


Figure B.4 First Floor Displacement and Acceleration Transducers

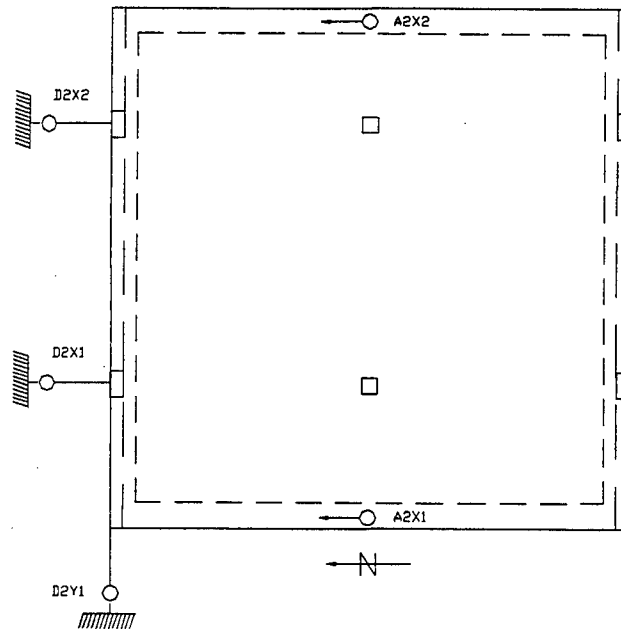


Figure B.5 Second Floor Displacement and Acceleration Transducers

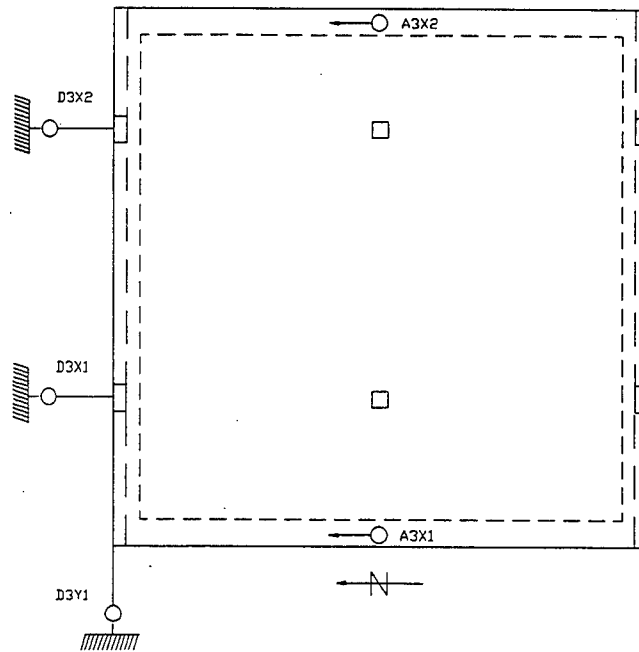


Figure B.6 Third Floor Displacement and Acceleration Transducers

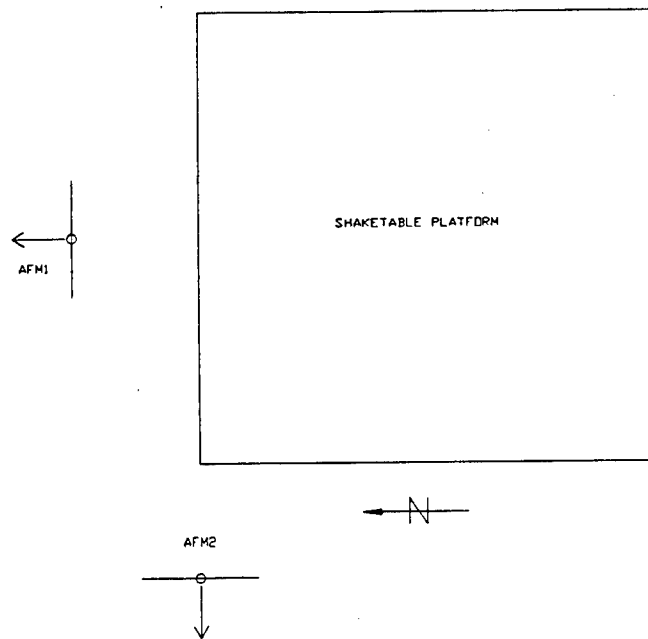


Figure B.7 Displacement Frame Acceleration Transducers

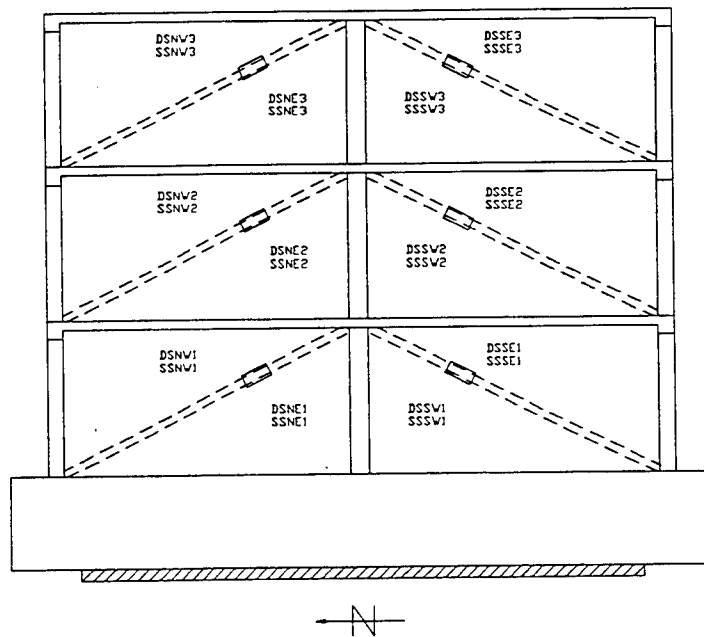


Figure B.8 Damper Displacement and Load Transducers

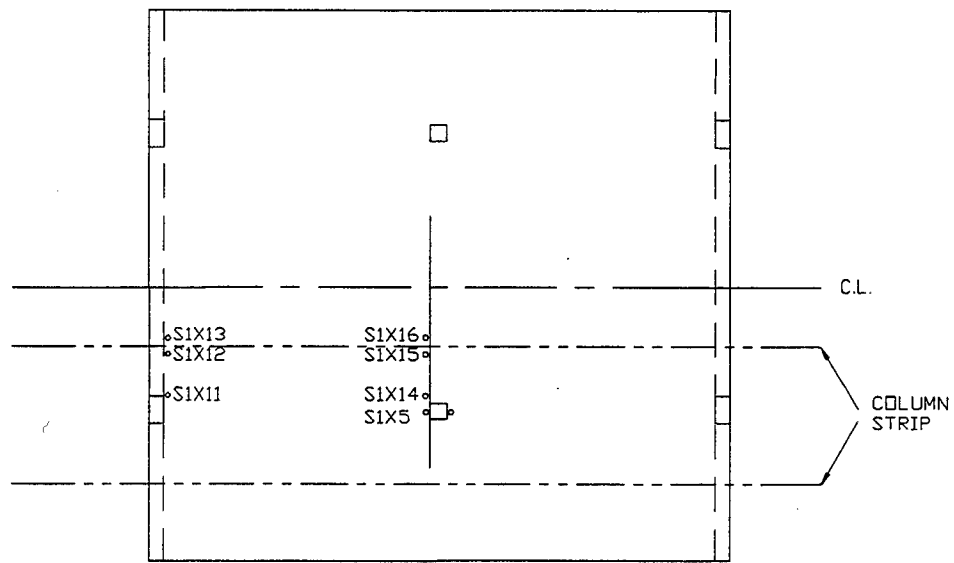


Figure B.9 Active Reinforcement Strain Gages in First Floor Slab

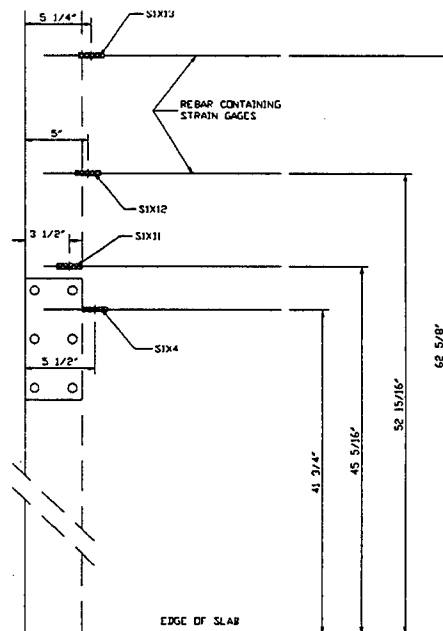


Figure B.10 Slab Reinforcement Gage Locations, Exterior Column

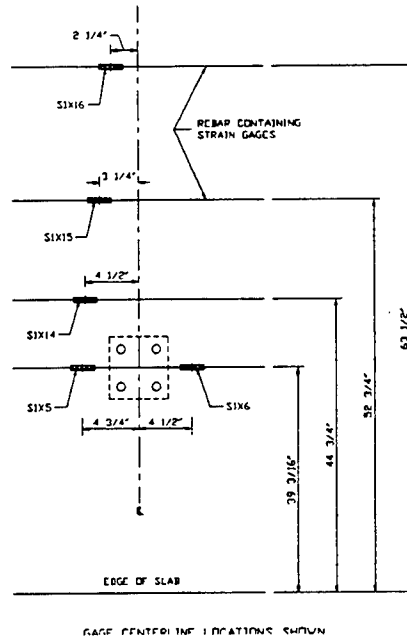


Figure B.11 Slab Reinforcement Strain Gage Locations, Interior Column

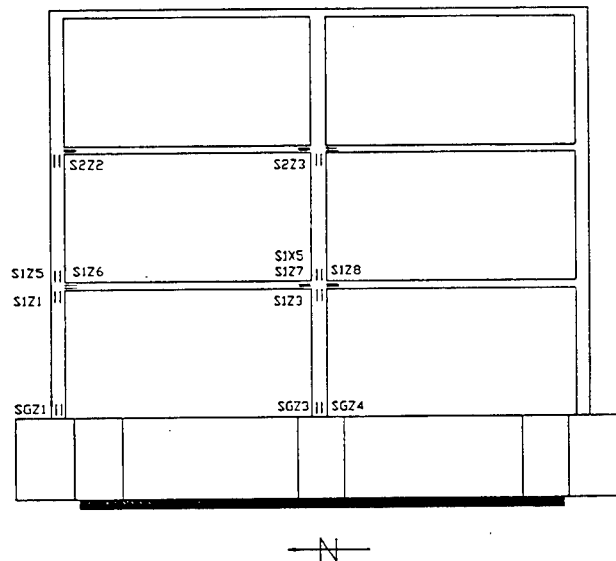


Figure B.12 Active Column and Slab Reinforcement Strain Gages

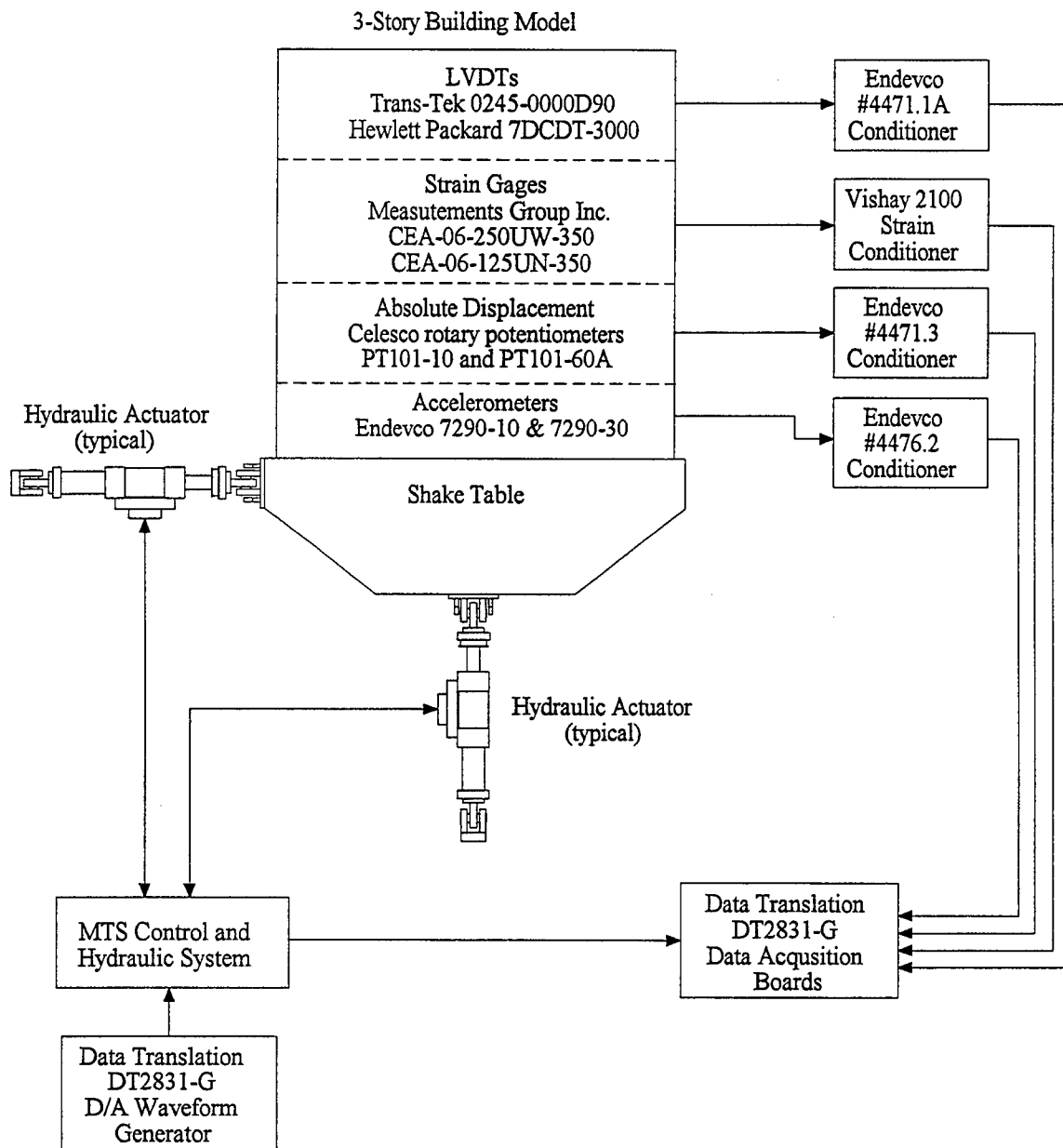


Figure B.13 Block Diagram Showing Shake Table Controls and Data Acquisition Systems

APPENDIX C

SEISMIC SIMULATION TEST DATA

This appendix presents all data that were recorded in the seismic simulations covered by this report. Both basic recorded data and derived quantity data are presented. Procedures used for derived quantities are explained briefly. Presented data include floor accelerations; floor relative displacements; interstory displacements; story shears; hysteretic behavior of the structure; overturning moments; viscoelastic damper (VED) forces and displacements; VED hysteretic behavior; comparisons of VED forces, column forces and story shears; column shears; relative floor velocities; dynamic characterizations of the model; derived energy input and dissipation quantities; and reinforcement strains.

C.1. Recorded Data Descriptions

All motions input to the model by the shaking table were uniaxial, north-south translations. Shaking table, base girder, and slab displacements, and accelerations in the east-west direction, were recorded to check for torsional response in the model. Measured east-west quantities were negligible, indicating torsion did not occur, and they are not reported. For each instance in which two like transducers recorded parallel data for the north-south displacements or accelerations, the average of the two transducer readings is reported.

For each floor level, the absolute north-south acceleration, expressed as a fraction of g , is reported. Acceleration was measured as positive for accelerations to the north of the origin.

For each floor level, relative and interstory displacements are reported. *Absolute displacement* was measured as positive for displacements south of the zero displacement origin. *Relative displacement* is calculated as the difference between the absolute displacement of the target floor level and the base girder. The *interstory displacement* is calculated as the difference between the absolute displacement of the target floor level and the absolute displacement of the next lower floor level. Where reported, the *interstory drift* represents, in percent, the interstory displacement divided by the story height measured to the center of the

relevant floor slabs. For the first floor, the story height is 38.81". For the second and third floors, the story height is 40.00".

VED LVDT displacements are reported as VED shear deformations. VED brace forces are reported as VED forces.

C.2. Data Plots

All seismic simulation data are plotted in Figures C.1.1 - C.23.12. All data were recorded at a sampling frequency of 300 Hz, while all plots are shown at a sampling frequency of 80 Hz. The lower resolution for the plots was found not to affect plot fidelity, as the significant structural response frequencies were all lower than this frequency.

(a) Acceleration Histories

Figures C.1.1 - C.1.17 present floor accelerations vs. elapsed time. Figures C.1.18 - C.1.24 present maximum floor acceleration profiles.

(b) Structural Displacement Histories

Figures C.2.1 - C.2.17 present relative displacements of all floors vs. elapsed time. Figures C.2.18 - C.2.24 present maximum relative story displacement profiles. Figures C.3.1 - C.3.17 present interstory displacements of all stories vs. elapsed time. Figures C.3.18 - C.3.30 present interstory drifts of all stories vs. elapsed time; these plots focus on the ten seconds of maximum interstory displacements in each simulation. Figures C.3.31 - C.3.35 present maximum interstory drift ratio profiles for all simulations.

(c) Story Shear Histories

Inertial forces for each floor were calculated as the product of floor acceleration and floor mass. Floor masses were derived from the floor weights (Table A.5). Story shears are reported for each floor. Story shear is calculated as the sum of target floor inertial force and the inertial forces of all floors above the target floor level, at any instant. Base shear is the sum of all floor inertial forces at any instant and is

also the “first story shear.” Figures C.4.1 - C.4.17 present story shears vs. elapsed time. Figures C.4.18 - C.4.24 present maximum story shear profiles, measured in kips. Figures C.4.25 - C.4.31 present maximum story shear profiles, normalized by the total model weight.

(d) Story Shear-Displacement Hystereses

Figures C.5.1 - C.5.17 present story shears vs. corresponding interstory displacements for all tests. These plots represent the combination of the story shear and interstory displacement histories. These plots facilitate evaluation of stiffness and energy dissipation characteristics of each story of the model. Figures C.6.1 - C.6.5 present base shear vs. third floor relative displacement. These plots facilitate evaluation of the overall stiffness and energy dissipation characteristics of the model. The sign conventions for both story shear and displacement have been adjusted to portray conventional first-third quadrant behavior.

(e) Overtuning Moments

Overtuning moments (OTMs) for each floor level were calculated as the sums of the products of the floor inertial forces and the distances from floor centers of mass to the reference location for calculating OTMs, for each floor above the reference location. The reference locations were the top of the base girder, for base OTM; the top of the first floor slab, for first floor OTM; and the top of the second floor slab, for second floor OTM. Floor masses and distances from the top of the base girder to the floor centers of mass are listed for each floor in Table A.5. Figures C.7.1 - C.7.7 present maximum OTM profiles for all tests.

(f) Damper Force Histories

Figures C.8.1 - C.8.46 present VED force vs. elapsed time for all tests with VEDs installed. The sign conventions for both shear deformation and displacement have been adjusted to portray conventional first-third quadrant behavior for all VEDs. Therefore, the plots for the northeast (NE) and northwest (NW) VEDs are opposite in sign to those of the southeast (SE) and southwest (SW) VEDs.

(g) Damper Deformation Histories

Figures C.9.1 - C.9.46 present VED shear deformation vs. elapsed time for all tests with VEDs installed.

(h) Damper Force-Deformation Hystereses

Figures C.10.1 - C.10.46 present VED shear deformation vs. force for all tests with VEDs installed. These plots facilitate interpretation of the energy dissipation characteristics of the VEDs.

(i) Damper Force vs. Story Shear

The maximum sums of the horizontal components of the VED forces (using the undeformed geometry of the structure) were calculated. This sum corresponds closely with the story shear quantity, and thus provides a means to compare the VED force with total inertial force in the structure. Figures C.11.1 - C.11.5 present profiles of the maximum sum of the horizontal components of the VED forces, overlaid on the corresponding story shears.

For all tests for which viscoelastic damper braces were installed, *column shear* is also reported. The column shear is derived as the difference between the story shear and the sum of the horizontal components of all VED brace forces for the subject story level. It provides a means of evaluating the shear forces that are carried by the columns in the regions not strengthened by the VED collars. Figures C.12.1 - C.12.13 present column shear vs. elapsed time, for all tests with VEDs installed. Figures C.13.1 - C.13.13 present column shears vs. corresponding interstory displacements for all tests with VEDs installed. Figures C.13.14 - C.13.18 present profiles of the maximum column shears, overlaid on the corresponding story shears.

Figures C.14.1 - C.14.17 present overlays of the story shears, column shears, and sums of the horizontal components of VED forces for all simulations with VEDs installed, plotted against elapsed time. The four seconds of maximum story shear are presented for each simulation. These plots are helpful for discerning the interrelationships of the three main force quantities, particularly with respect to the effect that the phase angle that exists between VED force and displacement has on the force distribution in the model.

(j) Relative Floor Velocities

Figures C.15.1 - C.15.9 plot the relative floor velocities vs. elapsed time in each of the earthquake simulations. Since the VEDs are mounted in diagonal braces in the structure, their shear deformation velocities are directly related to the relative velocities of the adjacent floor levels through the geometry of the structure. Since the energy dissipation contributed to a structure by a VED is often modeled using a linear viscous damper, or “dashpot,” in which damper force is the product of a viscous damping coefficient, c_d , and damper excitation velocity, reflection on relative floor velocities in the model is helpful in understanding the VED effects on the structural response. Relative floor velocities were derived by first integrating the acceleration time-histories for the base and each floor, to calculate base and floor velocities, and then subtracting the velocities for the floor level immediately below the floor being analyzed from the velocities for that floor. For example, to derive the relative velocity of Floor 3 with respect to Floor 2, the velocity of Floor 2 was subtracted from the velocity of Floor 3. To eliminate the tendency for the integrated velocity values to drift from a non-zero velocity at the end of the simulation, tenth order curve fits of the acceleration time-histories were subtracted from the acceleration time histories before the integration was performed.

(k) Dynamic Characterizations of Model

Figures C.16.1 - C.16.6 present acceleration-based *transfer functions* that were derived from the acceleration histories of the base and the floors in the model, where:

$$TF(f) = \frac{FL(f)}{B(f)} \quad (C.1)$$

In Equation C.1, $TF(f)$ is the system transfer function (TF), while $B(f)$ is the Fast Fourier Transform (FFT) of the base acceleration history, and $FL(f)$ is the FFT of the appropriate floor acceleration time-history. The TF quantifies the dynamic amplification of the input accelerations as a function of the frequency (f) of the input. The TF is analogous to the “transmissibility” of a dynamic system. The computation assumes linear behavior. Since this structural system has nonlinear components in both the VEDs and the reinforced concrete structure, the observations made from the TFs are approximate. The TF signal

typically has electronic noise associated with it. Particularly for low input levels, signal noise magnitude can be significant with respect to the primary signal. It was found that a degree of "smoothing" of the TFs helped to facilitate pinpointing modal frequencies and calculating modal damping. The plots shown are the results of smoothing the actual TFs using two algorithms available in the software package DPLOT, which was developed by the U.S. Army Waterways Experiment Station. The first algorithm removes random "spikes" from each FFT, where the spikes are single data points with very high amplitudes, with respect to the data points immediately adjacent to each spike point. The second algorithm, actually called smoothing in DPLOT, operates on groups (windows) of successive data points and consists of removing the linear trend in each window, performing a low-pass filter, and reinserting the linear trend. Several window sizes were used in initial trials, to balance noise reduction with the remaining signal fidelity. For the plots from simulations with VEDs installed on the model, eight successive data points, a frequency bandwidth of approximately 0.137 Hz, was used in each window. For the plots from simulations without VED installed on the model, six successive data points, a frequency bandwidth of approximately 0.098 Hz, was used in each window. In Figure C.16.2, the FL 3 TF plot for simulation E100DL shows the original (unedited) and edited (using DPLOT) TFs, indicating the significance of the noise in the unedited signals.

Figures C.16.7 - C.16.19 present Fourier amplitude spectra for the interstory displacements in each simulation. Since VED properties are typically characterized in terms of the frequencies and magnitudes of their shear strains or displacements, it is helpful to examine the frequency characteristics of their displacements. VED displacement may be related directly to interstory displacement through the geometry of the model.

Figures C.16.20 - C.16.25 present the acceleration-based TFs from low level white noise tests that were conducted on numerous occasions during the experimental program. Those tests are described in Section 3.4 of this report. The TFs and dynamic properties were derived using the same procedures as those described above, except that the FFTs of the base and floor motions were taken directly from an in-line spectrum analyzer, which recorded the data in larger frequency steps. The smoothing windows used included five successive data points, for a window bandwidth of 0.25 Hz, in the white noise tests without VEDs installed on the model, and seven successive data points, for a window bandwidth of 0.375 Hz, in the white noise tests with VEDs installed on the model.

Figures C.16.26 and C.16.27 present the results of free vibration decay and pullback tests that were conducted during the experimental program. Those tests are also described in Section 3.4 of this report.

(I) Energy Input and Dissipation

A structure that is subjected to earthquake-induced motion must dissipate the energy that is input by the ground motion. In a structure without supplemental energy dissipation devices, the input energy is largely dissipated by elastic strain energy, kinetic energy, viscous-damped energy, and irrecoverable dissipated energy [3]. The irrecoverable energy takes the form of permanent damage in the structure. When VEDs are added to the structure, energy dissipation also occurs in the VEDs. Mathematically, this relationship may be expressed as:

$$E_I = E_K + E_S + E_H + E_\xi + E_D \quad (C.2)$$

In Equation C.2, E_I is the input energy; E_K is the kinetic energy; E_S is the elastic strain energy, which is recoverable; E_ξ is the viscous-damped energy; E_H is the hysteretic energy that is dissipated by the structure through inelastic action; and, E_D is the energy dissipated by supplemental dampers (if any are present). References 3 and 45 present detailed discussions of the derivations of the terms in Equation C.2. A brief summary of those discussions is included here to provide an explanation of how these parameters were calculated from the test data.

The *input energy* is the time integral of the input power and is a function of the ground motion velocity and the structural base shear:

$$E_I = \int P_I dt = \int \left(\sum_{i=1}^n m_i \ddot{v}_{t_i} \right) dv_g = \int \left(\sum_{i=1}^n m_i \ddot{v}_{t_i} \right) \dot{v}_g dt \approx \int V_b \dot{v}_g dt \quad (C.3)$$

The terms in parentheses in Equation C.3 represent the products of the floor mass and floor acceleration, which are summed over “ n ” floors; in this study, there are three floors, with associated masses and absolute acceleration response histories. The term dv_g represents the incremental ground displacement, which is then expressed as the product of the ground velocity, \dot{v}_g , and the incremental time step, dt . Reference 85 points out that, strictly speaking, the terms in parentheses do not equal the base shear, V_b , because the base shear should theoretically also include the internal damping force. However, the internal damping force has been shown to be generally negligible and thus may be ignored in approximating the base shear. This

approximation is usually made when presenting base shear quantities and has been made elsewhere in this report. Equation C.3 may summarily be thought of as the work done by the base shear moving through the ground, or base, displacement.

For this study, the input energy has been calculated in three manners, to provide checks on the consistency of the data. First, it has been calculated as the time integral of the product of the base shear and the base velocity, as derived by integrating the base accelerations to obtain velocity. Second, it has been calculated as the time integral of the product of the base shear and the base velocity, as derived by differentiating the base displacements to obtain velocity. Third, it has been calculated directly as the displacement integral of the base shear. In each of these three instances, the approximation on the far right side of Equation C.3 represents the mathematical operation that is performed. V_b is applied in each case. In the first two instances, the ground velocity, \dot{v}_g , term has been derived in the two different manners that are mentioned. In the third instance the product $\dot{v}_g dt$ is summarily represented by $d\dot{v}_g$, the incremental ground displacement

The *kinetic energy* at any instant is a function of the absolute velocities of the three floor levels:

$$E_K = \frac{1}{2} \sum_{i=1}^n m_i (\dot{v}_i)^2 \quad (C.4)$$

In Equation C.4, the term in parentheses represents the absolute velocity of each floor, at any time, t . Again there are three floor levels, with associated floor masses. Floor velocities may be calculated by integrating floor accelerations or by differentiating the absolute floor displacements; in this report, the velocities were derived by integrating the floor accelerations. The absence of an integral operator indicates that the kinetic energy is an instantaneous, recoverable quantity.

The *elastic strain energy* at any instant is a function of the story shears and the story stiffnesses:

$$E_S = \sum_{i=1}^n \frac{V_i^2}{2 K_i} \quad (C.5)$$

For each of the three floor levels, V_i is the story shear at any time t . The term K_i is the story stiffness from the story shear vs. interstory drift relationship. As implied by the term elastic strain energy, this relationship assumes elastic behavior, and the story stiffness is the elastic stiffness. Since for a reinforced

concrete structure, this stiffness quantity can only be approximate, the “backbone” stiffnesses for each of the three stories were used in the calculations in this report. The backbone stiffness derivations is provided in Chapter 5. As with the kinetic energy, the elastic strain energy is an instantaneous, recoverable quantity.

The *hysteretic energy*, E_H , occurs largely through inelastic action and quantifies the permanent damage that is sustained by the structure. In a reinforced concrete structure, this damage consists largely of concrete cracking and reinforcement yielding. Another mechanism that may contribute to the hysteretic energy dissipation is frictional losses in bolted connections. There are several bolted connections in the model structure; all are associated with the VED braces. Since there is no ready means of quantifying these losses, they have been assumed to be included in E_H .

The *viscous-damped energy*, E_δ in Equation C.3 is very difficult to quantify from experimental data [3] and is essentially indistinguishable from the hysteretic energy. Therefore, in this report, the portion of the input energy that is not balanced by kinetic, elastic strain, or supplemental damper energies, is assumed to be a combination of hysteretic and viscous-damped energy dissipation, which is termed “hysteretic” energy.

The energy dissipated by a *single* VED is [3]:

$$E_D = \int f_{vd} d\delta_{vd} - \frac{1}{2} K_e \delta_{vd}^2 \quad (C.6)$$

In Equation C.6, f_{vd} is the VED force, δ_{vd} is the VED shear deformation, and K_e is the effective stiffness of the VED. The first term represents the area of the VED load-deformation hysteresis loop, integrated over the duration of the input motion. The second term represents the recoverable elastic strain energy. Since the structure returns to rest at its initial position in all of the tests with VEDs installed, the elastic strain energy is zero at the end of each of those tests, and the second term may be ignored. For the simulations reported herein, E_D is the summation of energy dissipated by all six VEDs in the model structure.

Figures C.17.1 - C.17.9 present the energy input and dissipation quantities for a number of the earthquake simulations. Plots for the low-level simulations are not shown, because the energy quantities were very small. For the plots that are presented, the input energy is based on the base girder velocities that were derived from the integrated accelerations. Those values were used simply as common reference points. Either of the other methods for calculating the input energy would have yielded essentially the same plots.

(m) Reinforcement Strain Histories

Figures C.18.1 - C.23.12 present reinforcement bar strain histories for all tests.

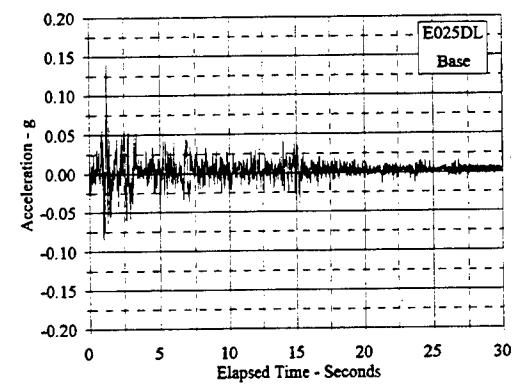
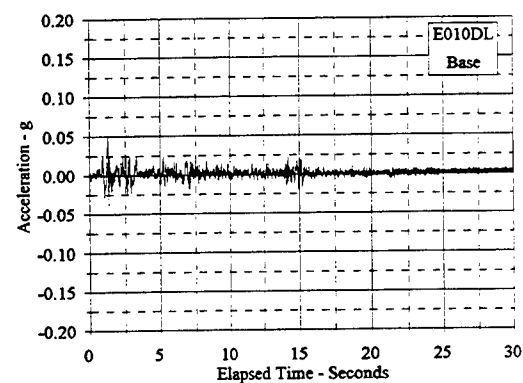
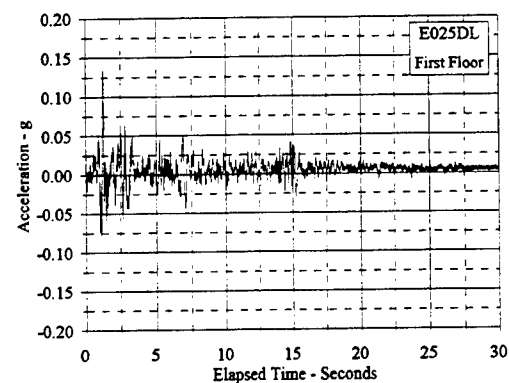
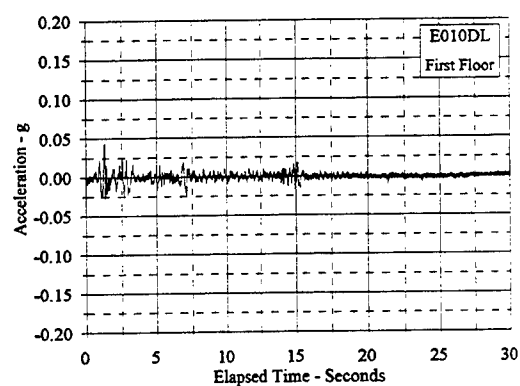
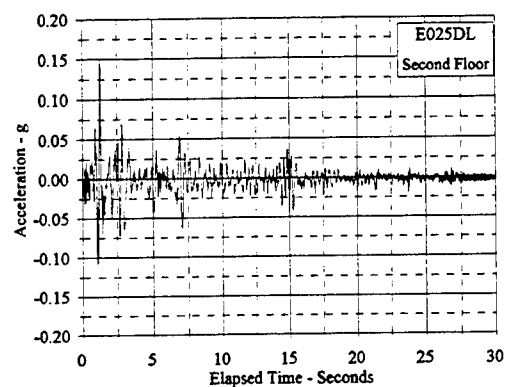
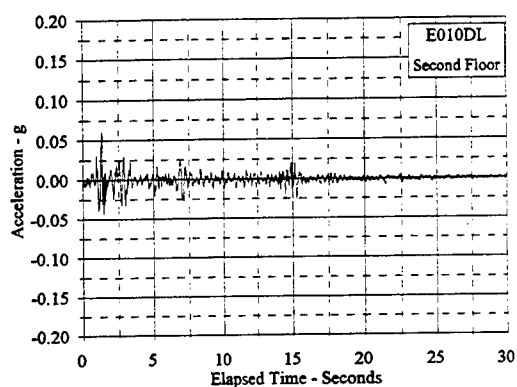
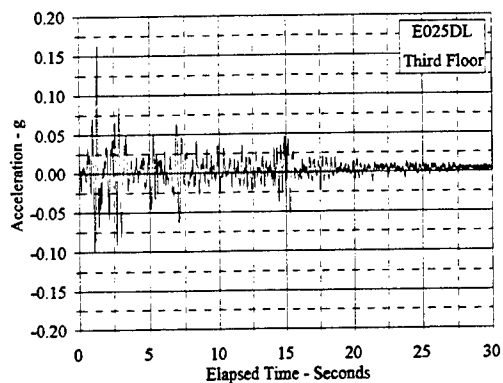
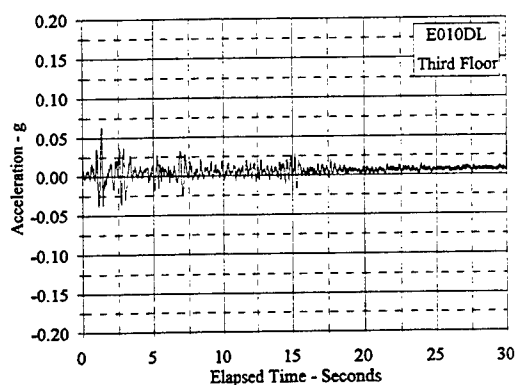


Figure C.1.1 Acceleration Vs. Elapsed Time: E010DL, E025DL

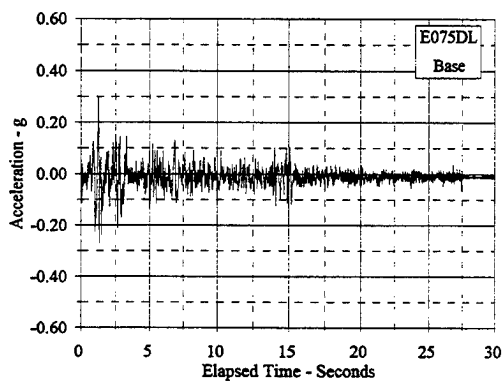
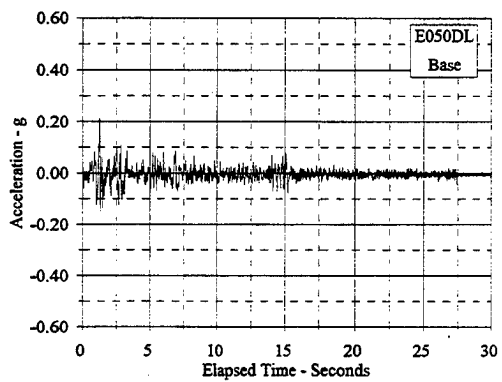
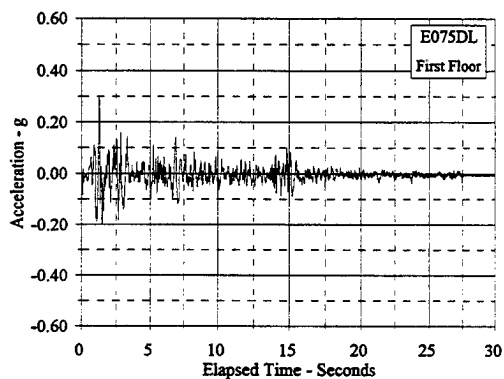
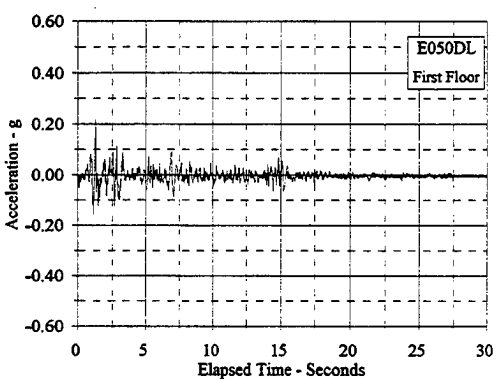
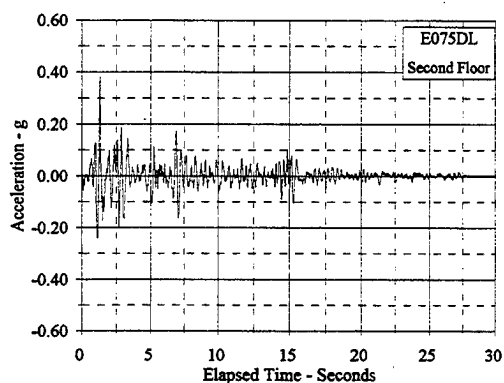
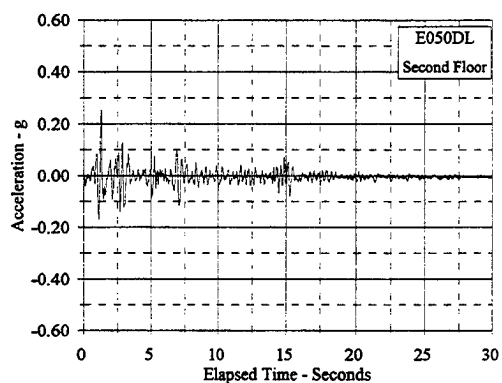
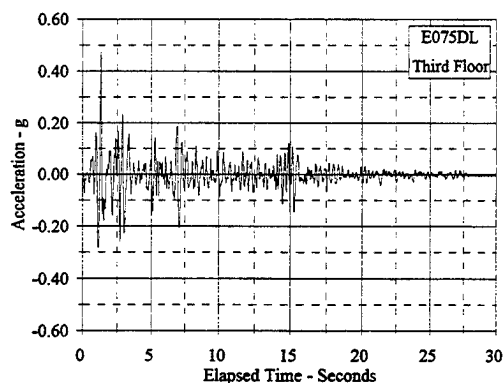
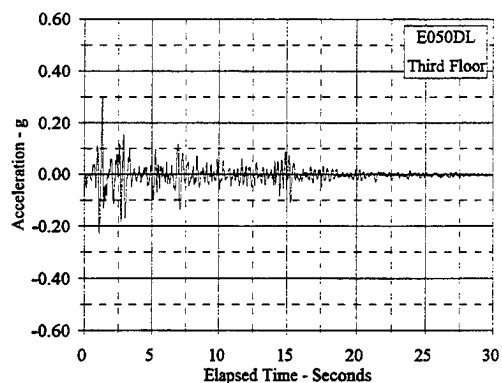


Figure C.1.2 Acceleration Vs. Elapsed Time: E050DL, E075DL

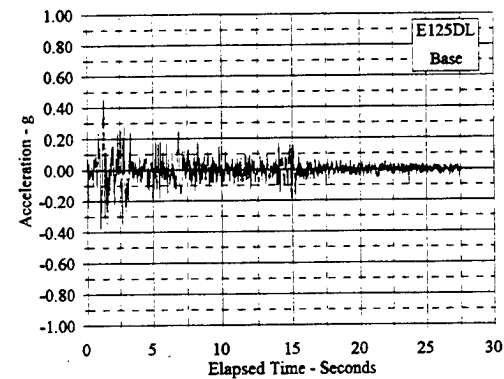
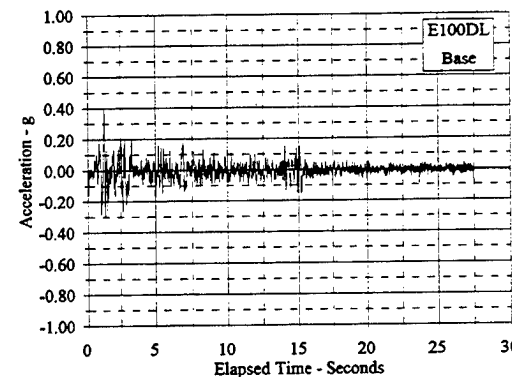
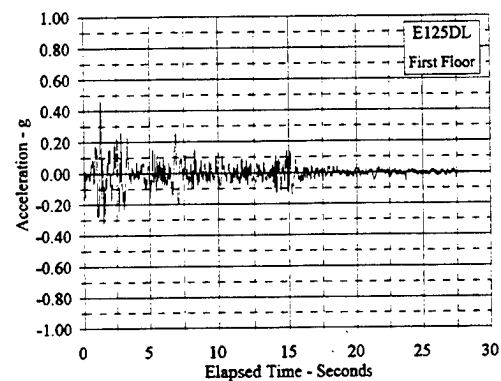
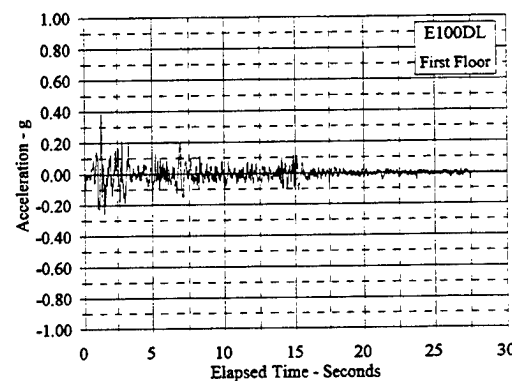
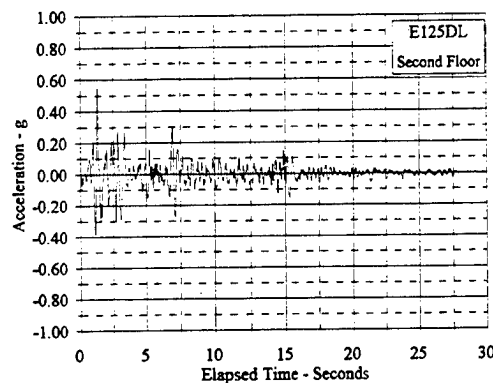
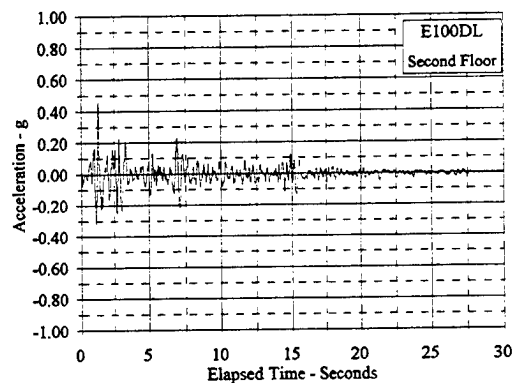
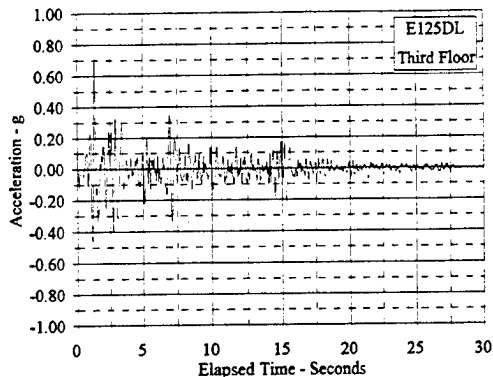
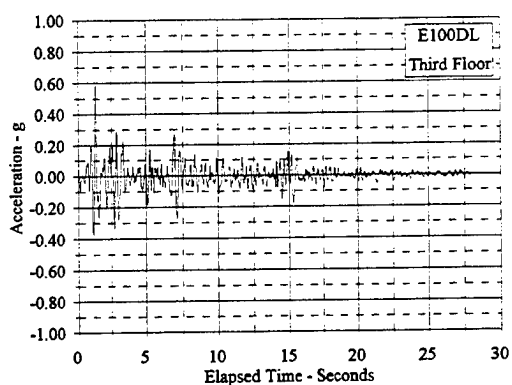


Figure C.1.3 Acceleration Vs. Elapsed Time: E100DL, E125DL

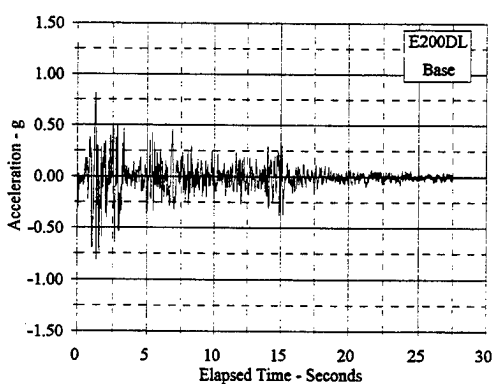
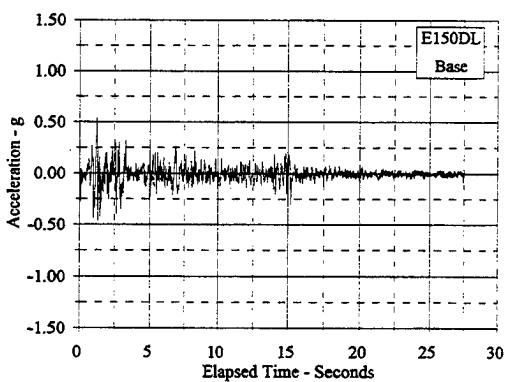
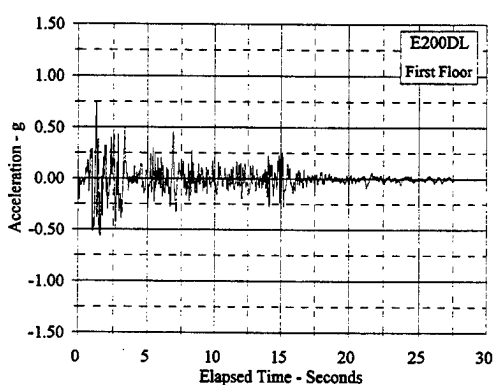
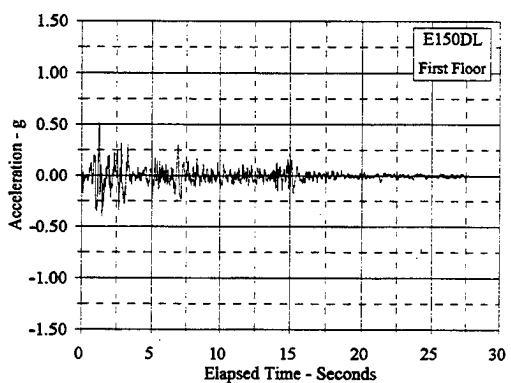
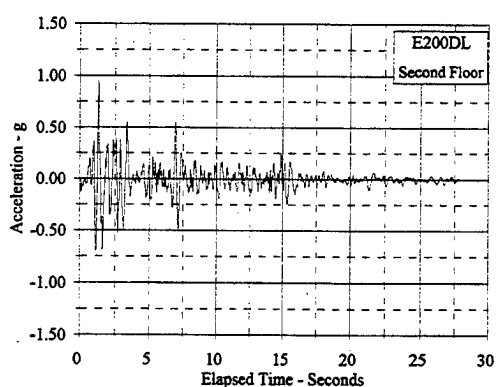
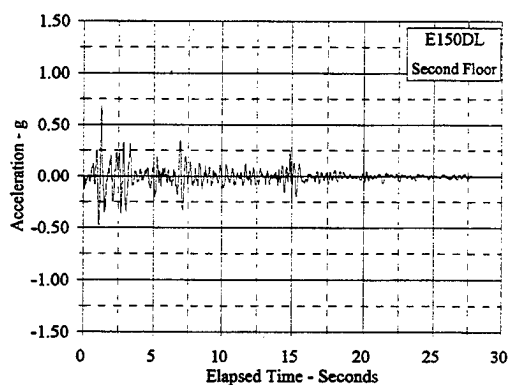
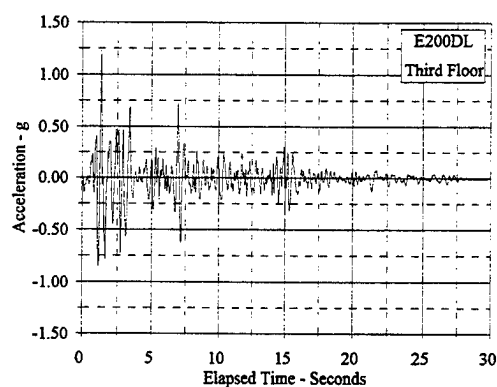
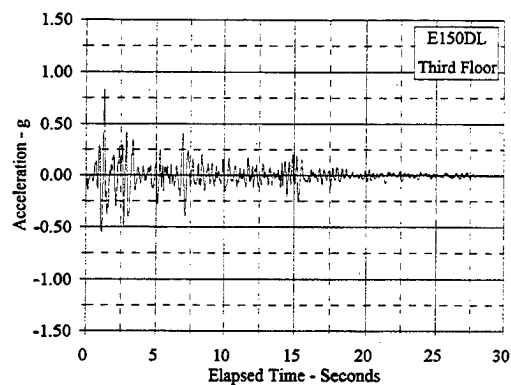


Figure C.1.4 Acceleration Vs. Elapsed Time: E150DL, E200DL

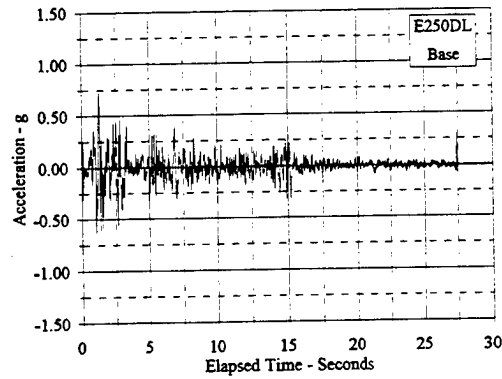
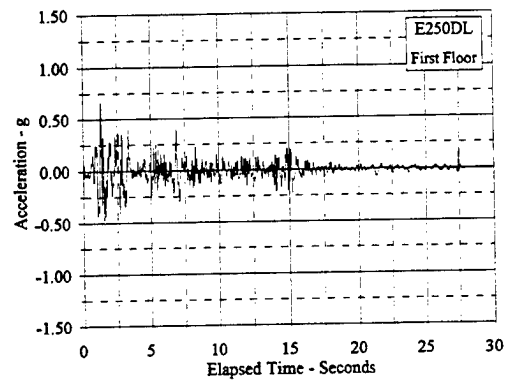
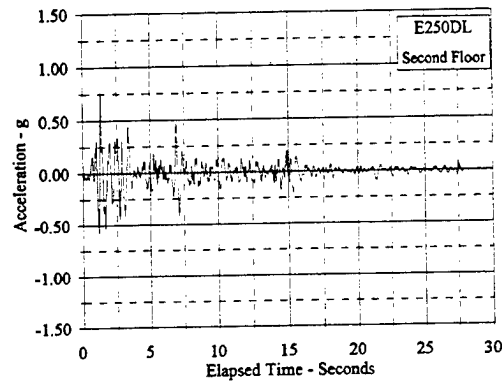
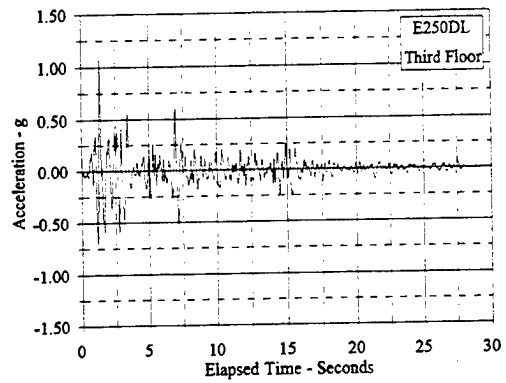


Figure C.1.5 Acceleration Vs. Elapsed Time: E250DL

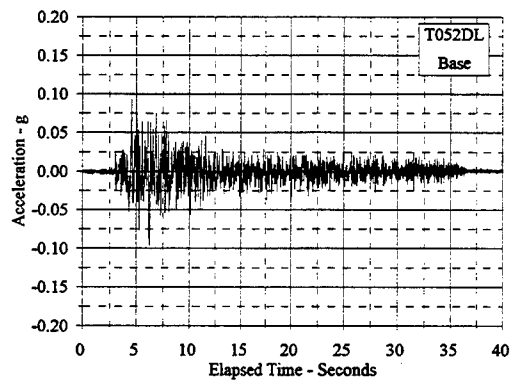
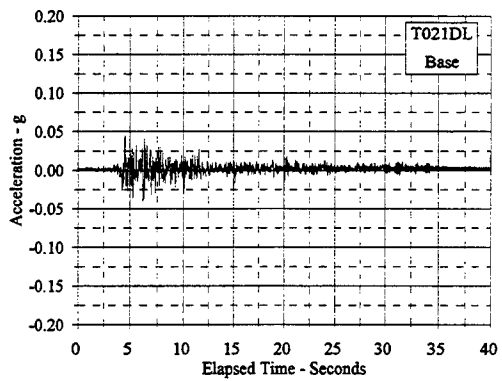
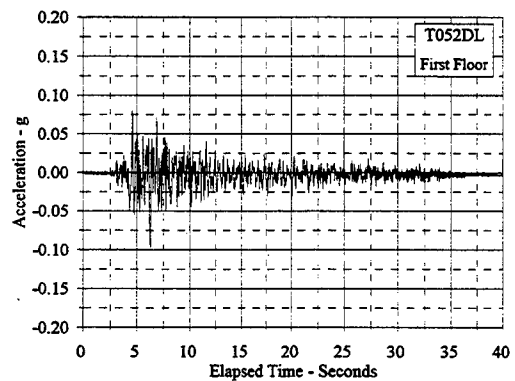
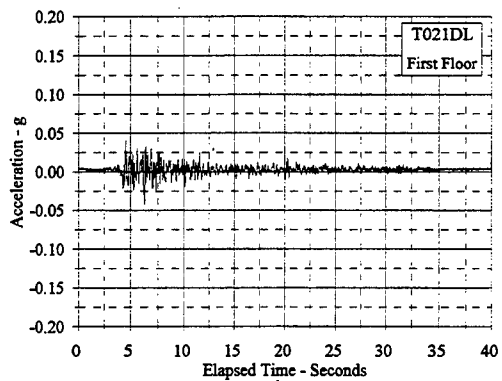
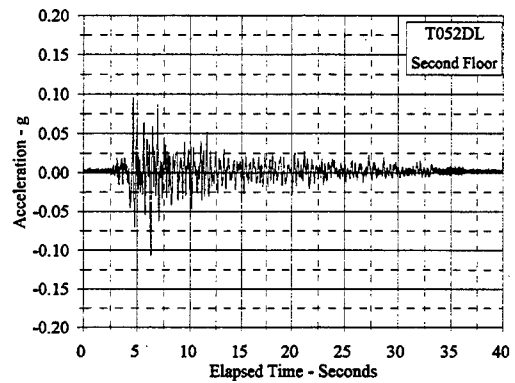
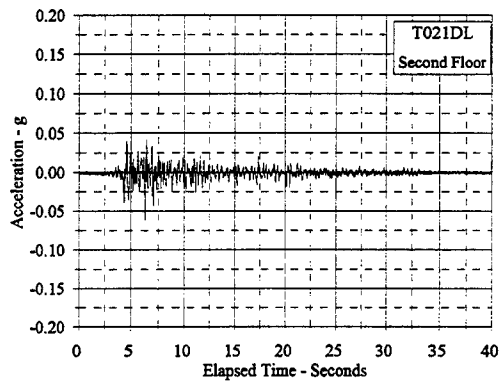
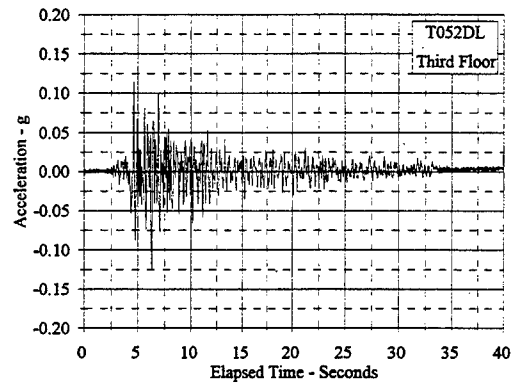
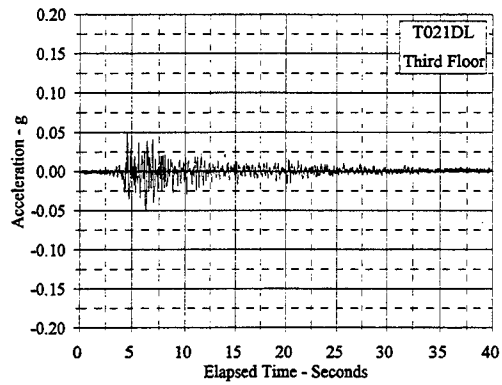


Figure C.1.6 Acceleration Vs. Elapsed Time: T021DL, T052DL

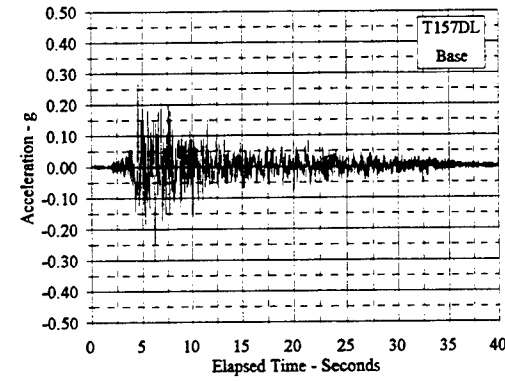
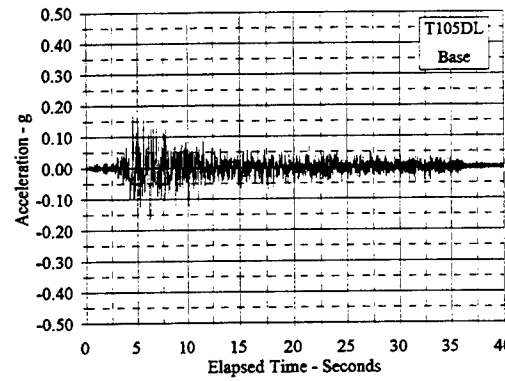
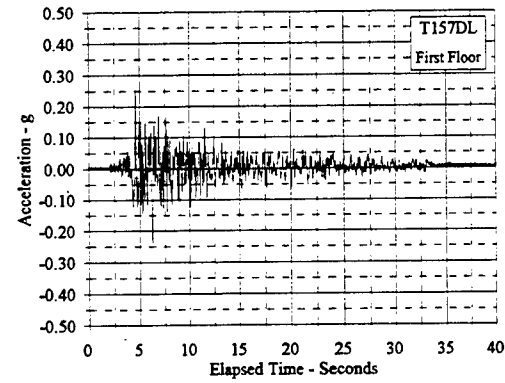
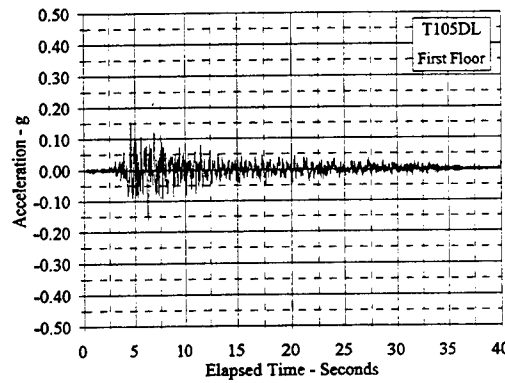
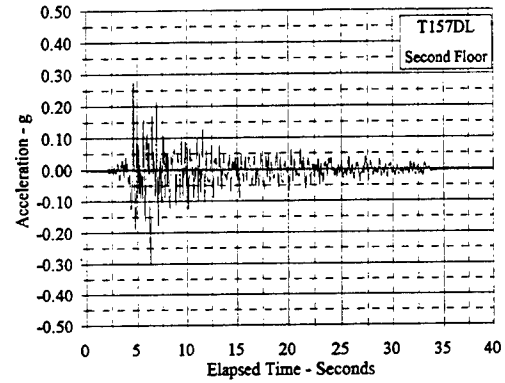
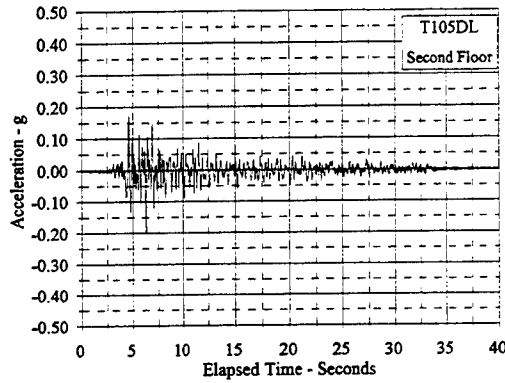
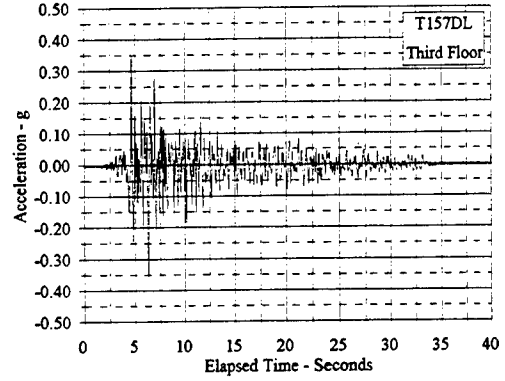
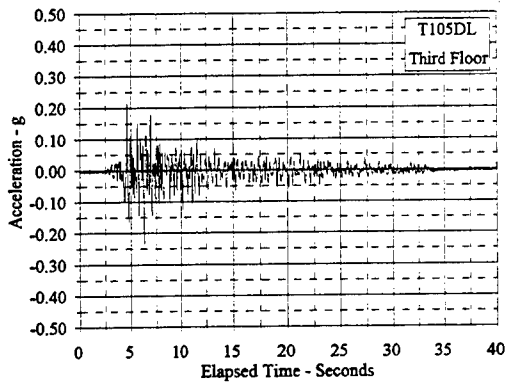


Figure C.1.7 Acceleration Vs. Elapsed Time: T105DL, T157DL

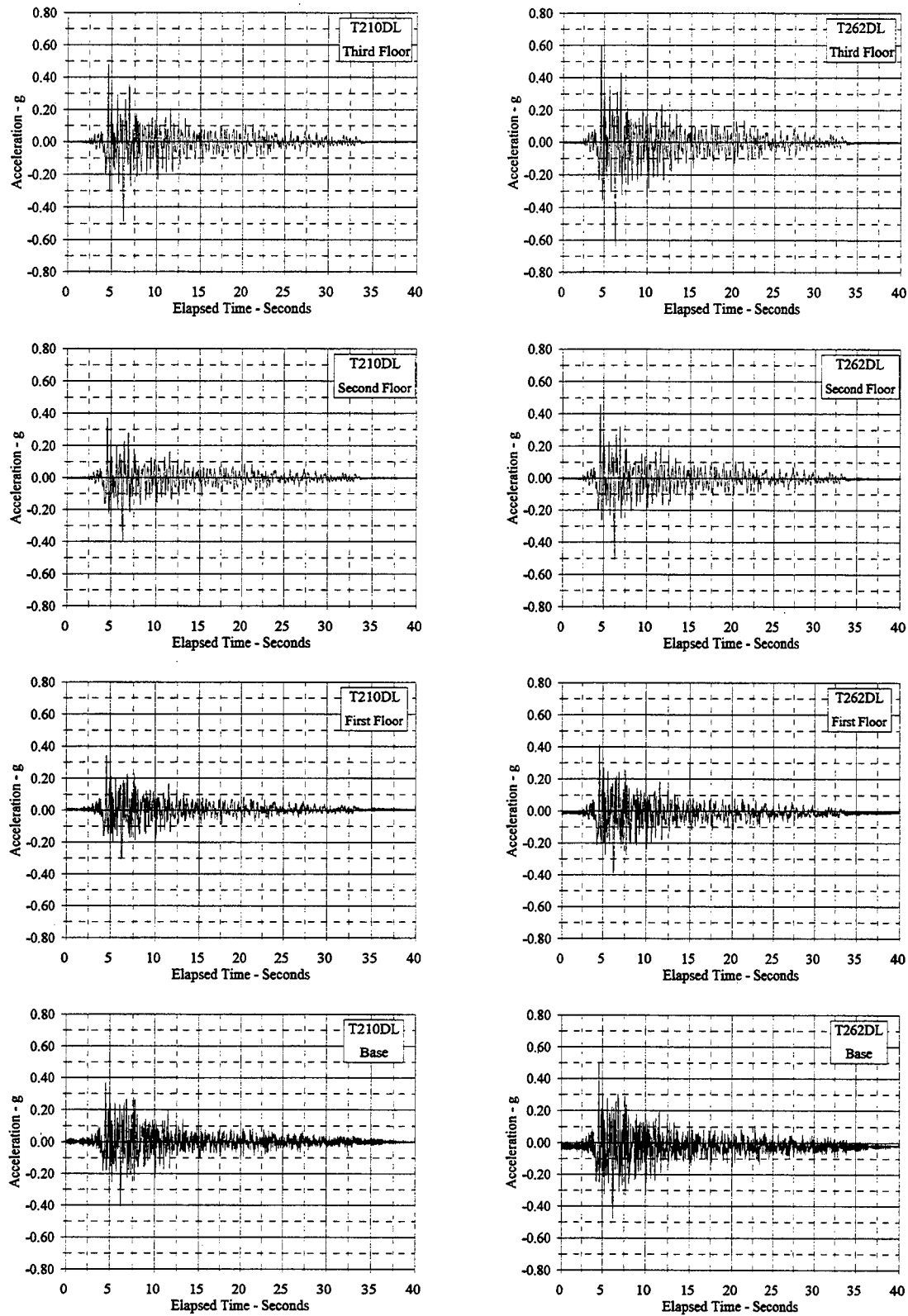


Figure C.1.8 Acceleration Vs. Elapsed Time: T210DL, T262DL

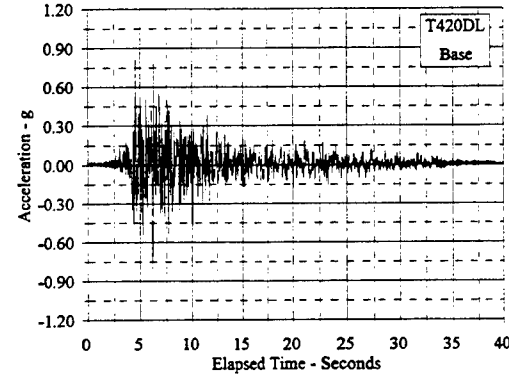
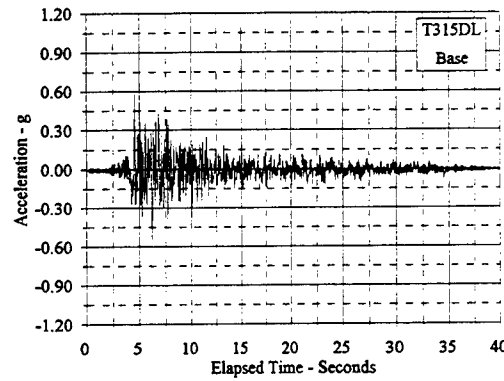
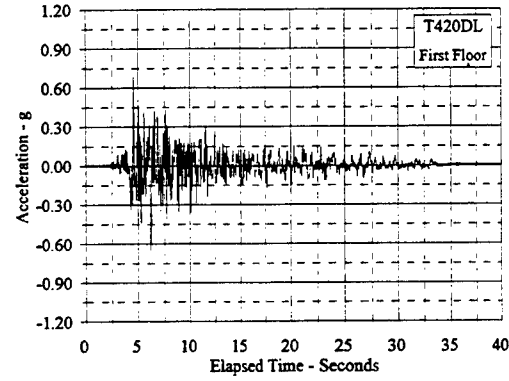
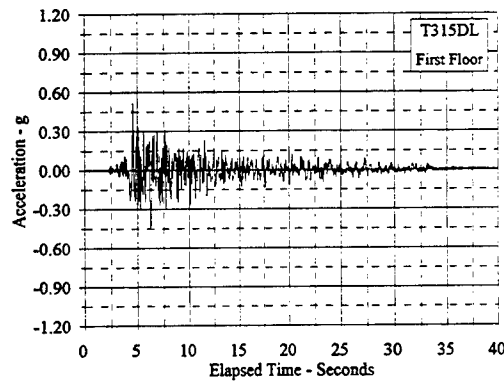
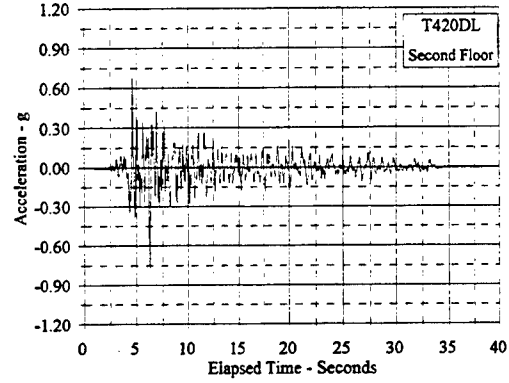
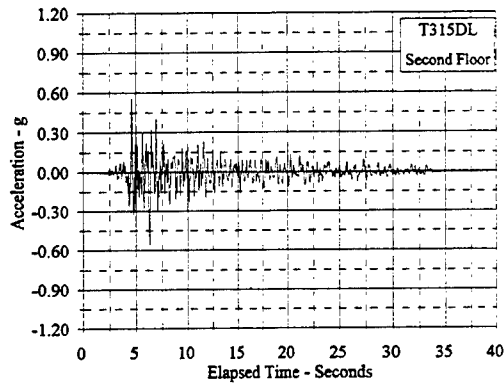
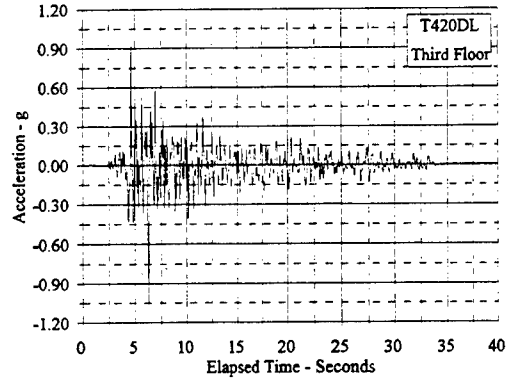
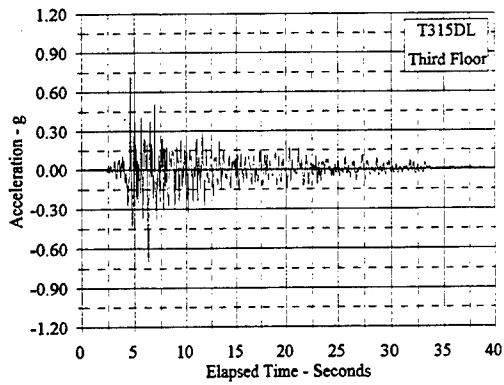


Figure C.1.9 Acceleration Vs. Elapsed Time: T315DL, T420DL

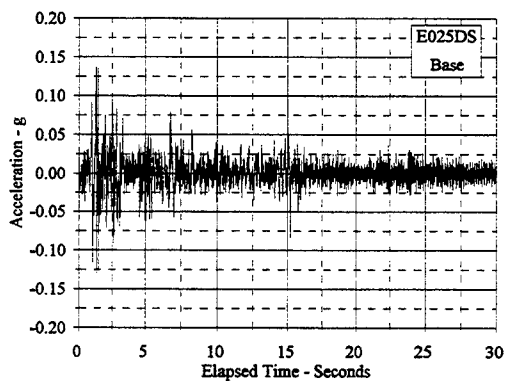
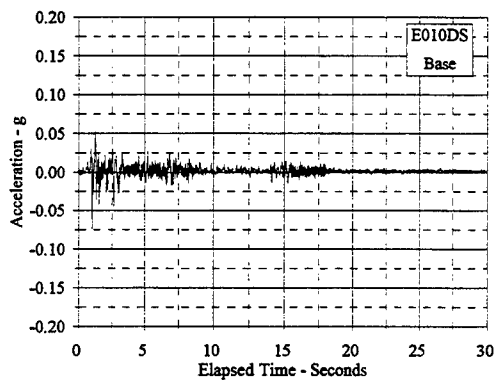
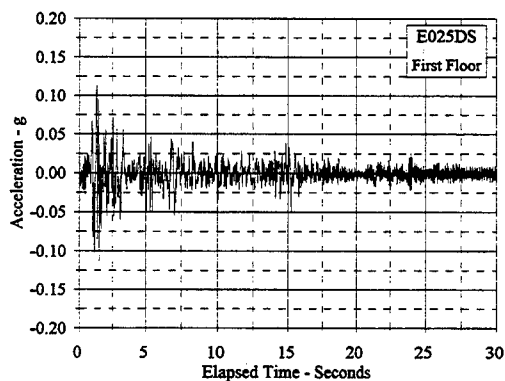
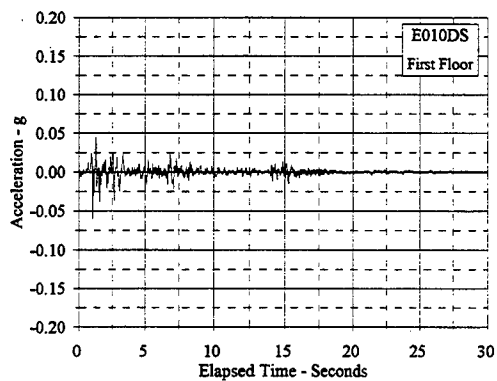
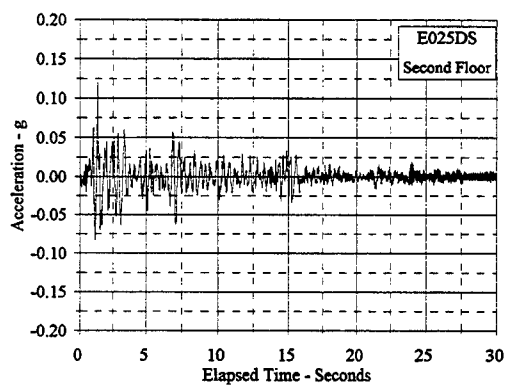
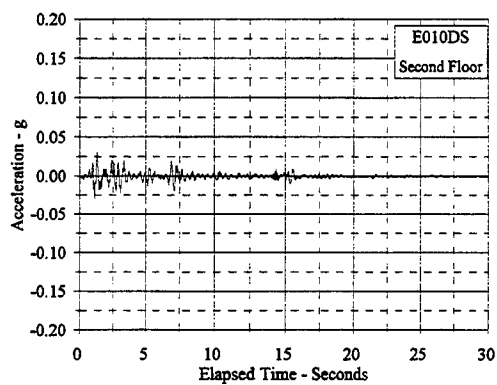
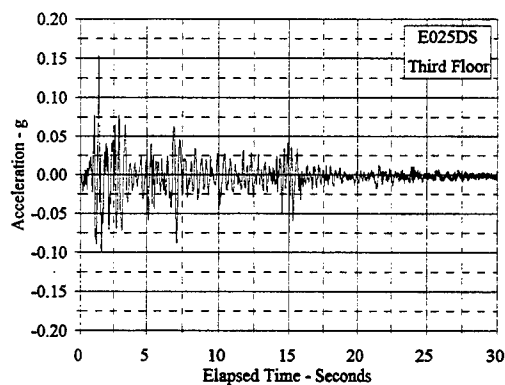
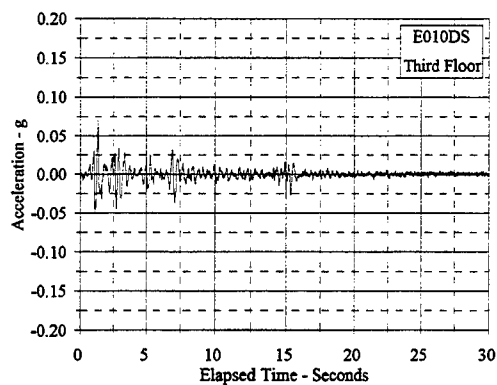


Figure C.1.10 Acceleration Vs. Elapsed Time: E010DS, E025DS

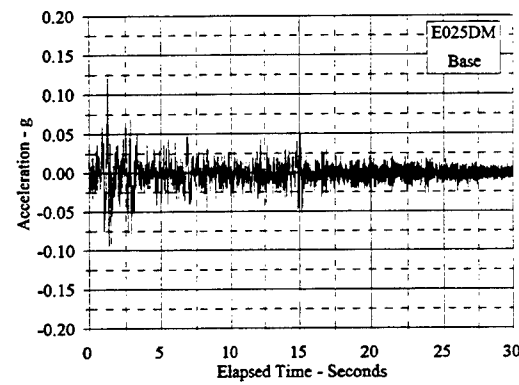
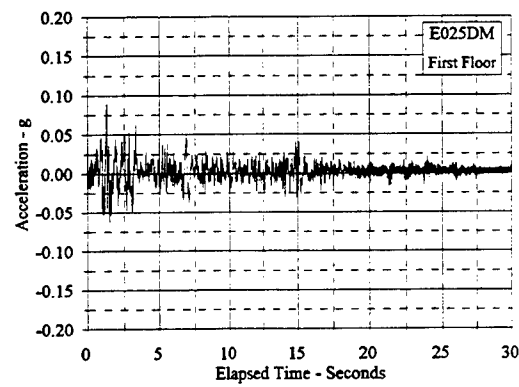
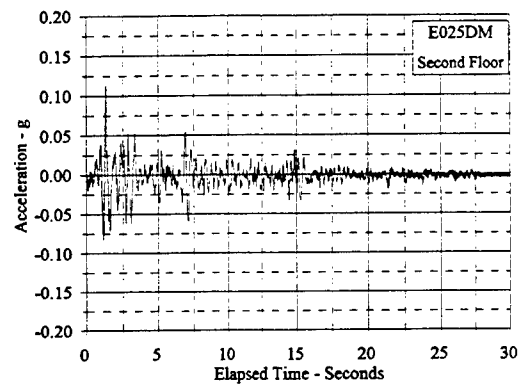
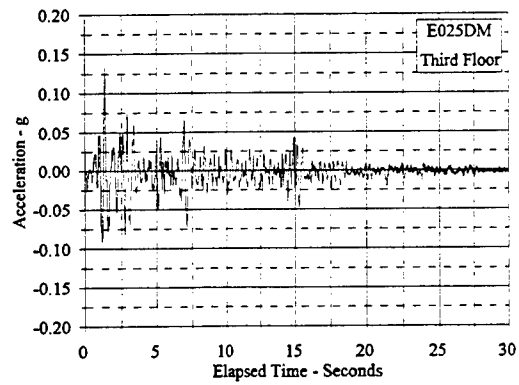


Figure C.1.11 Acceleration Vs. Elapsed Time: E025DM

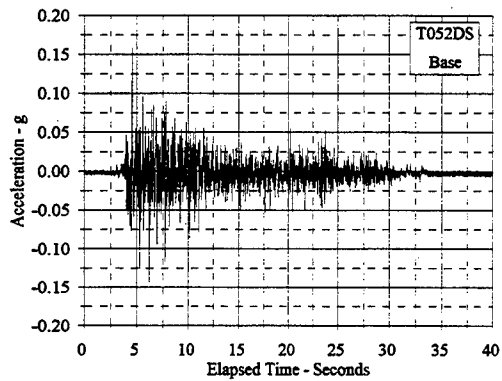
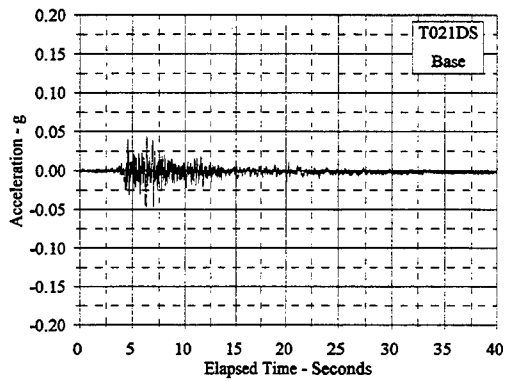
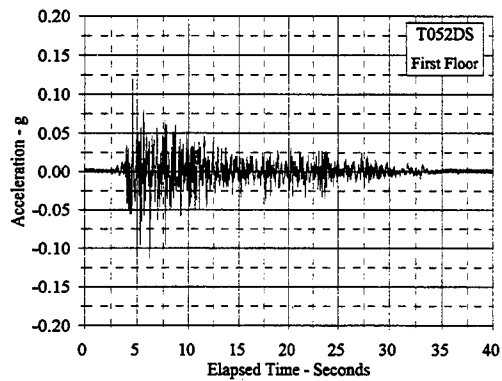
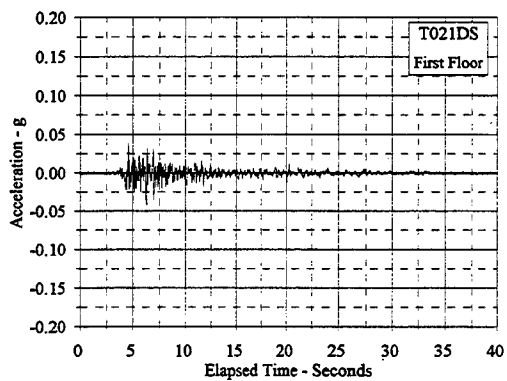
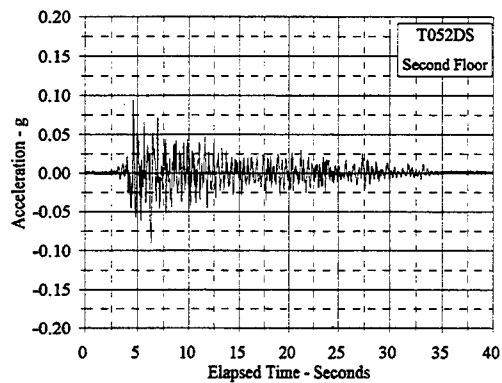
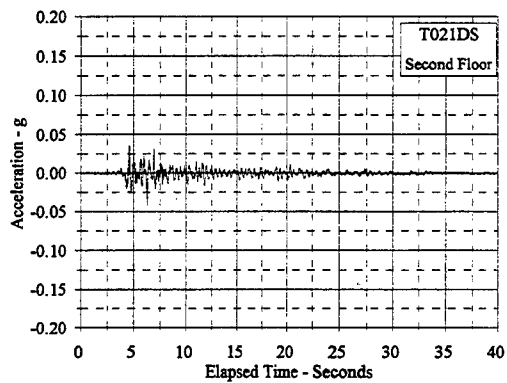
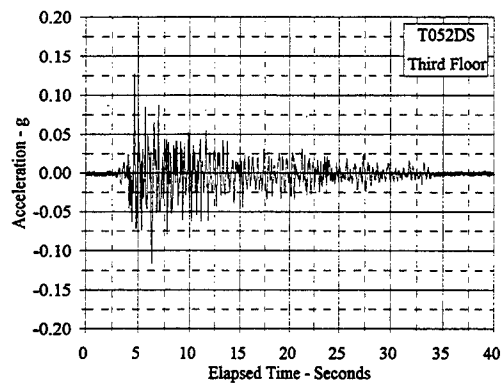
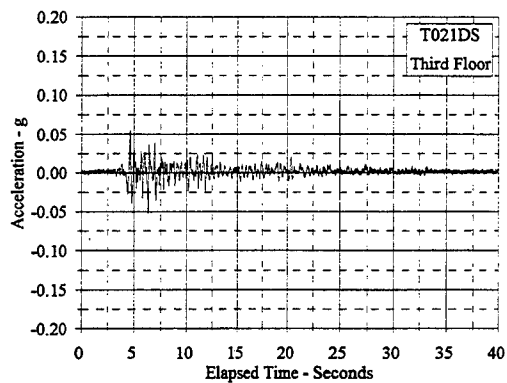


Figure C.1.12 Acceleration Vs. Elapsed Time: T021DS, T052DS

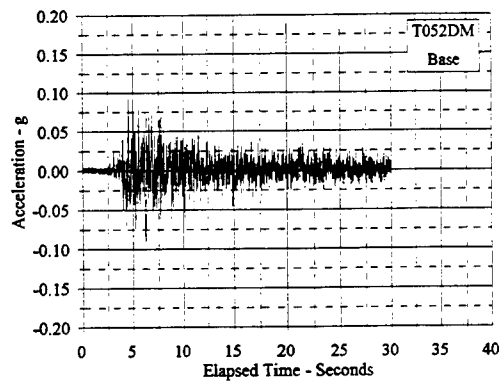
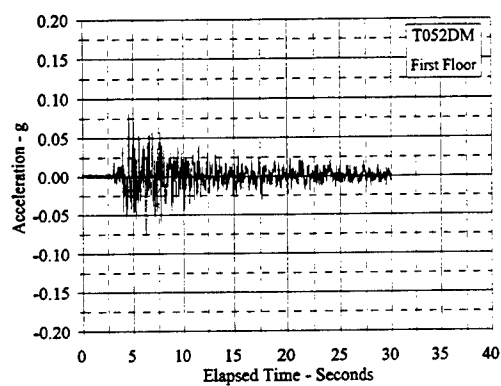
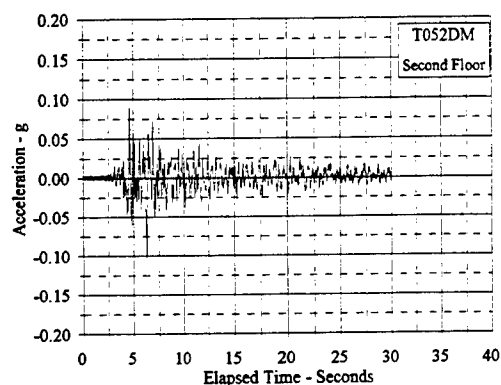
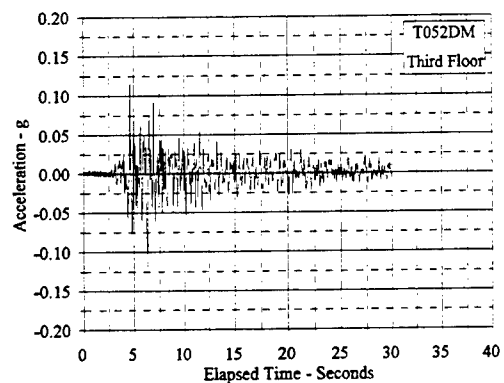


Figure C.1.13 Acceleration Vs. Elapsed Time: T052DM

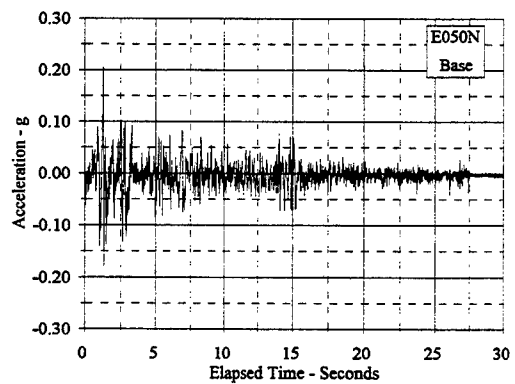
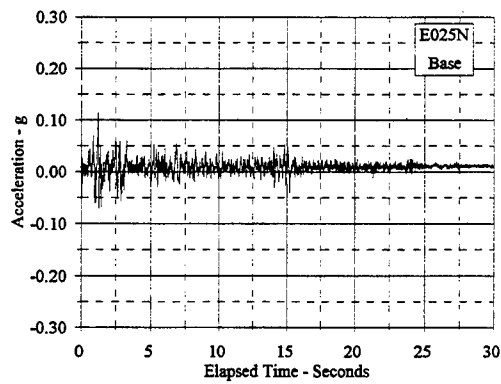
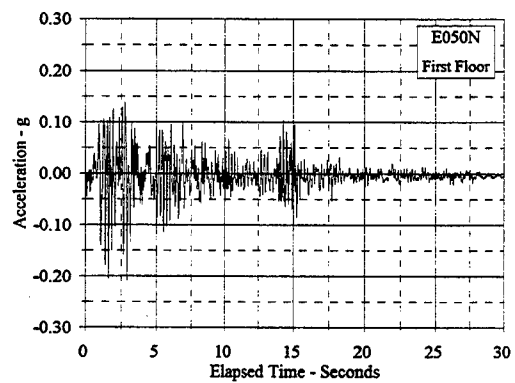
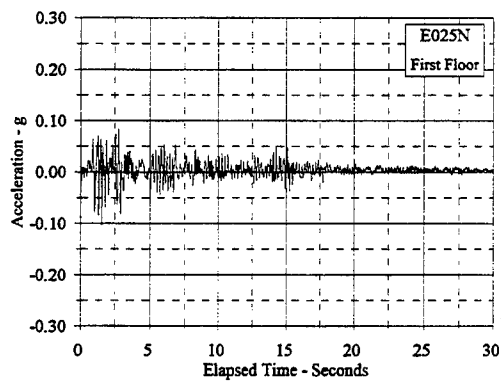
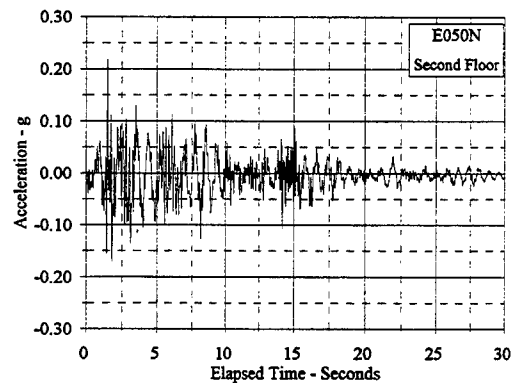
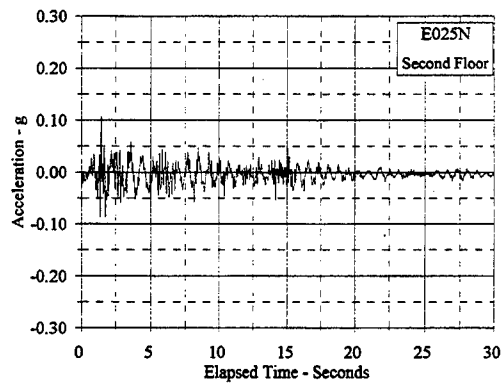
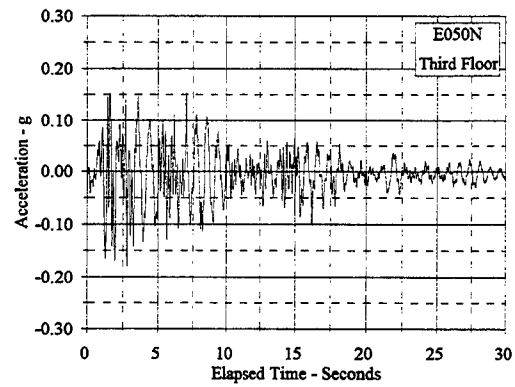
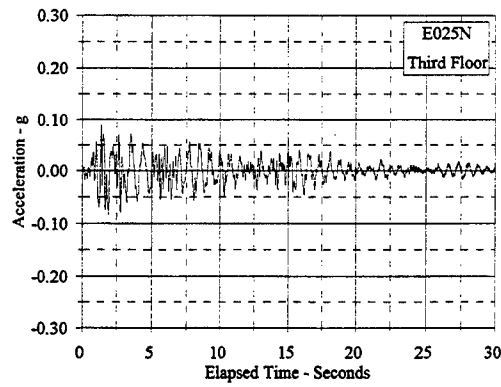


Figure C.1.14 Acceleration Vs. Elapsed Time: E025N, E050N

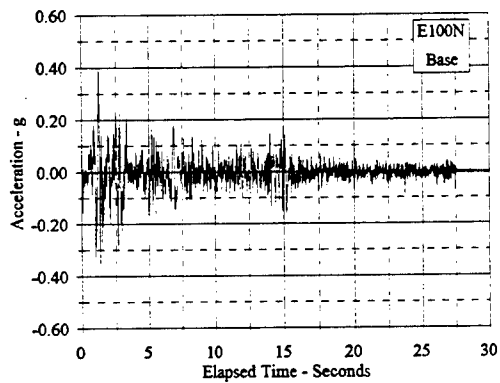
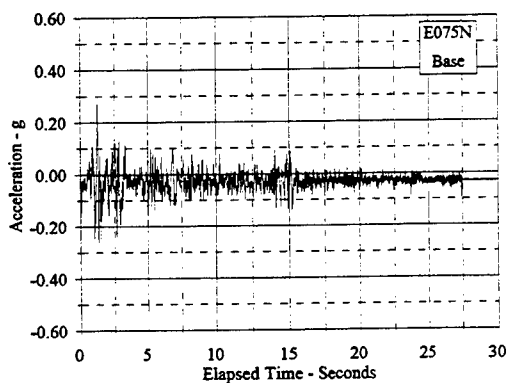
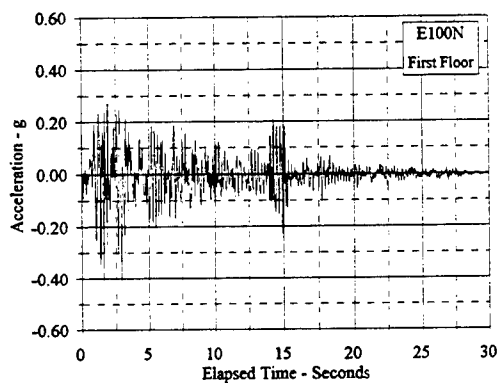
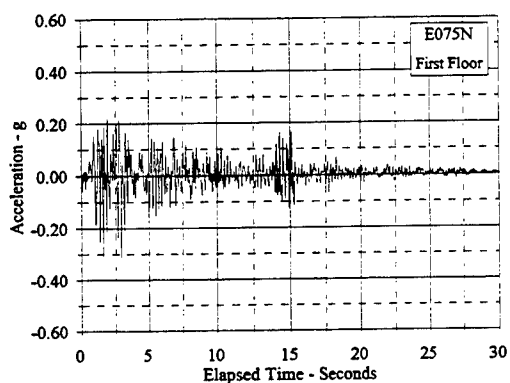
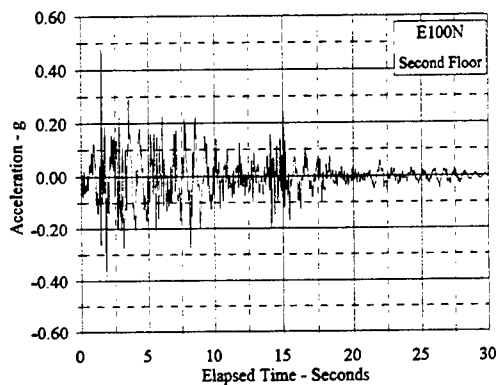
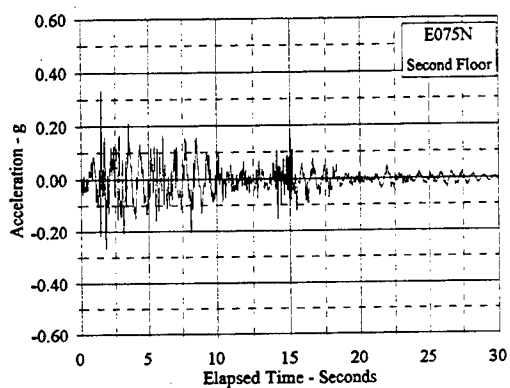
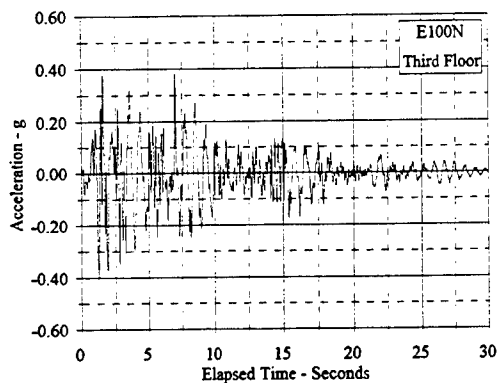
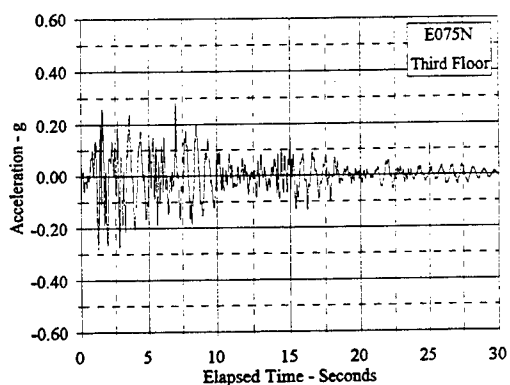


Figure C.1.15 Acceleration Vs. Elapsed Time: E075N, E100N

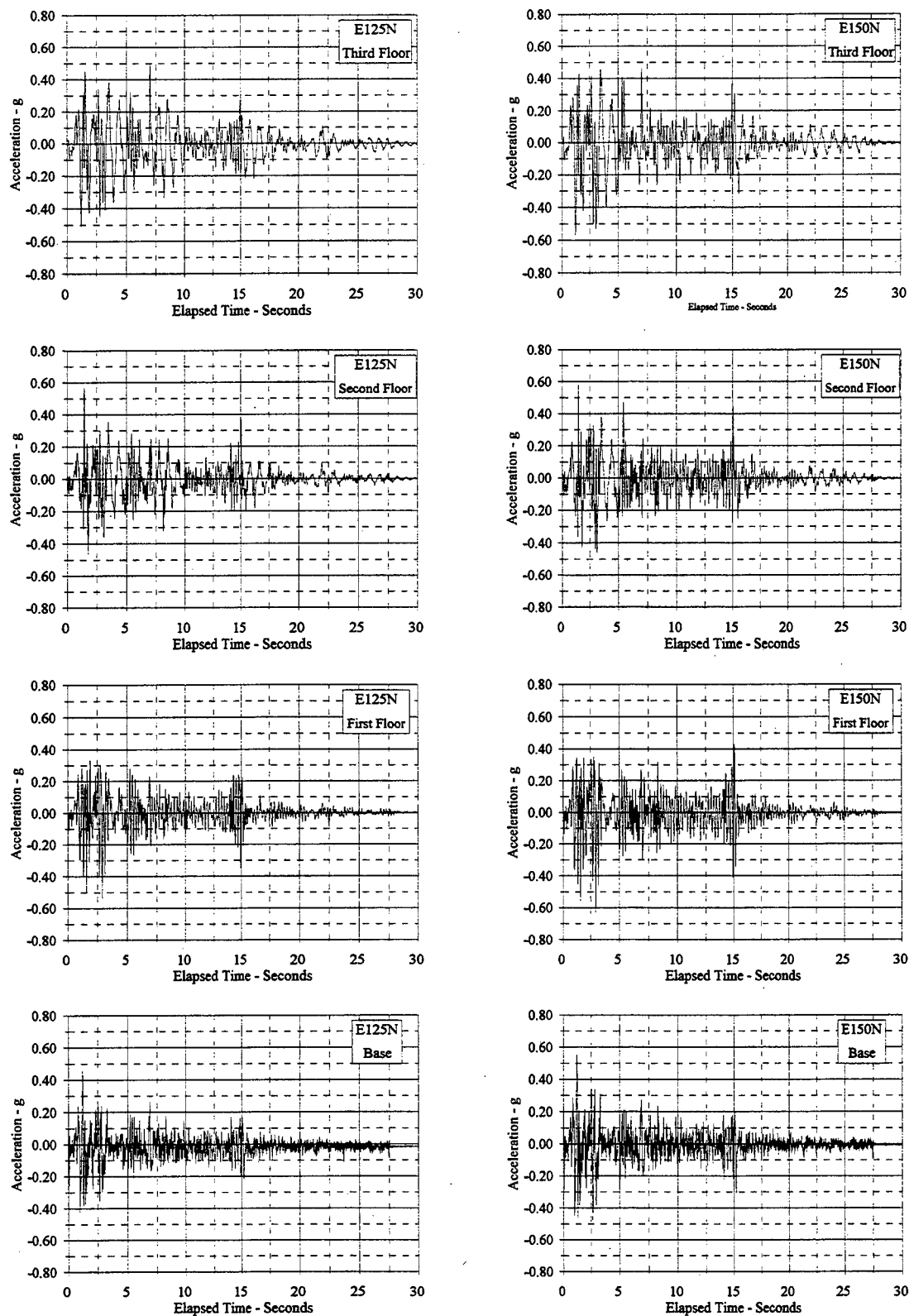


Figure C.1.16 Acceleration Vs. Elapsed Time: E125N, E150N

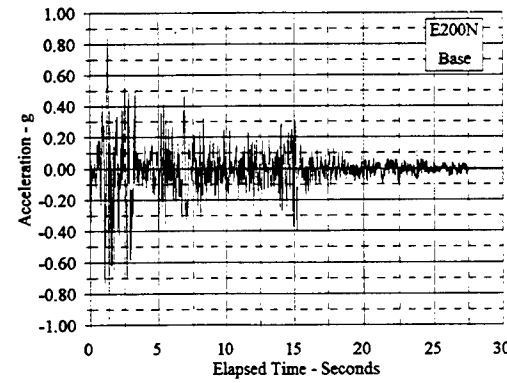
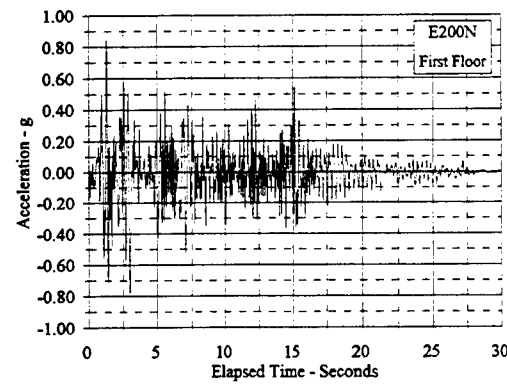
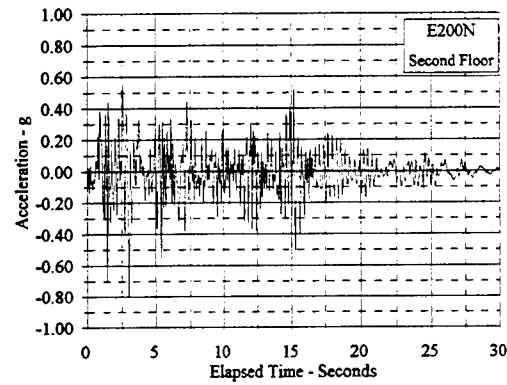
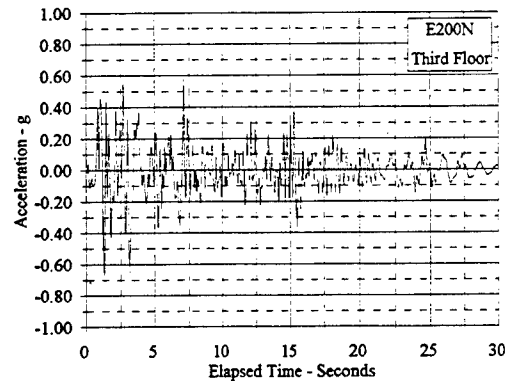


Figure C.1.17 Acceleration Vs. Elapsed Time: E200N

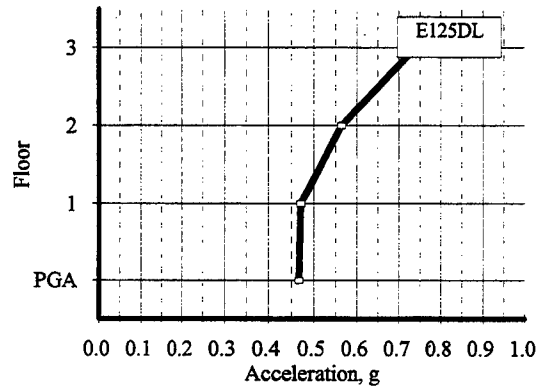
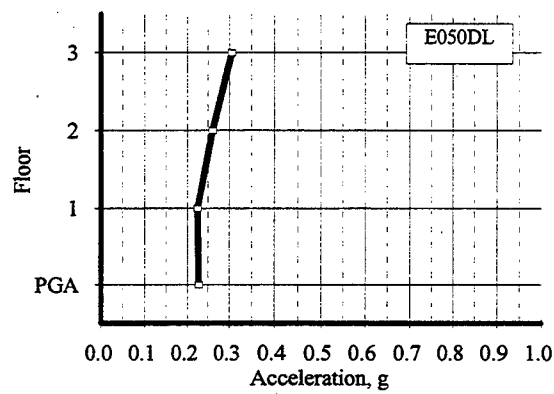
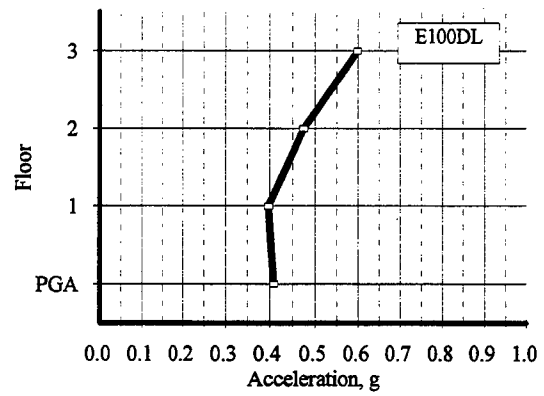
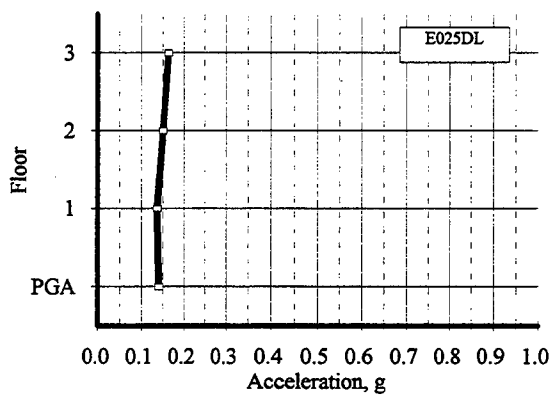
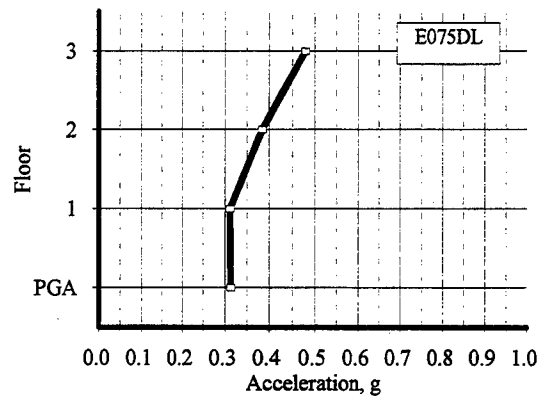
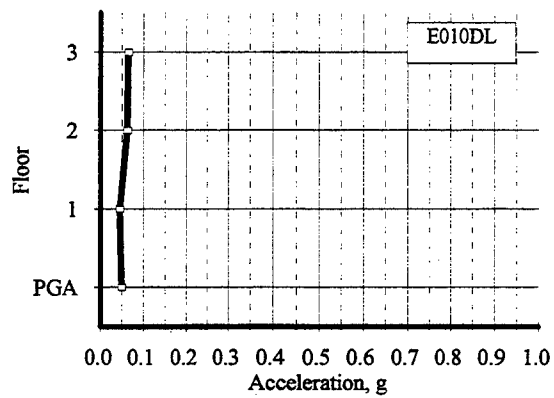


Figure C.1.18 Maximum Floor Acceleration Profiles: E010DL - E125DL

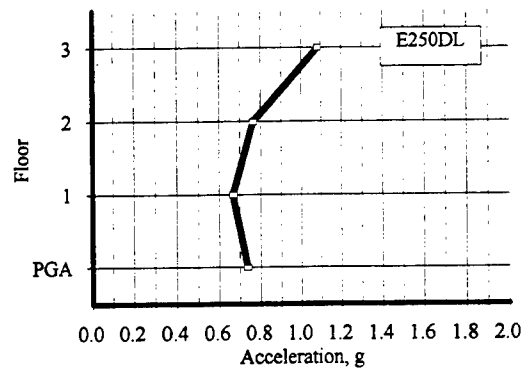
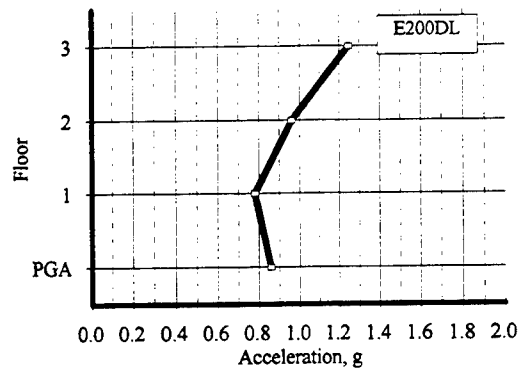
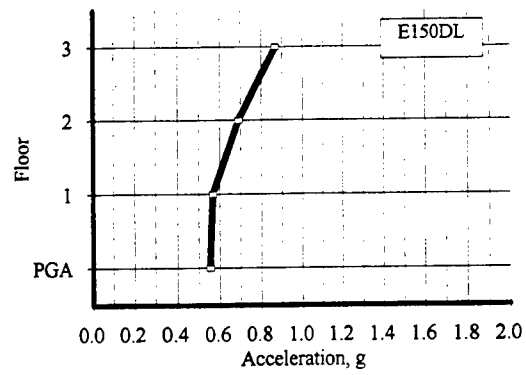


Figure C.1.19 Maximum Floor Acceleration Profiles: E150DL - E250DL

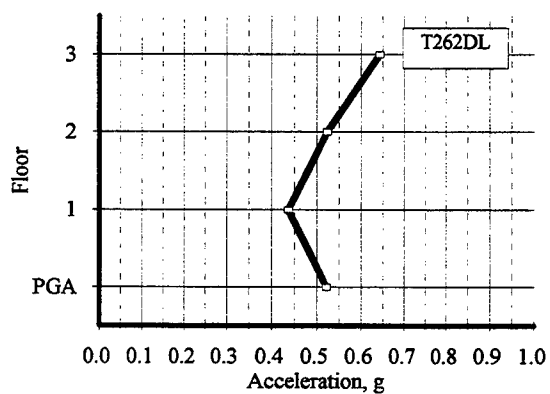
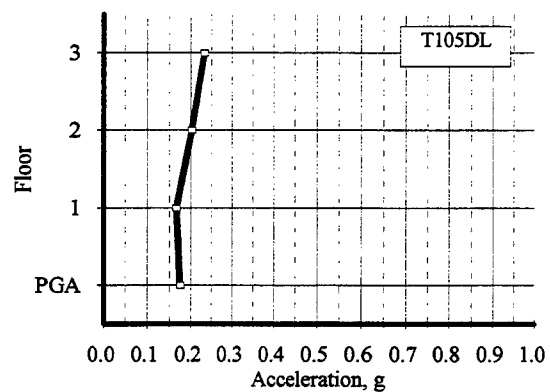
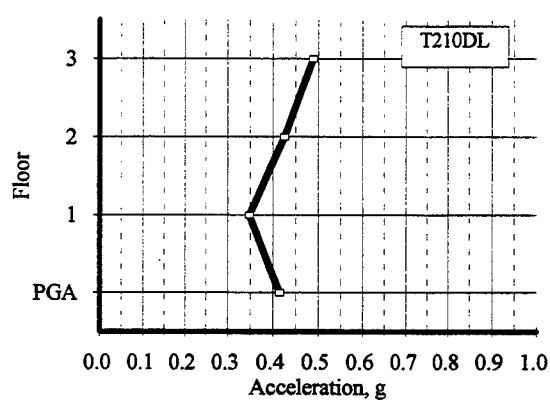
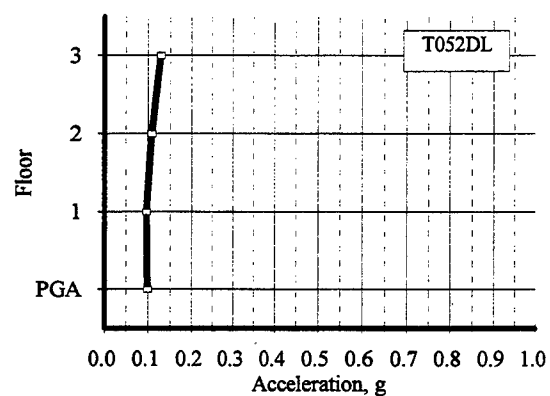
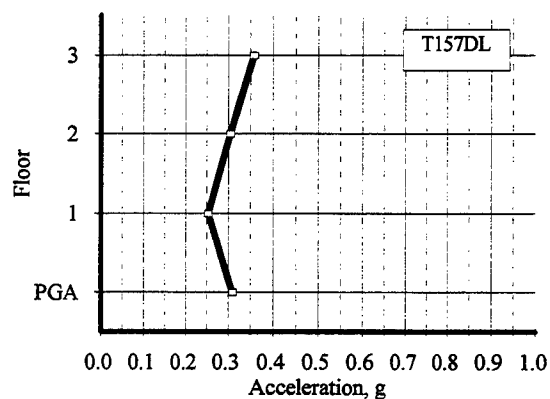
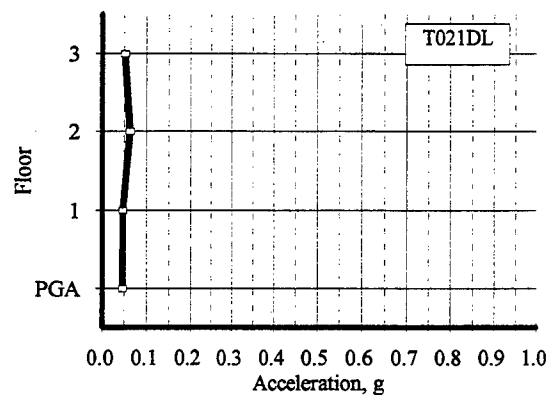


Figure C.1.20 Maximum Floor Acceleration Profiles: T021DL - T262DL

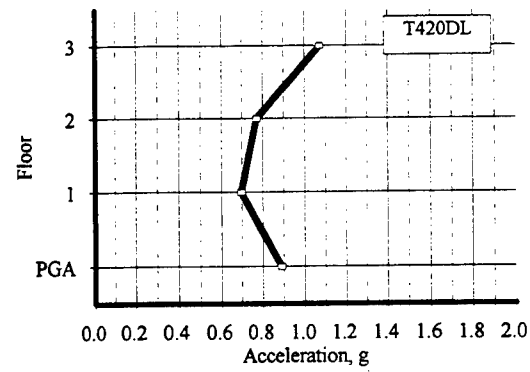
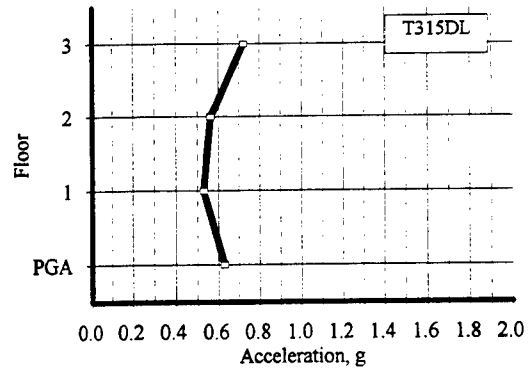


Figure C.1.21 Maximum Floor Acceleration Profiles: T315DL - T420DL

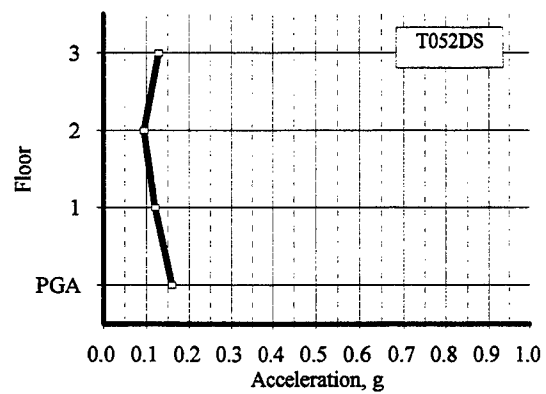
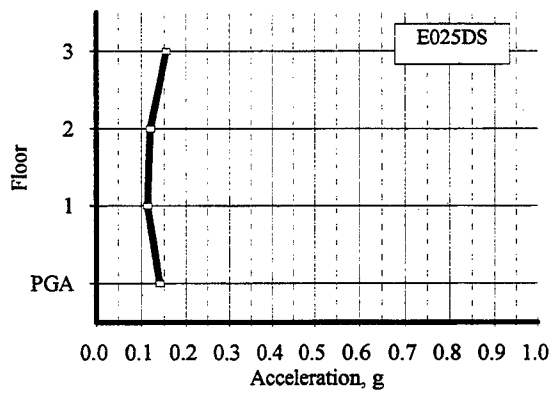
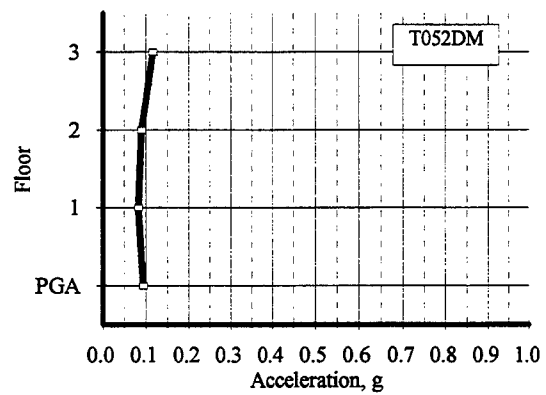
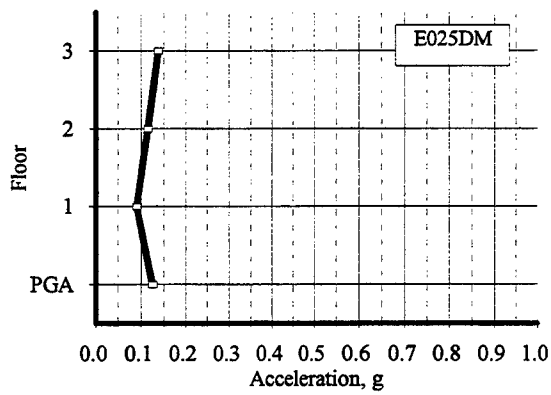
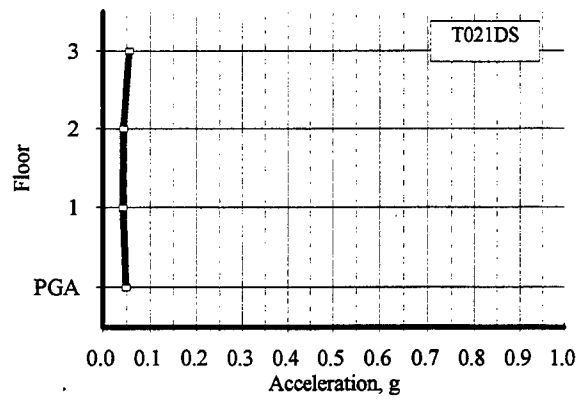
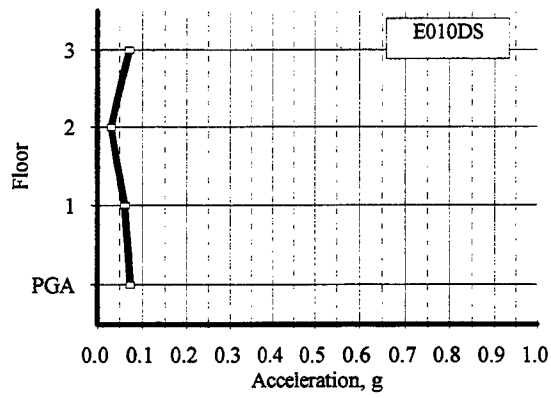


Figure C.1.22 Maximum Floor Acceleration Profiles: E010DS -T052DS

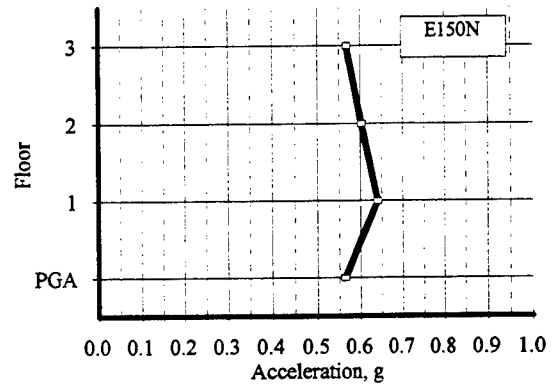
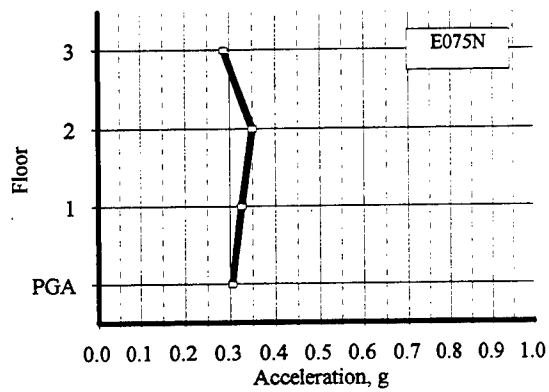
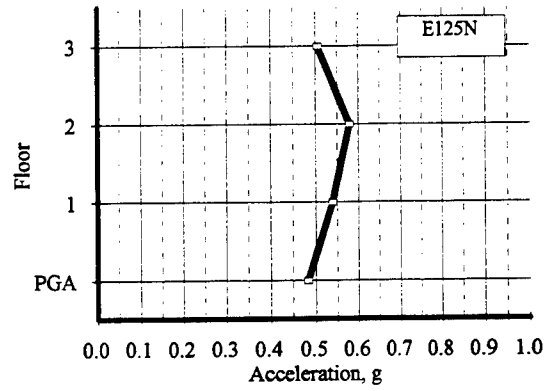
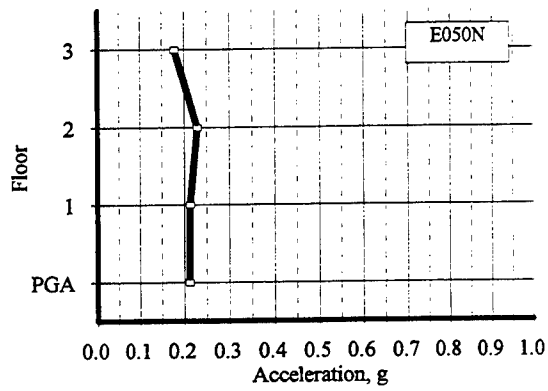
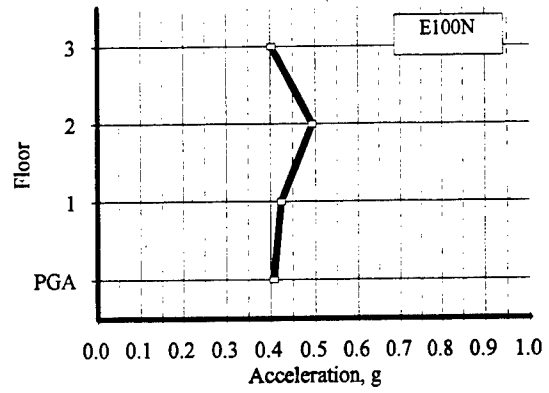
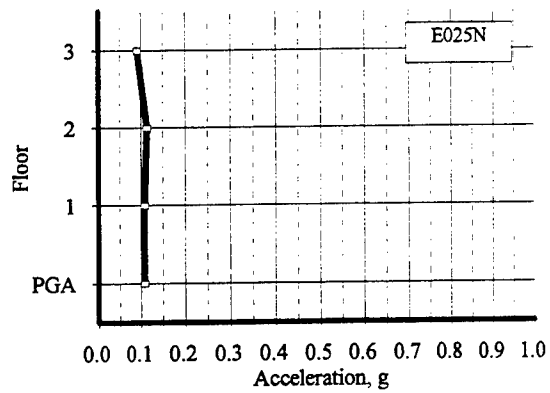


Figure C.1.23 Maximum Floor Acceleration Profiles: E025N - E150N

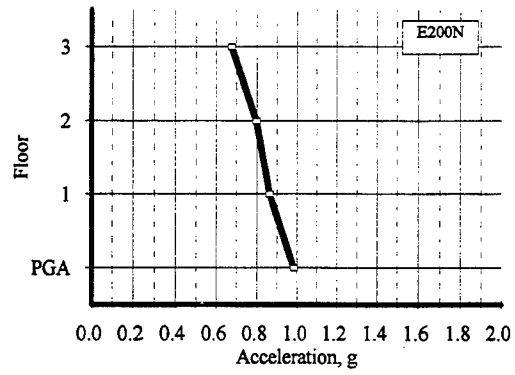


Figure C.1.24 Maximum Floor Acceleration Profile: E200N

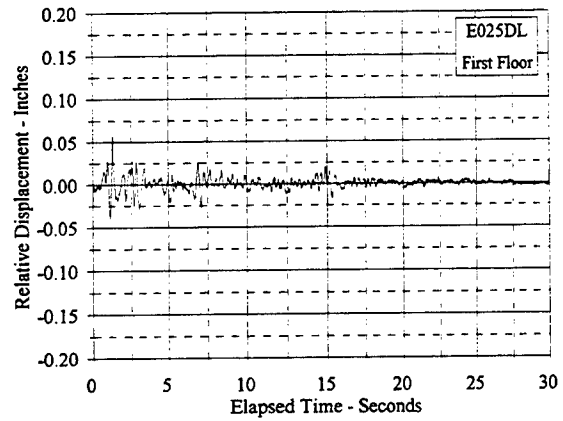
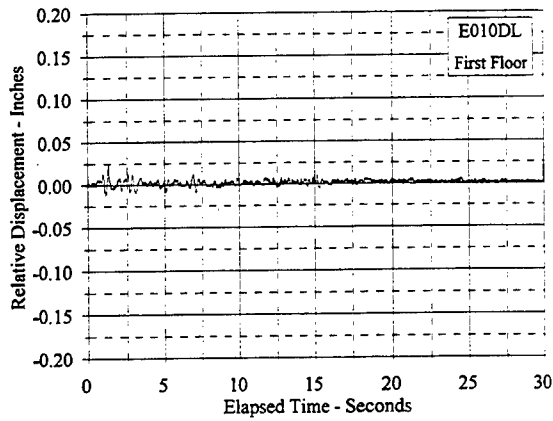
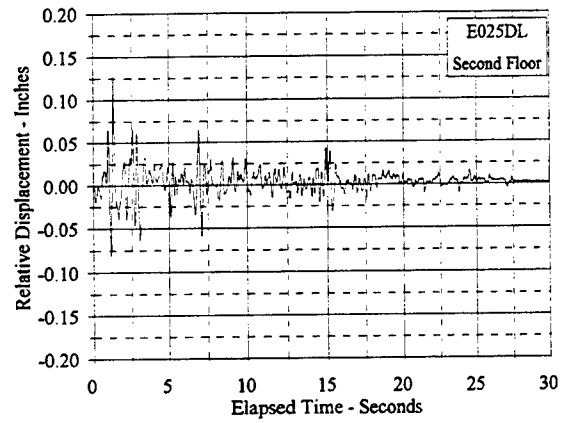
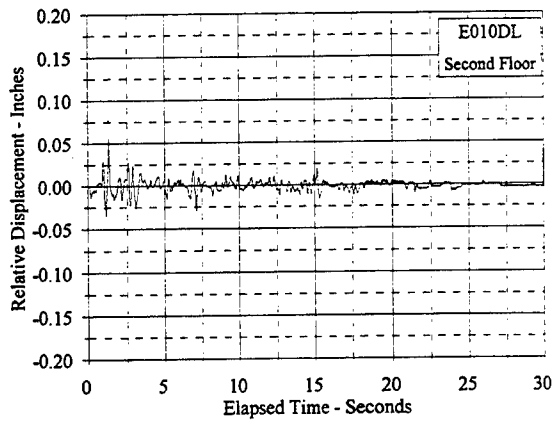
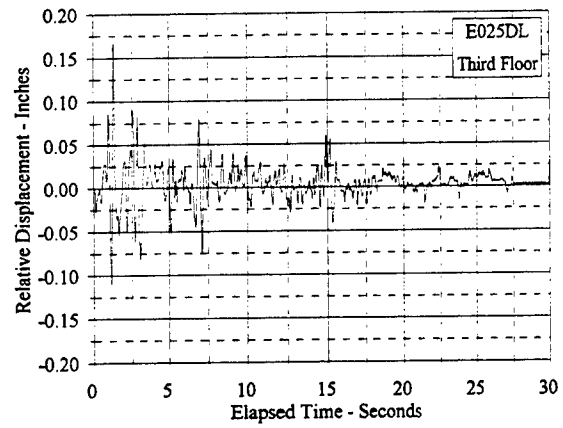
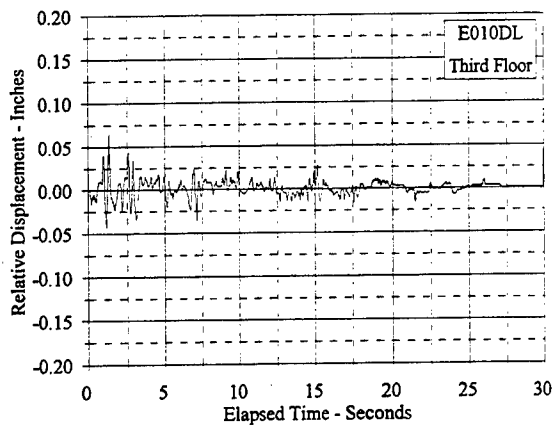


Figure C.2.1 Relative Displacement Vs. Elapsed Time: E010DL, E025DL

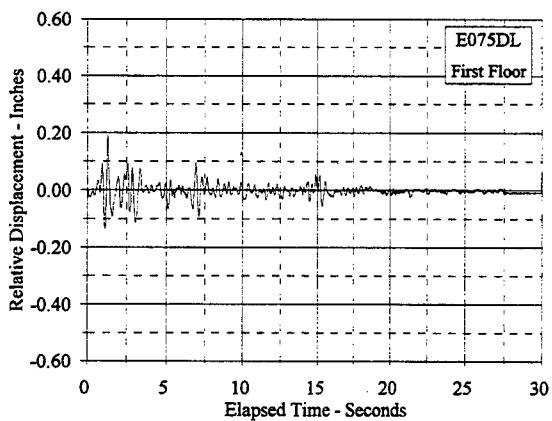
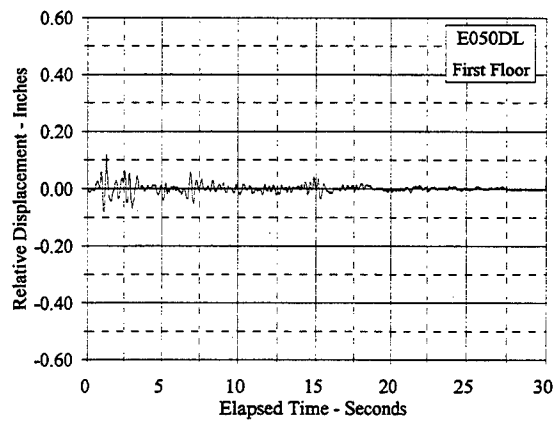
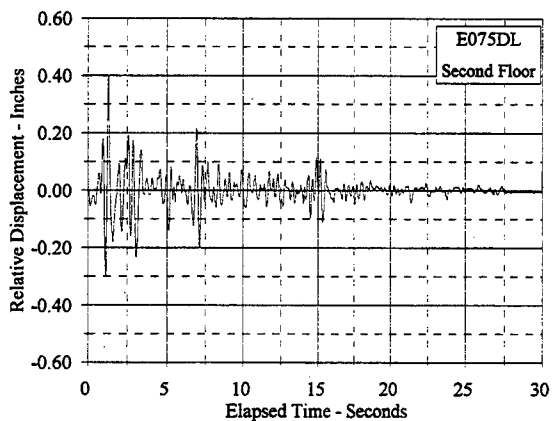
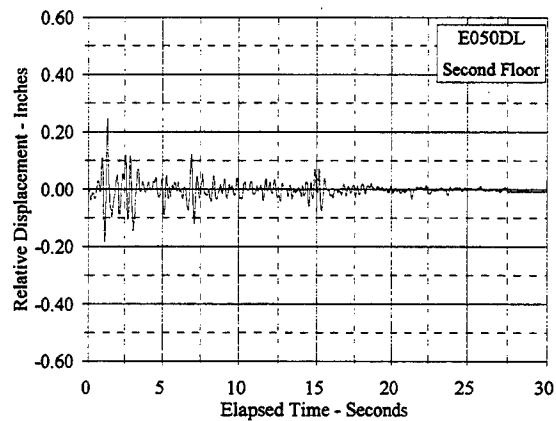
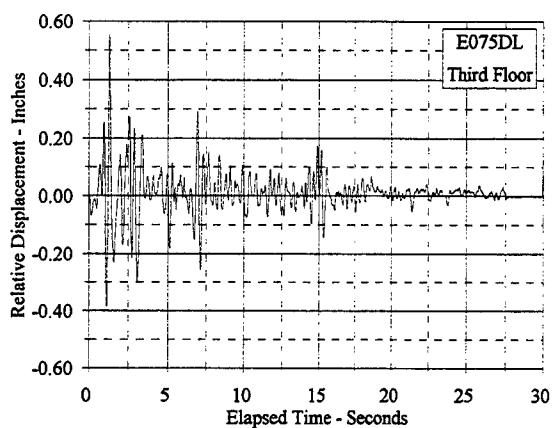
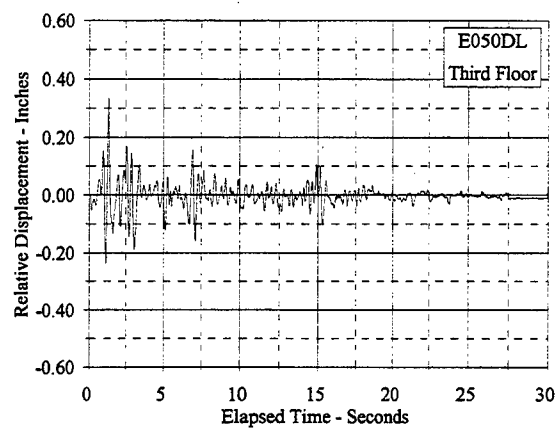


Figure C.2.2 Relative Displacement Vs. Elapsed Time: E050DL, E075DL

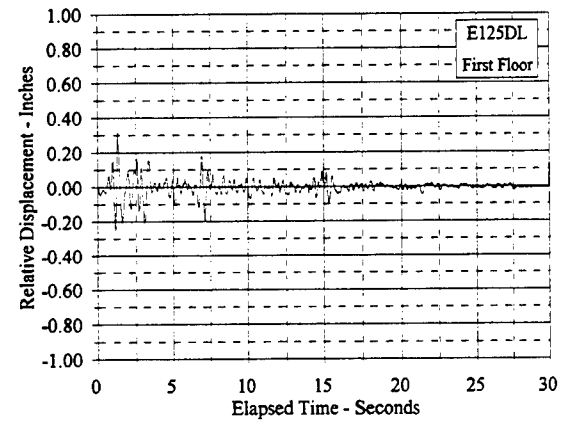
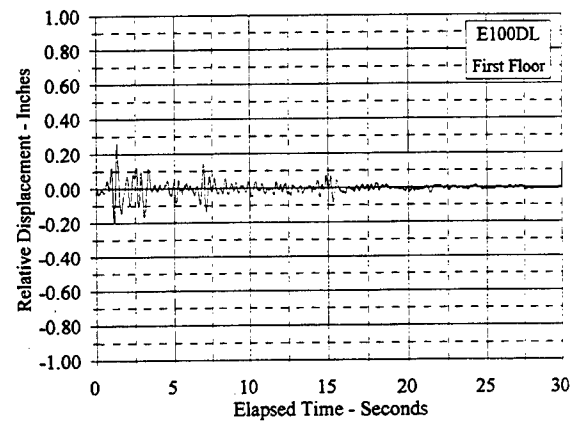
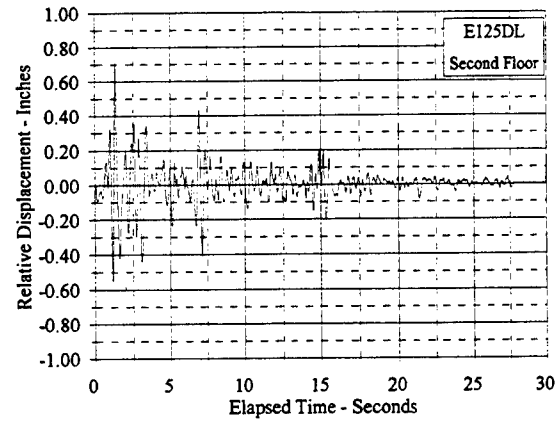
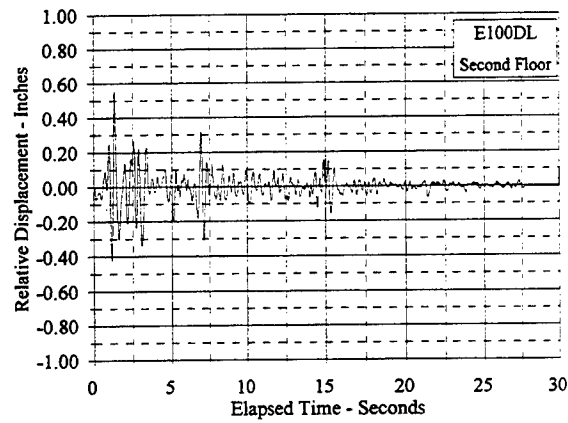
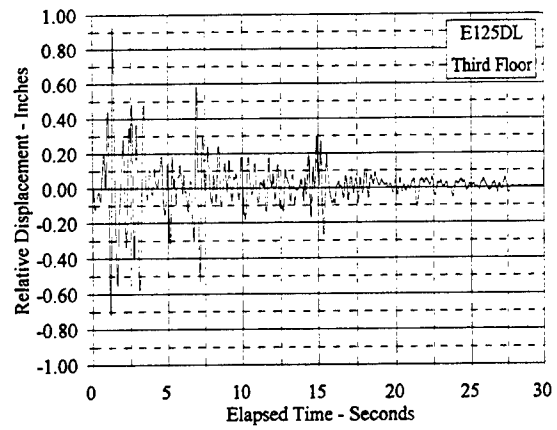
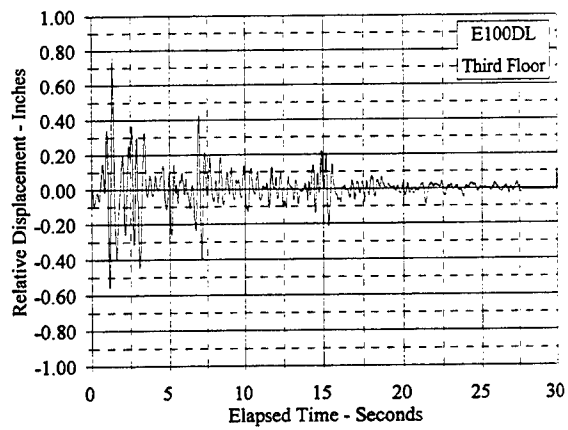


Figure C.2.3 Relative Displacement Vs. Elapsed Time: E100DL, E125DL

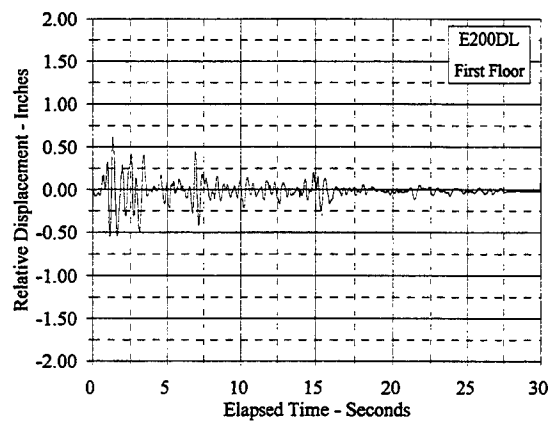
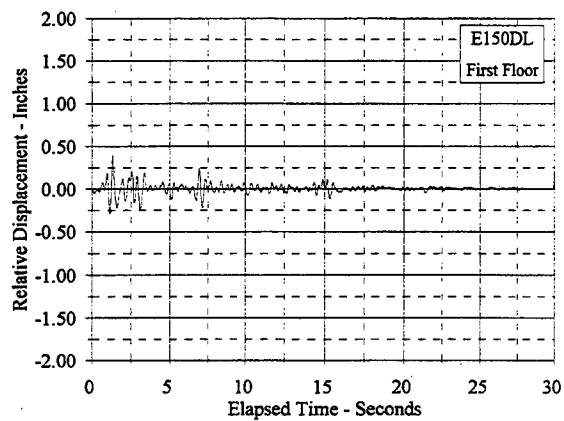
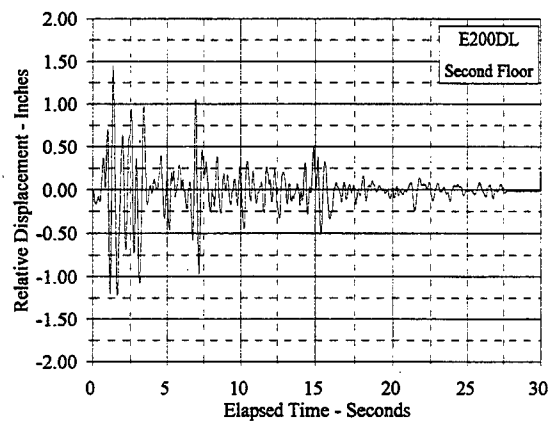
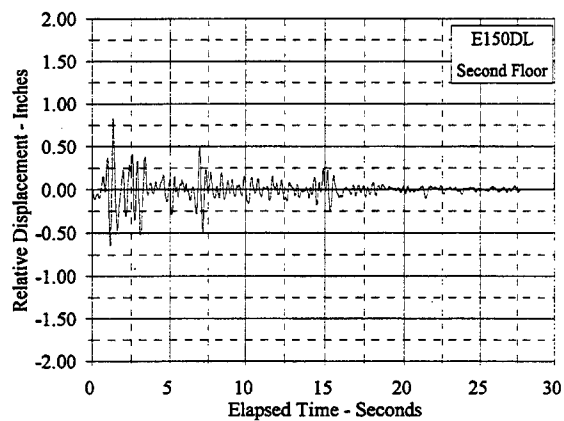
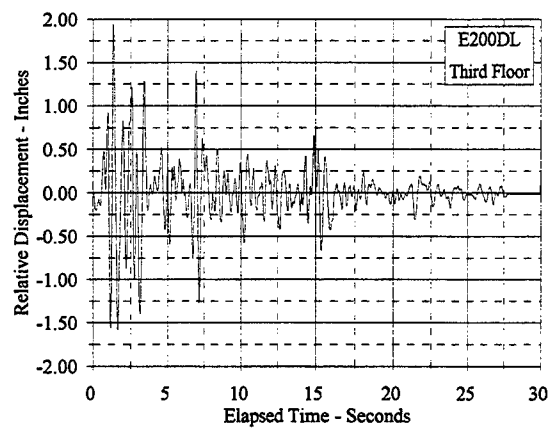
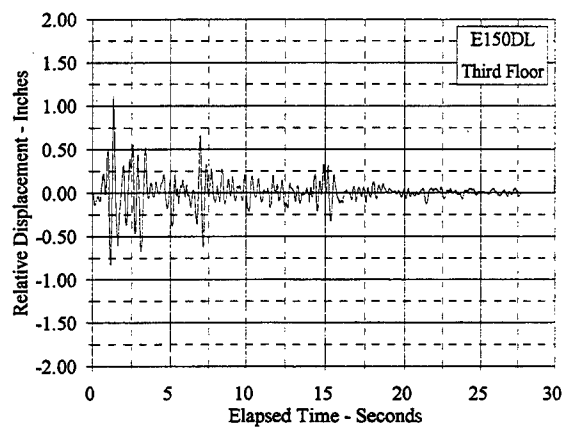


Figure C.2.4 Relative Displacement Vs. Elapsed Time: E150DL, E200DL

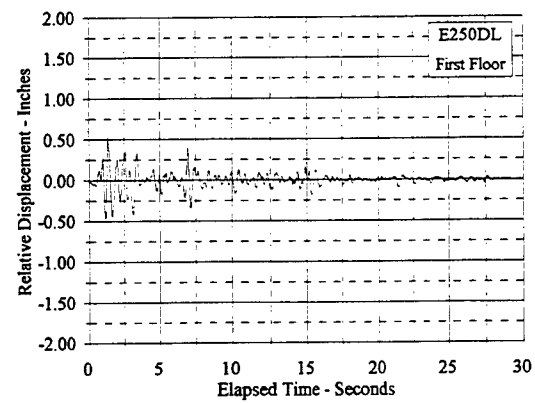
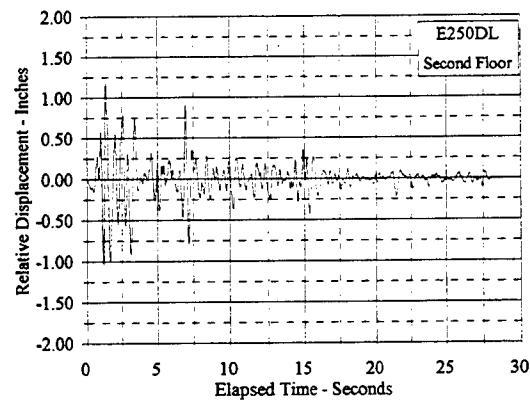
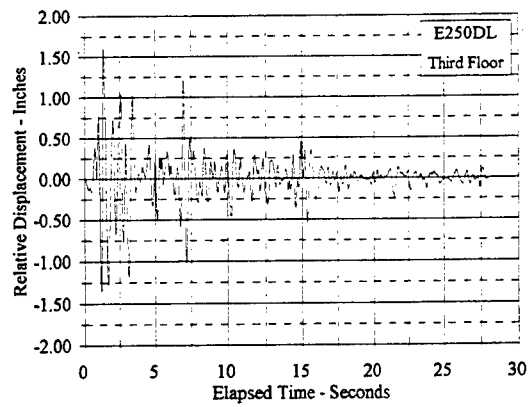


Figure C.2.5 Relative Displacement Vs. Elapsed Time: E250DL

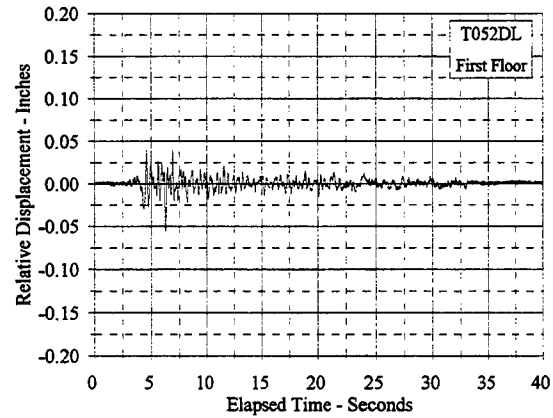
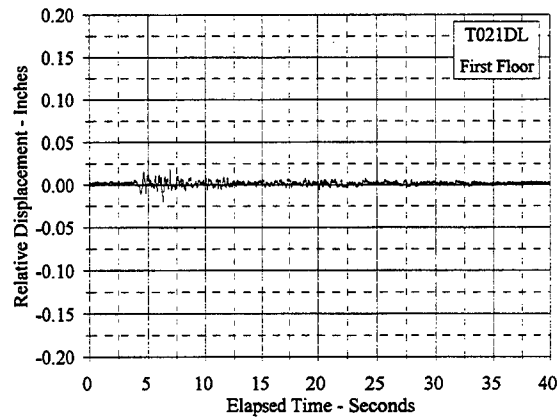
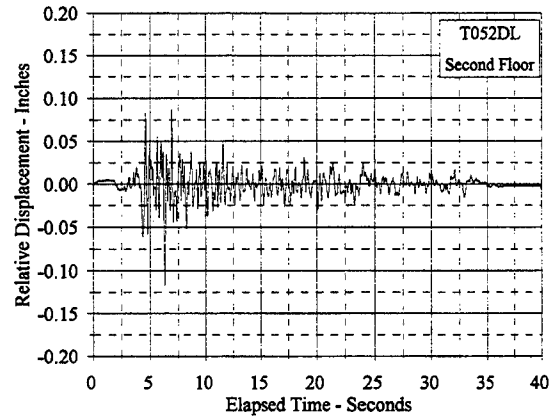
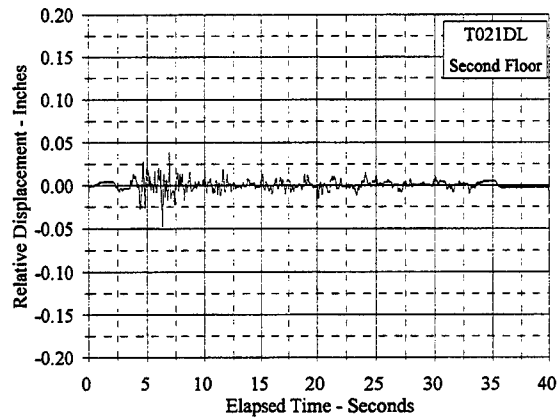
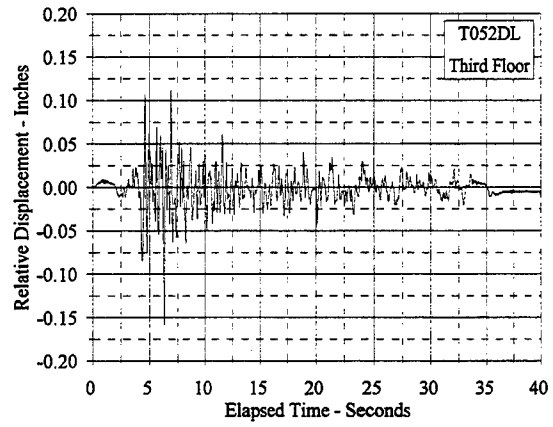
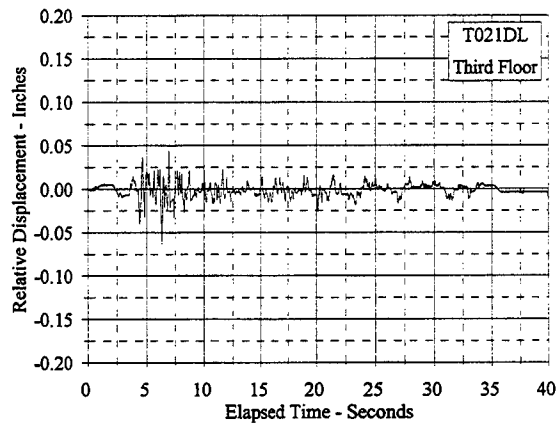


Figure C.2.6 Relative Displacement Vs. Elapsed Time: T021DL, T052DL

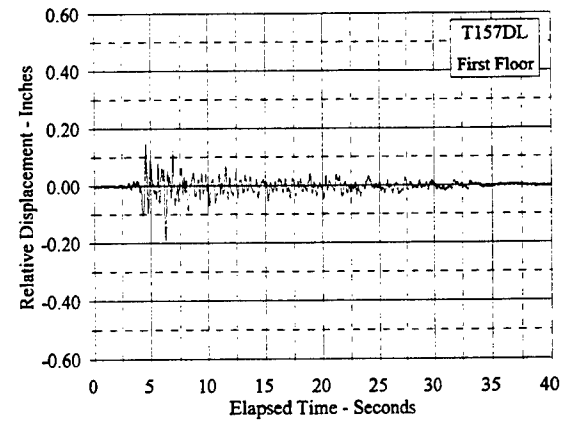
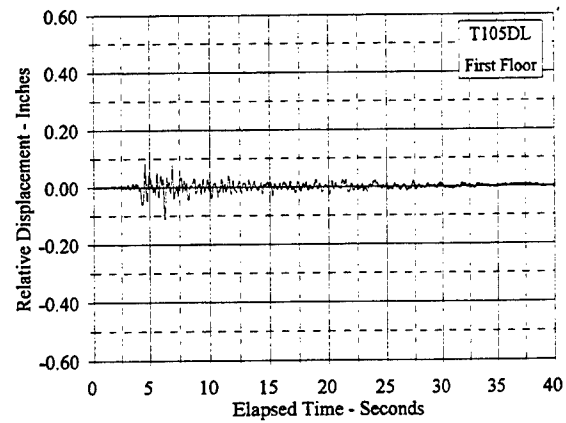
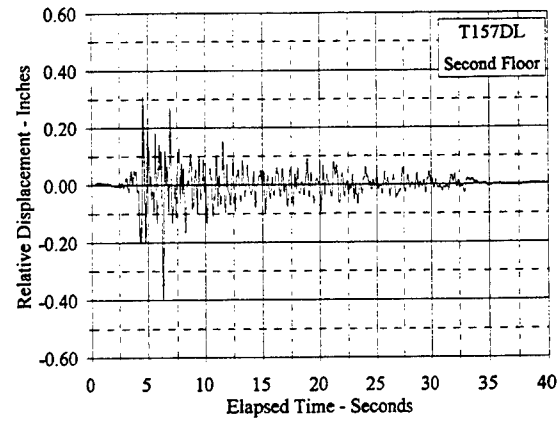
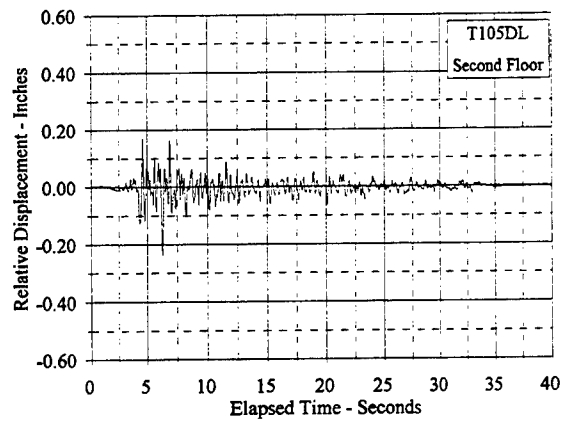
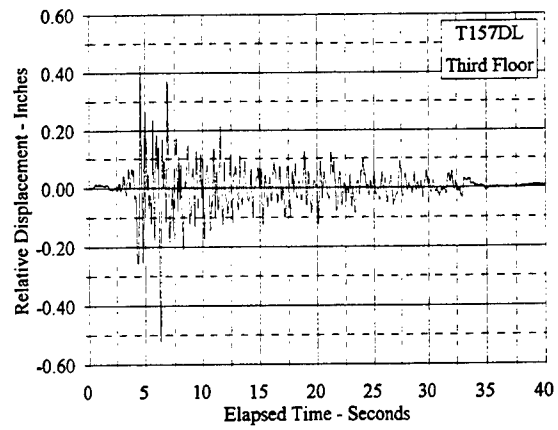
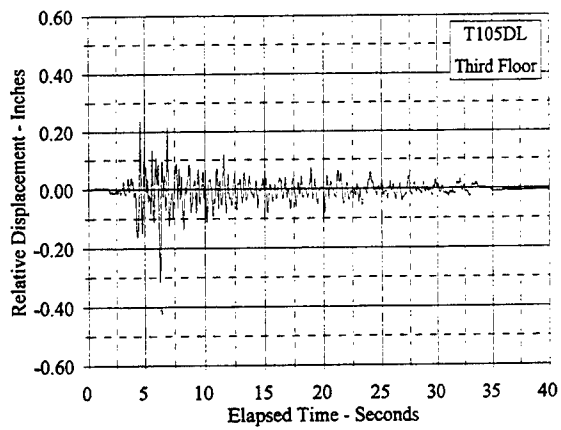


Figure C.2.7 Relative Displacement Vs. Elapsed Time: T105DL, T157DL

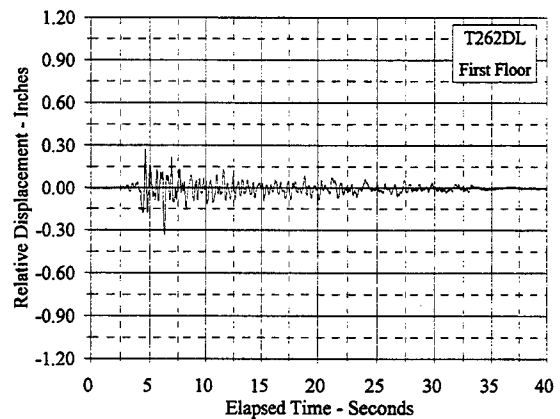
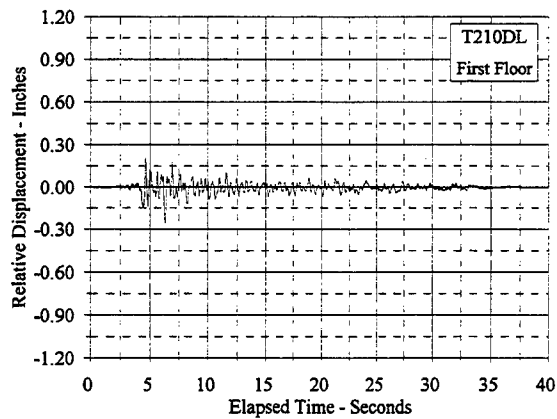
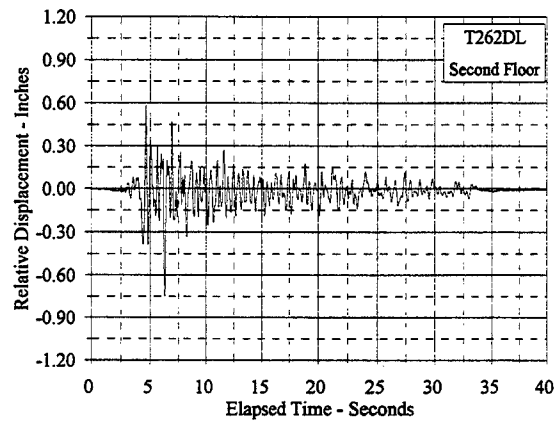
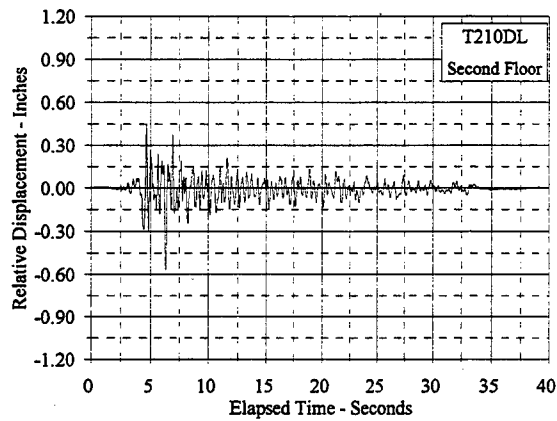
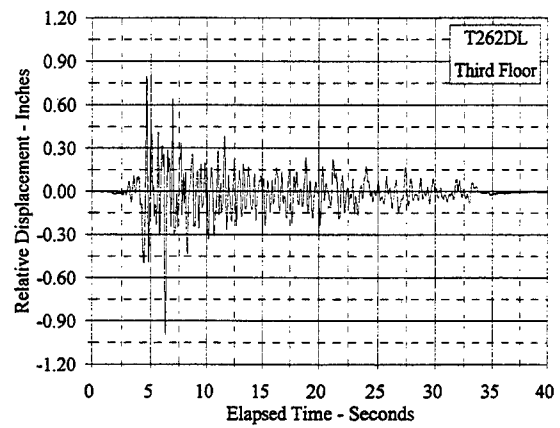
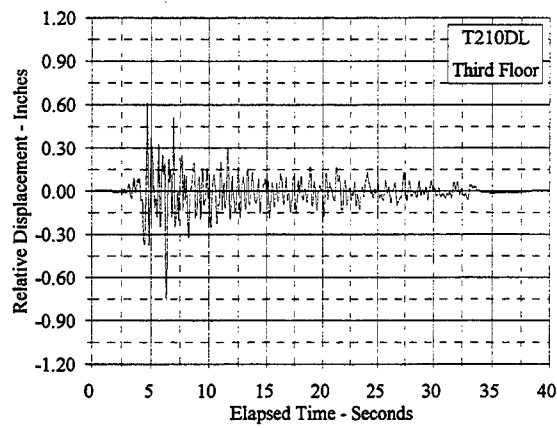


Figure C.2.8 Relative Displacement Vs. Elapsed Time: T210DL, T262DL

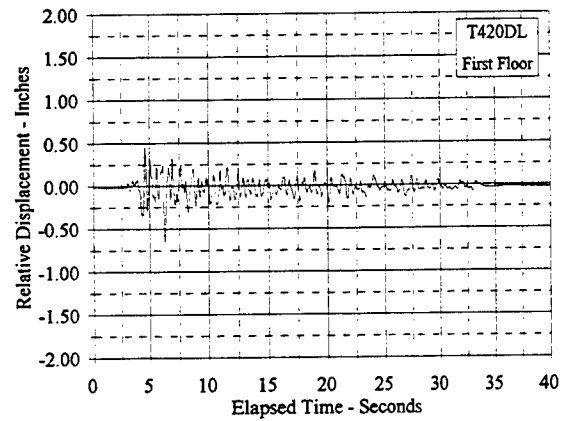
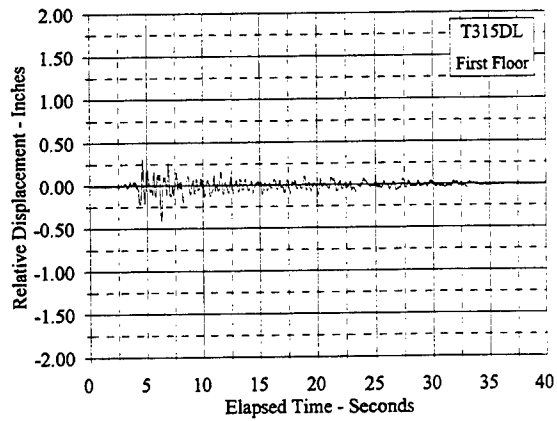
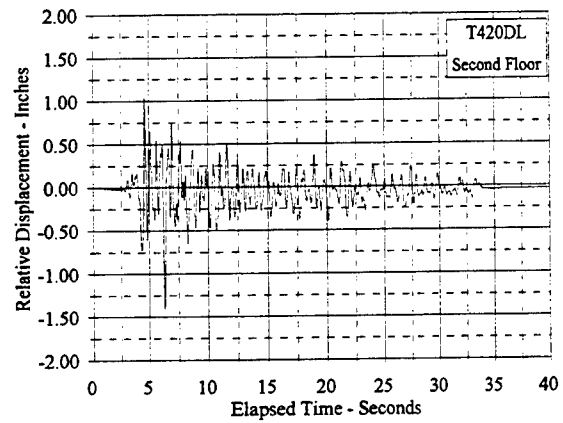
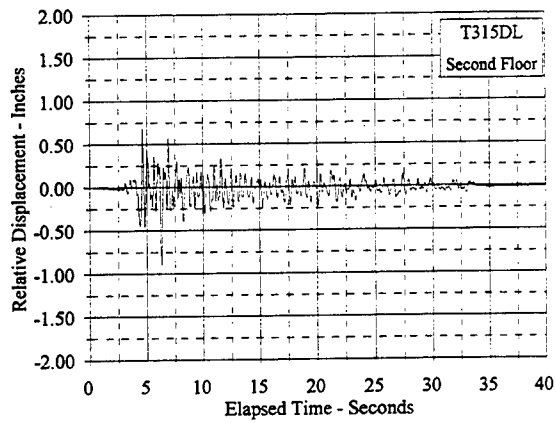
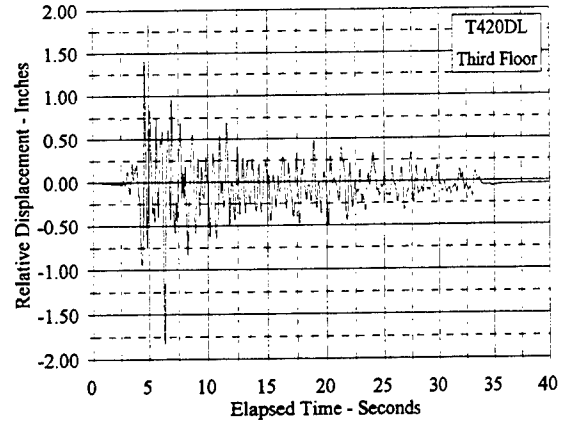
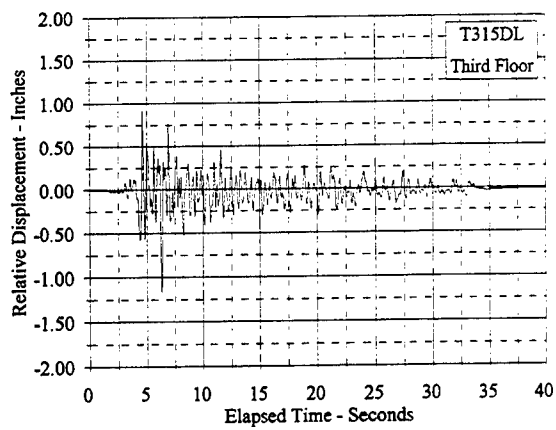


Figure C.2.9 Relative Displacement Vs. Elapsed Time: T315DL, T420DL

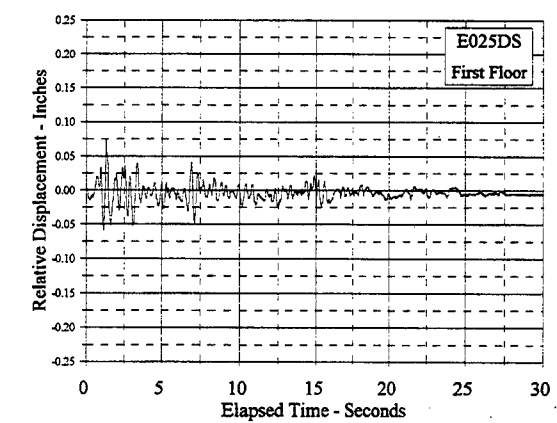
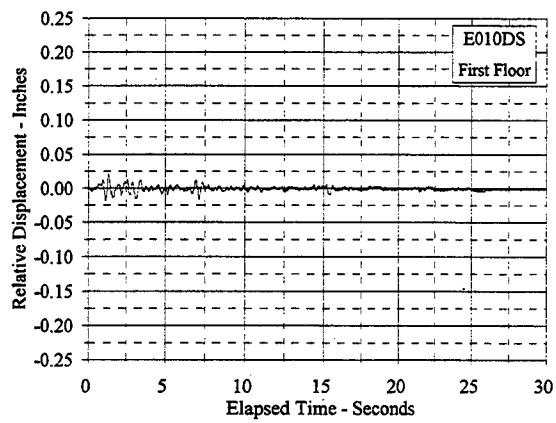
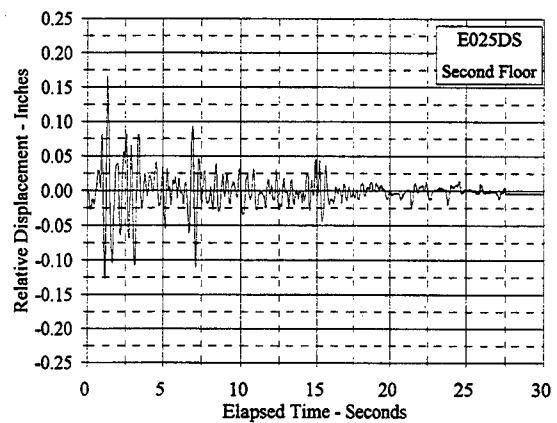
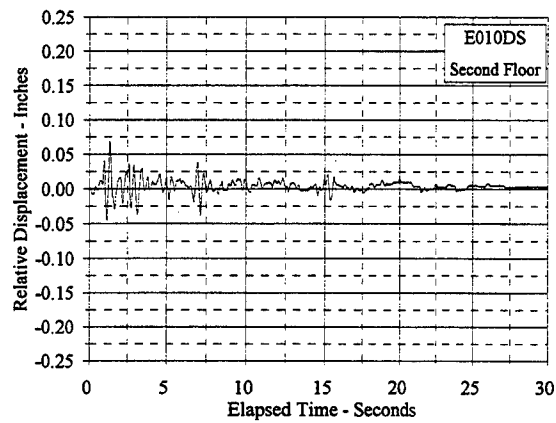
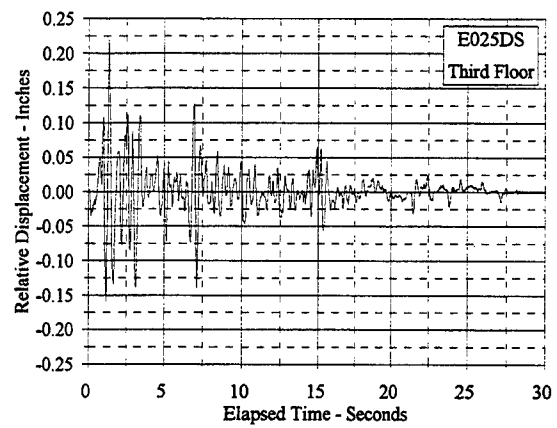
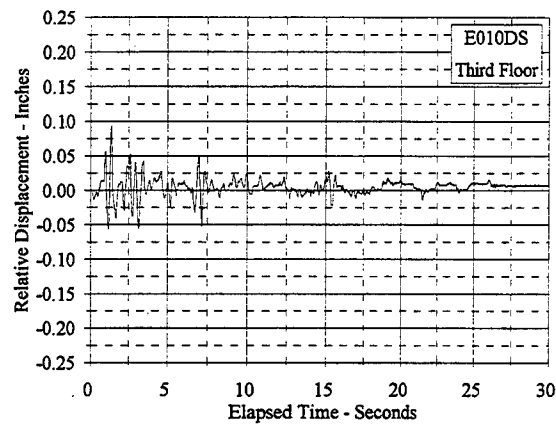


Figure C.2.10 Relative Displacement Vs. Elapsed Time: E010DS, E025DS

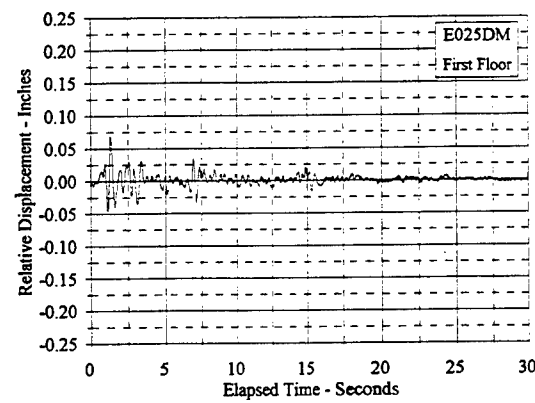
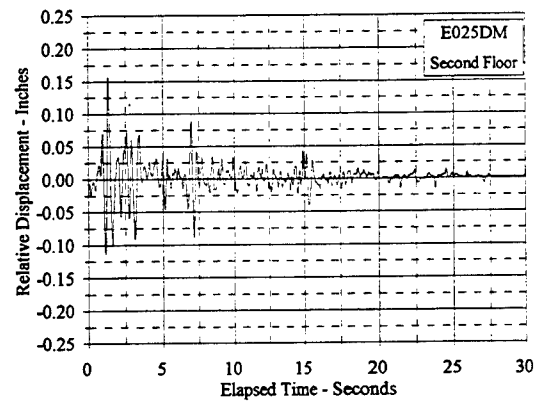
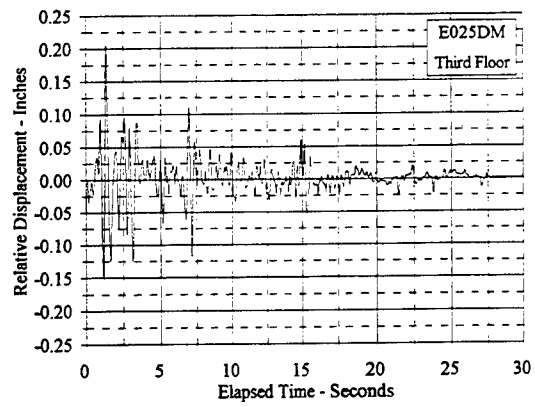


Figure C.2.11 Relative Displacement Vs. Elapsed Time: E025DM

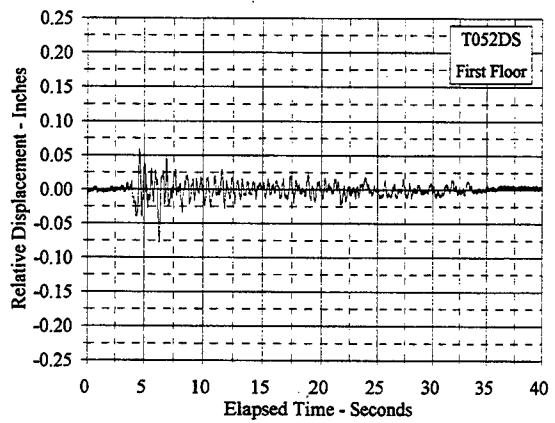
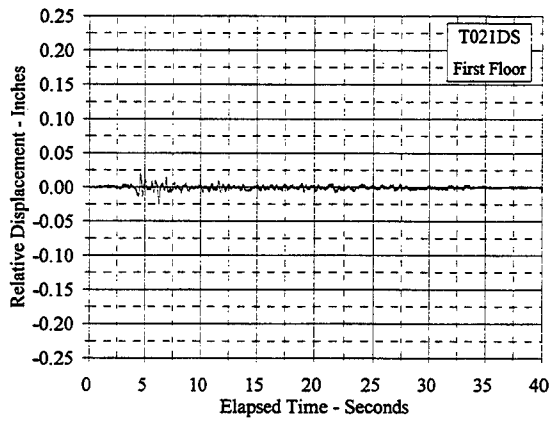
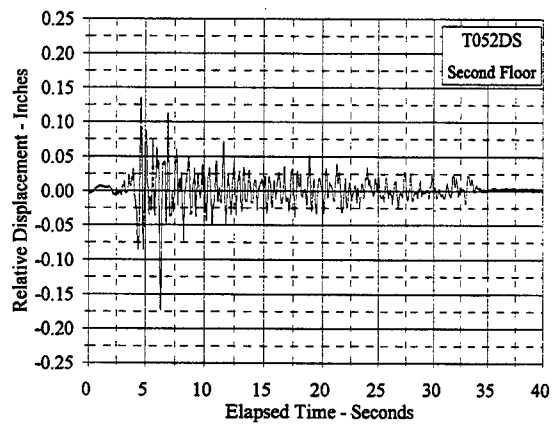
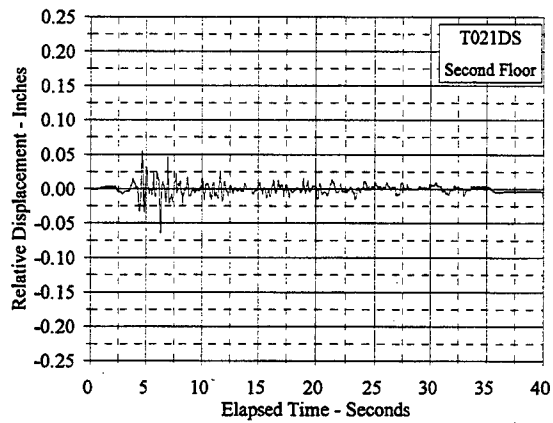
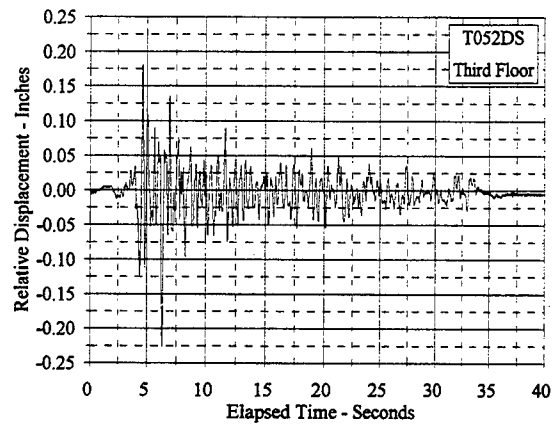
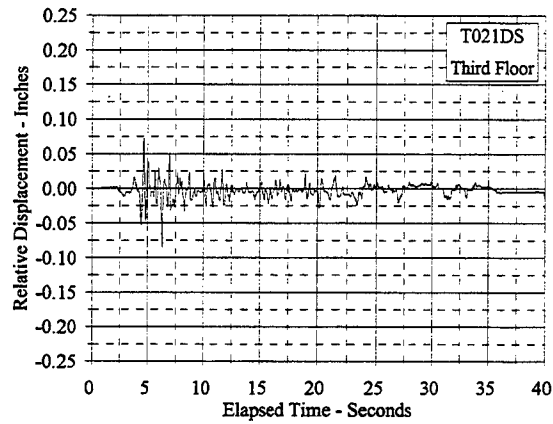


Figure C.2.12 Relative Displacement Vs. Elapsed Time: T021DS, T052DS

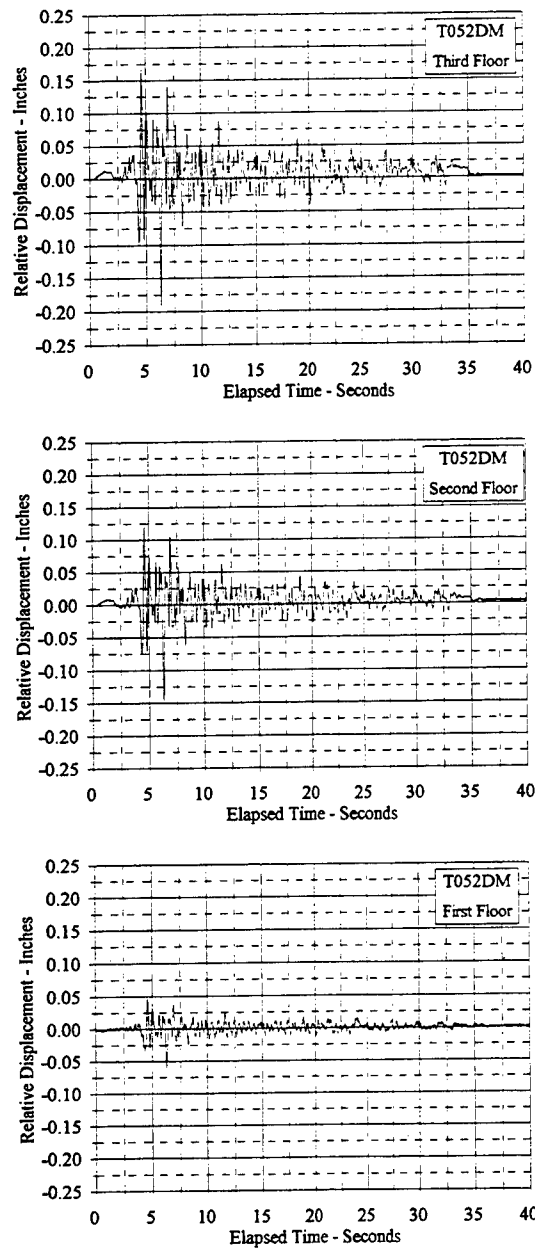


Figure C.2.13 Relative Displacement Vs. Elapsed Time: T052DM

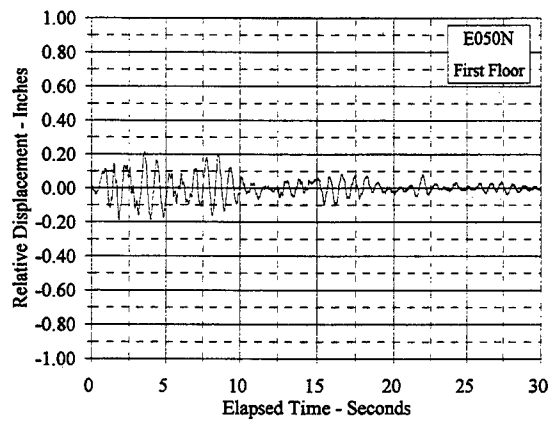
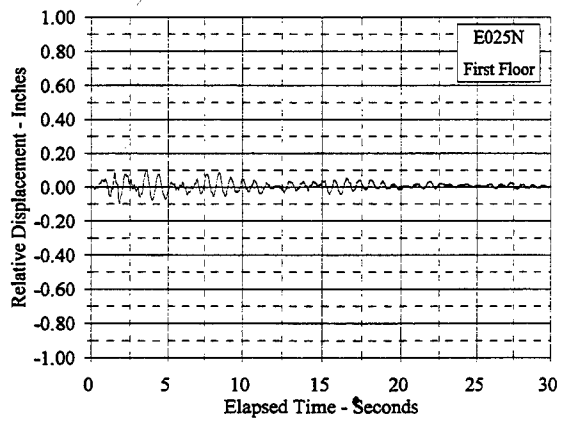
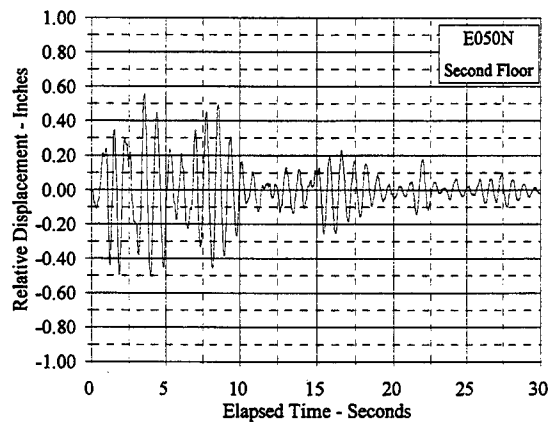
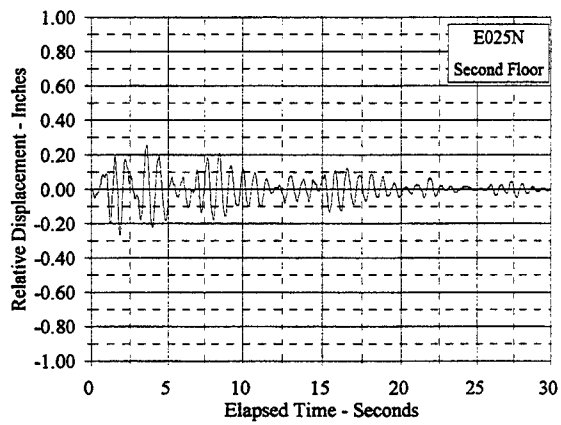
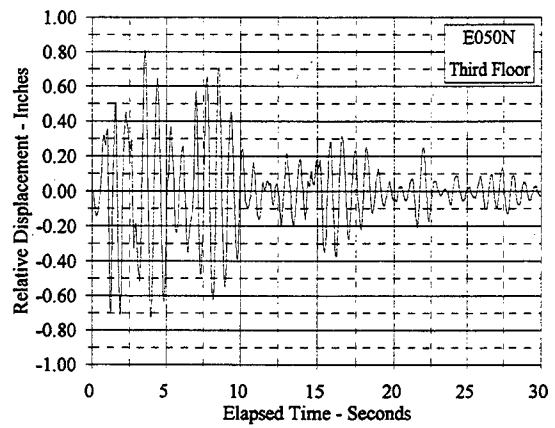
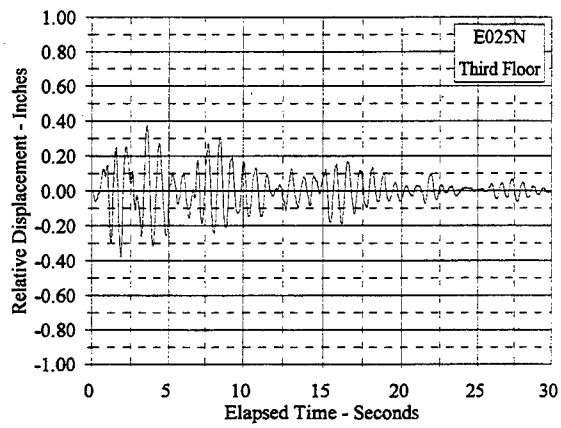


Figure C.2.14 Relative Displacement Vs. Elapsed Time: E025N, E050N

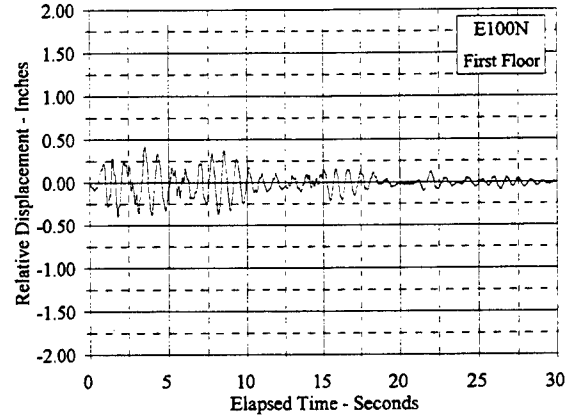
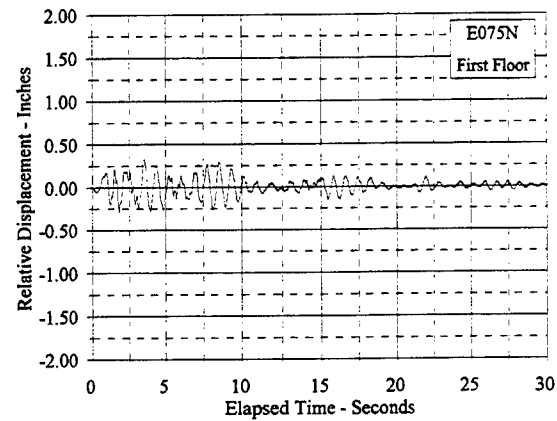
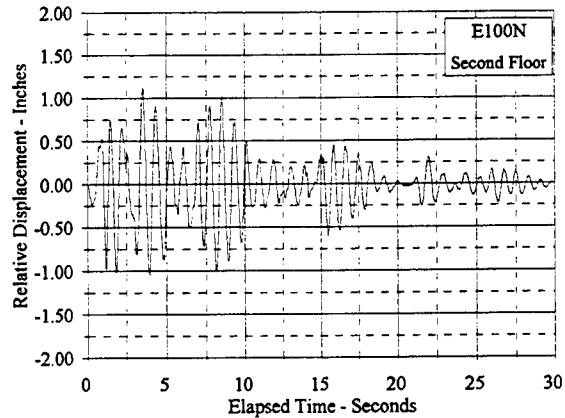
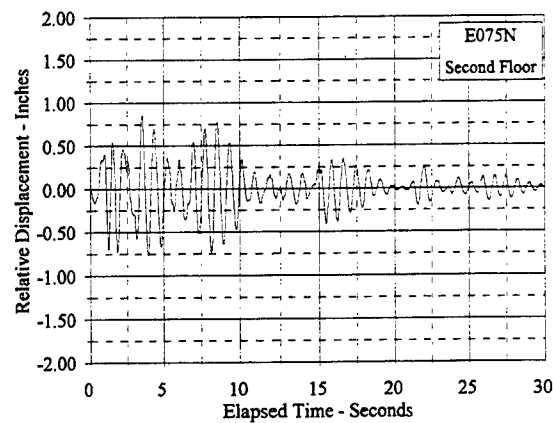
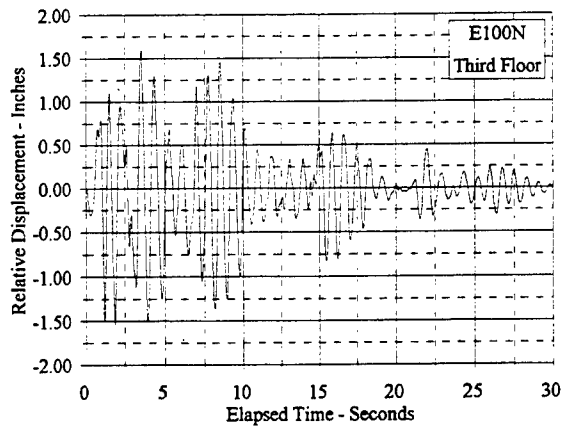
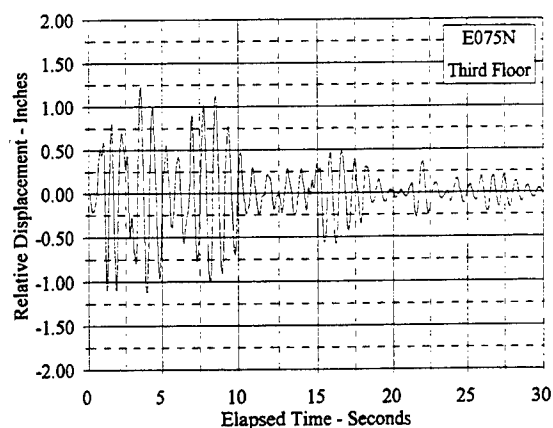


Figure C.2.15 Relative Displacement Vs. Elapsed Time: E075N, E100N

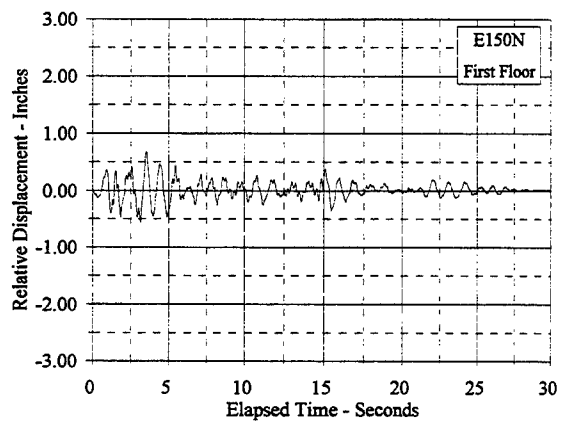
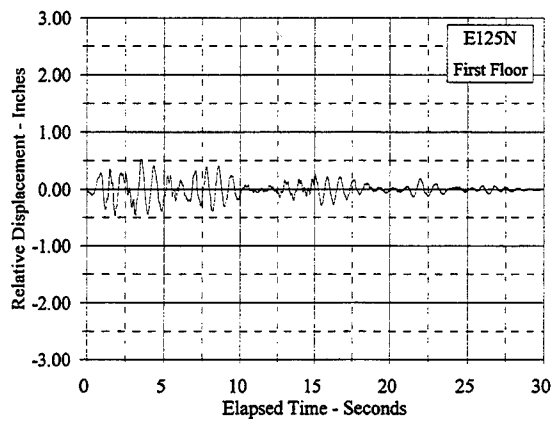
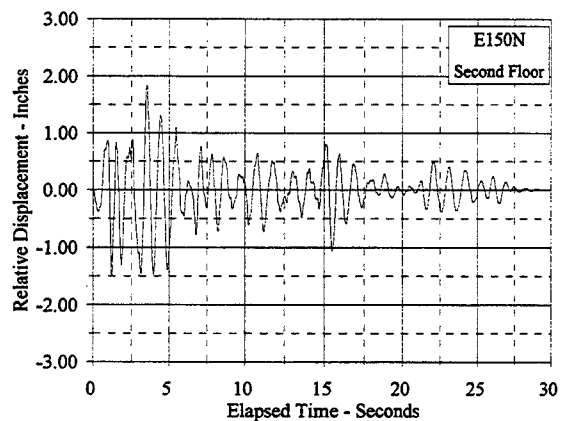
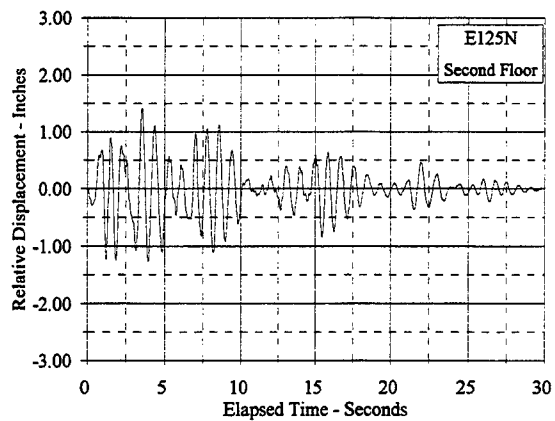
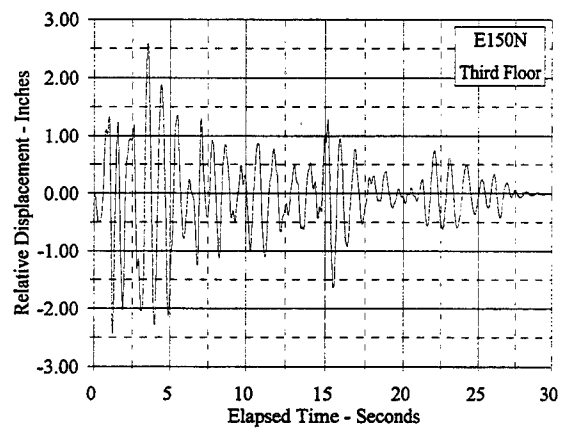
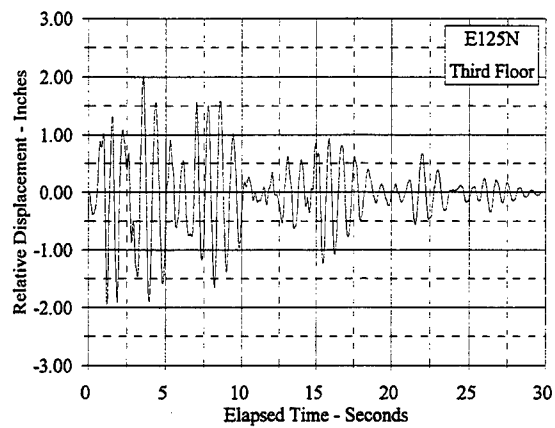


Figure C.2.16 Relative Displacement Vs. Elapsed Time: E125N, E150N

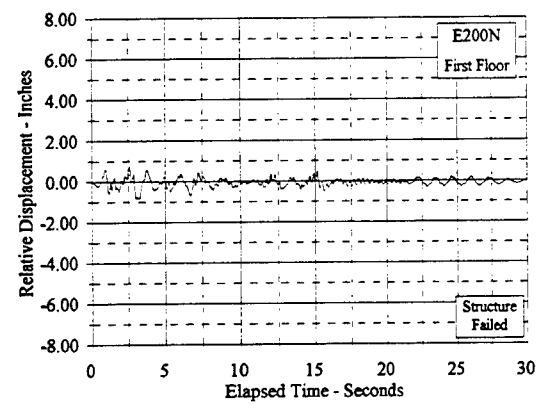
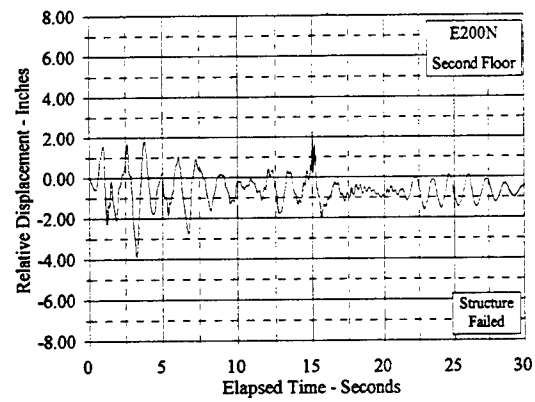
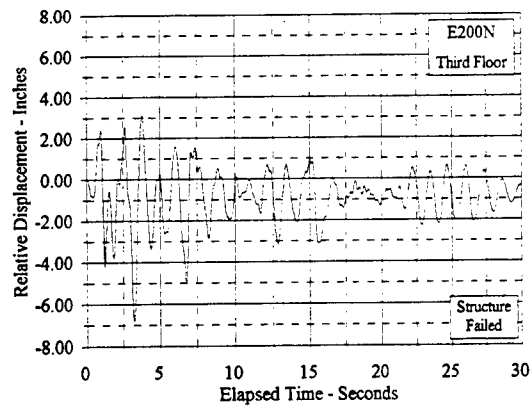


Figure C.2.17 Relative Displacement Vs. Elapsed Time: E200N

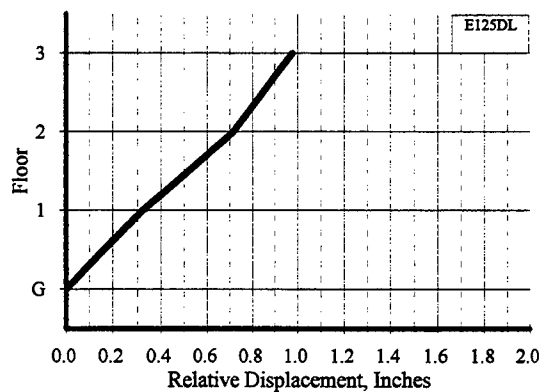
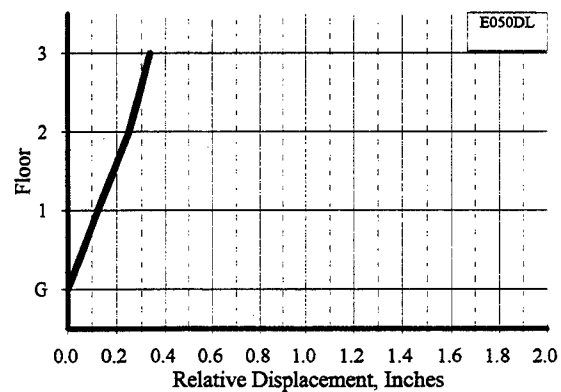
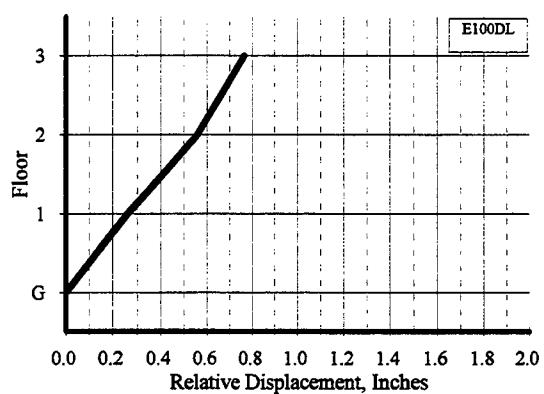
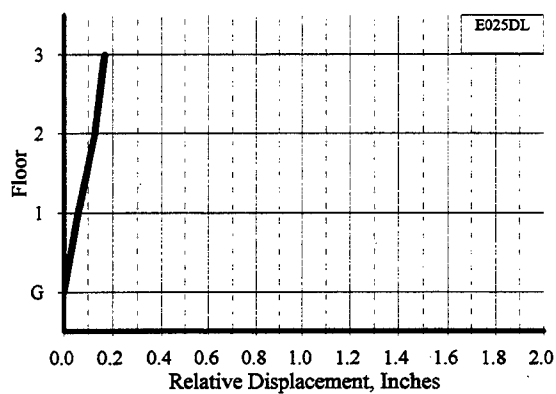
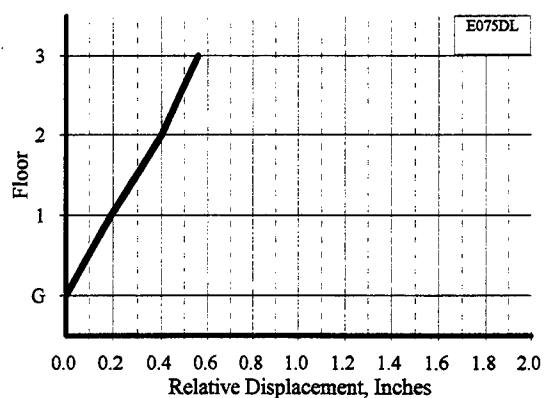
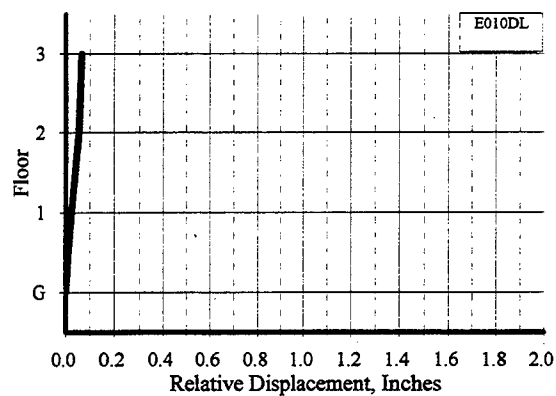


Figure C.2.18 Maximum Relative Story Displacement Profiles: E010DL - E125DL

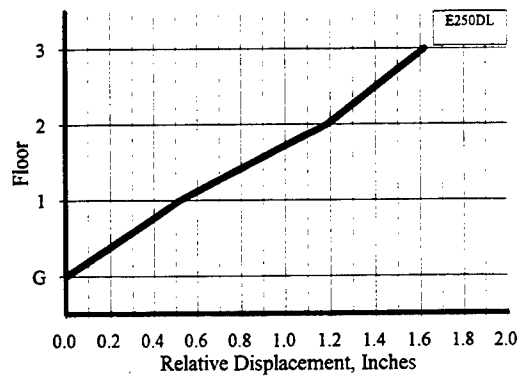
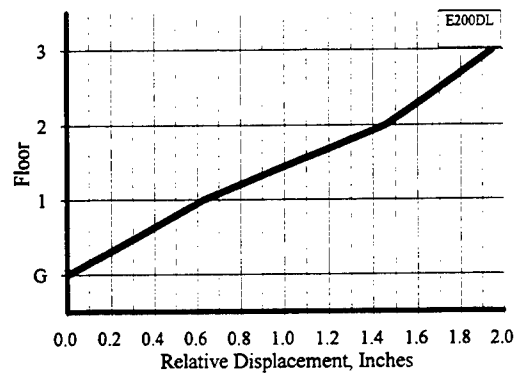
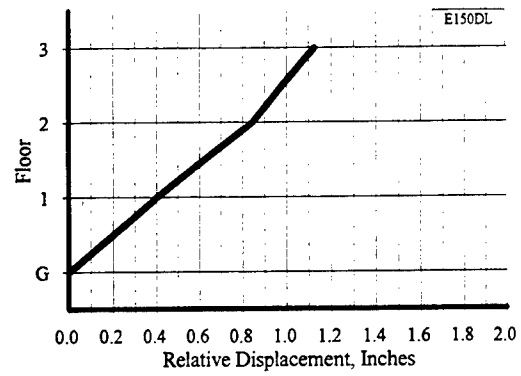


Figure C.2.19 Maximum Relative Story Displacement Profiles: E150DL - E250DL

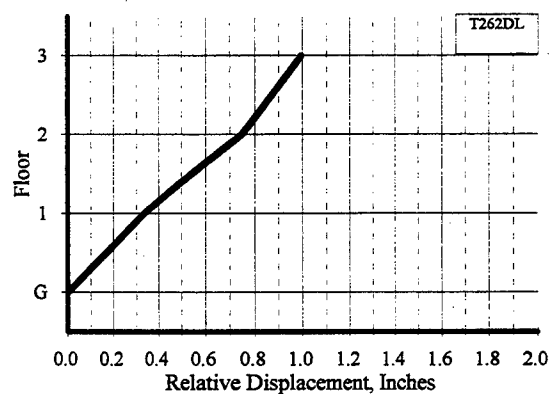
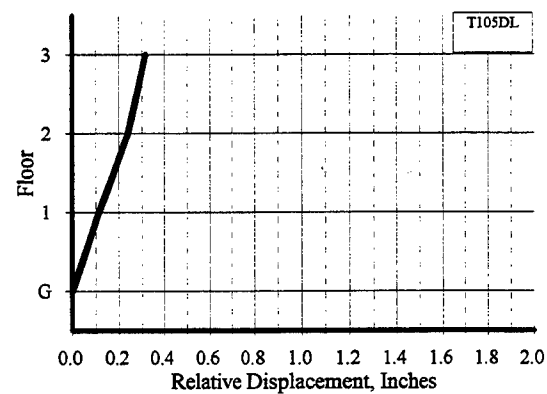
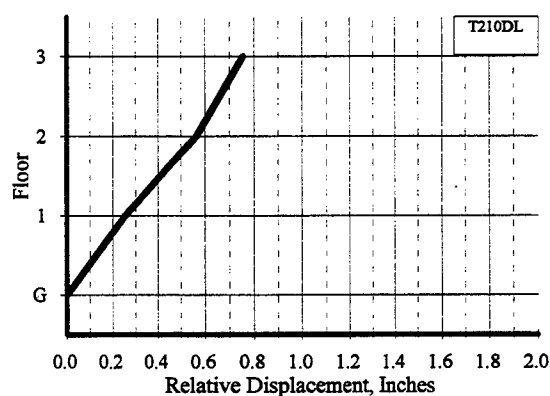
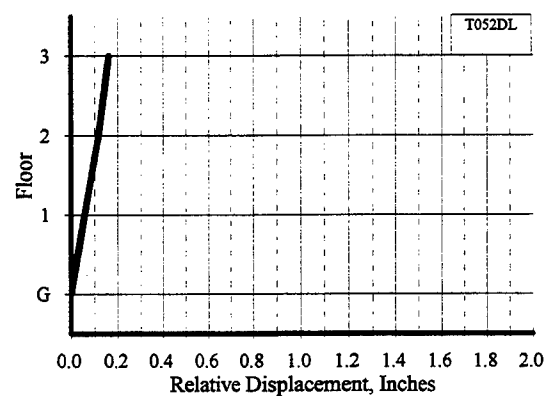
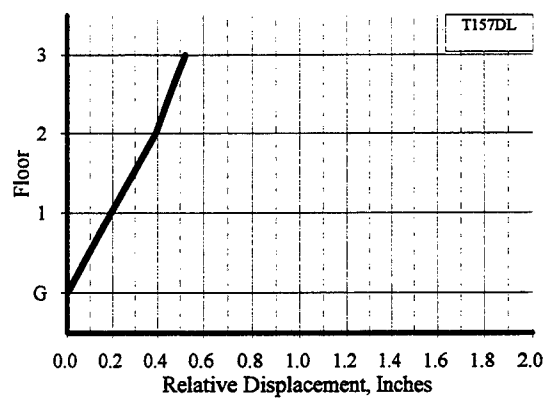
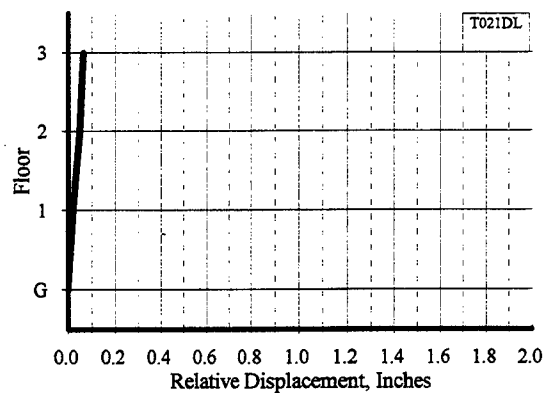


Figure C.2.20 Maximum Relative Story Displacement Profiles: T021DL - T262DL

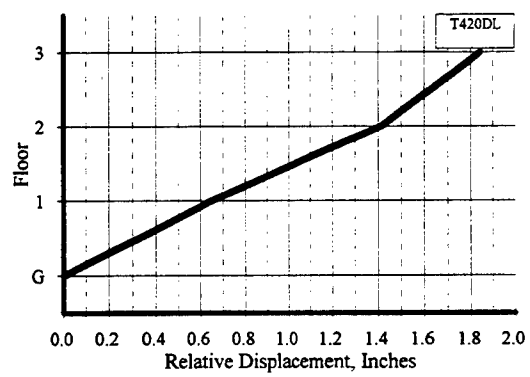
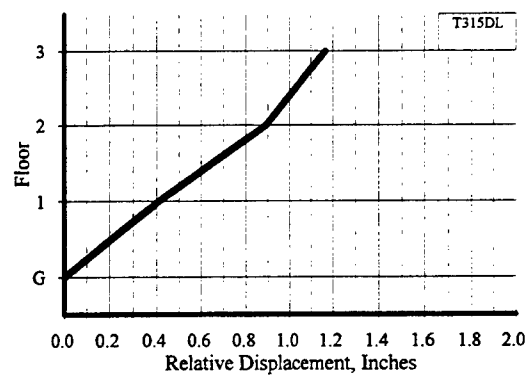


Figure C.2.21 Maximum Relative Story Displacement Profiles: T315DL - T420DL

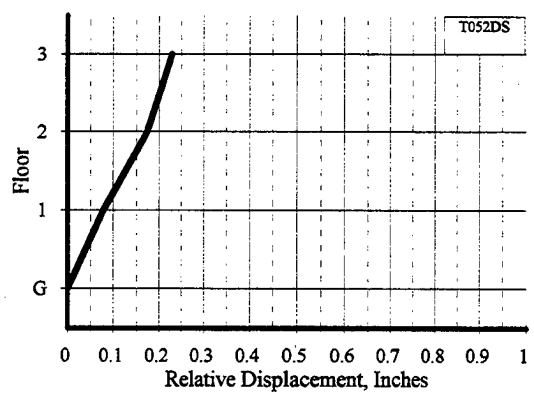
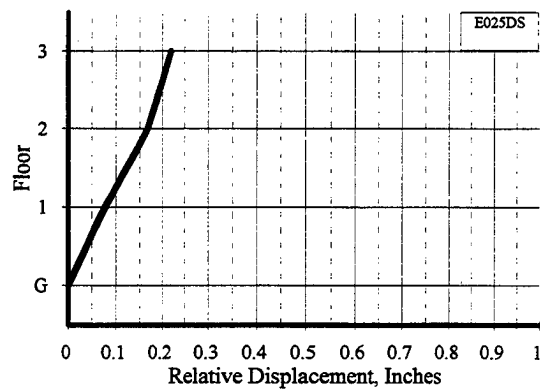
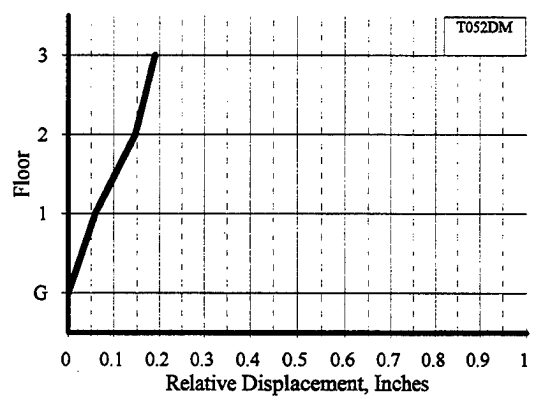
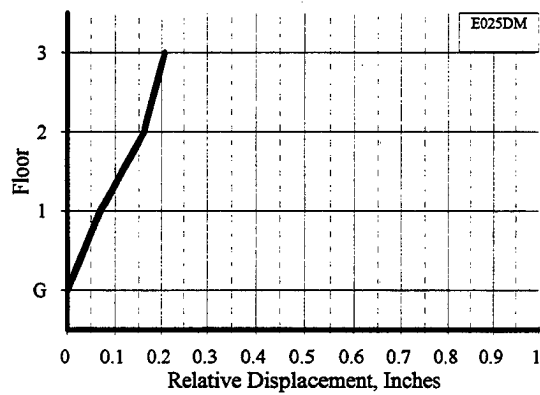
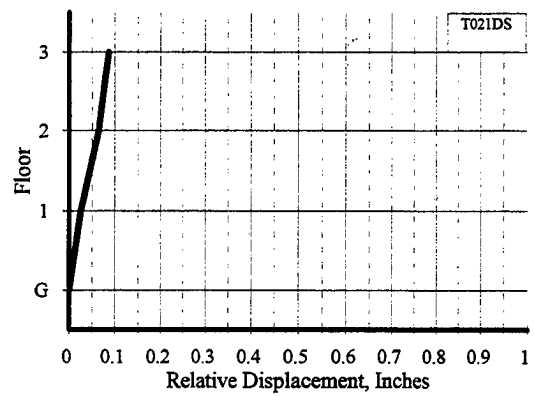
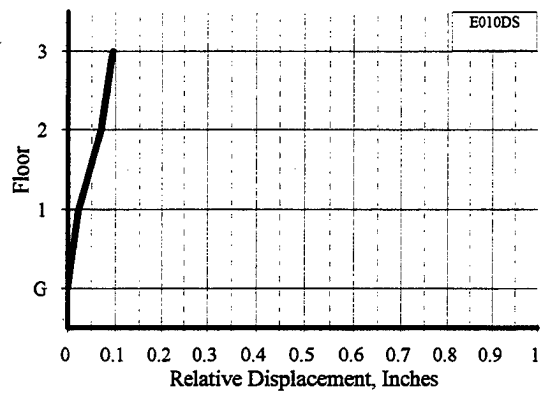


Figure C.2.22 Maximum Relative Story Displacement Profiles: E010DS - T052DS

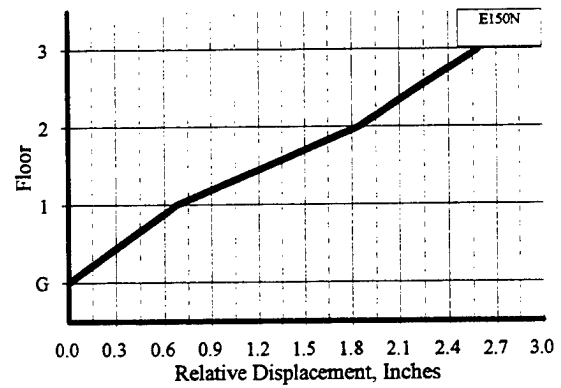
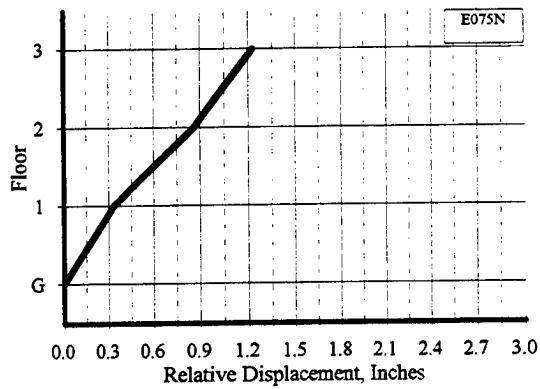
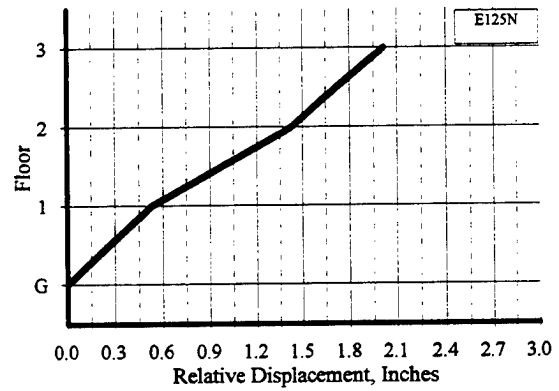
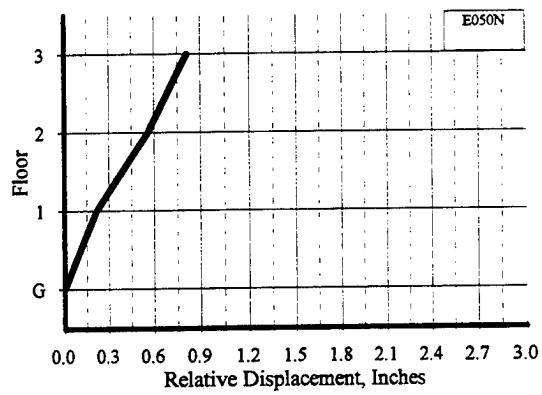
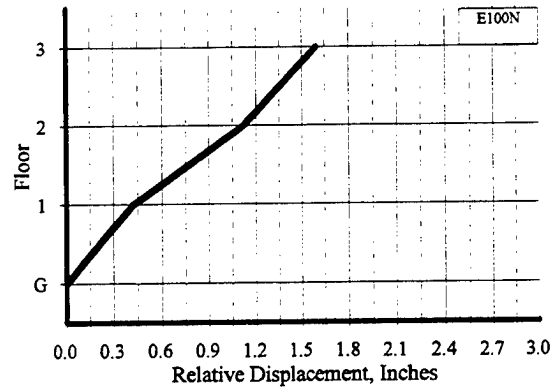
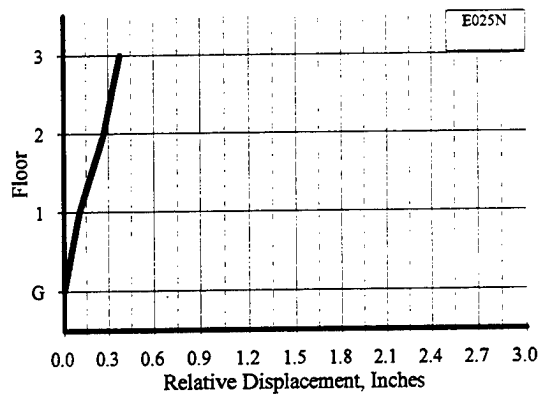


Figure C.2.23 Maximum Relative Story Displacement Profiles: E025N - E150N

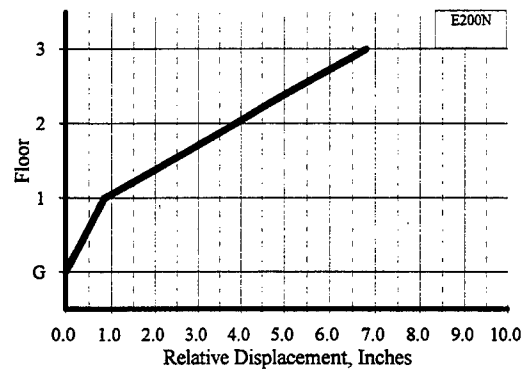


Figure C.2.24 Maximum Relative Story Displacement Profile: E200N

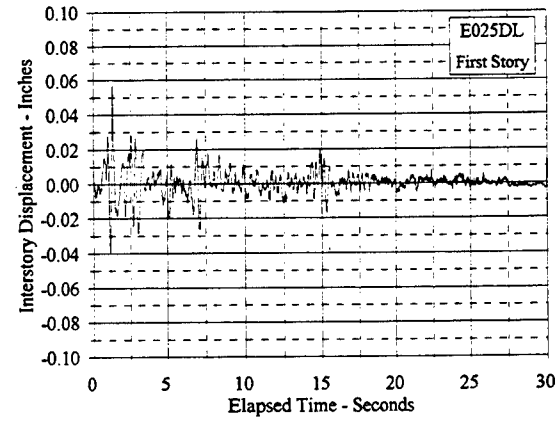
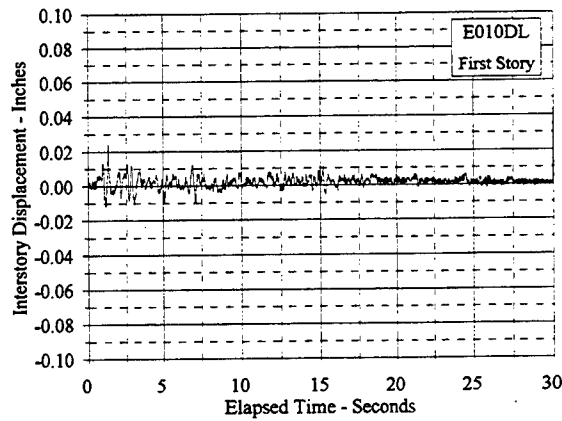
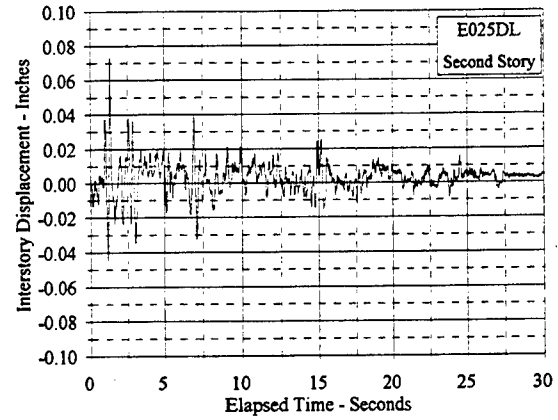
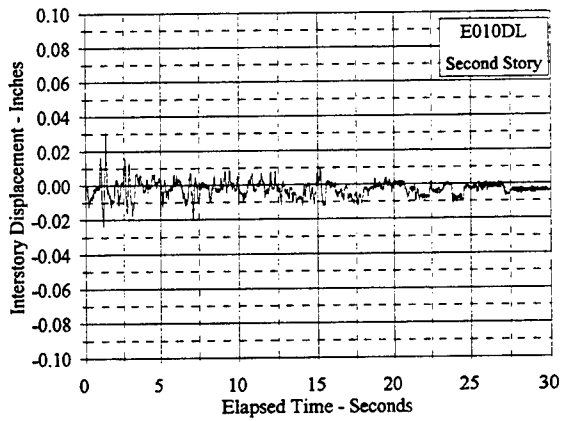
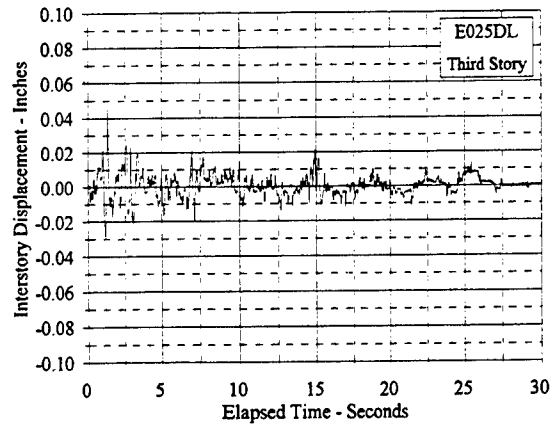
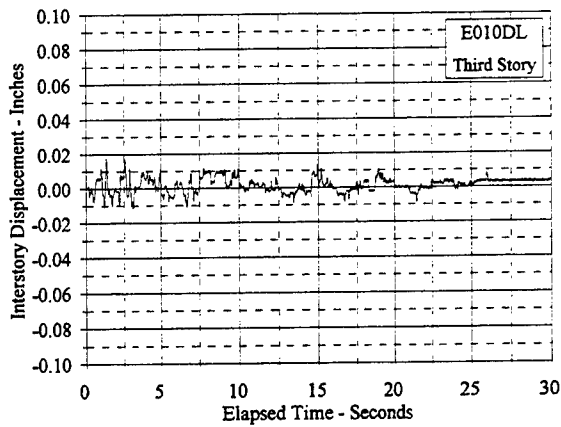


Figure C.3.1 Interstory Displacement Vs. Elapsed Time: E010DL, E025DL

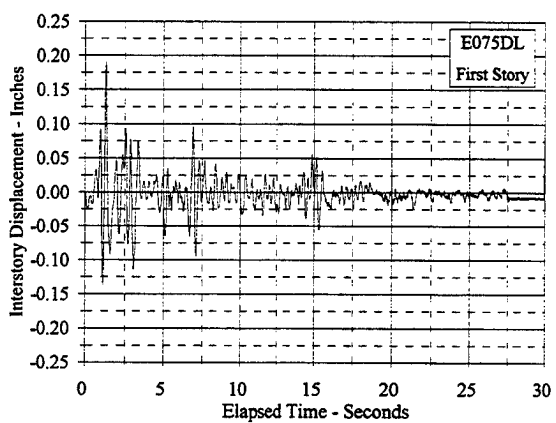
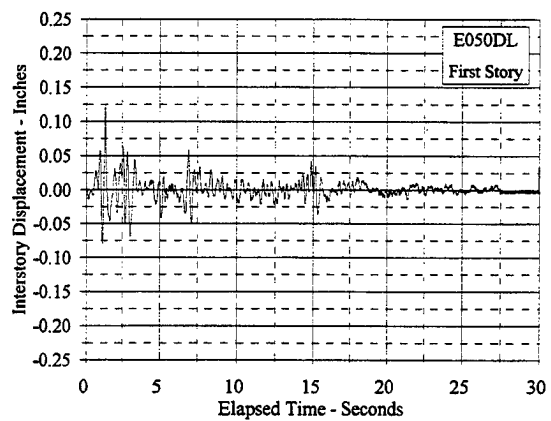
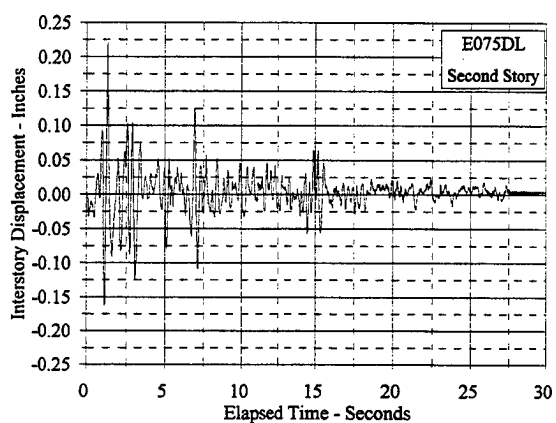
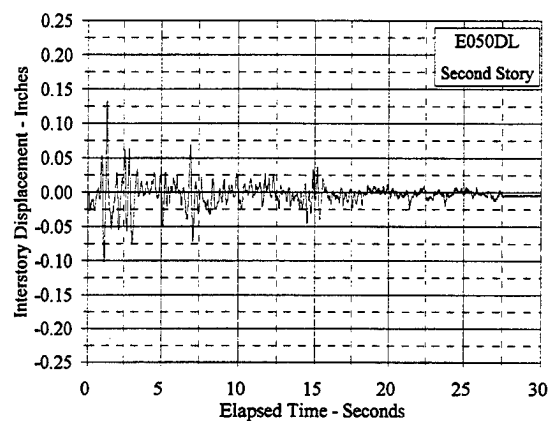
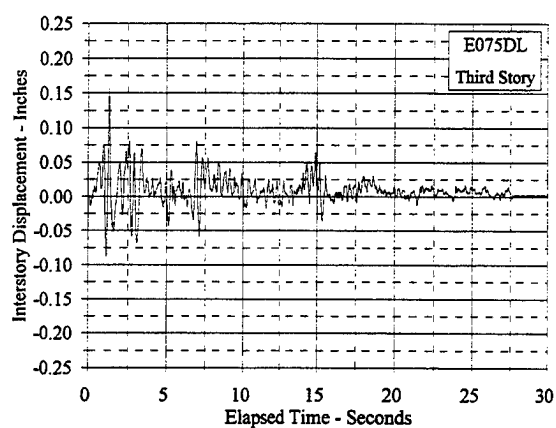
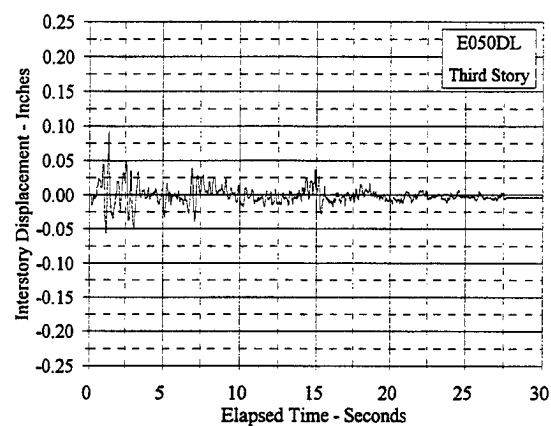


Figure C.3.2 Interstory Displacement Vs. Elapsed Time: E050DL, E075DL

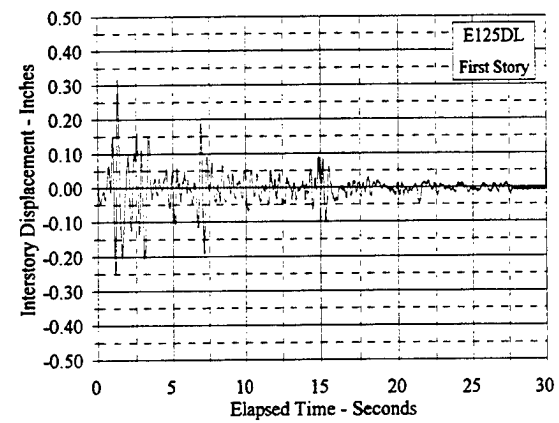
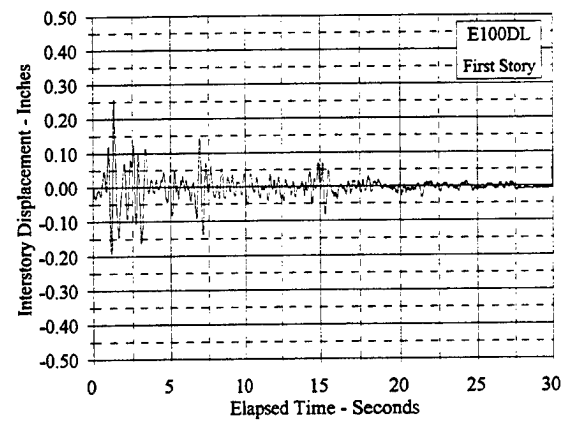
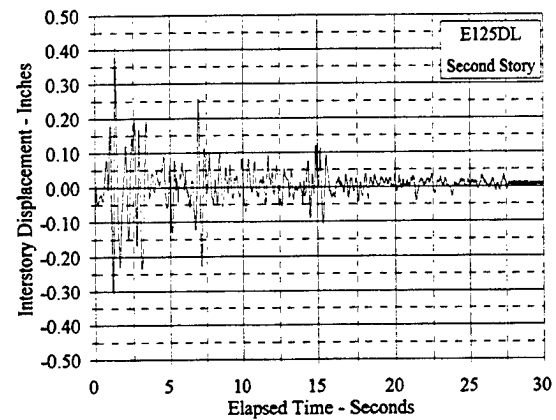
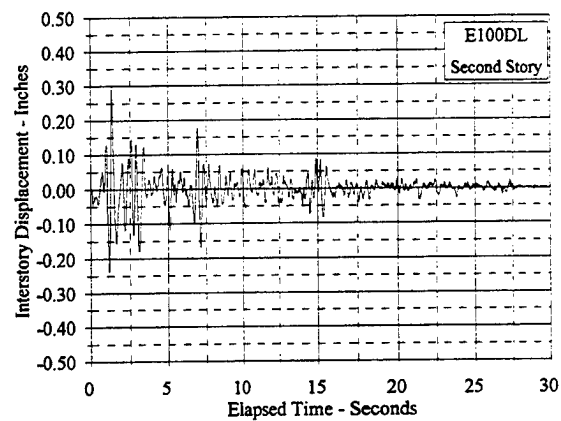
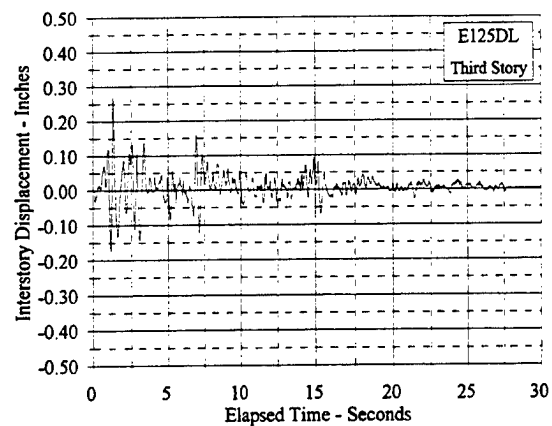
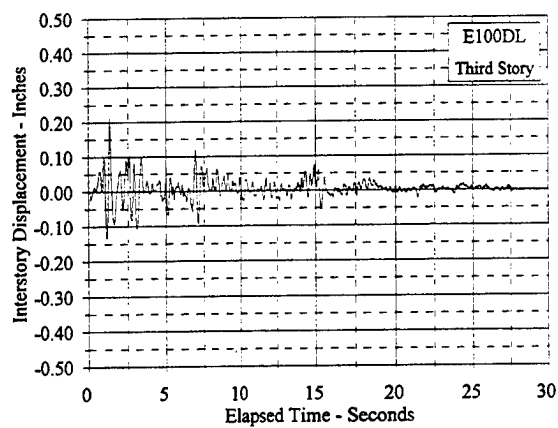


Figure C.3.3 Interstory Displacement Vs. Elapsed Time: E100DL, E125DL

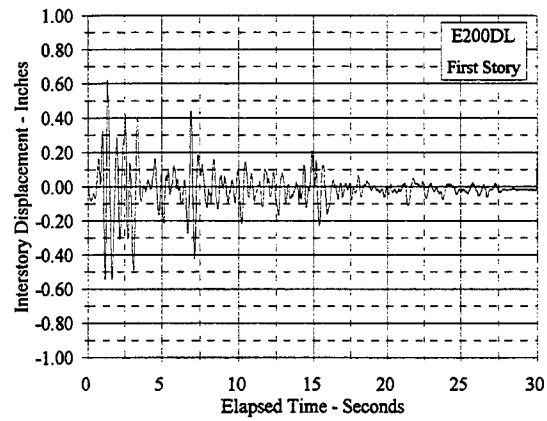
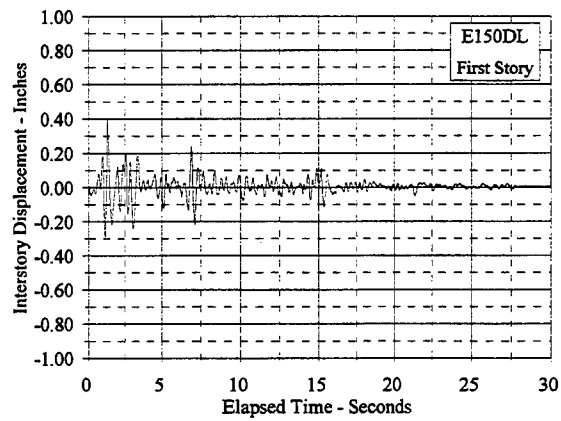
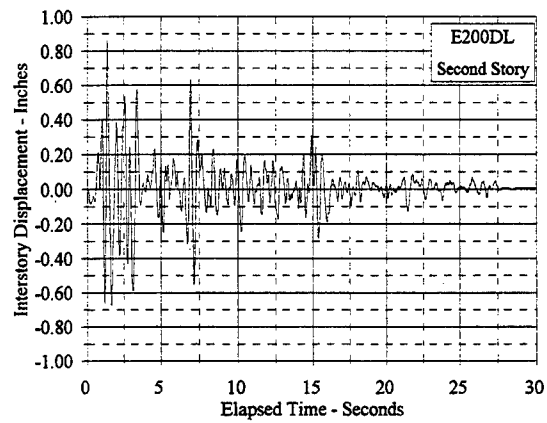
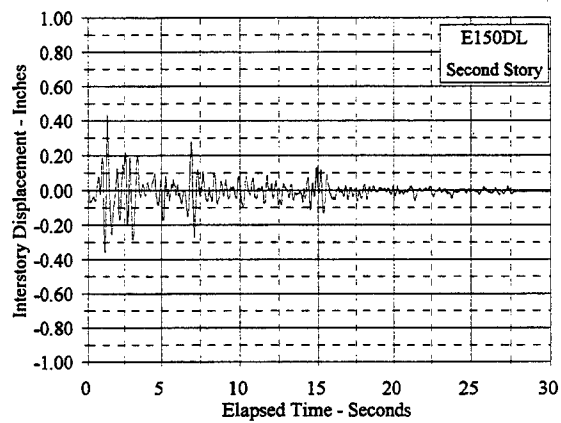
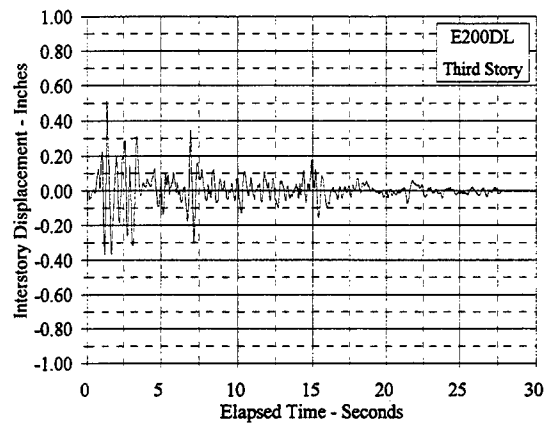
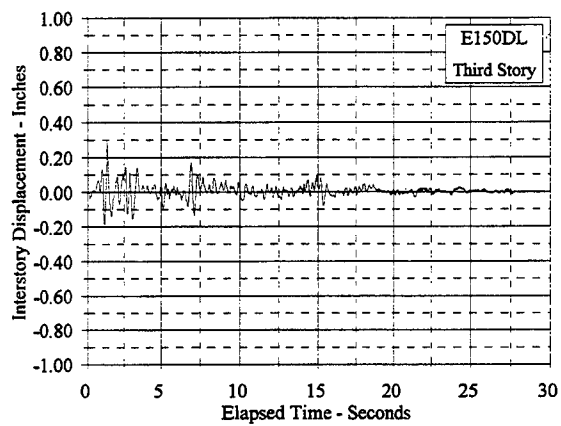


Figure C.3.4 Interstory Displacement Vs. Elapsed Time: E150DL, E200DL

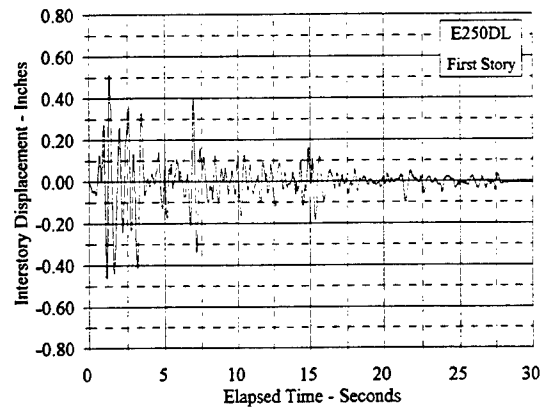
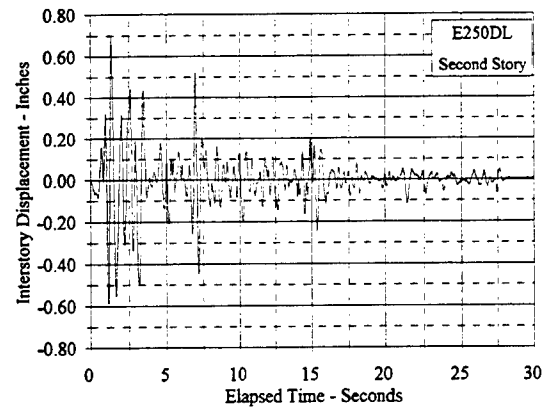
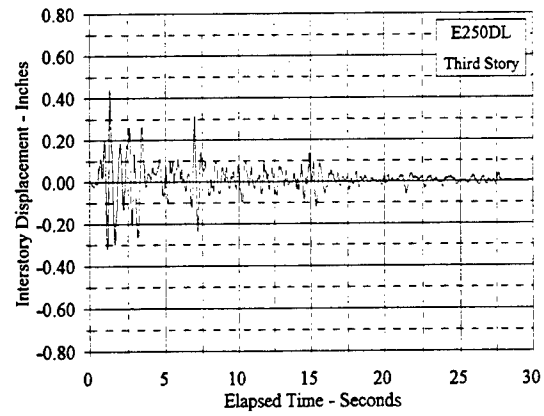


Figure C.3.5 Interstory Displacement Vs. Elapsed Time: E250DL

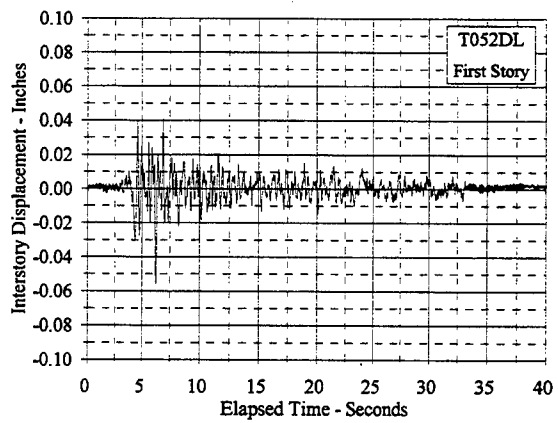
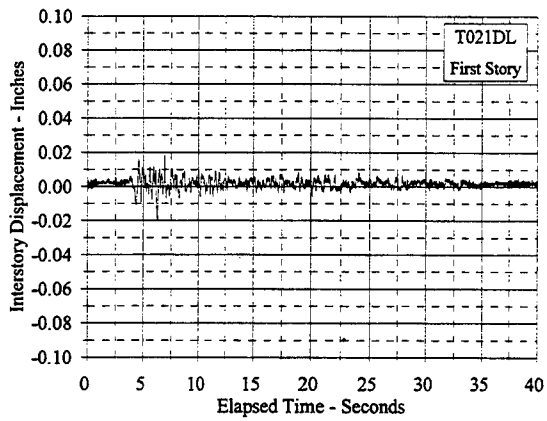
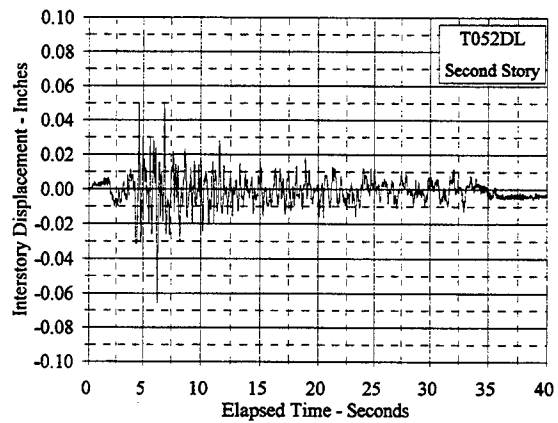
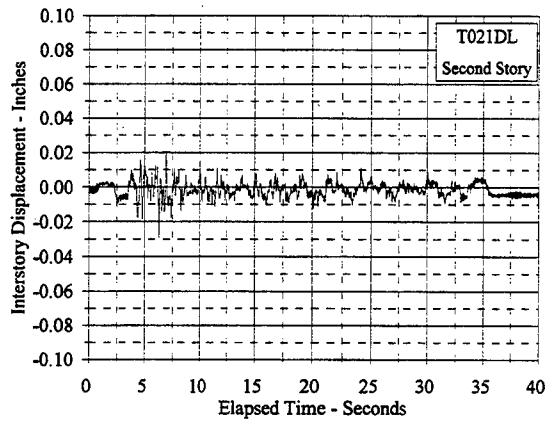
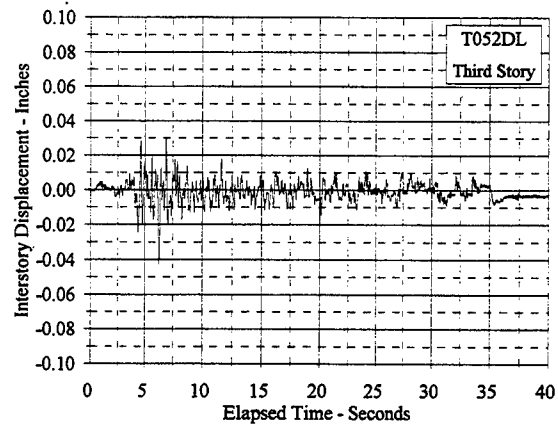
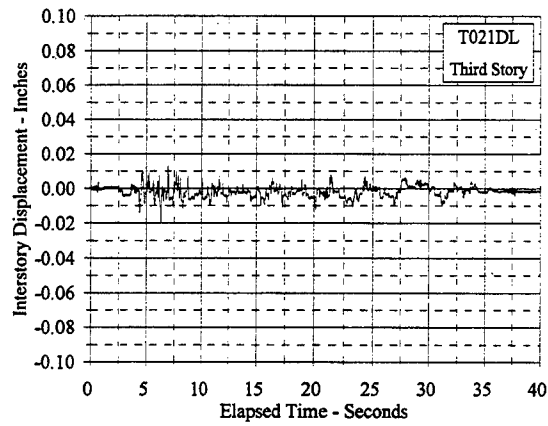


Figure C.3.6 Interstory Displacement Vs. Elapsed Time: T021DL, T052DL

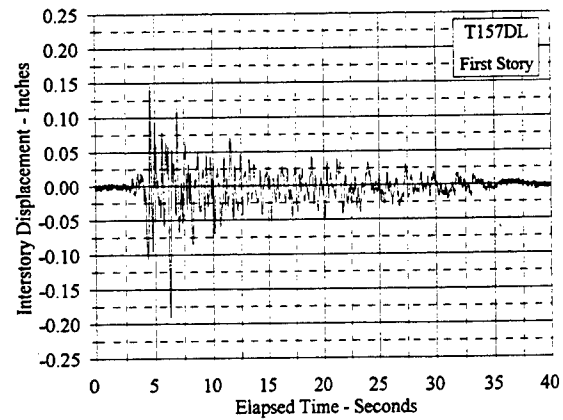
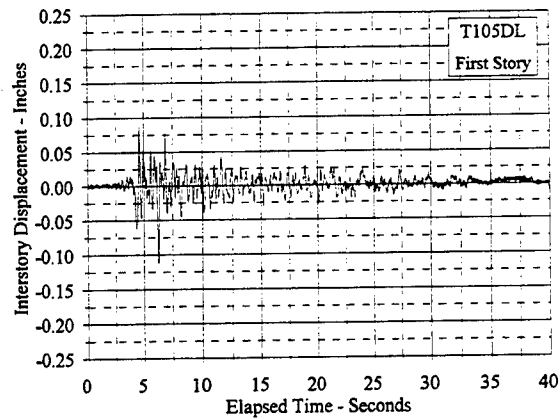
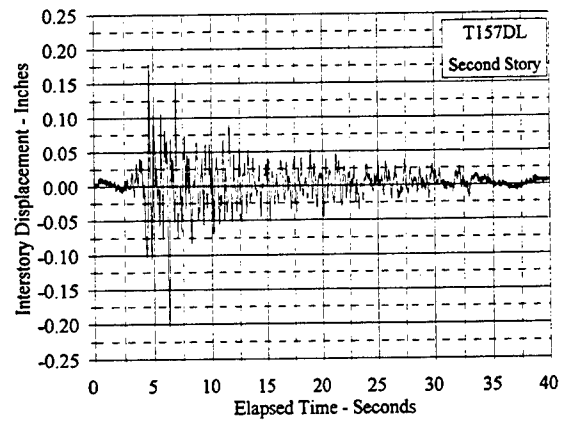
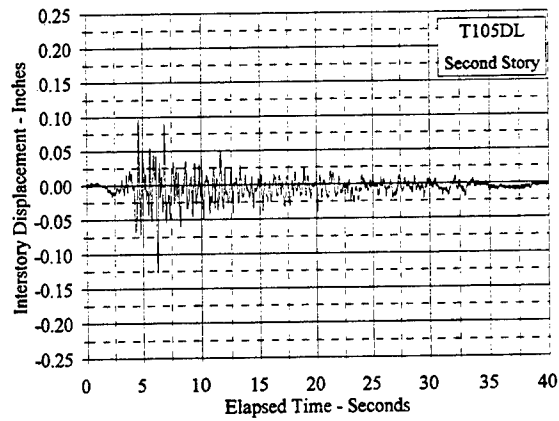
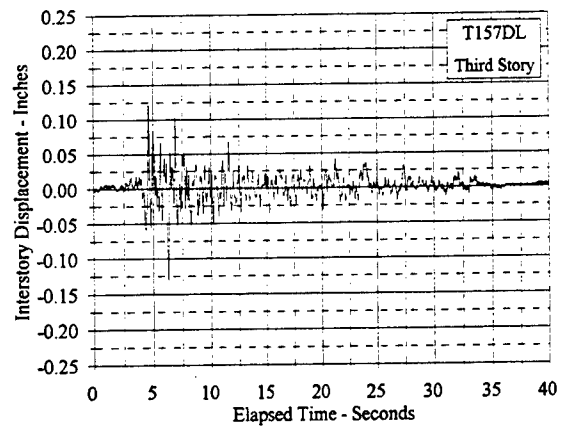
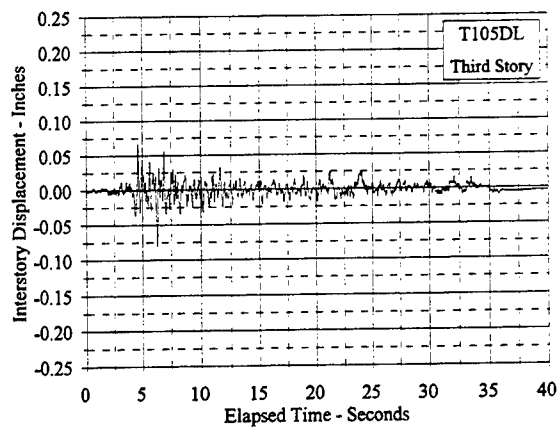


Figure C.3.7 Interstory Displacement Vs. Elapsed Time: T105DL, T157DL

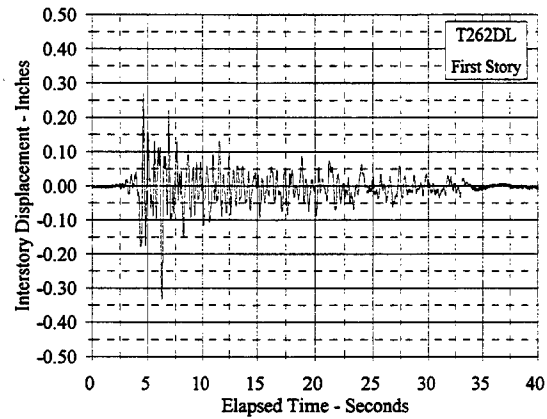
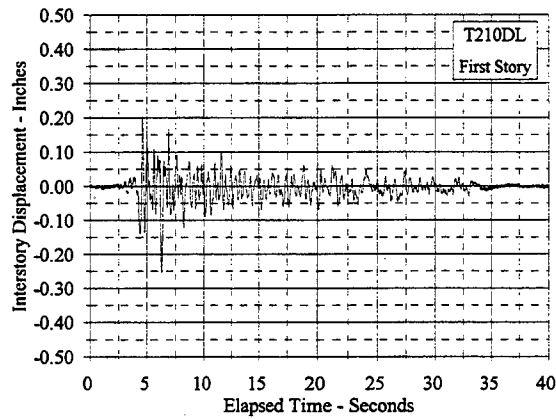
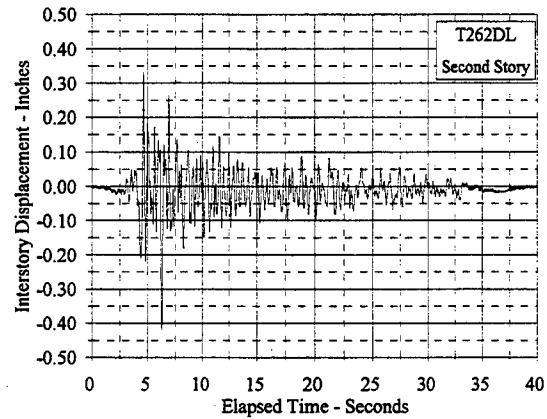
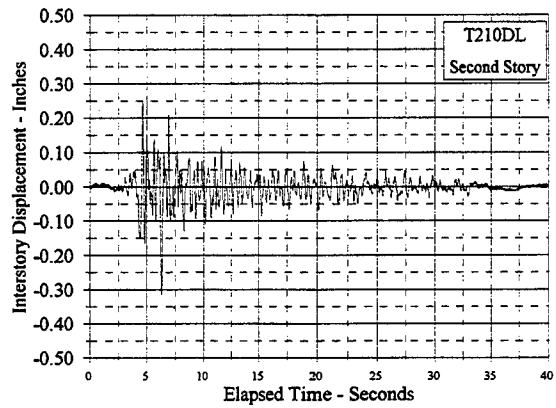
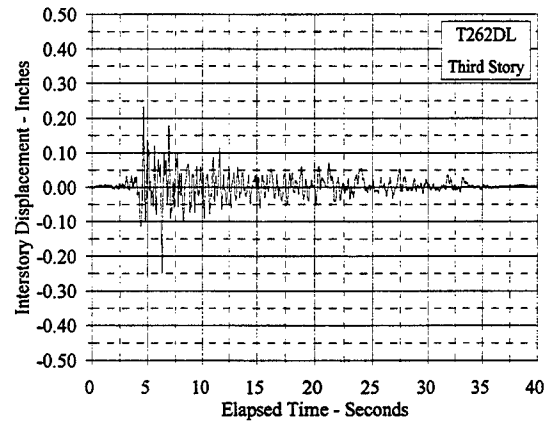
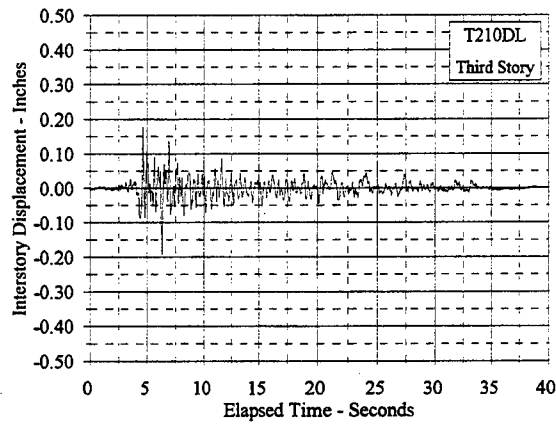


Figure C.3.8 Interstory Displacement Vs. Elapsed Time: T210DL, T262DL

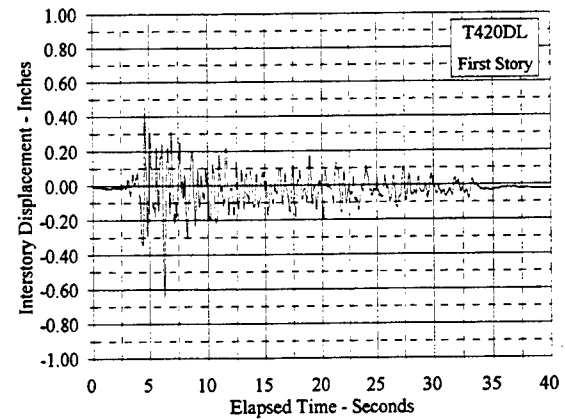
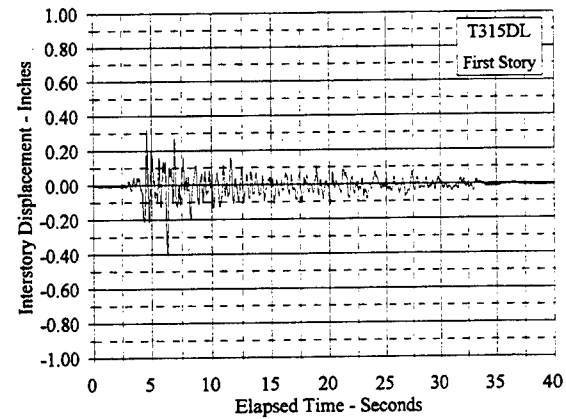
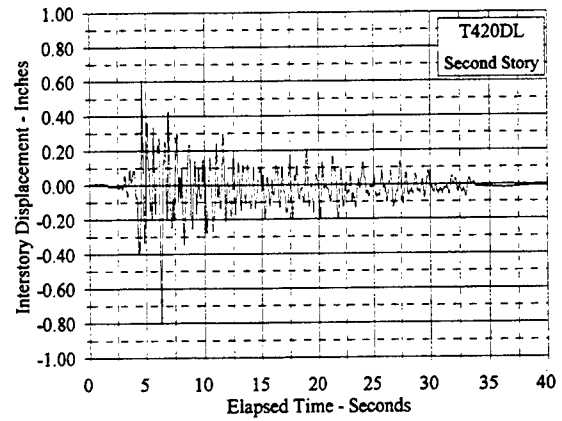
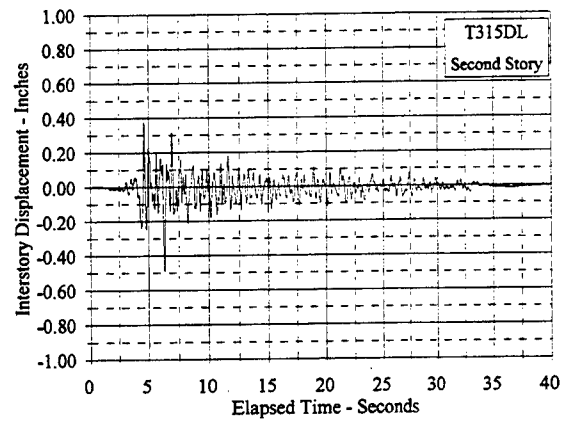
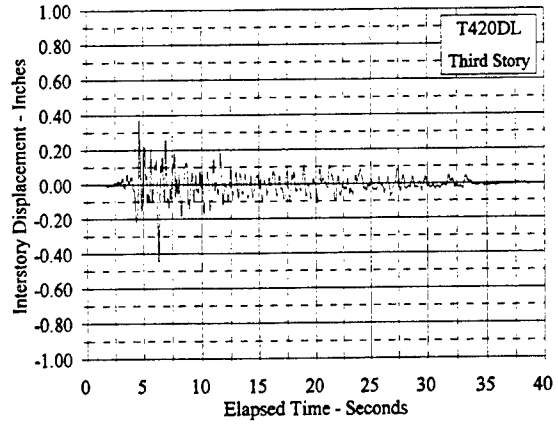
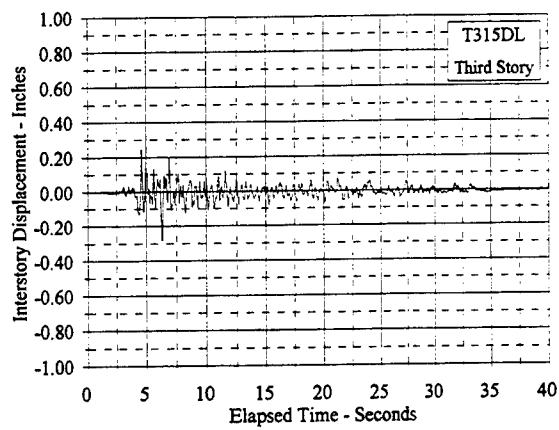


Figure C.3.9 Interstory Displacement Vs. Elapsed Time: T315DL, T420DL

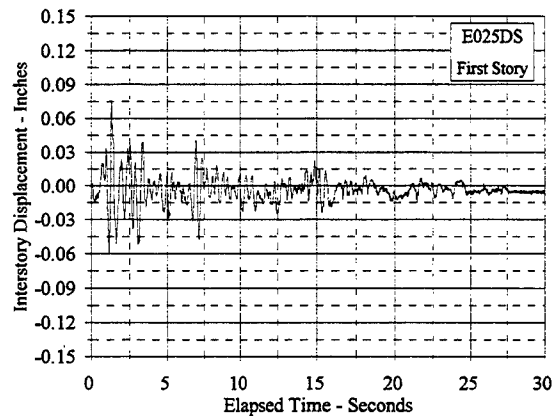
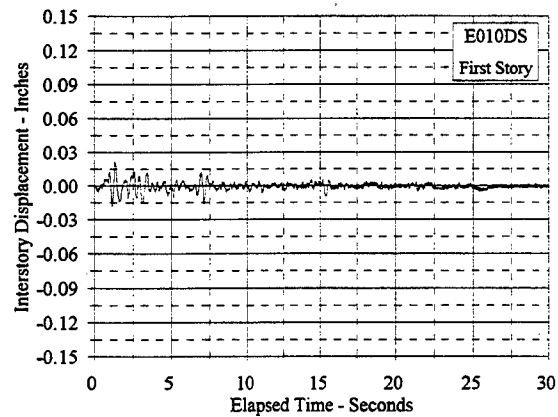
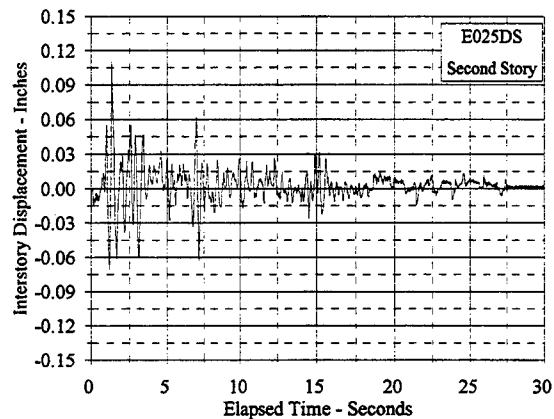
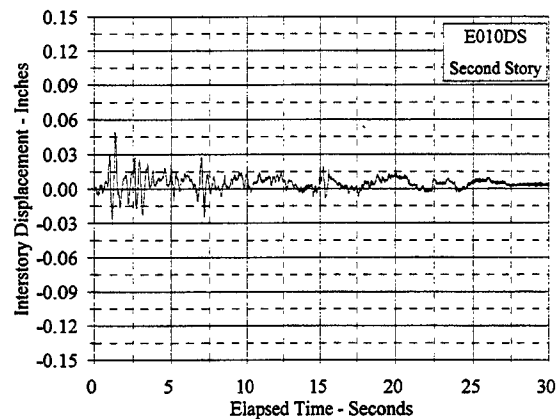
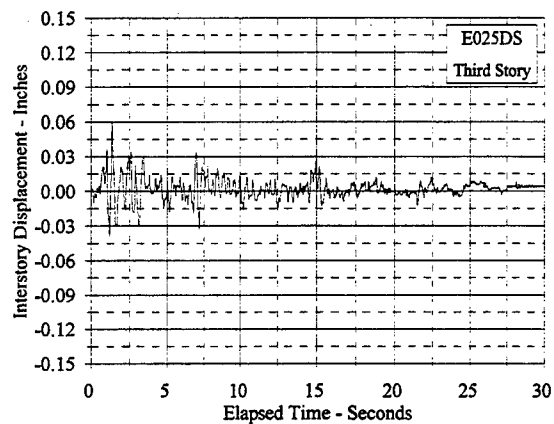
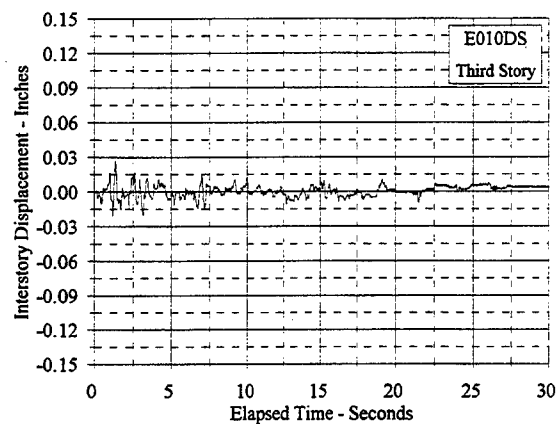


Figure C.3.10 Interstory Displacement Vs. Elapsed Time: E010DS, E025DS

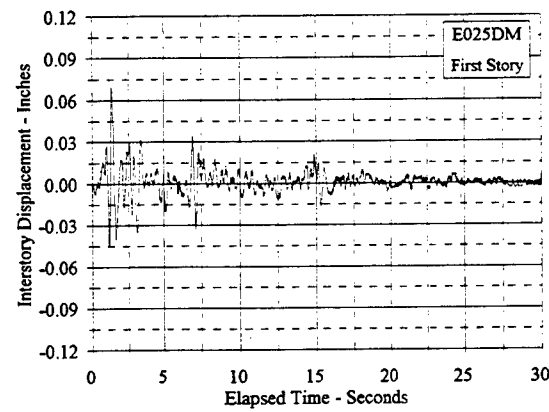
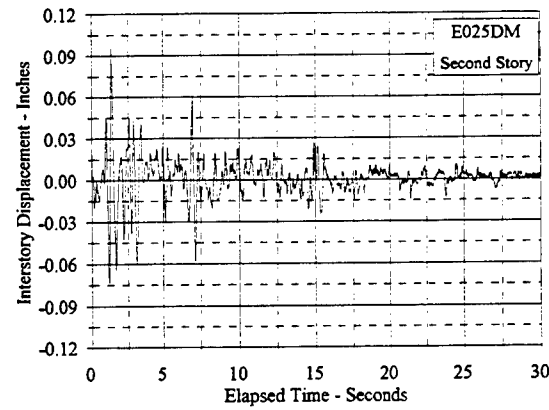
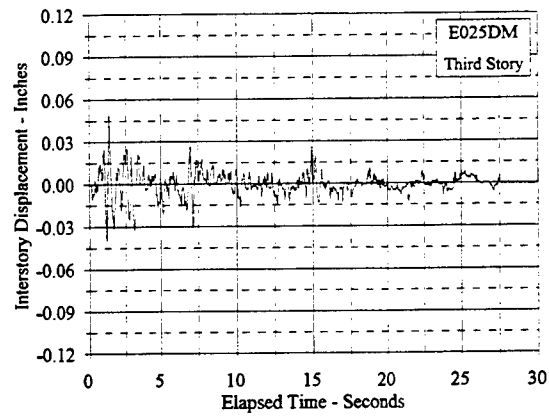


Figure C.3.11 Interstory Displacement Vs. Elapsed Time: E025DM

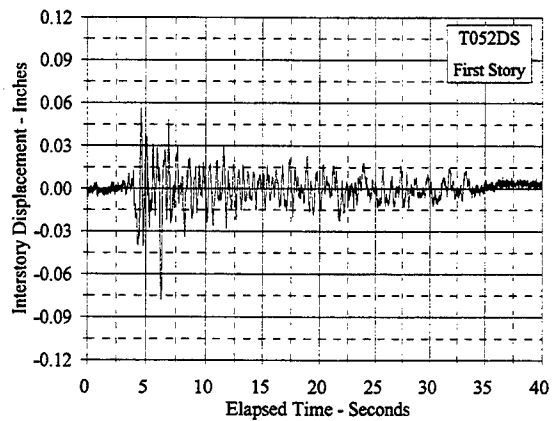
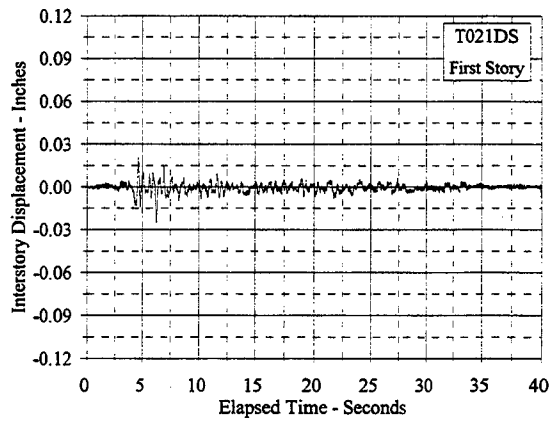
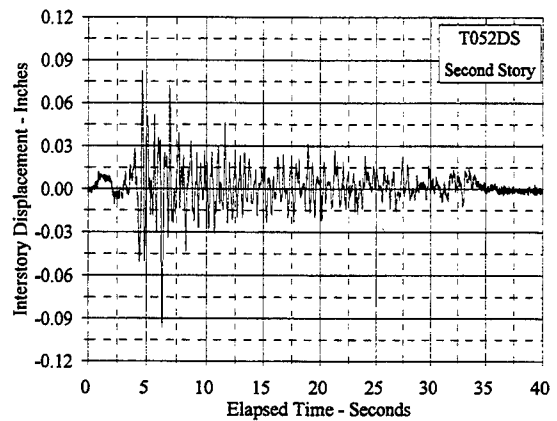
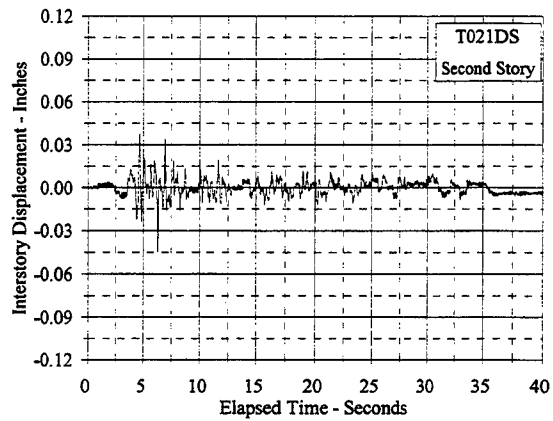
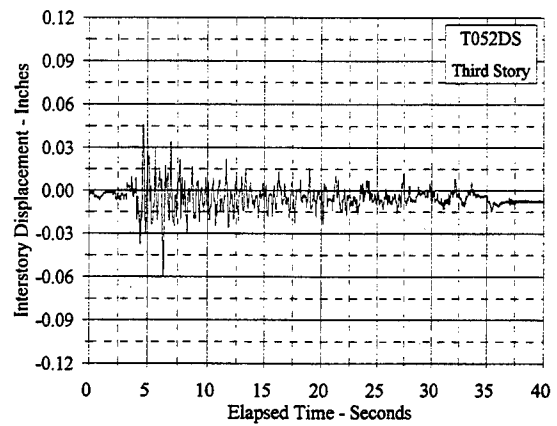
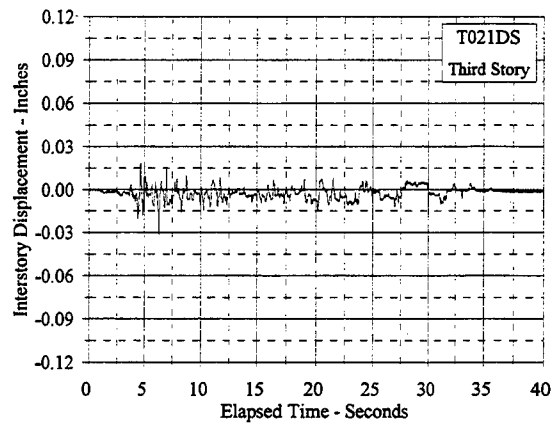


Figure C.3.12 Interstory Displacement Vs. Elapsed Time: T021DS, T052DS

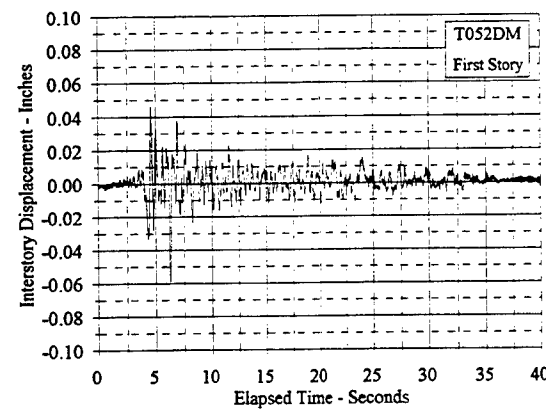
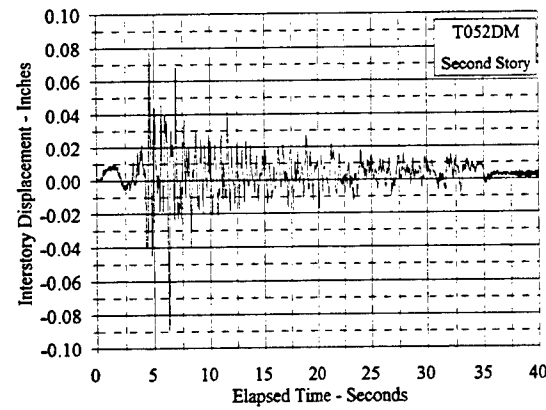
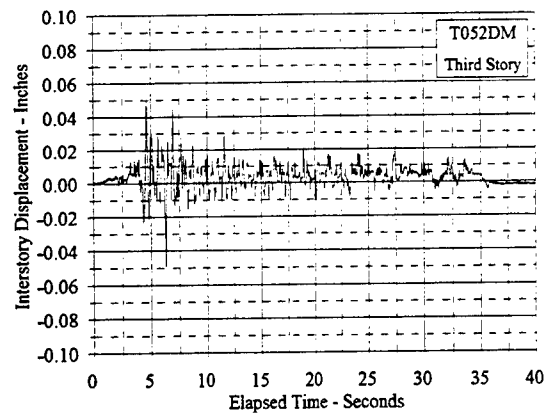


Figure C.3.13 Interstory Displacement Vs. Elapsed Time: T052DM

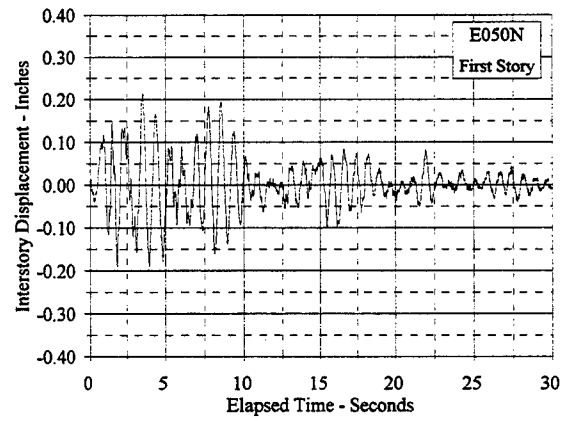
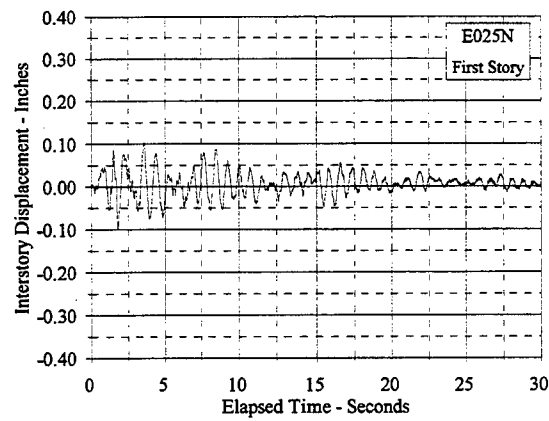
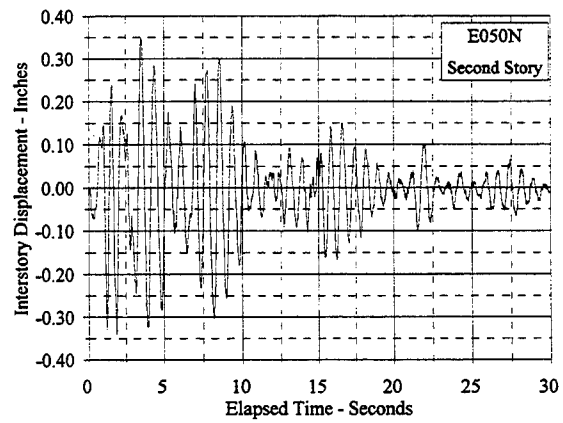
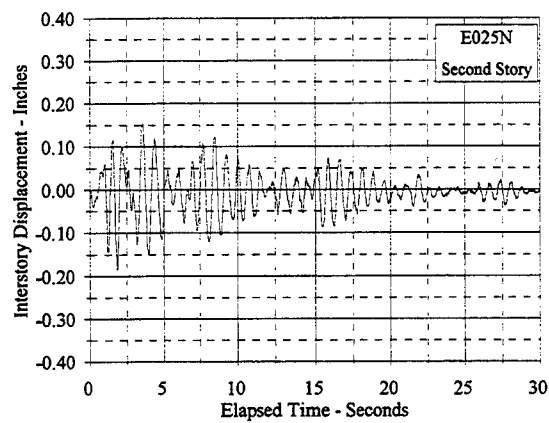
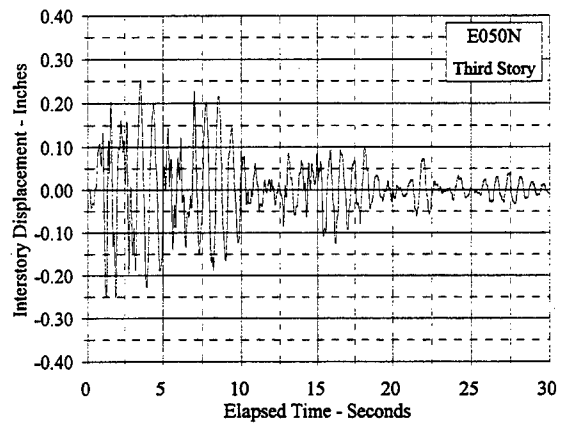
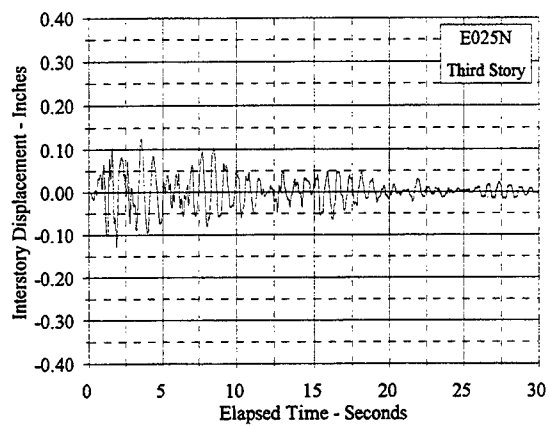


Figure C.3.14 Interstory Displacement Vs. Elapsed Time: E025N, E050N

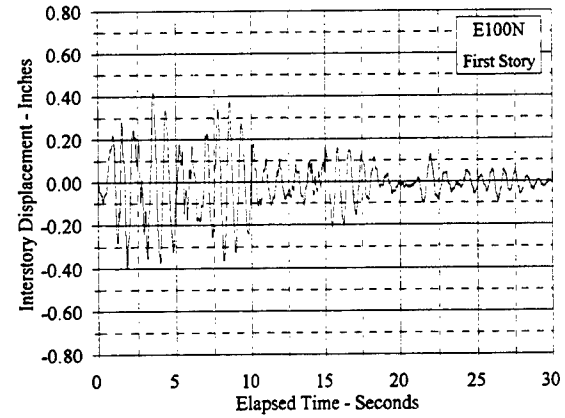
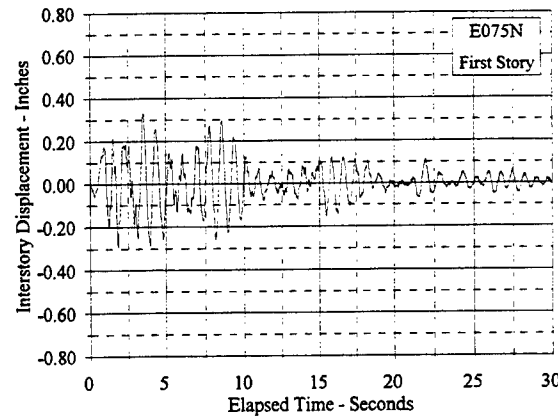
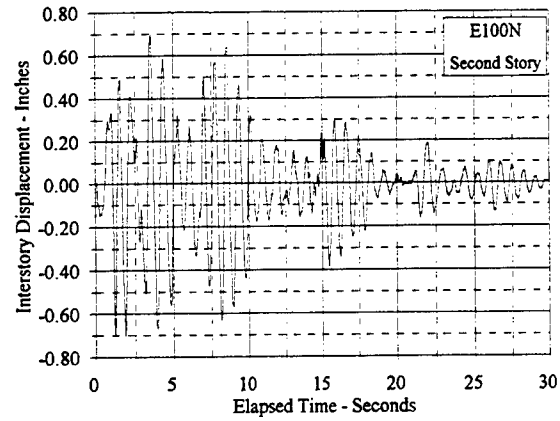
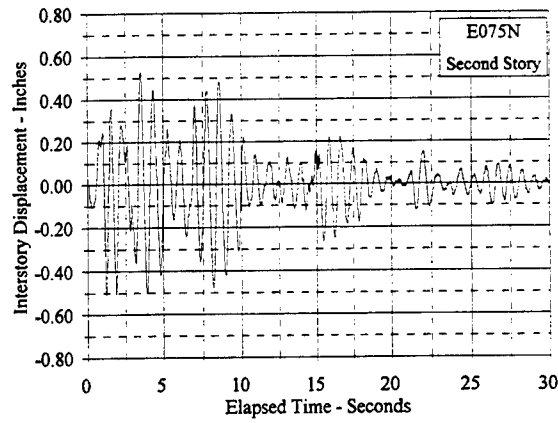
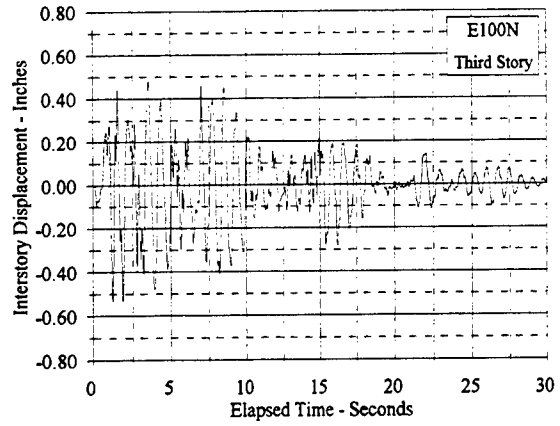
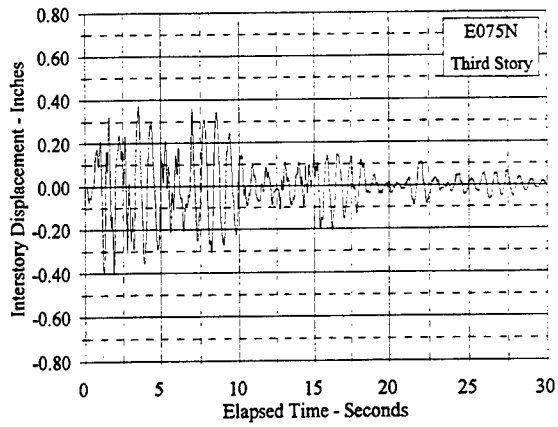


Figure C.3.15 Interstory Displacement Vs. Elapsed Time: E075N, E100N

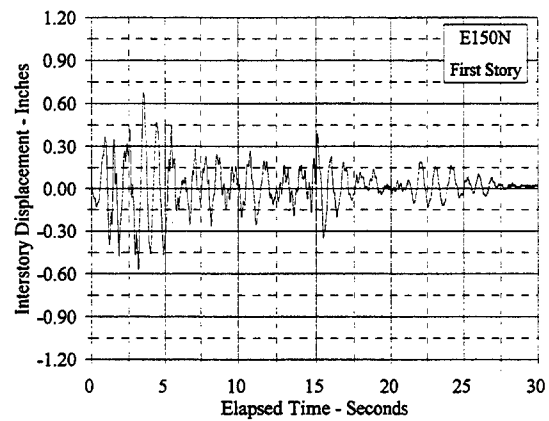
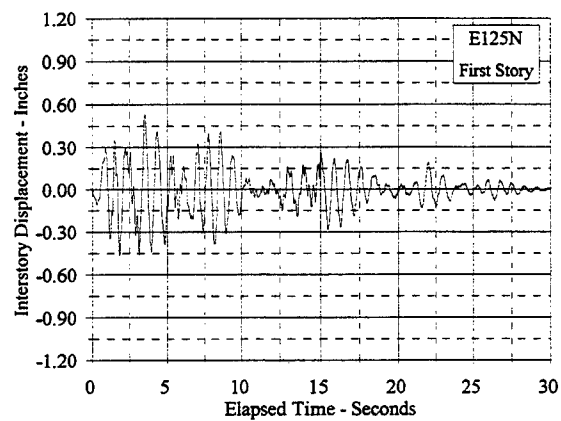
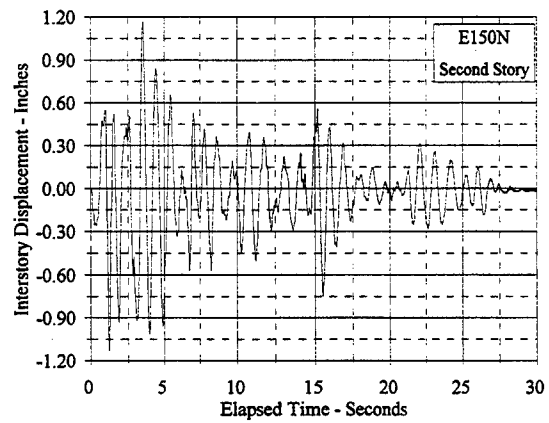
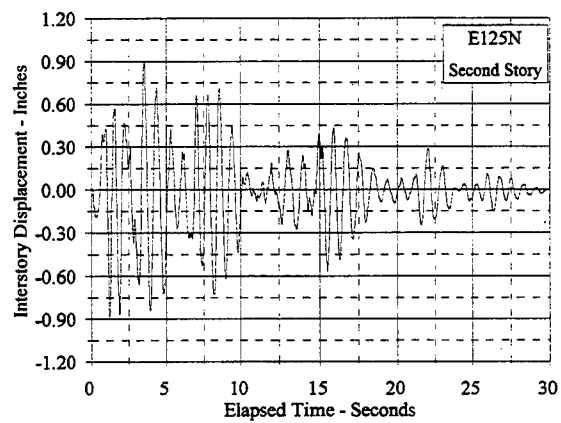
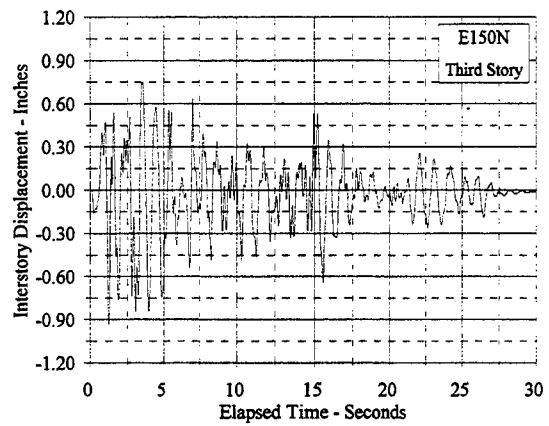
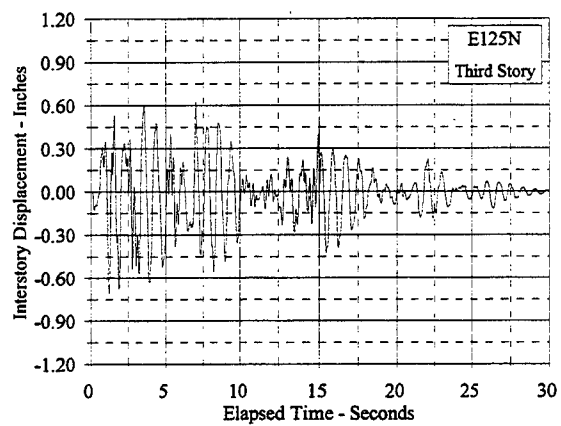


Figure C.3.16 Interstory Displacement Vs. Elapsed Time: E125N, E150N

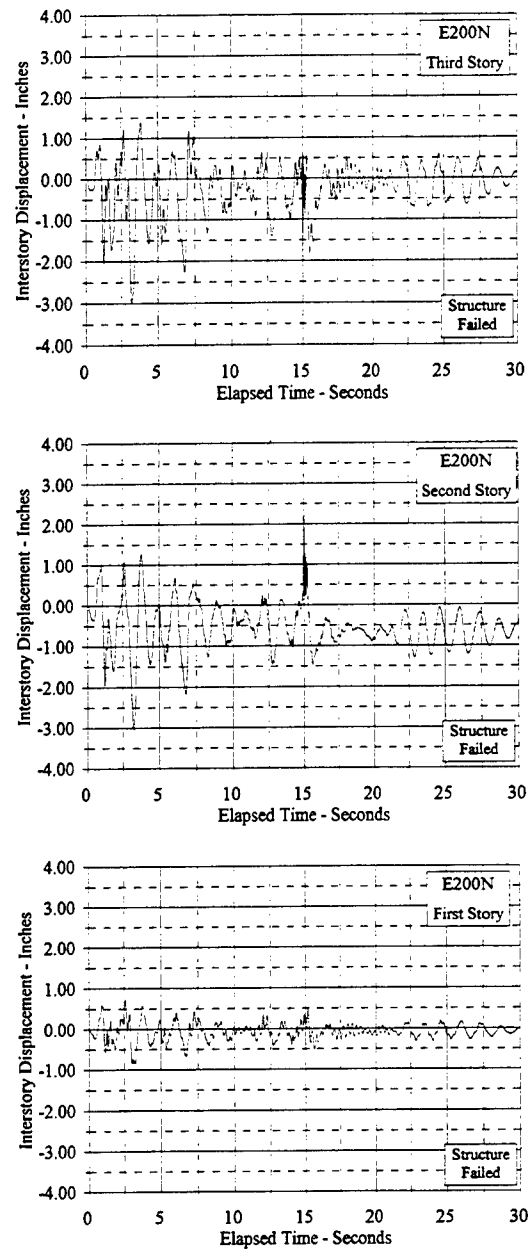


Figure C.3.17 Interstory Displacement Vs. Elapsed Time: E200N

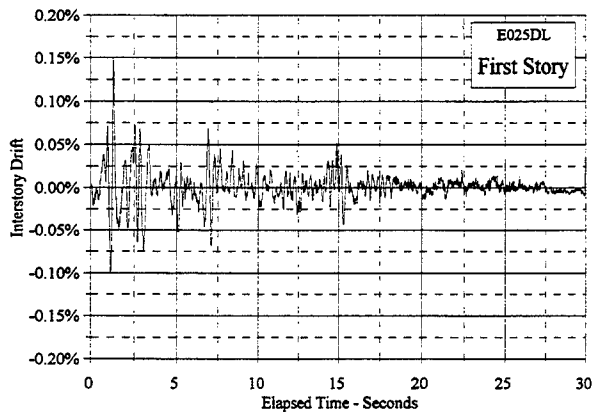
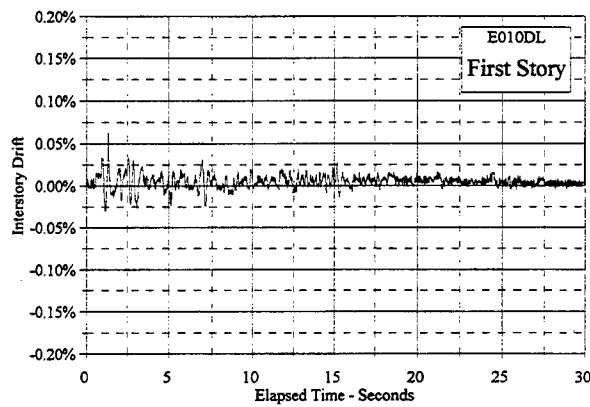
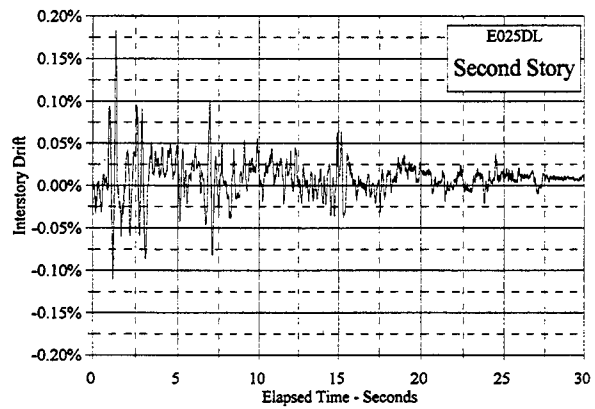
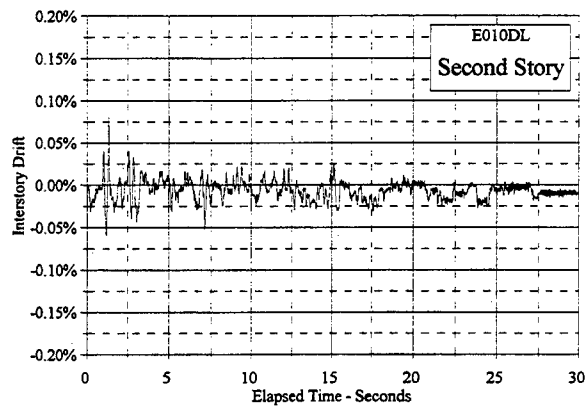
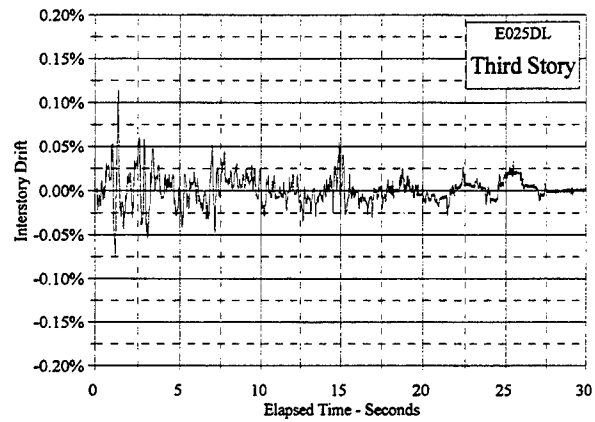
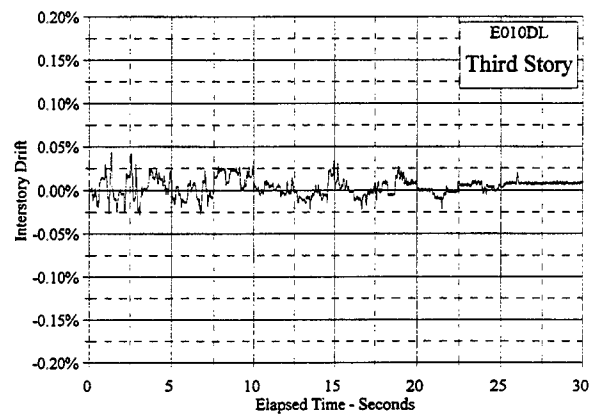


Figure C.3.18 Interstory Drift Vs. Elapsed Time: E010DL, E025DL

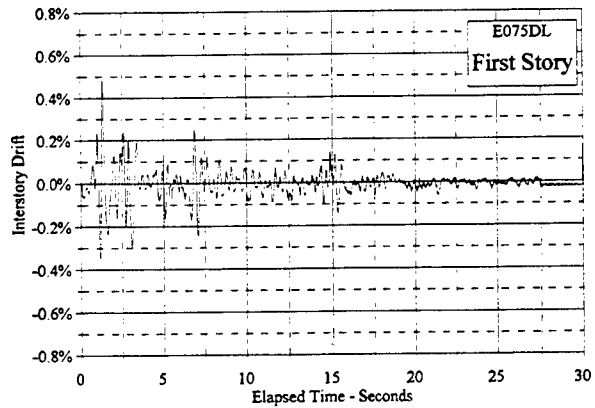
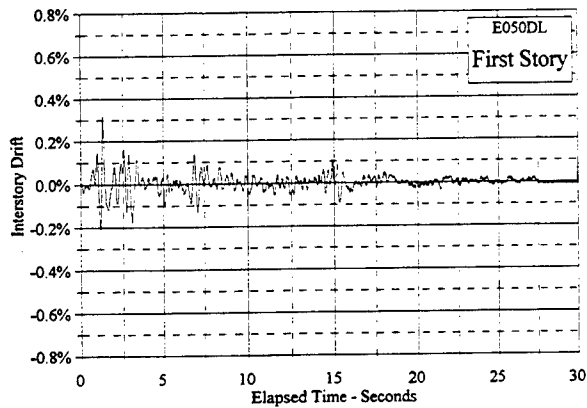
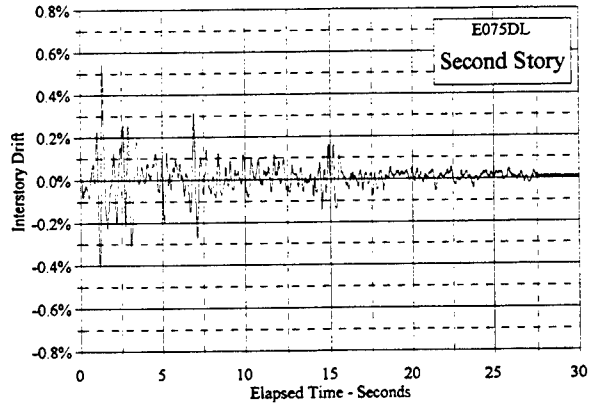
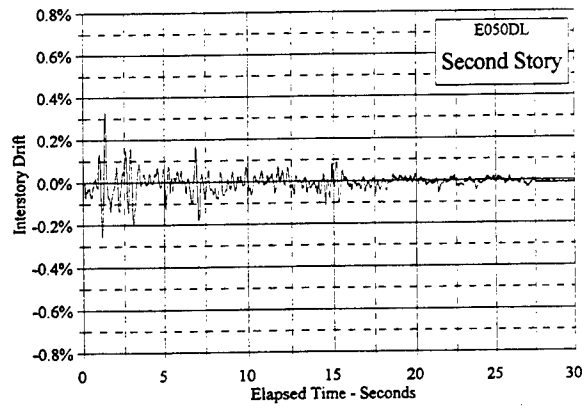
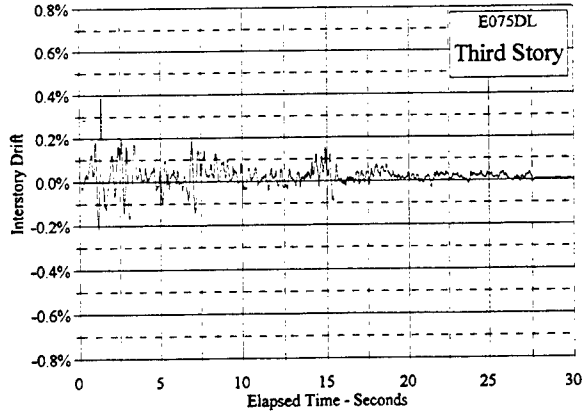
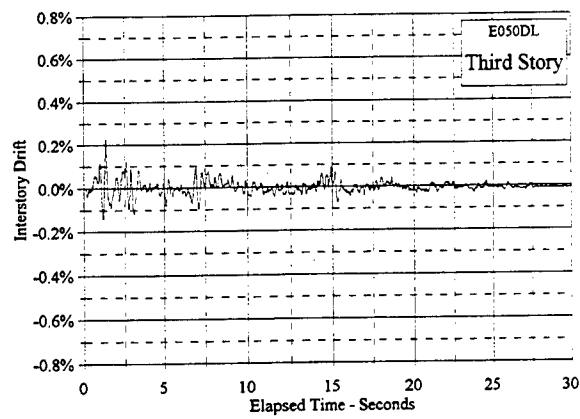


Figure C.3.19 Interstory Drift Vs. Elapsed Time: E050DL, E075DL

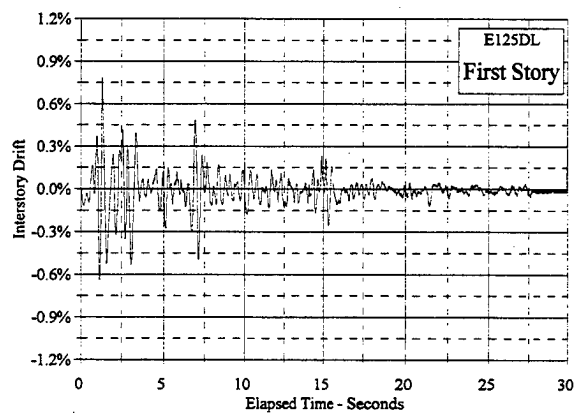
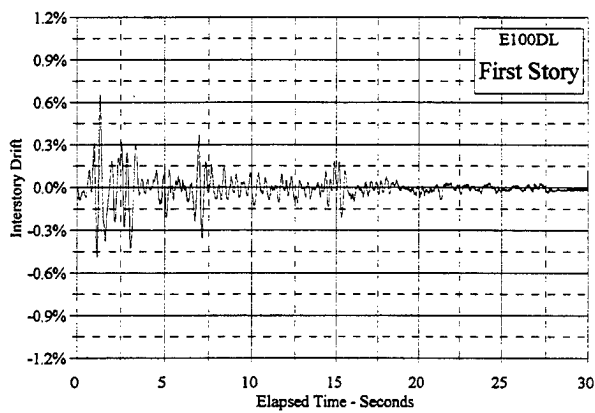
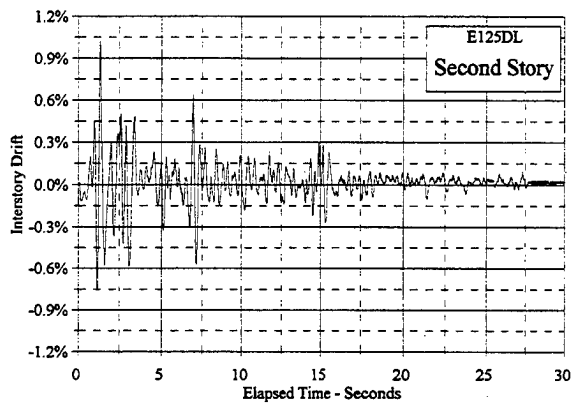
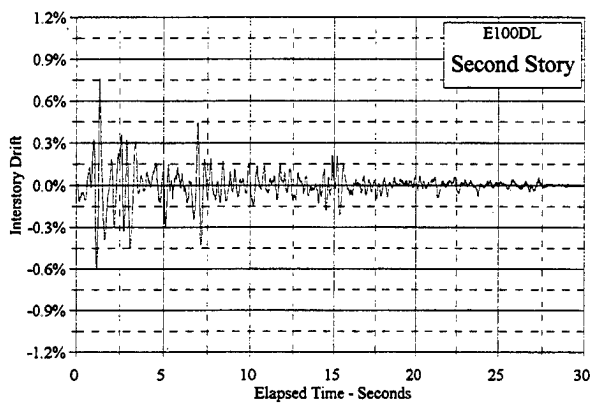
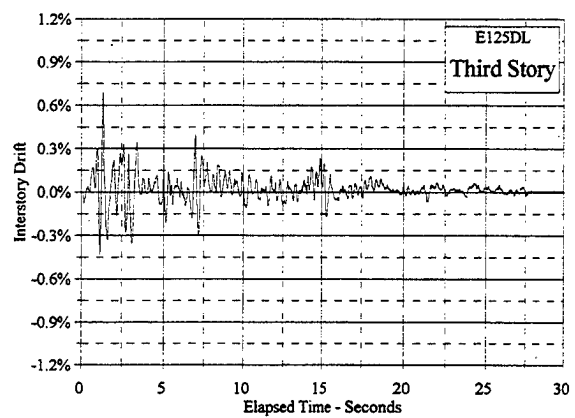
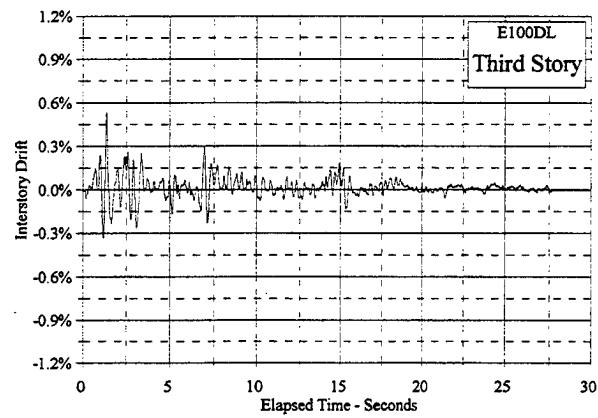


Figure C.3.20 Interstory Drift Vs. Elapsed Time: E100DL, E125DL

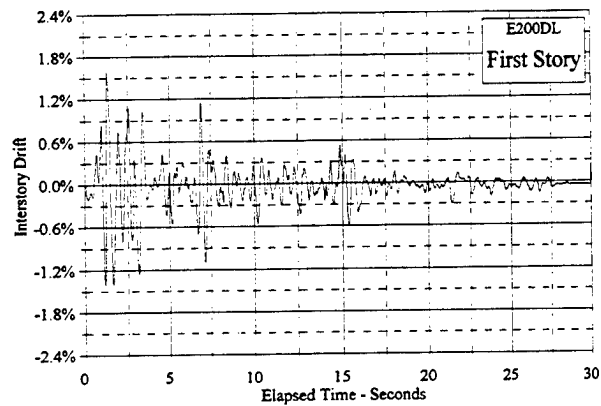
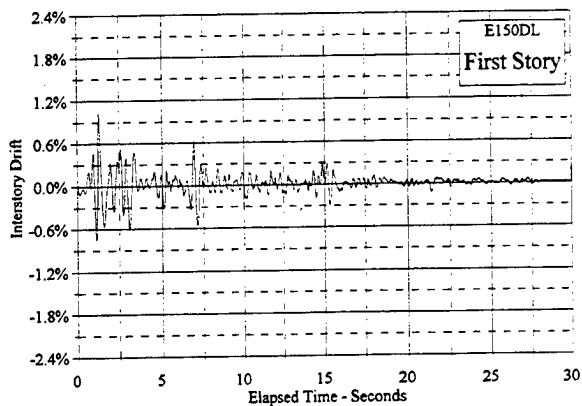
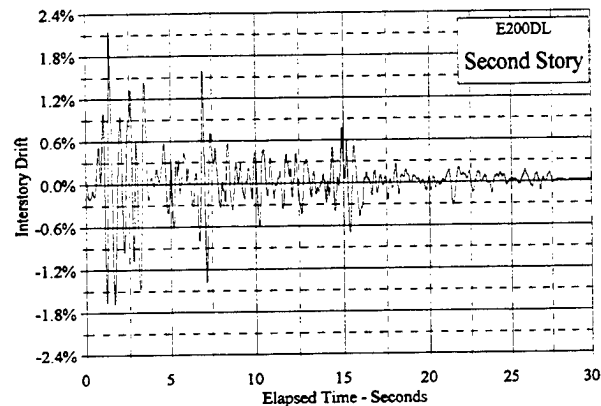
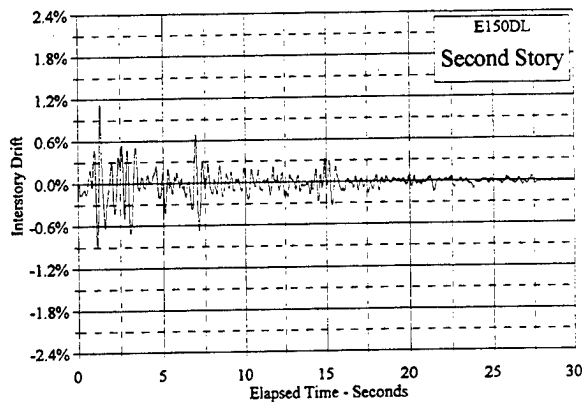
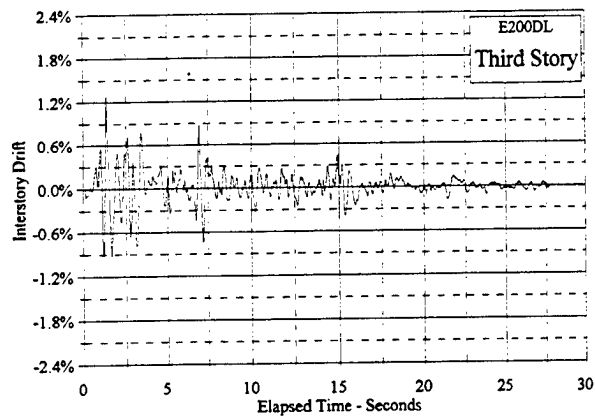
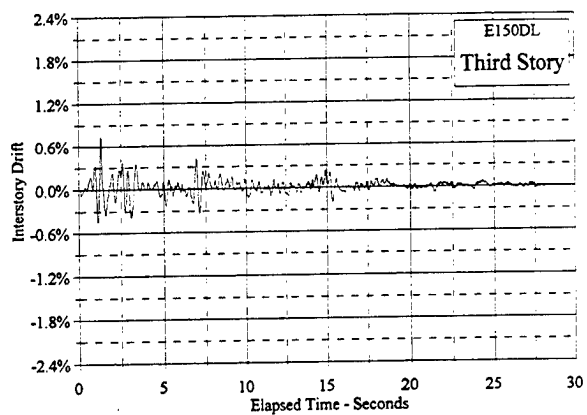


Figure C.3.21 Interstory Drift Vs. Elapsed Time: E150DL, E200DL

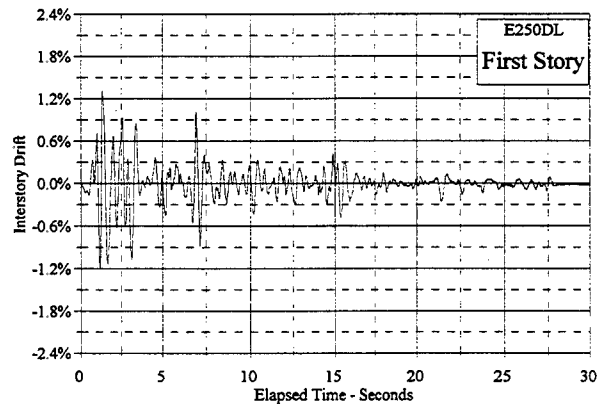
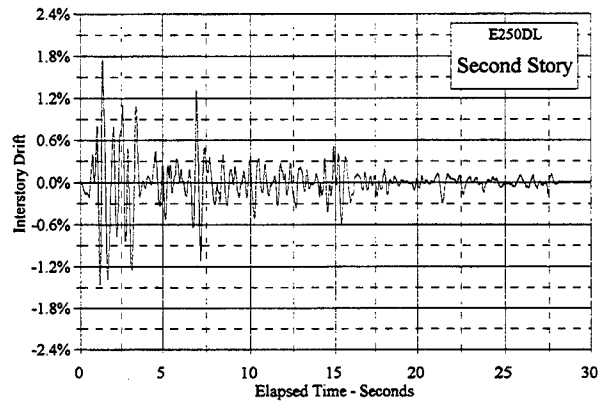
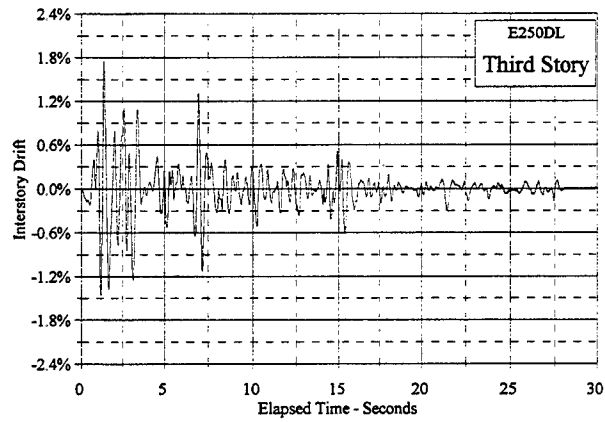


Figure C.3.22 Interstory Drift Vs. Elapsed Time: E250DL

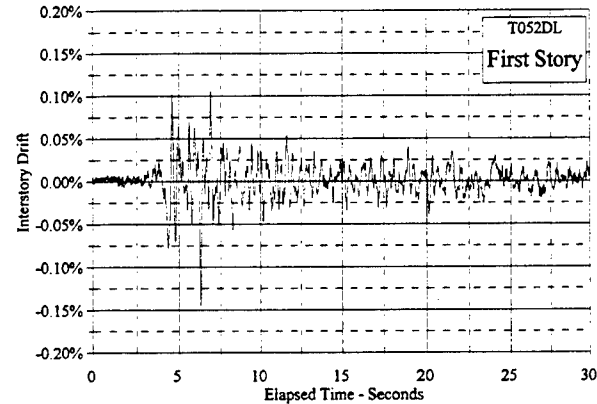
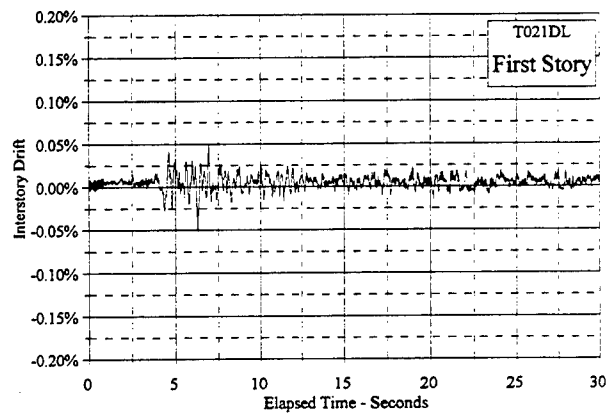
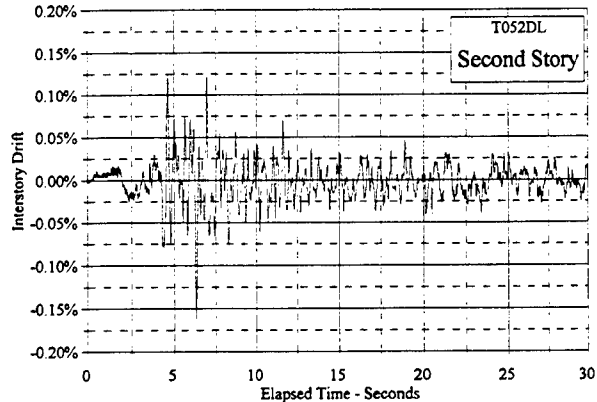
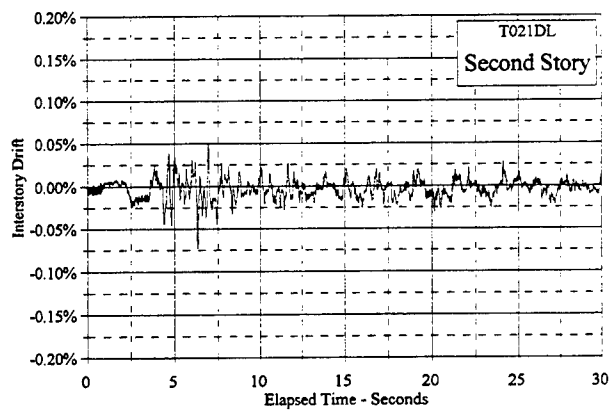
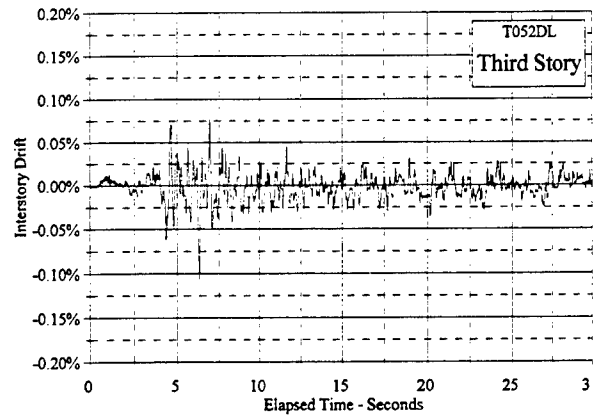
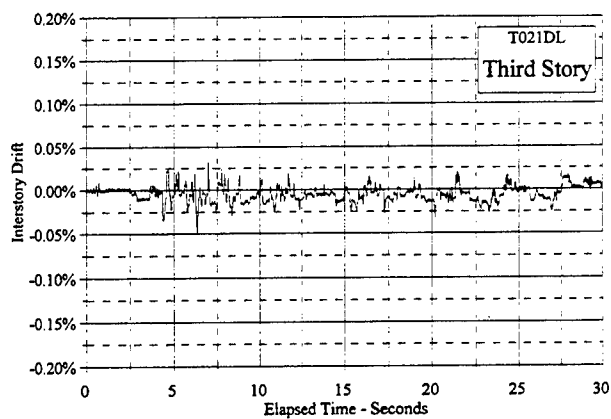


Figure C.3.23 Interstory Drift Vs. Elapsed Time: T021DL, T052DL

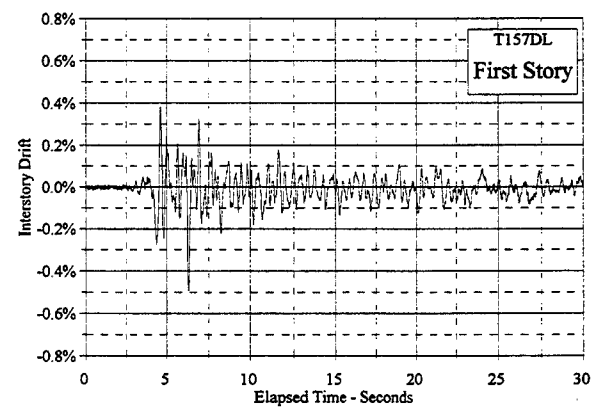
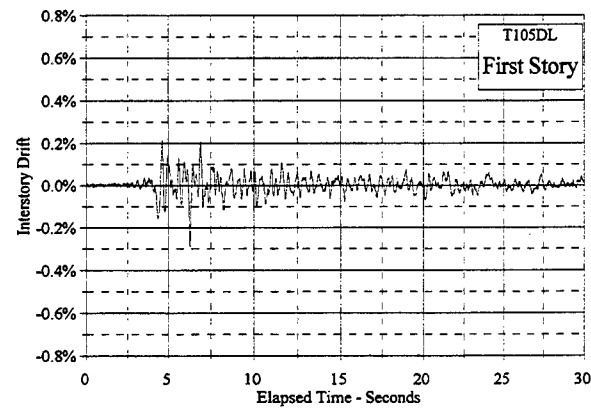
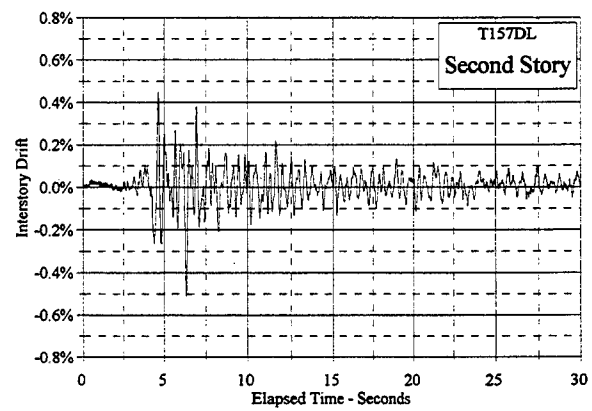
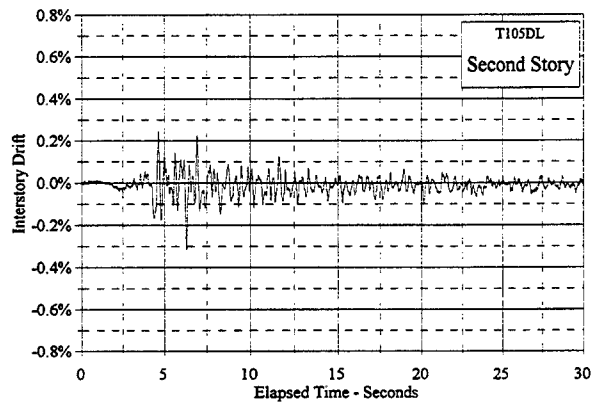
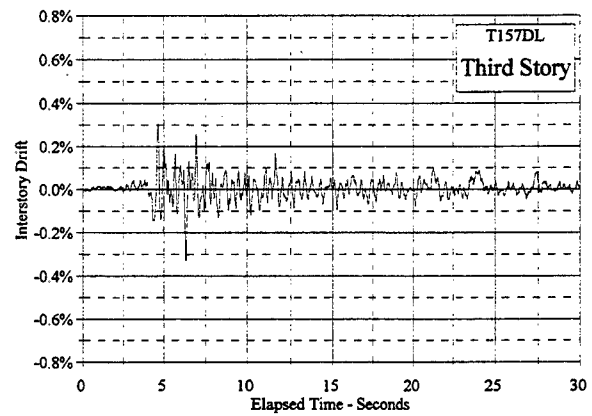
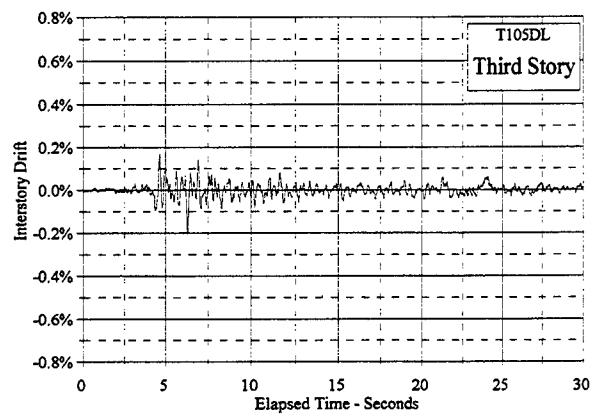


Figure C.3.24 Interstory Drift Vs. Elapsed Time: T105DL, T157DL

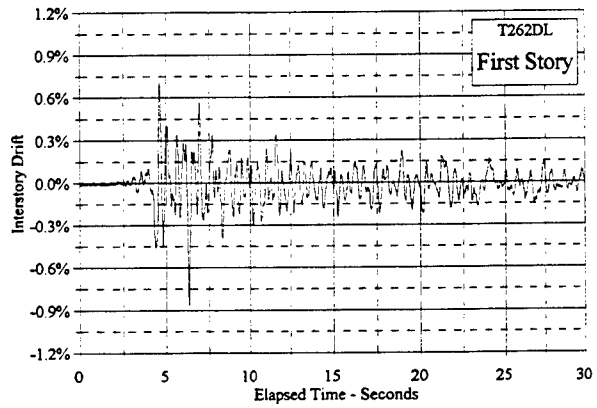
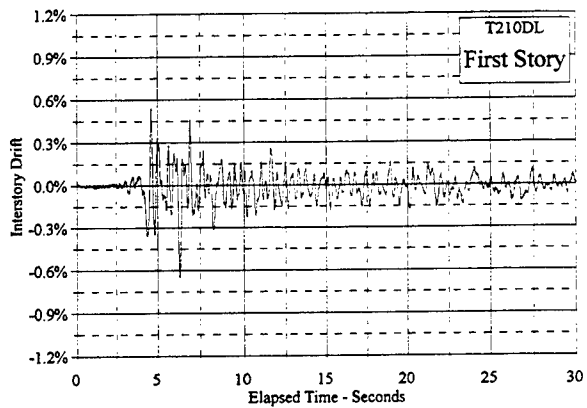
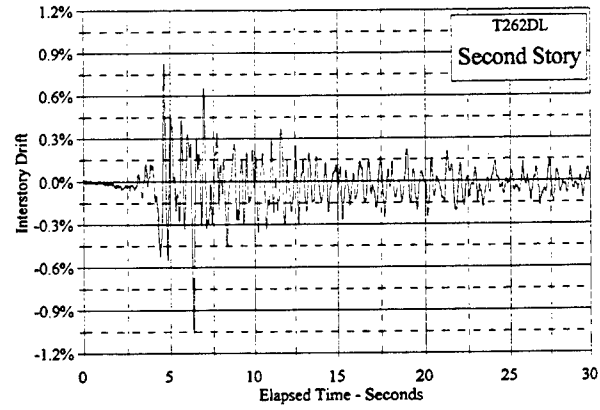
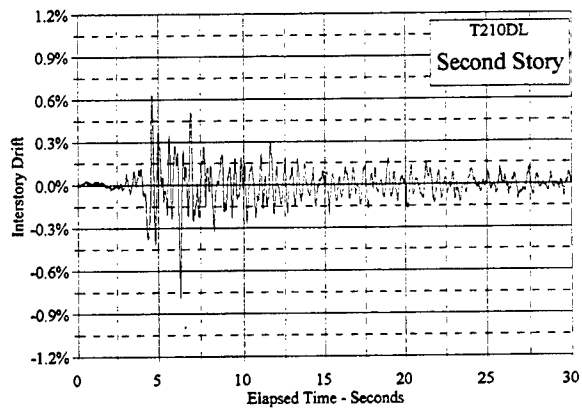
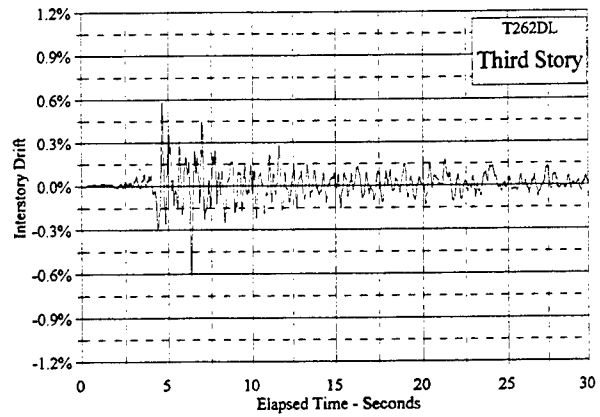
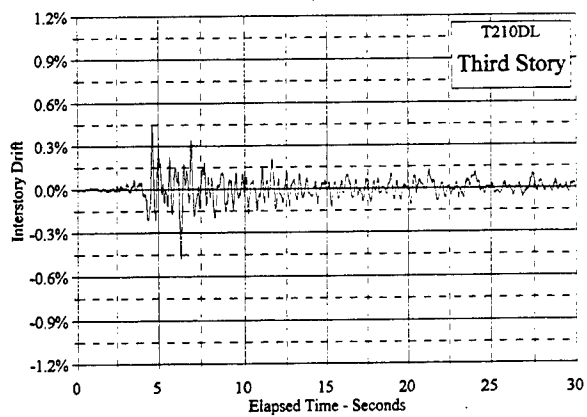


Figure C.3.25 Interstory Drift Vs. Elapsed Time: T210DL, T262DL

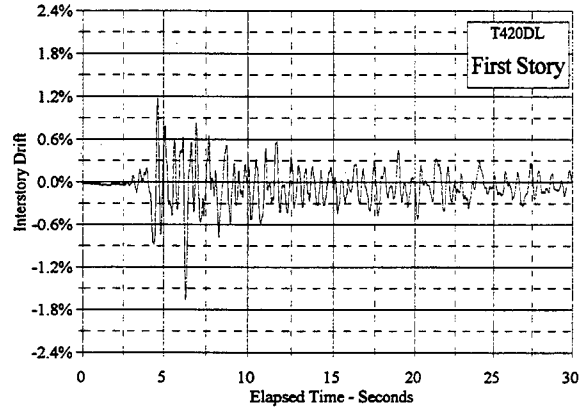
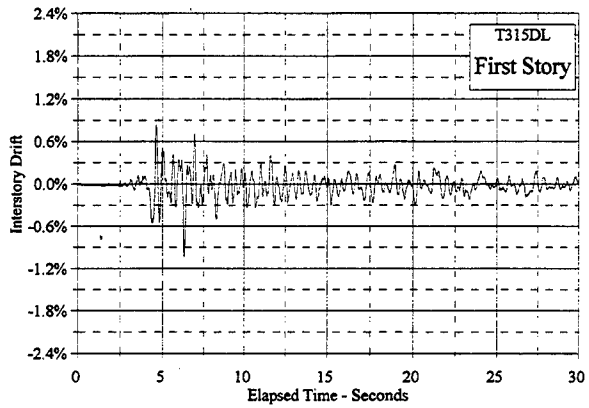
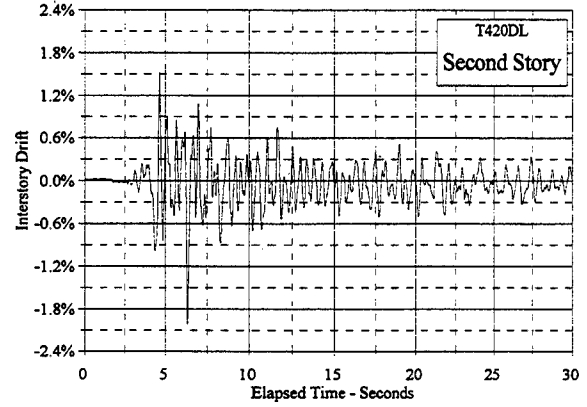
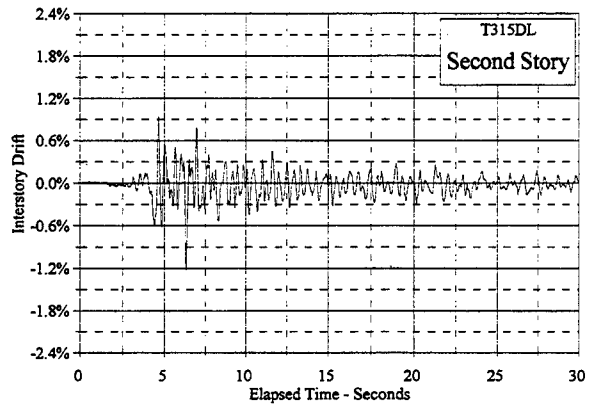
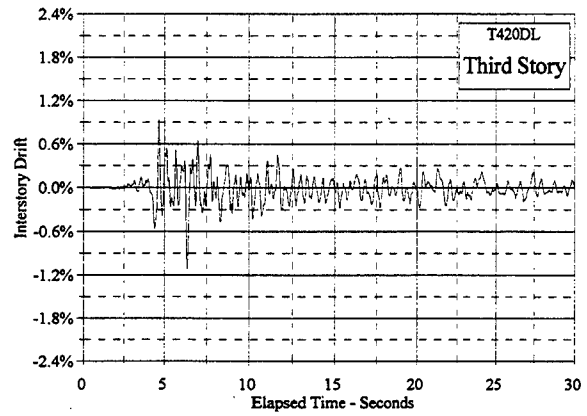
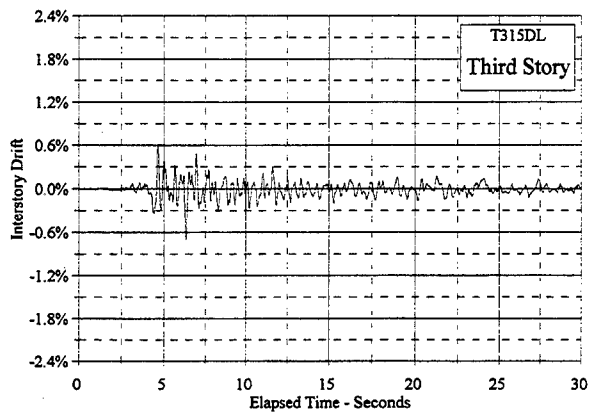


Figure C.3.26 Interstory Drift Vs. Elapsed Time: T315DL, T420DL

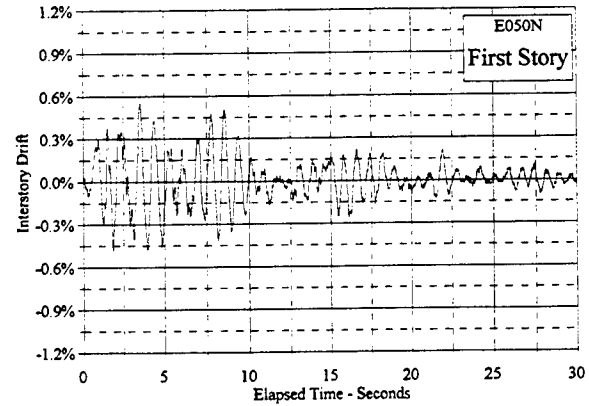
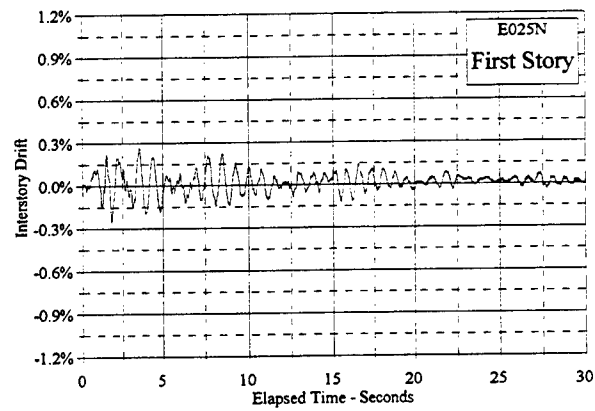
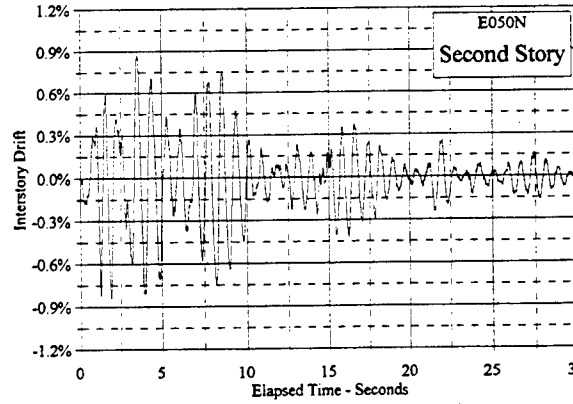
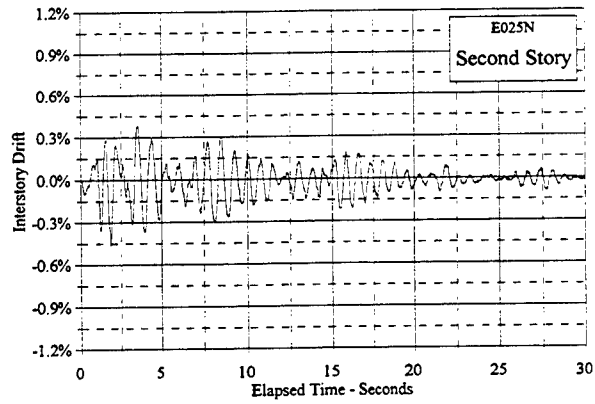
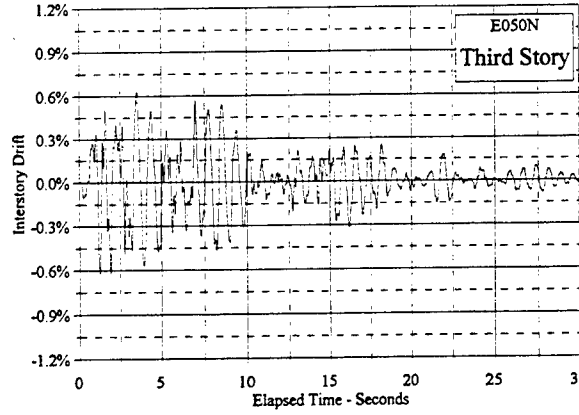
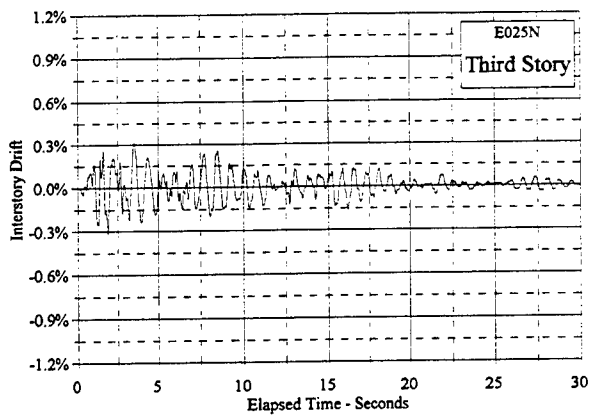


Figure C.3.27 Interstory Drift Vs. Elapsed Time: E025N, E050N

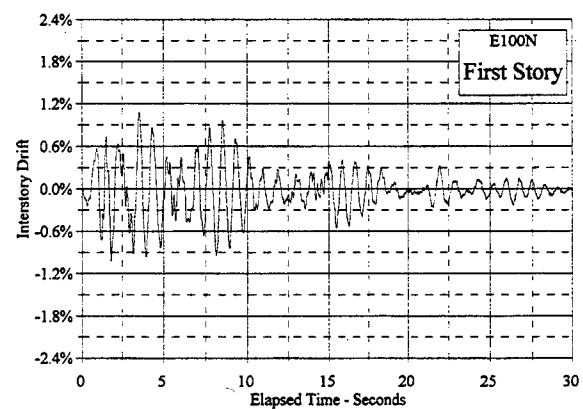
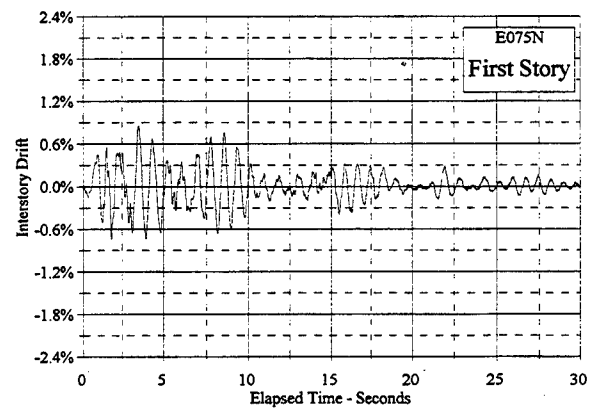
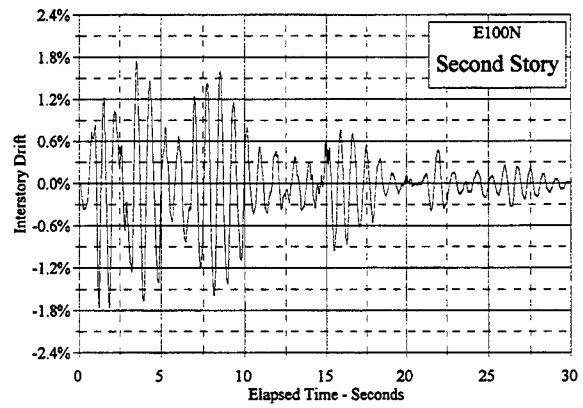
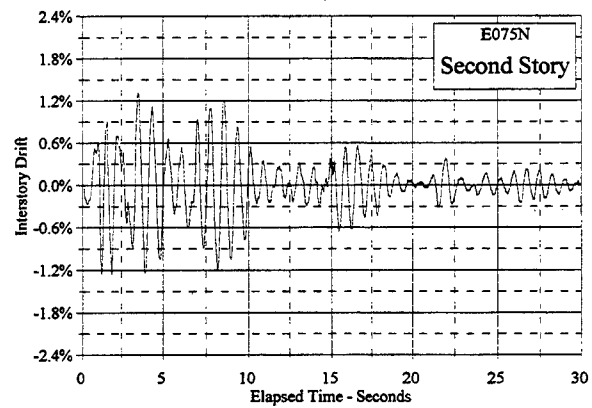
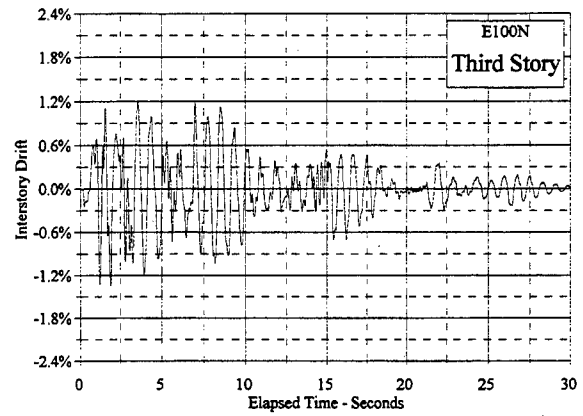
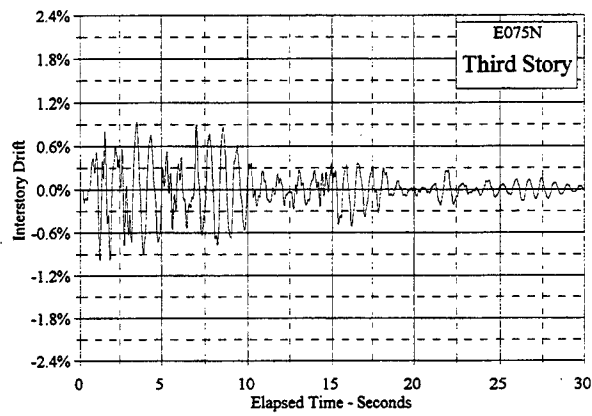


Figure C.3.28 Interstory Drift Vs. Elapsed Time: E075N, E100N

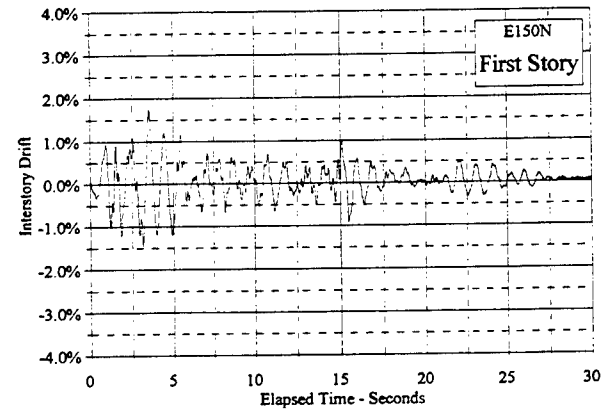
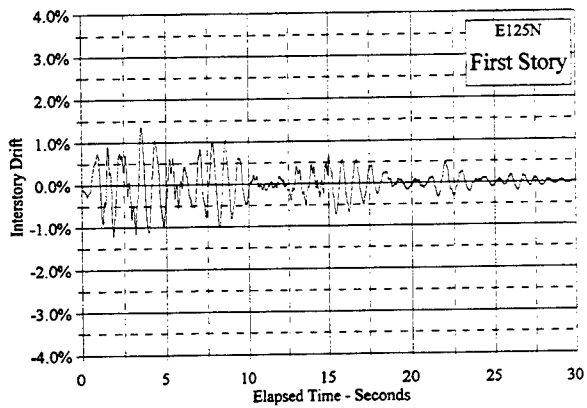
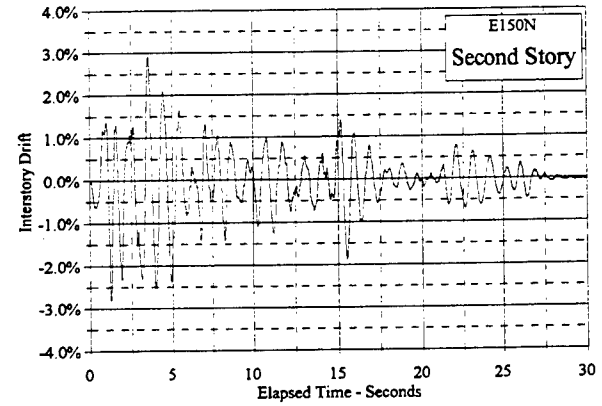
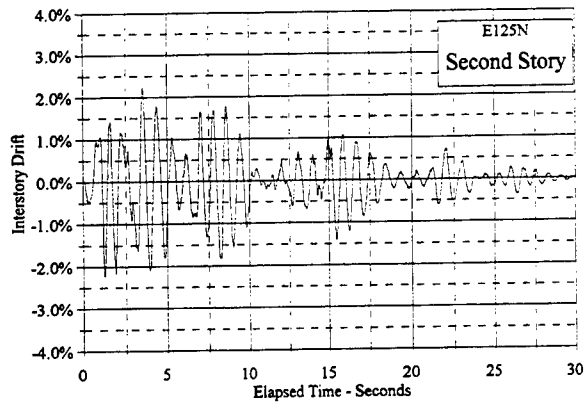
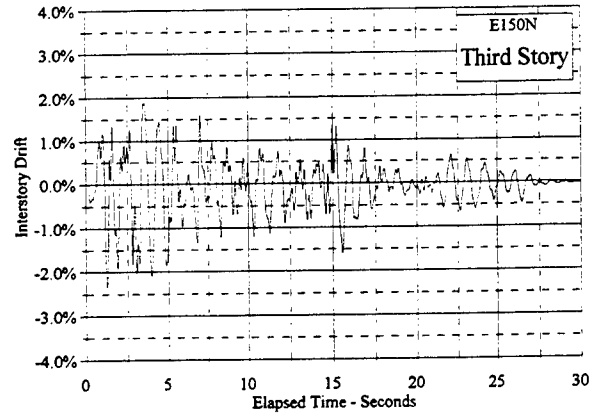
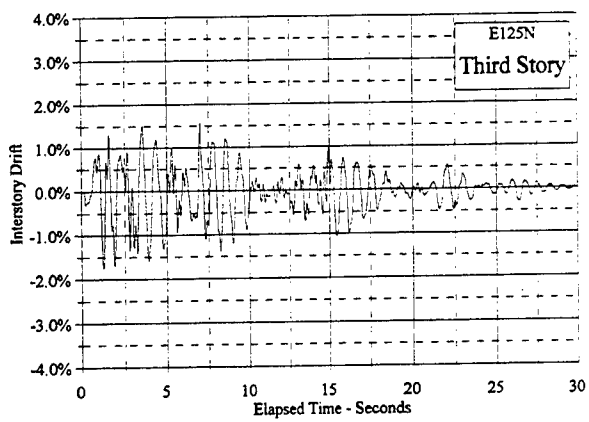


Figure C.3.29 Interstory Drift Vs. Elapsed Time: E125N, E150N

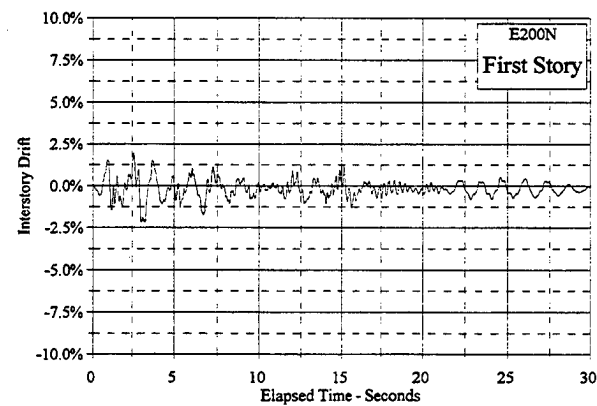
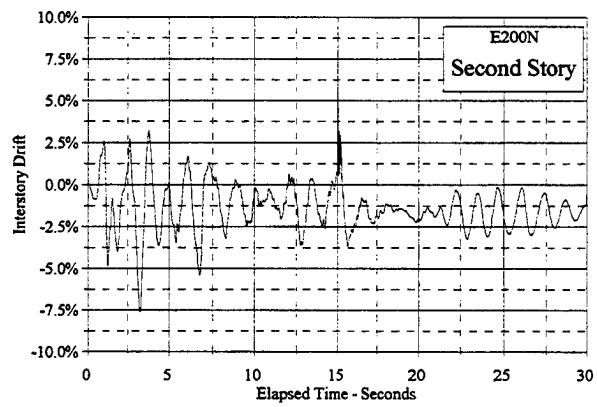
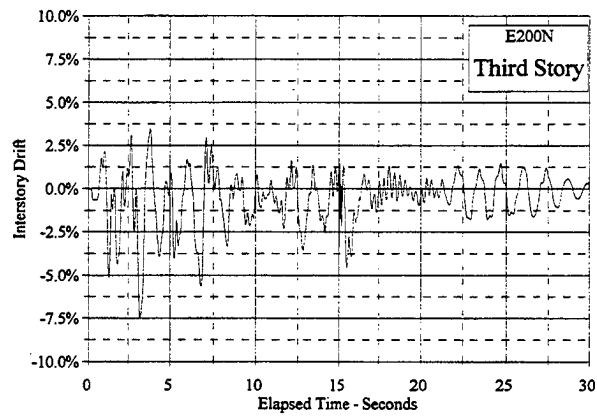


Figure C.3.30 Interstory Drift Vs. Elapsed Time: E200N

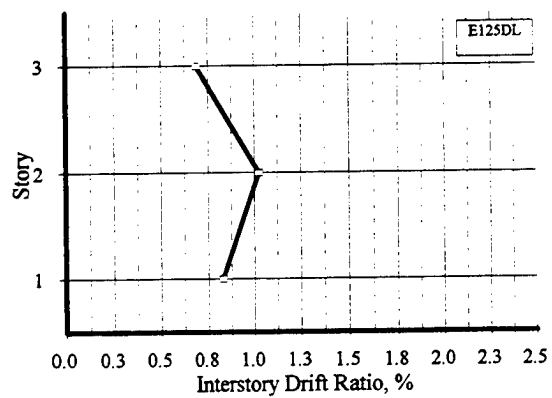
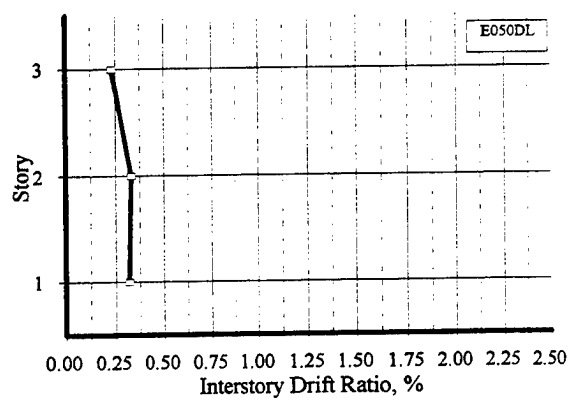
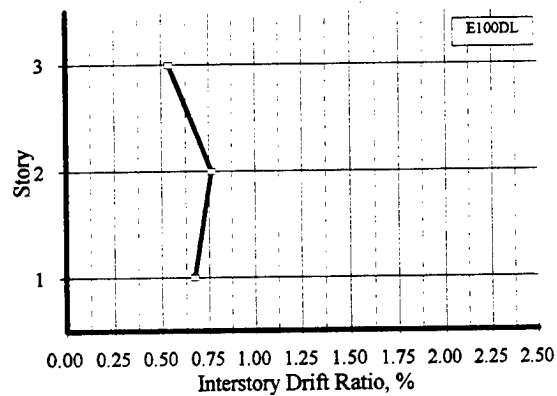
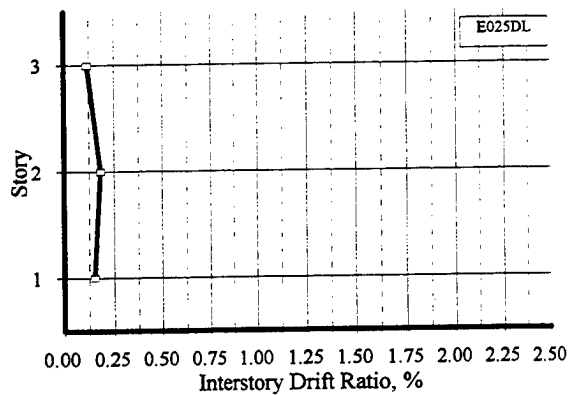
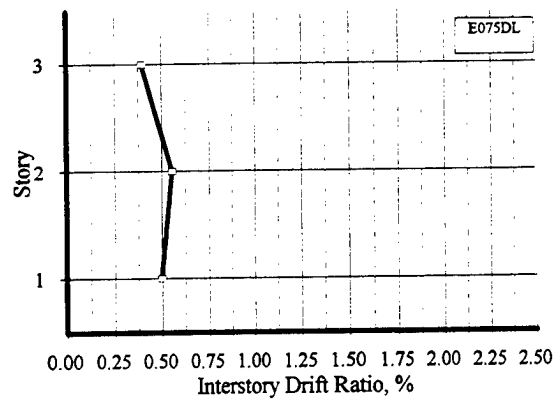
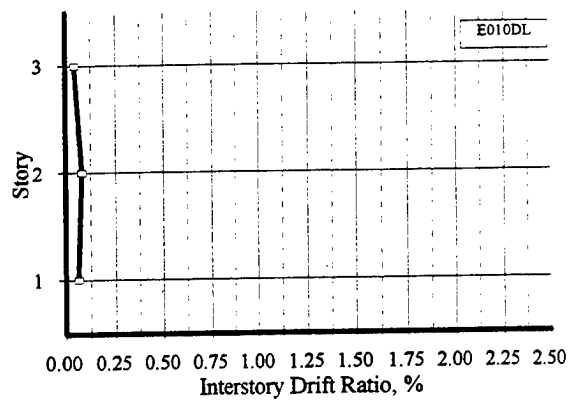


Figure C.3.31 Maximum Interstory Drift Ratios: E010DL - E125DL

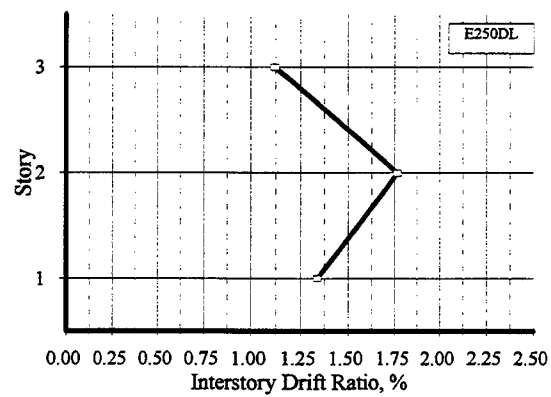
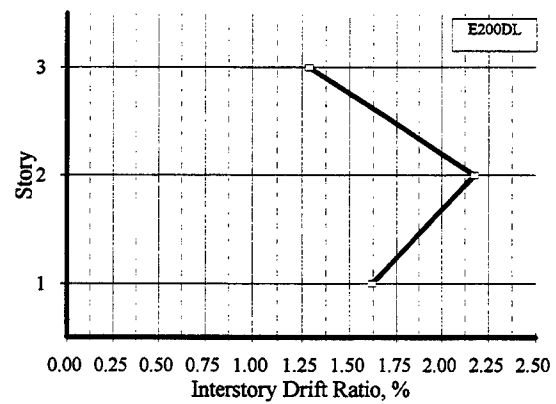
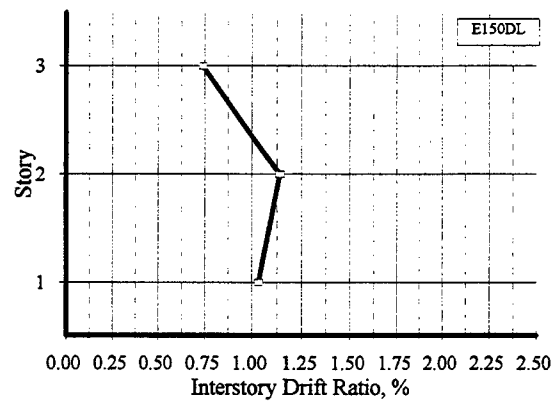


Figure C.3.32 Maximum Interstory Drift Ratios: E150DL - E250DL

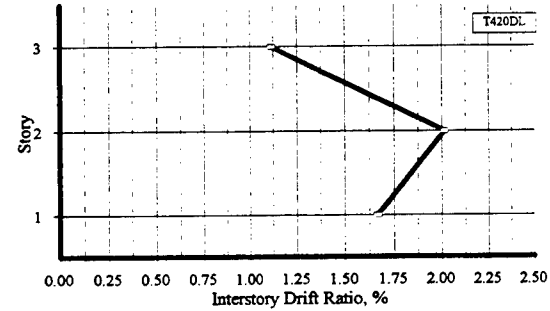
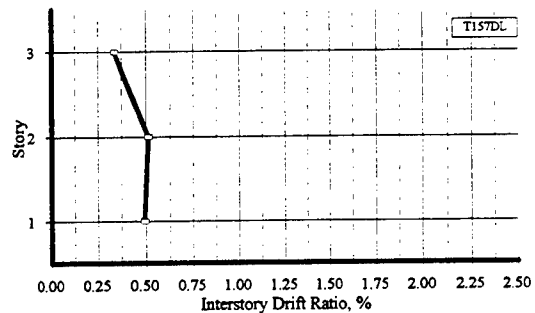
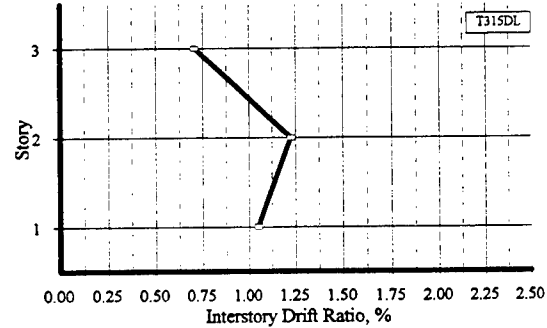
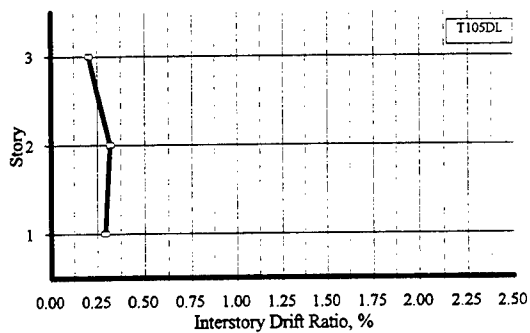
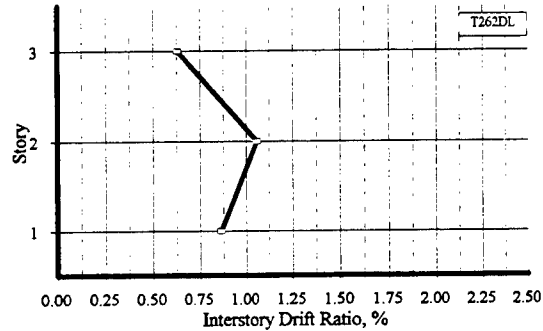
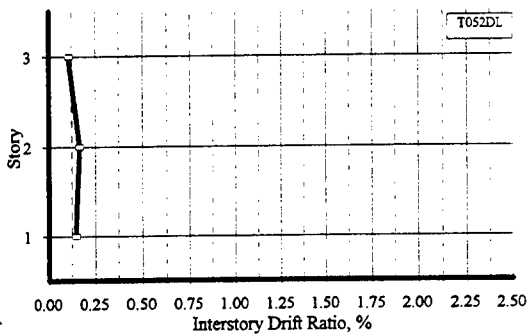
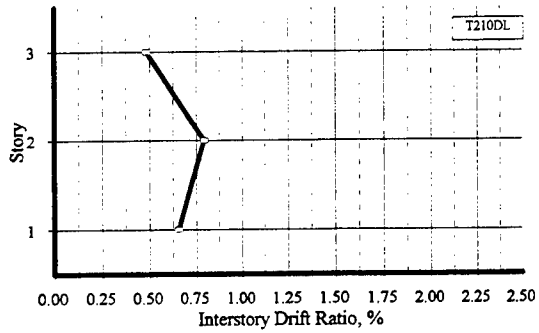
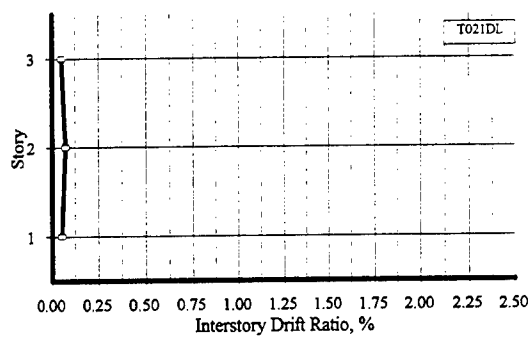


Figure C.3.33 Maximum Interstory Drift Ratios: T021DL - T420DL

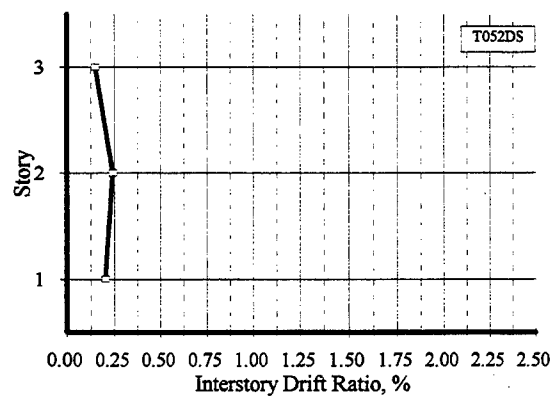
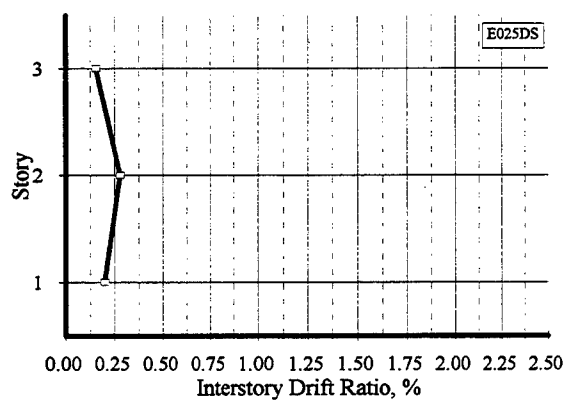
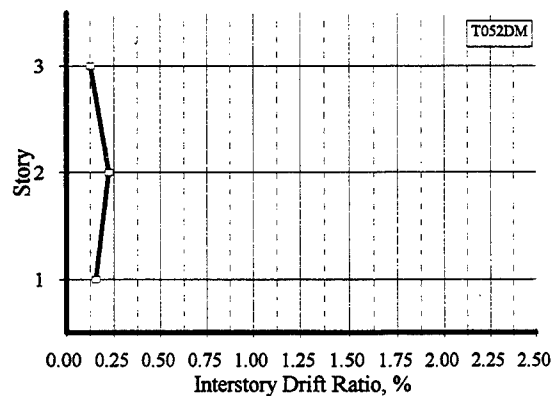
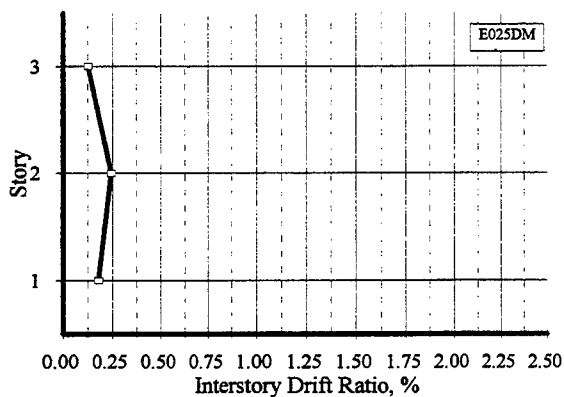
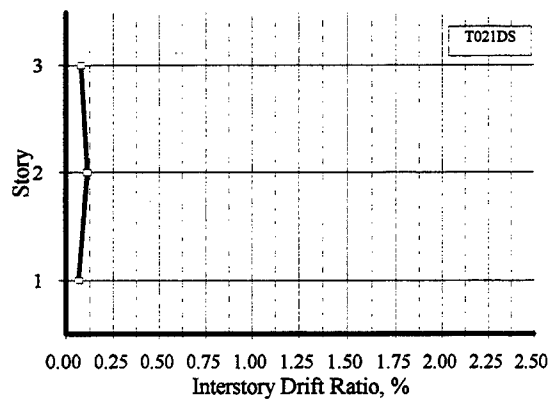
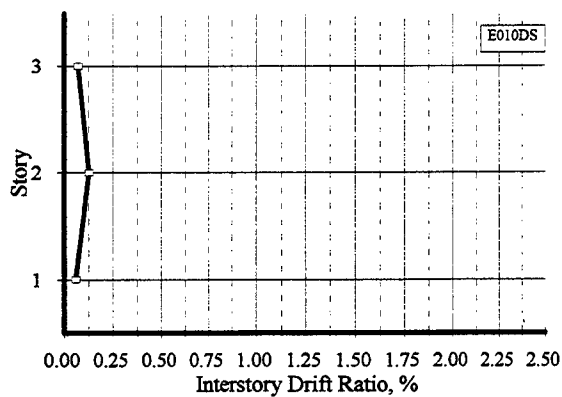


Figure C.3.34 Maximum Interstory Drift Ratios: E010DS - T052DS

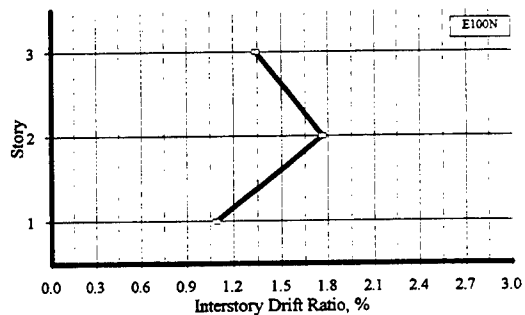
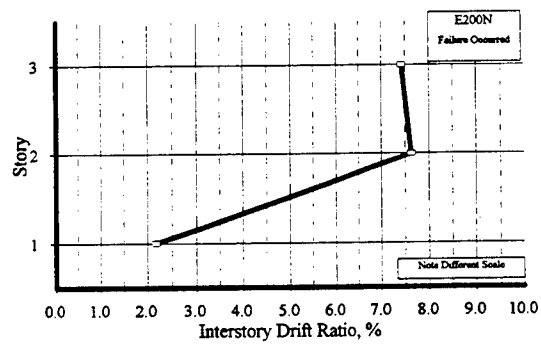
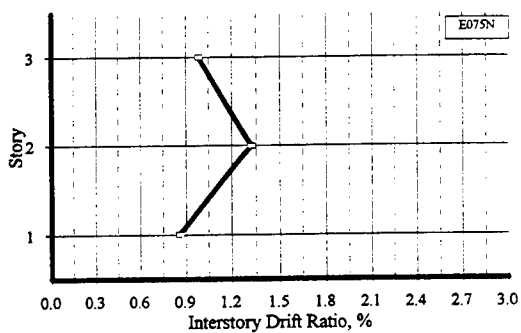
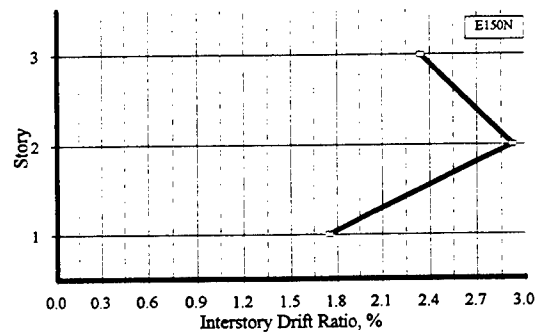
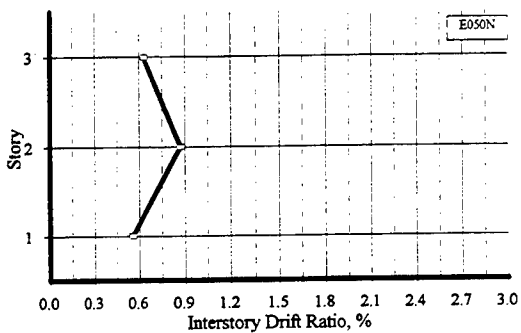
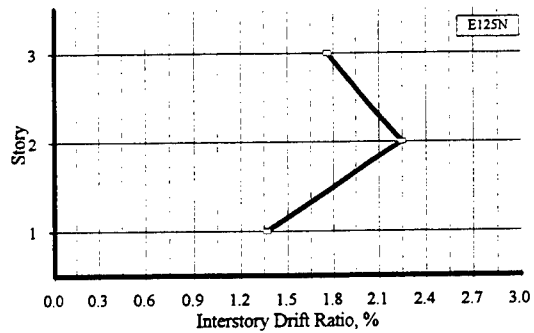
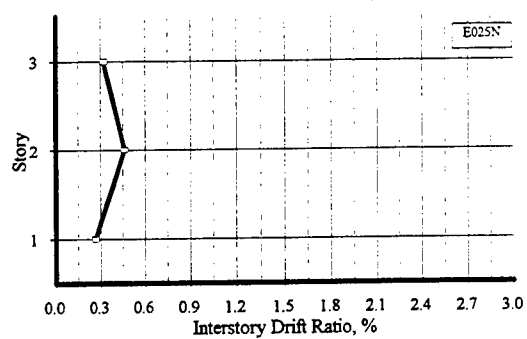


Figure C.3.35 Maximum Interstory Drift Ratios: E025N - E200N

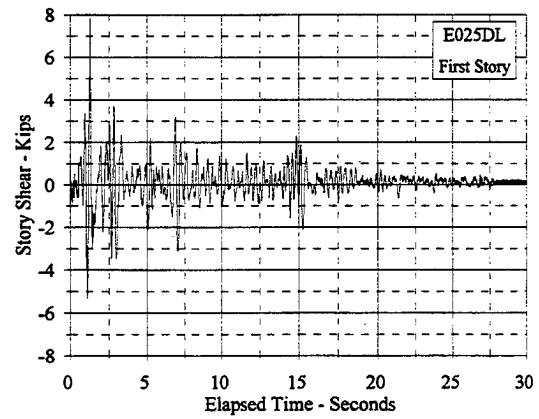
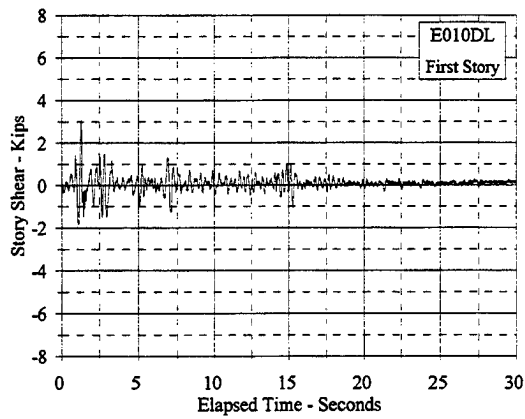
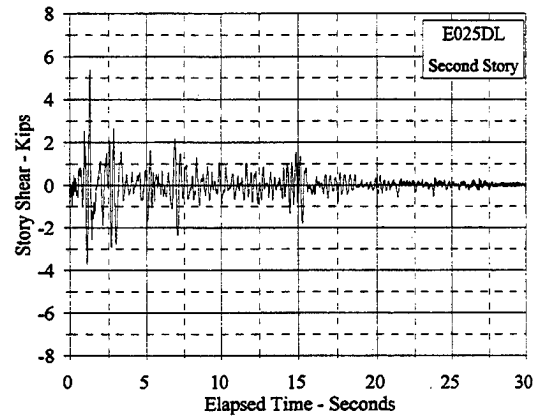
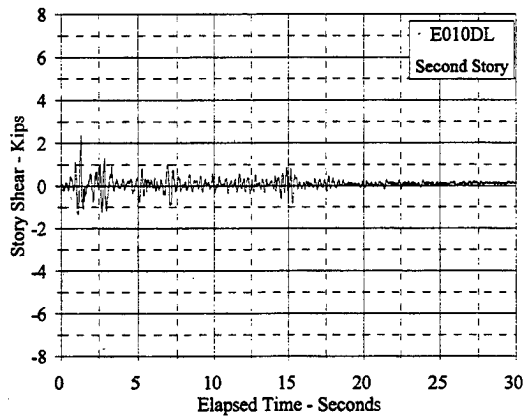
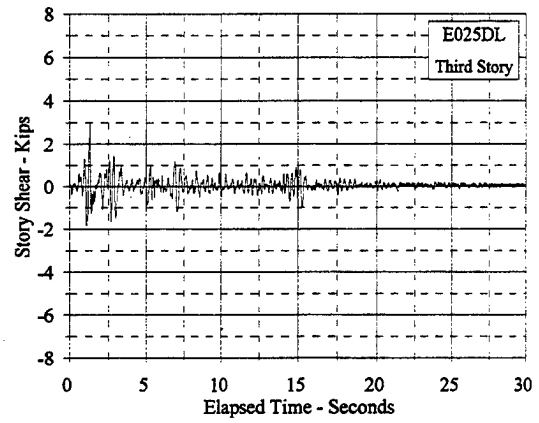
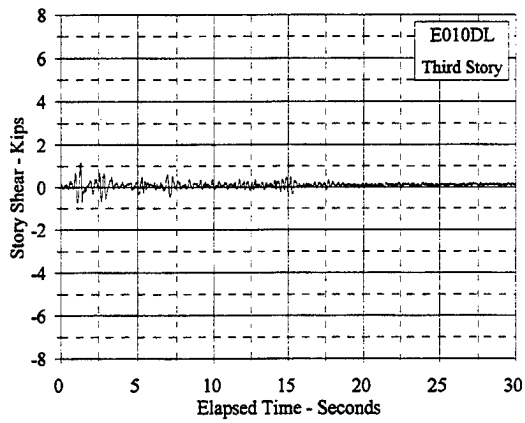


Figure C.4.1 Story Shear Vs. Elapsed Time: E010DL, E025DL

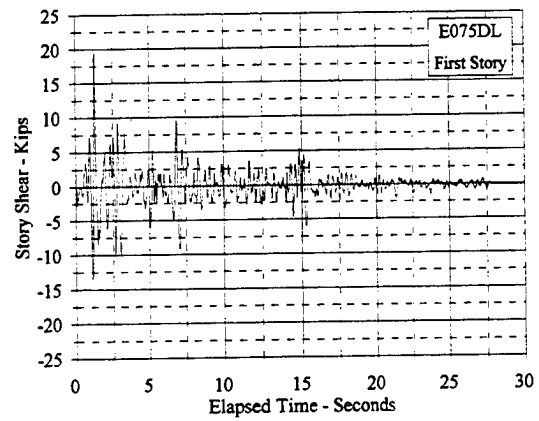
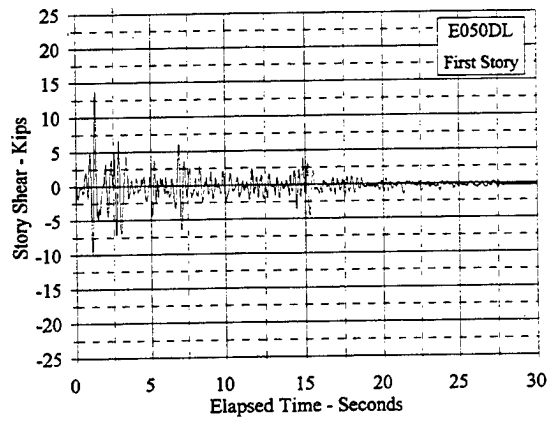
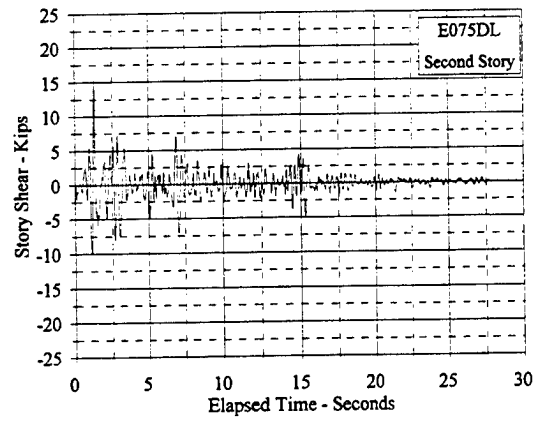
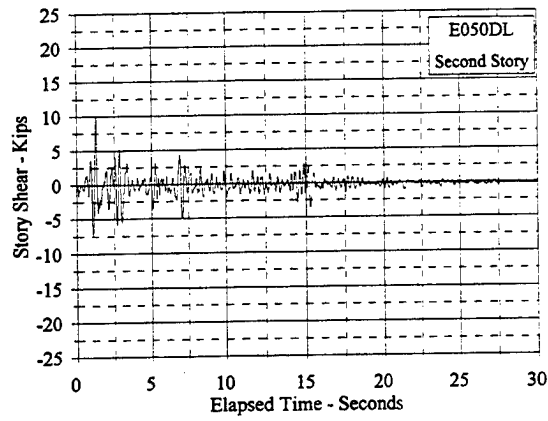
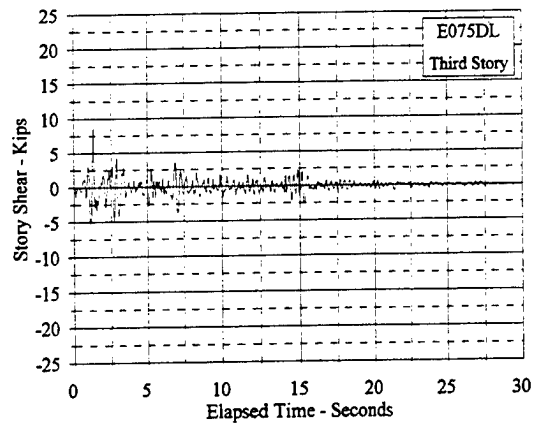
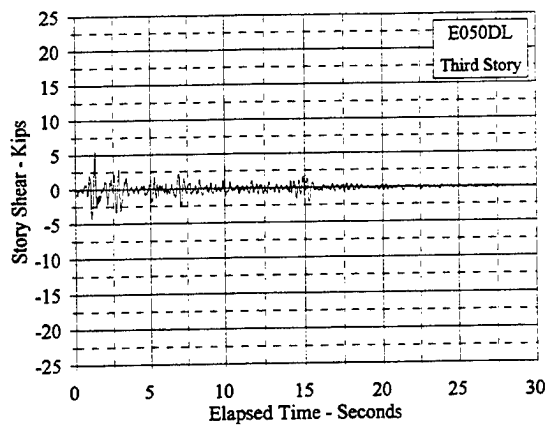


Figure C.4.2 Story Shear Vs. Elapsed Time: E050DL, E075DL

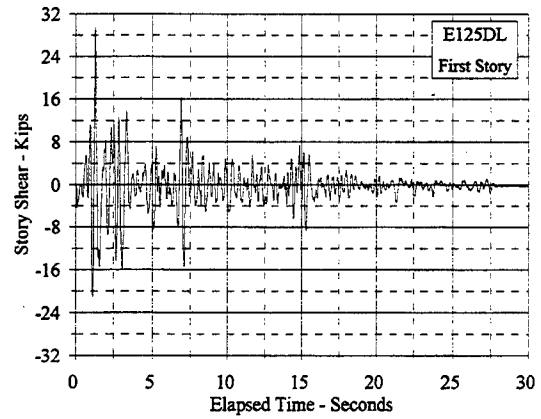
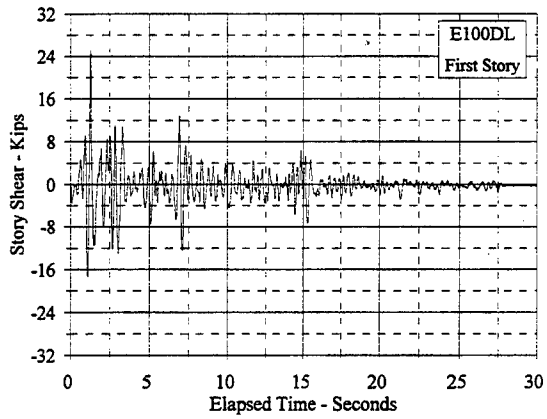
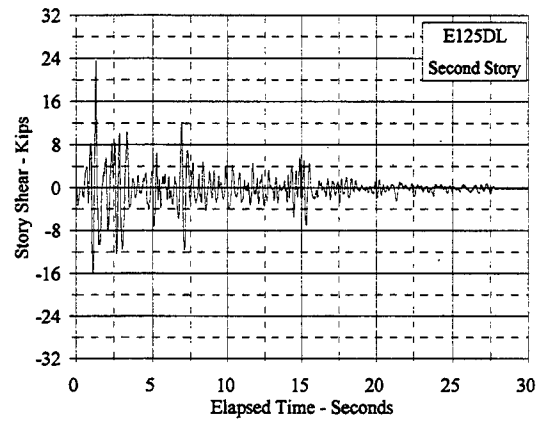
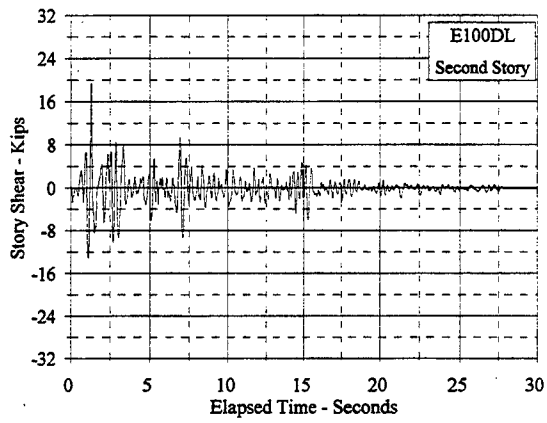
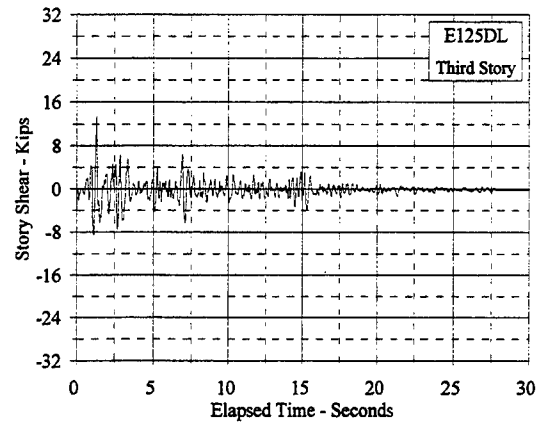
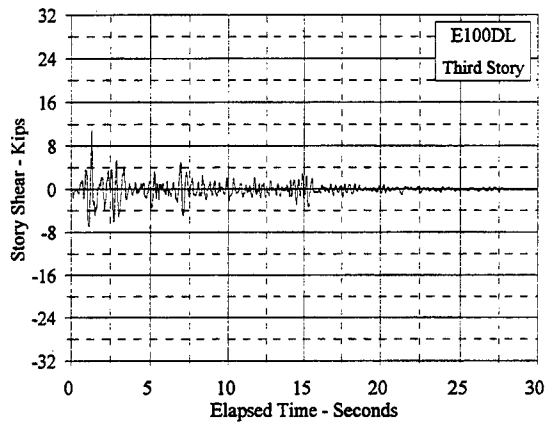


Figure C.4.3 Story Shear Vs. Elapsed Time: E100DL, E125DL

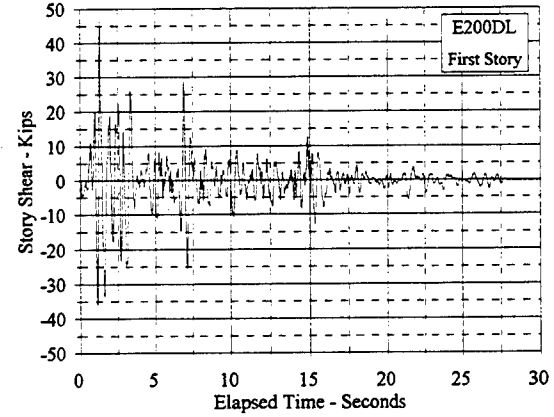
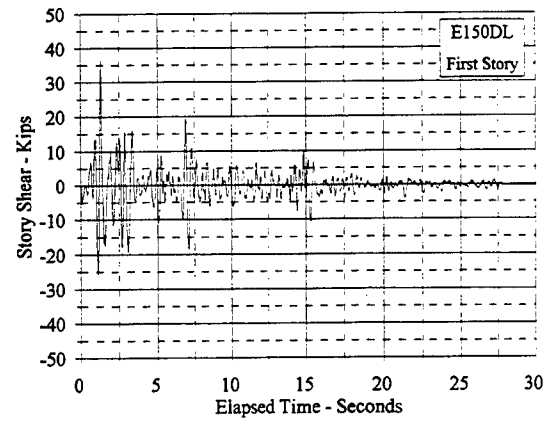
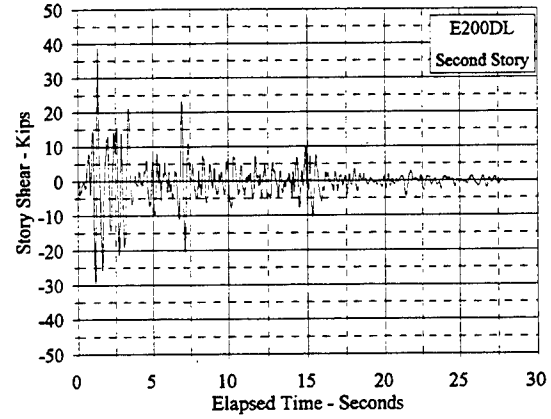
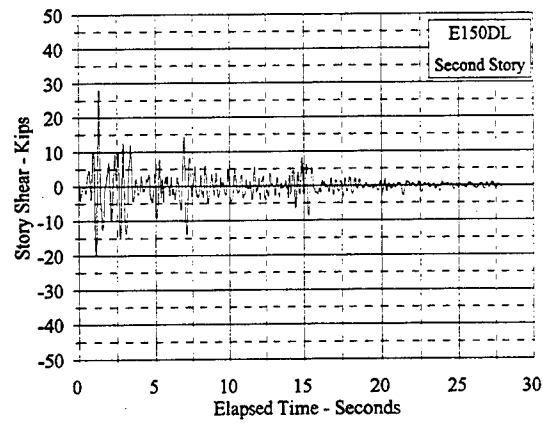
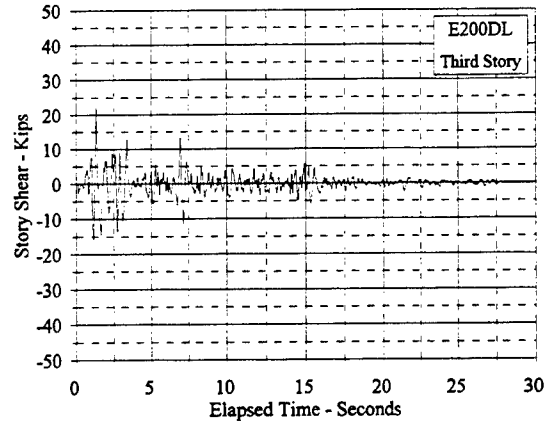
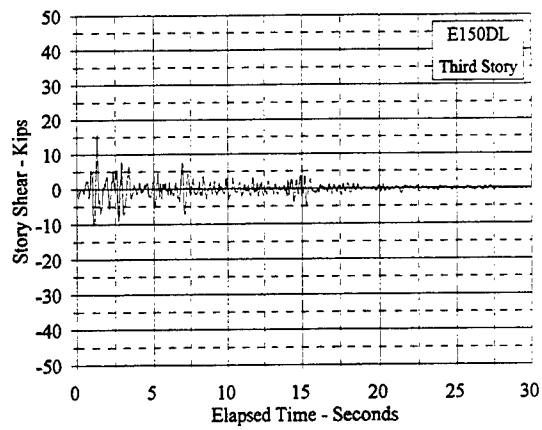


Figure C.4.4 Story Shear Vs. Elapsed Time: E150DL, E200DL

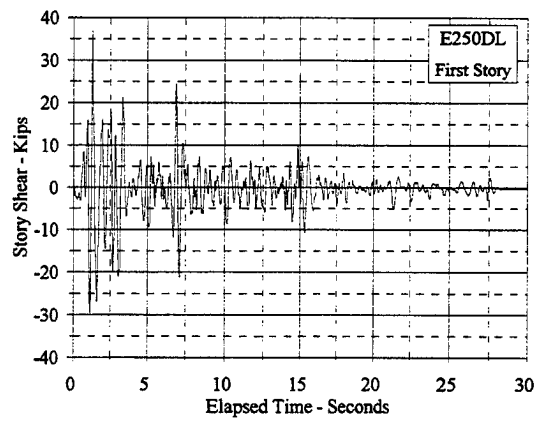
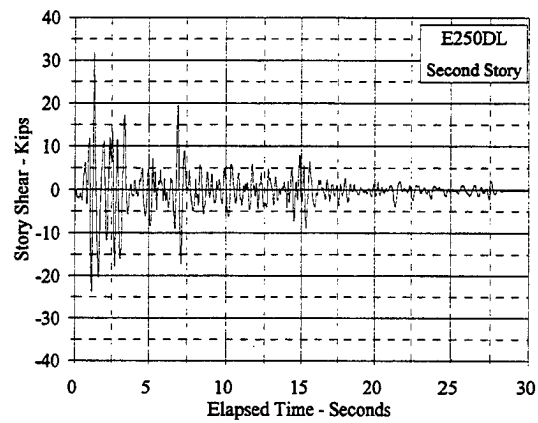
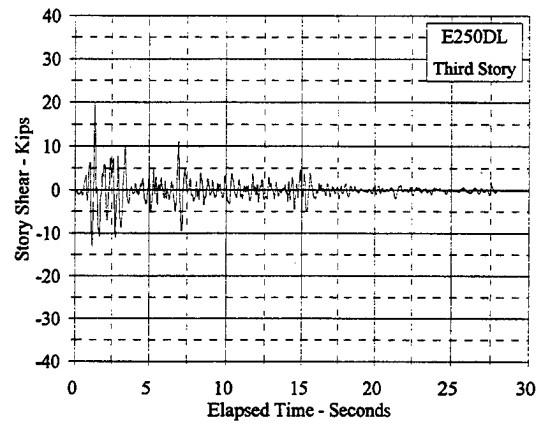


Figure C.4.5 Story Shear Vs. Elapsed Time: E200DL

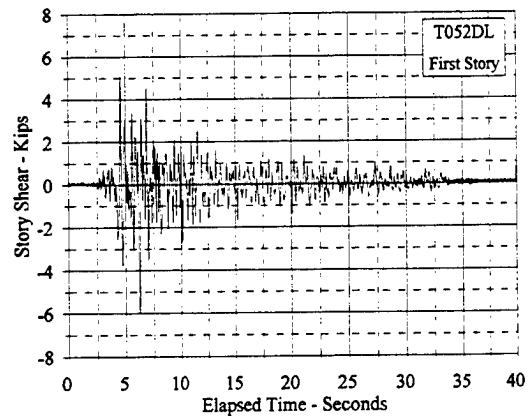
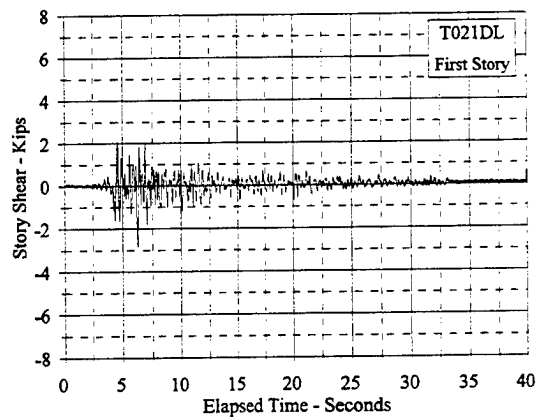
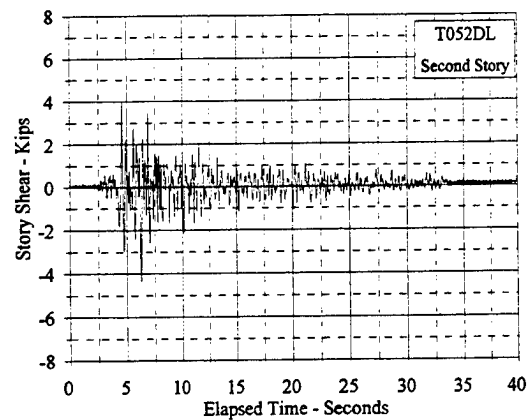
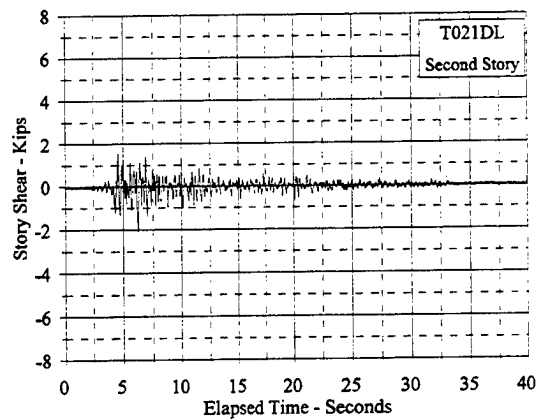
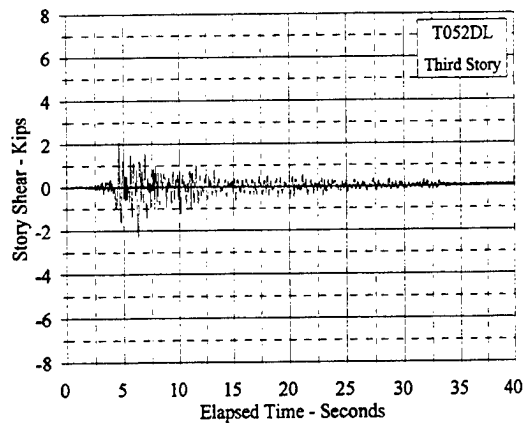
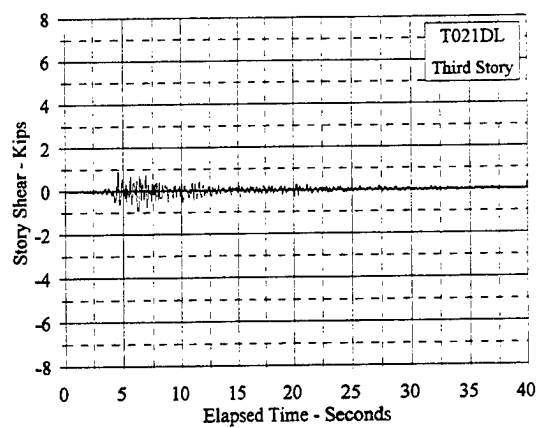


Figure C.4.6 Story Shear Vs. Elapsed Time: T021DL, T052DL

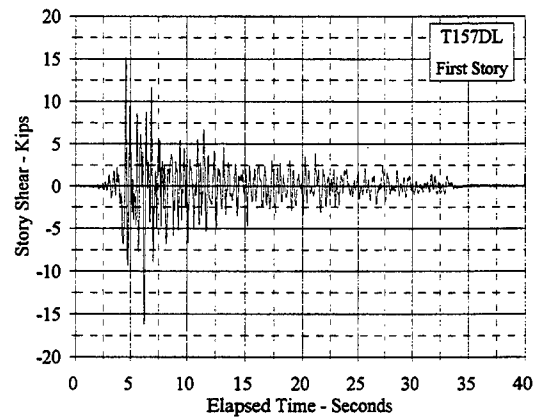
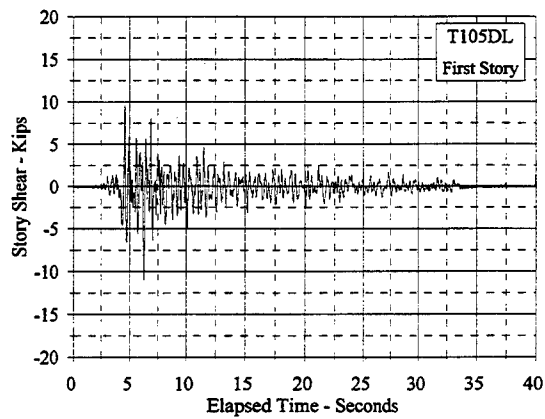
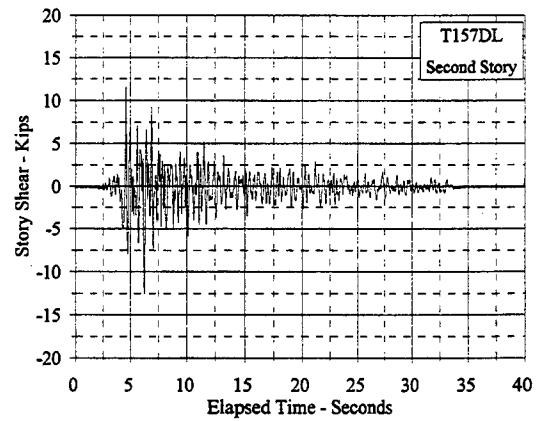
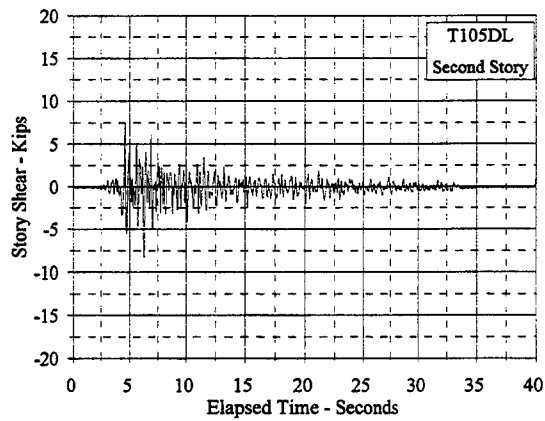
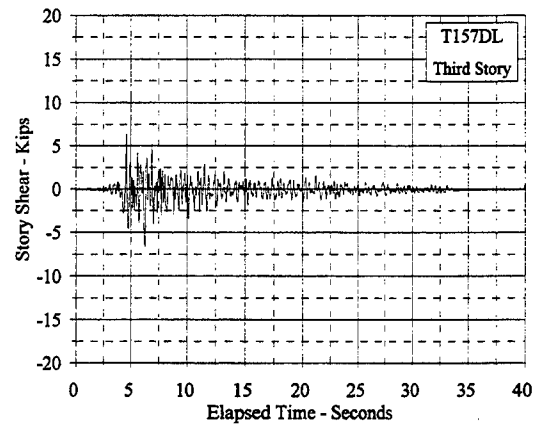
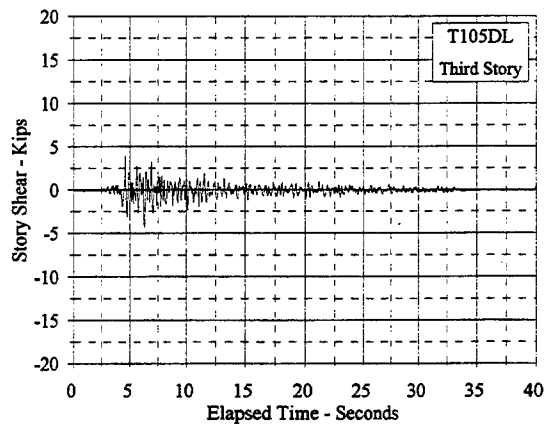


Figure C.4.7 Story Shear Vs. Elapsed Time: T105DL, T157DL

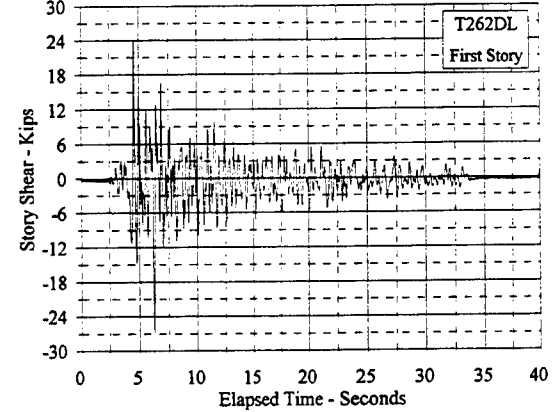
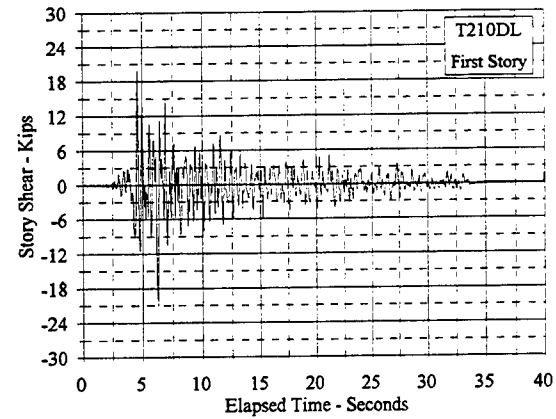
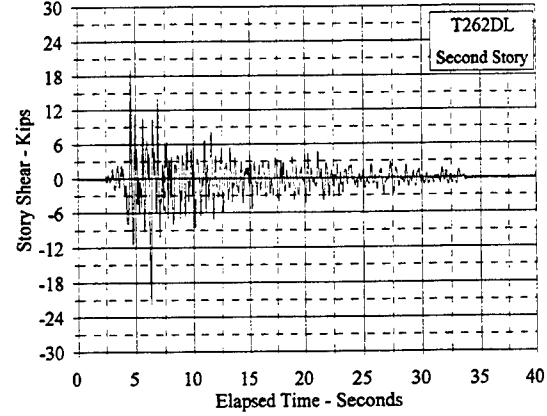
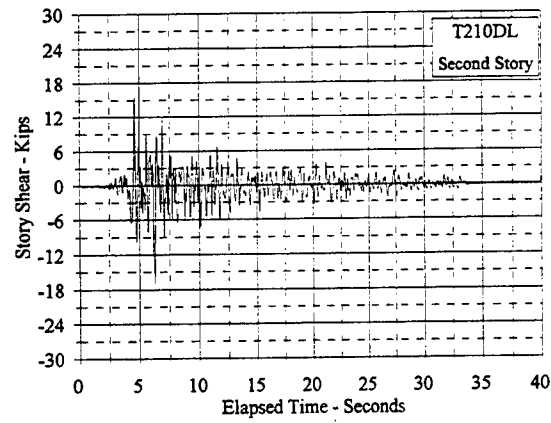
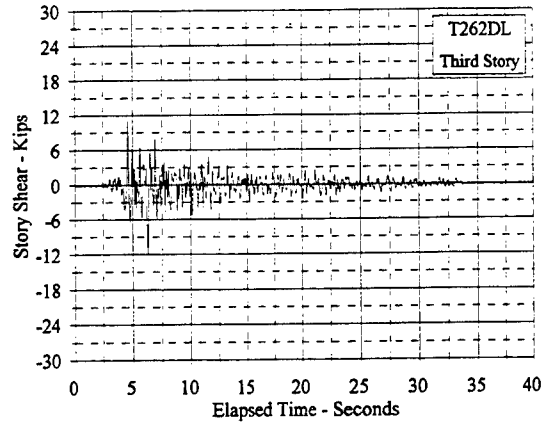
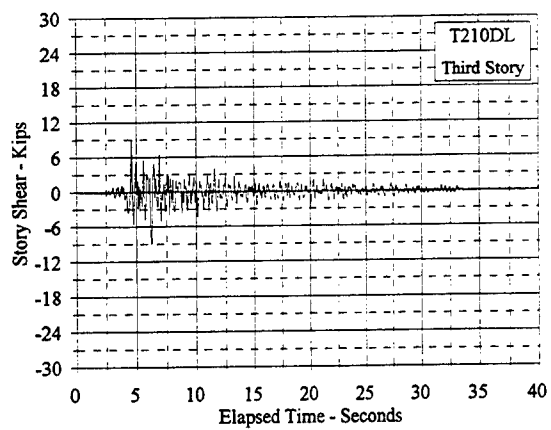


Figure C.4.8 Story Shear Vs. Elapsed Time: T210DL, T262DL

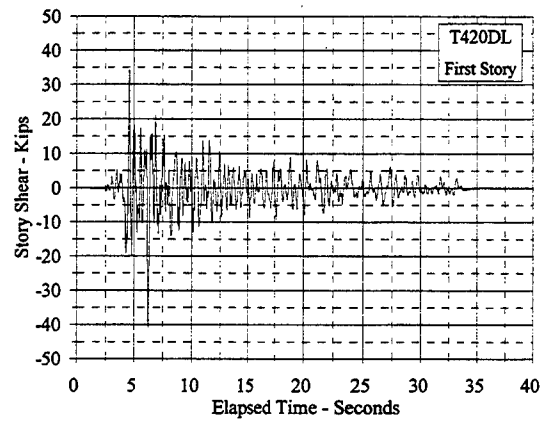
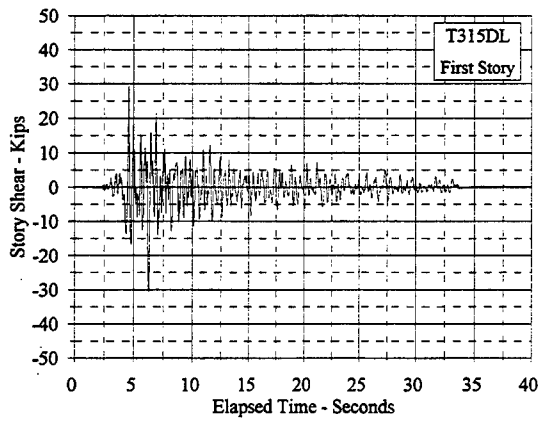
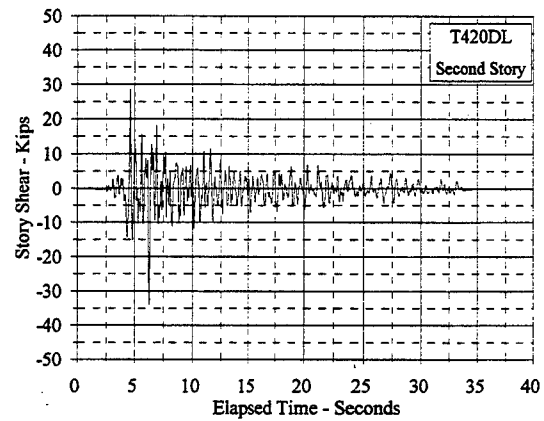
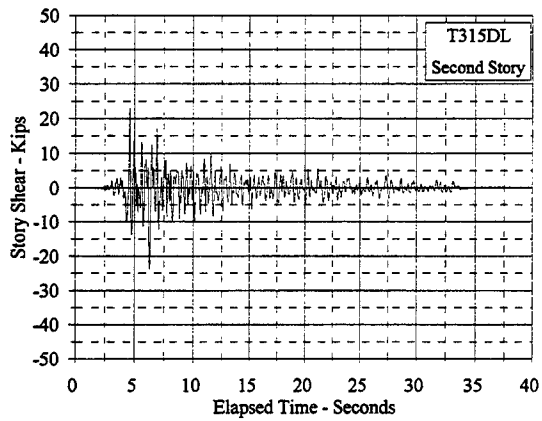
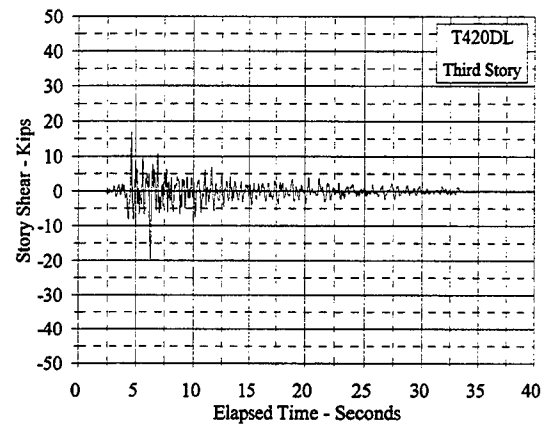
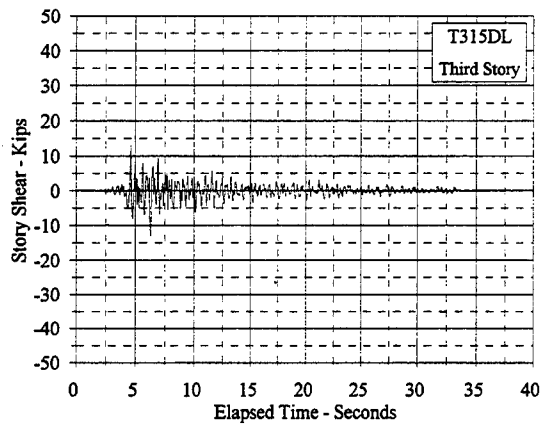


Figure C.4.9 Story Shear Vs. Elapsed Time: T315DL, T420DL

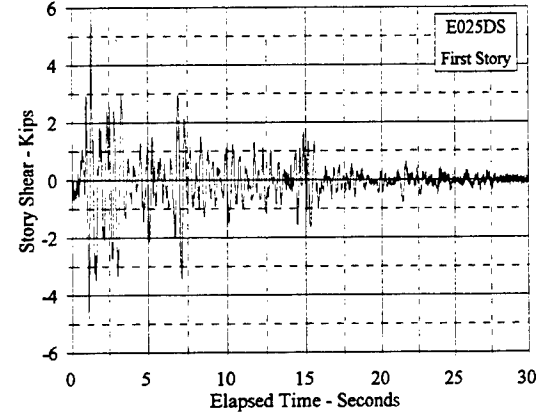
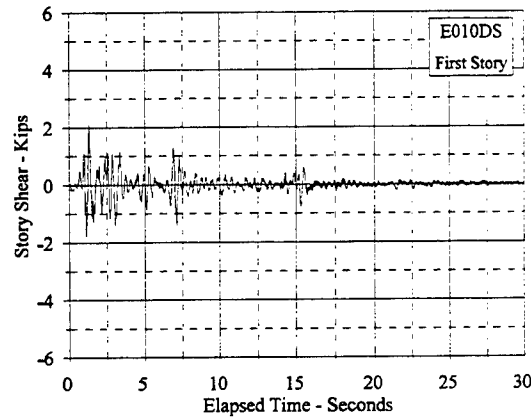
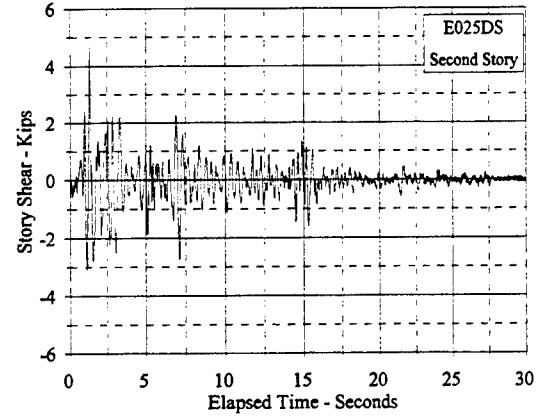
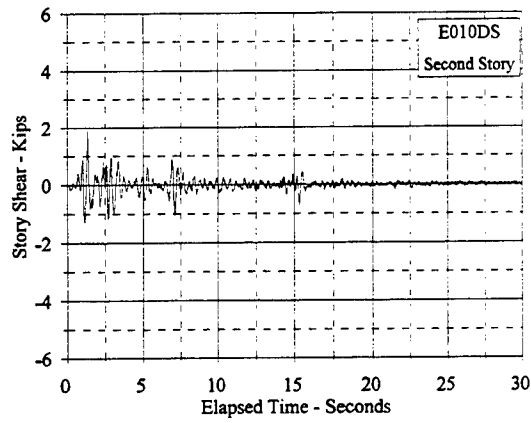
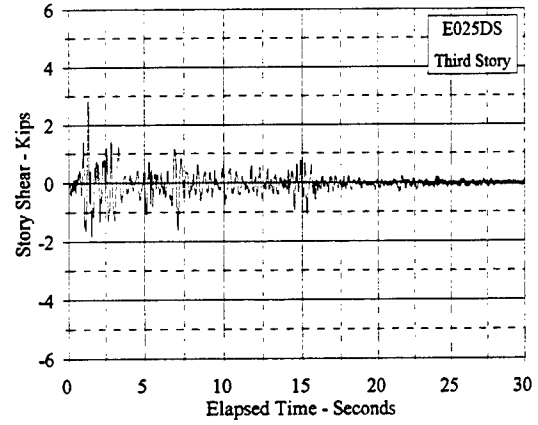
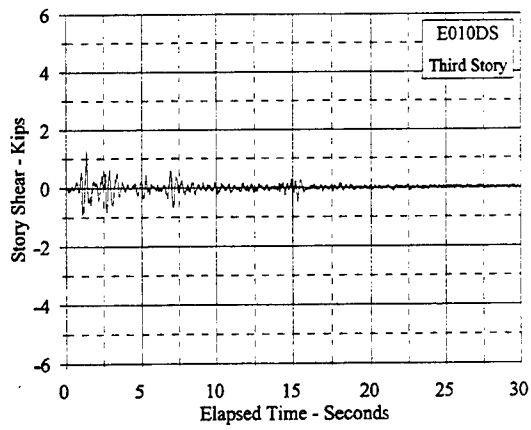


Figure C.4.10 Story Shear Vs. Elapsed Time: E010DS, E025DS

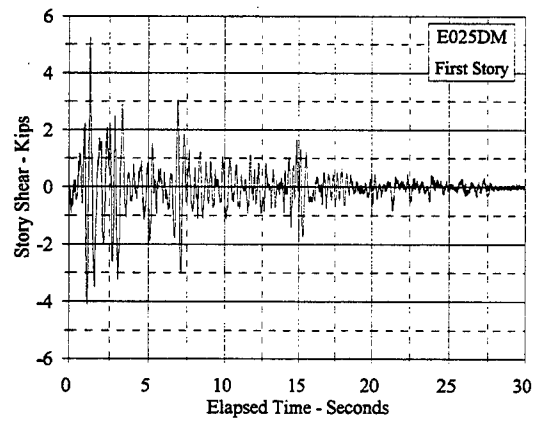
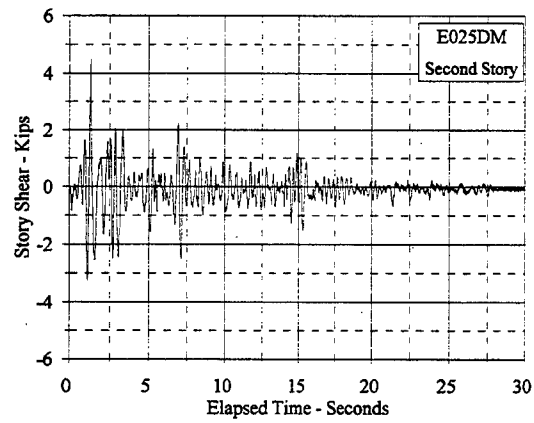
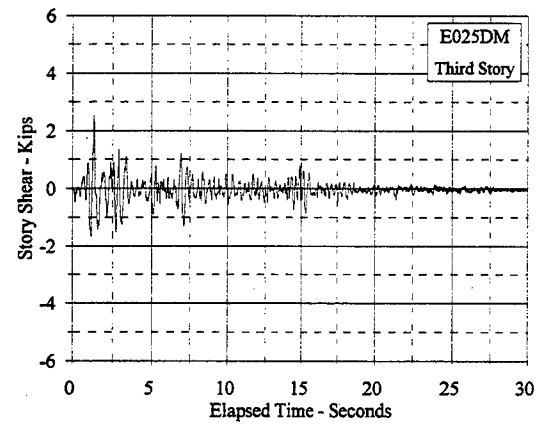


Figure C.4.11 Story Shear Vs. Elapsed Time: E025DM

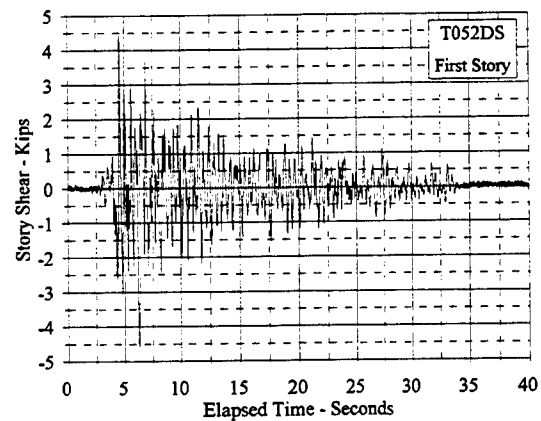
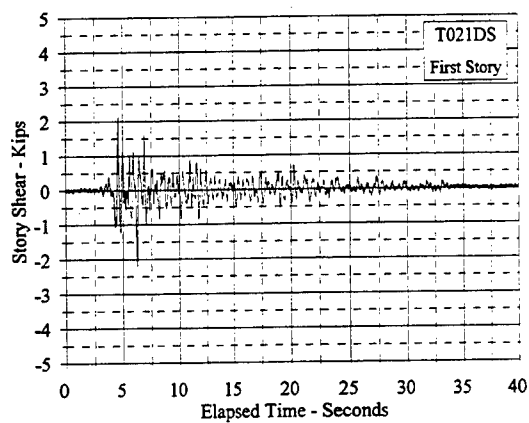
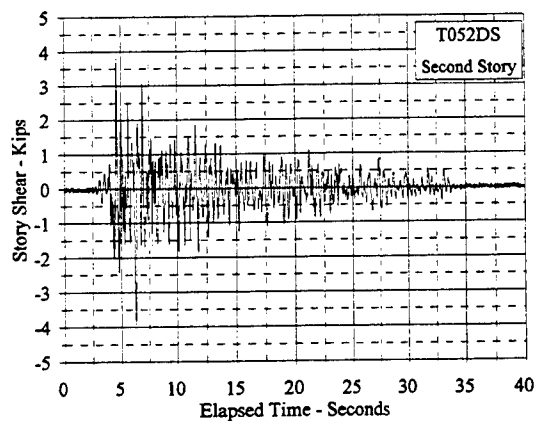
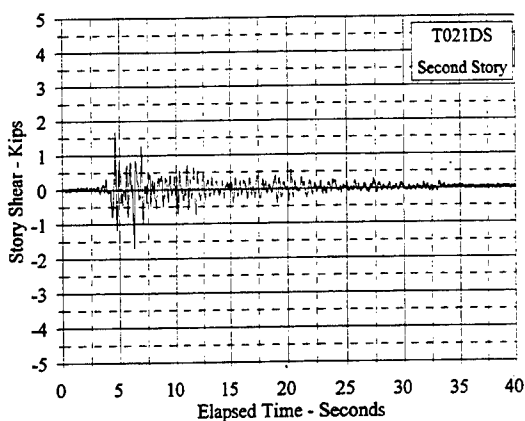
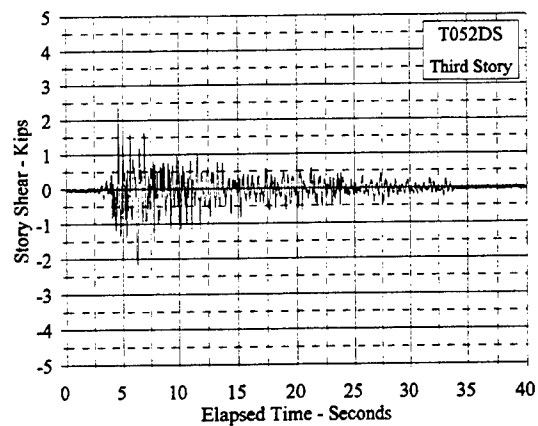
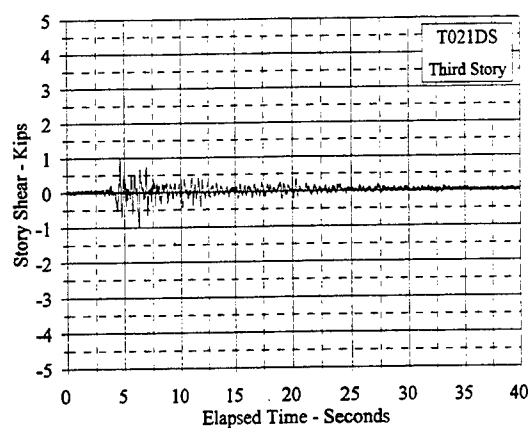


Figure C.4.12 Story Shear Vs. Elapsed Time: T021DS, T052DS

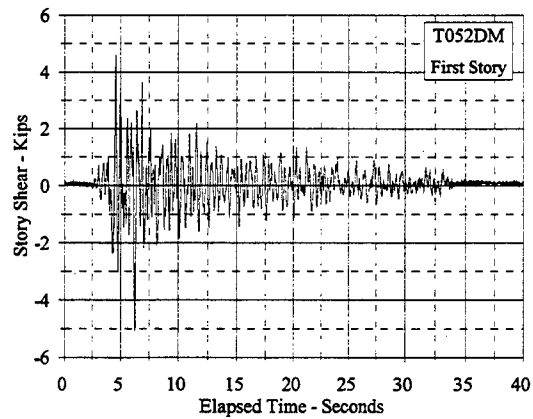
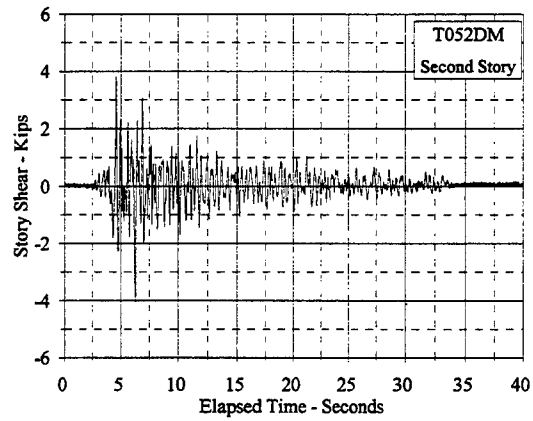
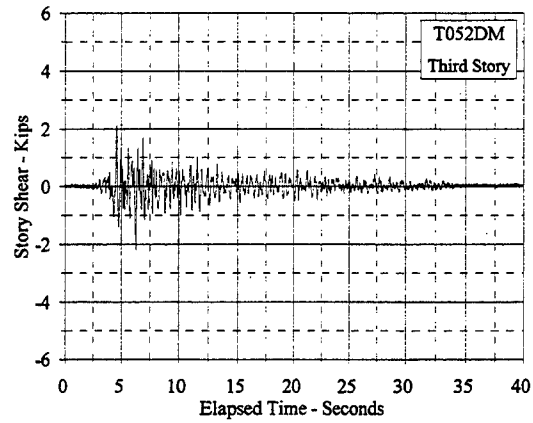


Figure C.4.13 Story Shear Vs. Elapsed Time: T052DM

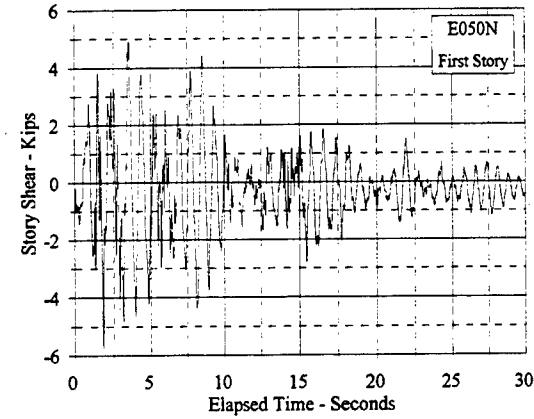
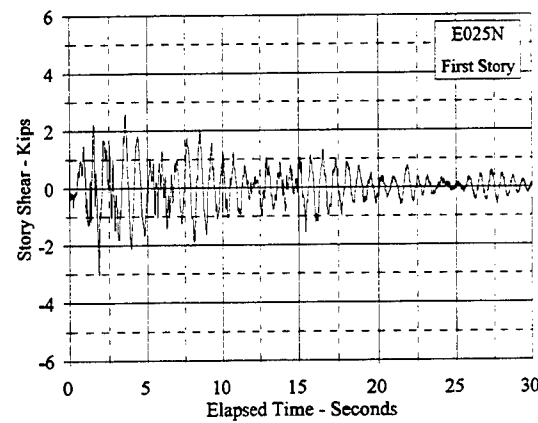
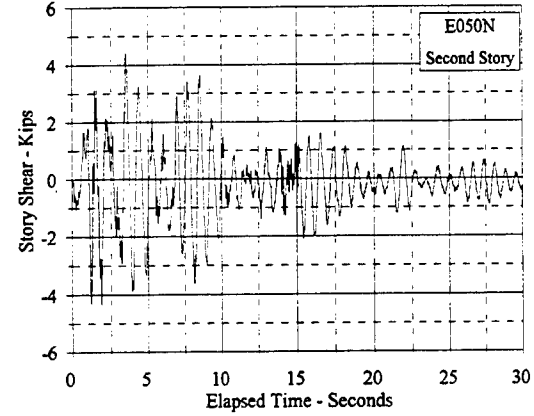
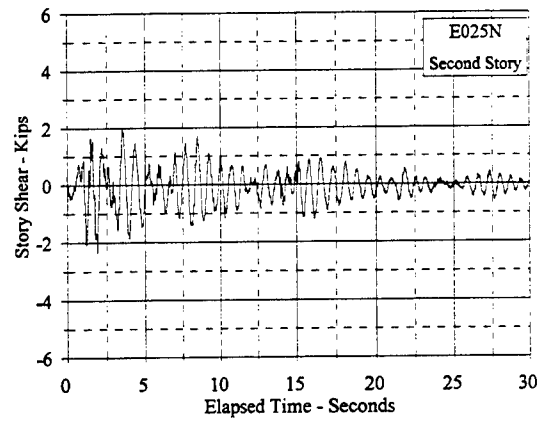
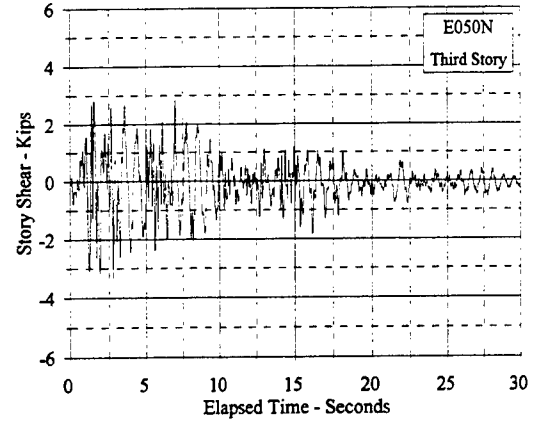
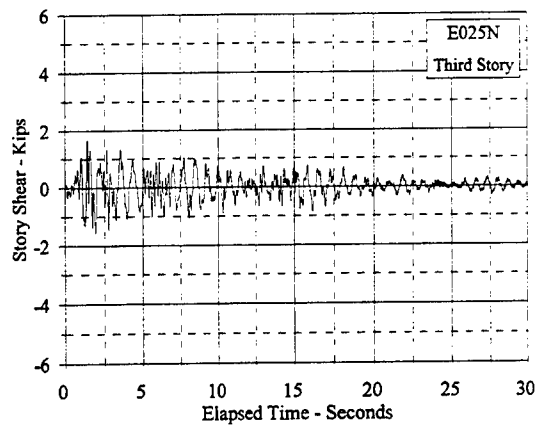


Figure C.4.14 Story Shear Vs. Elapsed Time: E025N, E050N

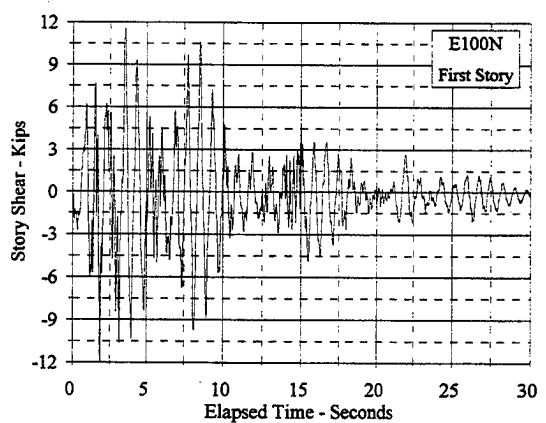
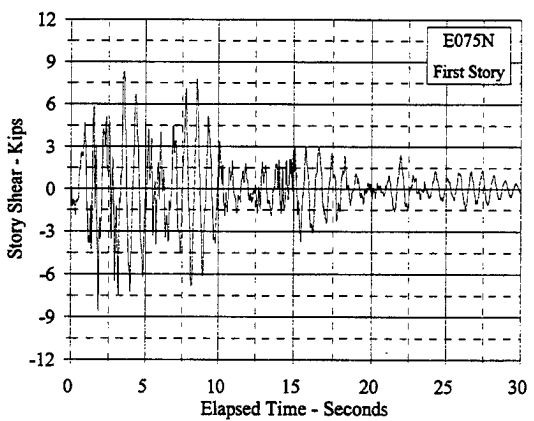
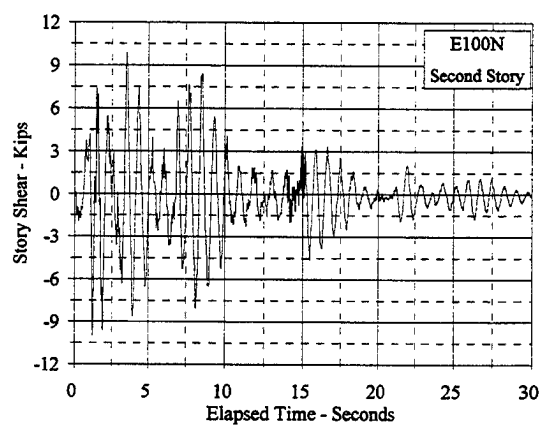
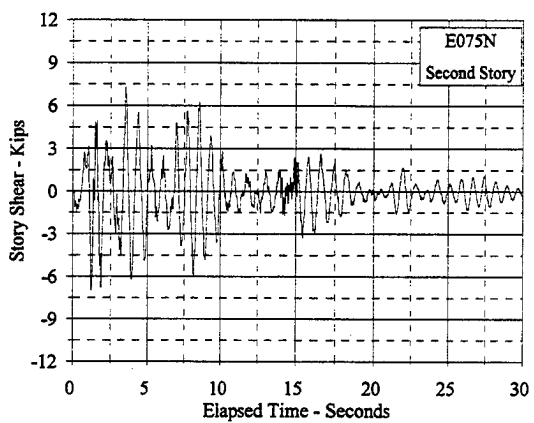
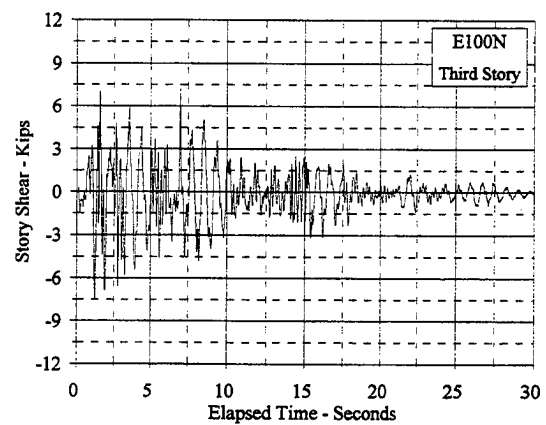
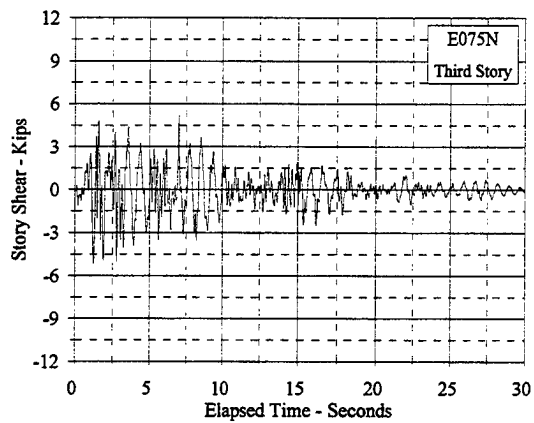


Figure C.4.15 Story Shear Vs. Elapsed Time: E075N, E100N

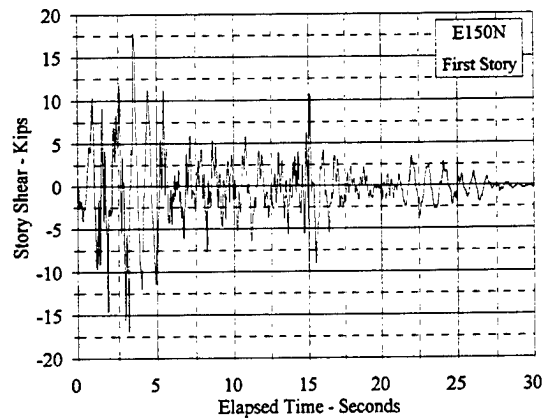
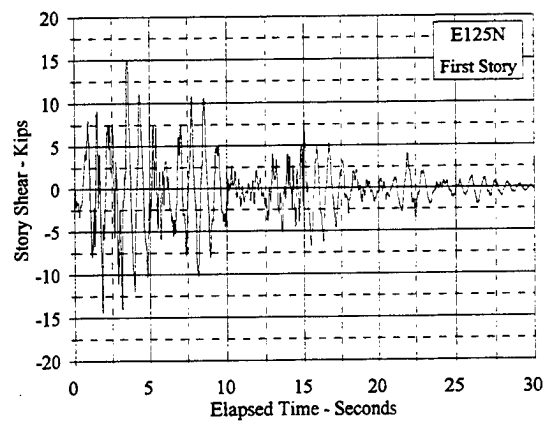
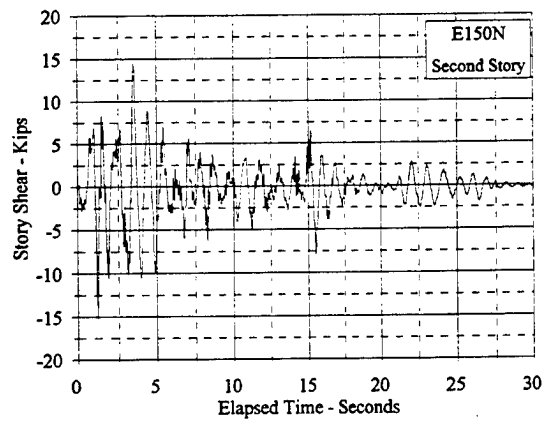
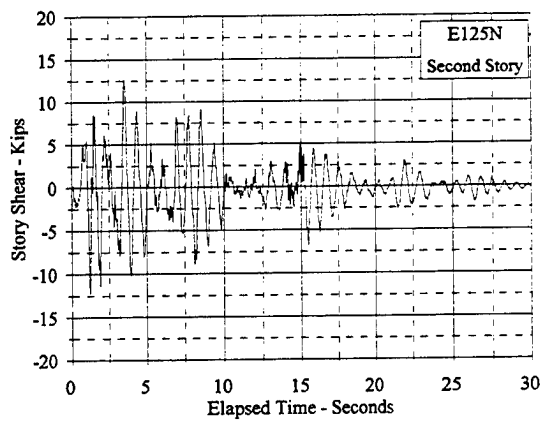
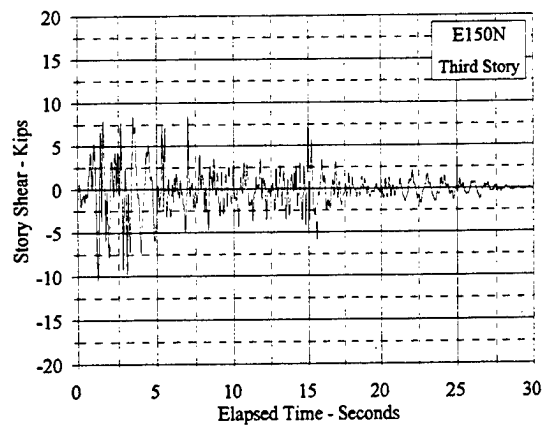
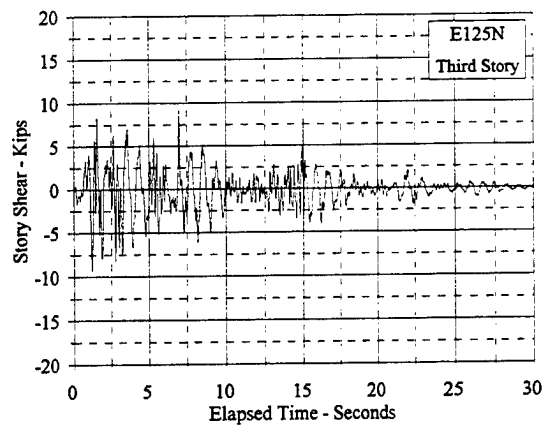


Figure C.4.16 Story Shear Vs. Elapsed Time: E125N, E150N

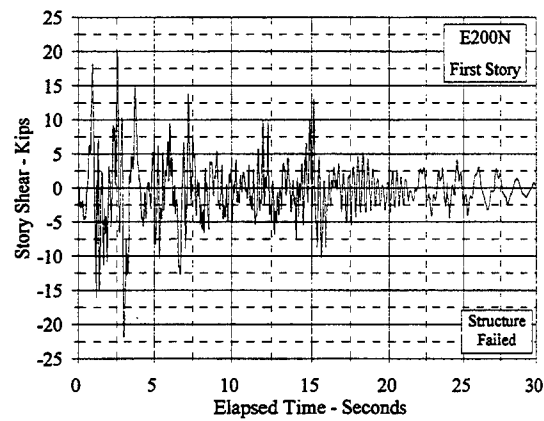
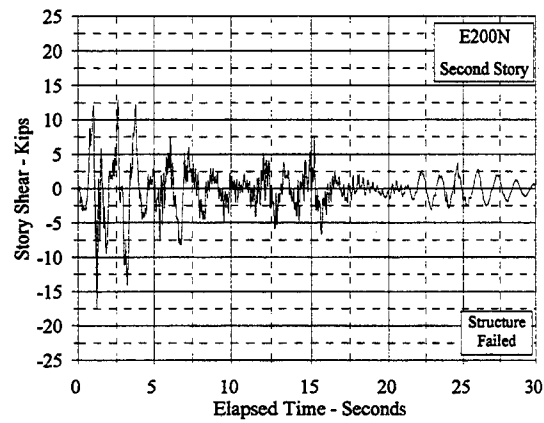
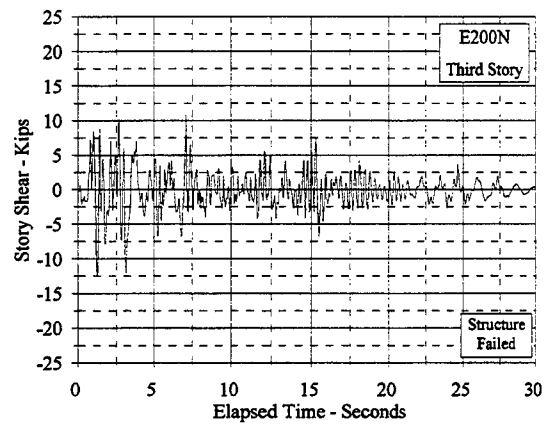


Figure C.4.17 Story Shear Vs. Elapsed Time: E200N

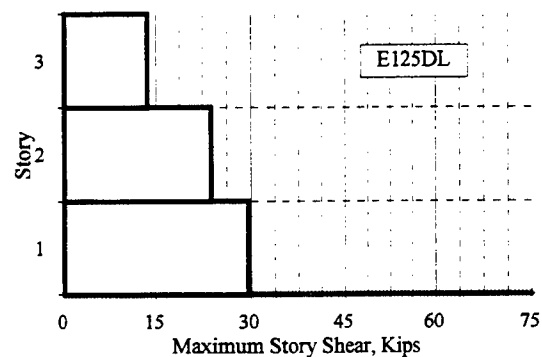
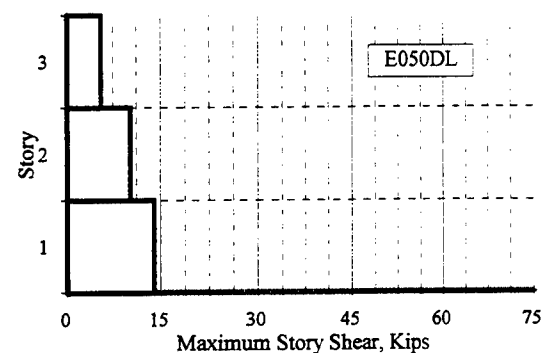
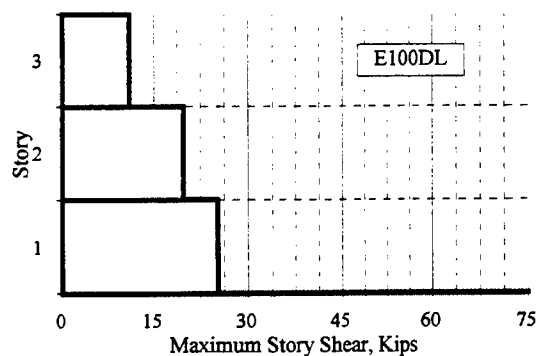
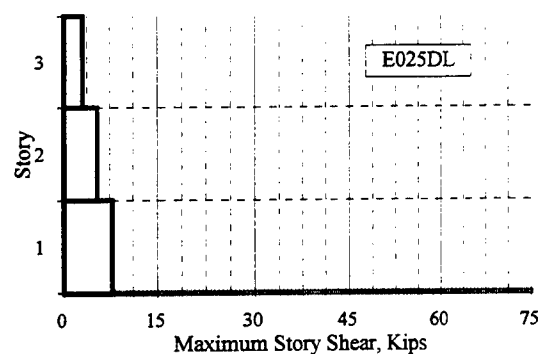
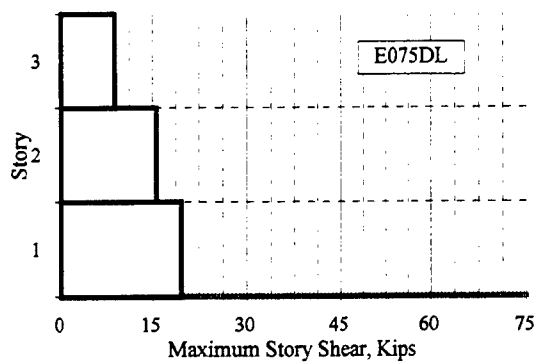
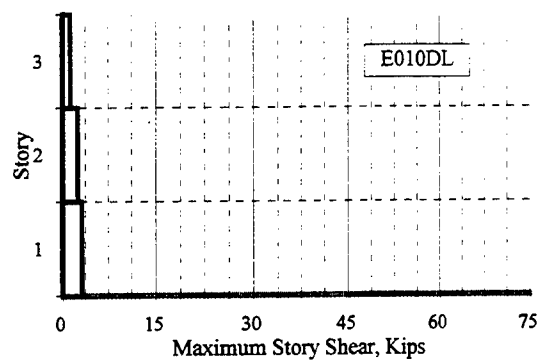


Figure C.4.18 Maximum Measured Story Shears: E010DL - E125DL

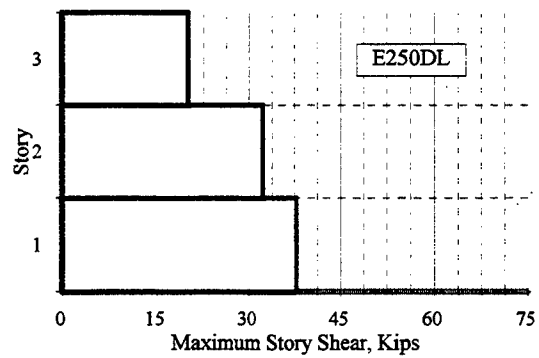
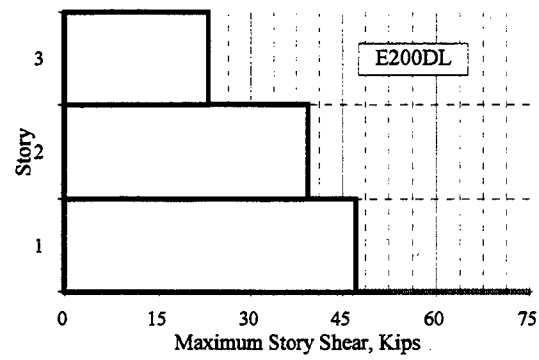
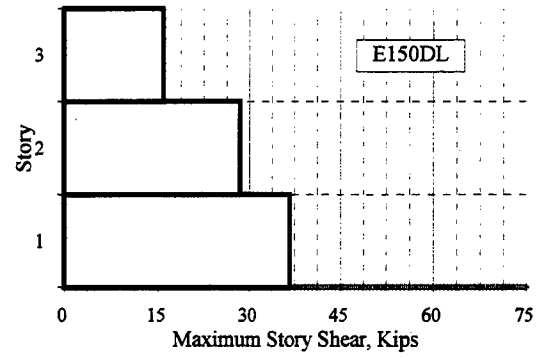


Figure C.4.19 Maximum Measured Story Shears: E150DL - E250DL

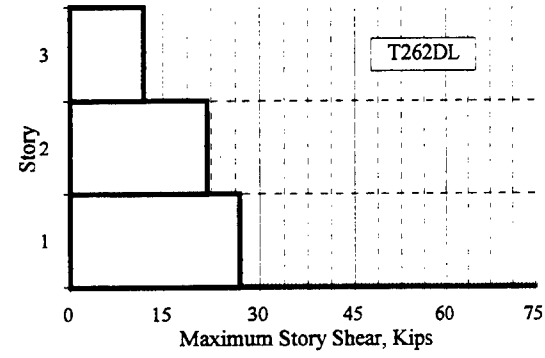
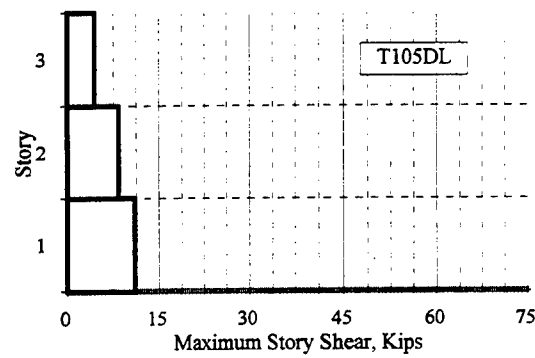
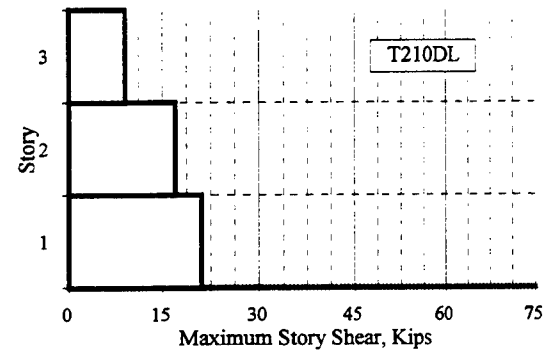
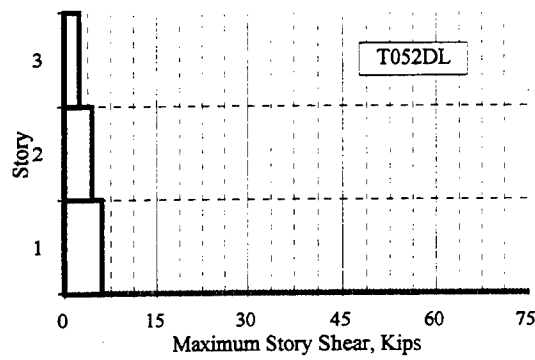
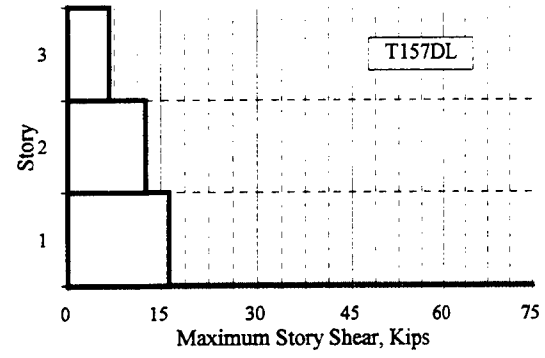
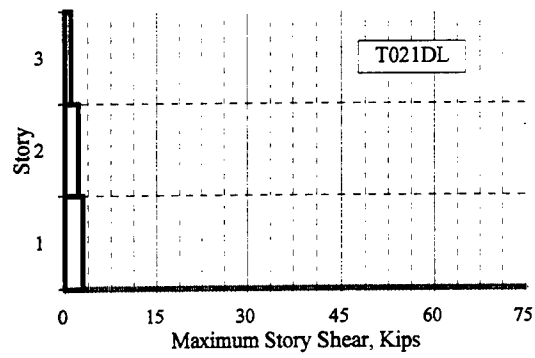


Figure C.4.20 Maximum Measured Story Shears: T021DL - T262DL

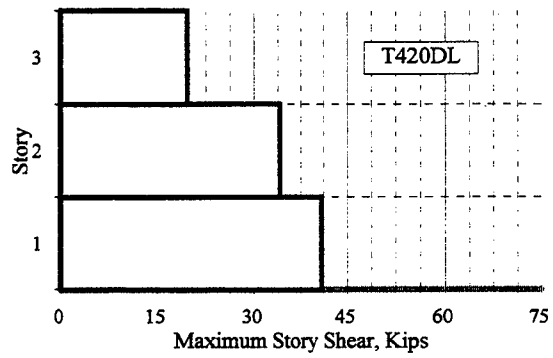
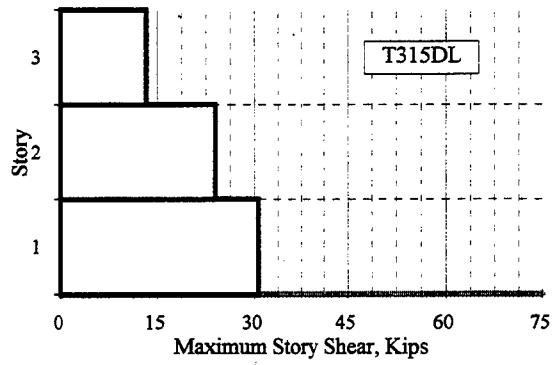


Figure C.4.21 Maximum Measured Story Shears: T315DL - T420DL

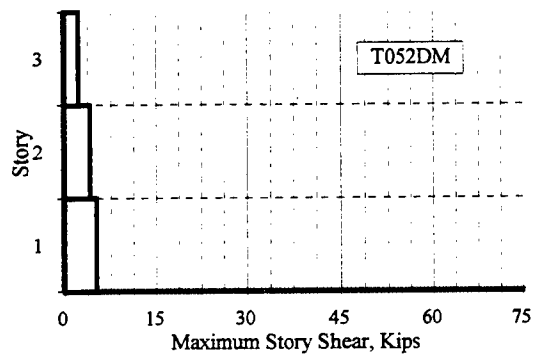
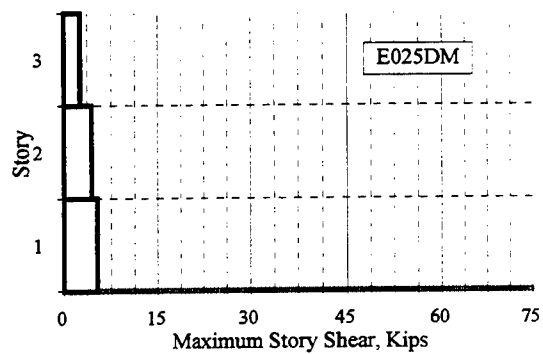
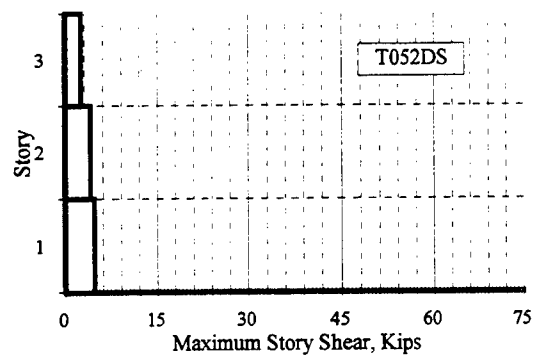
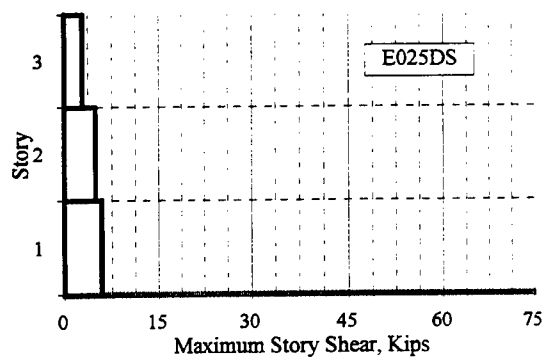
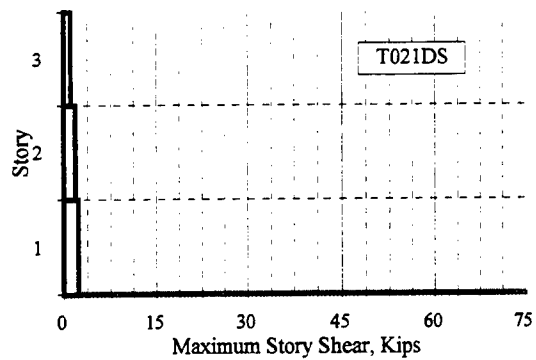
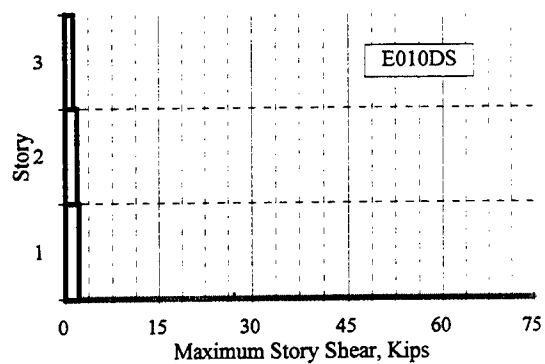


Figure C.4.22 Maximum Measured Story Shears: E010DS - T052DM

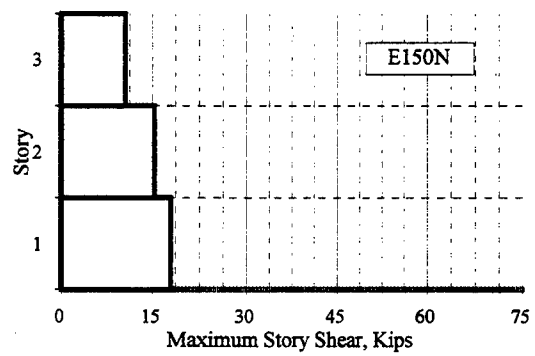
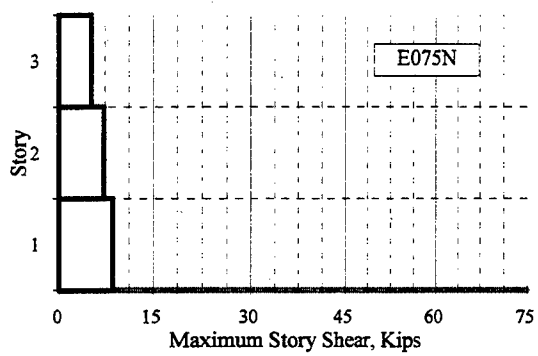
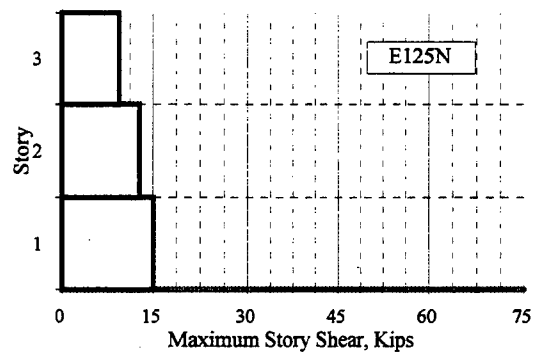
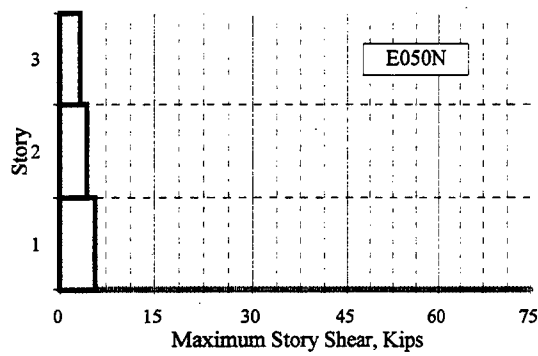
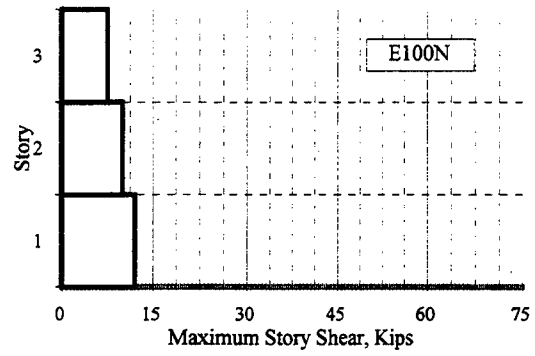
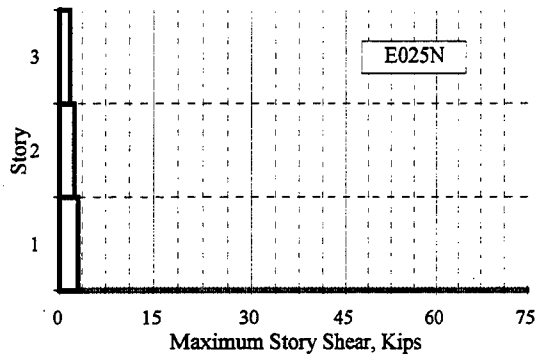


Figure C.4.23 Maximum Measured Story Shears: E025N - E150N

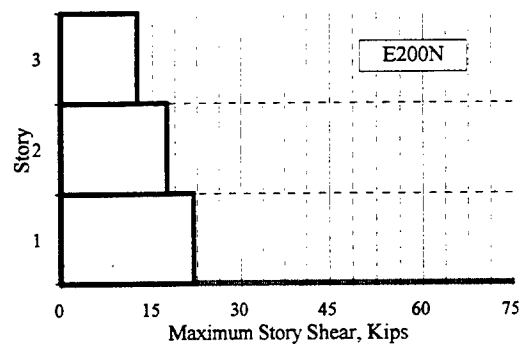


Figure C.4.24 Maximum Measured Story Shears: E200N

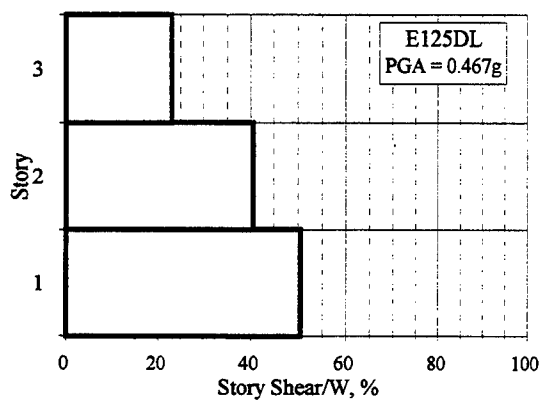
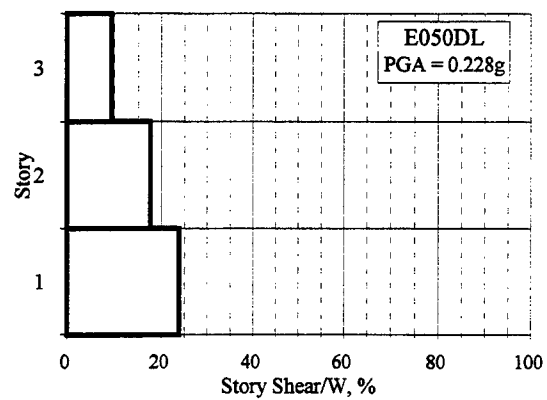
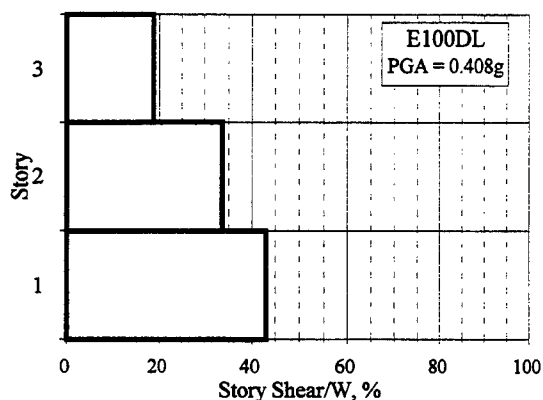
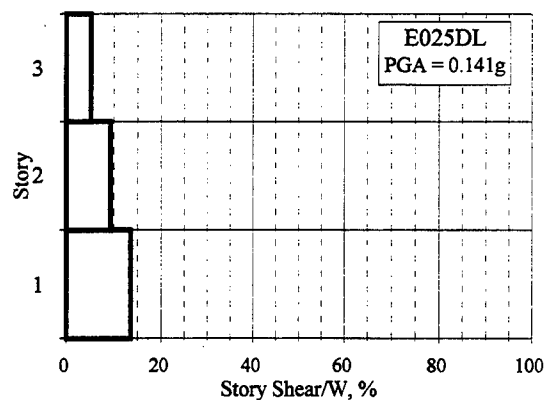
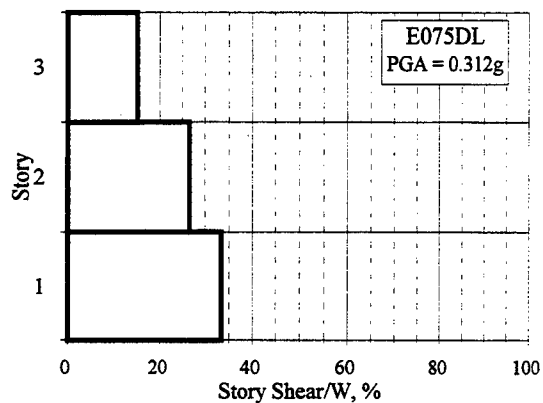
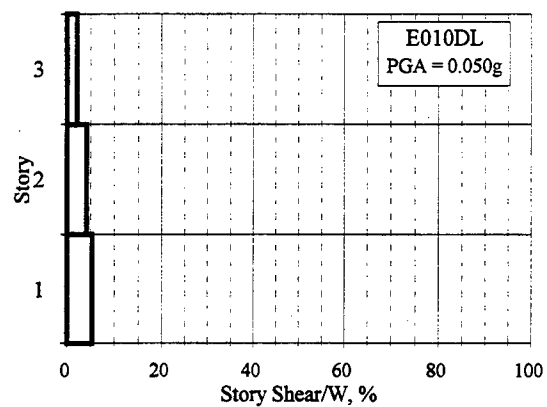


Figure C.4.25 Maximum Story Shear Normalized by Total Model Weight: E010DL - E125DL

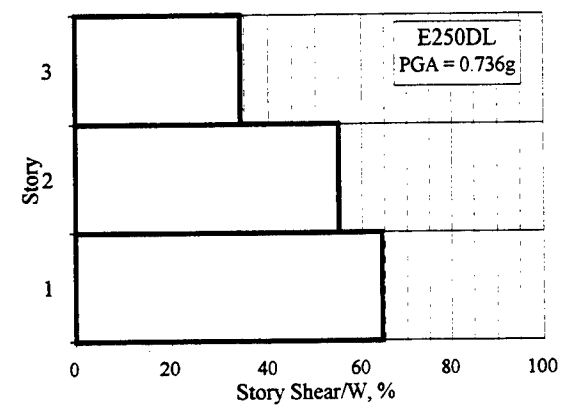
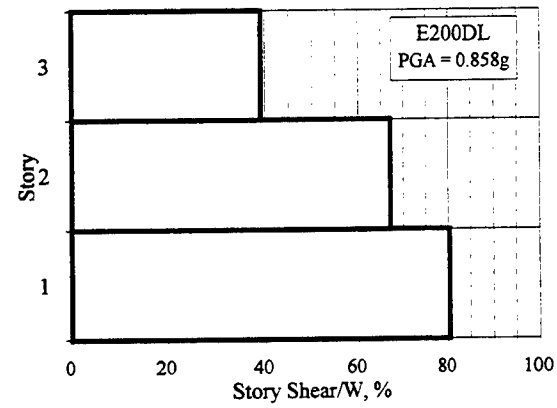
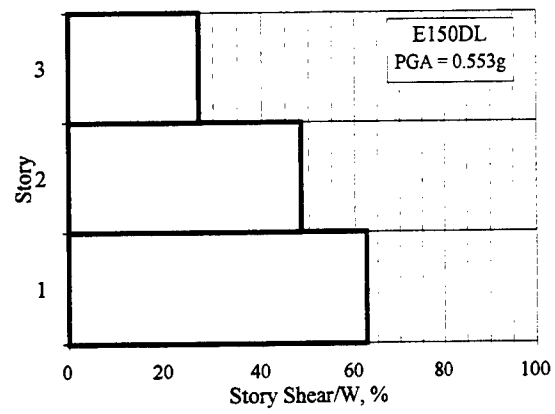


Figure C.4.26 Maximum Story Shear Normalized by Total Model Weight: E150DL - E250DL

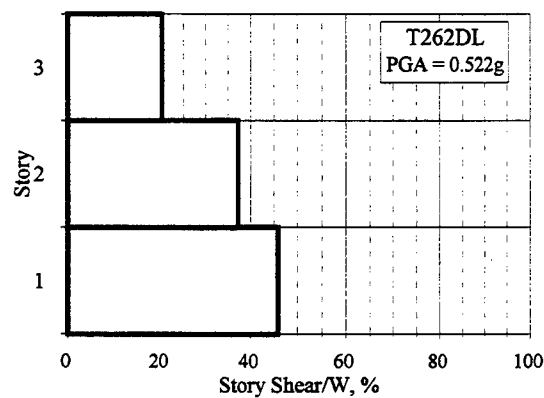
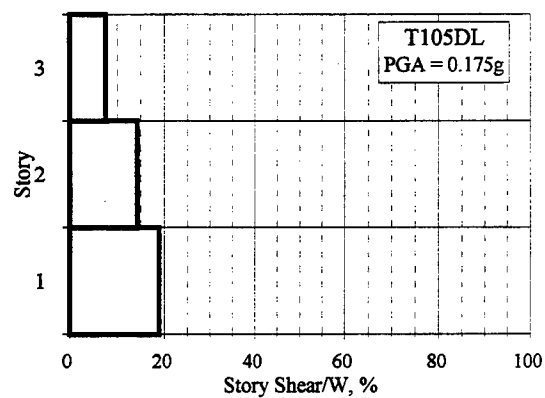
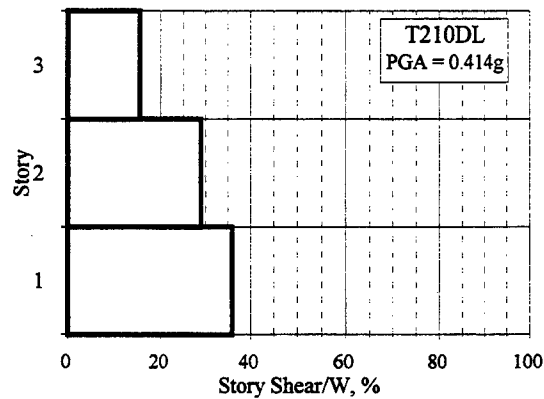
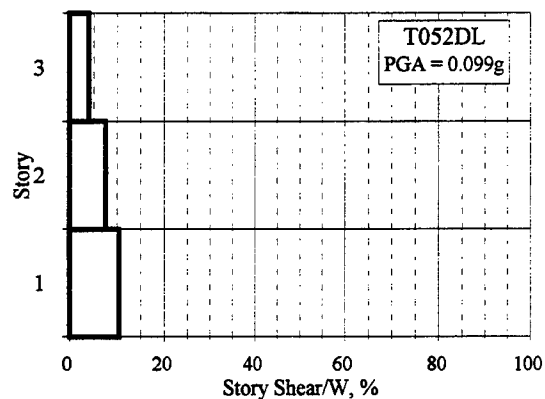
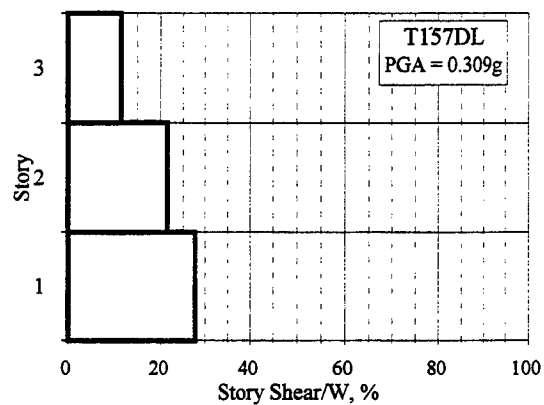
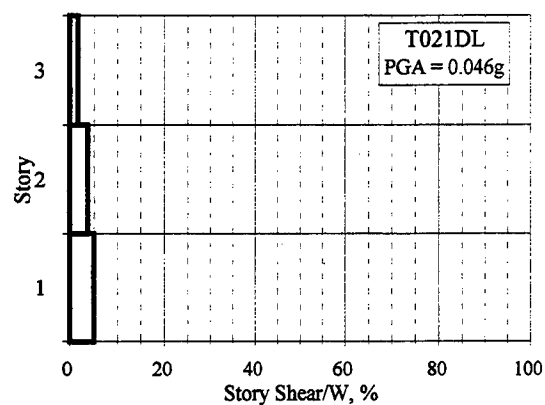


Figure C.4.27 Maximum Story Shear Normalized by Total Model Weight: T021DL - T262DL

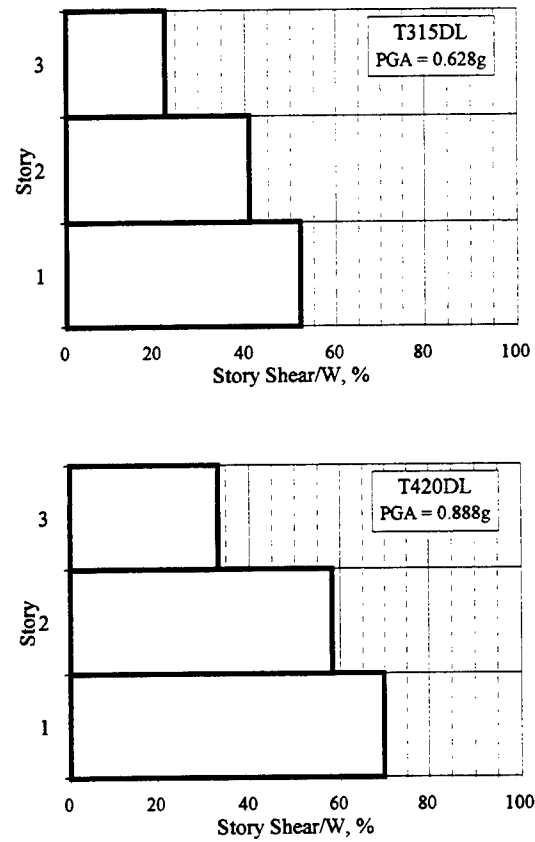


Figure C.4.28 Maximum Story Shear Normalized by Total Model Weight: T315DL - T420DL

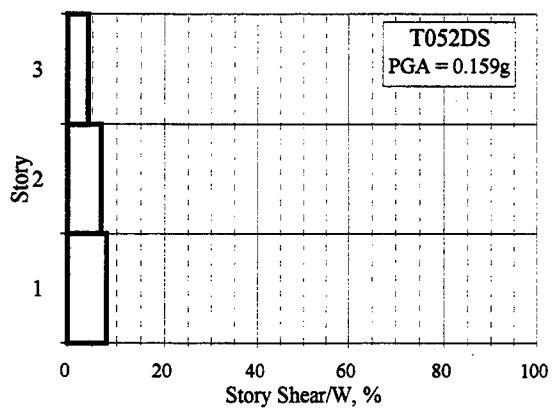
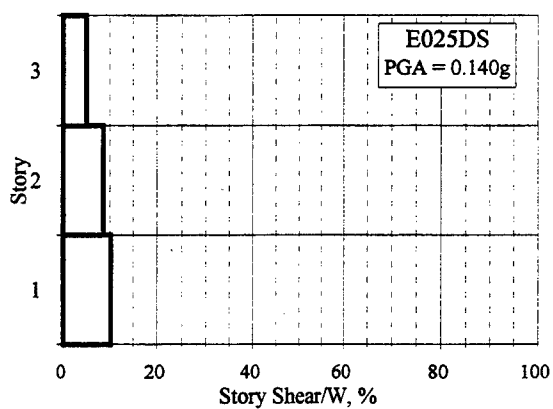
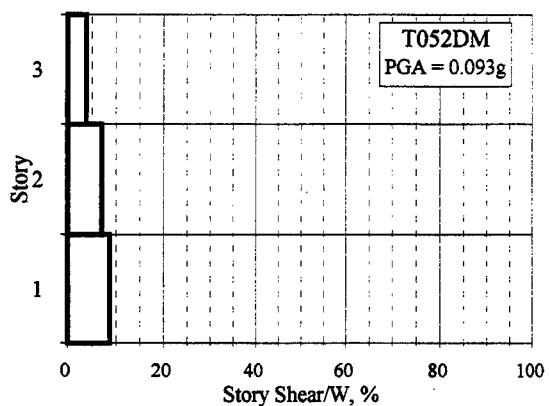
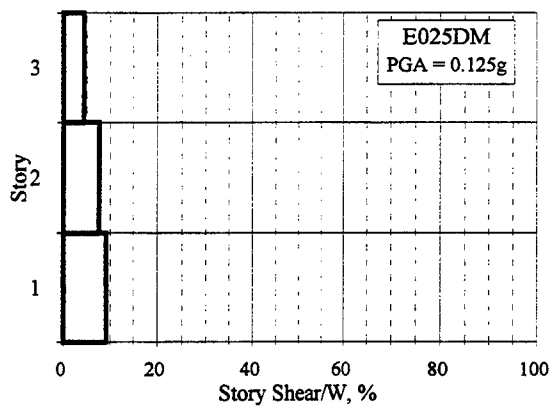
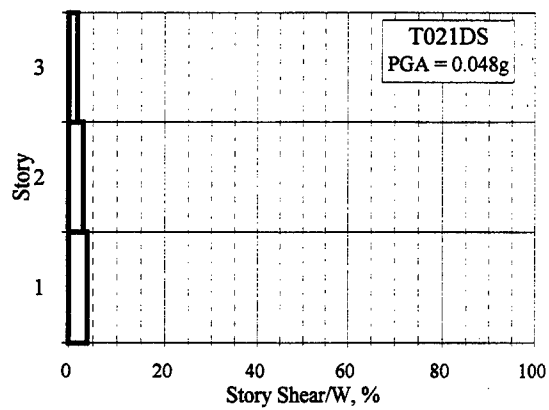
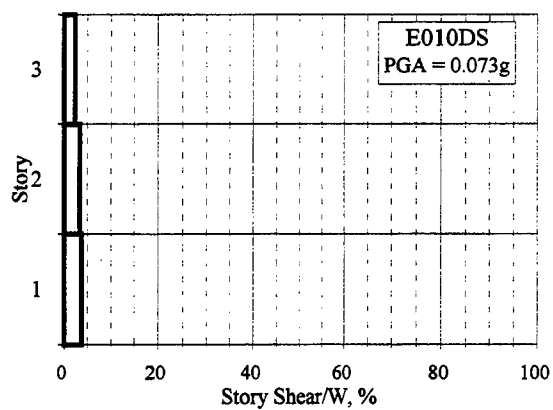


Figure C.4.29 Maximum Story Shear Normalized by Total Model Weight: E010DS - T052DS

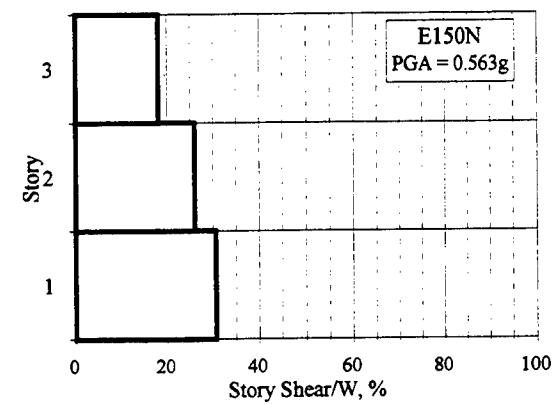
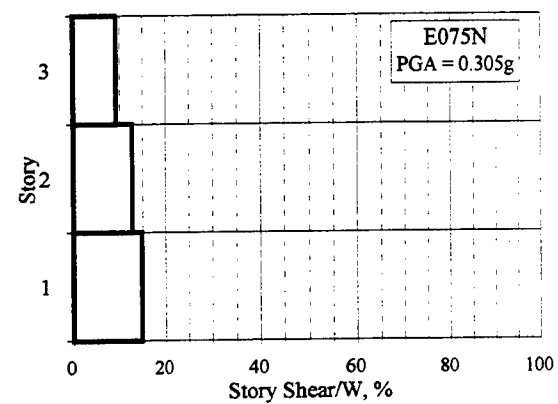
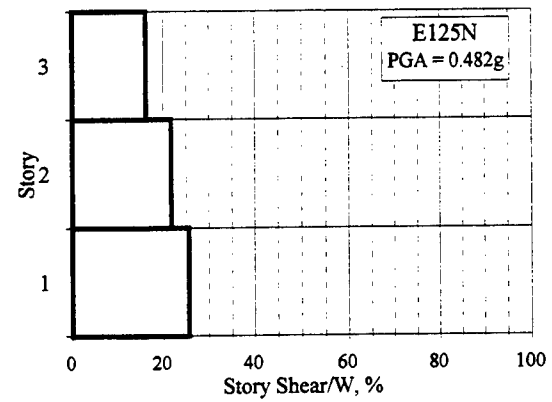
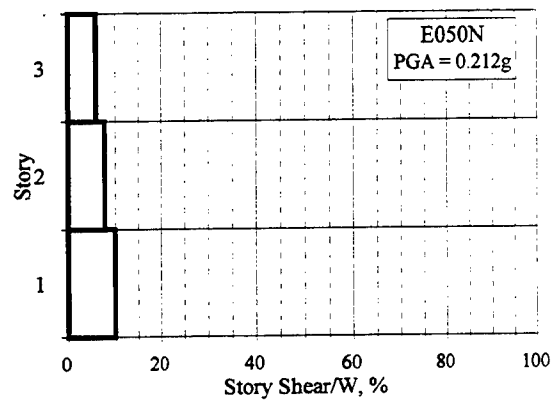
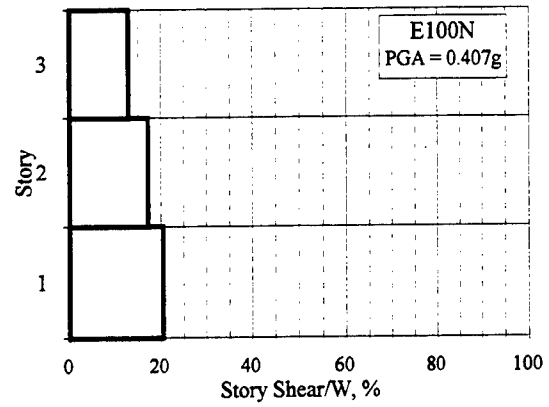
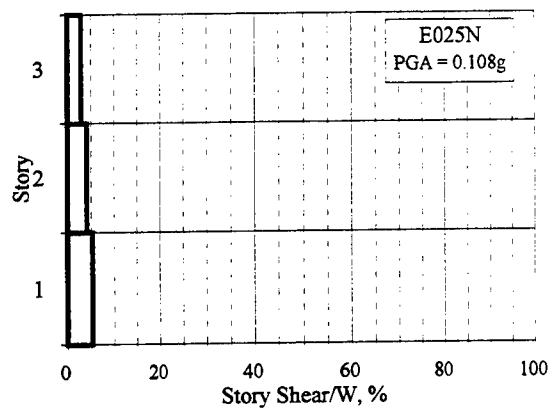


Figure C.4.30 Maximum Story Shear Normalized by Total Model Weight: E025N - E150N

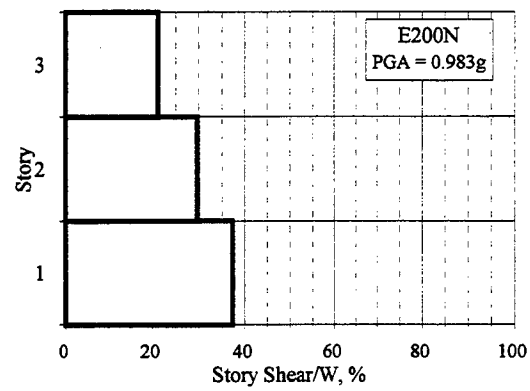


Figure C.4.31 Maximum Story Shear Normalized by Total Model Weight: E200N

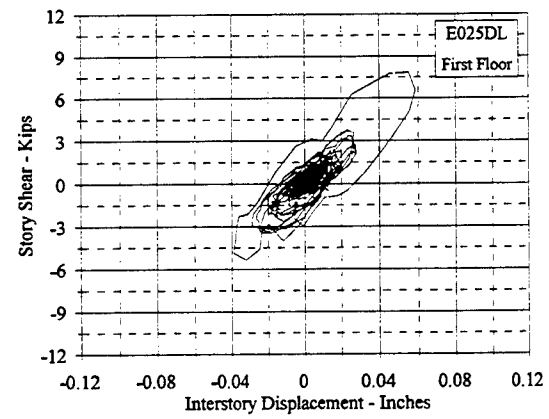
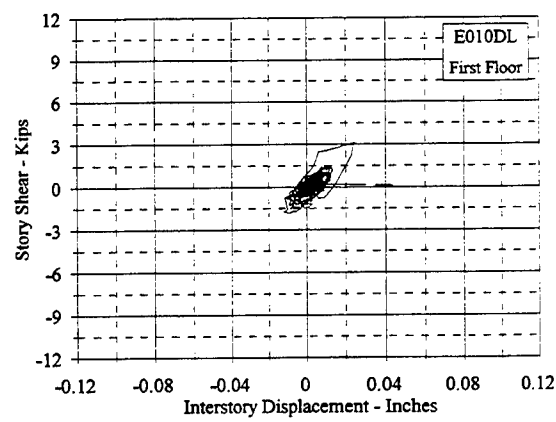
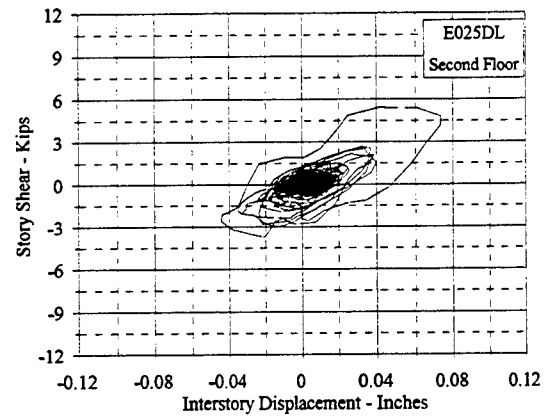
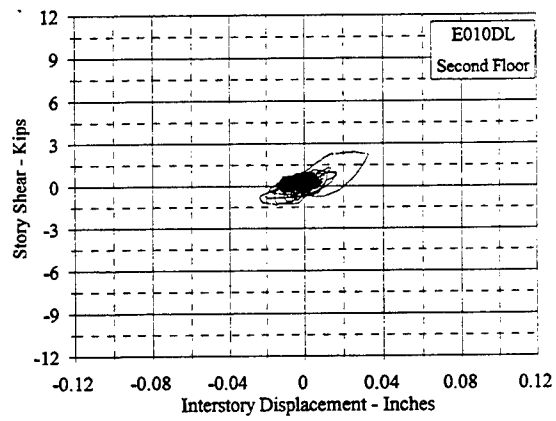
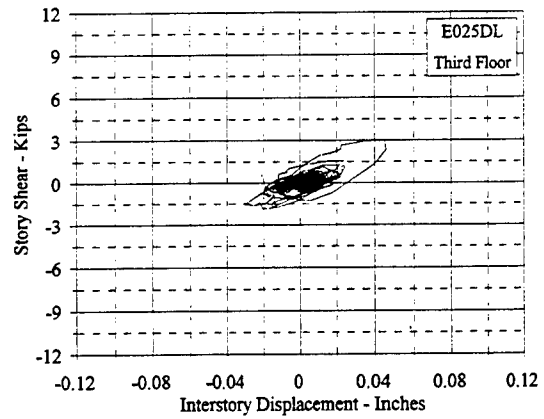
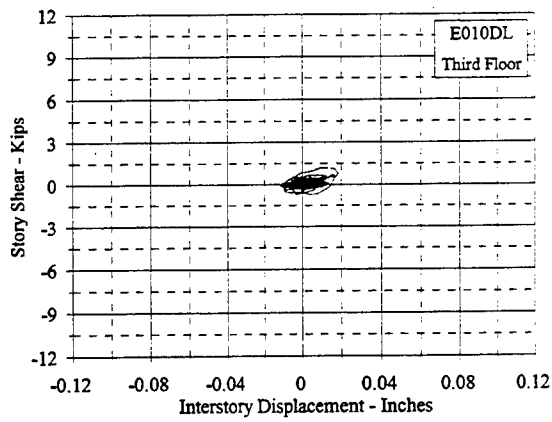


Figure C.5.1 Story Shear Vs. Interstory Displacement: E010DL, E025DL

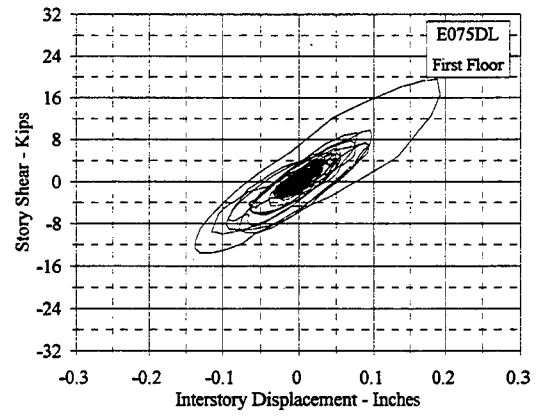
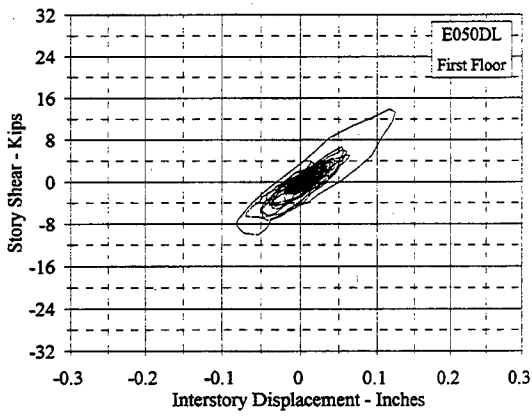
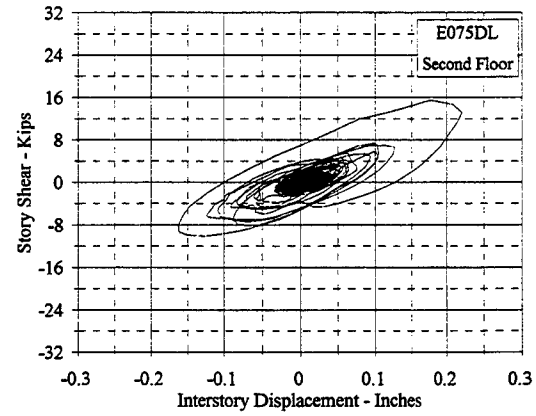
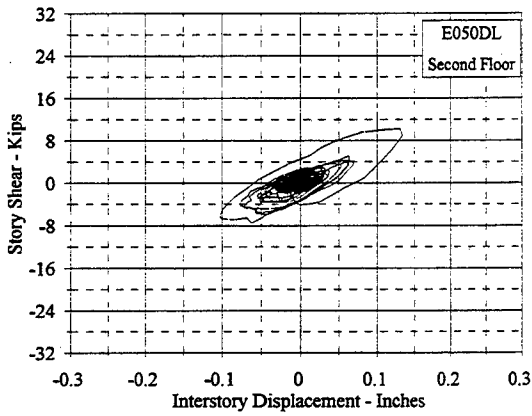
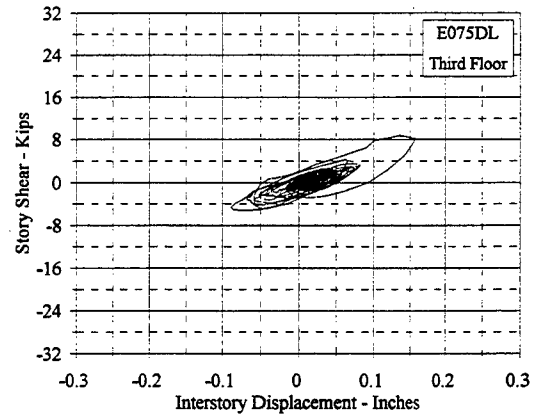
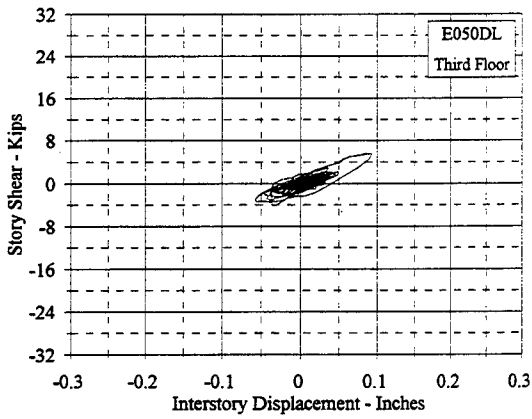


Figure C.5.2 Story Shear Vs. Interstory Displacement : E050DL, E075DL

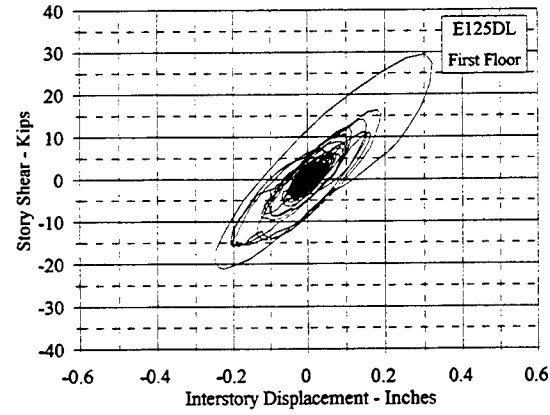
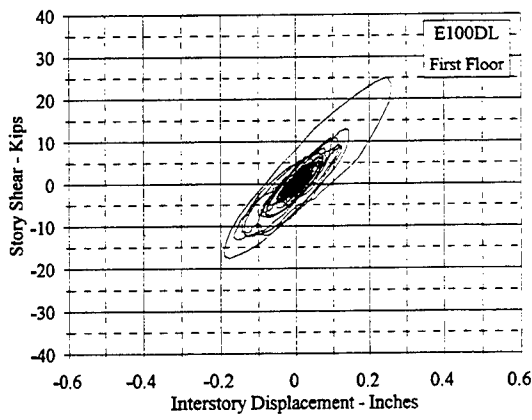
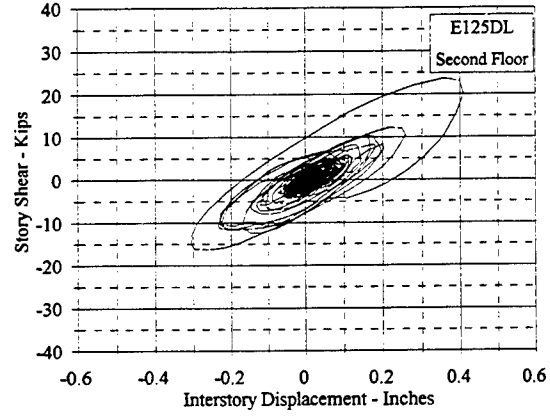
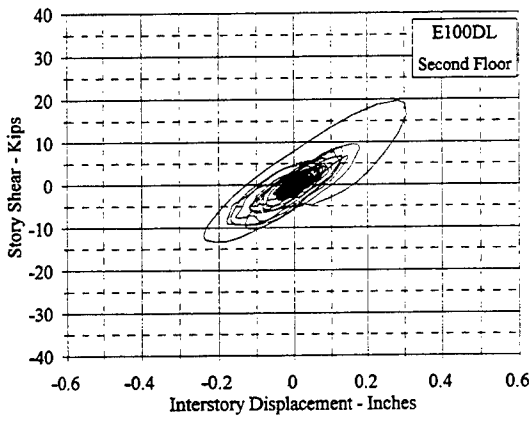
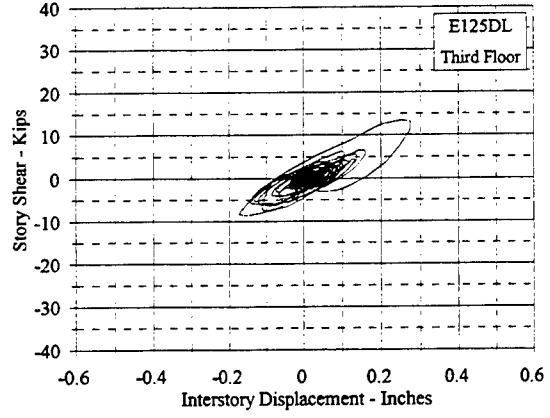
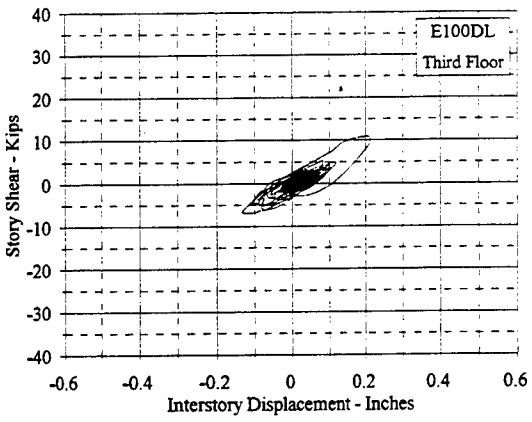


Figure C.5.3 Story Shear Vs. Interstory Displacement: E100DL, E125DL

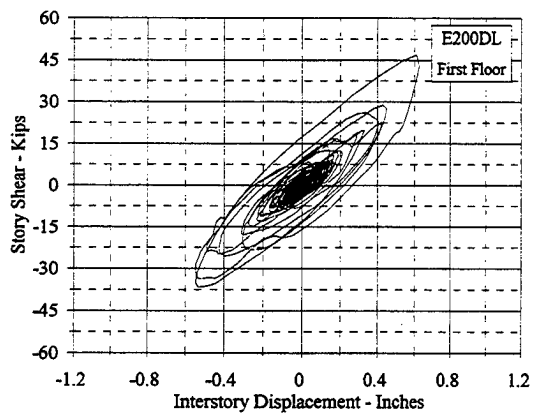
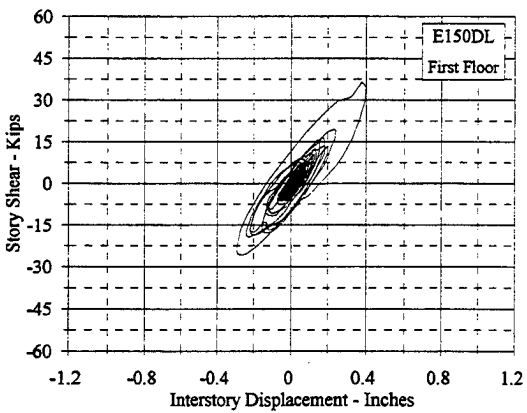
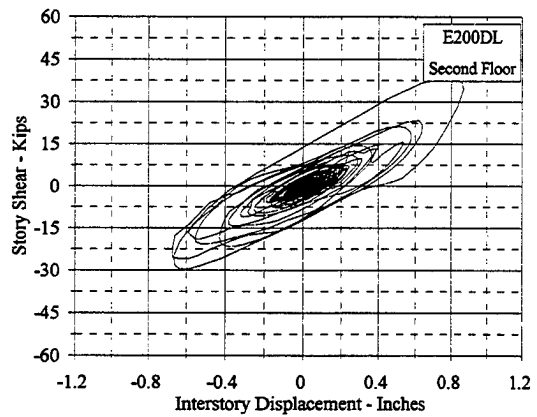
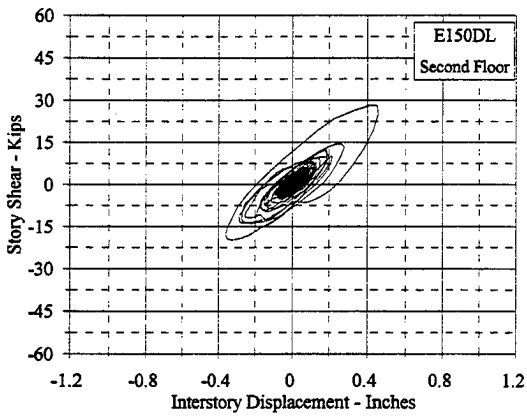
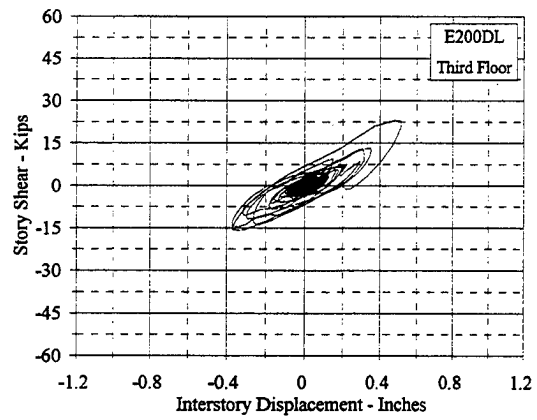
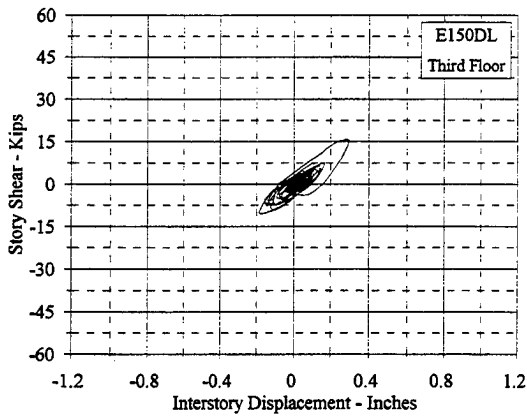


Figure C.5.4 Story Shear Vs. Interstory Displacement: E150DL, E200DL

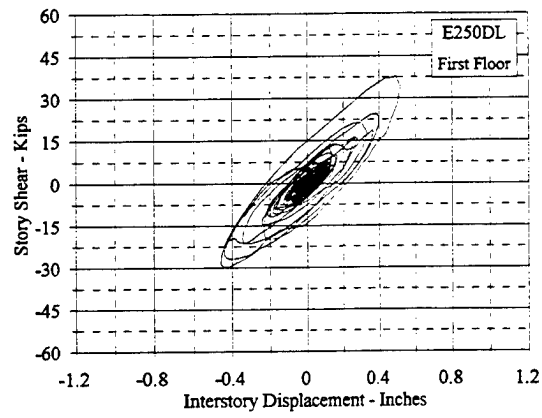
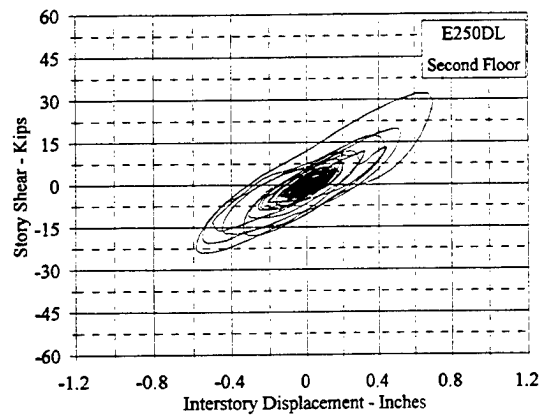
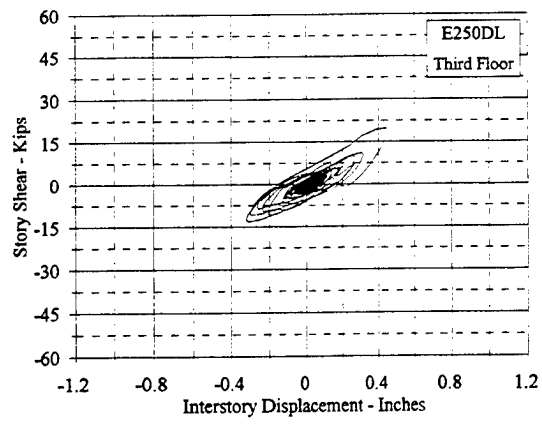


Figure C.5.5 Story Shear Vs. Interstory Displacement: E250DL

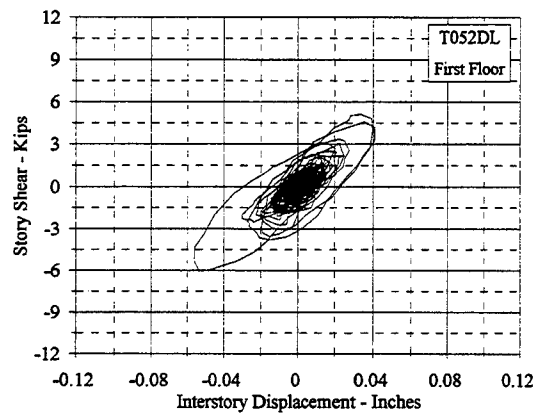
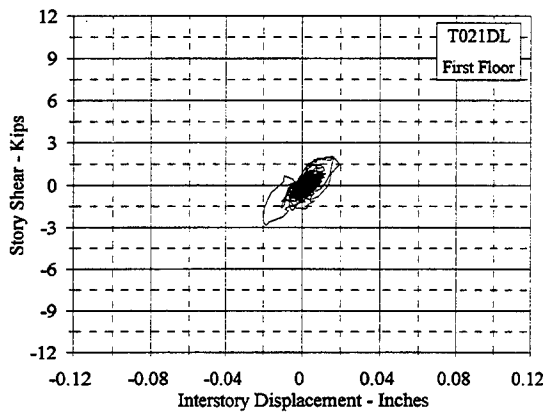
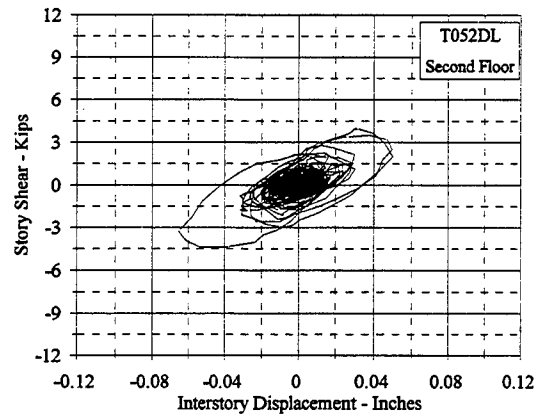
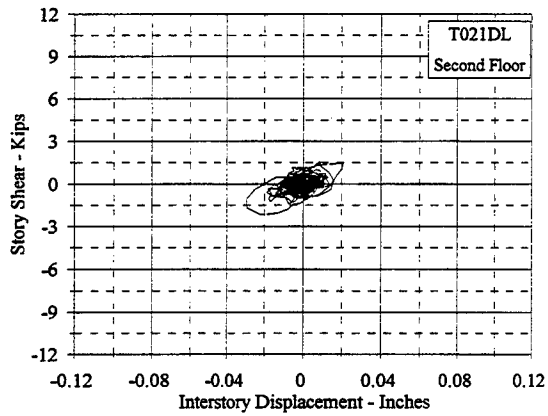
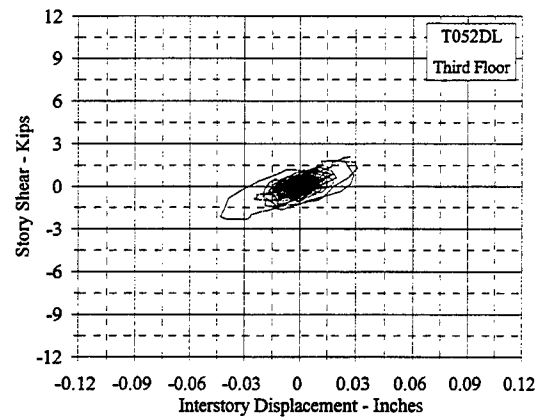
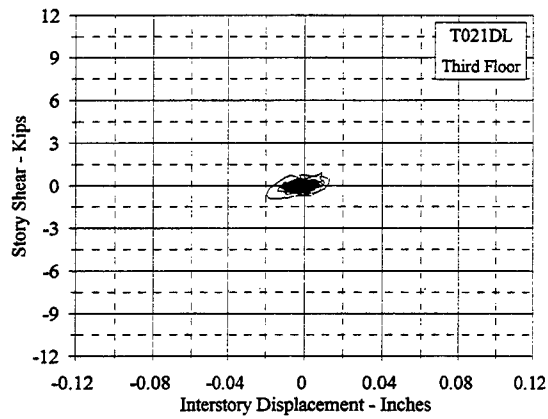


Figure C.5.6 Story Shear Vs. Interstory Displacement: T021DL, T052DL

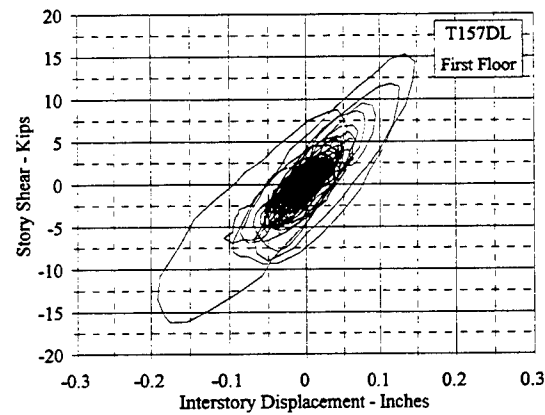
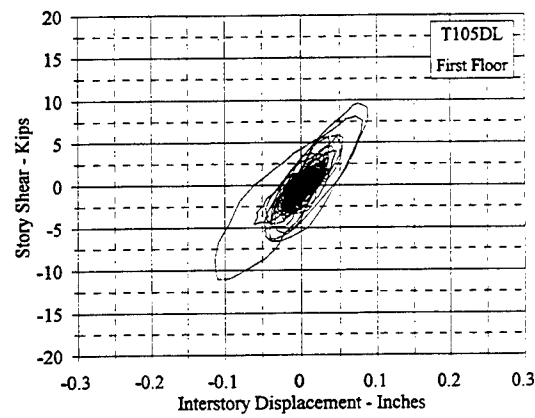
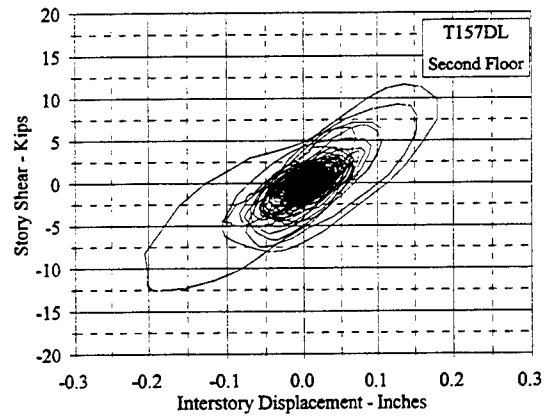
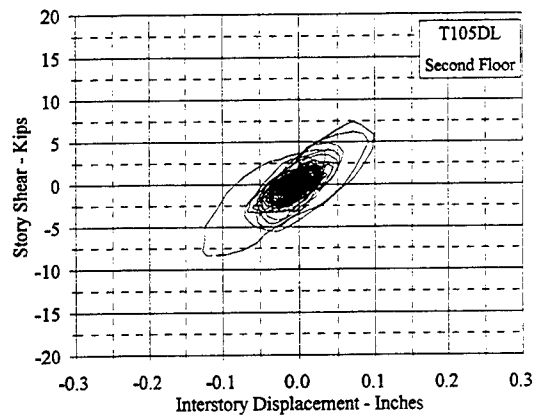
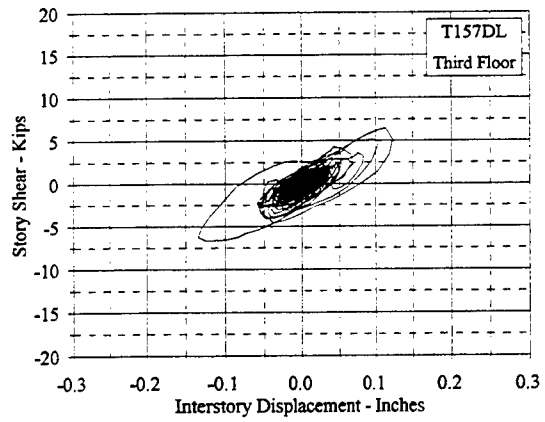
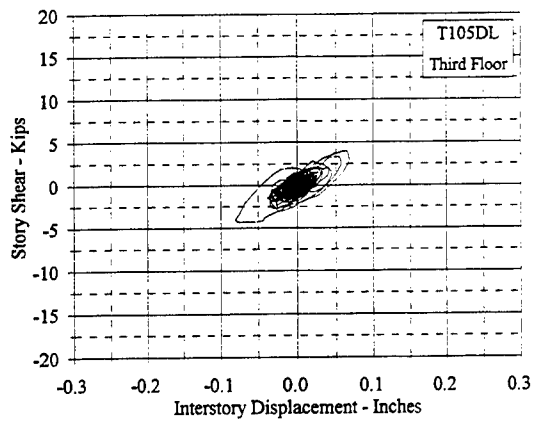


Figure C.5.7 Story Shear Vs. Interstory Displacement: T105DL, T157DL

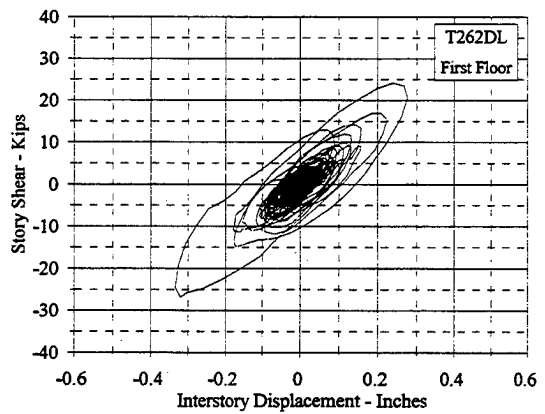
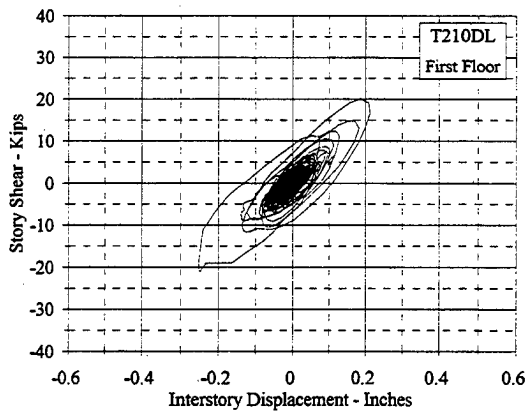
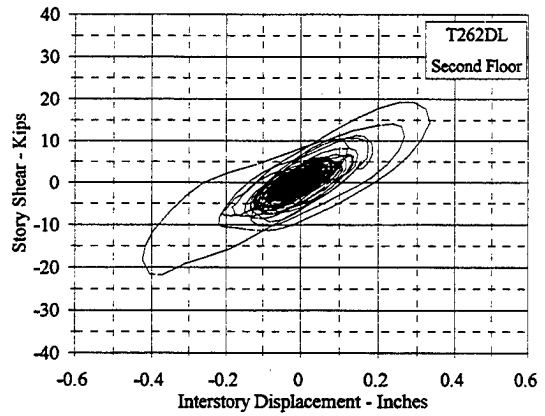
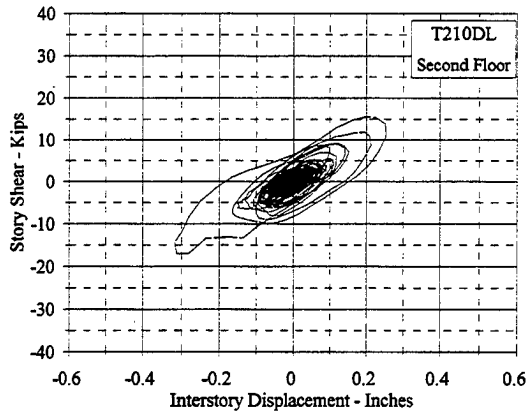
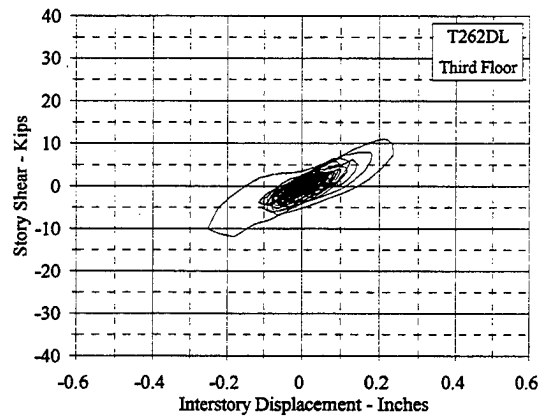
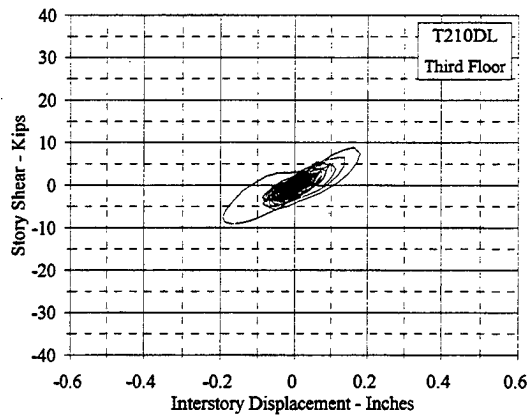


Figure C.5.8 Story Shear Vs. Interstory Displacement: T210DL, T262DL

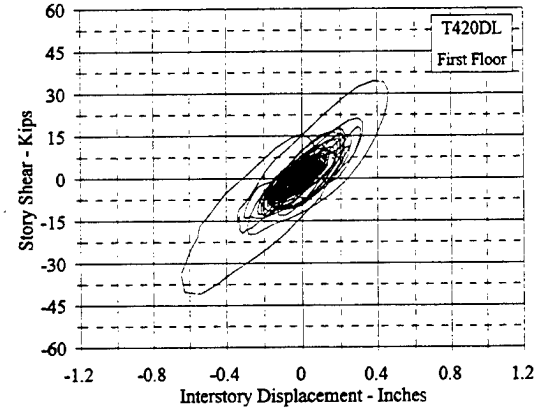
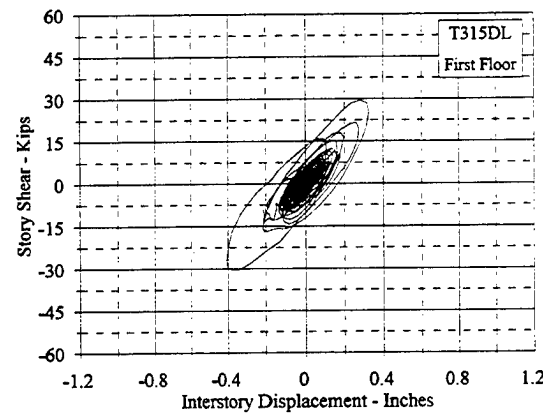
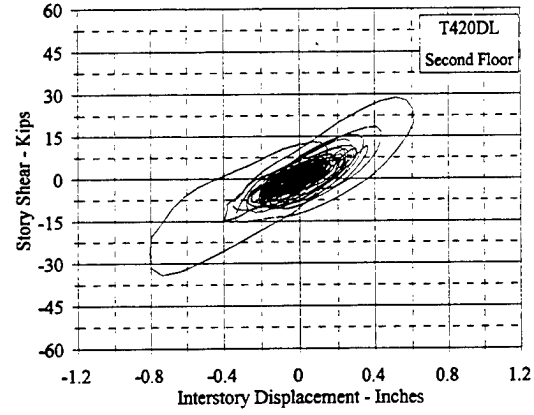
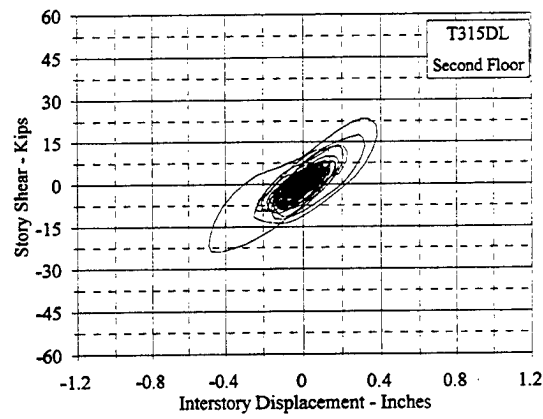
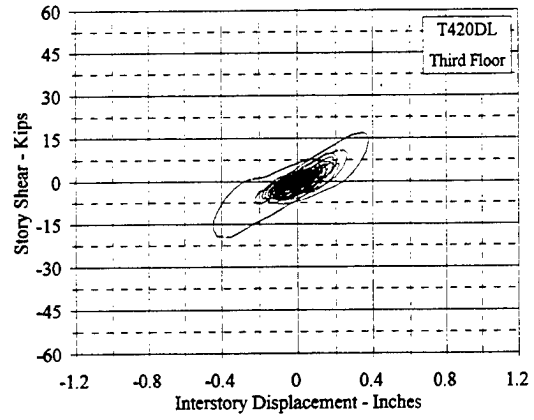
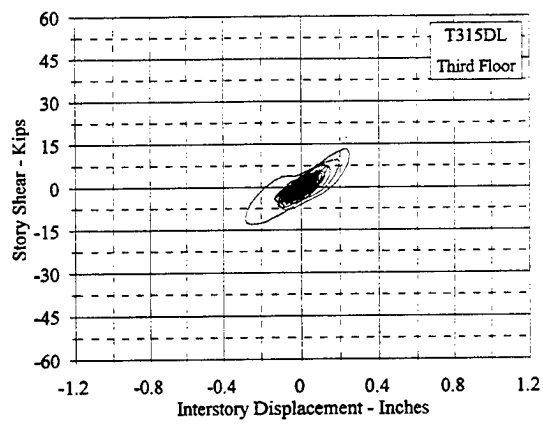


Figure C.5.9 Story Shear Vs. Interstory Displacement: T315DL, T420DL

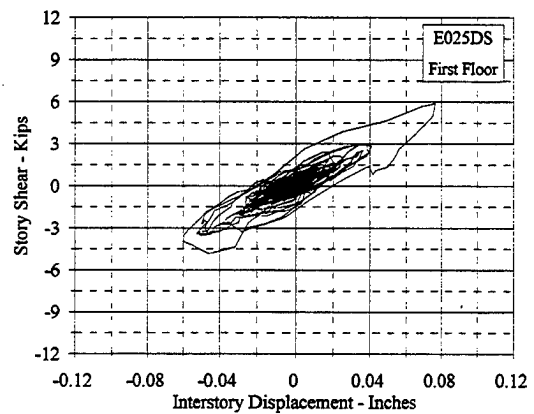
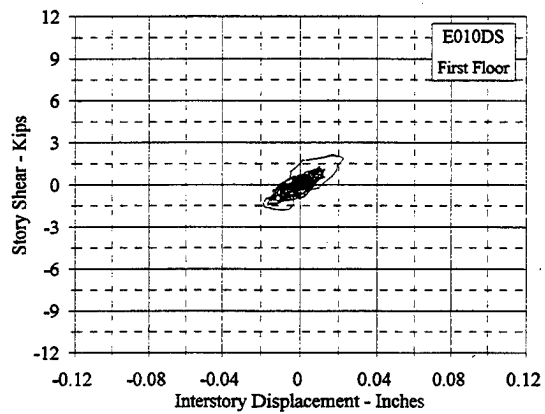
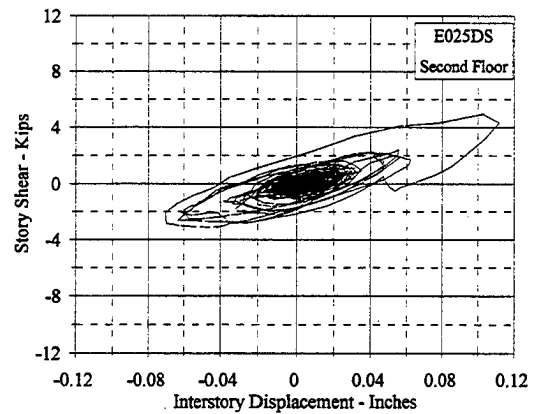
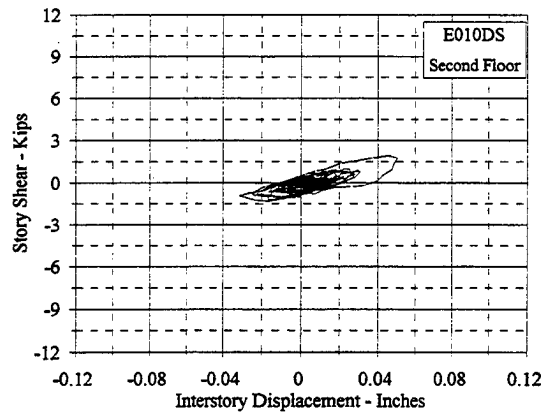
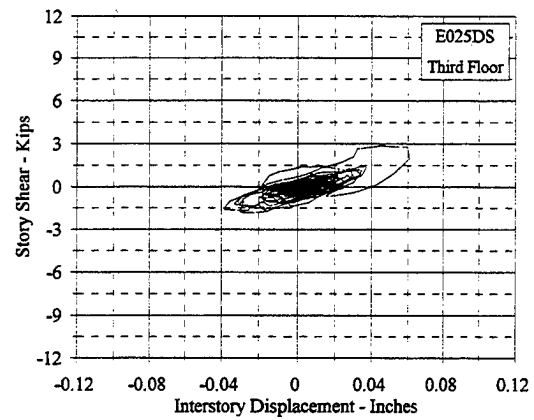
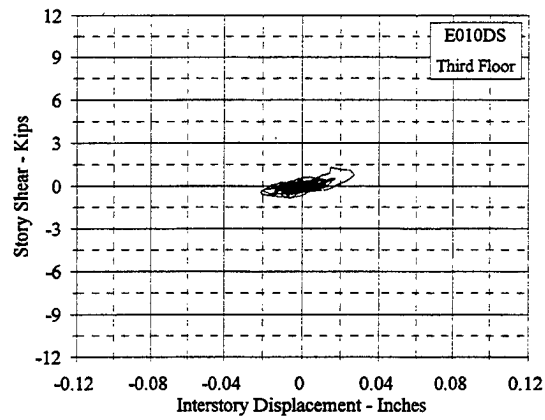


Figure C.5.10 Story Shear Vs. Interstory Displacement: E010DS, E025DS

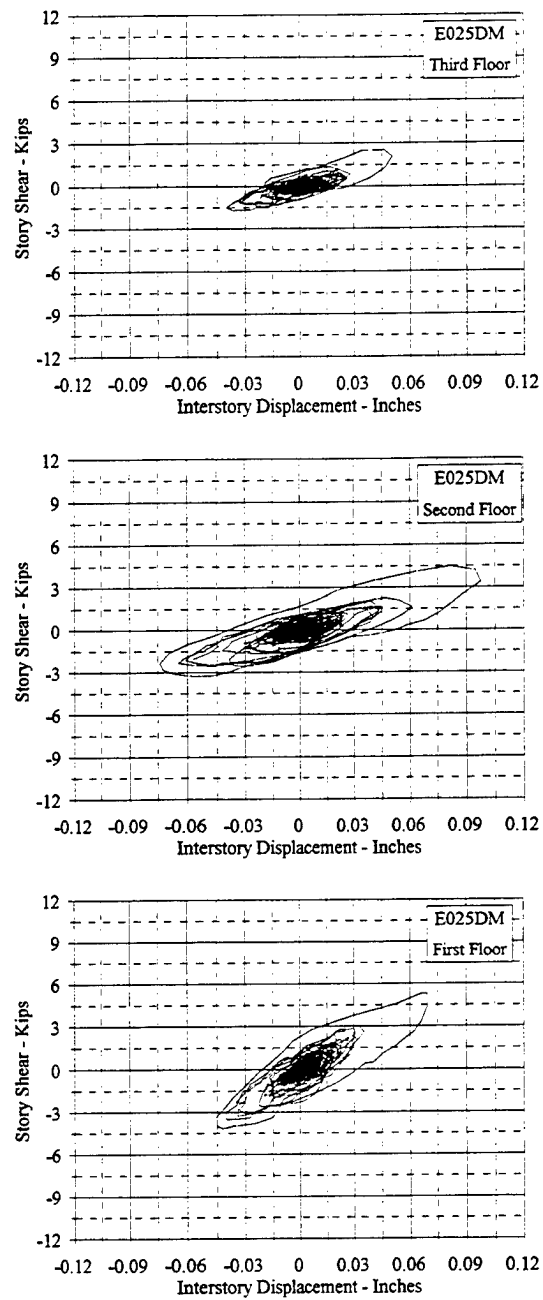


Figure C.5.11 Story Shear Vs. Interstory Displacement: E025DM

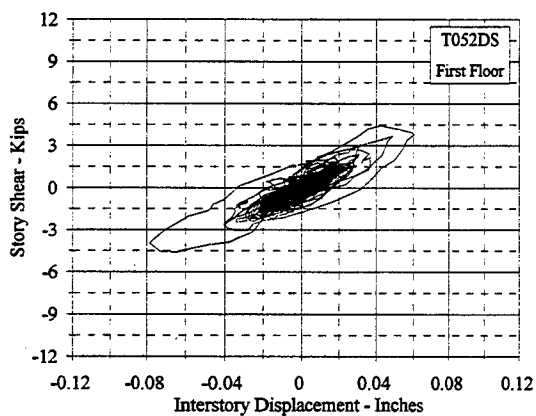
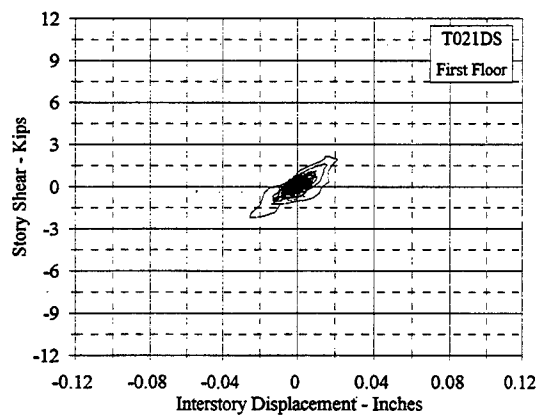
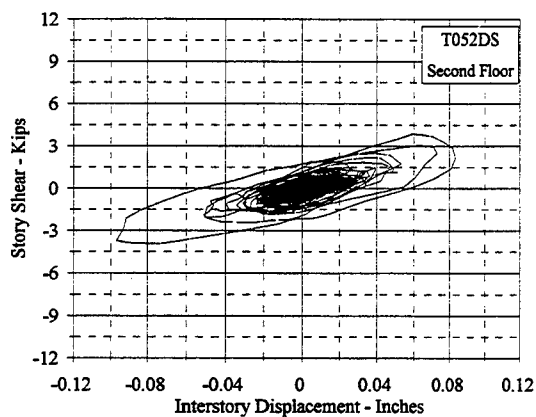
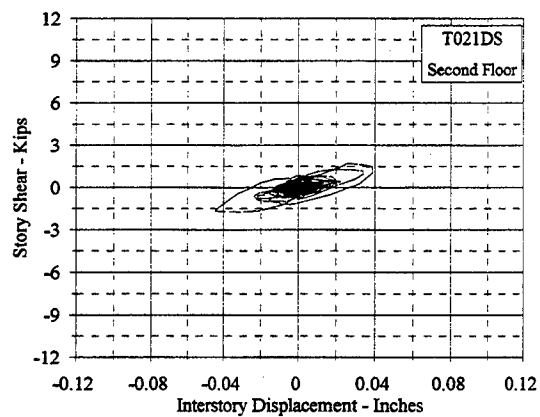
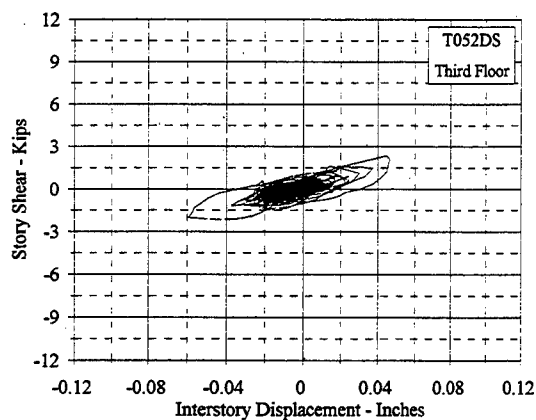
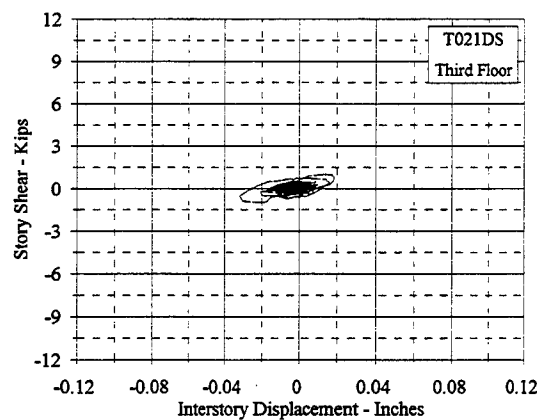


Figure C.5.12 Story Shear Vs. Interstory Displacement: T021DS, T052DS

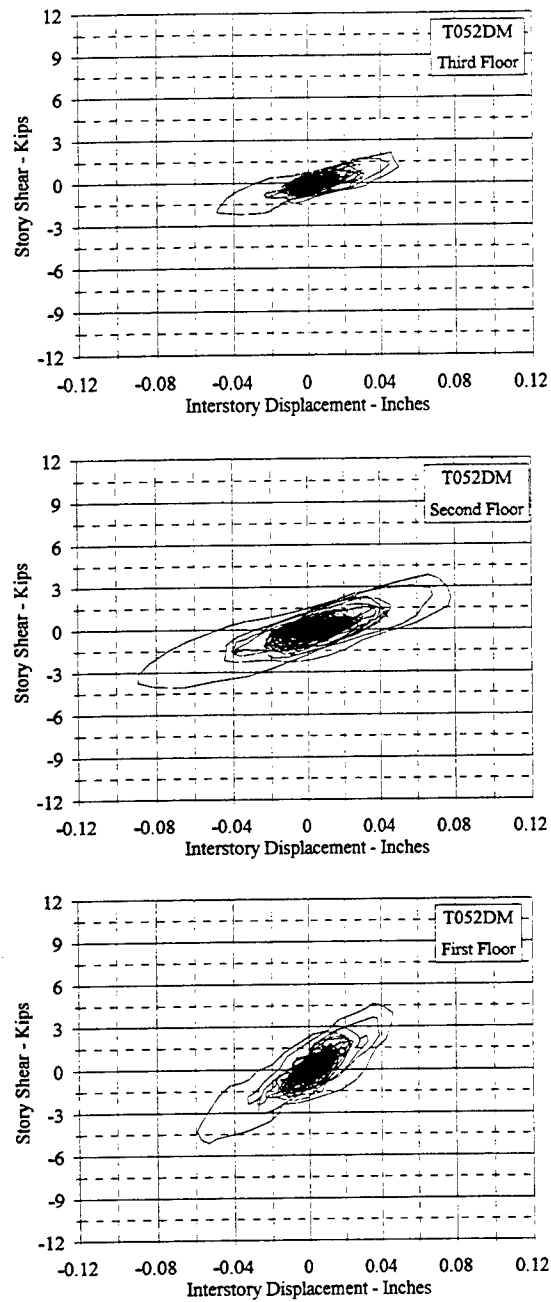


Figure C.5.13 Story Shear Vs. Interstory Displacement: T052DM

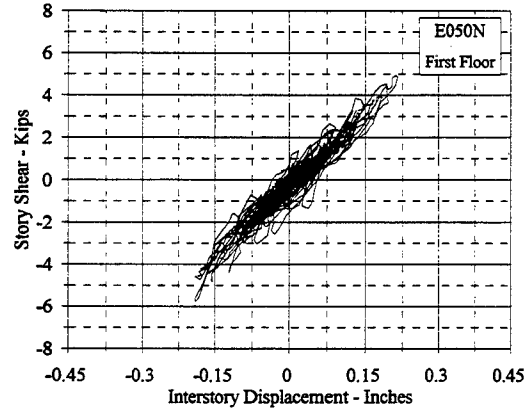
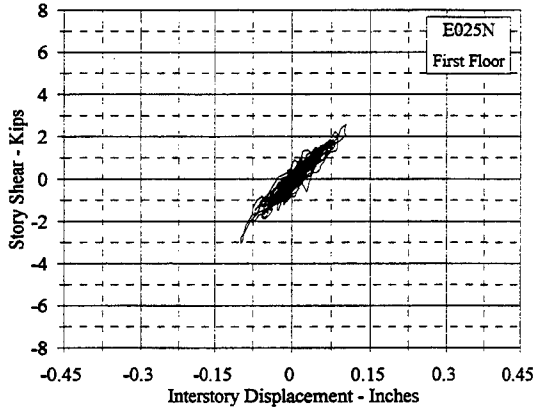
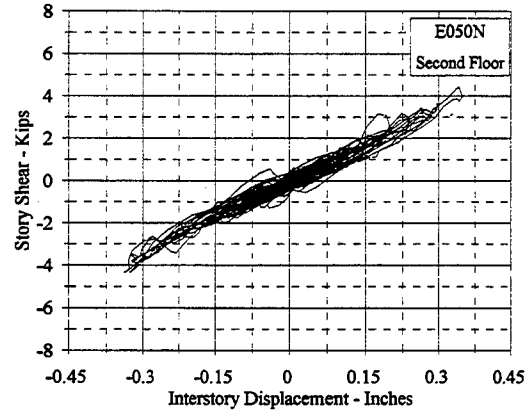
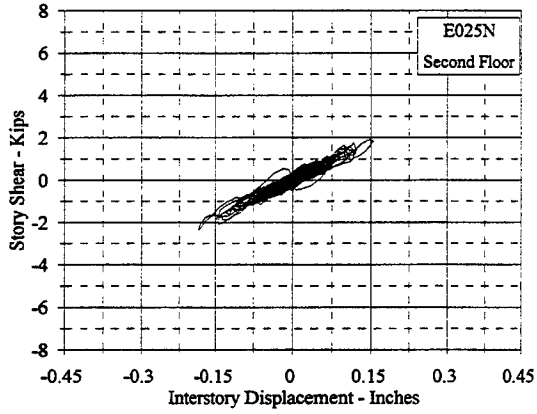
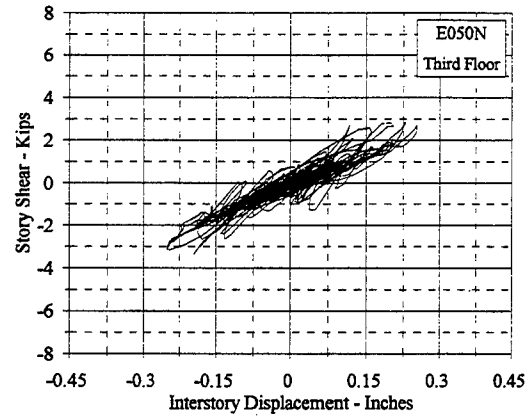
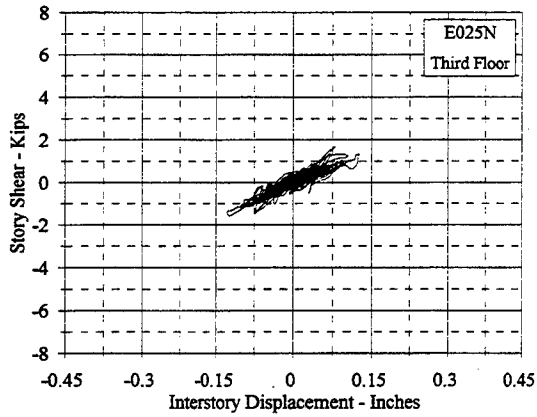


Figure C.5.14 Story Shear Vs. Interstory Displacement: E025N, E050N

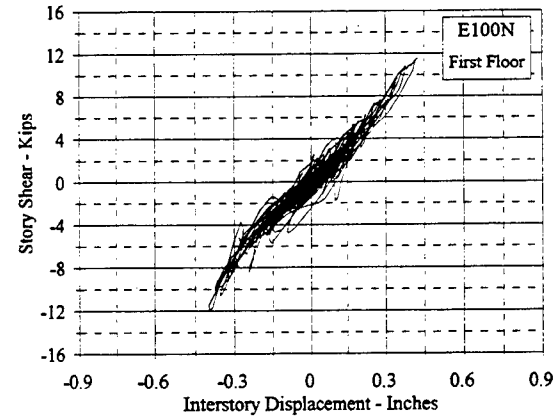
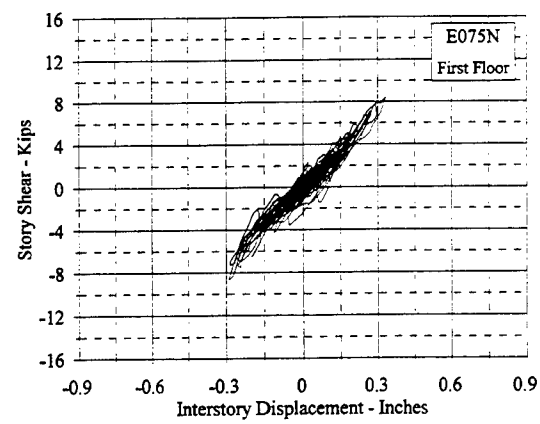
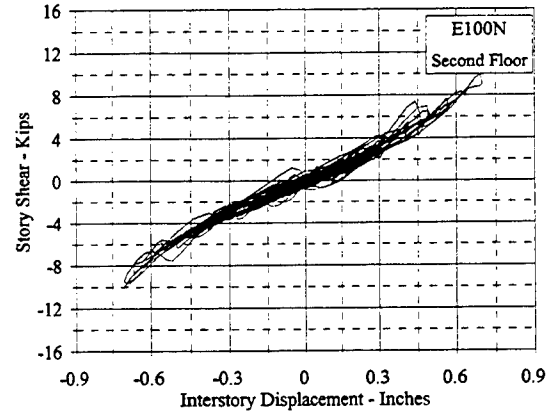
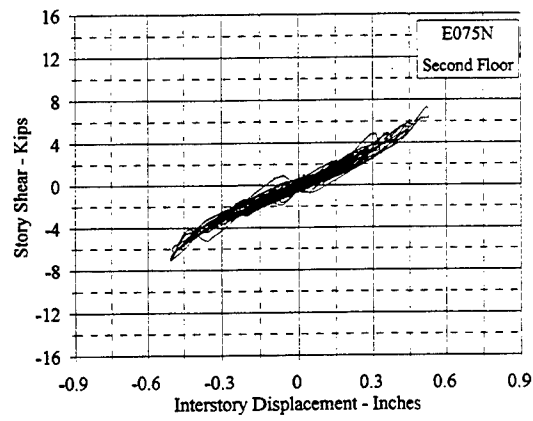
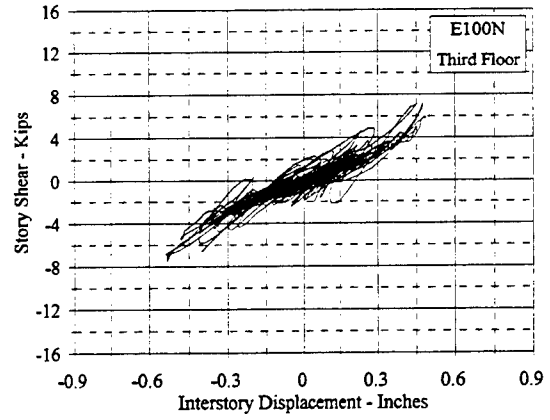
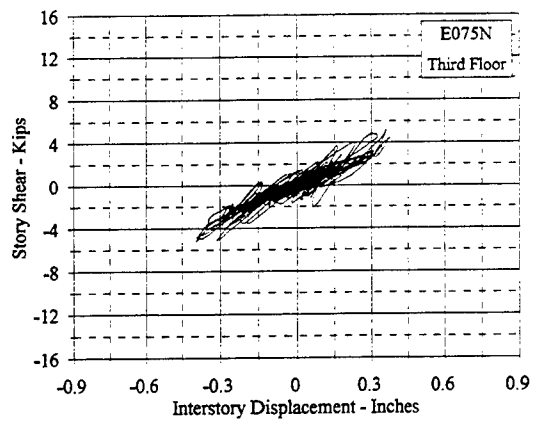


Figure C.5.15 Story Shear Vs. Interstory Displacement: E075N, E100N

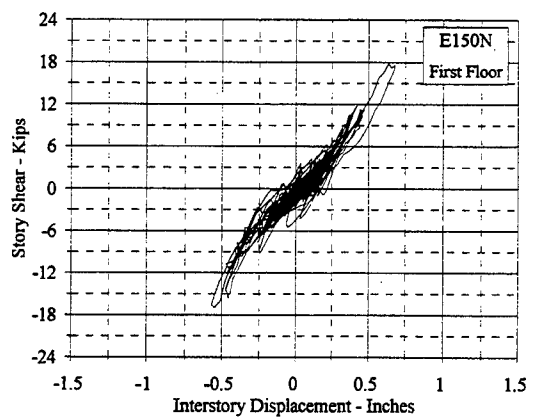
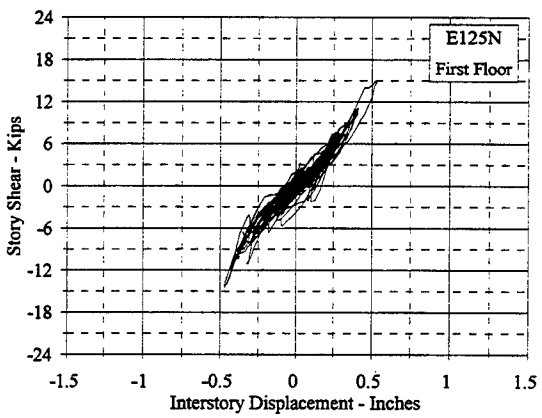
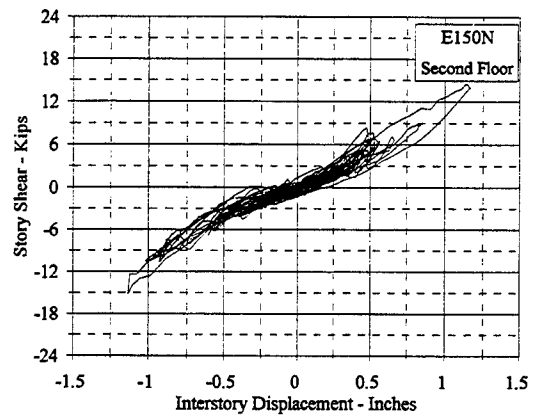
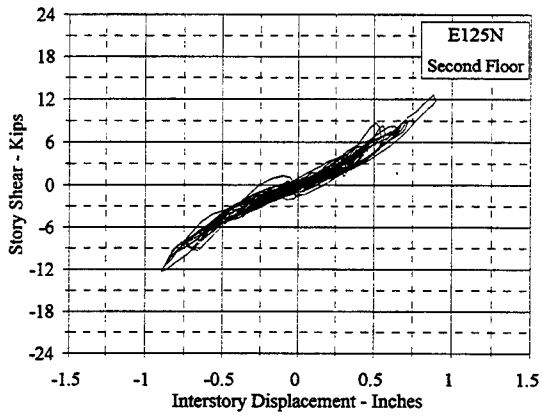
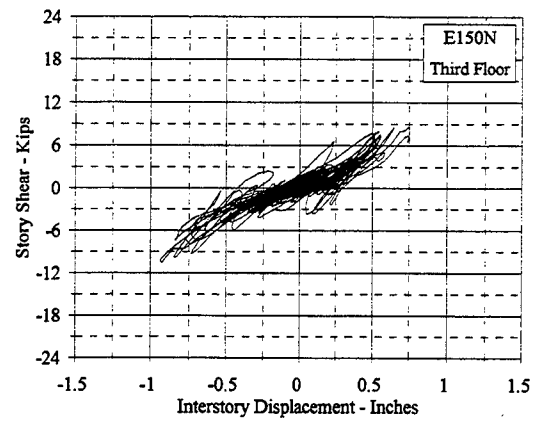
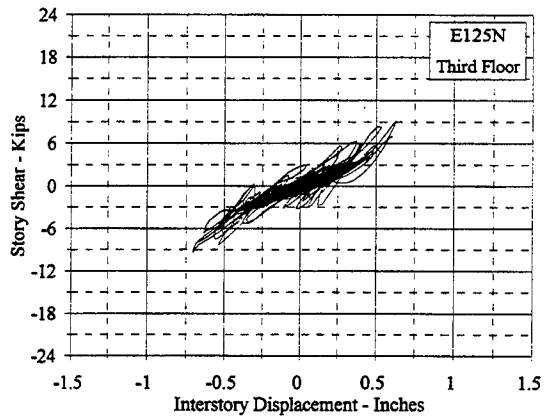


Figure C.5.16 Story Shear Vs. Interstory Displacement: E125N, E150N

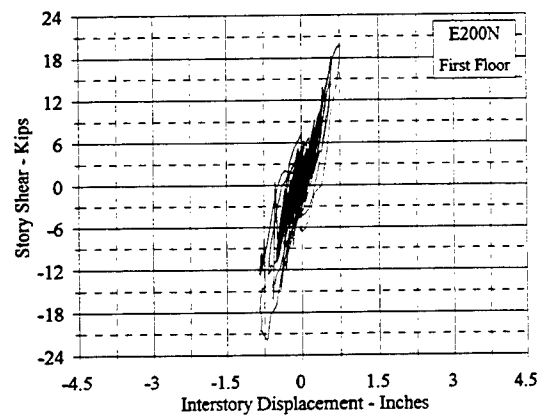
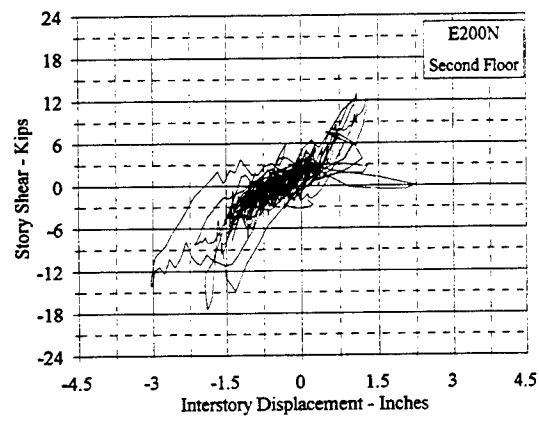
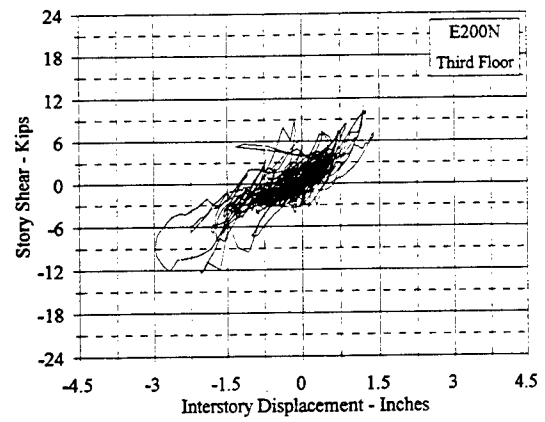


Figure C.5.17 Story Shear Vs. Interstory Displacement: E200N

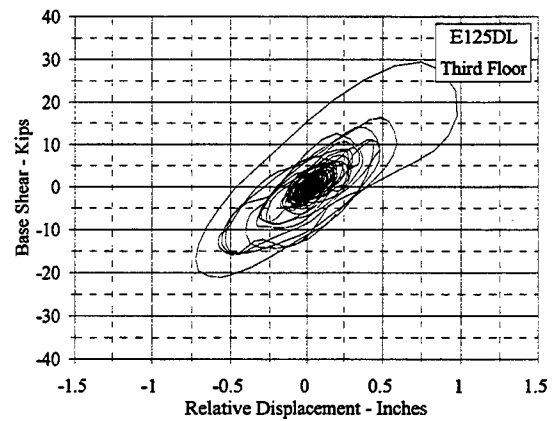
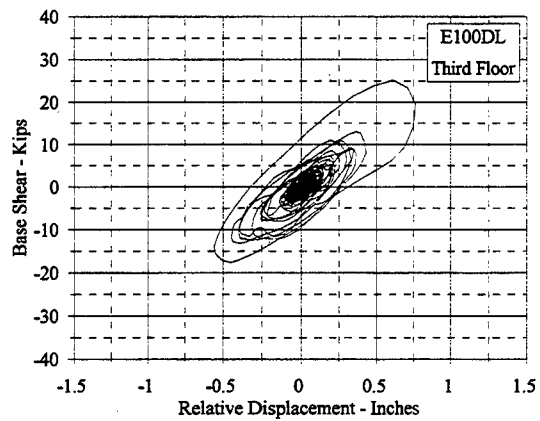
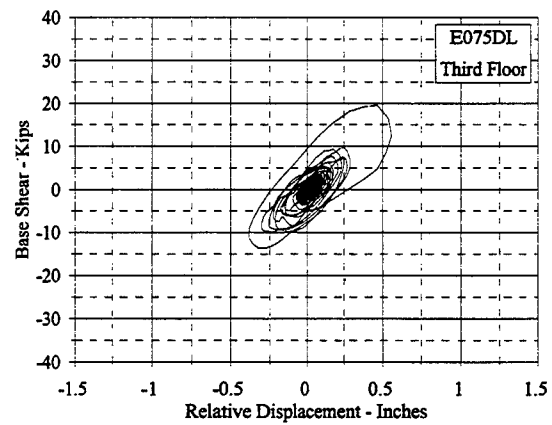
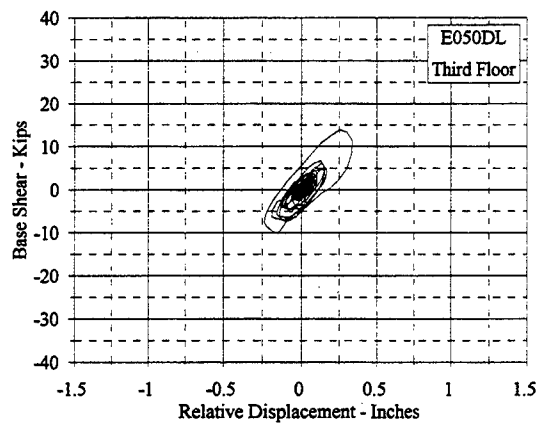
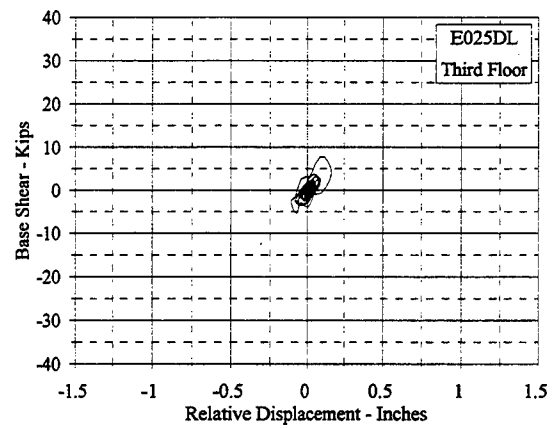
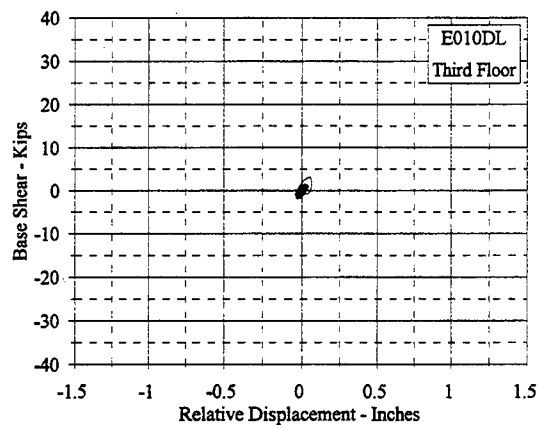


Figure C.6.1 Base Shear Vs. Relative Third Floor Displacement: E010DL - E125DL

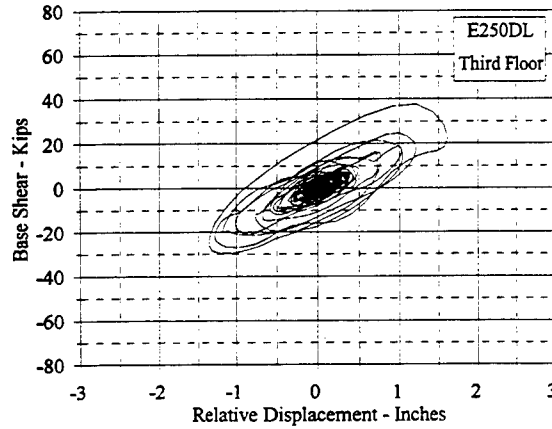
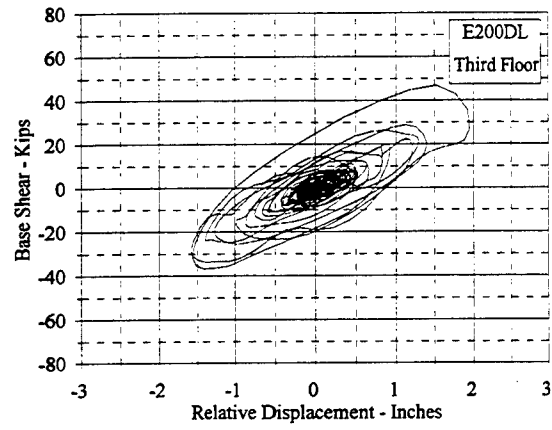
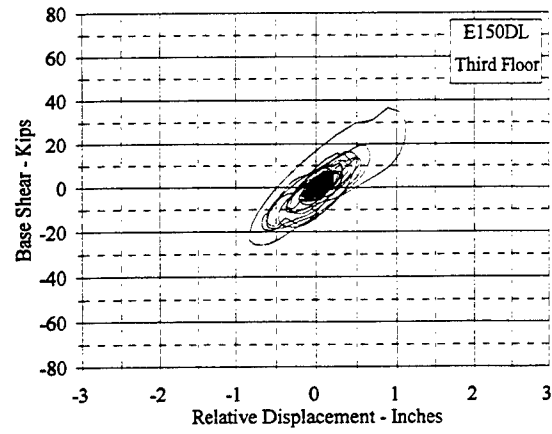


Figure C.6.2 Base Shear Vs. Third Floor Relative Displacement: E150DL - E250DL

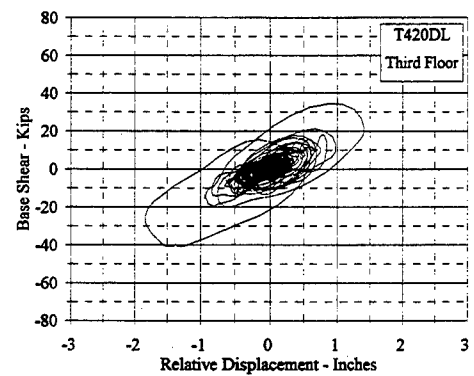
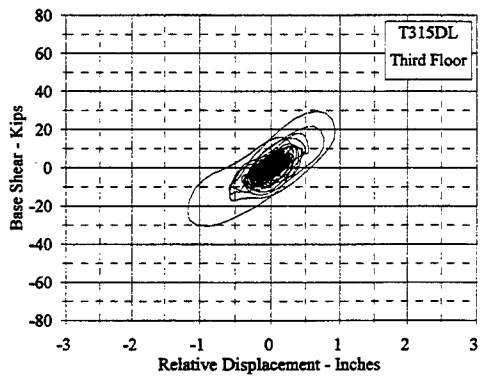
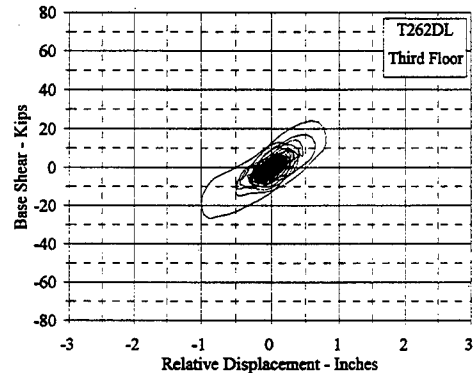
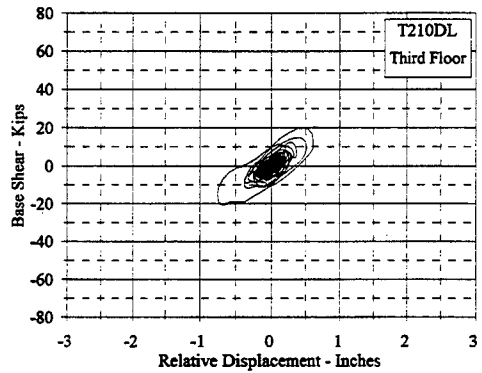
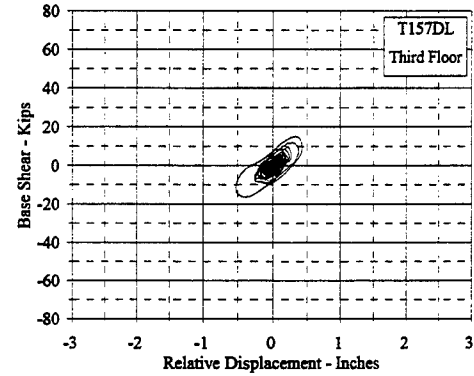
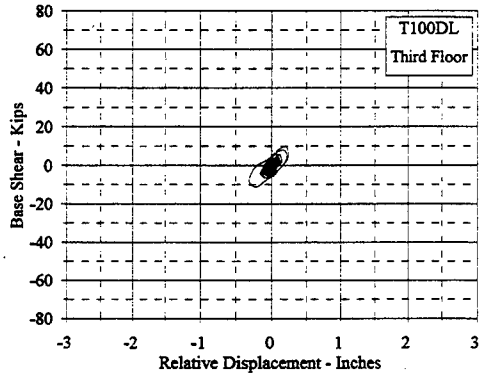
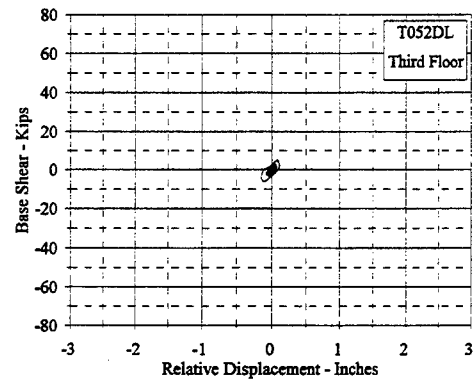
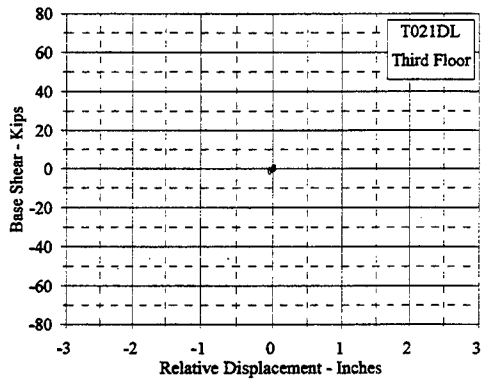


Figure C.6.3 Base Shear Vs. Third Floor Relative Displacement: T021DL - T420DL

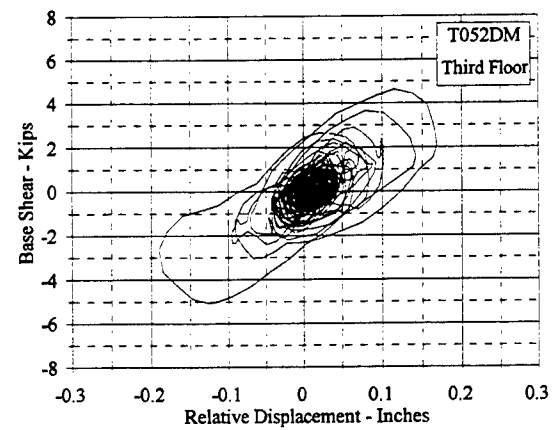
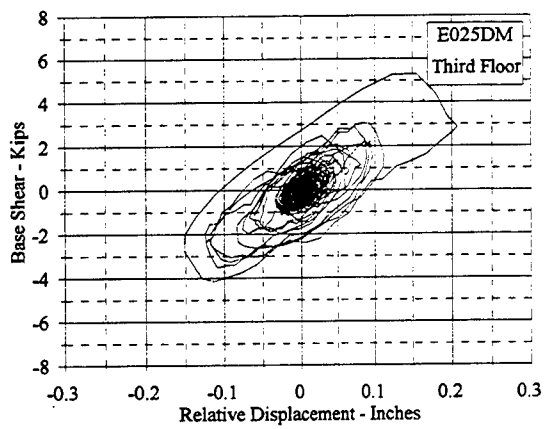
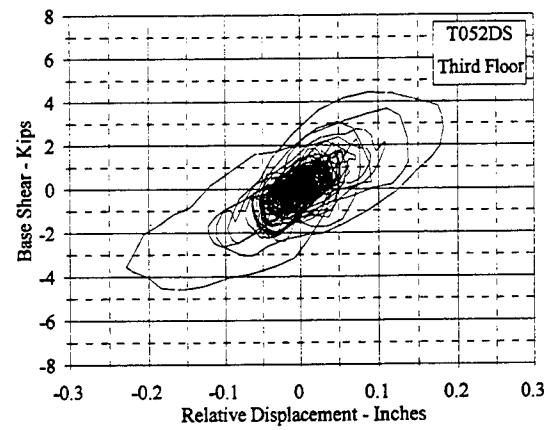
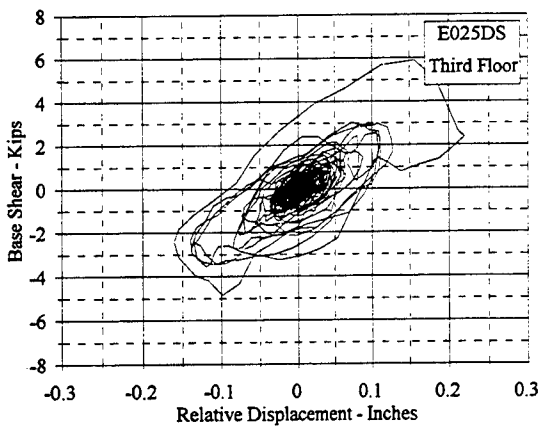
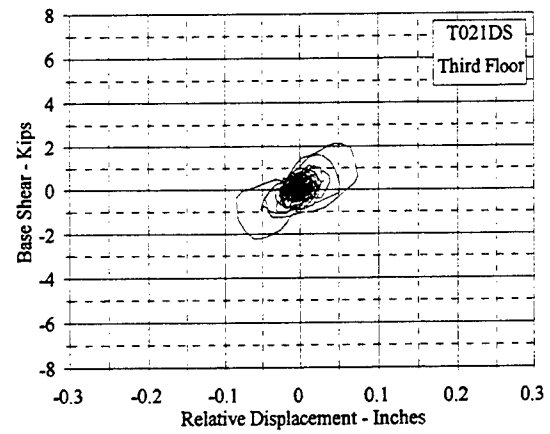
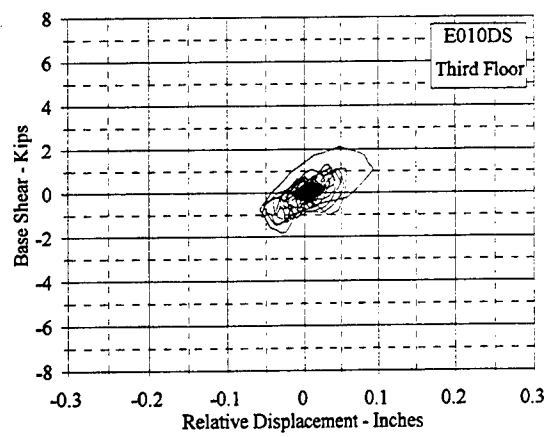


Figure C.6.4 Base Shear Vs. Third Floor Relative Displacement: E010DS - T052DM

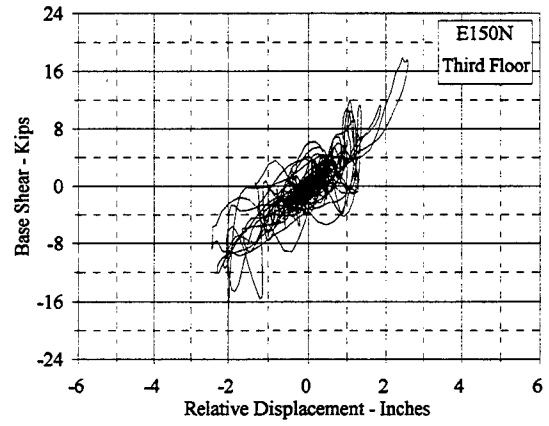
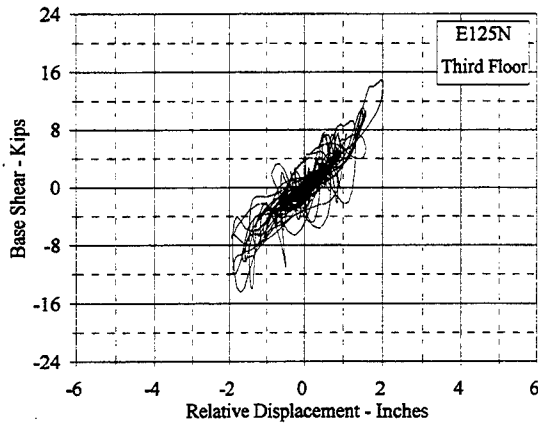
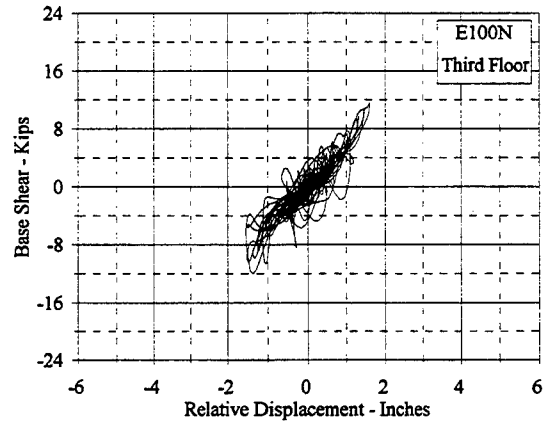
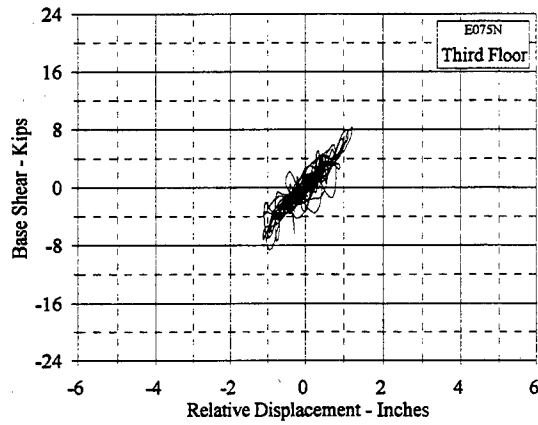
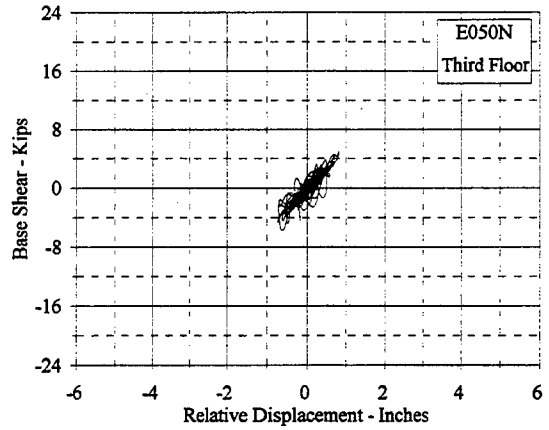
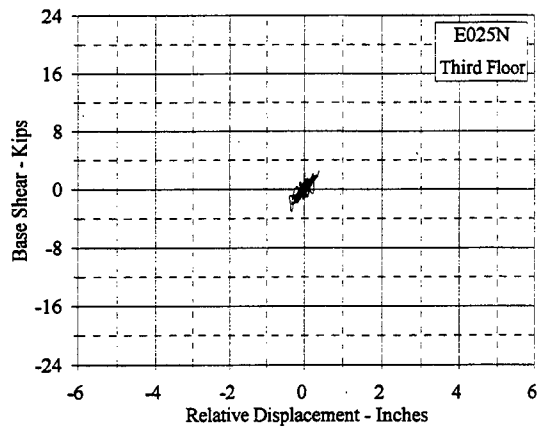


Figure C.6.5 Base Shear Vs. Third Floor Relative Displacement: E025N - E150N

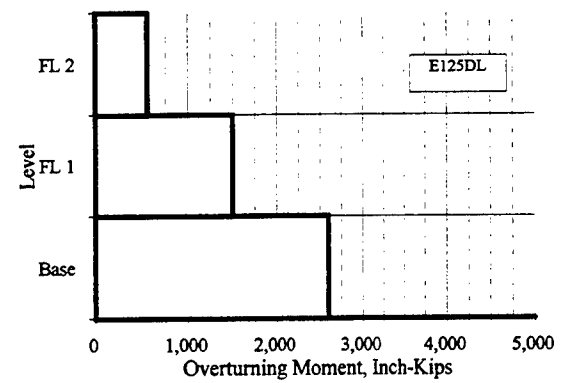
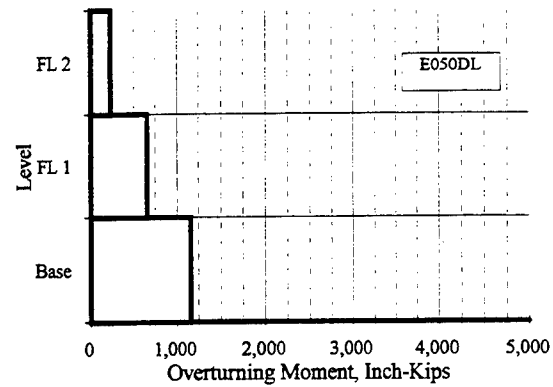
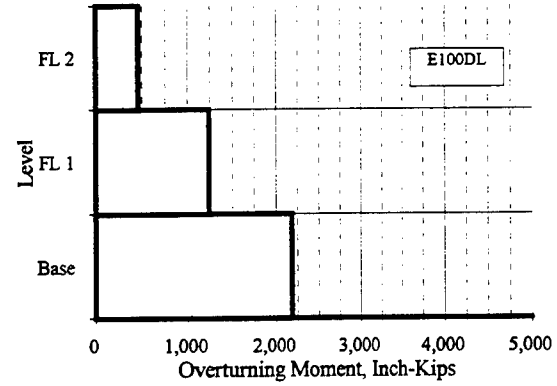
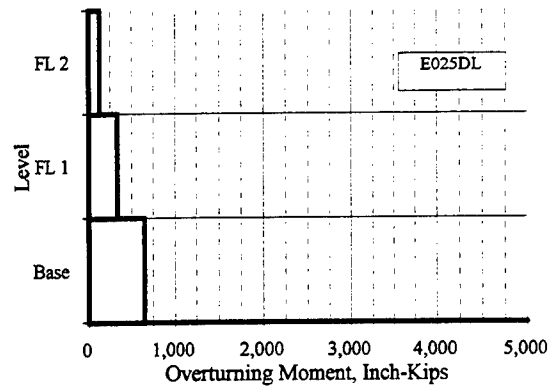
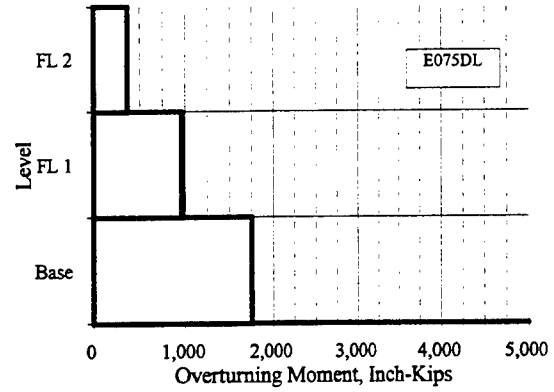
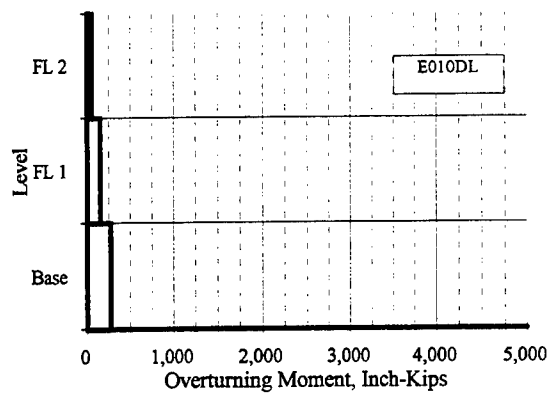


Figure C.7.1 Maximum Overturning Moments: E010DL - E125DL

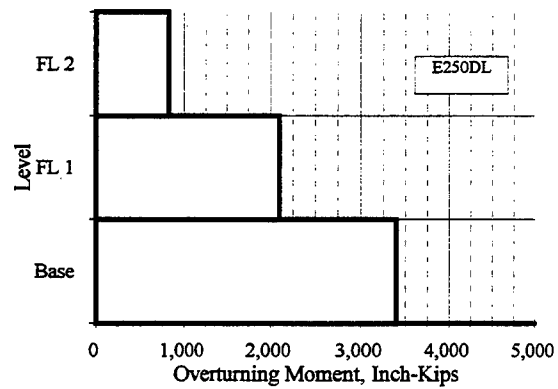
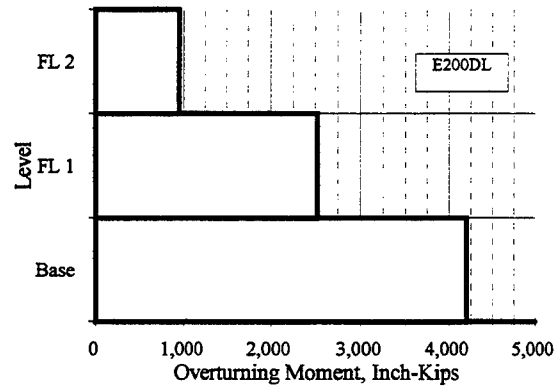
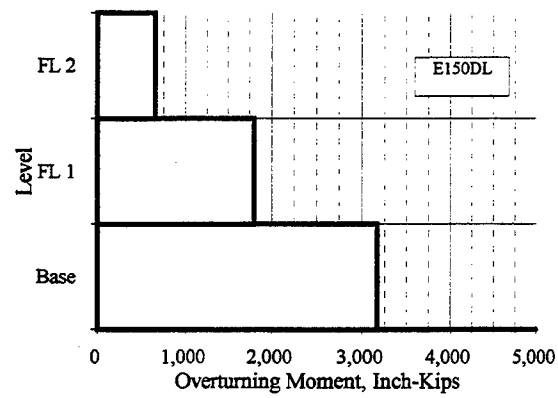


Figure C.7.2 Maximum Overturning Moments: E150DL - E250DL

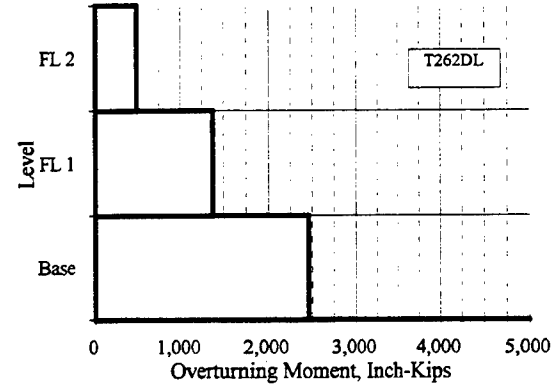
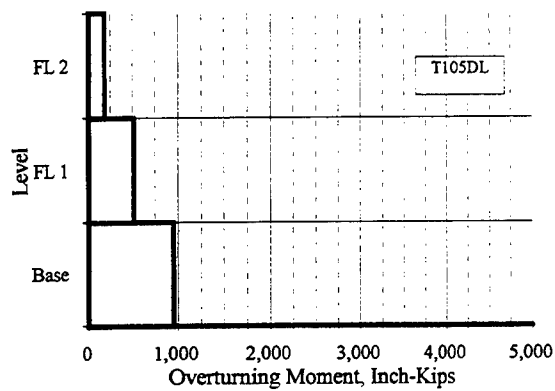
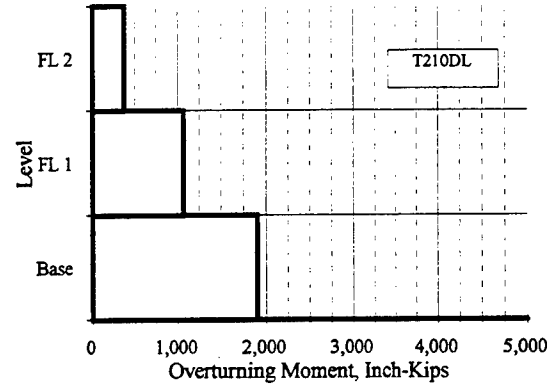
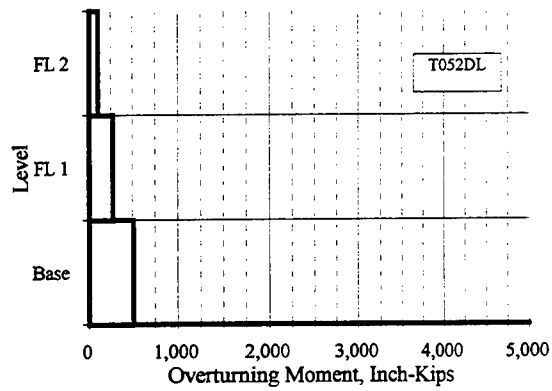
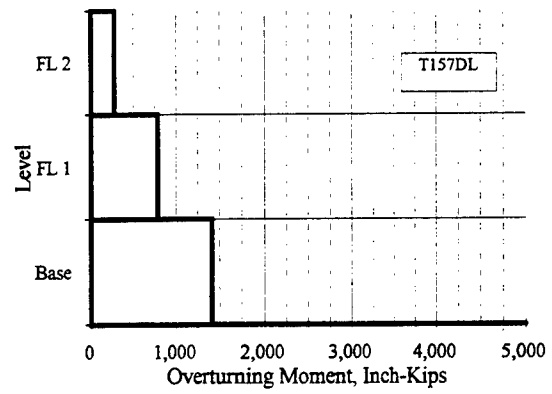
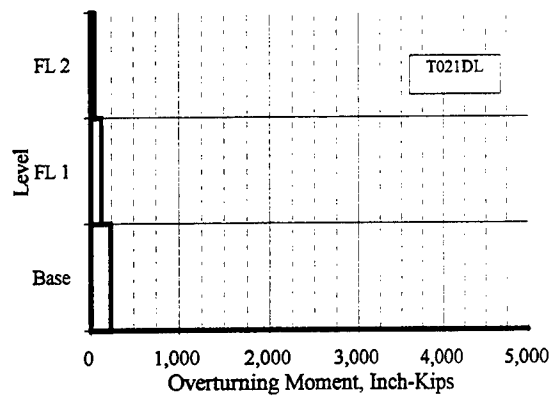


Figure C.7.3 Maximum Overturning Moments: T021DL - T262DL

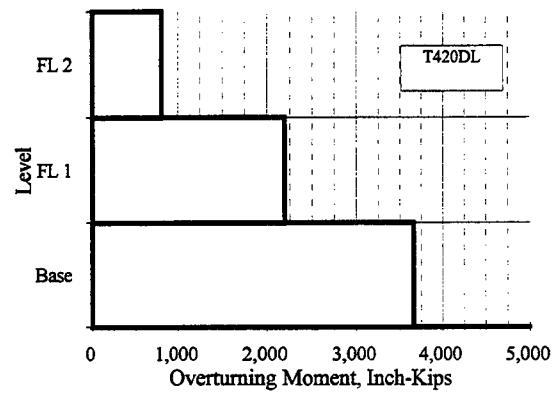
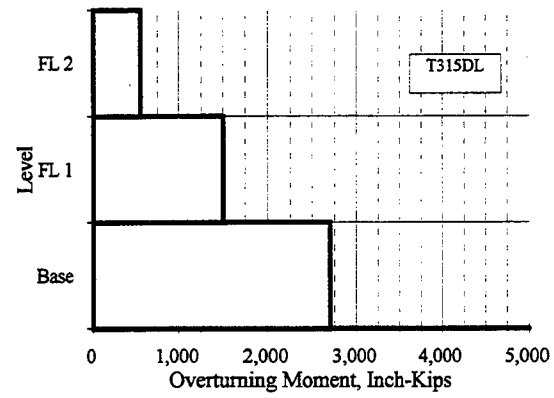


Figure C.7.4 Maximum Overturning Moments: T315DL - T420DL

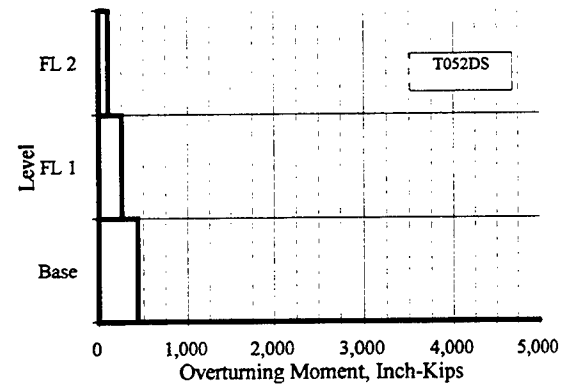
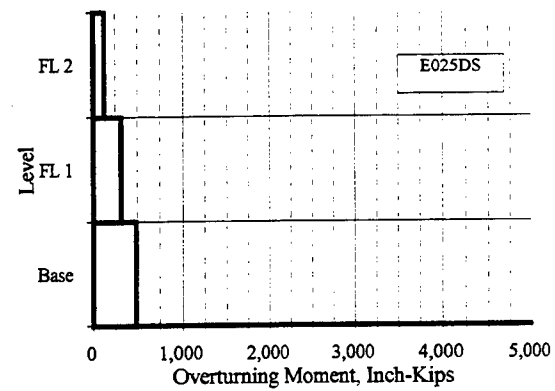
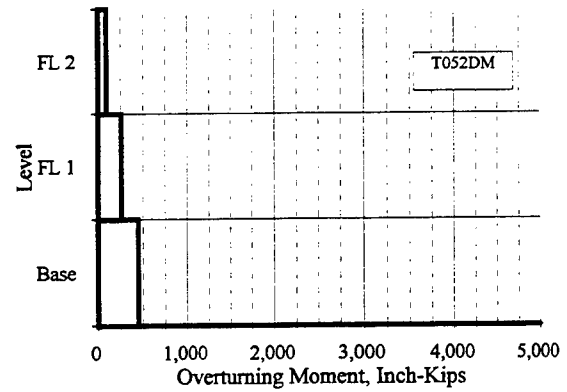
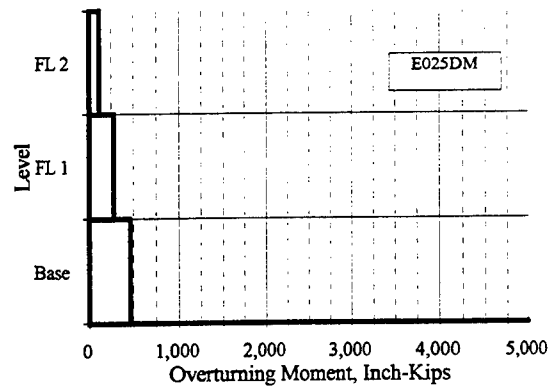
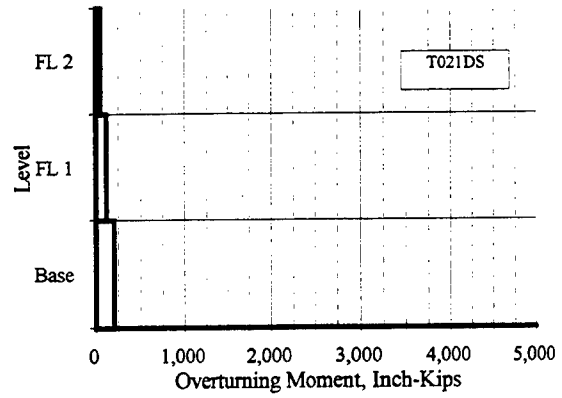
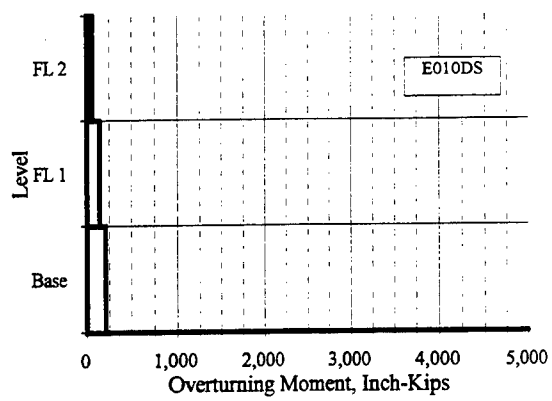


Figure C.7.5 Maximum Overturning Moments: E010DS -T052DS

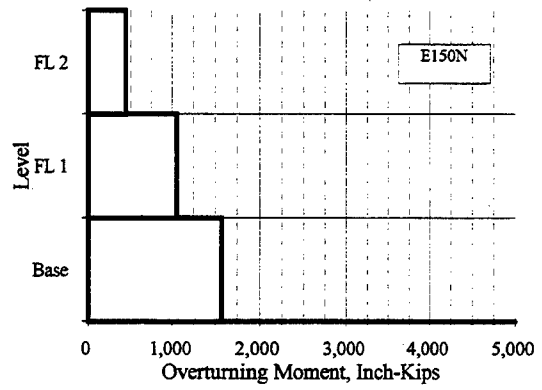
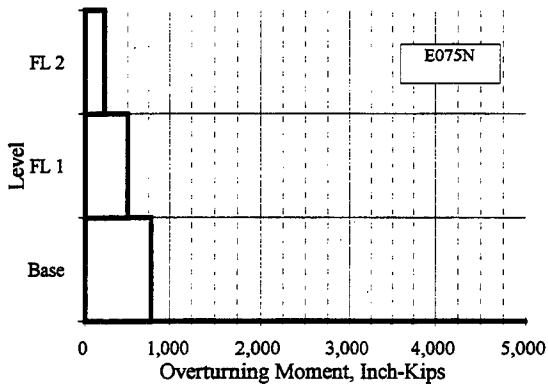
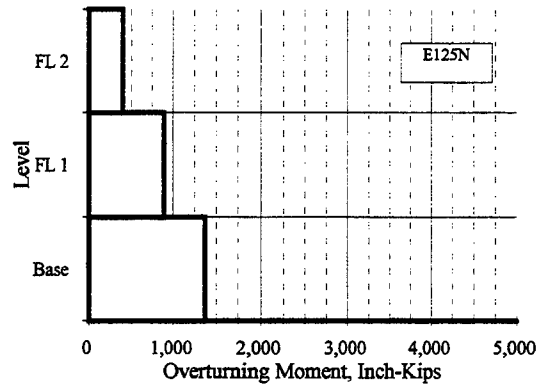
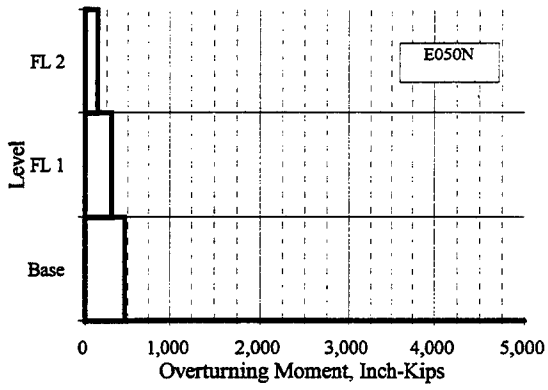
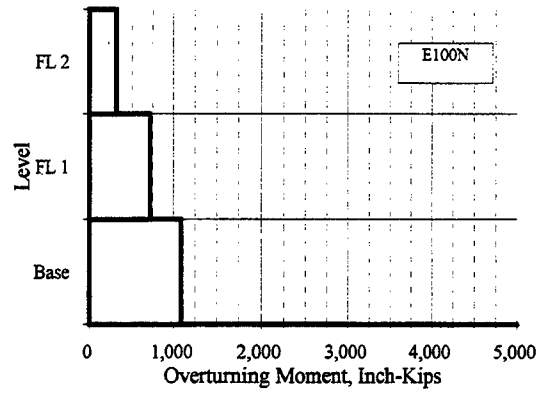
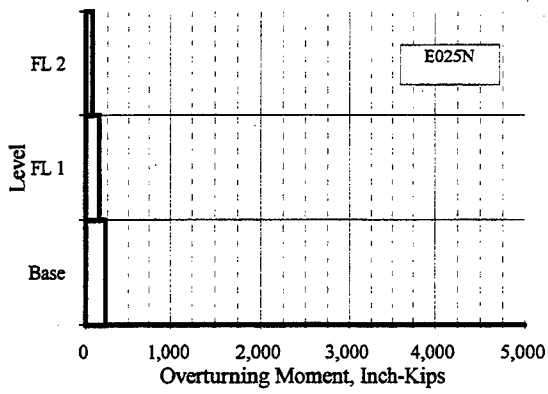


Figure C.7.6 Maximum Overturning Moments: E025N - E150N

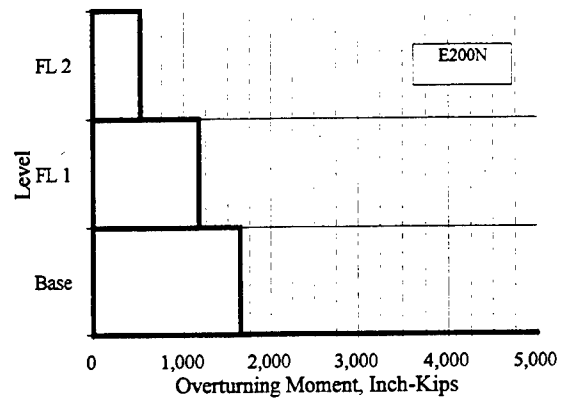


Figure C.7.7 Maximum Overturning Moments: E200N

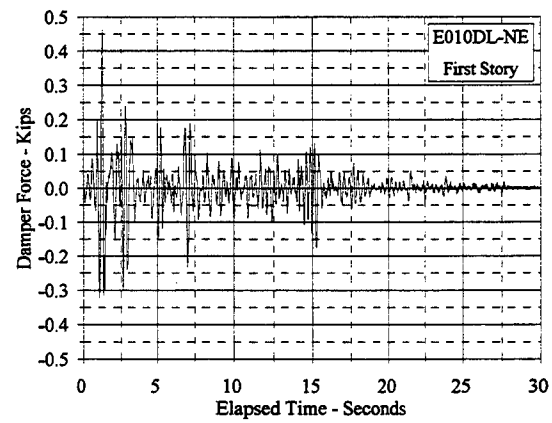
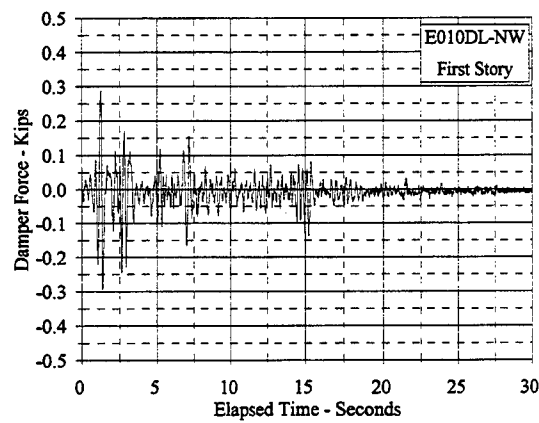
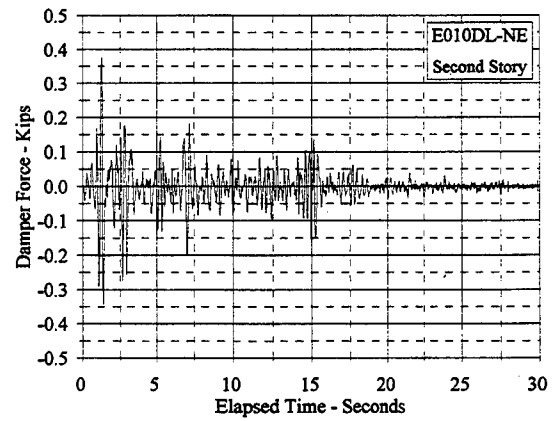
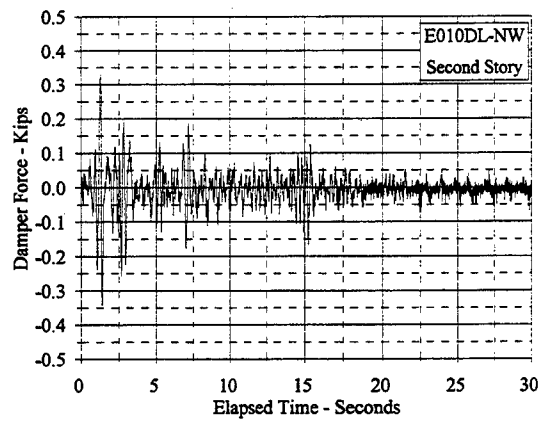
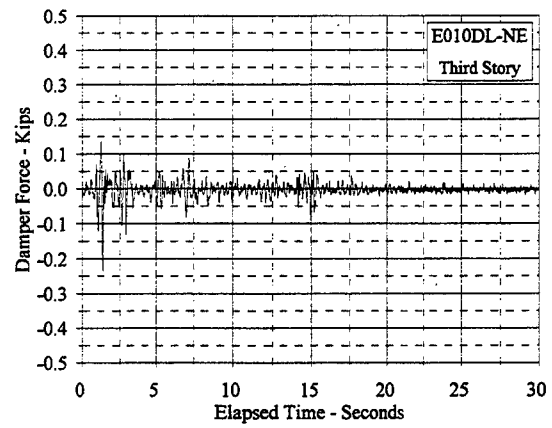
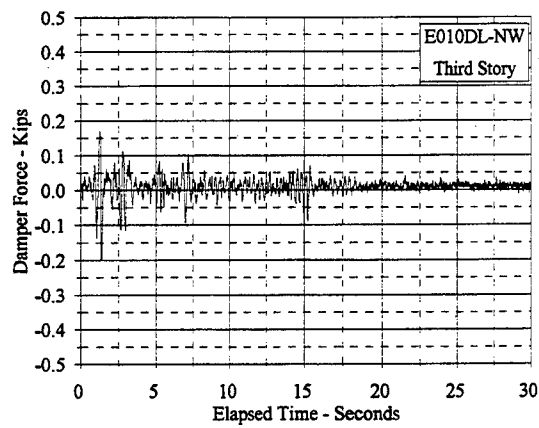


Figure C.8.1 Damper Force Vs. Elapsed Time: E010DL, NW and NE

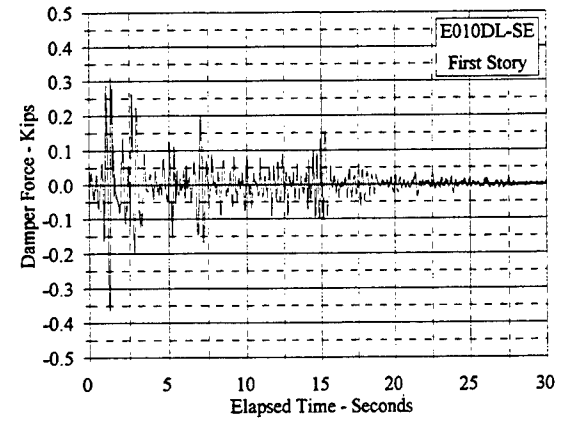
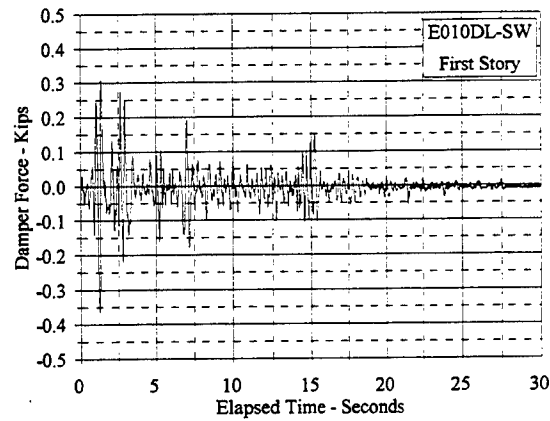
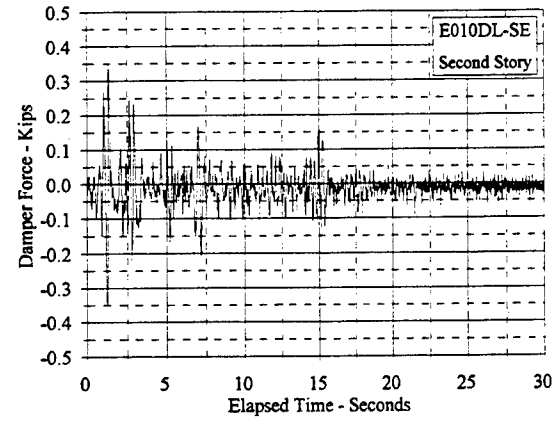
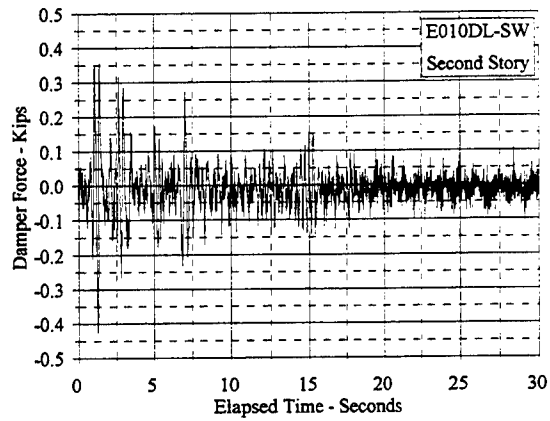
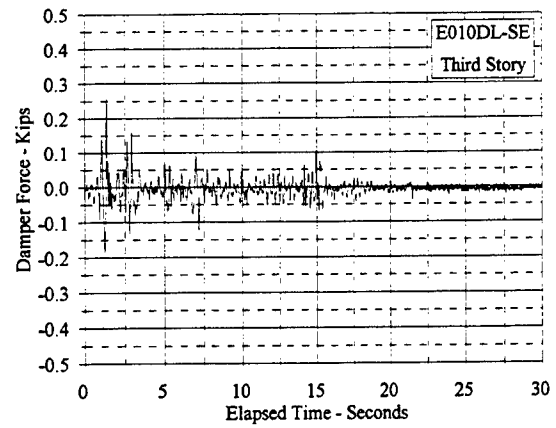
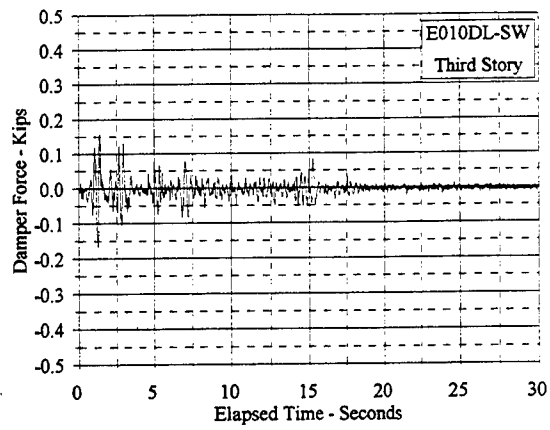


Figure C.8.2 Damper Force Vs. Elapsed Time: E010DL, SW and SE

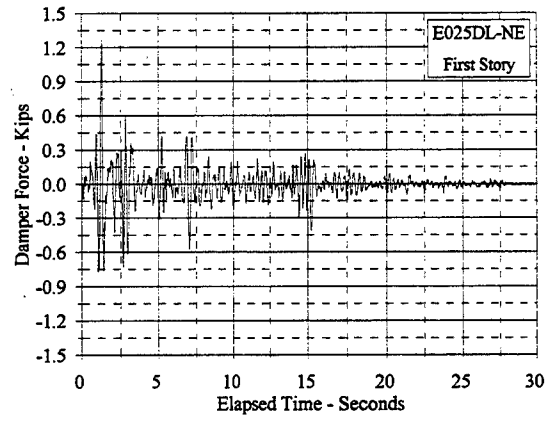
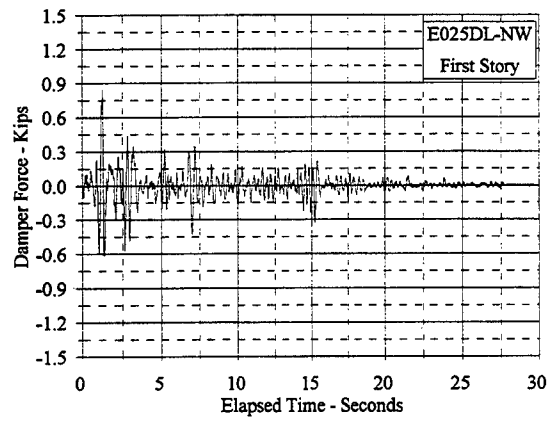
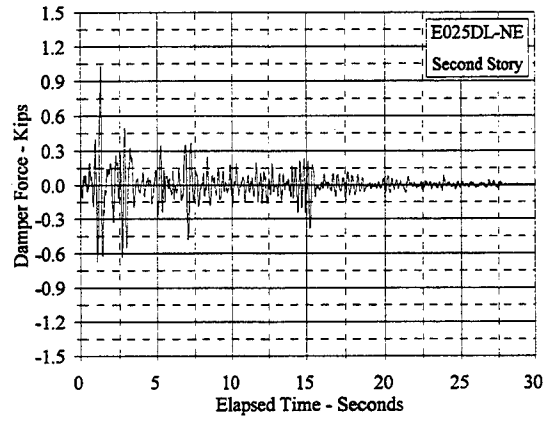
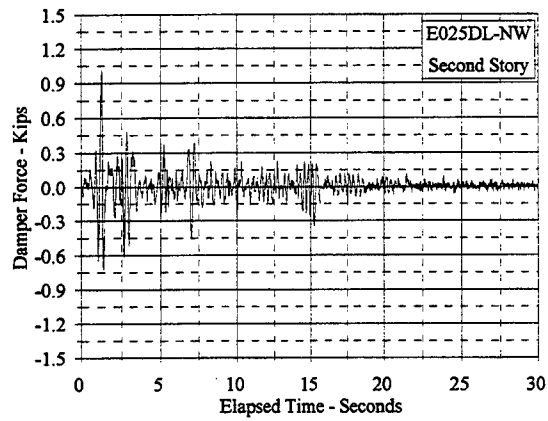
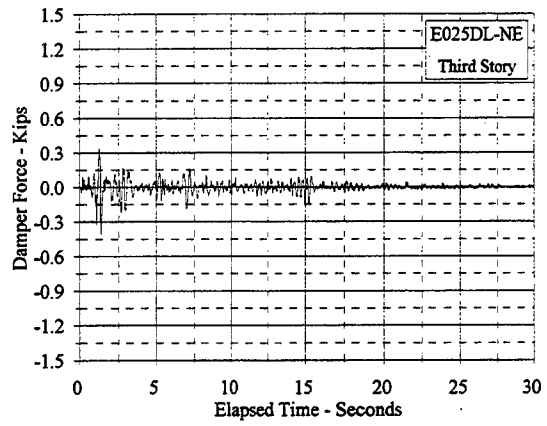
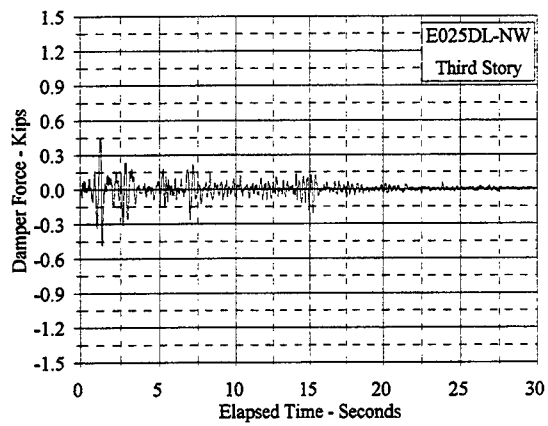


Figure C.8.3 Damper Force Vs. Elapsed Time: E025DL, NW and NE

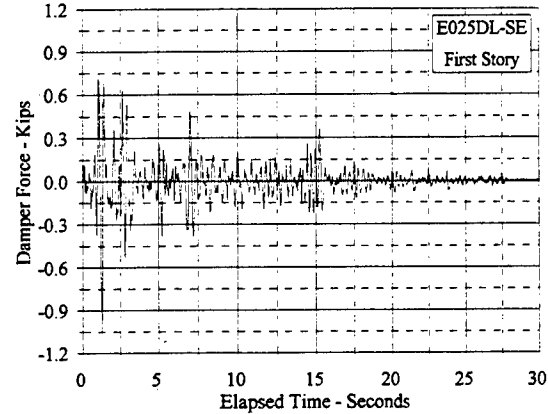
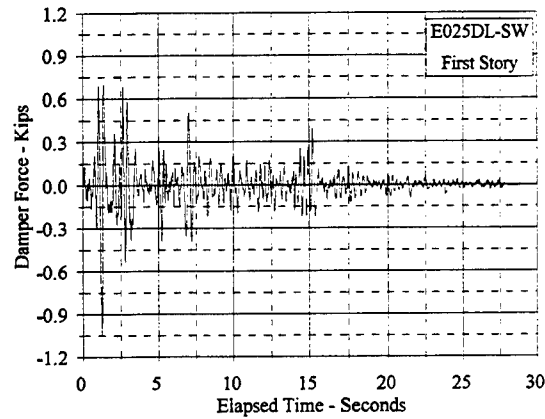
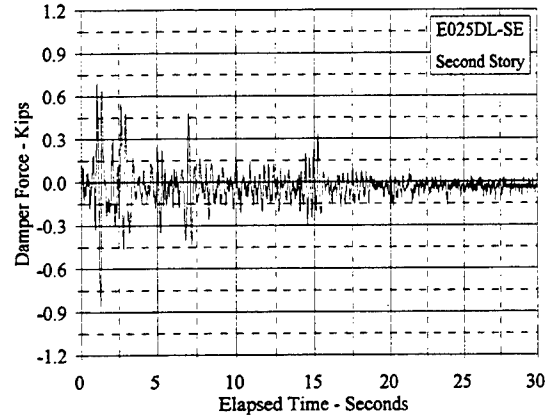
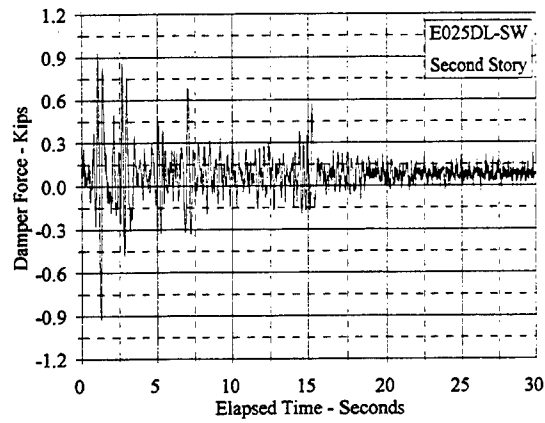
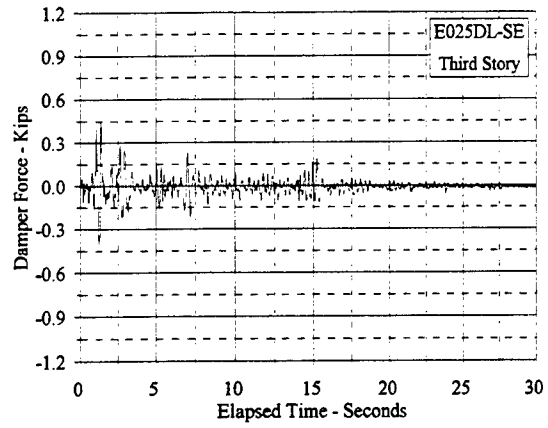
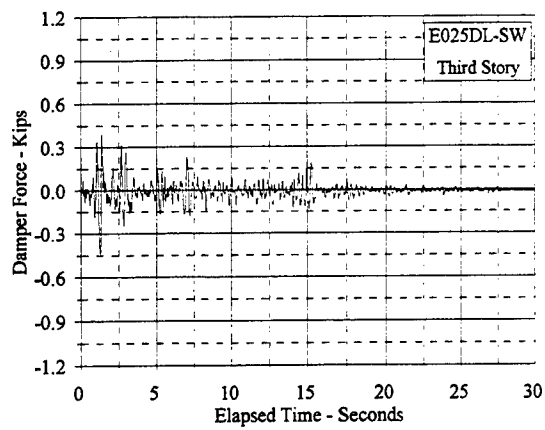


Figure C.8.4 Damper Force Vs. Elapsed Time: E025DL, SW and SE

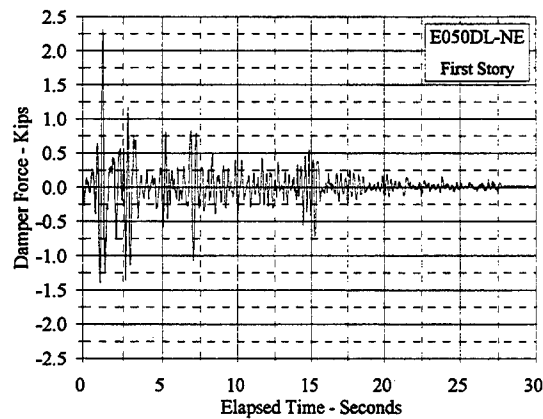
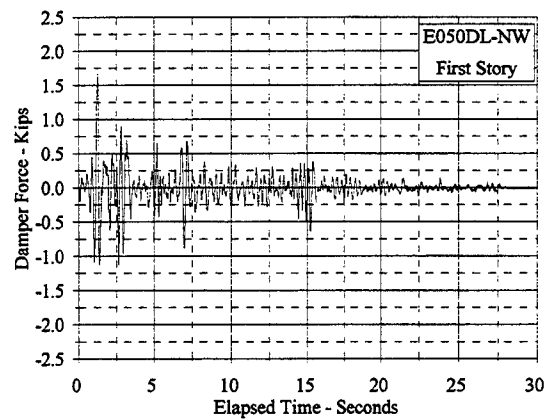
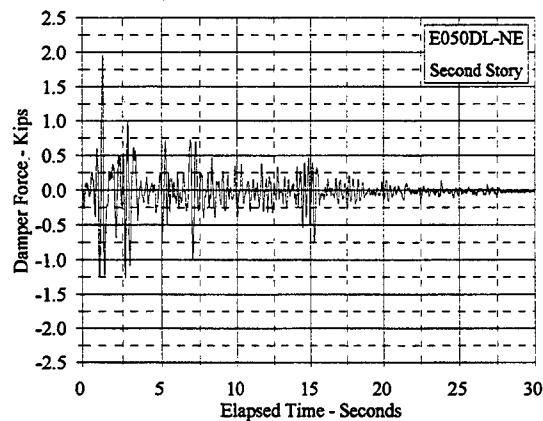
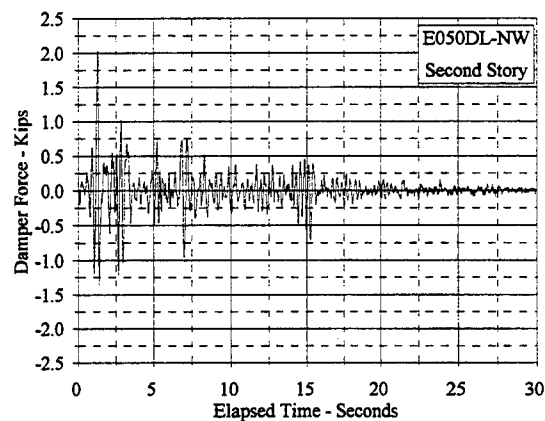
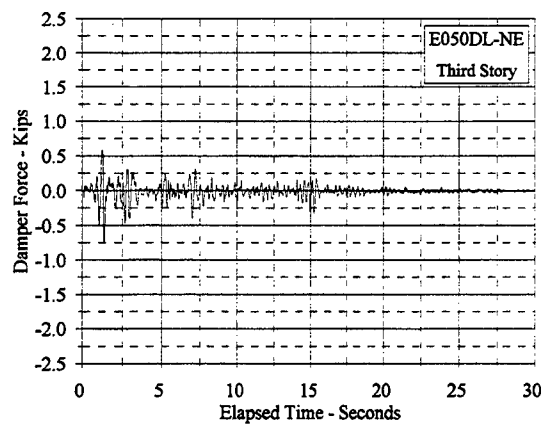
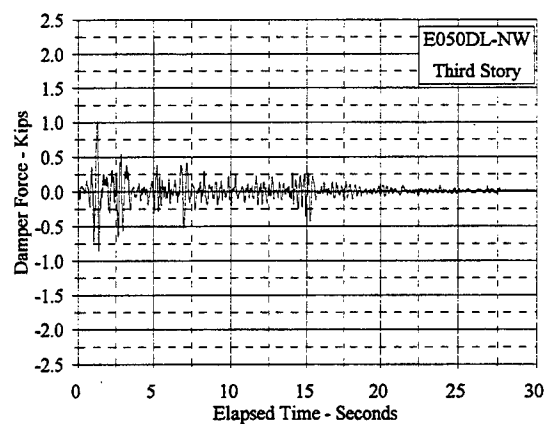


Figure C.8.5 Damper Force Vs. Elapsed Time: E050DL, NW and NE

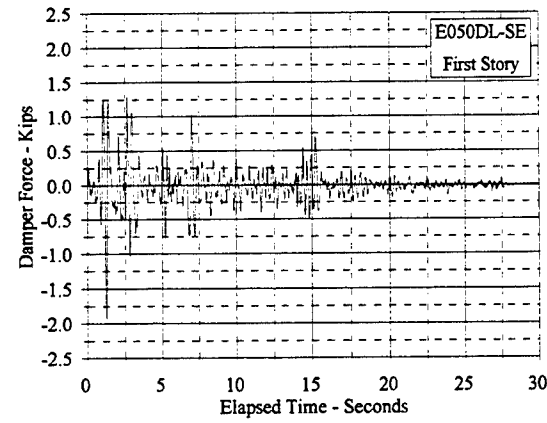
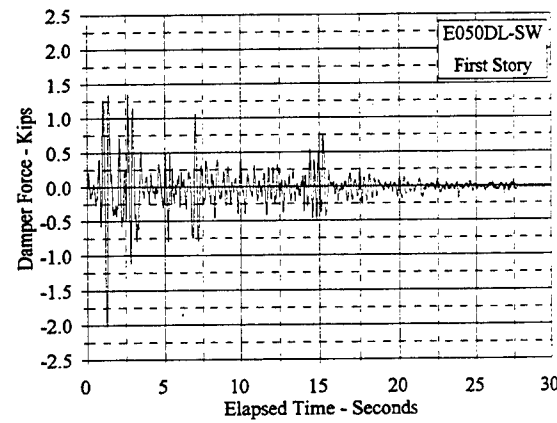
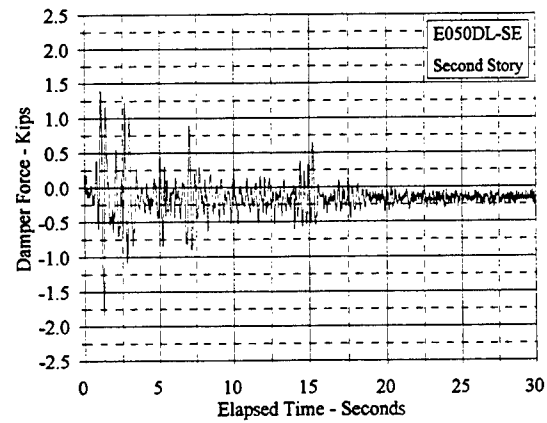
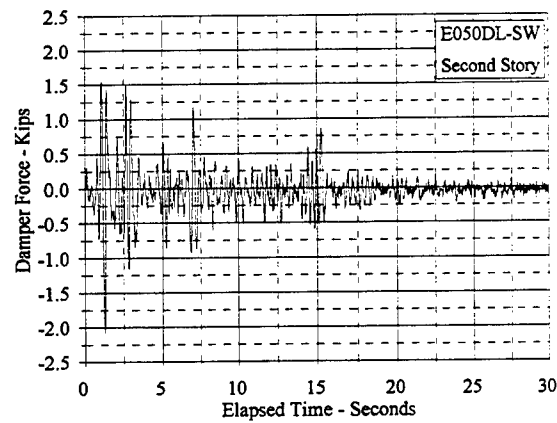
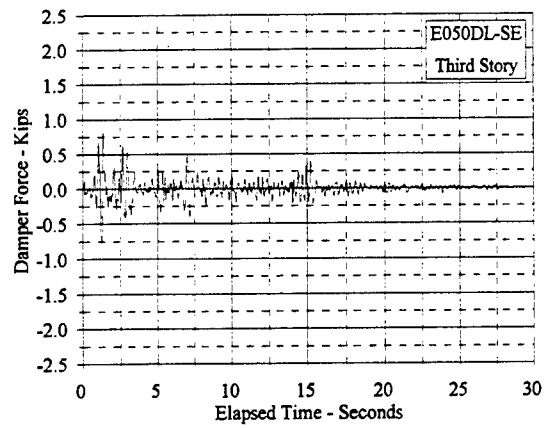
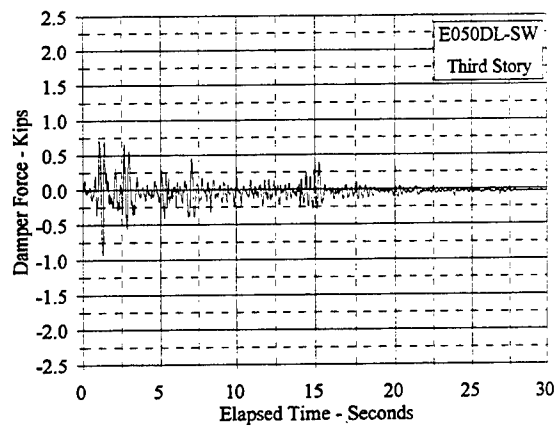


Figure C.8.6 Damper Force Vs. Elapsed Time: E050DL, SW and SE

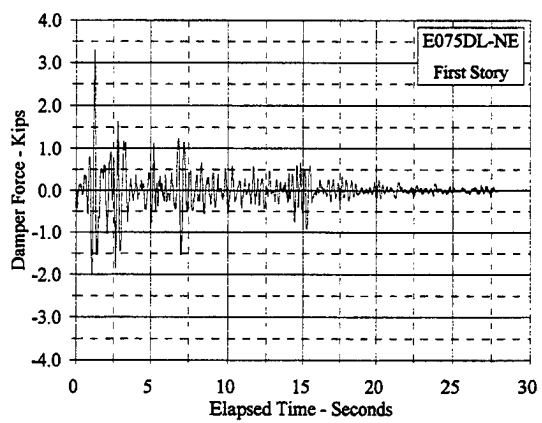
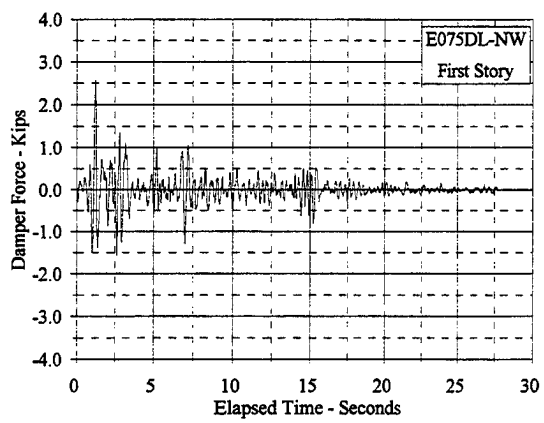
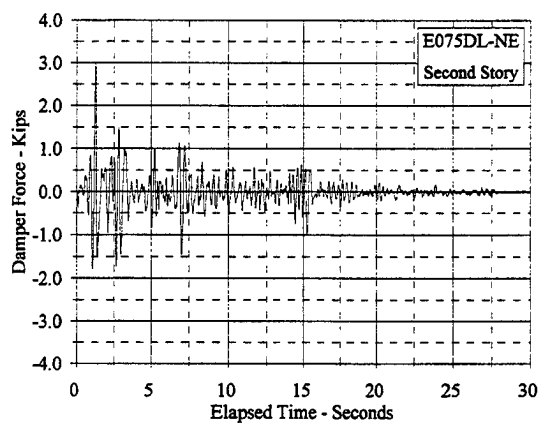
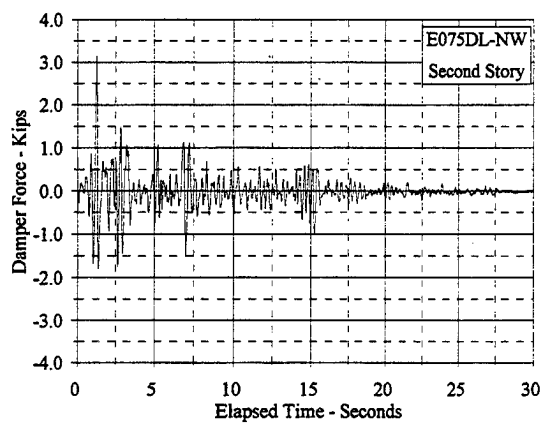
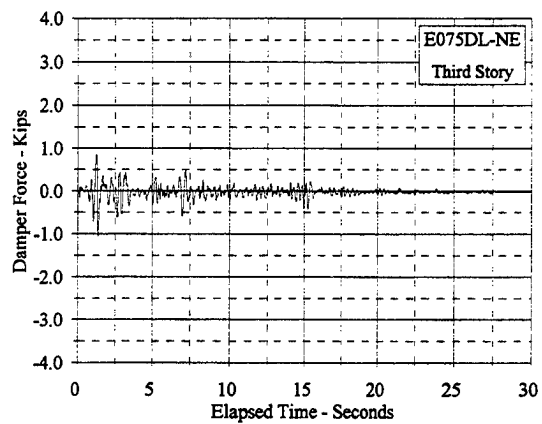
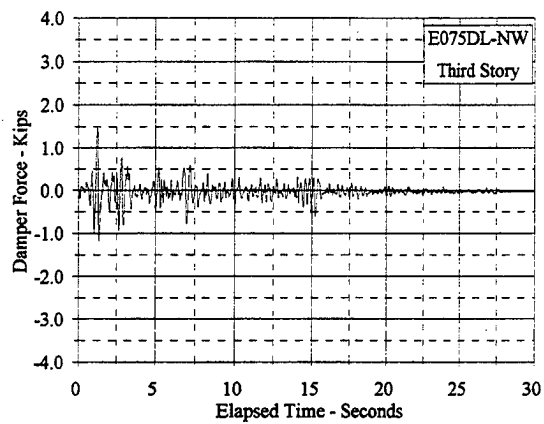


Figure C.8.7 Damper Force Vs. Elapsed Time: E075DL, NW and NE

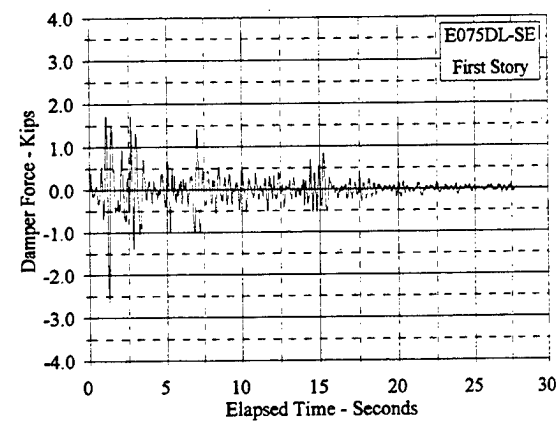
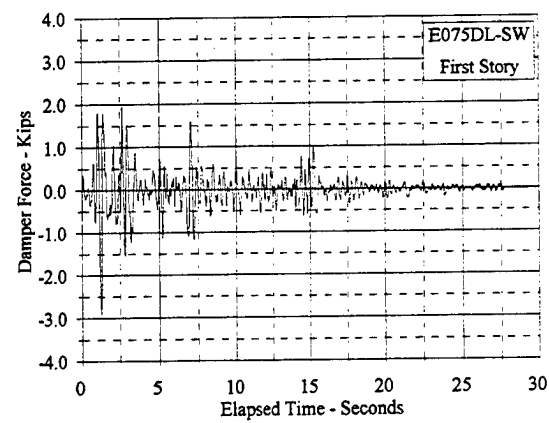
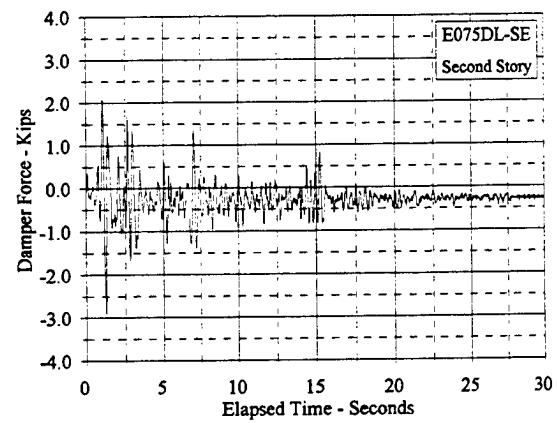
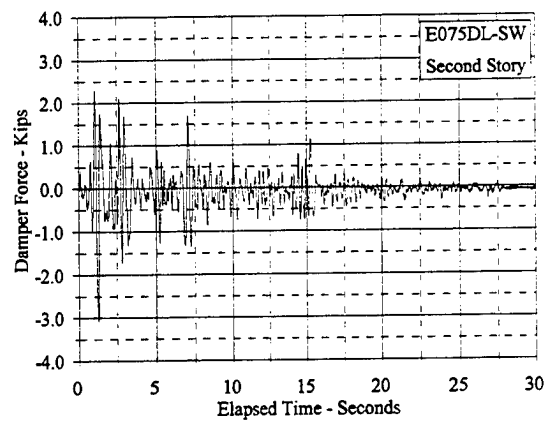
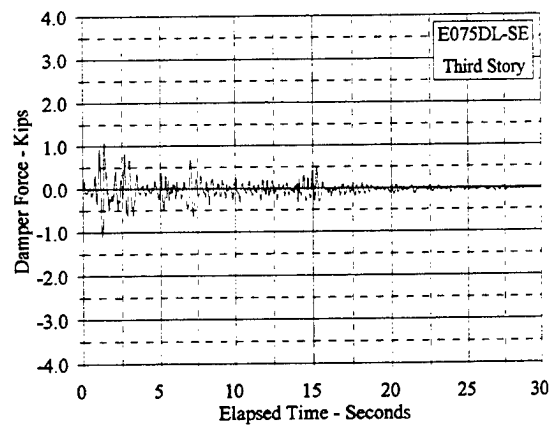
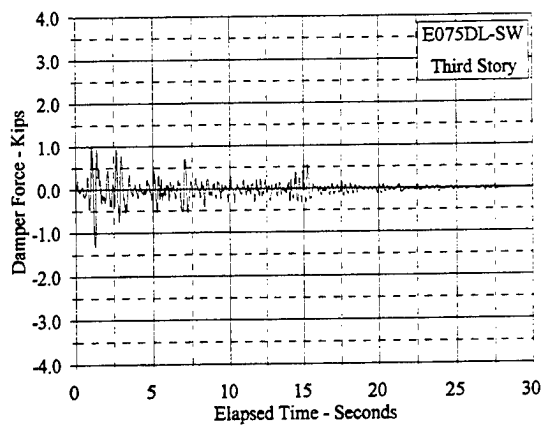


Figure C.8.8 Damper Force Vs. Elapsed Time: E075DL, SW and SE

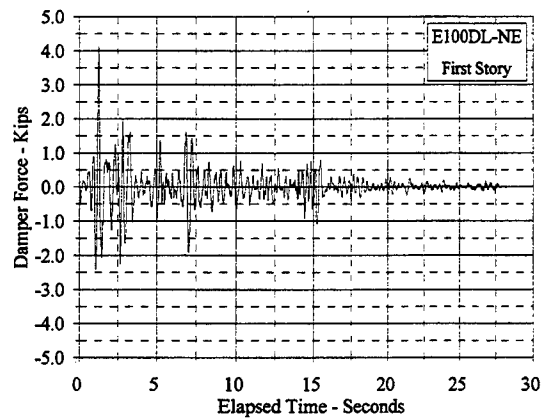
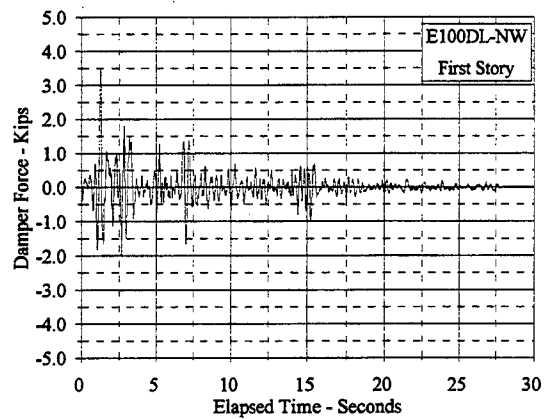
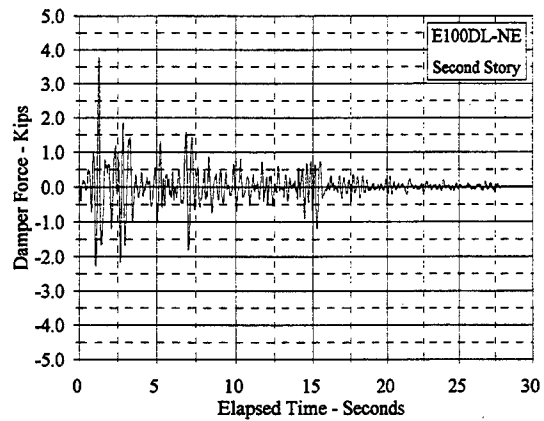
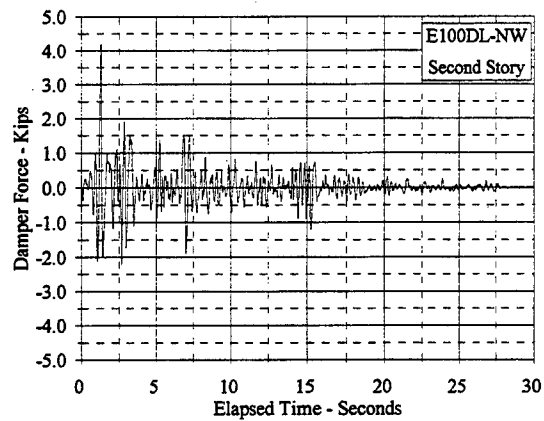
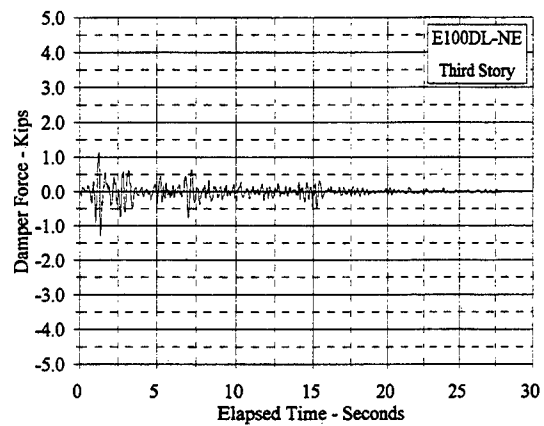
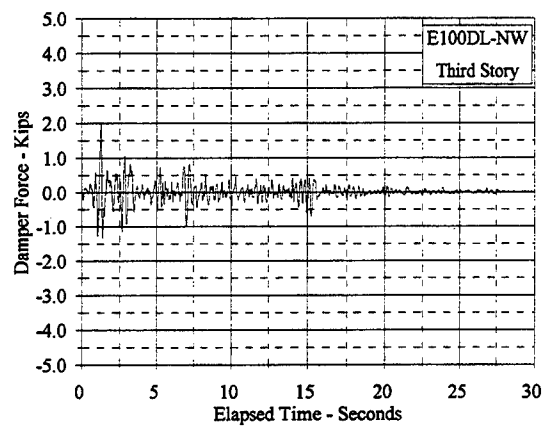


Figure C.8.9 Damper Force Vs. Elapsed Time: E100DL, NW and NE

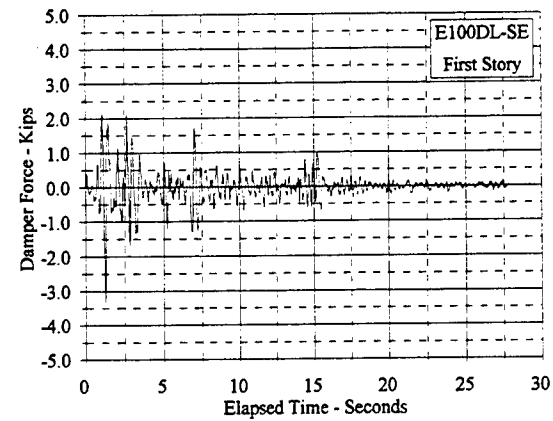
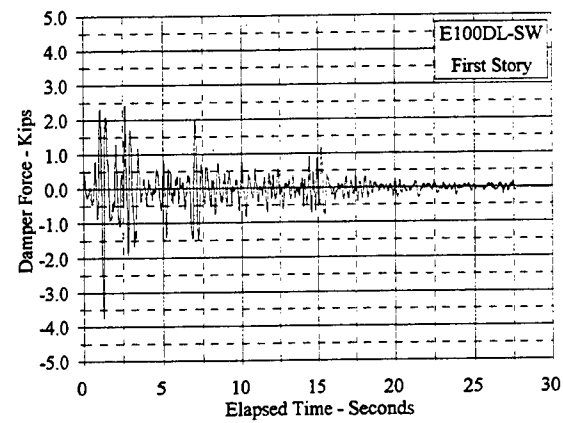
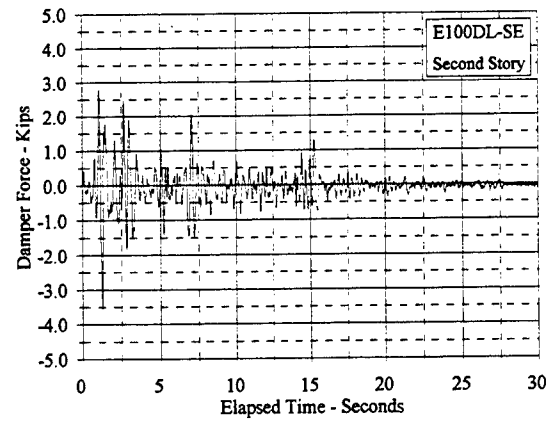
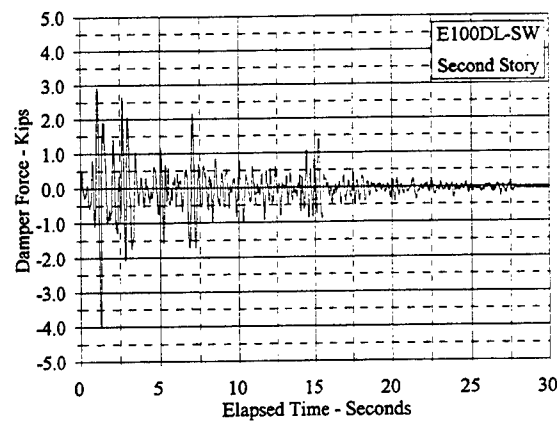
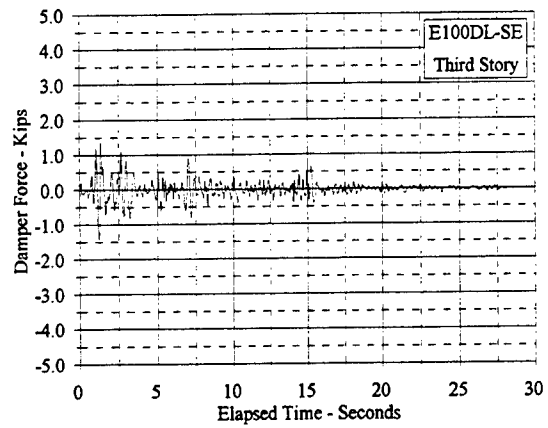
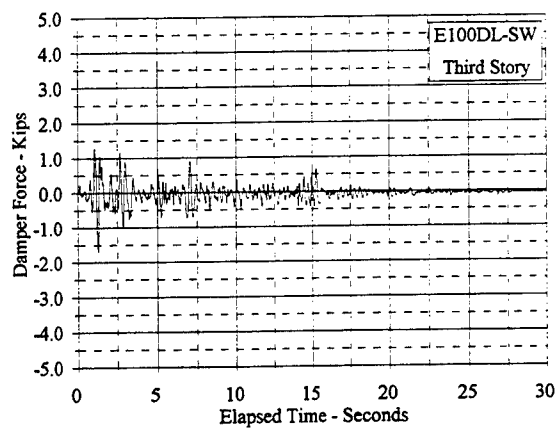


Figure C.8.10 Damper Force Vs. Elapsed Time: E100DL, SW and SE

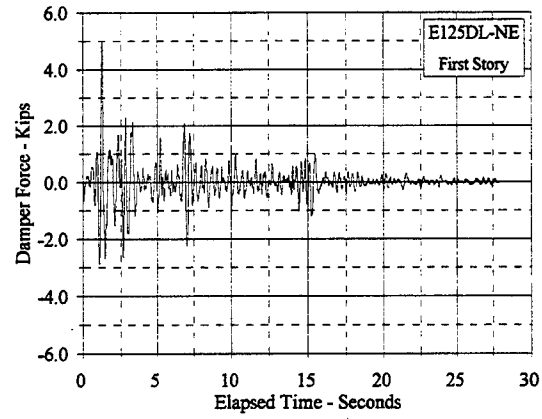
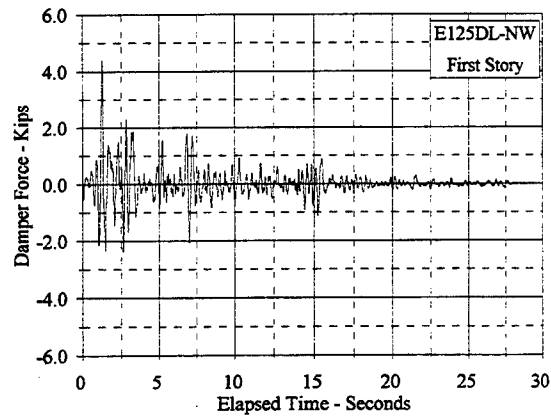
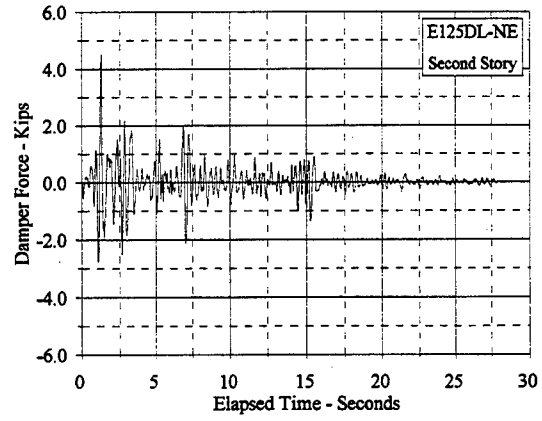
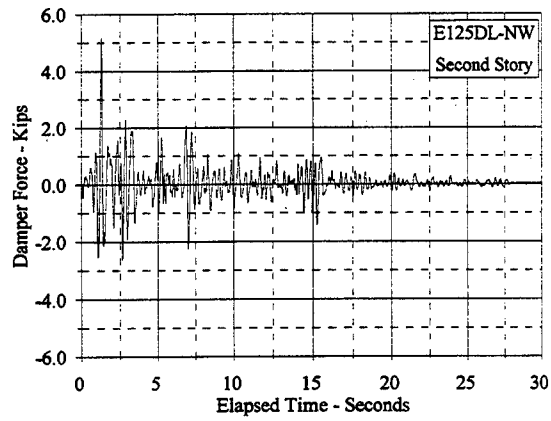
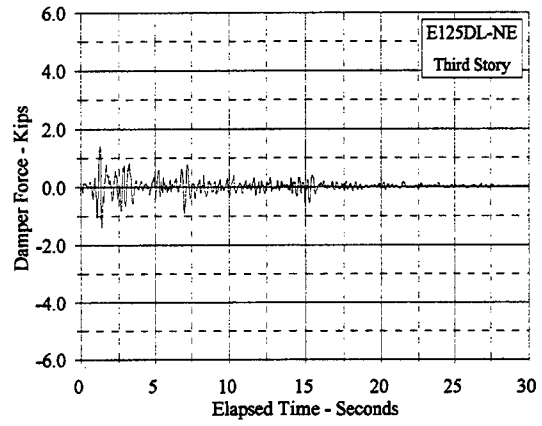
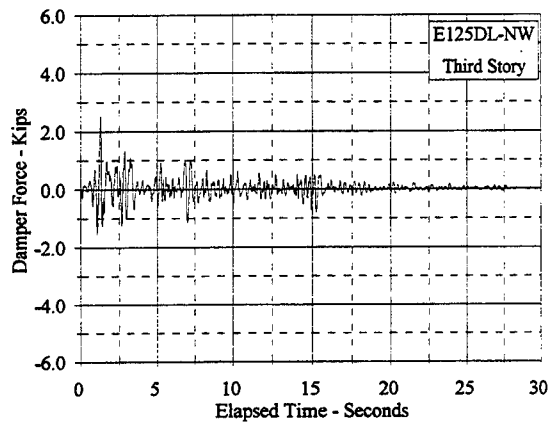


Figure C.8.11 Damper Force Vs. Elapsed Time: E125DL, NW and NE

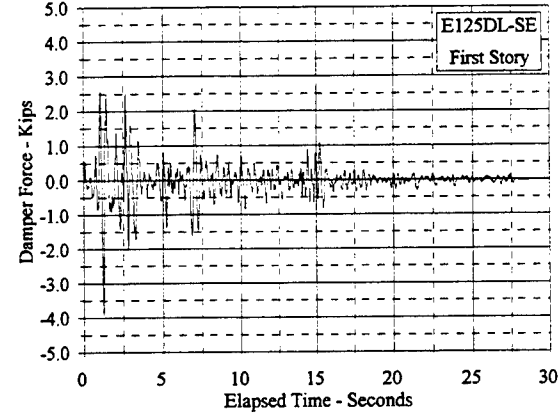
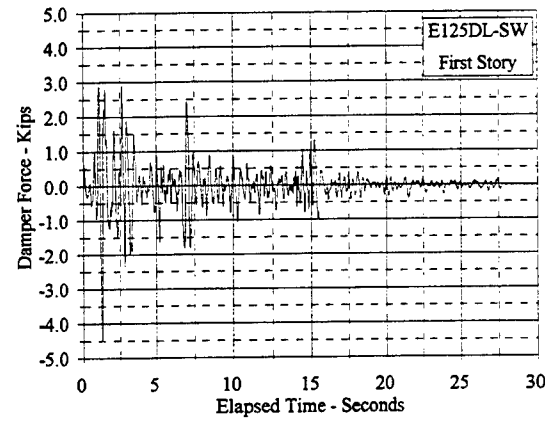
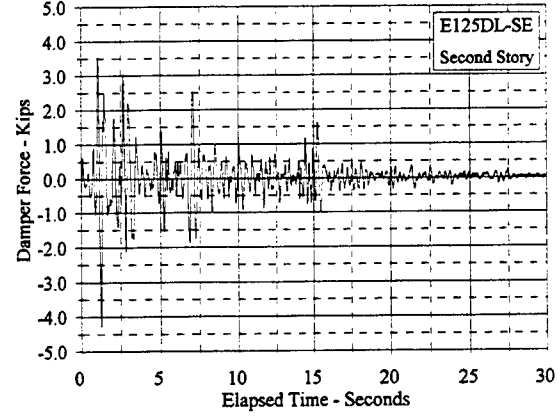
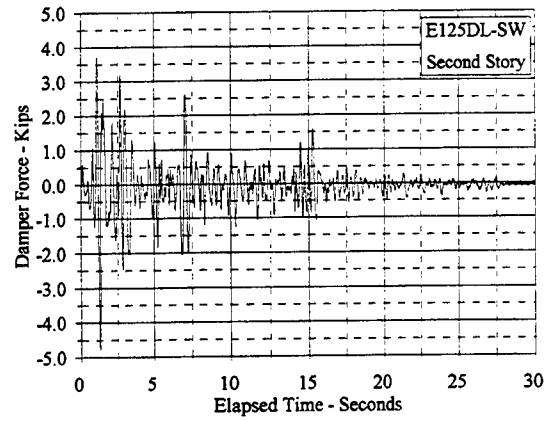
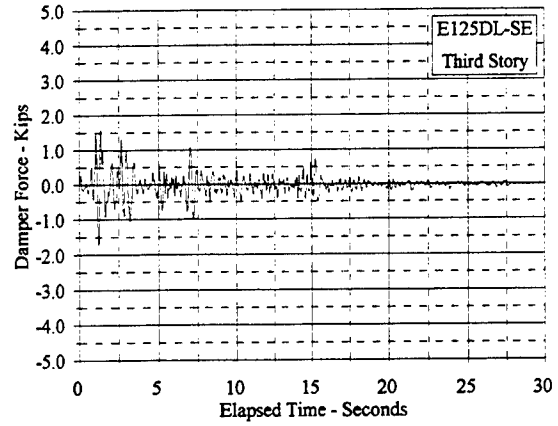
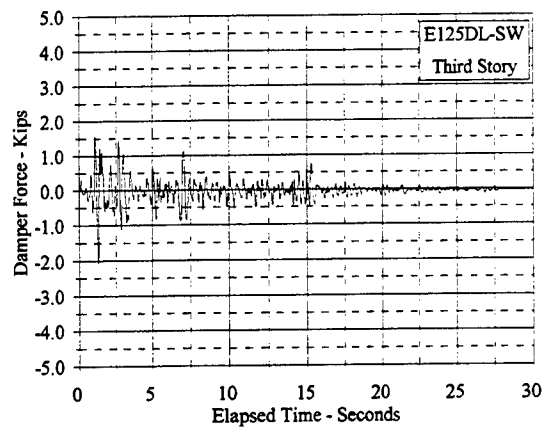


Figure C.8.12 Damper Force Vs. Elapsed Time: E125DL, SW and SE

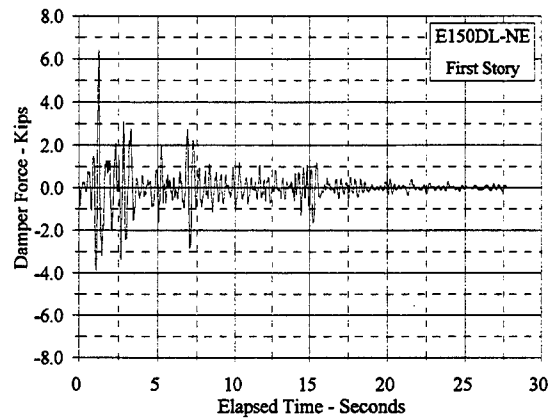
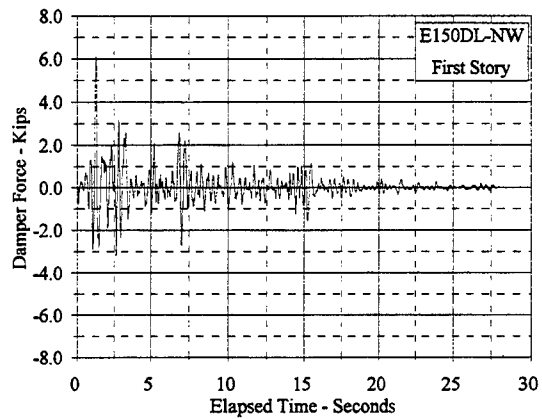
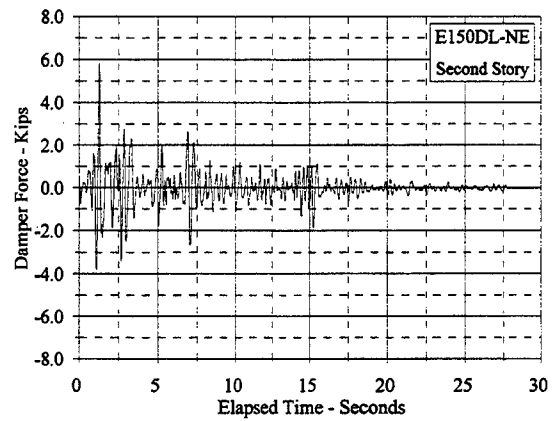
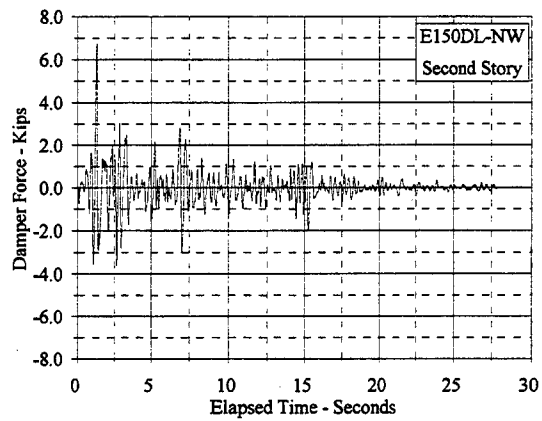
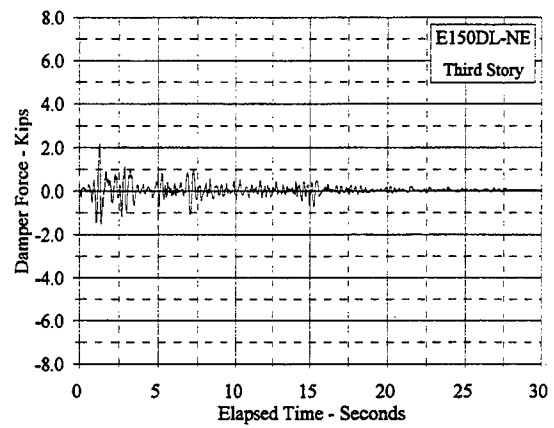
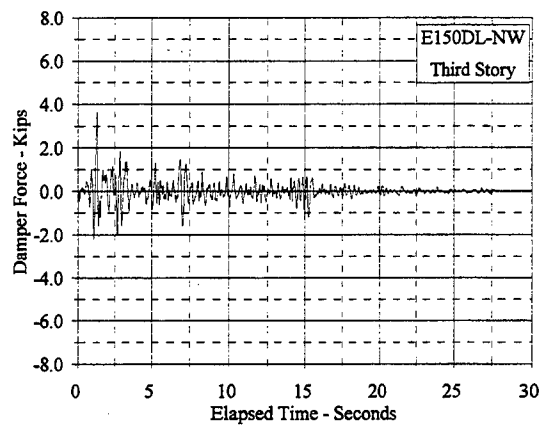


Figure C.8.13 Damper Force Vs. Elapsed Time: E150DL, NW and NE

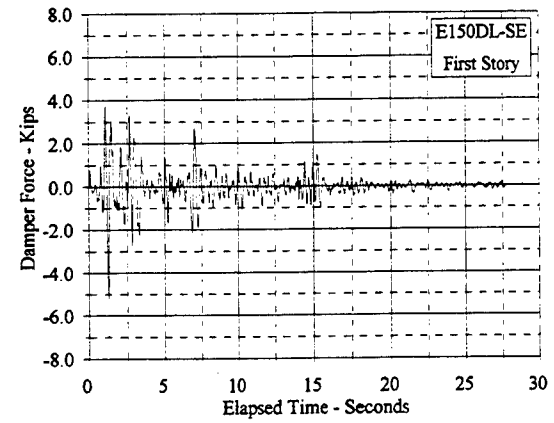
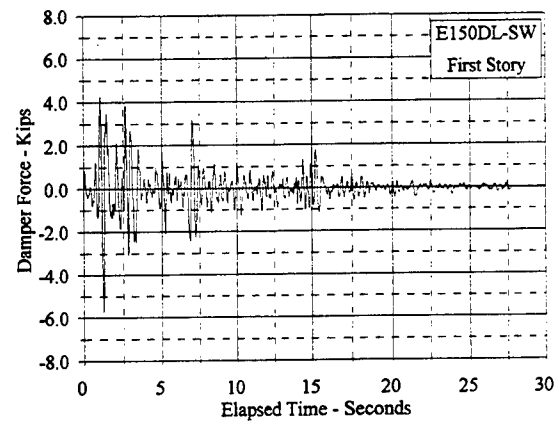
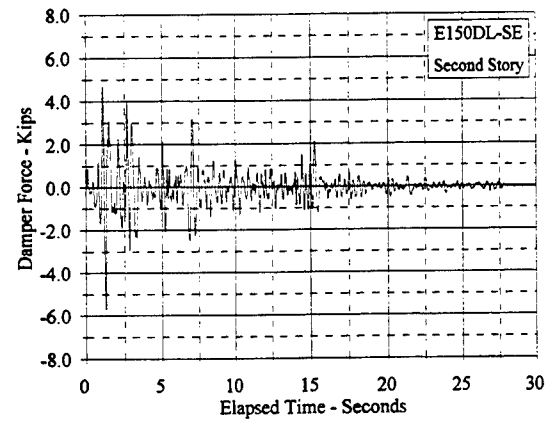
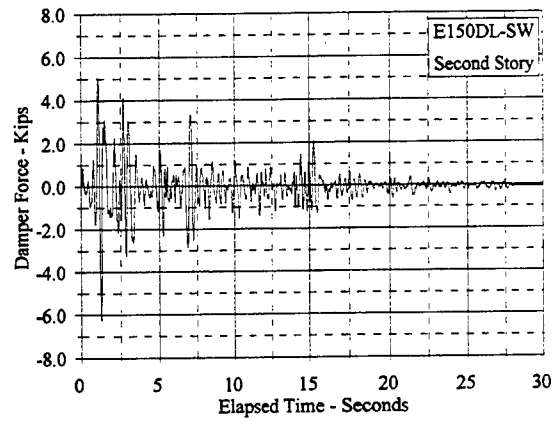
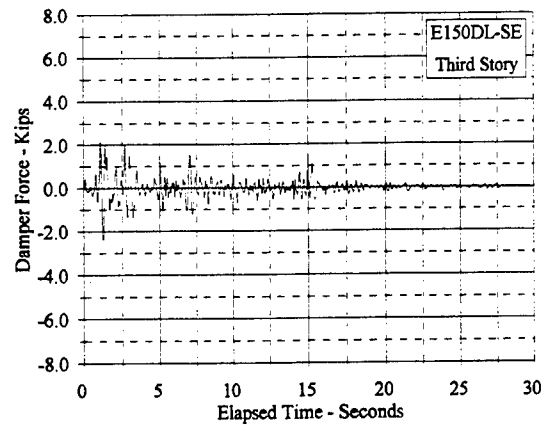
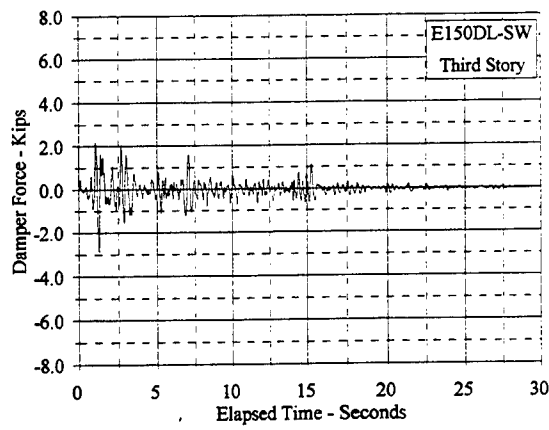


Figure C.8.14 Damper Force Vs. Elapsed Time: E150DL, SW and SE

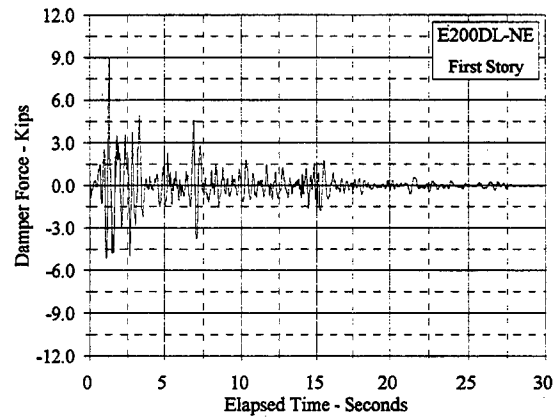
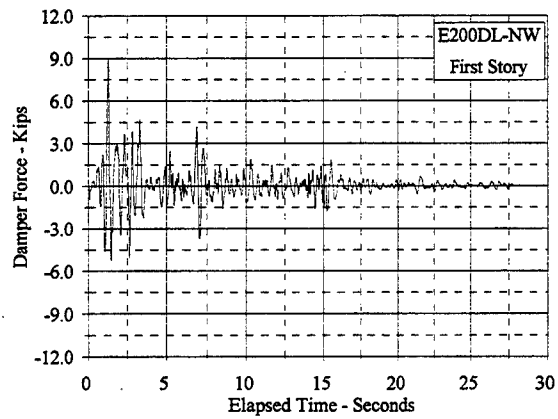
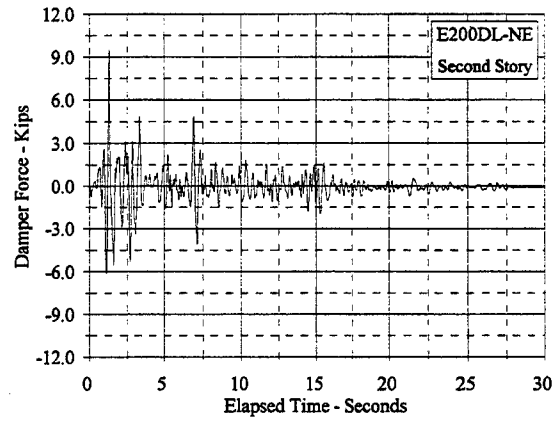
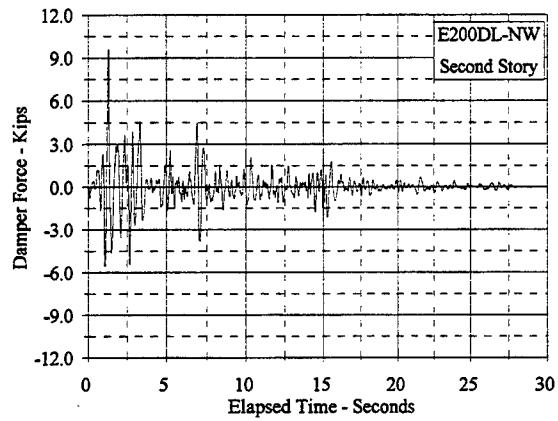
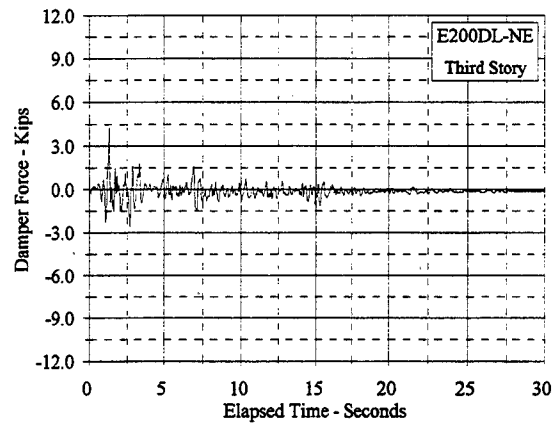
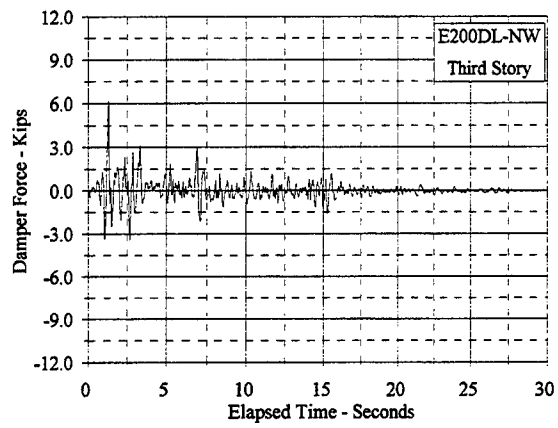


Figure C.8.15 Damper Force Vs. Elapsed Time: E200DL, NW and NE

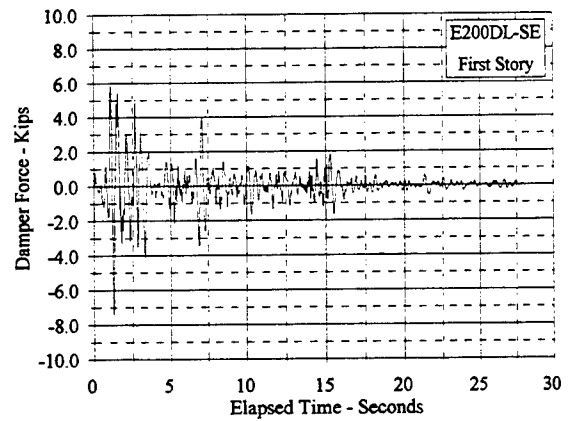
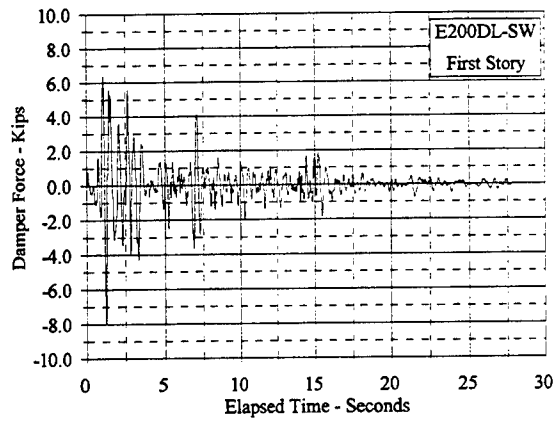
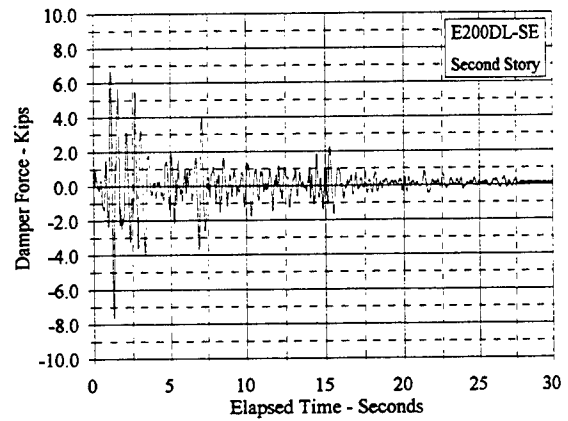
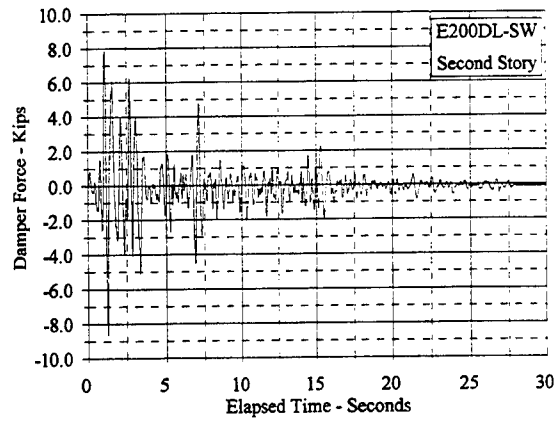
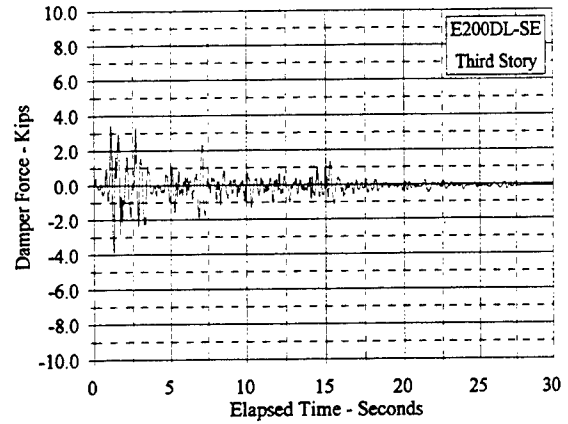
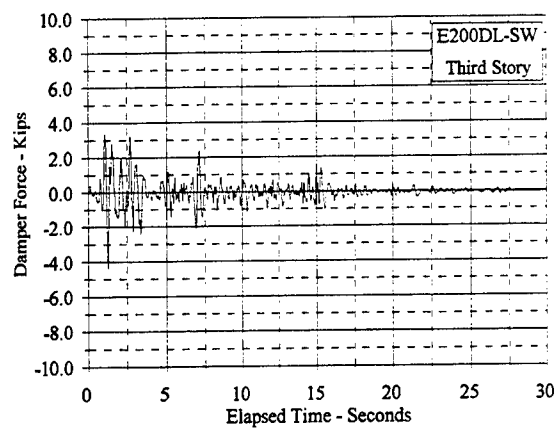


Figure C.8.16 Damper Force Vs. Elapsed Time: E200DL, SW and SE

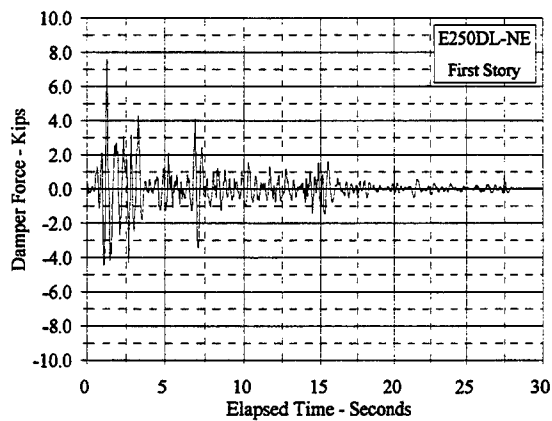
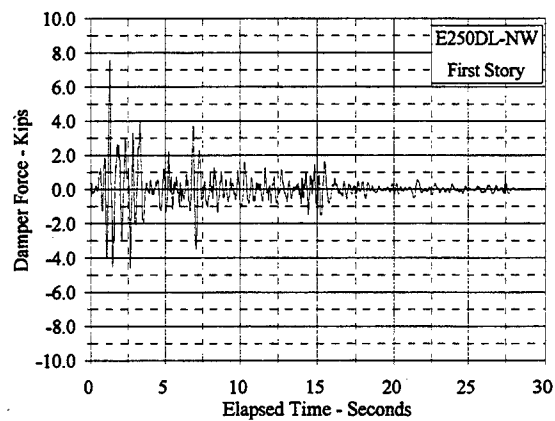
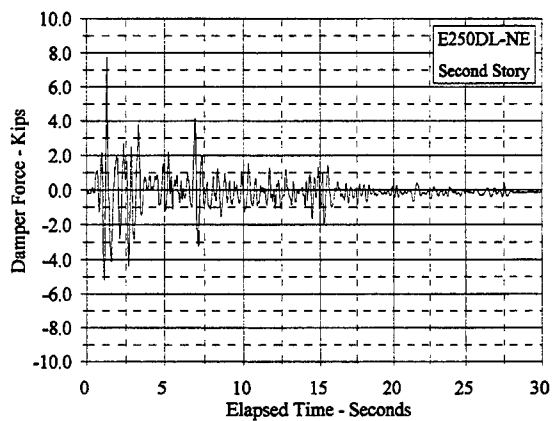
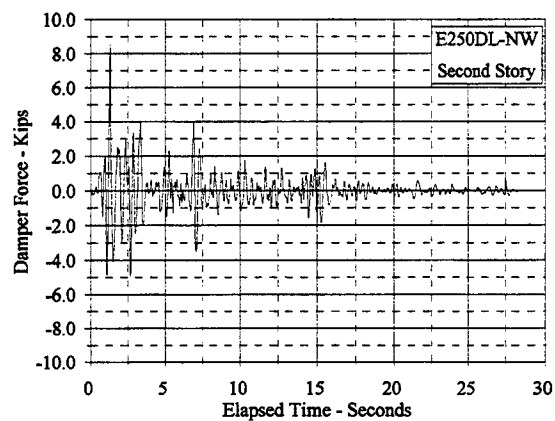
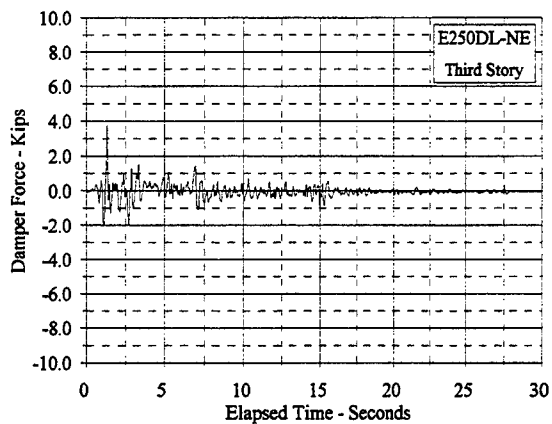
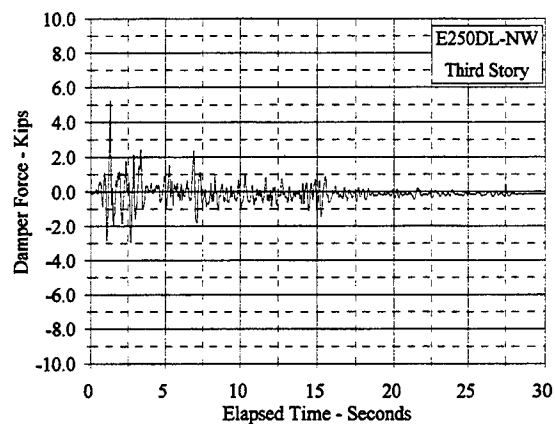


Figure C.8.17 Damper Force Vs. Elapsed Time: E250DL, NW and NE

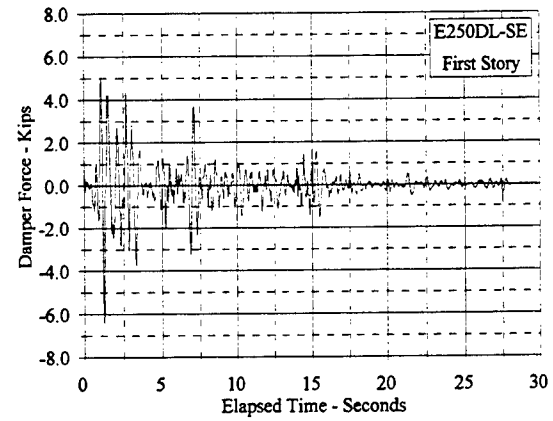
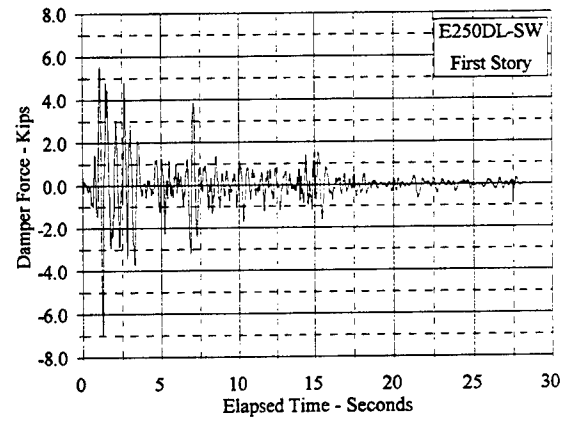
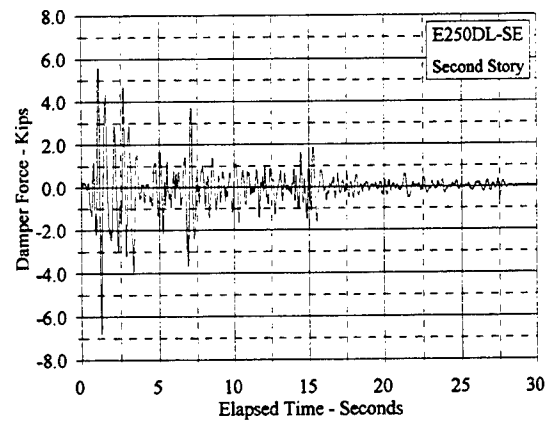
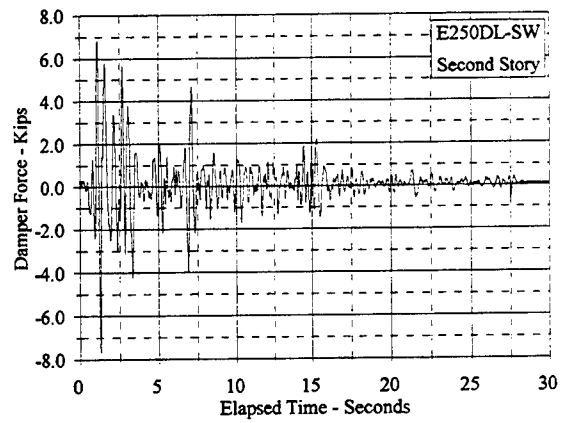
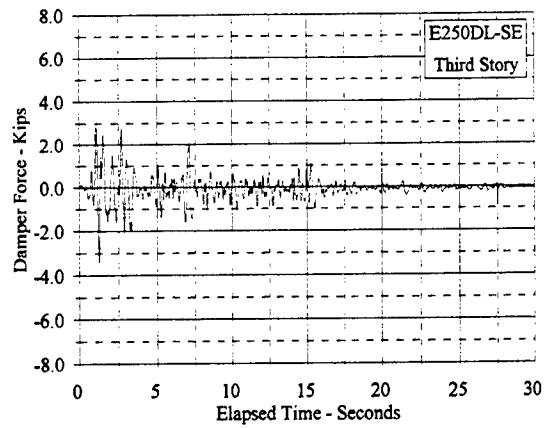
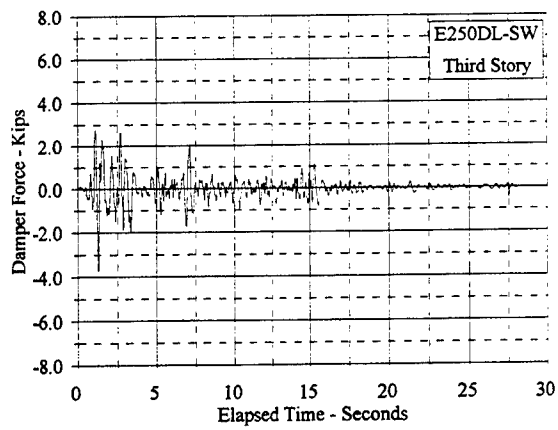


Figure C.8.18 Damper Force Vs. Elapsed Time: E250DL, SW and SE

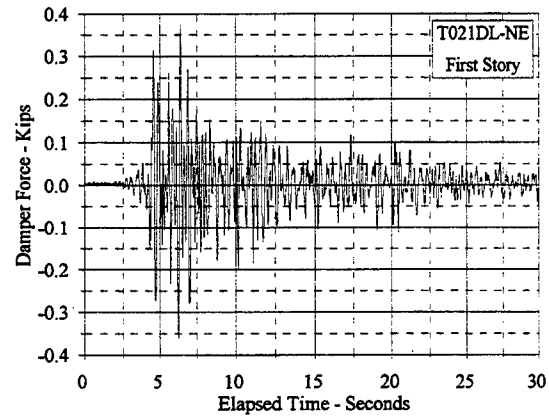
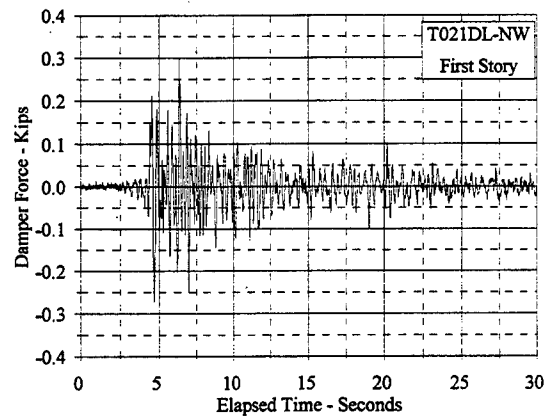
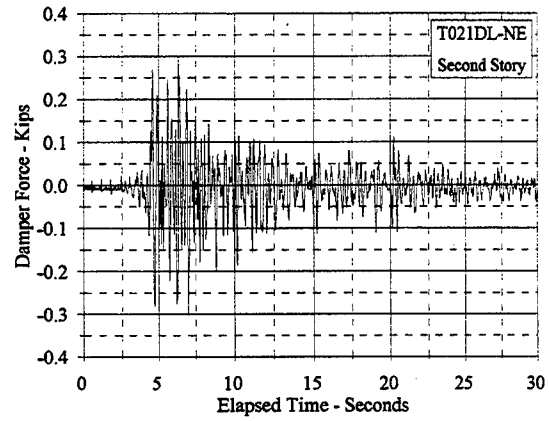
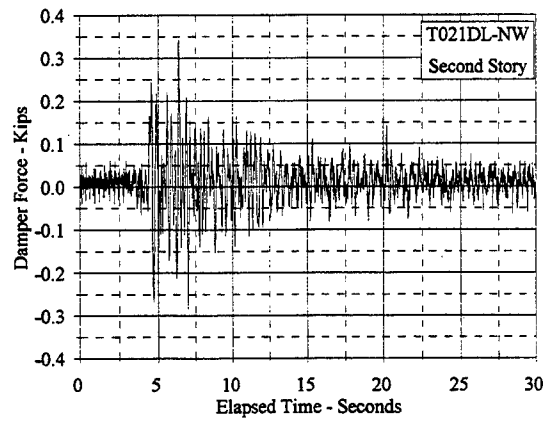
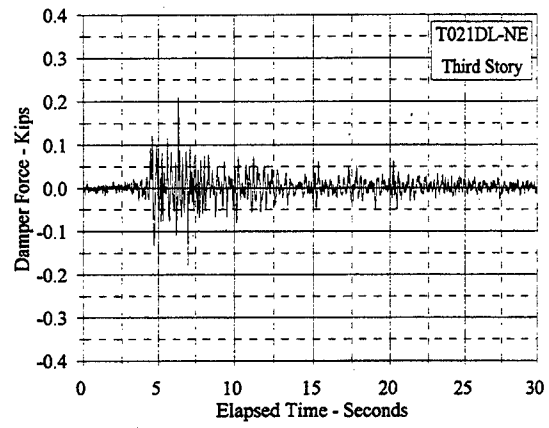
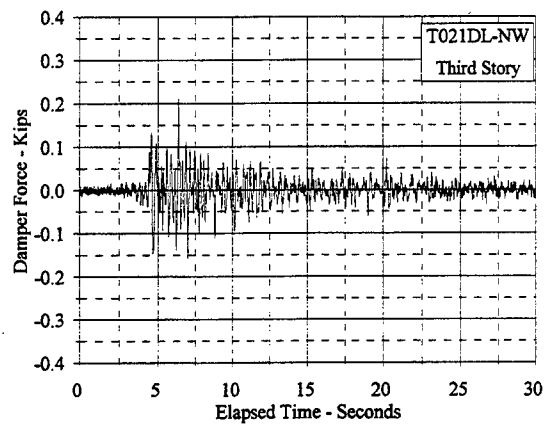


Figure C.8.19 Damper Force Vs. Elapsed Time: T021DL, NW and NE

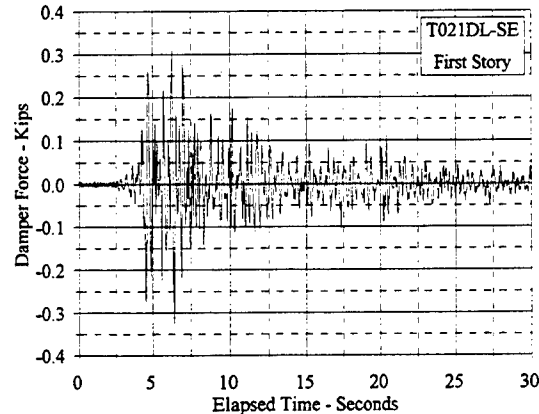
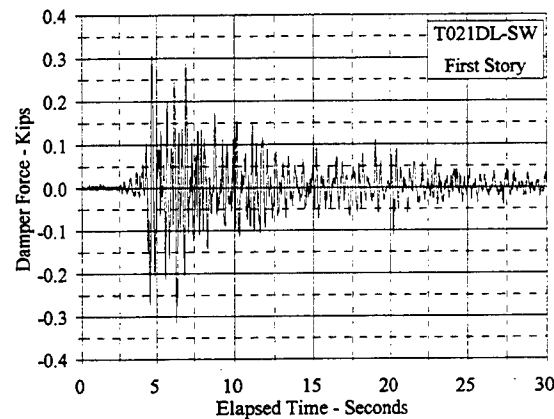
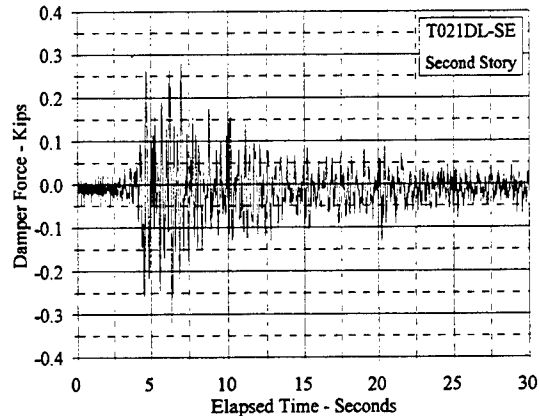
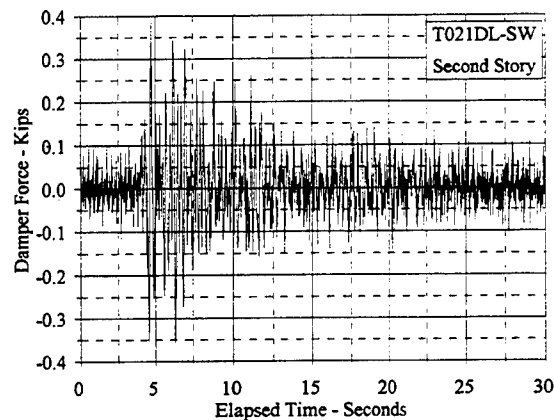
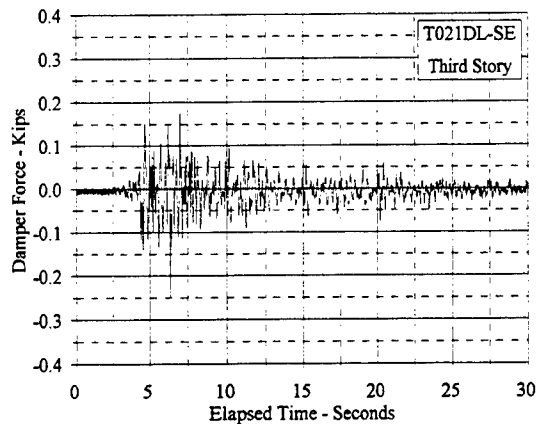
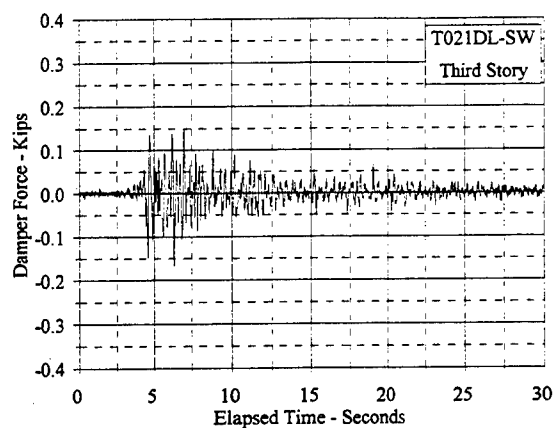


Figure C.8.20 Damper Force Vs. Elapsed Time: T021DL, SW and SE

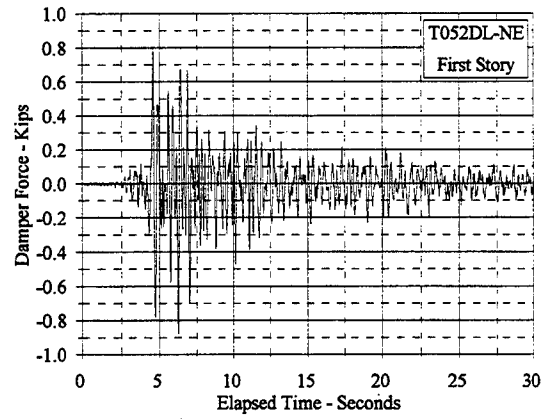
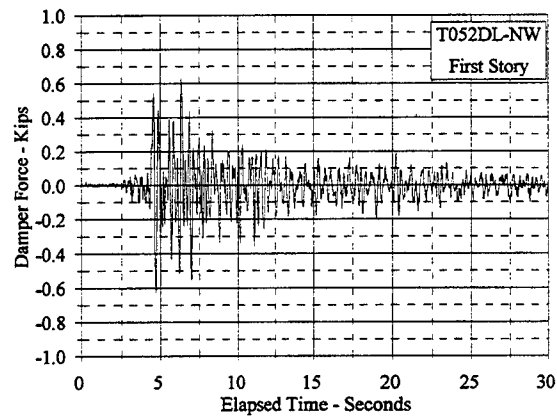
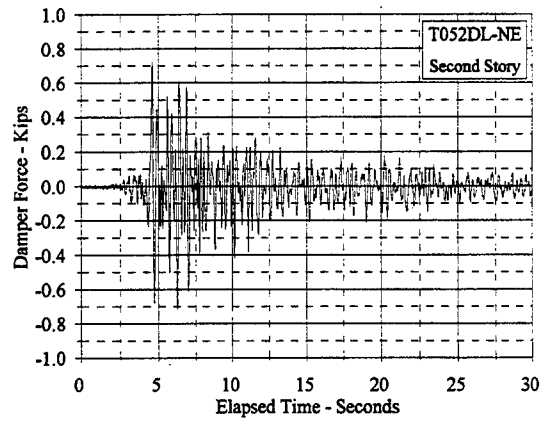
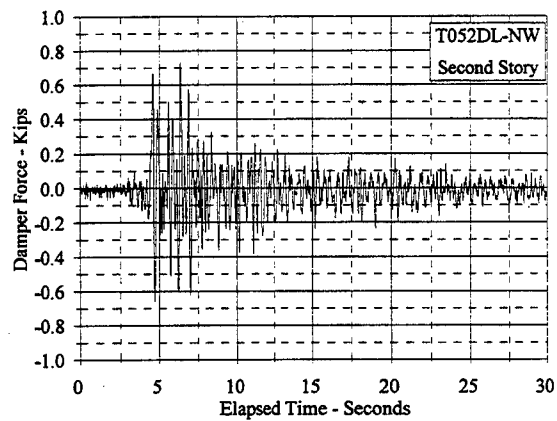
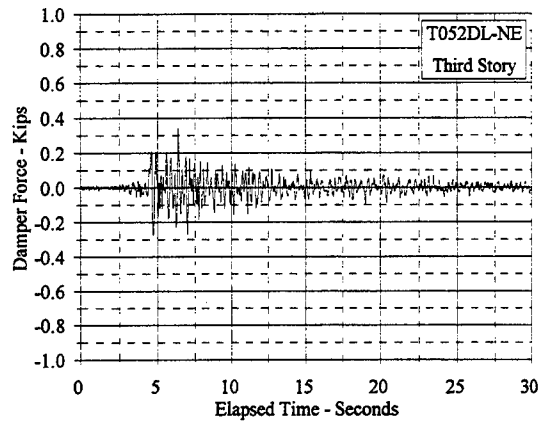
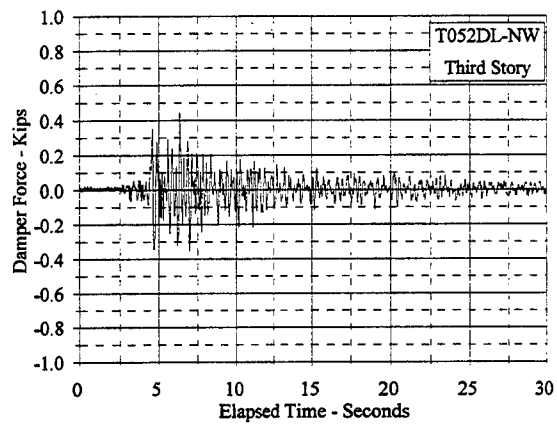


Figure C.8.21 Damper Force Vs. Elapsed Time: T052DL, NW and NE

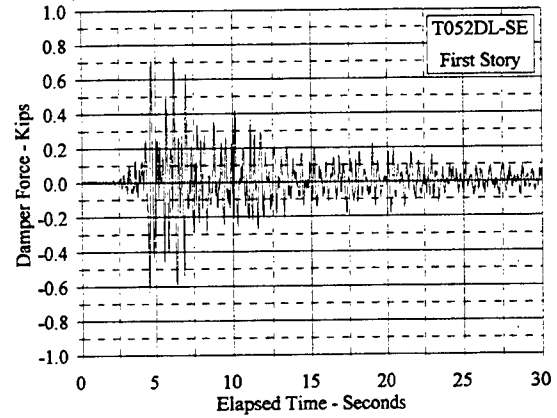
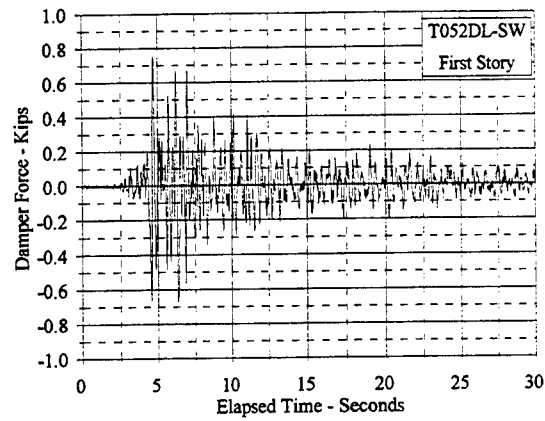
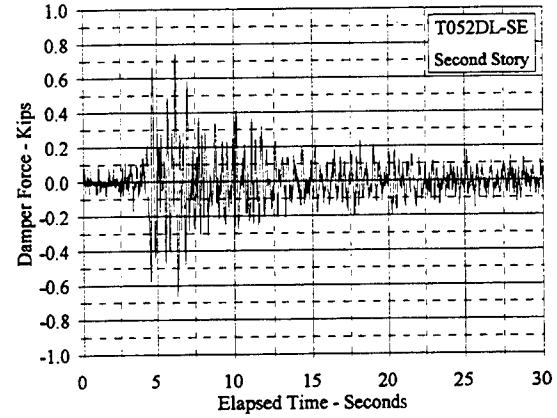
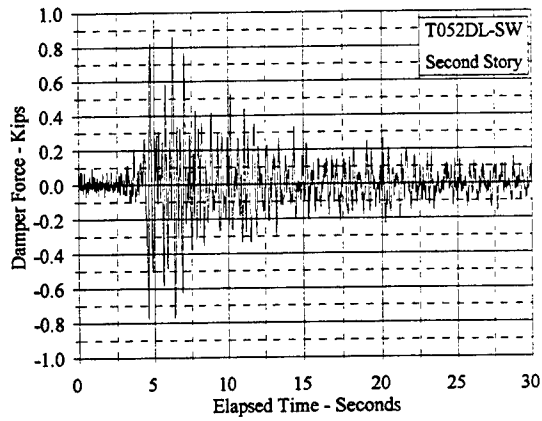
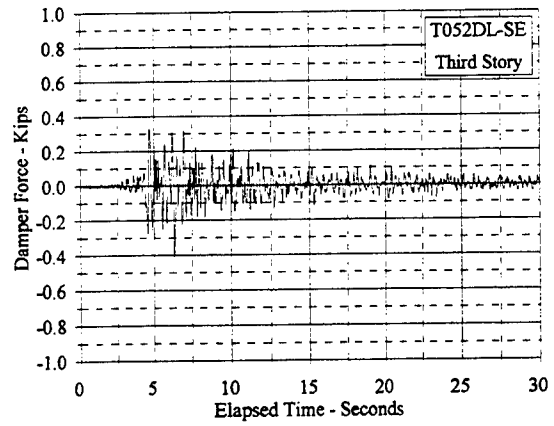
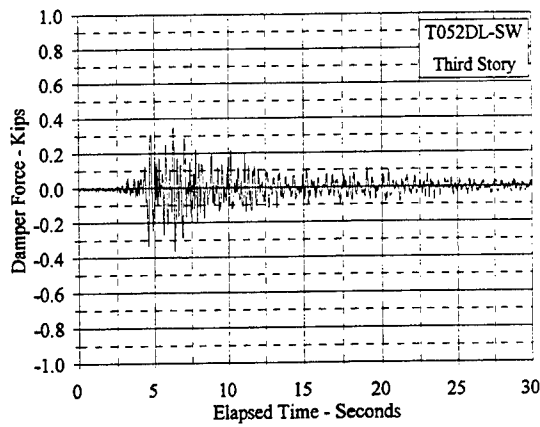


Figure C.8.22 Damper Force Vs. Elapsed Time: T052DL, SW and SE

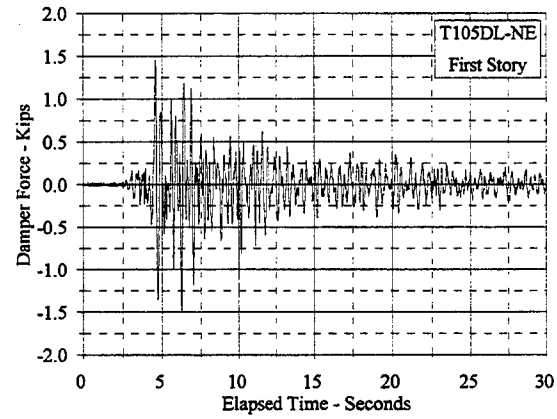
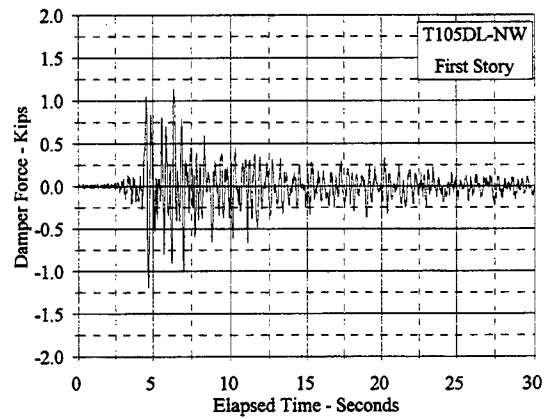
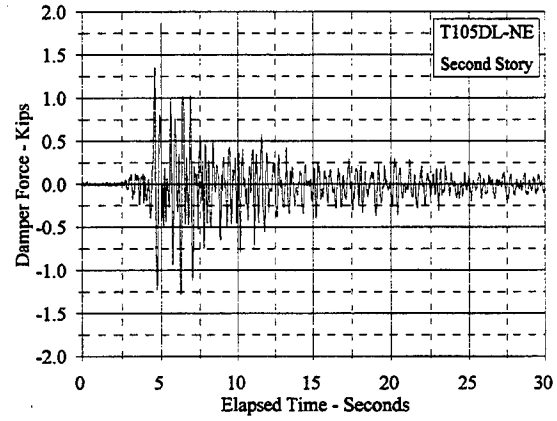
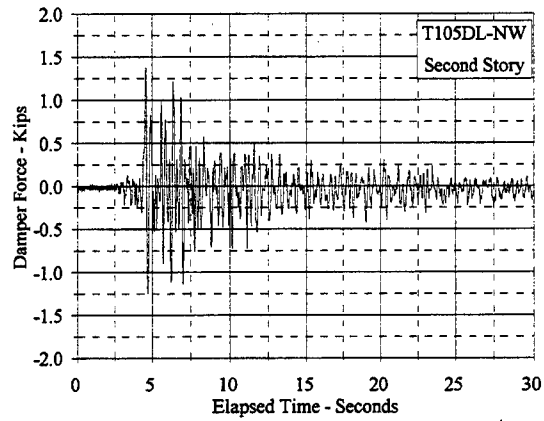
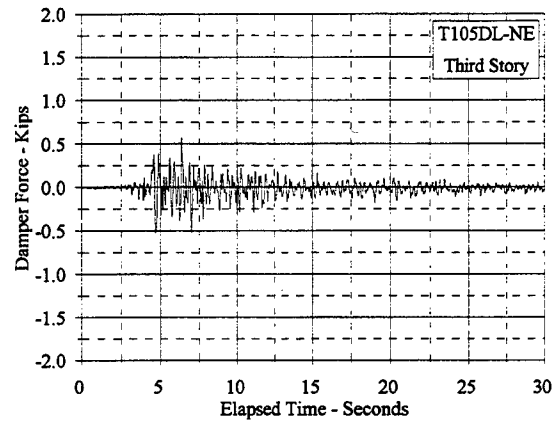
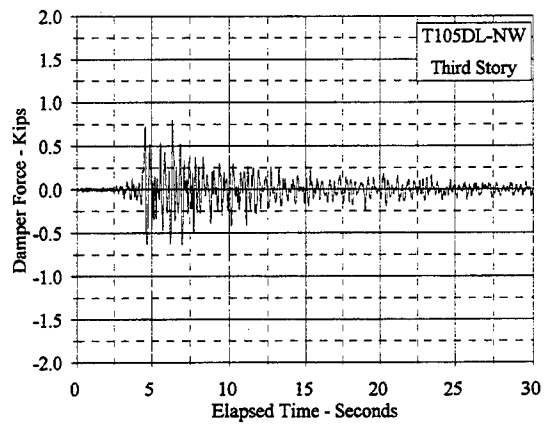


Figure C.8.23 Damper Force Vs. Elapsed Time: T105DL, NW and NE

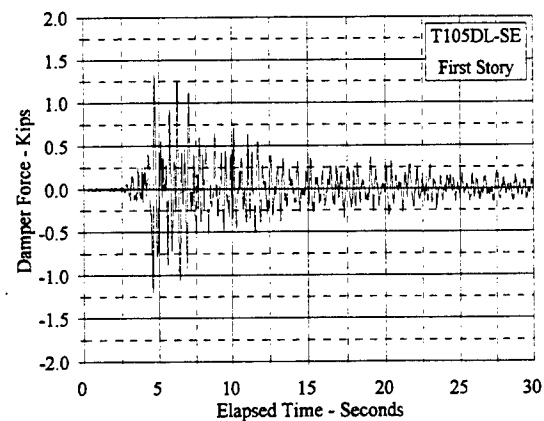
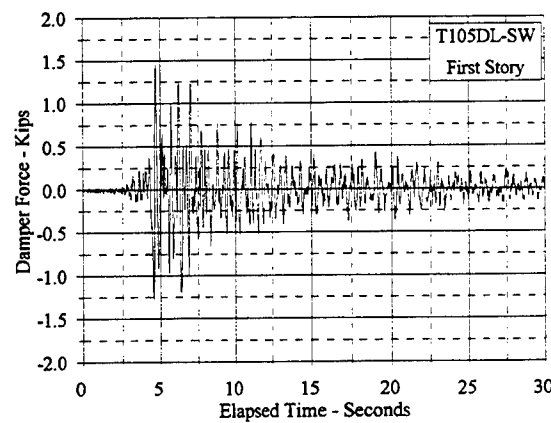
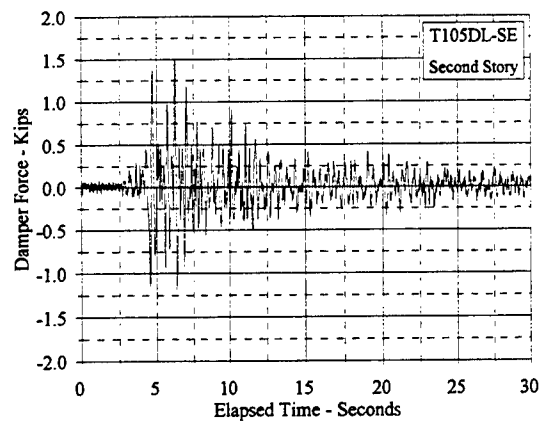
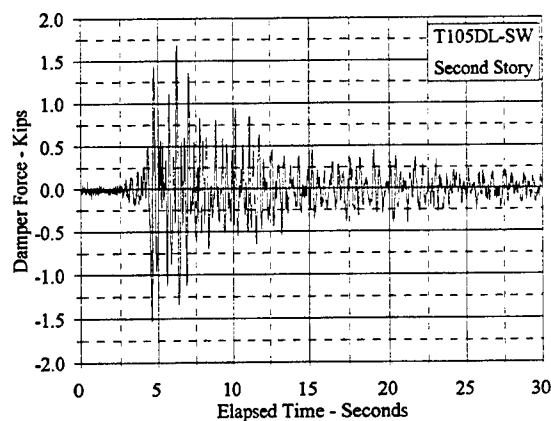
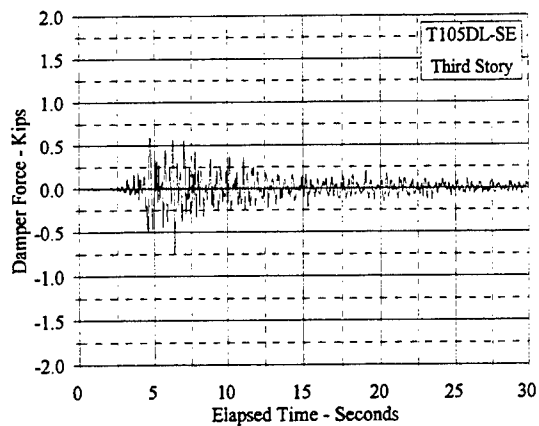
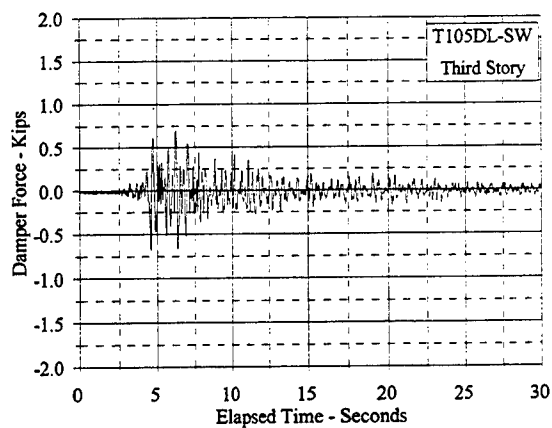


Figure C.8.24 Damper Force Vs. Elapsed Time: T105DL, SW and SE

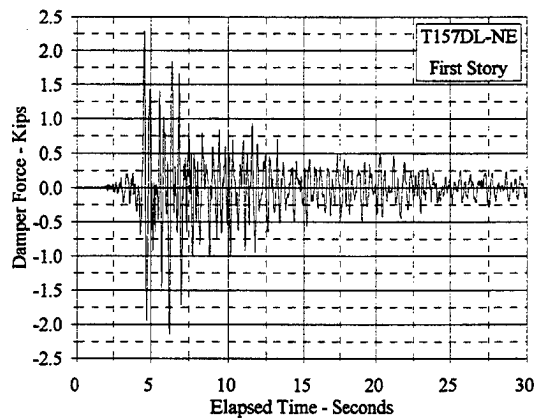
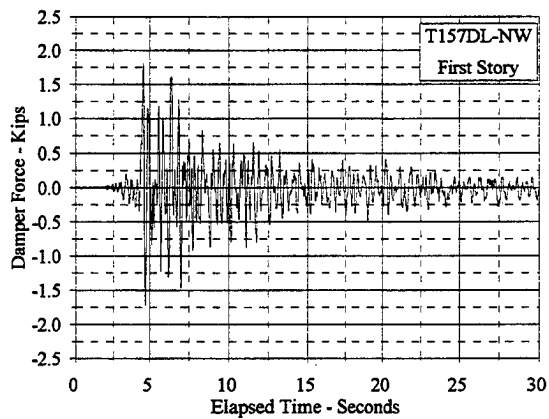
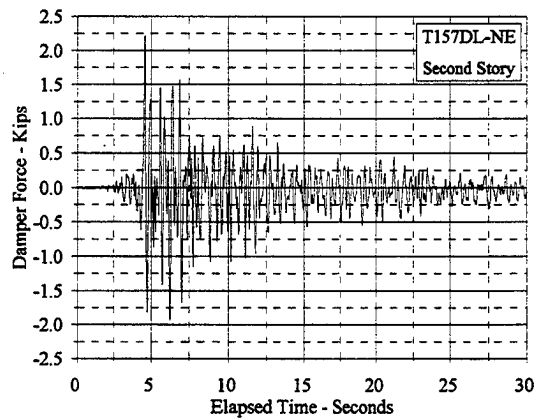
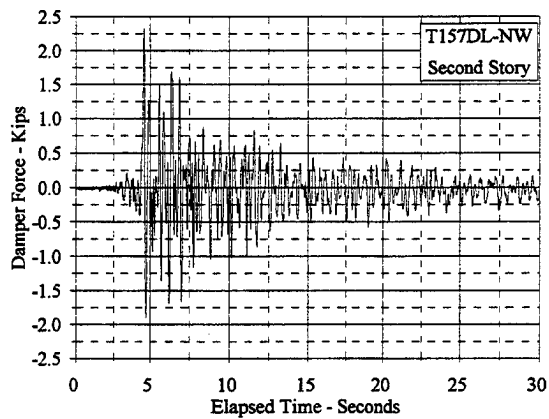
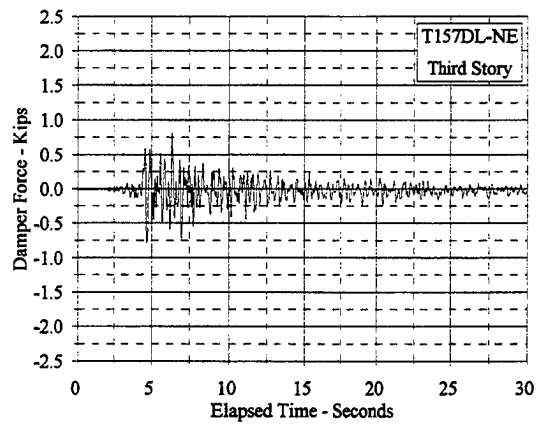
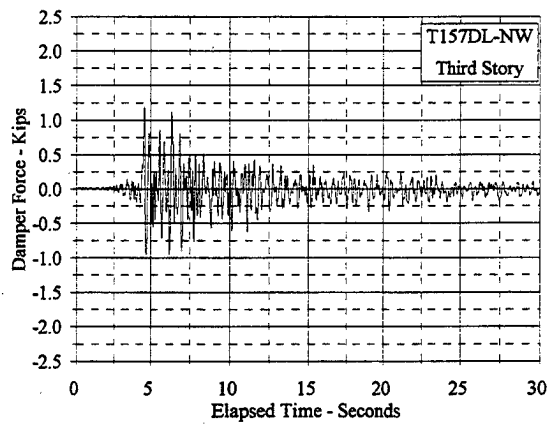


Figure C.8.25 Damper Force Vs. Elapsed Time: T157DL, NW and NE

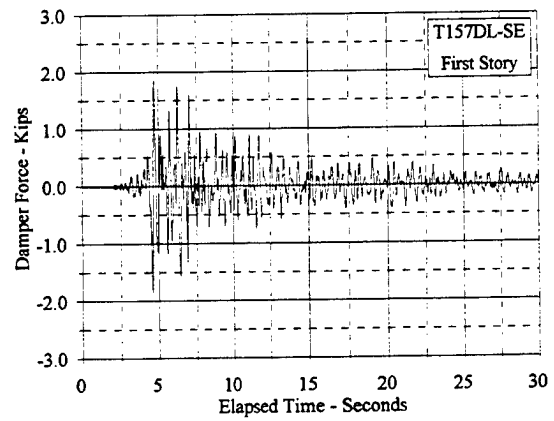
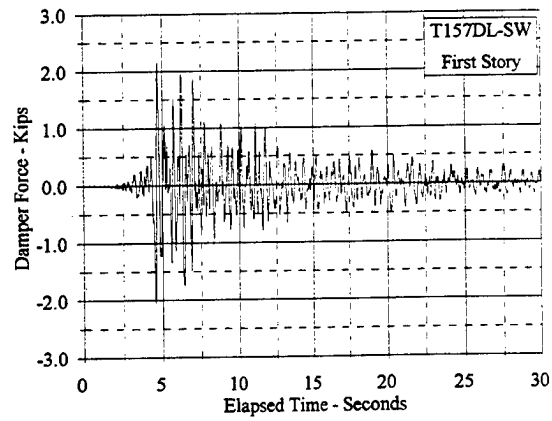
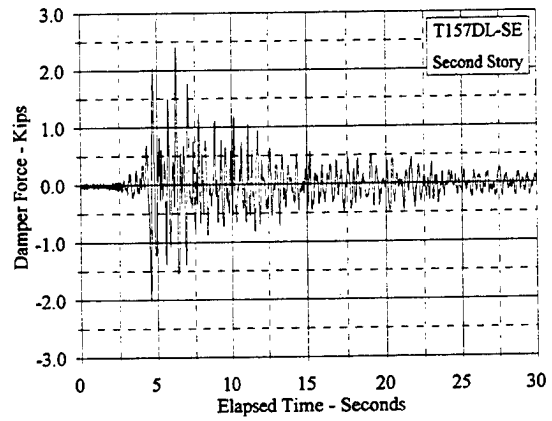
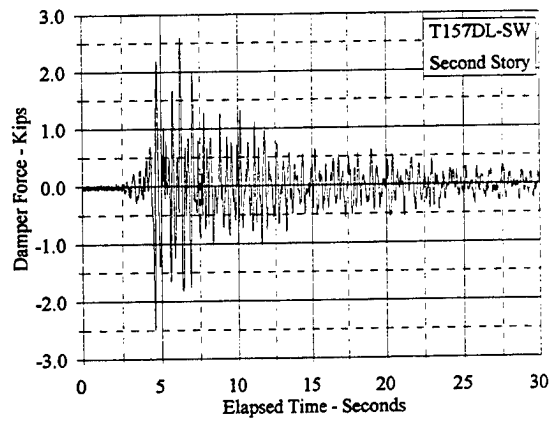
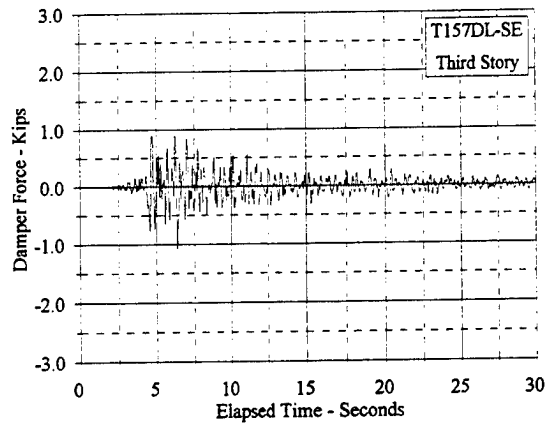
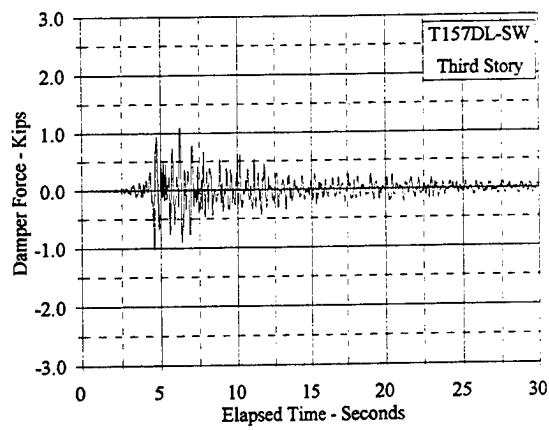


Figure C.8.26 Damper Force Vs. Elapsed Time: T157DL, SW and SE

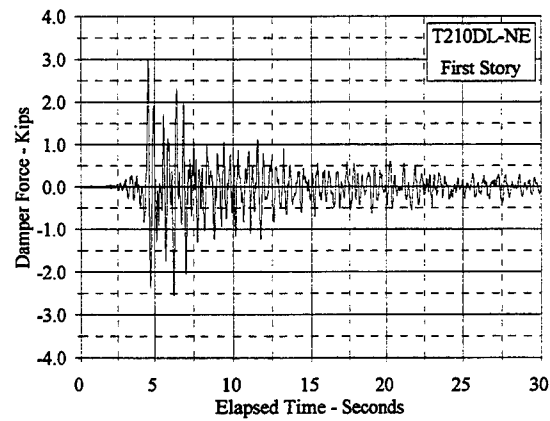
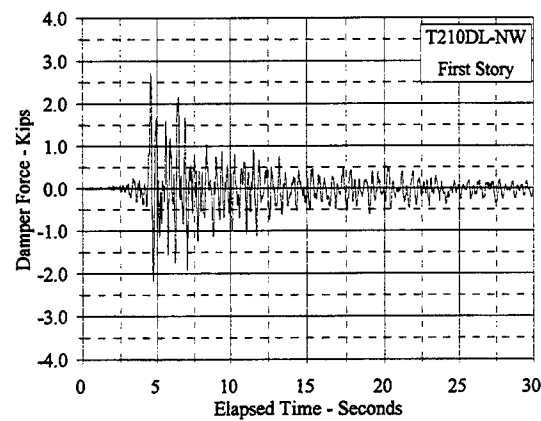
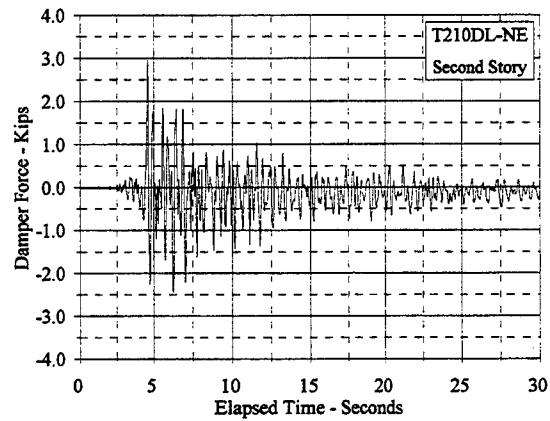
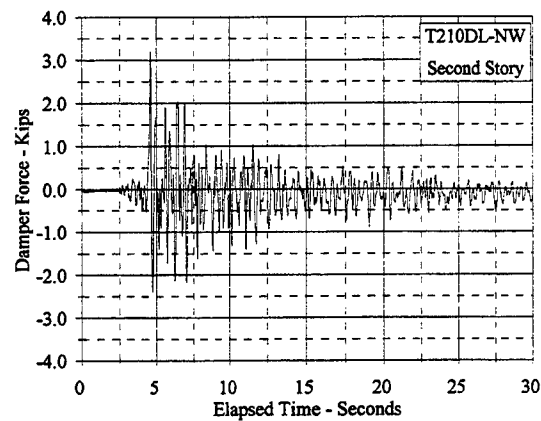
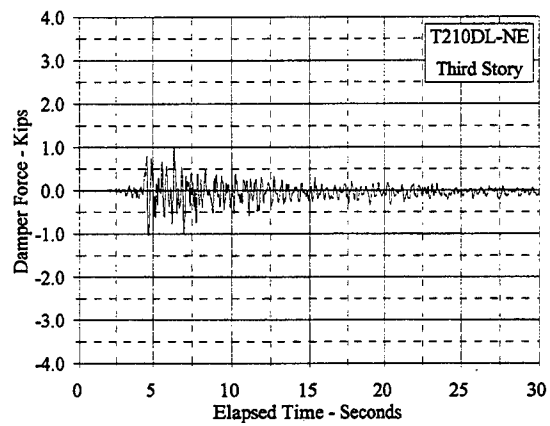
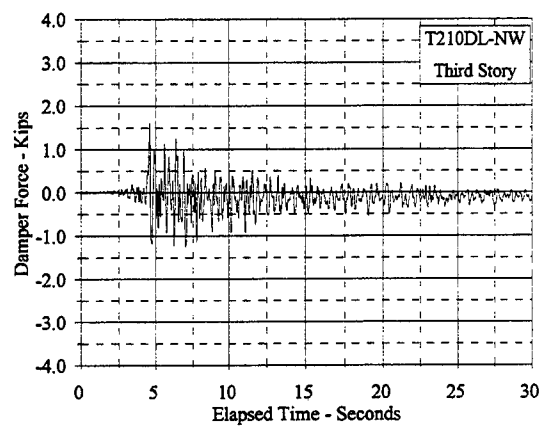


Figure C.8.27 Damper Force Vs. Elapsed Time: T210DL, NW and NE

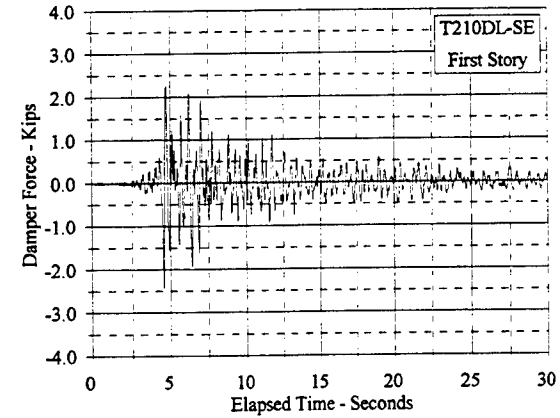
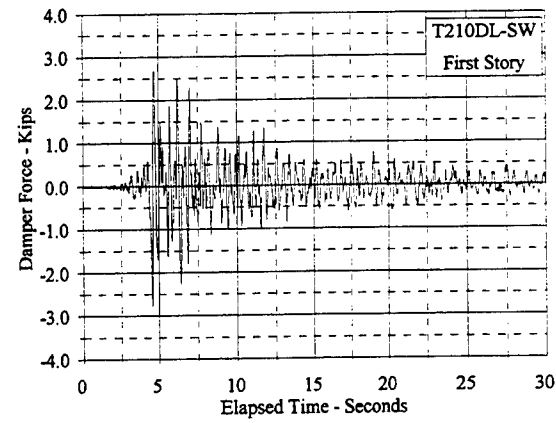
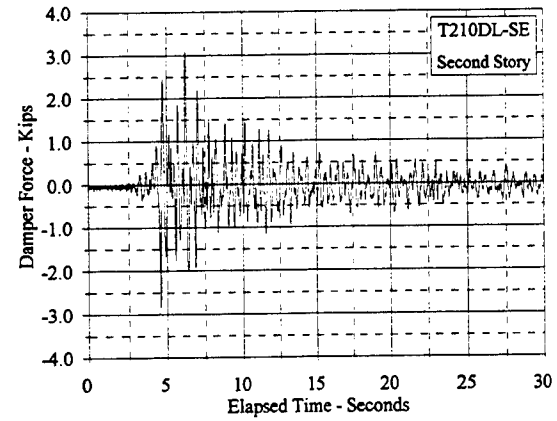
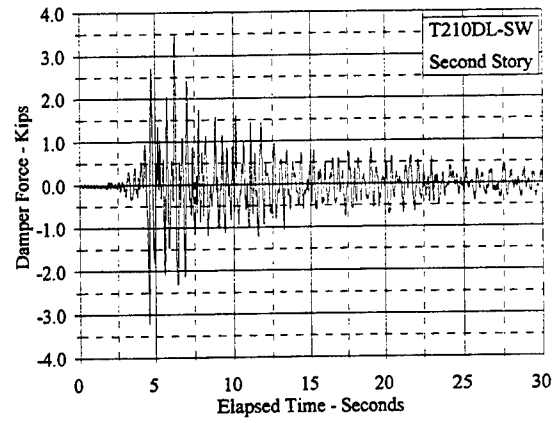
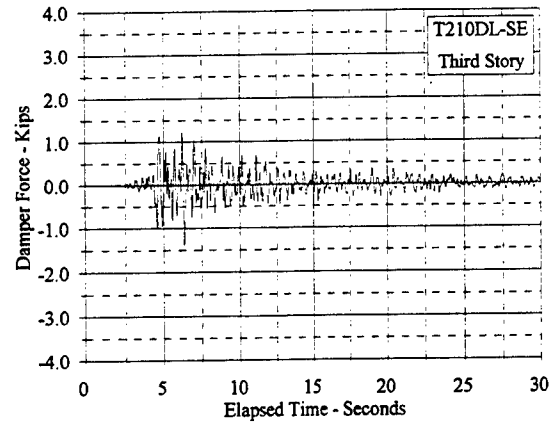
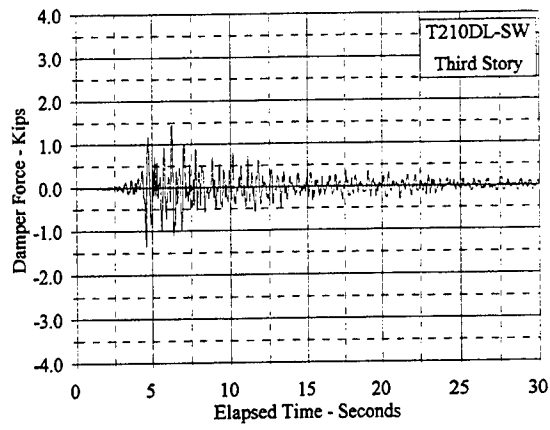


Figure C.8.28 Damper Force Vs. Elapsed Time: T210DL, SW and SE

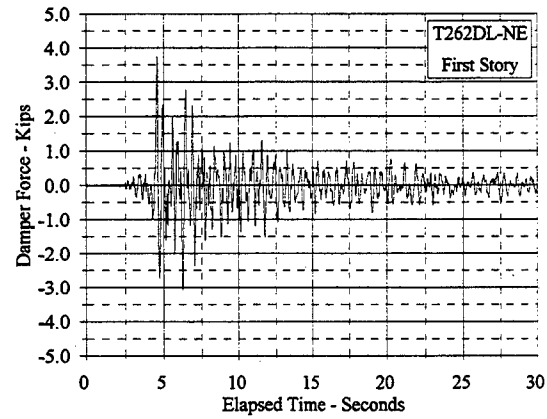
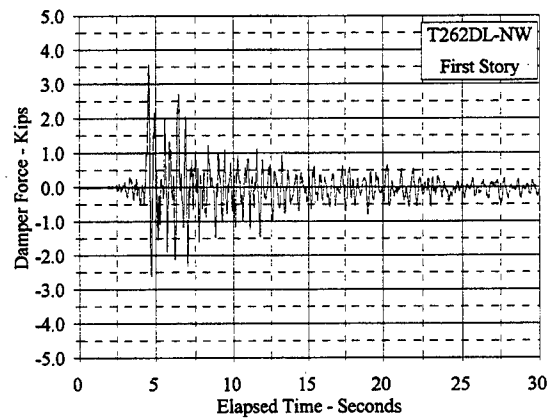
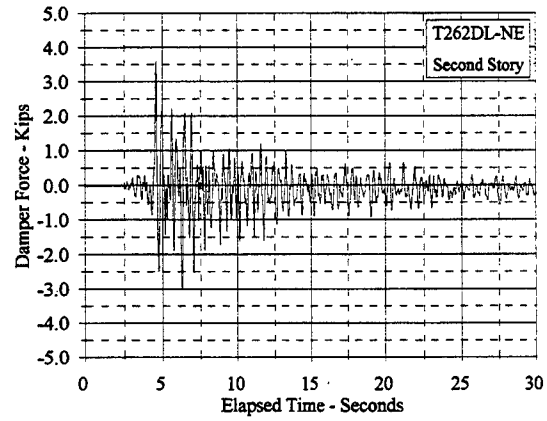
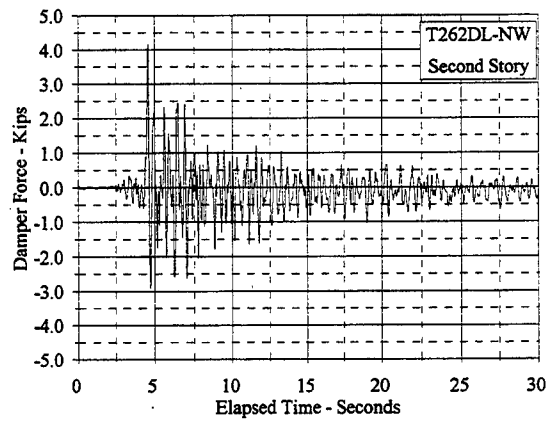
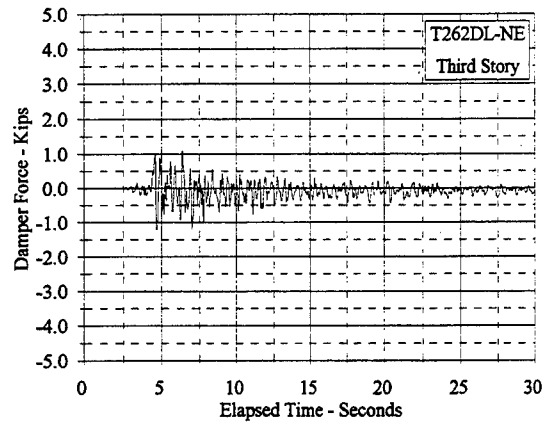
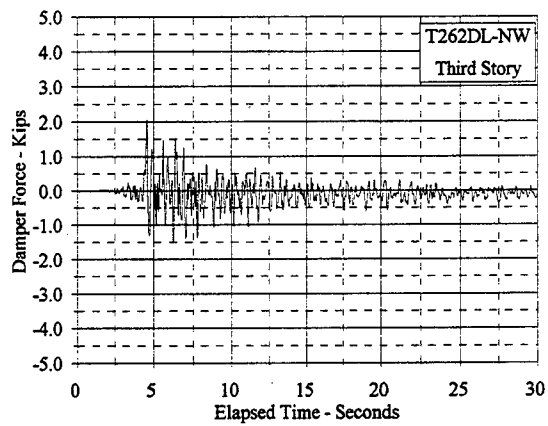


Figure C.8.29 Damper Force Vs. Elapsed Time: T262DL, NW and NE

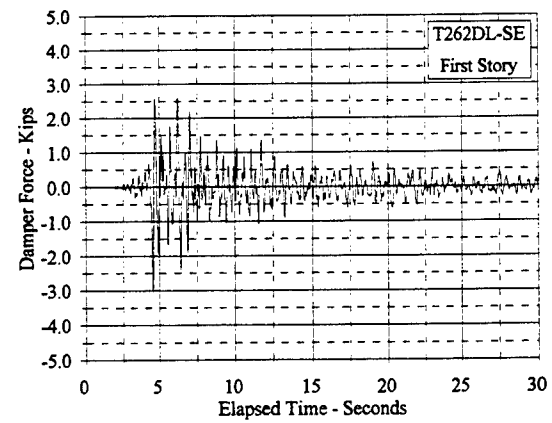
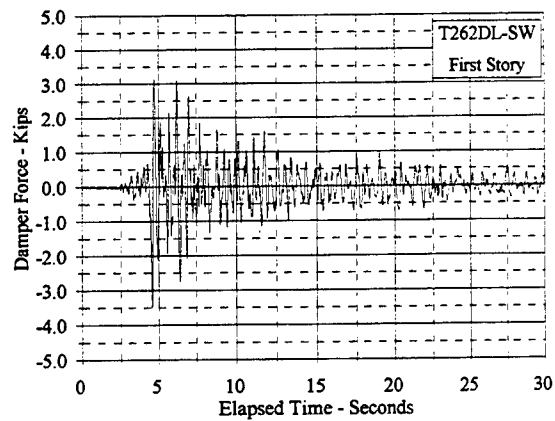
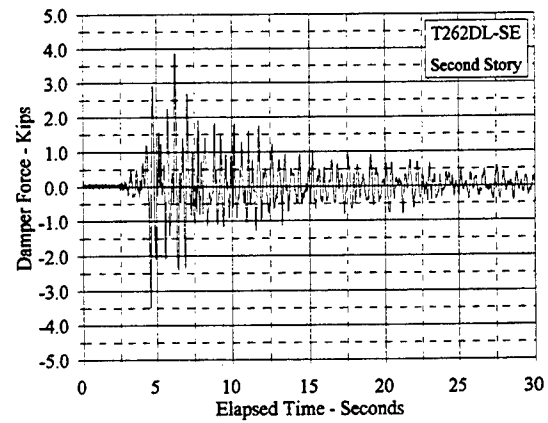
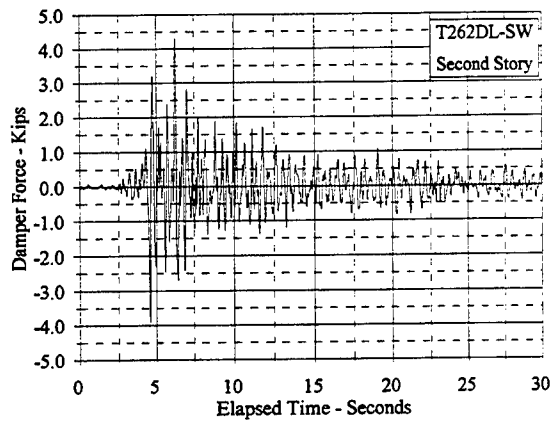
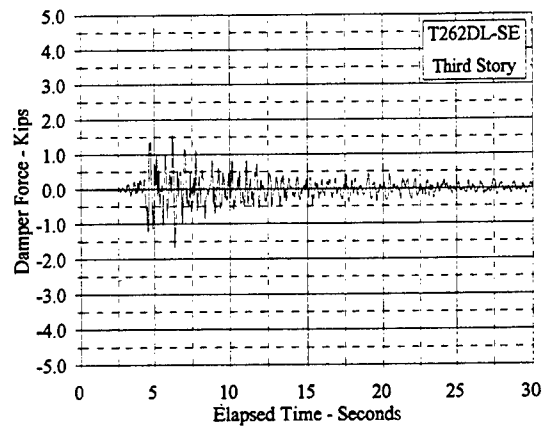
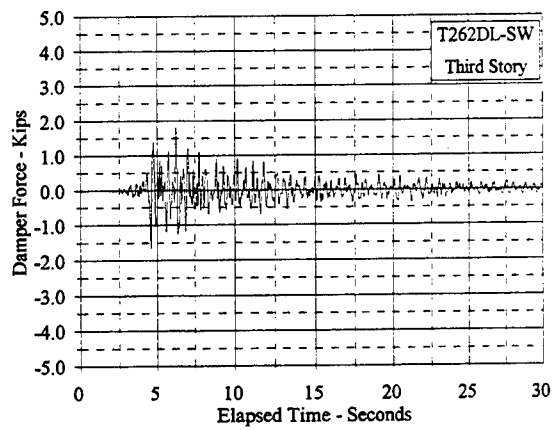


Figure C.8.30 Damper Force Vs. Elapsed Time: T262DL, SW and SE

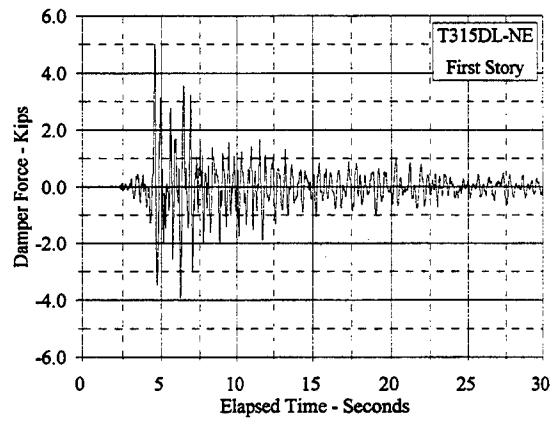
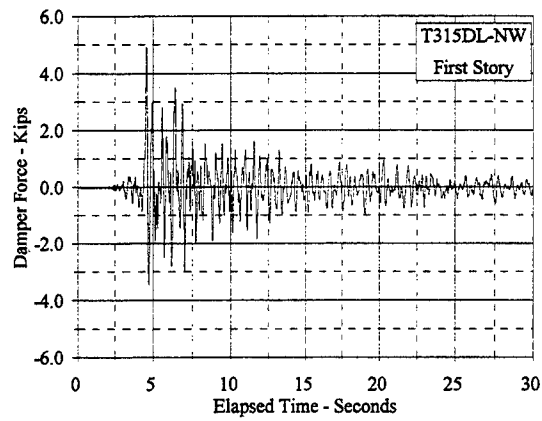
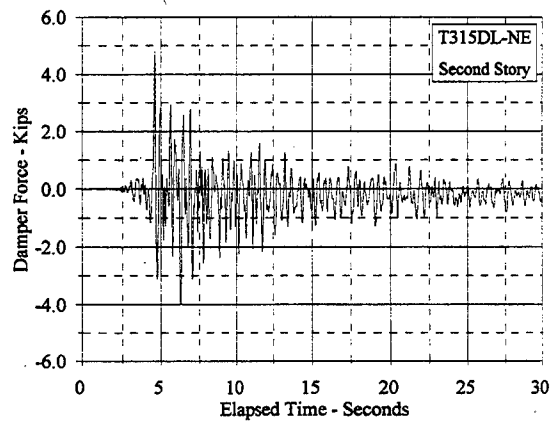
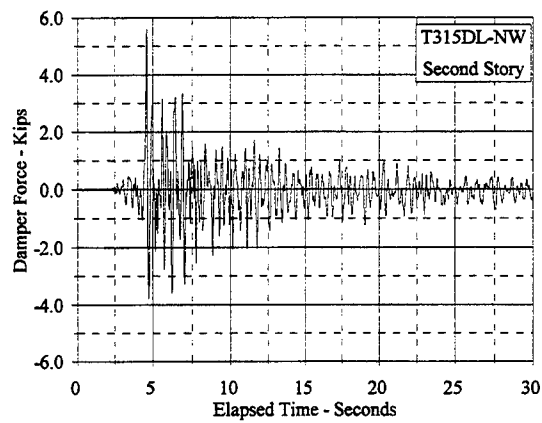
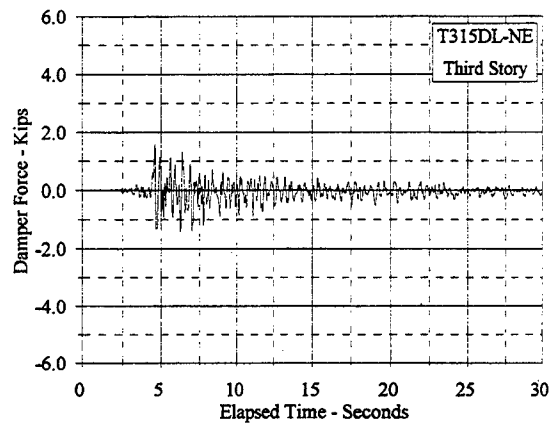
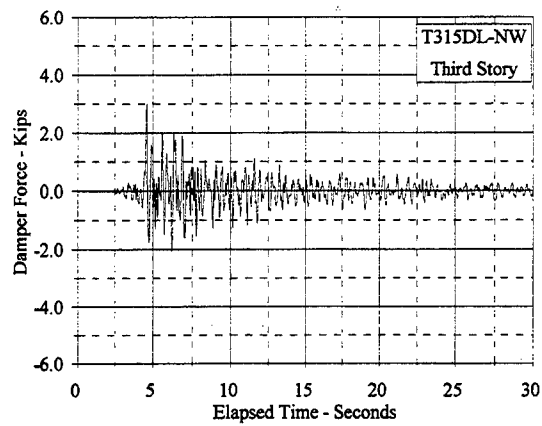


Figure C.8.31 Damper Force Vs. Elapsed Time: T315DL, NW and NE

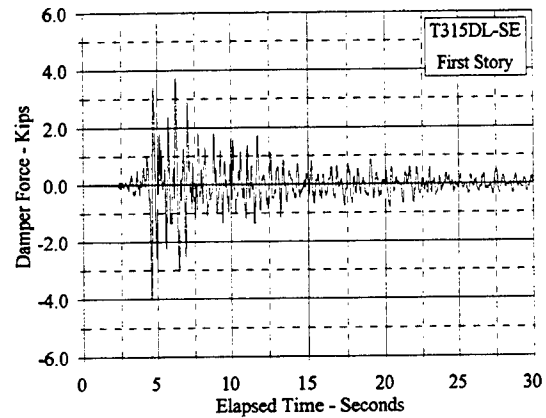
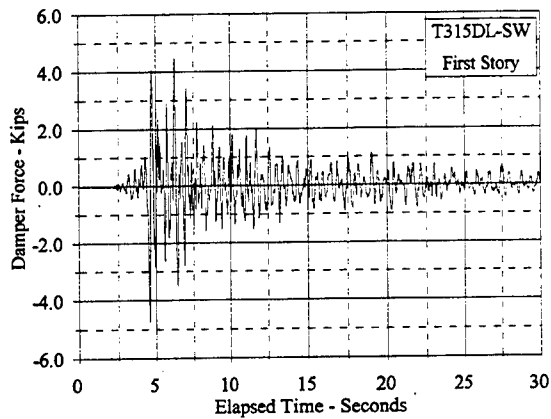
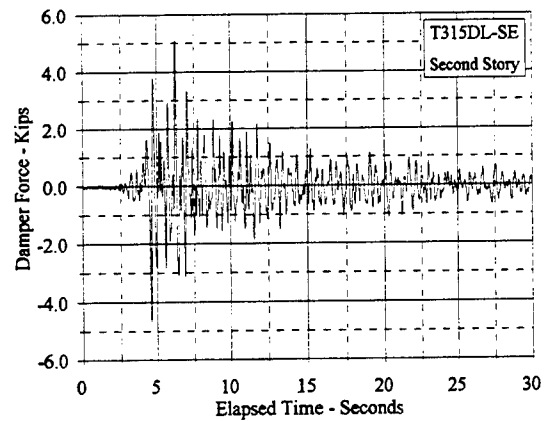
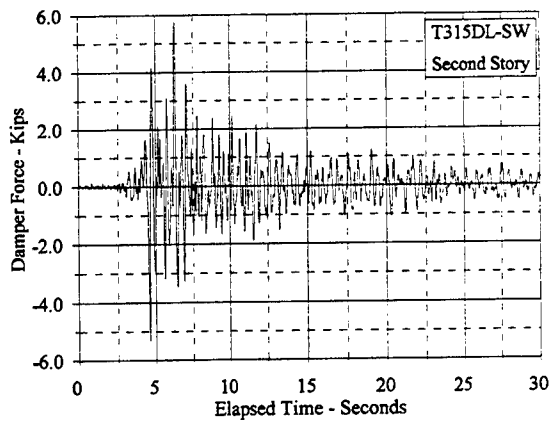
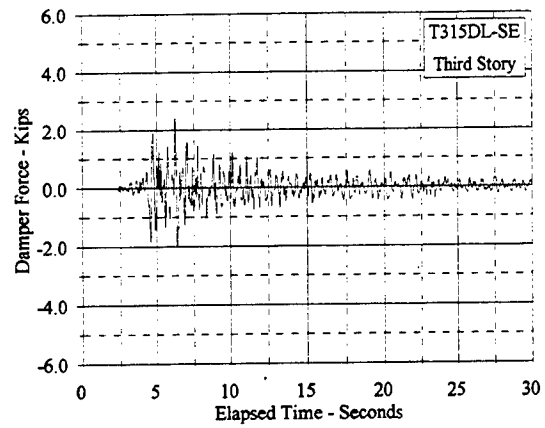
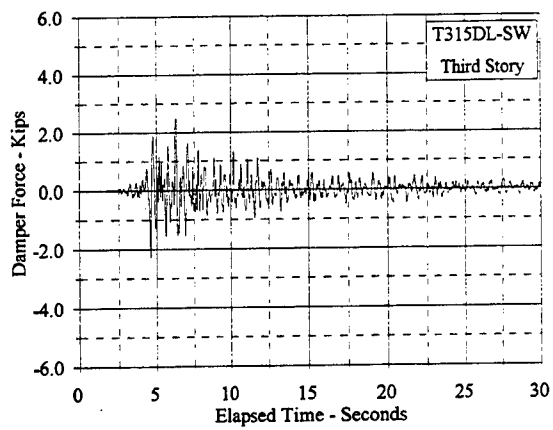


Figure C.8.32 Damper Force Vs. Elapsed Time: T315DL, SW and SE

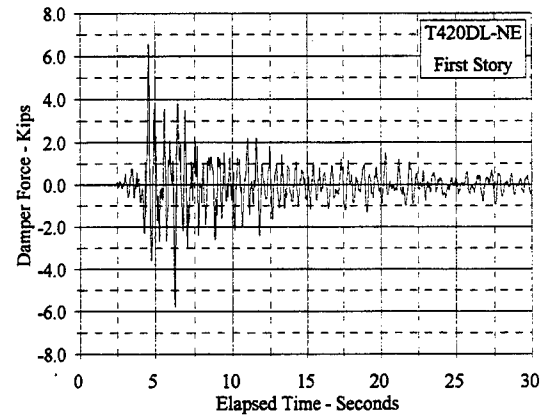
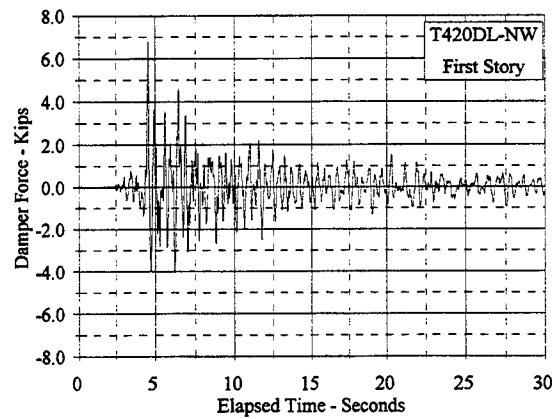
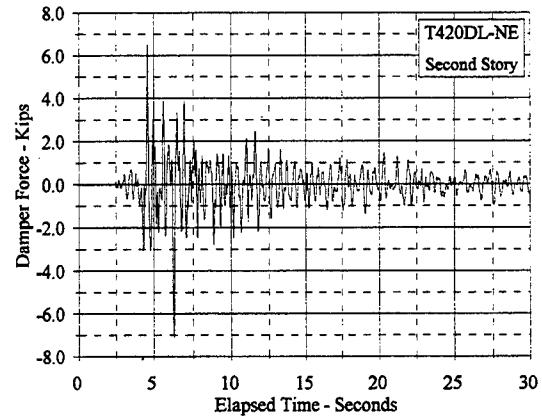
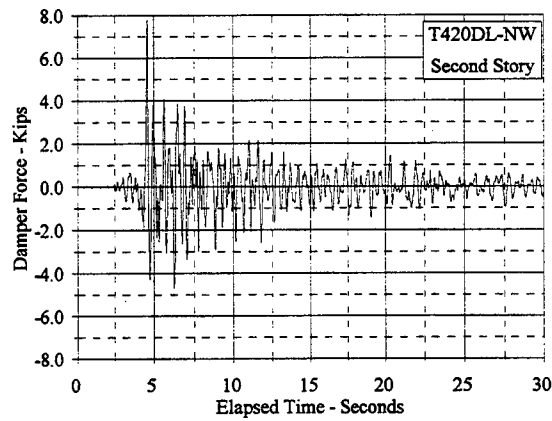
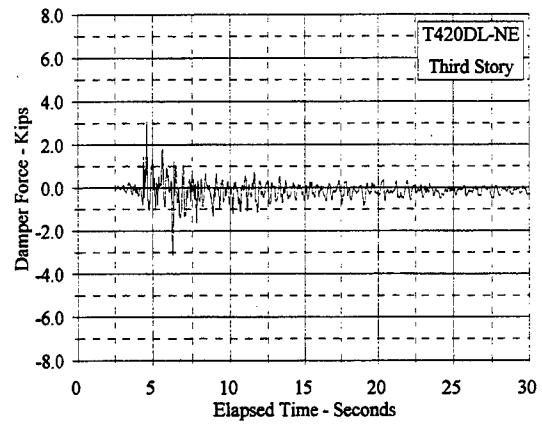
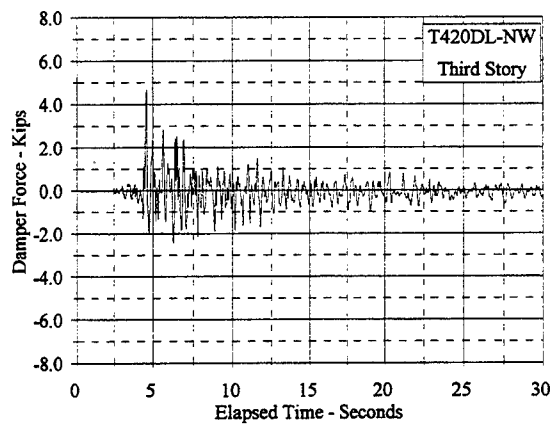


Figure C.8.33 Damper Force Vs. Elapsed Time: T420DL, NW and NE

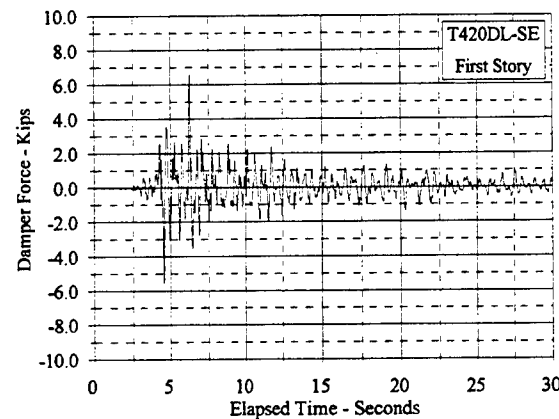
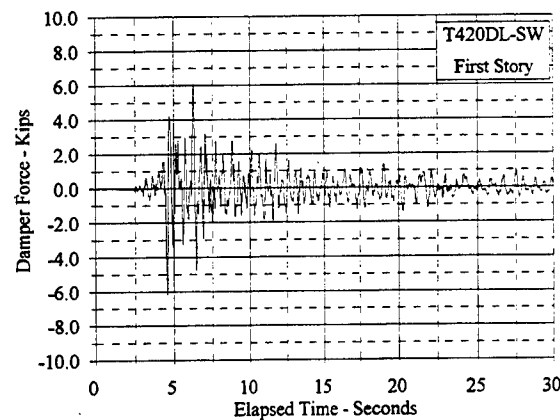
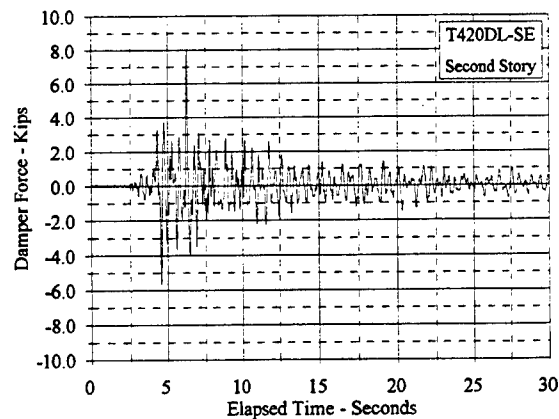
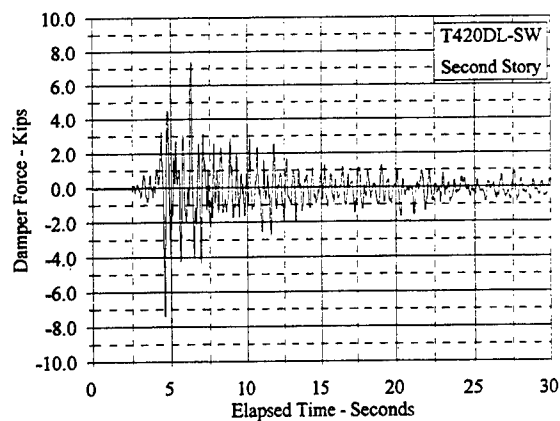
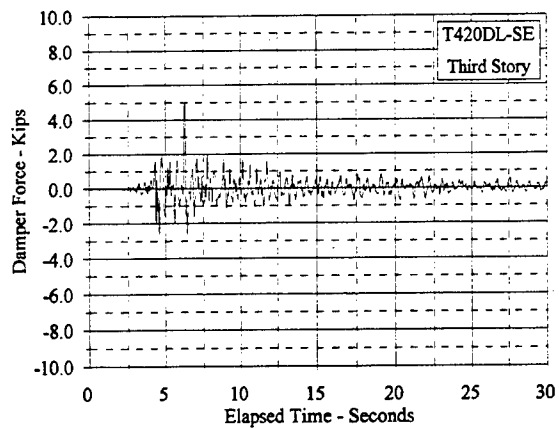
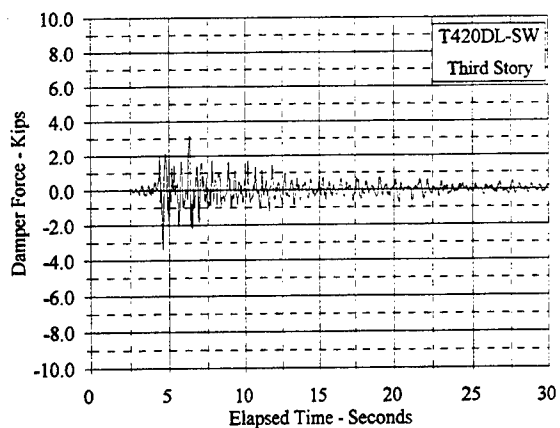


Figure C.8.34 Damper Force Vs. Elapsed Time: T420DL, SW and SE

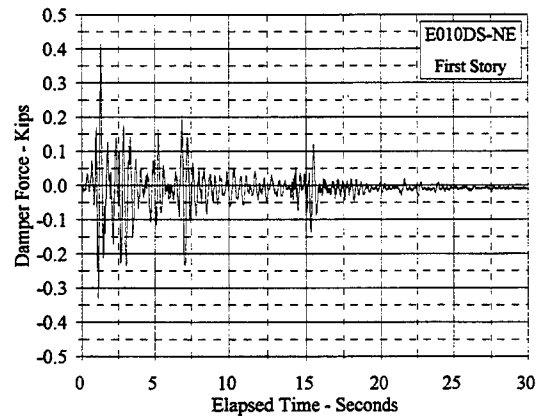
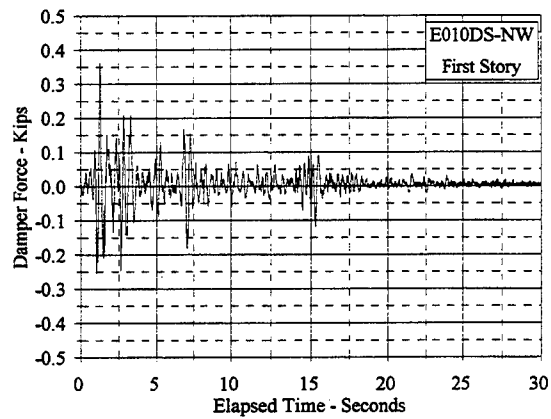
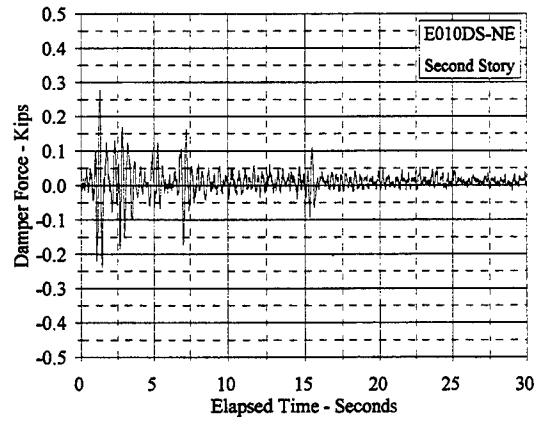
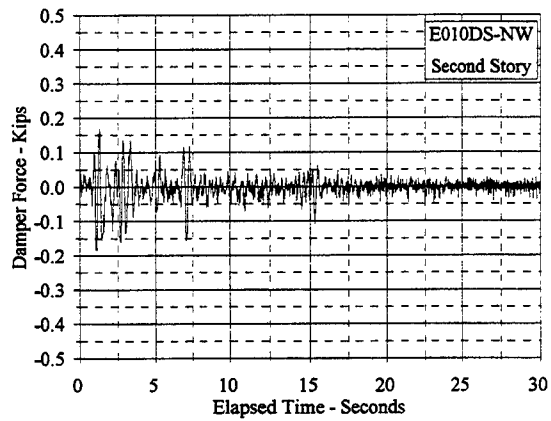
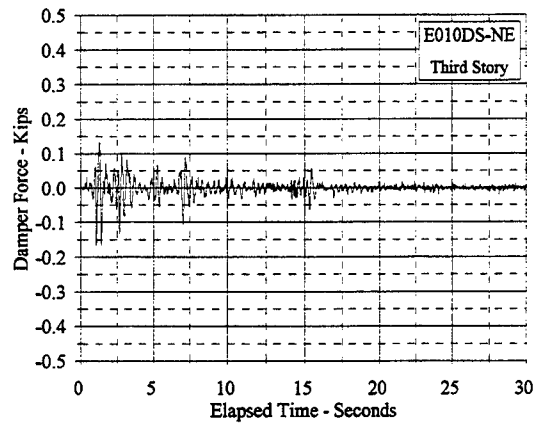
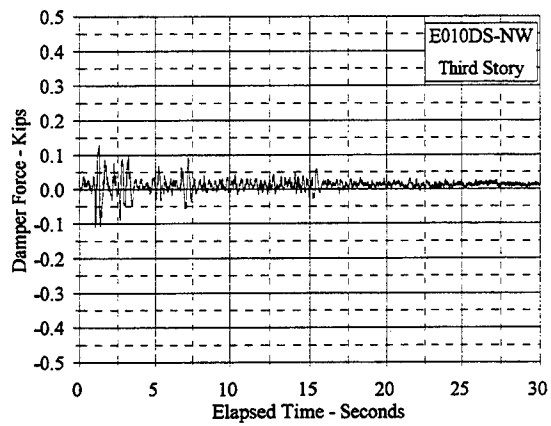


Figure C.8.35 Damper Force Vs. Elapsed Time: E010DS, NW and NE

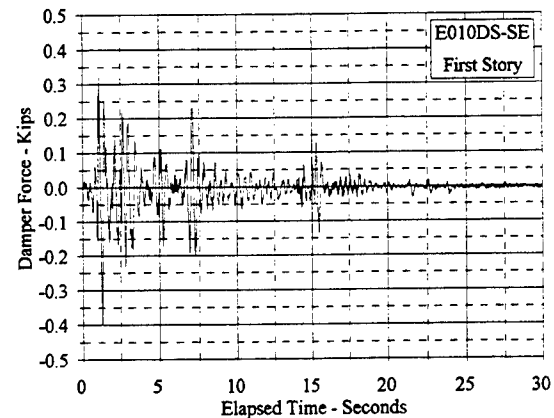
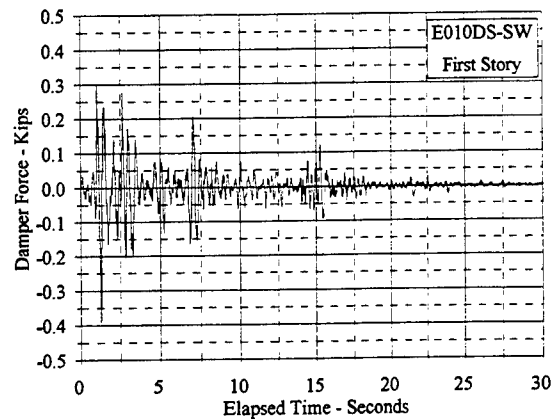
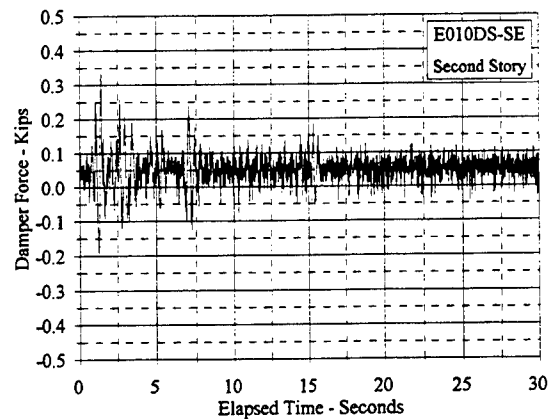
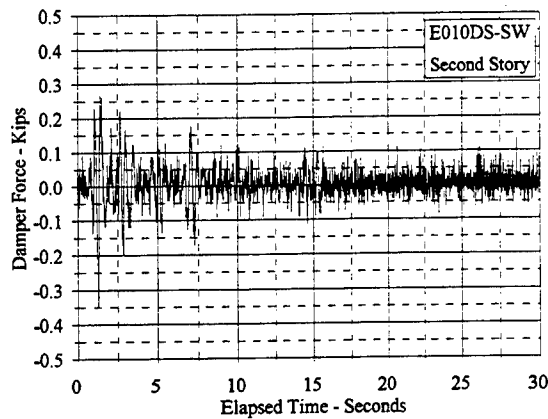
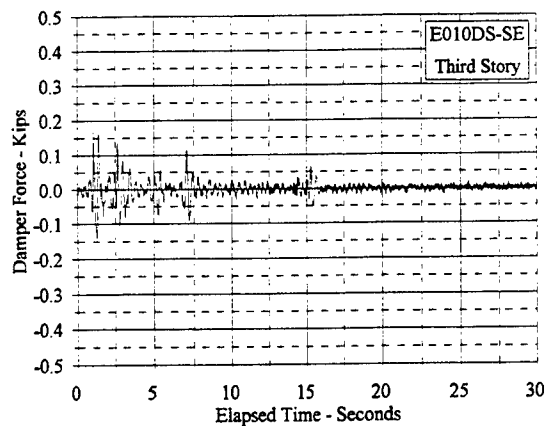
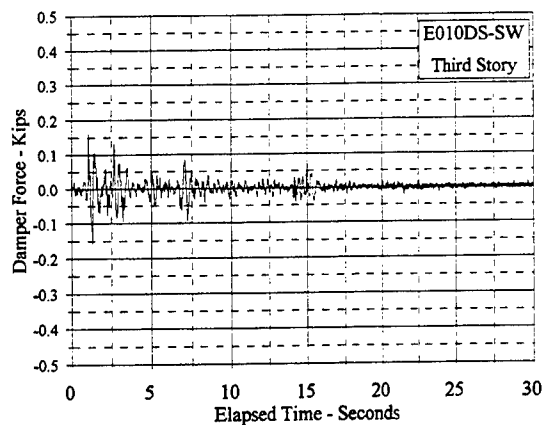


Figure C.8.36 Damper Force Vs. Elapsed Time: E010DS, SW and SE

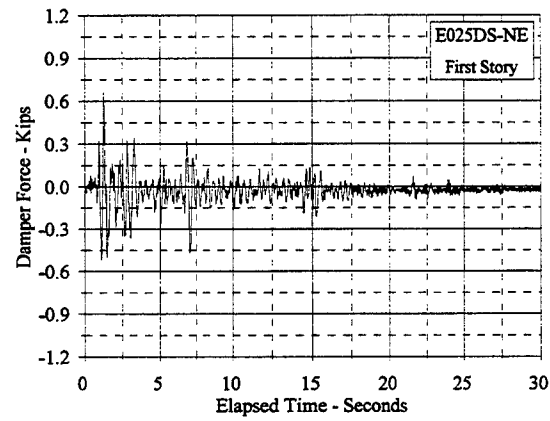
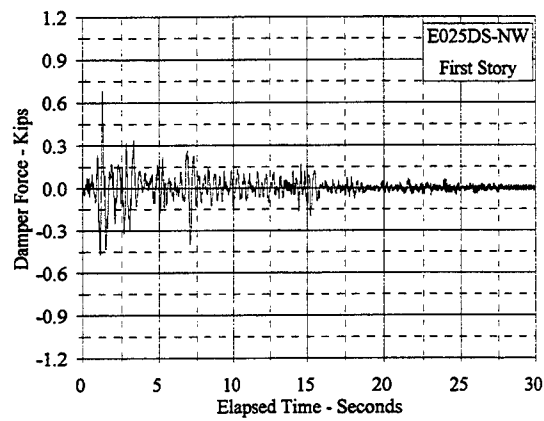
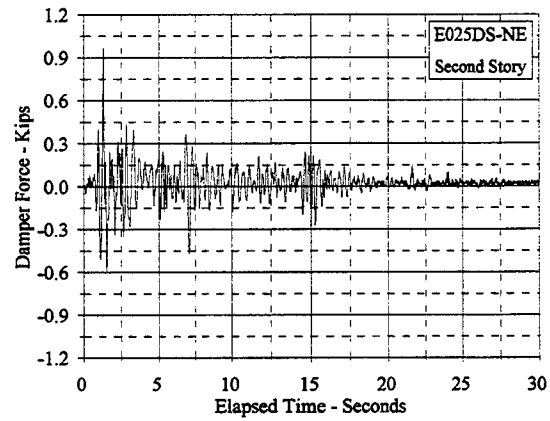
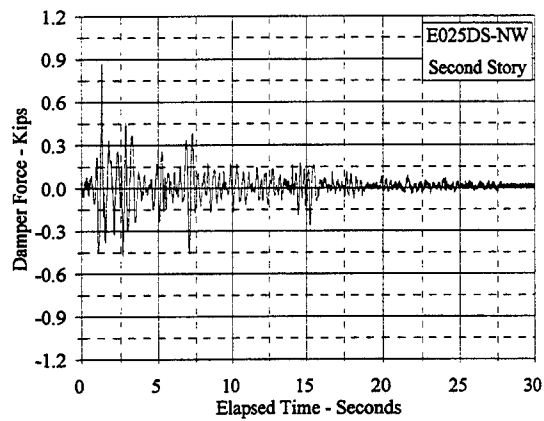
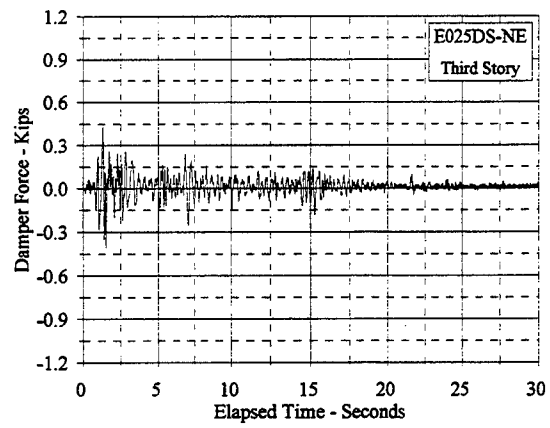
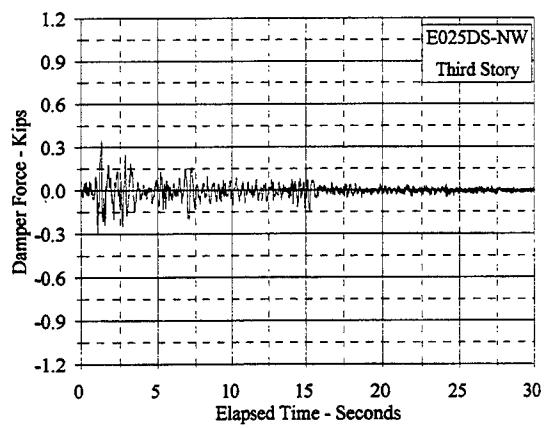


Figure C.8.37 Damper Force Vs. Elapsed Time: E025DS, NW and NE

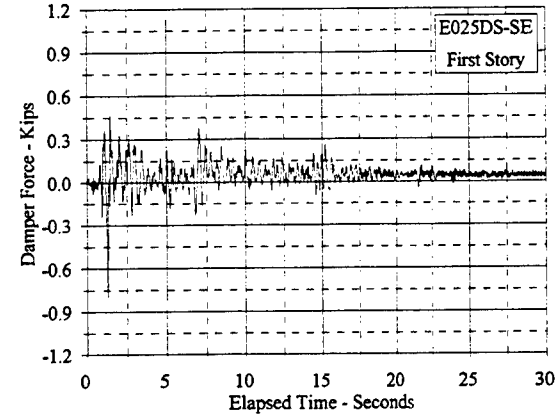
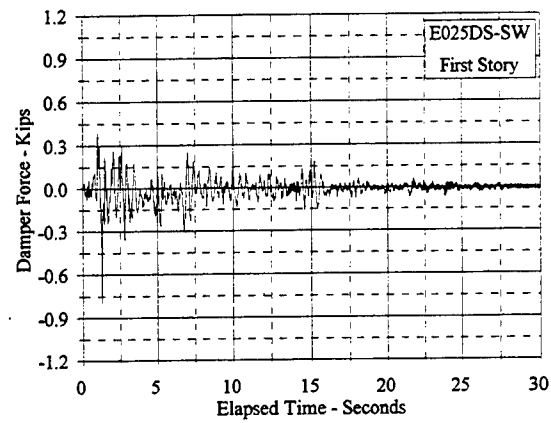
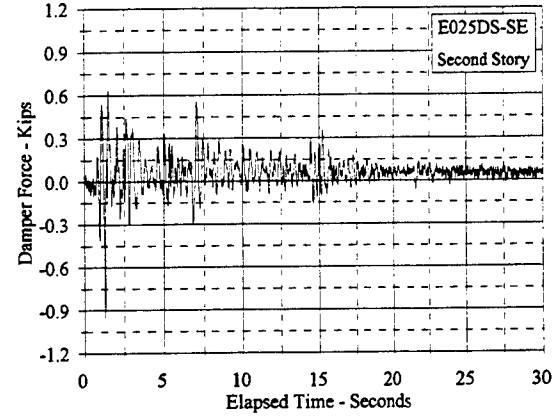
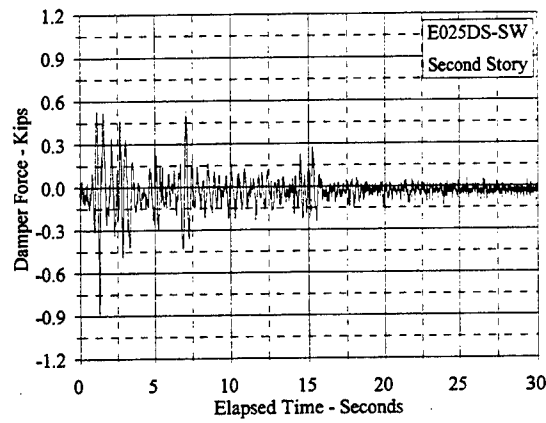
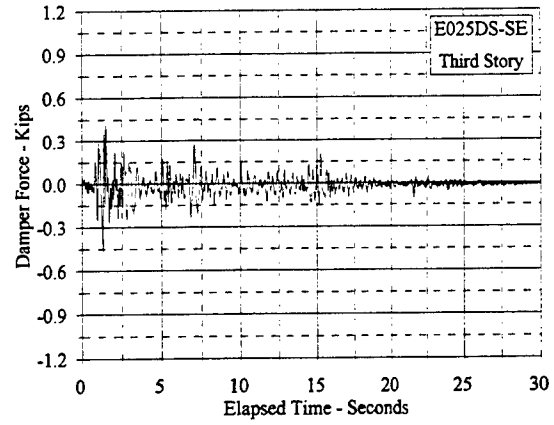
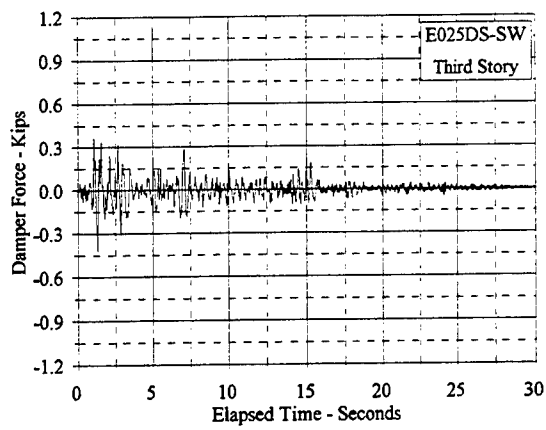


Figure C.8.38 Damper Force Vs. Elapsed Time: E025DS, SW and SE

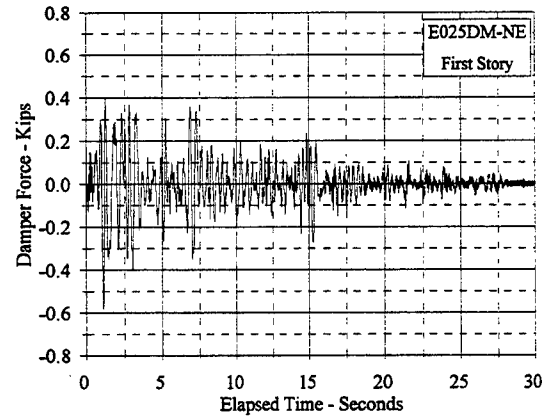
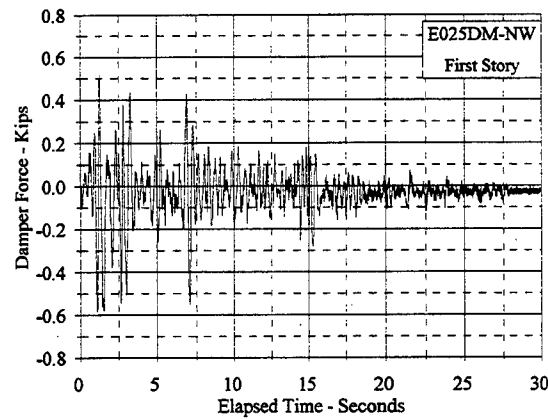
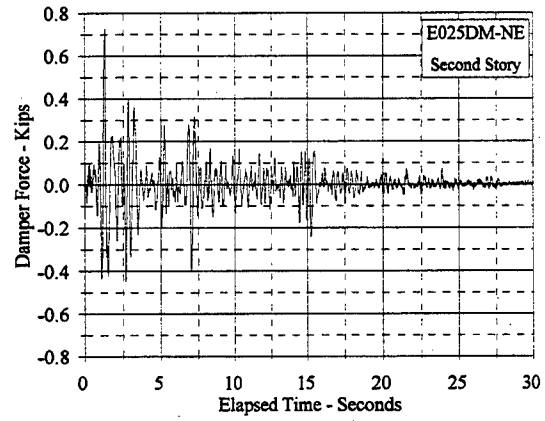
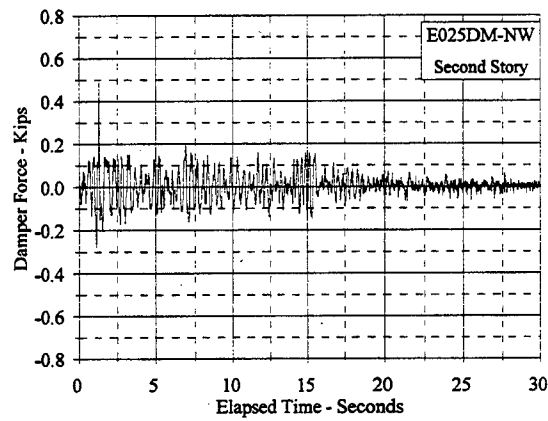
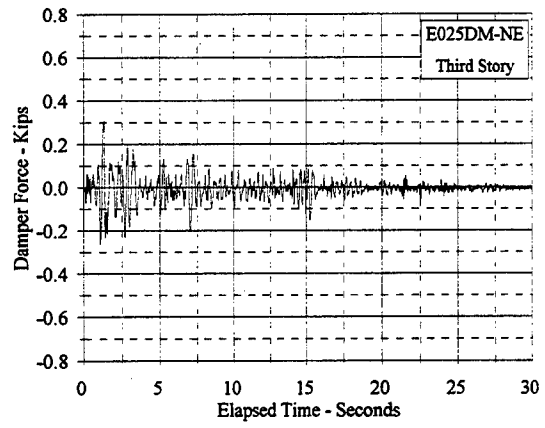
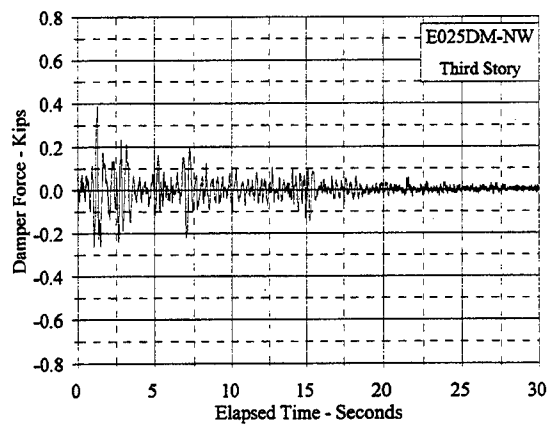


Figure C.8.39 Damper Force Vs. Elapsed Time: E025DM, NW and NE

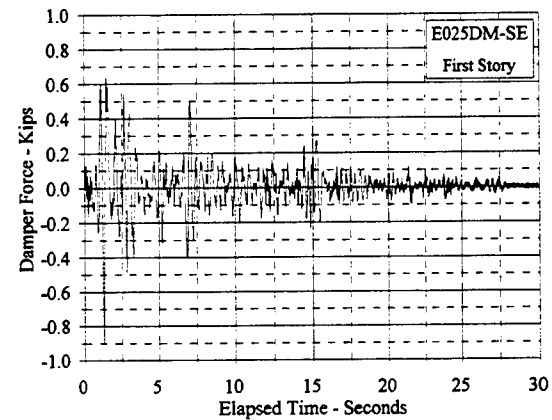
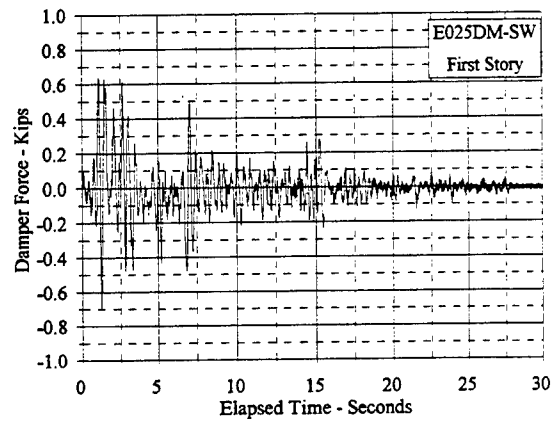
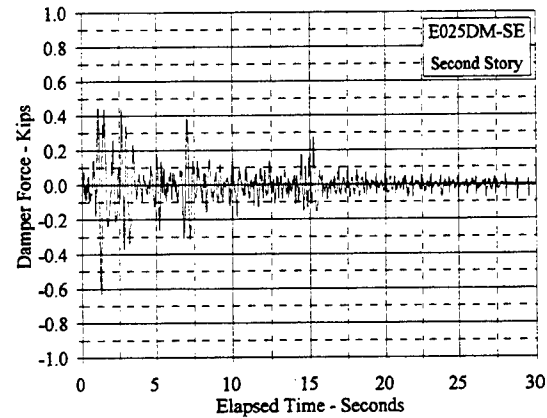
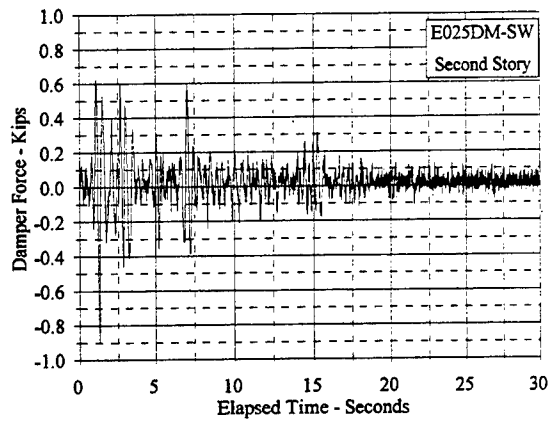
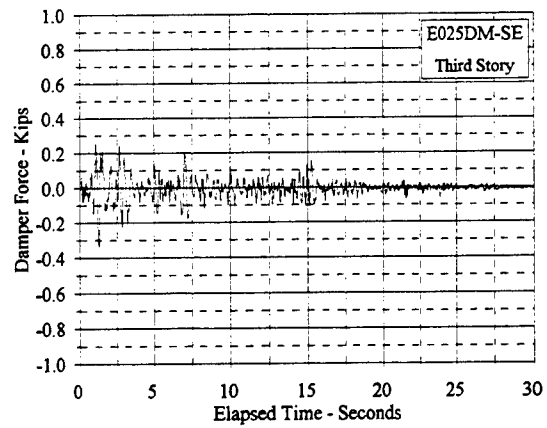
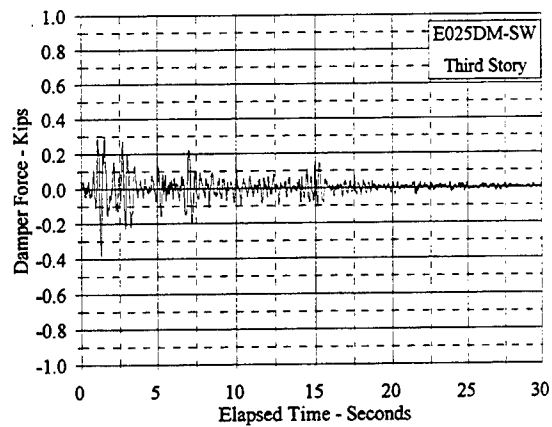


Figure C.8.40 Damper Force Vs. Elapsed Time: E025DM, SW and SE

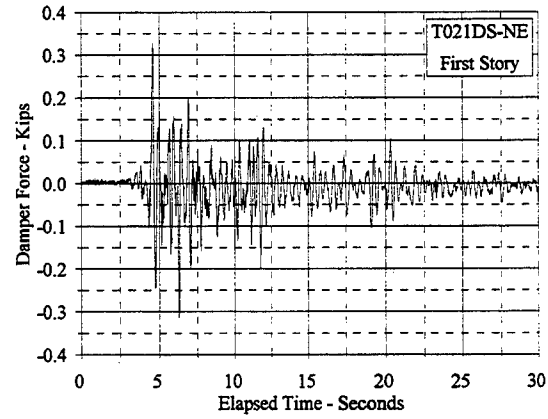
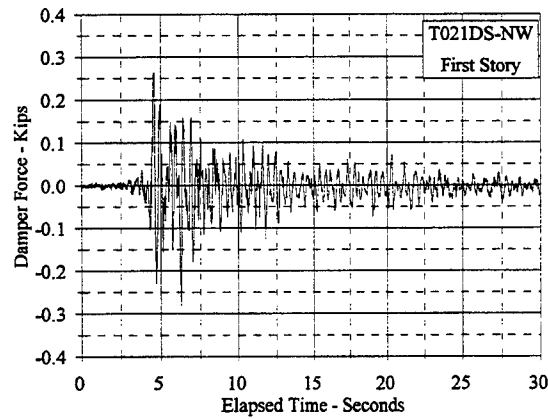
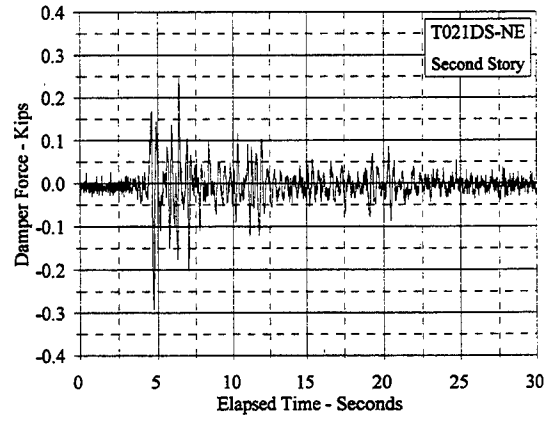
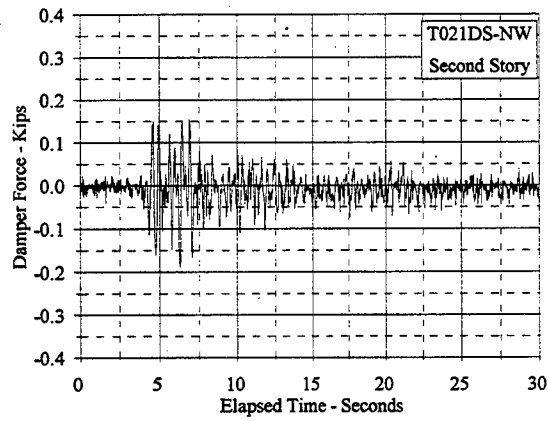
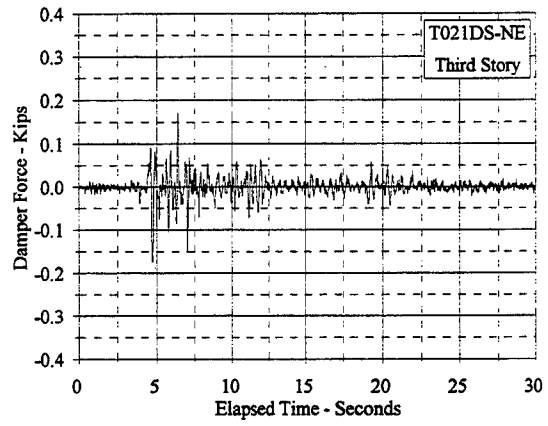
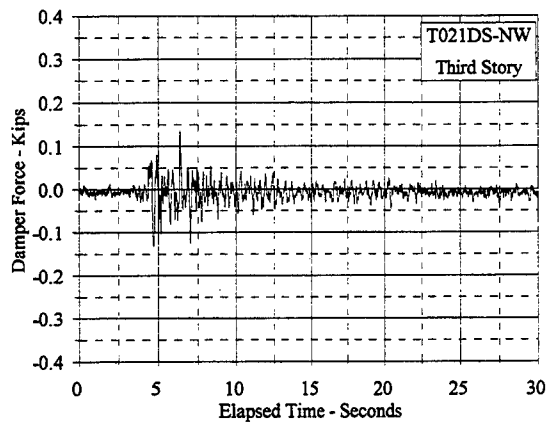


Figure C.8.41 Damper Force Vs. Elapsed Time: T021DS, NW and NE

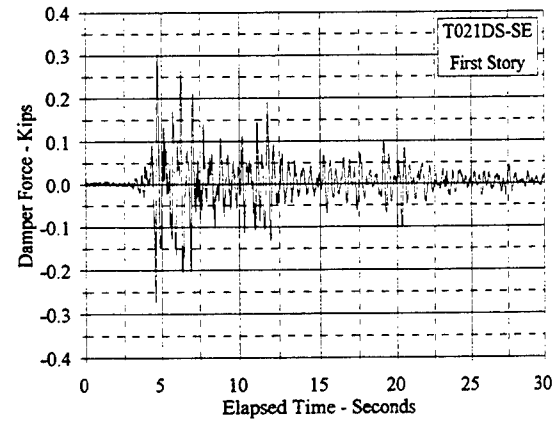
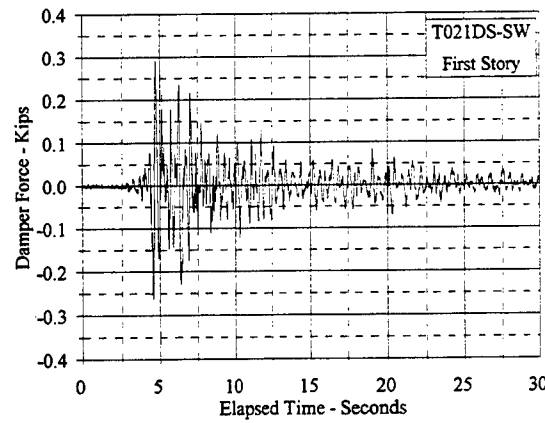
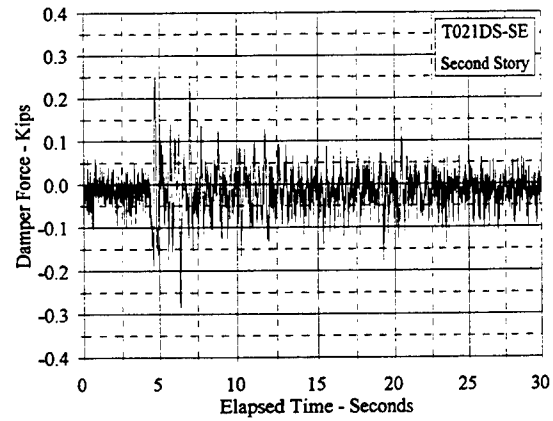
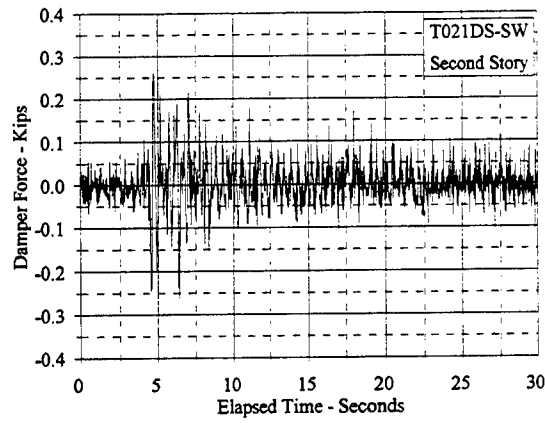
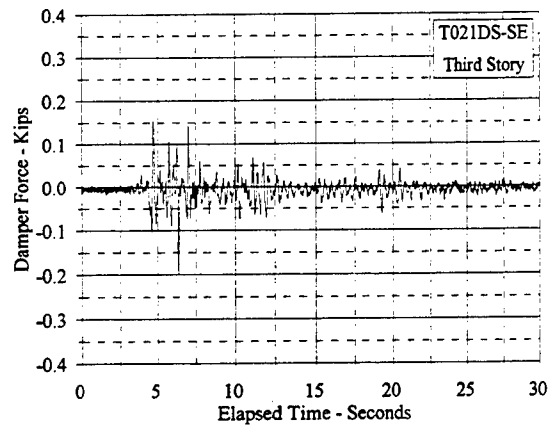
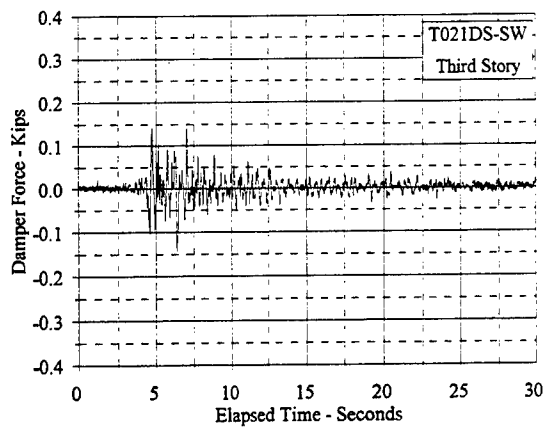


Figure C.8.42 Damper Force Vs. Elapsed Time: T021DS, SW and SE

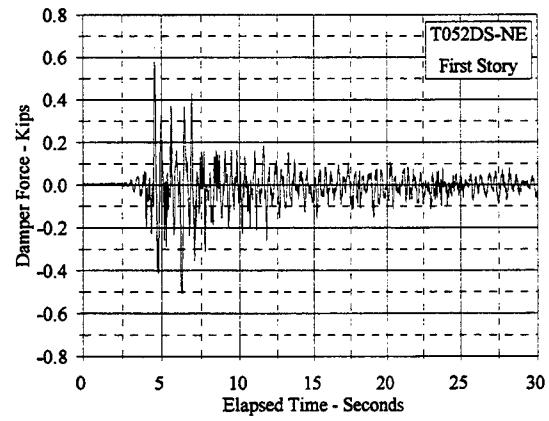
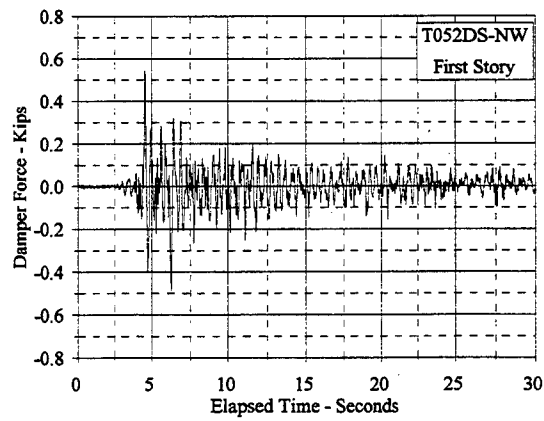
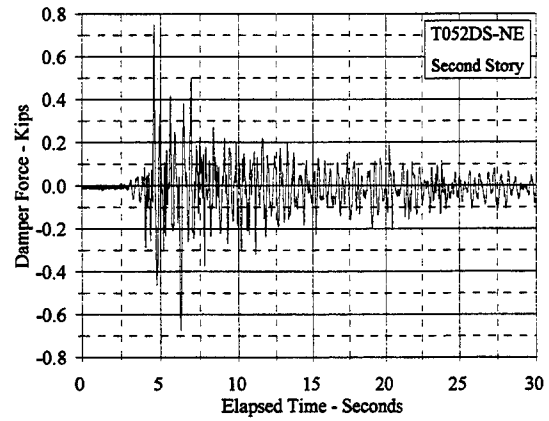
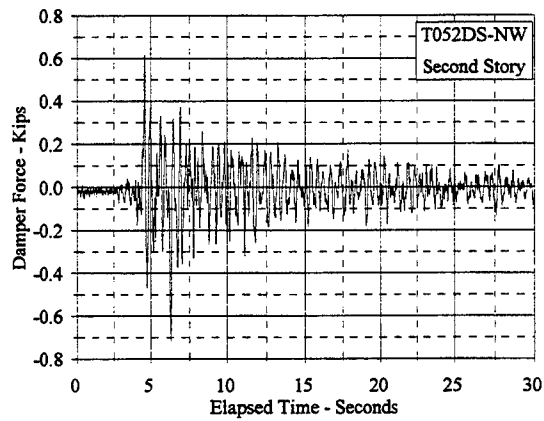
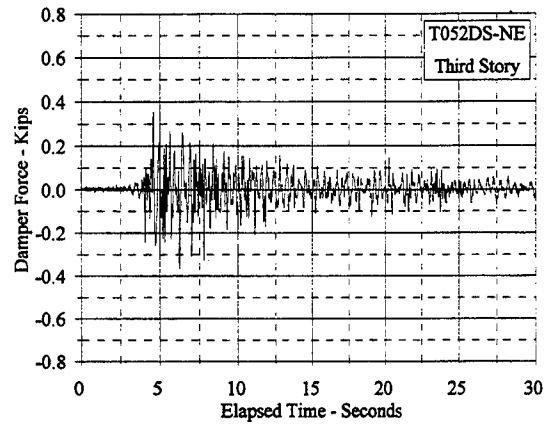
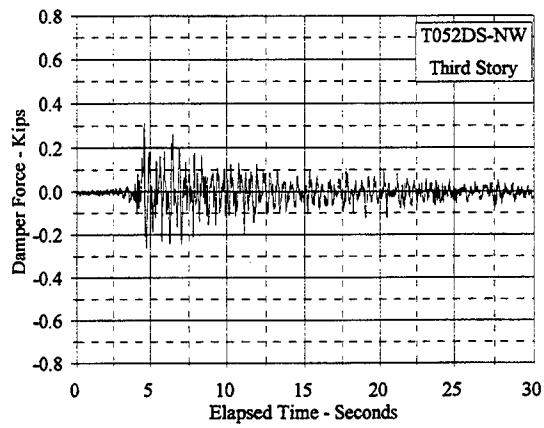


Figure C.8.43 Damper Force Vs. Elapsed Time: T052DS, NW and NE

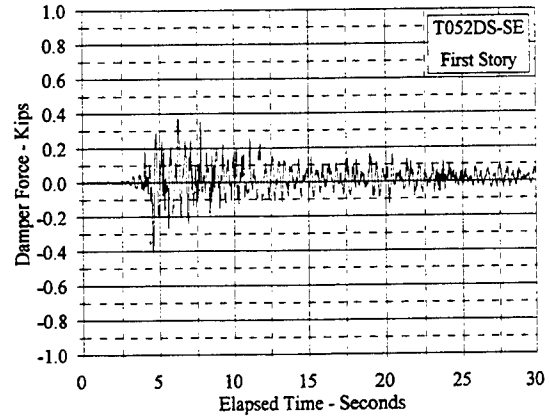
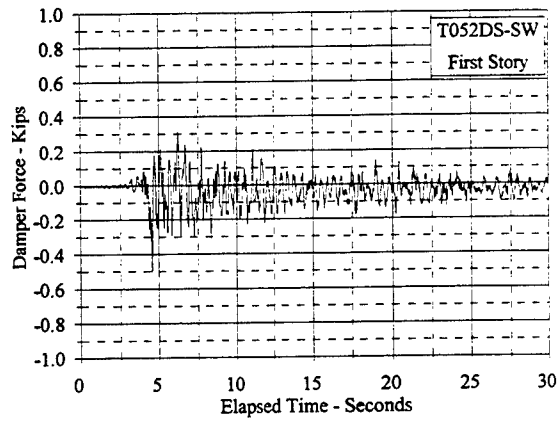
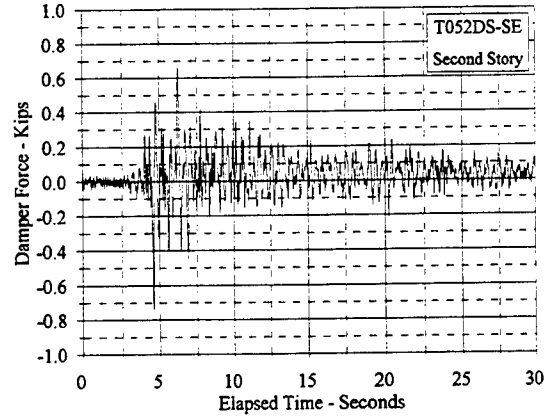
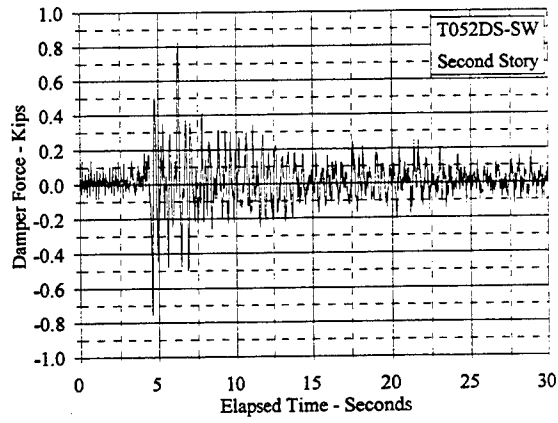
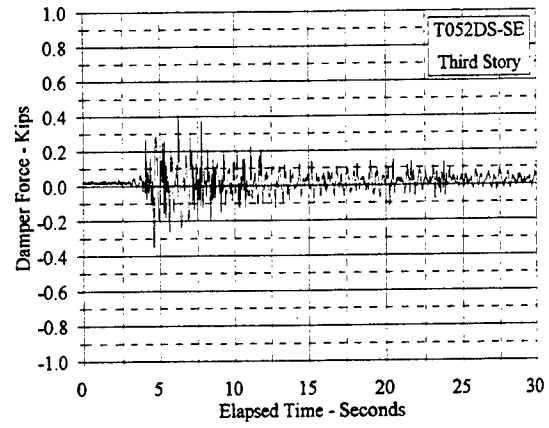
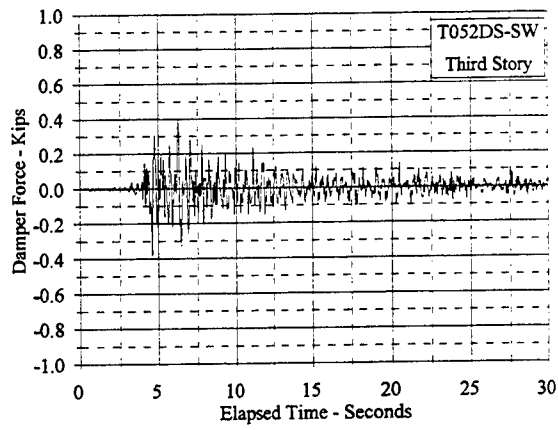


Figure C.8.44 Damper Force Vs. Elapsed Time: T052DS, SW and SE

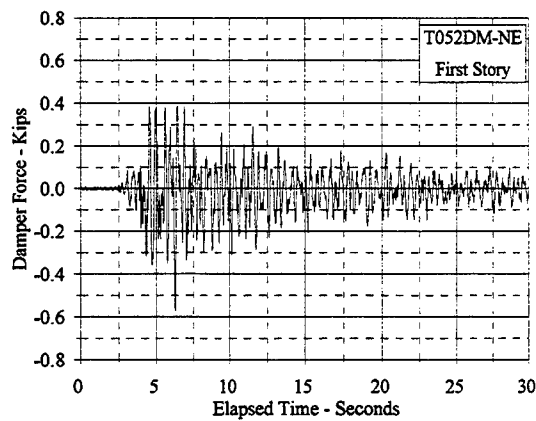
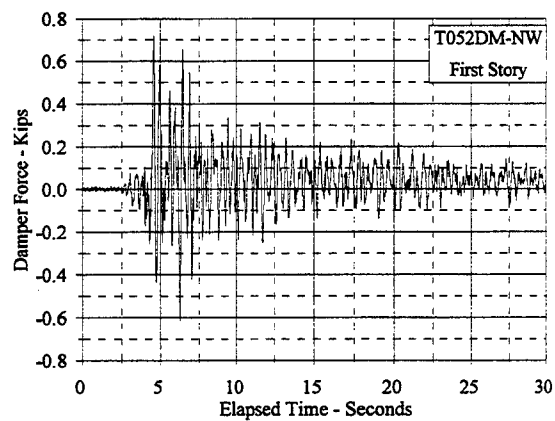
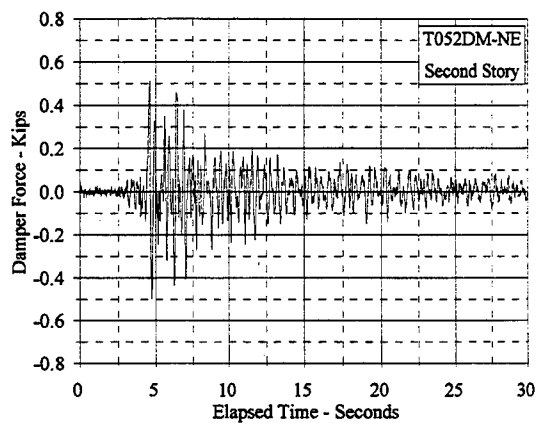
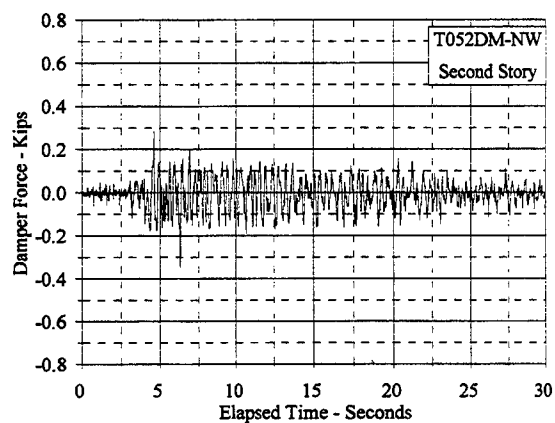
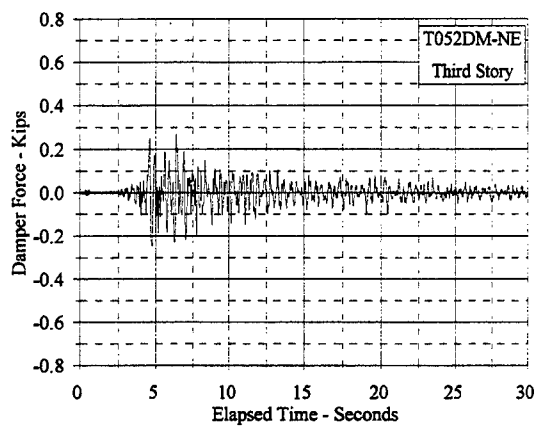
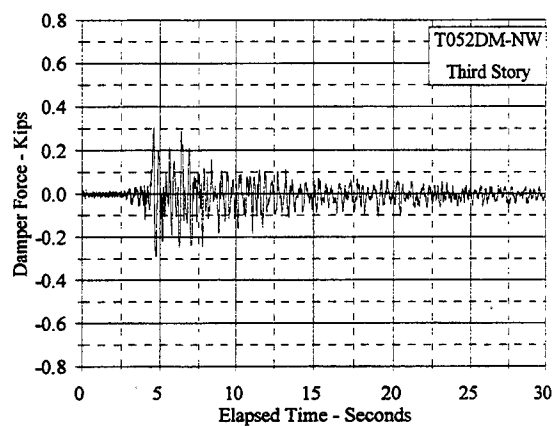


Figure C.8.45 Damper Force Vs. Elapsed Time: T052DM, NW and NE

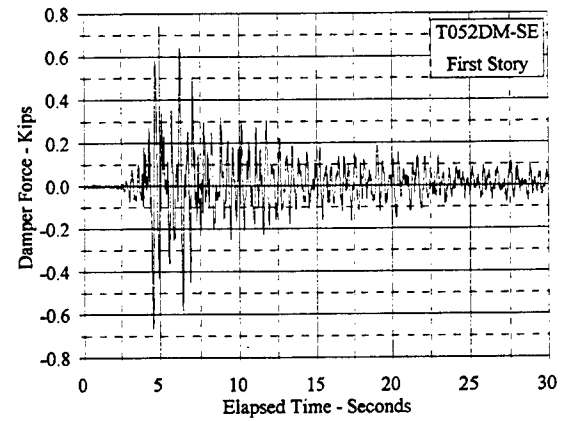
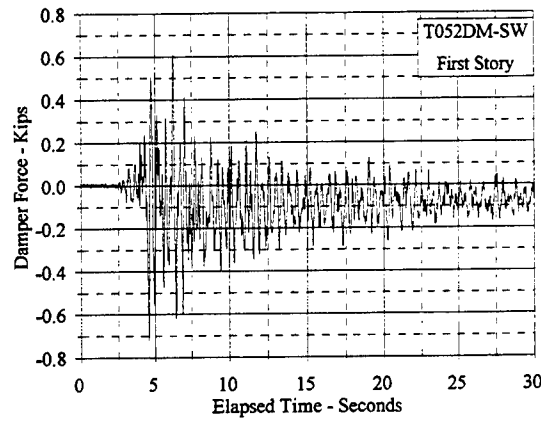
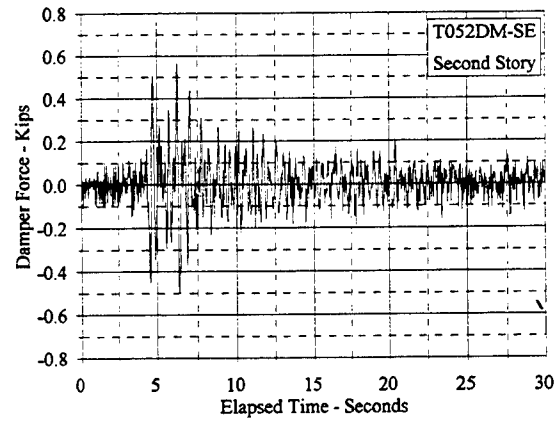
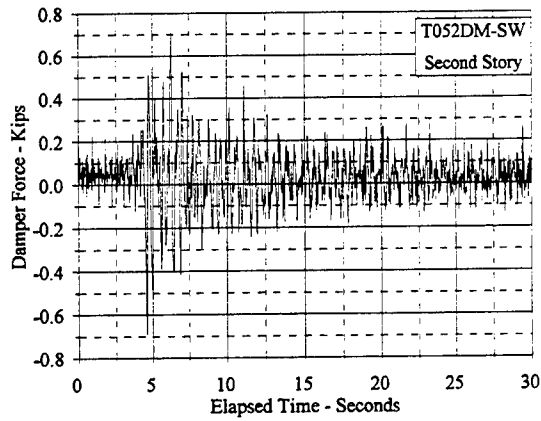
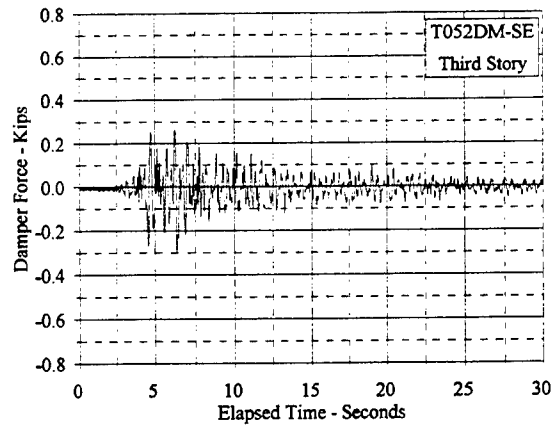
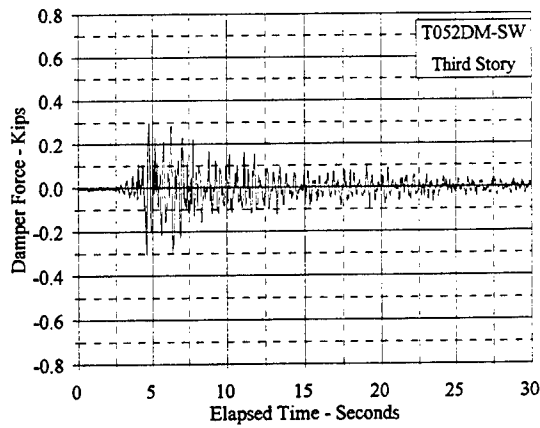


Figure C.8.46 Damper Force Vs. Elapsed Time: T052DM, SW and SE

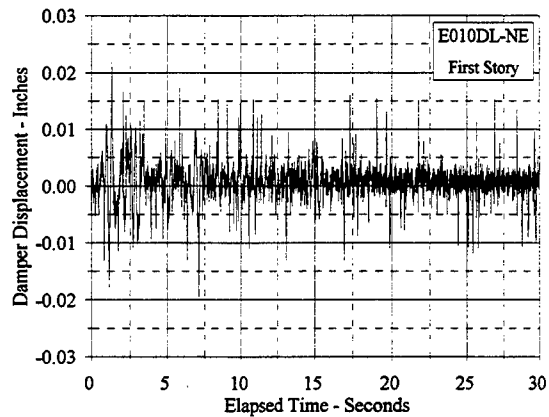
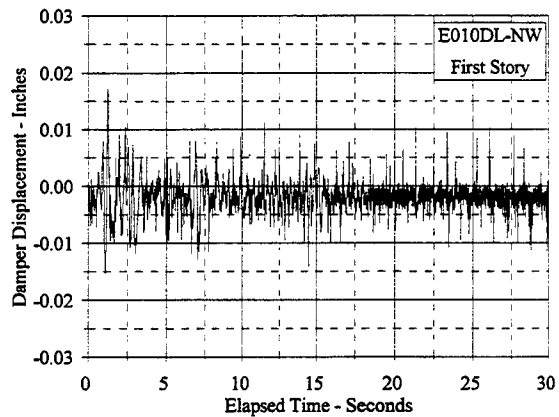
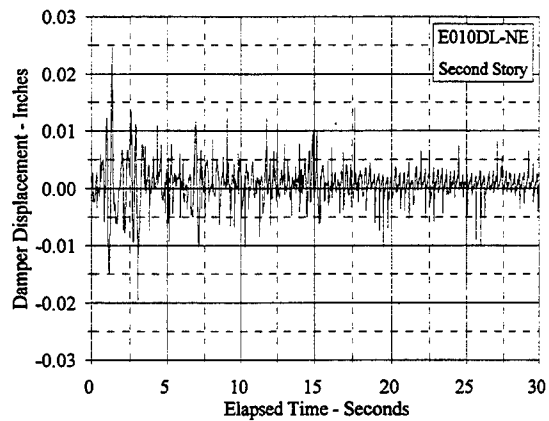
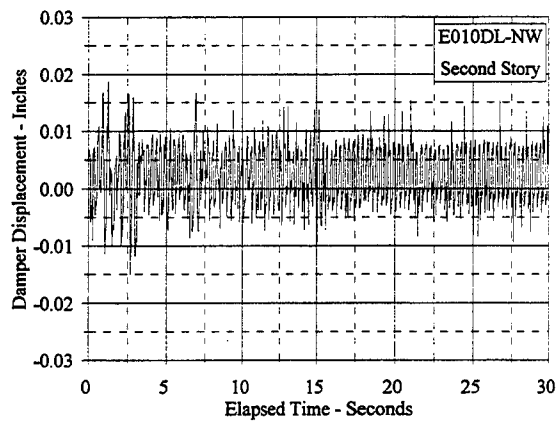
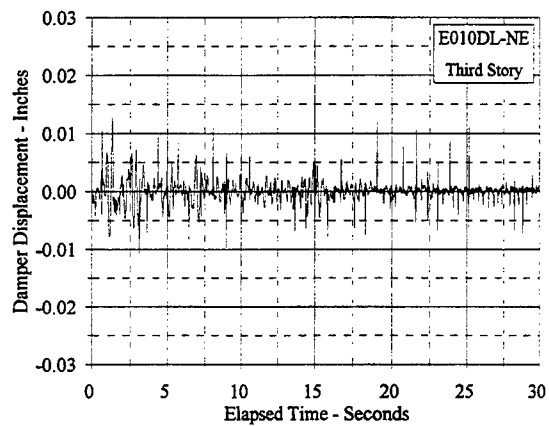
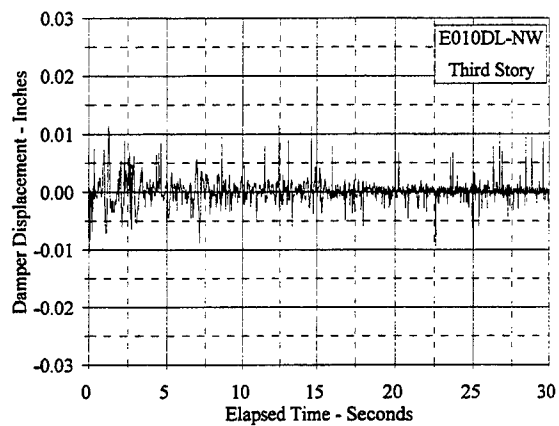


Figure C.9.1 Damper Displacement Vs. Elapsed Time: E010DL, NW and NE

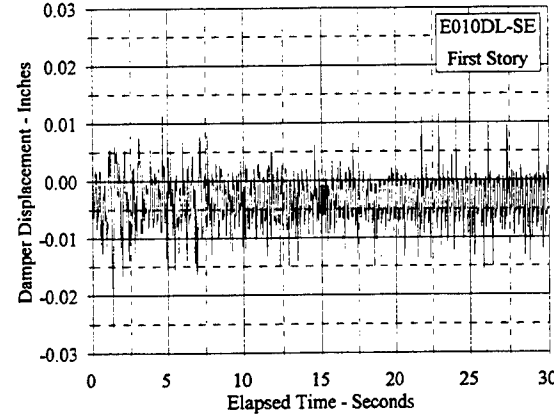
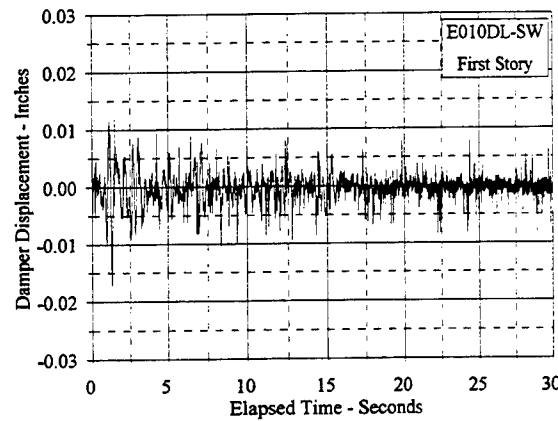
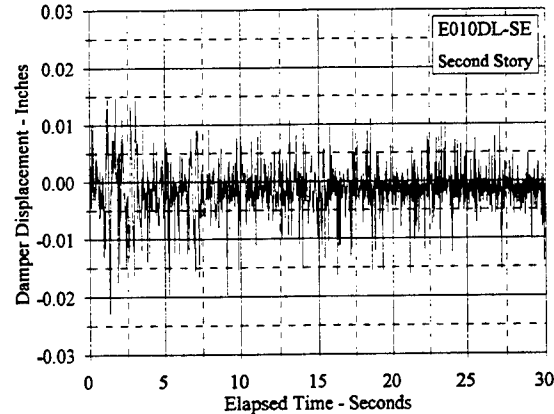
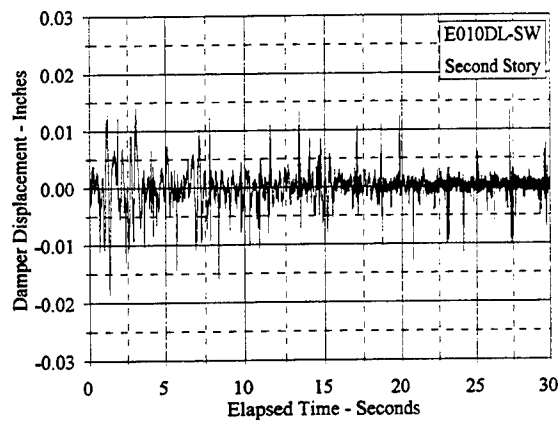
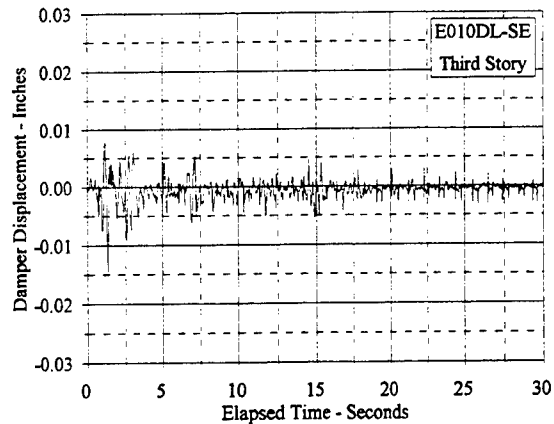
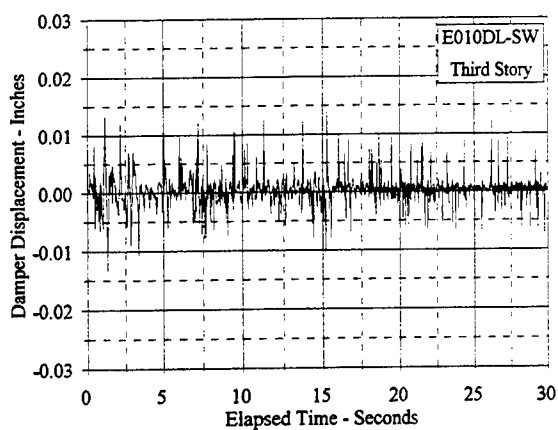


Figure C.9.2 Damper Displacement Vs. Elapsed Time: E010DL, SW and SE

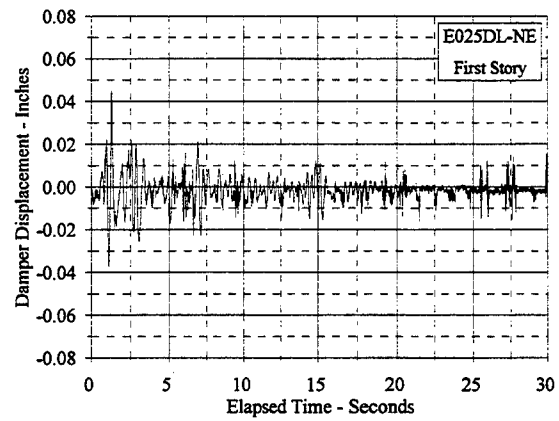
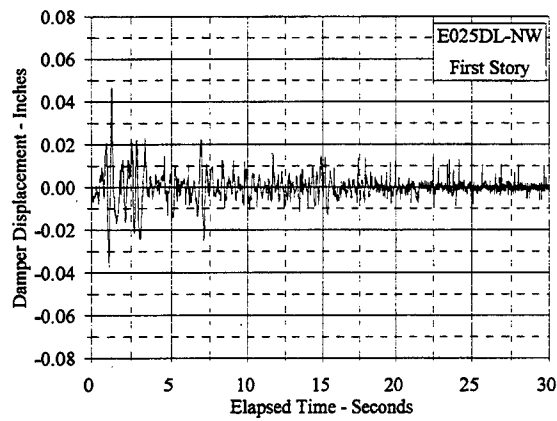
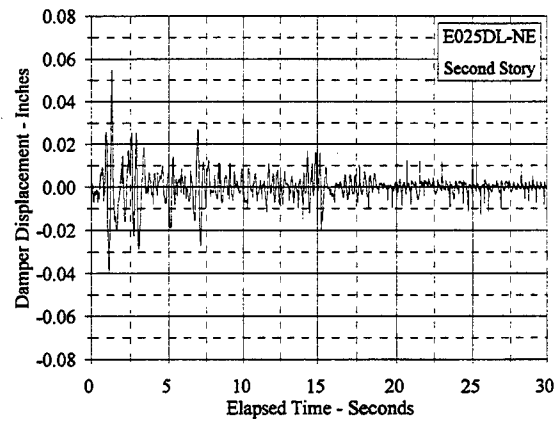
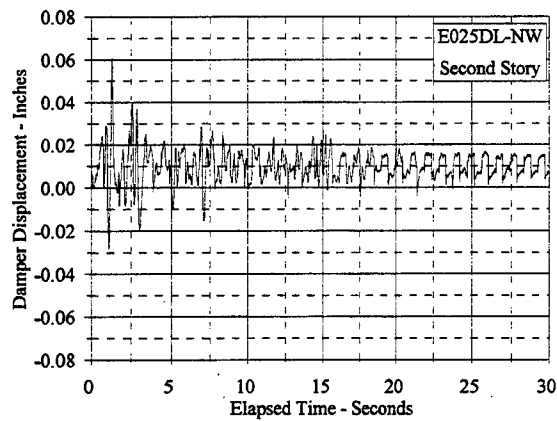
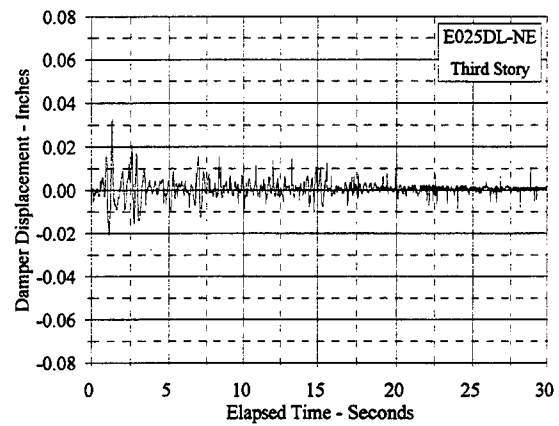
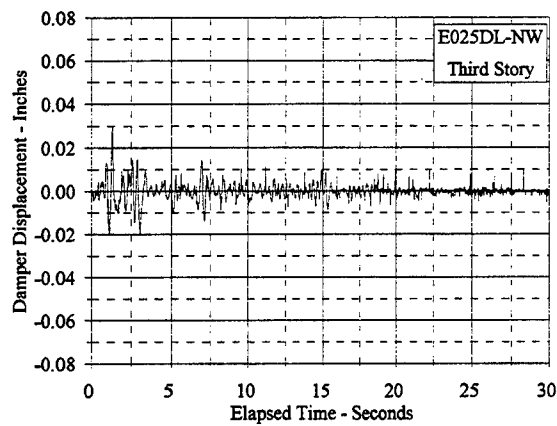


Figure C.9.3 Damper Displacement Vs. Elapsed Time: E025DL, NW and NE

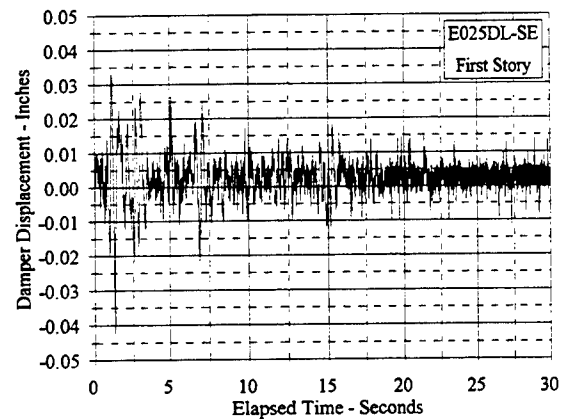
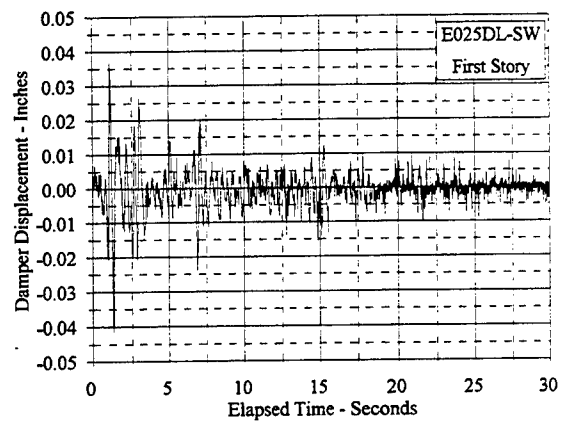
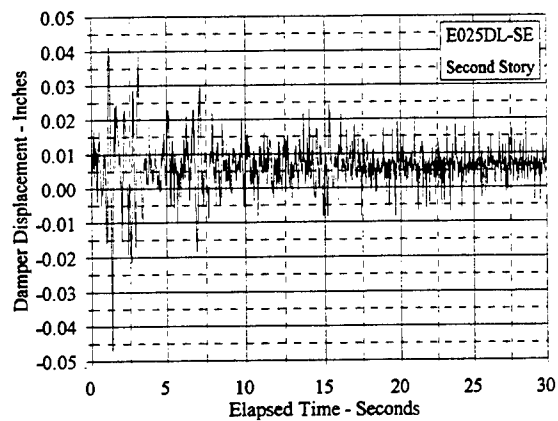
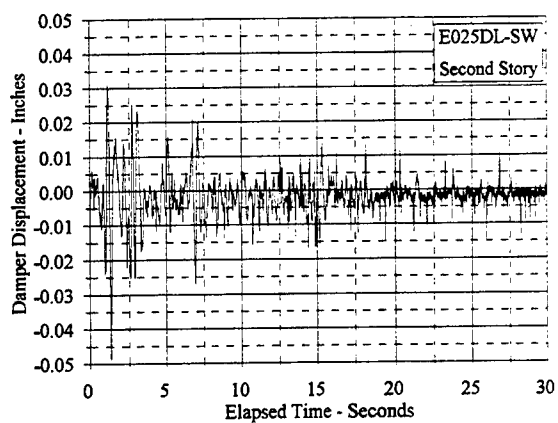
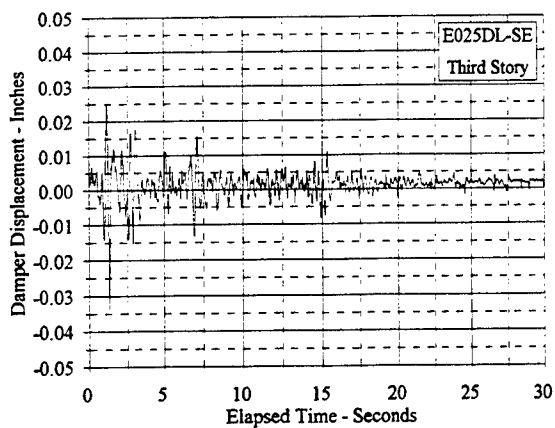
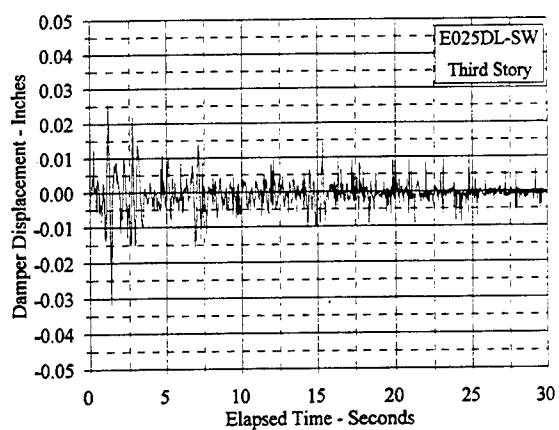


Figure C.9.4 Damper Displacement Vs. Elapsed Time: E025DL, SW and SE

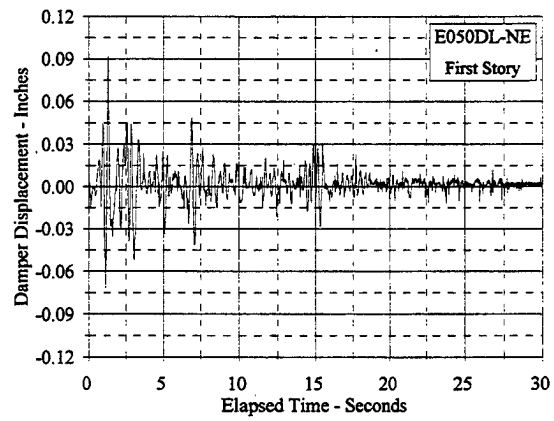
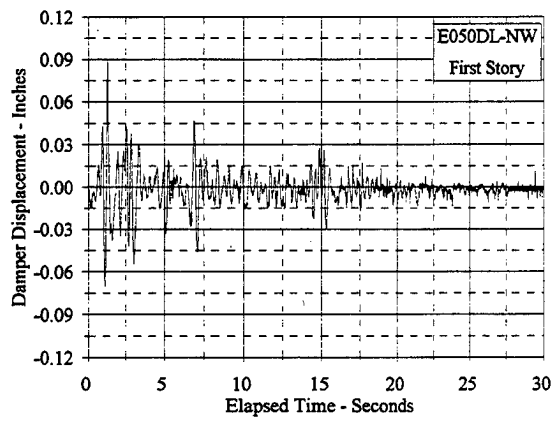
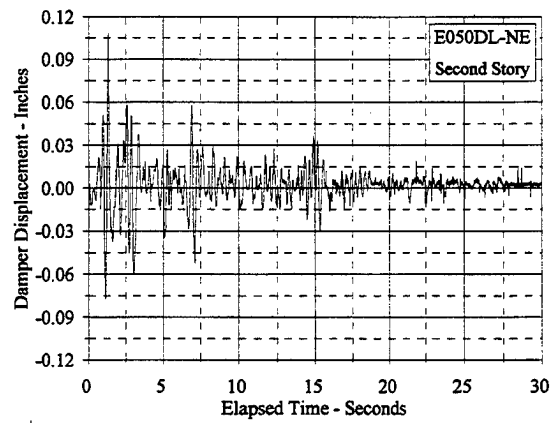
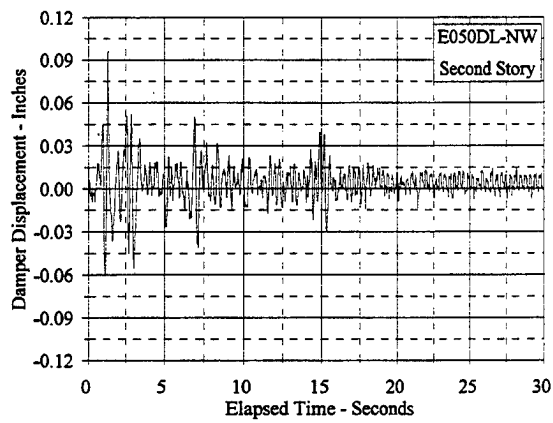
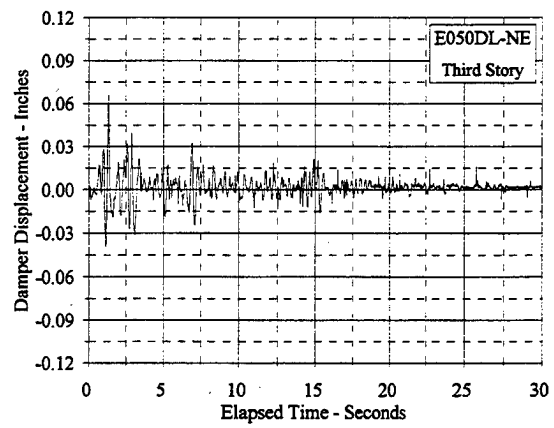
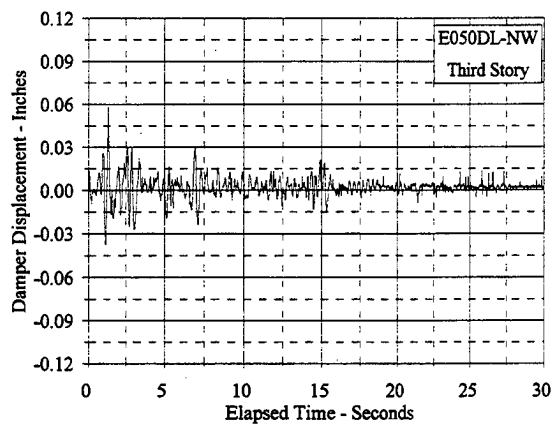


Figure C.9.5 Damper Displacement Vs. Elapsed Time: E050DL, NW and NE

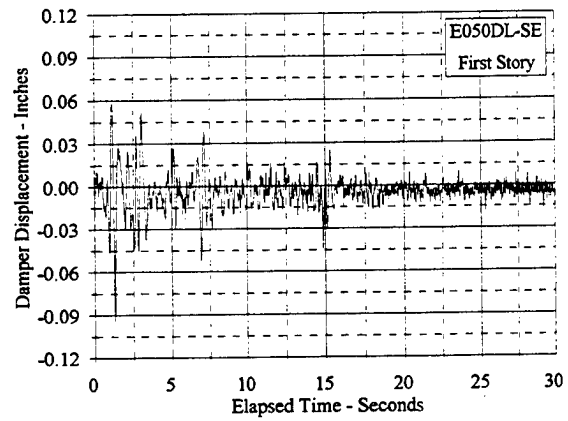
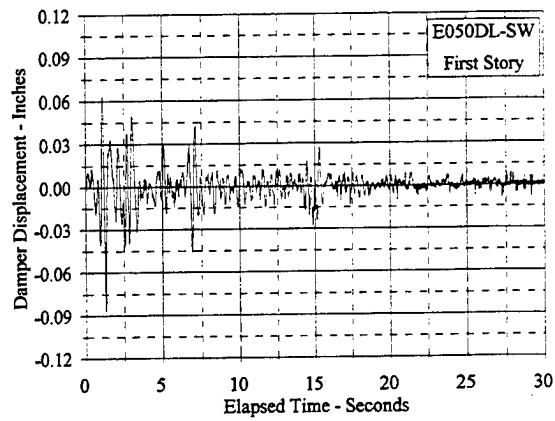
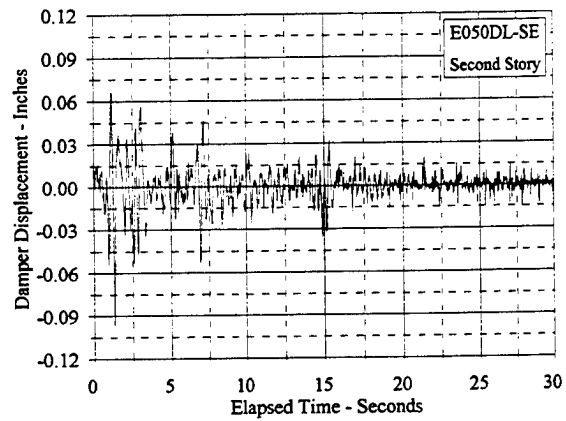
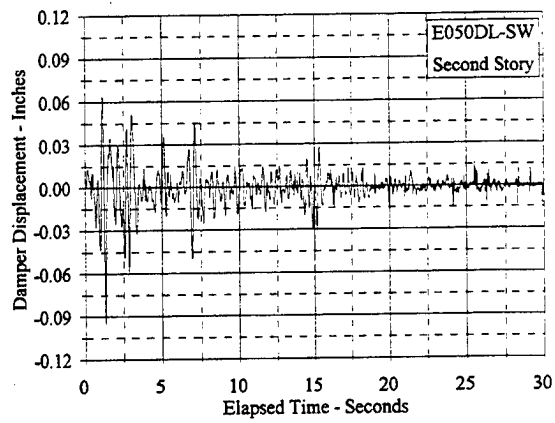
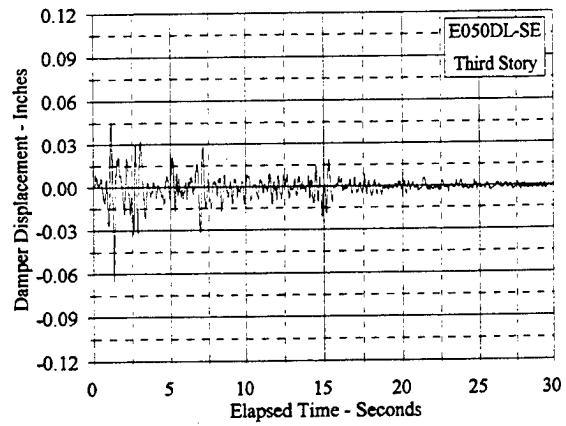
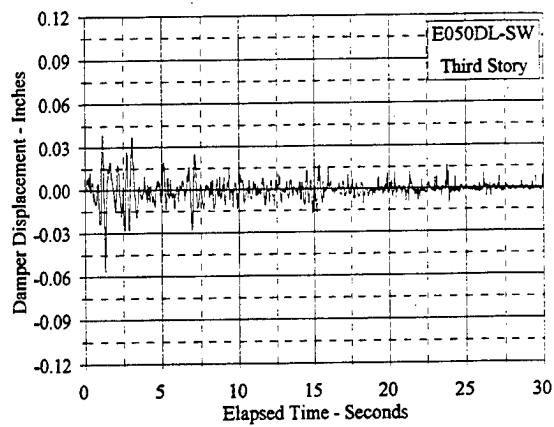


Figure C.9.6 Damper Displacement Vs. Elapsed Time: E050DL, SW and SE

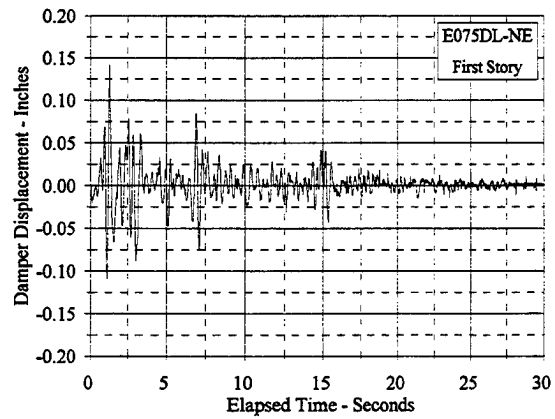
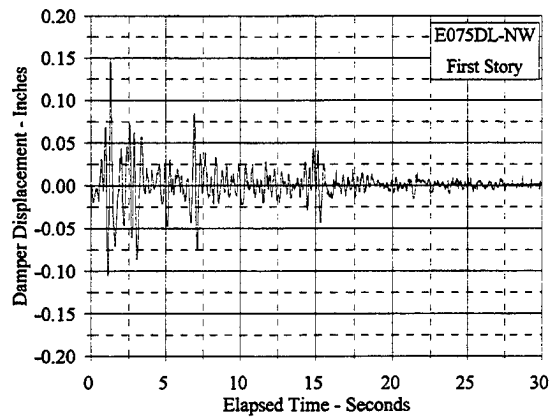
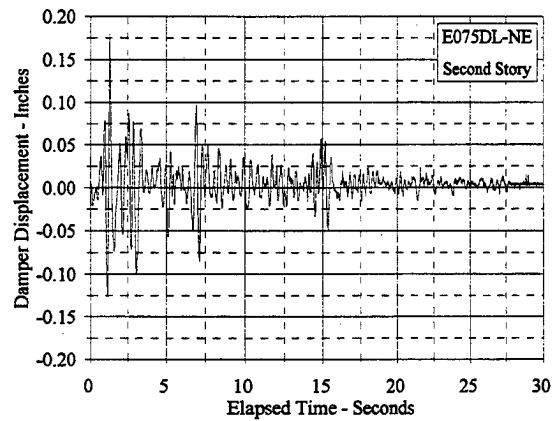
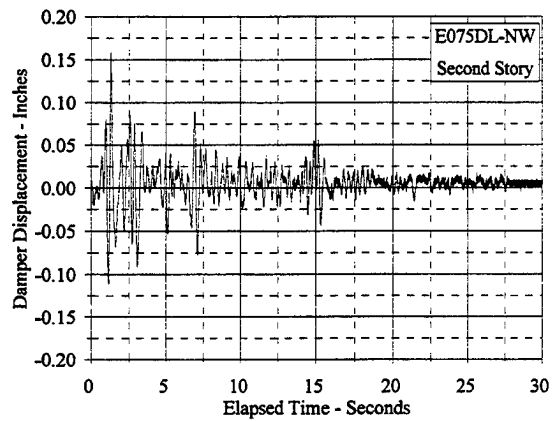
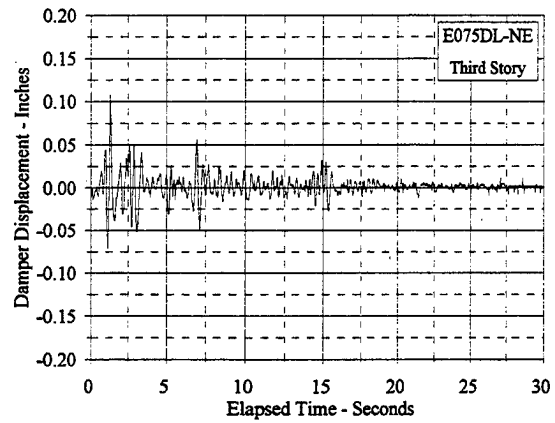
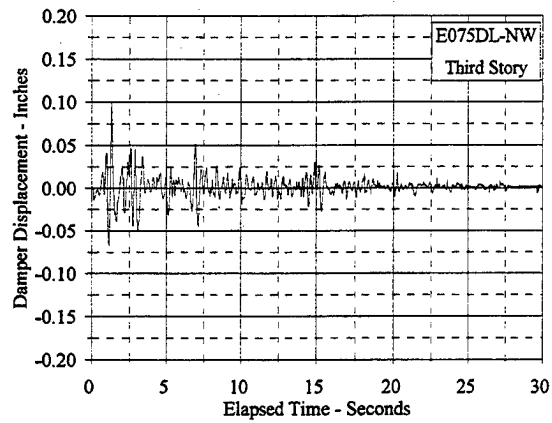


Figure C.9.7 Damper Displacement Vs. Elapsed Time: E075DL, NW and NE

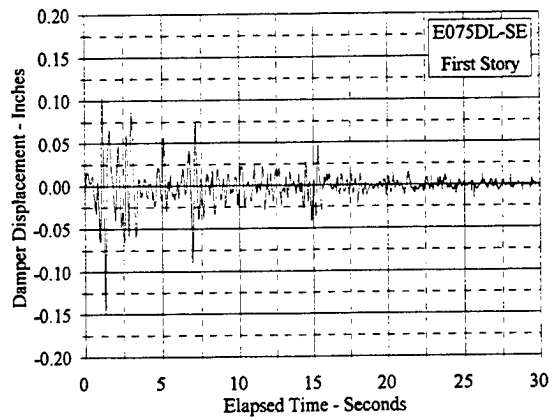
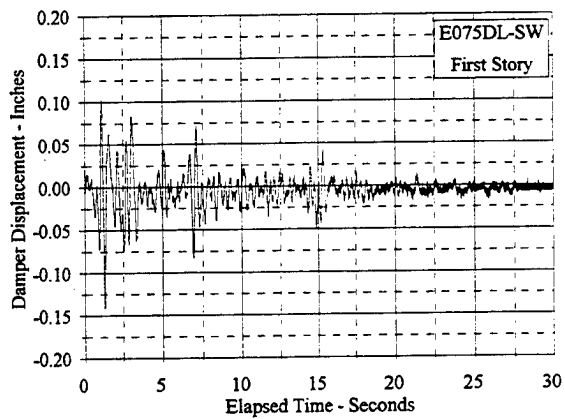
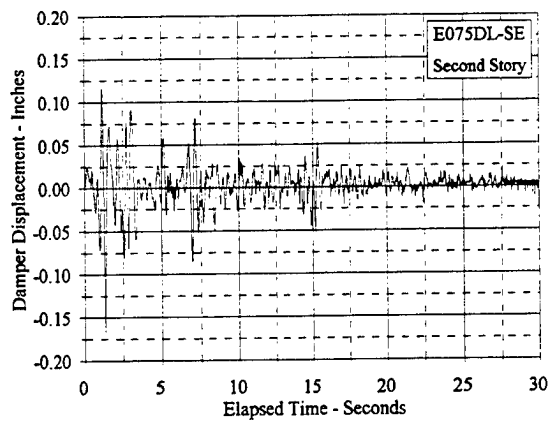
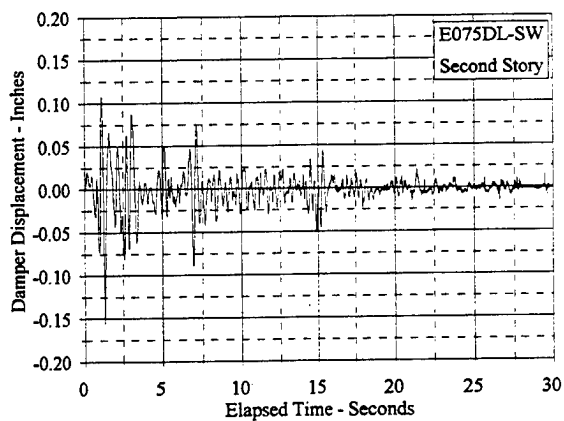
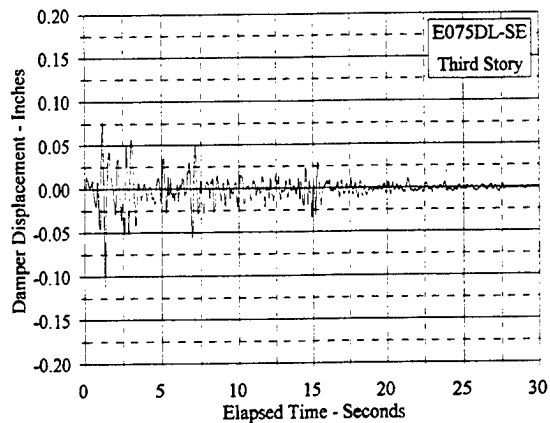
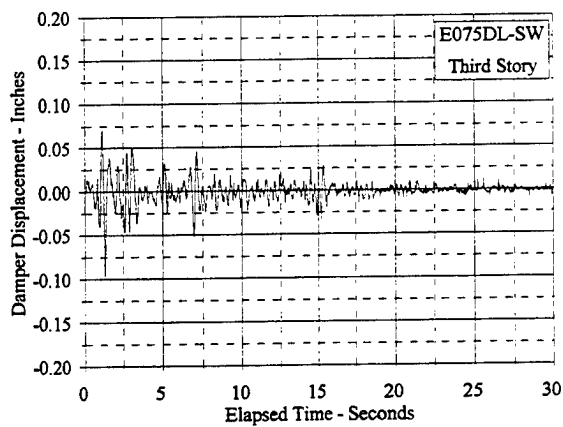


Figure C.9.8 Damper Displacement Vs. Elapsed Time: E075DL, SW and SE

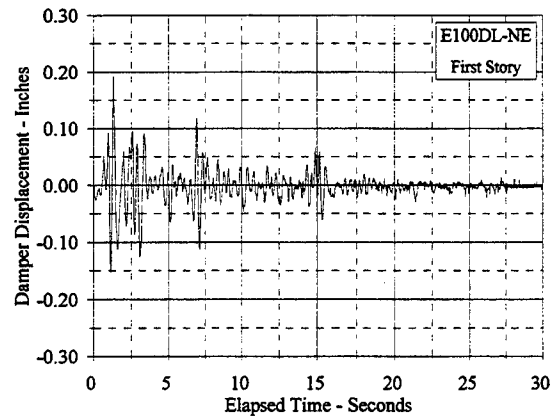
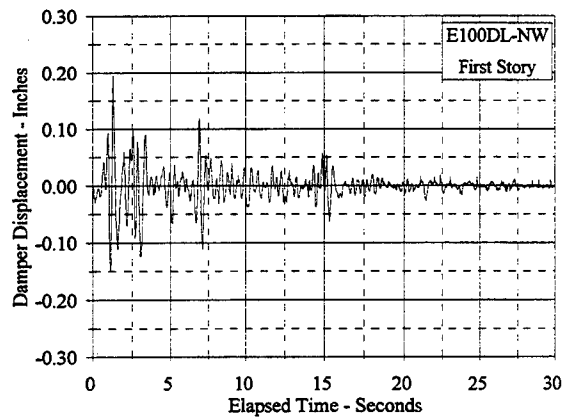
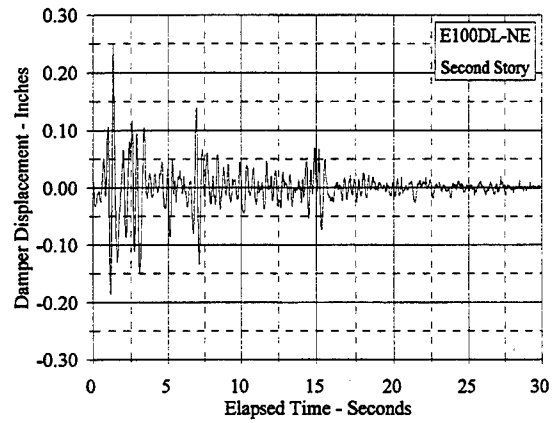
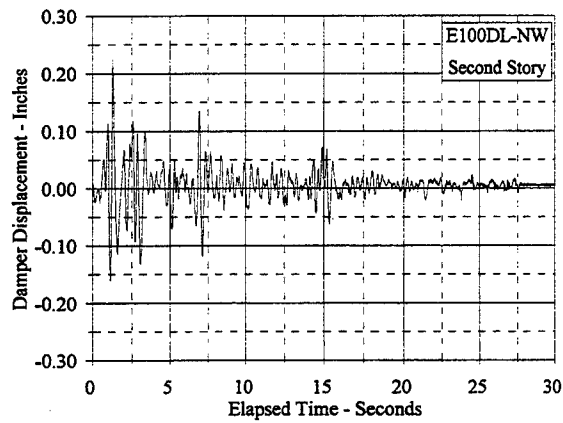
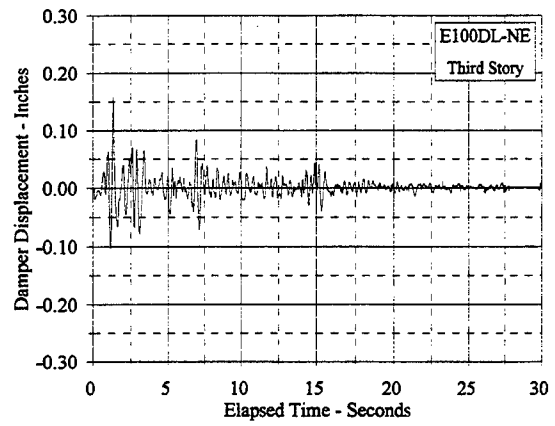
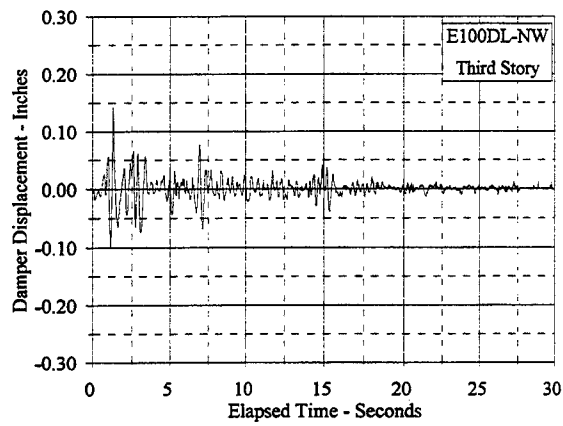


Figure C.9.9 Damper Displacement Vs. Elapsed Time: E100DL, NW and NE

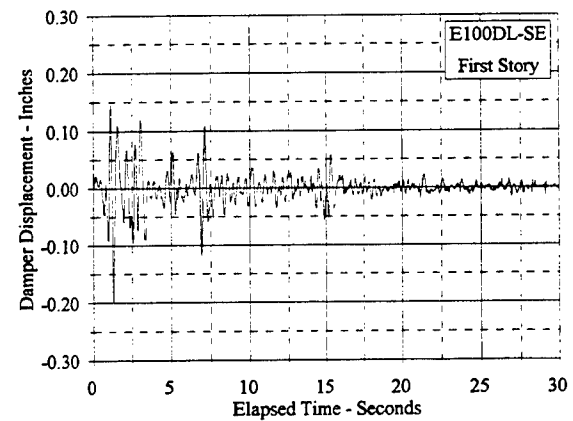
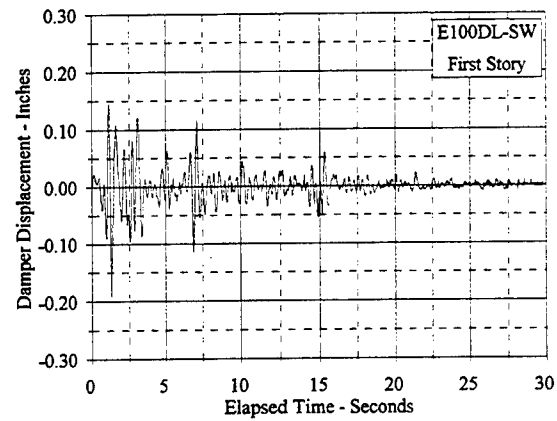
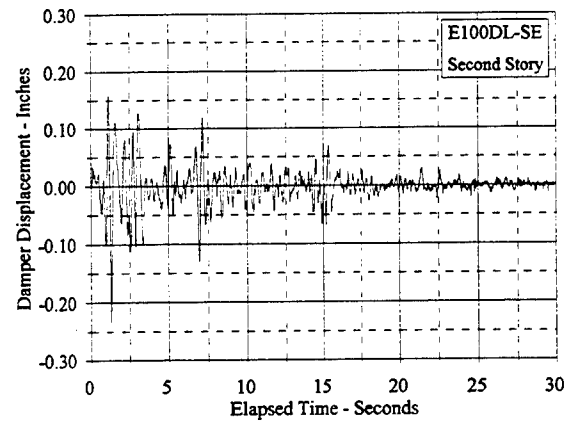
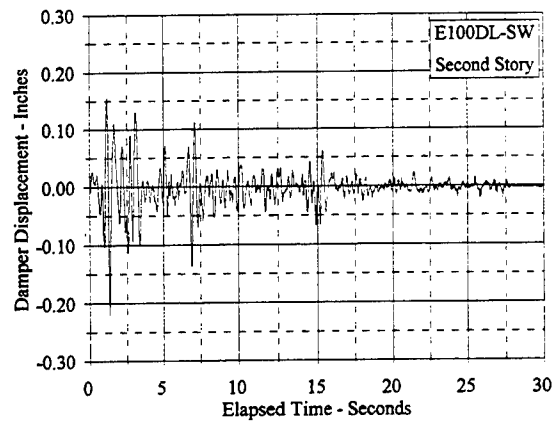
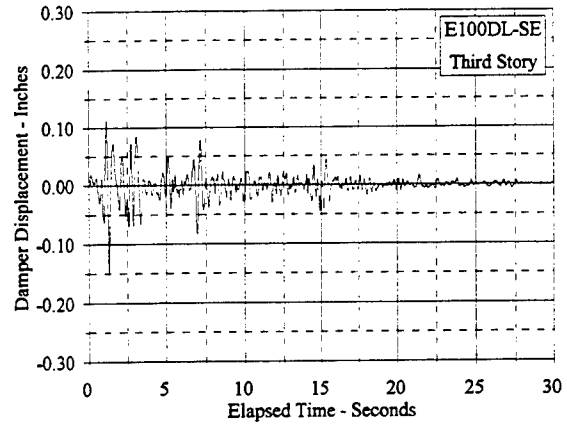
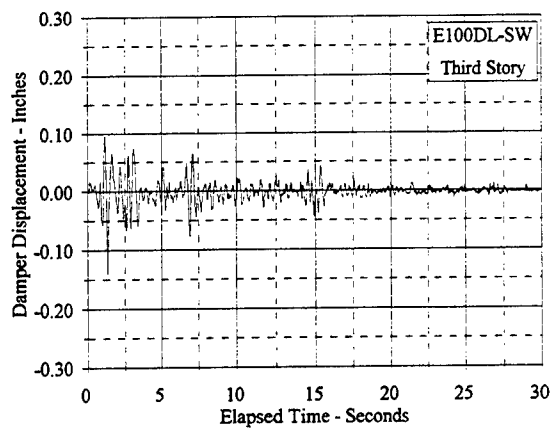


Figure C.9.10 Damper Displacement Vs. Elapsed Time: E100DL, SW and SE

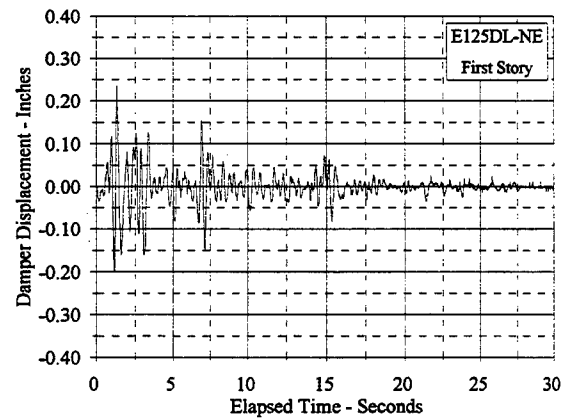
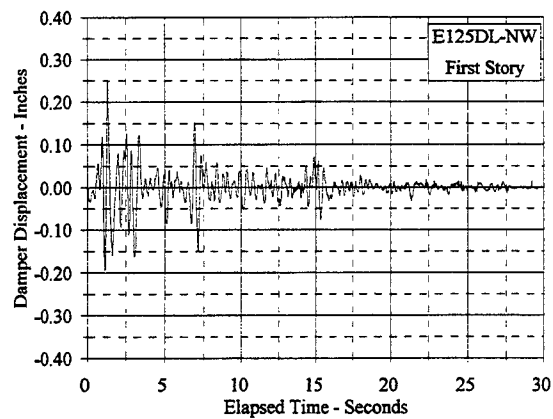
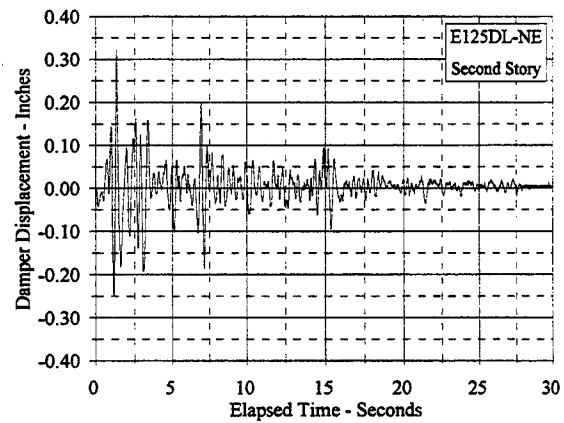
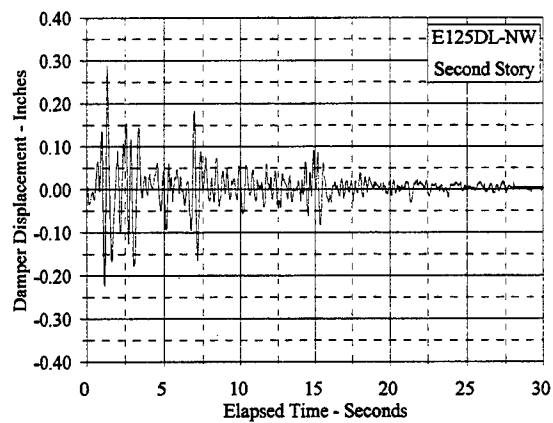
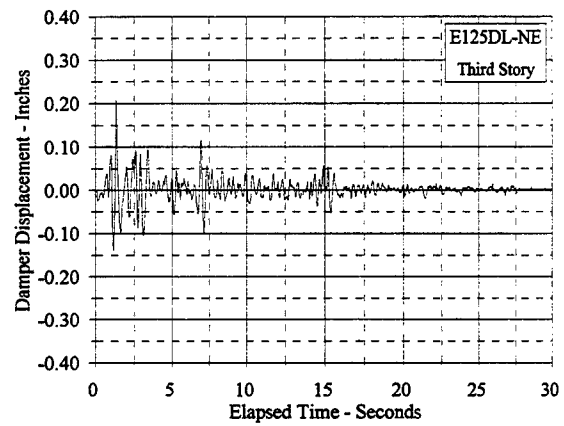
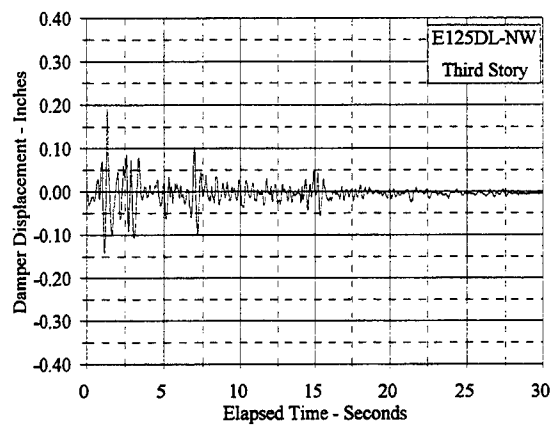


Figure C.9.11 Damper Displacement Vs. Elapsed Time: E125DL, NW and NE

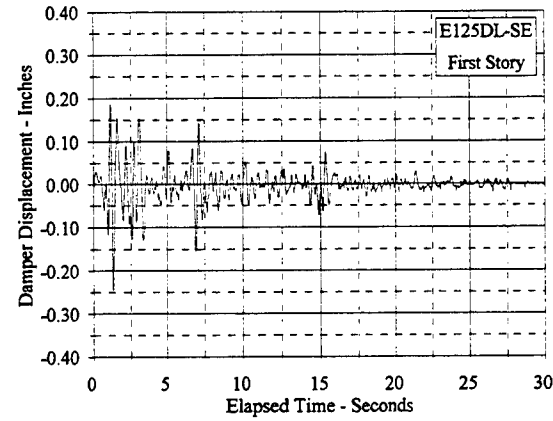
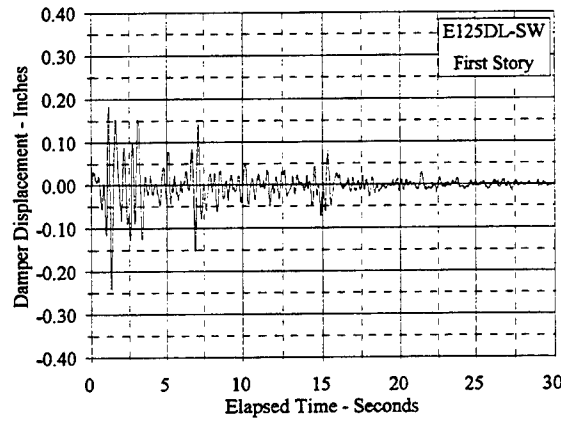
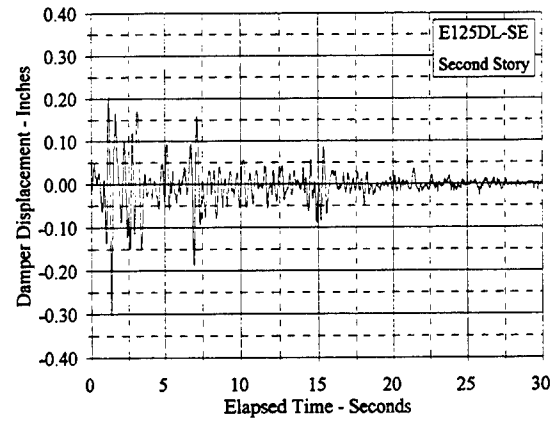
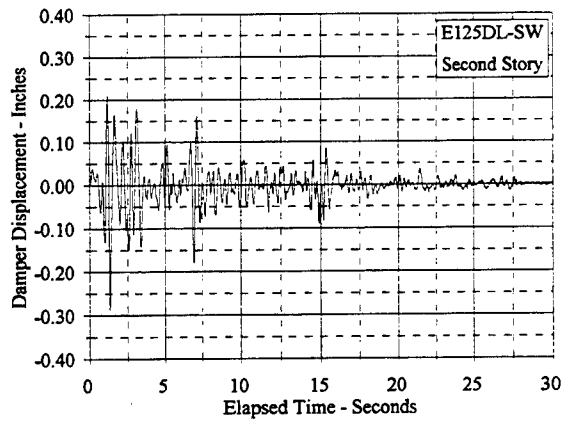
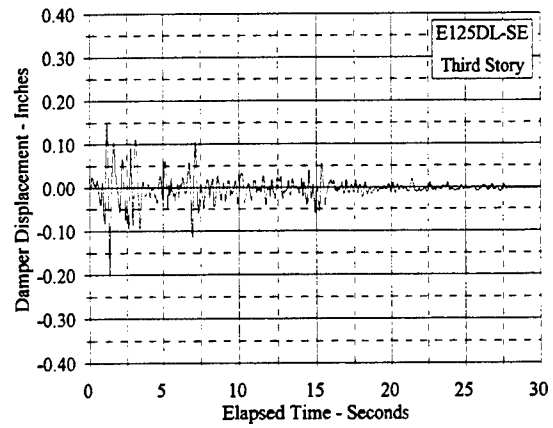
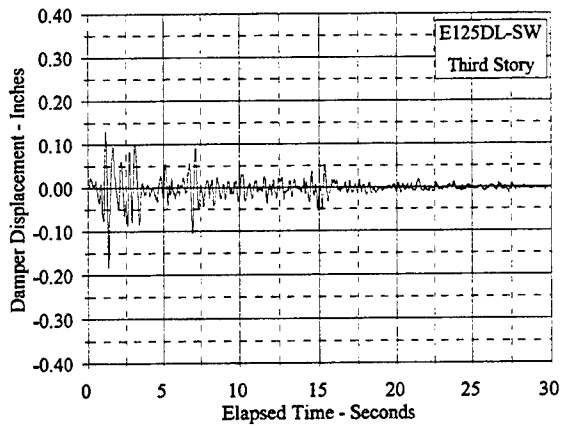


Figure C.9.12 Damper Displacement Vs. Elapsed Time: E125DL, SW and SE

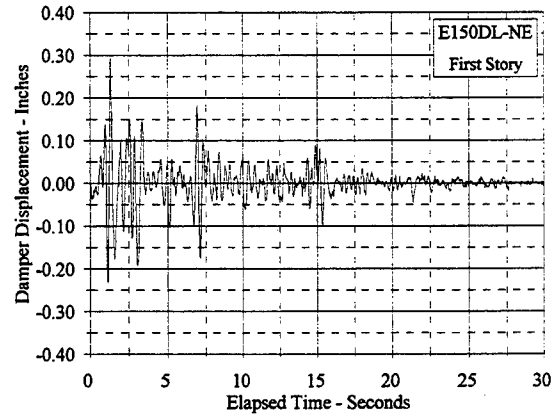
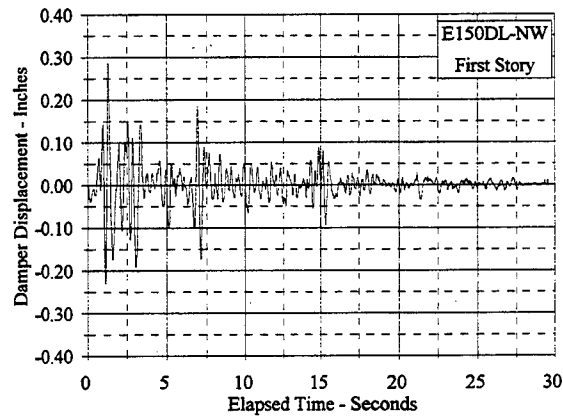
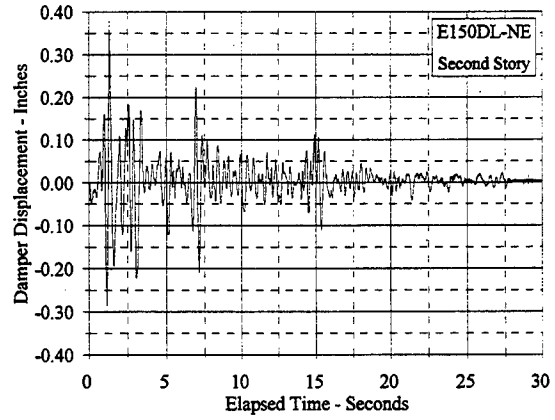
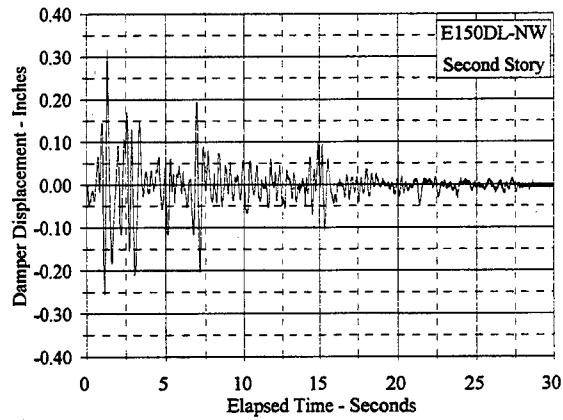
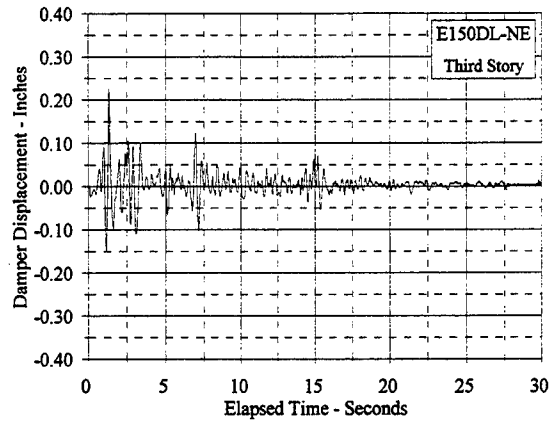
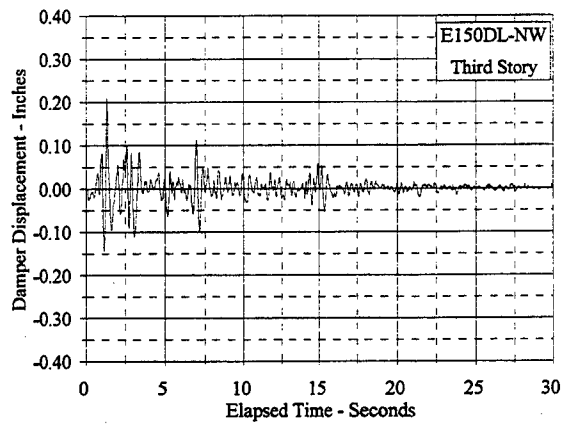


Figure C.9.13 Damper Displacement Vs. Elapsed Time: E150DL, NW and NE

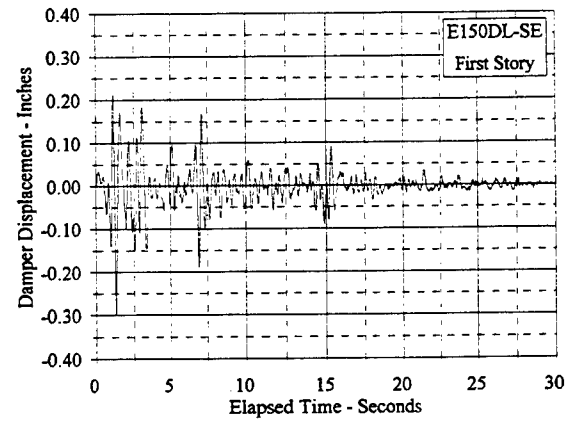
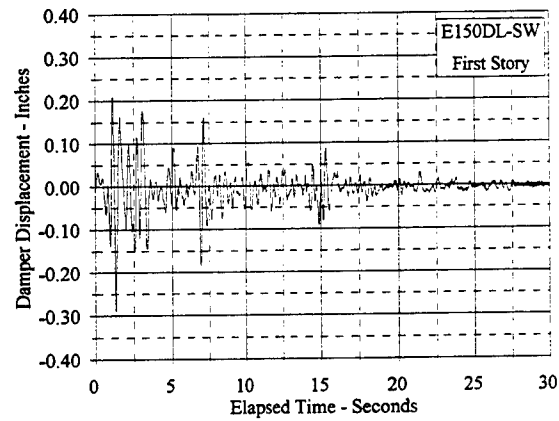
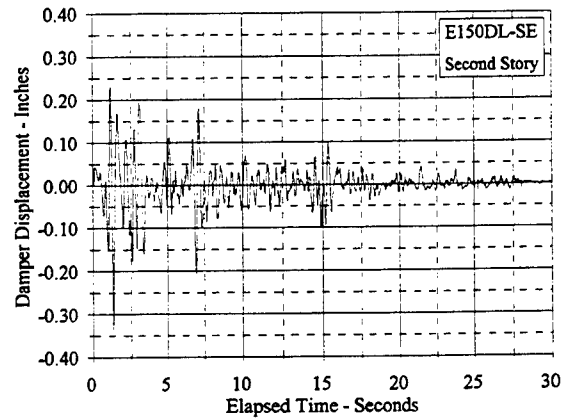
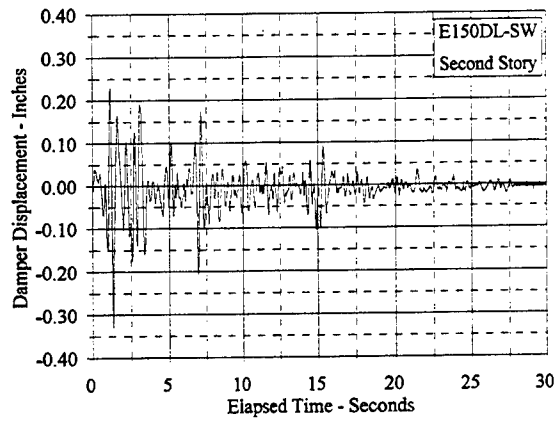
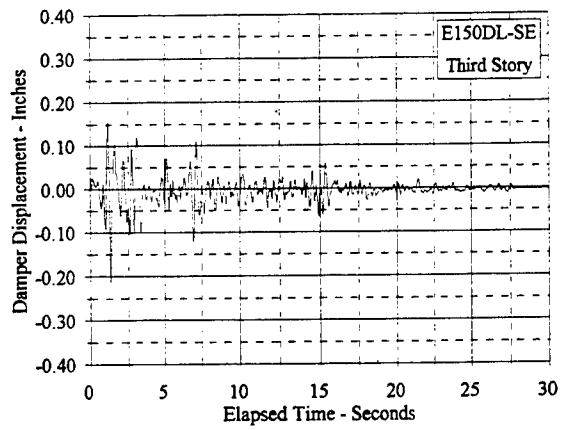
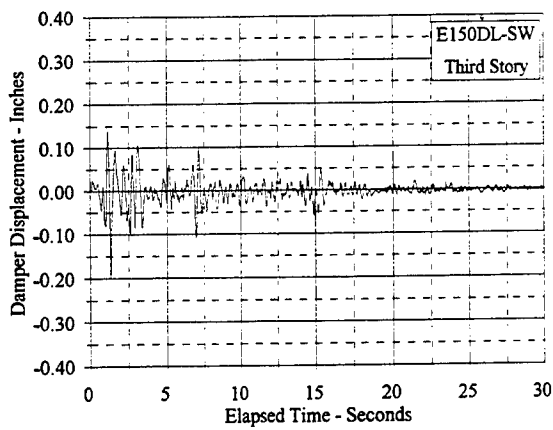


Figure C.9.14 Damper Displacement Vs. Elapsed Time: E150DL, SW and SE

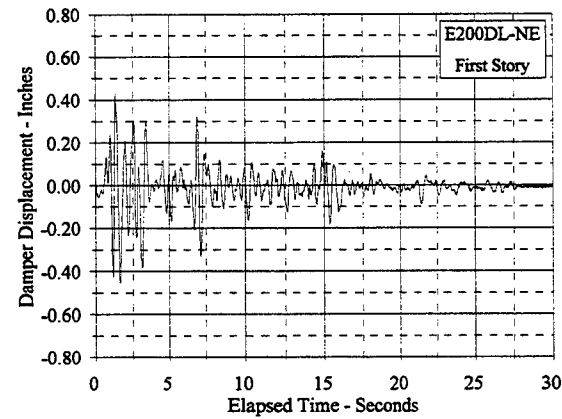
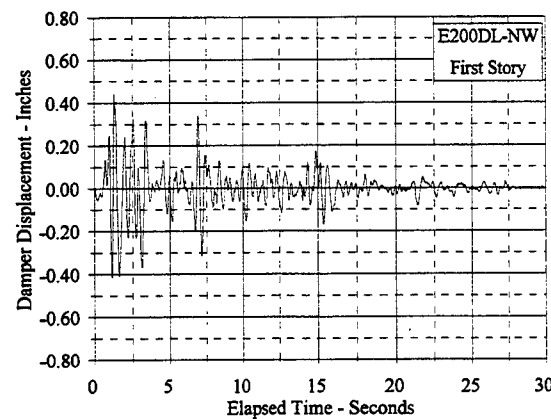
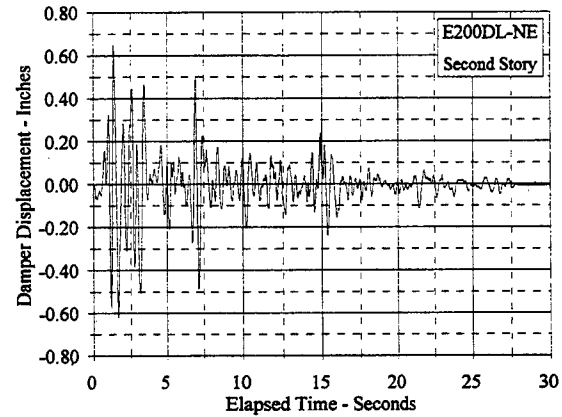
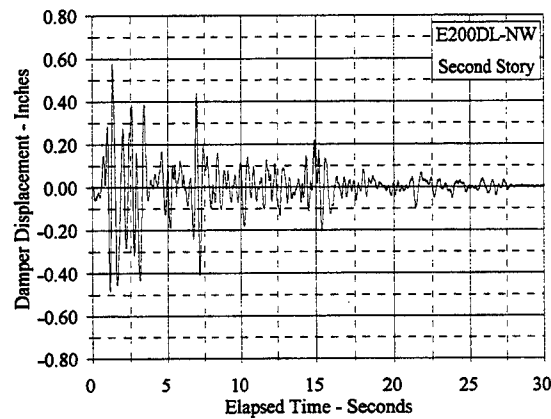
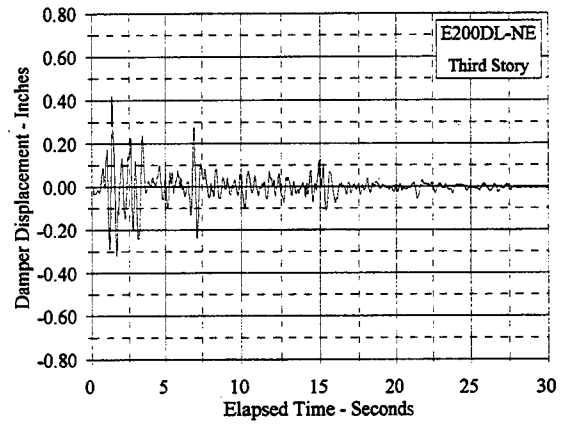
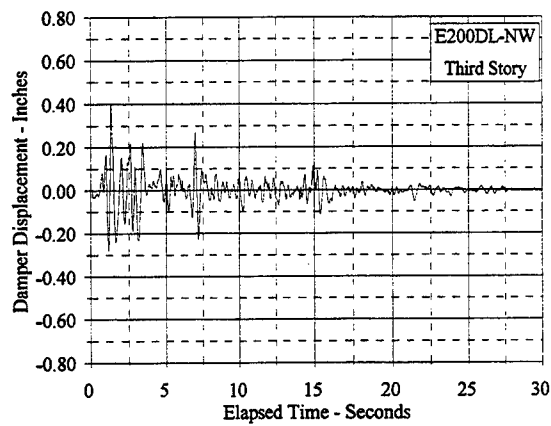


Figure C.9.15 Damper Displacement Vs. Elapsed Time: E200DL, NW and NE

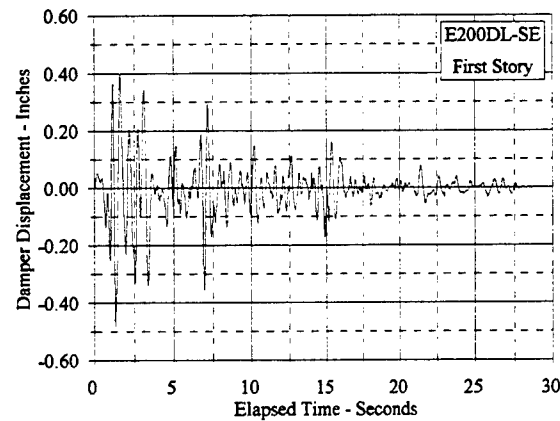
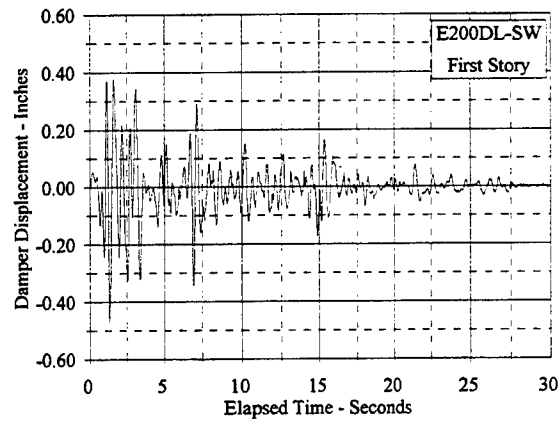
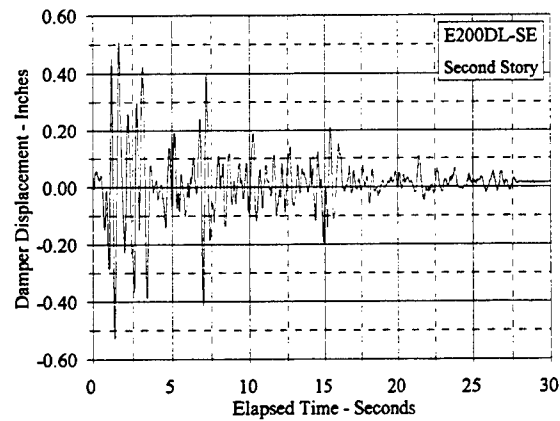
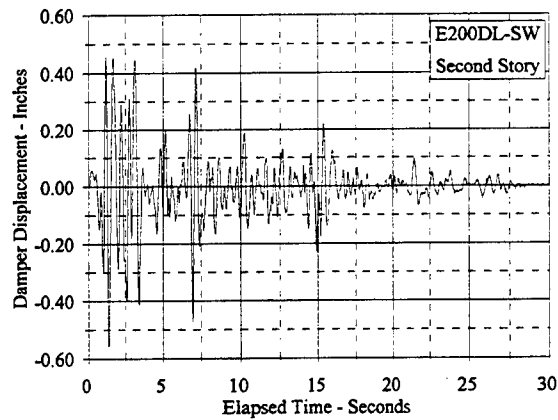
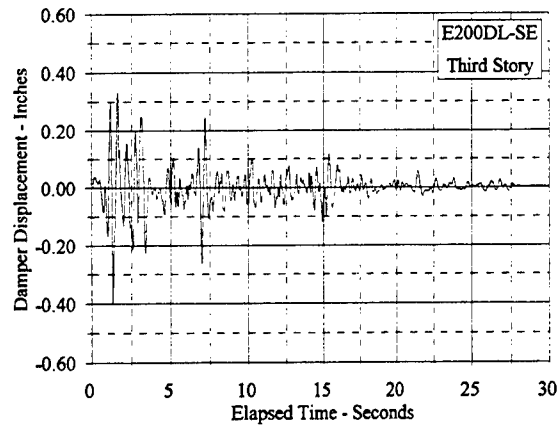
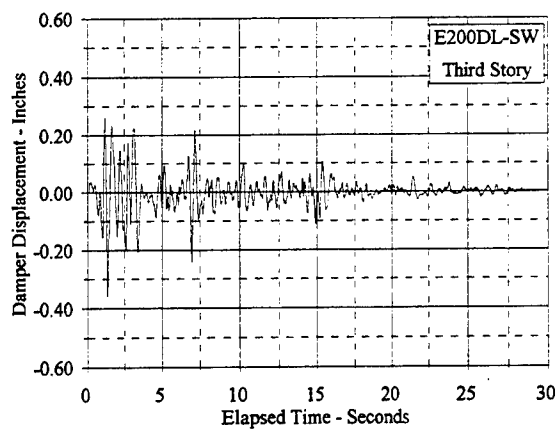


Figure C.9.16 Damper Displacement Vs. Elapsed Time: E200DL, SW and SE

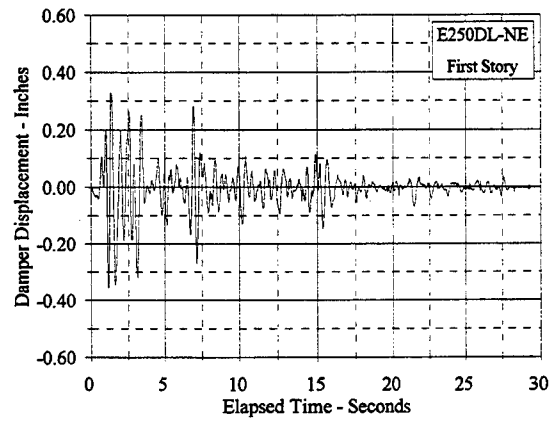
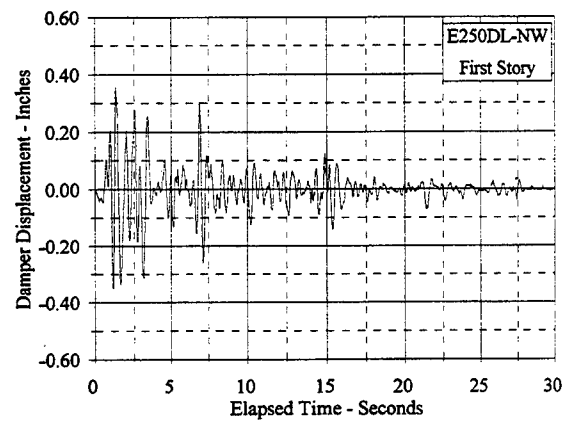
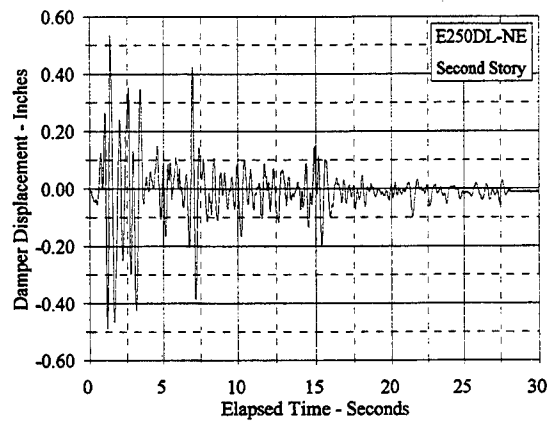
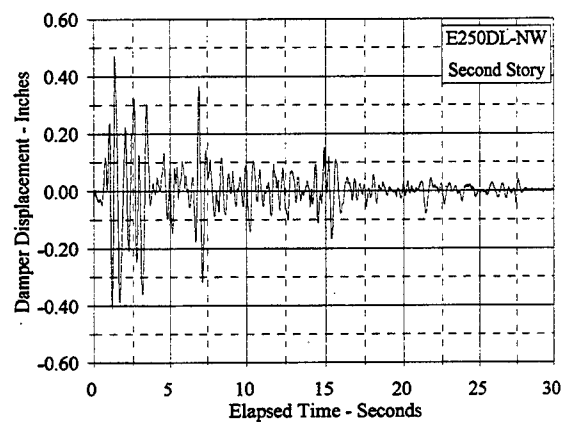
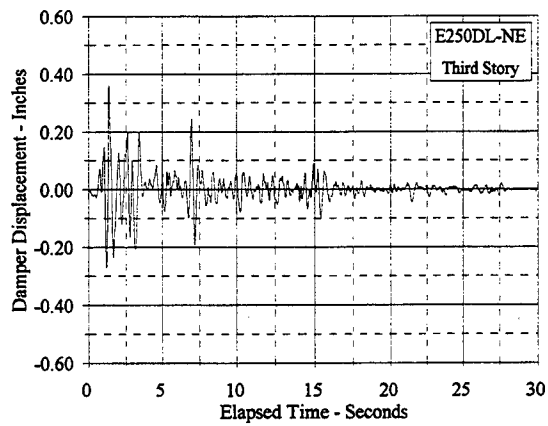
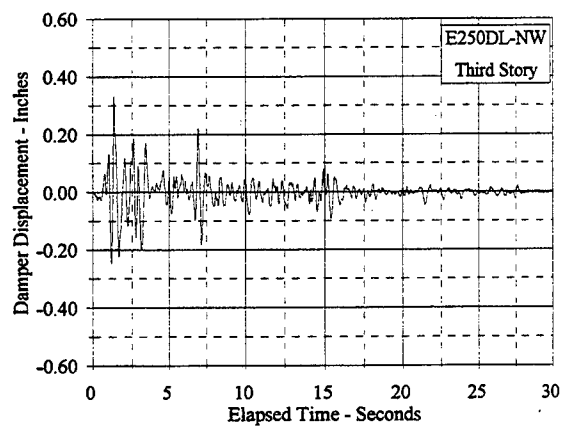


Figure C.9.17 Damper Displacement Vs. Elapsed Time: E250DL, NW and NE

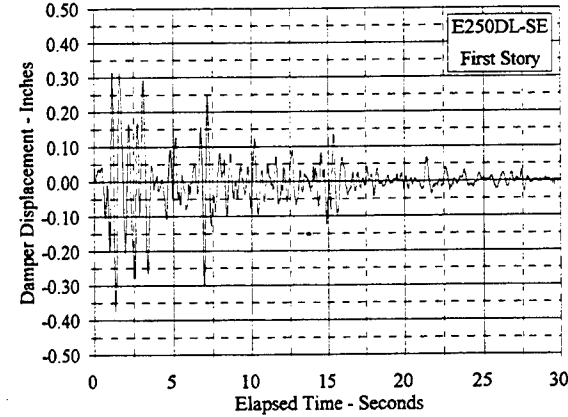
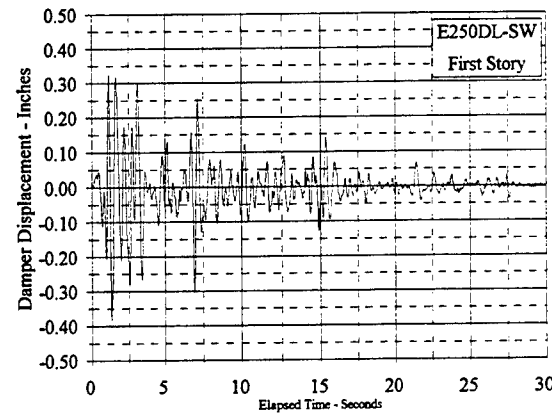
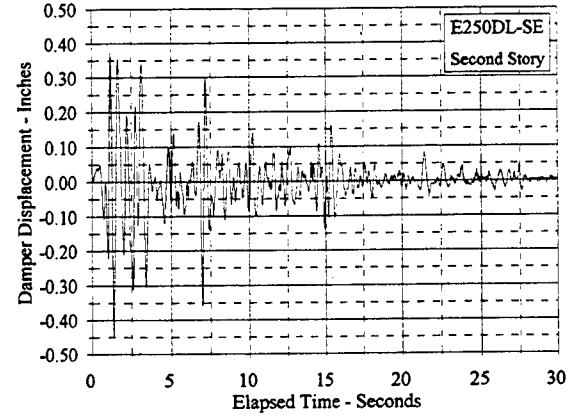
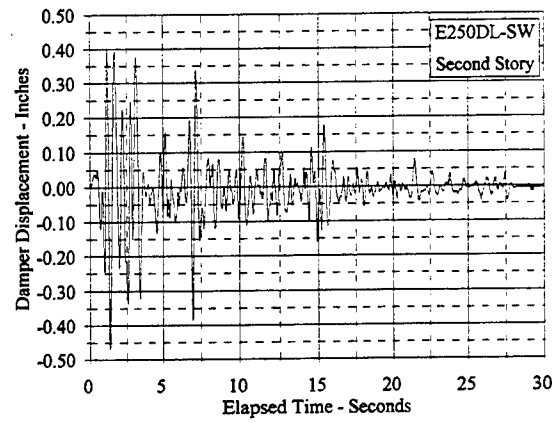
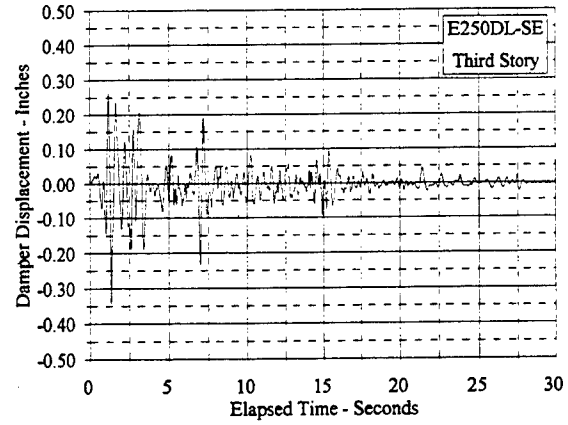
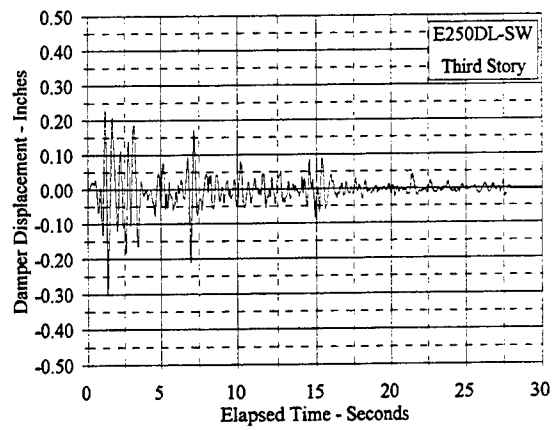


Figure C.9.18 Damper Displacement Vs. Elapsed Time: E250DL, SW and SE

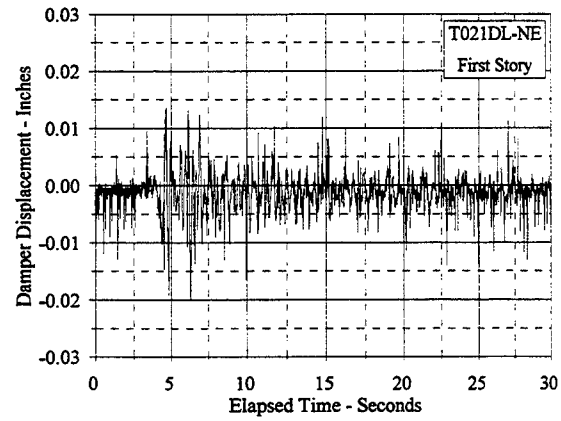
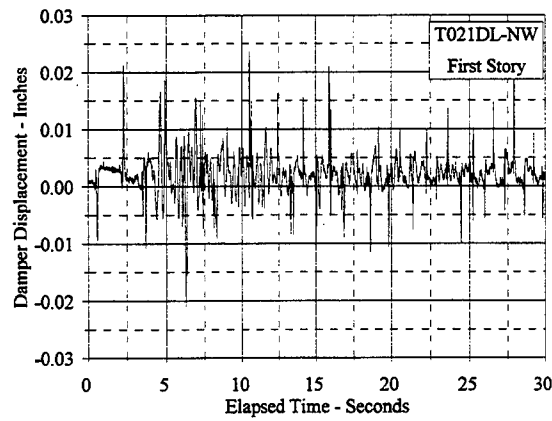
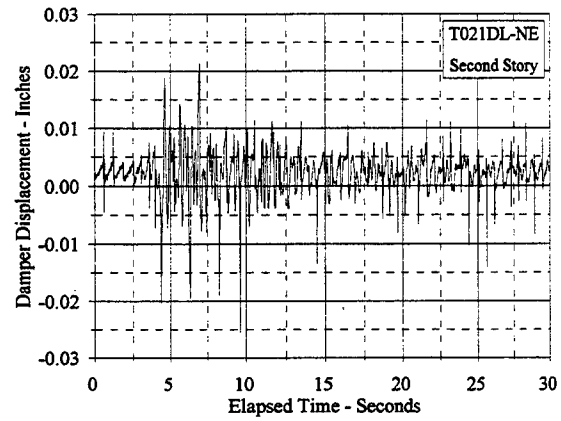
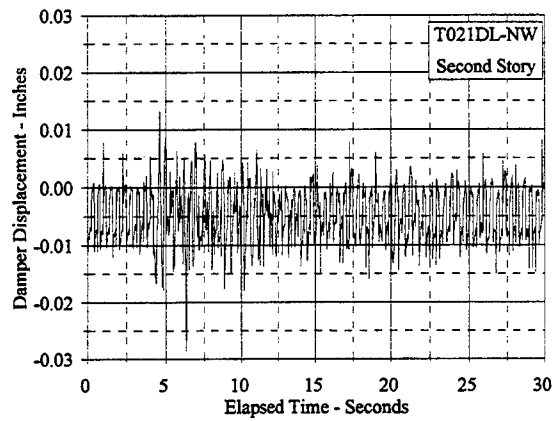
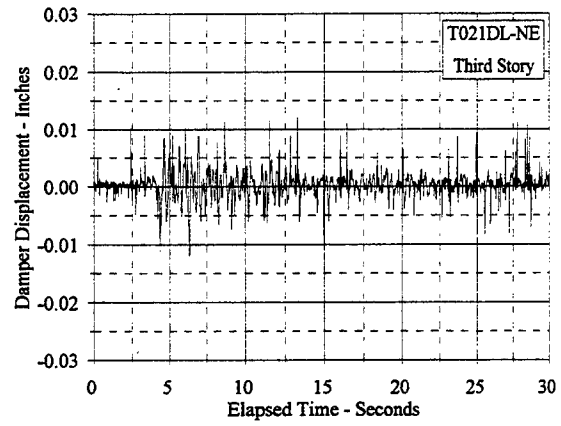
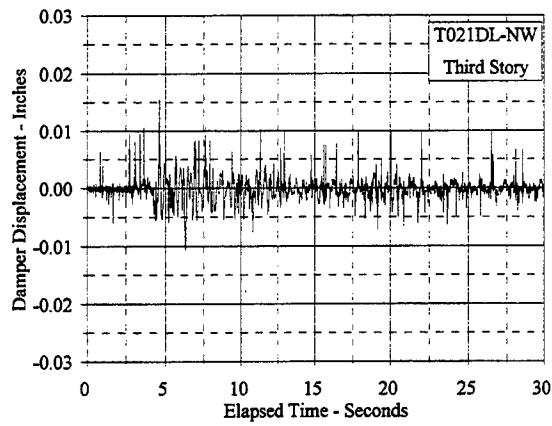


Figure C.9.19 Damper Displacement Vs. Elapsed Time: T021DL, NW and NE

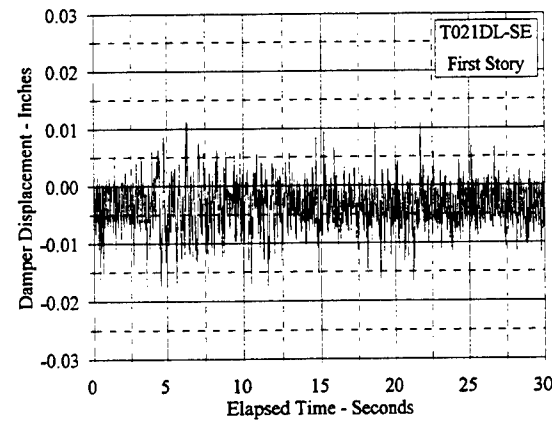
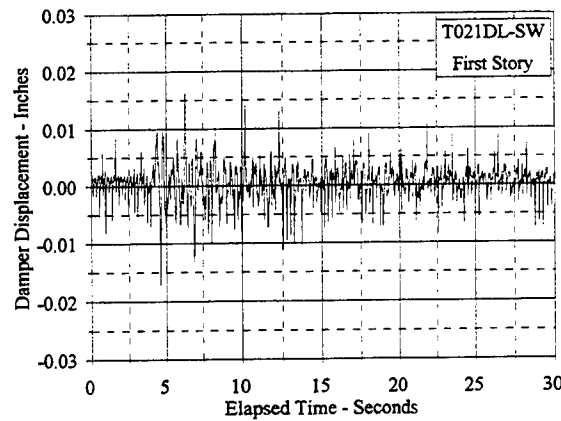
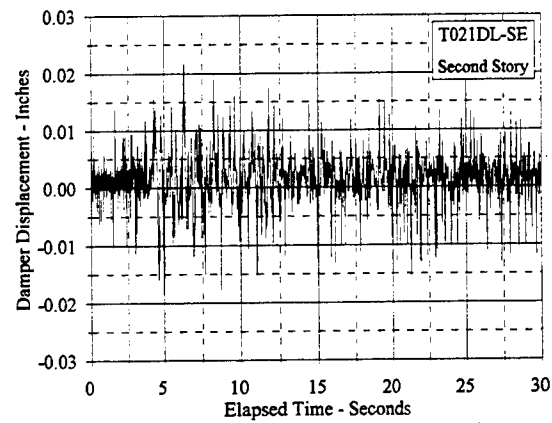
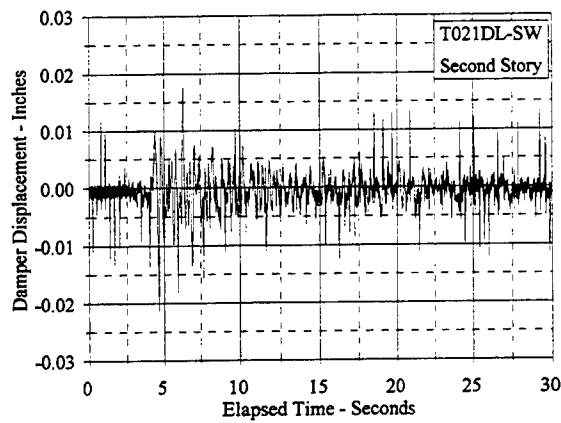
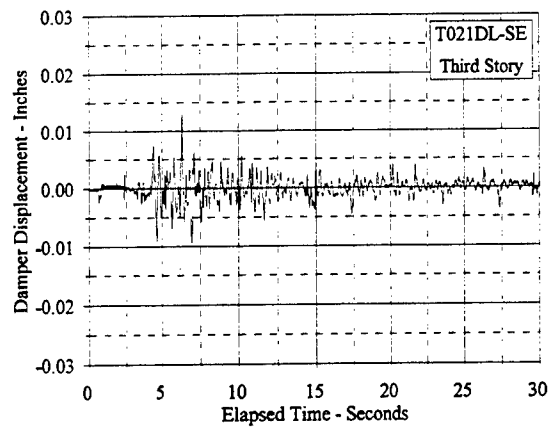
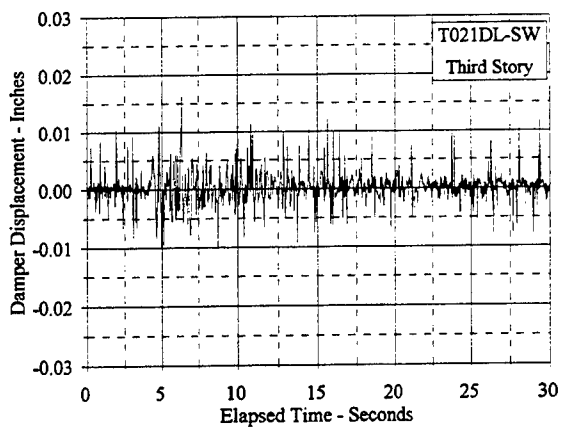


Figure C.9.20 Damper Displacement Vs. Elapsed Time: T021DL, SW and SE

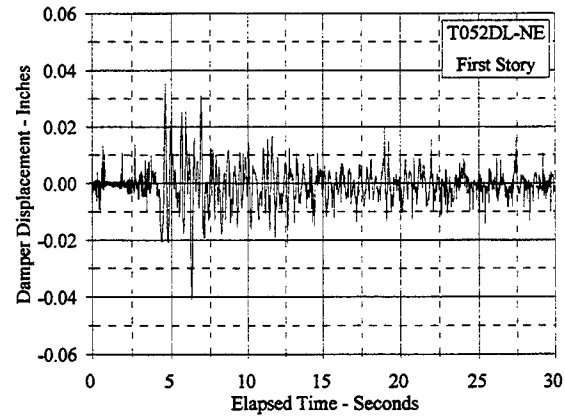
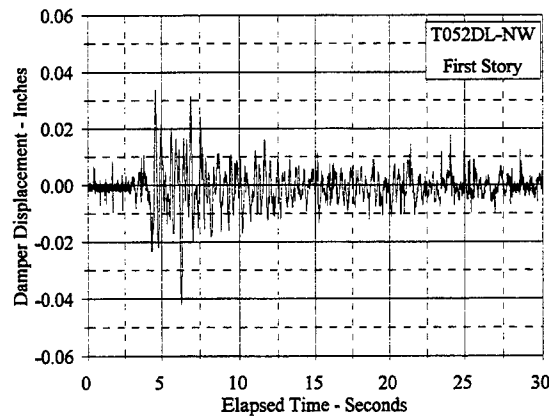
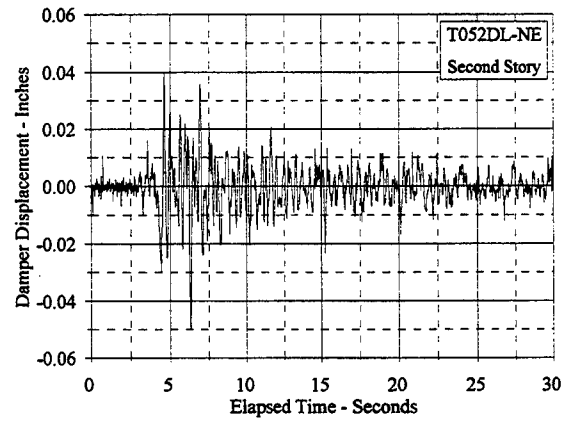
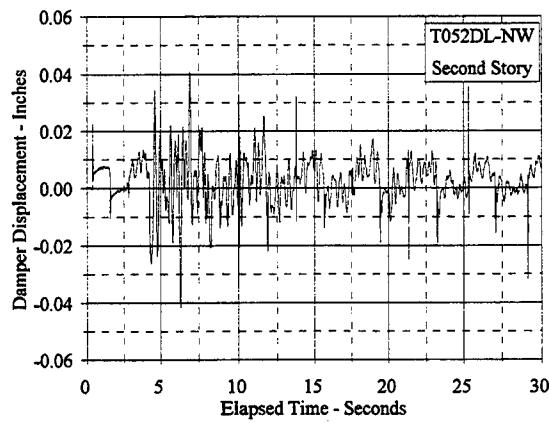
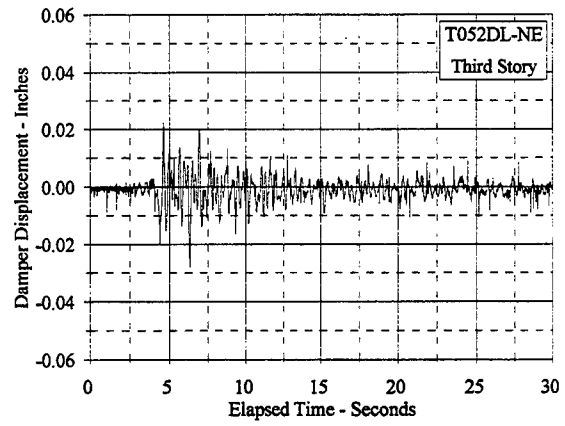
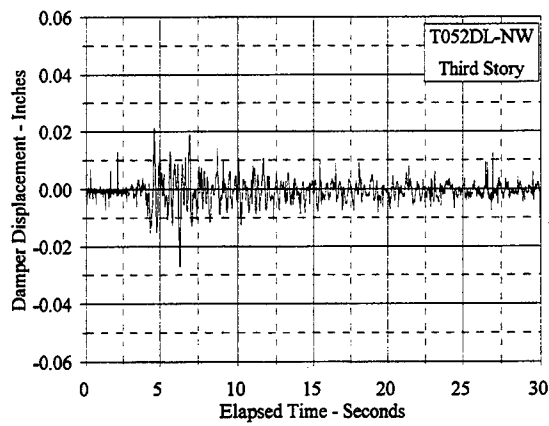


Figure C.9.21 Damper Displacement Vs. Elapsed Time: T052DL, NW and NE

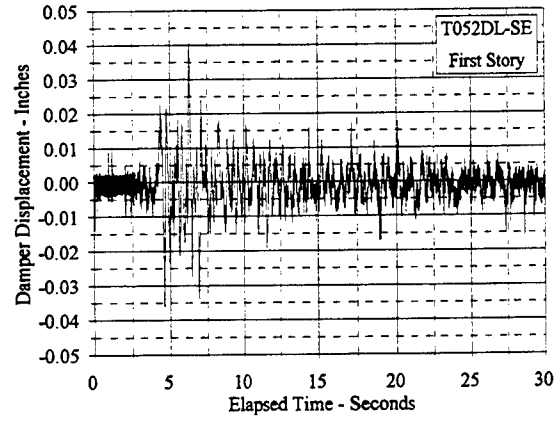
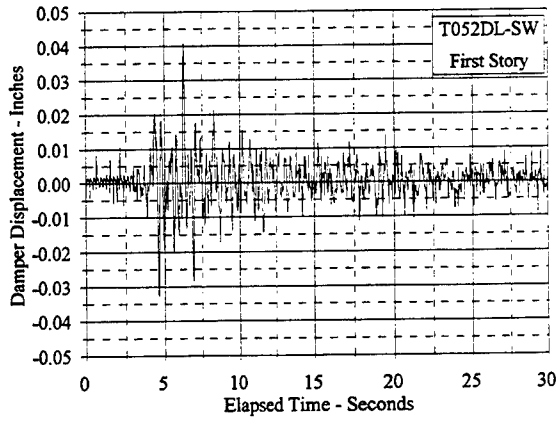
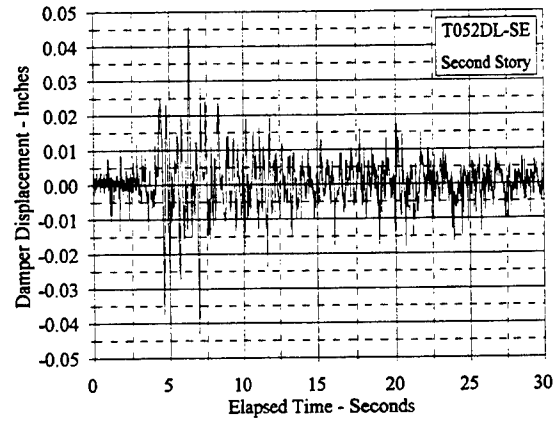
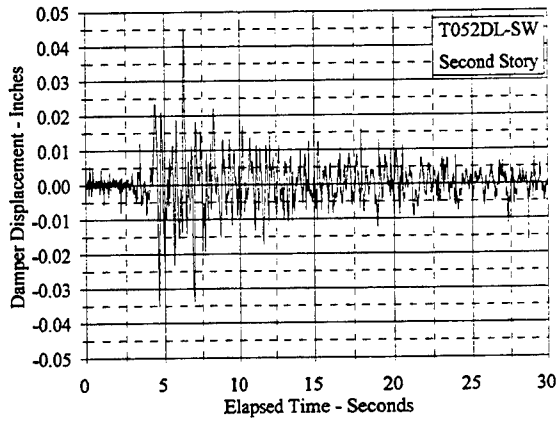
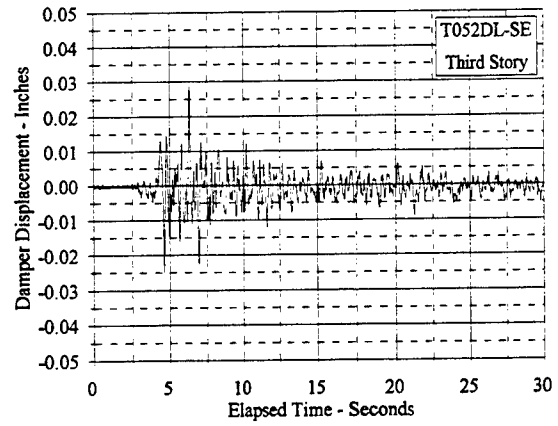
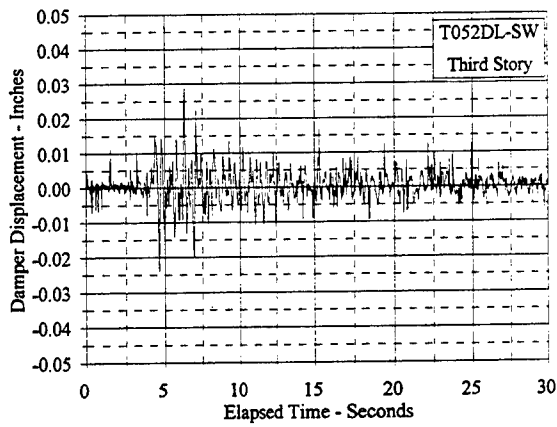


Figure C.9.22 Damper Displacement Vs. Elapsed Time: T052DL, SW and SE

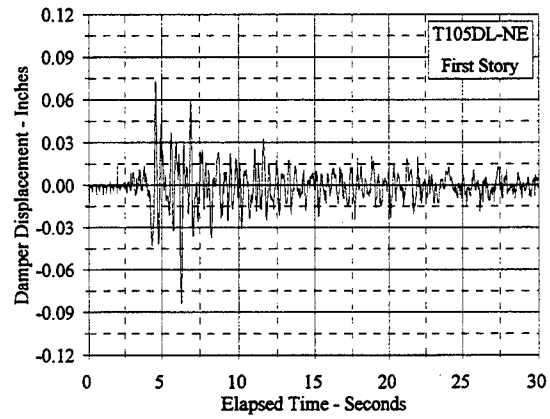
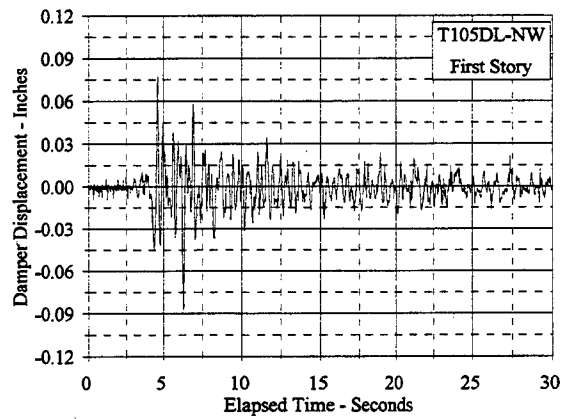
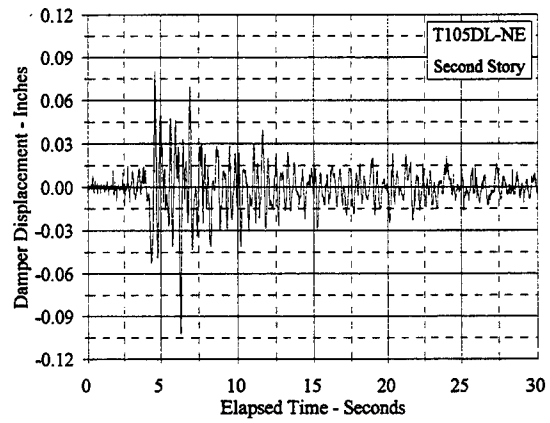
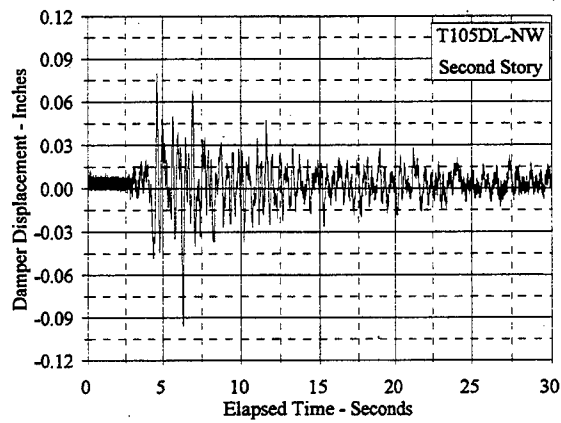
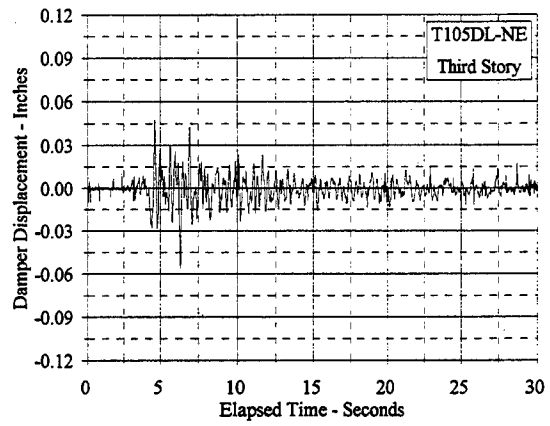
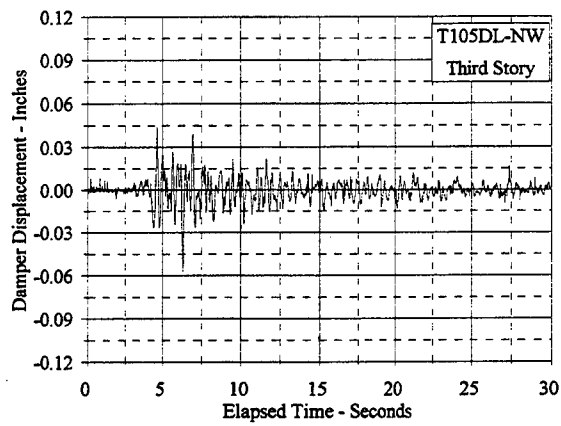


Figure C.9.23 Damper Displacement Vs. Elapsed Time: T105DL, NW and NE

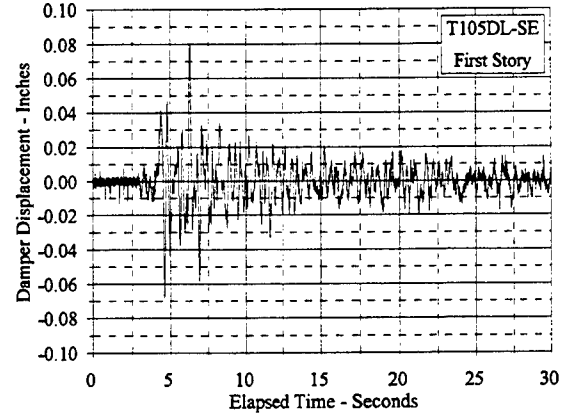
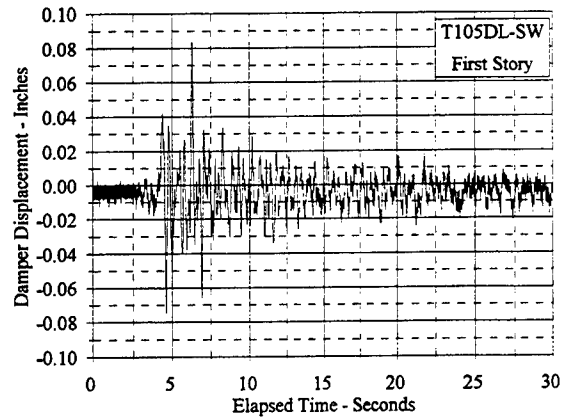
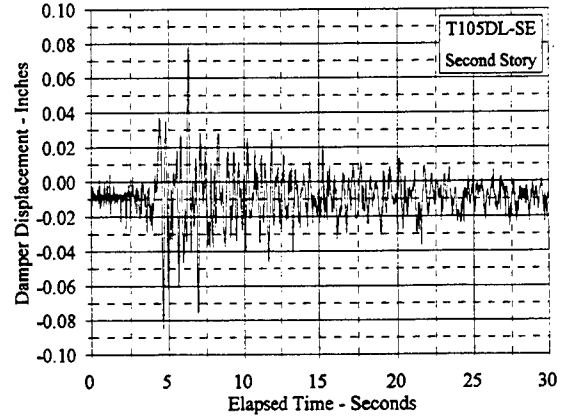
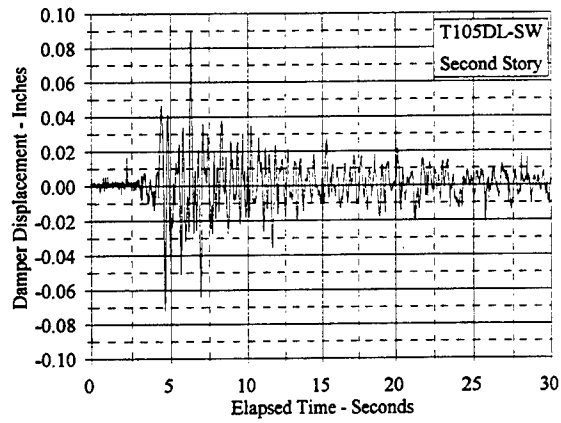
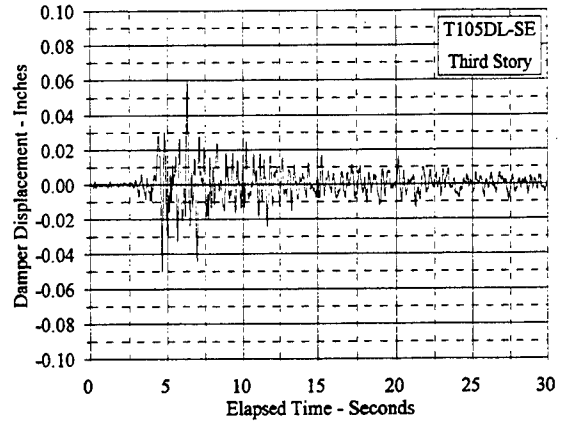
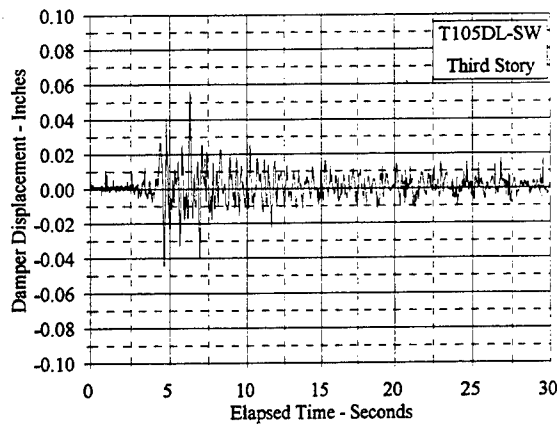


Figure C.9.24 Damper Displacement Vs. Elapsed Time: T105DL, SW and SE

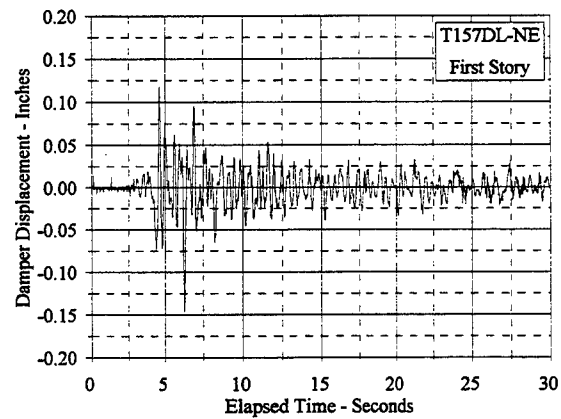
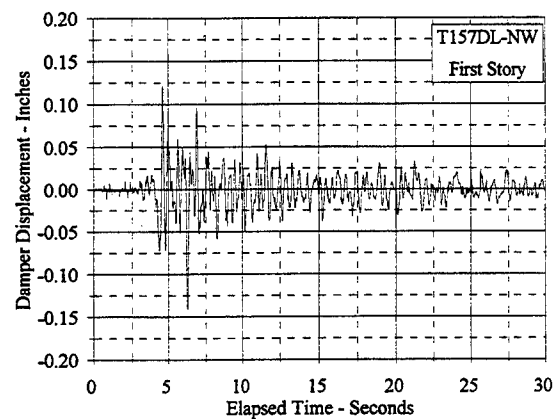
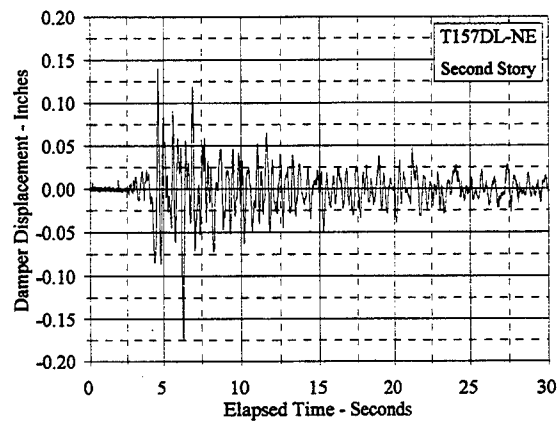
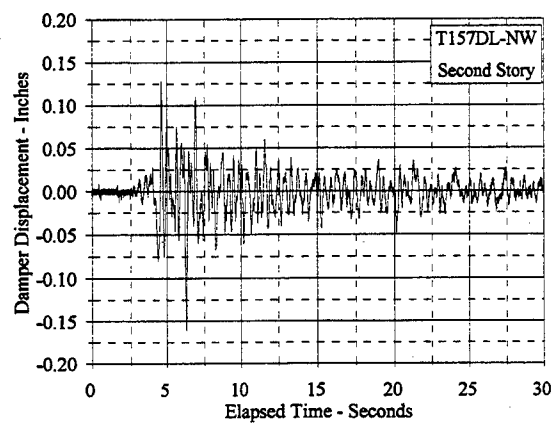
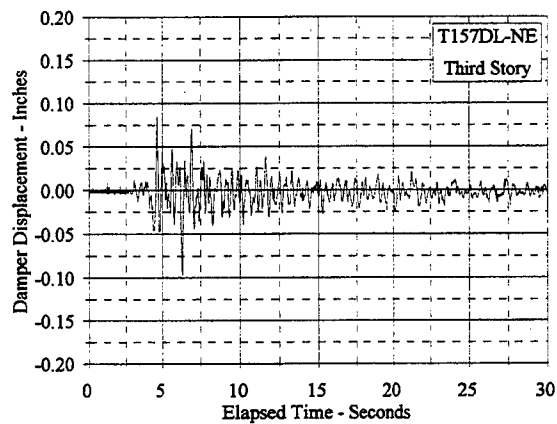
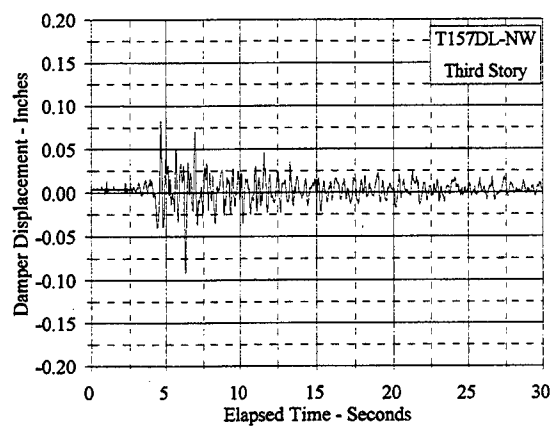


Figure C.9.25 Damper Displacement Vs. Elapsed Time: T157DL, NW and NE

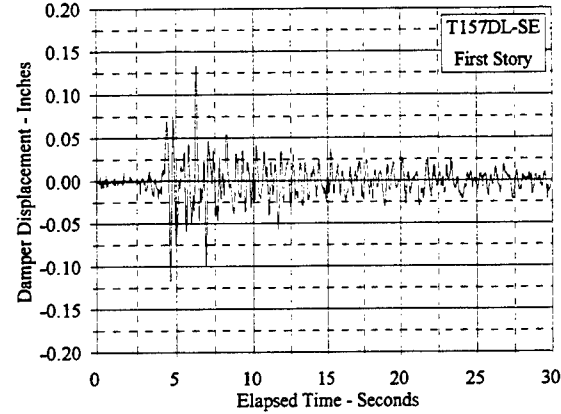
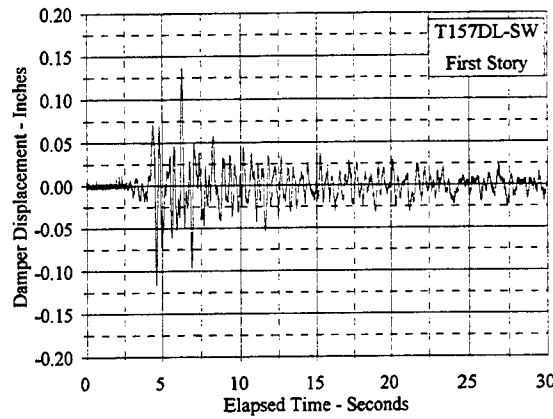
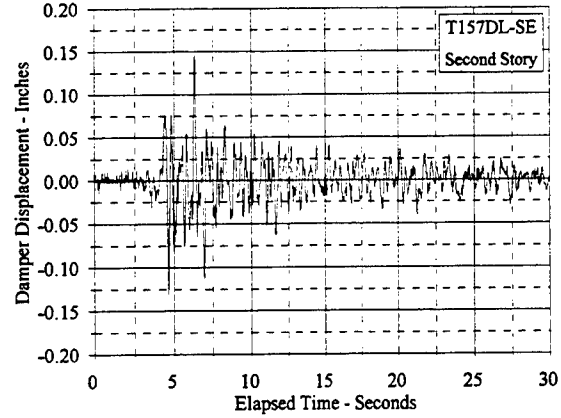
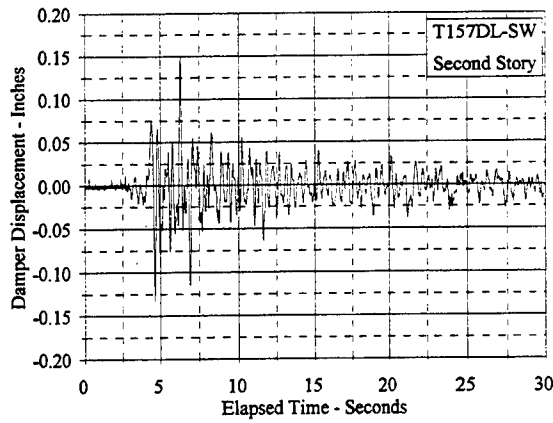
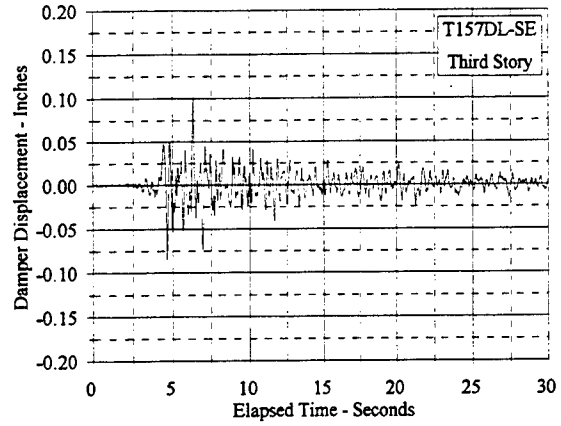
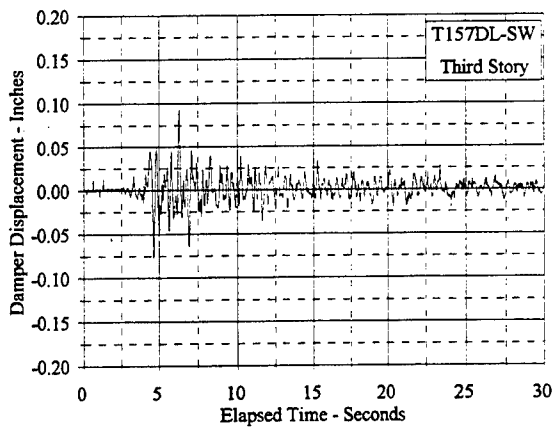


Figure C.9.26 Damper Displacement Vs. Elapsed Time: T157DL, SW and SE

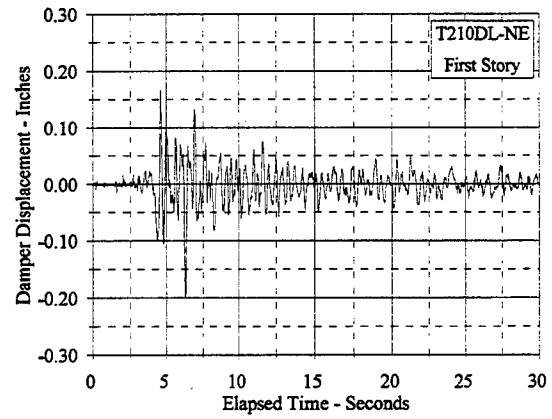
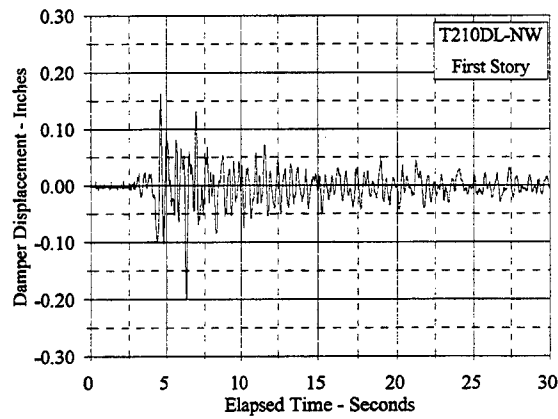
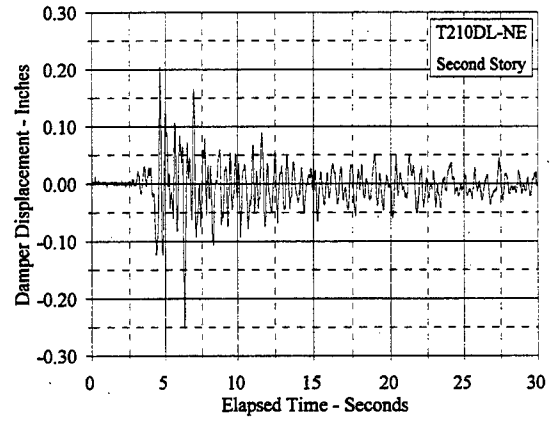
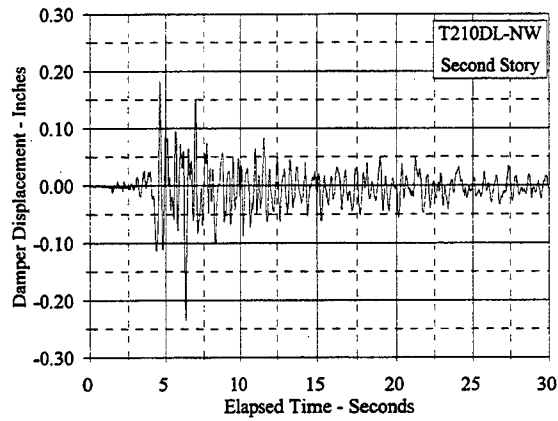
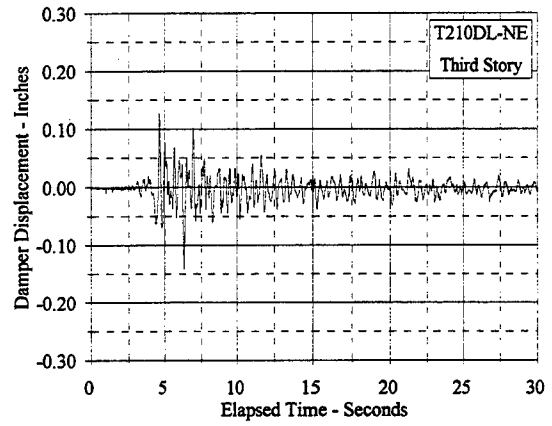
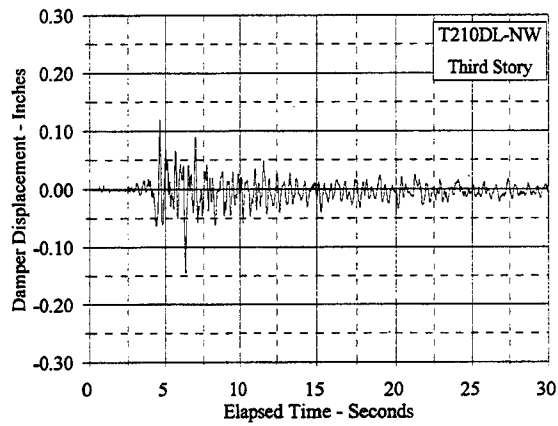


Figure C.9.27 Damper Displacement Vs. Elapsed Time: T210DL, NW and NE

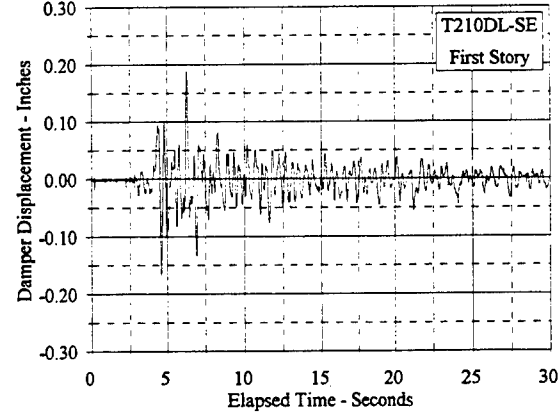
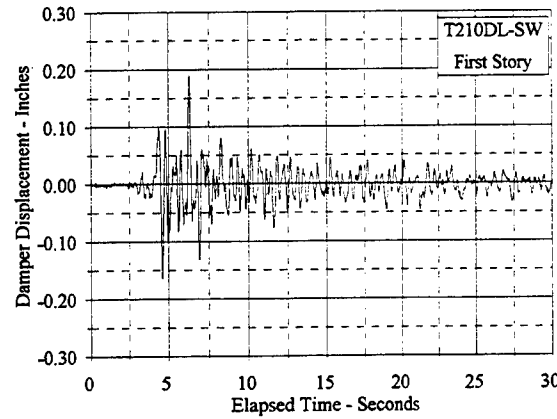
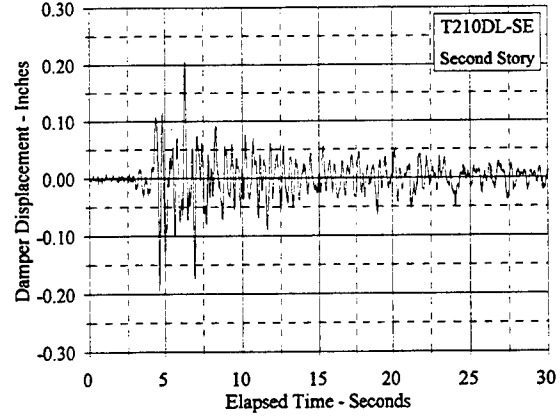
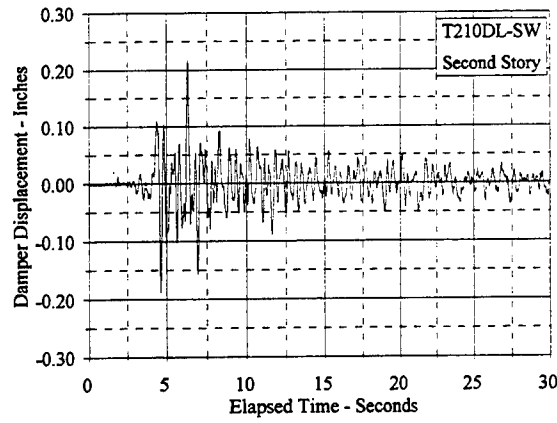
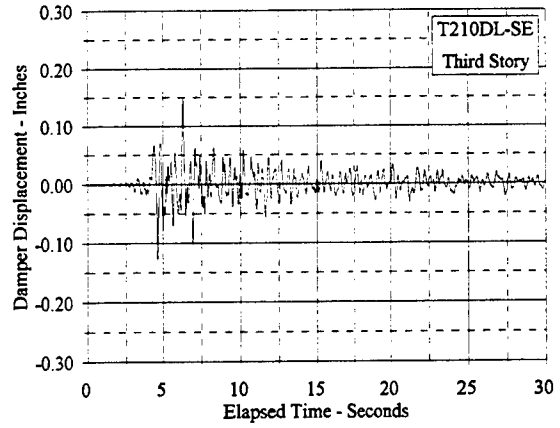
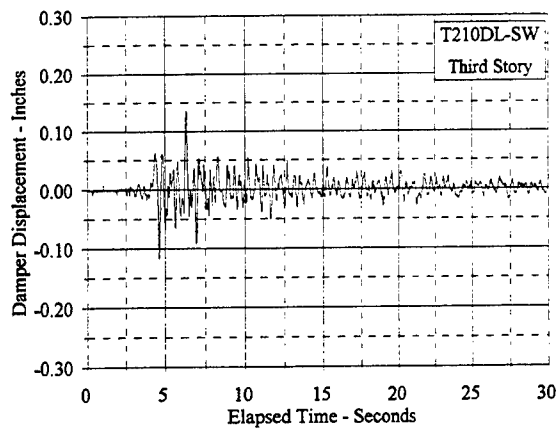


Figure C.9.28 Damper Displacement Vs. Elapsed Time: T210DL, SW and SE

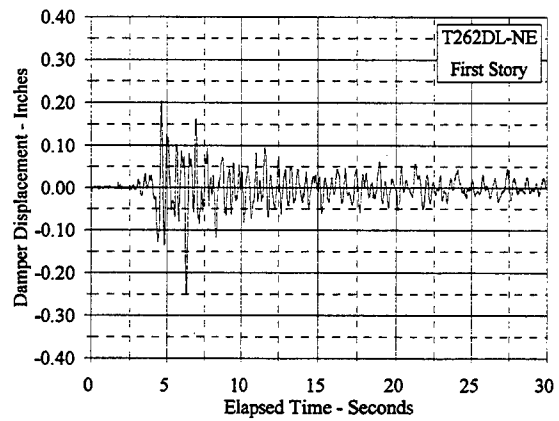
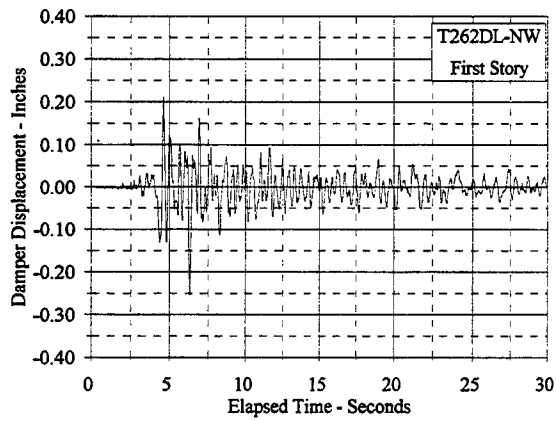
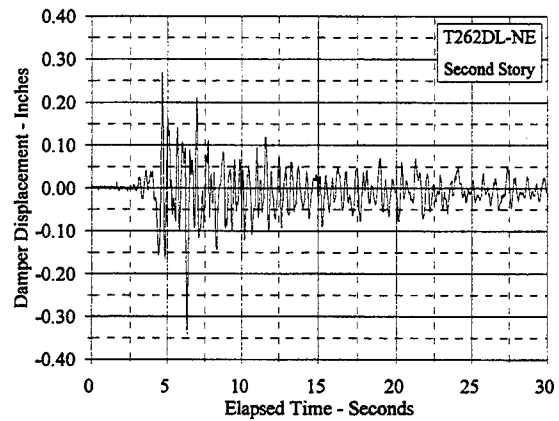
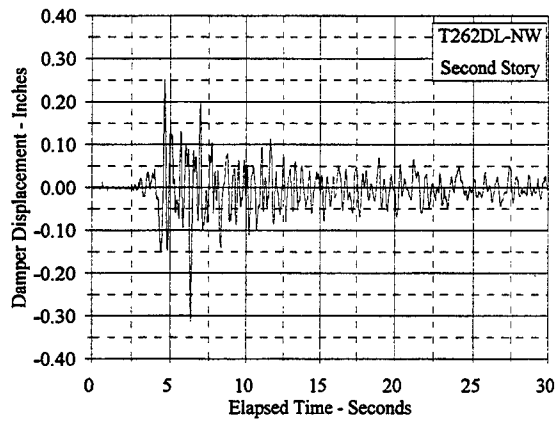
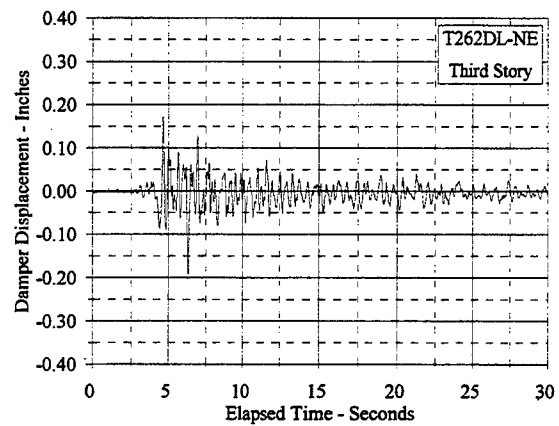
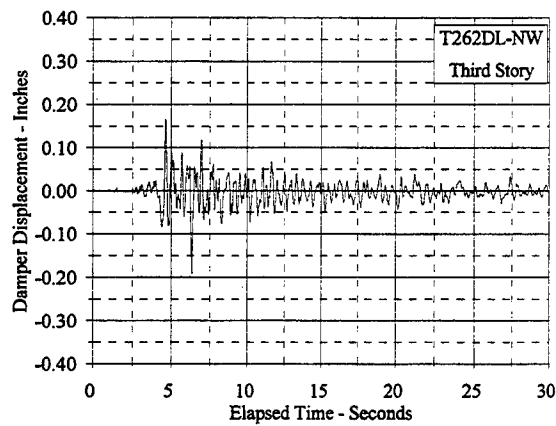


Figure C.9.29 Damper Displacement Vs. Elapsed Time: T262DL, NW and NE

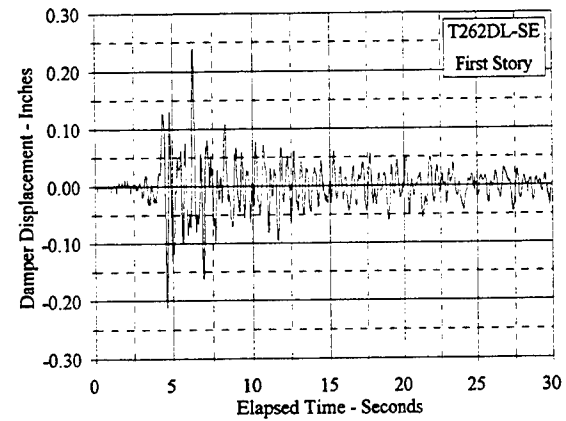
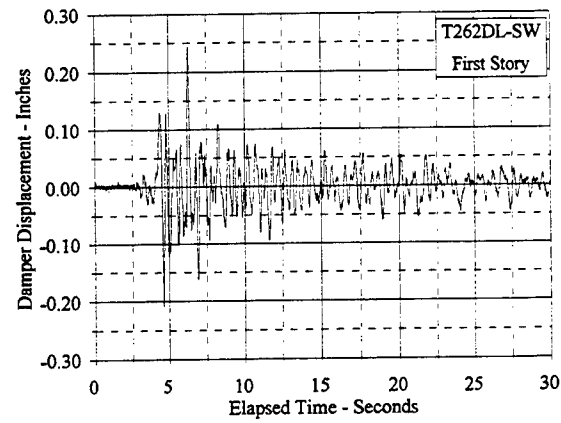
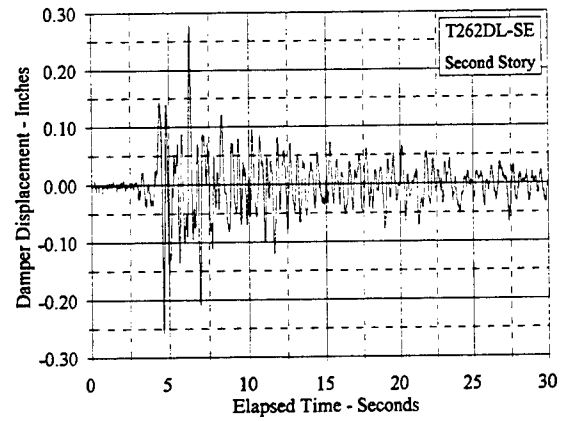
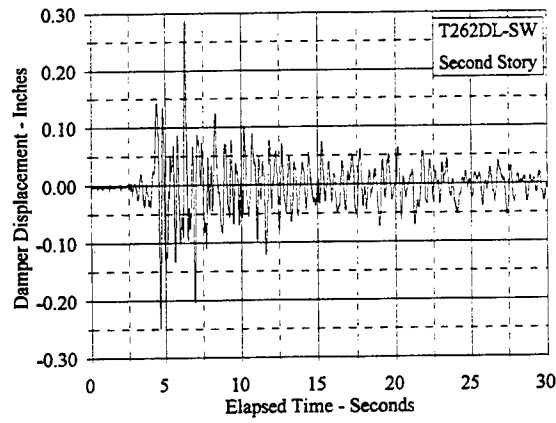
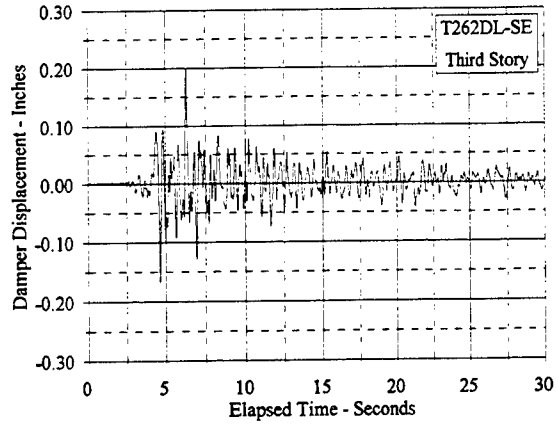
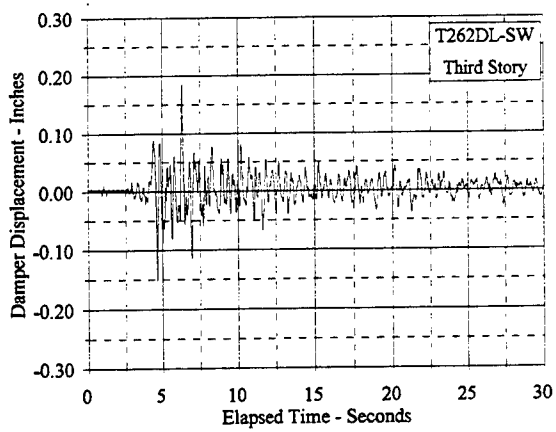


Figure C.9.30 Damper Displacement Vs. Elapsed Time: T262DL, SW and SE

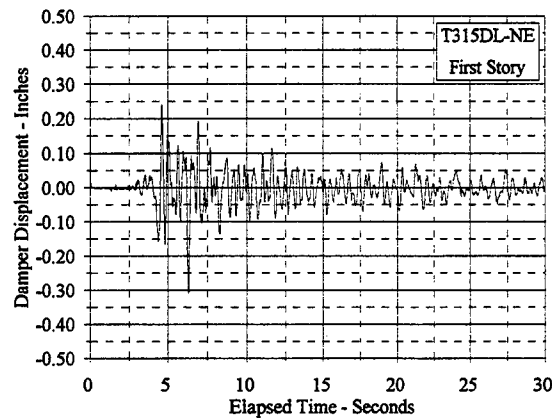
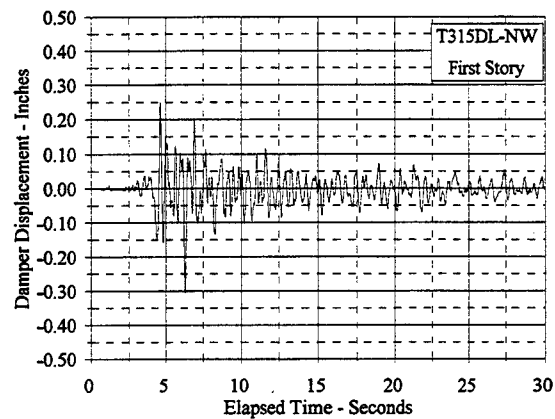
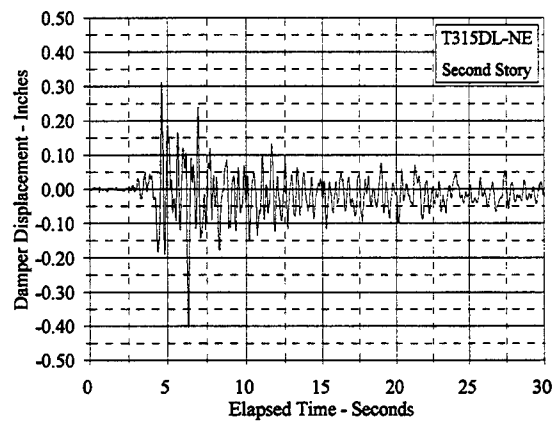
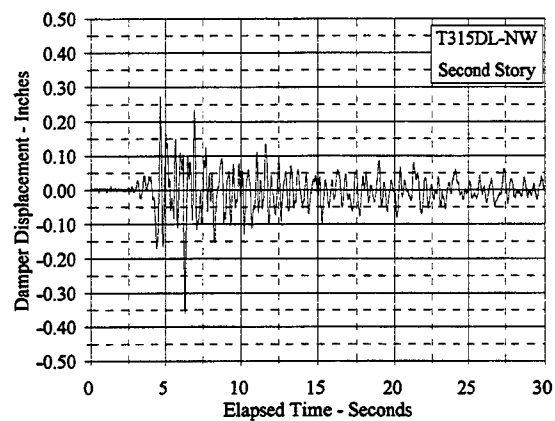
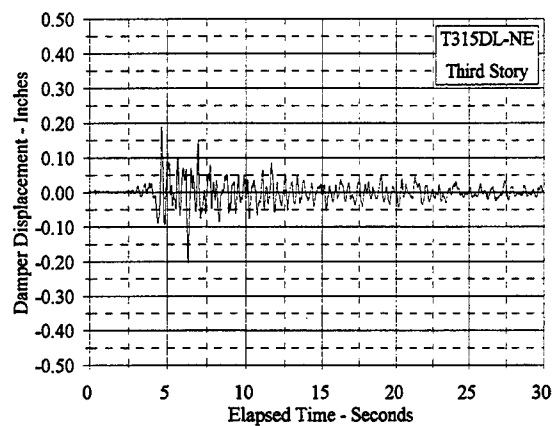
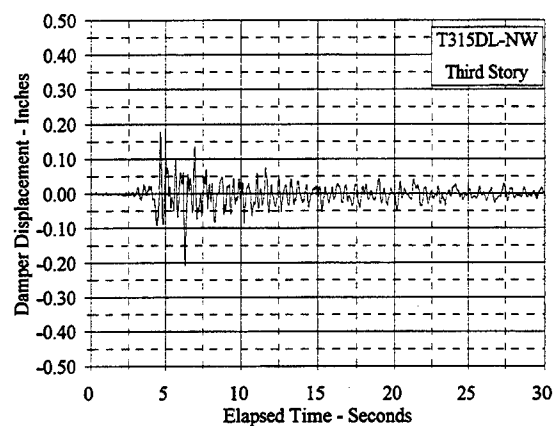


Figure C.9.31 Damper Displacement Vs. Elapsed Time: T315DL, NW and NE

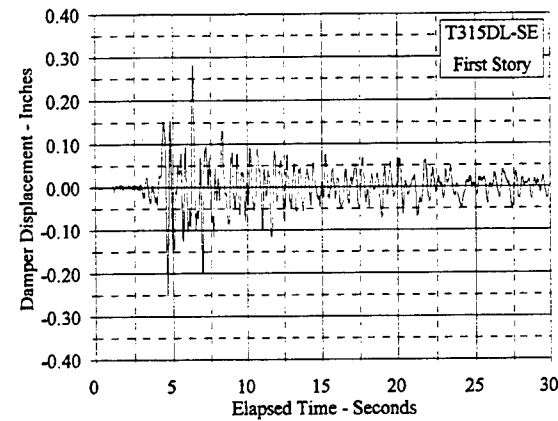
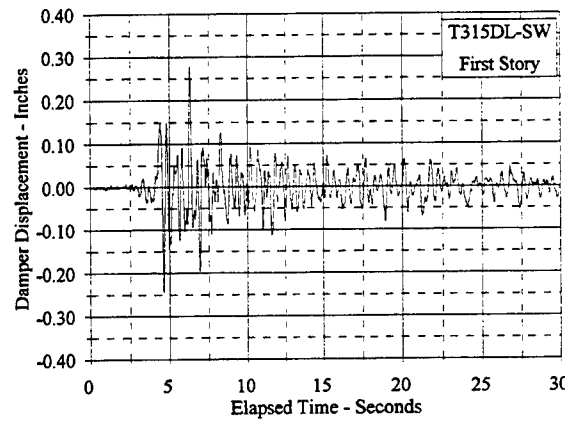
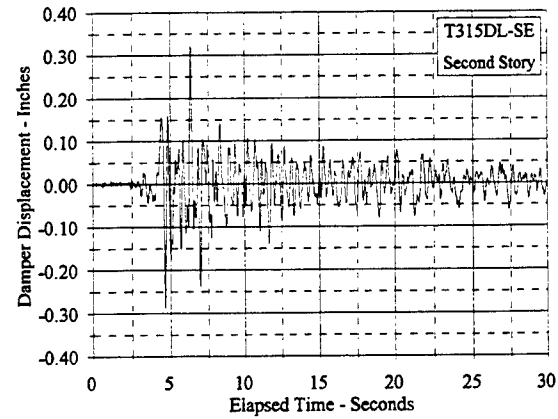
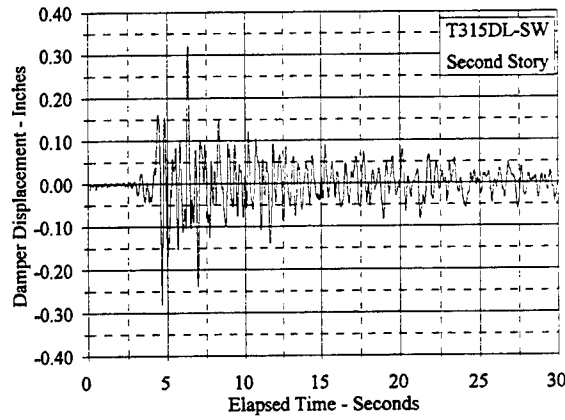
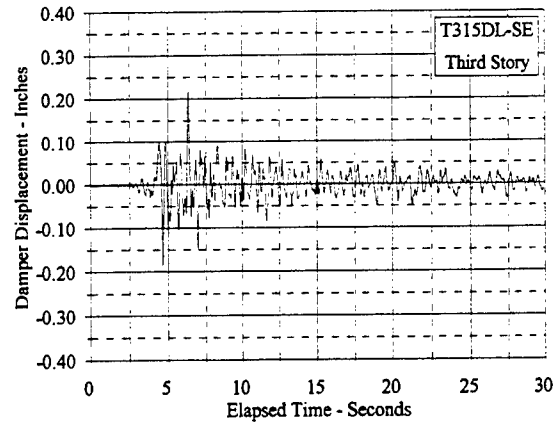
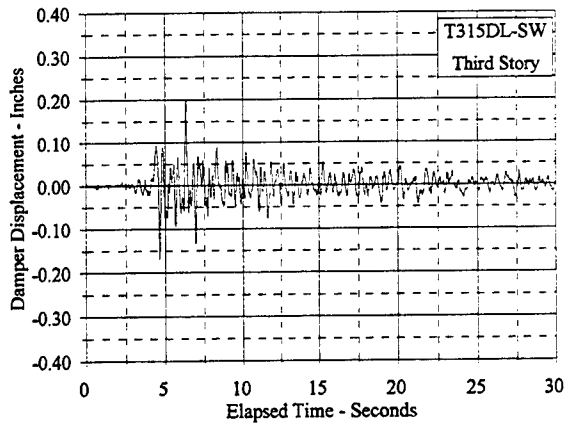


Figure C.9.32 Damper Displacement Vs. Elapsed Time: T315DL, SW and SE

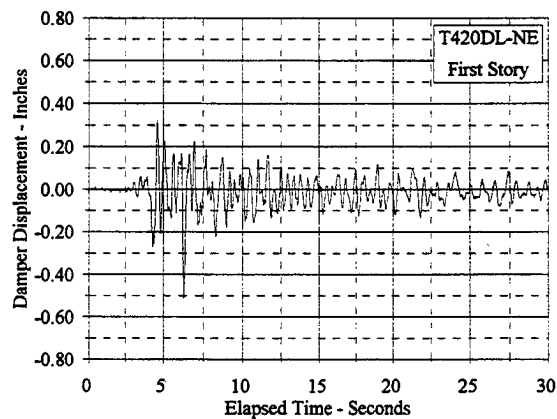
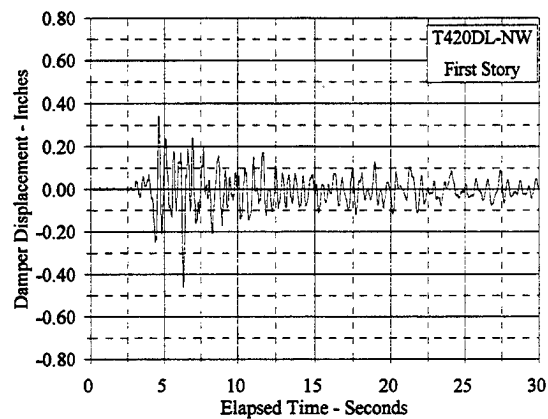
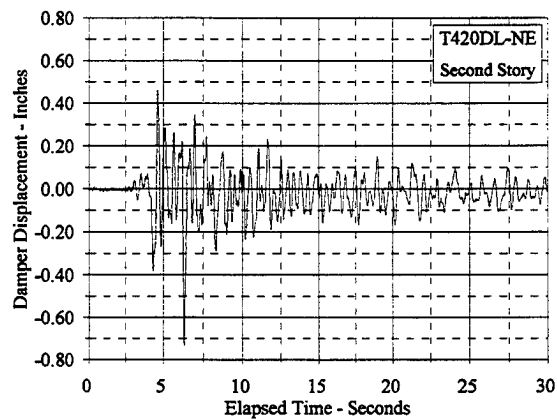
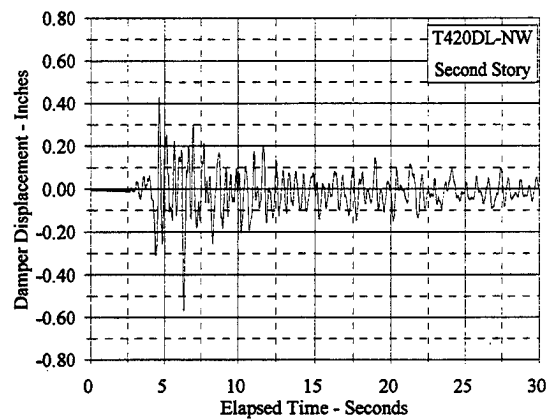
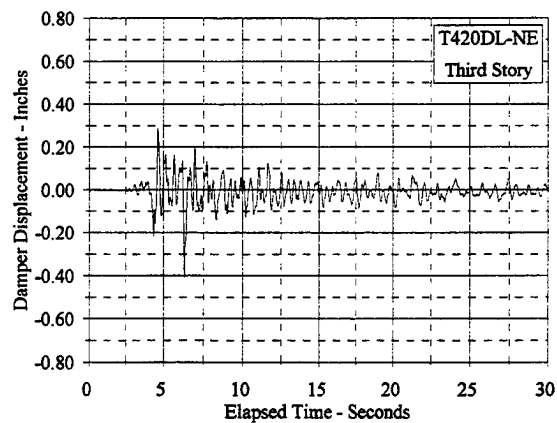
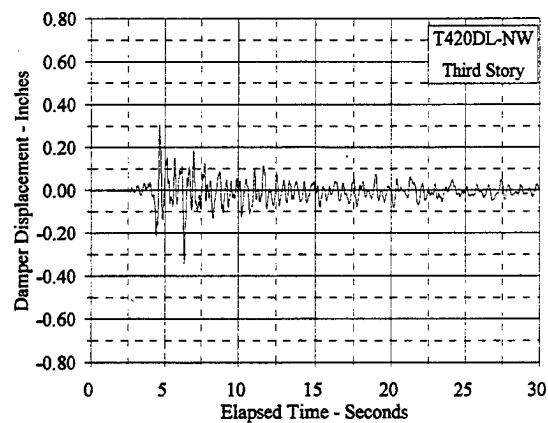


Figure C.9.33 Damper Displacement Vs. Elapsed Time: T420DL, NW and NE

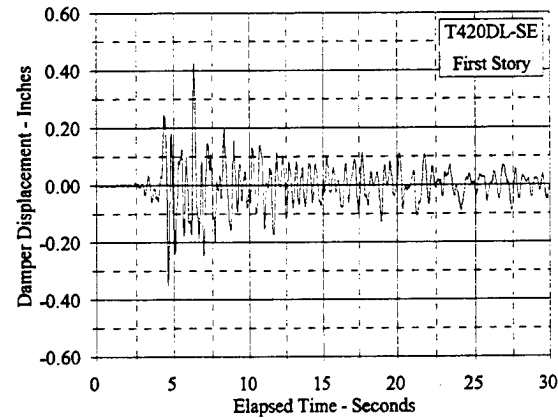
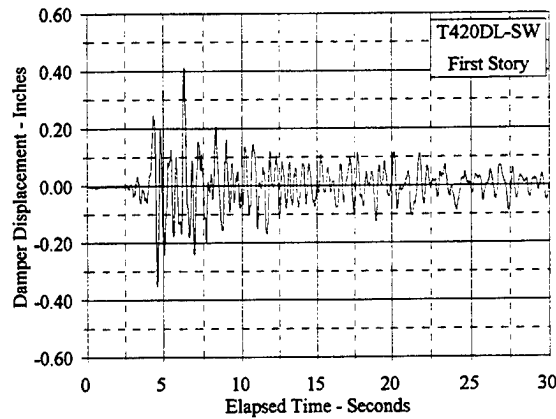
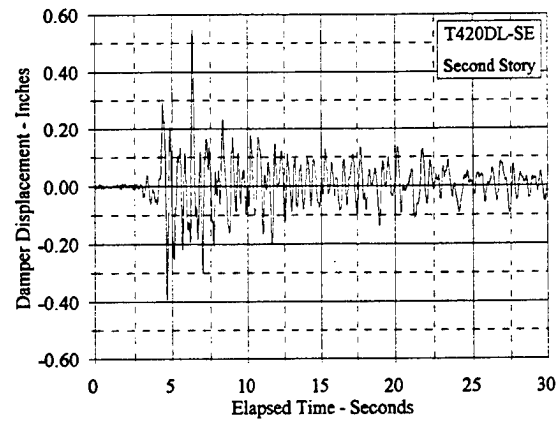
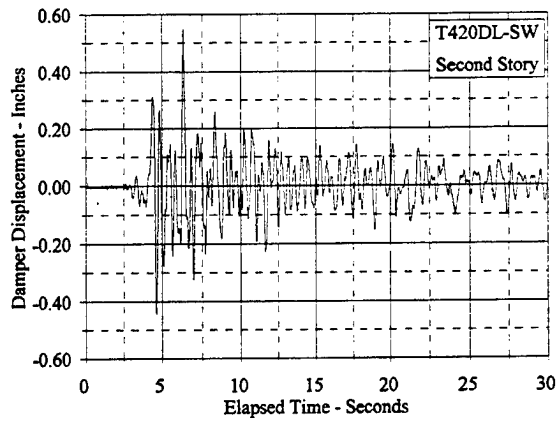
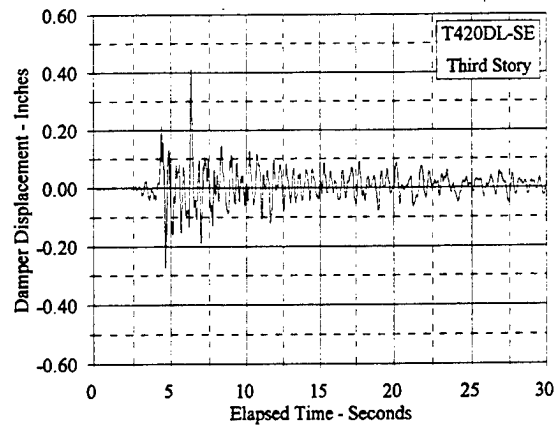
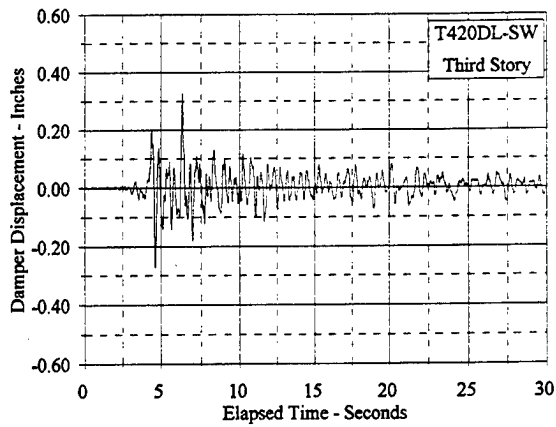


Figure C.9.34 Damper Displacement Vs. Elapsed Time: T420DL, SW and SE

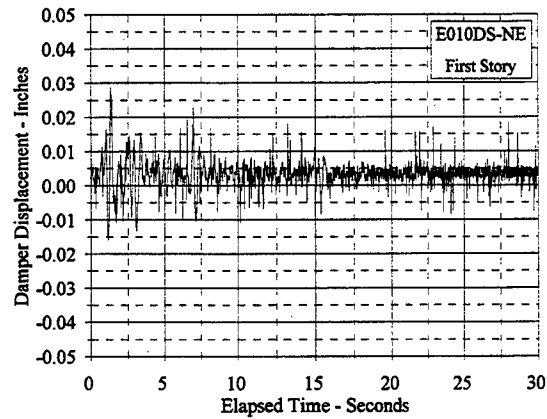
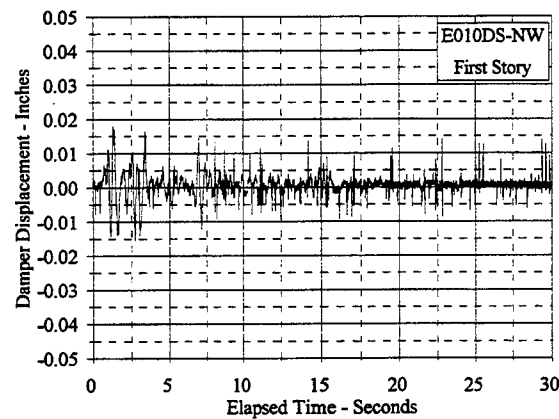
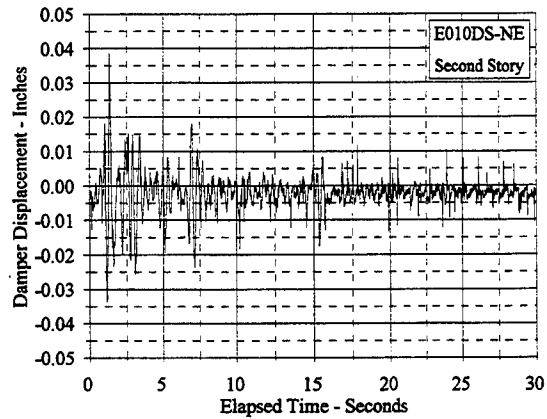
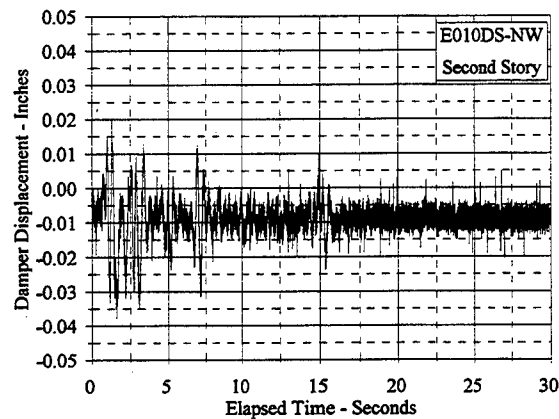
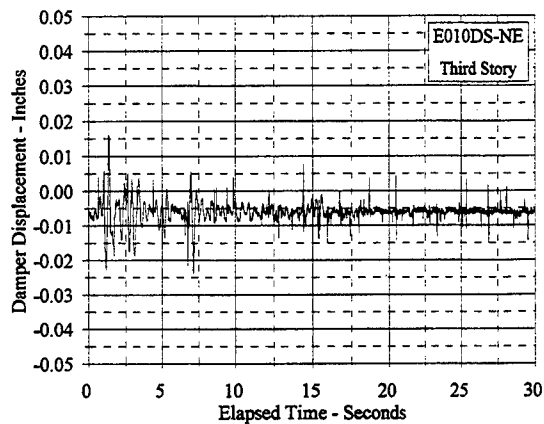
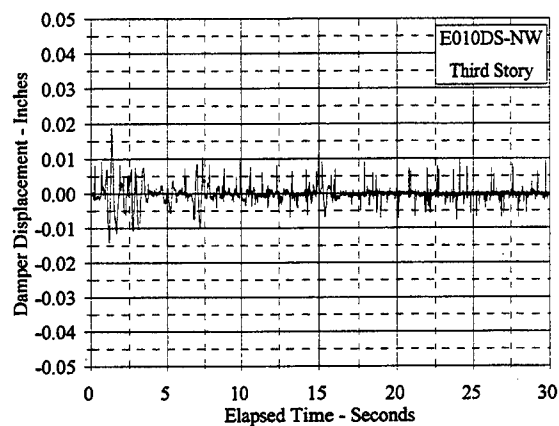


Figure C.9.35 Damper Displacement Vs. Elapsed Time: E010DS, NW and NE

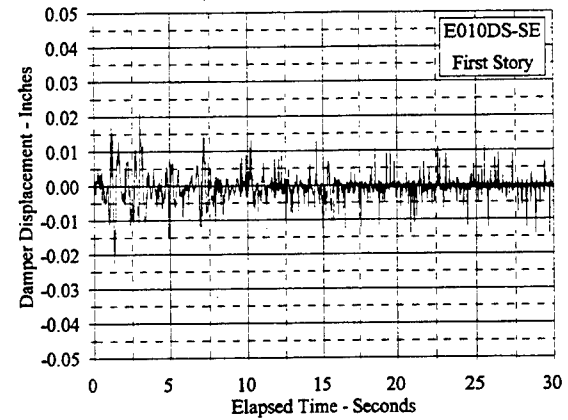
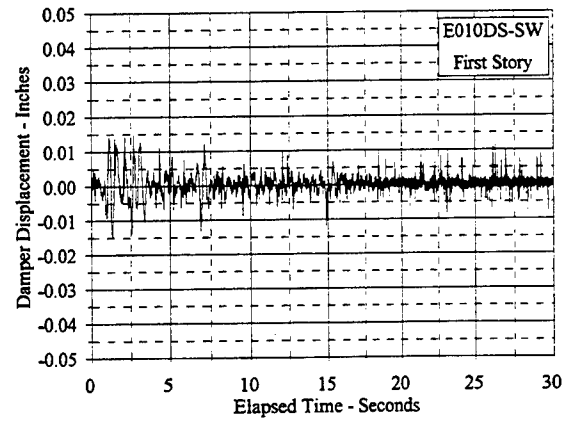
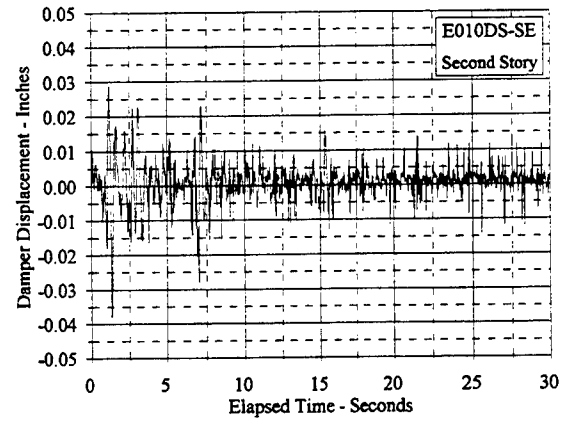
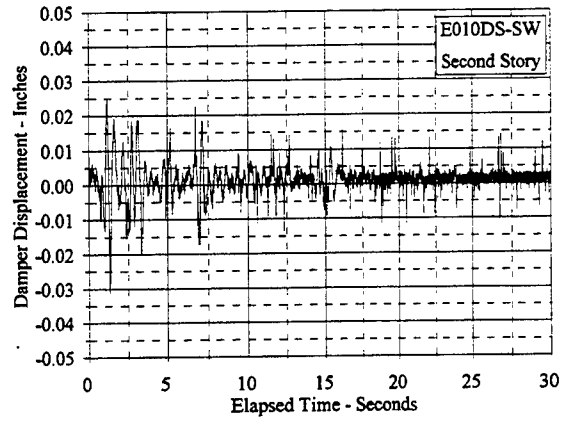
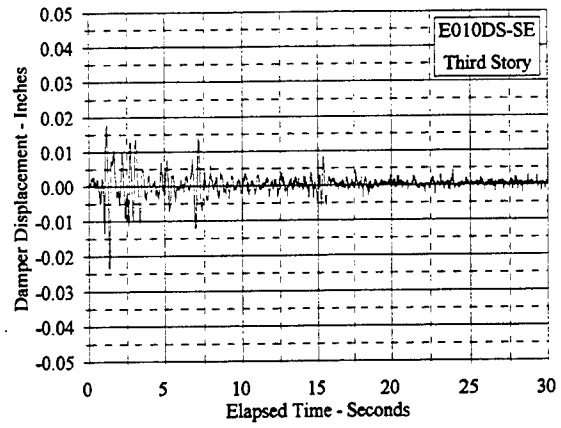
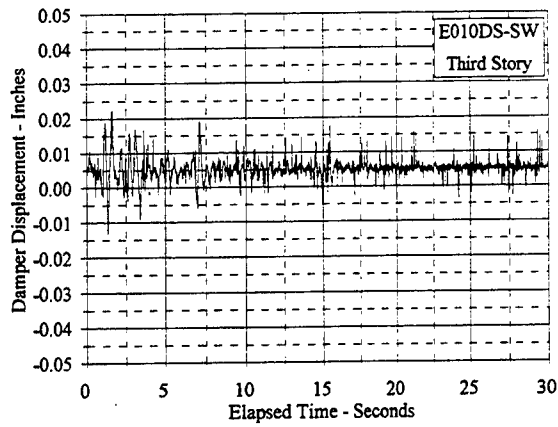


Figure C.9.36 Damper Displacement Vs. Elapsed Time: E010DS, SW and SE

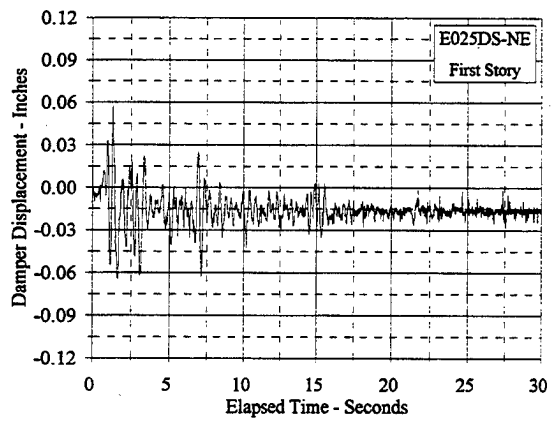
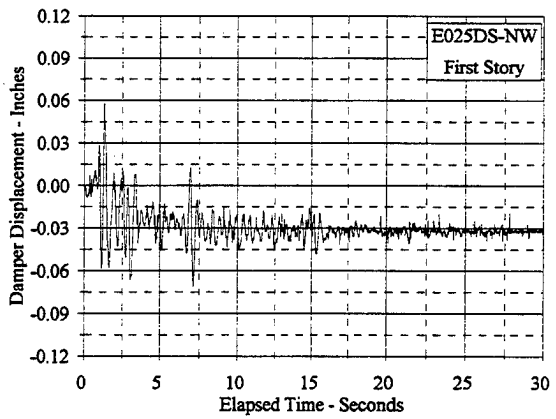
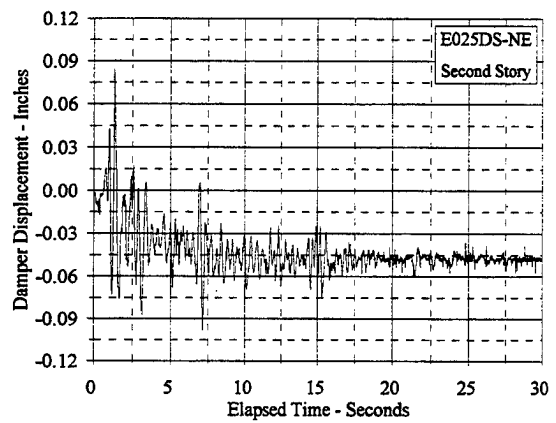
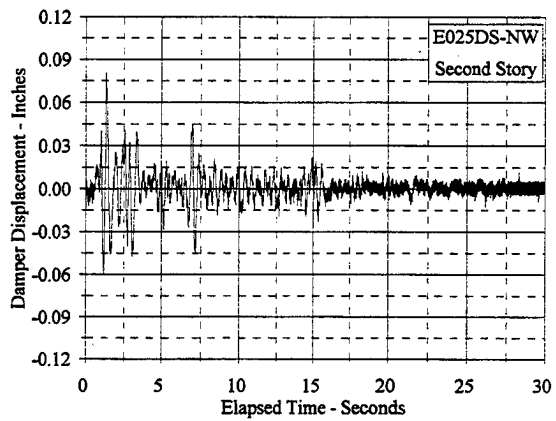
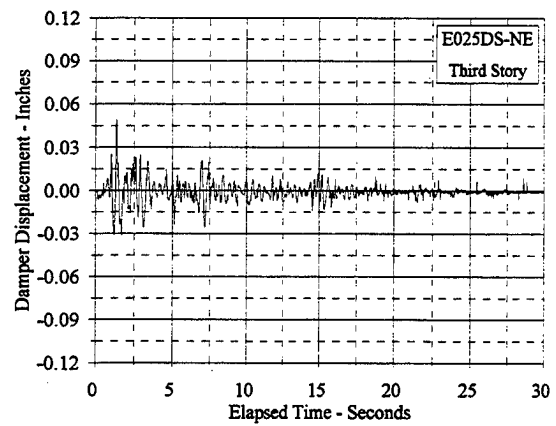
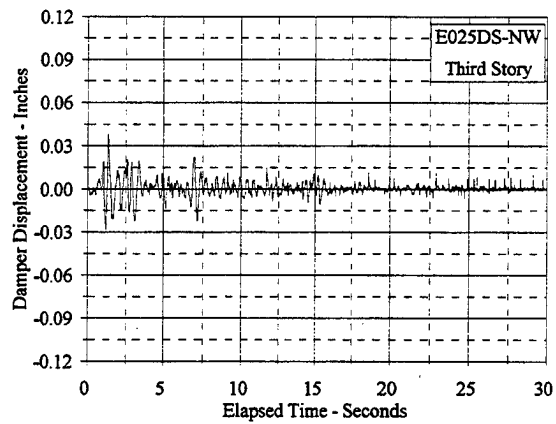


Figure C.9.37 Damper Displacement Vs. Elapsed Time: E025DS, NW and NE

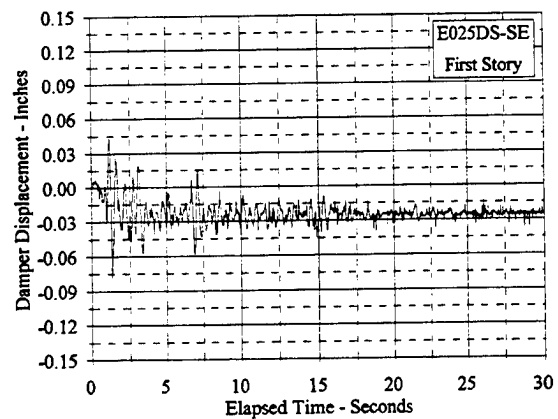
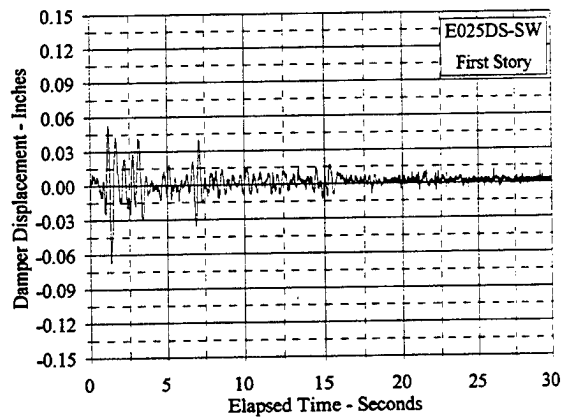
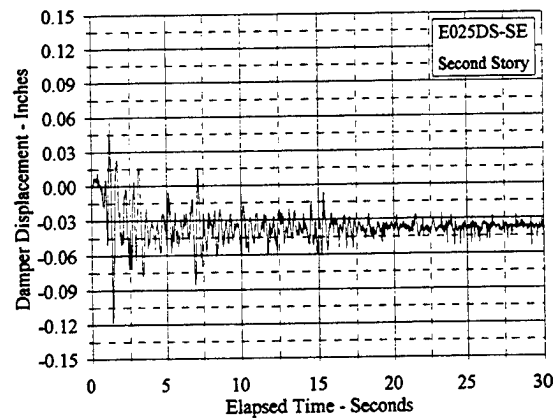
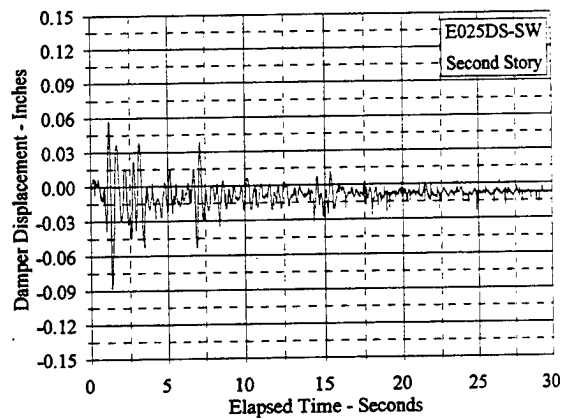
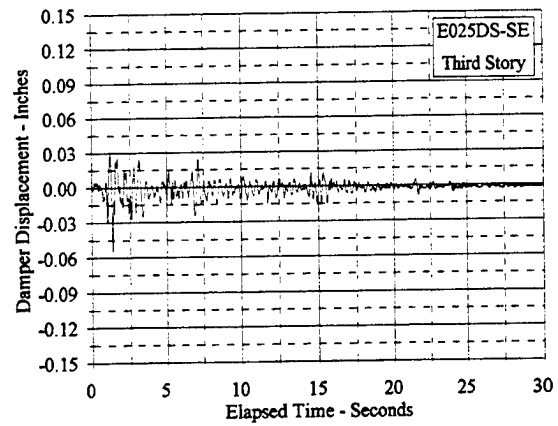
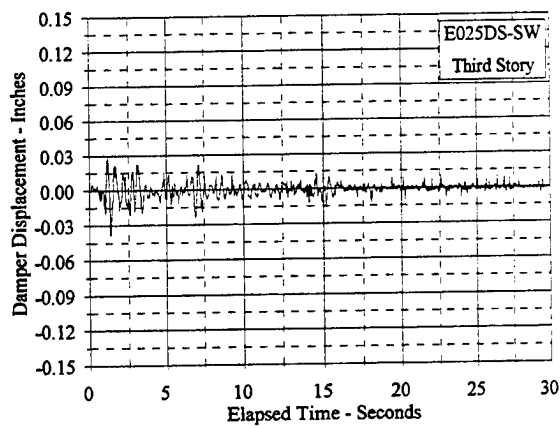


Figure C.9.38 Damper Displacement Vs. Elapsed Time: E025DS, SW and SE

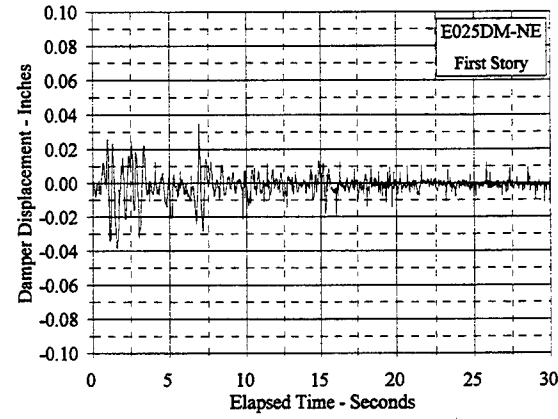
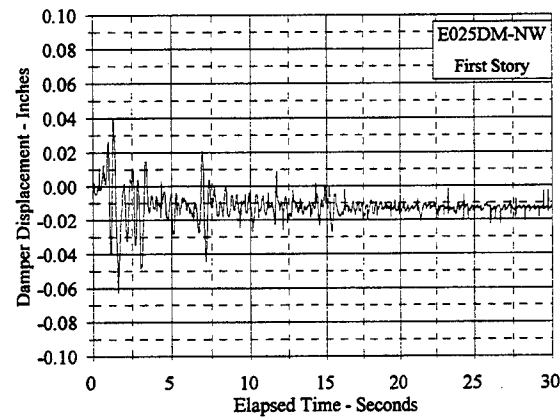
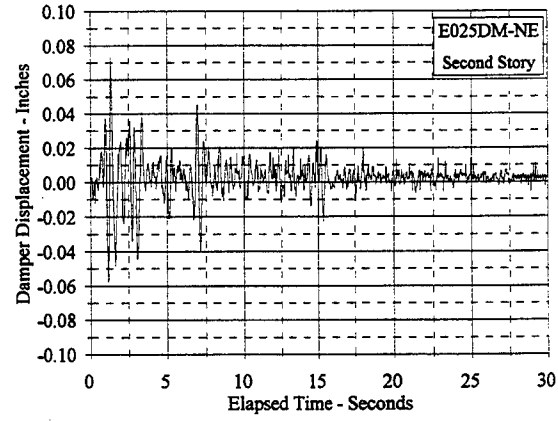
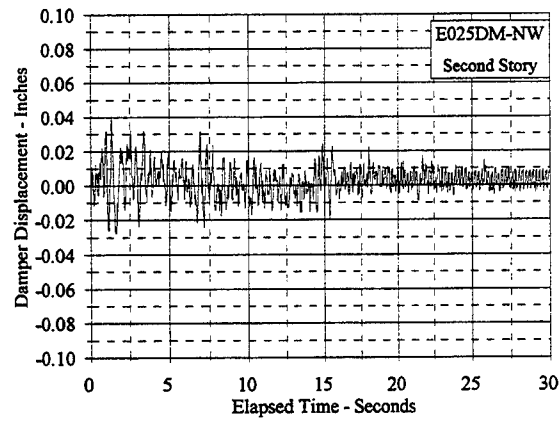
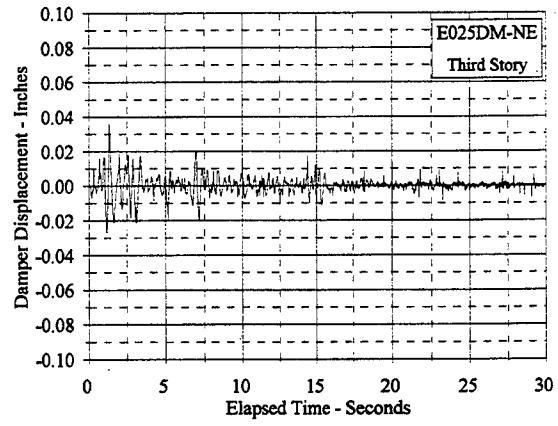
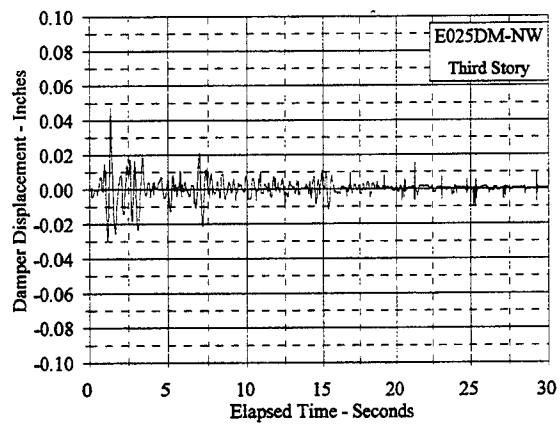


Figure C.9.39 Damper Displacement Vs. Elapsed Time: E025DM, NW and NE

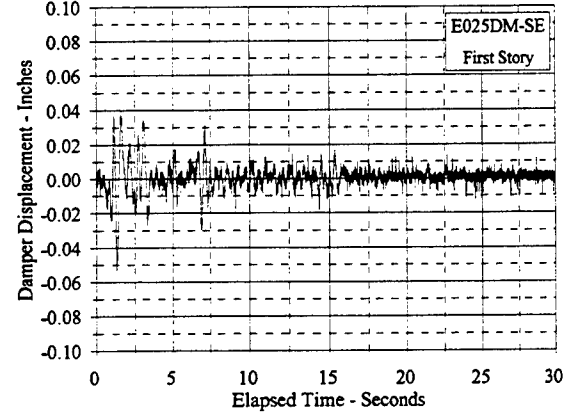
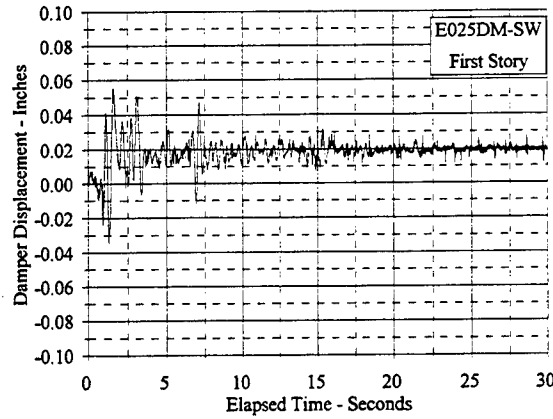
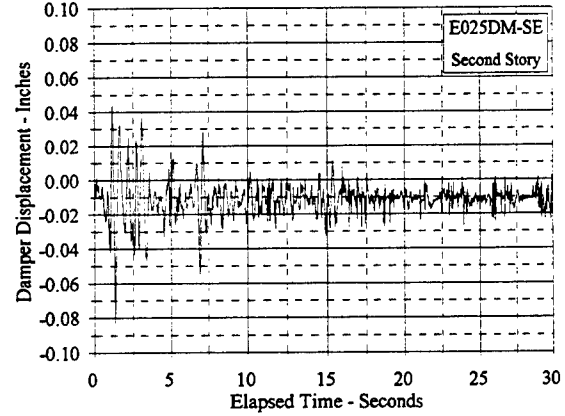
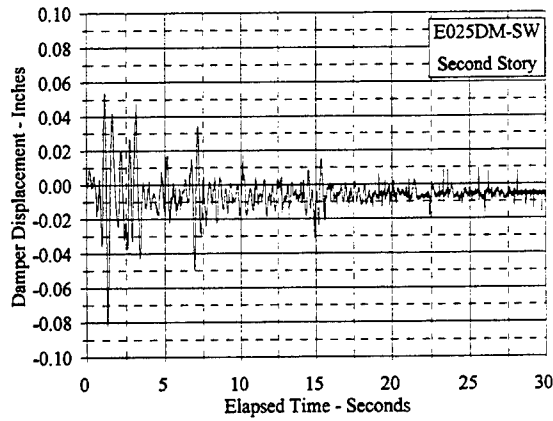
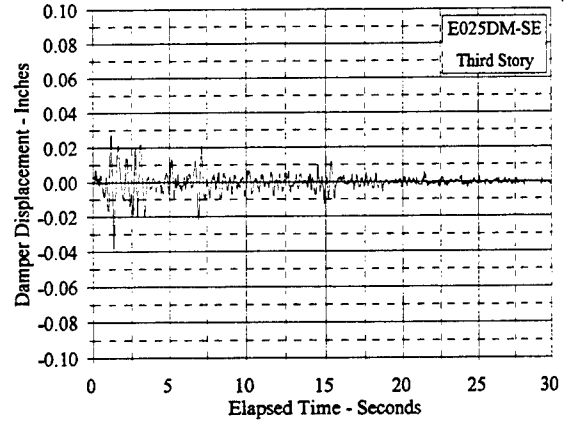
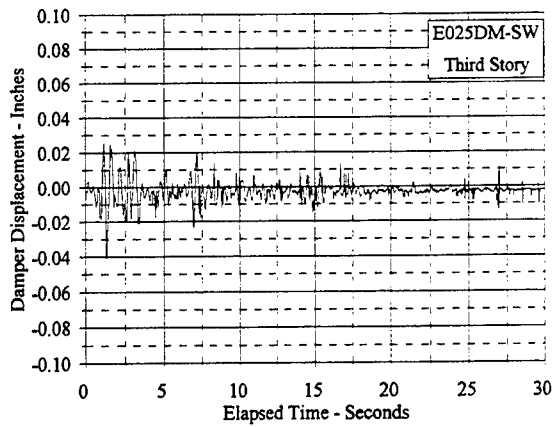


Figure C.9.40 Damper Displacement Vs. Elapsed Time: E025DM, SW and SE

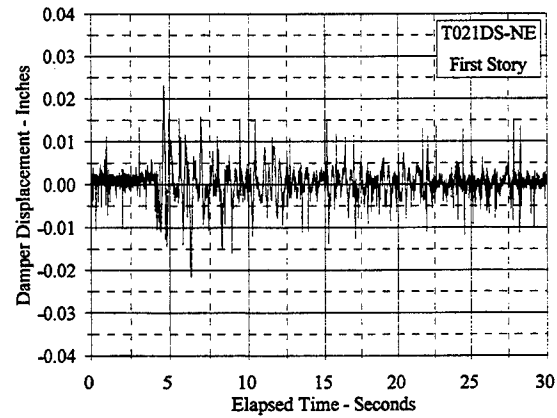
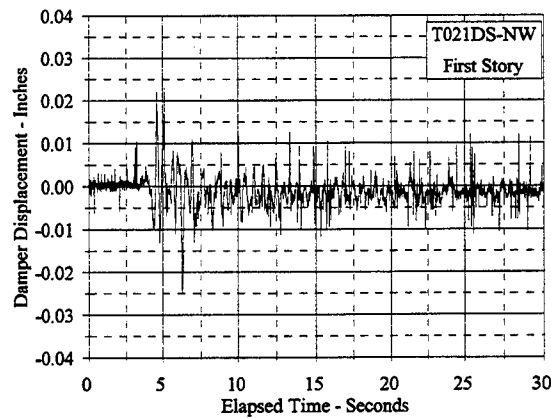
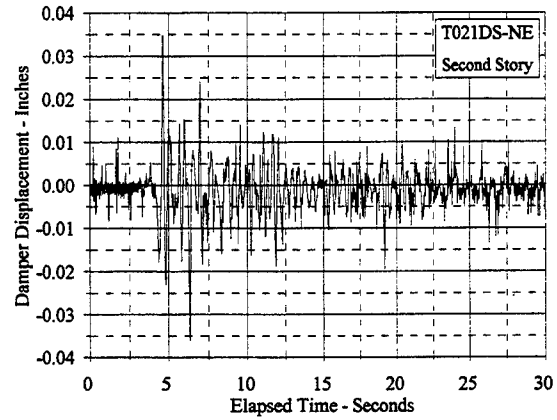
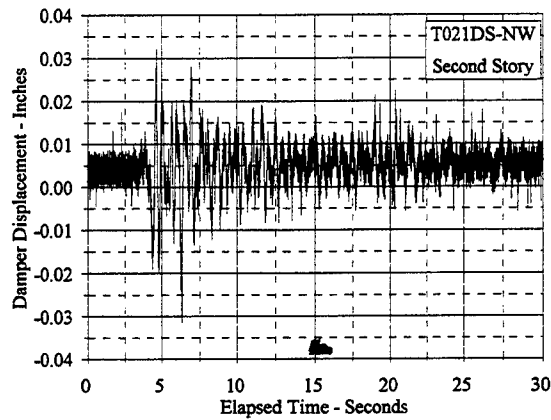
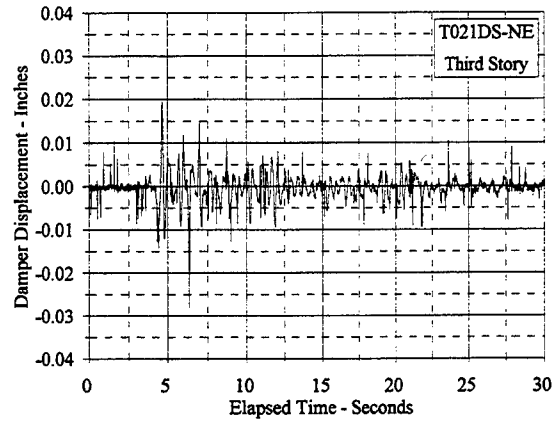
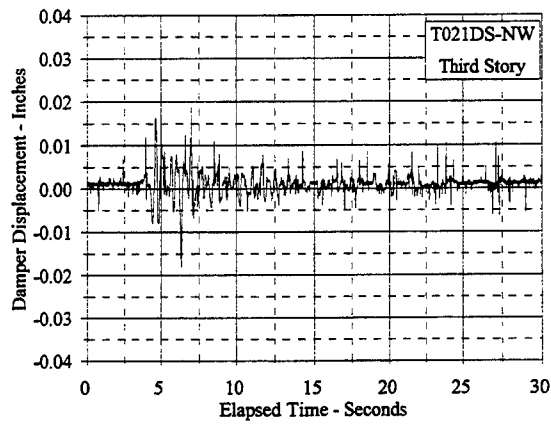


Figure C.9.41 Damper Displacement Vs. Elapsed Time: T021DS, NW and NE

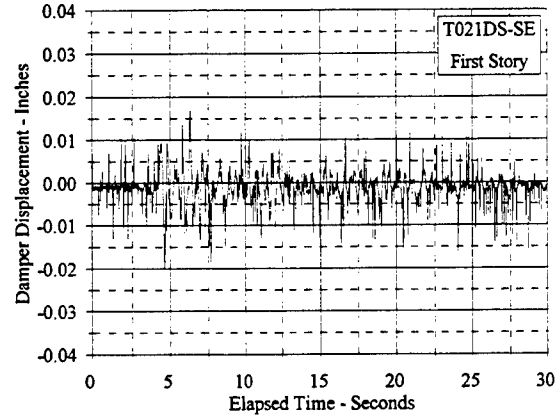
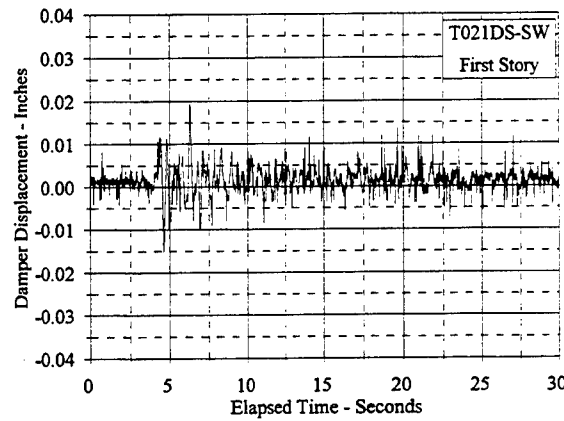
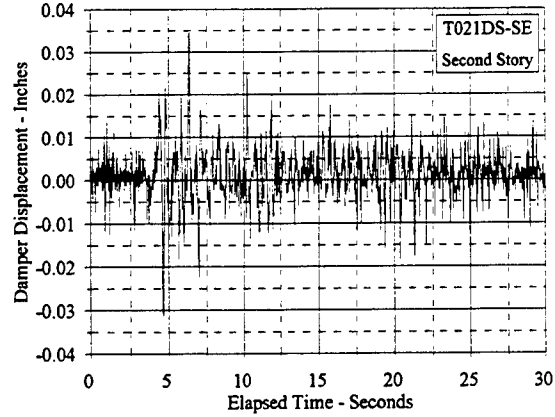
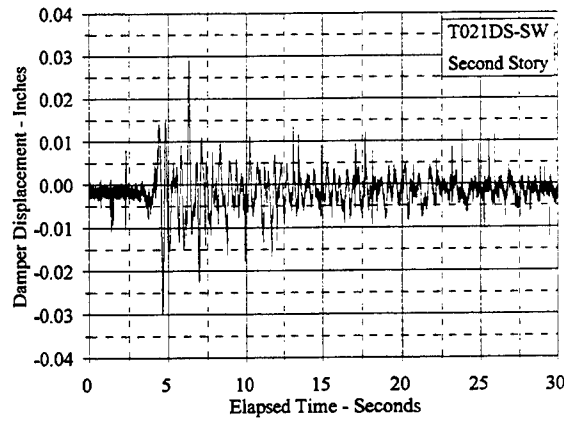
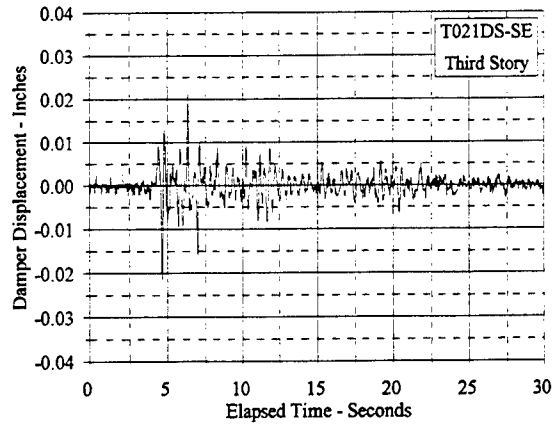
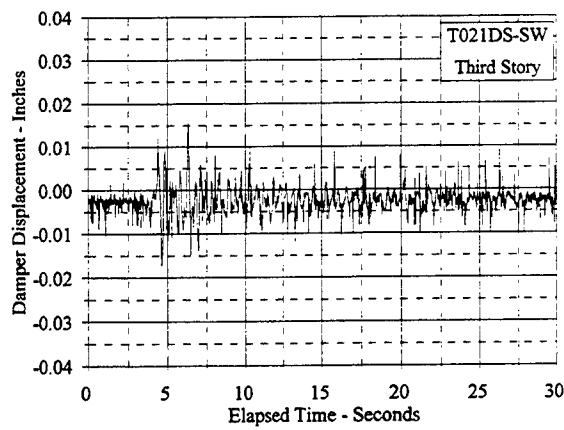


Figure C.9.42 Damper Displacement Vs. Elapsed Time: T021DS, SW and SE

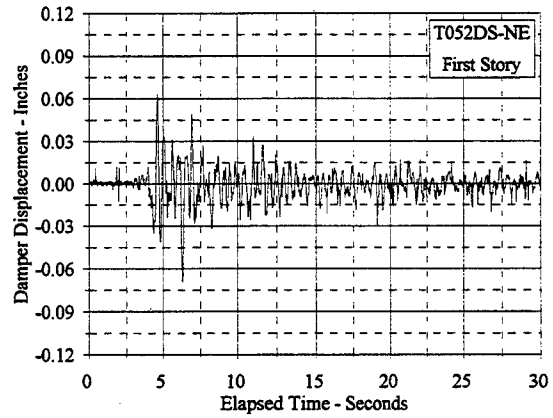
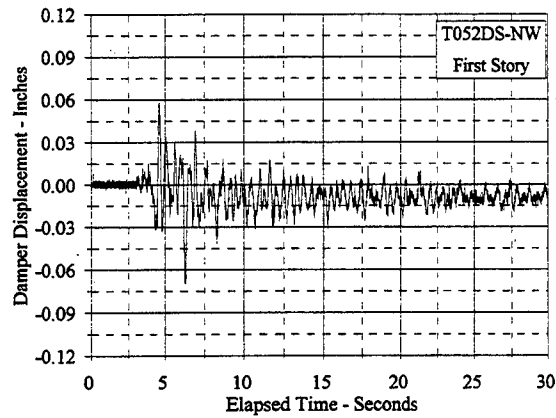
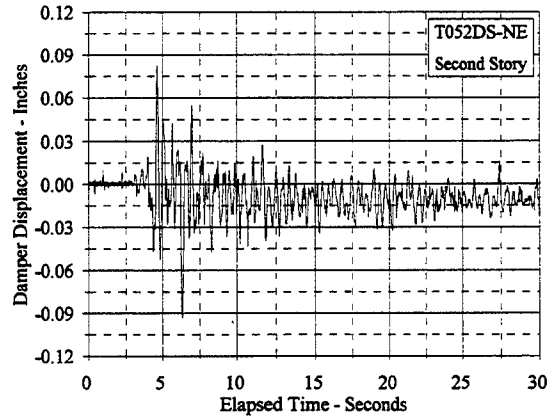
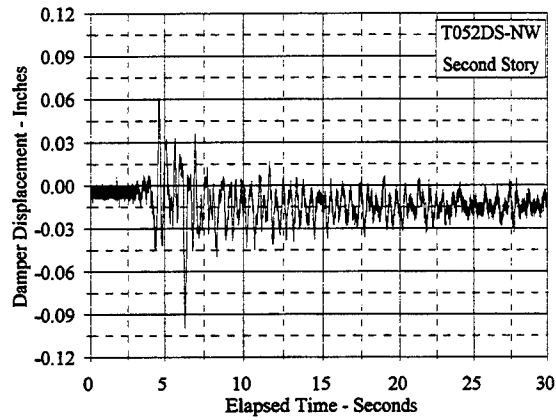
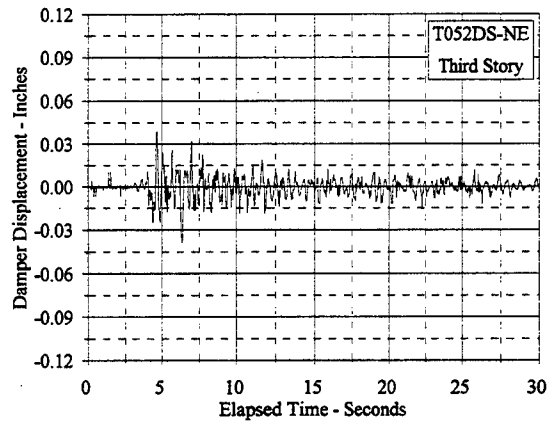
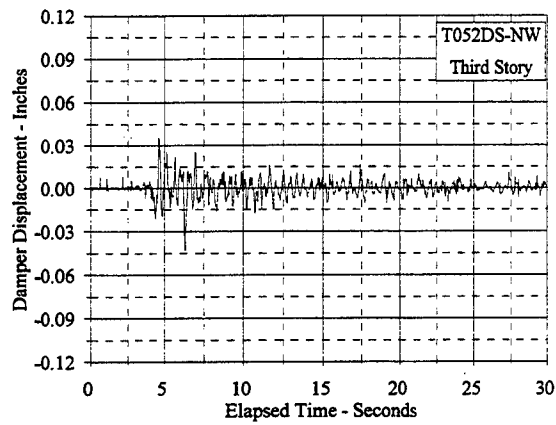


Figure C.9.43 Damper Displacement Vs. Elapsed Time: T052DS, NW and NE

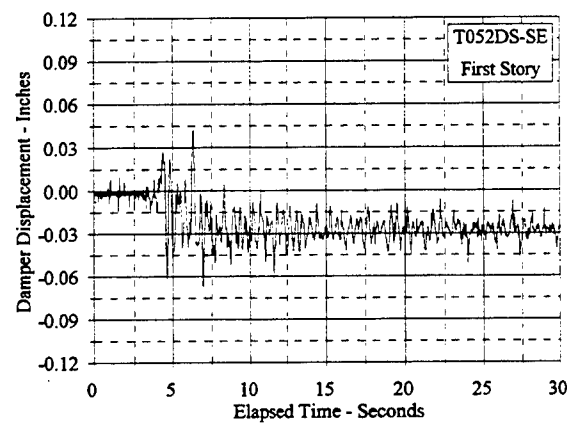
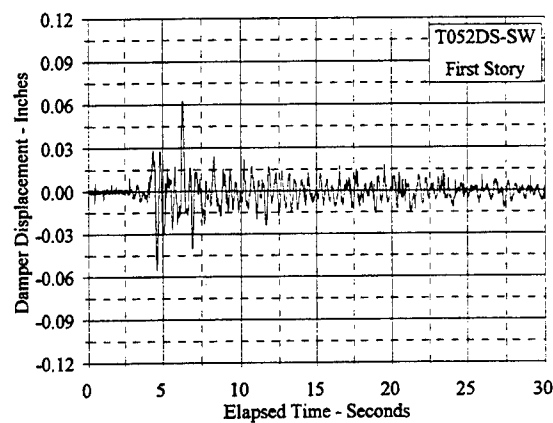
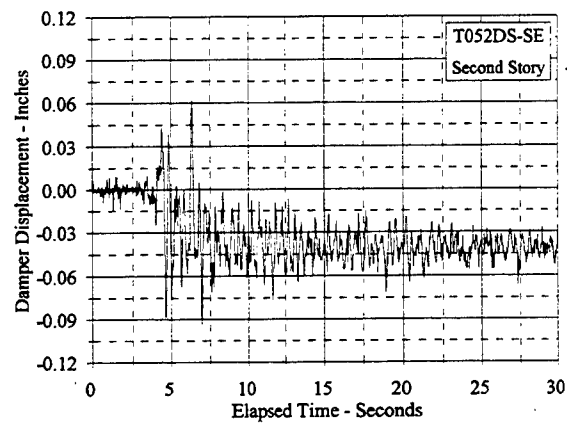
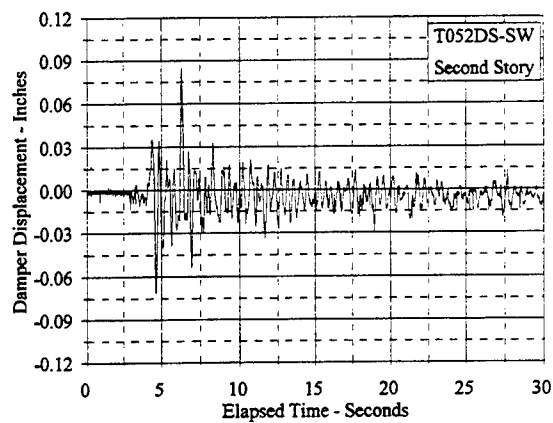
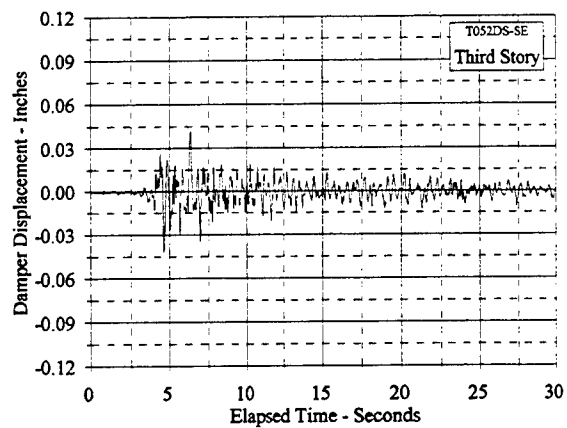
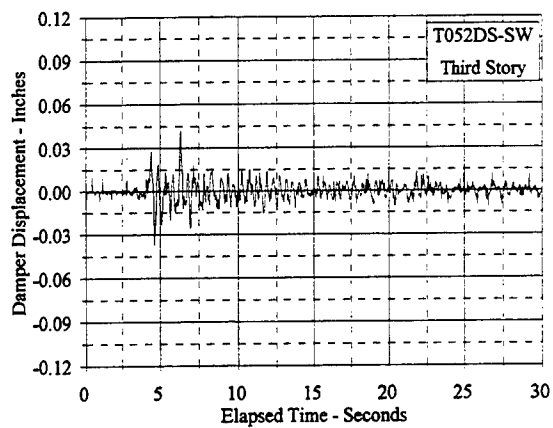


Figure C.9.44 Damper Displacement Vs. Elapsed Time: T052DS, SW and SE

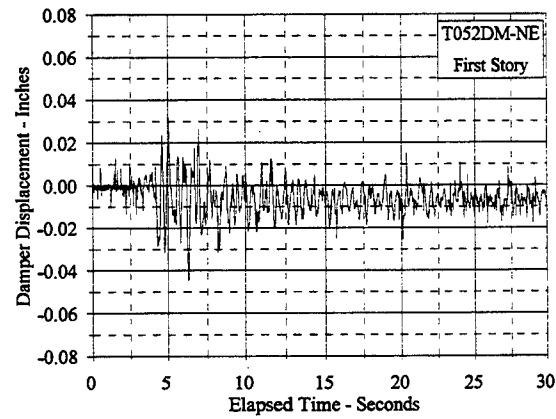
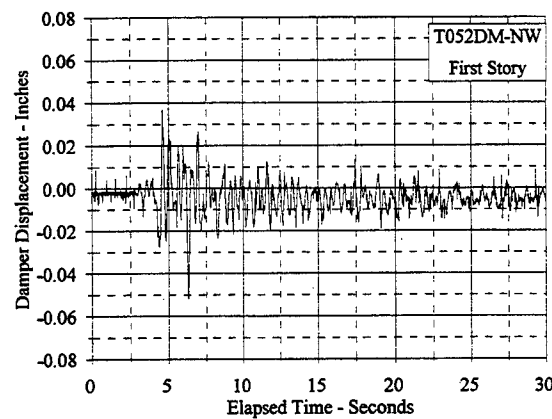
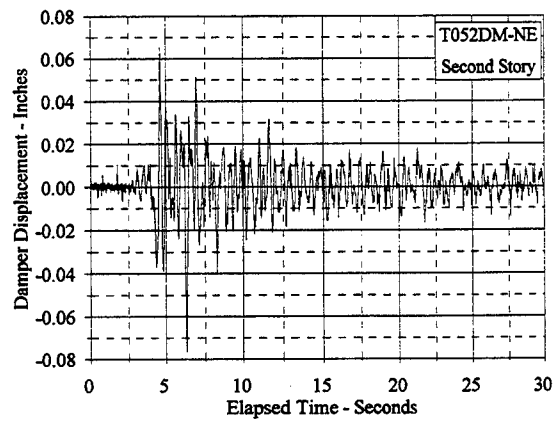
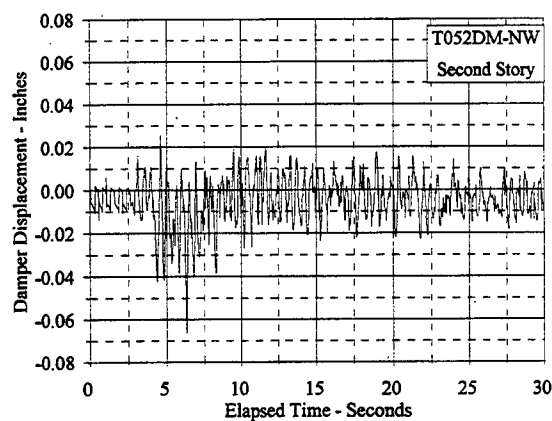
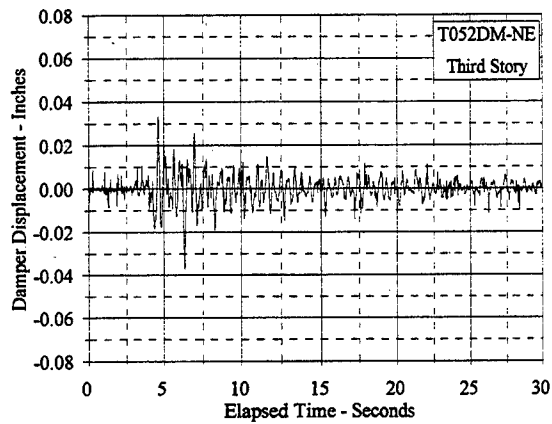
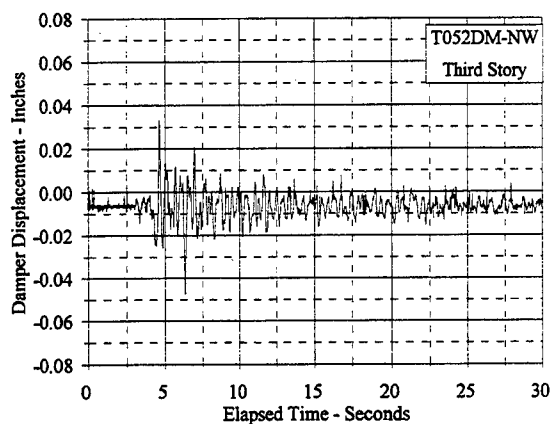


Figure C.9.45 Damper Displacement Vs. Elapsed Time: T052DM, NW and NE

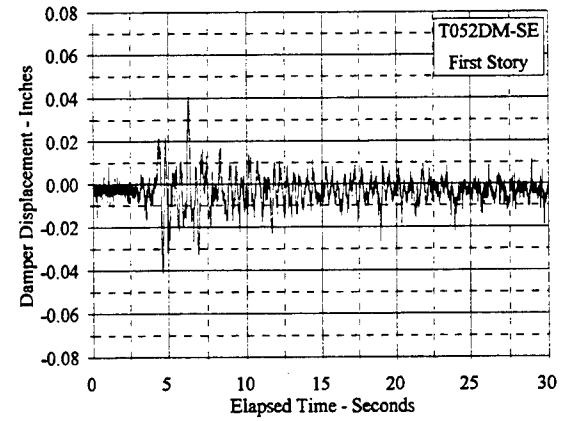
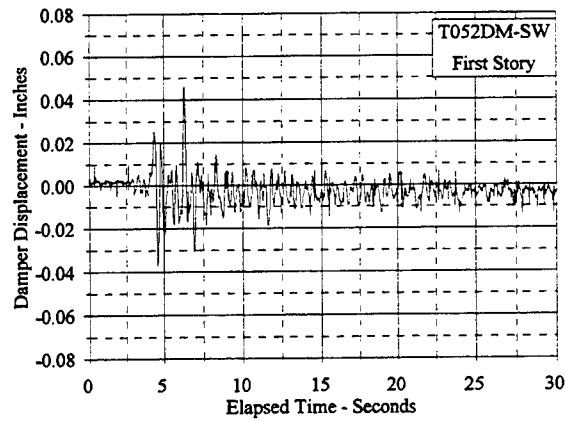
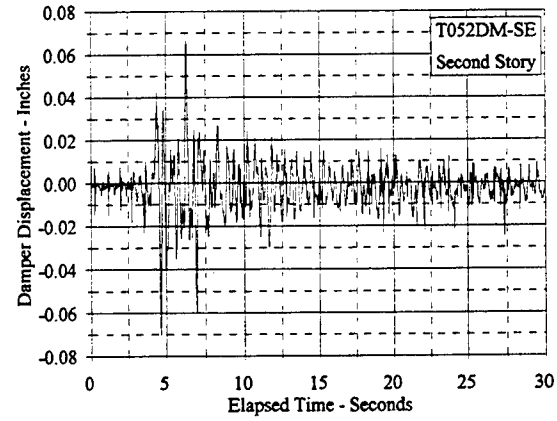
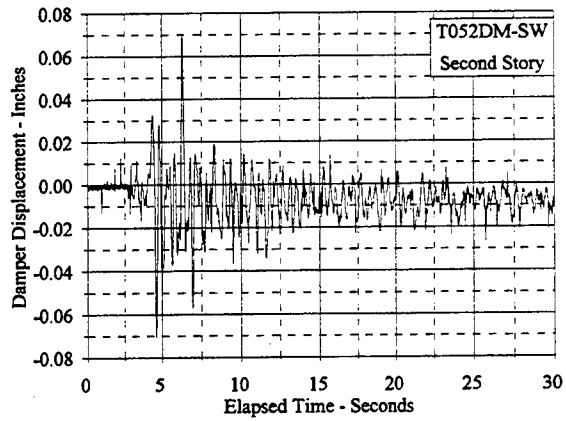
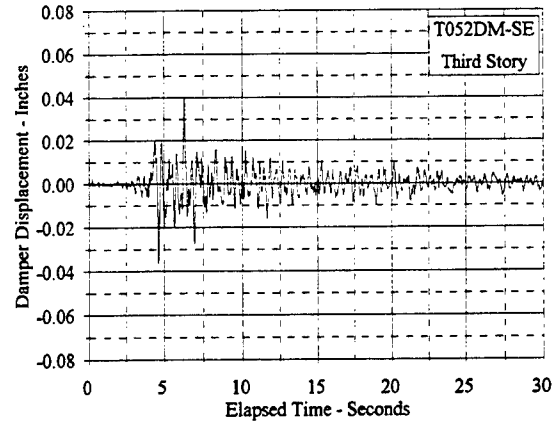
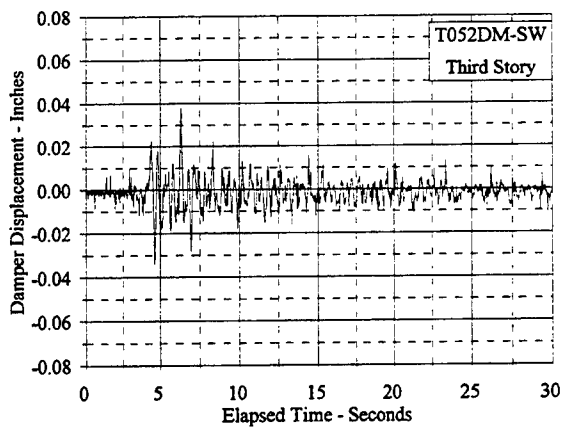


Figure C.9.46 Damper Displacement Vs. Elapsed Time: T052DM, SW and SE

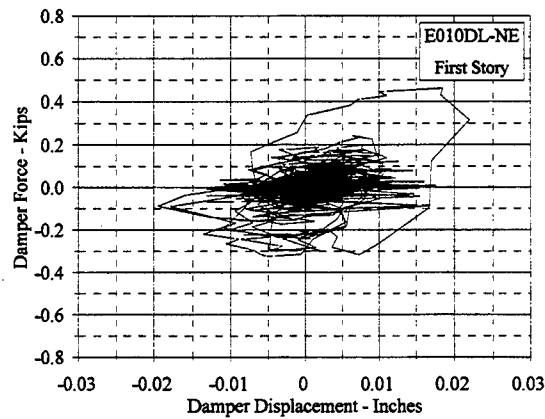
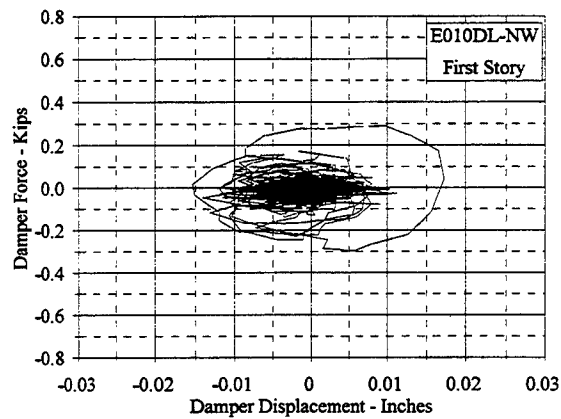
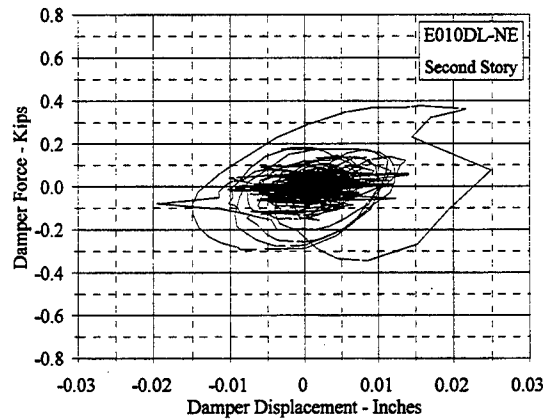
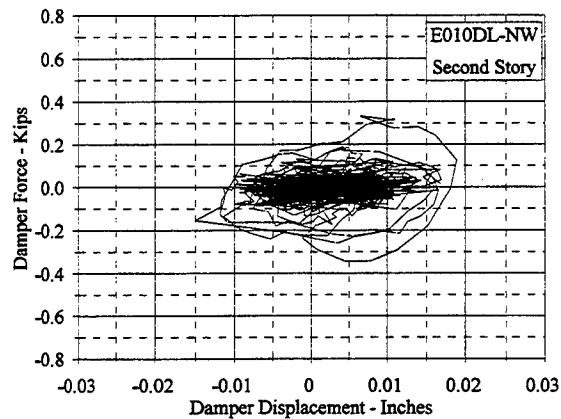
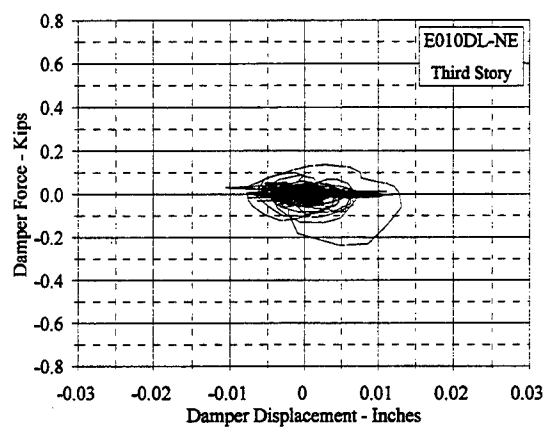
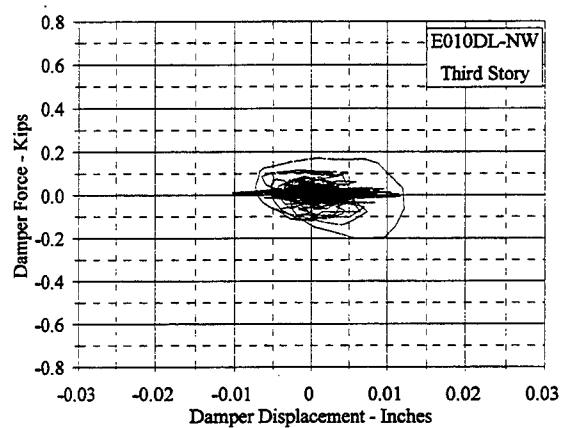


Figure C.10.1 Damper Force Vs. Displacement: E010DL, NW and NE

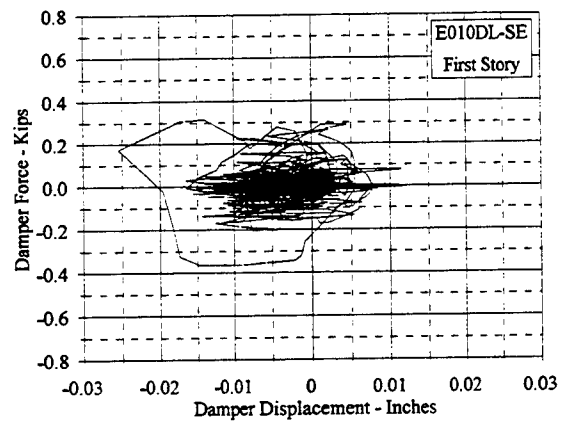
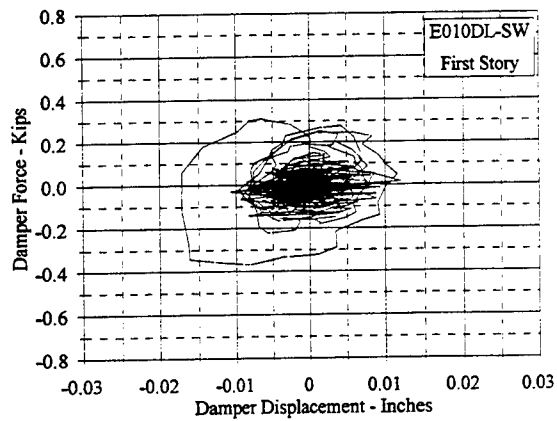
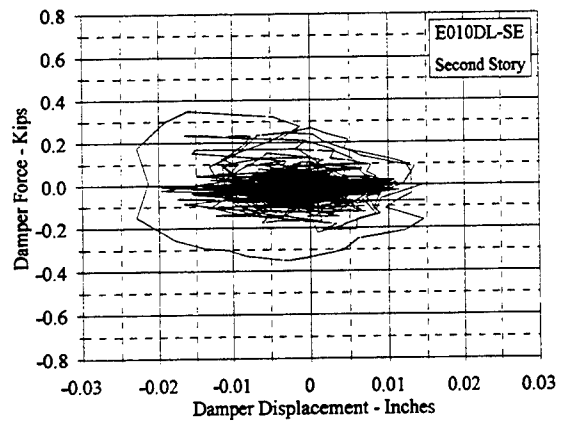
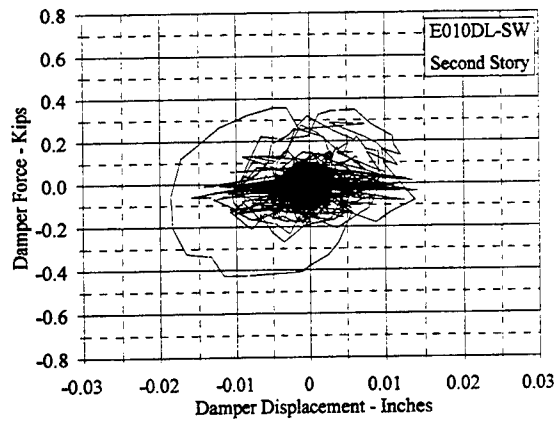
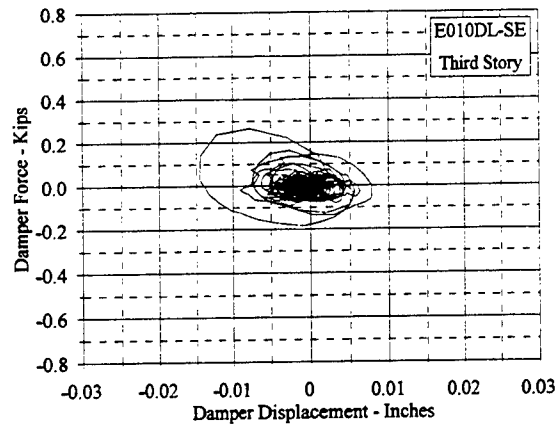
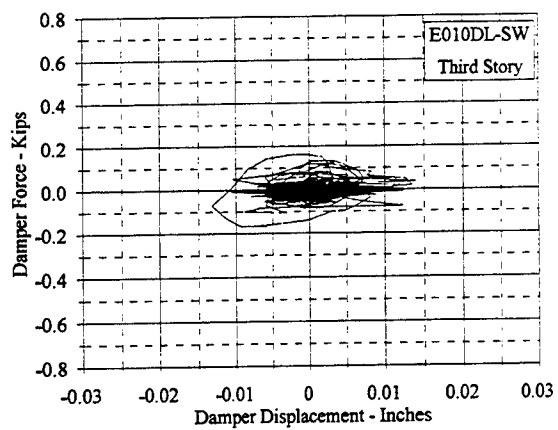


Figure C.10.2 Damping Force Vs. Displacement: E010DL, SW and SE

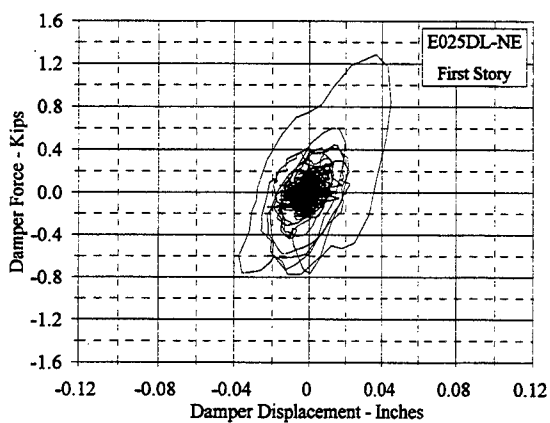
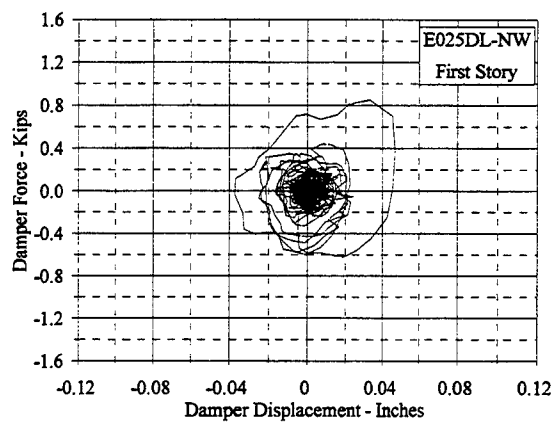
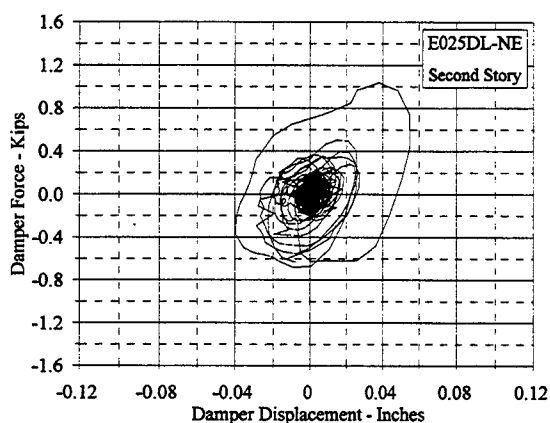
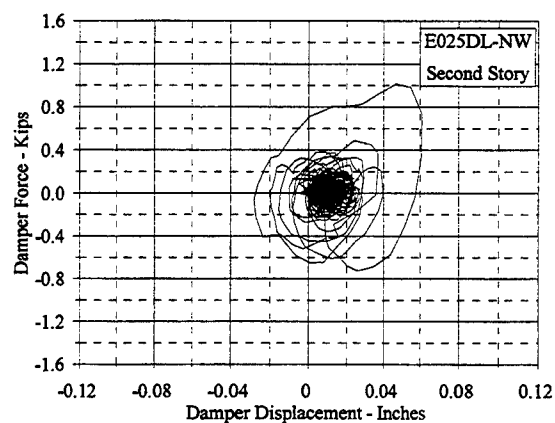
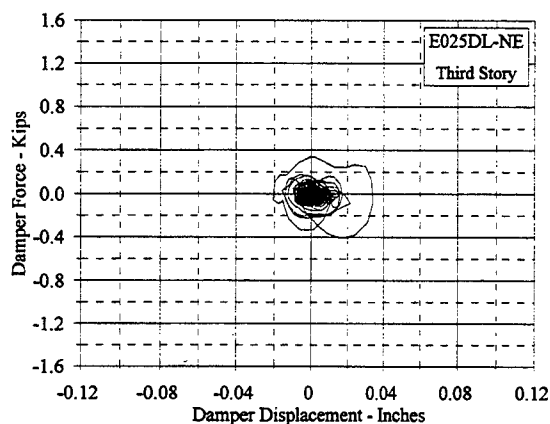
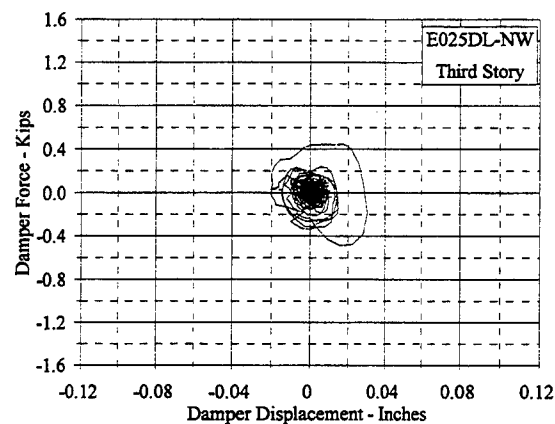


Figure C.10.3 Damper Force Vs. Displacement: E025DL, NW and NE

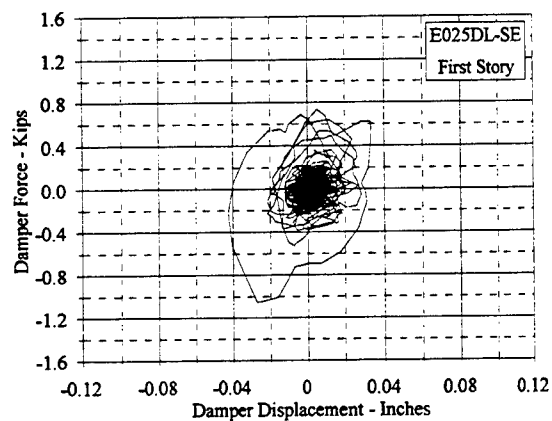
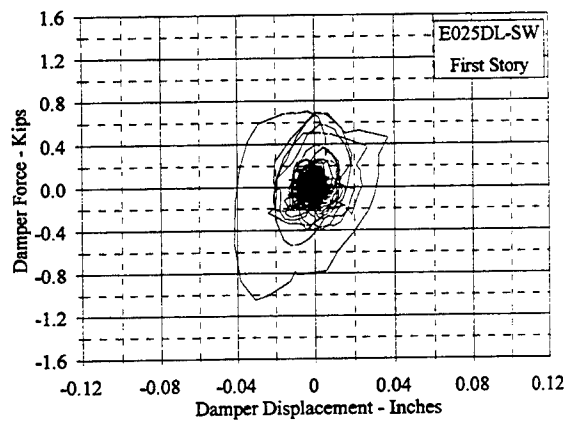
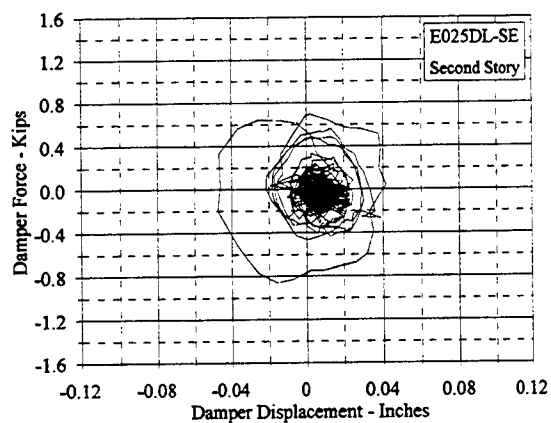
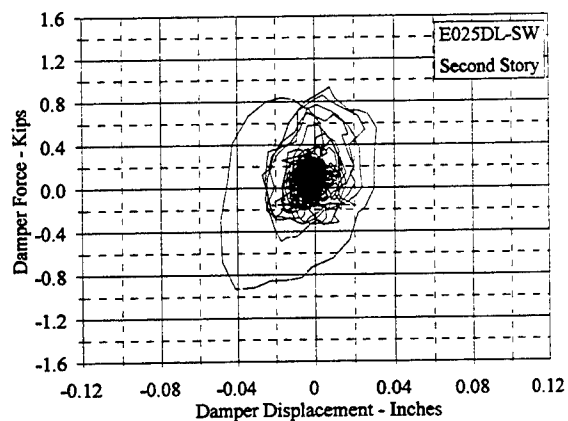
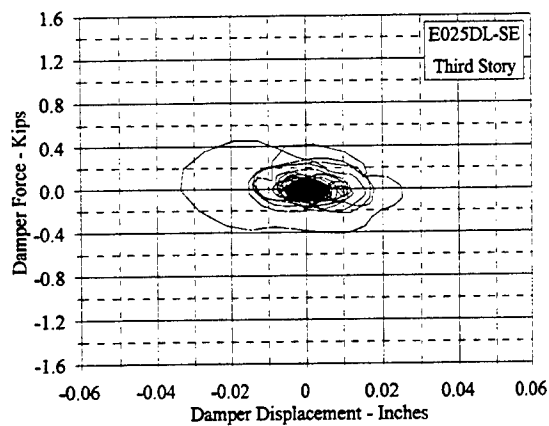
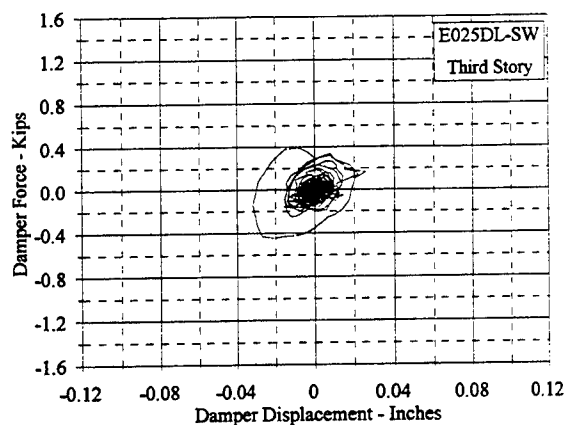


Figure C.10.4 Damper Force Vs. Displacement: E025DL, SW and SE

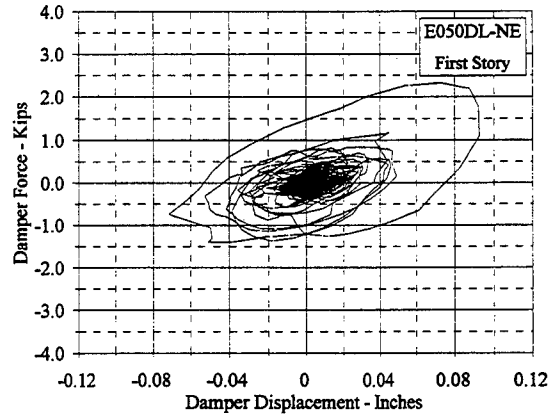
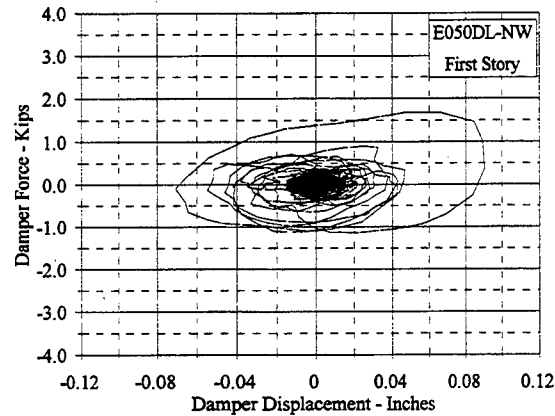
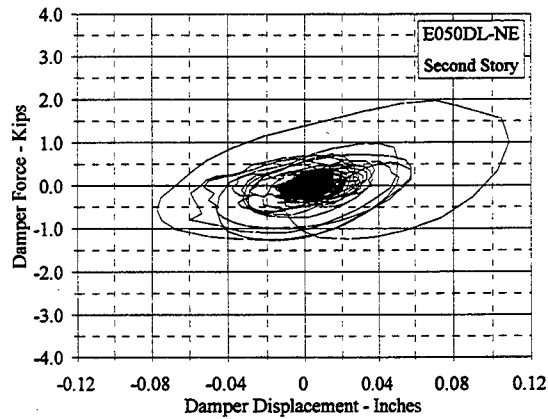
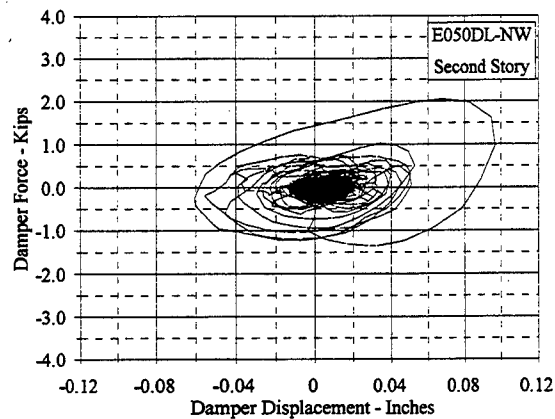
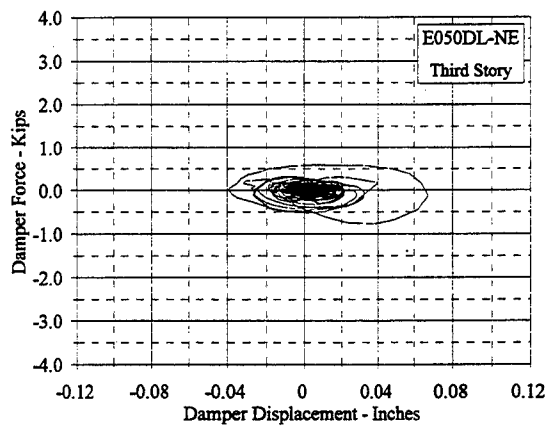
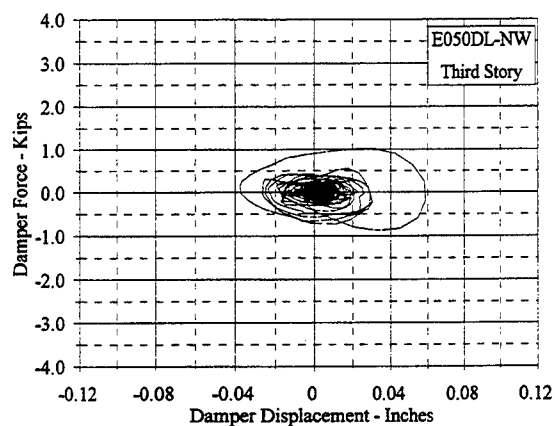


Figure C.10.5 Damper Force Vs. Displacement: E050DL, NW and NE

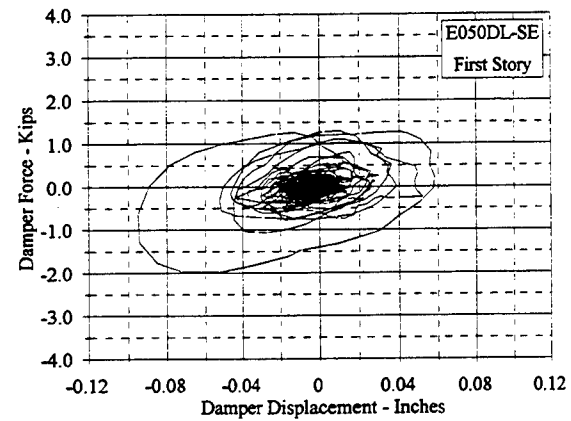
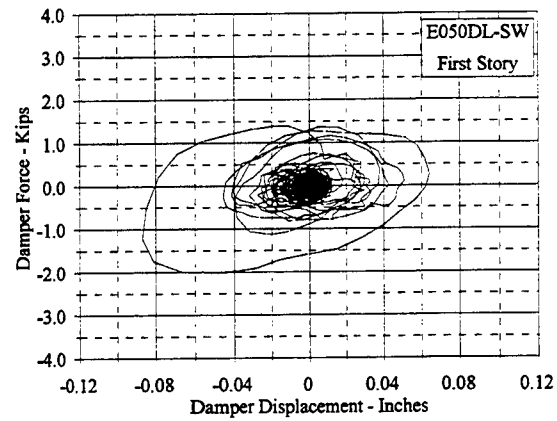
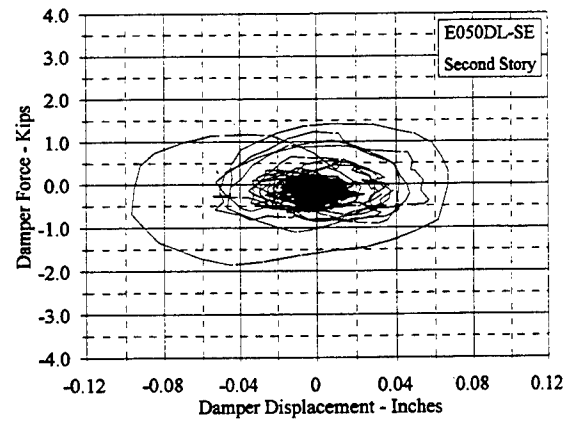
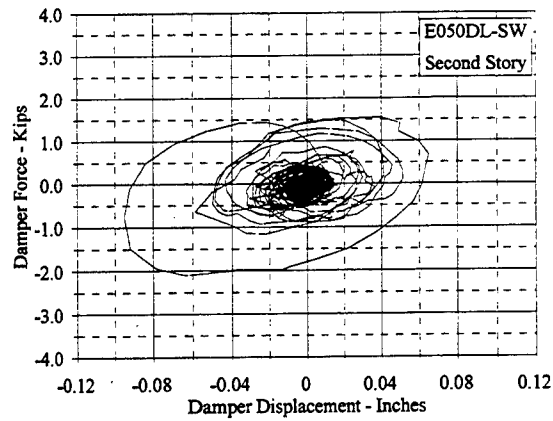
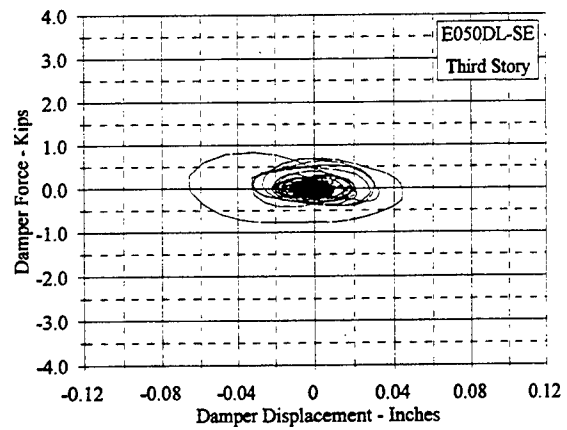
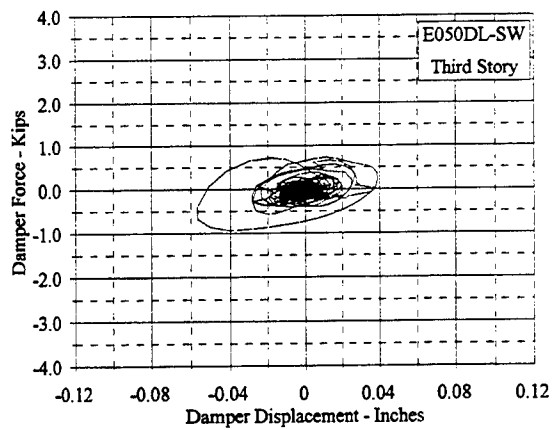


Figure C.10.6 Damper Force Vs. Displacement: E050DL, SW and SE

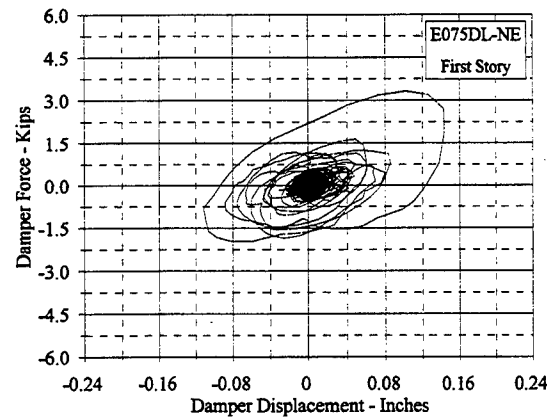
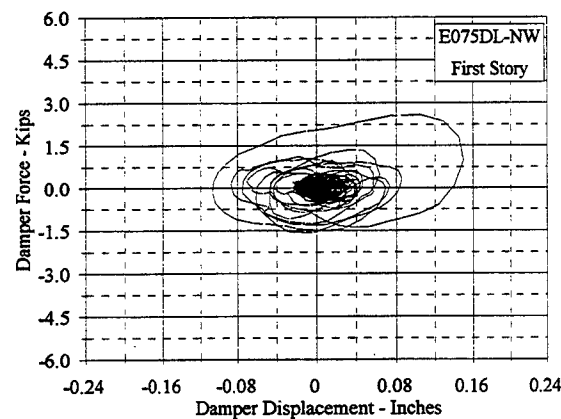
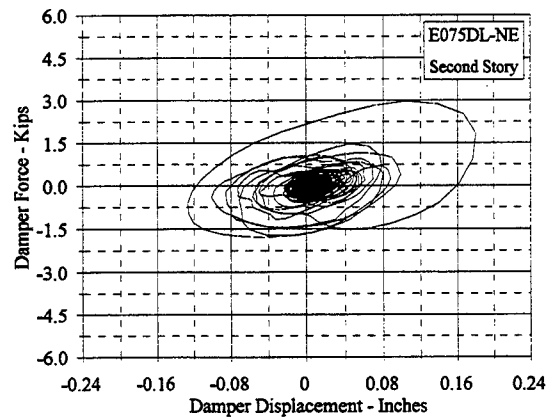
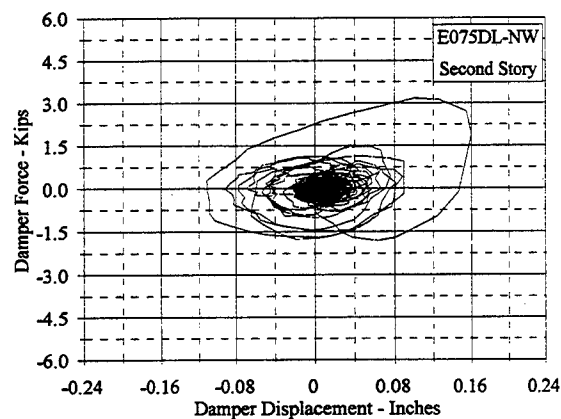
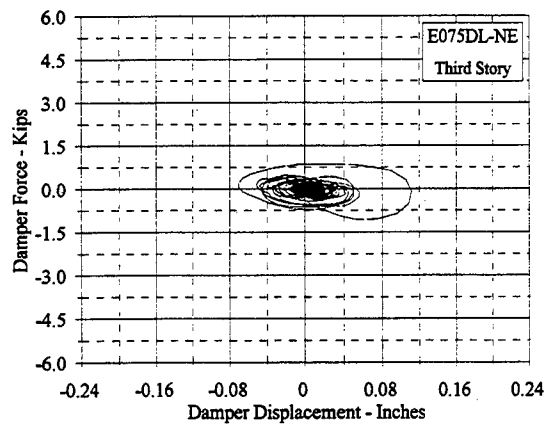
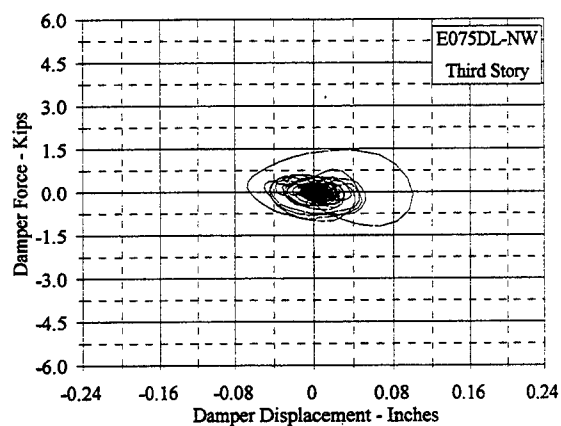


Figure C.10.7 Damper Force Vs. Displacement: E075DL, NW and NE

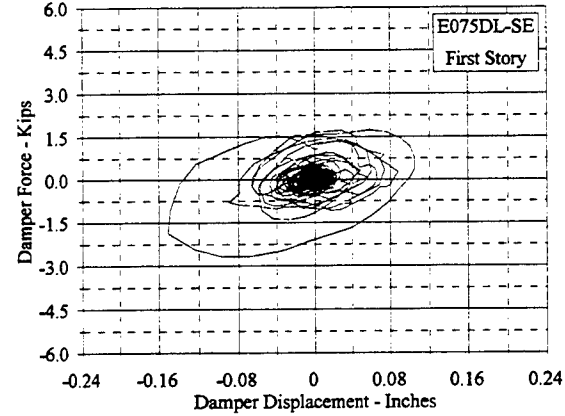
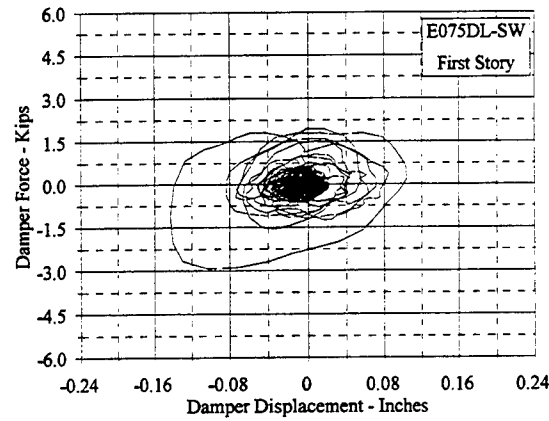
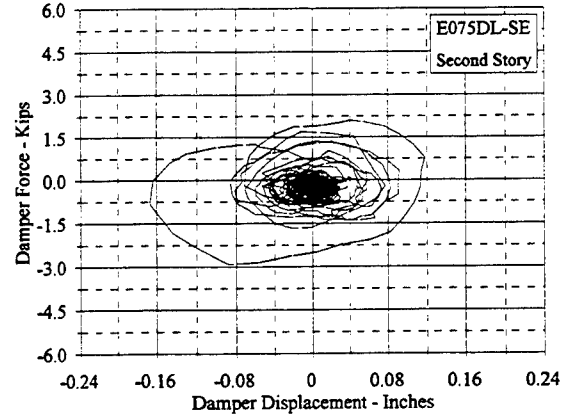
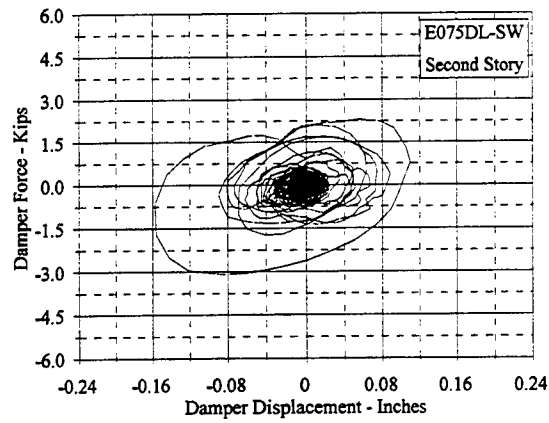
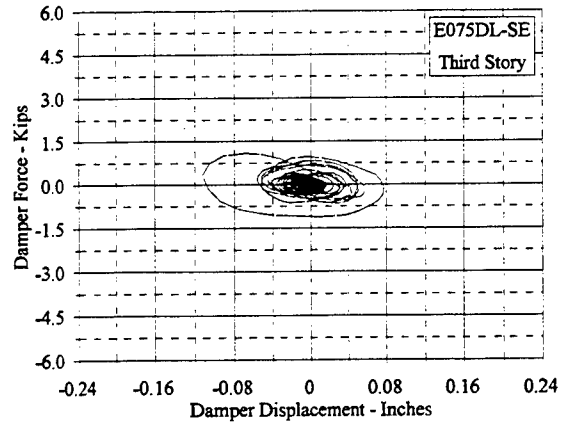
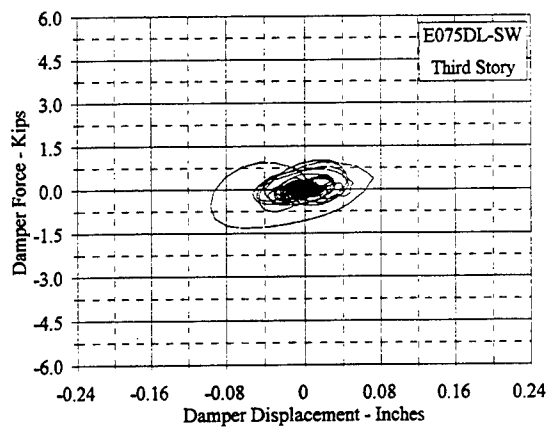


Figure C.10.8 Damper Force Vs. Displacement: E075DL, SW and SE

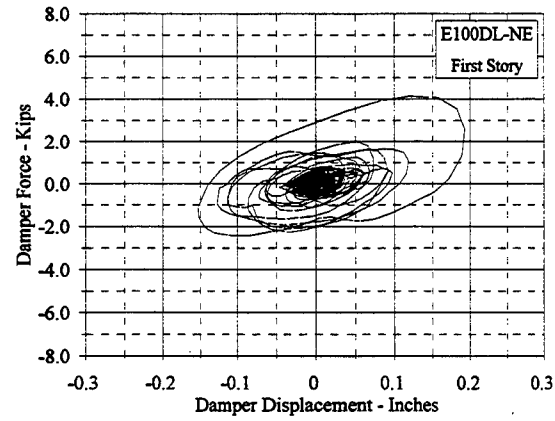
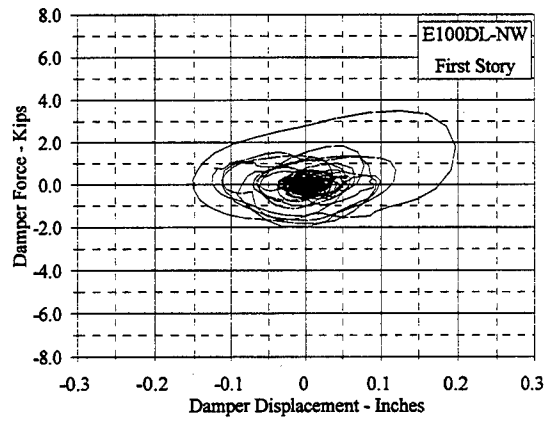
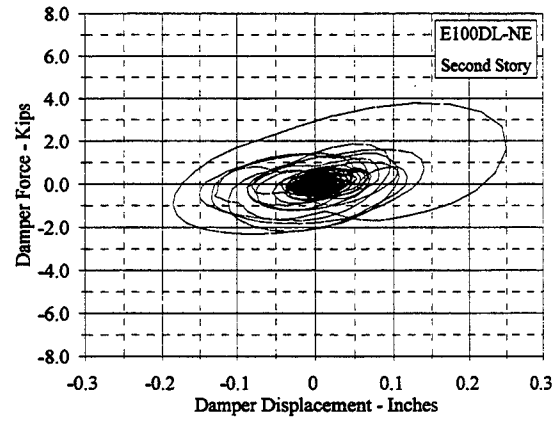
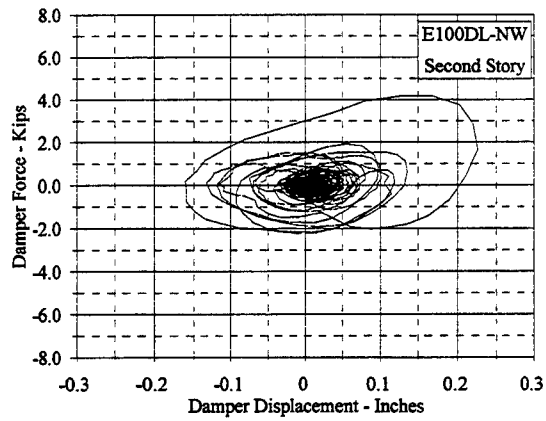
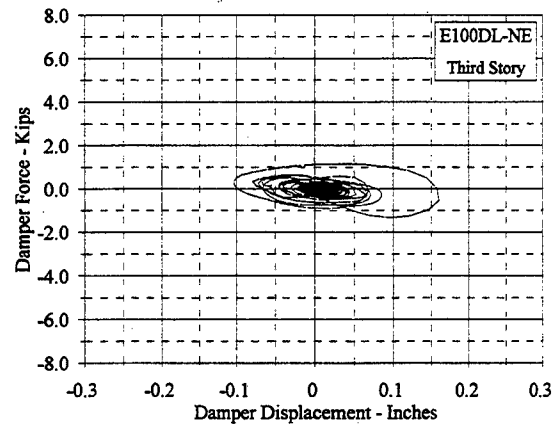
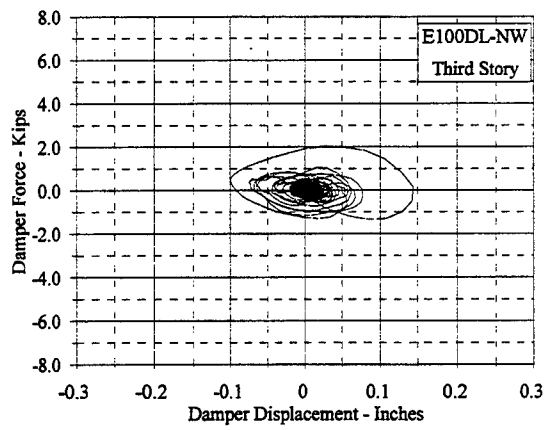


Figure C.10.9 Damper Force Vs. Displacement: E100DL, NW and NE

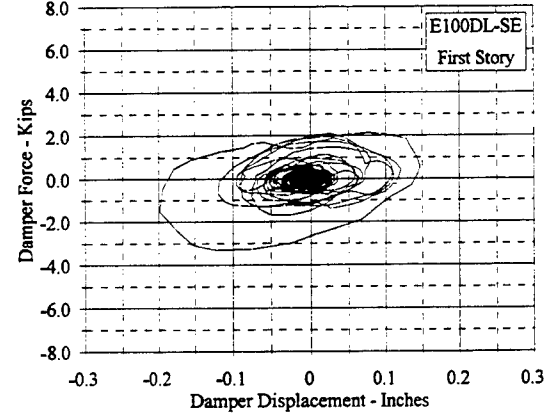
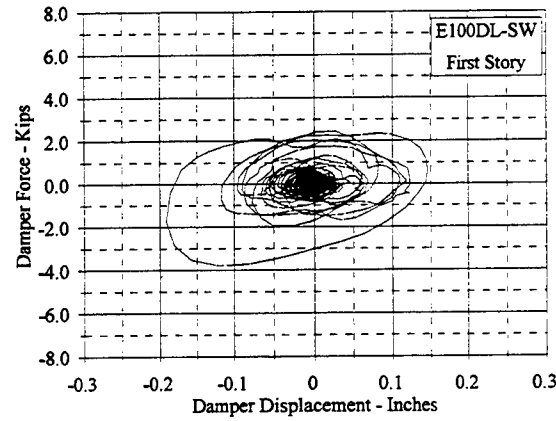
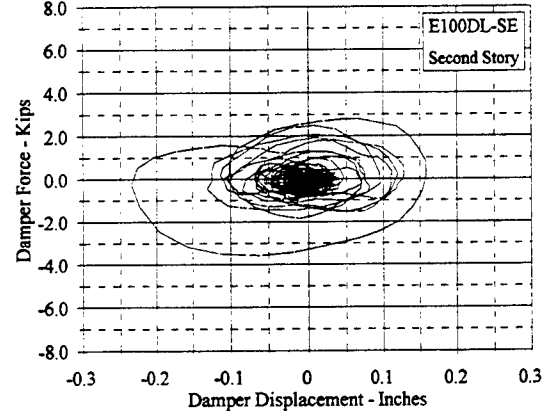
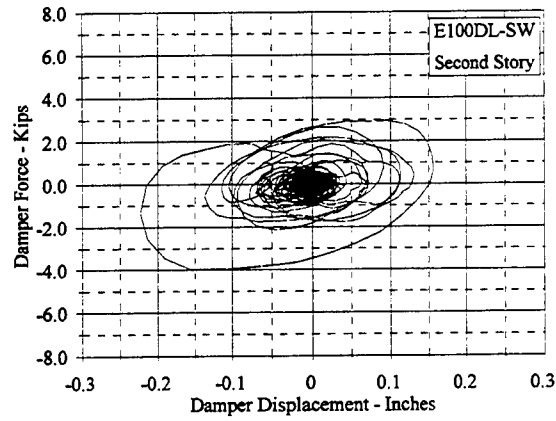
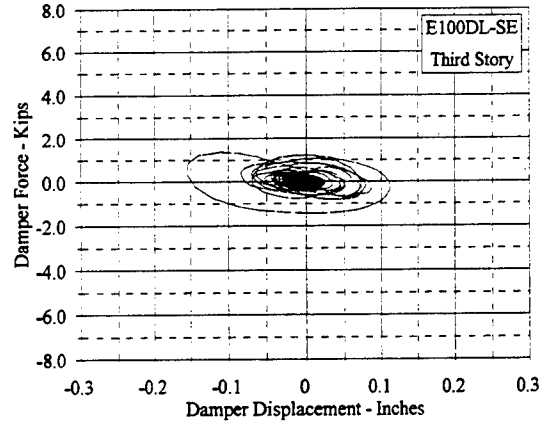
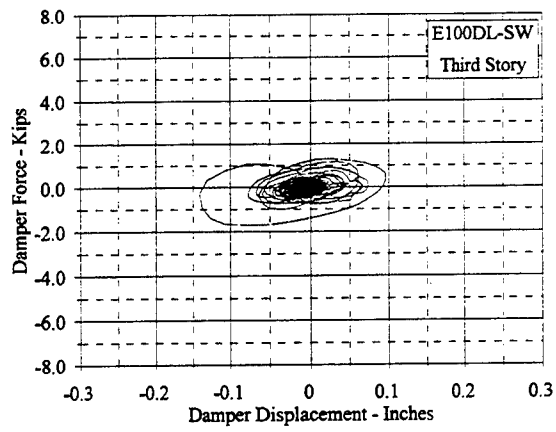


Figure C.10.10 Damper Force Vs. Displacement: E100DL, SW and SE

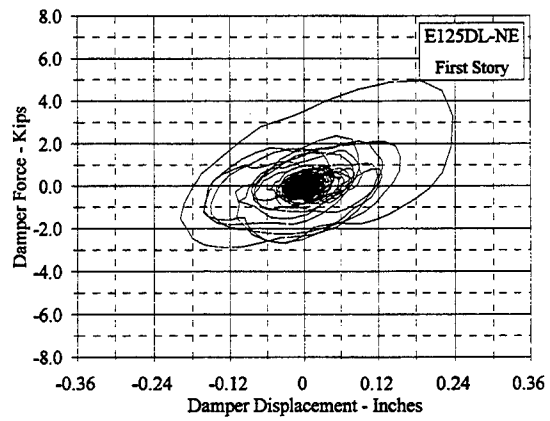
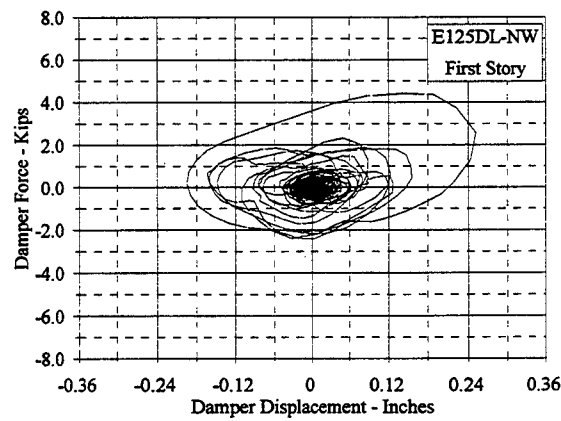
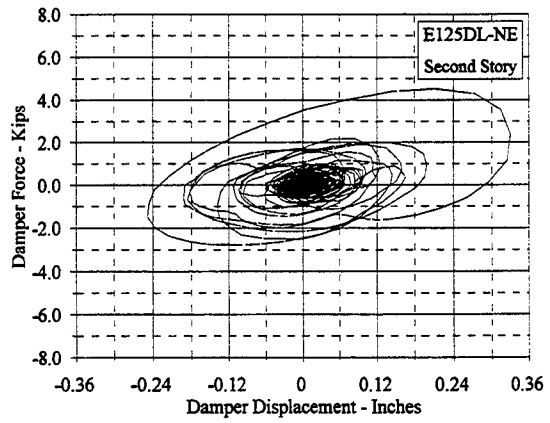
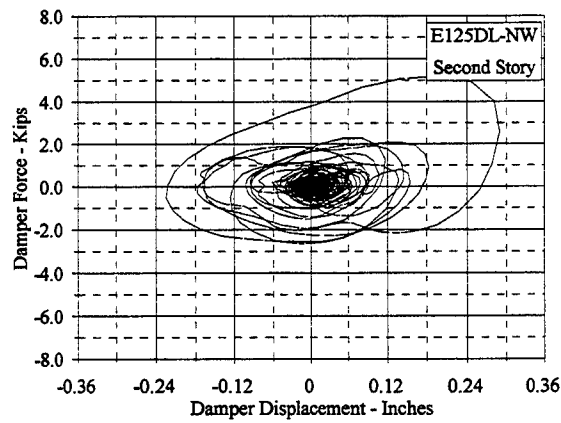
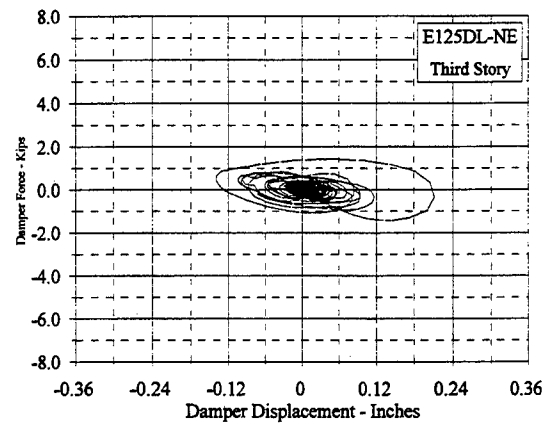
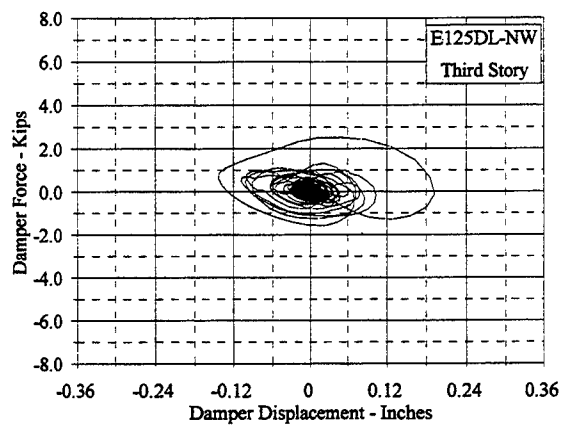


Figure C.10.11 Damper Force Vs. Displacement: E125DL, NW and NE

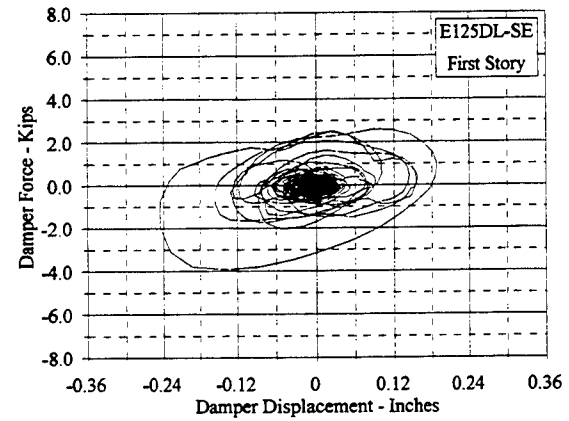
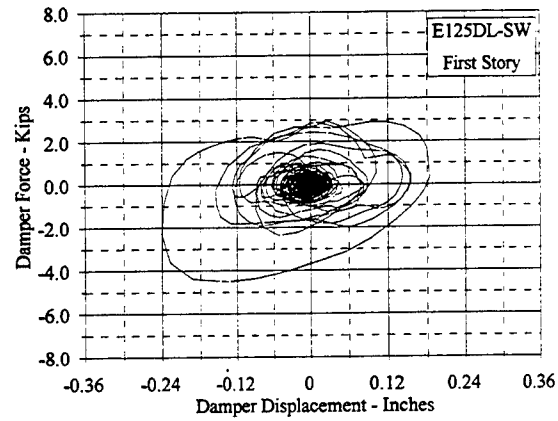
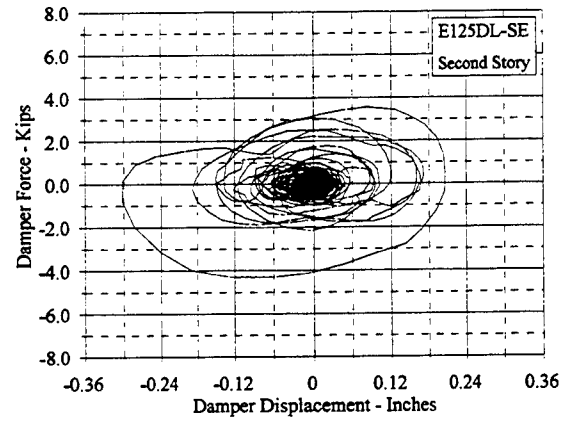
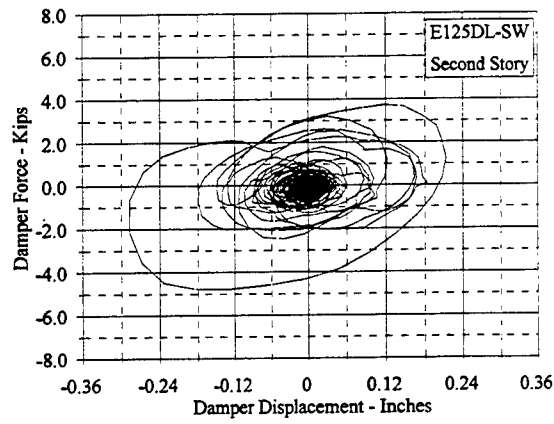
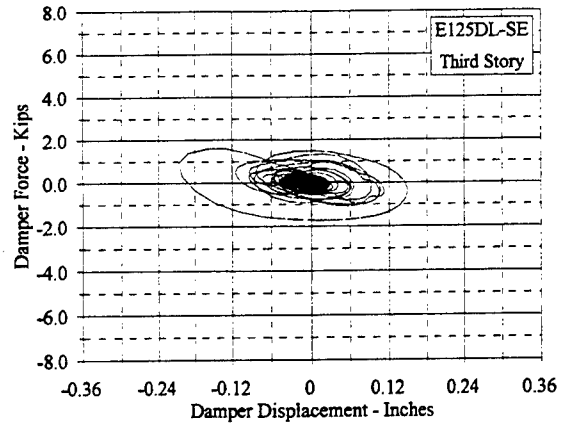
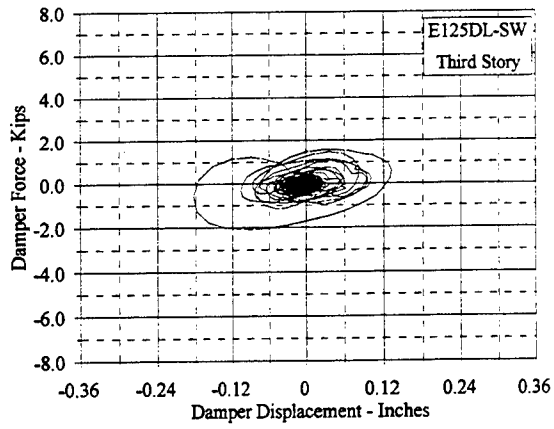


Figure C.10.12 Damper Force Vs. Displacement: E125DL, SW and SE

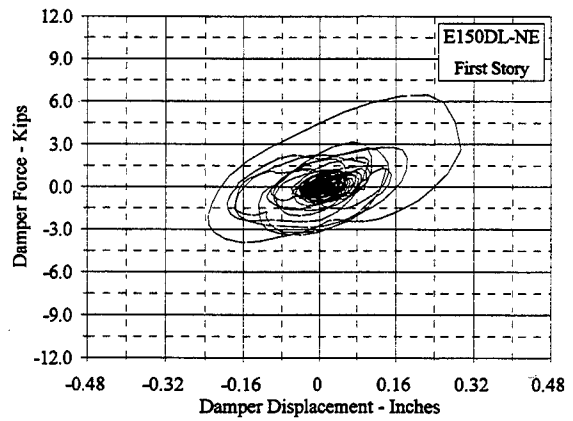
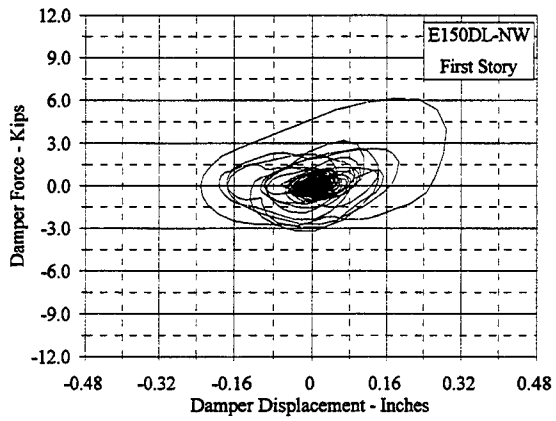
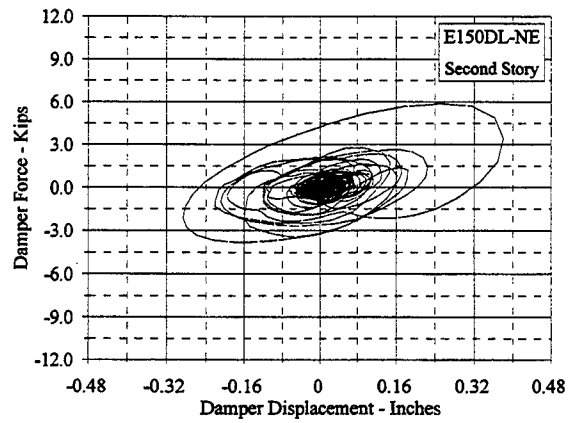
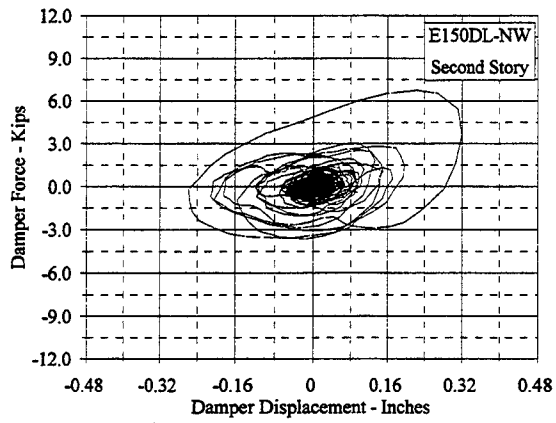
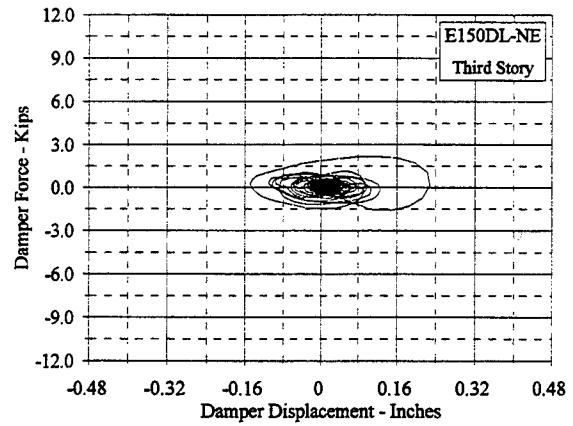
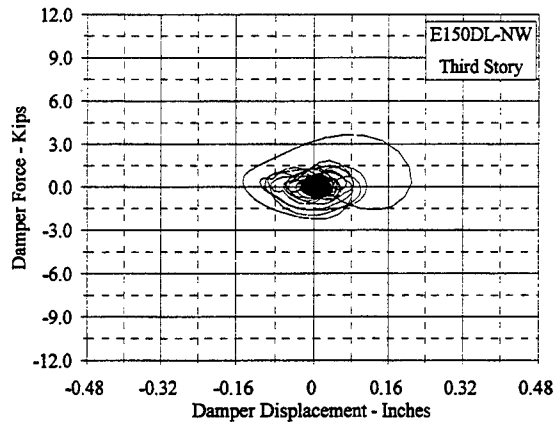


Figure C.10.13 Damper Force Vs. Displacement: E150DL, NW and NE

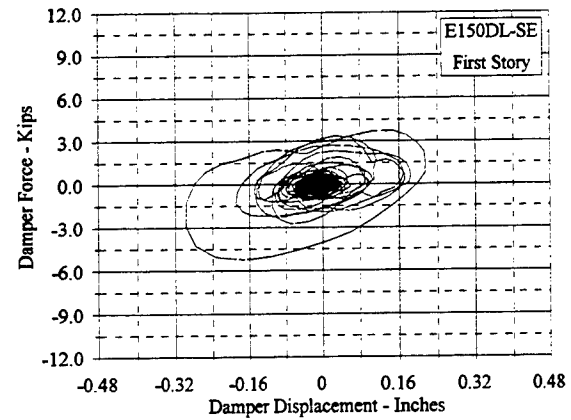
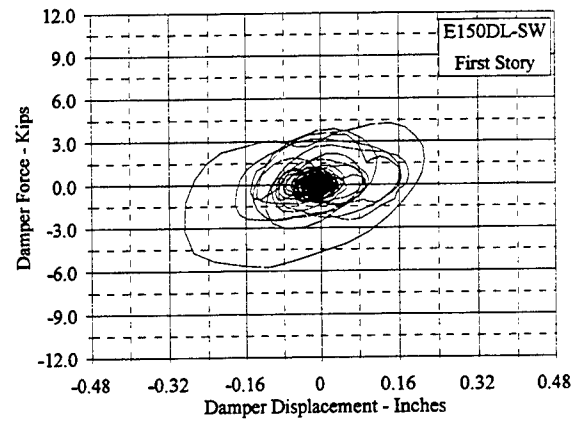
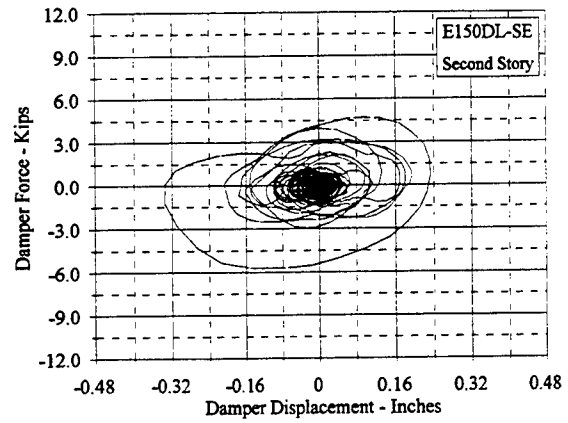
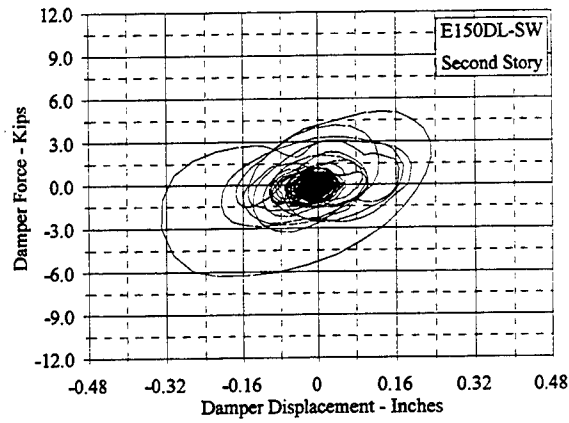
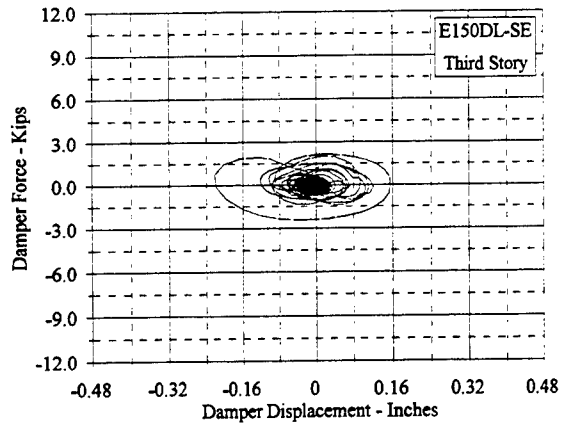
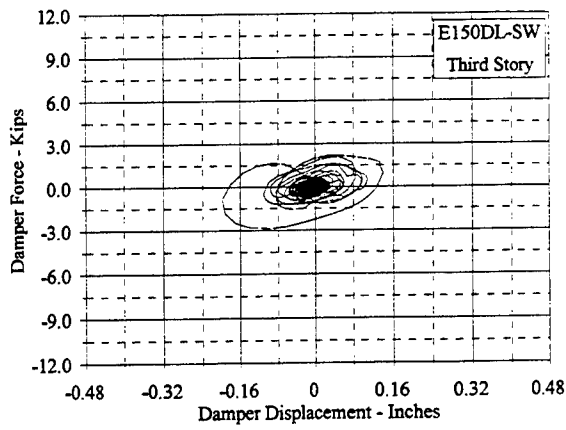


Figure C.10.14 Damper Force Vs. Displacement: E150DL, SW and SE

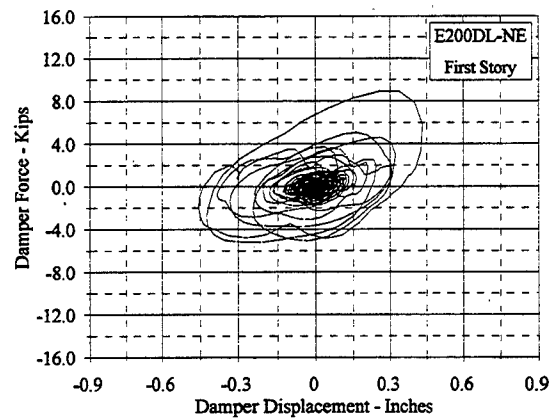
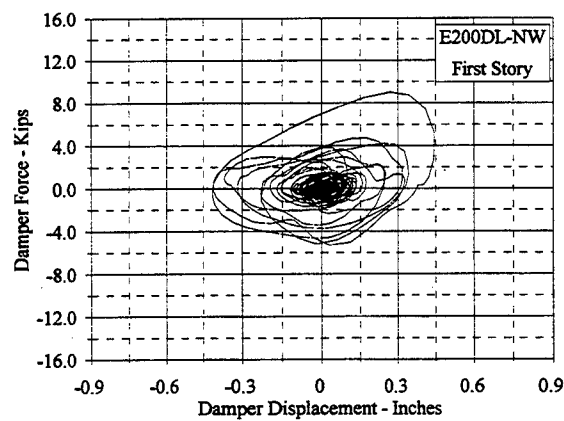
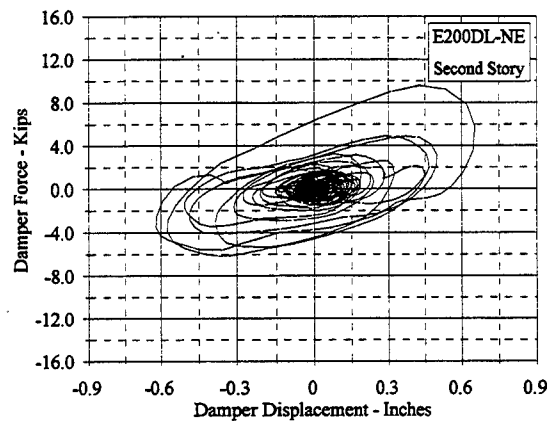
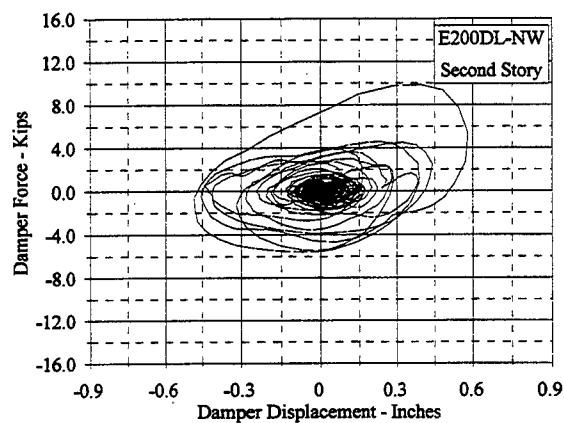
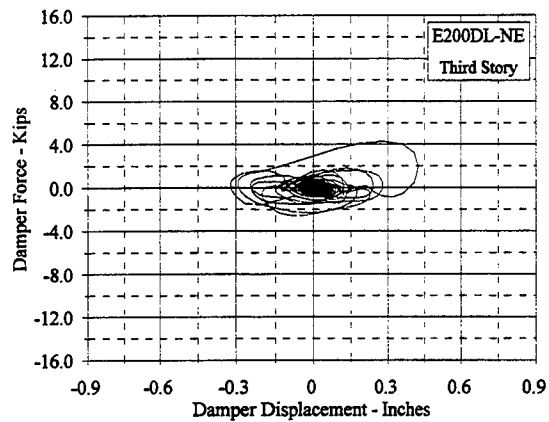
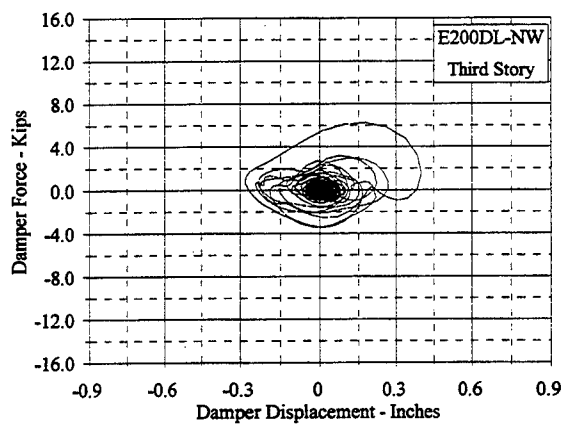


Figure C.10.15 Damper Force Vs. Displacement: E200DL, NW and NE

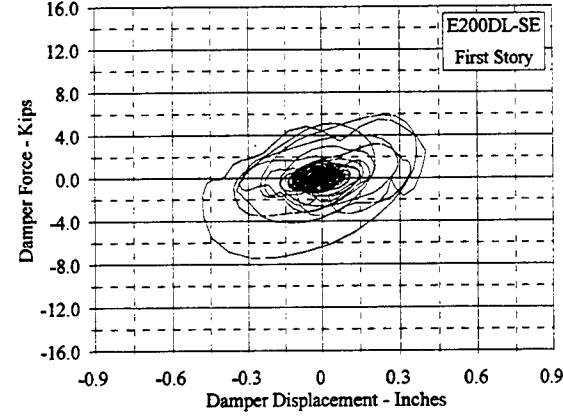
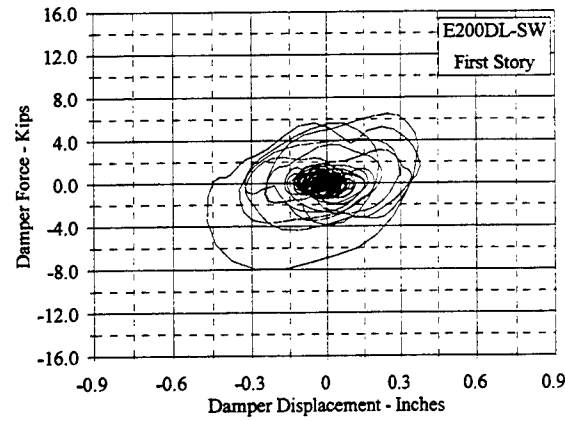
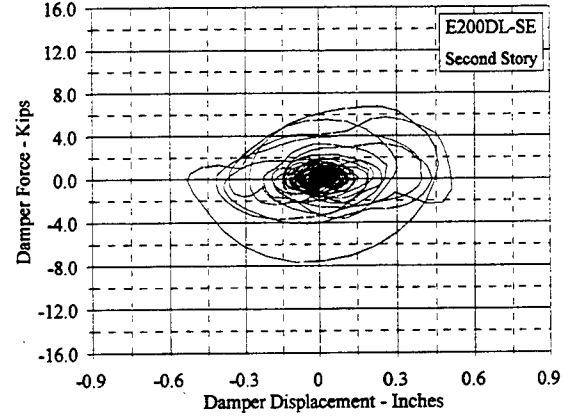
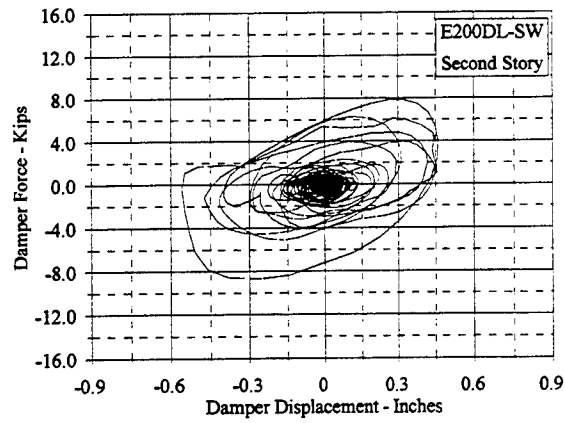
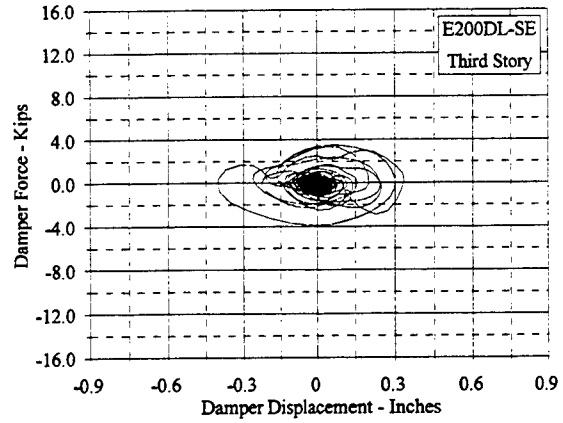
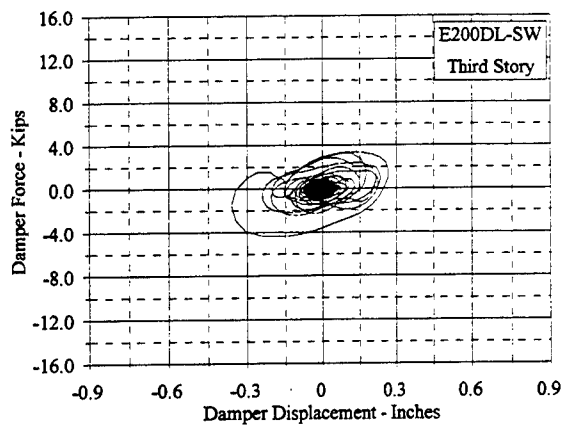


Figure C.10.16 Damper Force Vs. Displacement: E200DL, SW and SE

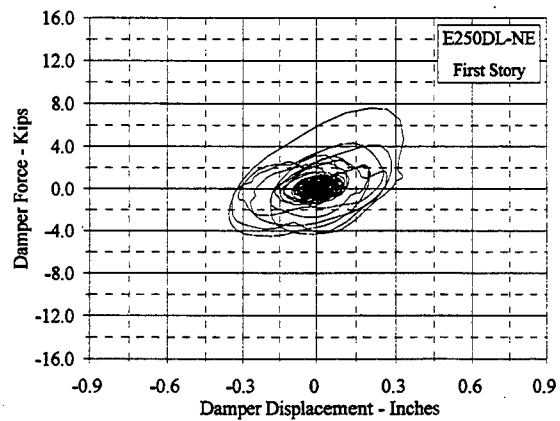
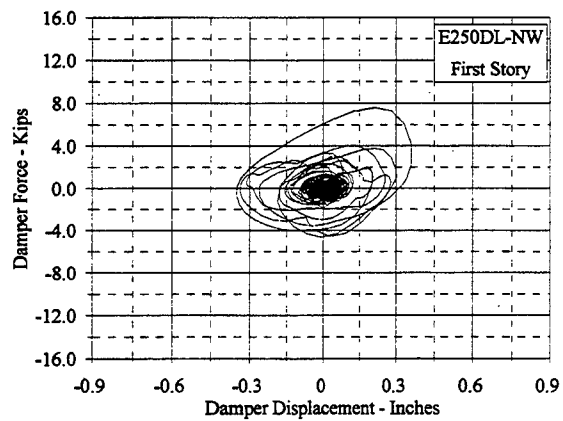
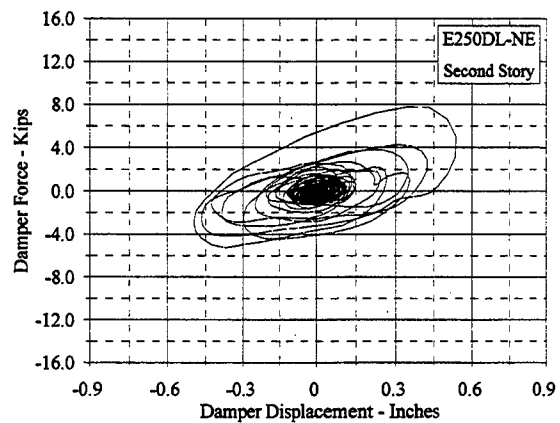
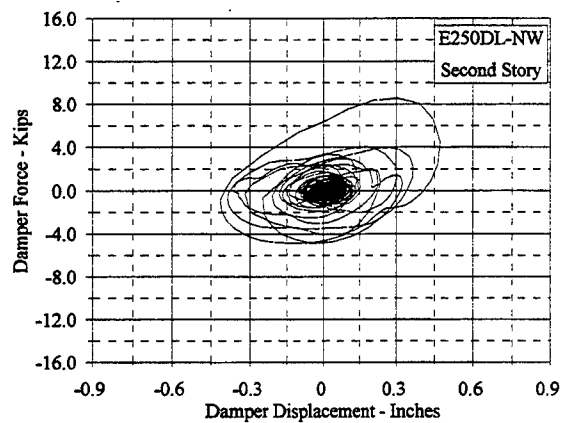
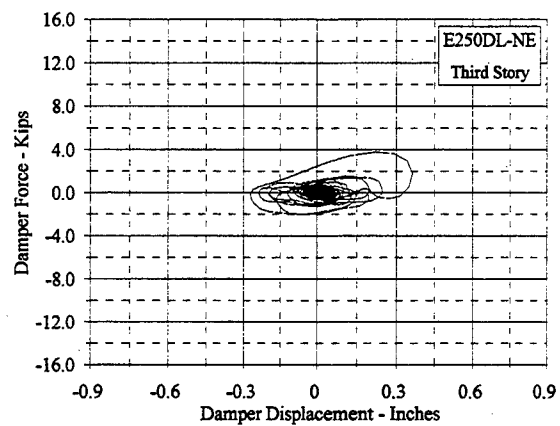
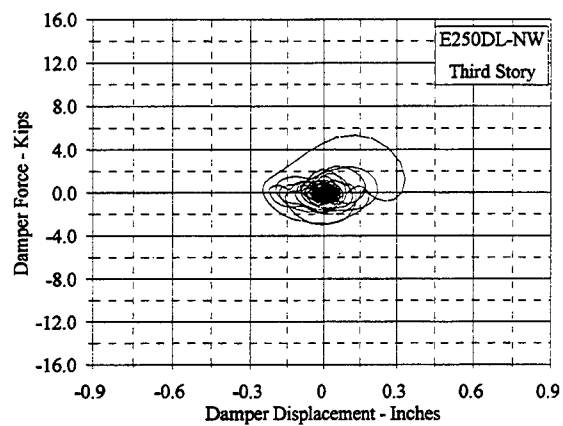


Figure C.10.17 Damper Force Vs. Displacement: E250DL, NW and NE

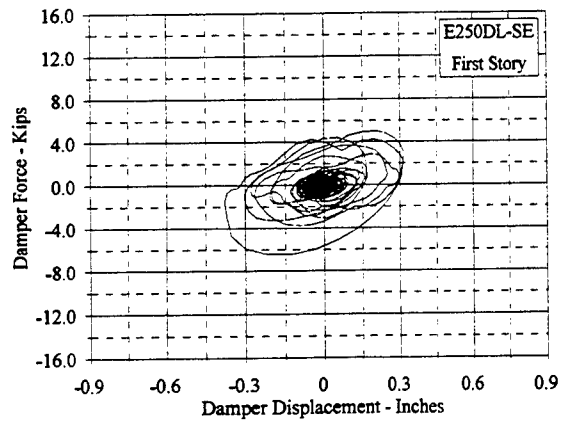
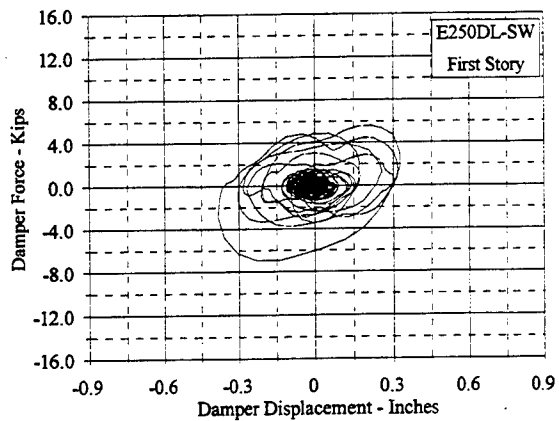
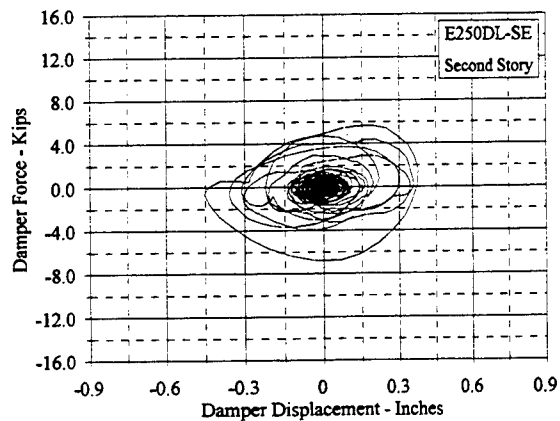
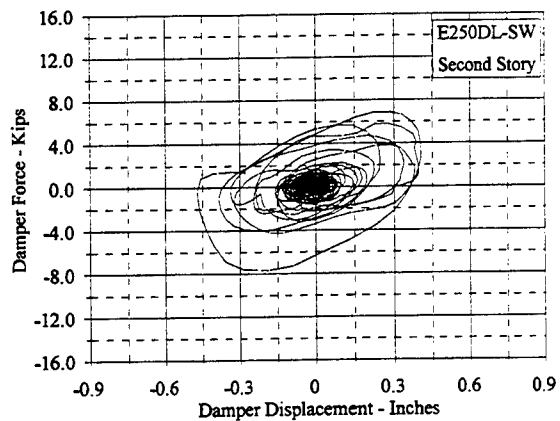
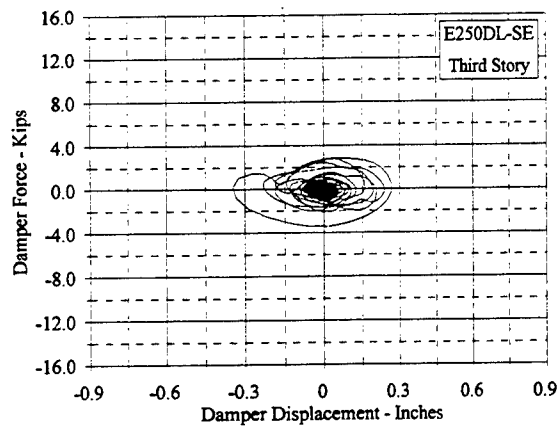
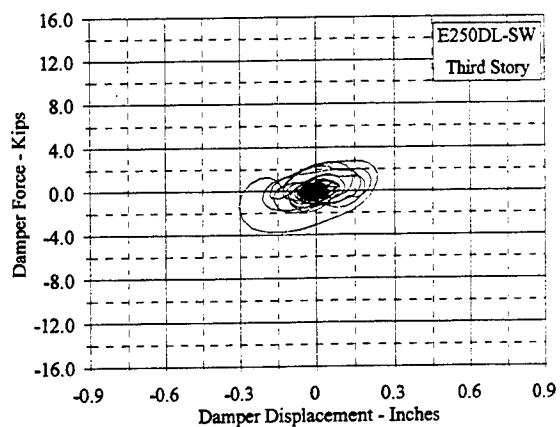


Figure C.10.18 Damper Force Vs. Displacement: E250DL, SW and SE

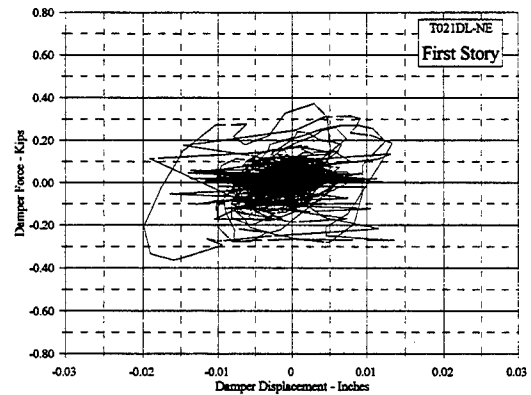
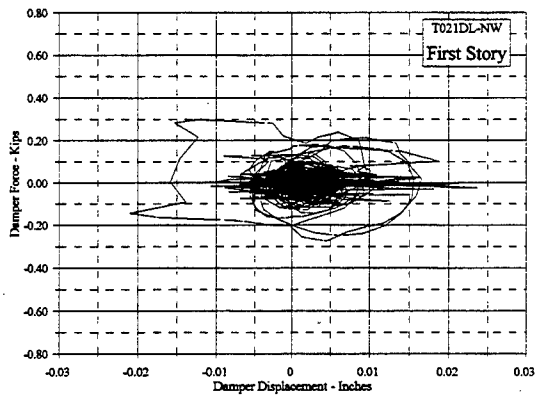
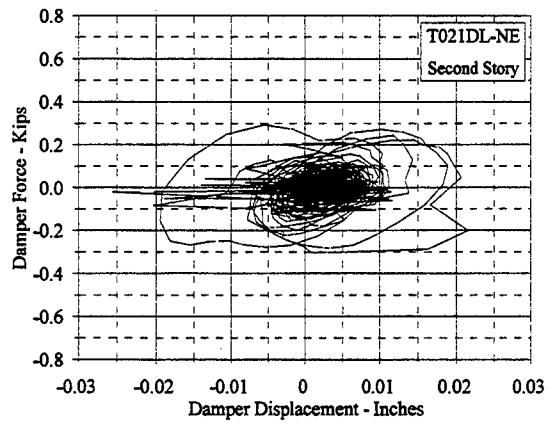
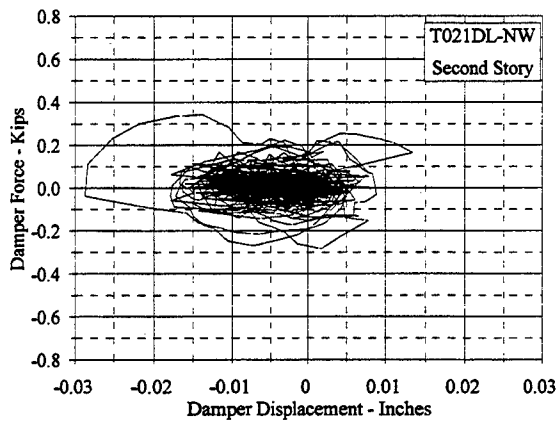
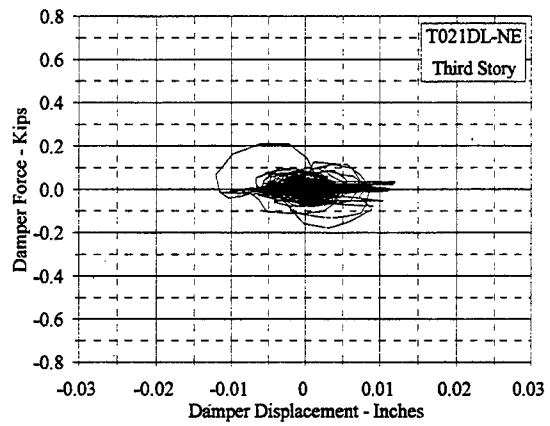
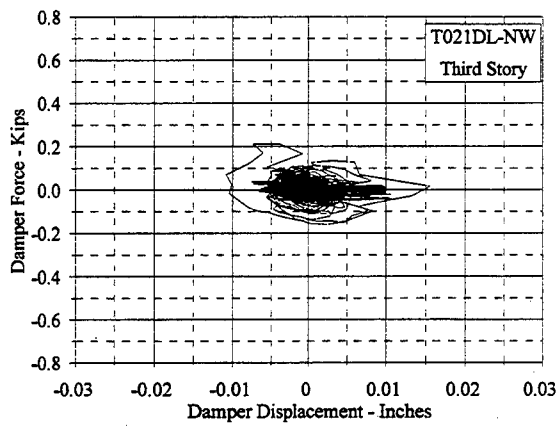


Figure C.10.19 Damper Force Vs. Displacement: T021DL, NW and NE

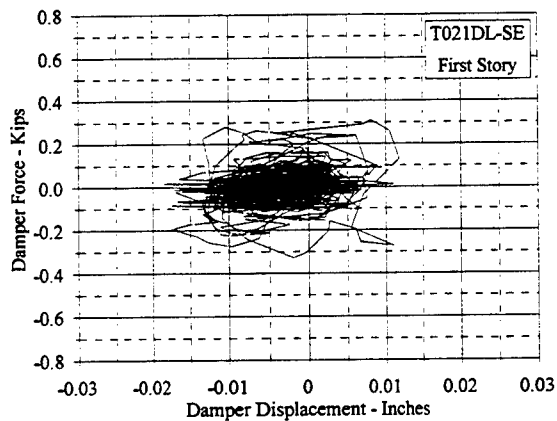
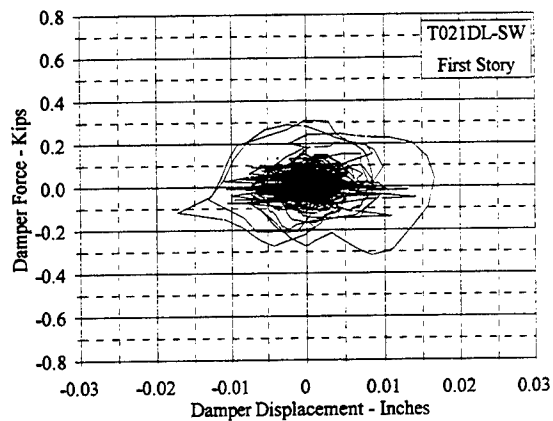
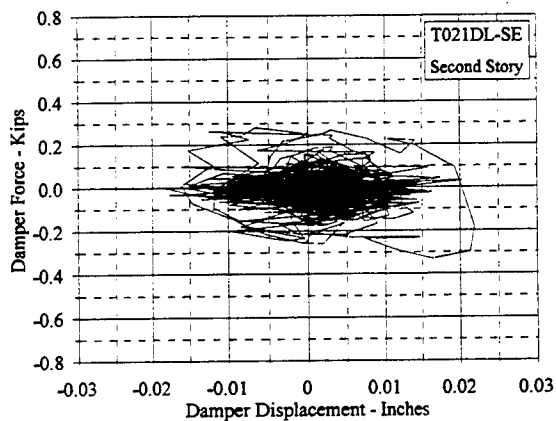
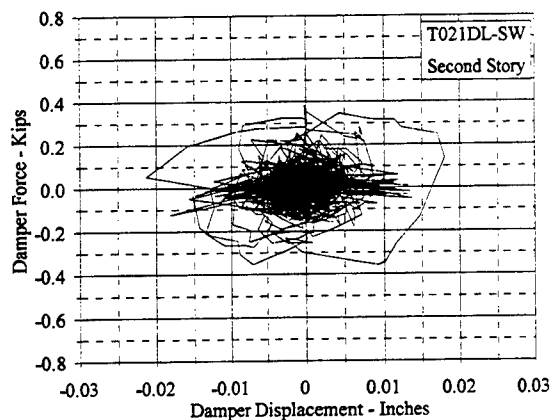
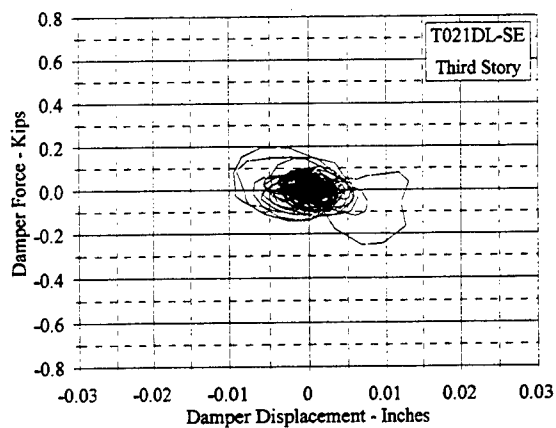
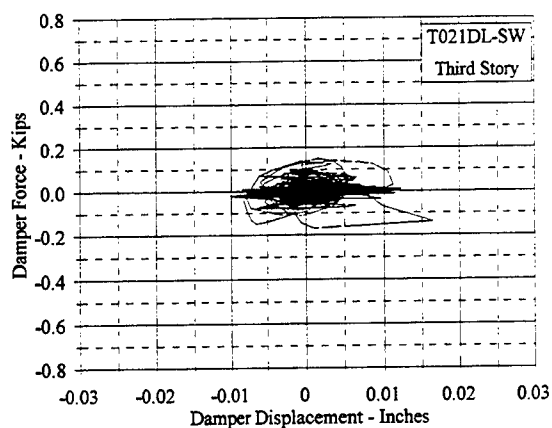


Figure C.10.20 Damper Force Vs. Displacement: T021DL, SW and SE

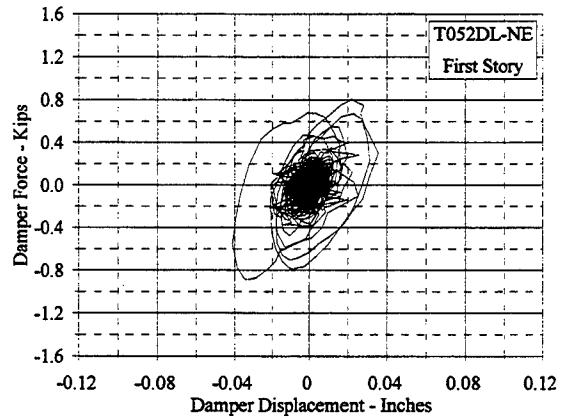
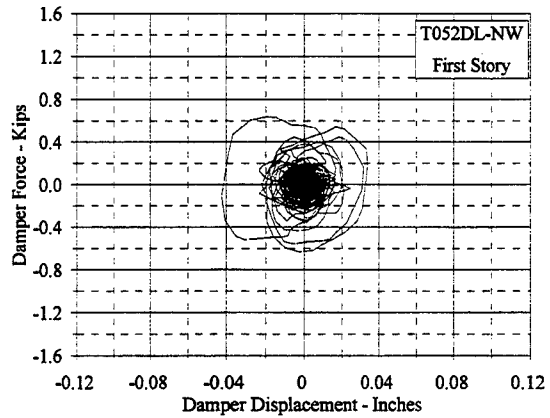
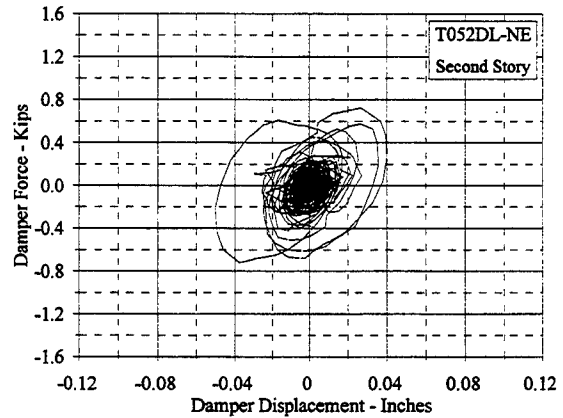
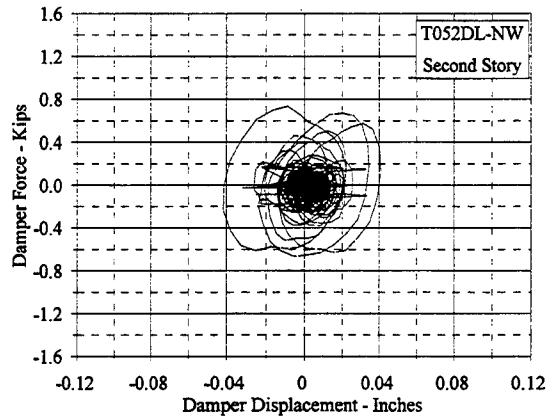
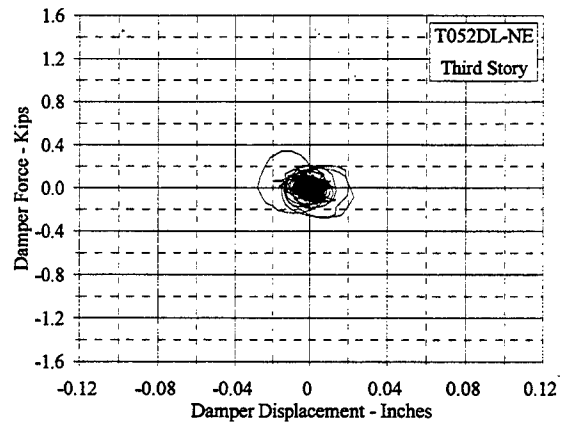
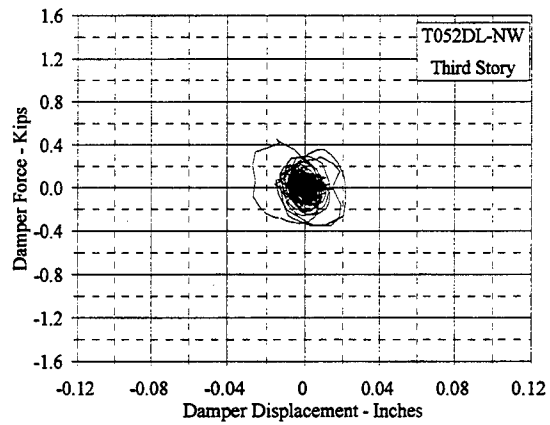


Figure C.10.21 Damper Force Vs. Displacement: T052DL, NW and NE

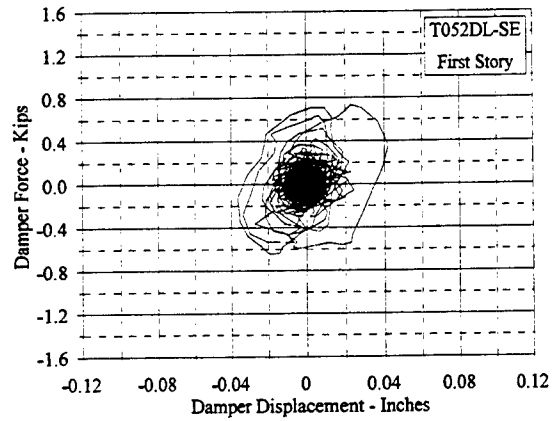
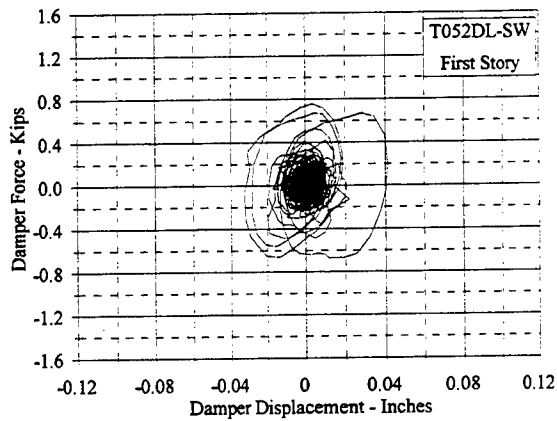
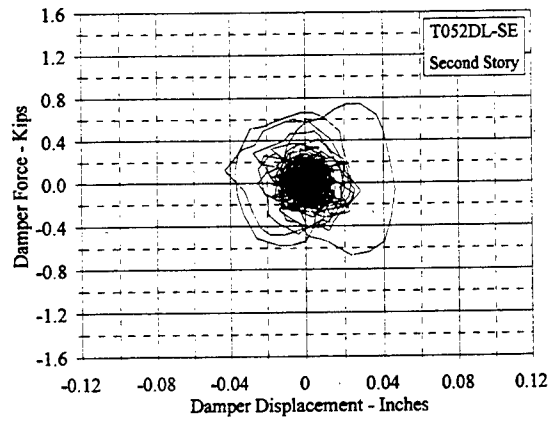
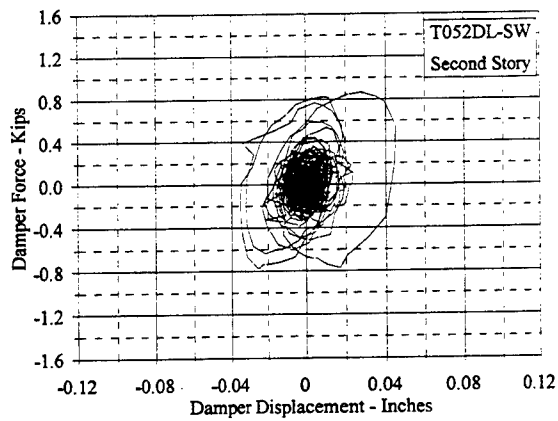
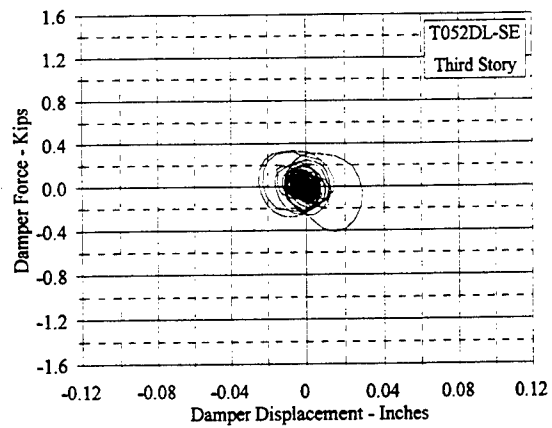
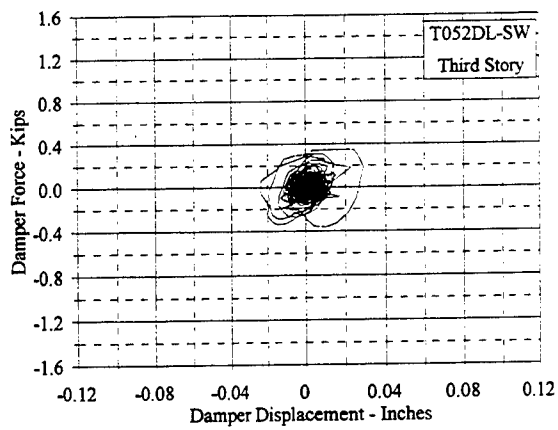


Figure C.10.22 Damper Force Vs. Displacement: T052DL, SW and SE

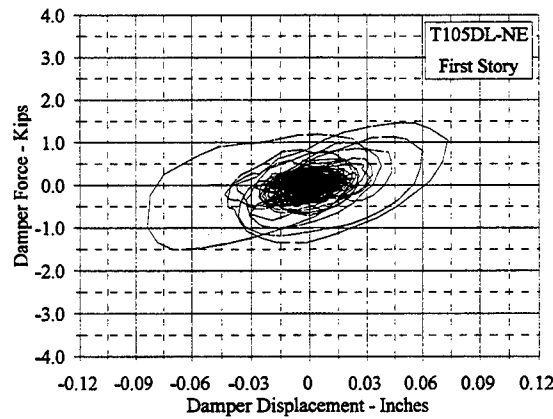
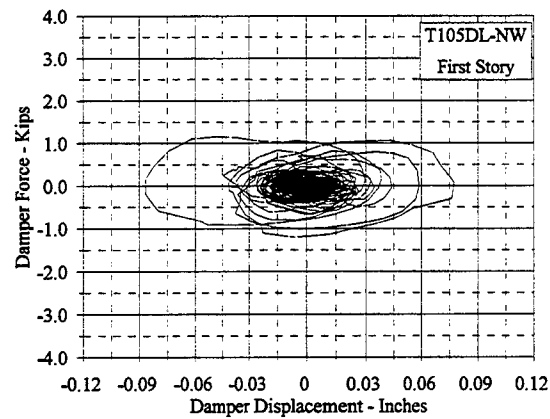
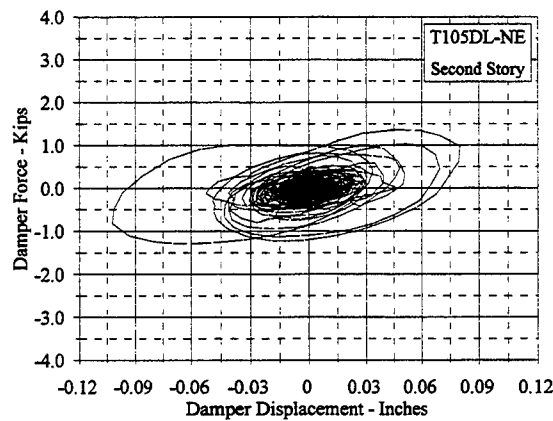
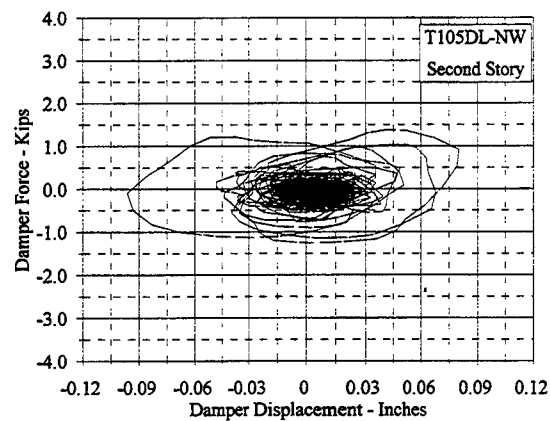
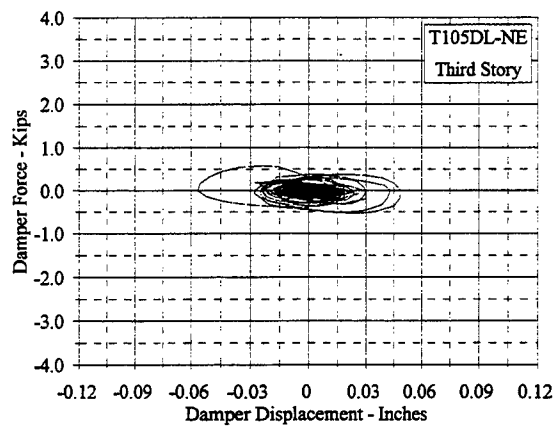
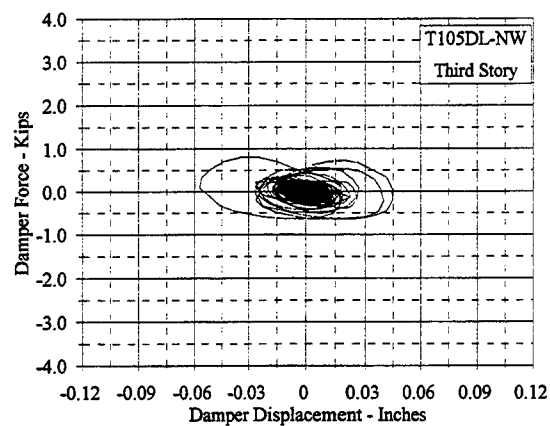


Figure C.10.23 Damper Force Vs. Displacement: T105DL, NW and NE

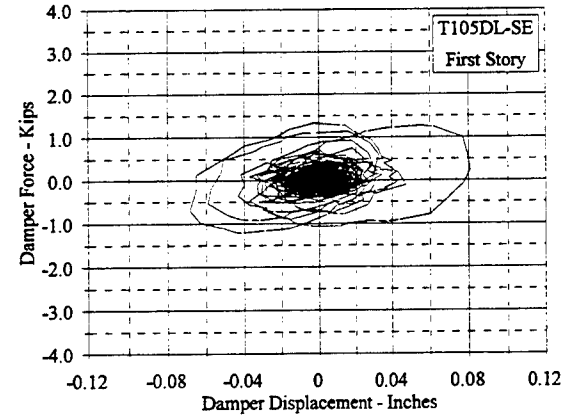
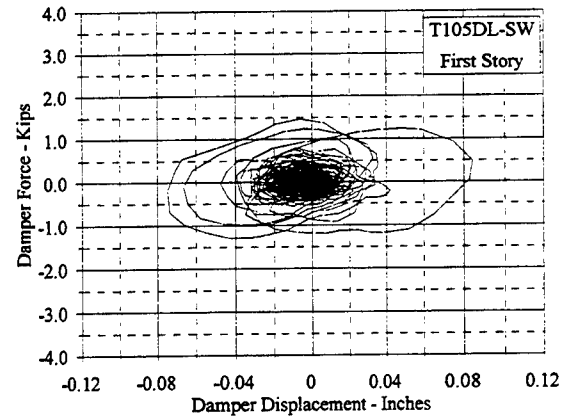
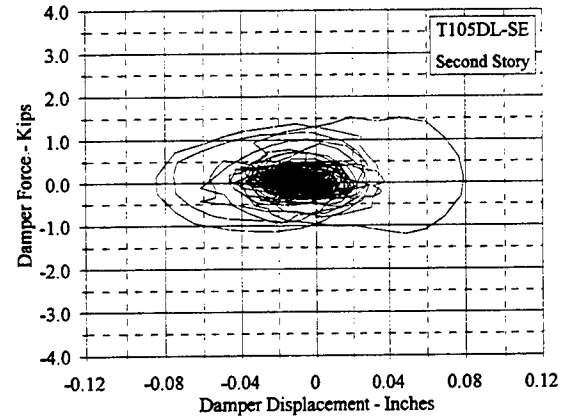
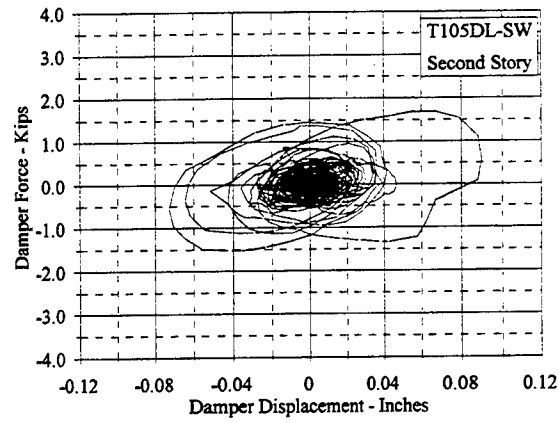
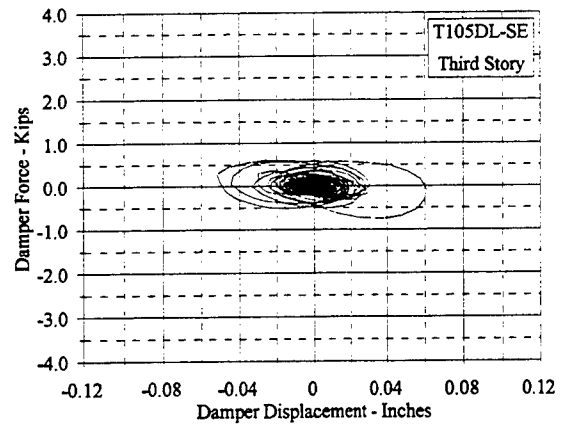
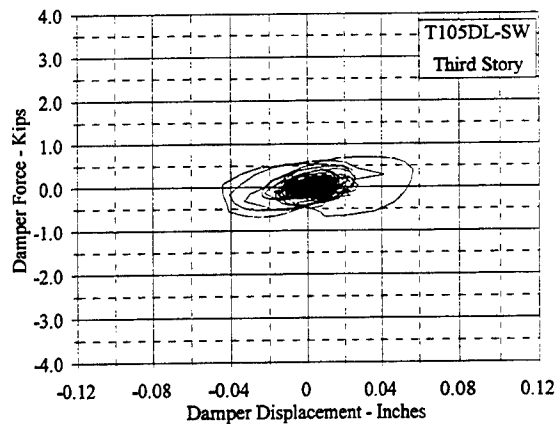


Figure C.10.24 Damper Force Vs. Displacement: T105DL, SW and SE

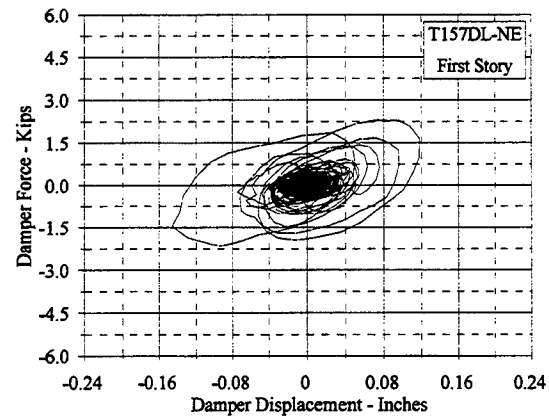
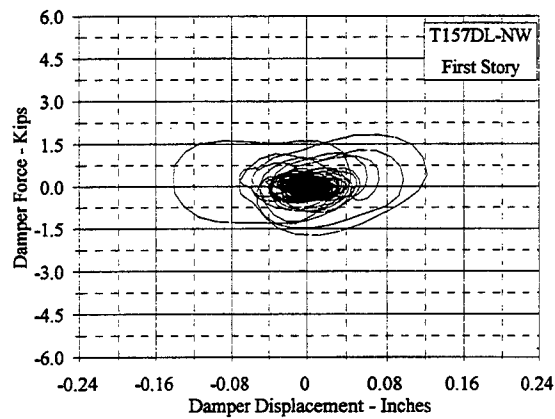
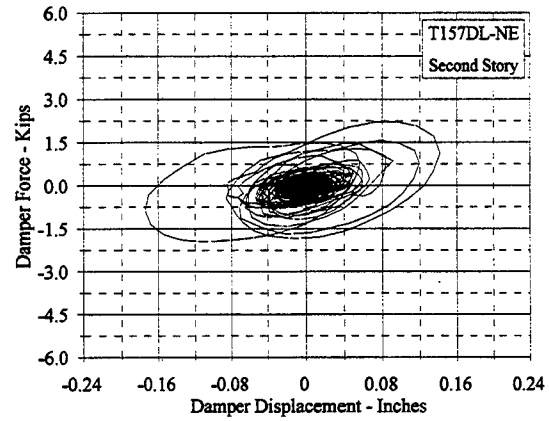
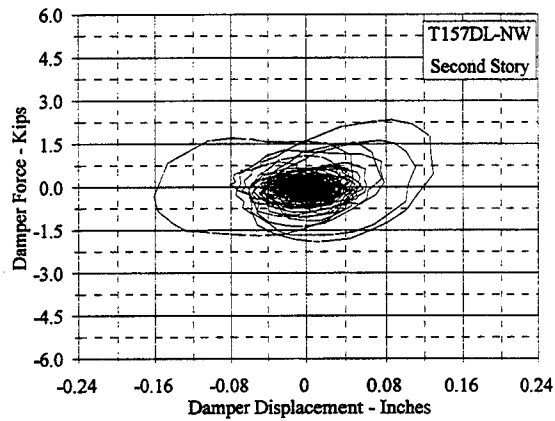
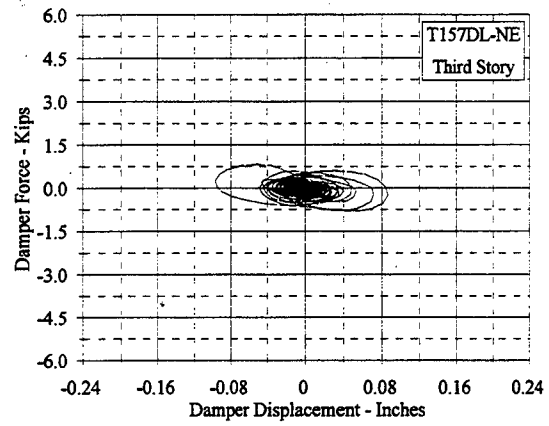
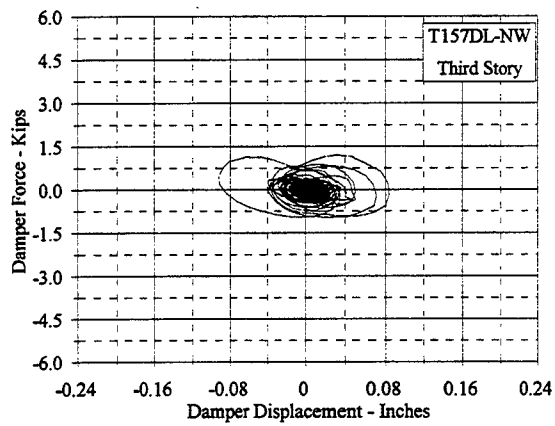


Figure C.10.25 Damper Force Vs. Displacement: T157DL, NW and NE

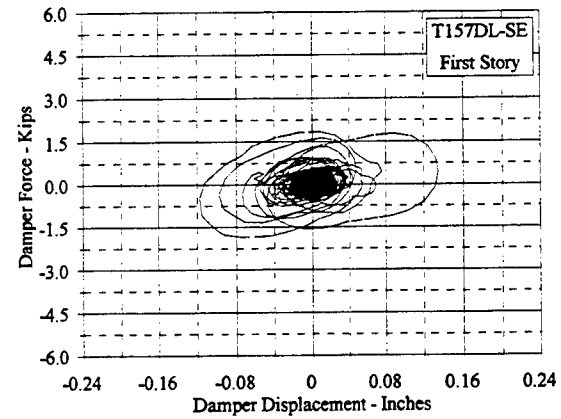
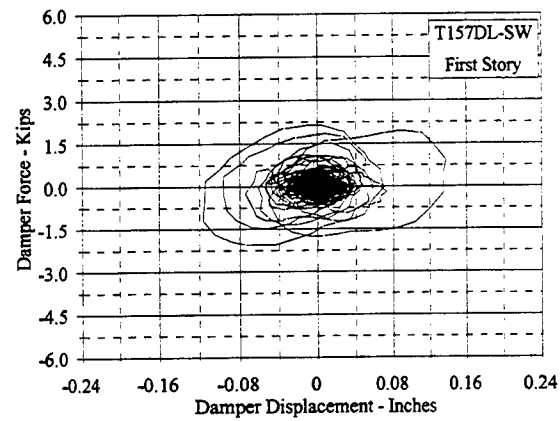
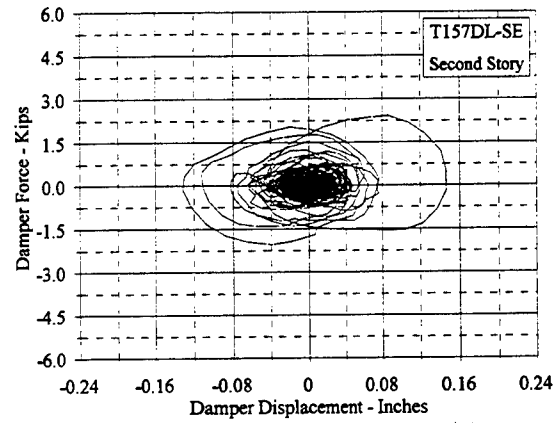
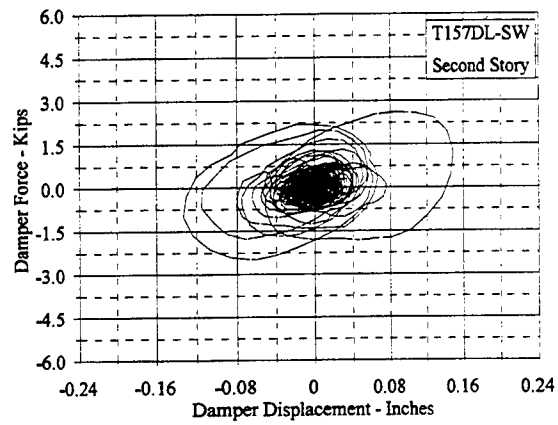
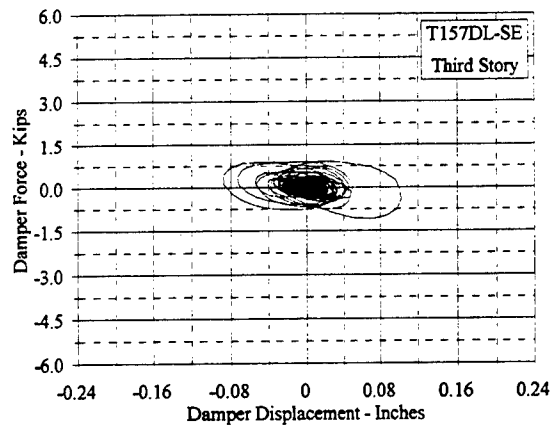
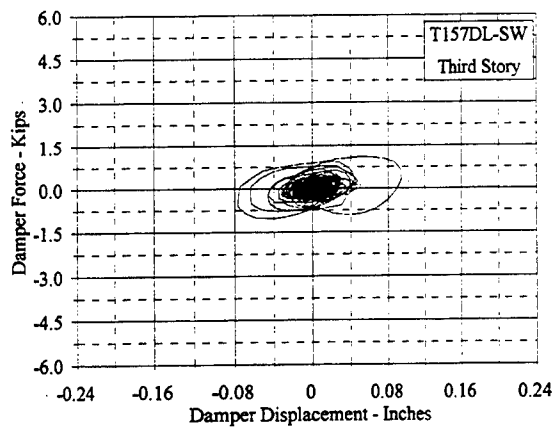


Figure C.10.26 Damper Force Vs. Displacement: T157DL, SW and SE

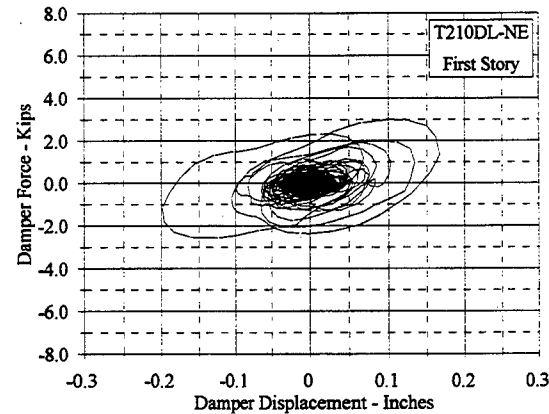
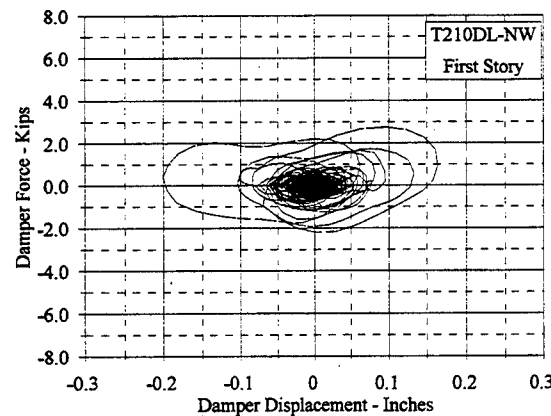
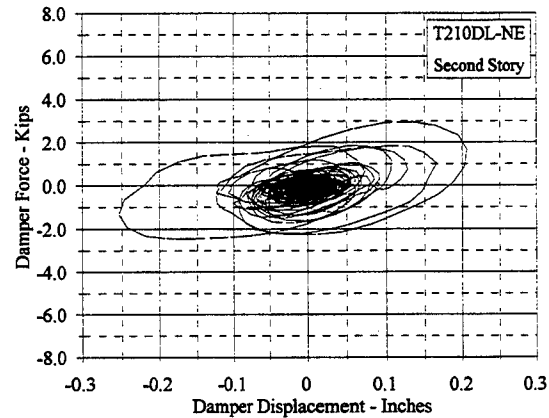
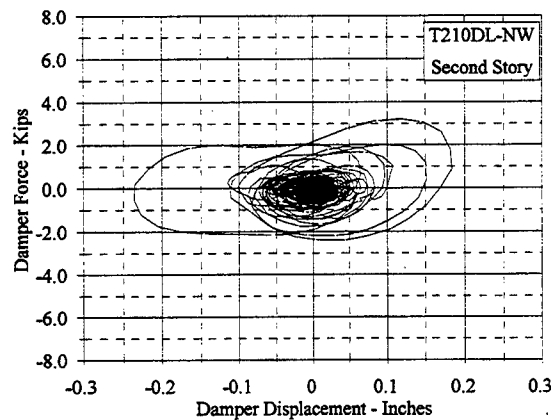
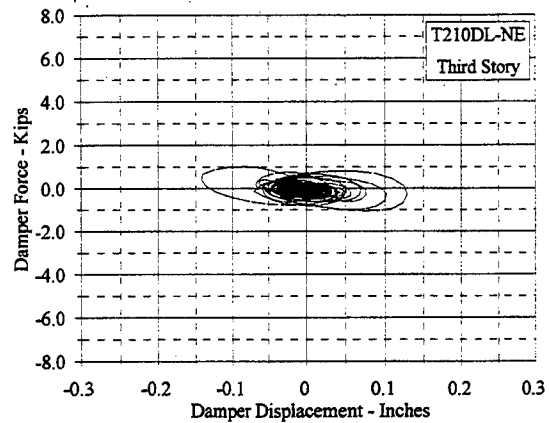
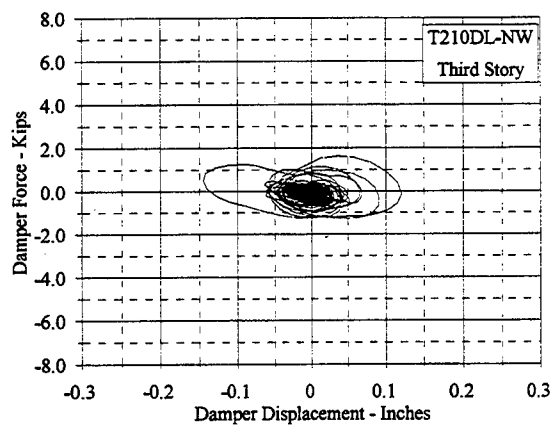


Figure C.10.27 Damper Force Vs. Displacement: T210DL, NW and NE

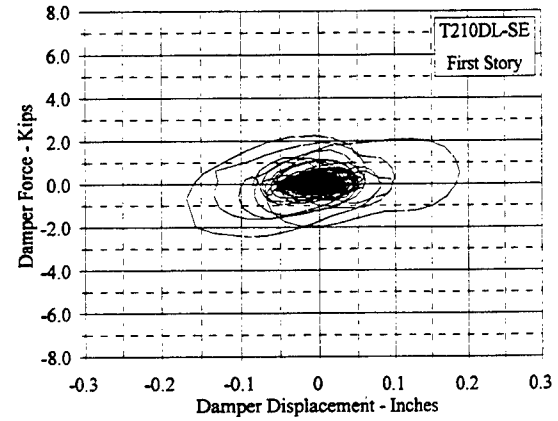
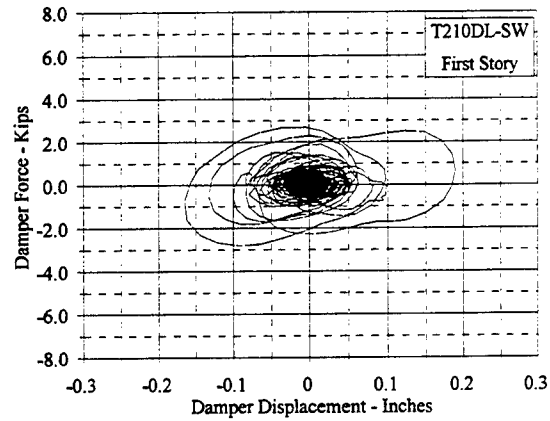
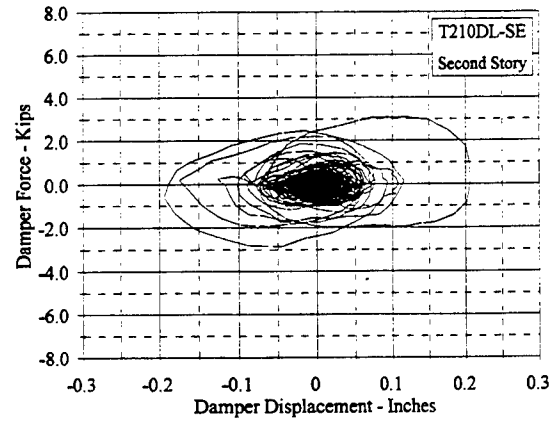
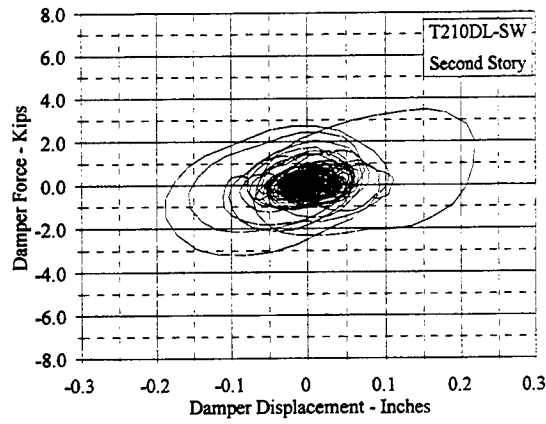
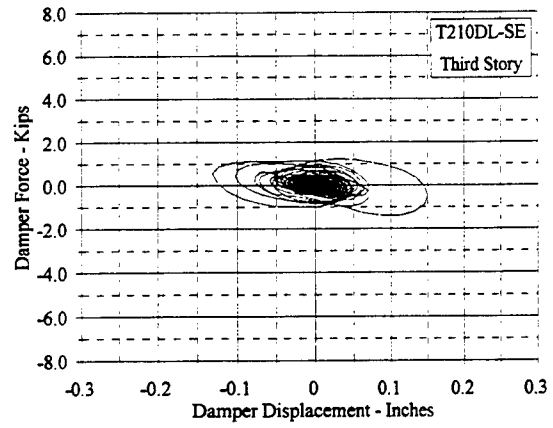
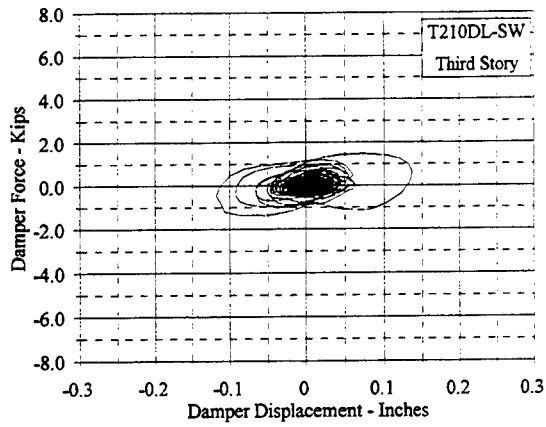


Figure C.10.28 Damper Force Vs. Displacement: T210DL, SW and SE

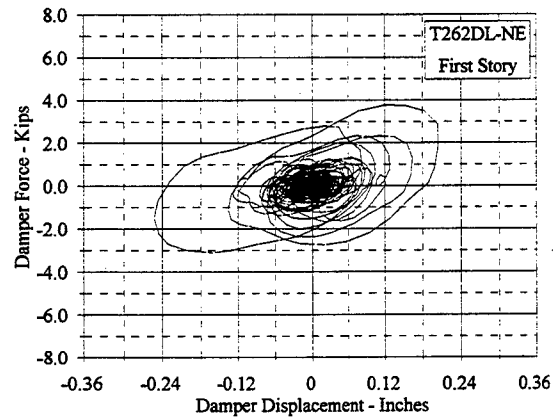
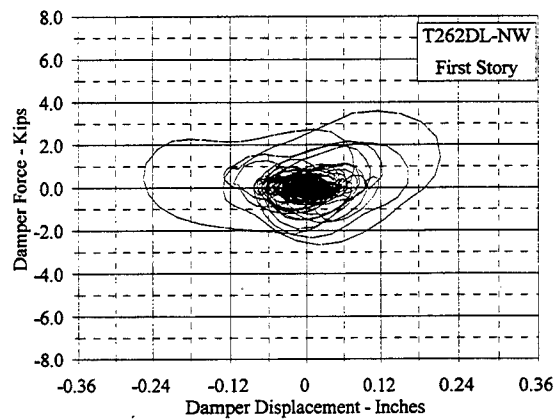
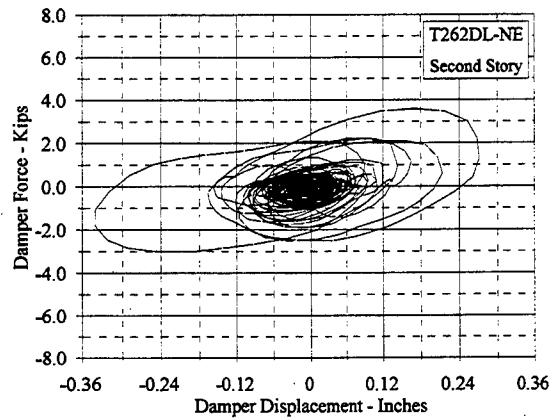
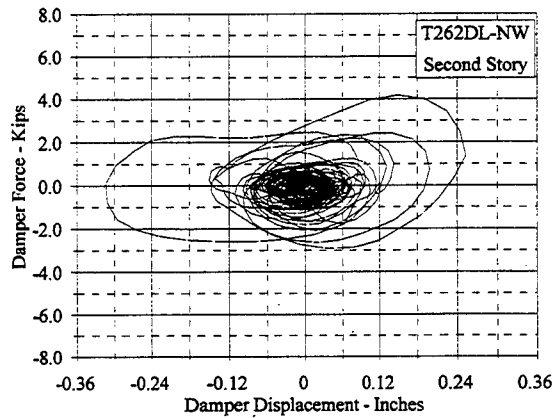
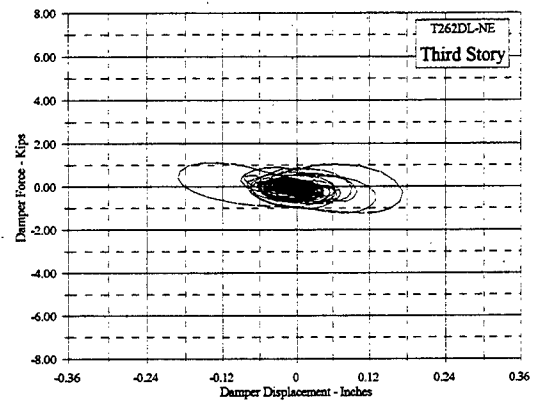
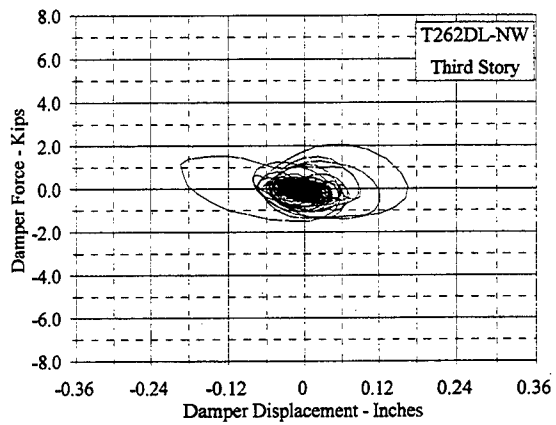


Figure C.10.29 Damper Force Vs. Displacement: T262DL, NW and NE

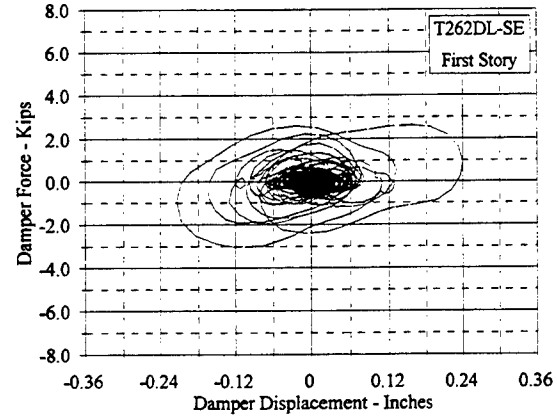
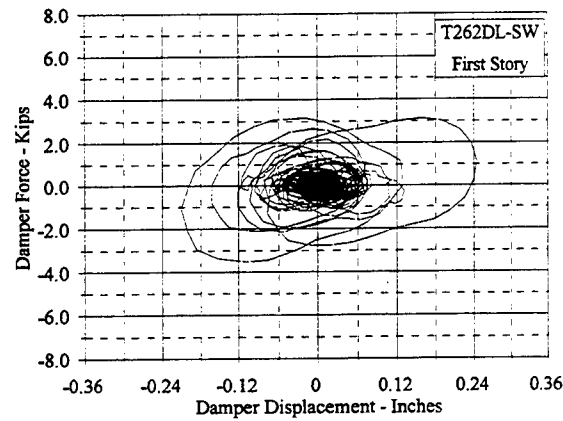
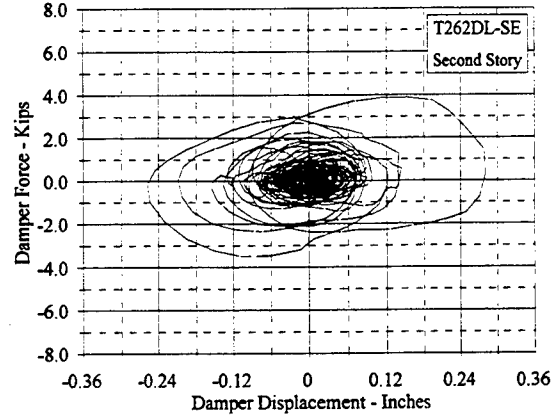
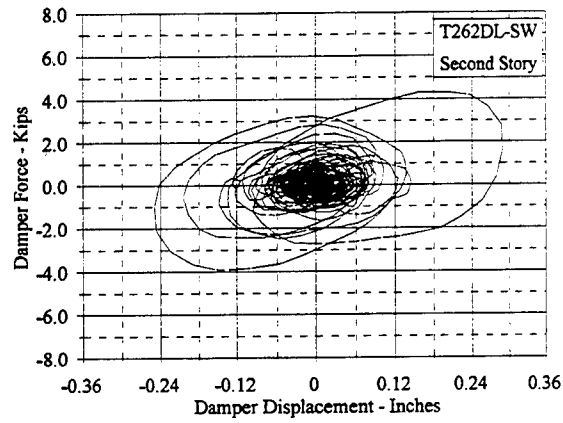
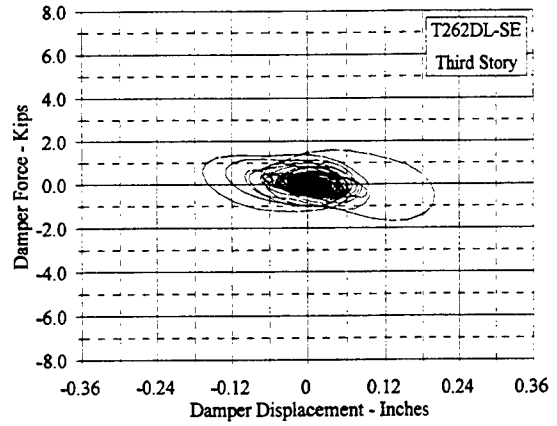
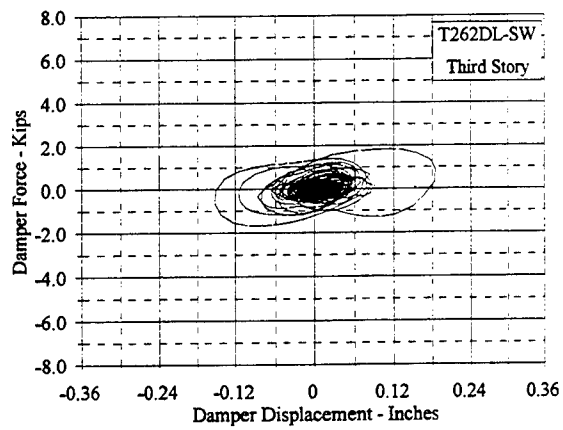


Figure C.10.30 Damper Force Vs. Displacement: T262DL, SW and SE

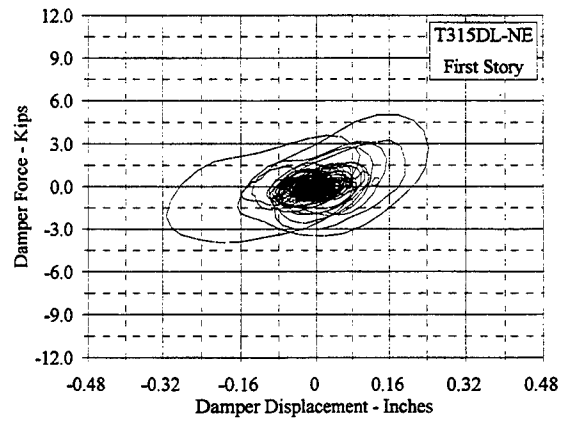
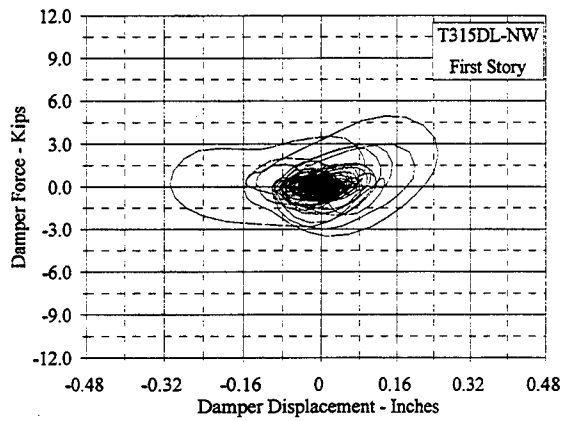
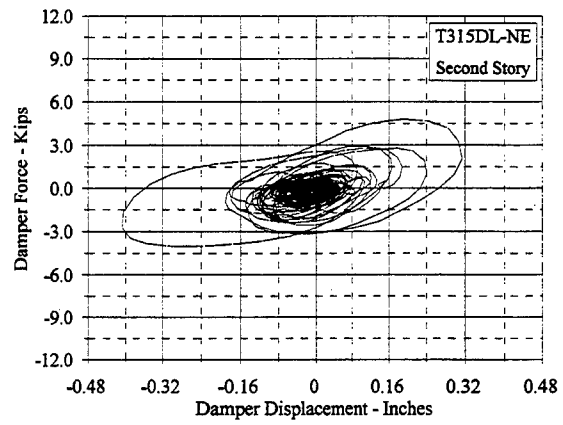
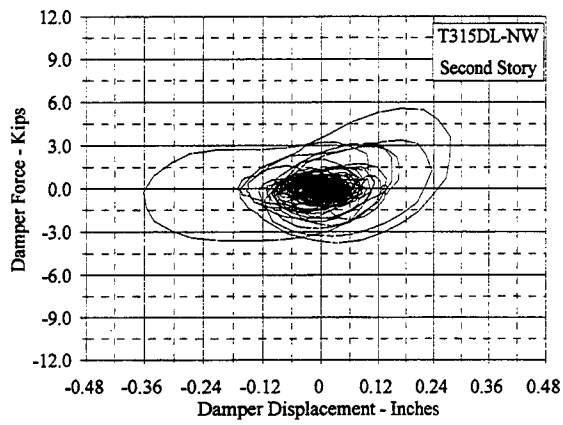
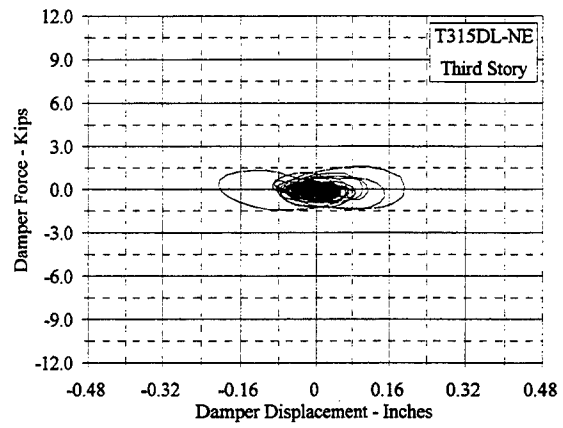
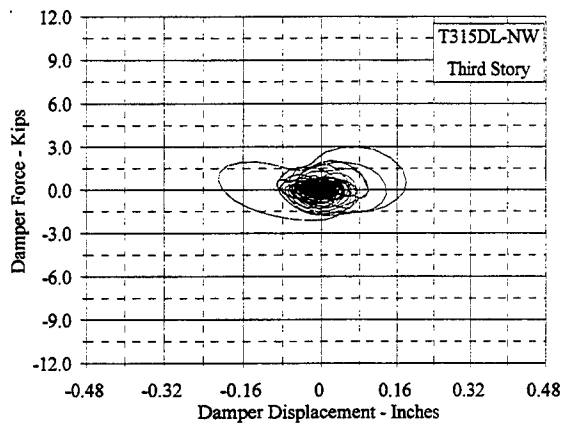


Figure C.10.31 Damper Force Vs. Displacement: T315DL, NW and NE

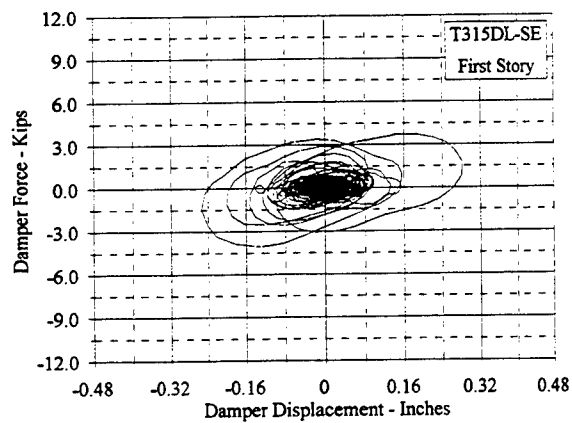
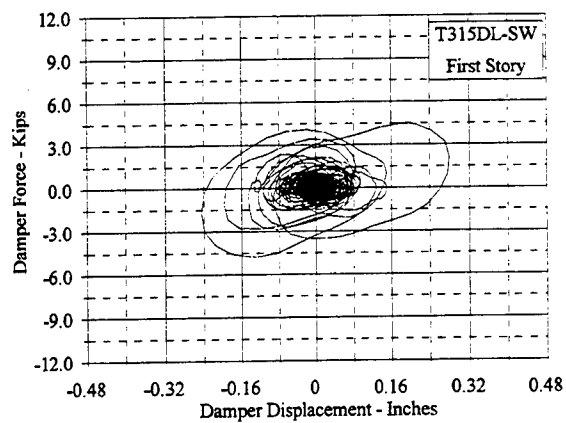
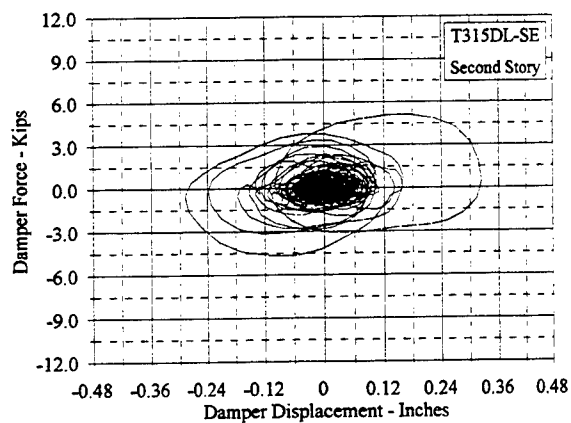
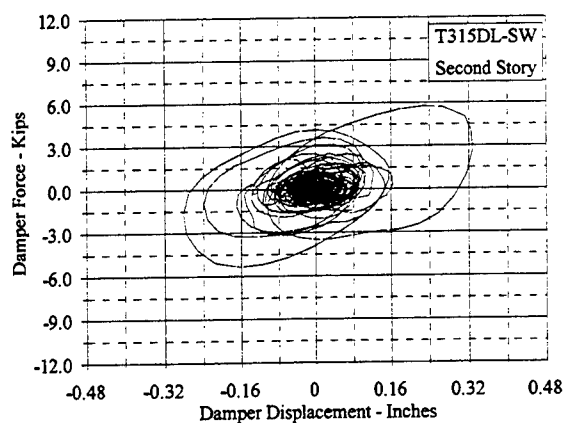
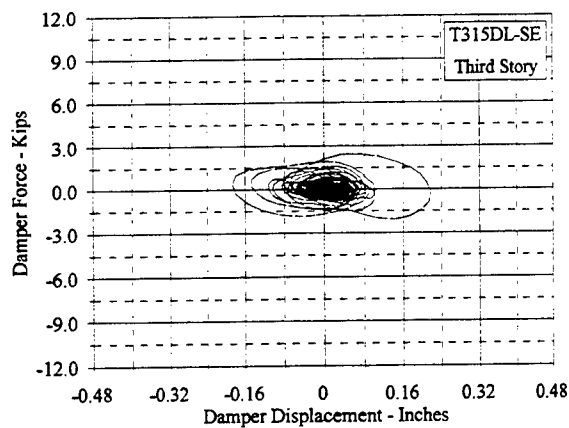
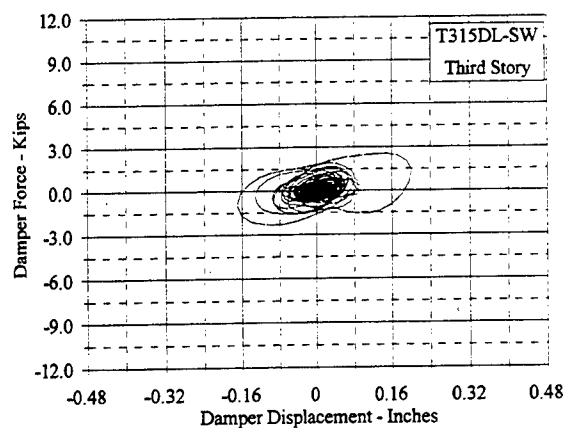


Figure C.10.32 Damper Force Vs. Displacement: T315DL, SW and SE

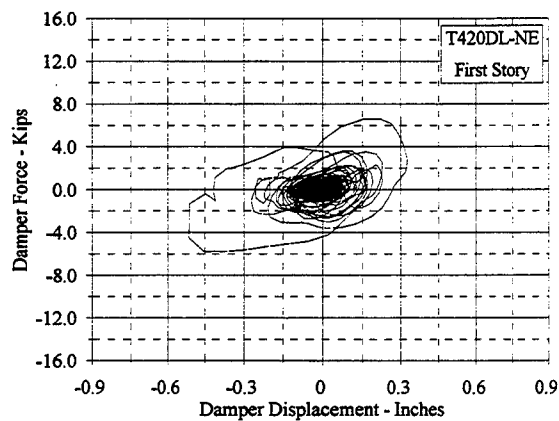
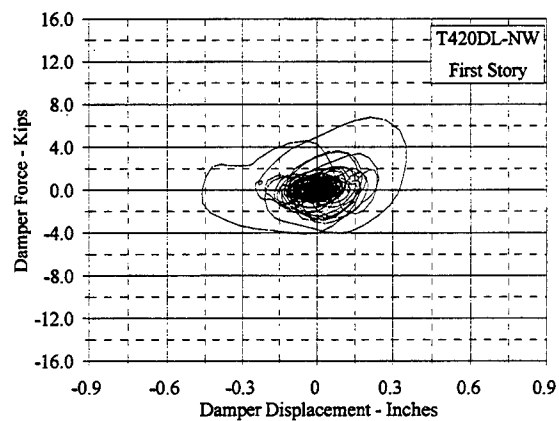
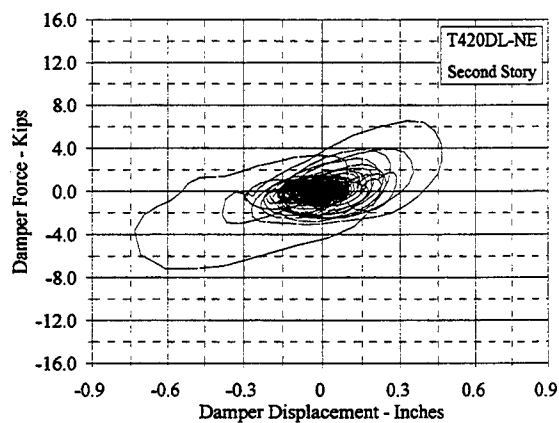
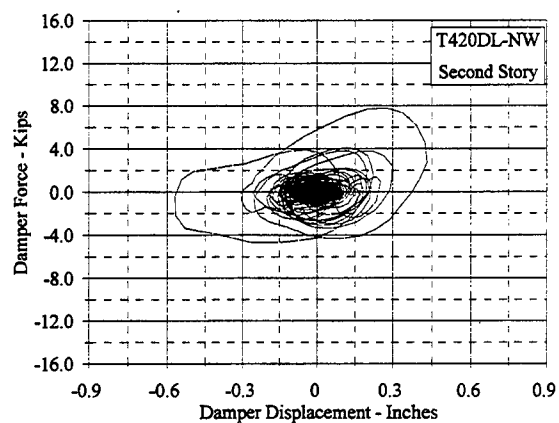
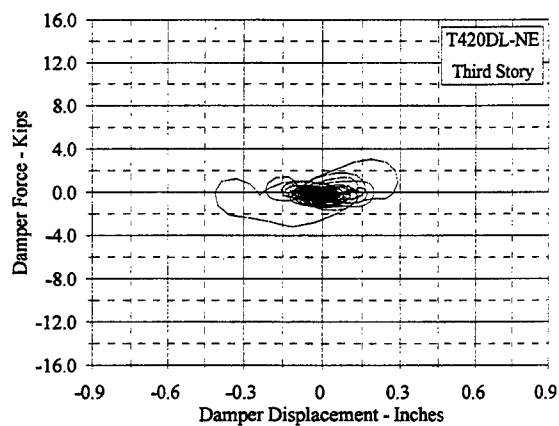
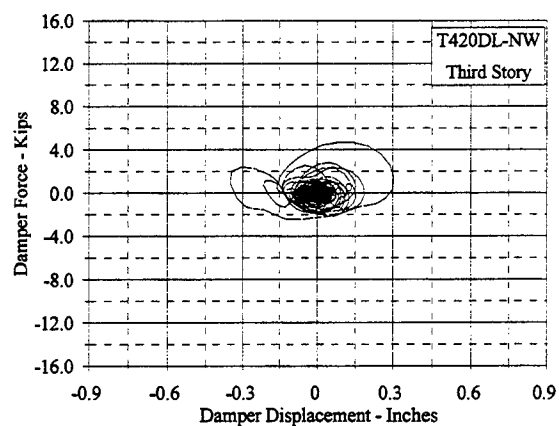


Figure C.10.33 Damper Force Vs. Displacement: T420DL, NW and NE

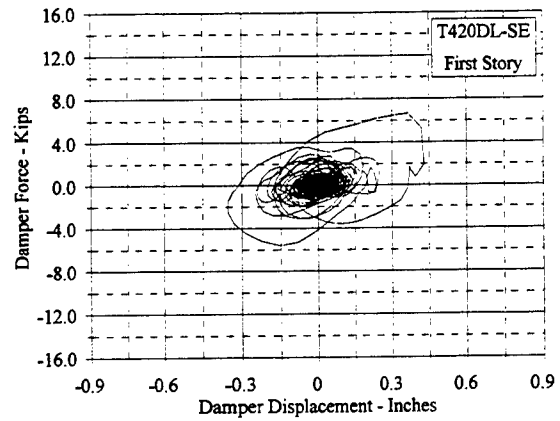
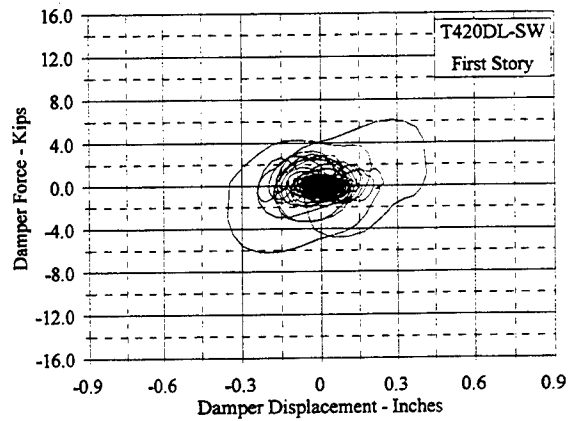
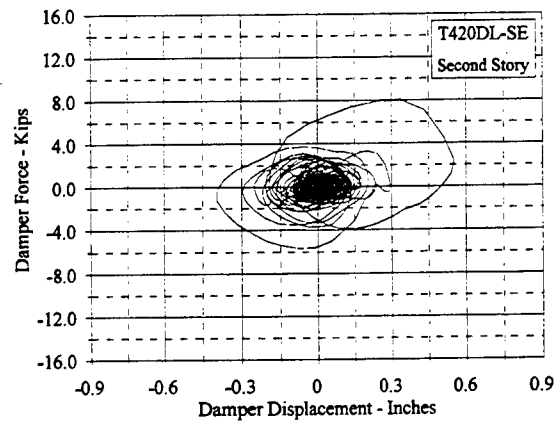
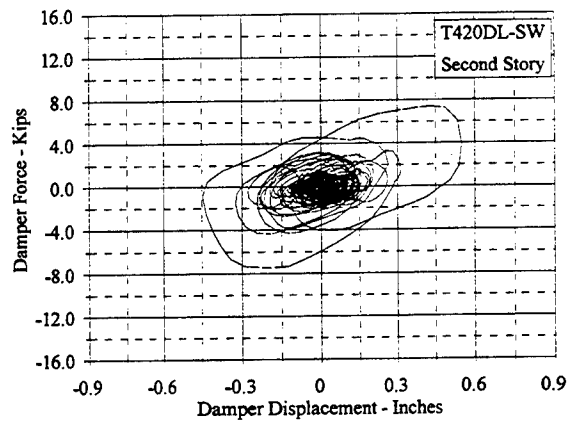
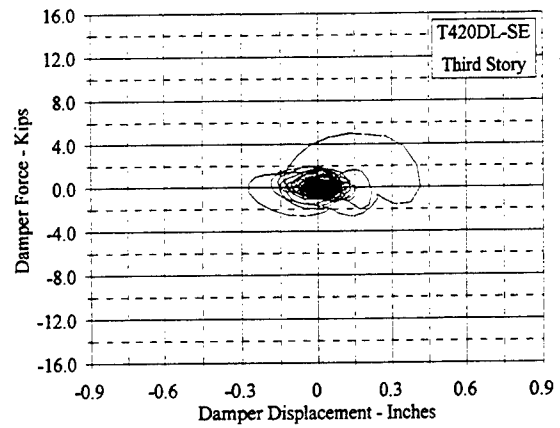
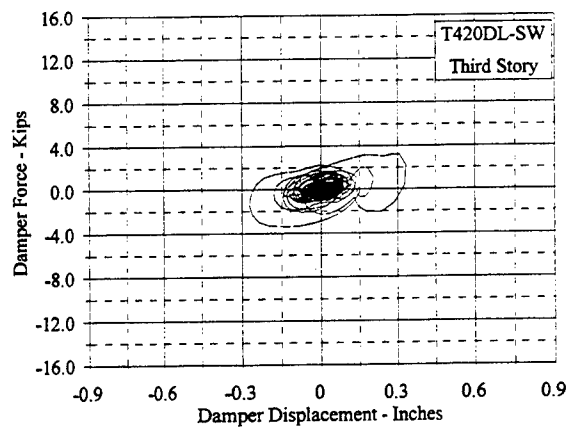


Figure C.10.34 Damper Force Vs. Displacement: T420DL, SW and SE

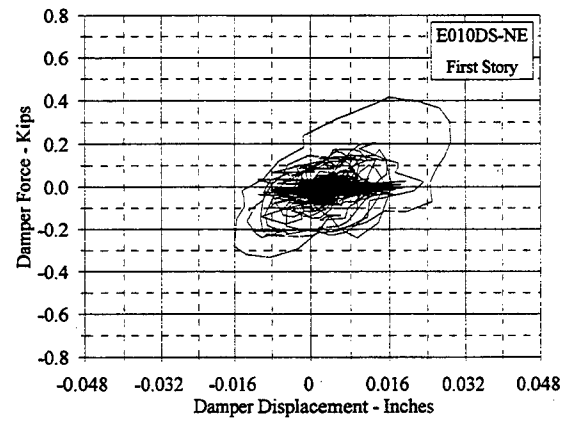
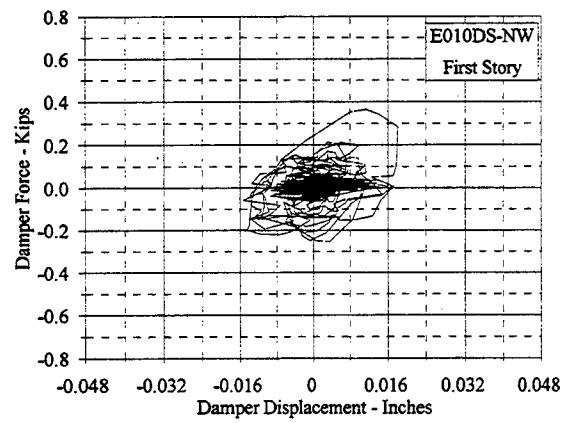
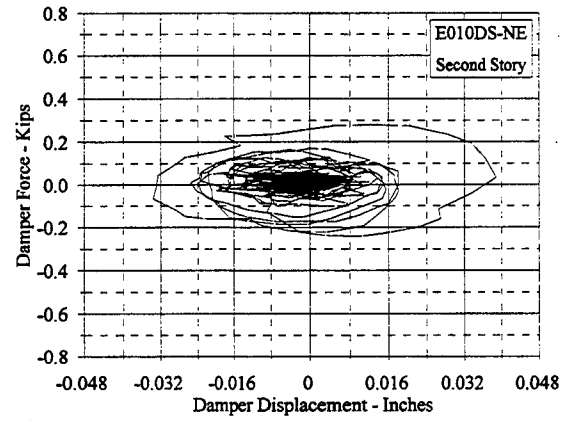
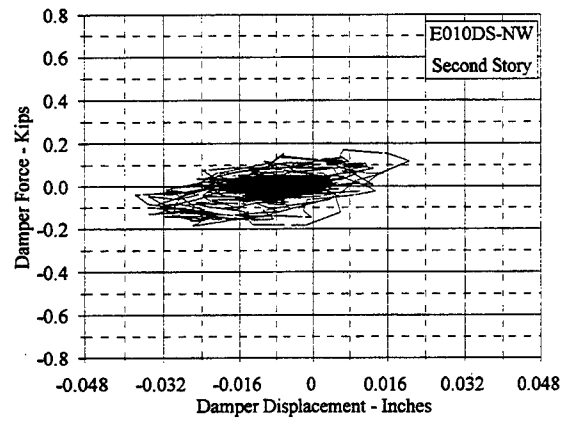
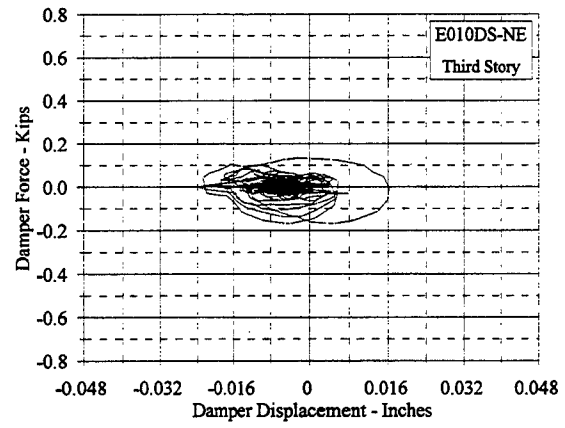
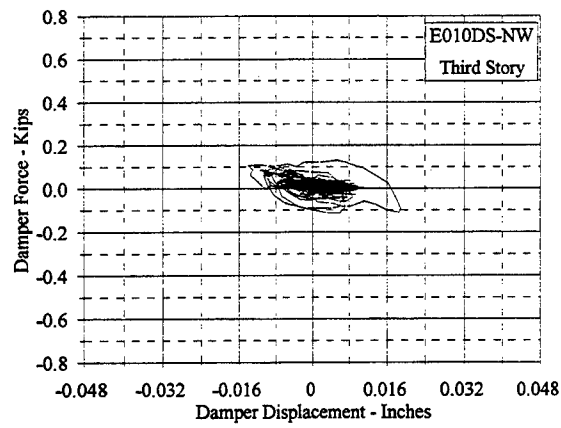


Figure C.10.35 Damper Force Vs. Displacement: E010DS, NW and NE

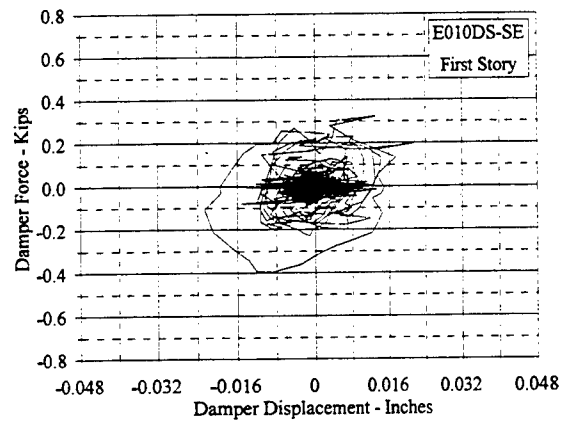
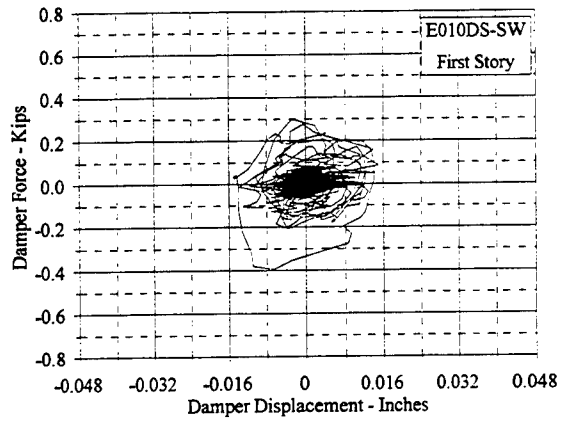
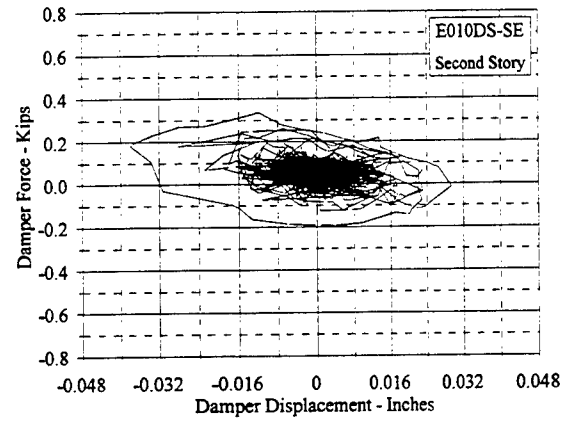
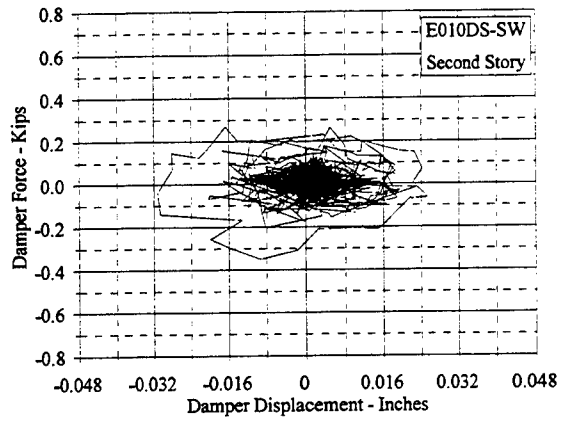
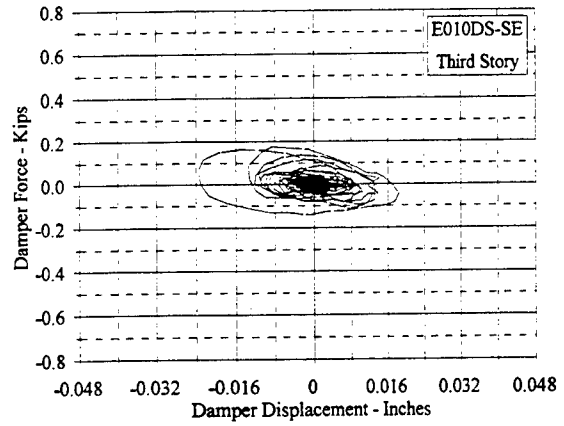
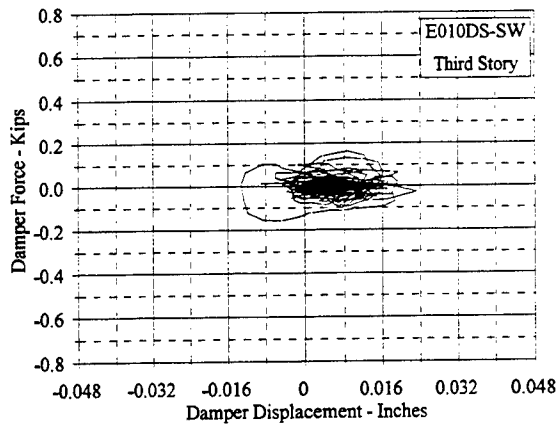


Figure C.10.36 Damper Force Vs. Displacement: E010DS, SW and SE

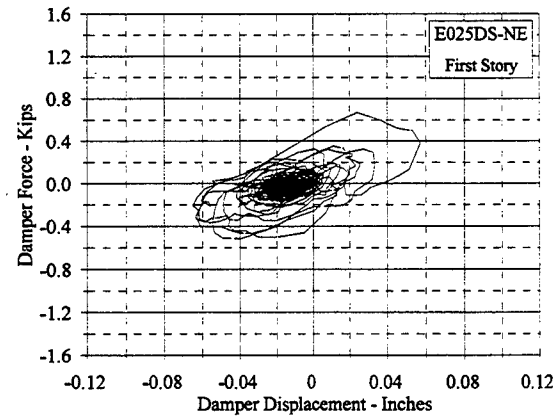
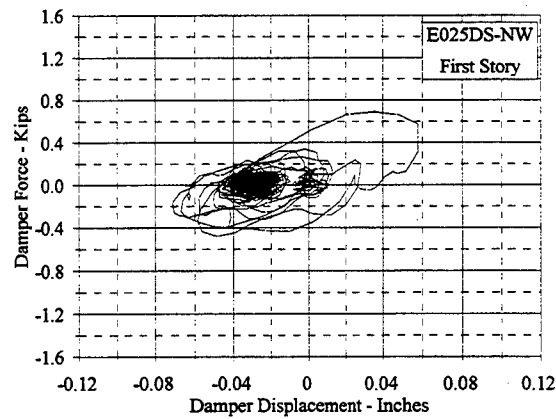
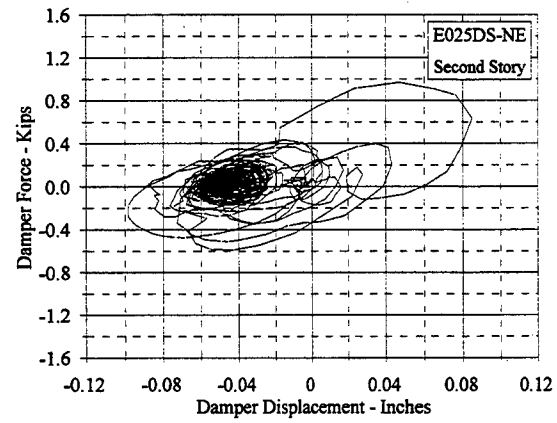
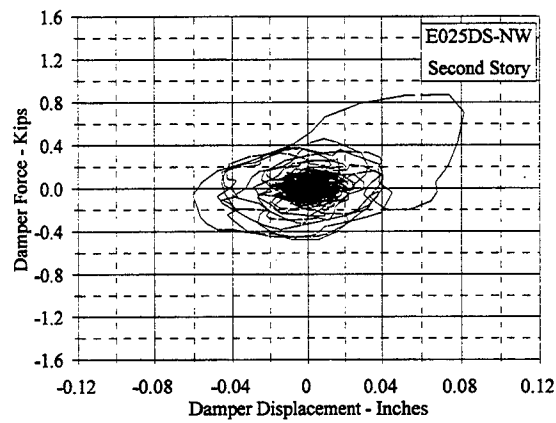
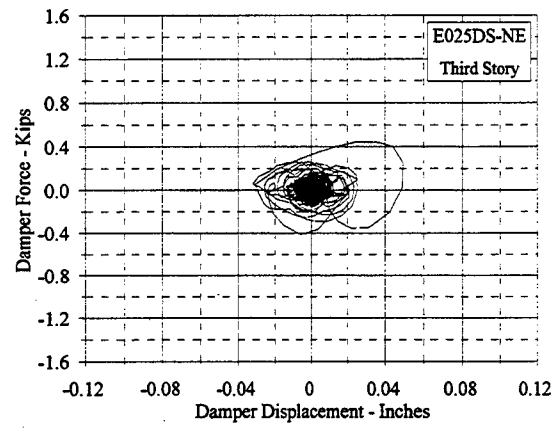
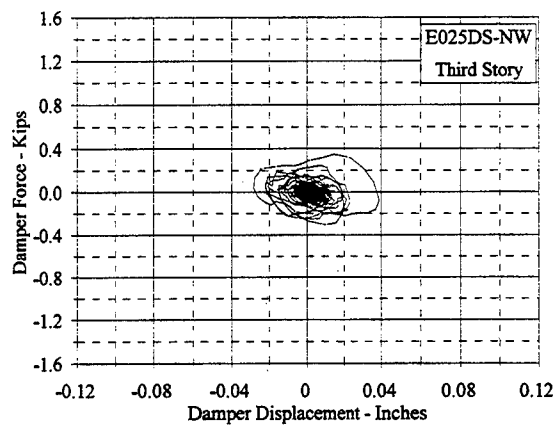


Figure C.10.37 Damper Force Vs. Displacement: E025DS, NW and NE

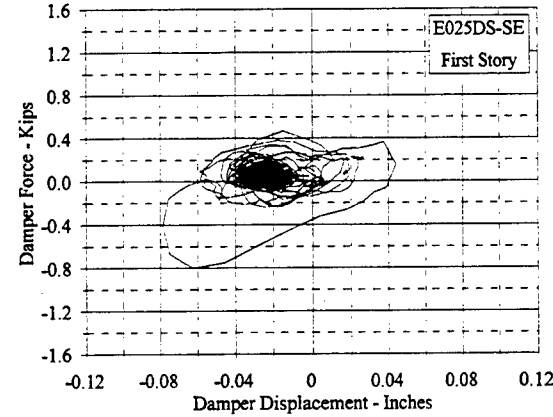
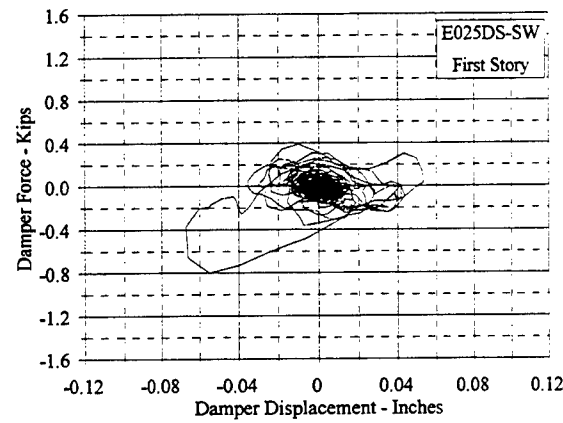
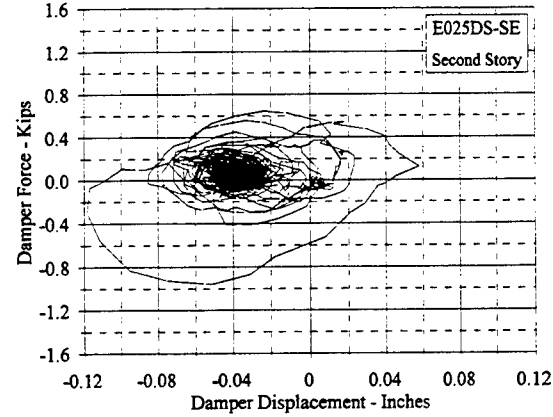
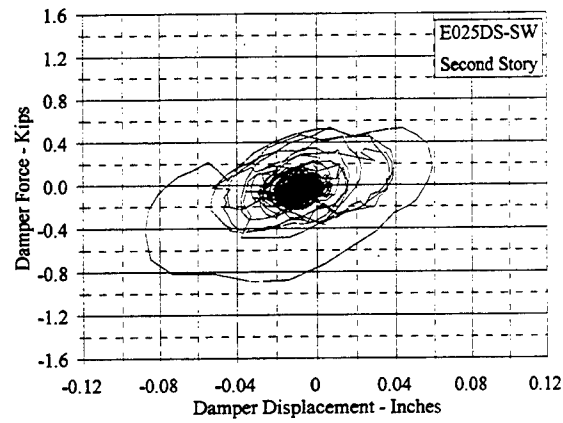
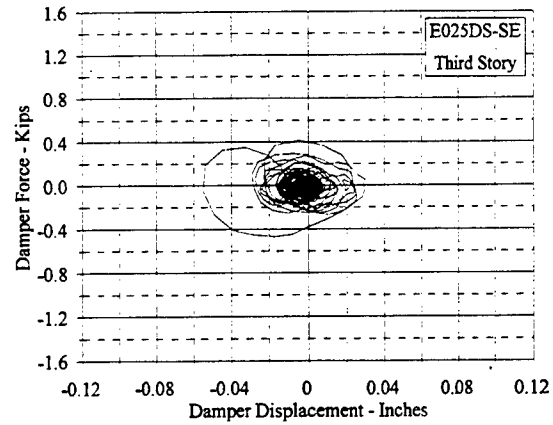
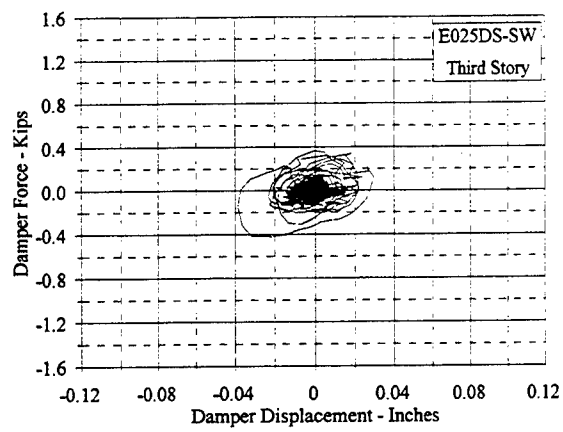


Figure C.10.38 Damper Force Vs. Displacement: E025DS, SW and SE

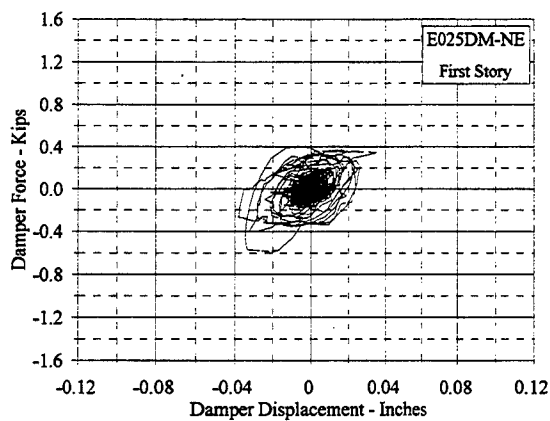
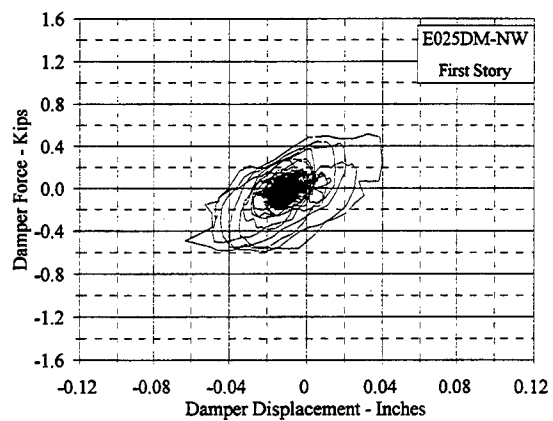
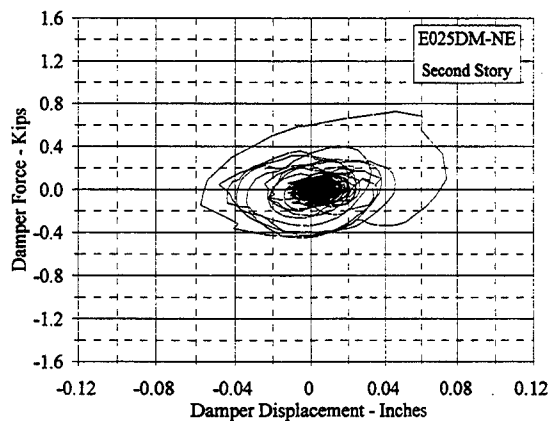
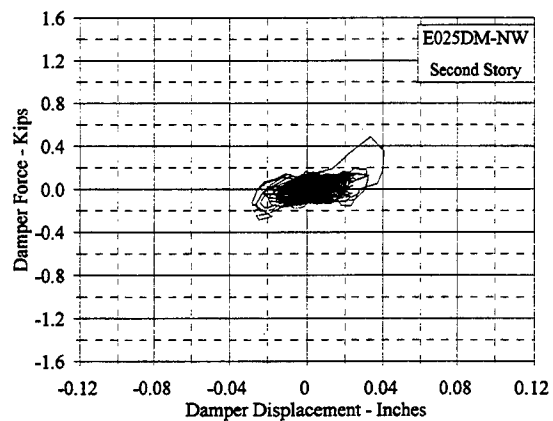
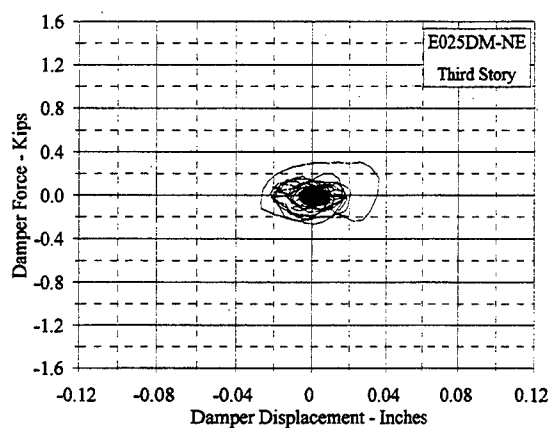
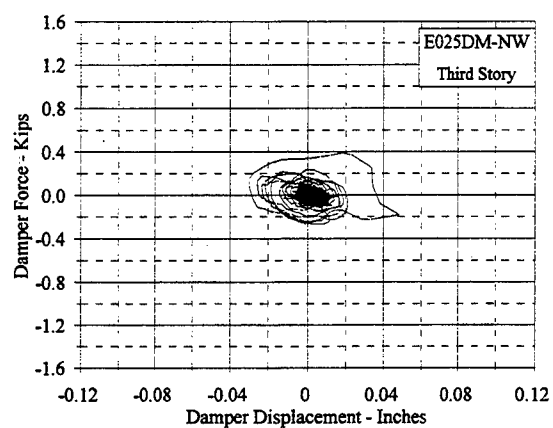


Figure C.10.39 Damper Force Vs. Displacement: E025DM, NW and NE

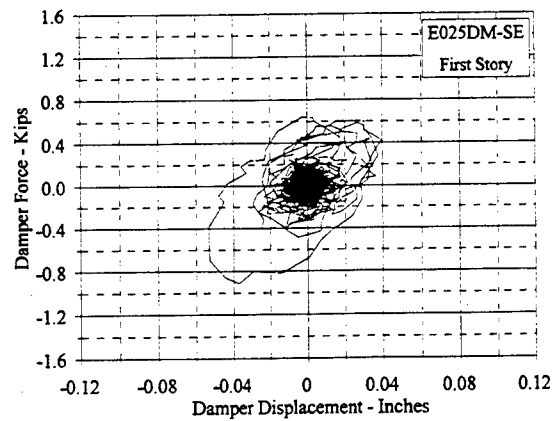
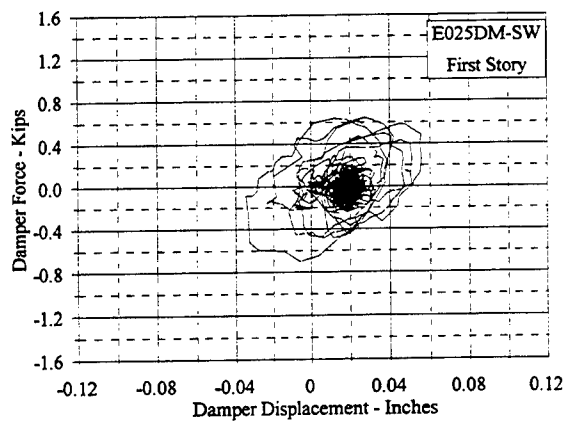
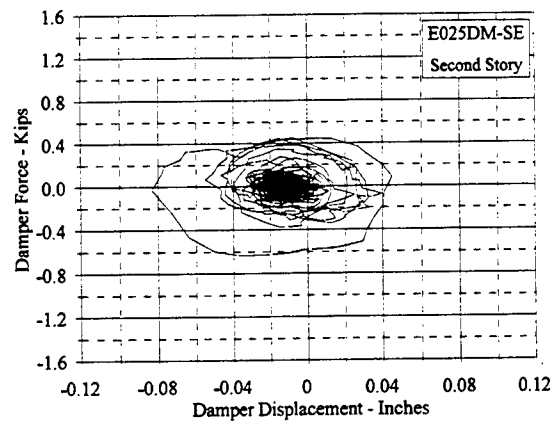
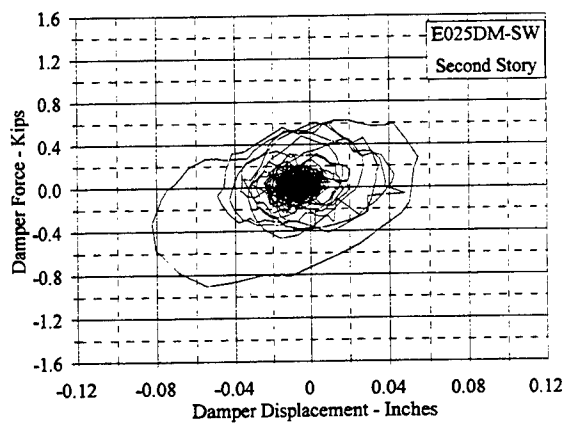
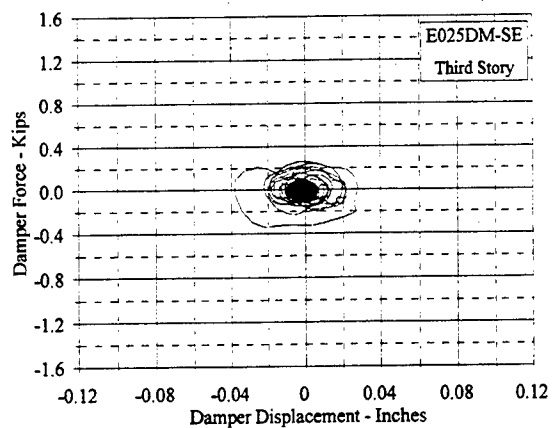
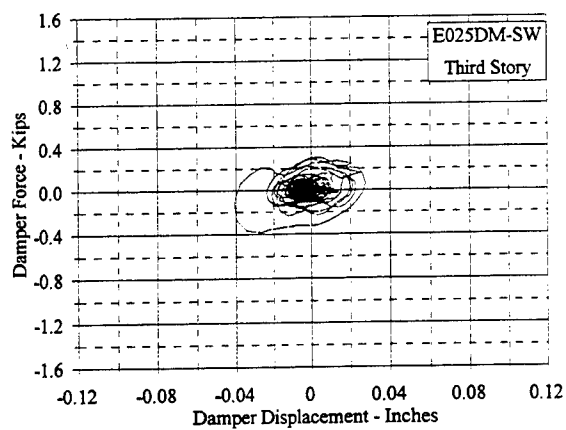


Figure C.10.40 Damper Force Vs. Displacement: E025DM, SW and SE

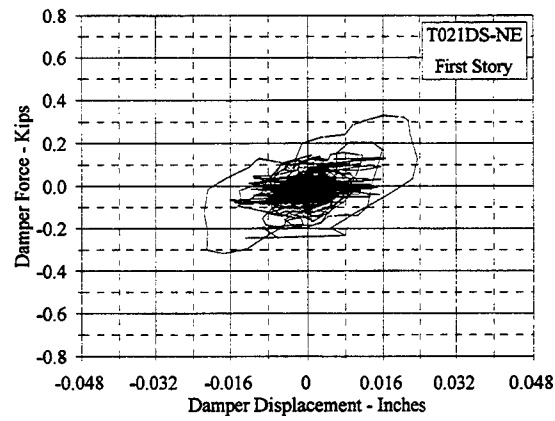
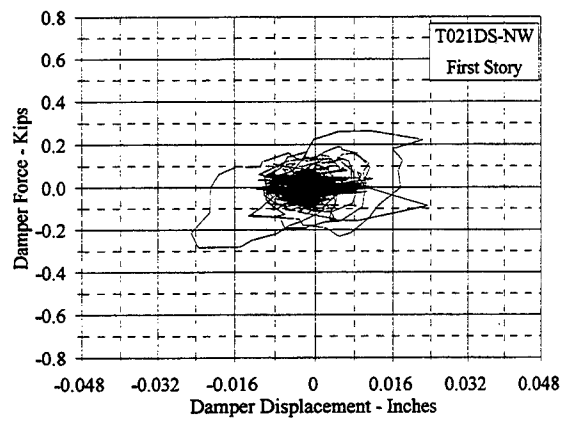
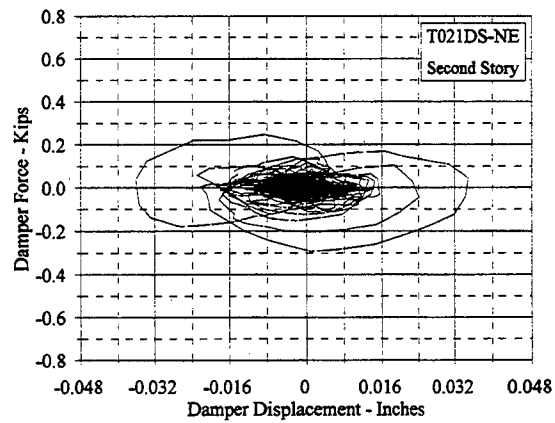
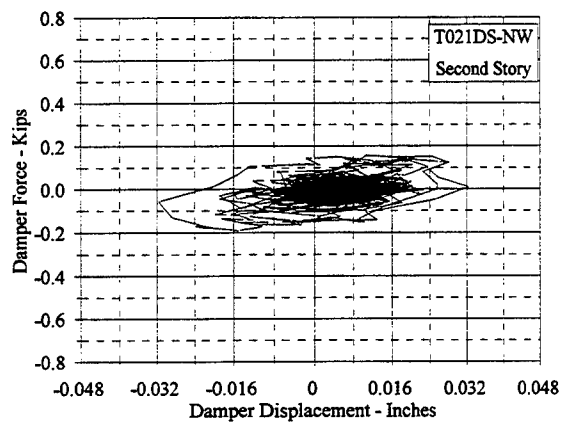
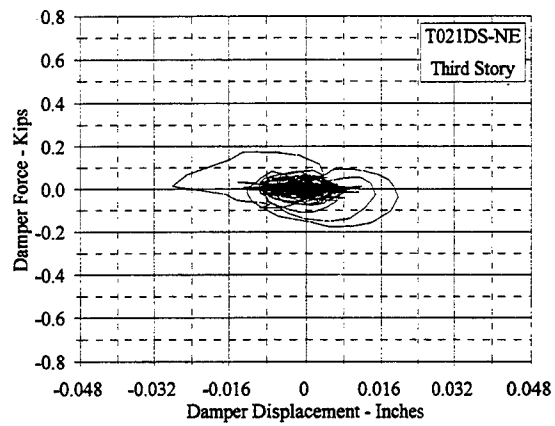
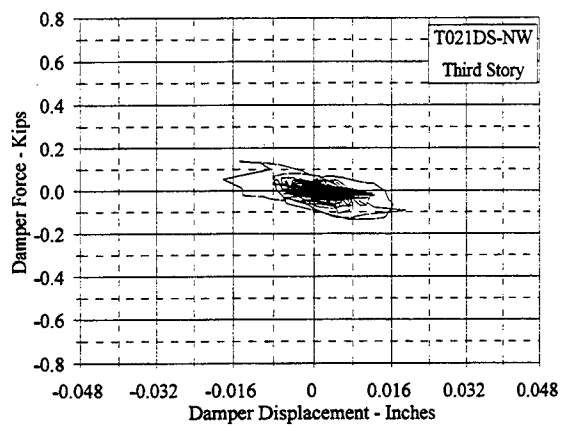


Figure C.10.41 Damper Force Vs. Displacement: T021DS, NW and NE

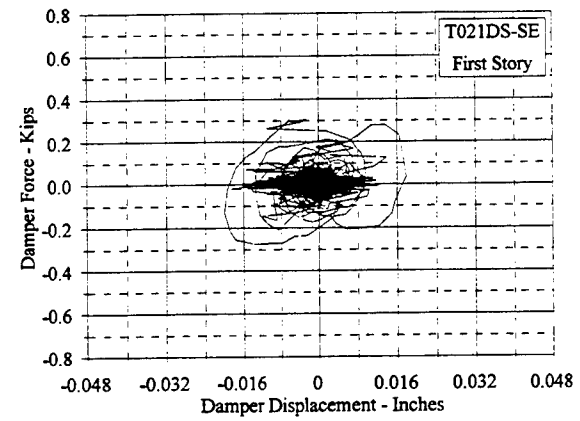
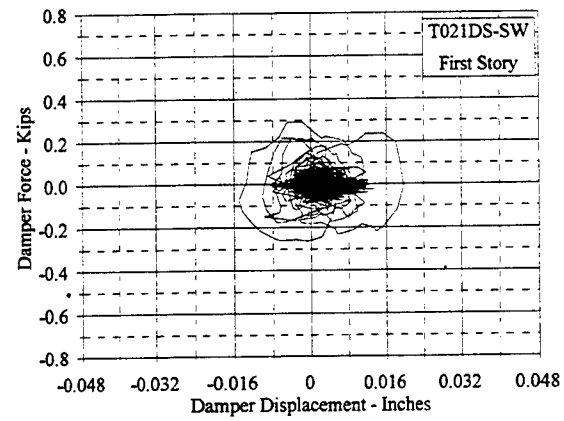
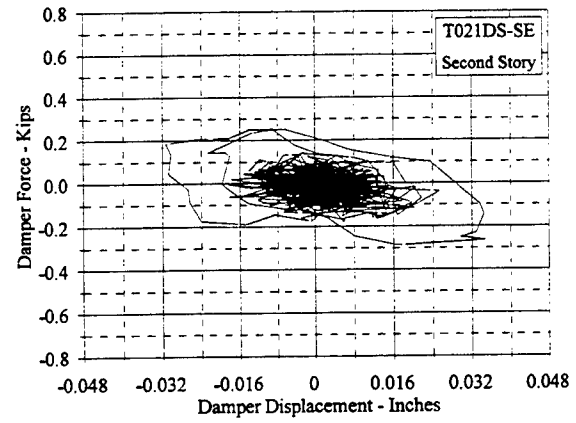
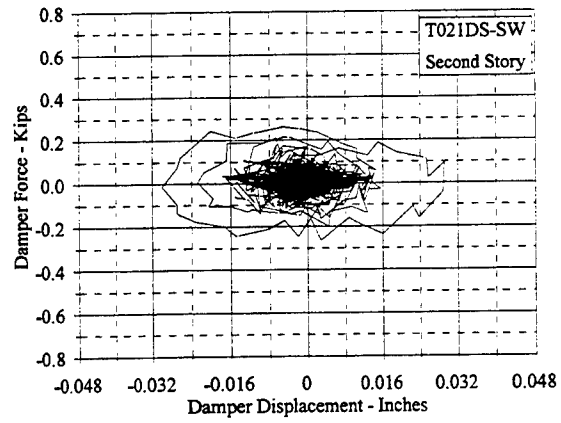
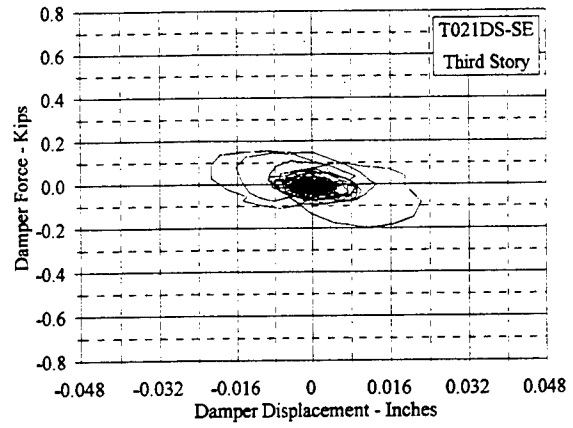
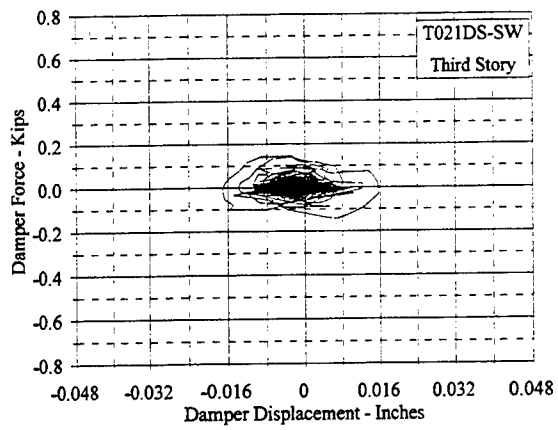


Figure C.10.42 Damper Force Vs. Displacement: T021DS, SW and SE

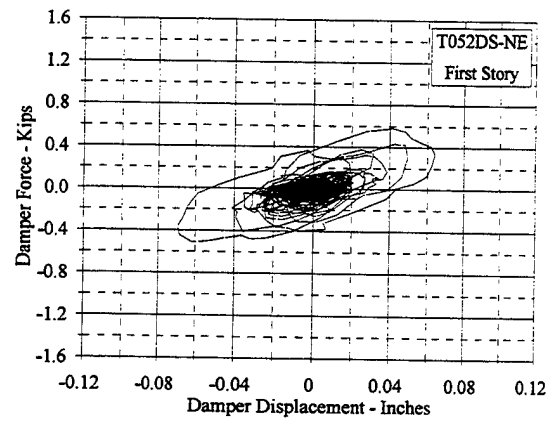
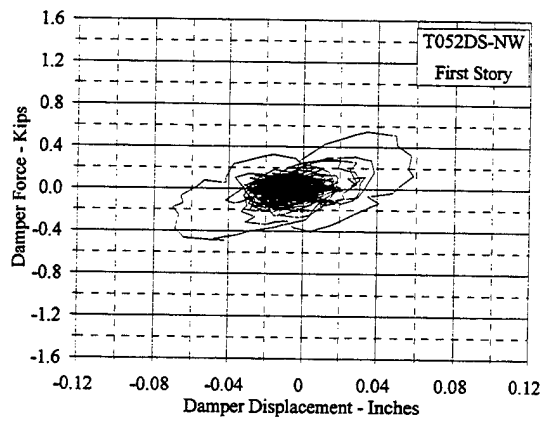
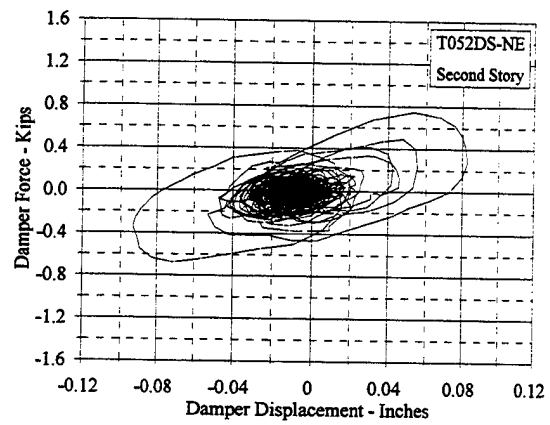
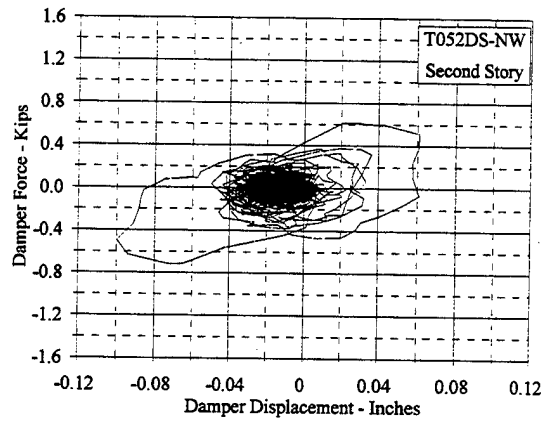
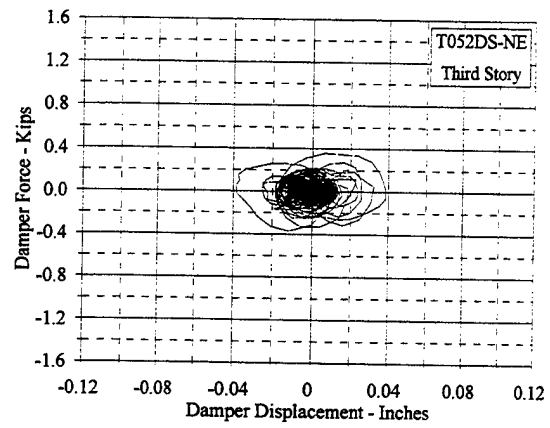
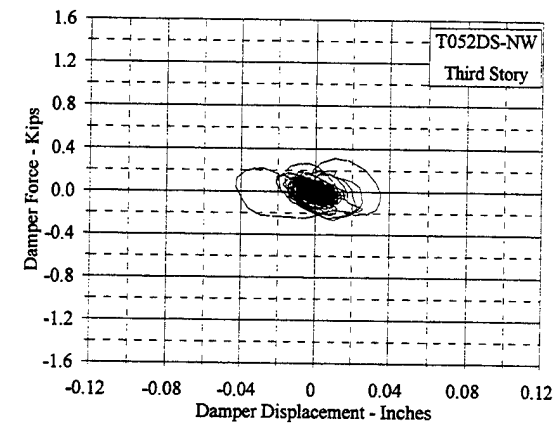


Figure C.10.43 Damper Force Vs. Displacement: T052DS, NW and NE

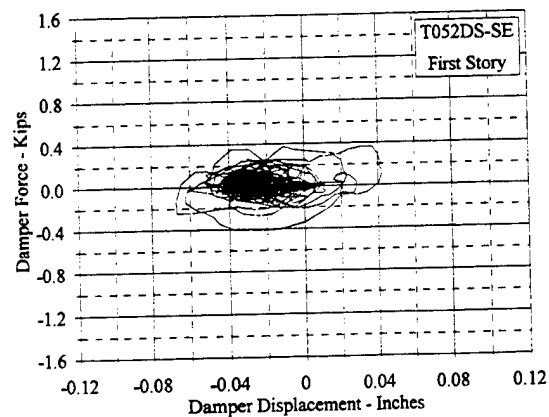
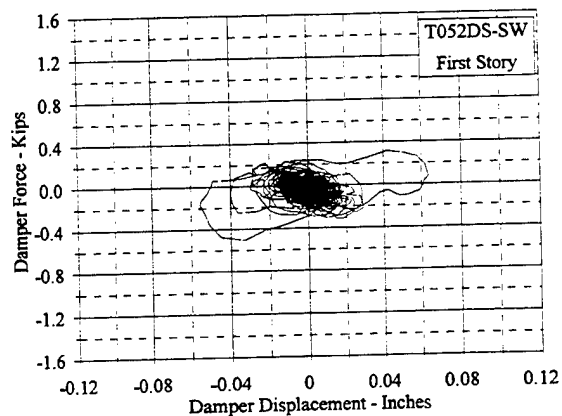
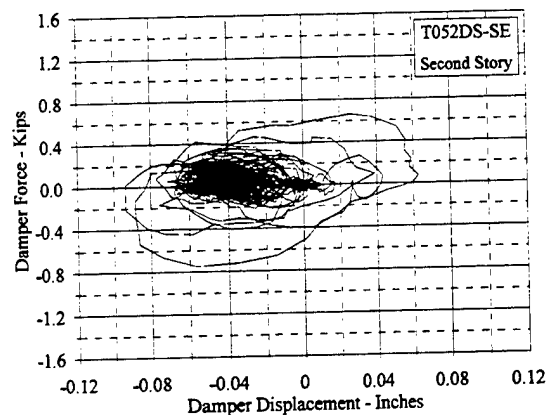
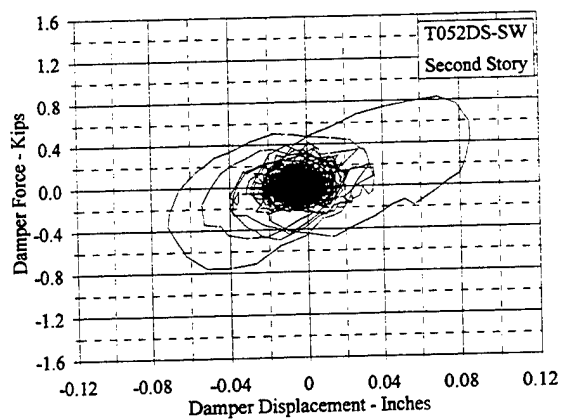
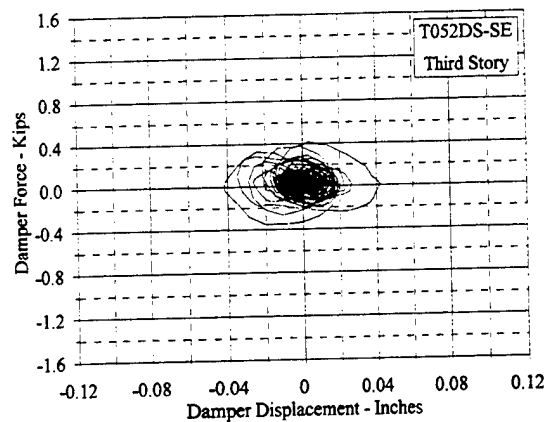
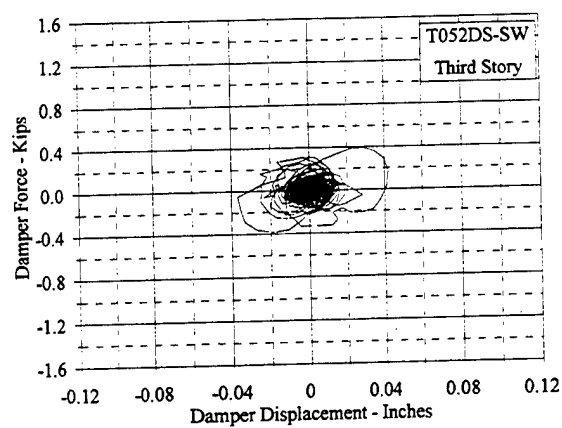


Figure C.10.44 Damper Force Vs. Displacement: T052DS, SW and SE

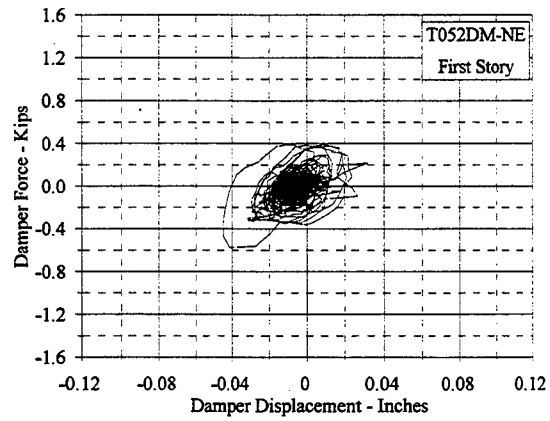
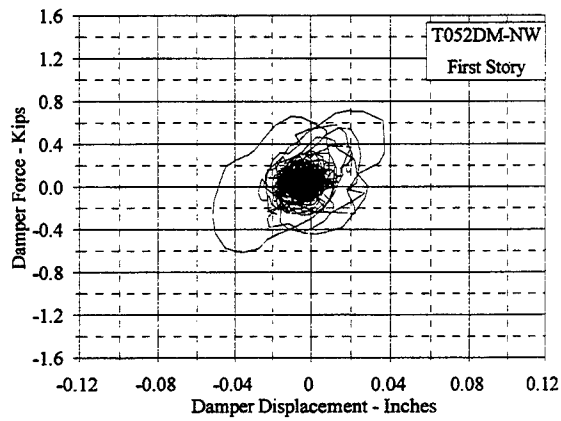
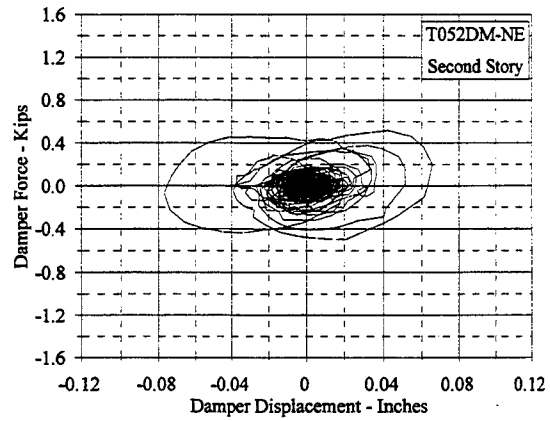
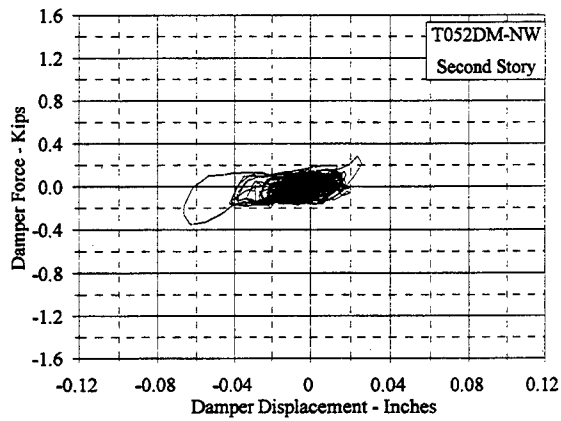
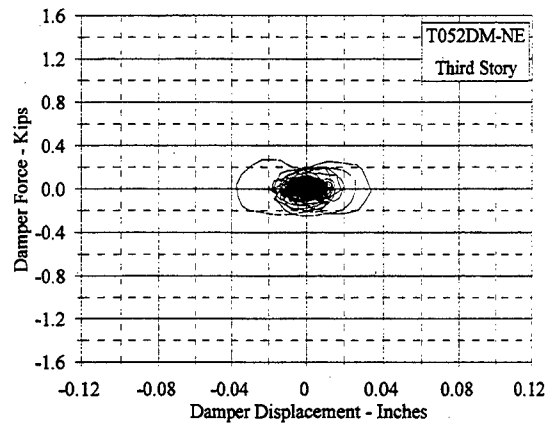
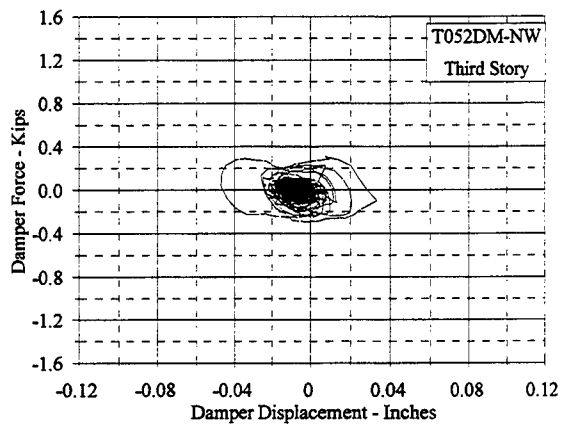


Figure C.10.45 Damper Force Vs. Displacement: T052DM, NW and NE

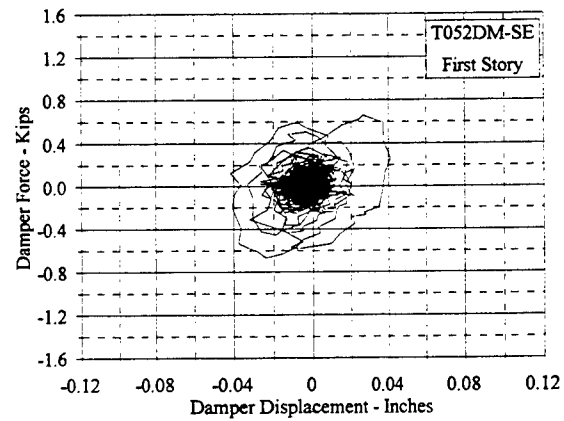
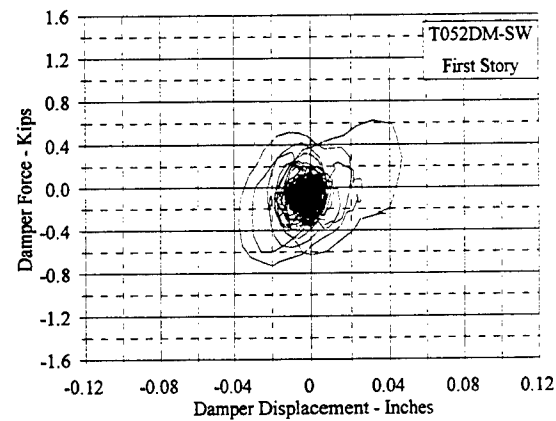
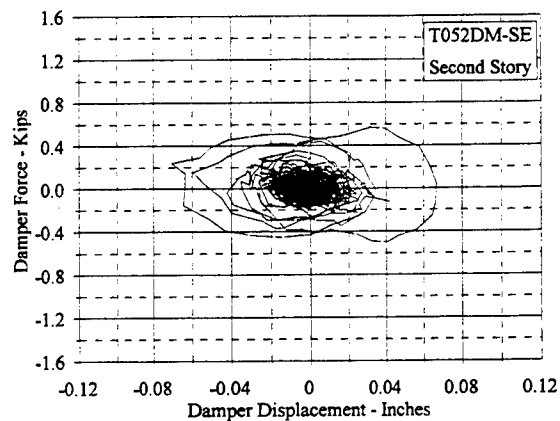
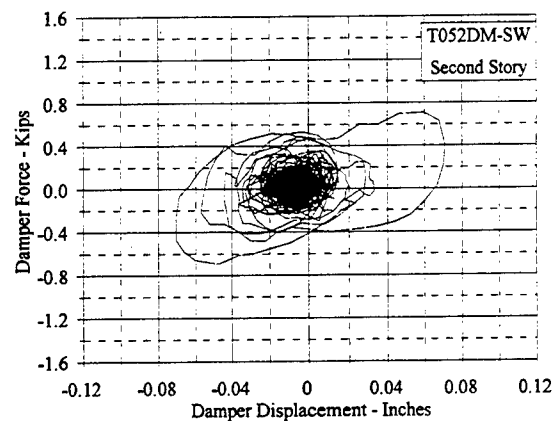
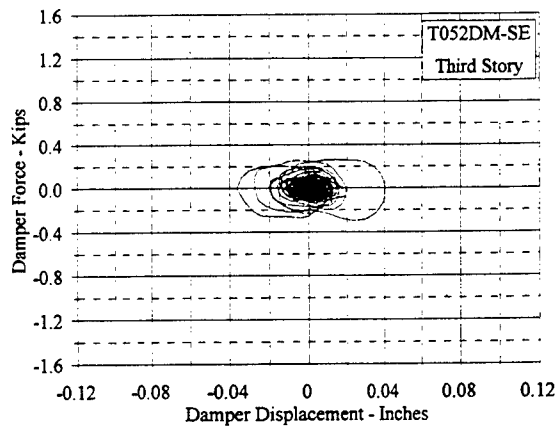
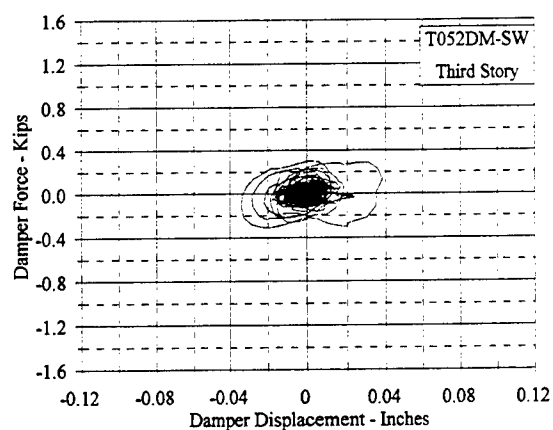
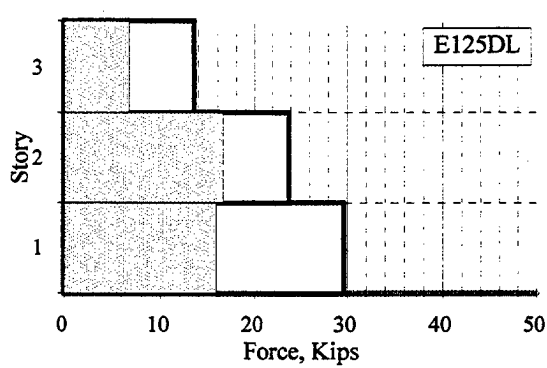
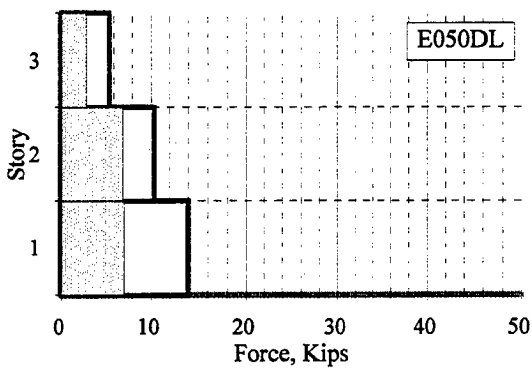
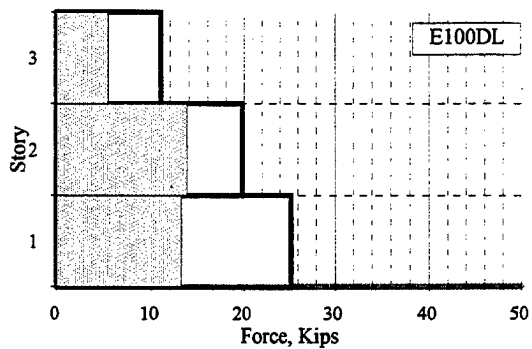
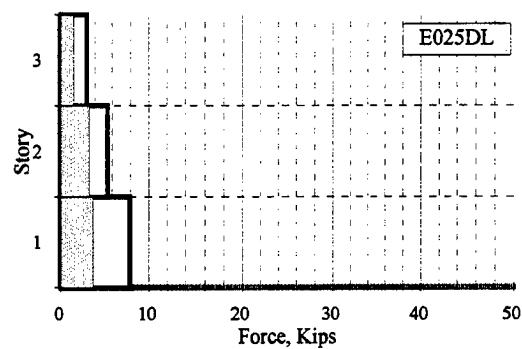
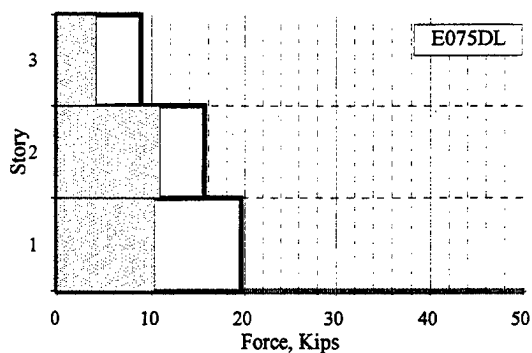
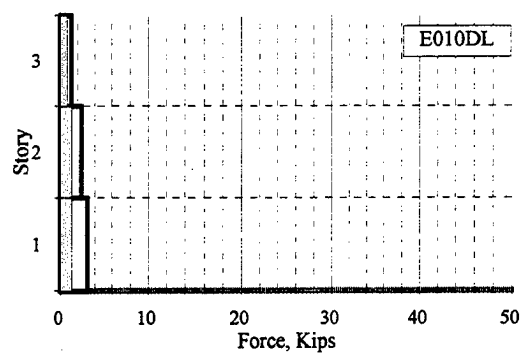


Figure C.10.46 Damper Force Vs. Displacement: T052DM, SW and SE



□ Story Shear ■ Damper Force Sum

□ Story Shear ■ Damper Force Sum

Figure C.11.1 Maximum Sum of Horizontal Components of Damper Forces Vs. Maximum Story Shear: E010DL - E125DL

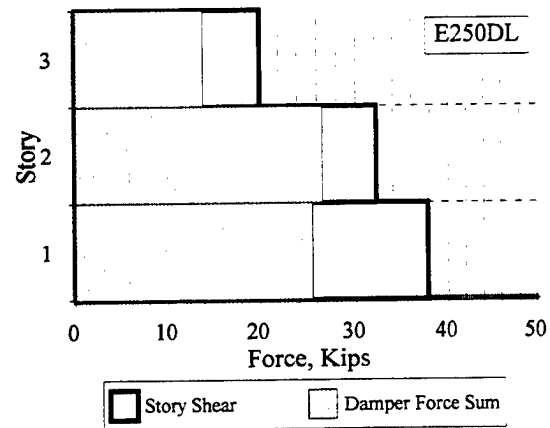
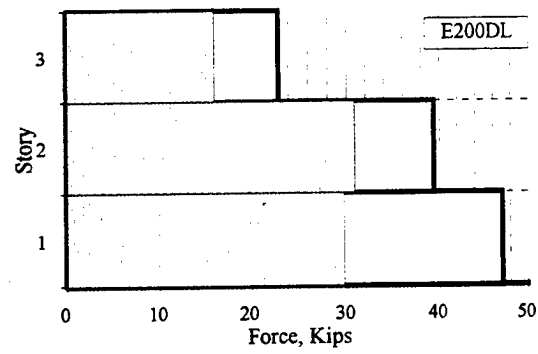
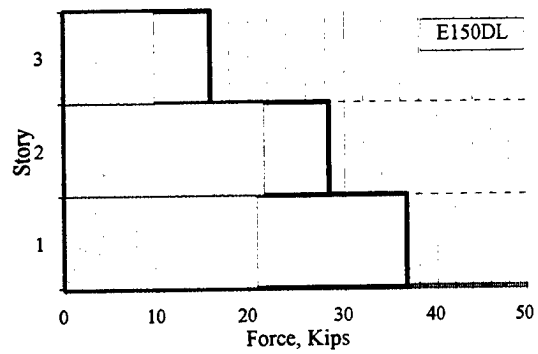


Figure C.11.2 Maximum Sum of Horizontal Components of Damper Forces Vs. Maximum Story Shear: E150DL - E250DL

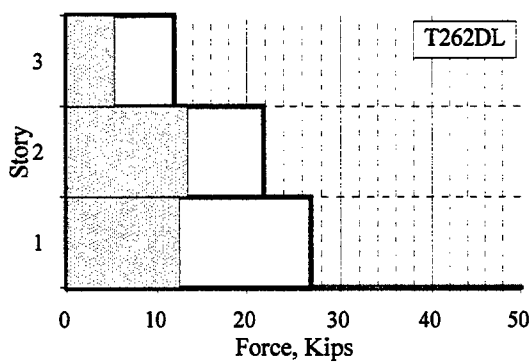
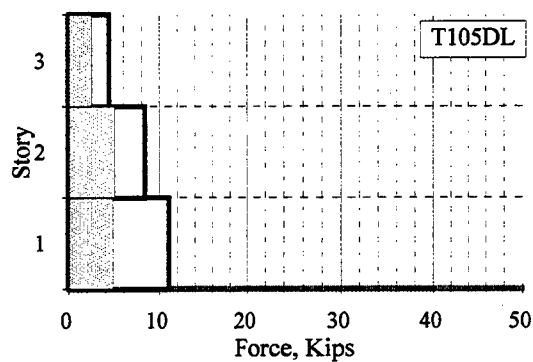
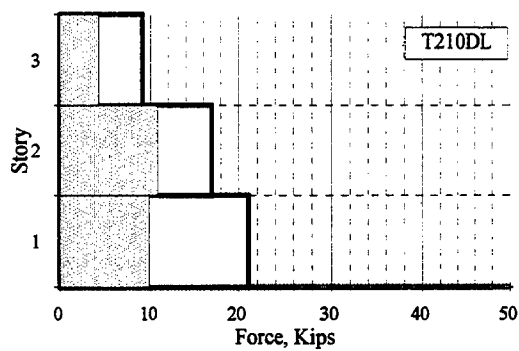
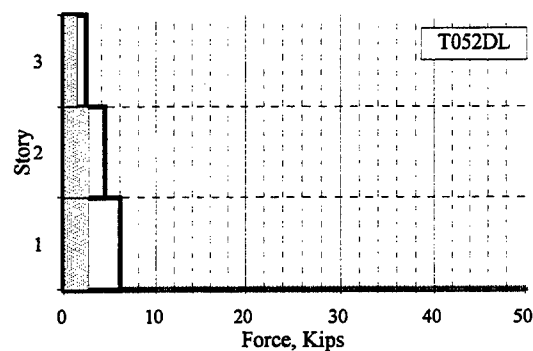
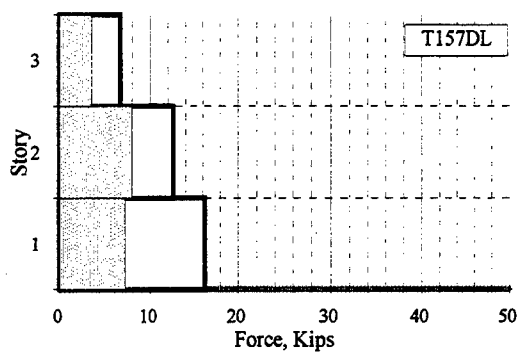
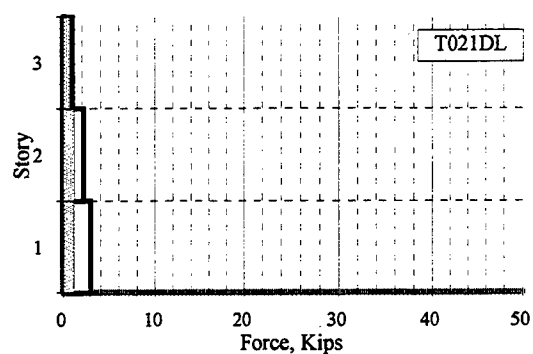


Figure C.11.3 Maximum Sum of Horizontal Components of Damper Forces Vs. Maximum Story Shear: T021DL - T262DL

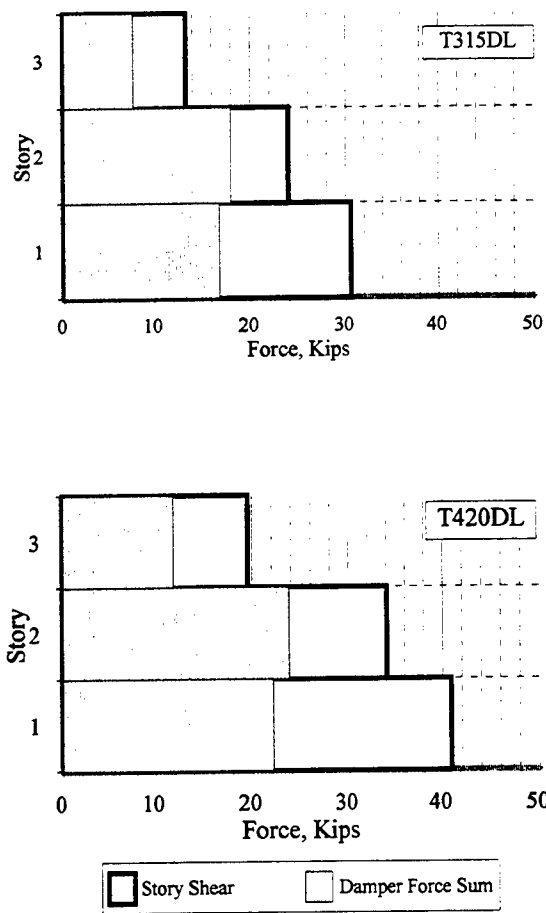
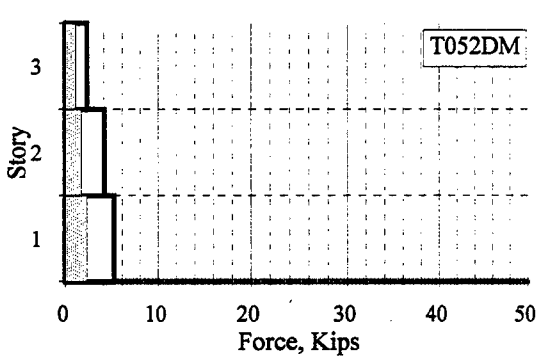
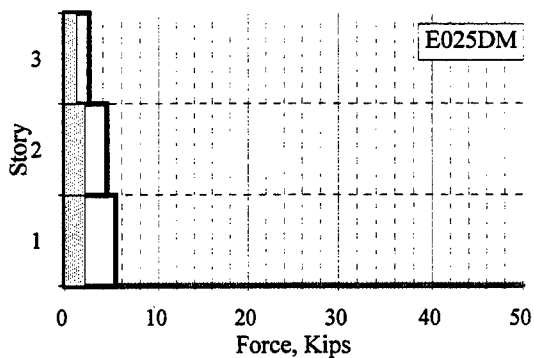
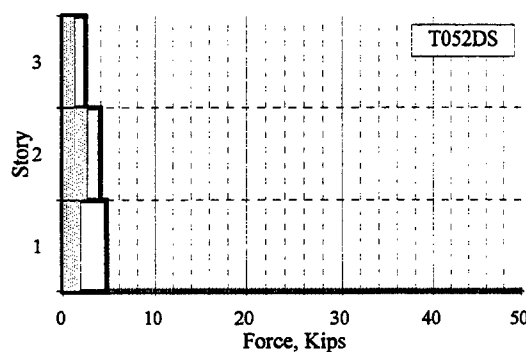
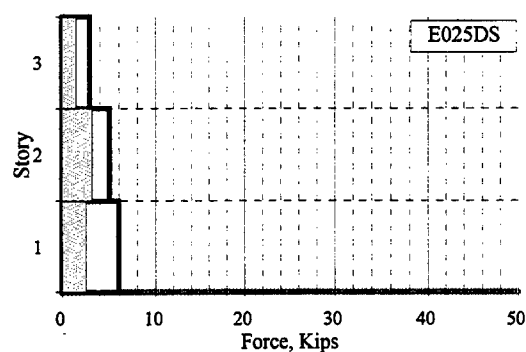
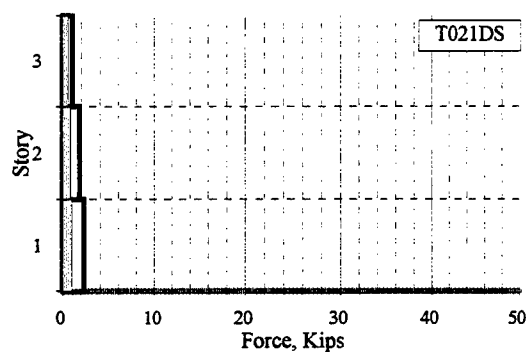
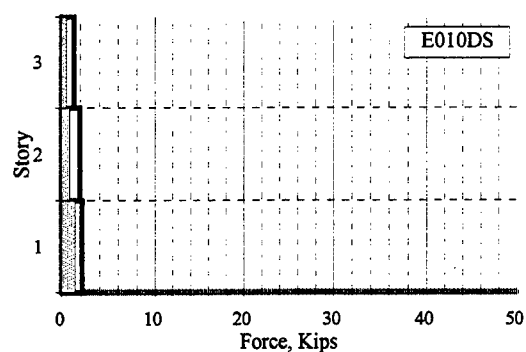


Figure C.11.4 Maximum Sum of Horizontal Components of Damper Forces Vs. Maximum Story Shear: T315DL - T420DL



☐ Story Shear
 ☐ Damper Force Sum

☐ Story Shear
 ☐ Damper Force Sum

Figure C.11.5 Maximum Sum of Horizontal Components of Damper Forces Vs. Maximum Story Shear: E010DS - T052DM

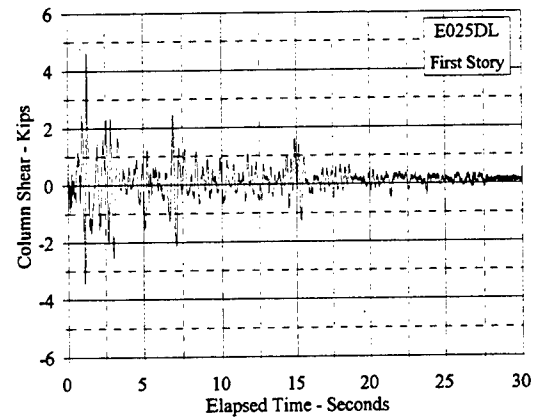
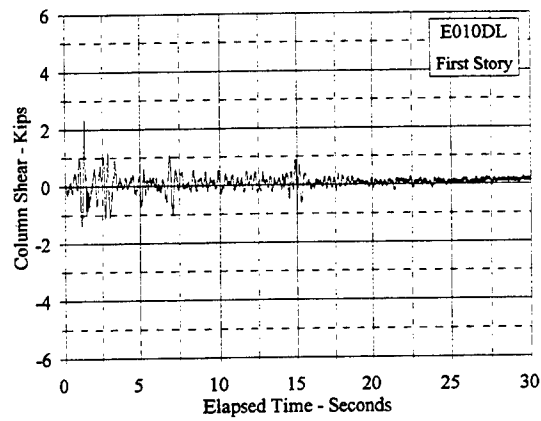
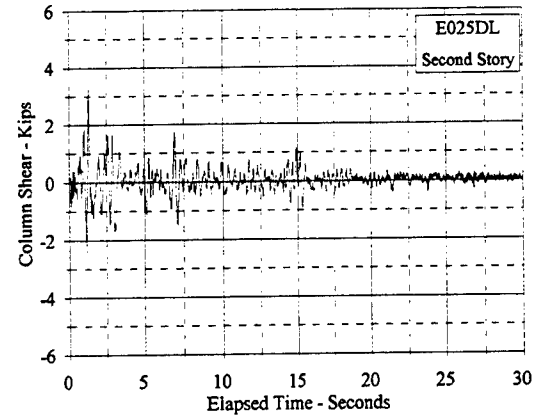
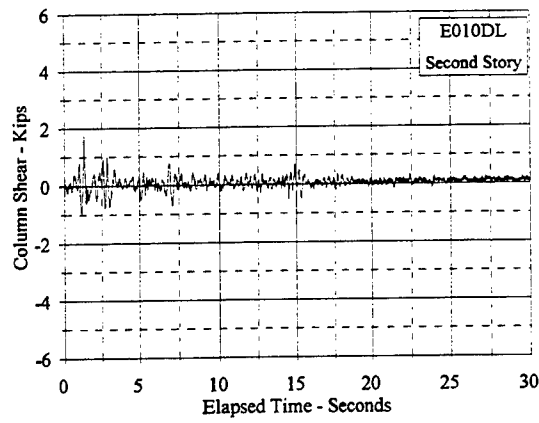
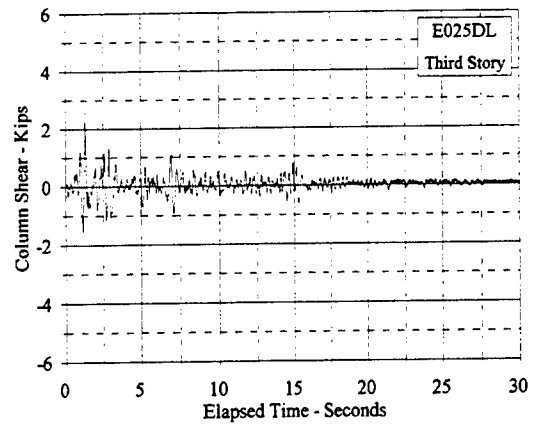
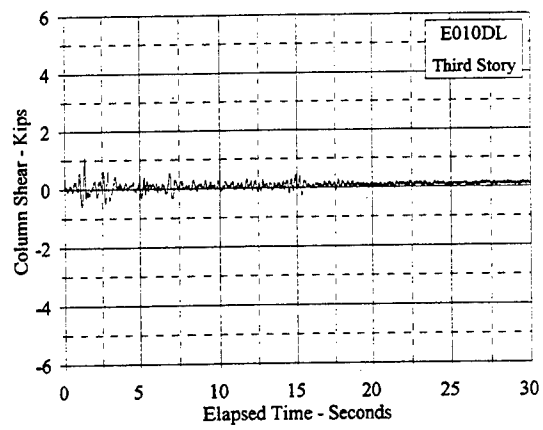


Figure C.12.1 Column Shear Vs. Elapsed Time: E010DL, E025DL

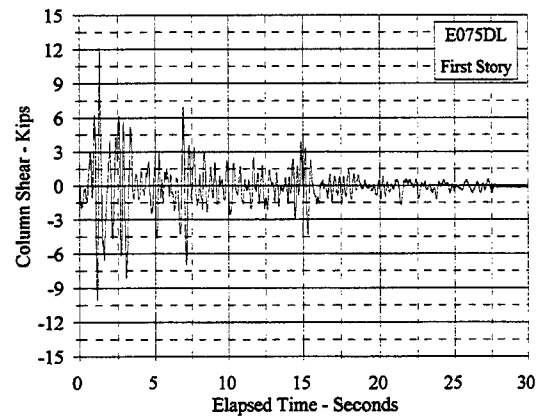
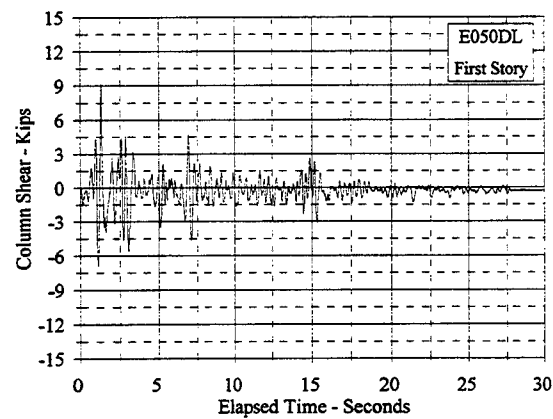
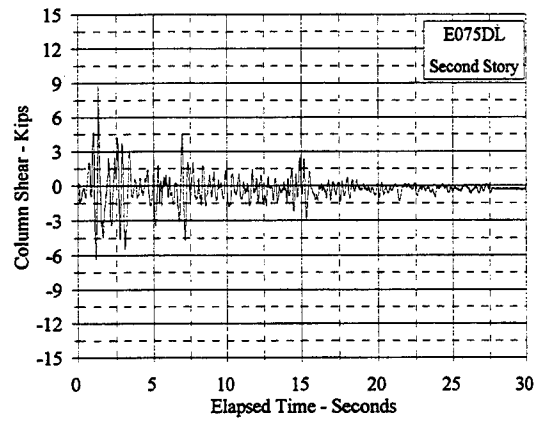
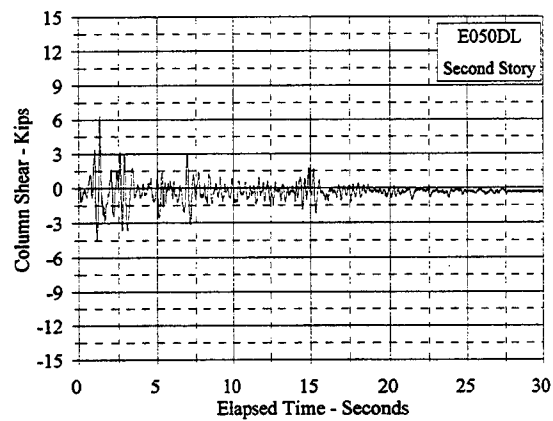
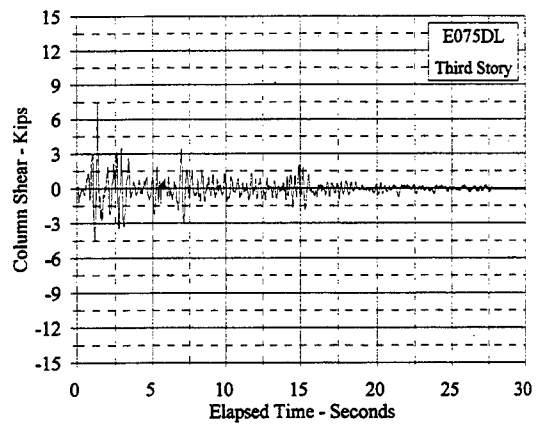
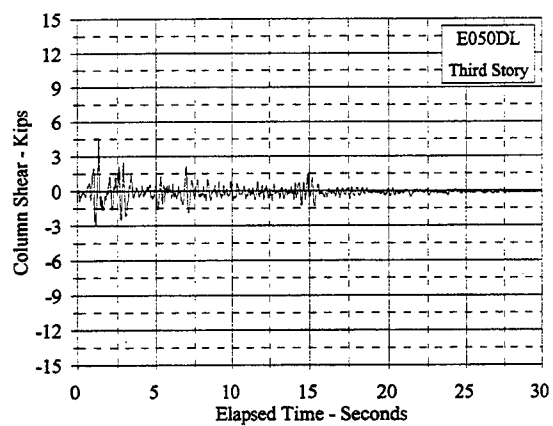


Figure C.12.2 Column Shear Vs. Elapsed Time: E050DL, E075DL

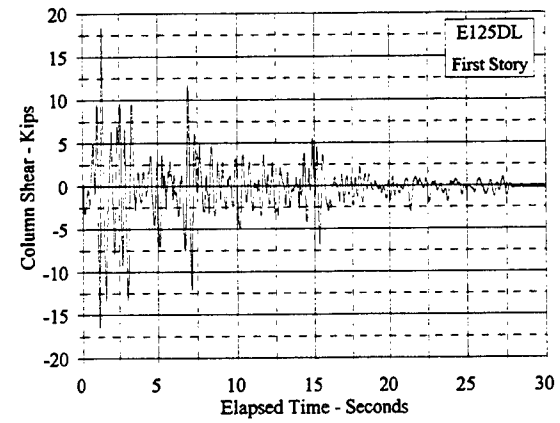
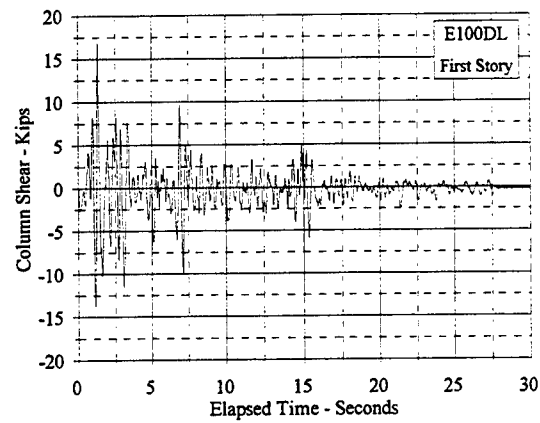
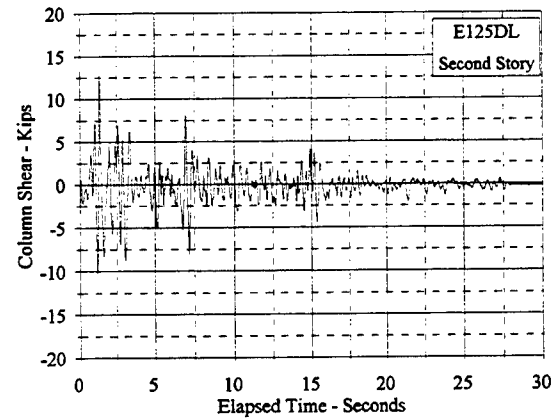
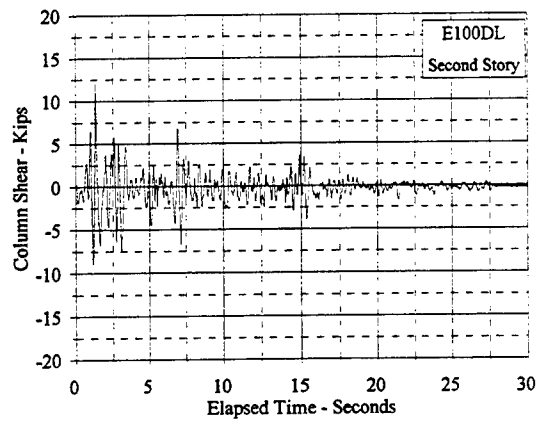
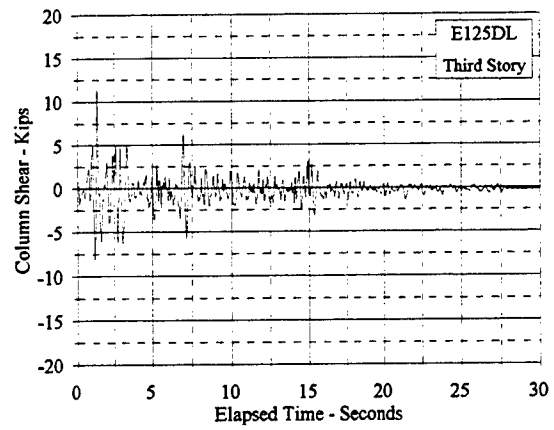
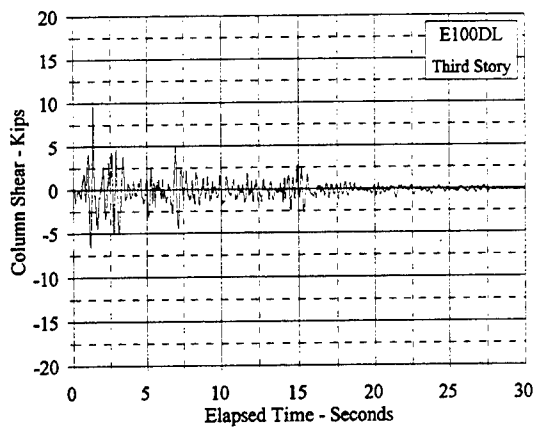


Figure C.12.3 Column Shear Vs. Elapsed Time: E100DL, E125DL

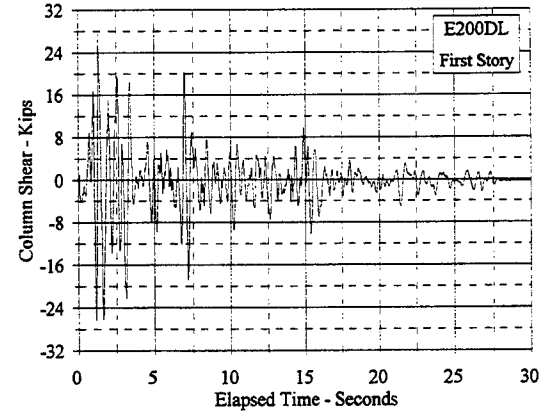
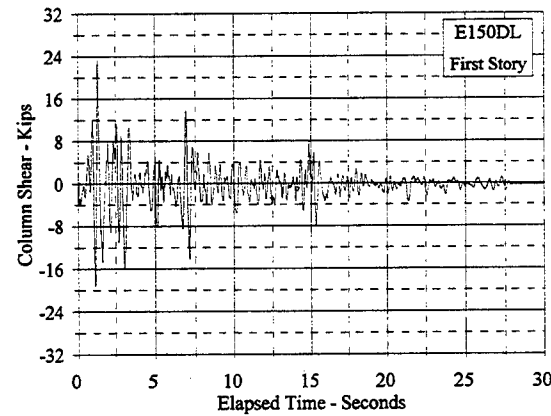
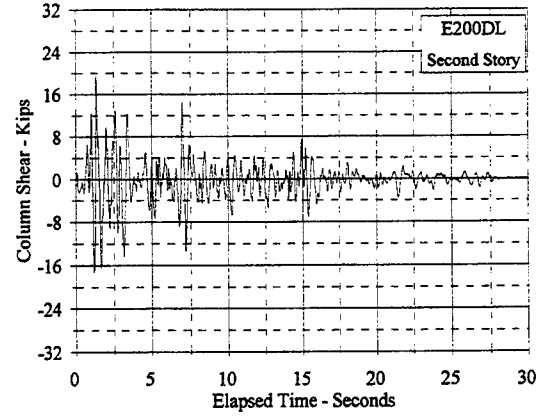
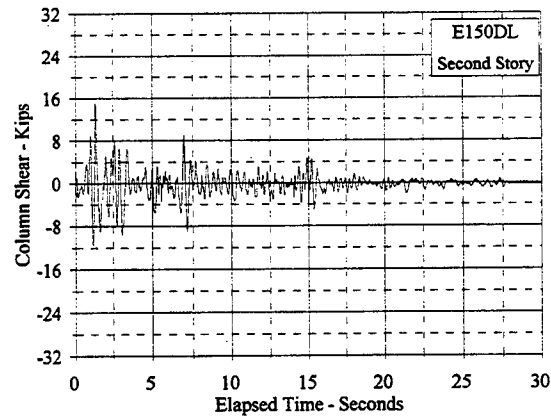
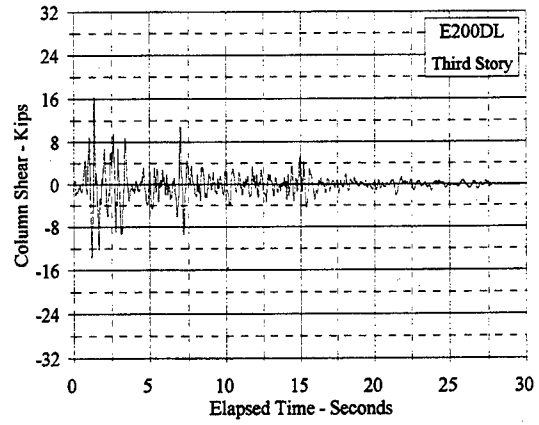
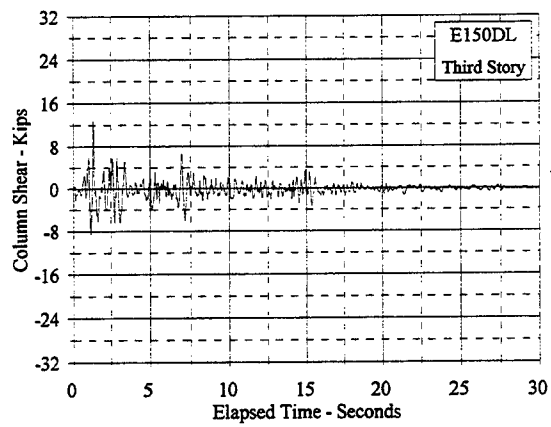


Figure C.12.4 Column Shear Vs. Elapsed Time: E150DL, E200DL

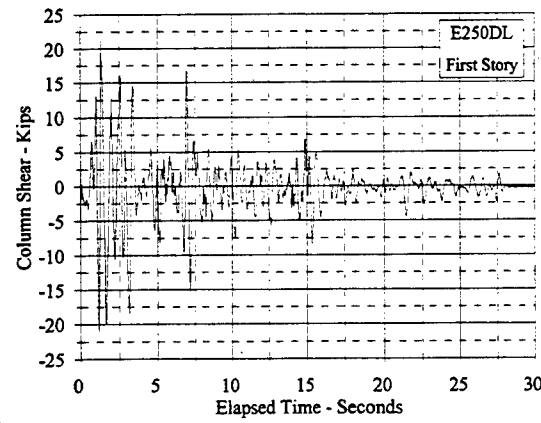
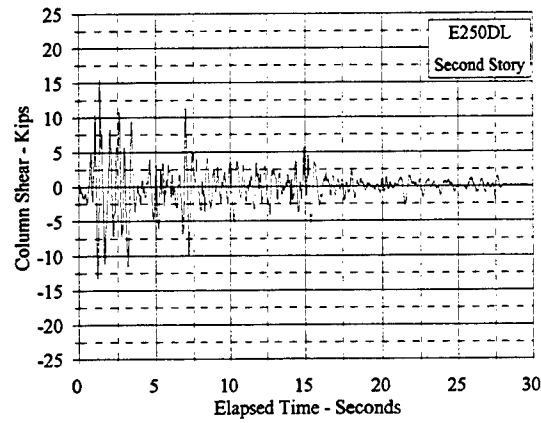
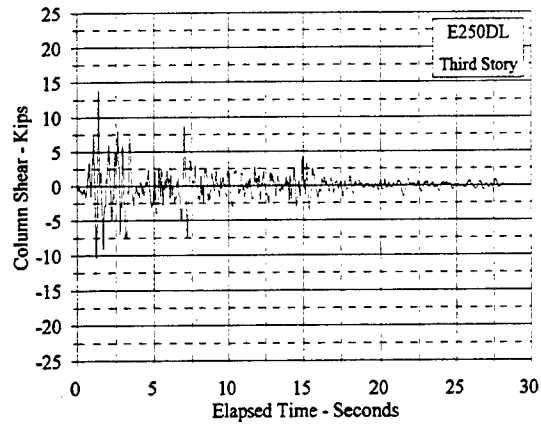


Figure C.12.5 Column Shear Vs. Elapsed Time: E250DL

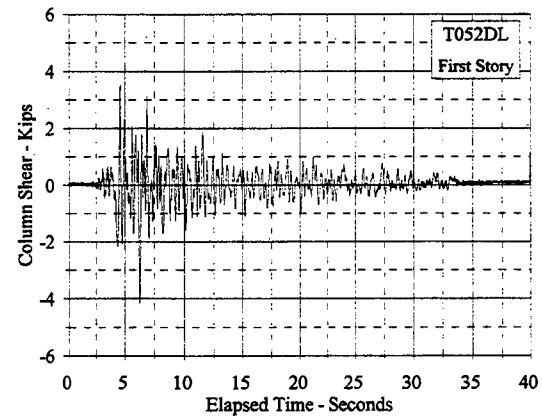
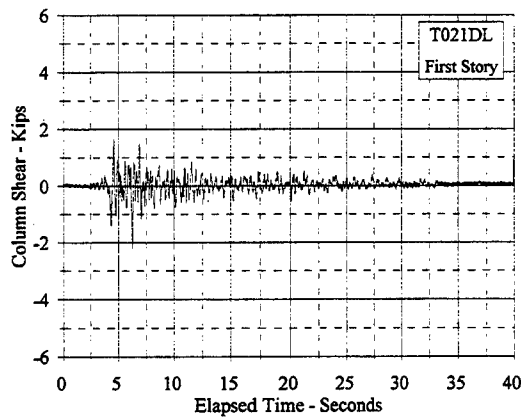
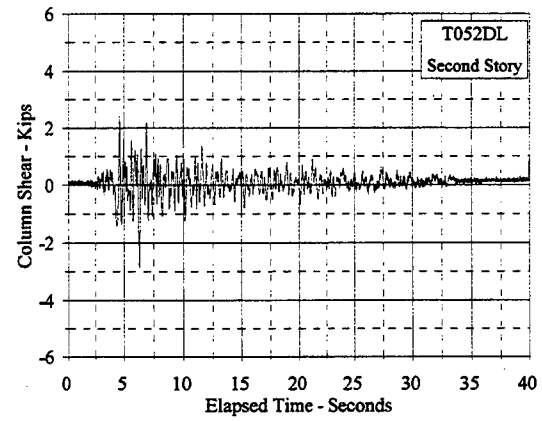
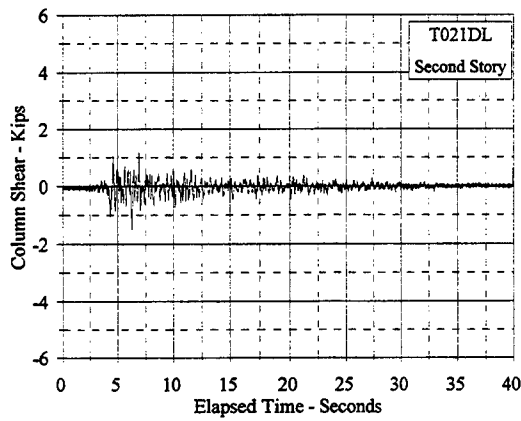
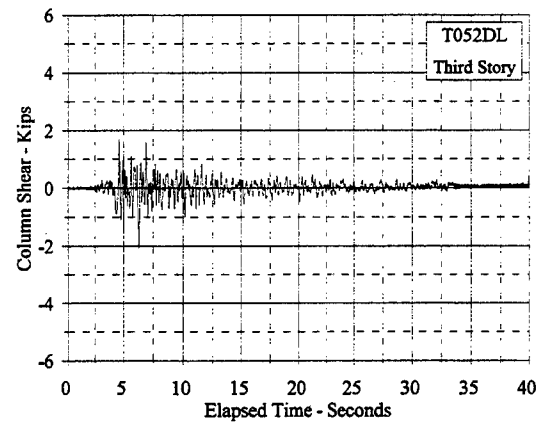
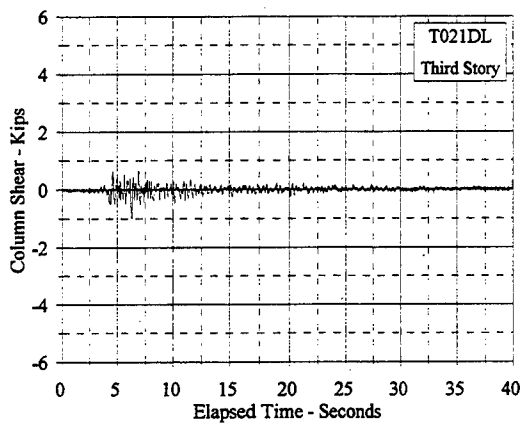


Figure C.12.6 Column Shear Vs. Elapsed Time: T021DL, T052DL

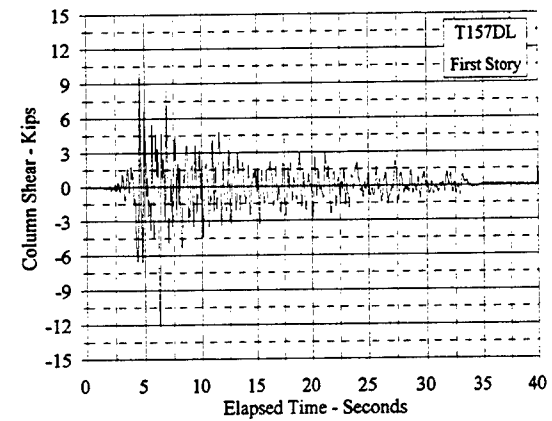
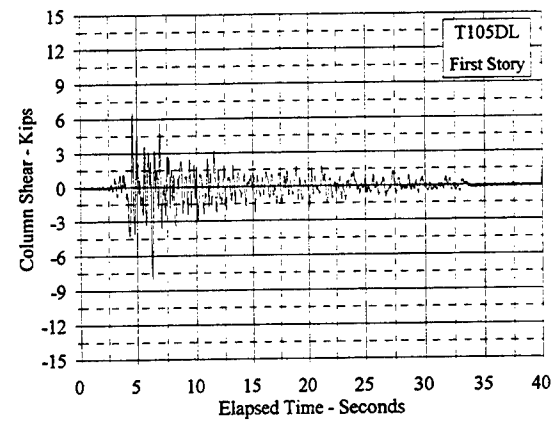
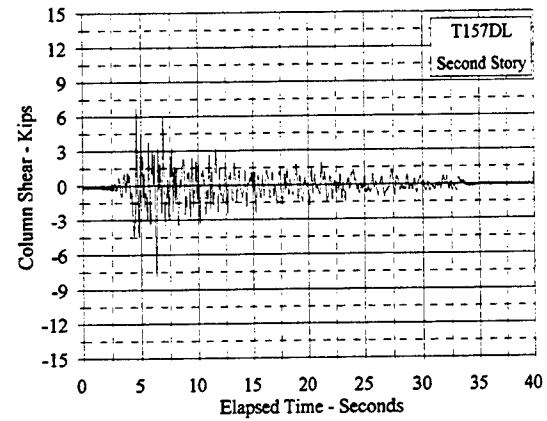
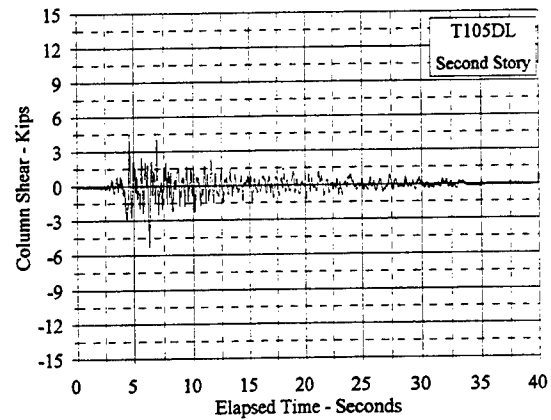
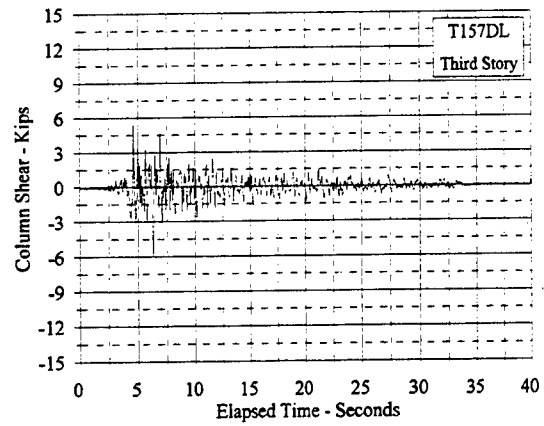
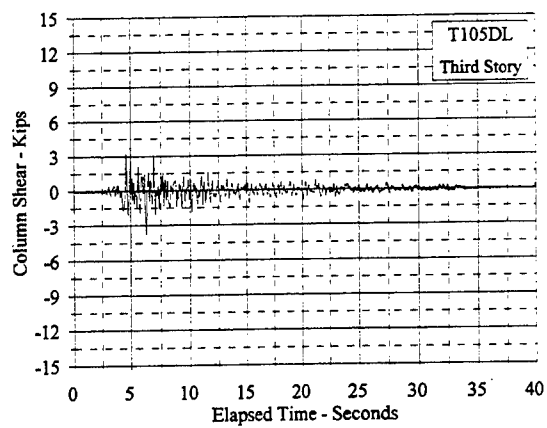


Figure C.12.7 Column Shear Vs. Elapsed Time: T105DL, T157DL

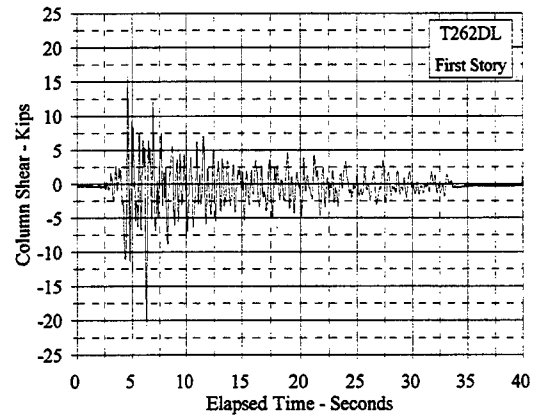
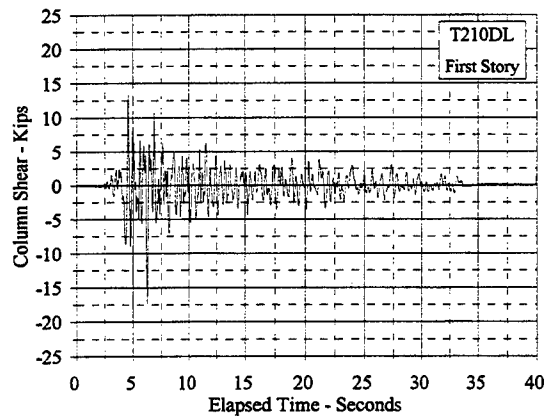
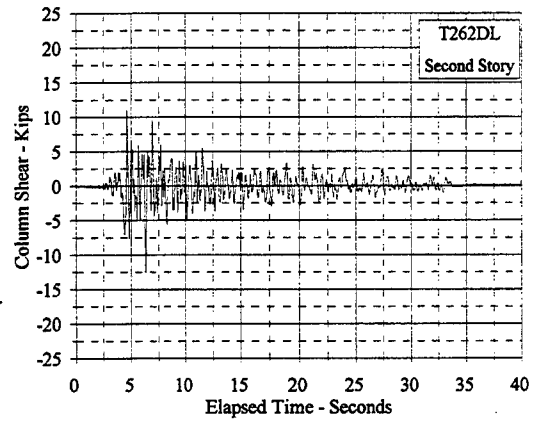
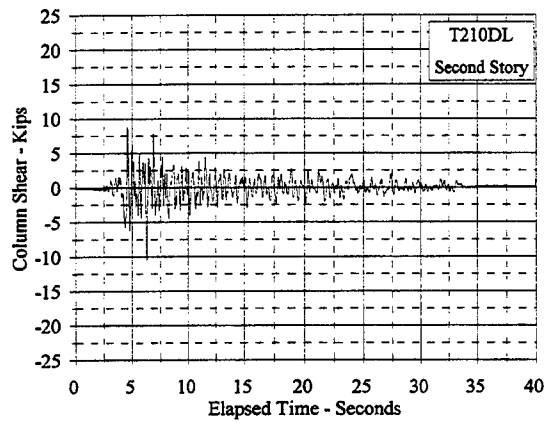
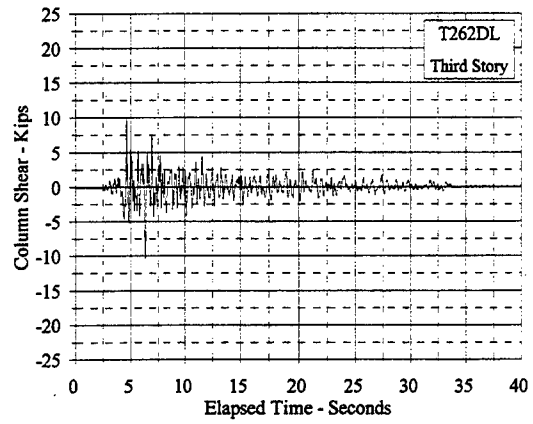
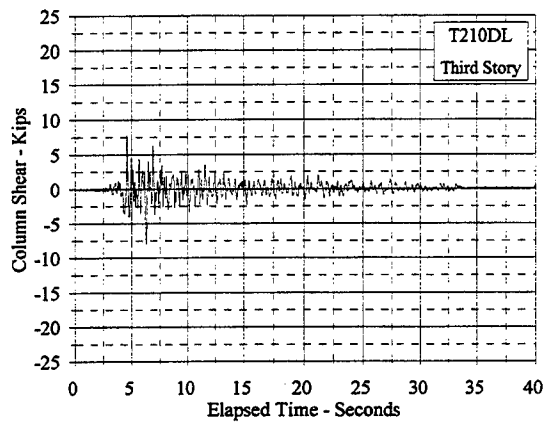


Figure C.12.8 Column Shear Vs. Elapsed Time: T210DL, T262DL

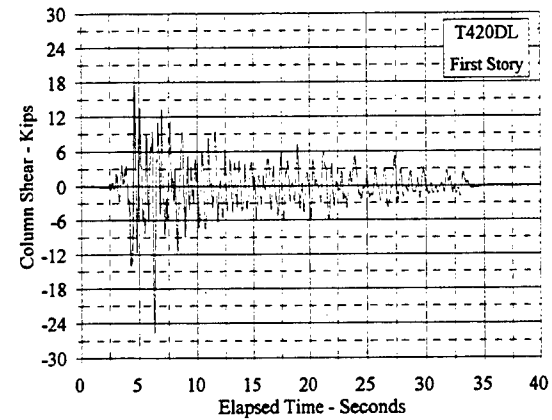
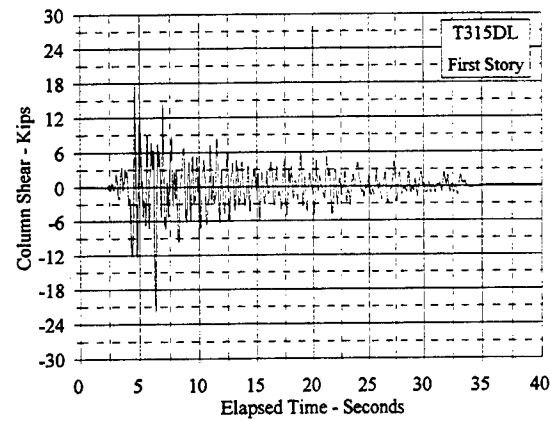
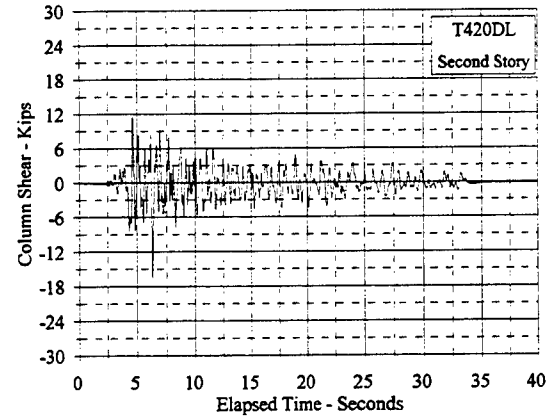
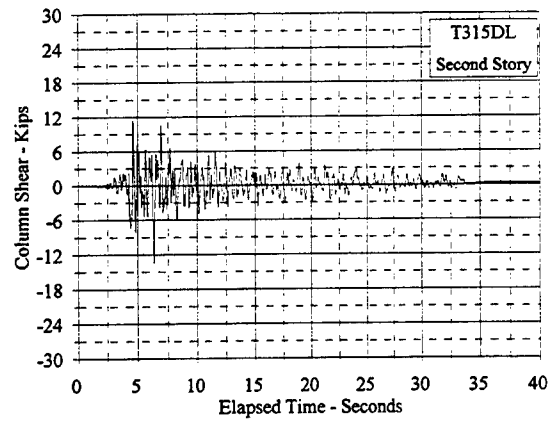
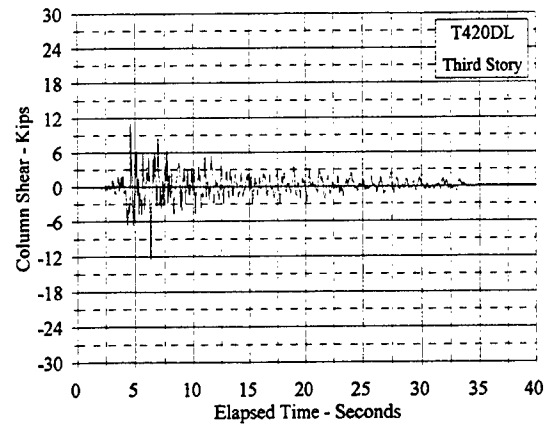
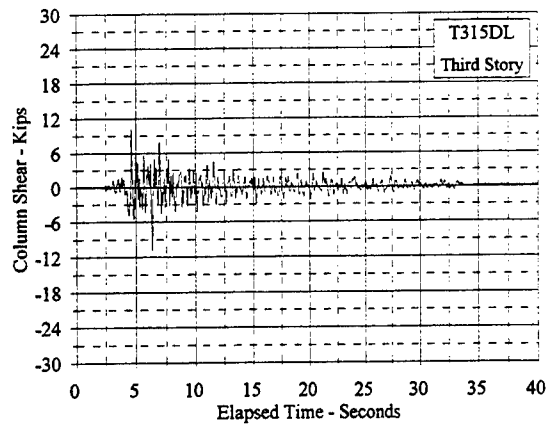


Figure C.12.9 Column Shear Vs. Elapsed Time: T315DL, T420DL

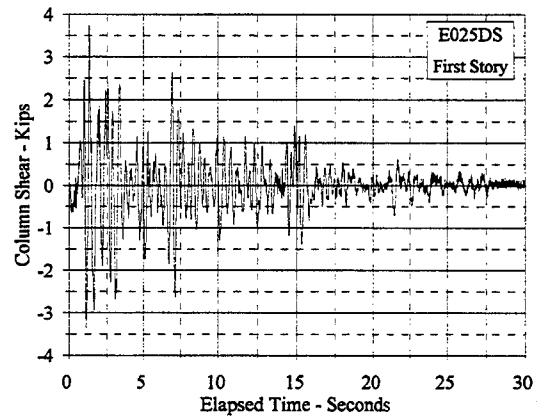
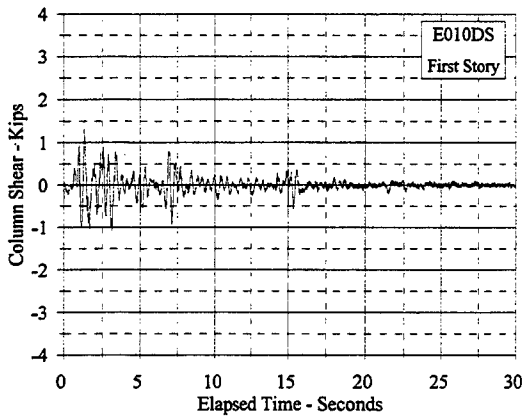
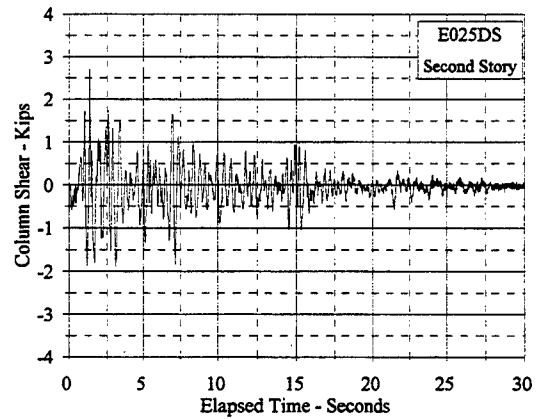
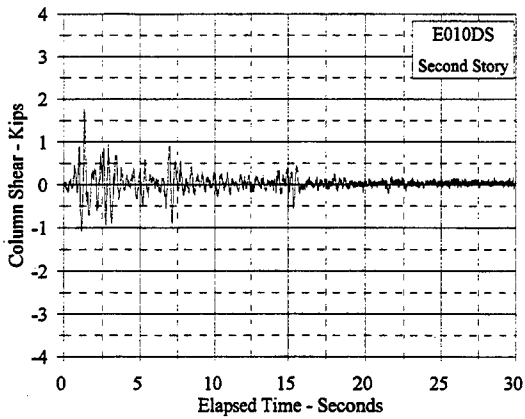
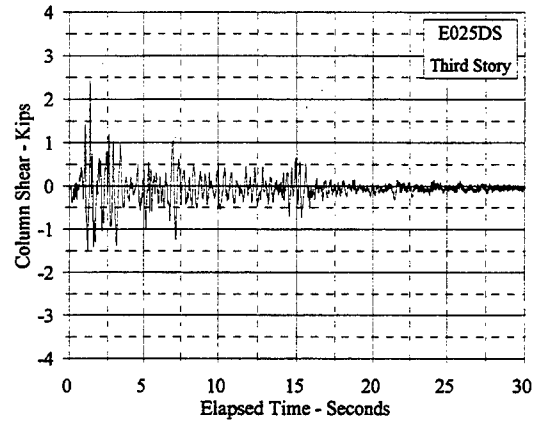
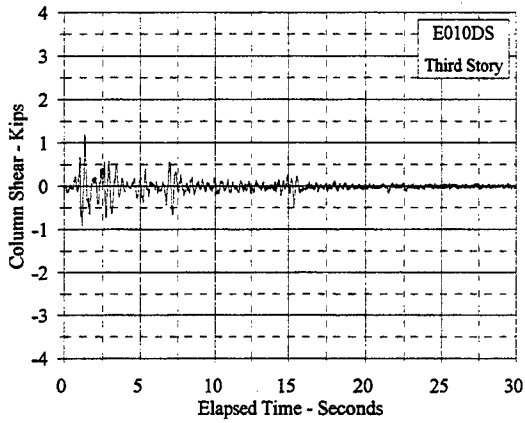


Figure C.12.10 Column Shear Vs. Elapsed Time: E010DS, E025DS

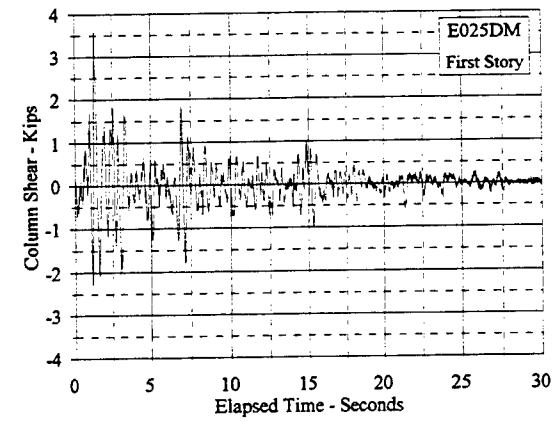
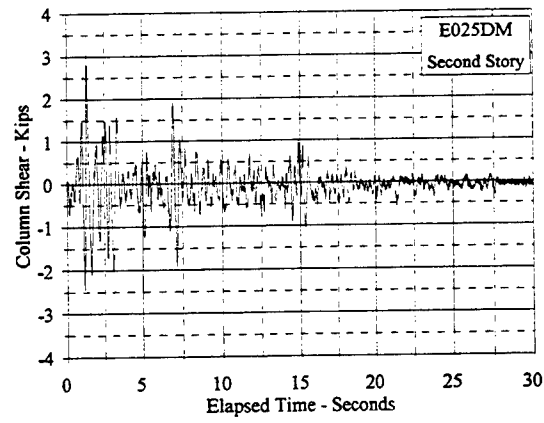
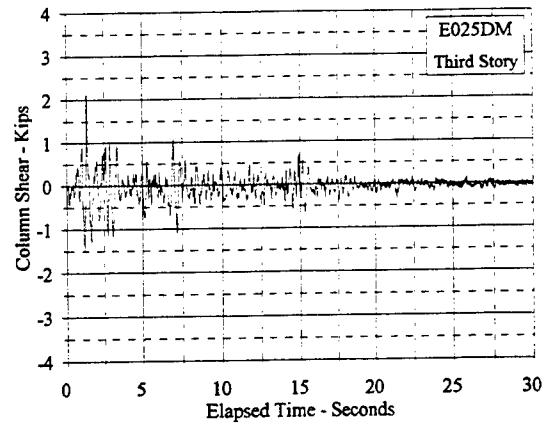


Figure C.12.11 Column Shear Vs. Elapsed Time: E025DM

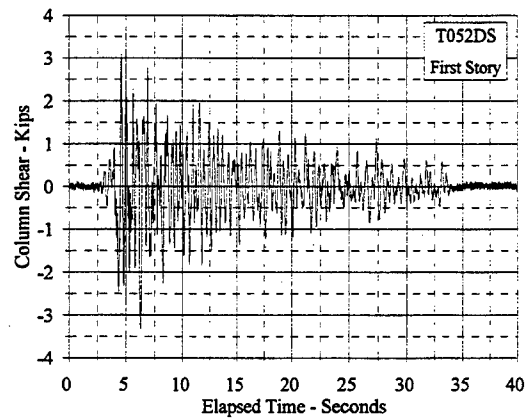
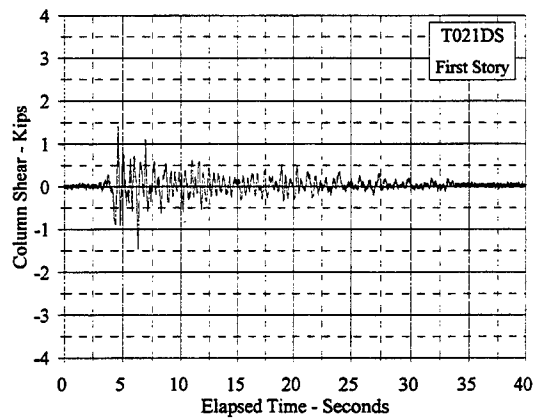
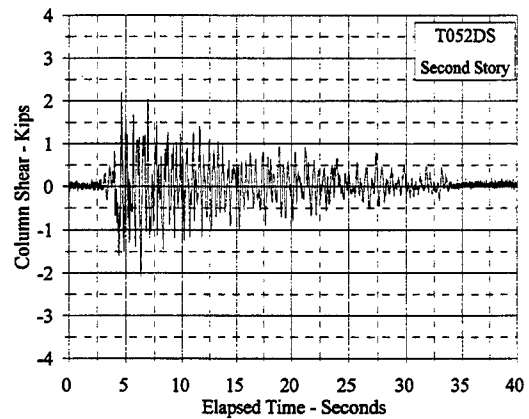
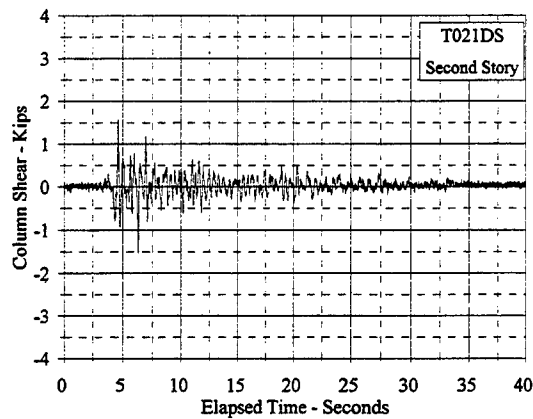
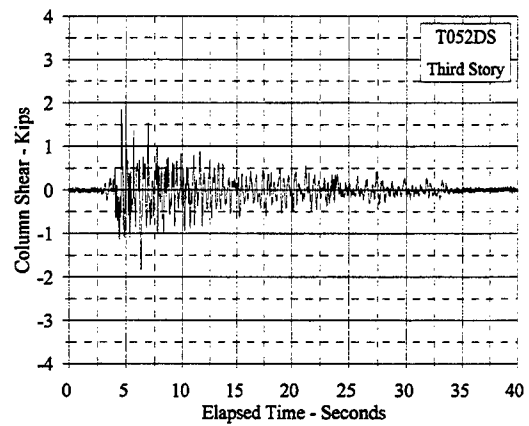
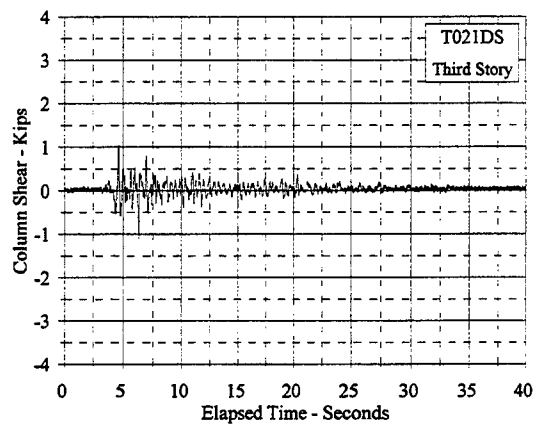


Figure C.12.12 Column Shear Vs. Elapsed Time: T021DS, T052DS

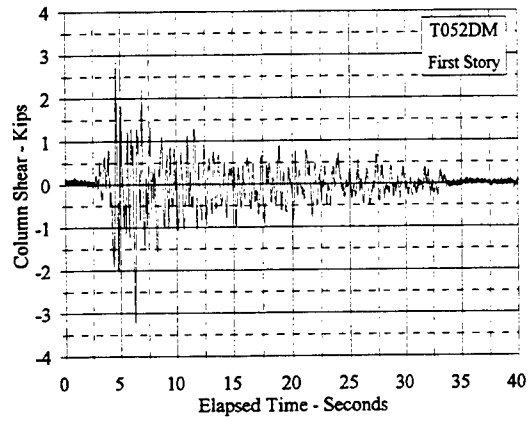
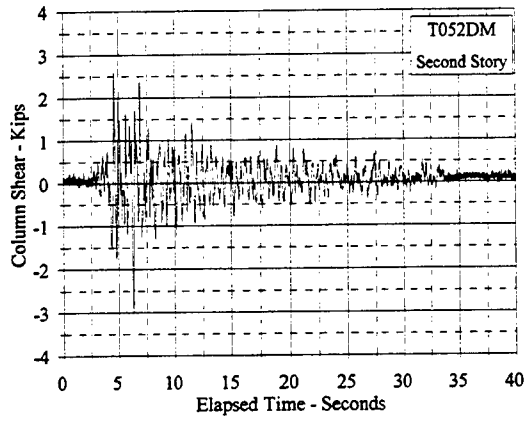
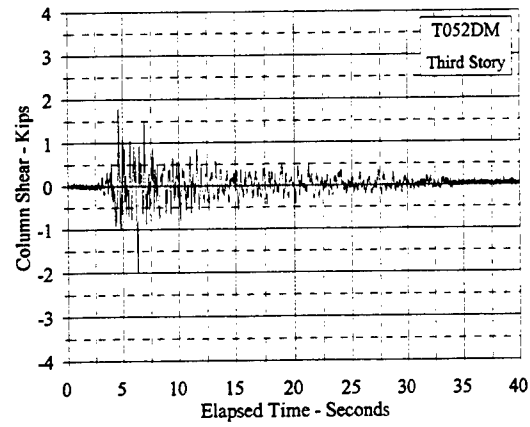


Figure C.12.13 Column Shear Vs. Elapsed Time: T052DM

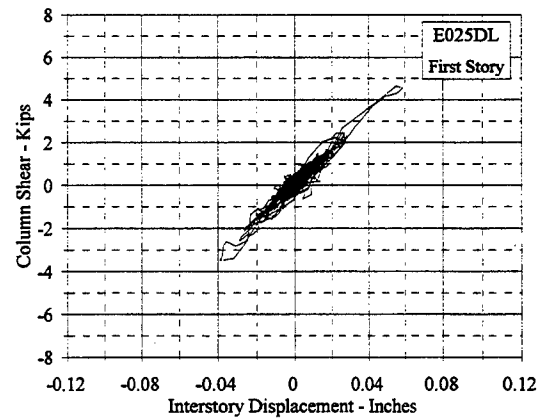
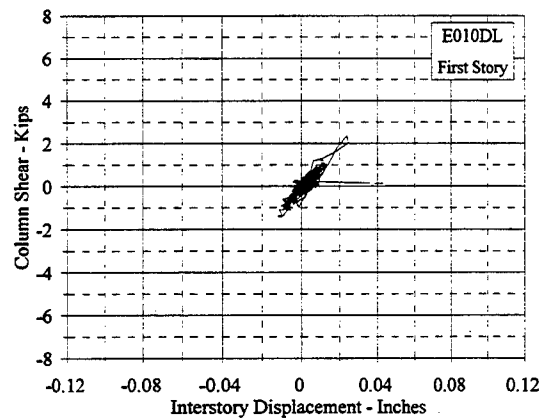
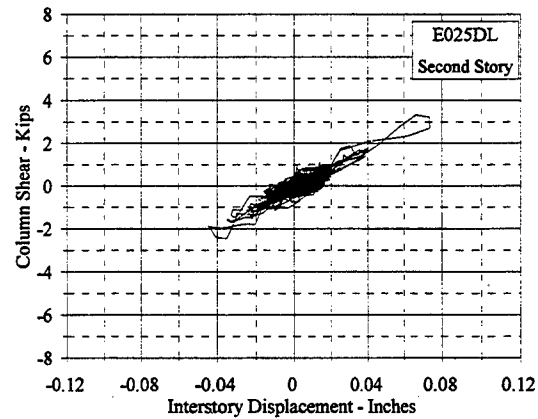
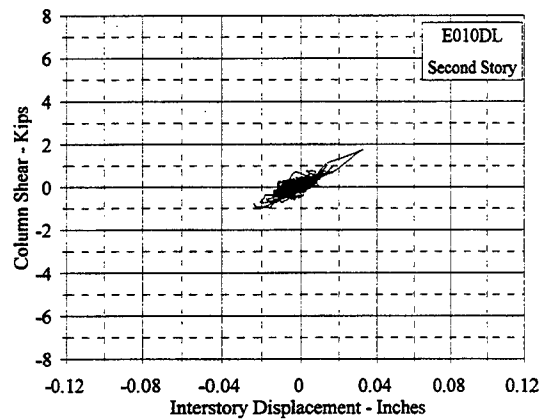
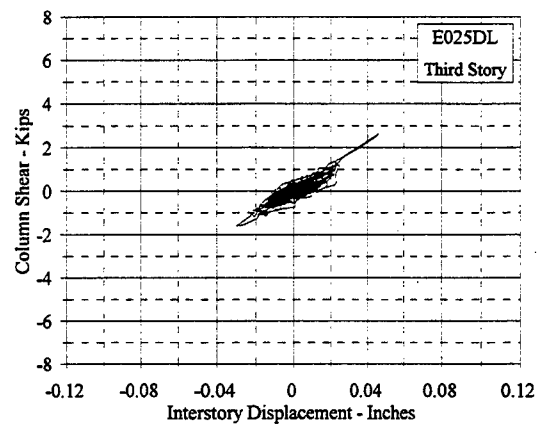
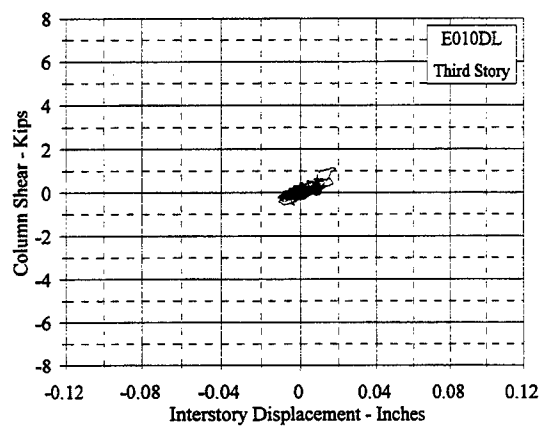


Figure C.13.1 Column Shear Vs. Interstory Displacement: E010DL, E025DL

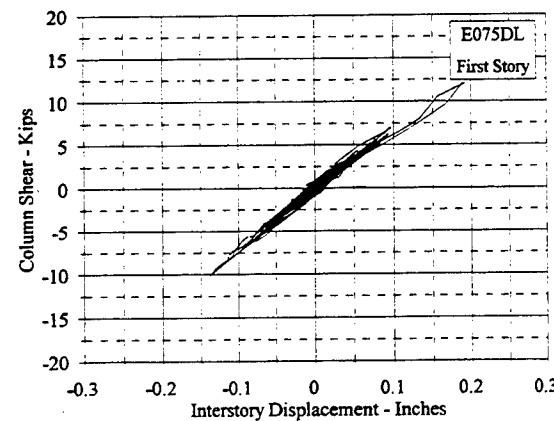
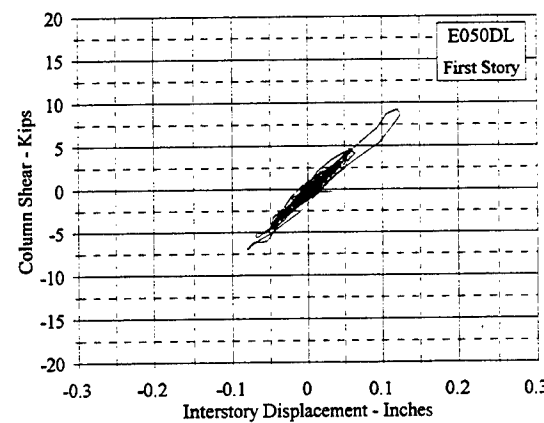
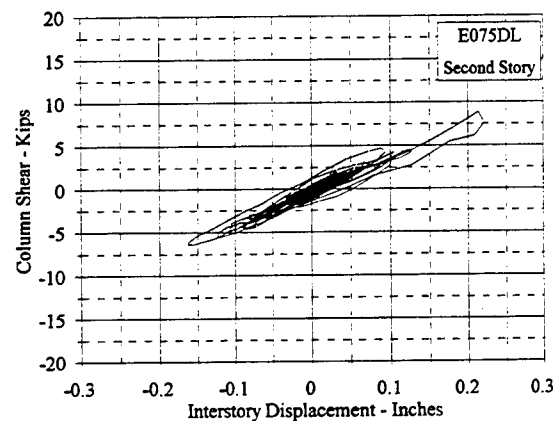
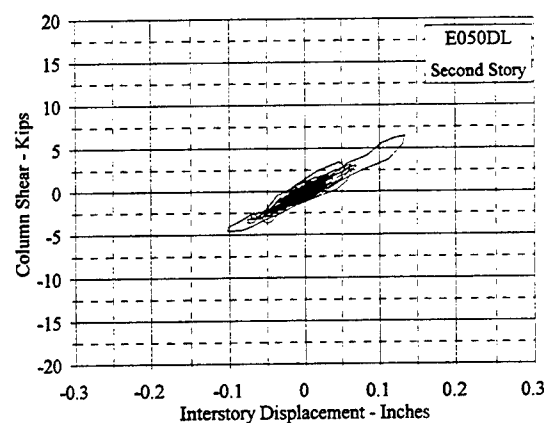
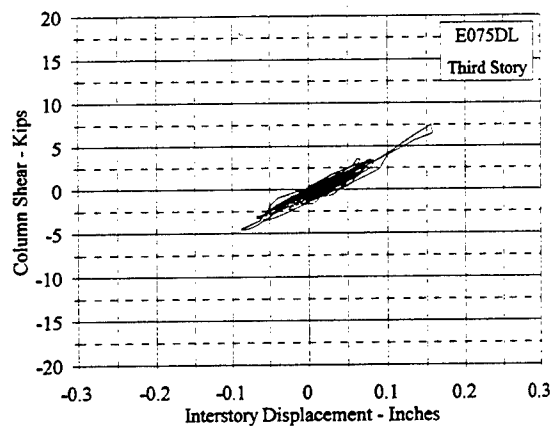
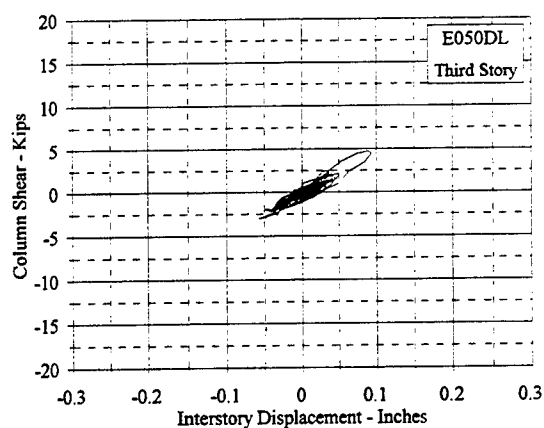


Figure C.13.2 Column Shear Vs. Interstory Displacement: E050DL, E075DL

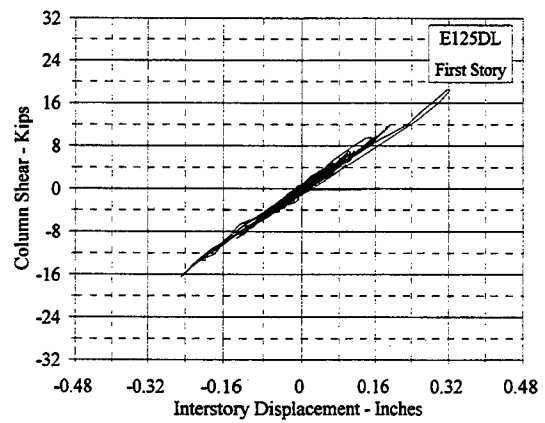
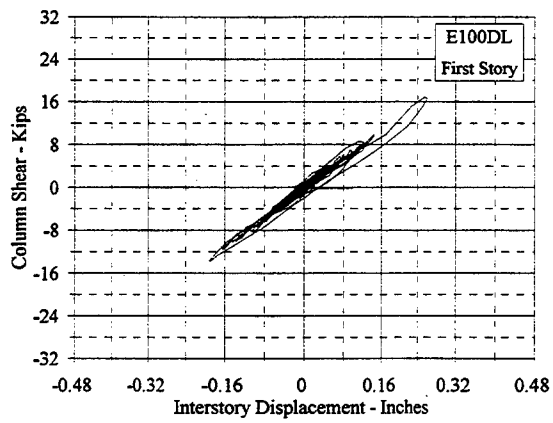
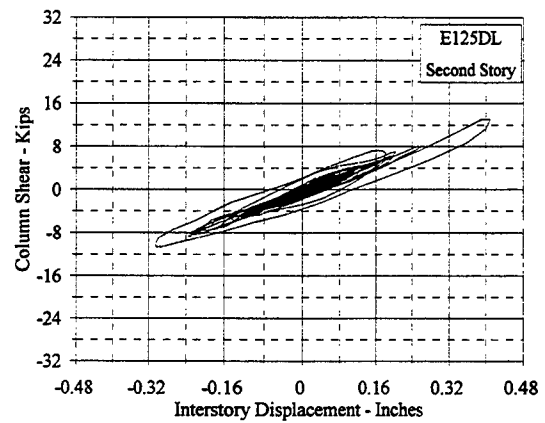
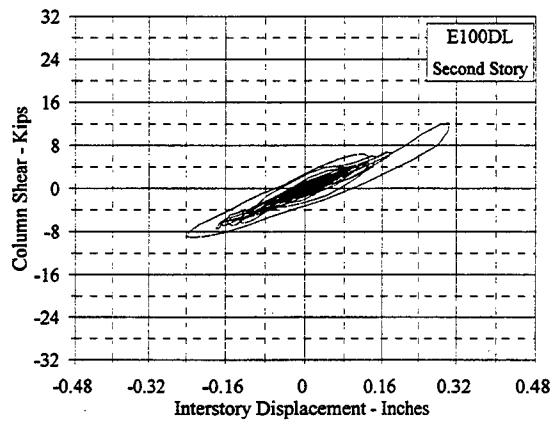
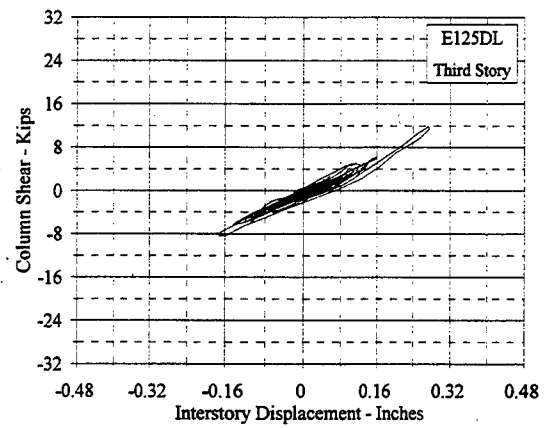
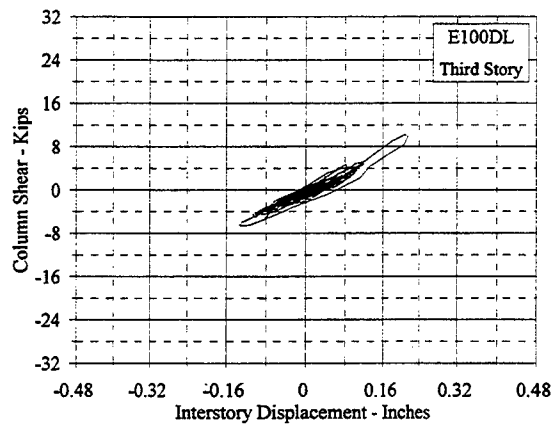


Figure C.13.3 Column Shear Vs. Interstory Displacement: E100DL, E125DL

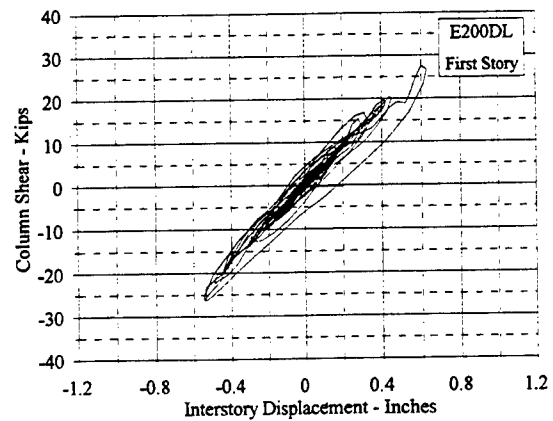
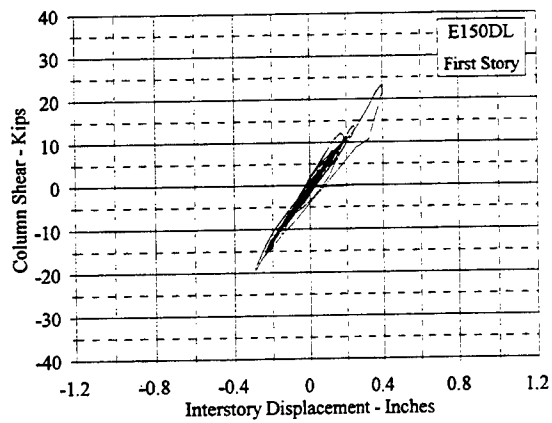
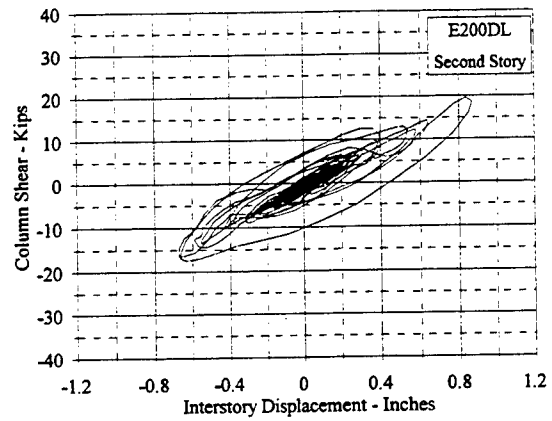
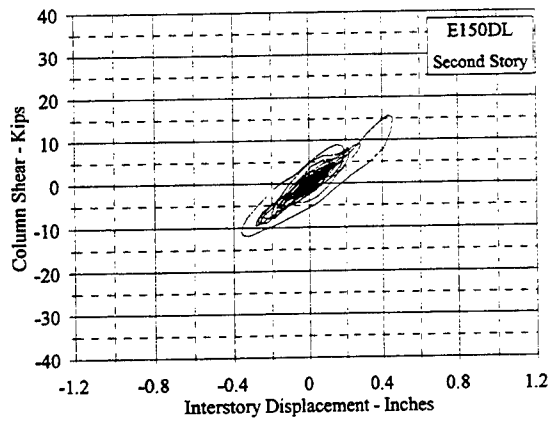
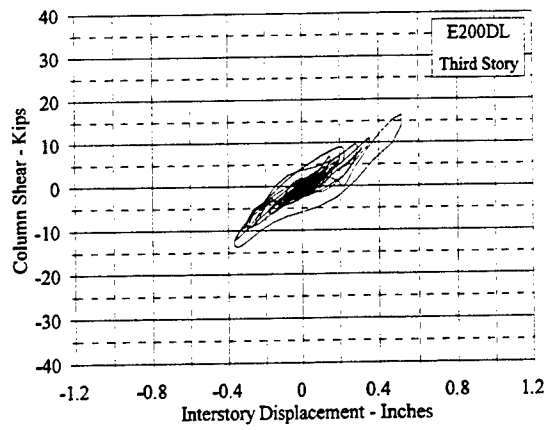
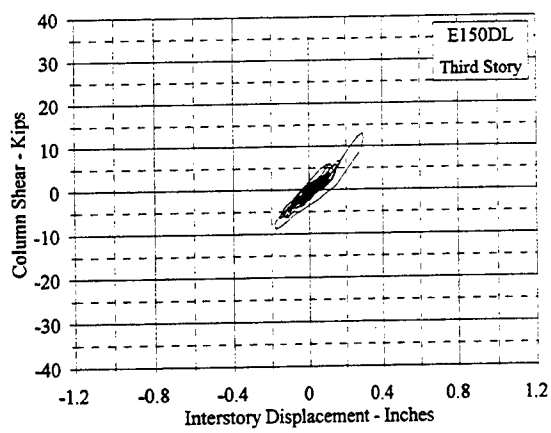


Figure C.13.4 Column Shear Vs. Interstory Displacement: E150DL, E200DL

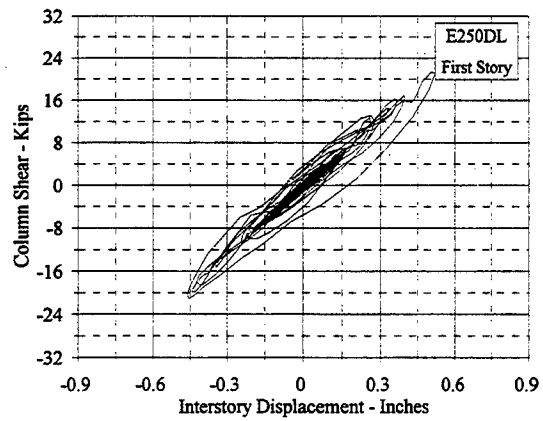
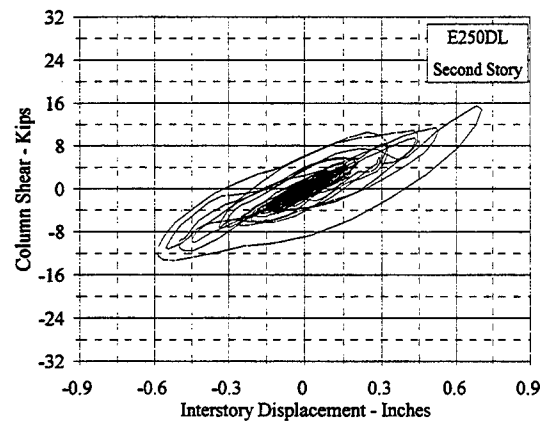
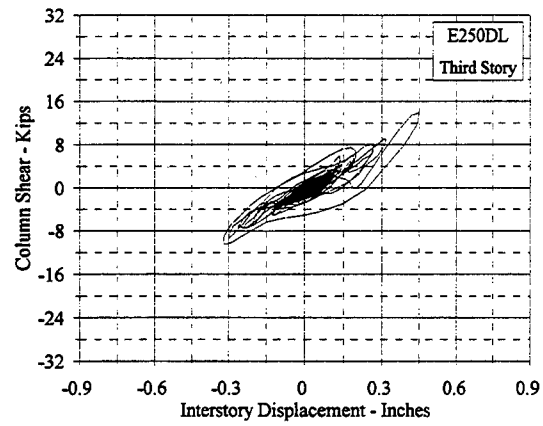


Figure C.13.5 Column Shear Vs. Interstory Displacement: E250DL

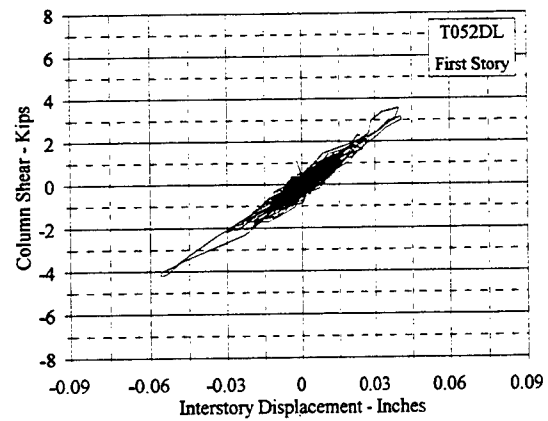
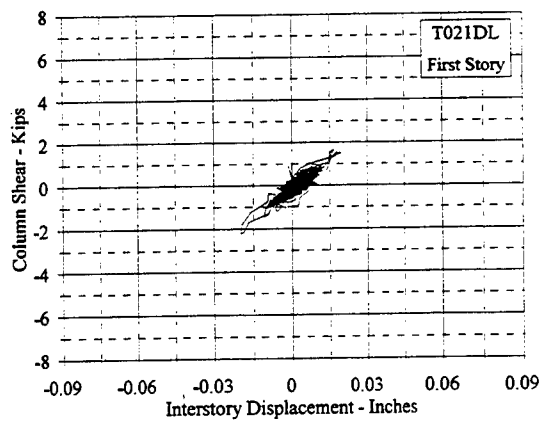
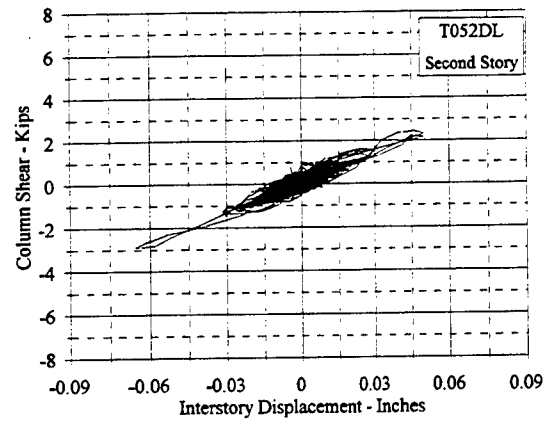
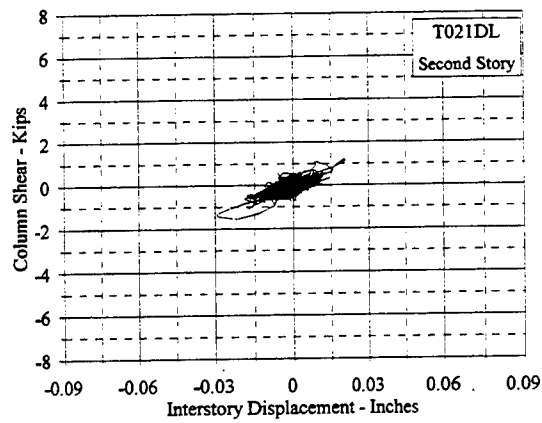
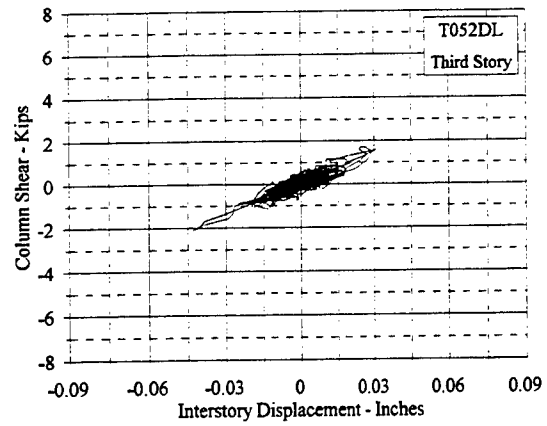
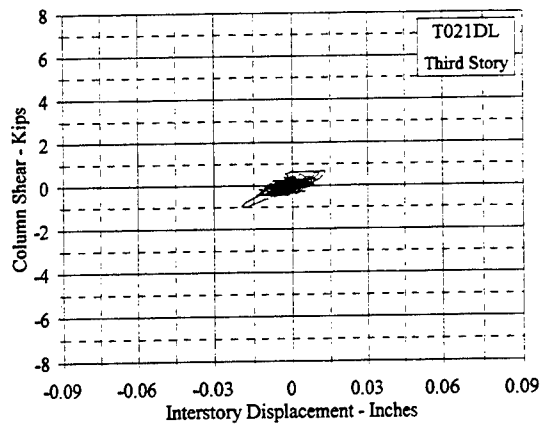


Figure C.13.6 Column Shear Vs. Interstory Displacement: T021DL, T052DL

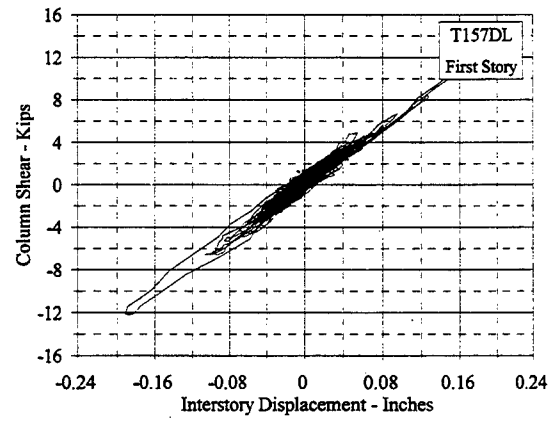
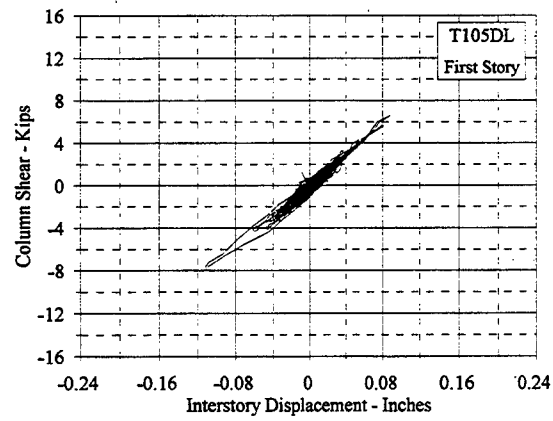
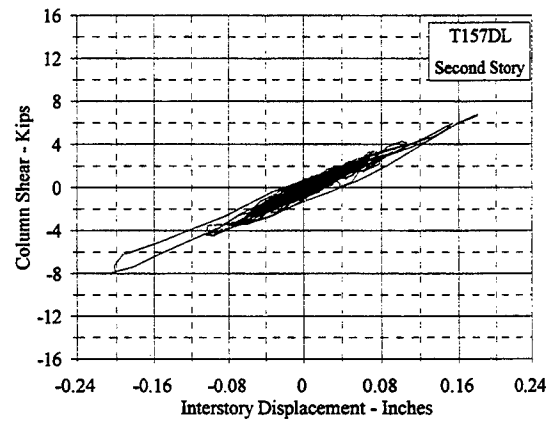
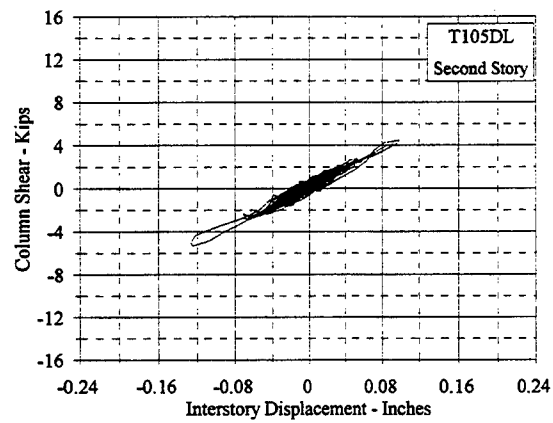
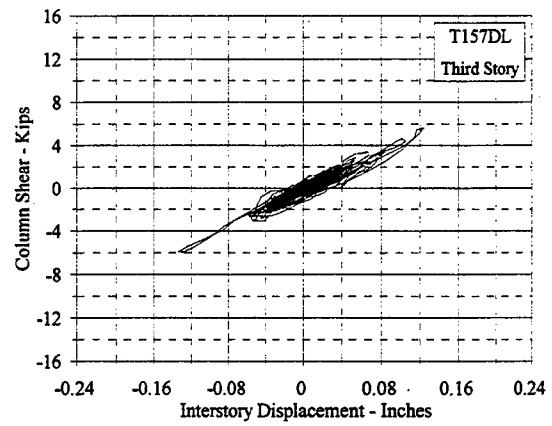
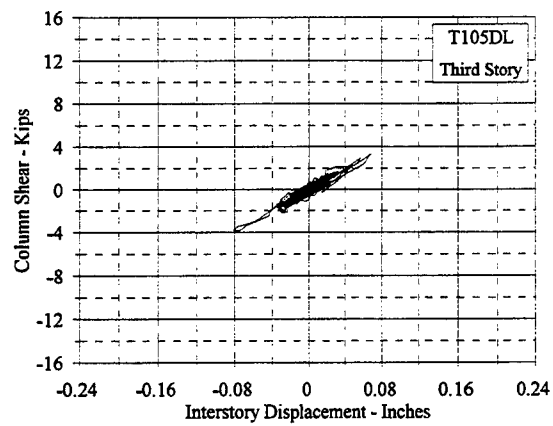


Figure C.13.7 Column Shear Vs. Interstory Displacement: T105DL, T157DL

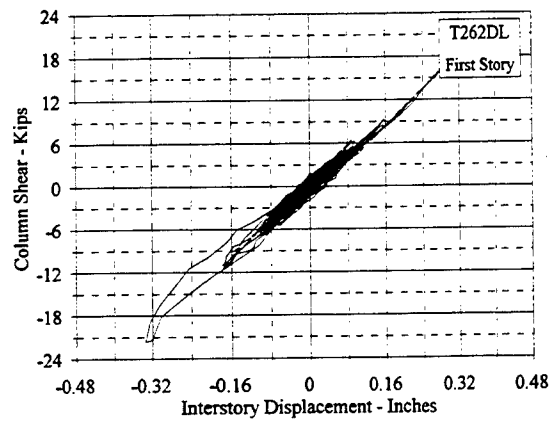
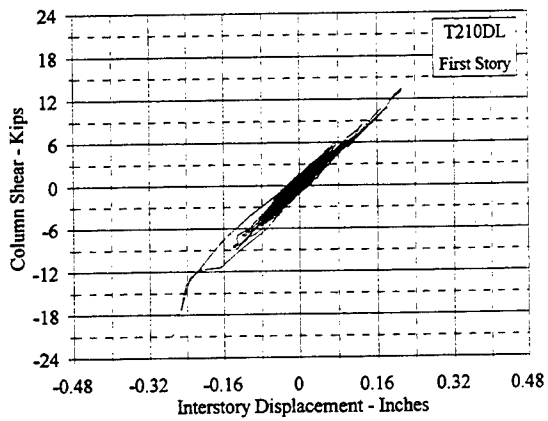
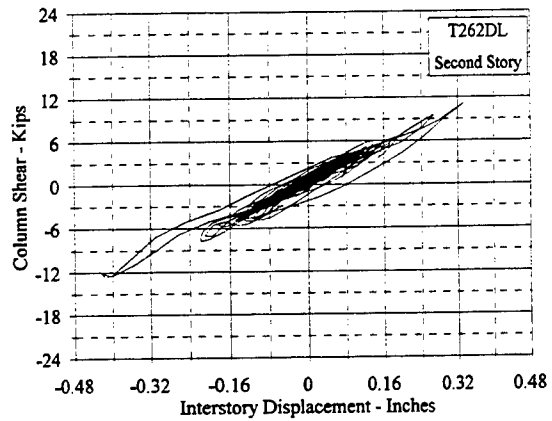
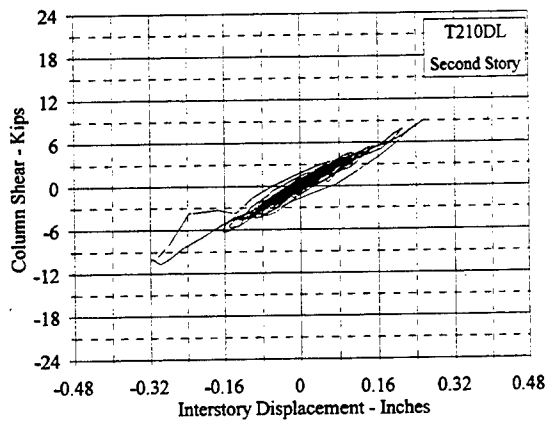
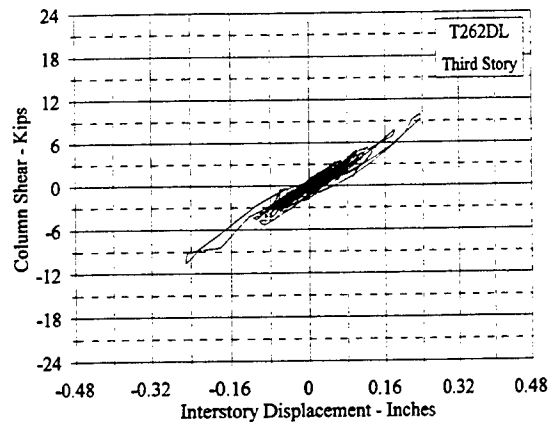
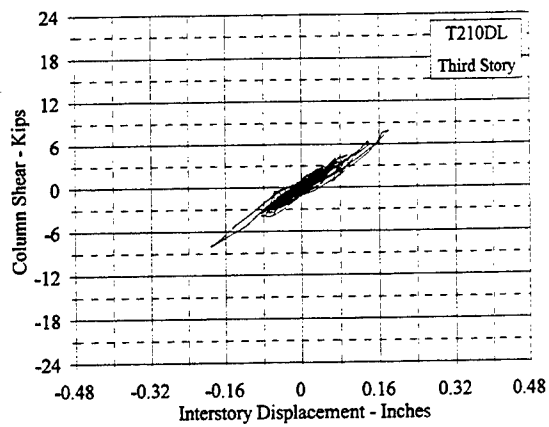


Figure C.13.8 Column Shear Vs. Interstory Displacement: T210DL, T262DL

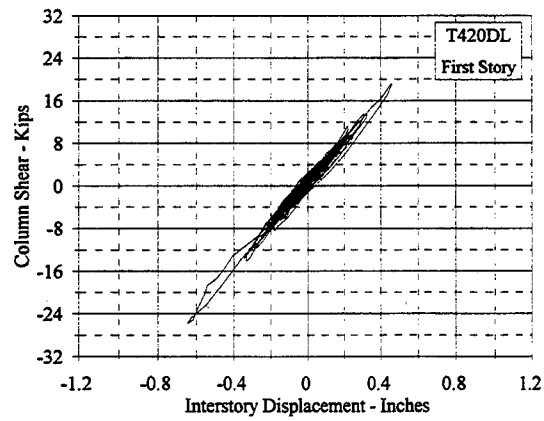
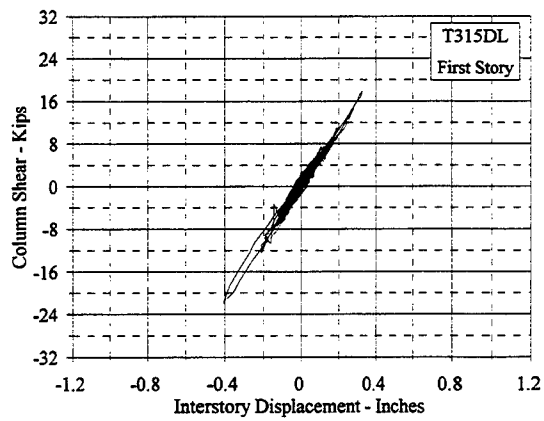
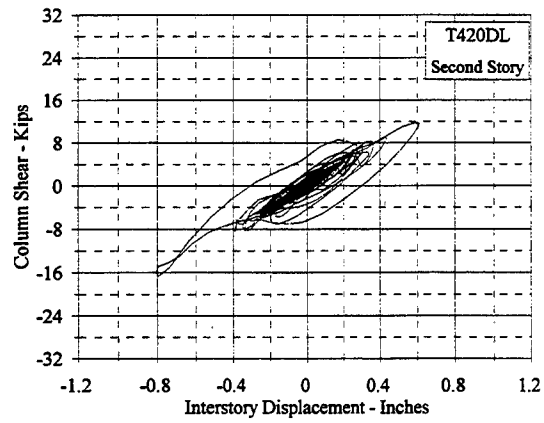
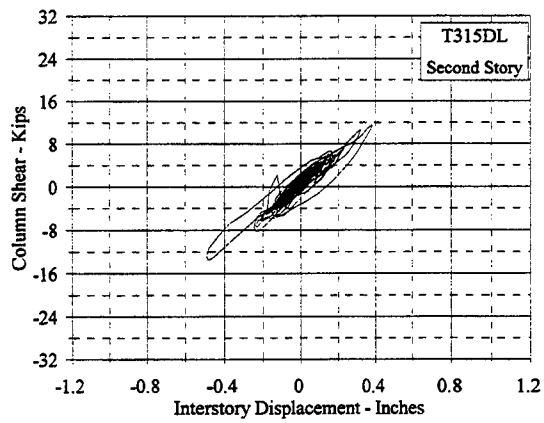
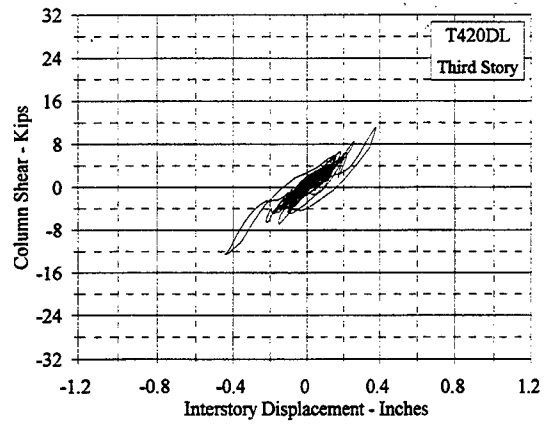
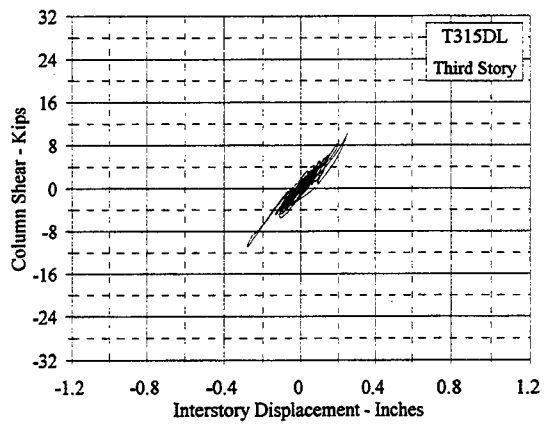


Figure C.13.9 Column Shear Vs. Interstory Displacement: T315DL, T420DL

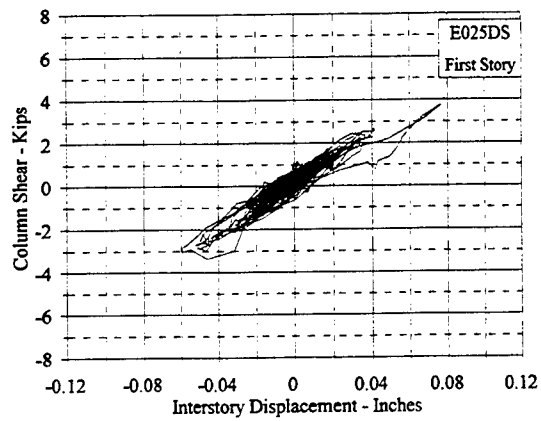
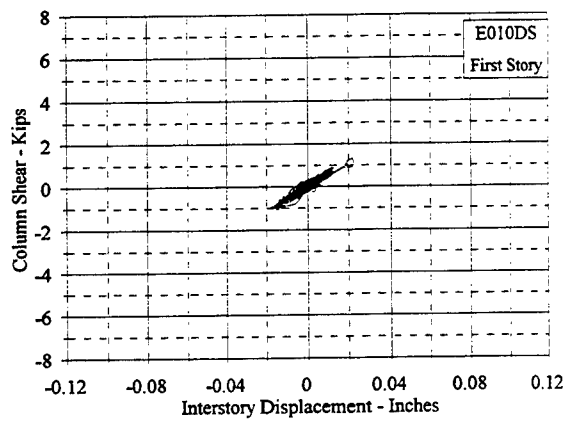
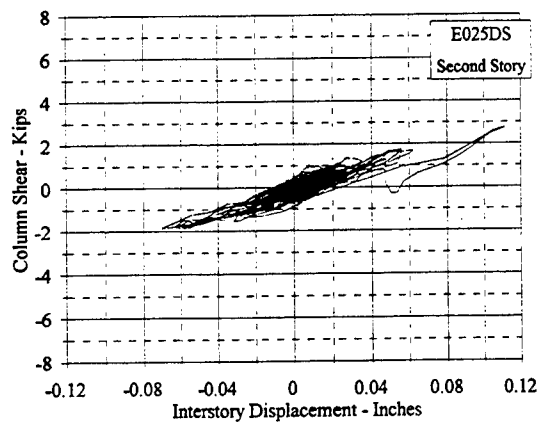
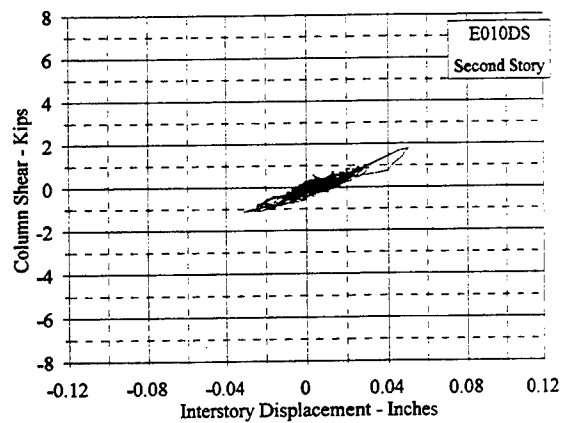
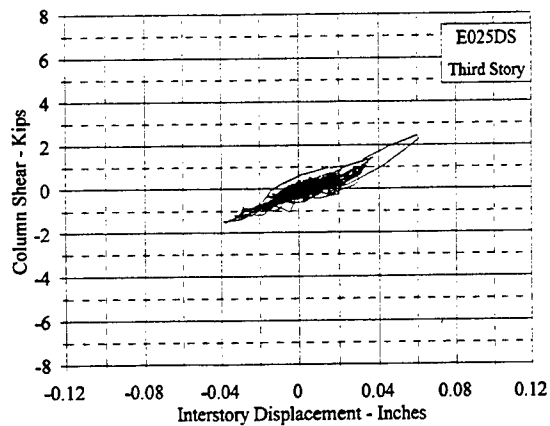
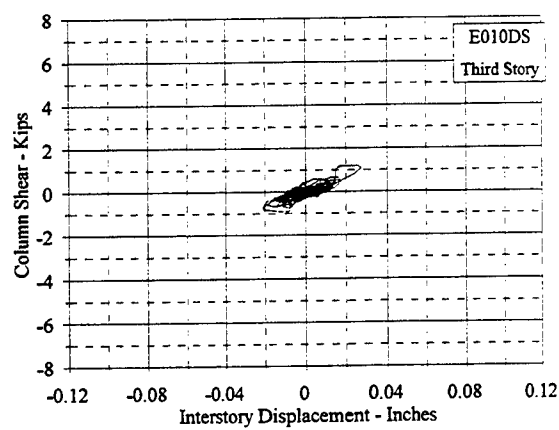


Figure C.13.10 Column Shear Vs. Interstory Displacement: E010DS, E025DS

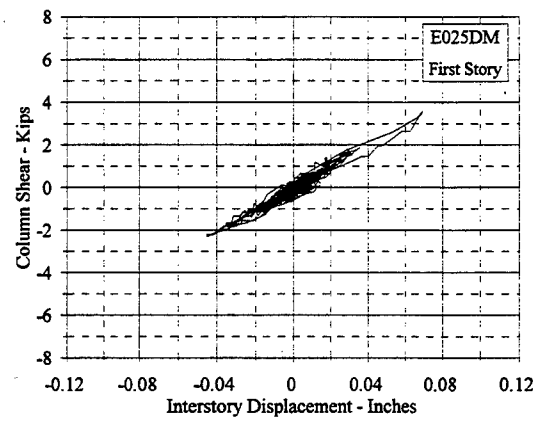
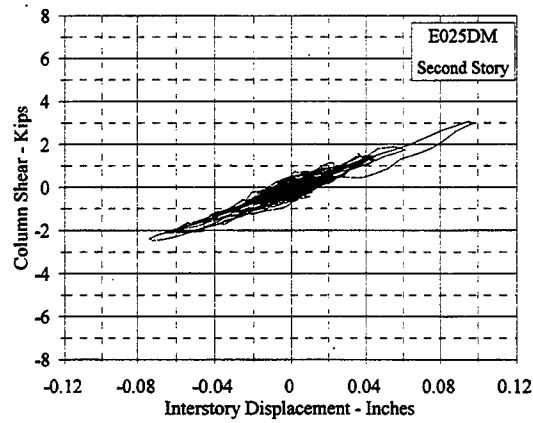
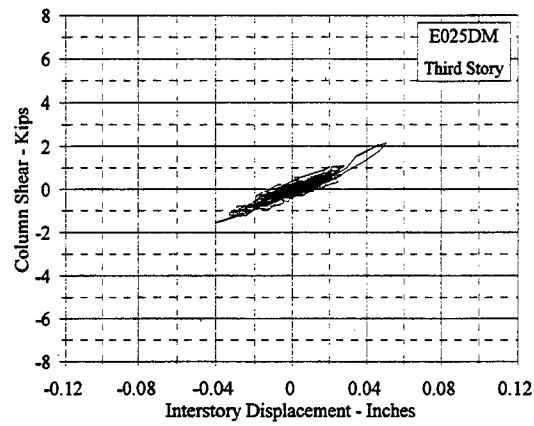


Figure C.13.11 Column Shear Vs. Interstory Displacement: E025DM

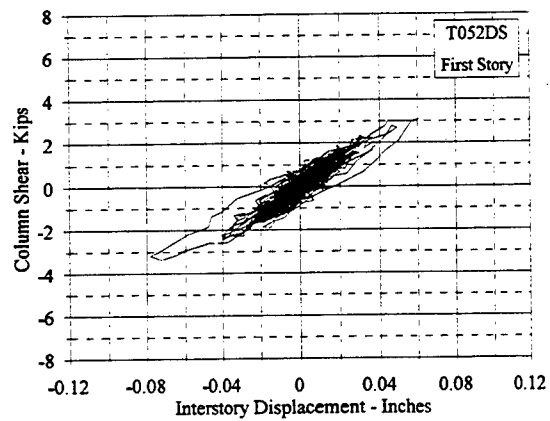
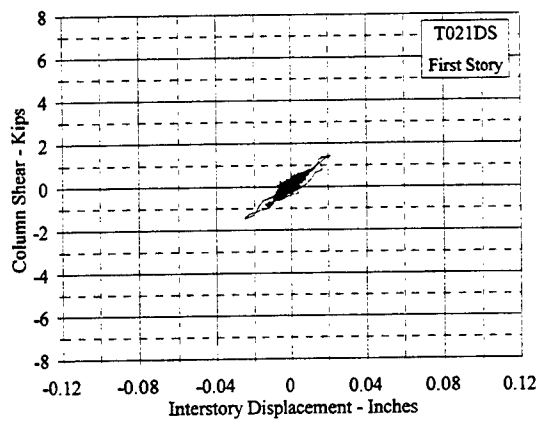
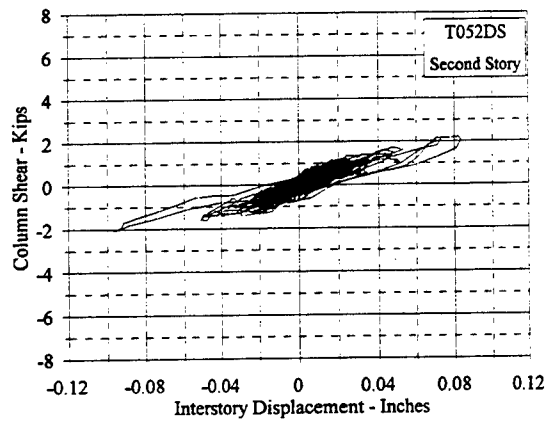
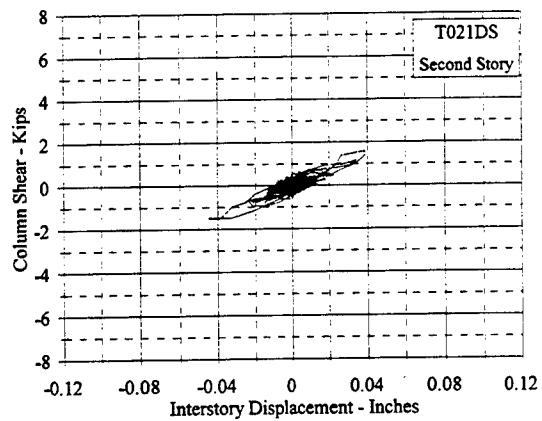
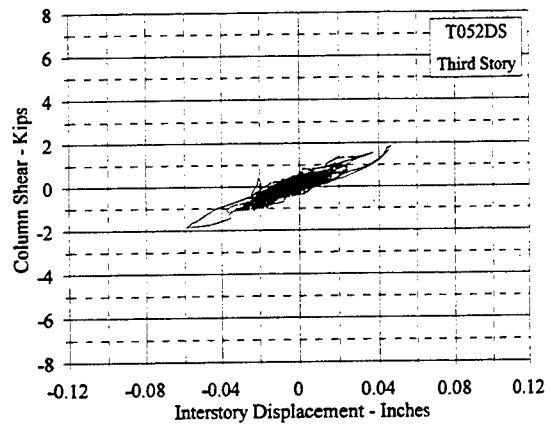
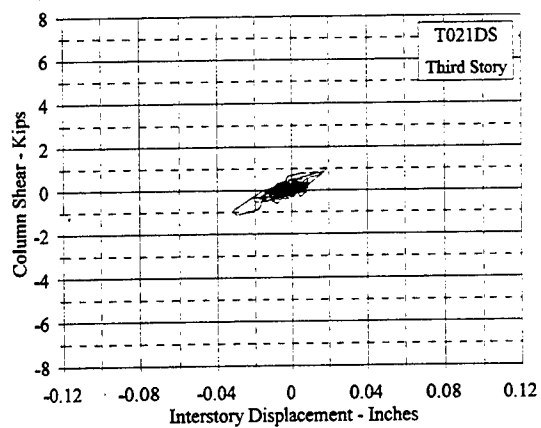


Figure C.13.12 Column Shear Vs. Interstory Displacement: T021DS, T052DS

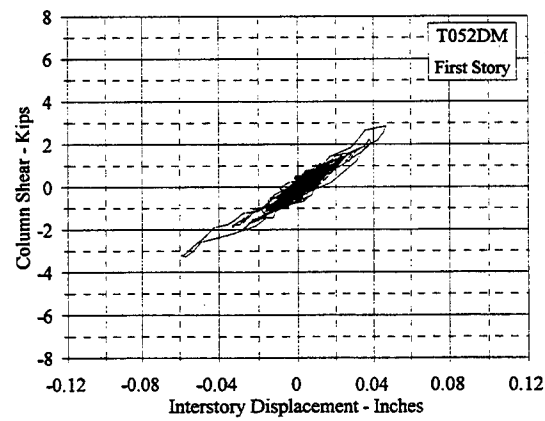
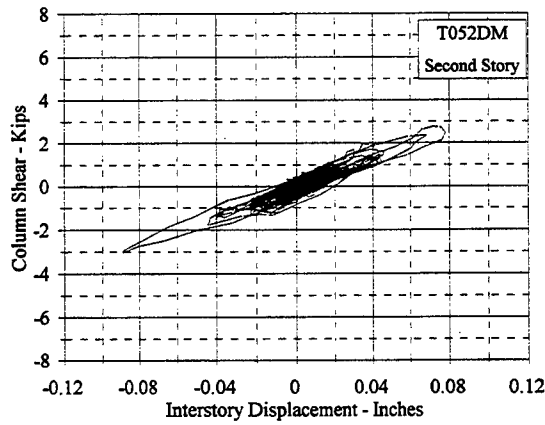
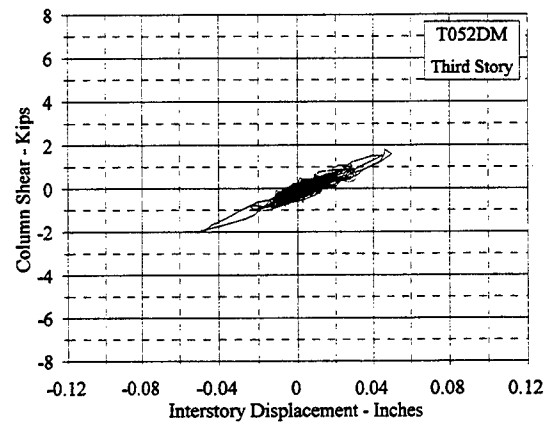
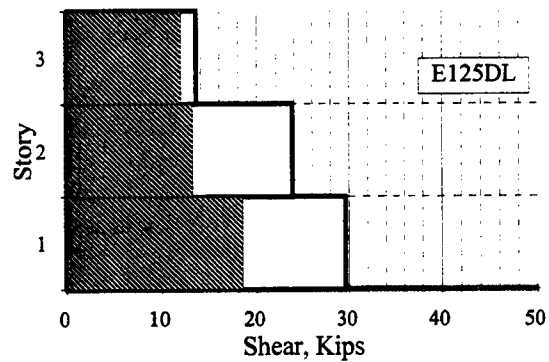
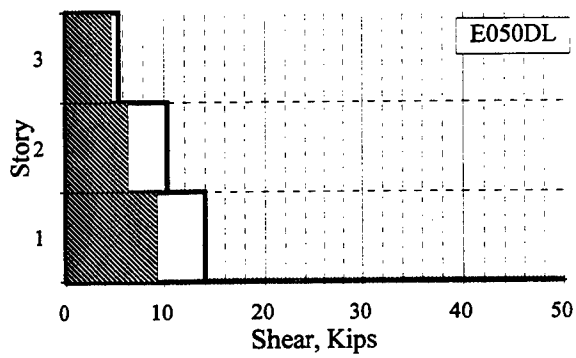
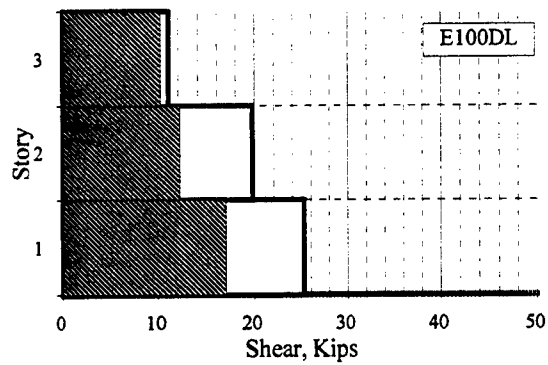
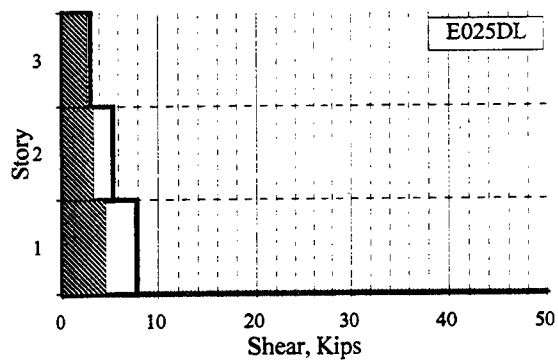
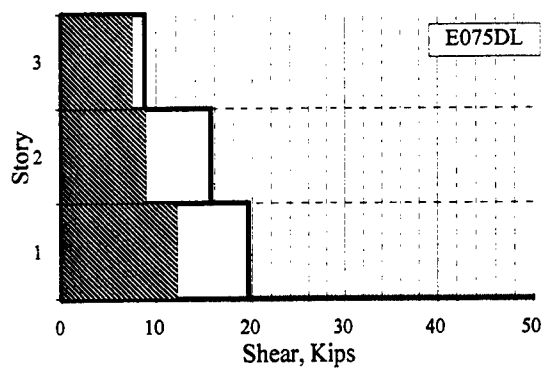
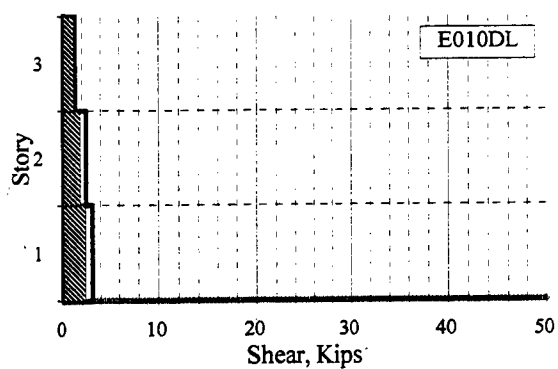


Figure C.13.13 Column Shear Vs. Interstory Displacement: T052DM



□ Story Shear ▨ Column Shear

□ Story Shear ▨ Column Shear

Figure C.13.14 Maximum Column Shear Vs. Maximum Story Shear: E010DL - E125DL

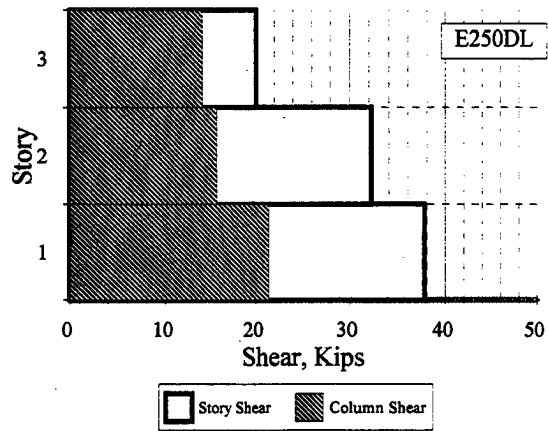
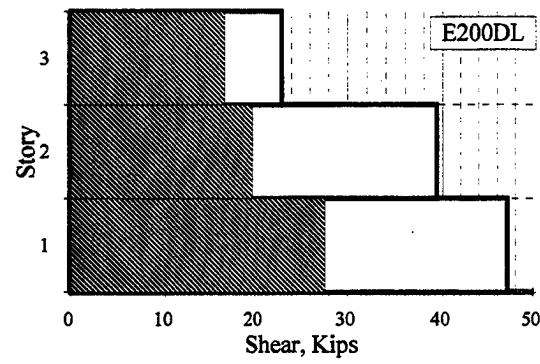
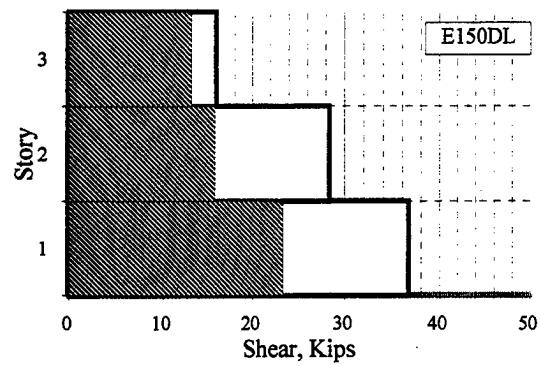
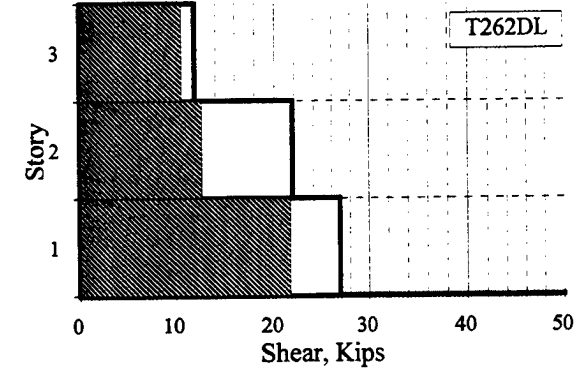
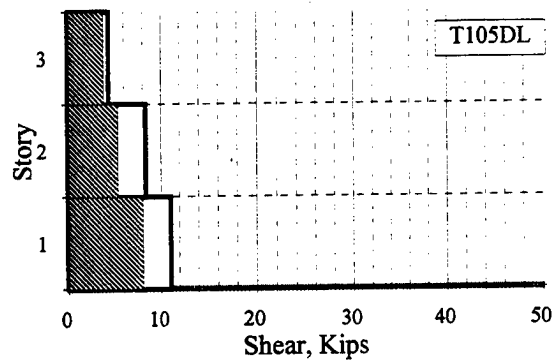
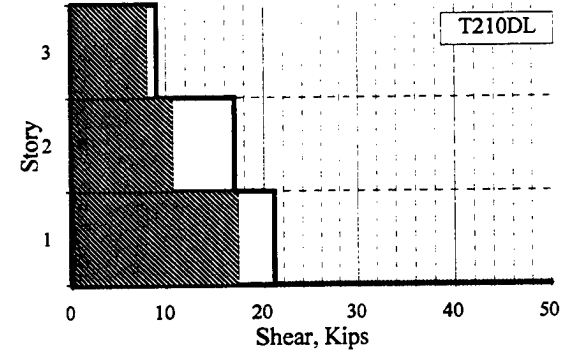
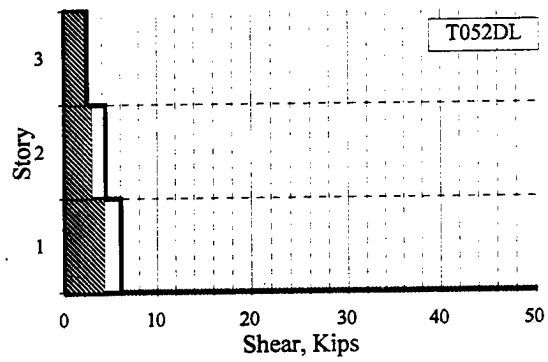
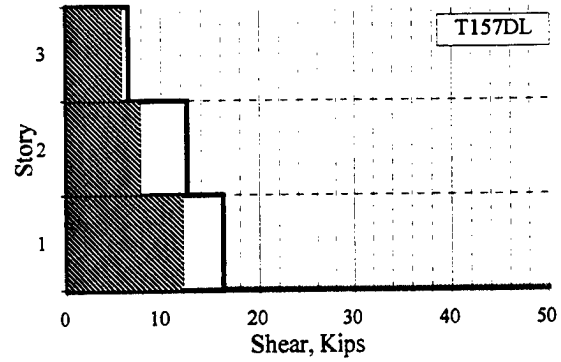
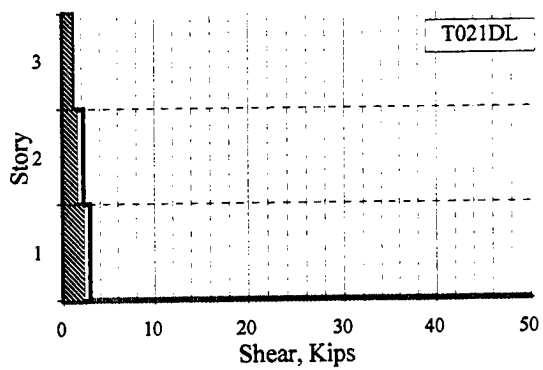


Figure C.13.15 Maximum Column Shear Vs. Maximum Story Shear: E150DL - E205DL



□ Story Shear ▨ Column Shear

□ Story Shear ▨ Column Shear

Figure C.13.16 Maximum Column Shear Vs. Maximum Story Shear: T021DL - T262DL

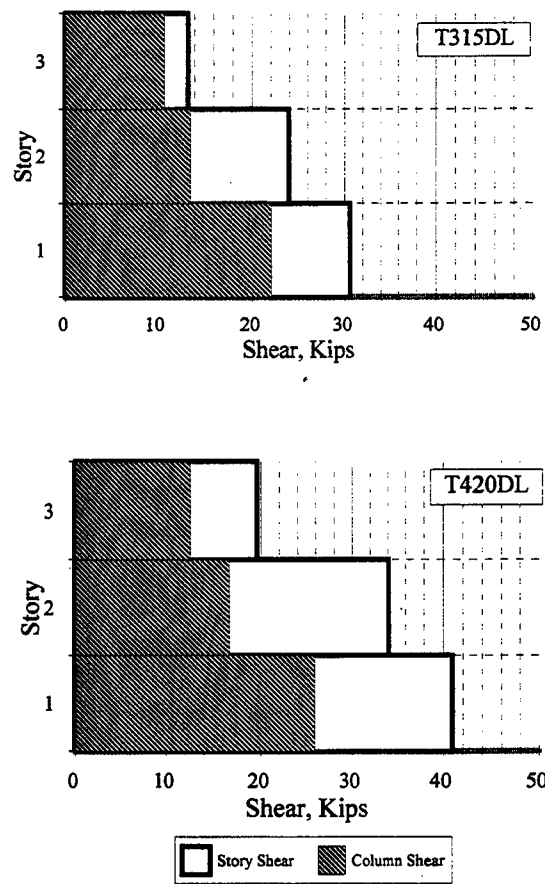


Figure C.13.17 Maximum Column Shear Vs. Maximum Story Shear: T315DL - T420DL

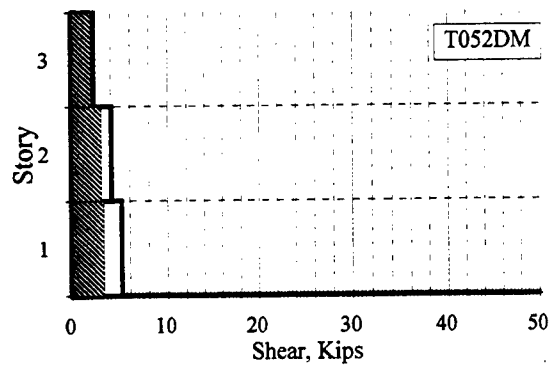
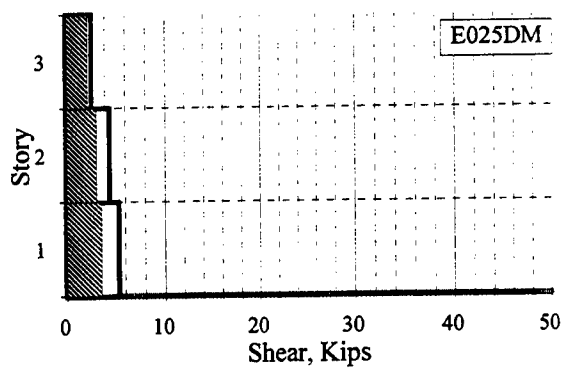
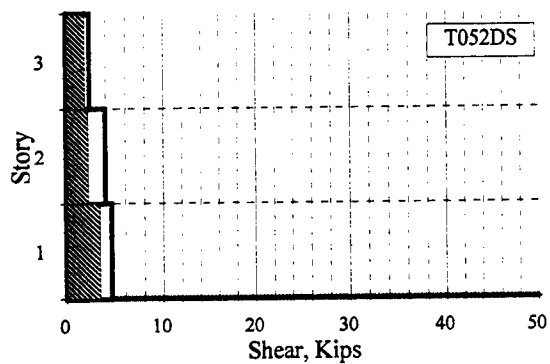
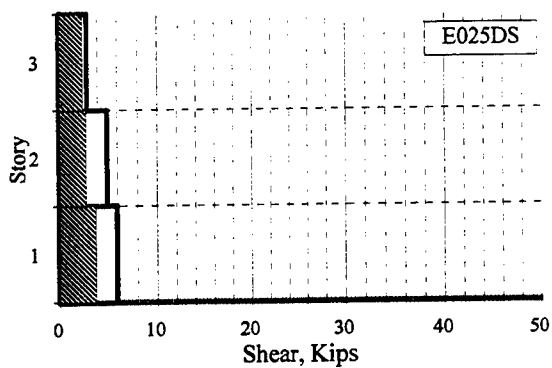
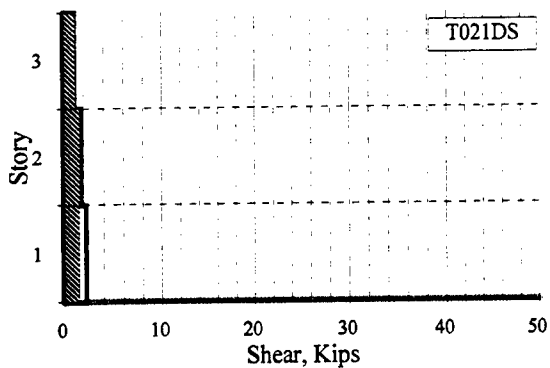
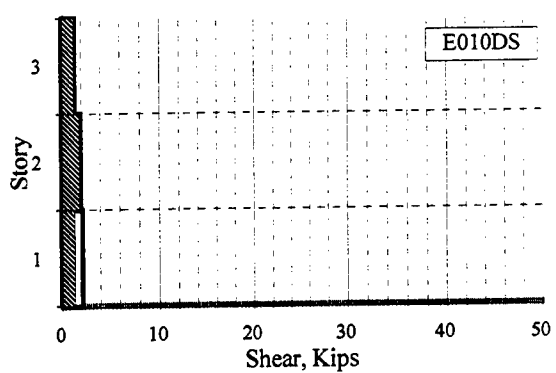


Figure C.13.18 Maximum Column Shear Vs. Maximum Story Shear: E010DS - T052DM

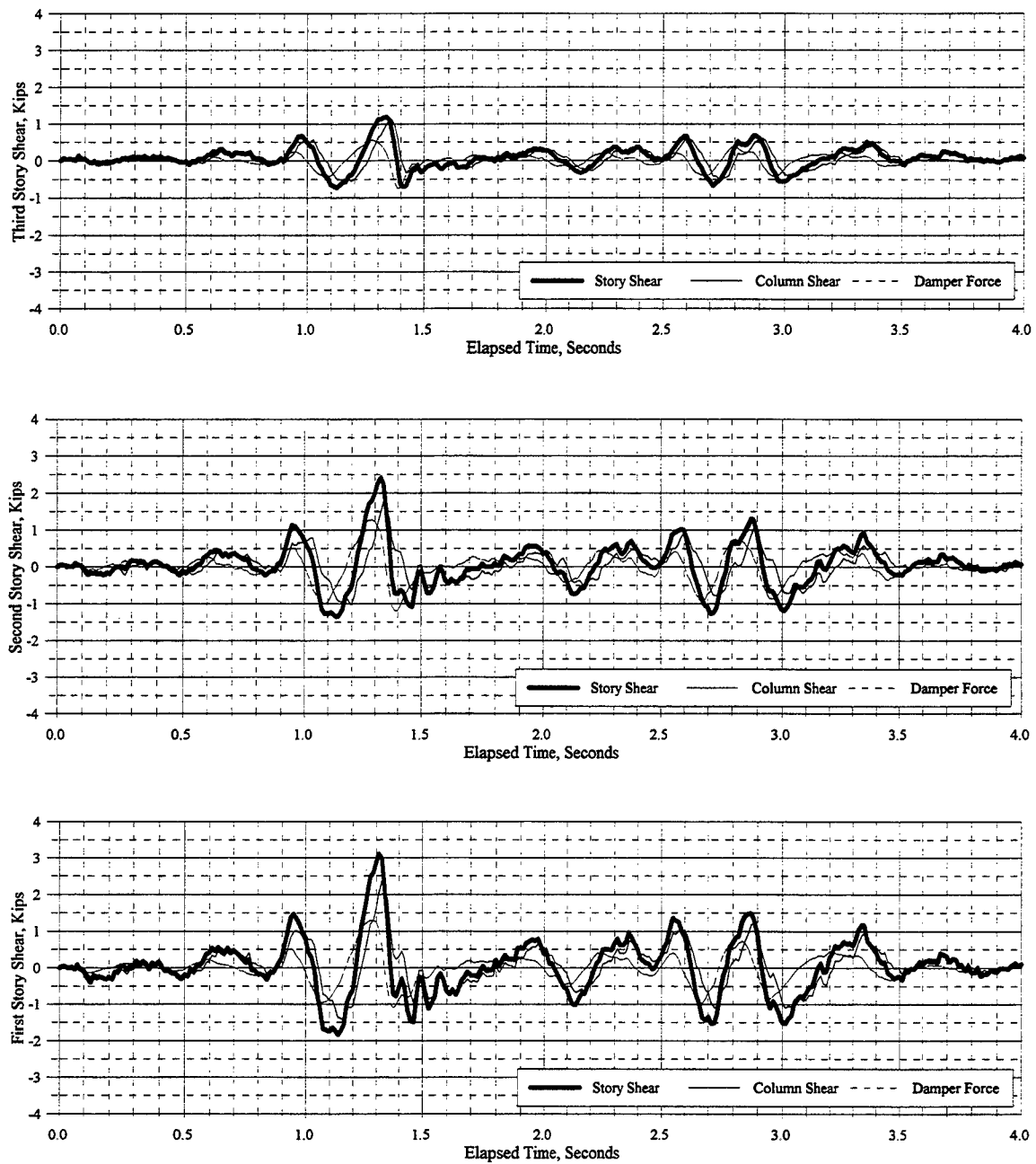


Figure C.14.1 Story Shear, Column Shear, and Sum of Horizontal Component of Damper Forces: E010DL

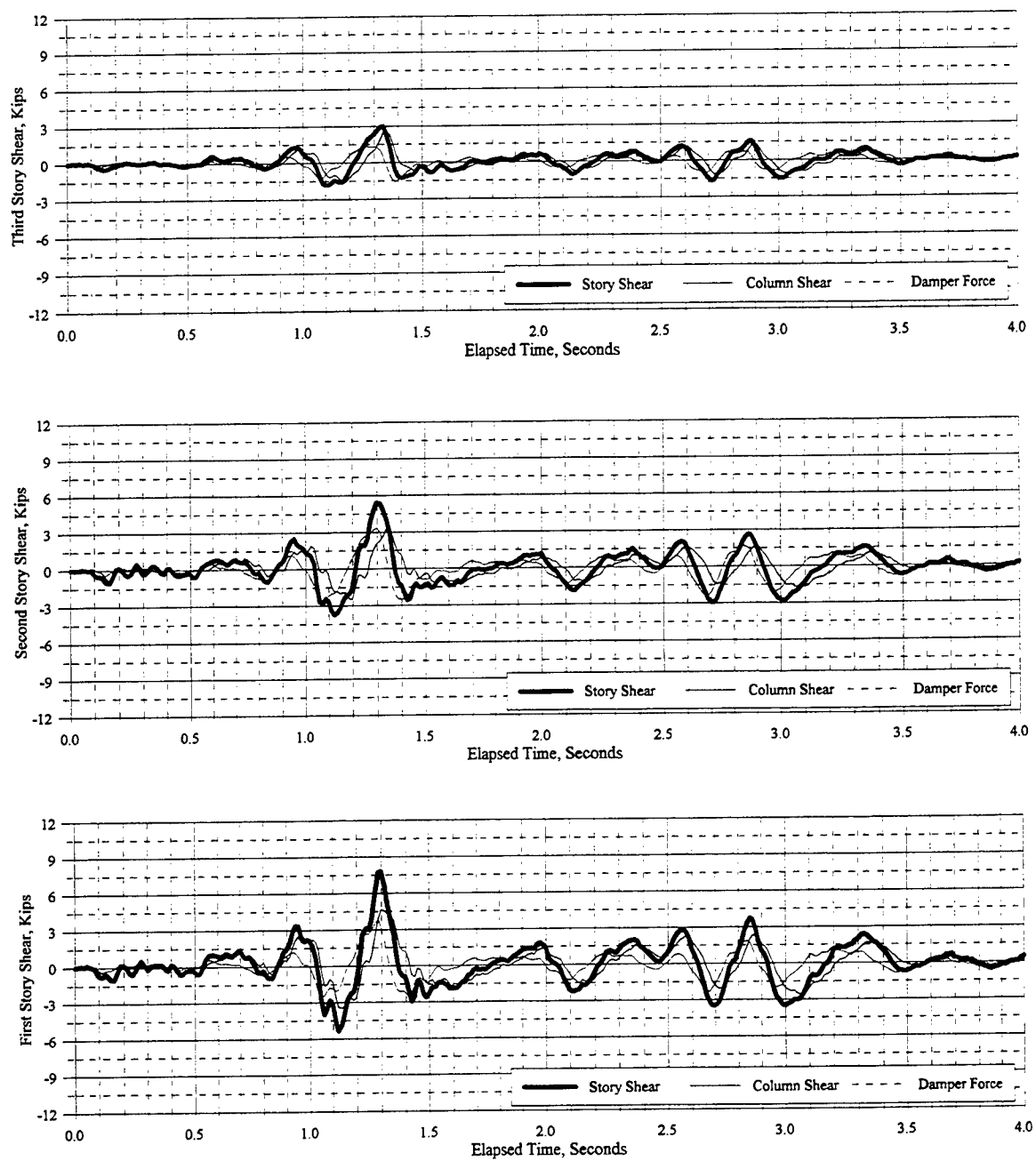


Figure C.14.2 Story Shear, Column Shear, and Sum of Horizontal Component of Damper Forces: E025DL

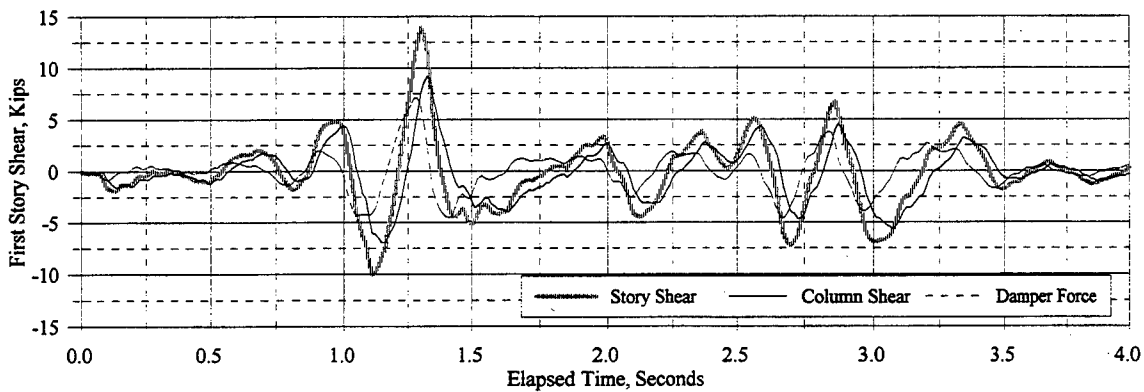
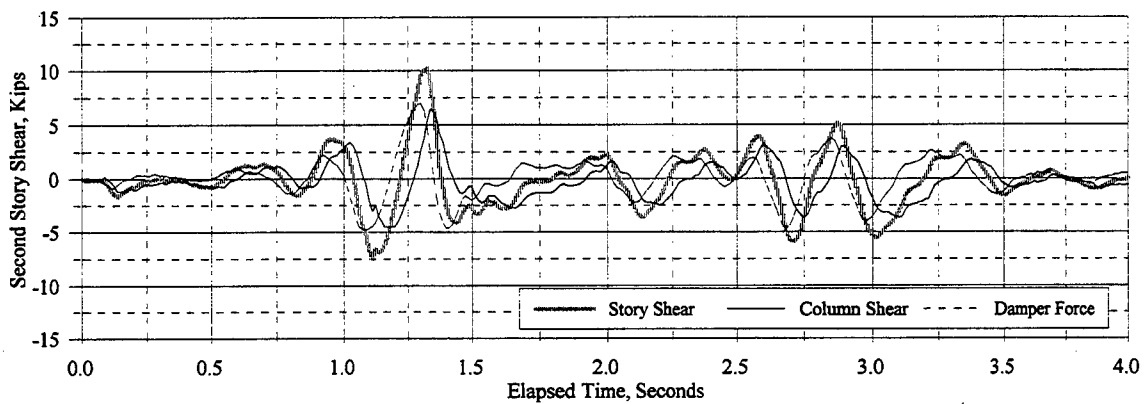
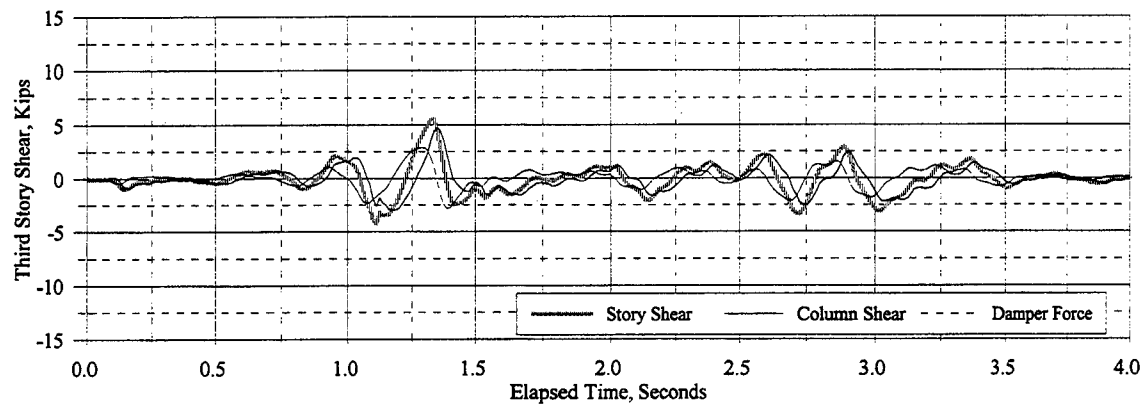


Figure C.14.3 Story Shear, Column Shear, and Sum of Horizontal Components of Damper Forces: E050DL

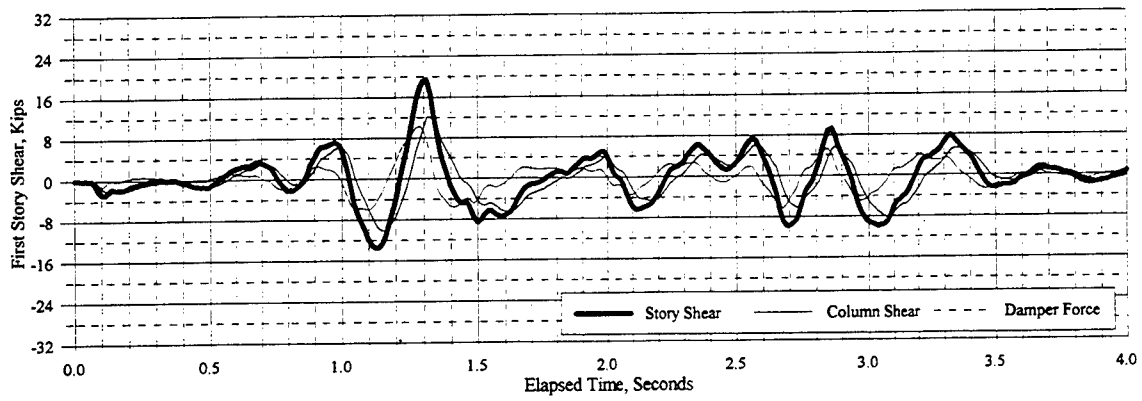
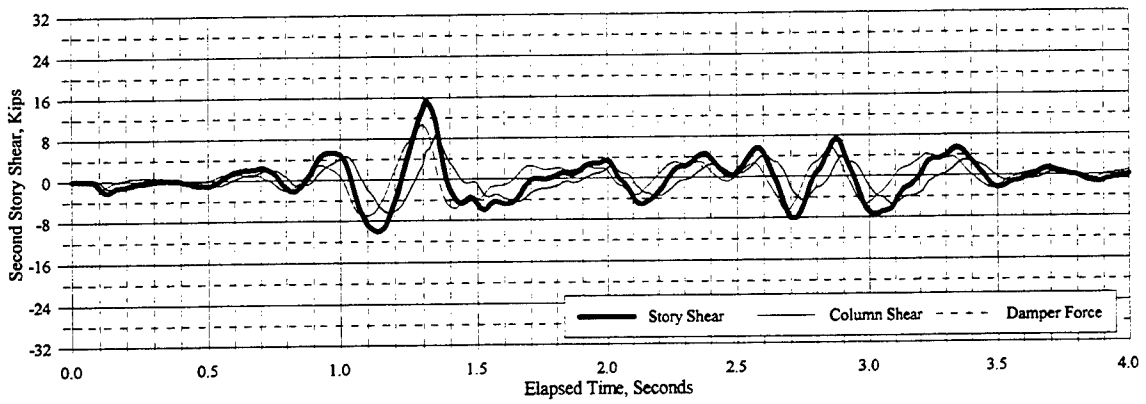
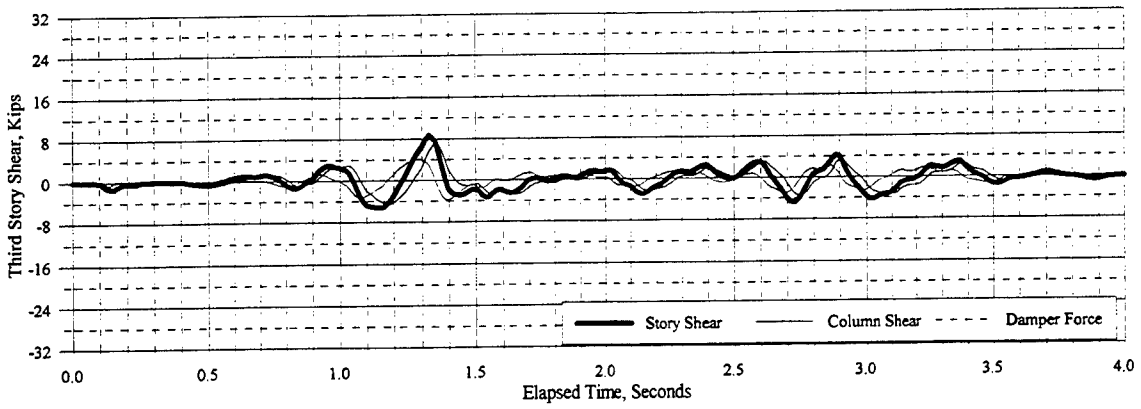


Figure C.14.4 Story Shear, Column Shear, and Sum of Horizontal Components of Damper Forces: E075DL

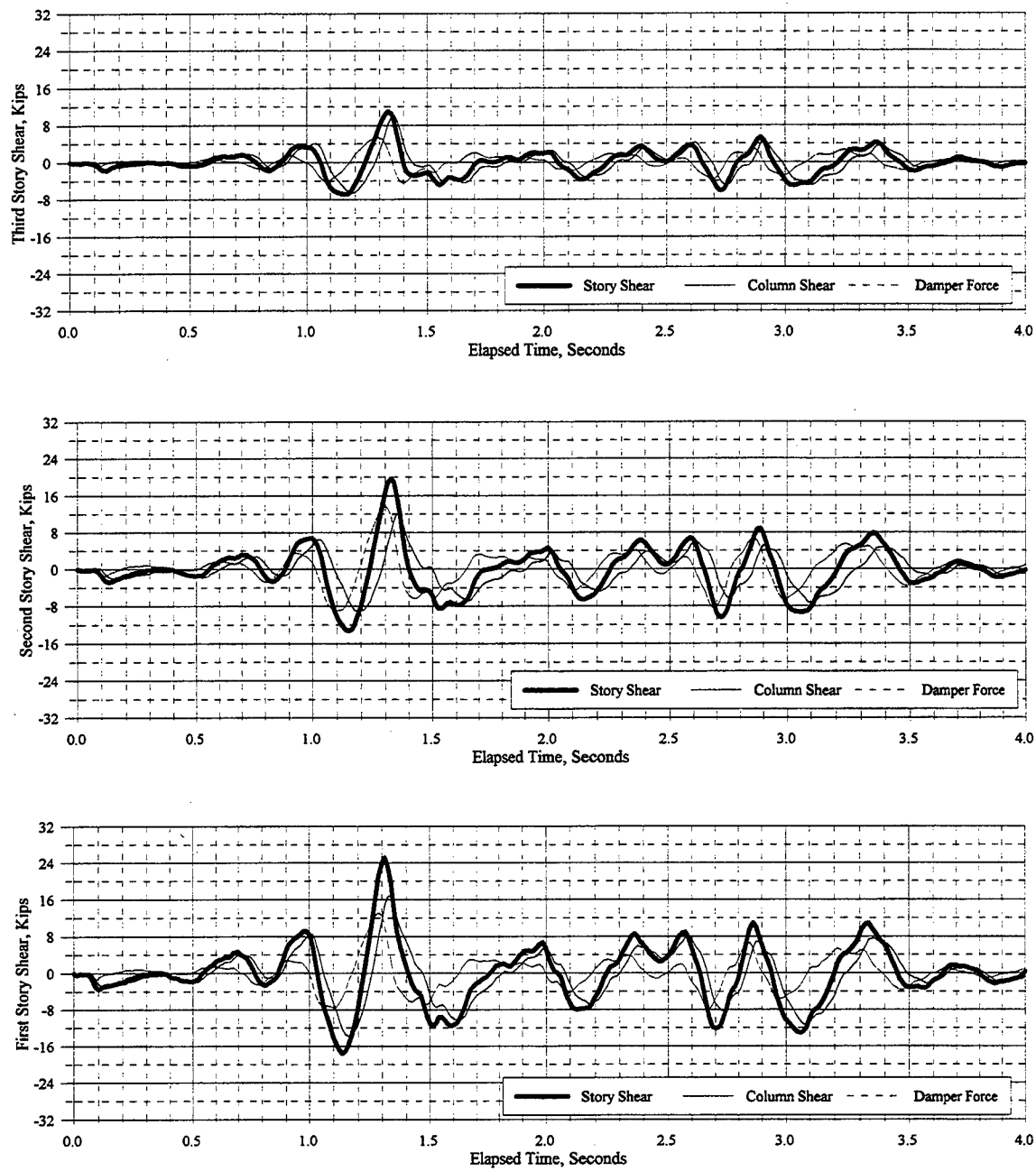


Figure C.14.5 Story Shear, Column Shear, and Sum of Horizontal Components of Damper Forces: E100DL

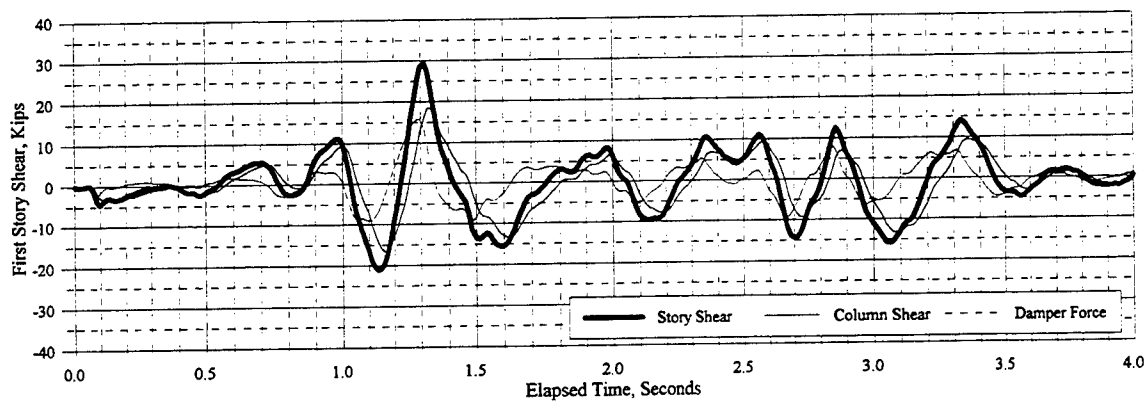
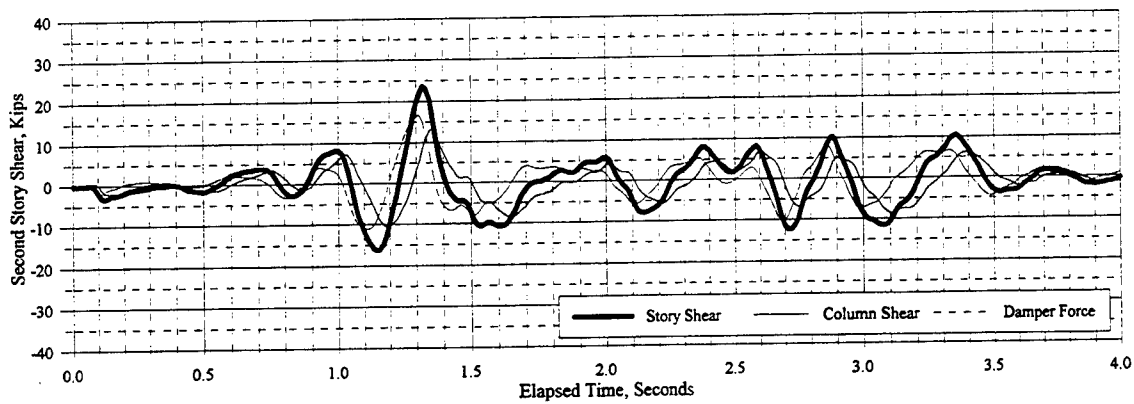
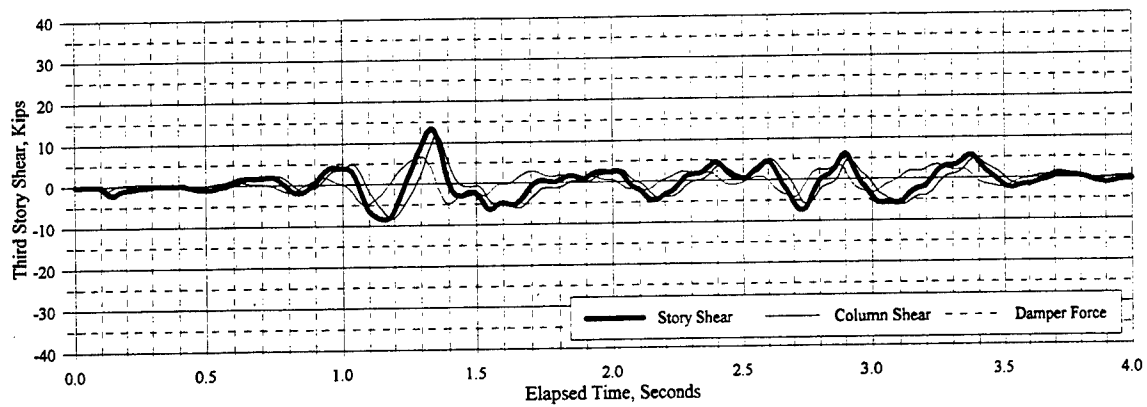


Figure C.14.6 Story Shear, Column Shear, and Sum of Horizontal Components of Damper Forces: E125DL

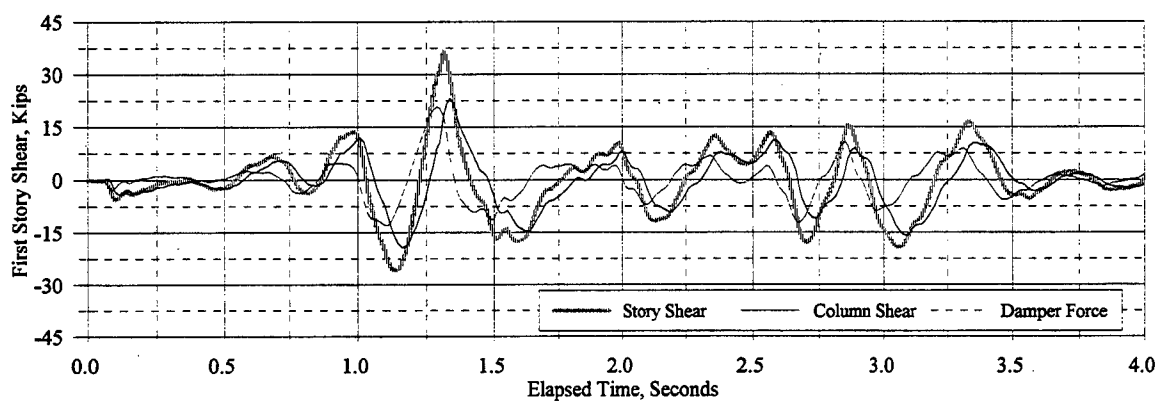
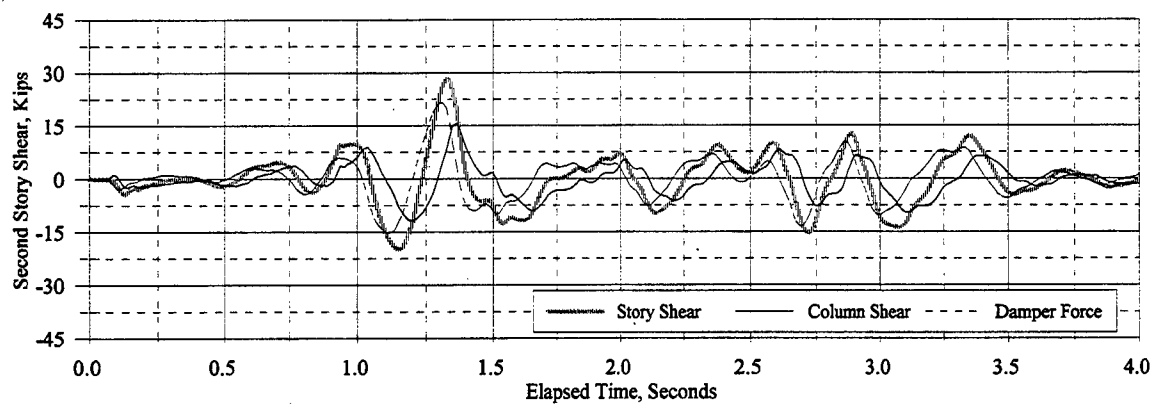
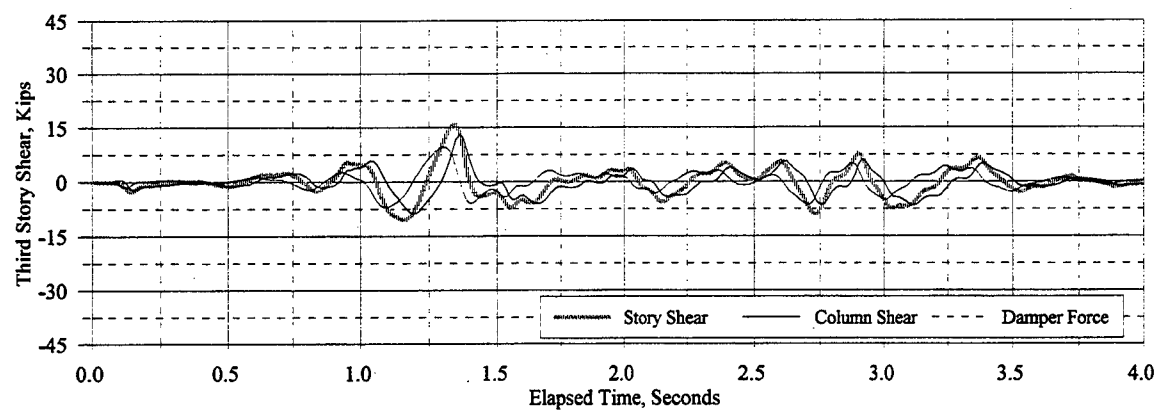


Figure C.14.7 Story Shear, Column Shear, and Sum of Horizontal Components of Damper Forces: E150DL

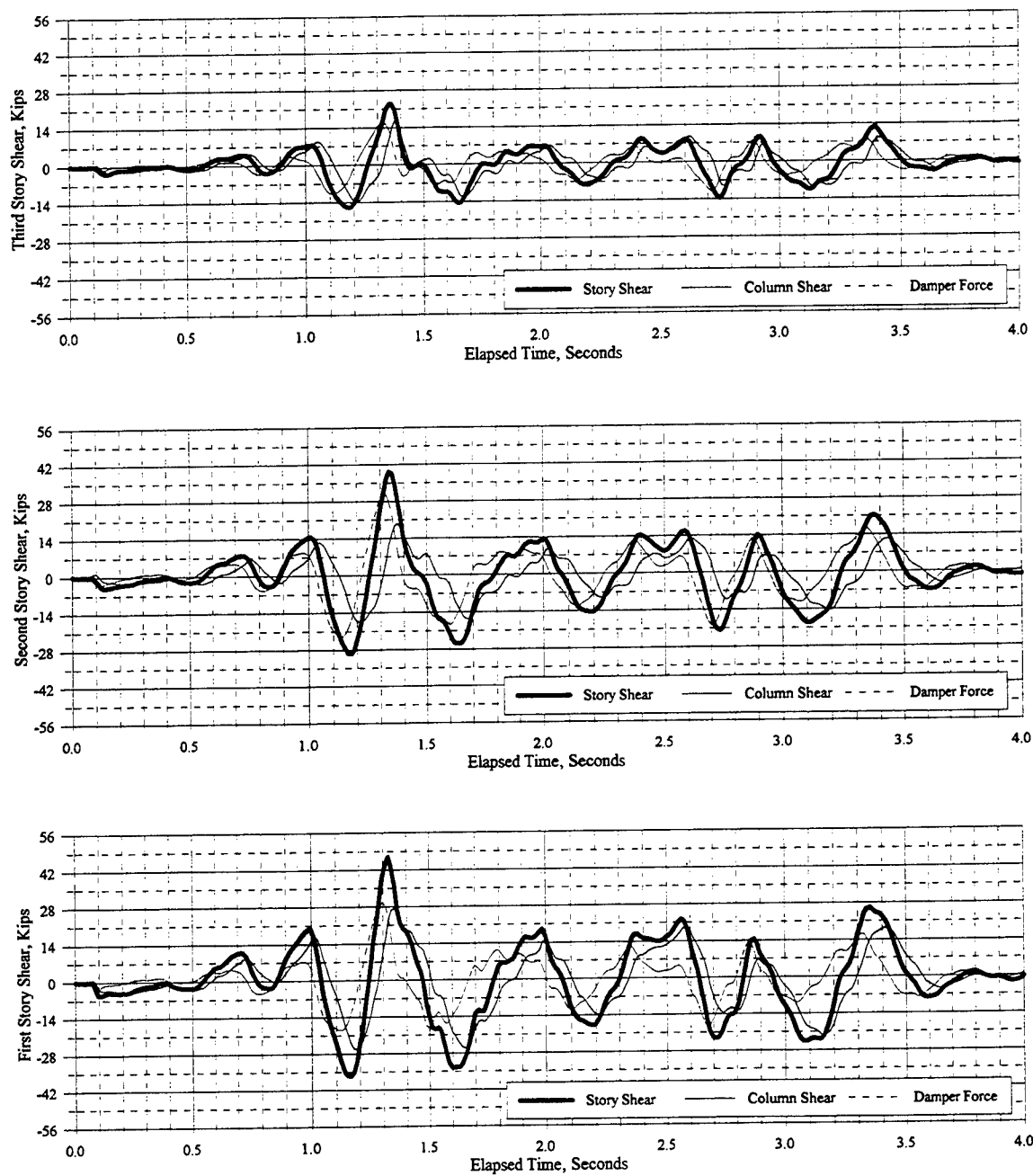


Figure C.14.8 Story Shear, Column Shear, and Sum of Horizontal Components of Damper Forces: E200DL

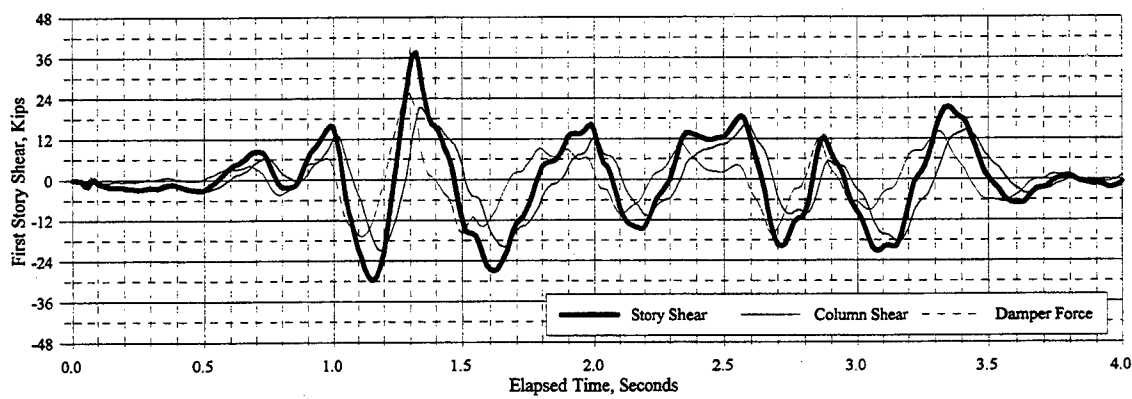
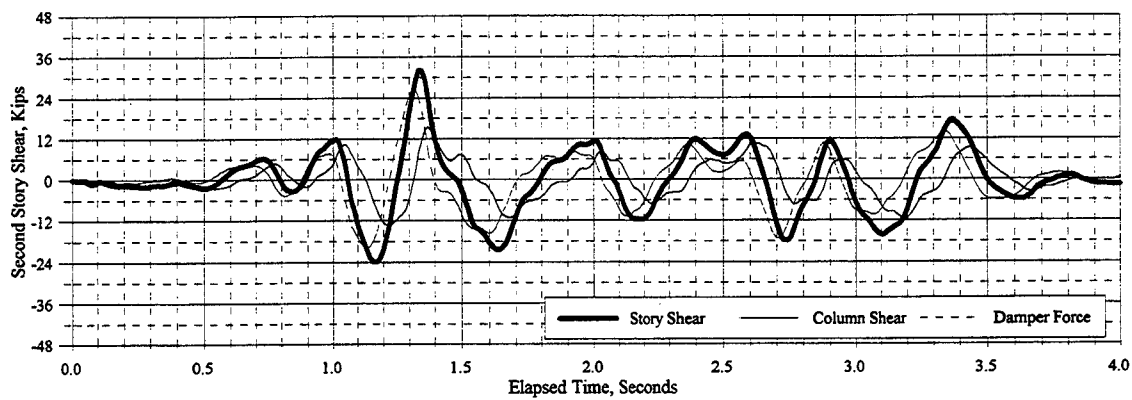
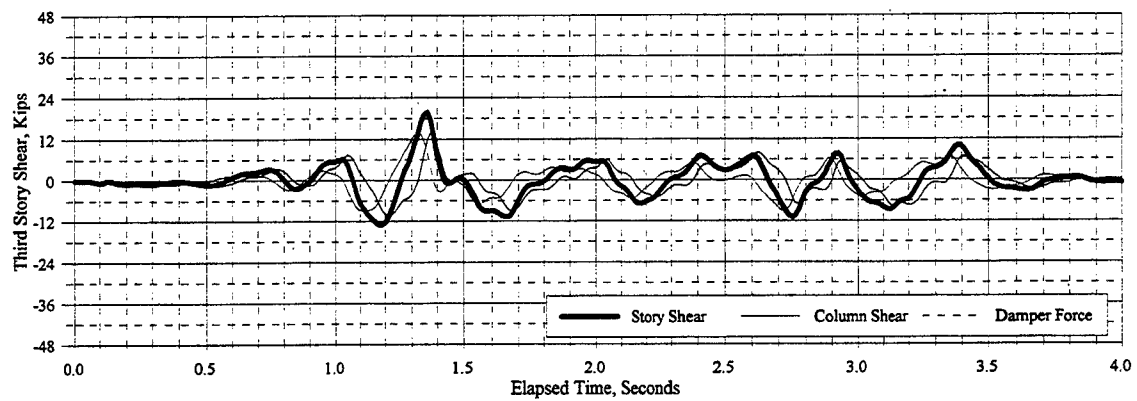


Figure C.14.9 Story Shear, Column Shear, and Sum of Horizontal Components of Damper Forces: E250DL

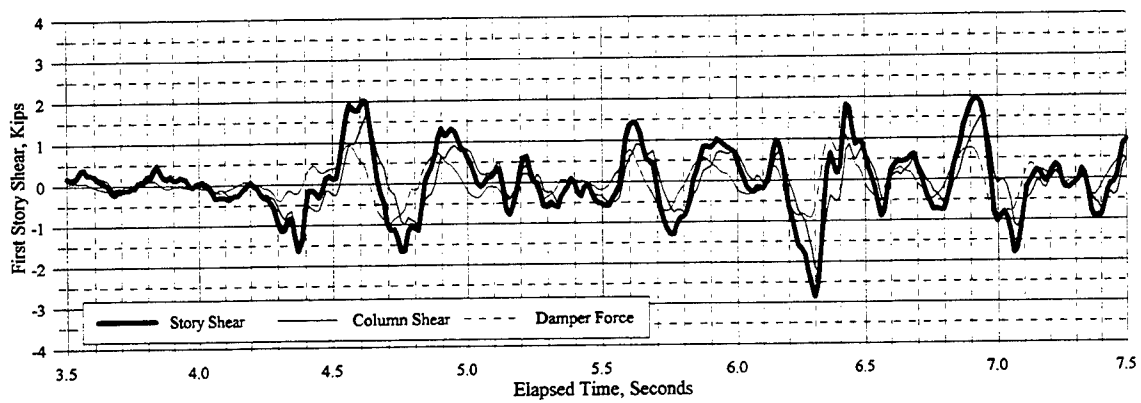
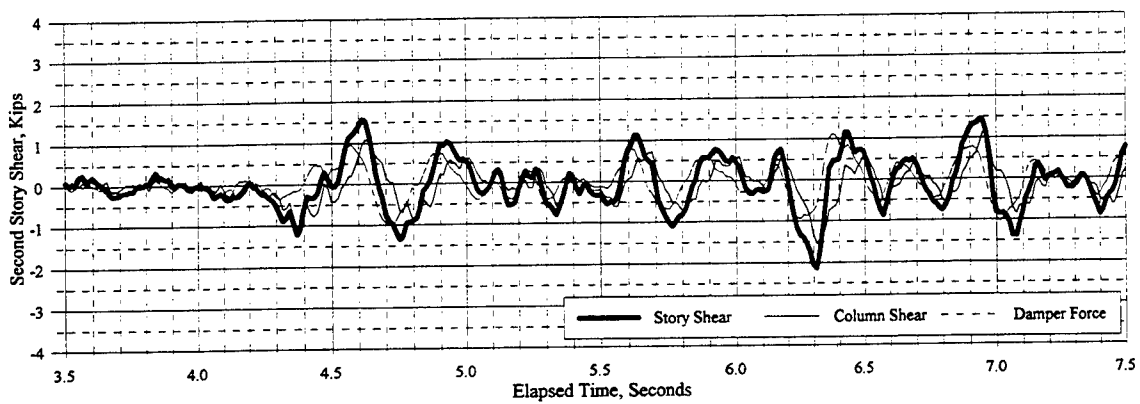
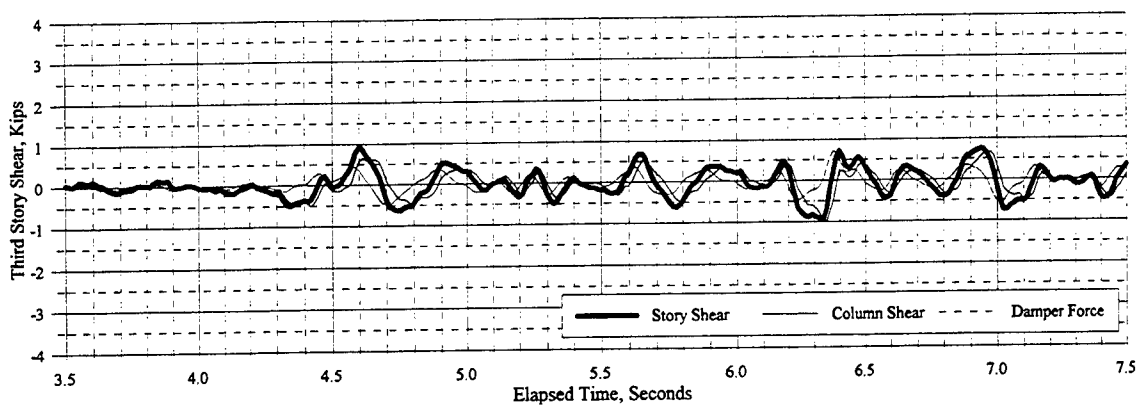


Figure C.14.10 Story Shear, Column Shear, and Sum of Horizontal Components of Damper Forces: T021DL

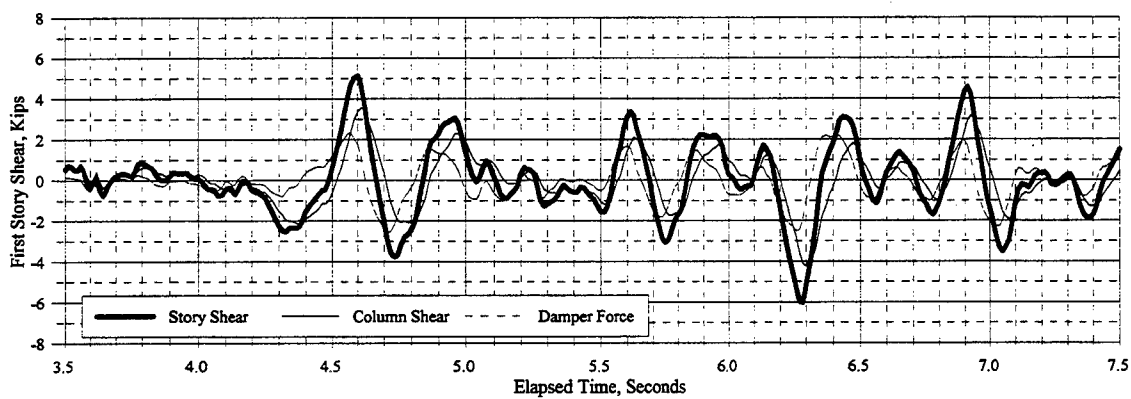
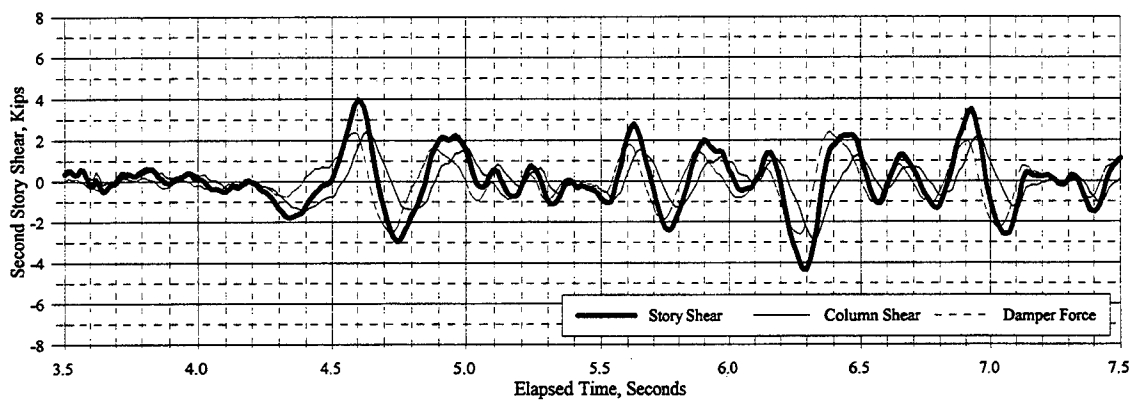
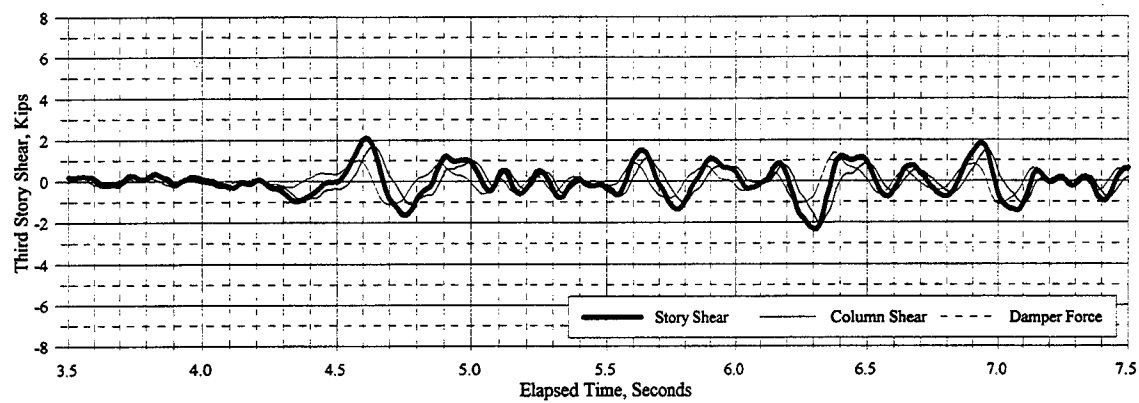


Figure C.14.11 Story Shear, Column Shear, and Sum of Horizontal Components of Damper Forces: T052DL

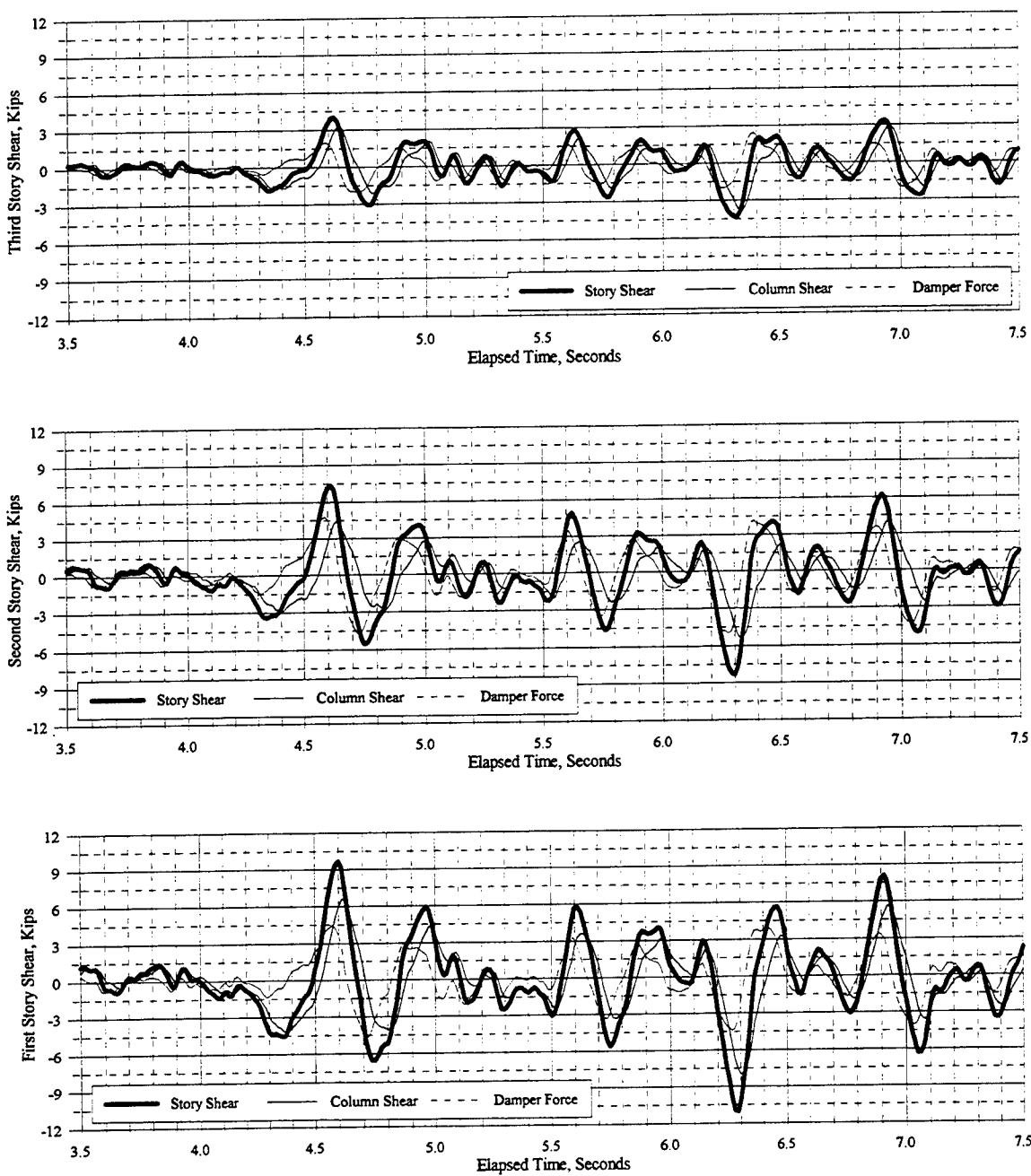


Figure C.14.12 Story Shear, Column Shear, and Sum of Horizontal Components of Damper Forces: T105DL

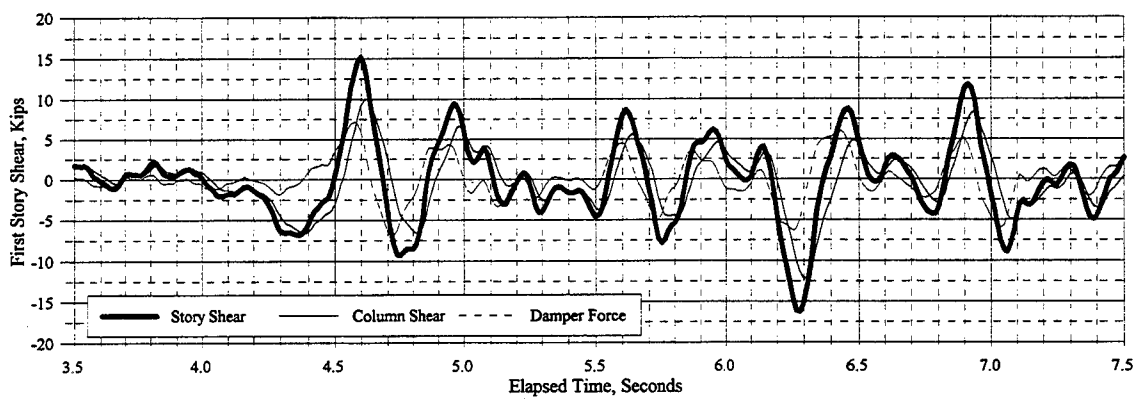
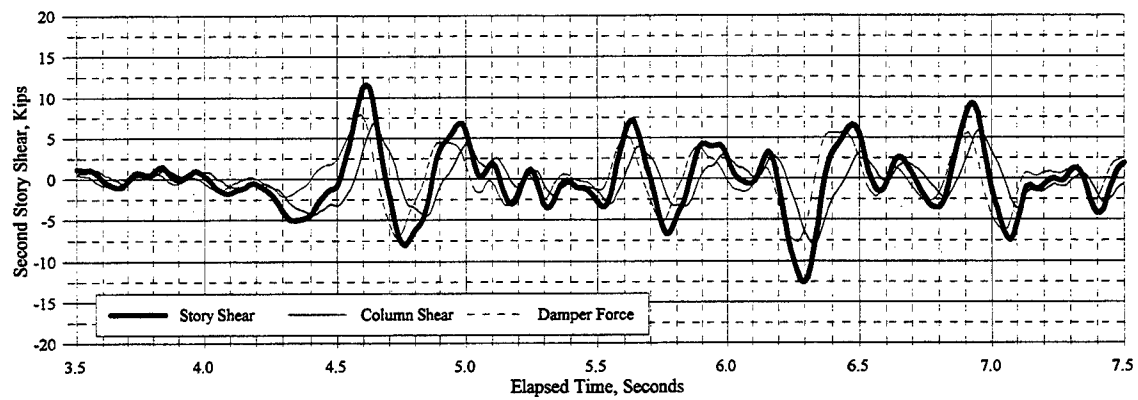
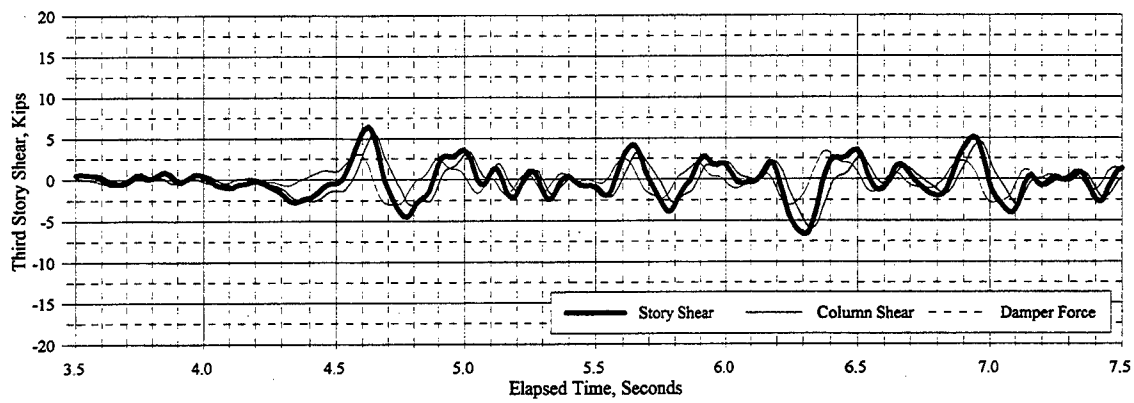


Figure C.14.13 Story Shear, Column Shear, and Sum of Horizontal Components of Damper Forces: T157DL

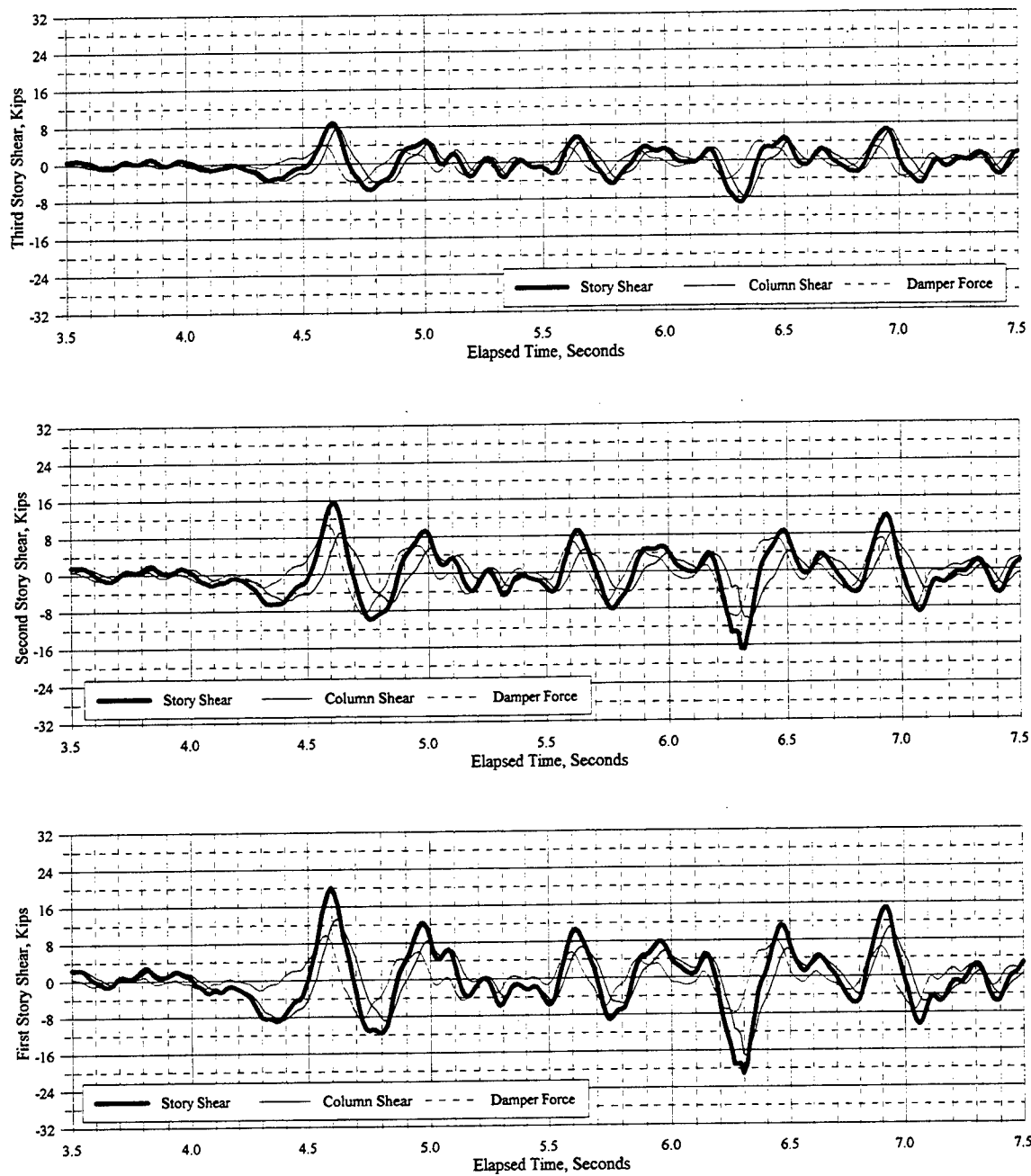


Figure C.14.14 Story Shear, Column Shear, and Sum of Horizontal Components of Damper Forces: T210DL

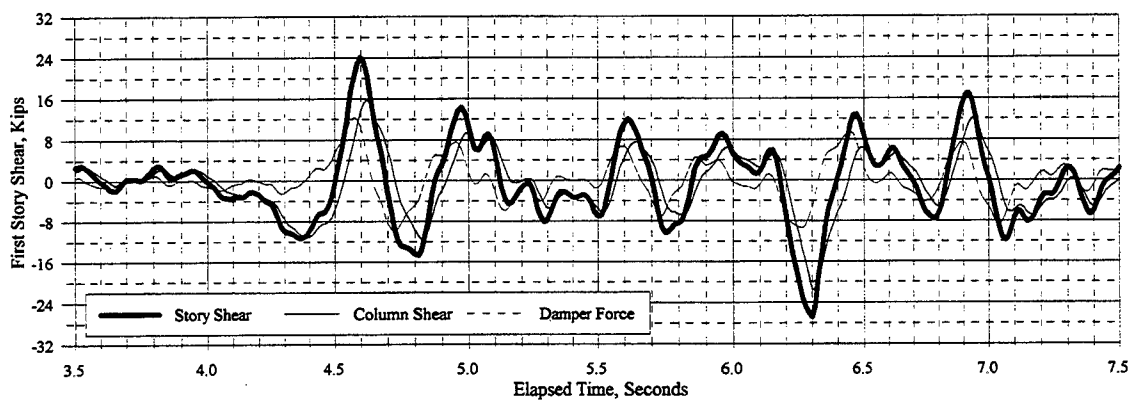
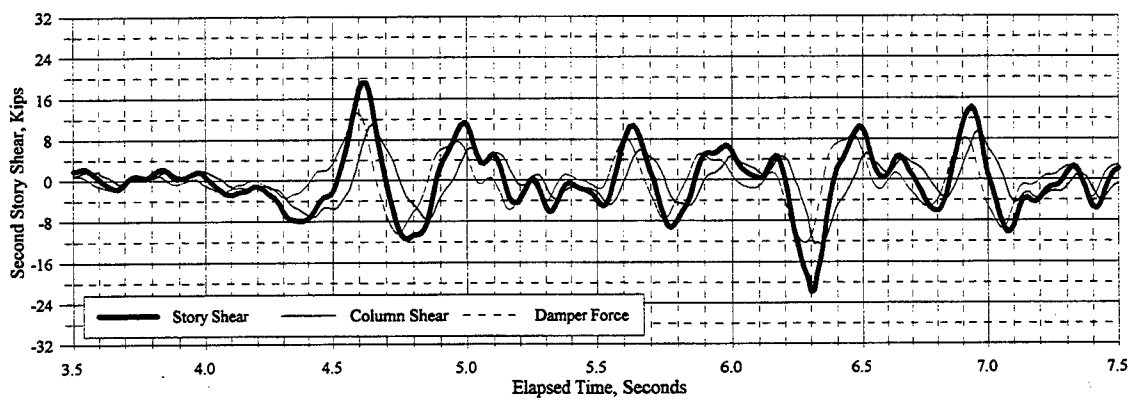
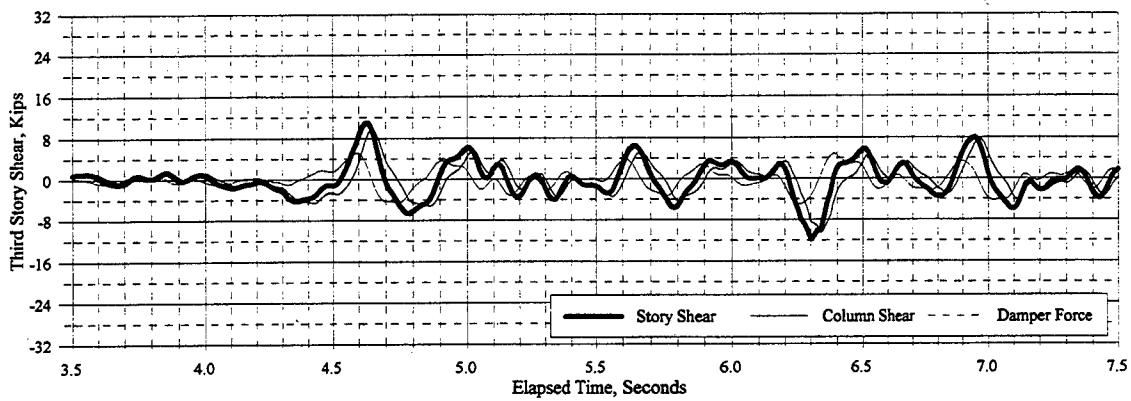


Figure C.14.15 Story Shear, Column Shear, and Sum of Horizontal Components of Damper Forces: T262DL

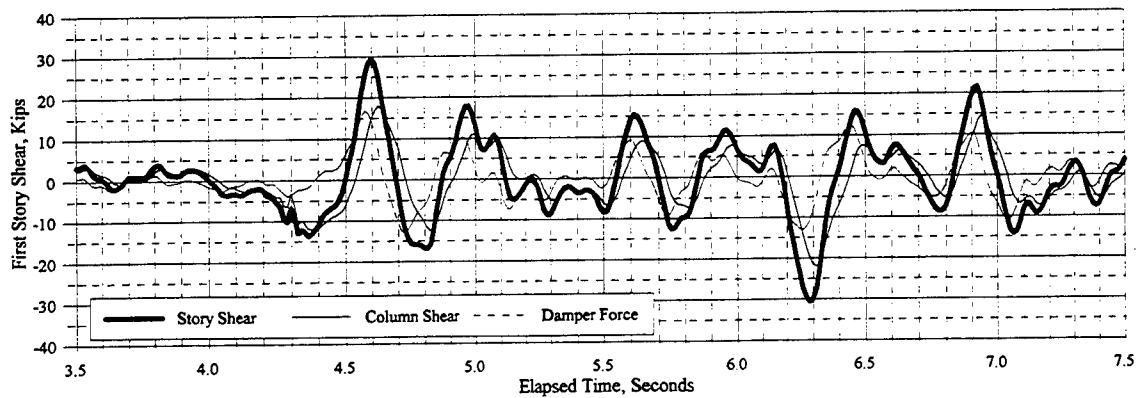
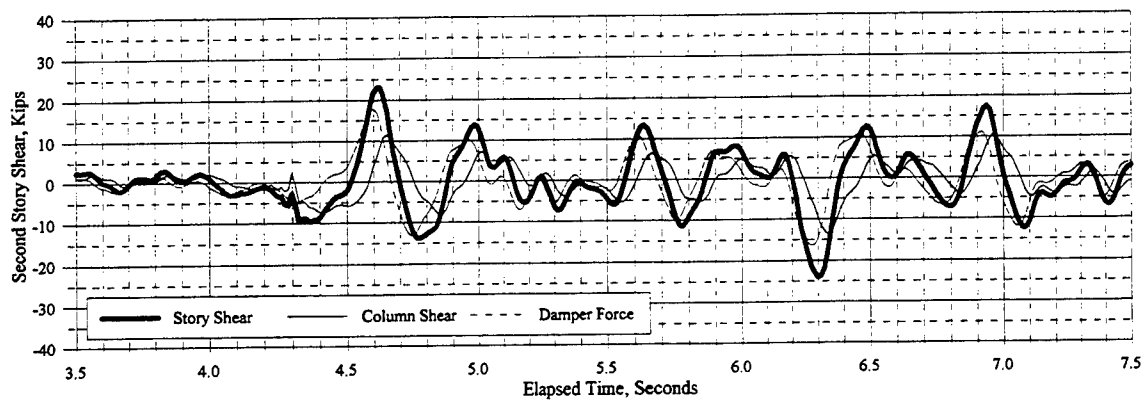
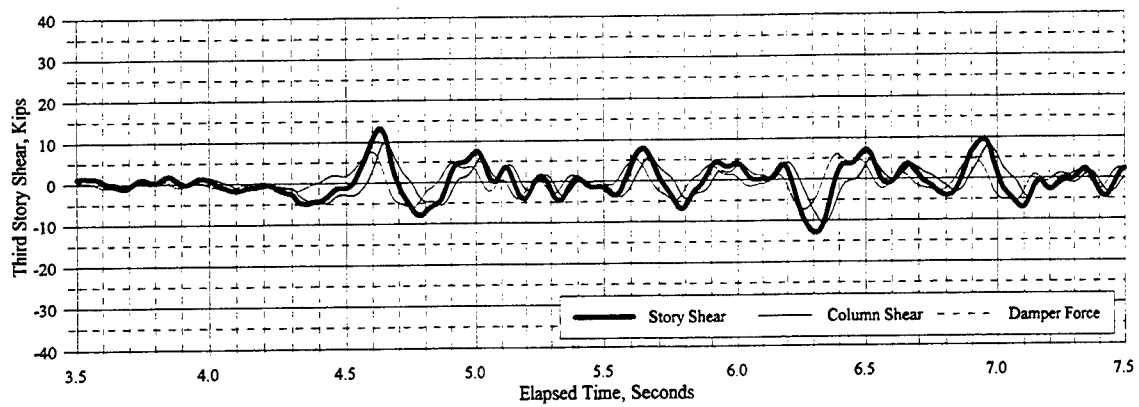


Figure C.14.16 Story Shear, Column Shear, and Sum of Horizontal Components of Damper Forces: T315DL

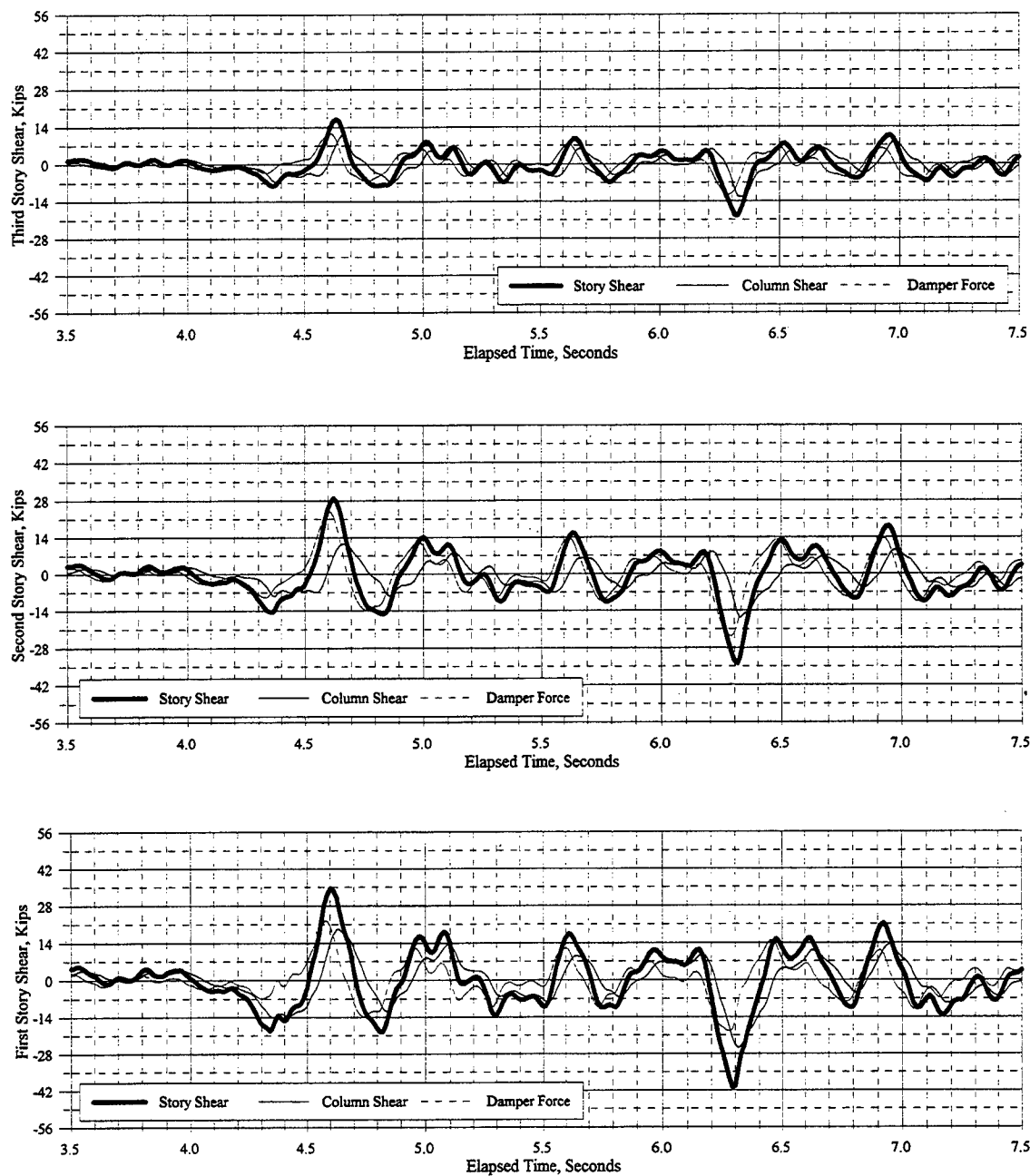


Figure C.14.17 Story Shear, Column Shear, and Sum of Horizontal Components of Damper Forces: T420DL

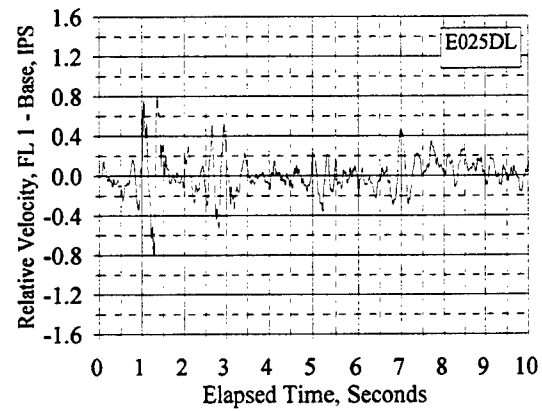
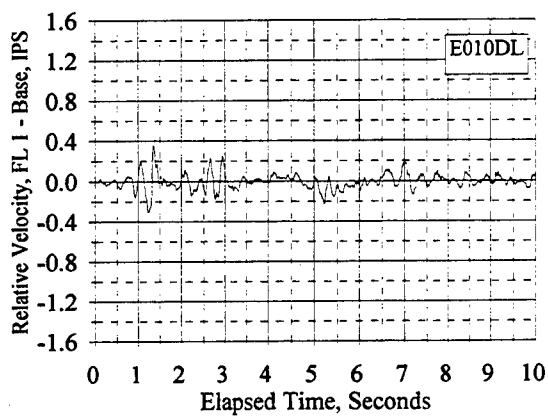
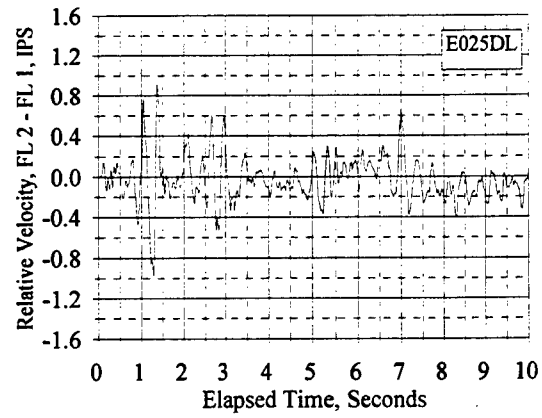
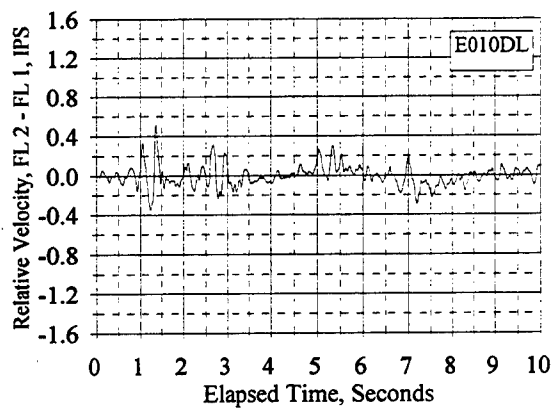
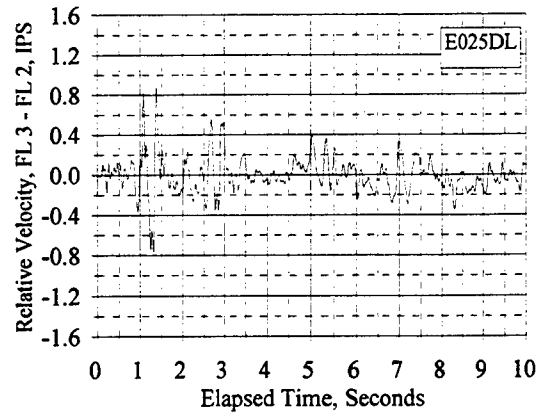
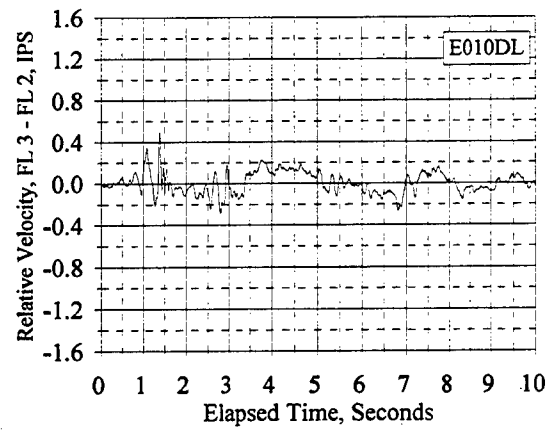


Figure C.15.1 Relative Floor Velocities: E010DL, E025DL

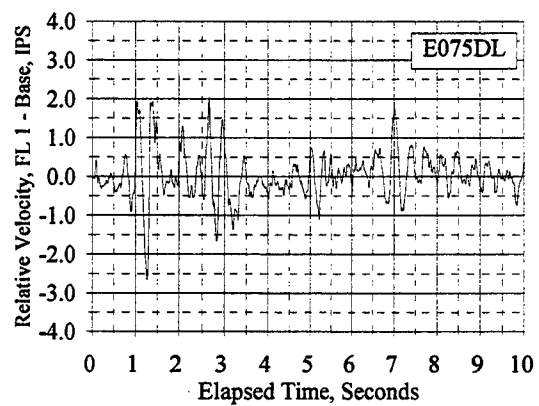
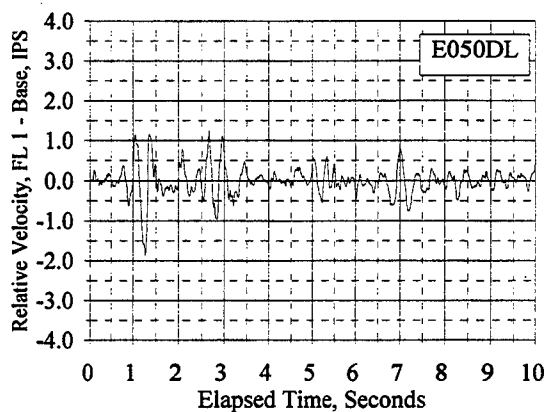
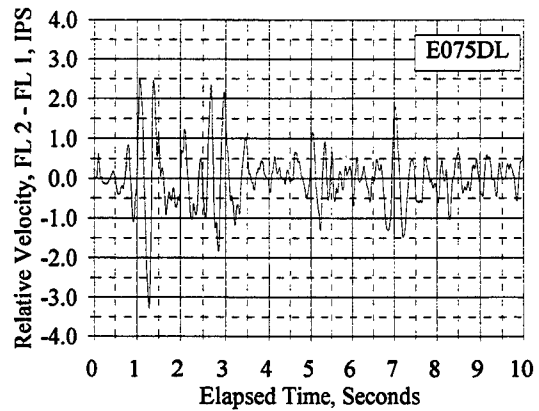
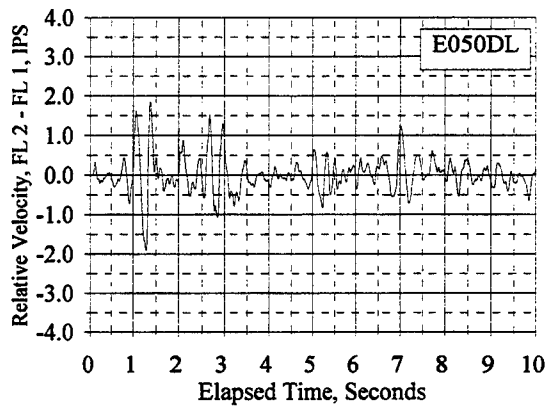
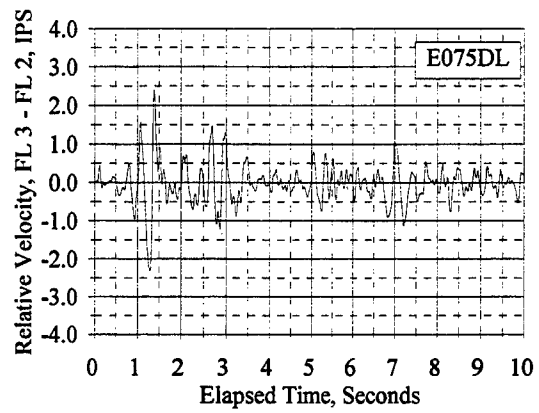
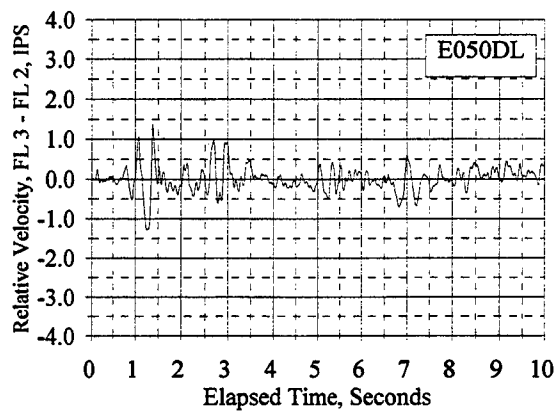


Figure C.15.2 Relative Floor Velocities: E050DL, E075DL

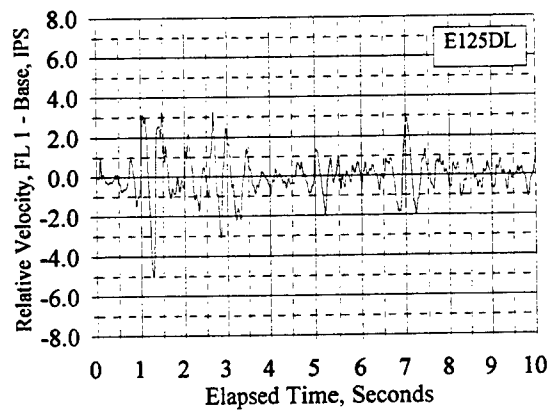
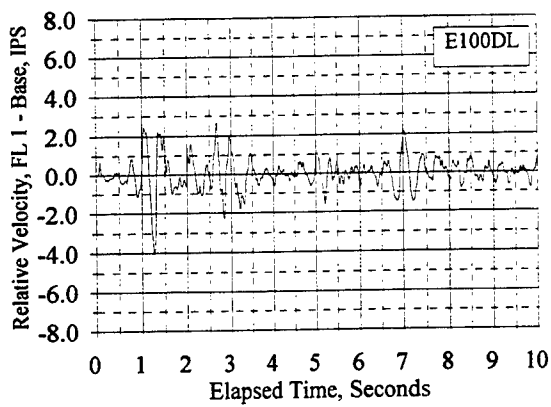
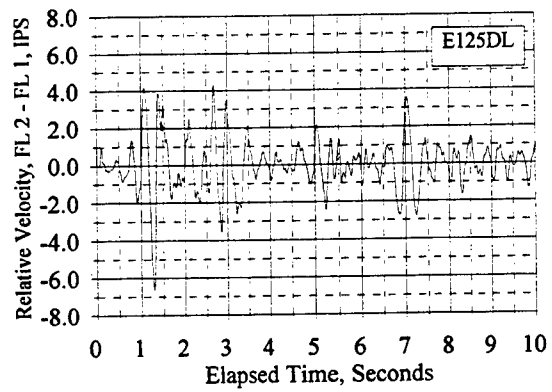
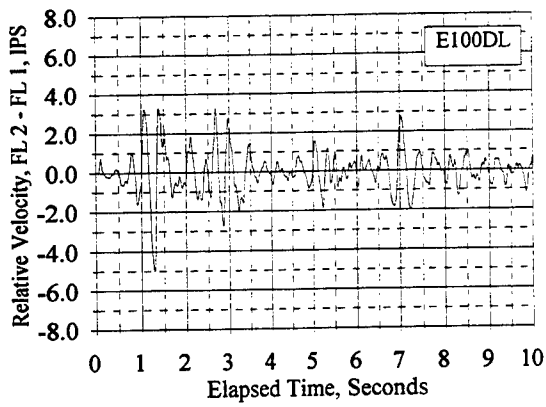
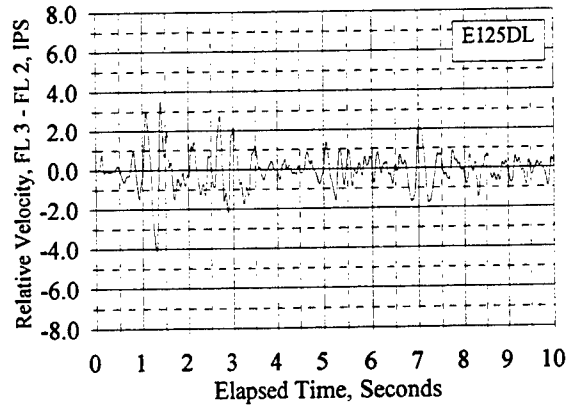
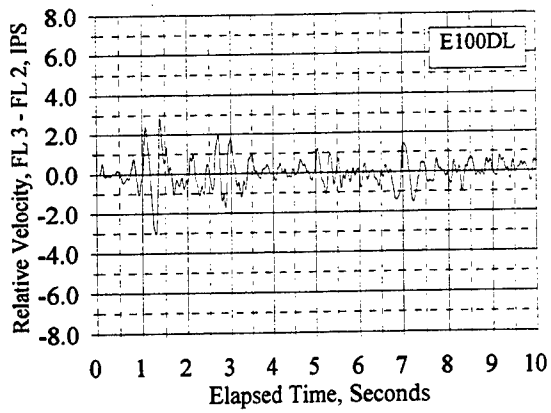


Figure C.15.3 Relative Floor Velocities: E100DL, E125DL

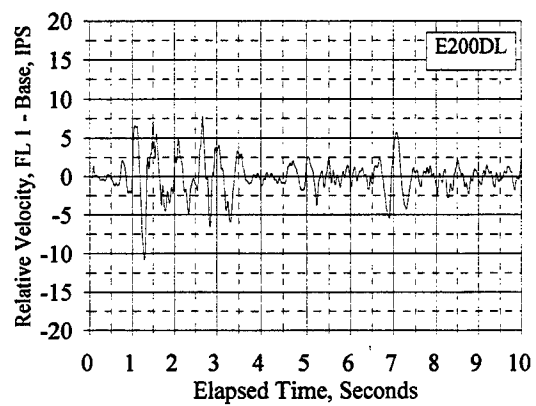
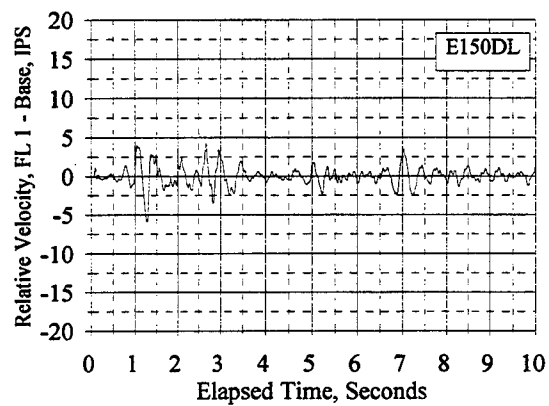
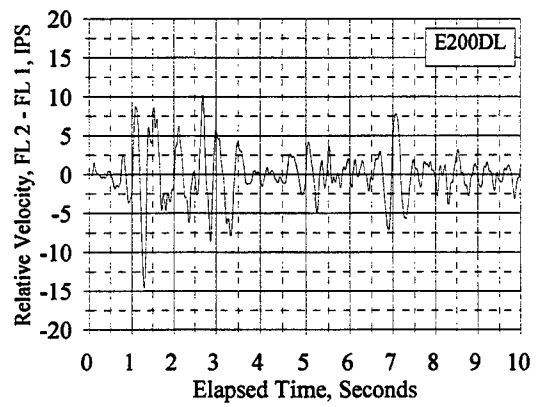
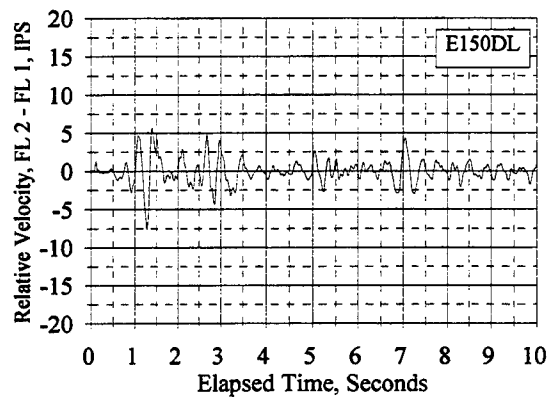
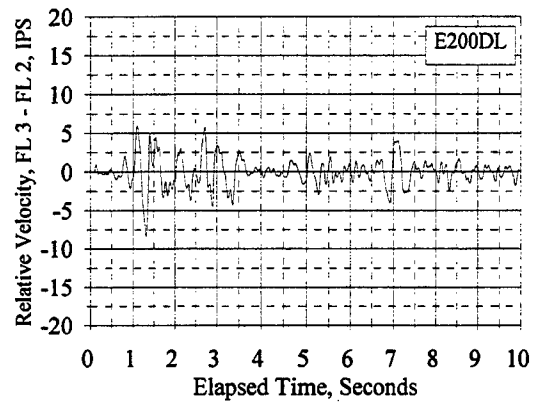
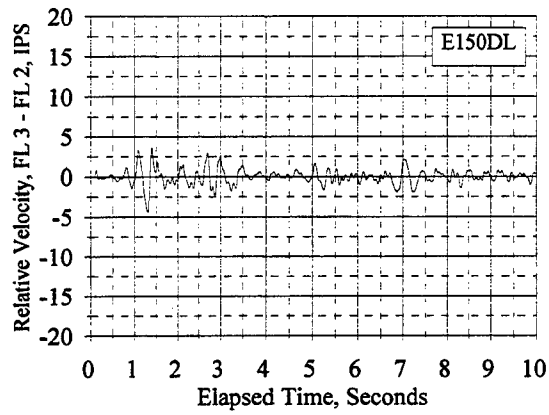


Figure C.15.4 Relative Floor Velocities: E150DL, E200DL

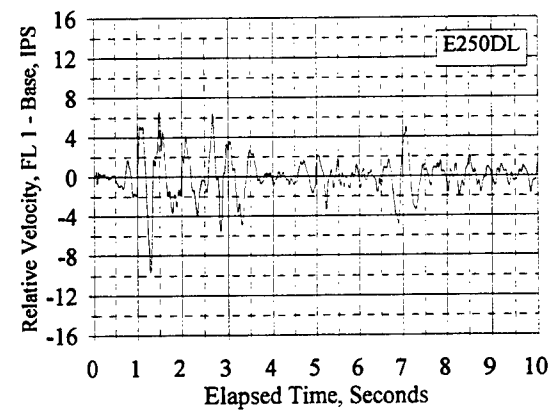
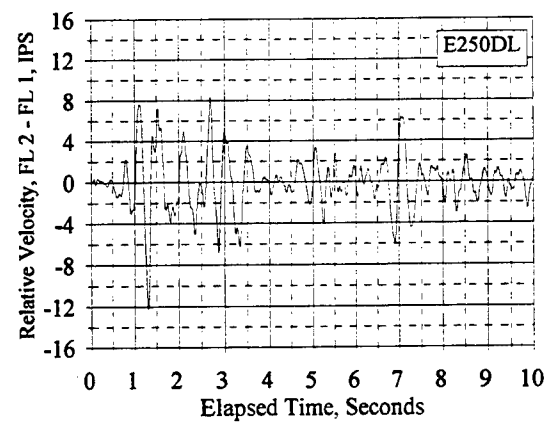
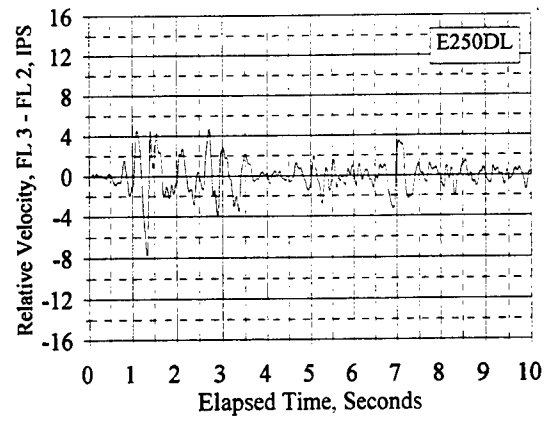


Figure C.15.5 Relative Floor Velocities: E250DL

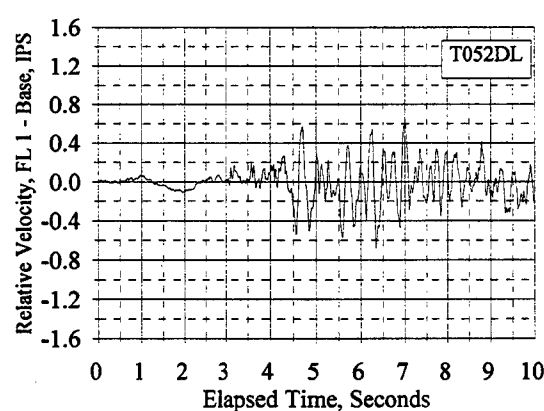
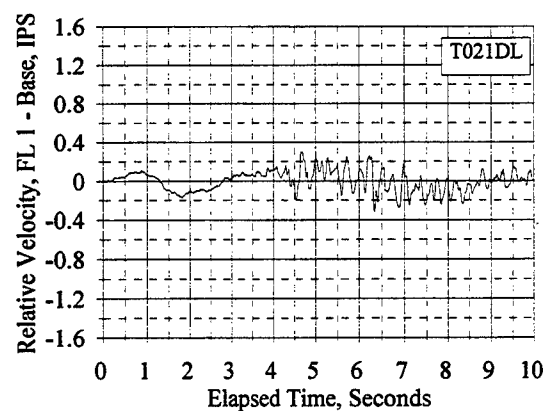
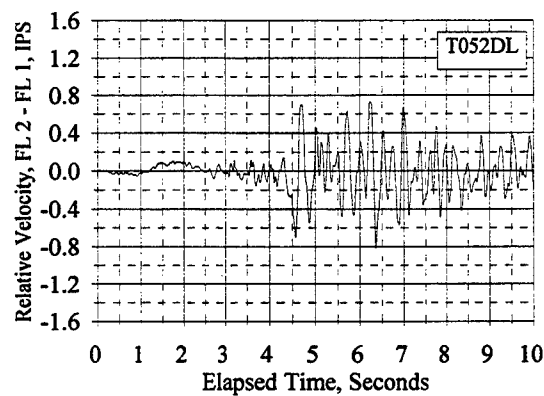
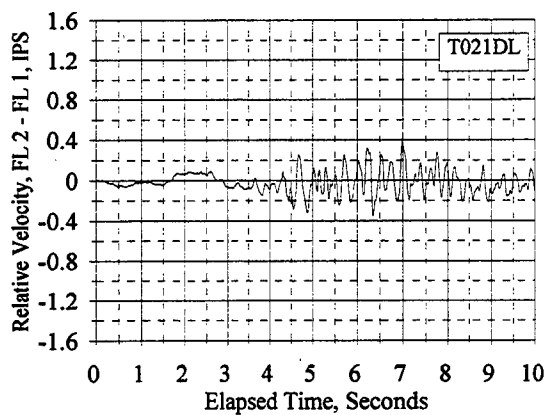
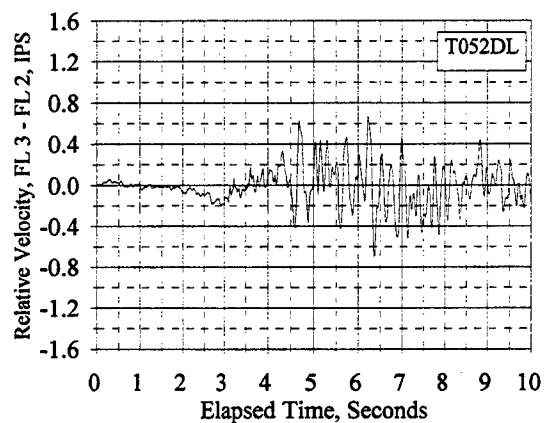
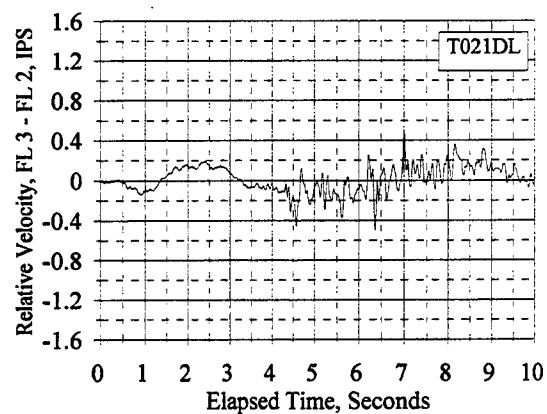


Figure C.15.6 Relative Floor Velocities: T021DL, T052DL

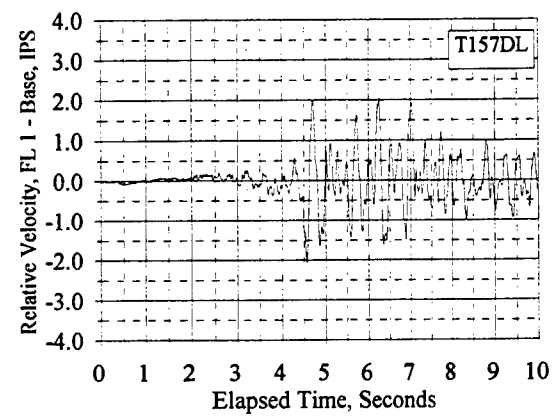
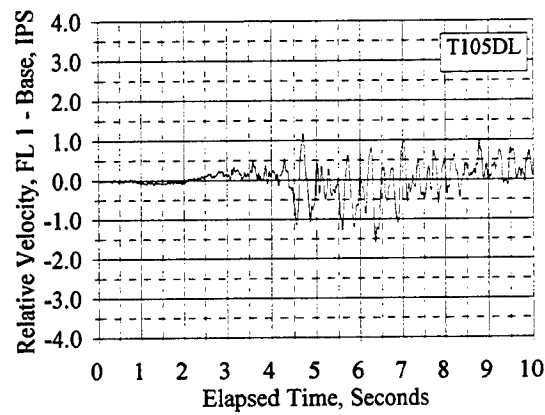
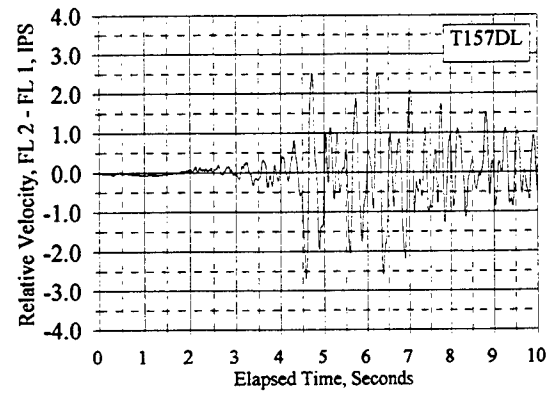
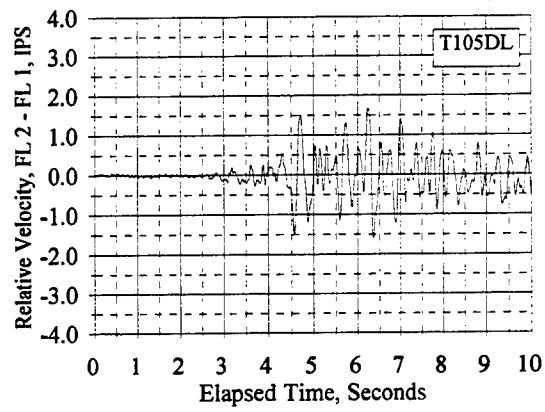
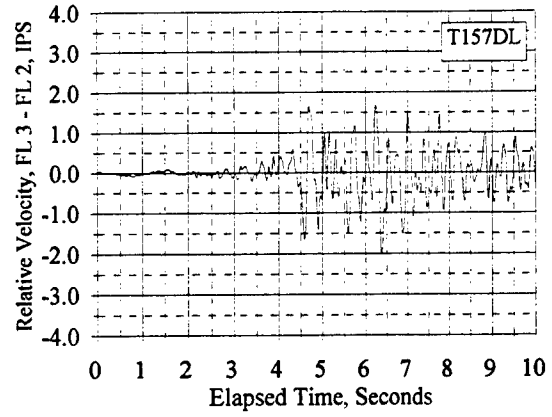
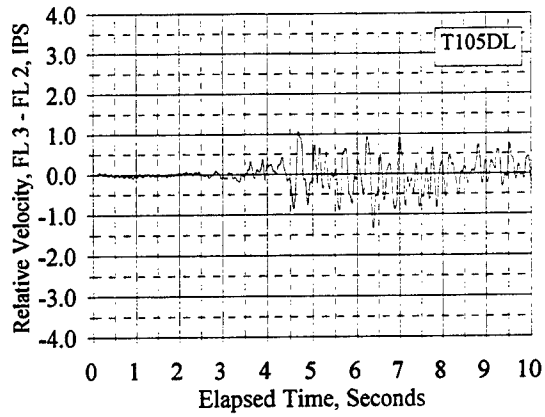


Figure C.15.7 Relative Floor Velocities: T105DL, T157DL

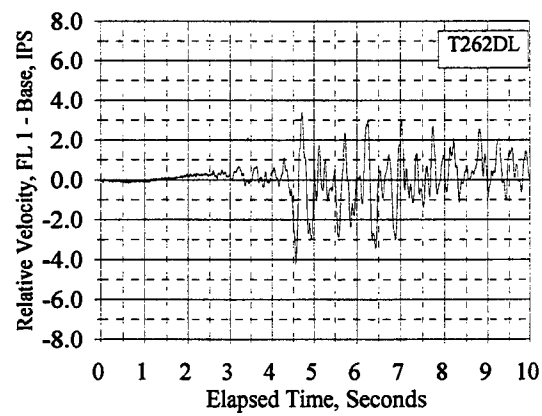
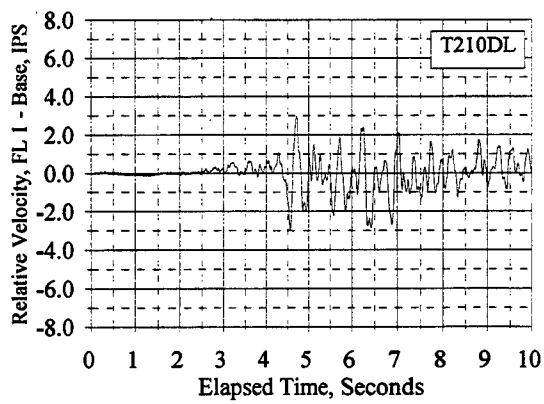
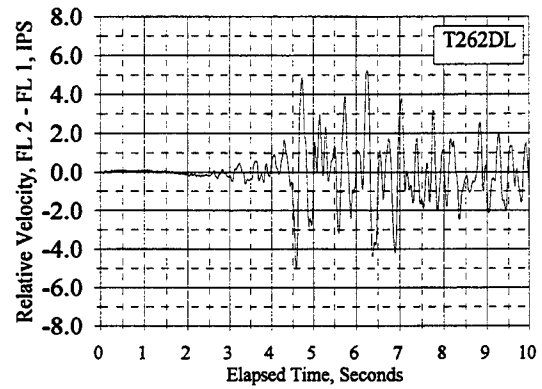
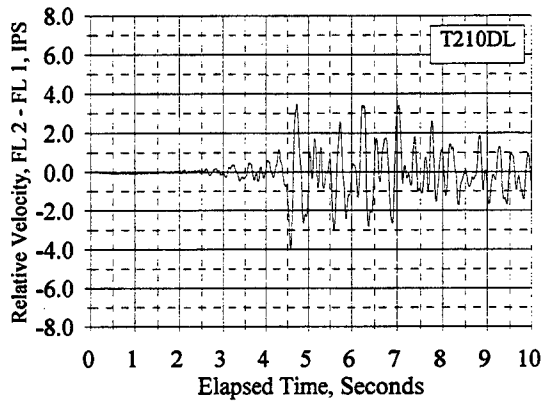
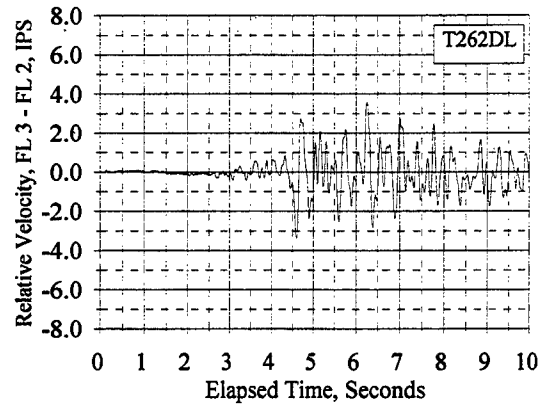
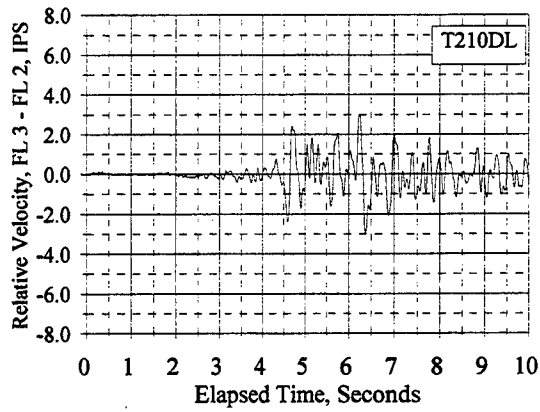


Figure C.15.8 Relative Floor Velocities: T210DL, T262DL

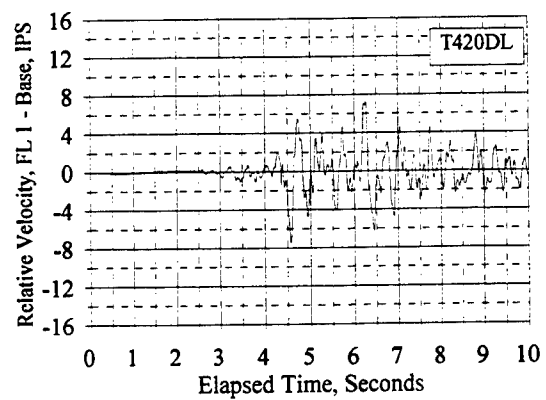
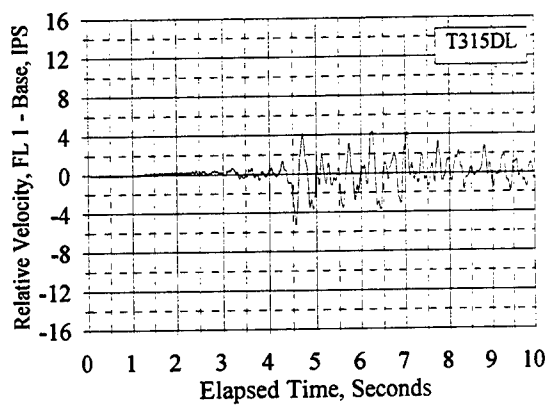
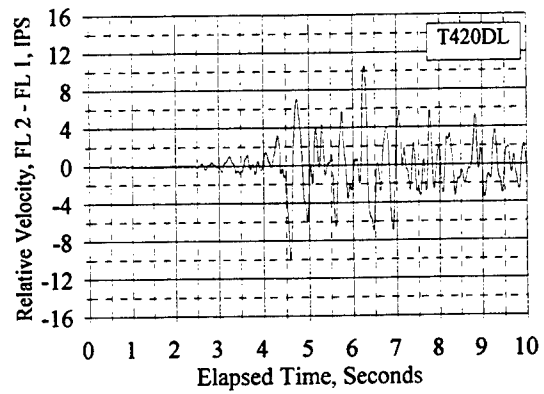
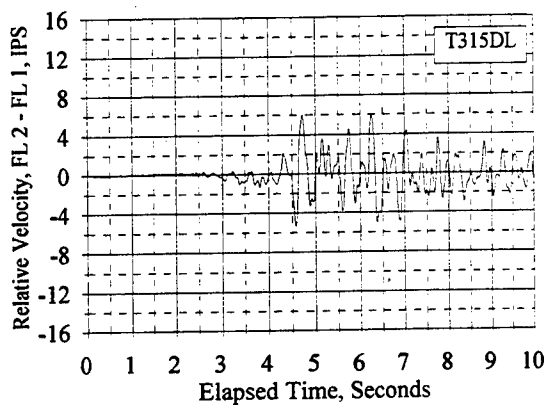
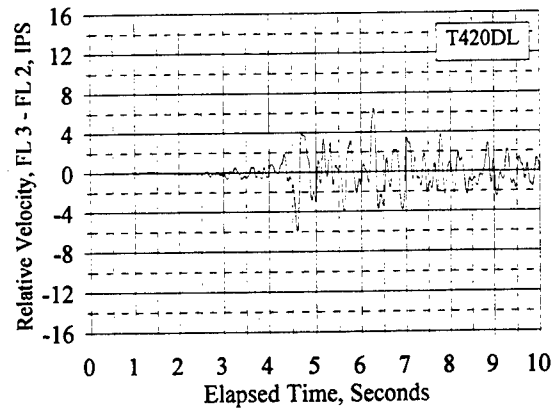
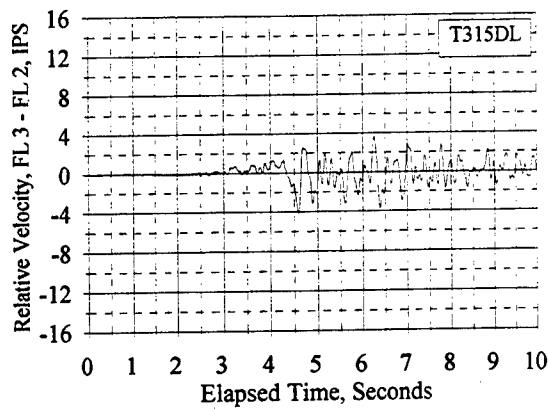


Figure C.15.9 Relative Floor Velocities: T315DL, T420DL

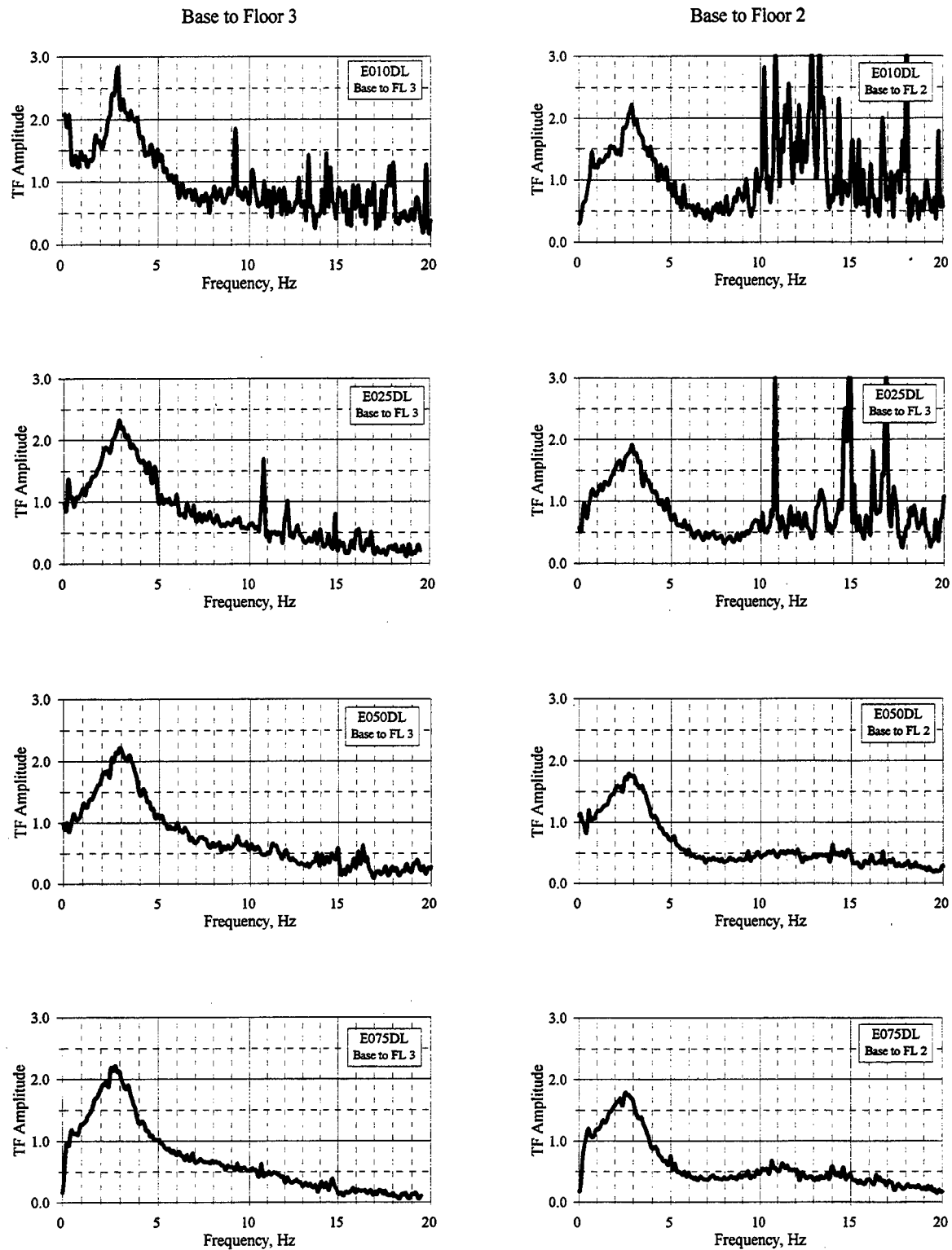


Figure C.16.1 Acceleration-Based Transfer Functions: E010DL - E075DL

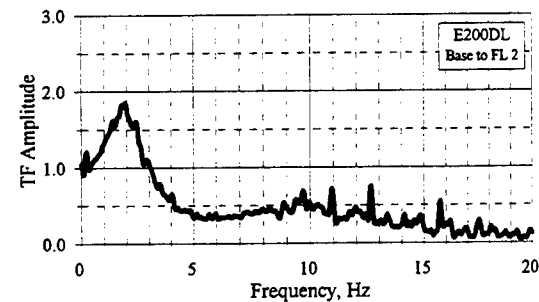
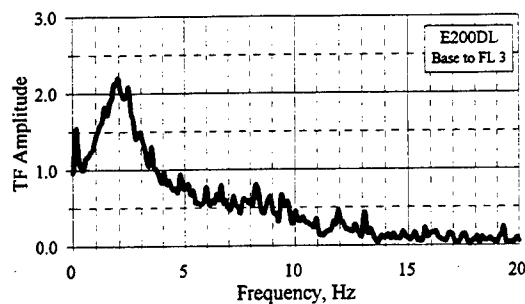
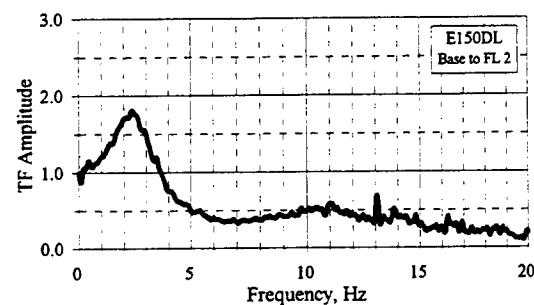
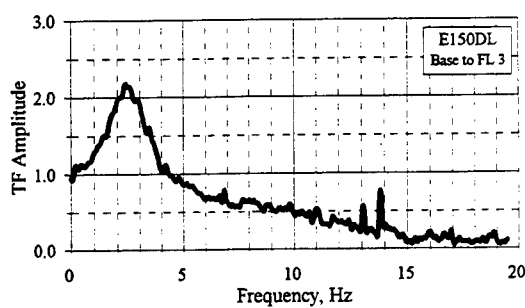
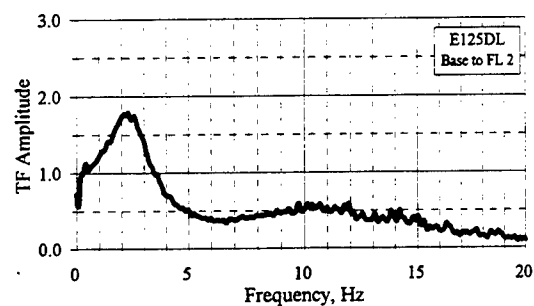
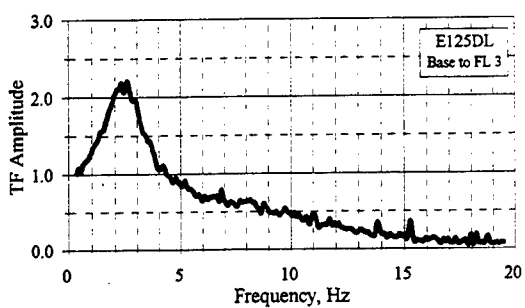
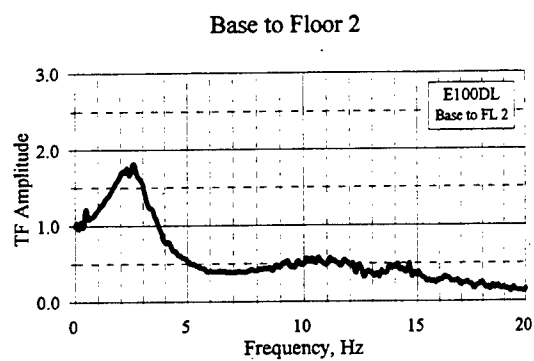
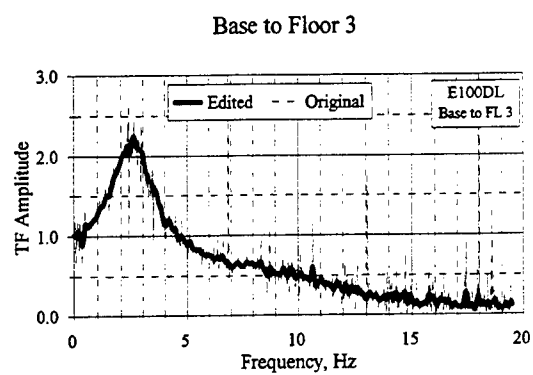


Figure C.16.2 Acceleration-Based Transfer Functions: E100DL - E200DL

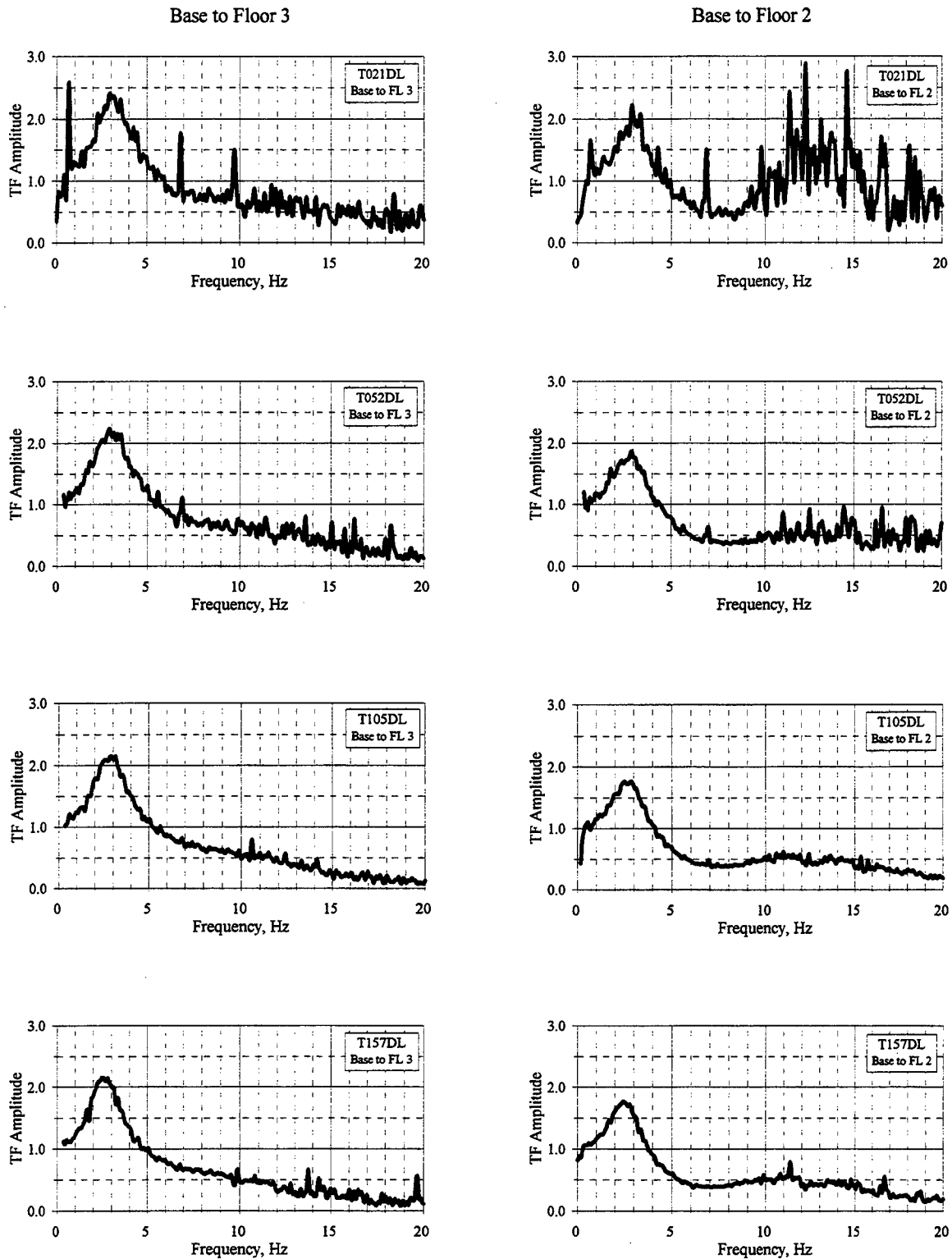


Figure C.16.3 Acceleration-Based Transfer Functions: T021DL - T157DL

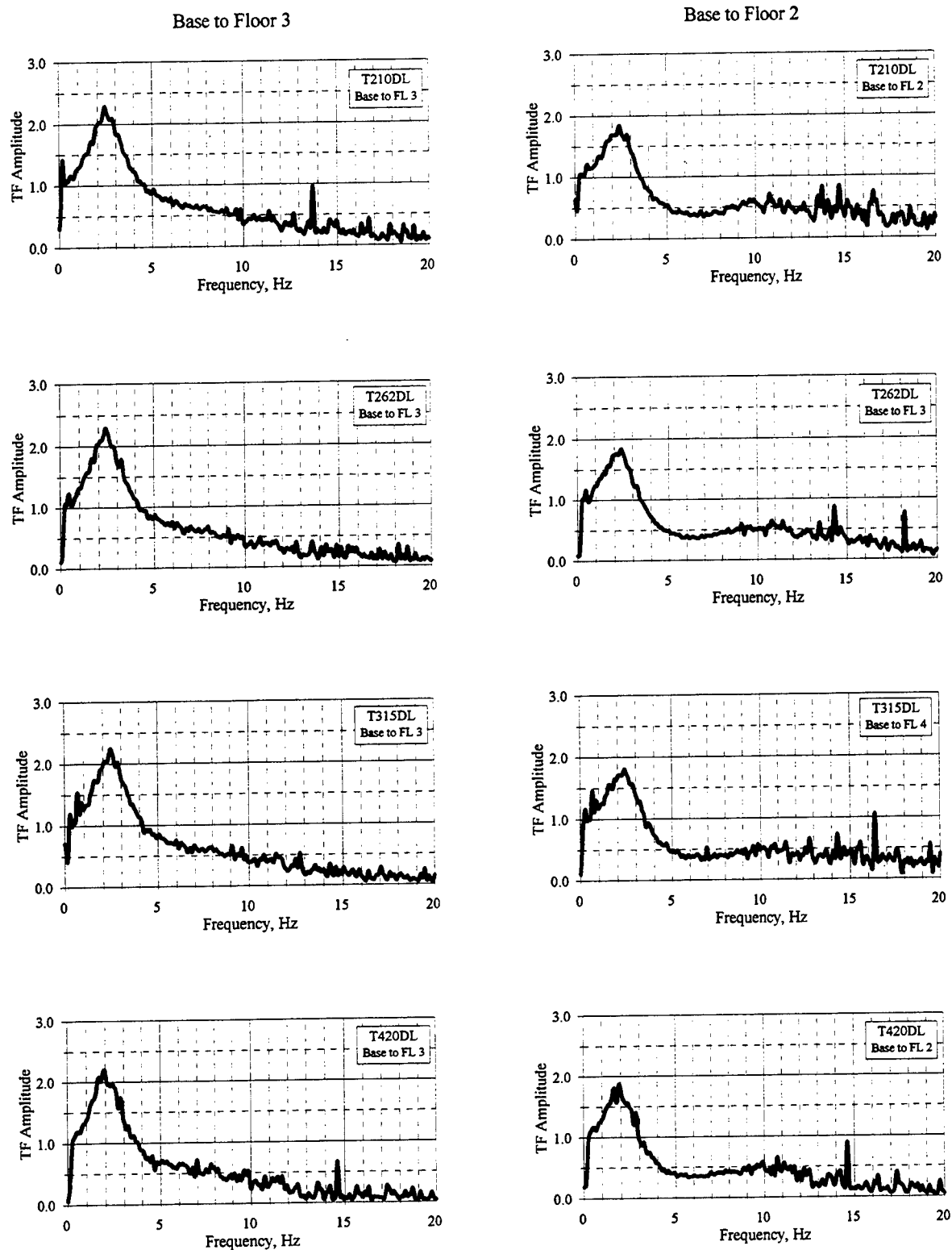


Figure C.16.4 Acceleration-Based Transfer Functions: T210DL - T420DL

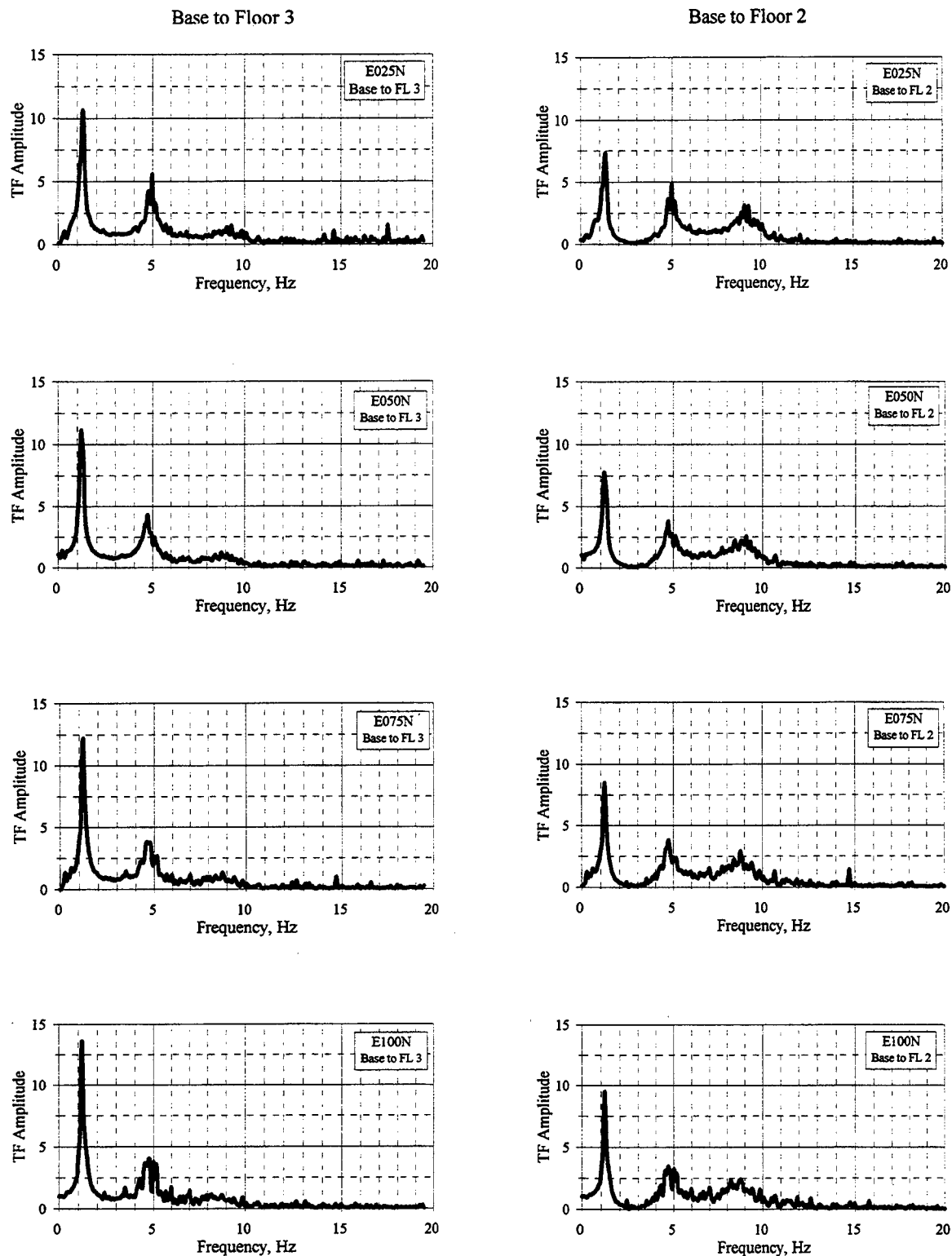


Figure C.16.5 Acceleration-Based Transfer Functions: E025N - E100N

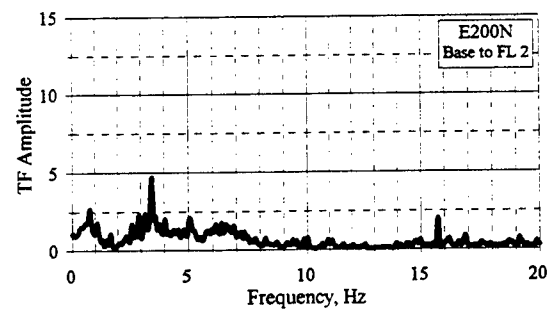
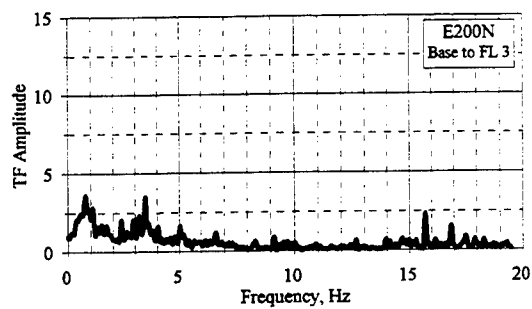
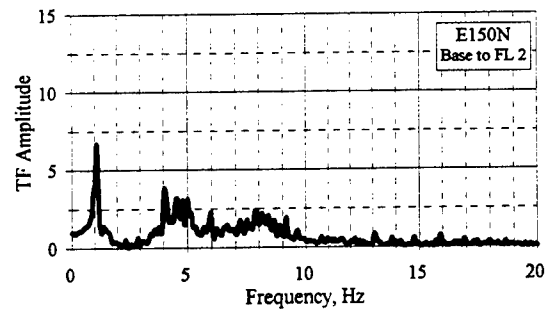
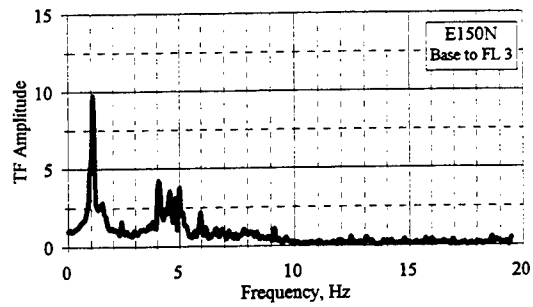
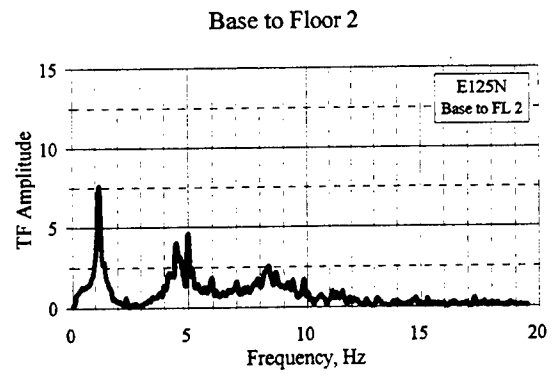
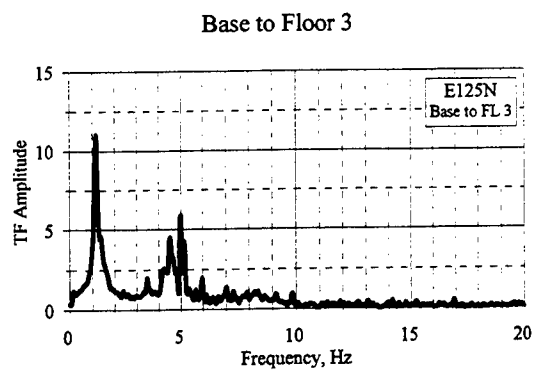


Figure C.16.6 Acceleration-Based Transfer Functions: E125N - E200N

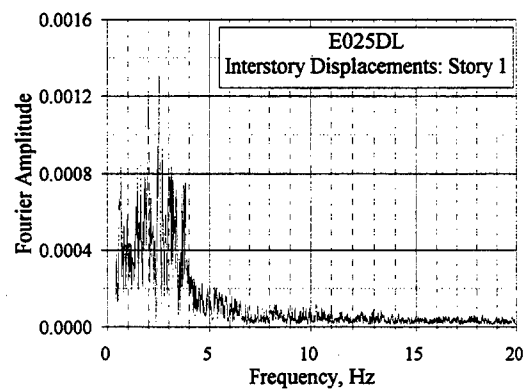
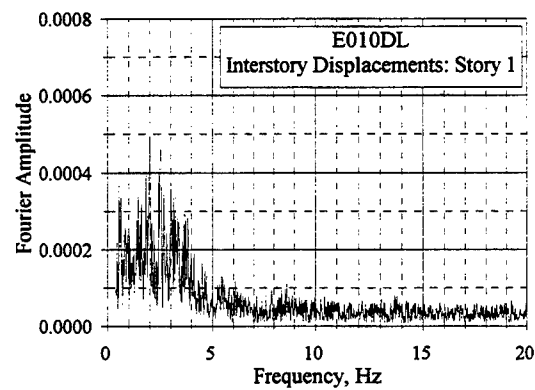
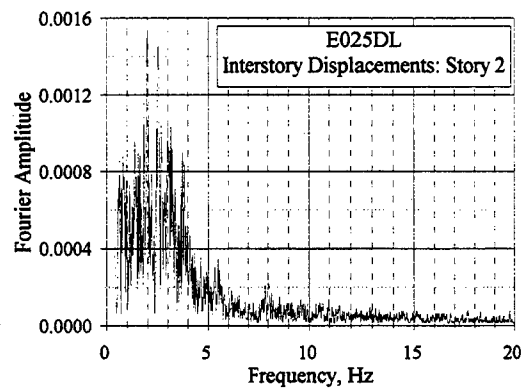
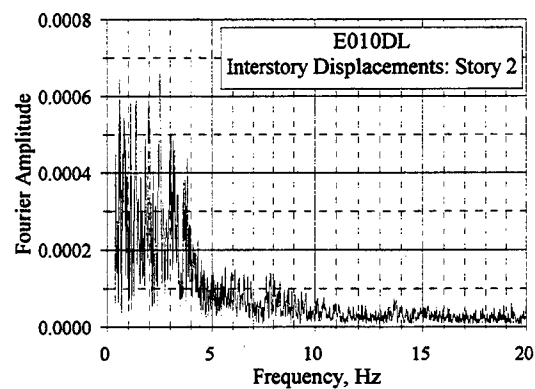
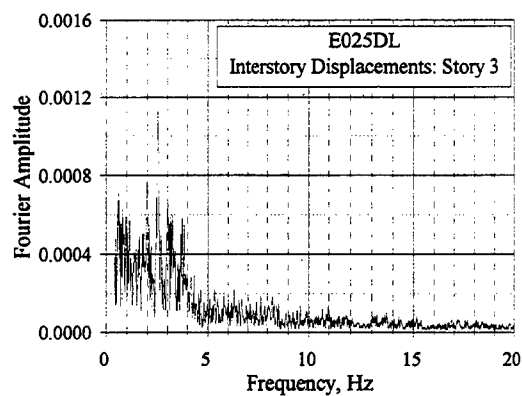
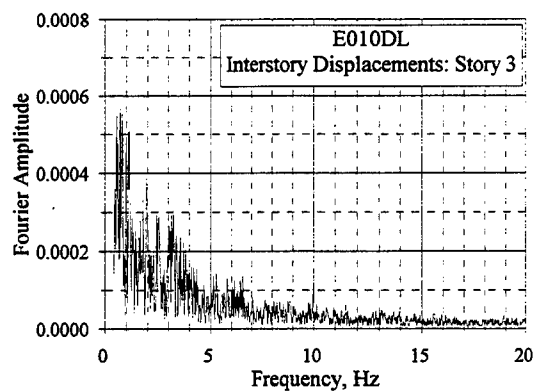


Figure C.16.7 Fourier Amplitude Spectra of Interstory Displacements: E010DL and E025DL

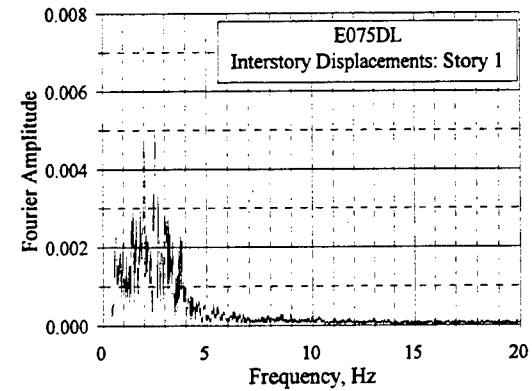
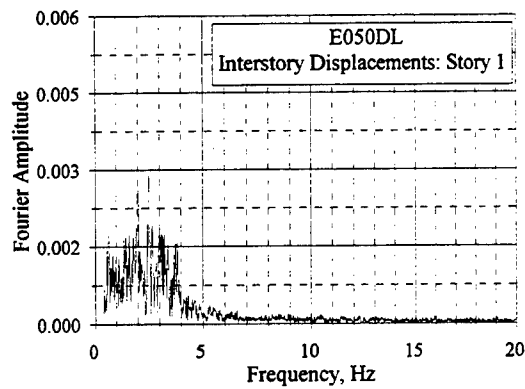
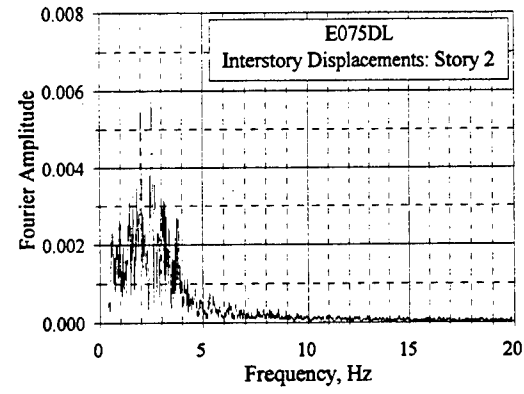
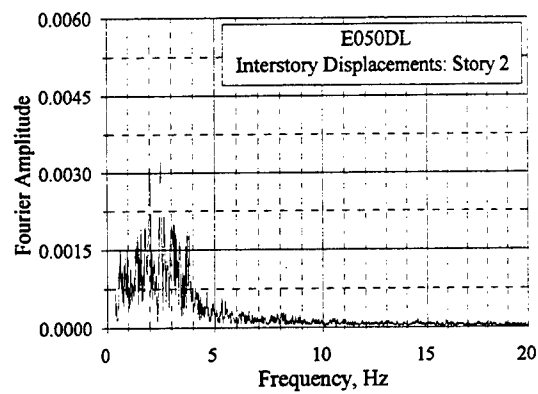
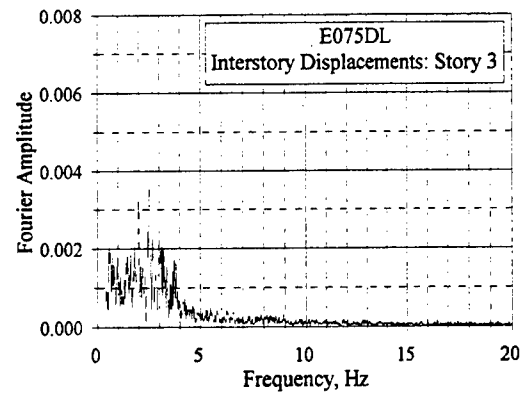
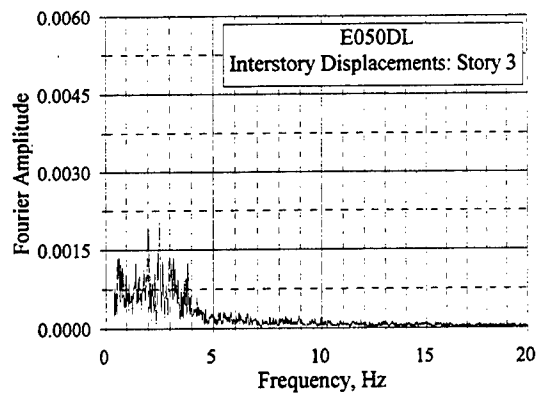


Figure C.16.8 Fourier Amplitude Spectra of Interstory Displacements: E050DL and E075DL

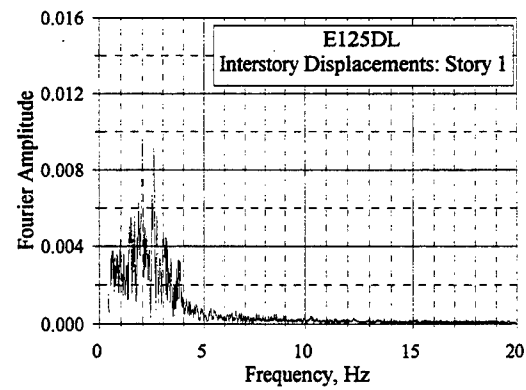
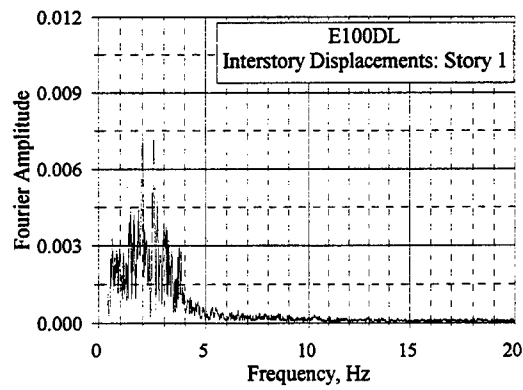
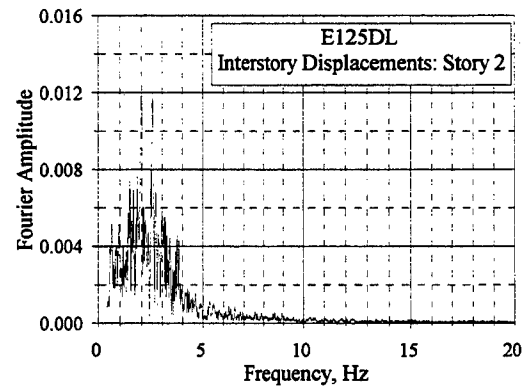
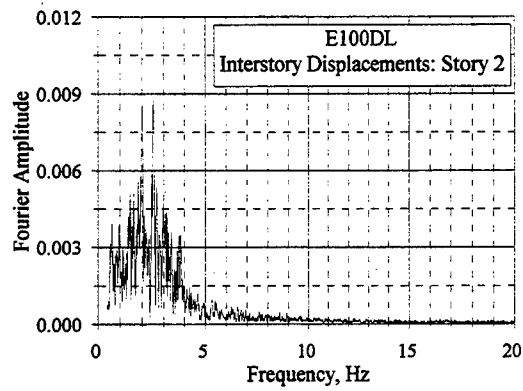
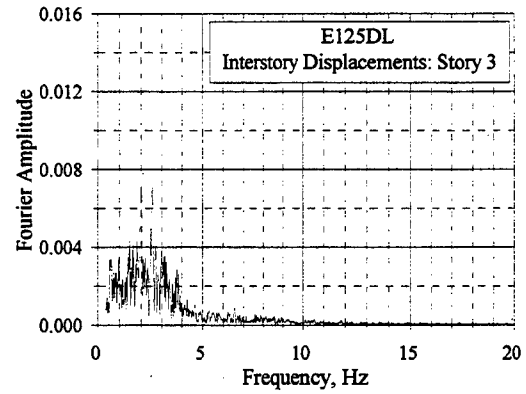
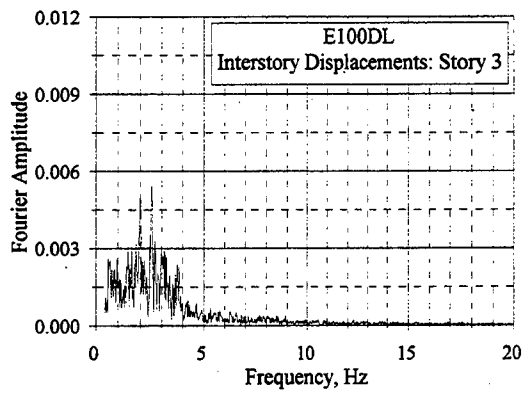


Figure C.16.9 Fourier Amplitude Spectra of Interstory Displacements: E100DL and E125DL

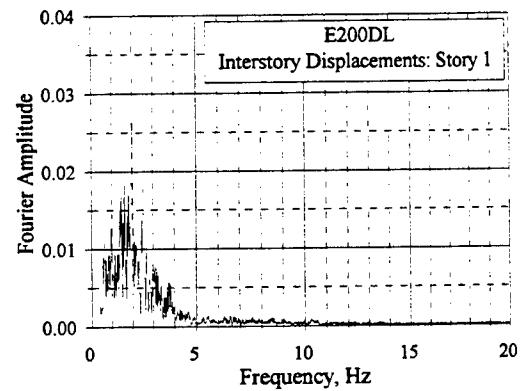
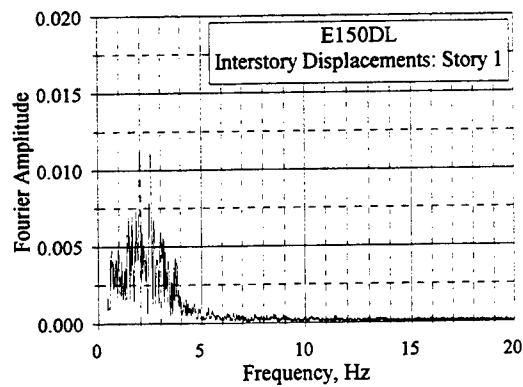
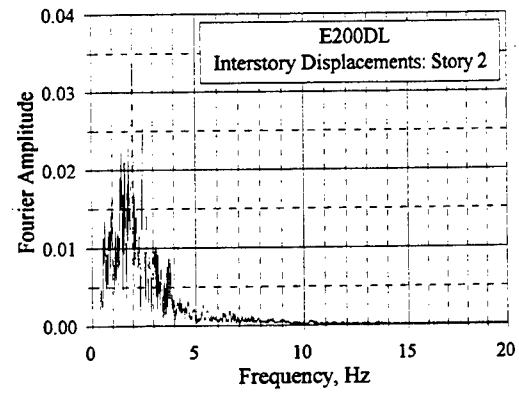
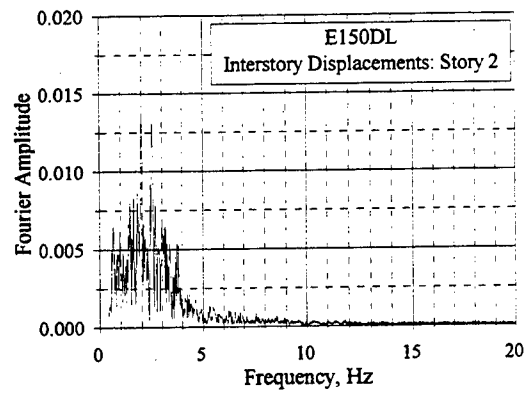
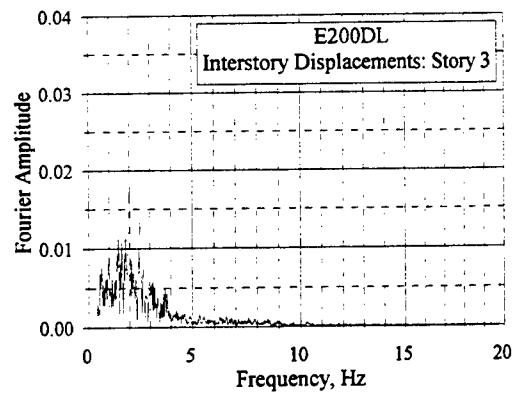
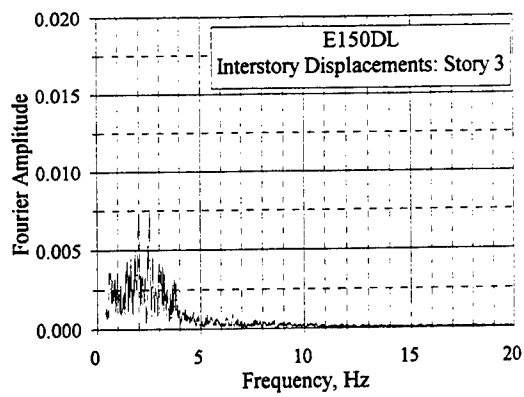


Figure C.16.10 Fourier Amplitude Spectra of Interstory Displacements: E150DL and E200DL

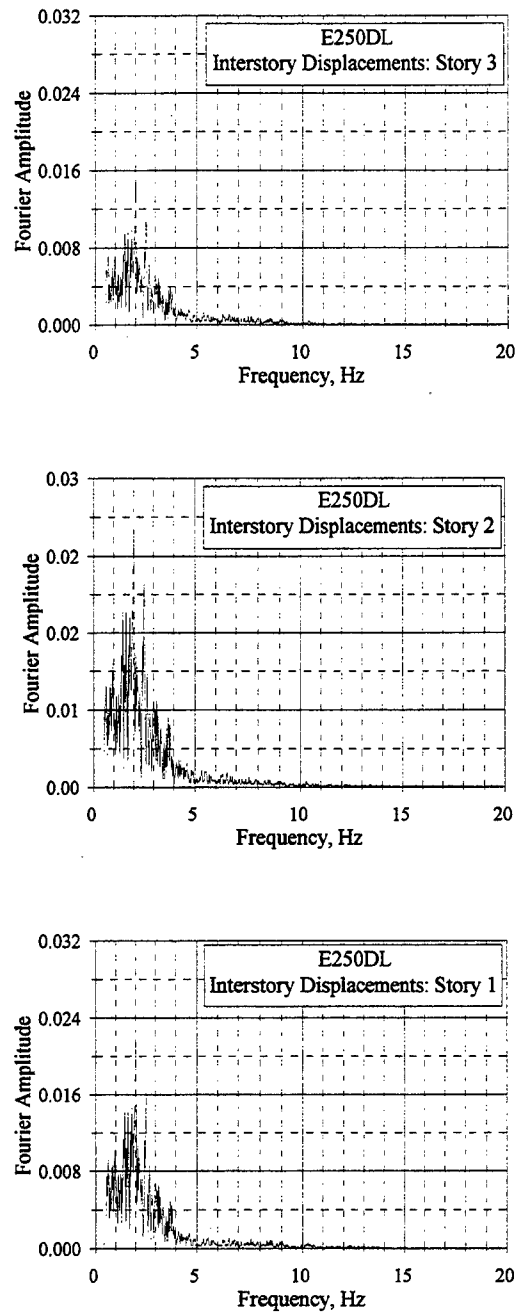


Figure C.16.11 Fourier Amplitude Spectra of Interstory Displacements: E250DL

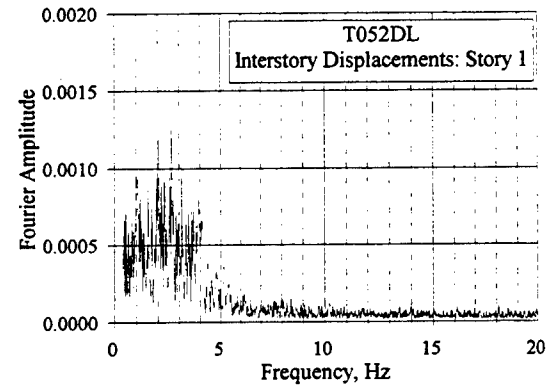
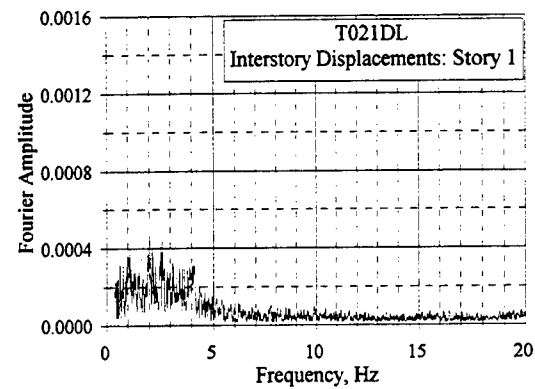
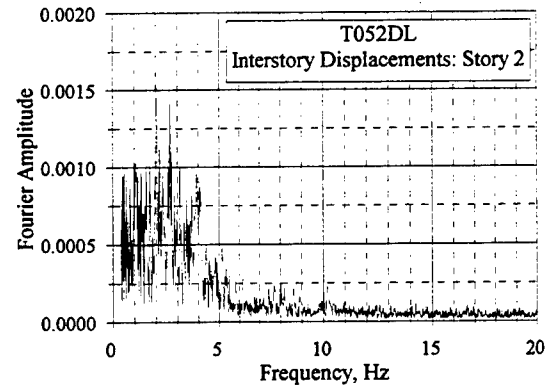
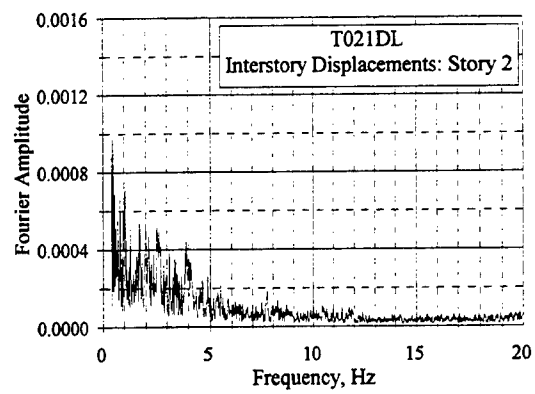
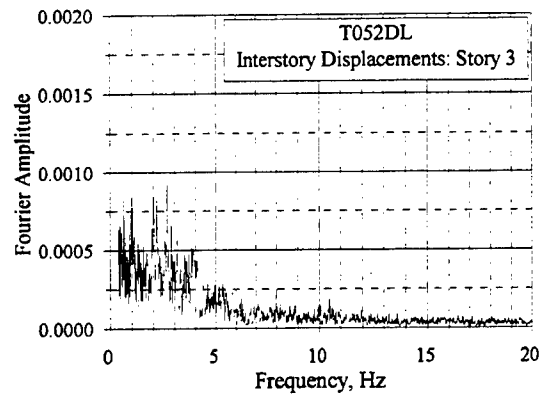
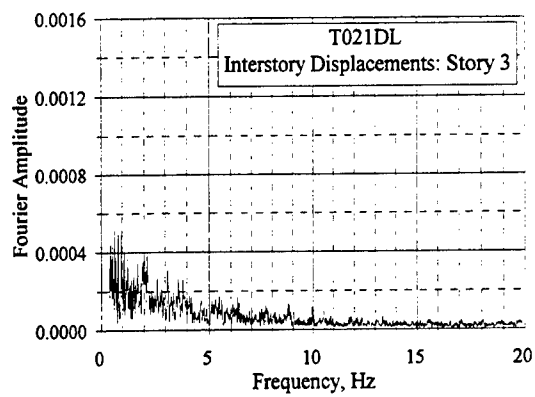


Figure C.16.12 Fourier Amplitude Spectra of Interstory Displacements: T021DL and T052DL

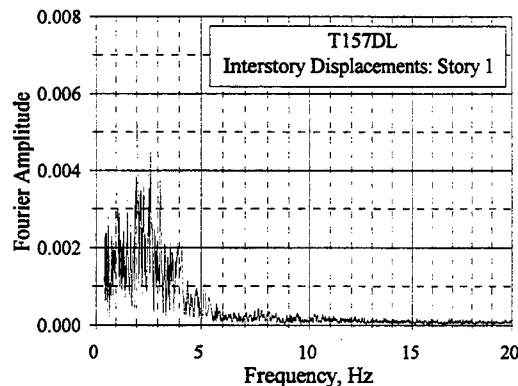
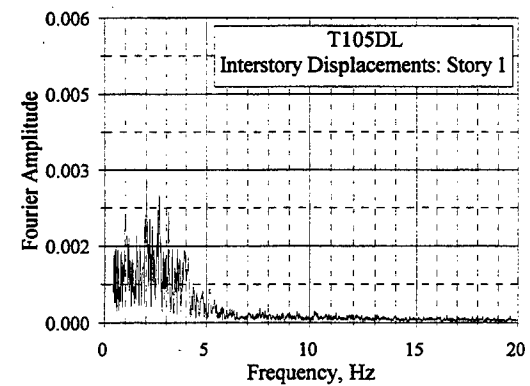
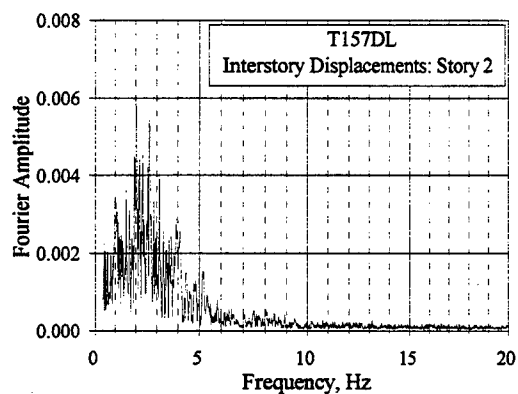
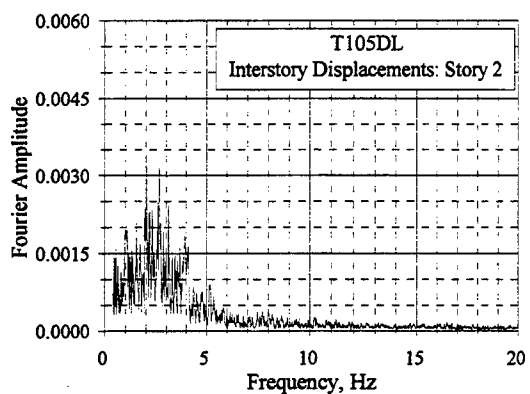
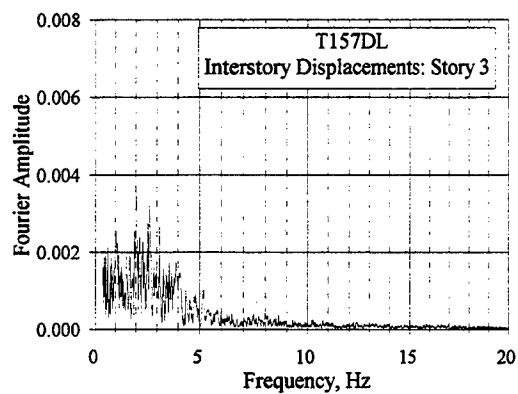
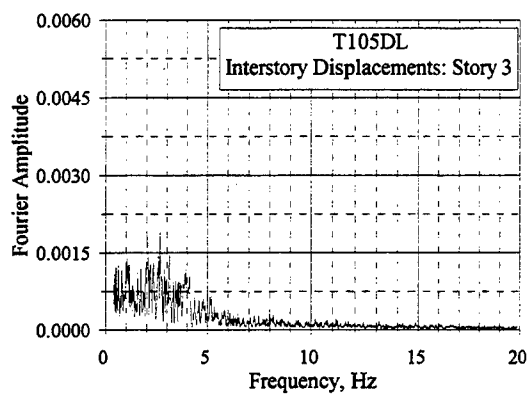


Figure C.16.13 Fourier Amplitude Spectra of Interstory Displacements: T105DL and T157DL

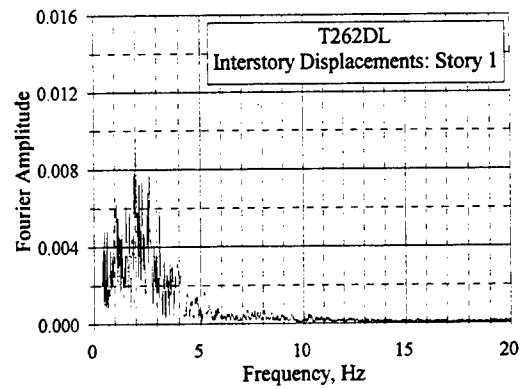
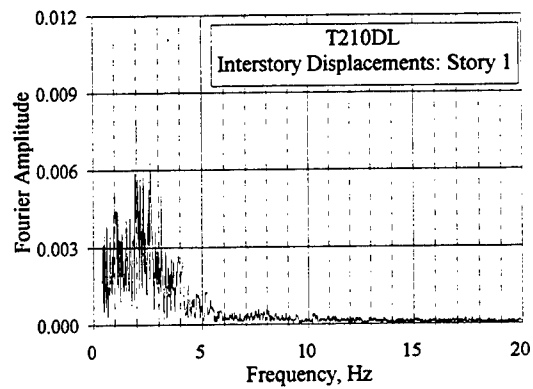
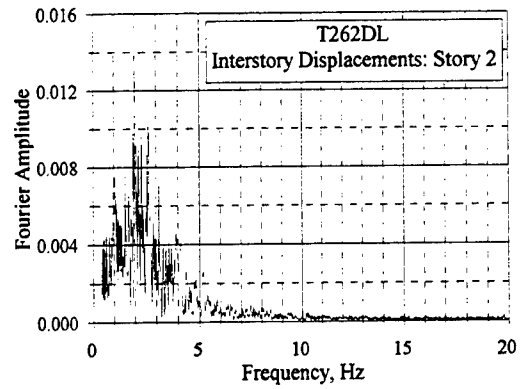
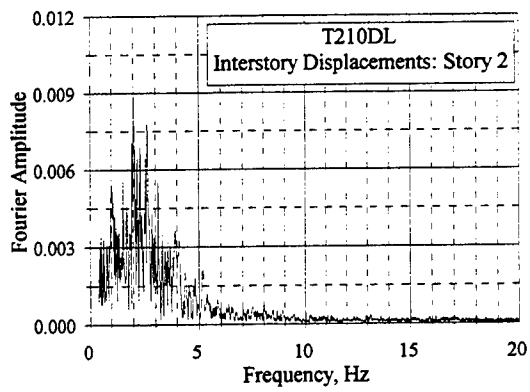
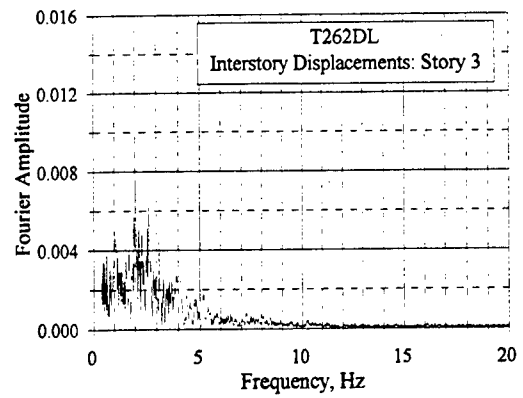
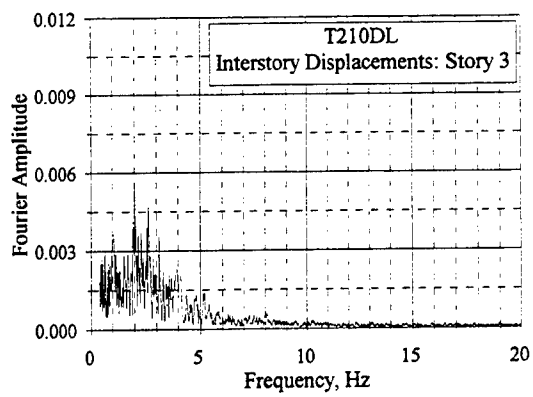


Figure C.16.14 Fourier Amplitude Spectra of Interstory Displacements: T210DL and T262DL

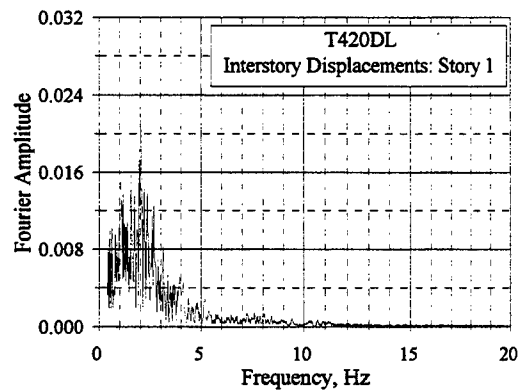
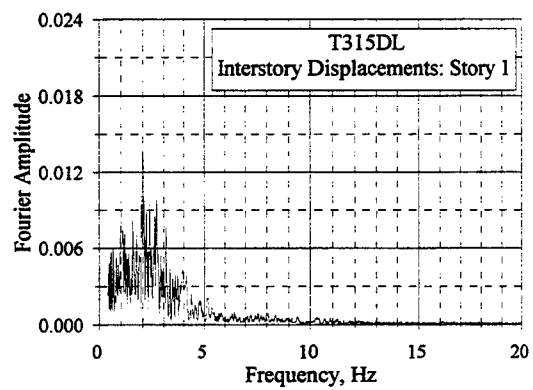
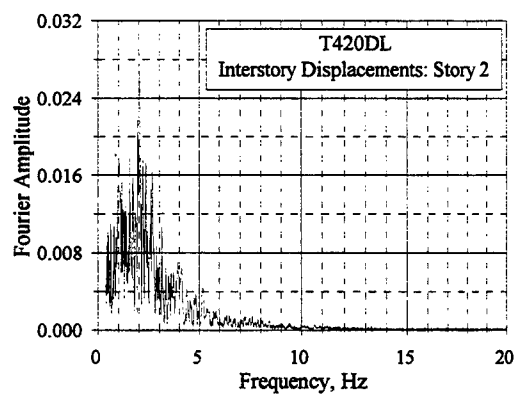
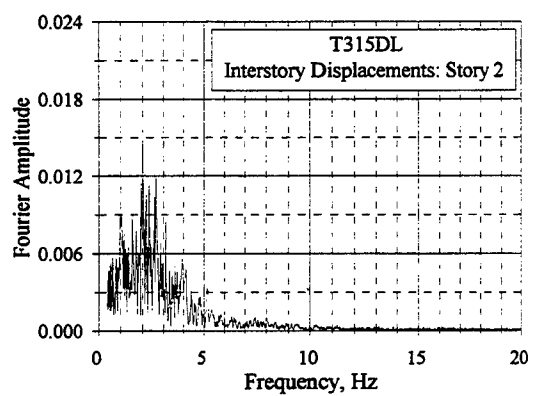
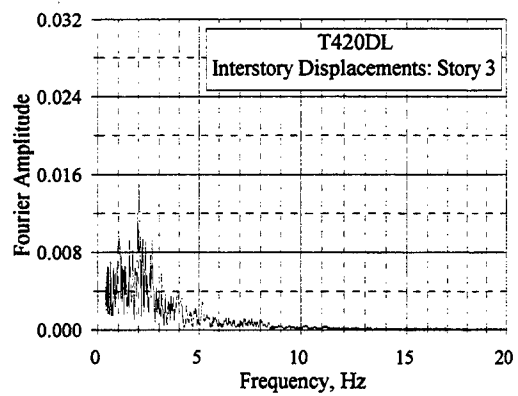
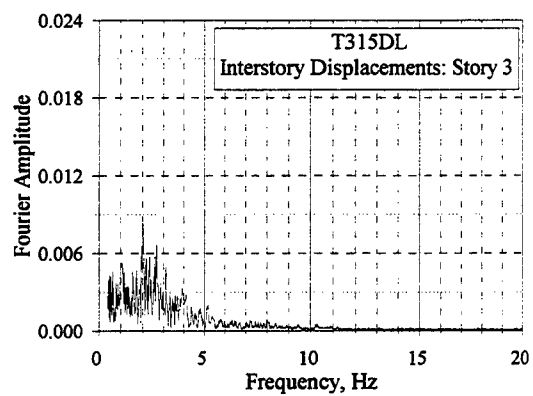


Figure C.16.15 Fourier Amplitude Spectra of Interstory Displacements: T315DL and T420DL

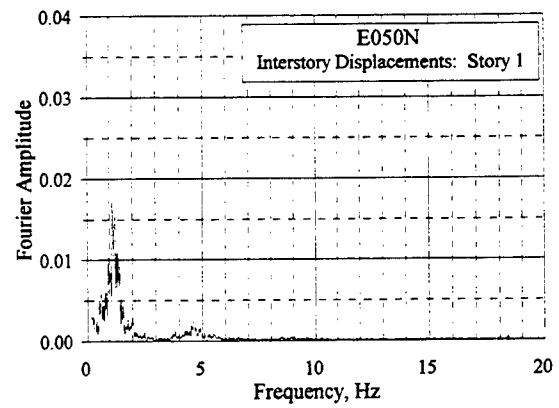
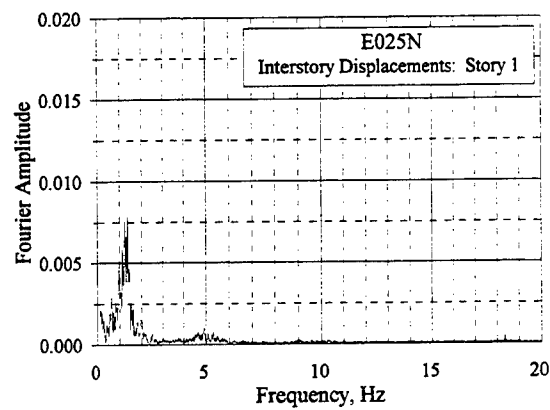
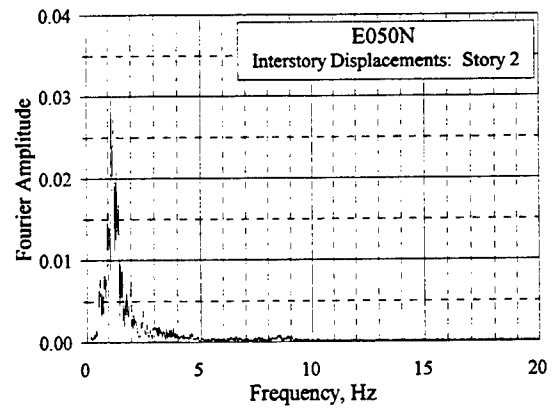
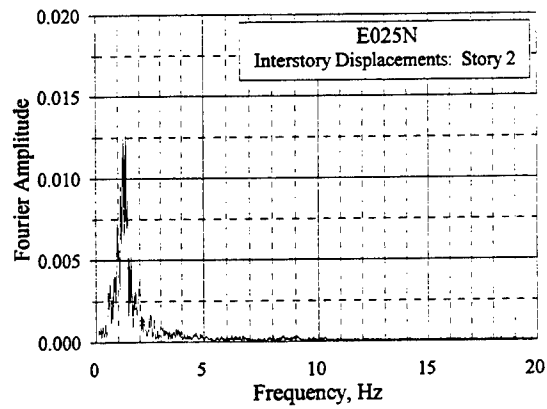
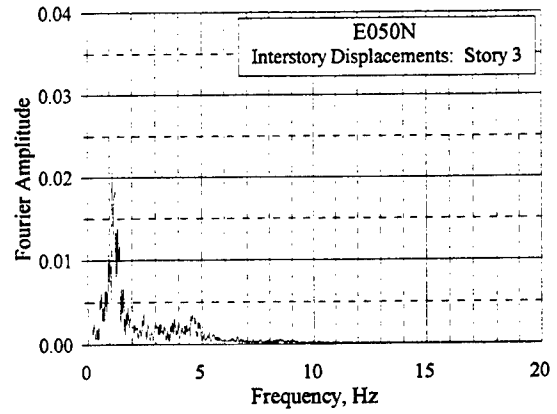
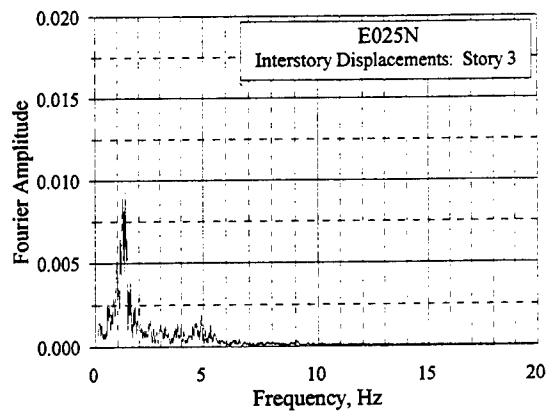


Figure C.16.16 Fourier Amplitude Spectra of Interstory Displacements: E025N and E050N

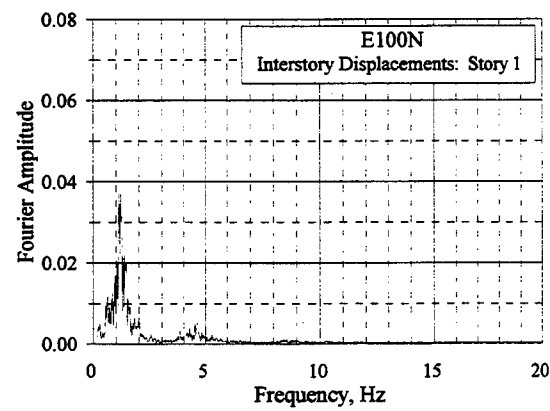
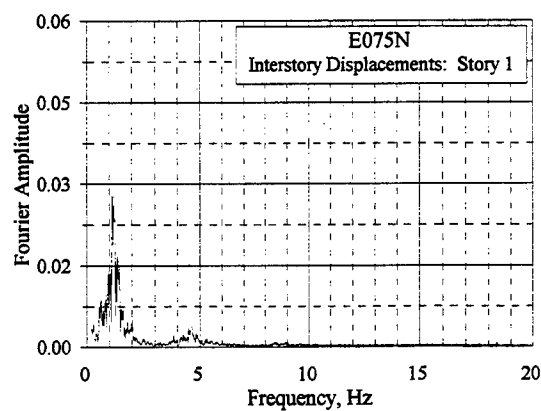
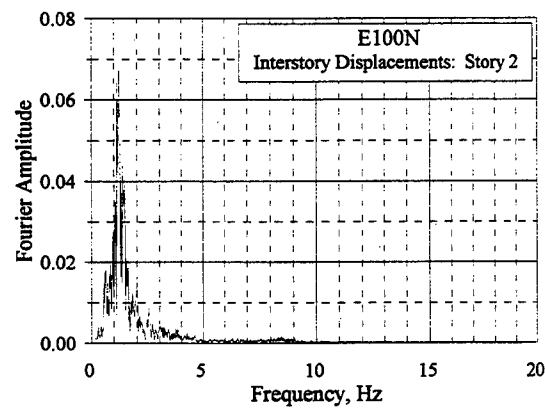
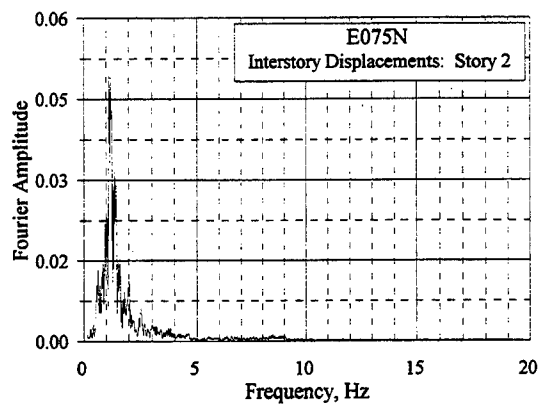
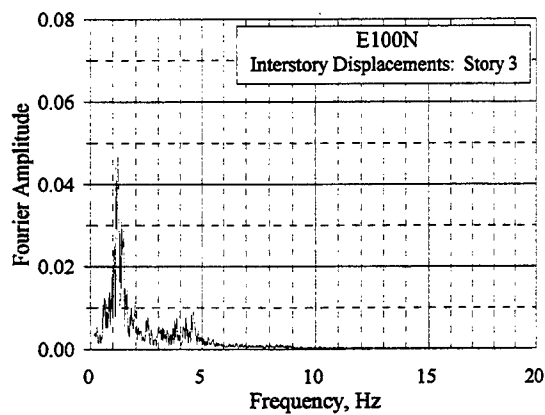
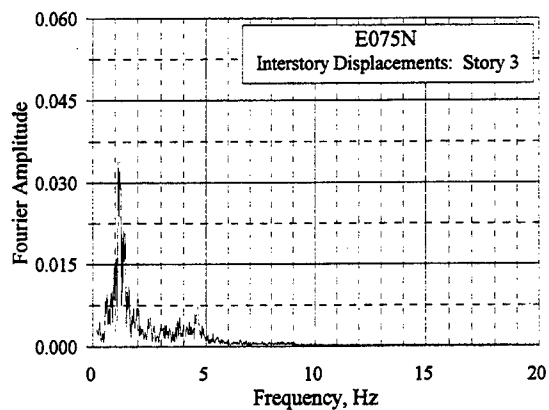


Figure C.16.17 Fourier Amplitude Spectra of Interstory Displacements: E075N and E100N

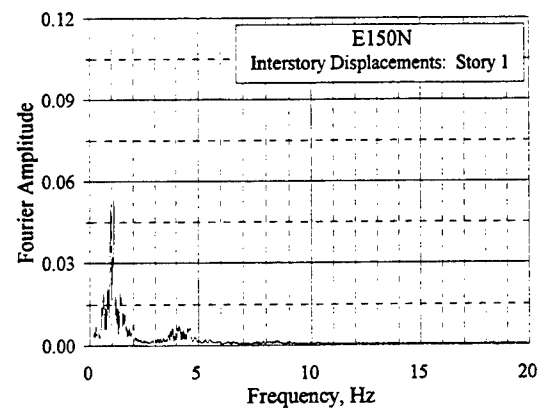
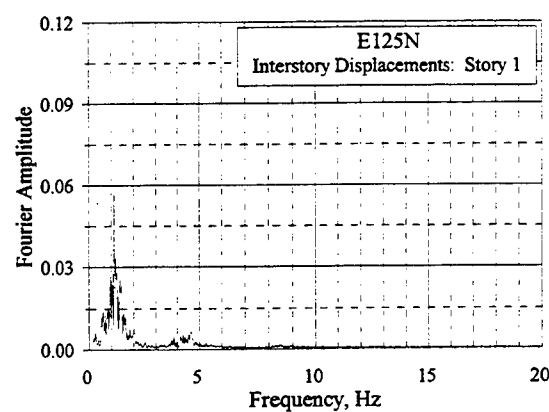
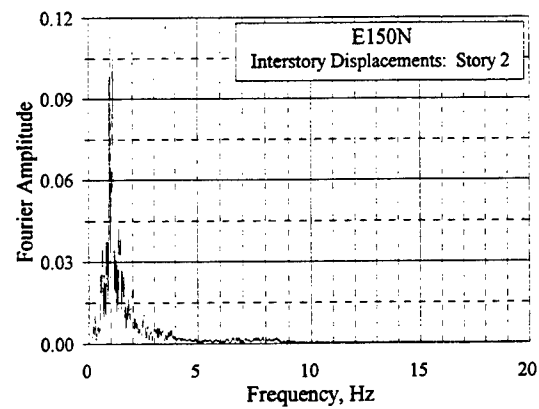
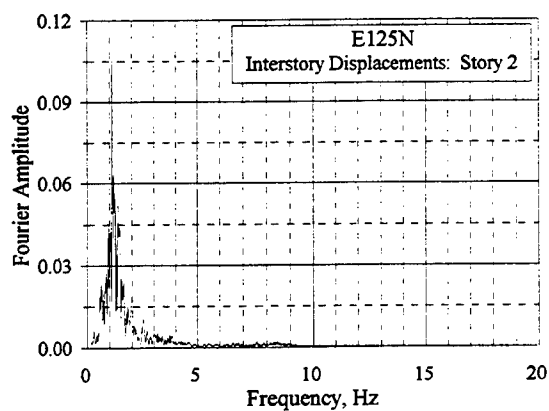
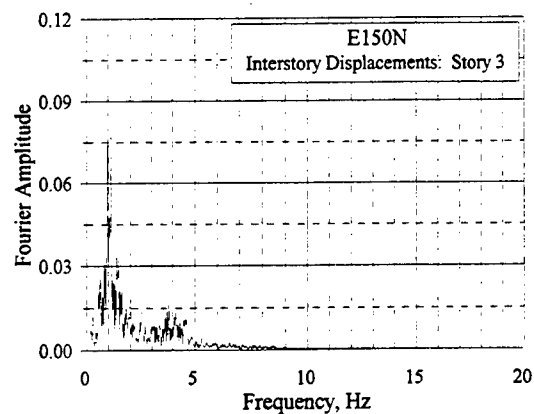
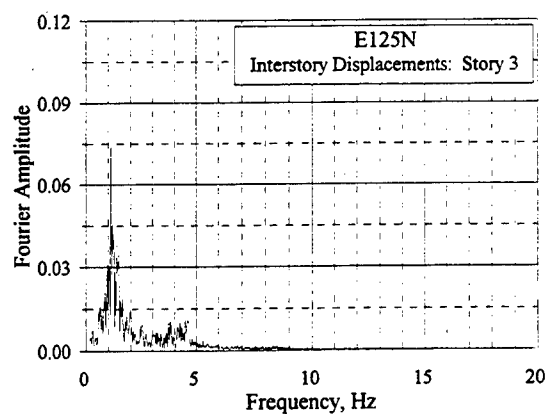


Figure C.16.18 Fourier Amplitude Spectra of Interstory Displacements: E125N and E150N

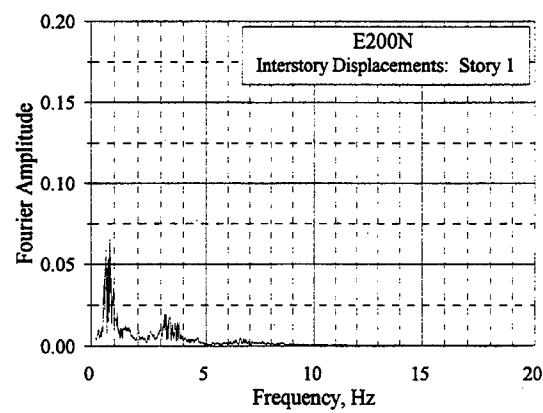
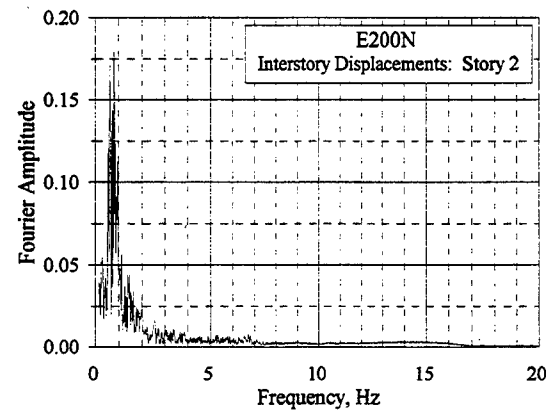
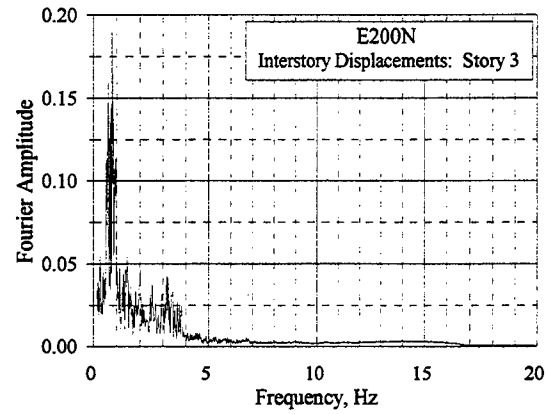


Figure C.16.19 Fourier Amplitude Spectra of Interstory Displacements: E200N

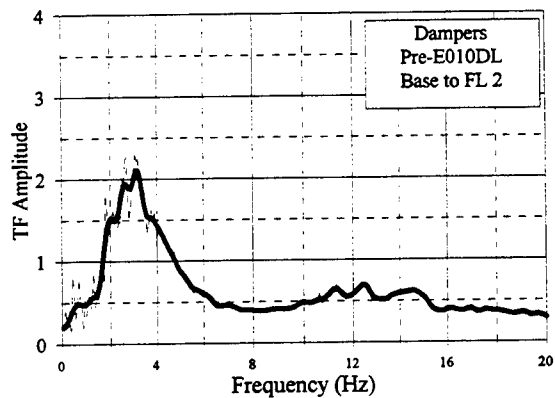
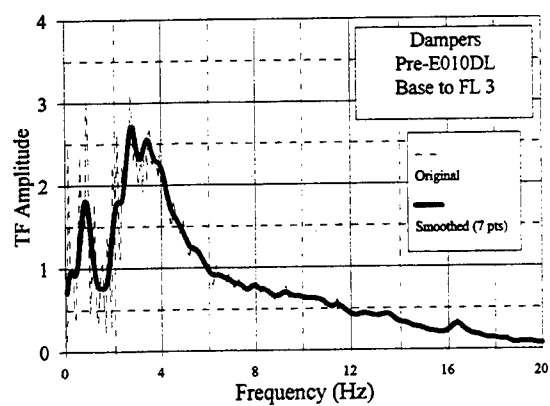
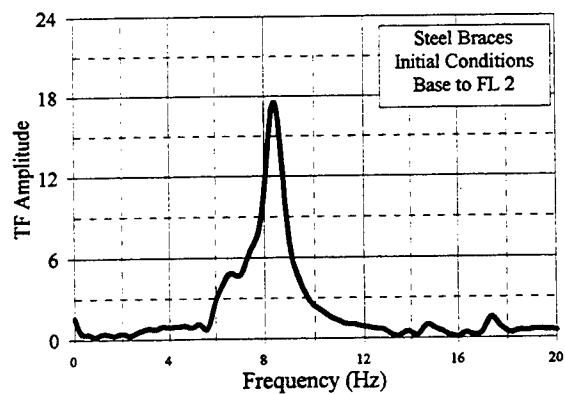
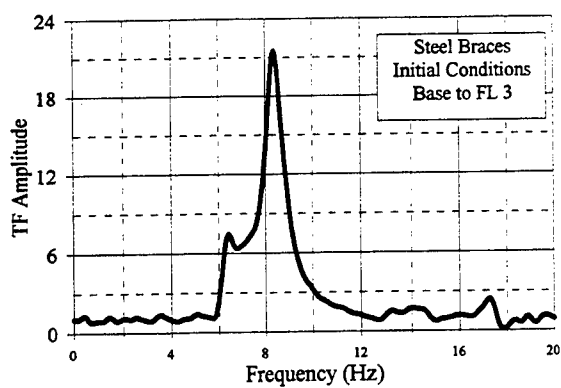
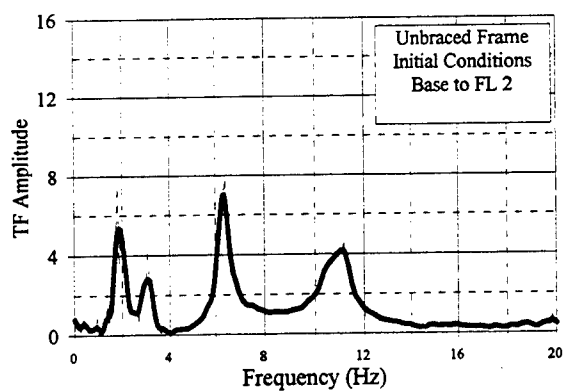
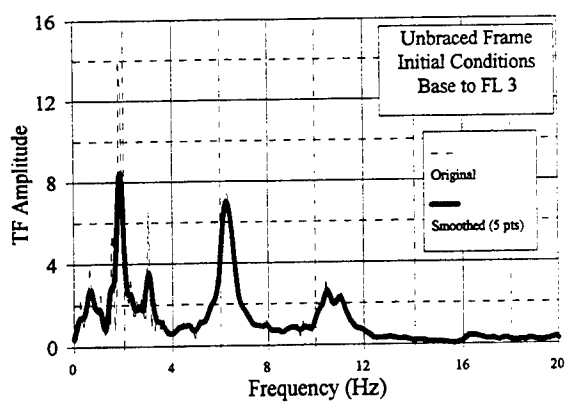


Figure C.16.20 Acceleration-Based Transfer Functions, White Noise Tests: Initial Conditions

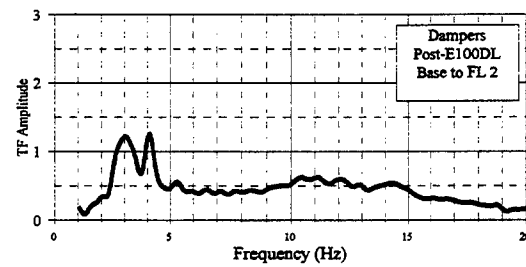
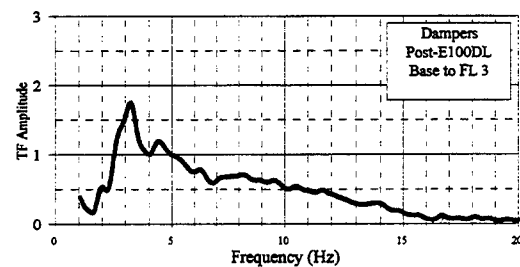
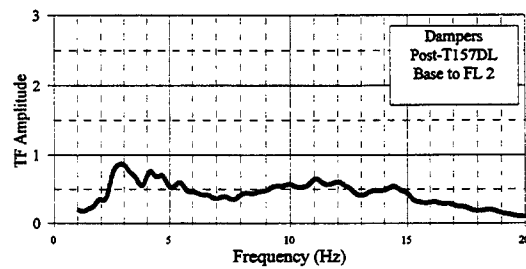
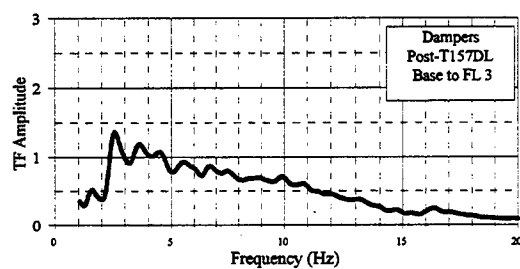
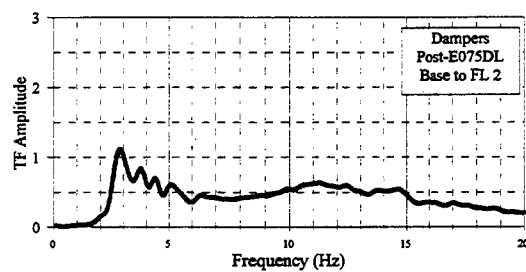
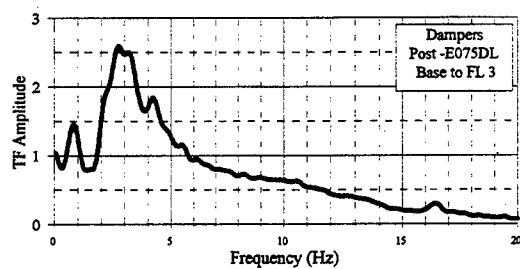
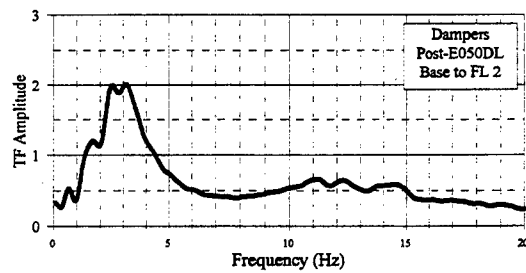
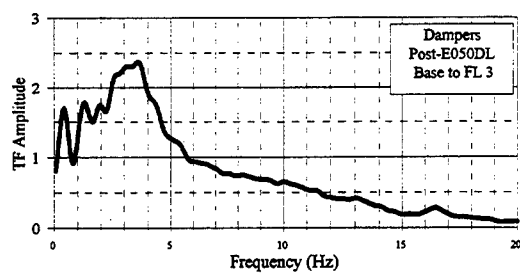


Figure C.16.21 Acceleration-Based Transfer Functions, White Noise Tests: E050DL - E100DL

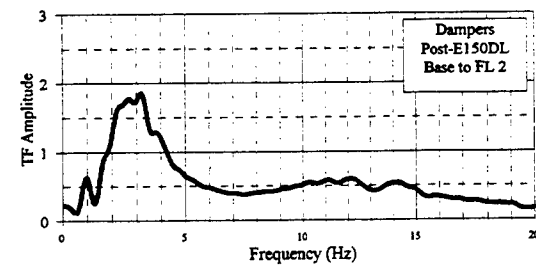
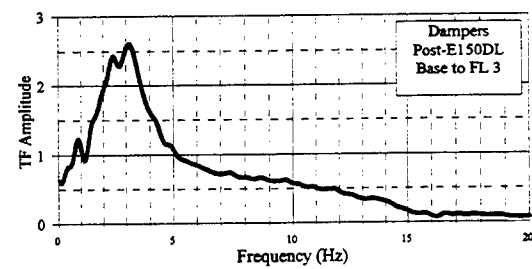
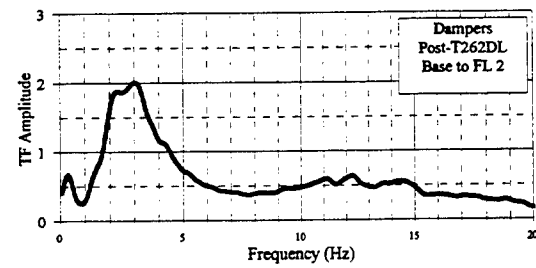
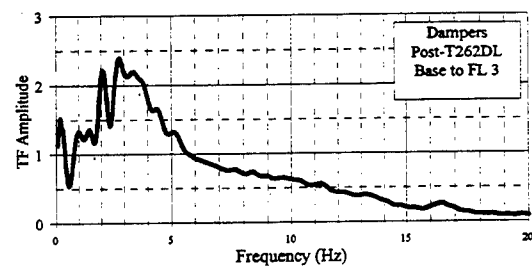
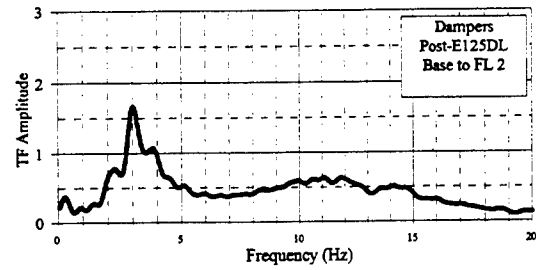
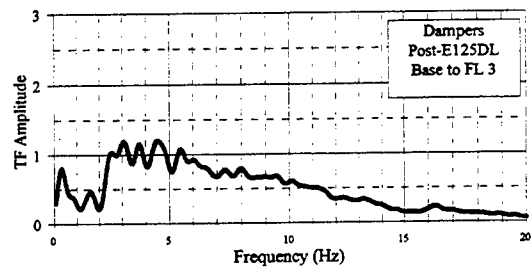
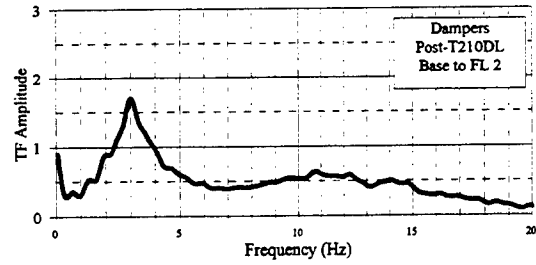
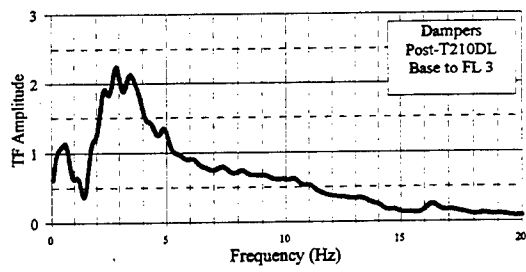


Figure C.16.22 Acceleration-Based Transfer Functions, White Noise Tests: T210DL - E150DL

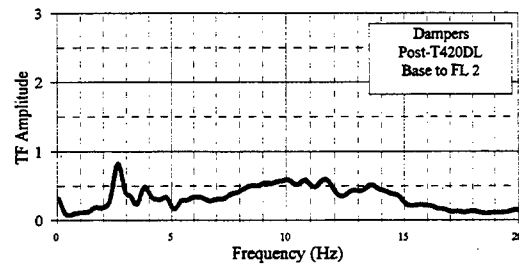
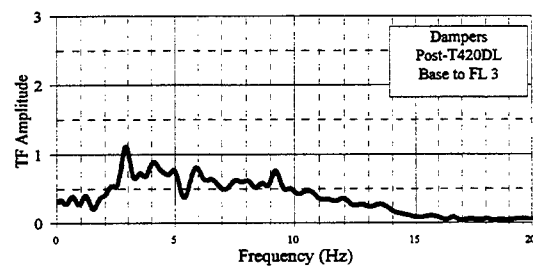
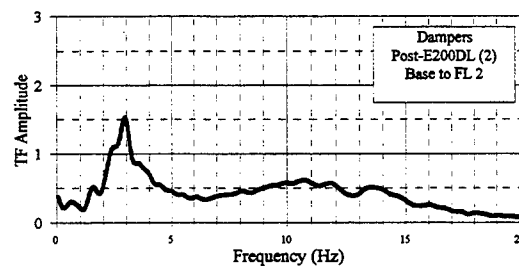
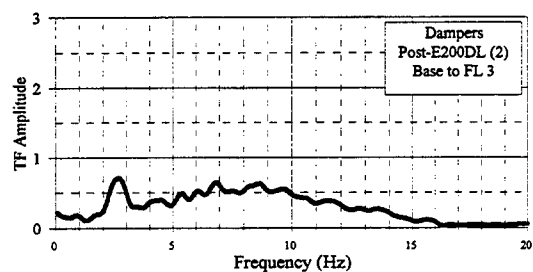
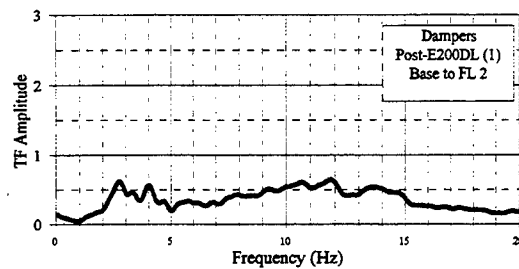
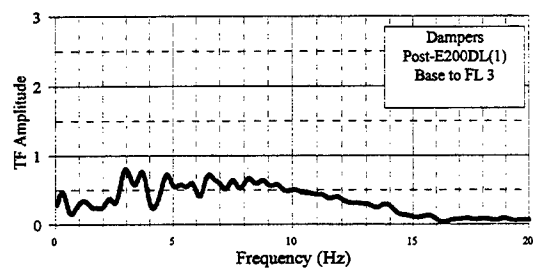
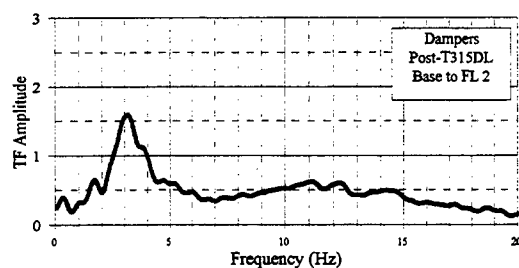
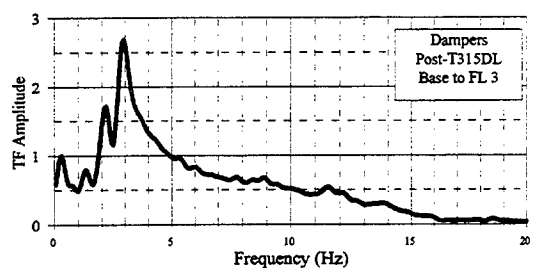


Figure C.16.23 Acceleration-Based Transfer Functions, White Noise Tests: T315DL - T420DL

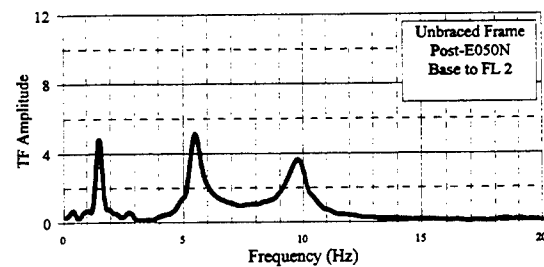
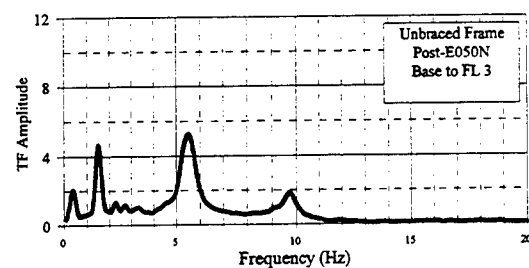
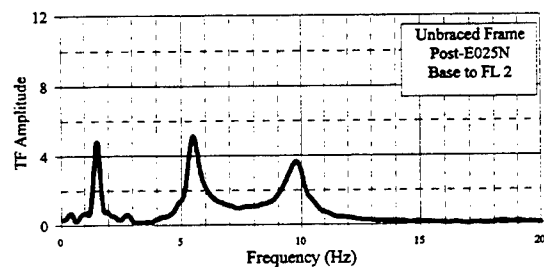
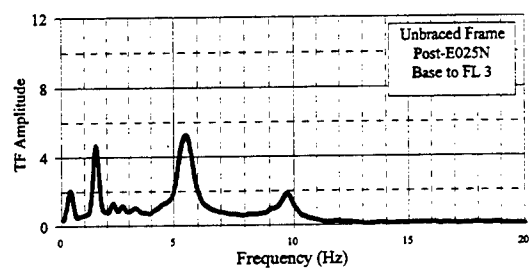
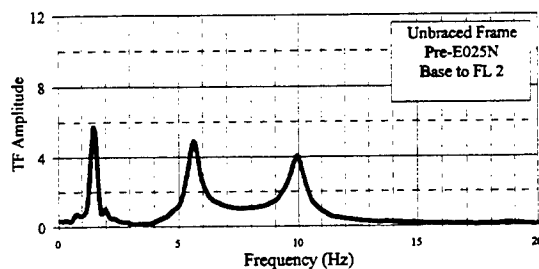
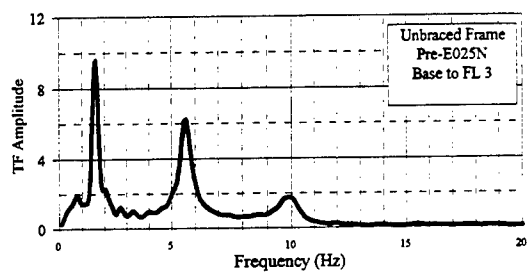
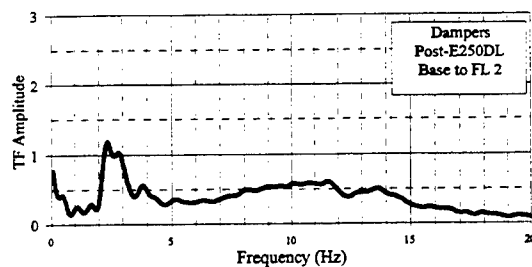
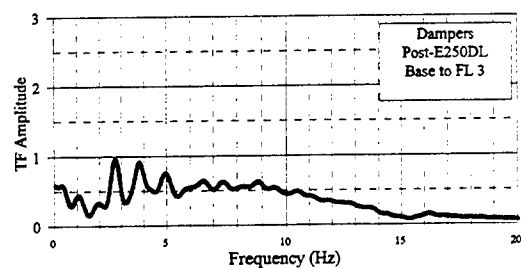


Figure C.16.24 Acceleration-Based Transfer Functions, White Noise Tests: E250DL - E050N

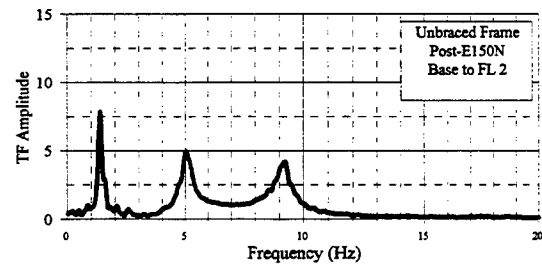
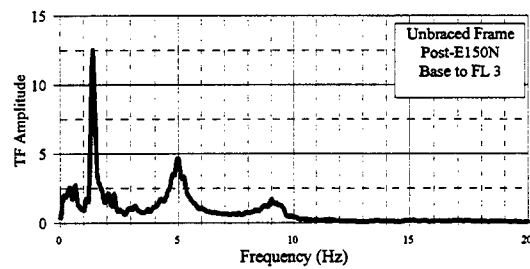
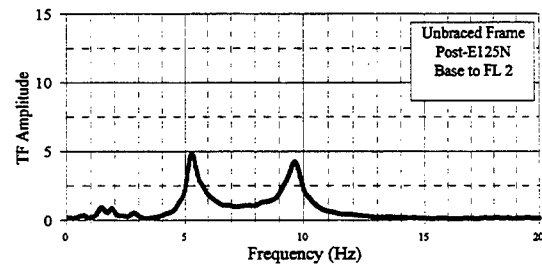
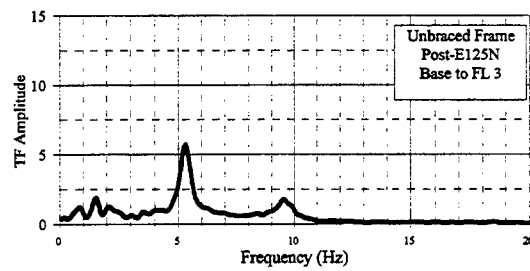
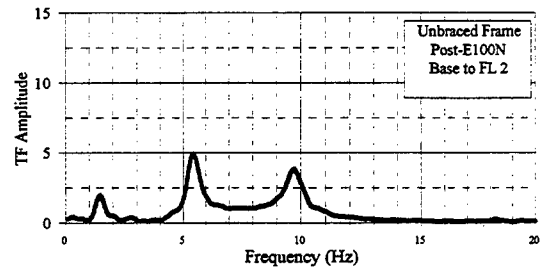
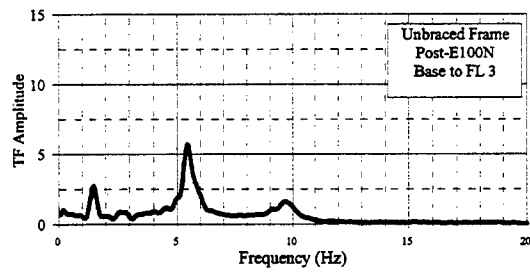
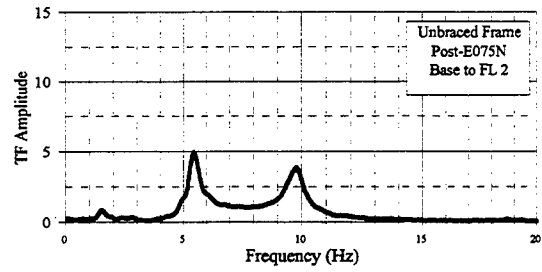
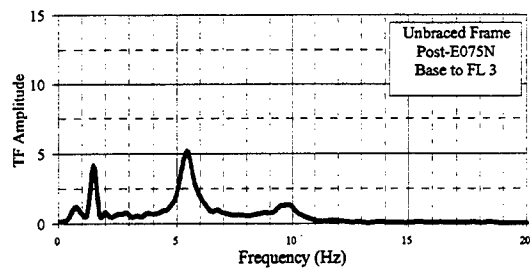


Figure C.16.25 Acceleration-Based Transfer Functions, White Noise Tests: E075N - E150N

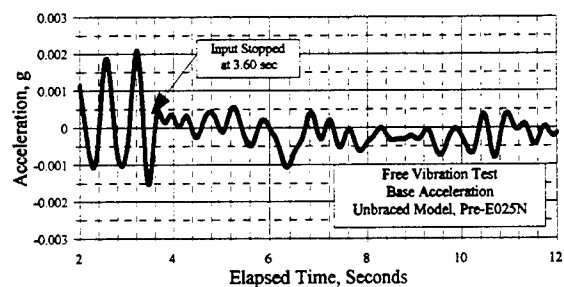
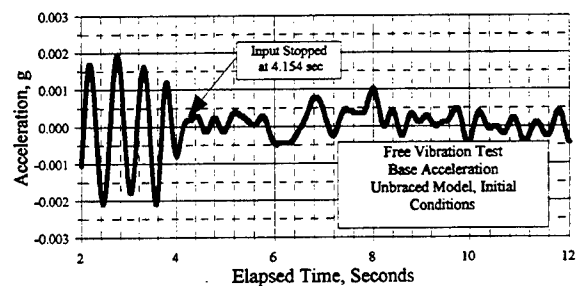
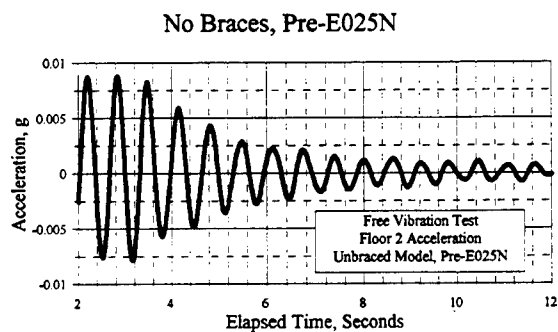
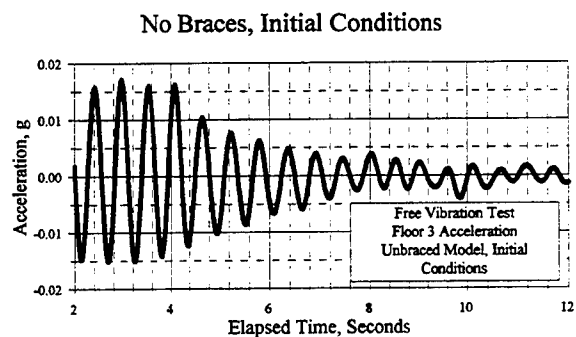
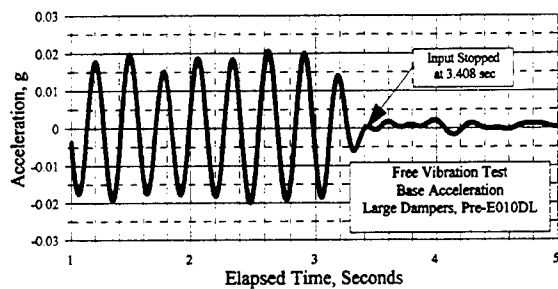
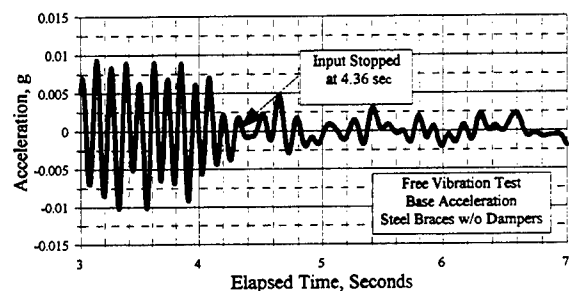
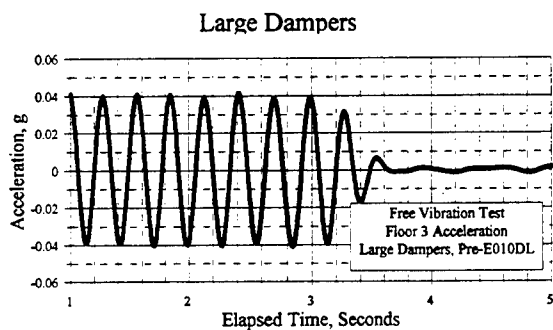
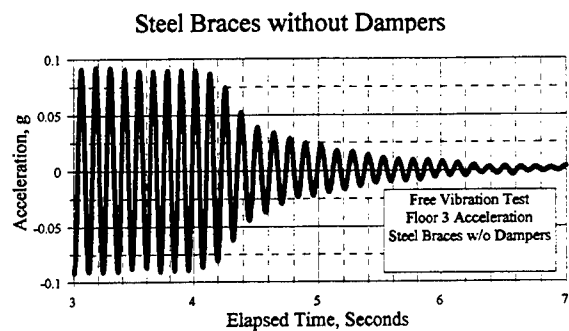


Figure C.16.26 Free Vibration Tests

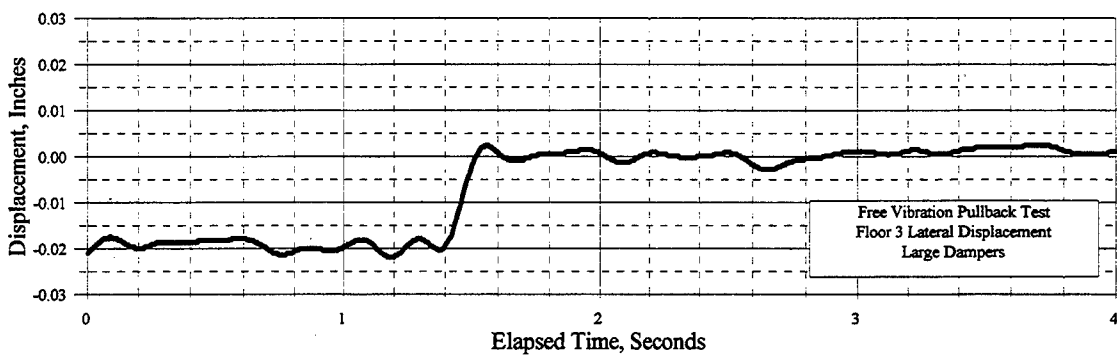
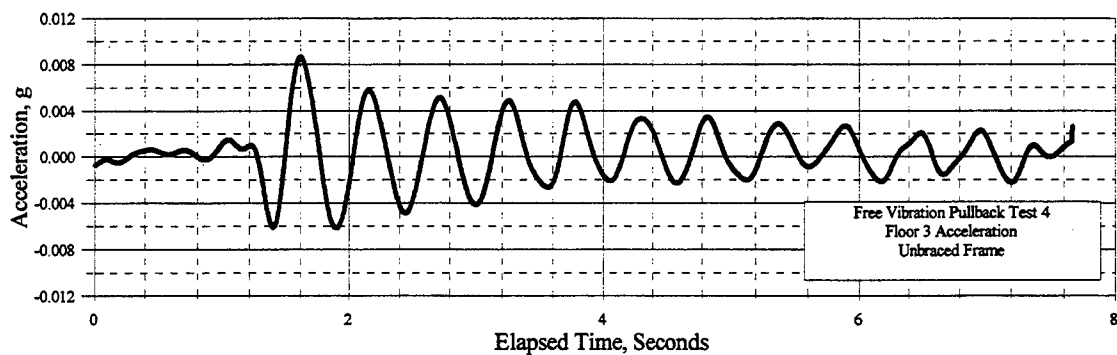
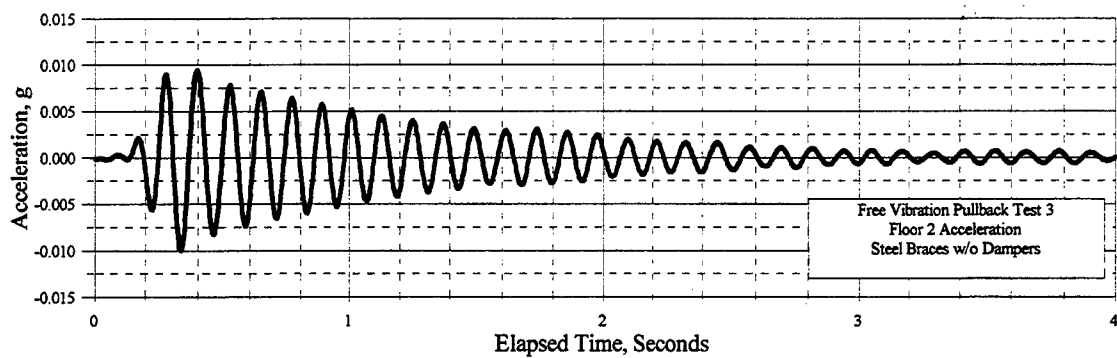


Figure C.16.27 Pullback Test Results

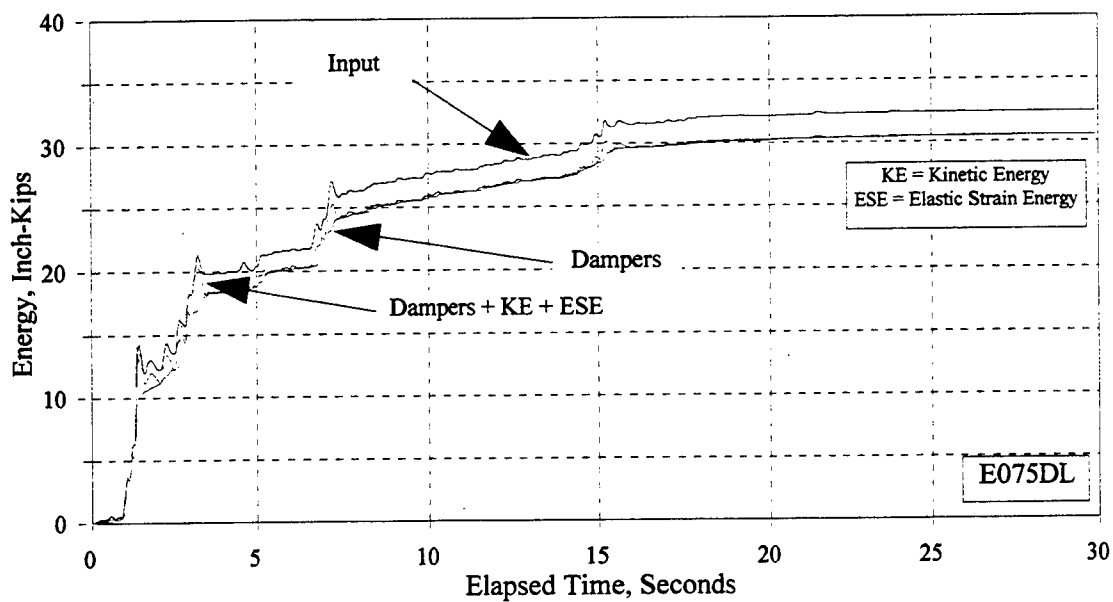
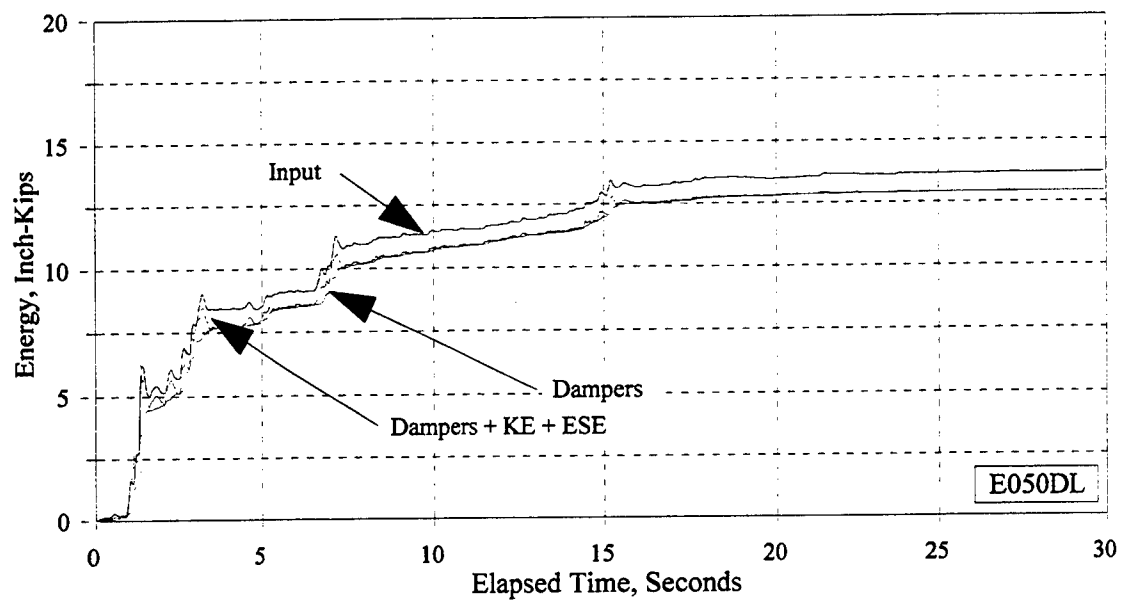


Figure C.17.1 Input, Damper Dissipation, Kinetic, and Elastic Strain Energies: E050DL and E075DL

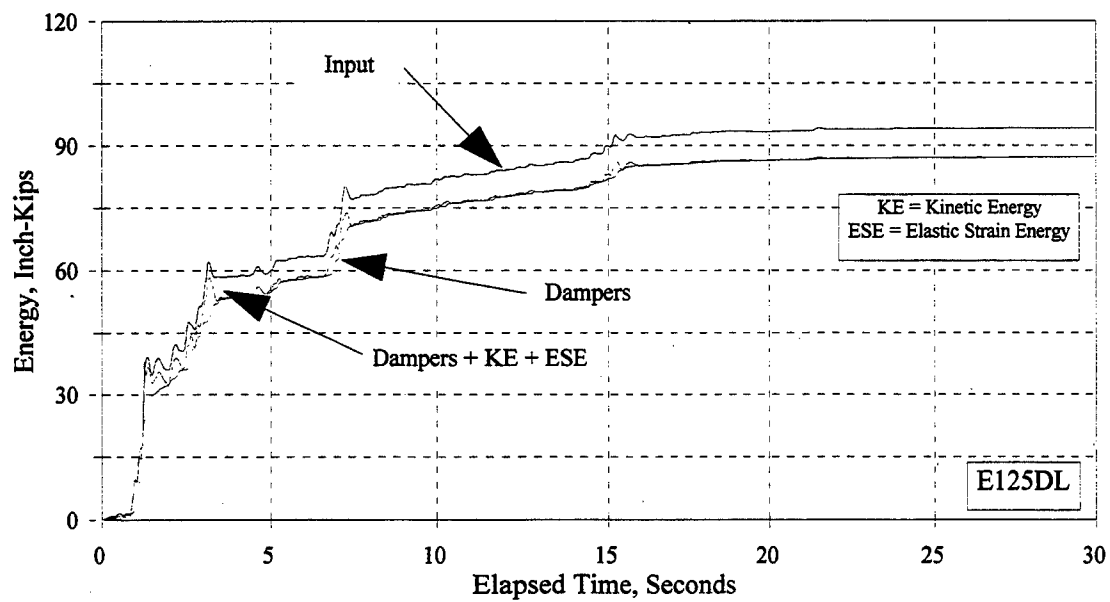
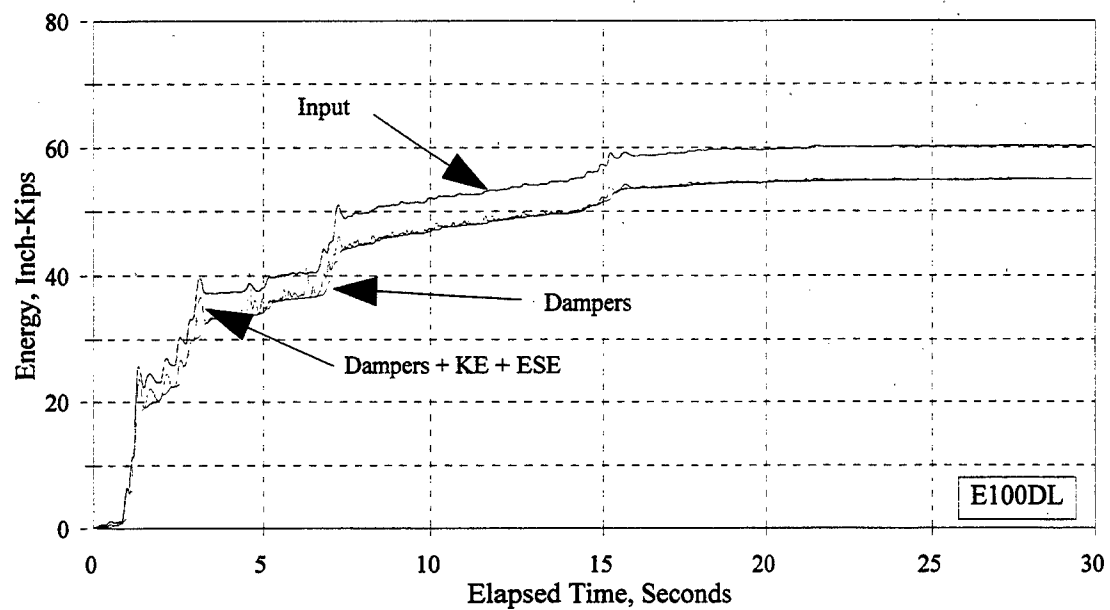


Figure C.17.2 Input, Damper Dissipation, Kinetic, and Elastic Strain Energies: E100DL and E125DL

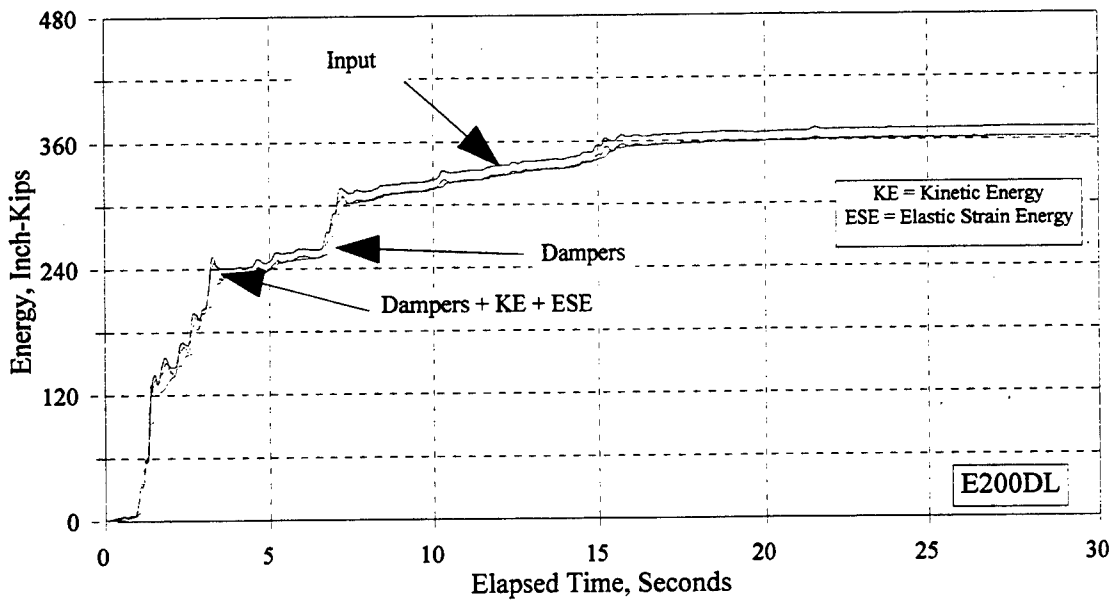
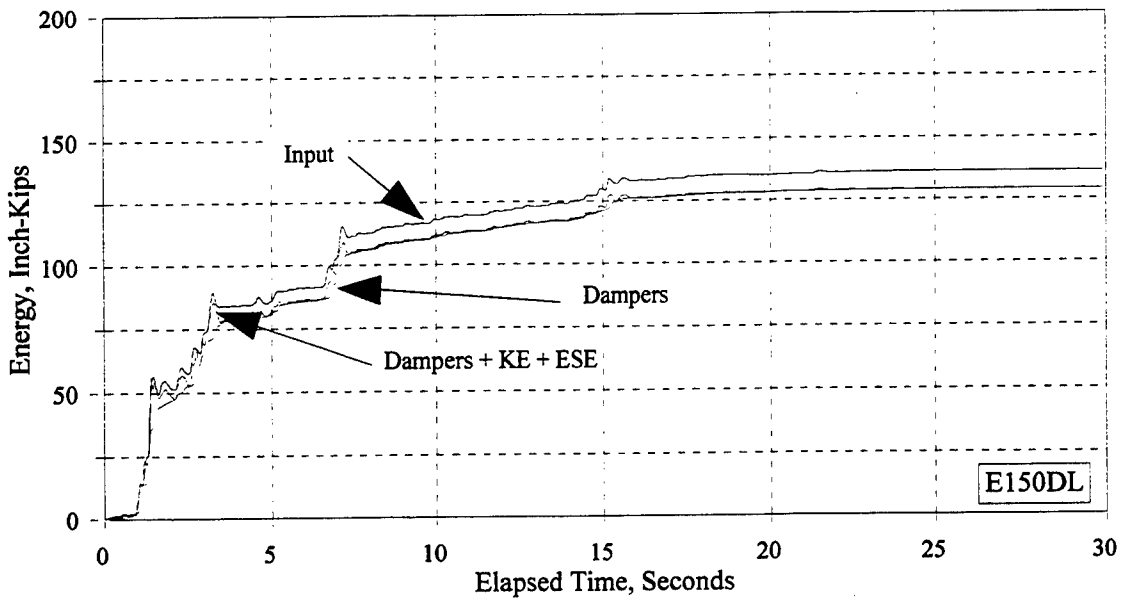


Figure C.17.3 Input, Damper Dissipation, Kinetic, and Elastic Strain Energies: E150DL and E200DL

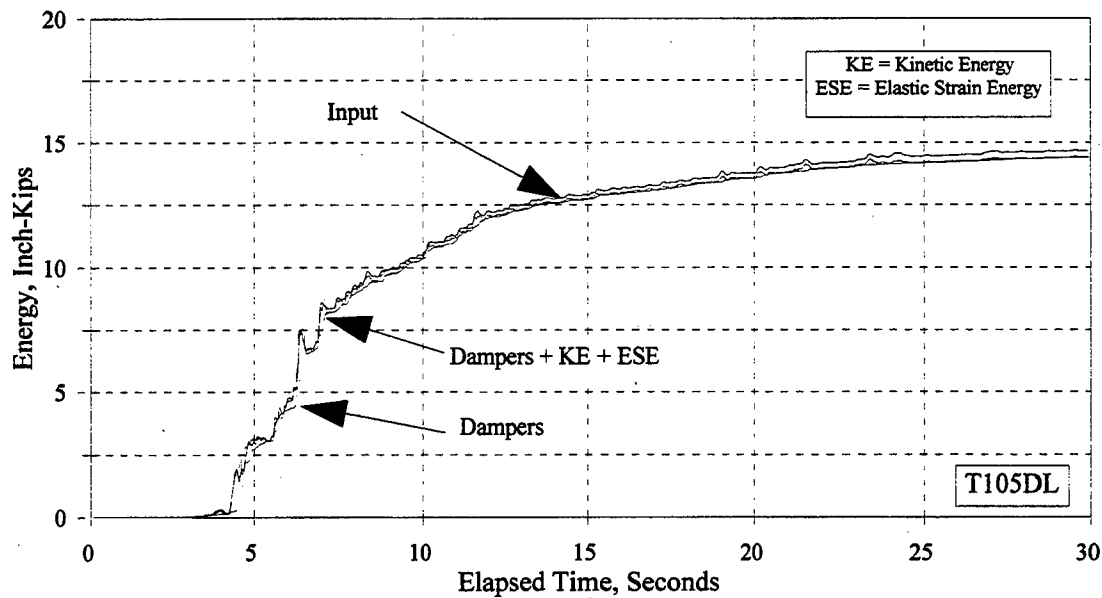
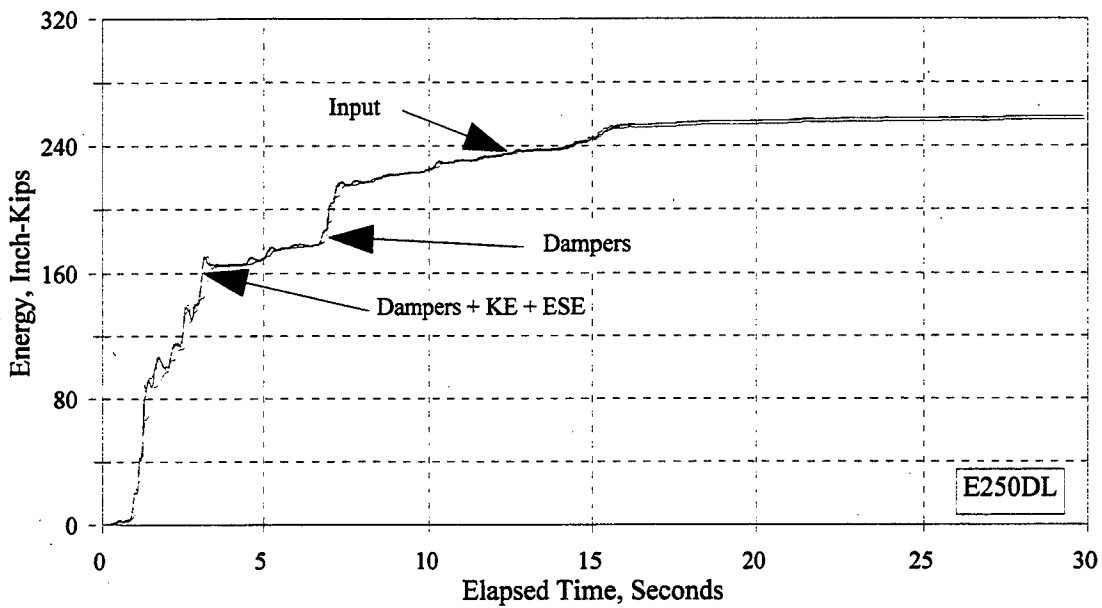


Figure C.17.4 Input, Damper Dissipation, Kinetic, and Elastic Strain Energies: E250DL and T105DL

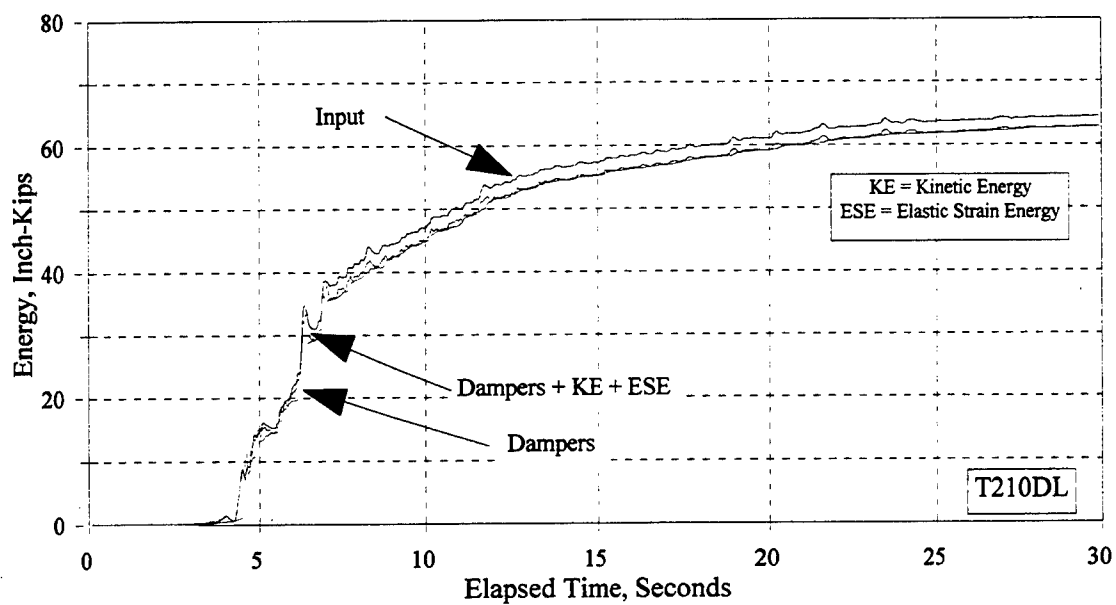
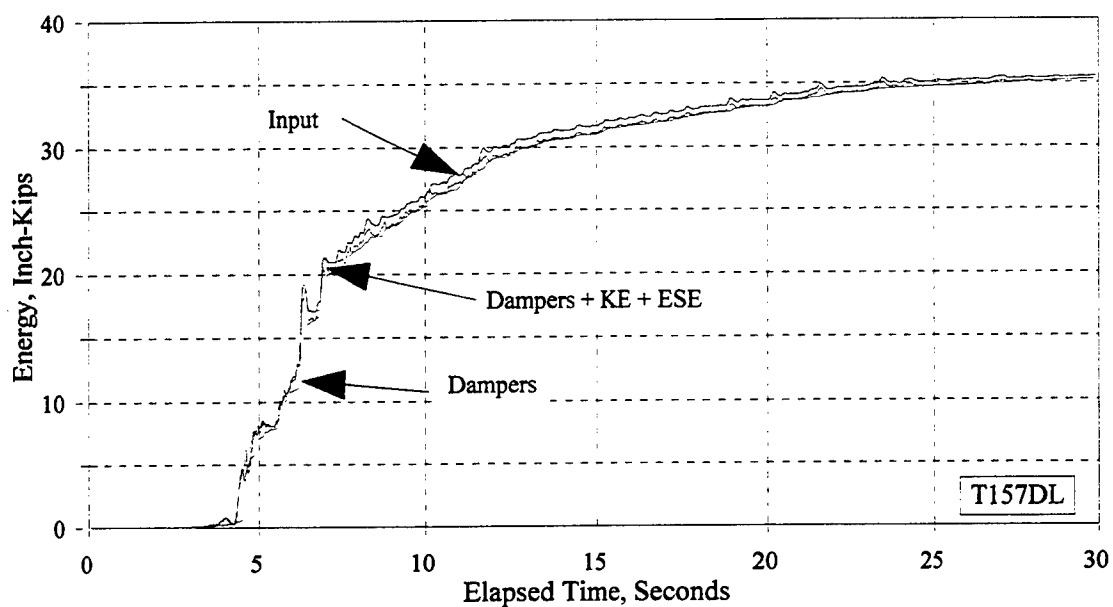


Figure C.17.5 Input, Damper Dissipation, Kinetic, and Elastic Strain Energies: T157DL and T210DL

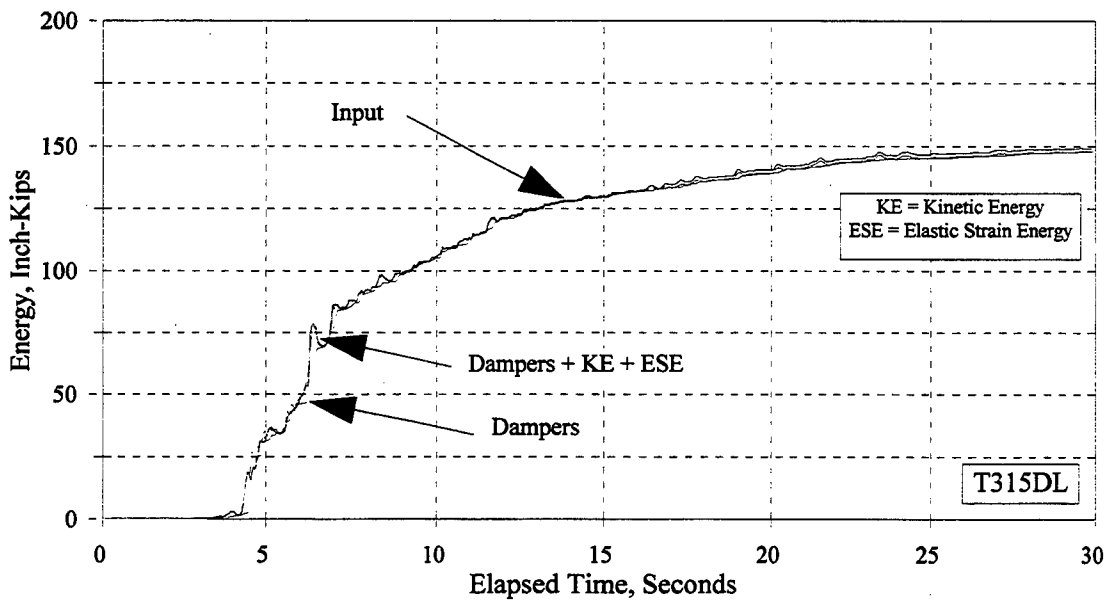
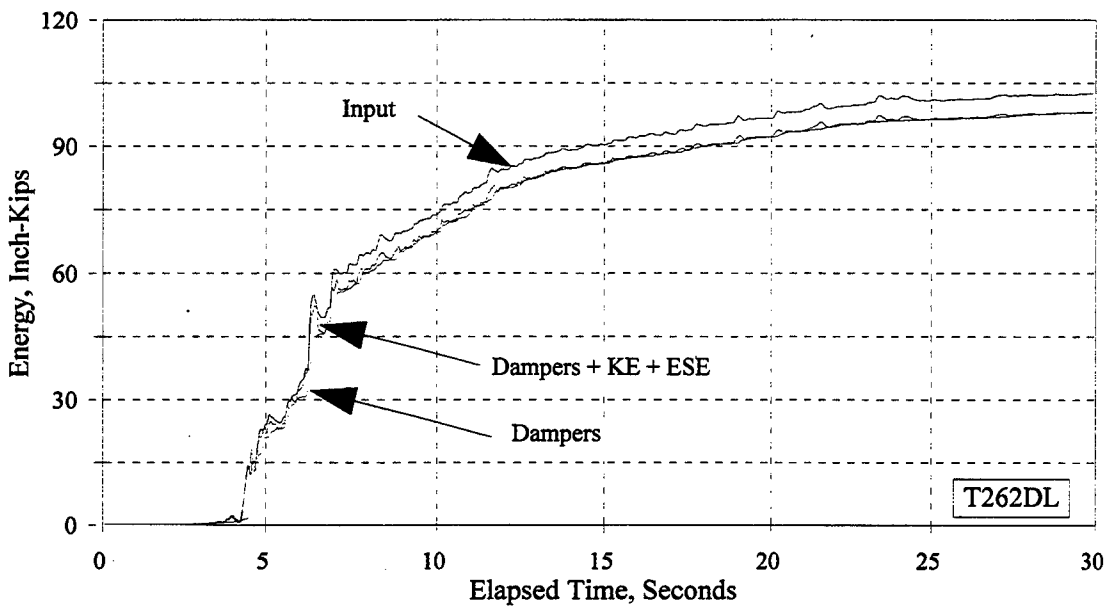


Figure C.17.6 Input, Damper Dissipation, Kinetic, and Elastic Strain Energies: T262DL and T315DL

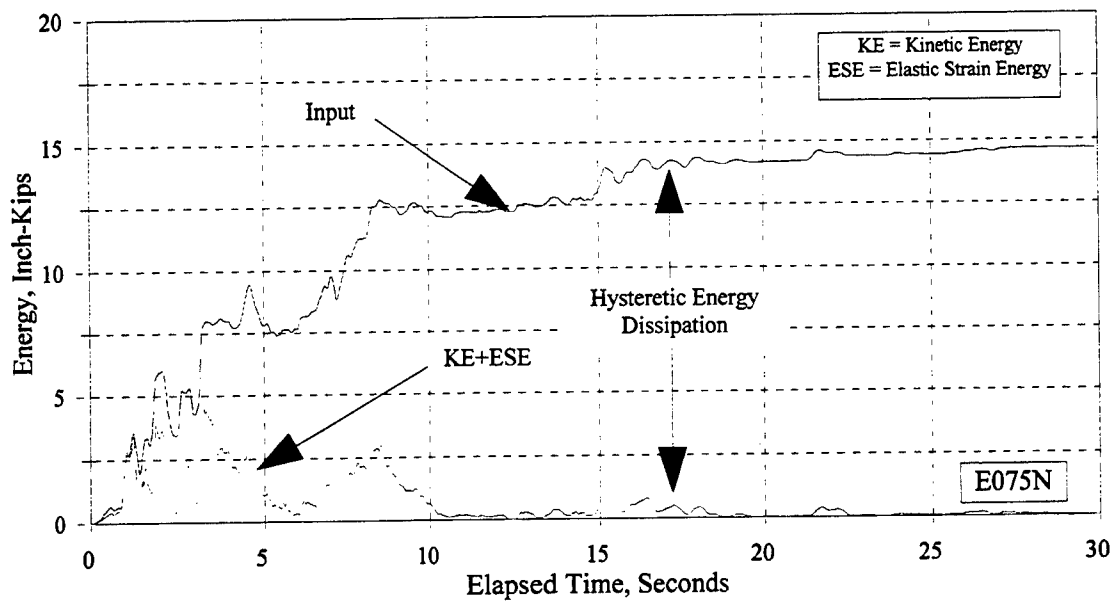
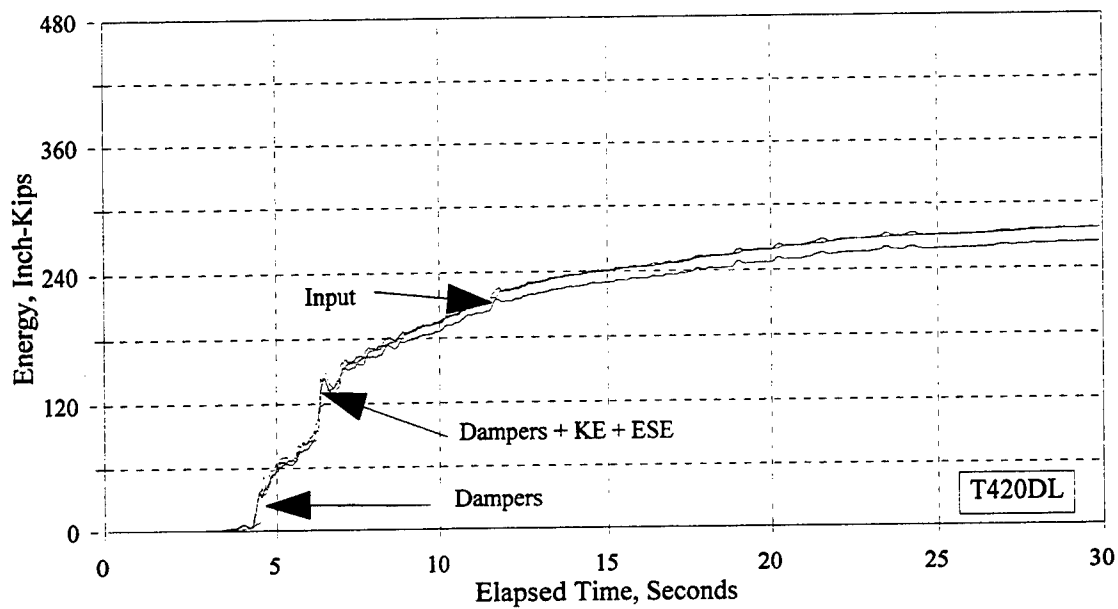


Figure C.17.7 Input, Damper Dissipation, Kinetic, and Elastic Strain Energies: T420DL and E075N

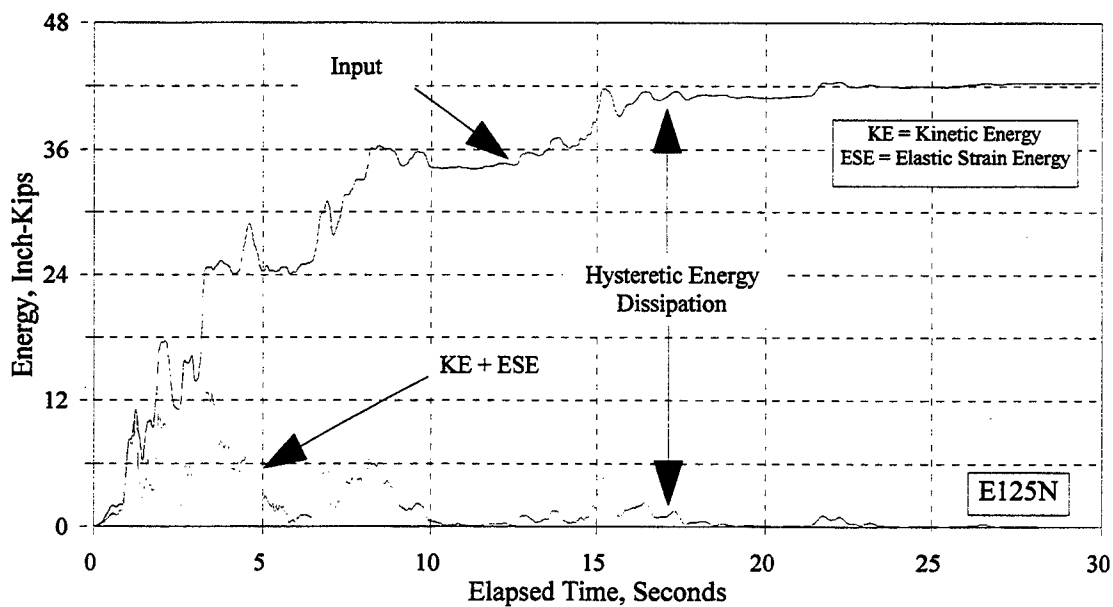
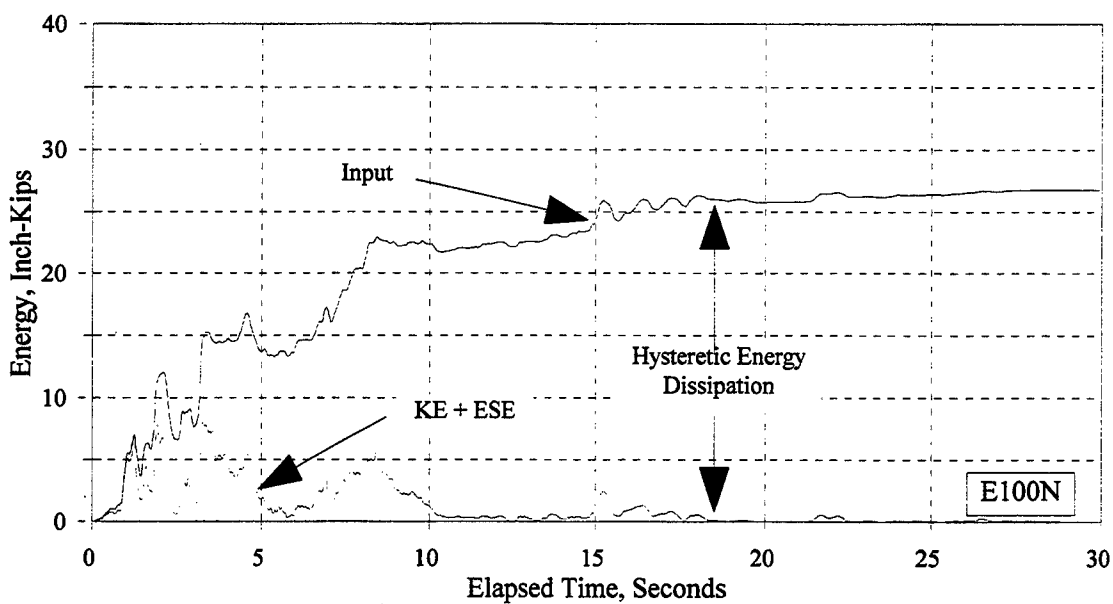


Figure C.17.8 Input, Kinetic, and Elastic Strain Energies: E100N and E125N

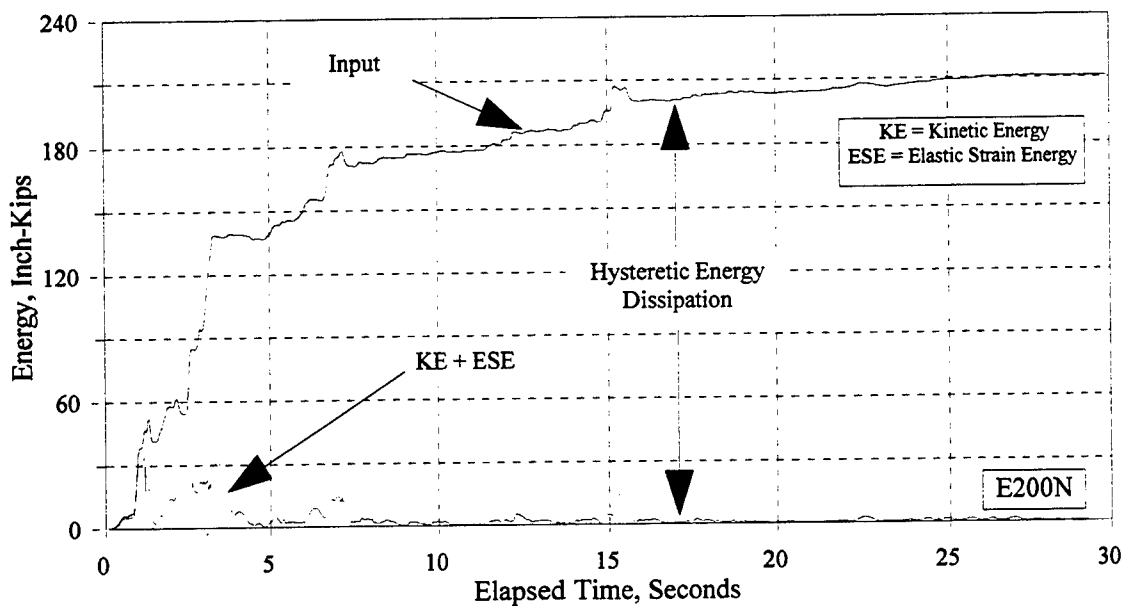
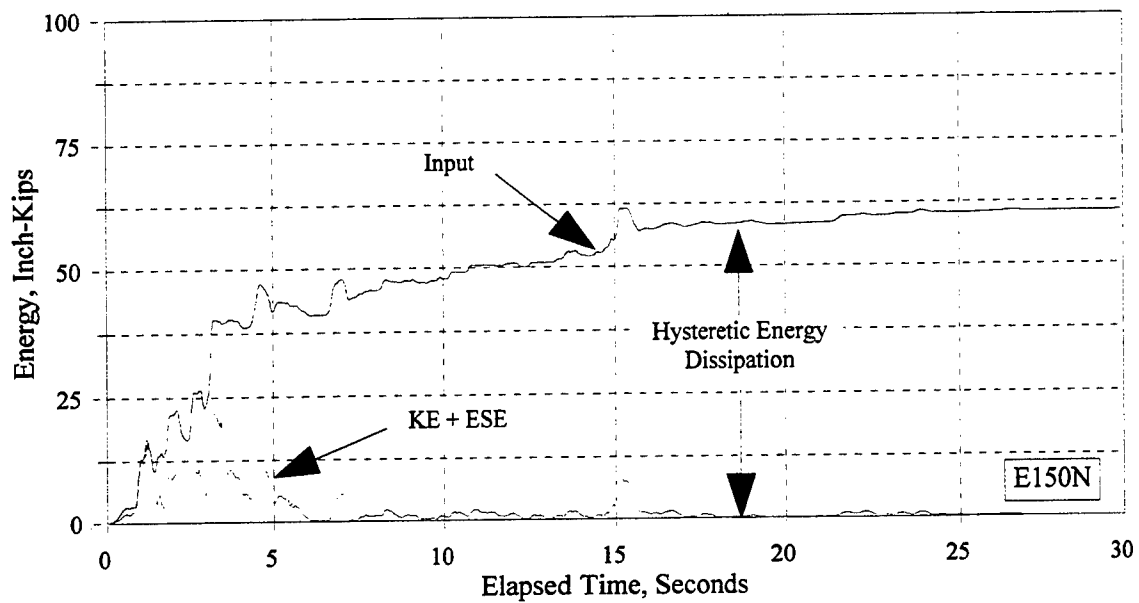


Figure C.17.9 Input, Kinetic, and Elastic Strain Energies: E150N and E200N

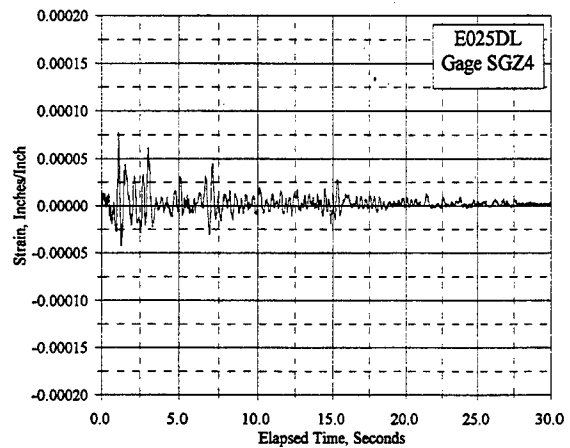
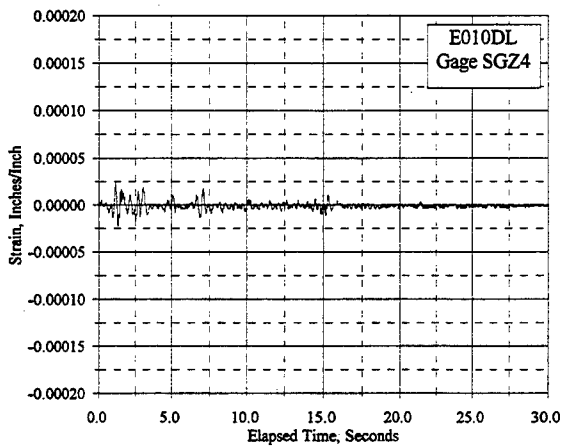
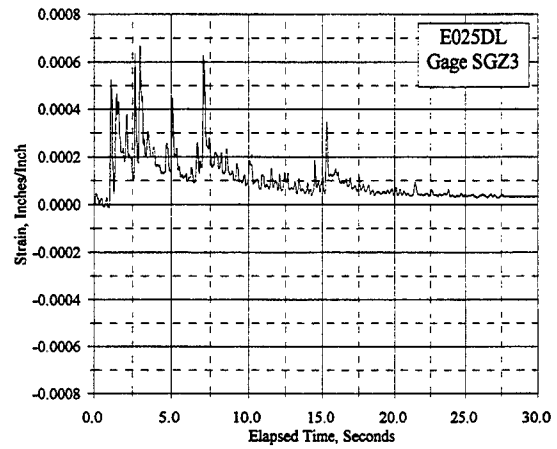
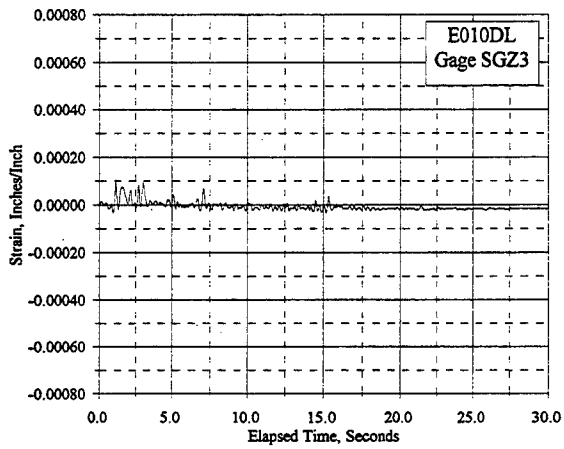
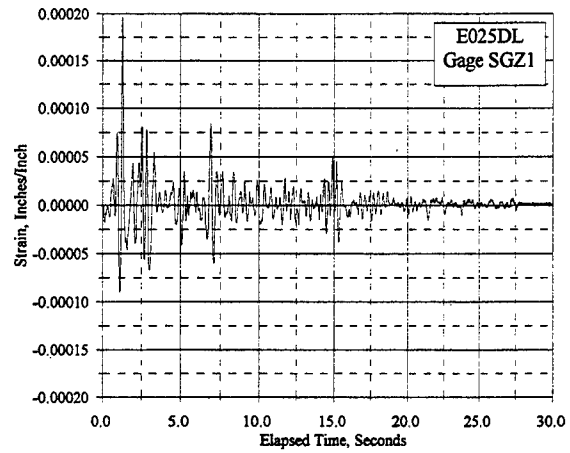
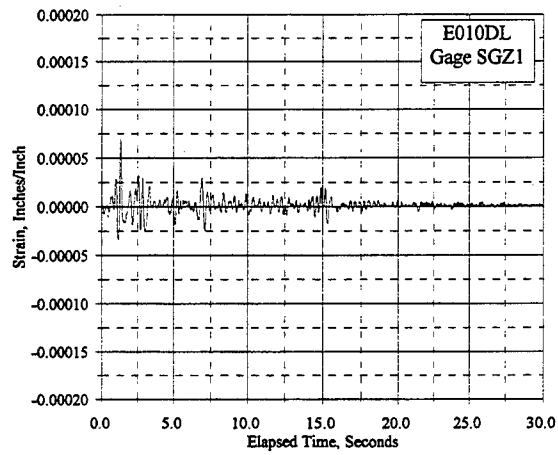


Figure C.18.1 Reinforcement Strain Vs. Elapsed Time, Gages SGZ1, SGZ3, SGZ4: E010DL, E025DL

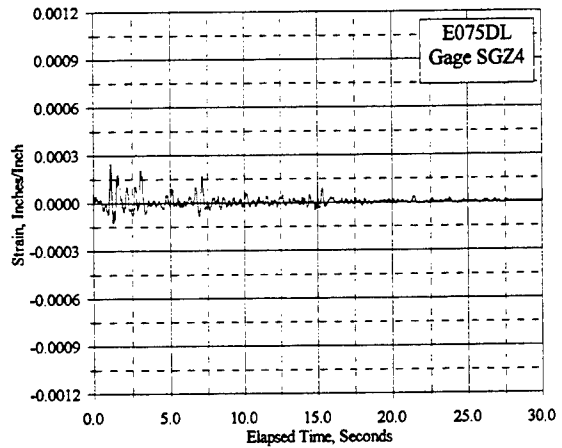
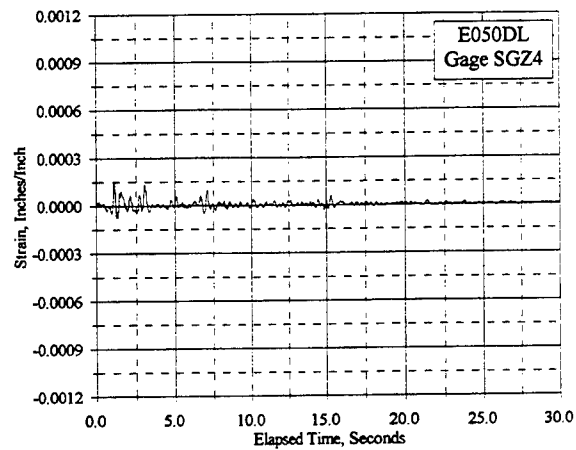
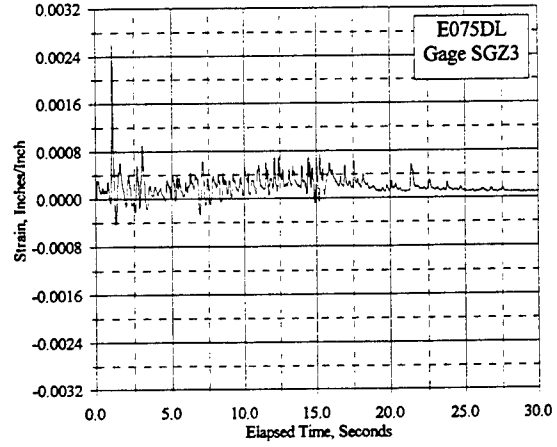
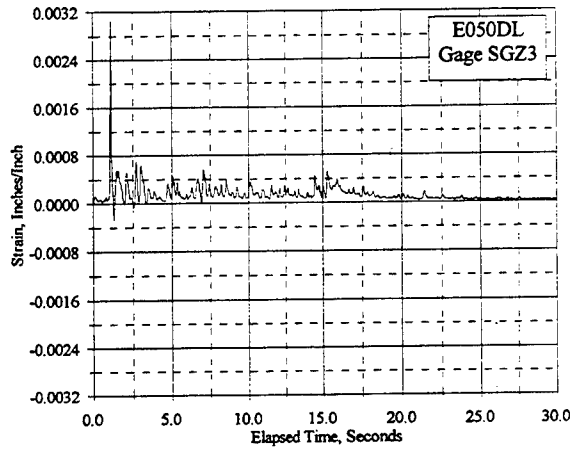
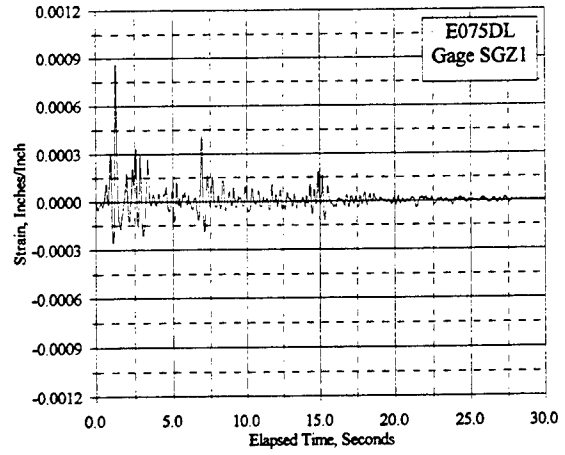
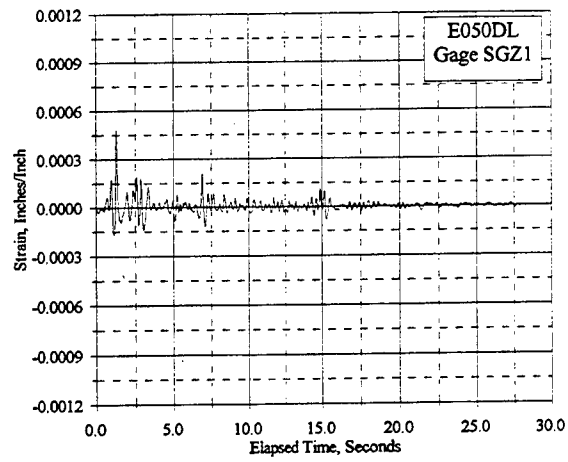


Figure C.18.2 Reinforcement Strain Vs. Elapsed Time, Gages SGZ1, SGZ3, SGZ4: E050DL, E075DL

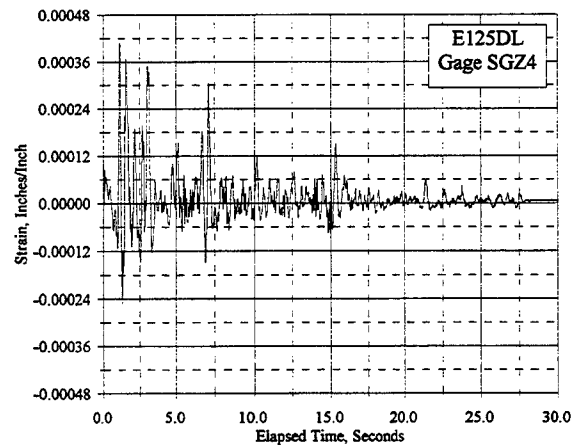
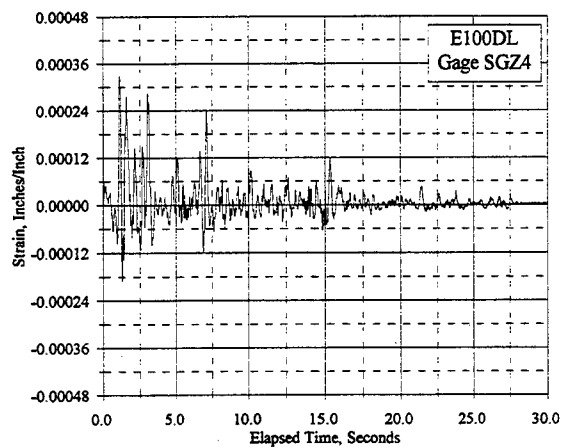
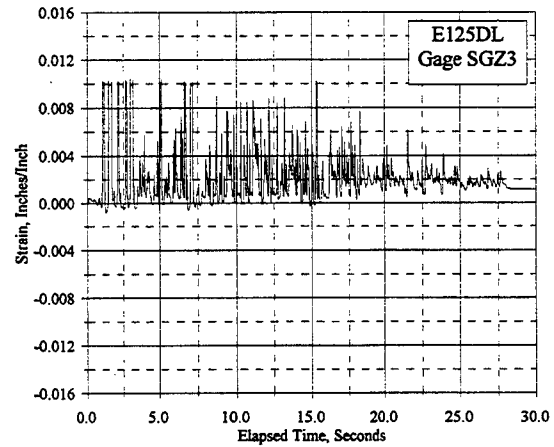
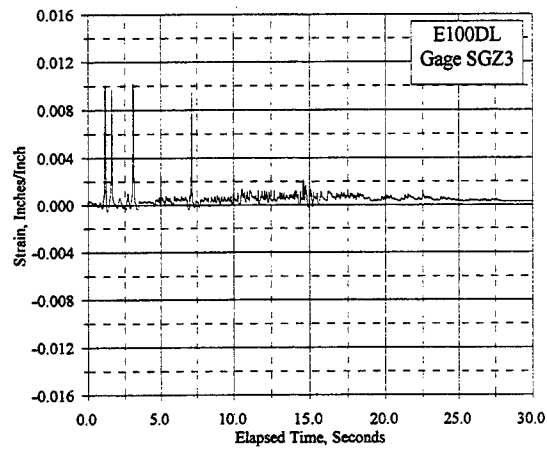
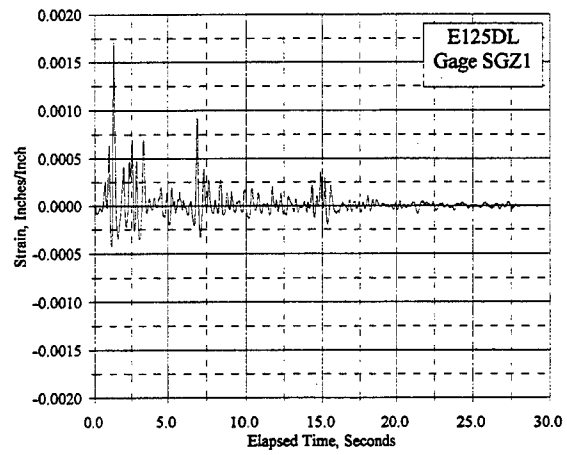
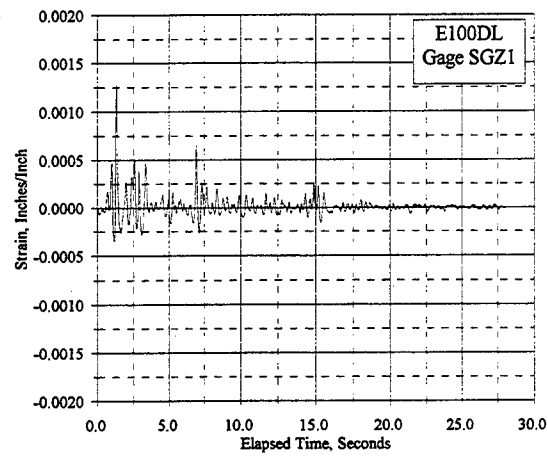


Figure C.18.3 Reinforcement Strain Vs. Elapsed Time, Gages SGZ1, SGZ3, SGZ4: E100DL, E125DL

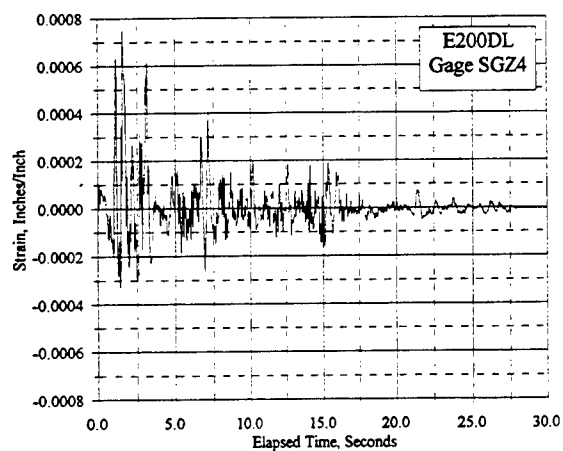
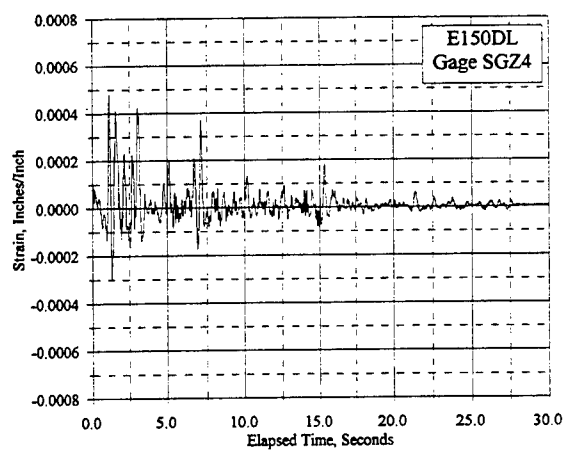
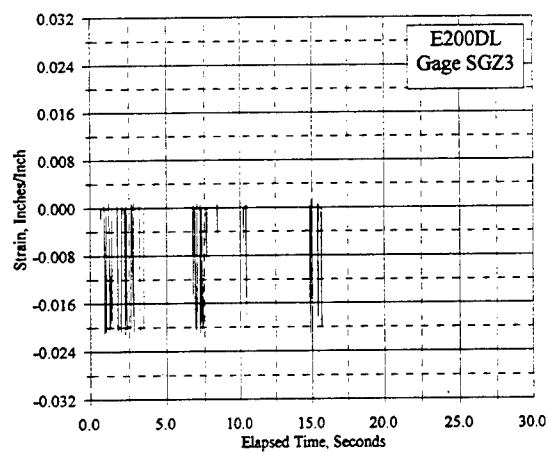
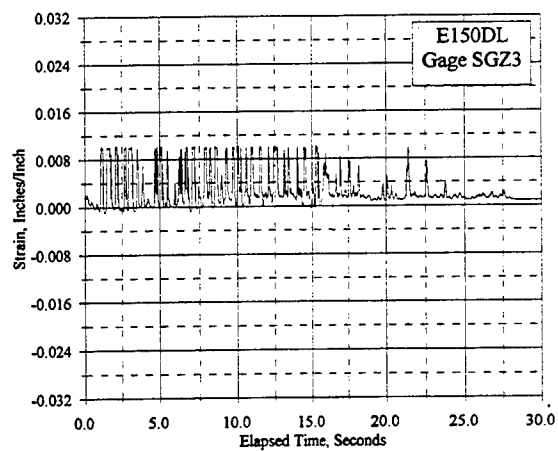
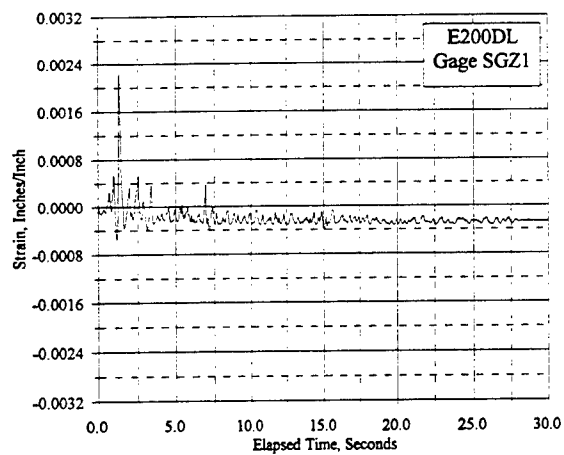
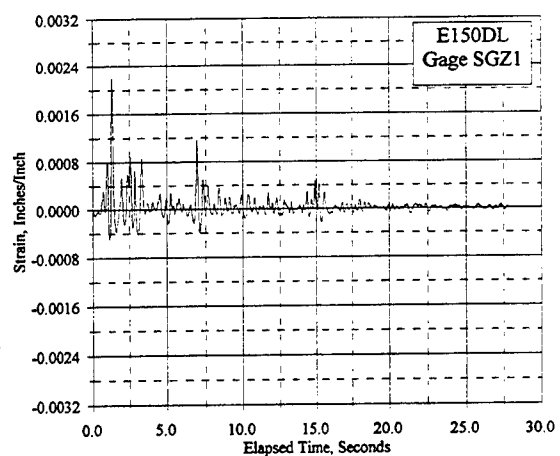


Figure C.18.4 Reinforcement Strain Vs. Elapsed Time, Gages SGZ1, SGZ3, SGZ4: E150DL, E200DL

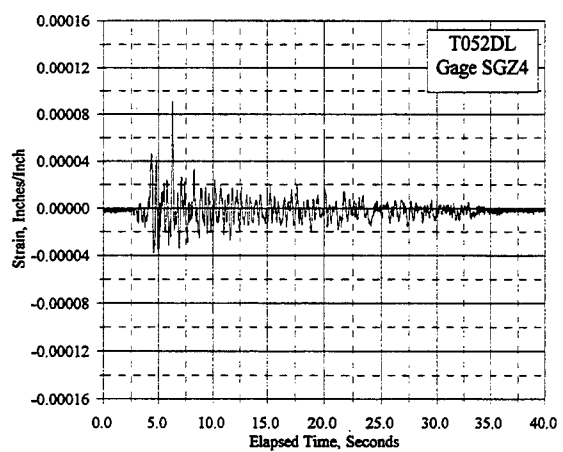
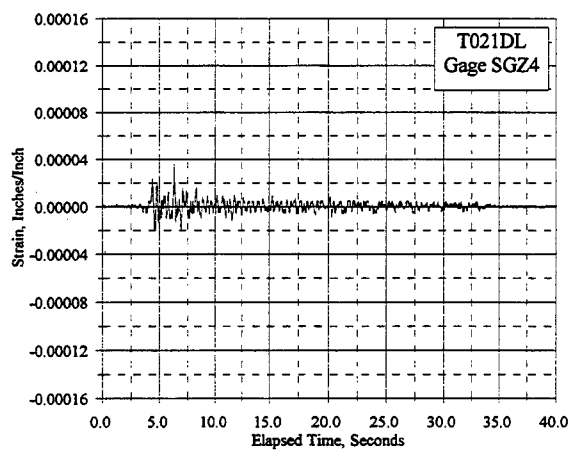
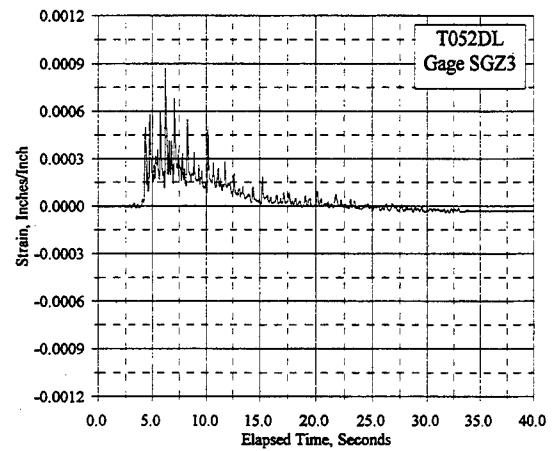
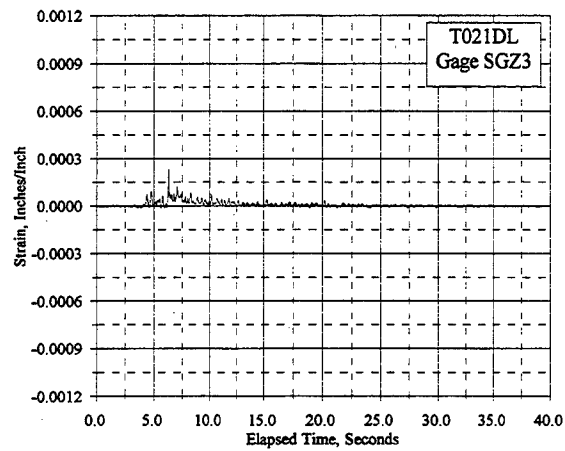
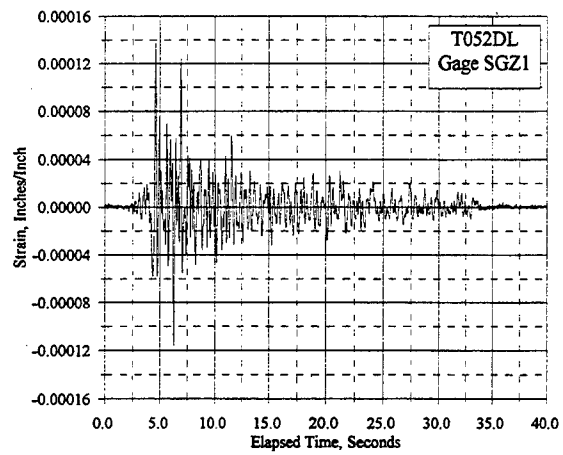
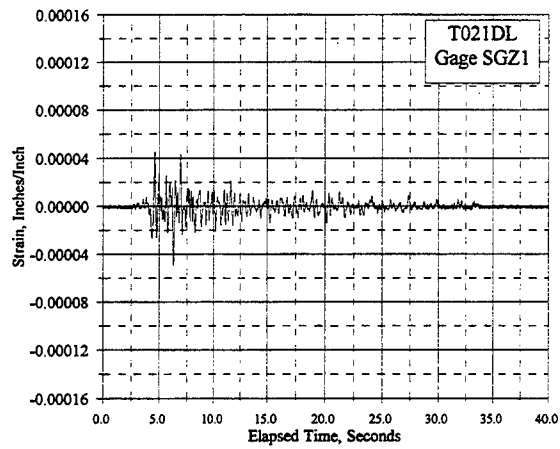


Figure C.18.5 Reinforcement Strain Vs. Elapsed Time, Gages SGZ1, SGZ3, SGZ4: T021DL, T052DL

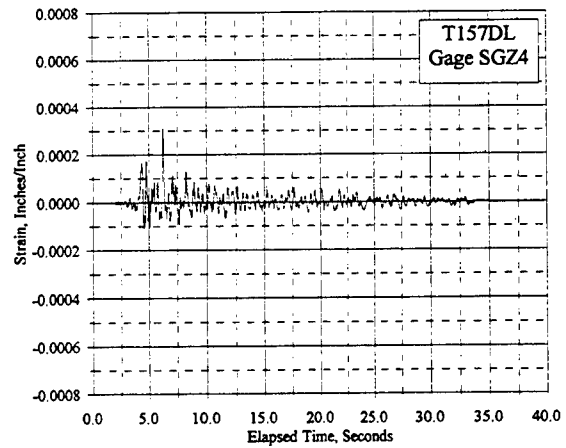
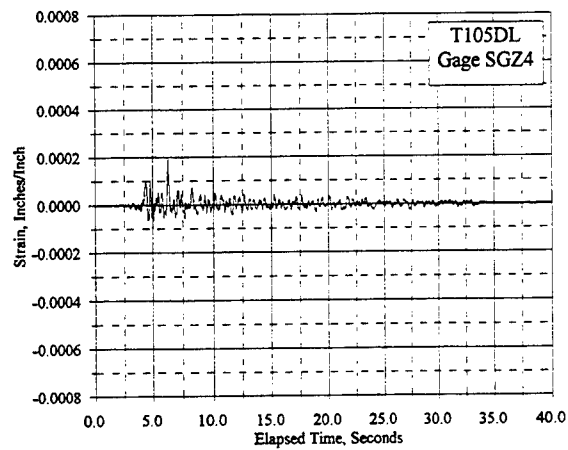
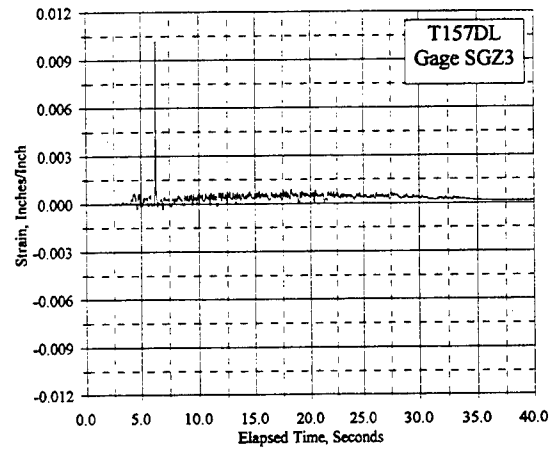
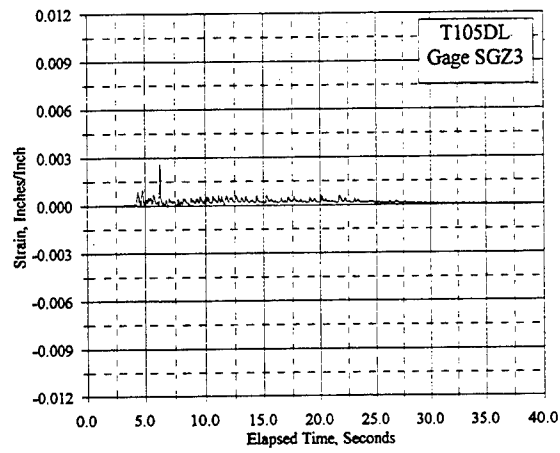
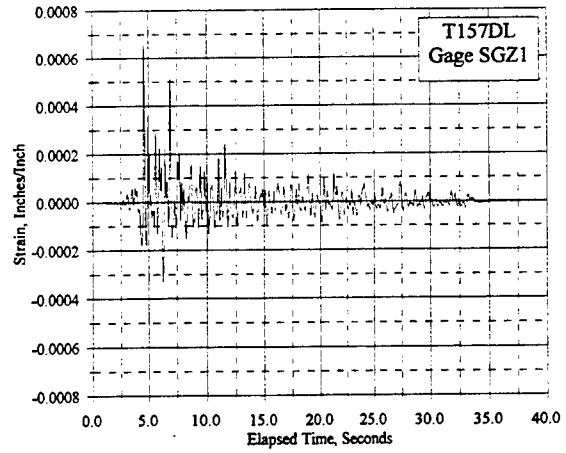
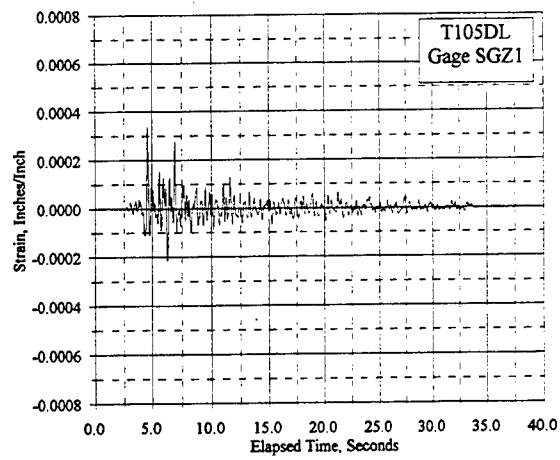


Figure C.18.6 Reinforcement Strain Vs. Elapsed Time, Gages SGZ1, SGZ3, SGZ4: T105DL, T157DL

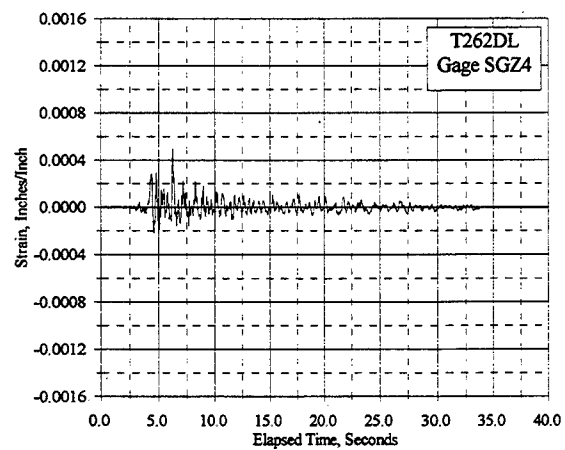
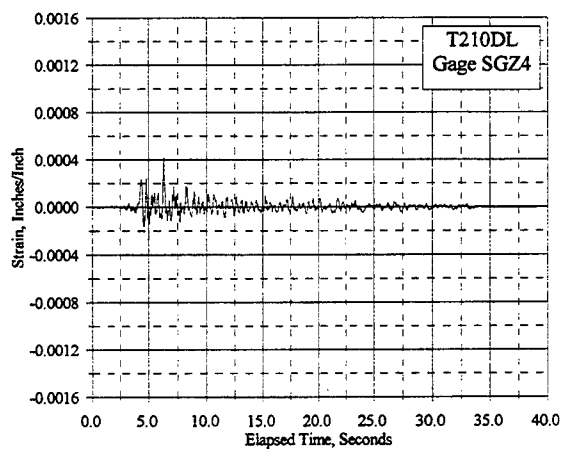
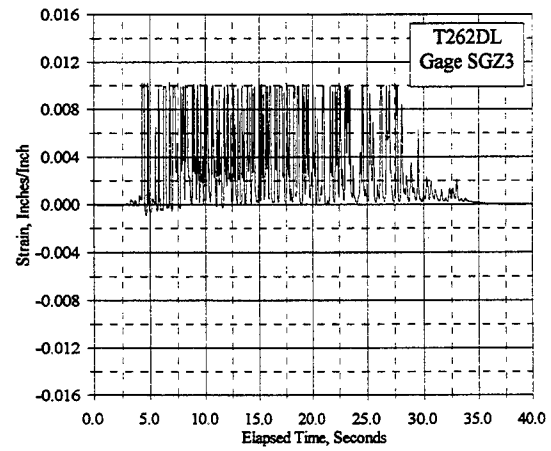
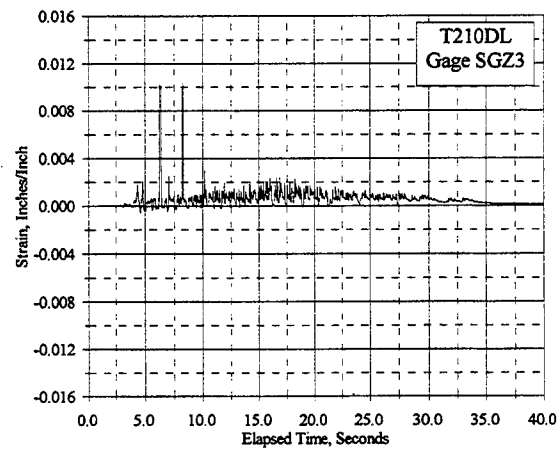
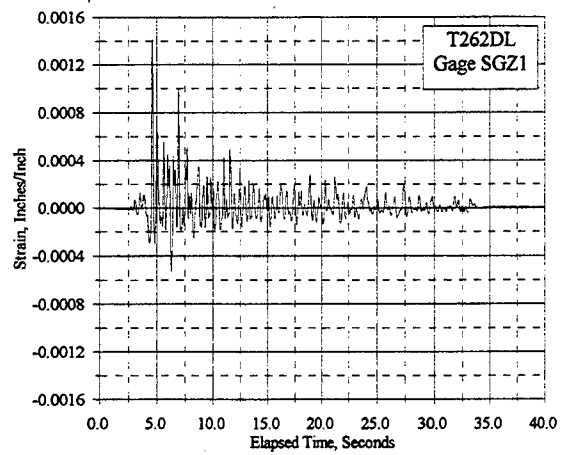
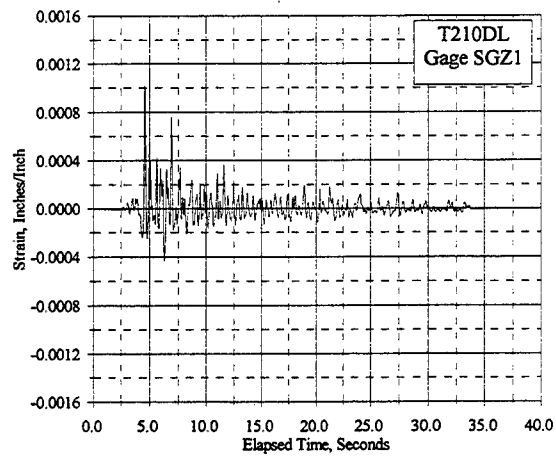


Figure C.18.7 Reinforcement Strain Vs. Elapsed Time, Gages SGZ1, SGZ3, SGZ4: T210DL, T262DL

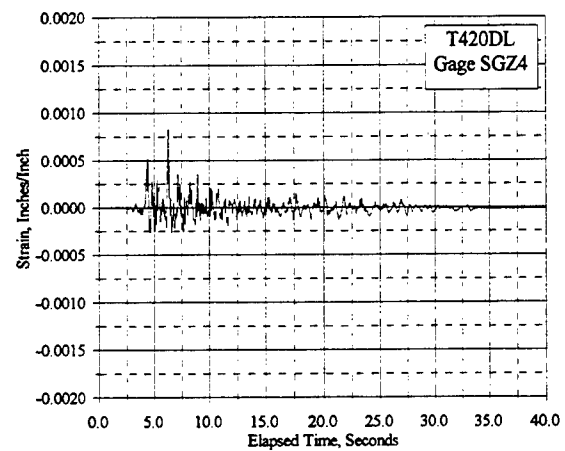
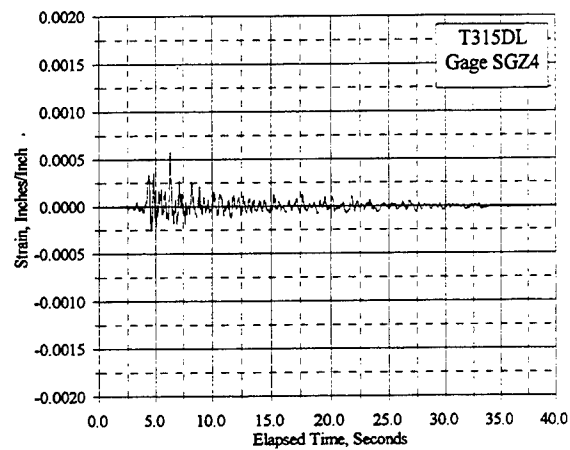
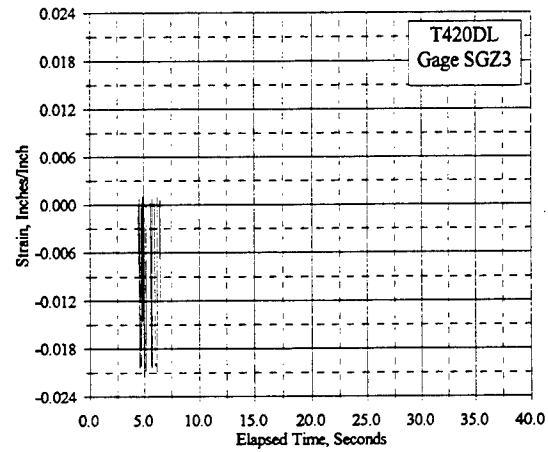
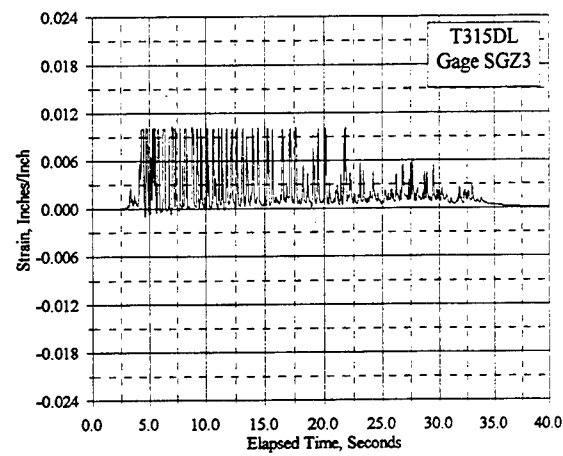
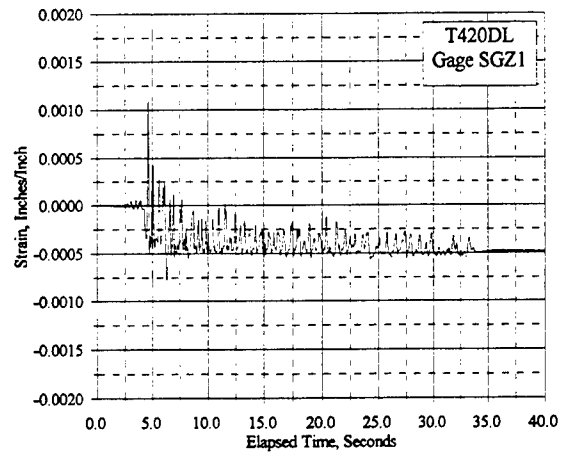
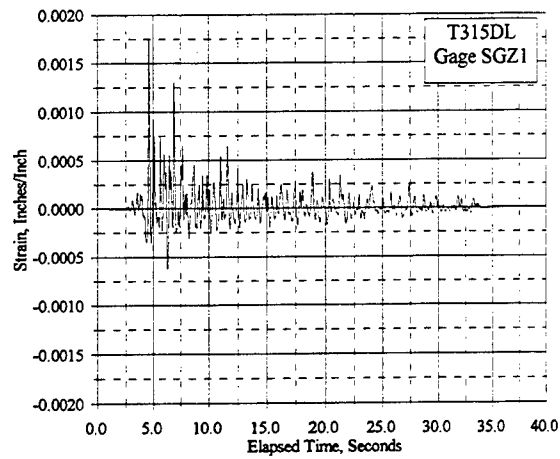


Figure C.18.8 Reinforcement Strain Vs. Elapsed Time, Gages SGZ1, SGZ3, SGZ4: T315DL, T420DL

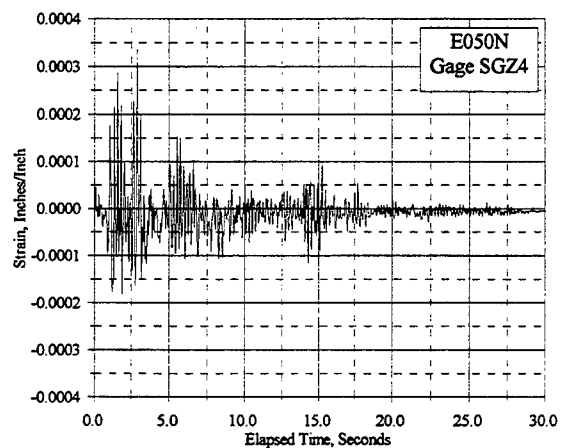
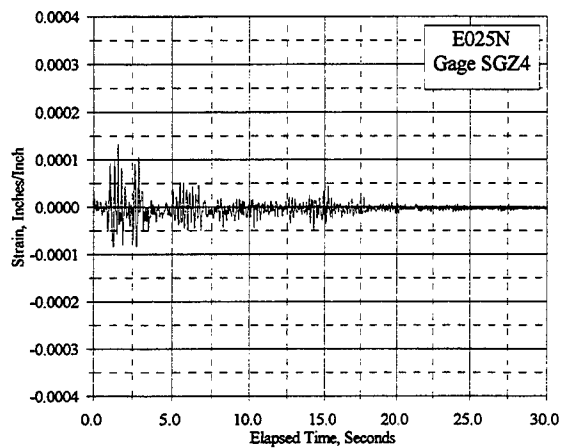
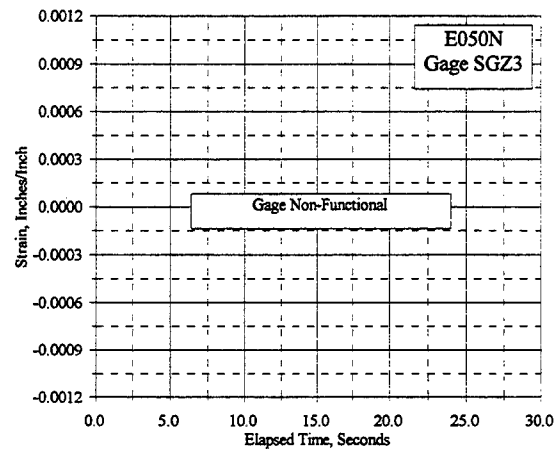
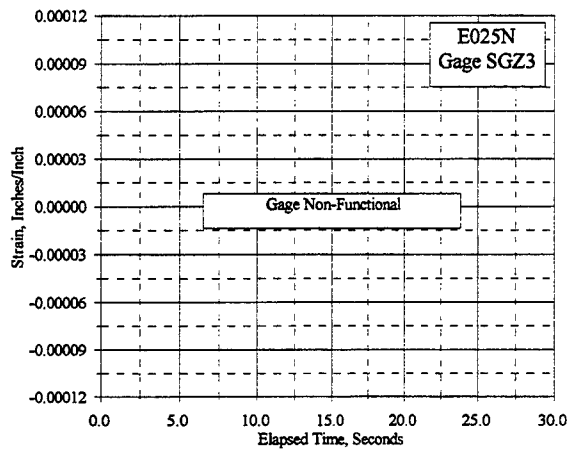
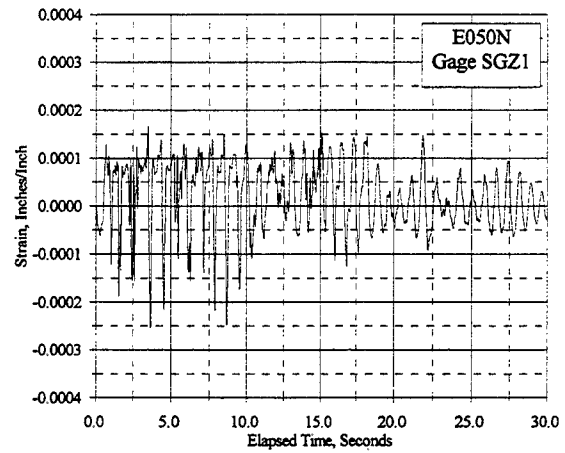
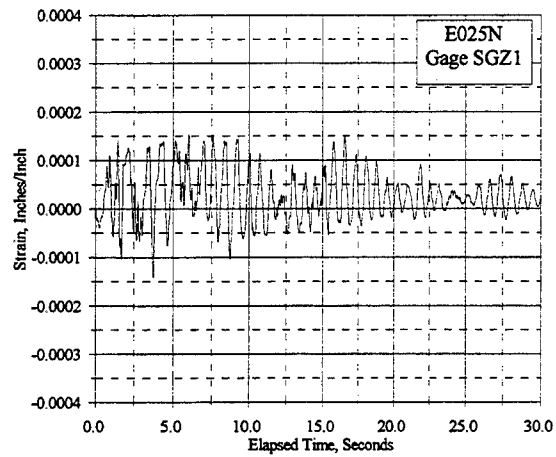


Figure C.18.9 Reinforcement Strain Vs. Elapsed Time, Gages SGZ1, SGZ3, SGZ4: E025N, E050N

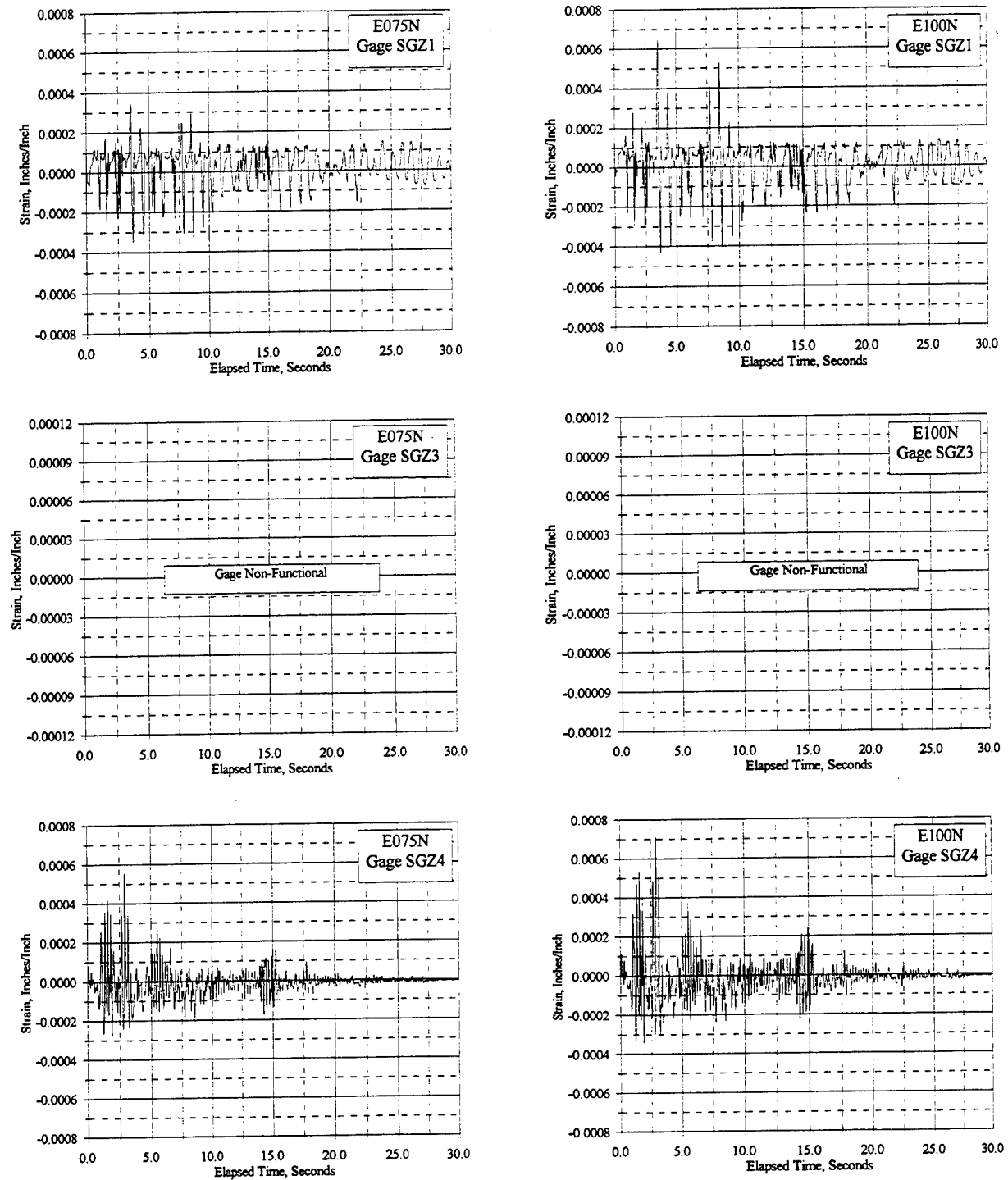


Figure C.18.10 Reinforcement Strain Vs. Elapsed Time, Gages SGZ1, SGZ3, SGZ4: E075N, E100N

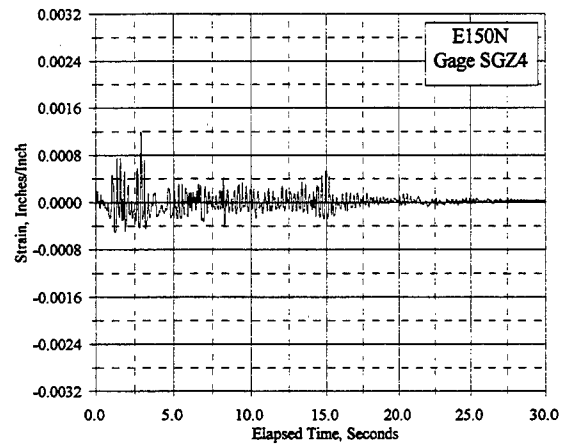
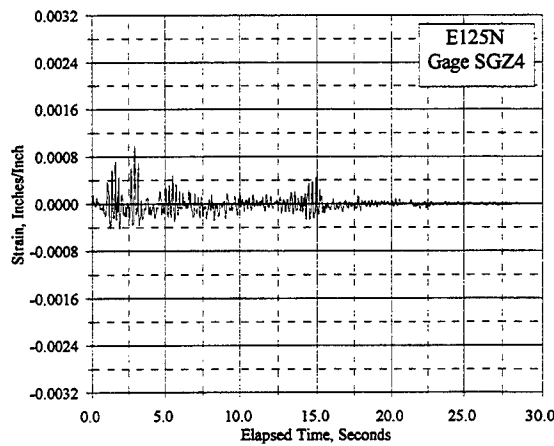
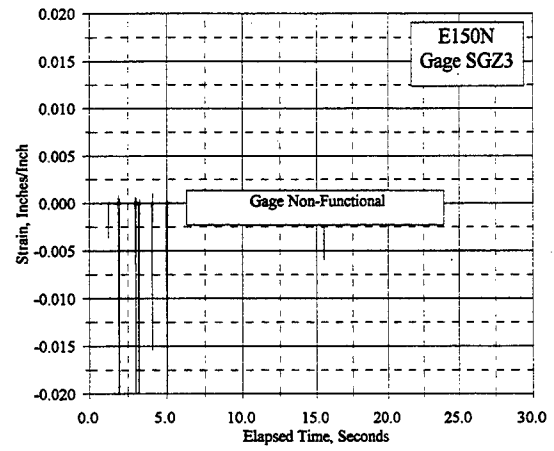
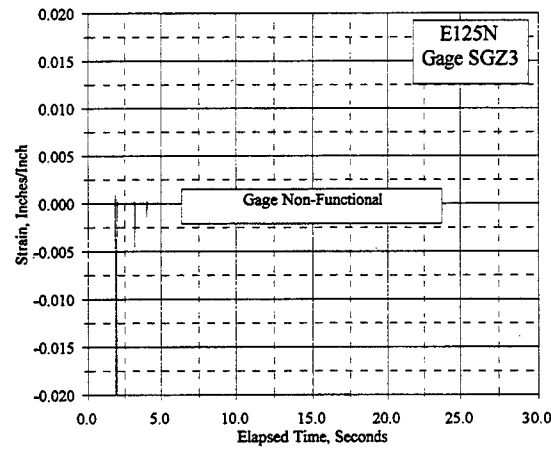
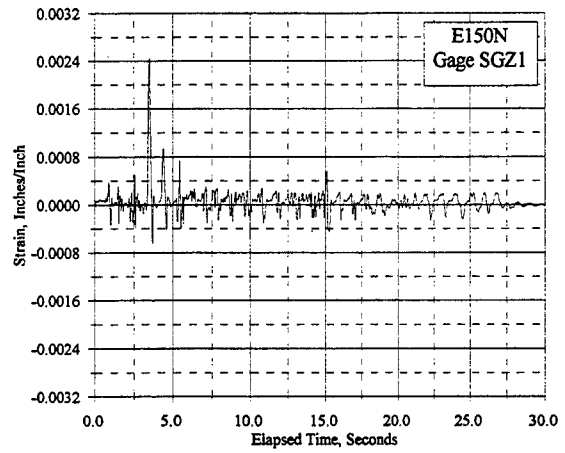
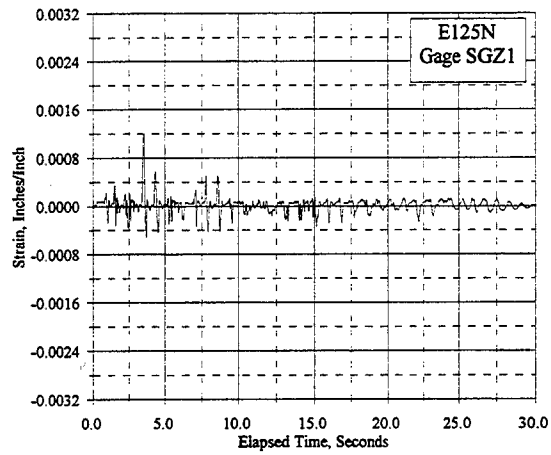


Figure C.18.11 Reinforcement Strain Vs. Elapsed Time, Gages SGZ1, SGZ3, SGZ4: E125N, E150N

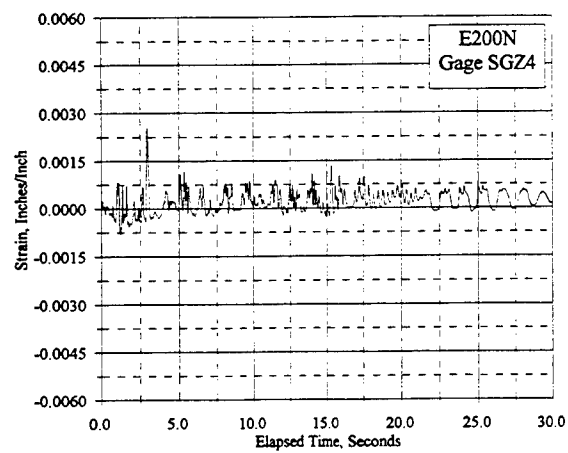
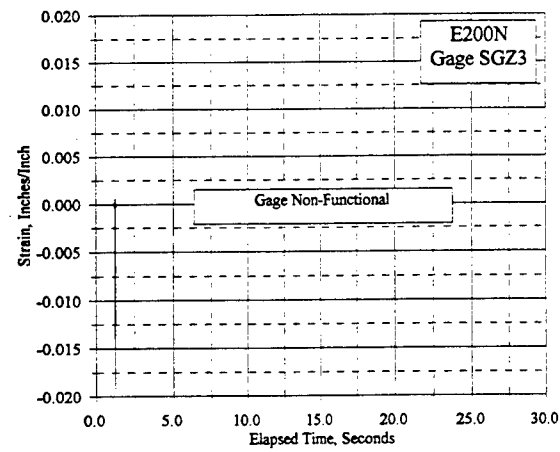
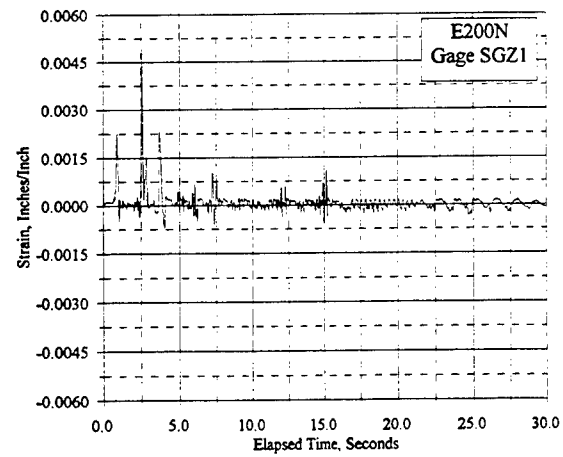


Figure C.18.12 Reinforcement Strain Vs. Elapsed Time, Gages SGZ1, SGZ3, SGZ4: E200N

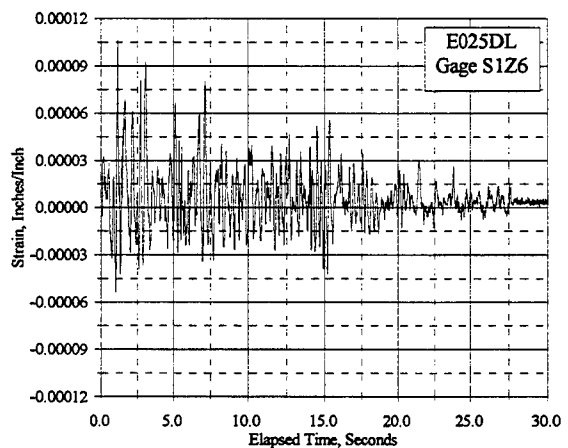
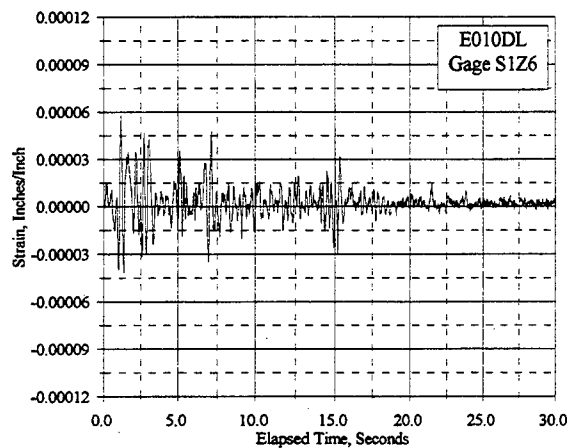
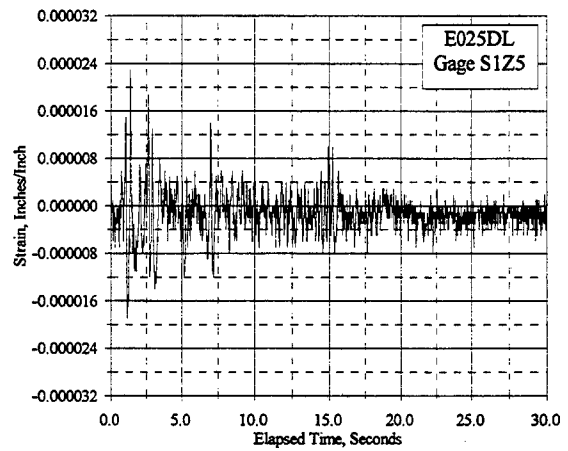
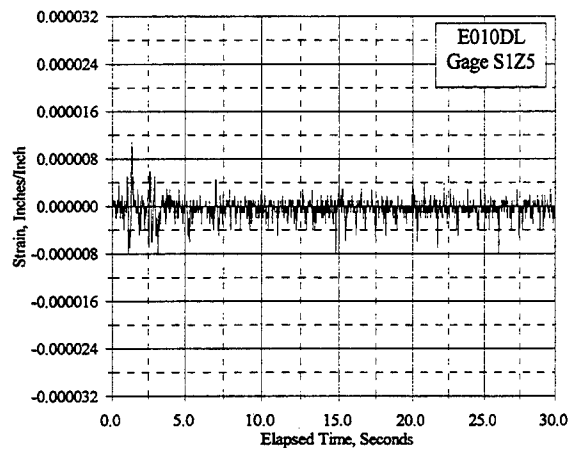
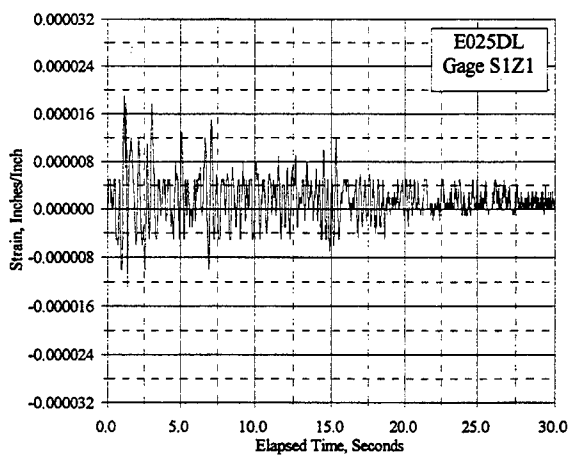
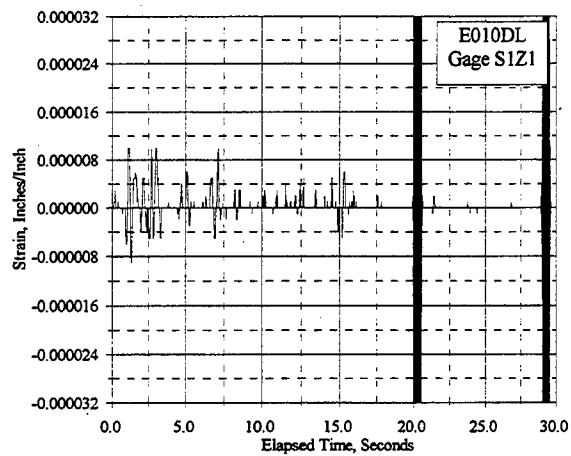


Figure C.19.1 Reinforcement Strain Vs. Elapsed Time, Gages S1Z1, S1Z5, S1Z6: E010DL, E025DL

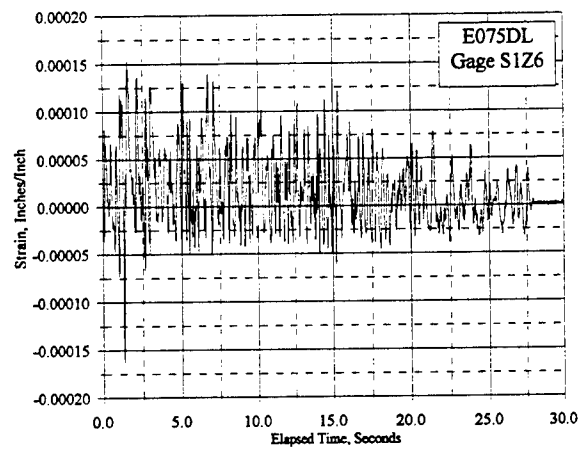
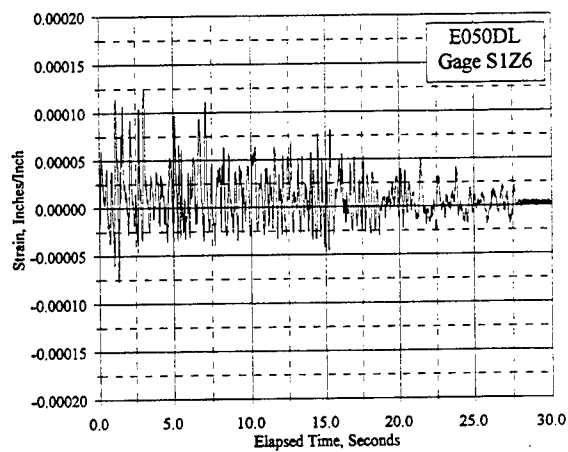
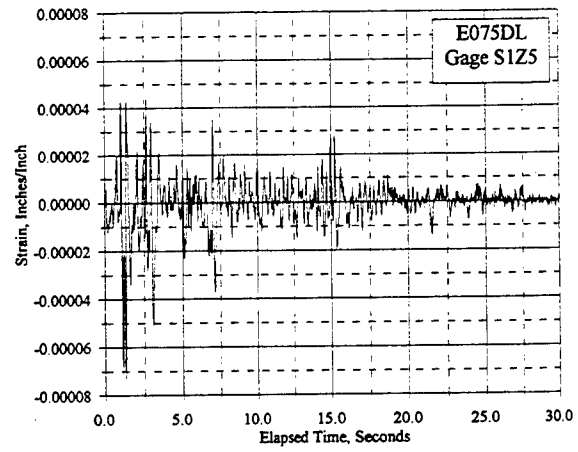
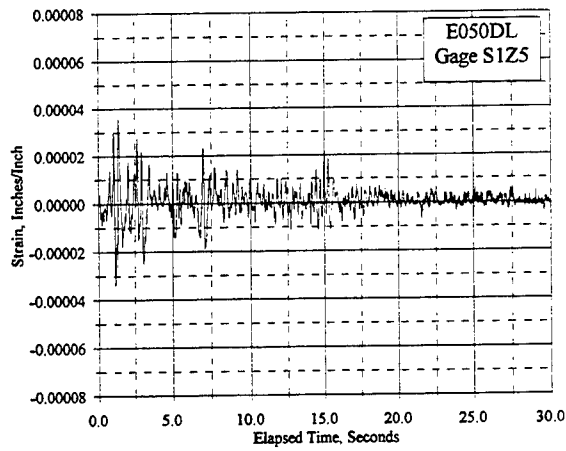
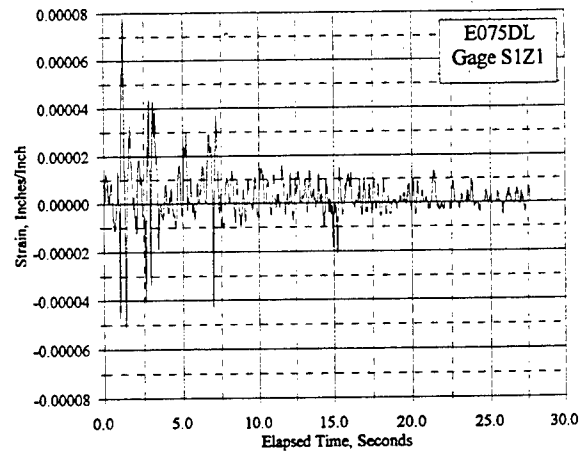
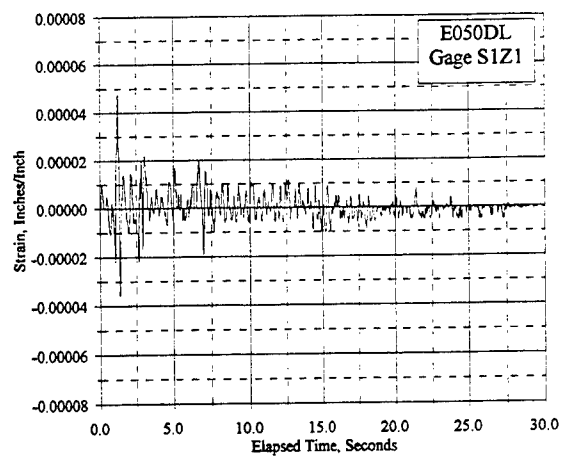


Figure C.19.2 Reinforcement Strain Vs. Elapsed Time, Gages S1Z1, S1Z5, S1Z6: E050DL, E075DL

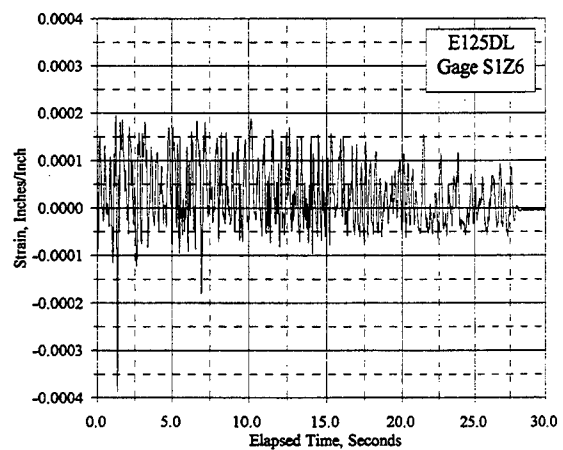
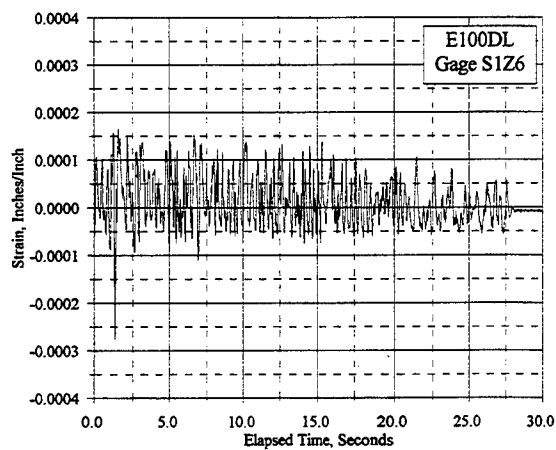
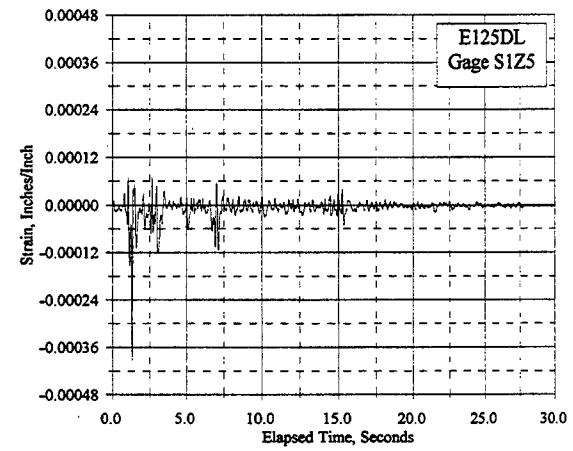
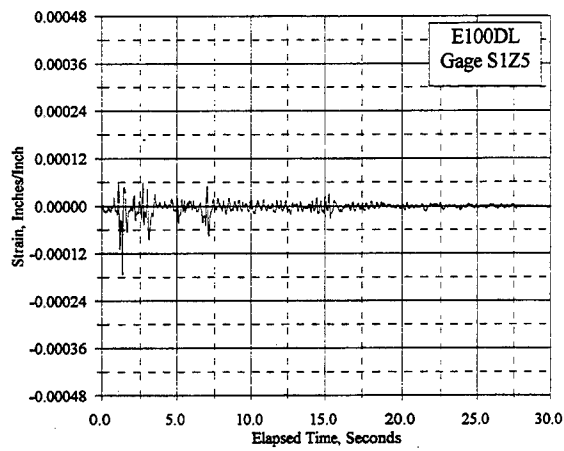
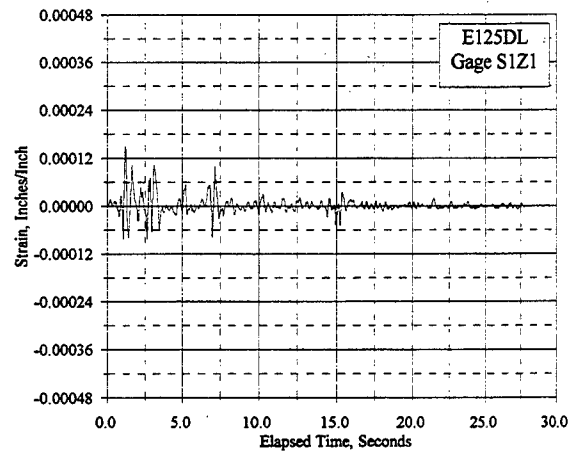
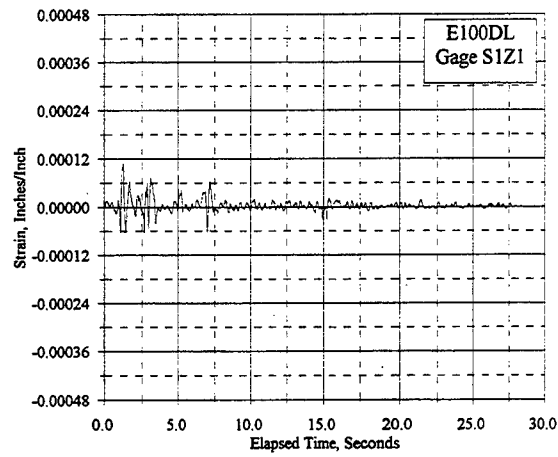


Figure C.19.3 Reinforcement Strain Vs. Elapsed Time, Gages S1Z1, S1Z5, S1Z6: E100DL, E125DL

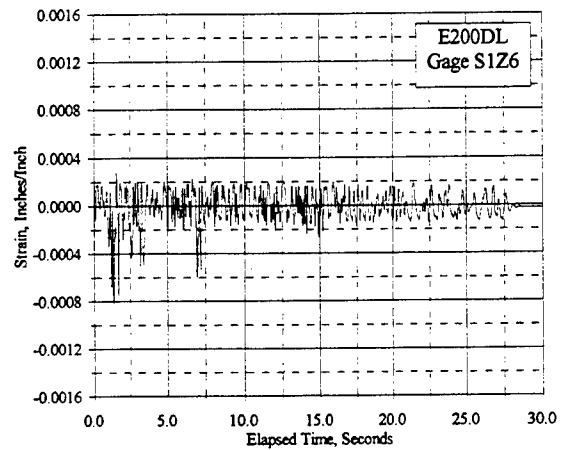
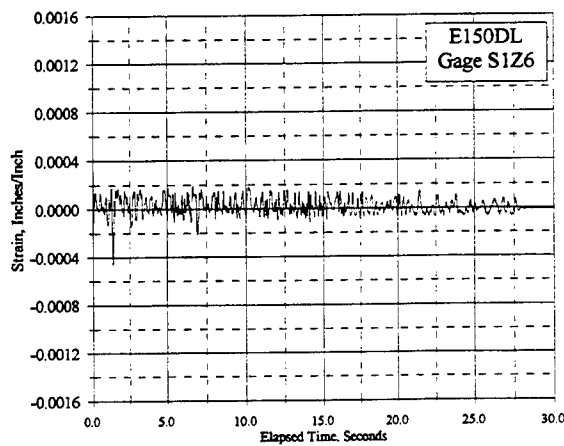
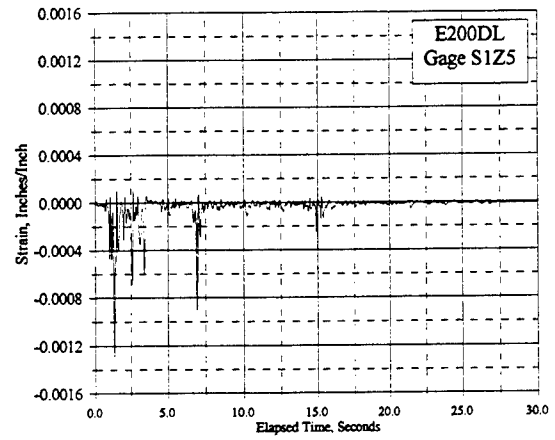
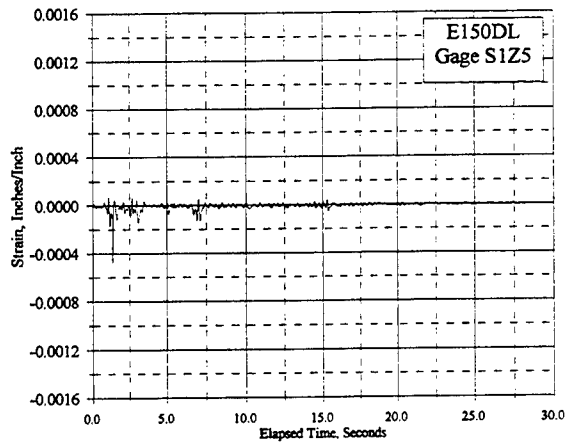
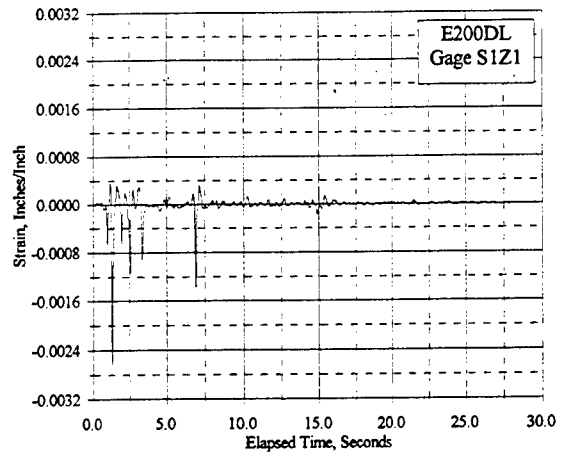
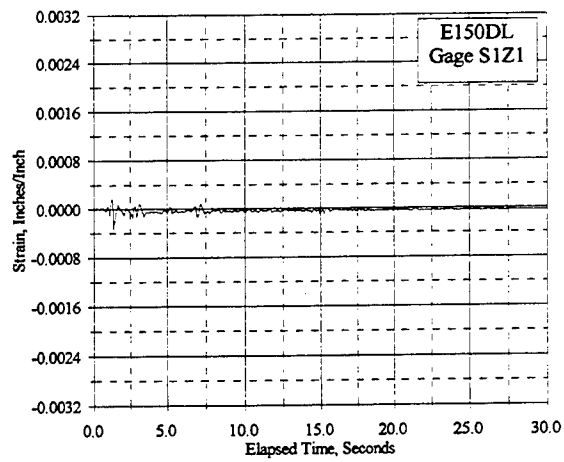


Figure C.19.4 Reinforcement Strain Vs. Elapsed Time, Gages S1Z1, S1Z5, S1Z6: E150DL, E200DL

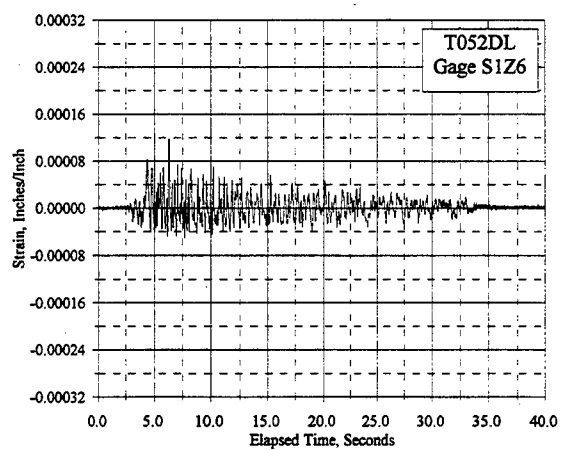
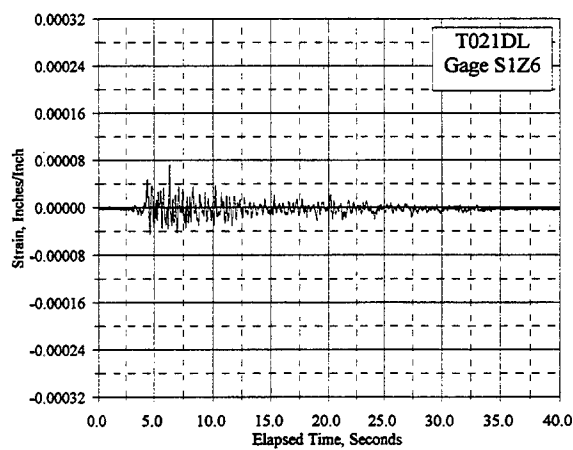
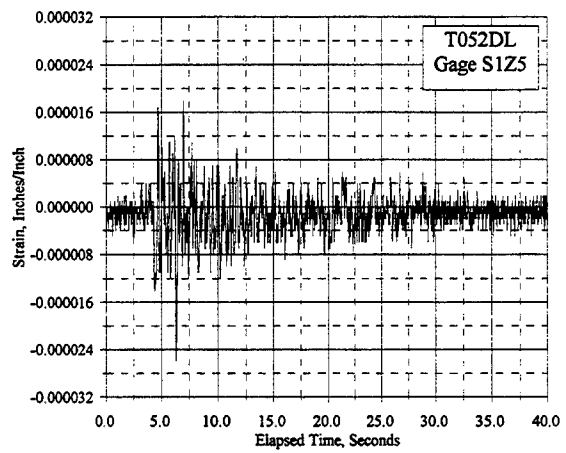
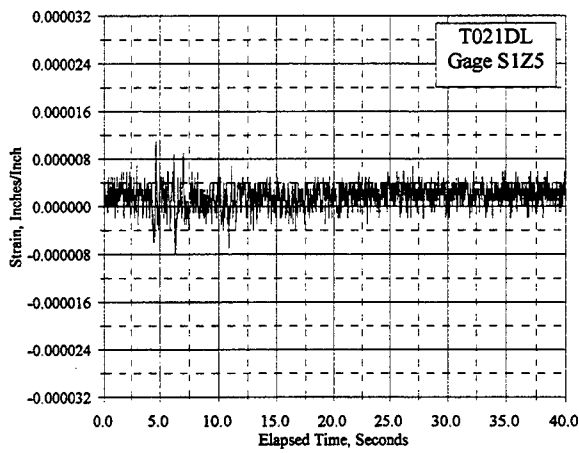
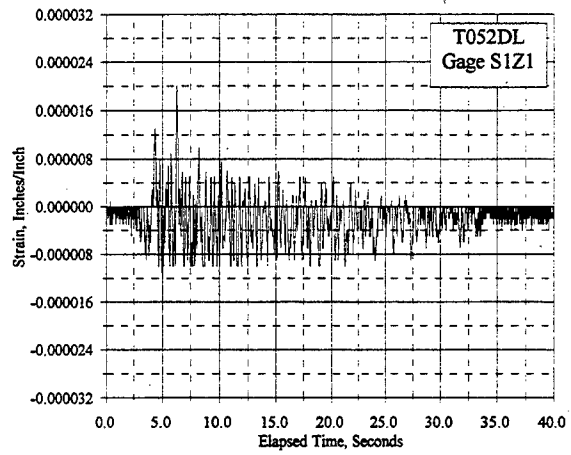
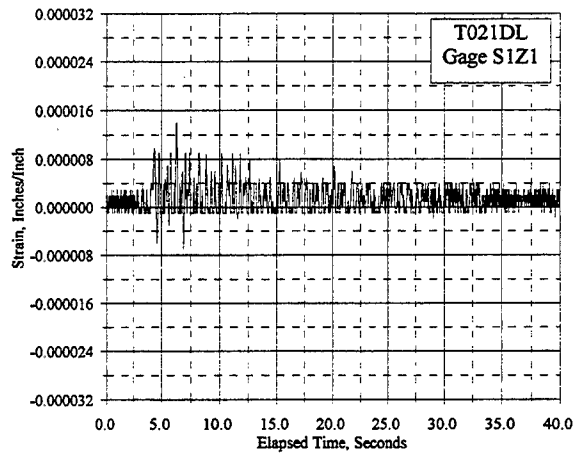


Figure C.19.5 Reinforcement Strain Vs. Elapsed Time, Gages S1Z1, S1Z5, S1Z6: T021DL, T052DL

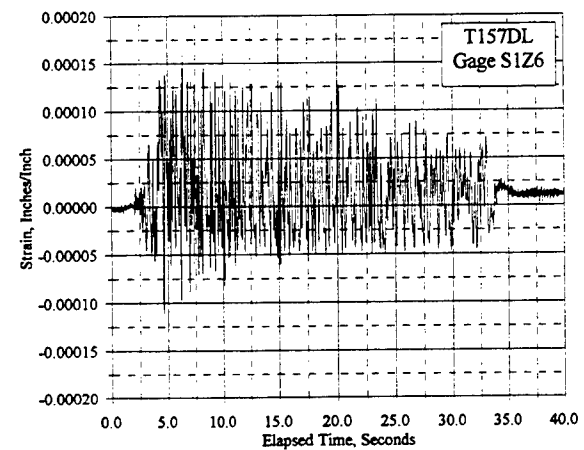
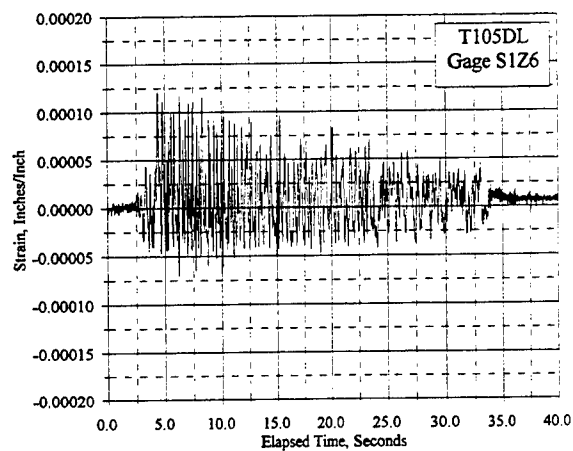
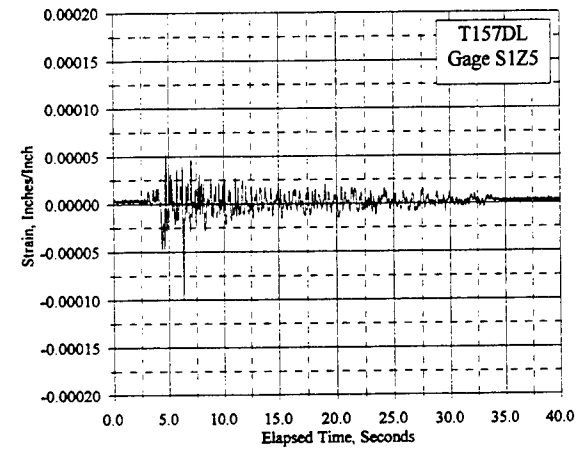
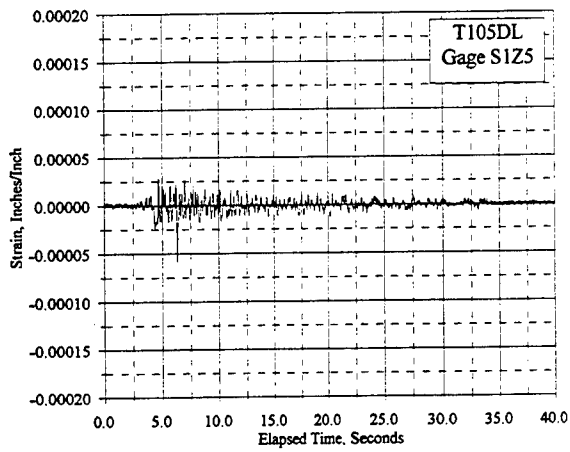
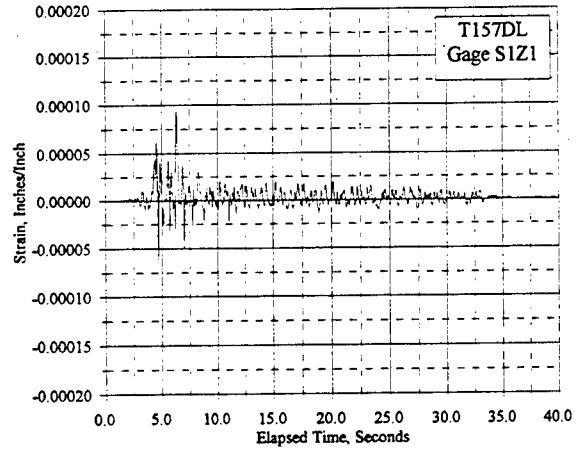
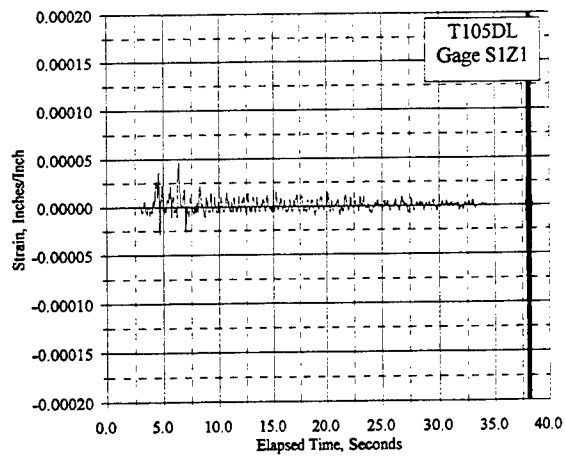


Figure C.19.6 Reinforcement Strain Vs. Elapsed Time, Gages S1Z1, S1Z5, S1Z6: T105DL, T157DL

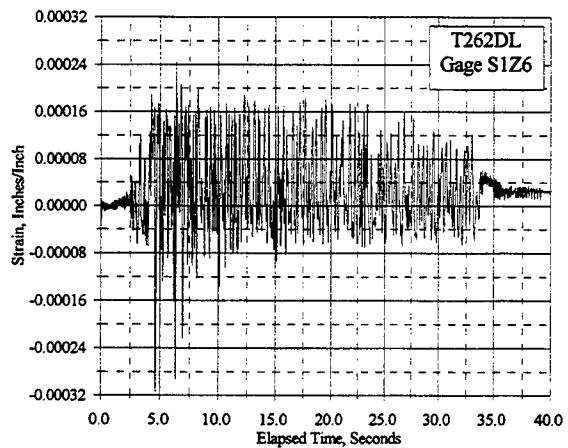
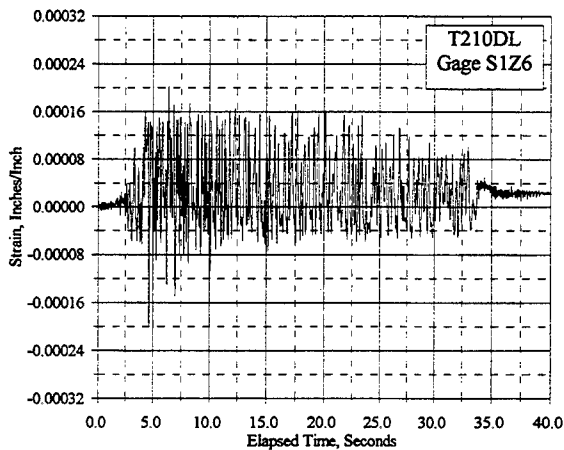
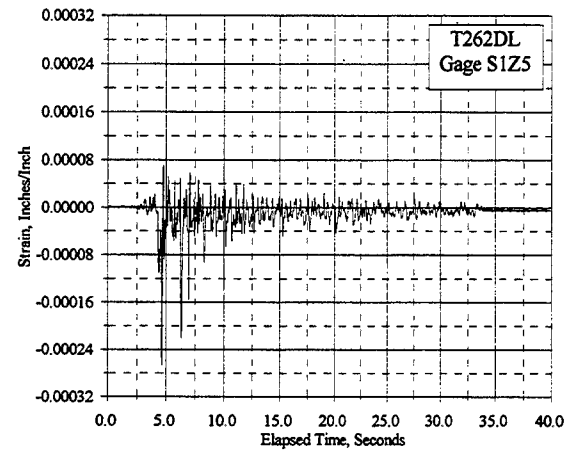
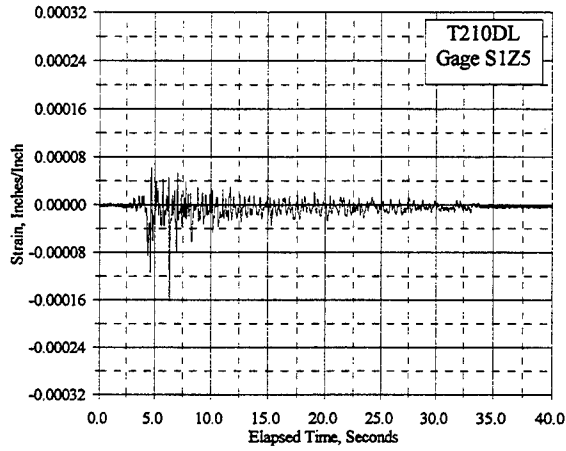
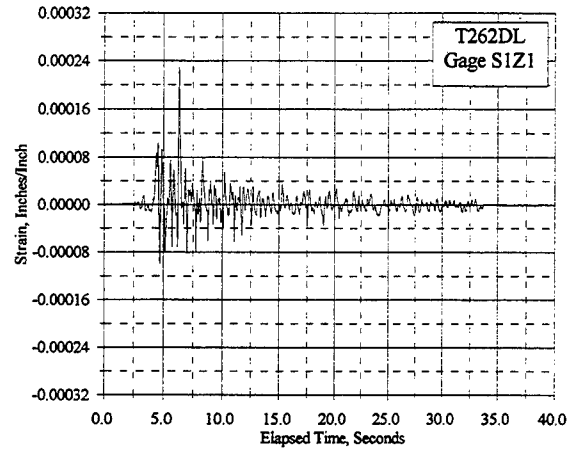
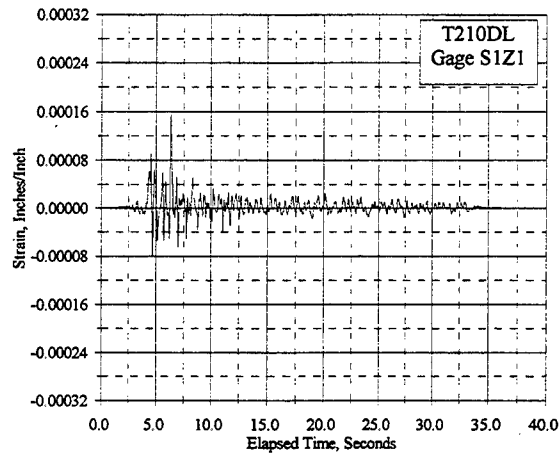


Figure C.19.7 Reinforcement Strain Vs. Elapsed Time, Gages S1Z1, S1Z5, S1Z6: T210DL, T262DL

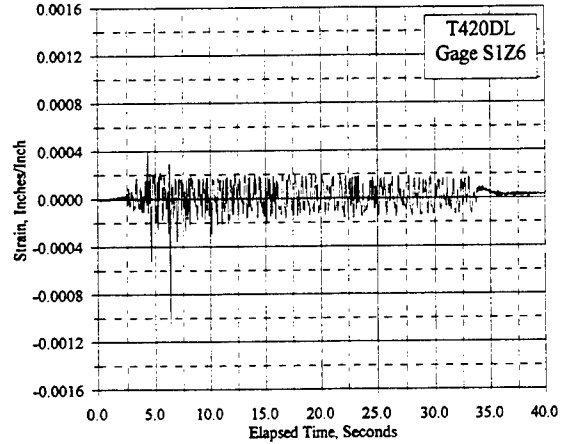
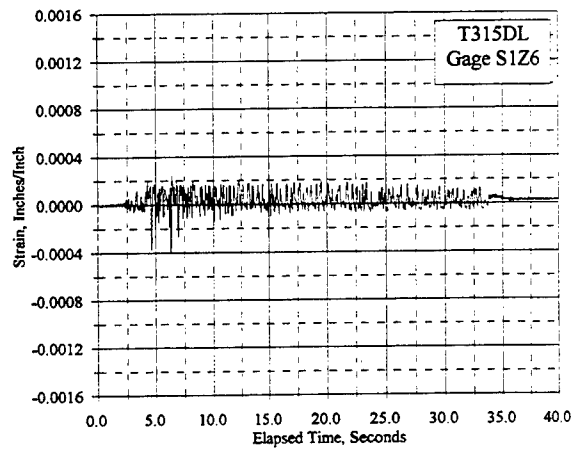
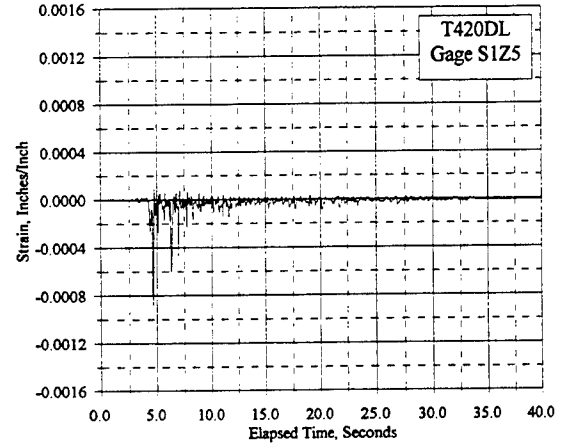
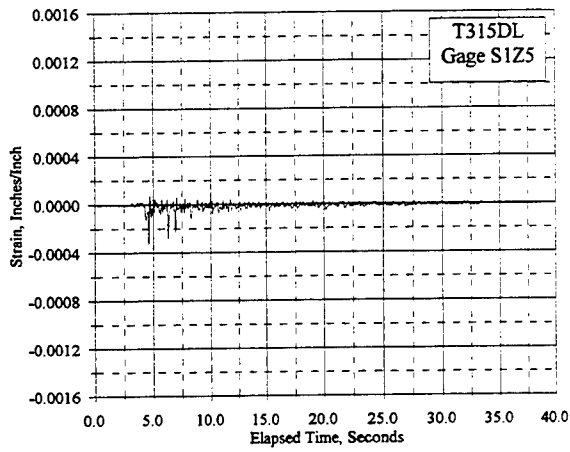
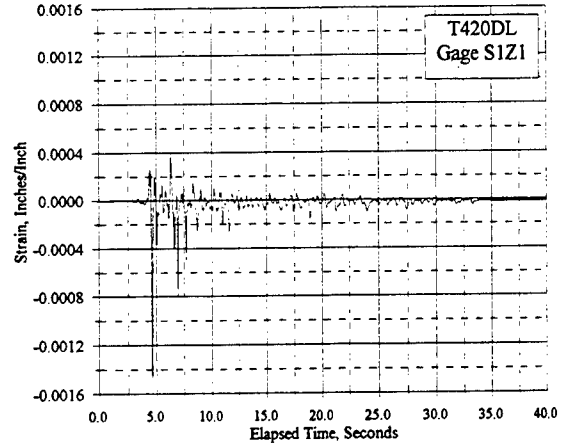
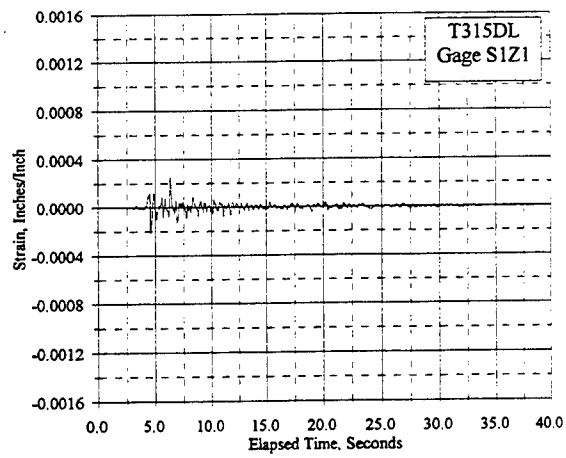


Figure C.19.8 Reinforcement Strain Vs. Elapsed Time, Gages S1Z1, S1Z5, S1Z6: T315DL, T420DL

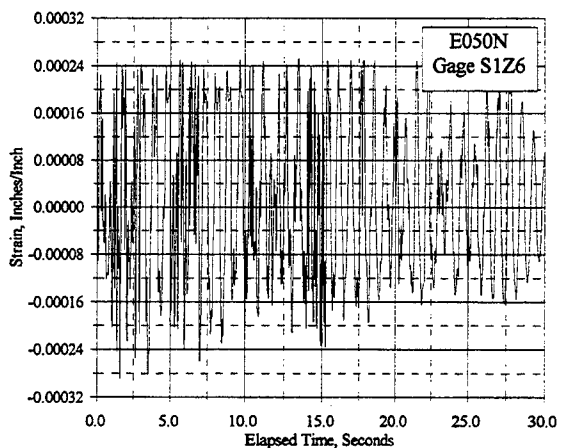
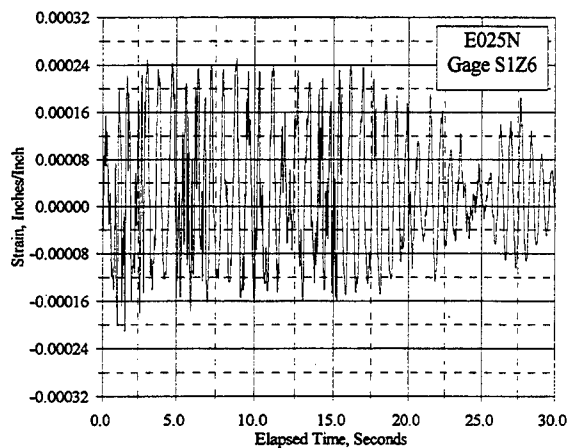
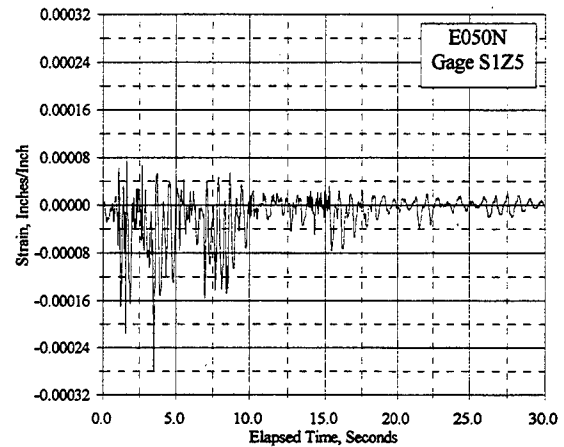
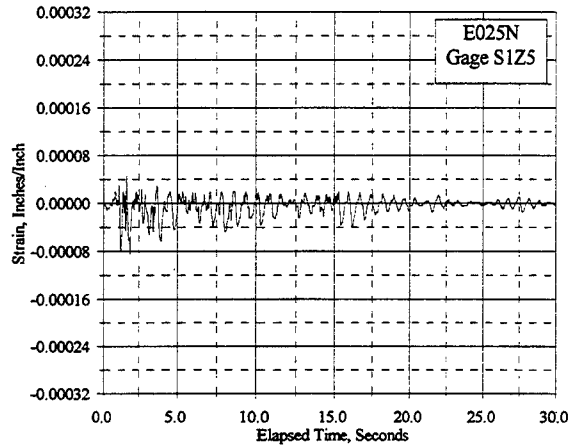
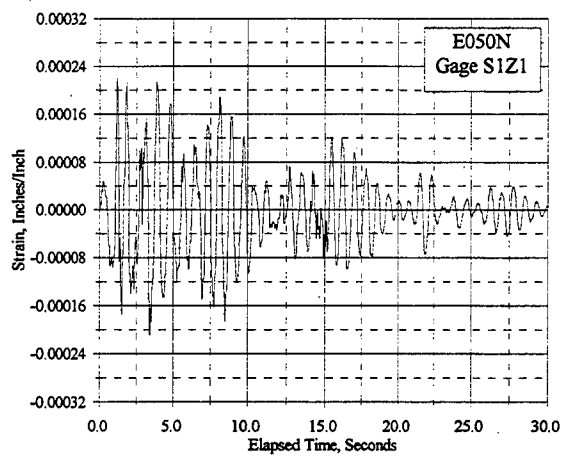
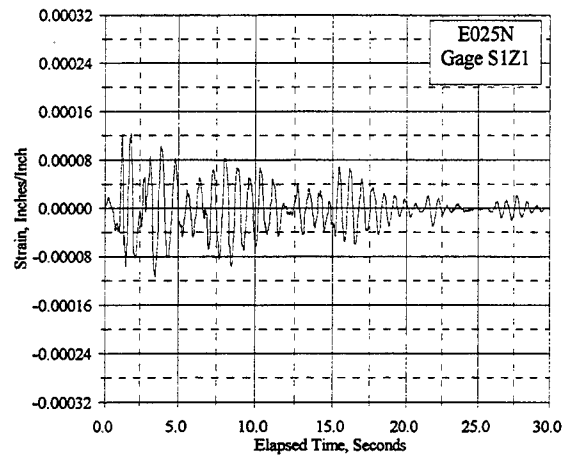


Figure C.19.9 Reinforcement Strain Vs. Elapsed Time, Gages S1Z1, S1Z5, S1Z6: E025N, E050N

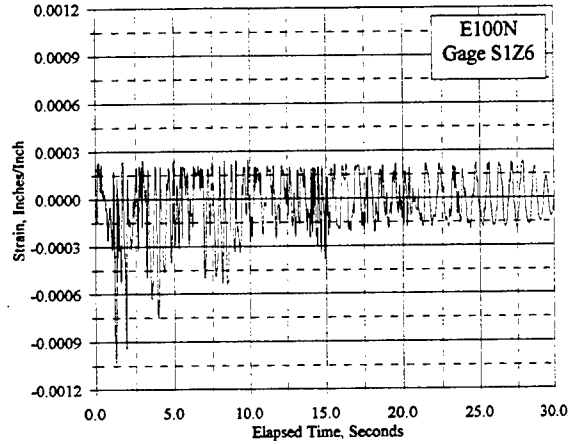
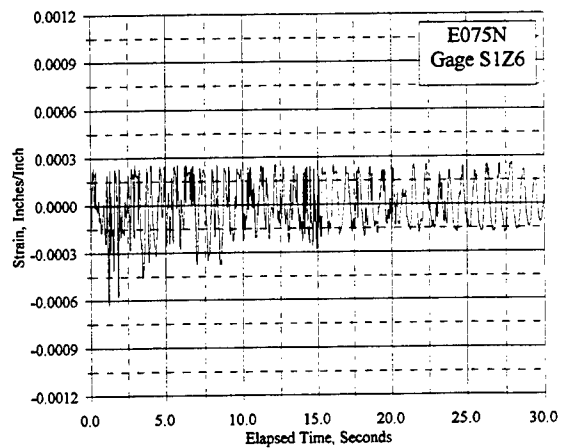
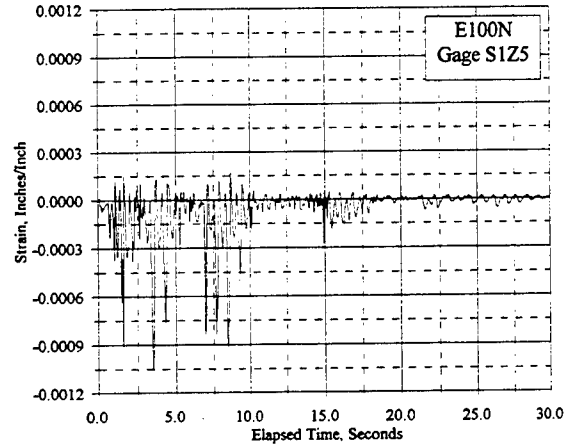
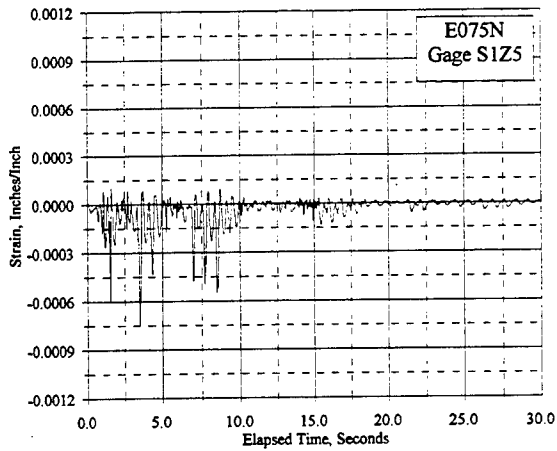
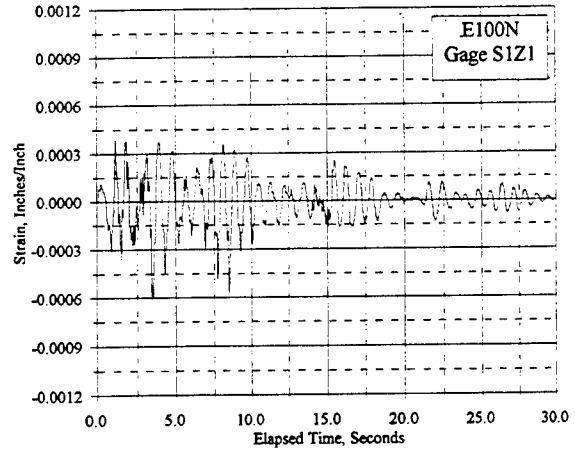
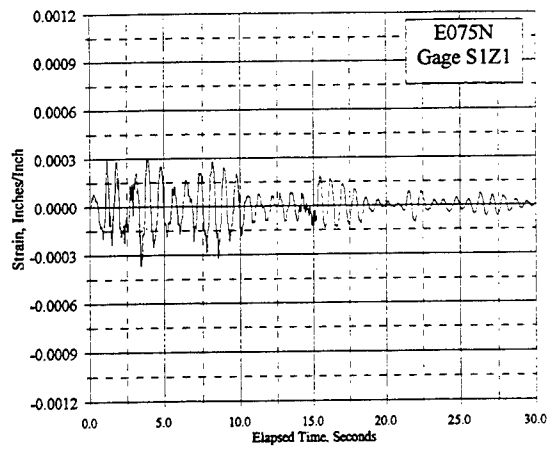


Figure C.19.10 Reinforcement Strain Vs. Elapsed Time, Gages S1Z1, S1Z5, S1Z6: E075N, E100N

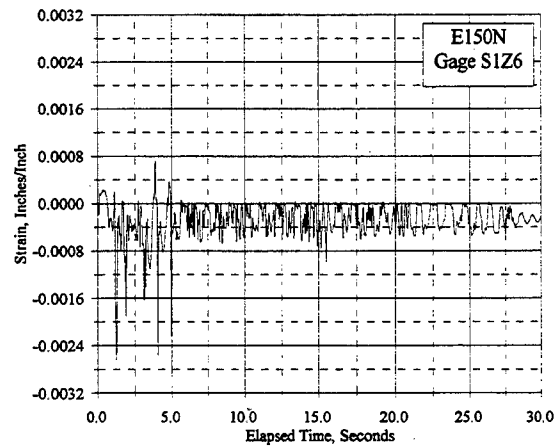
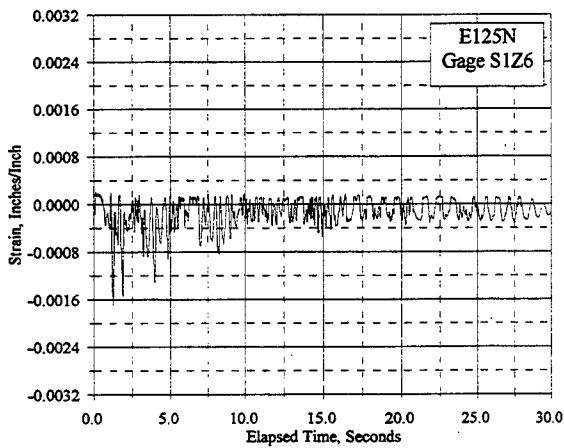
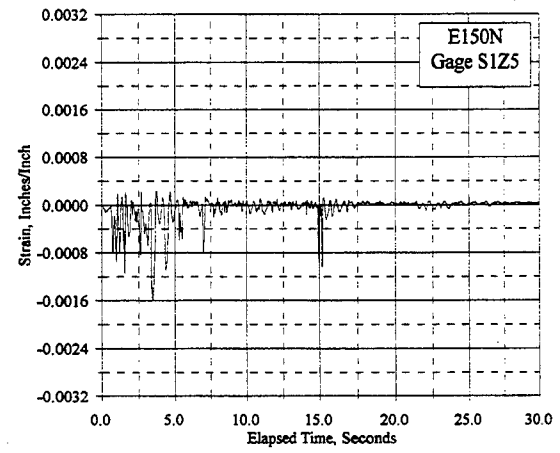
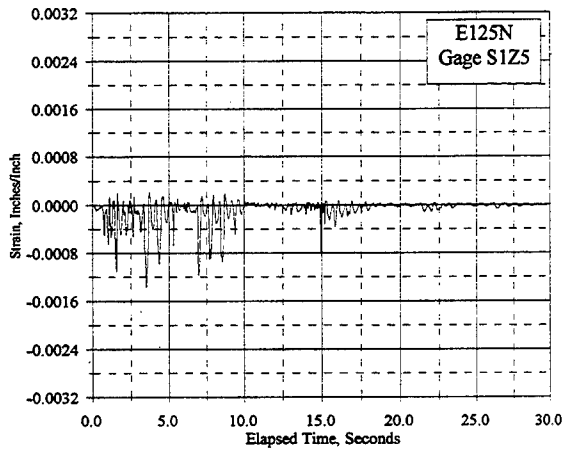
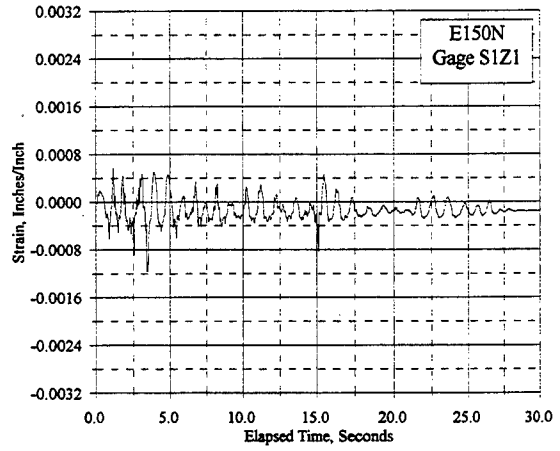
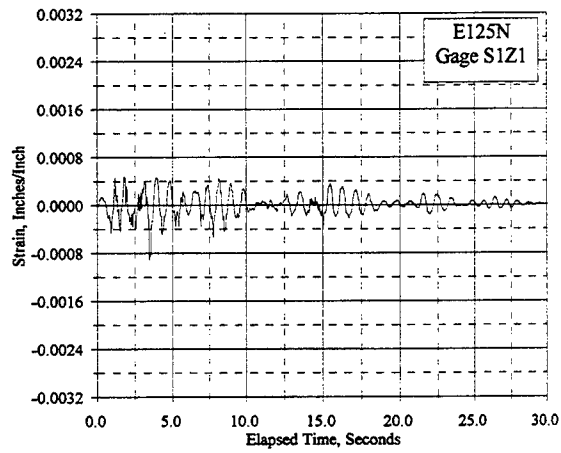


Figure C.19.11 Reinforcement Strain Vs. Elapsed Time, Gages S1Z1, S1Z5, S1Z6: E125N, E150N

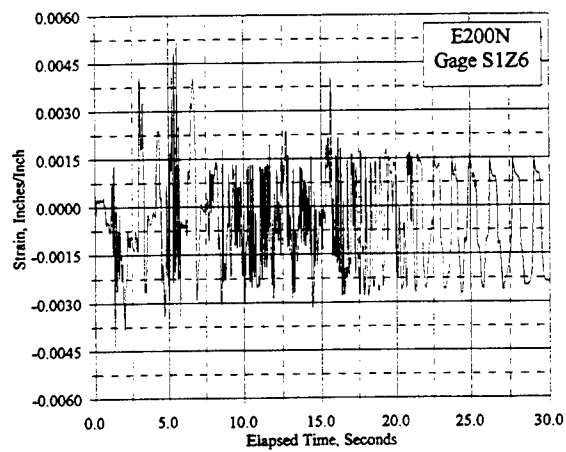
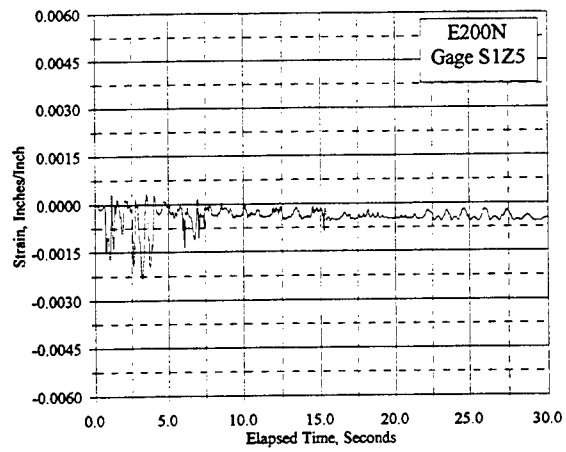
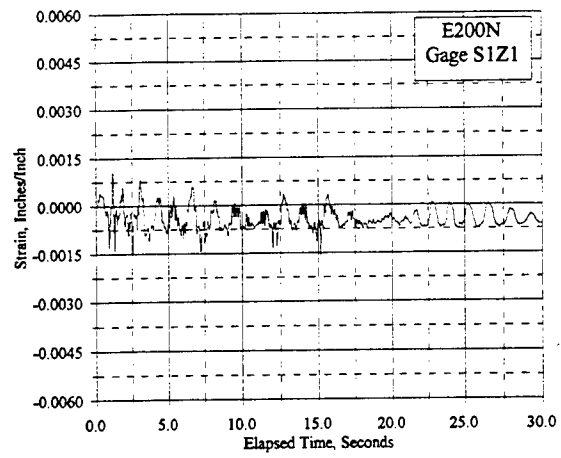


Figure C.19.12 Reinforcement Strain Vs. Elapsed Time, Gages S1Z1, S1Z5, S1Z6: E200N

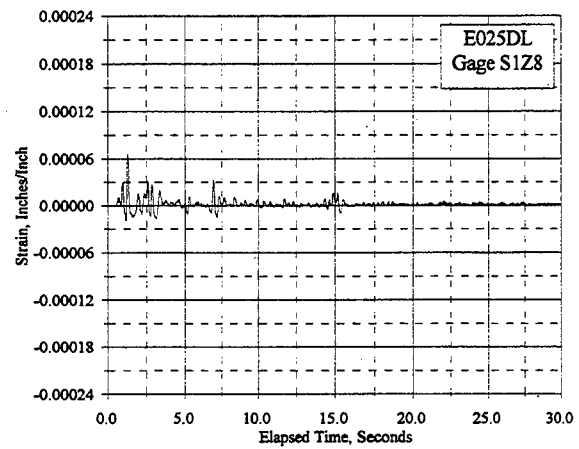
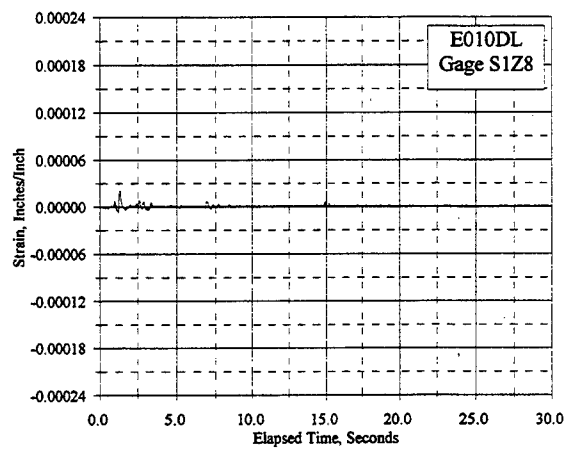
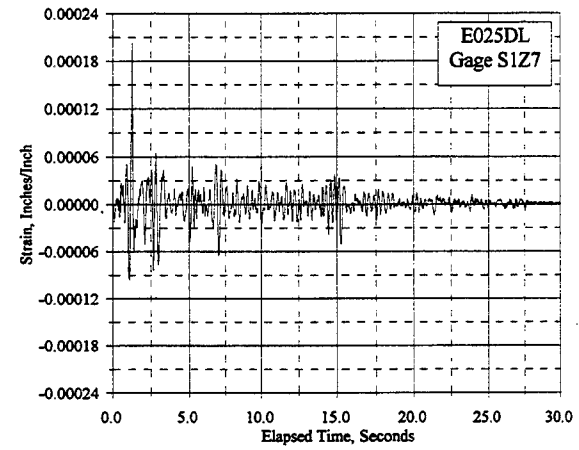
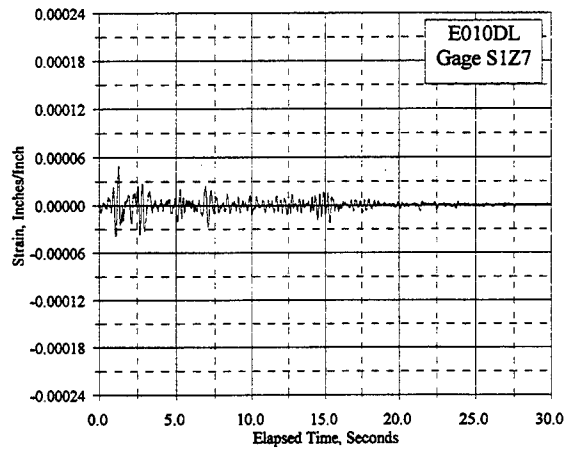
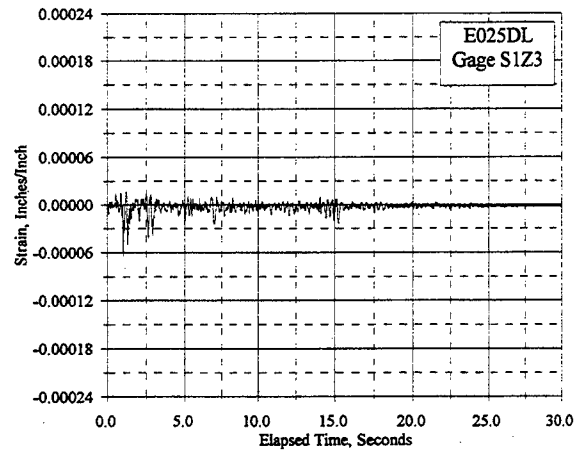
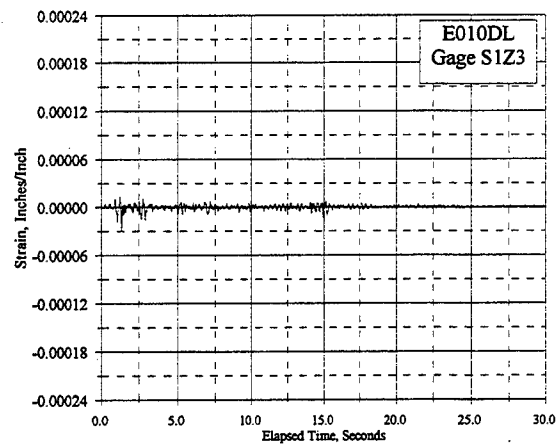


Figure C.20.1 Reinforcement Strain Vs. Elapsed Time, Gages S1Z3, S1Z7, S1Z8: E010DL, E025DL

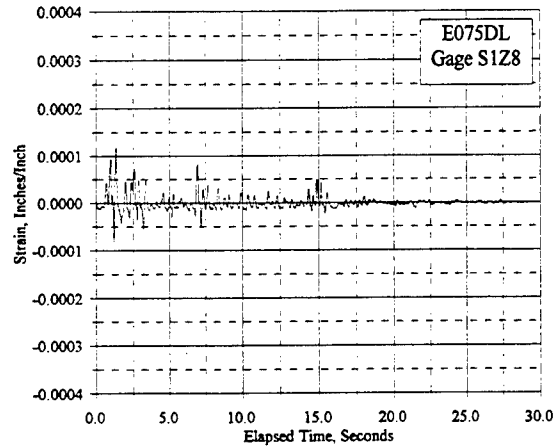
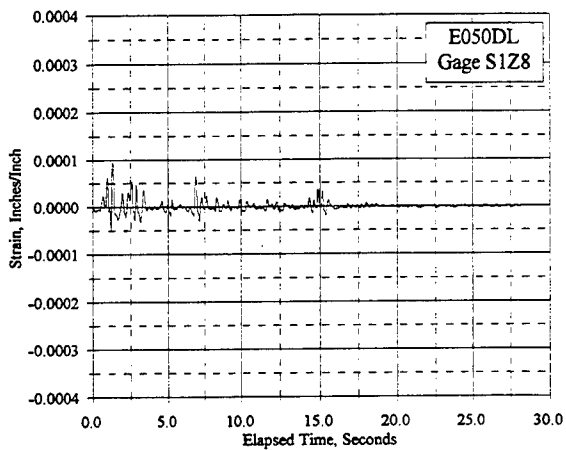
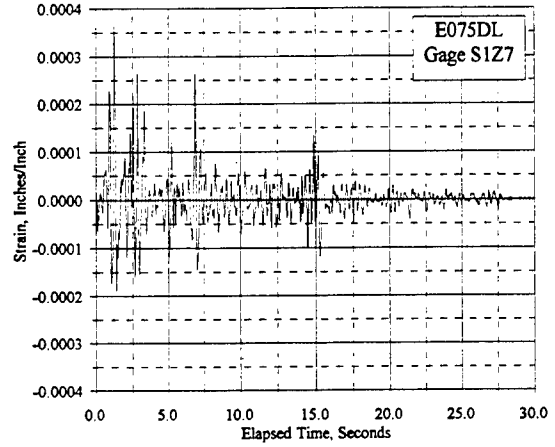
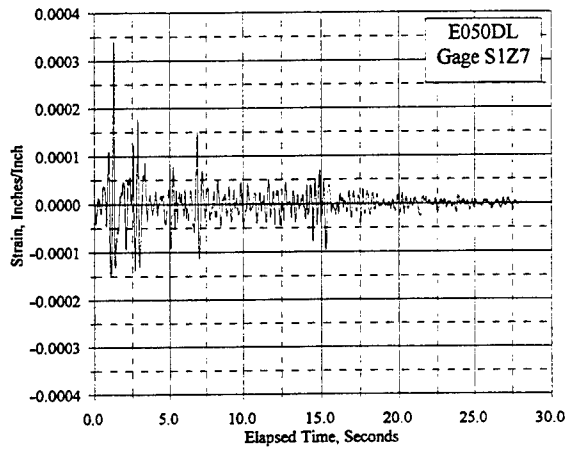
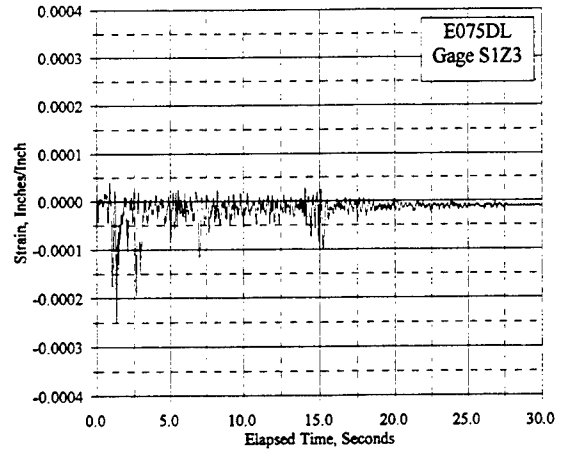
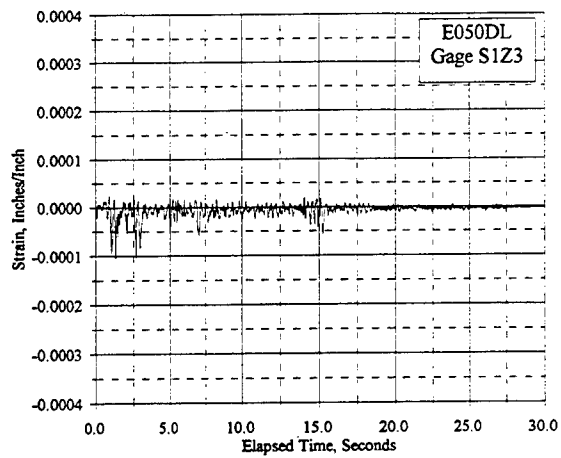


Figure C.20.2 Reinforcement Strain Vs. Elapsed Time, Gages S1Z3, S1Z7, S1Z8: E050DL, E075DL

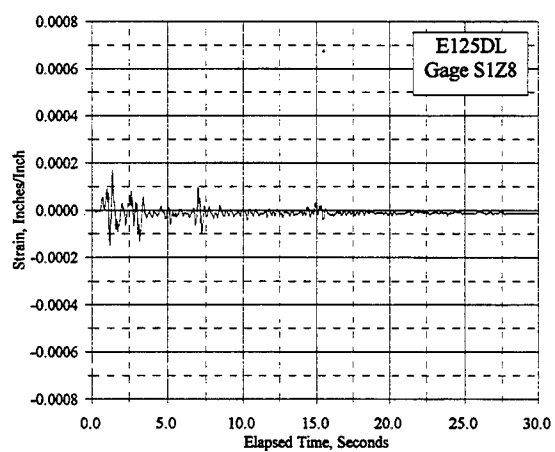
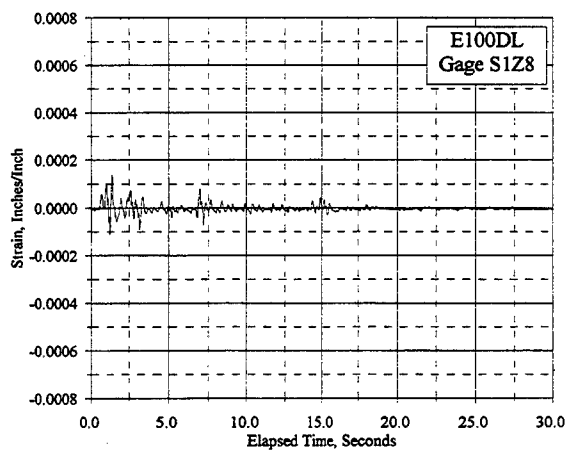
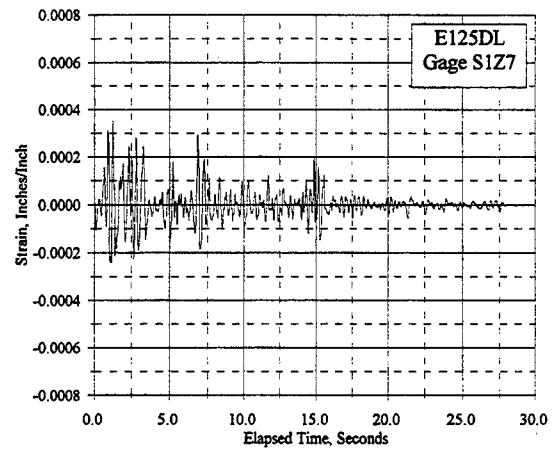
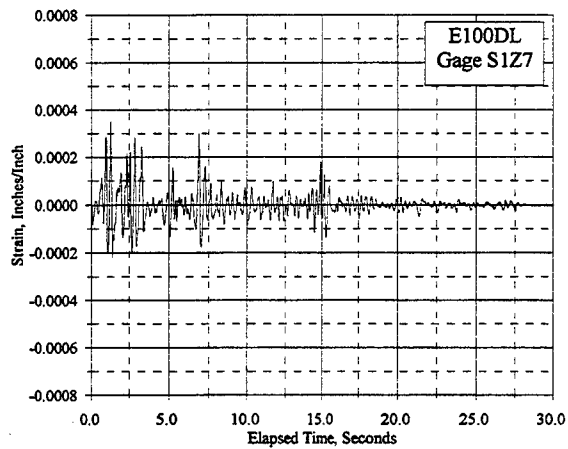
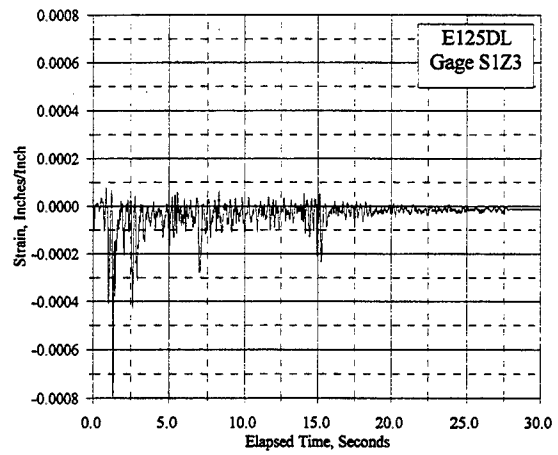
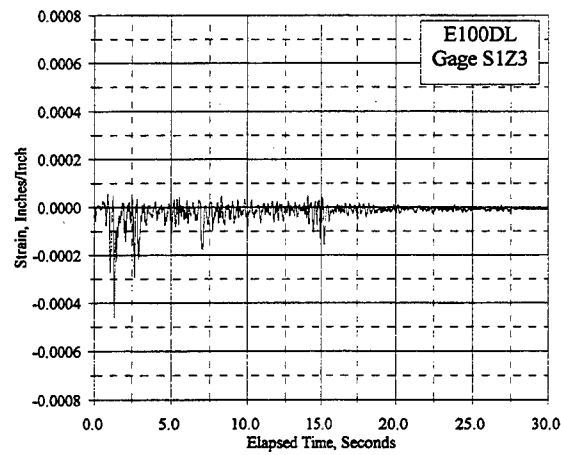


Figure C.20.3 Reinforcement Strain Vs. Elapsed Time, Gages S1Z3, S1Z7, S1Z8: E100DL, E125DL

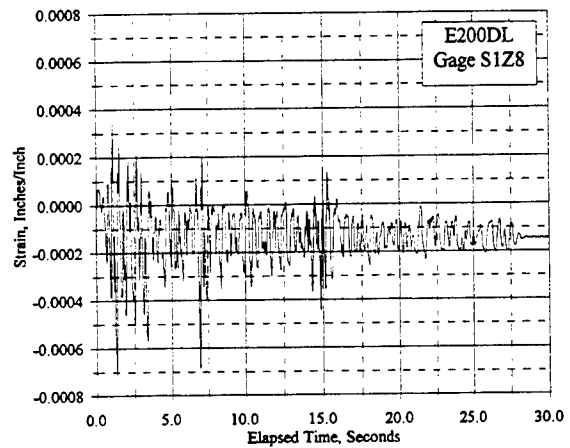
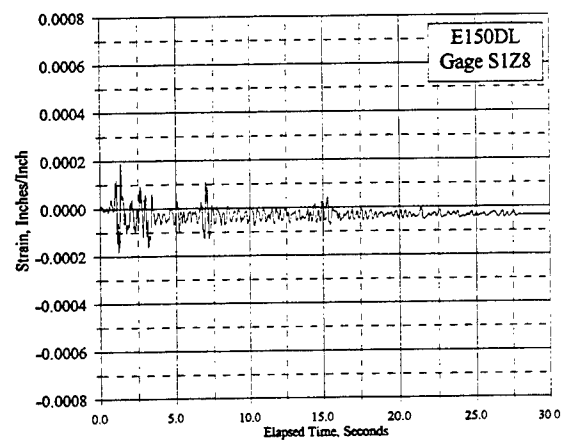
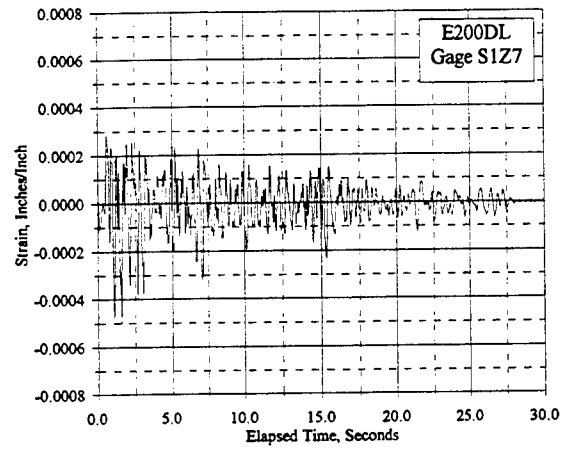
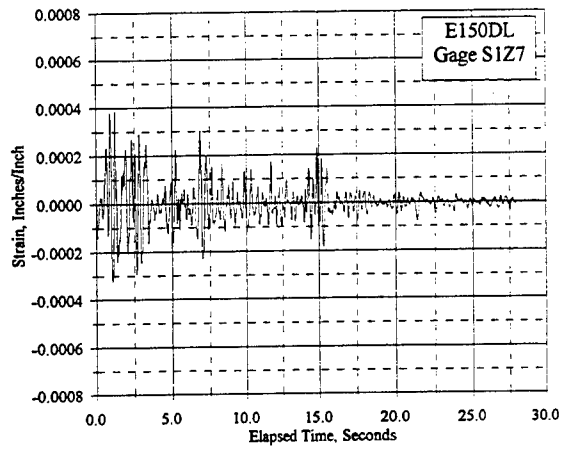
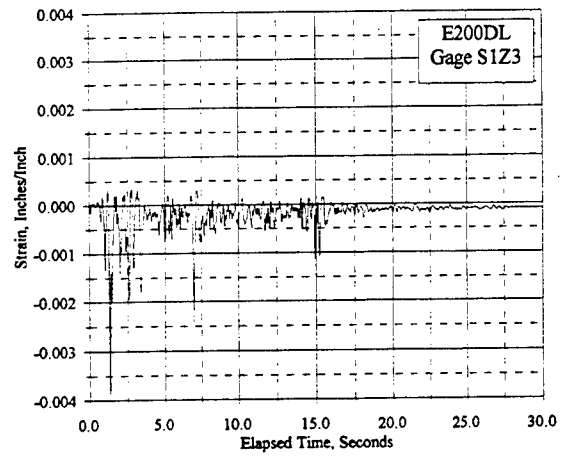
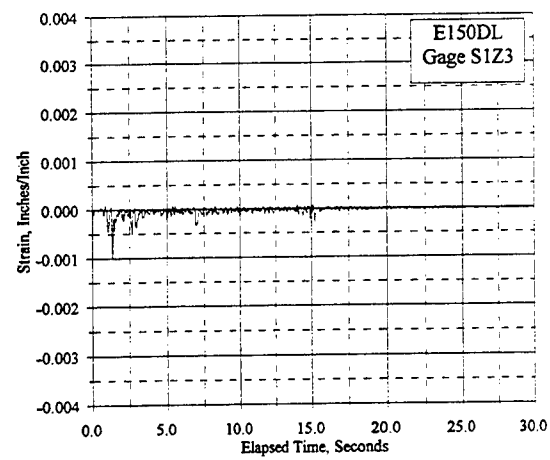


Figure C.20.4 Reinforcement Strain Vs. Elapsed Time, Gages S1Z3, S1Z7, S1Z8: E150DL, E200DL

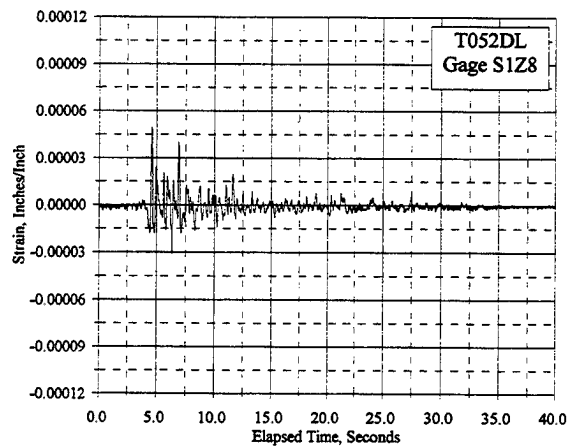
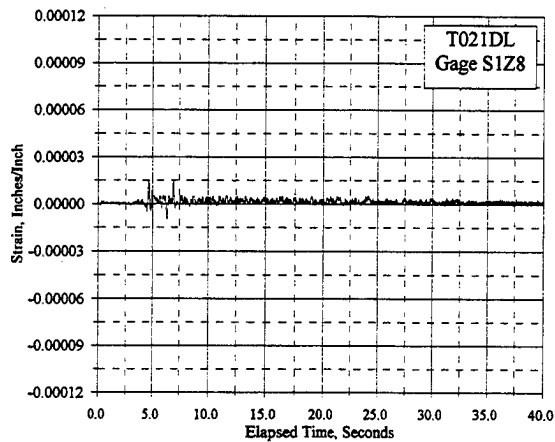
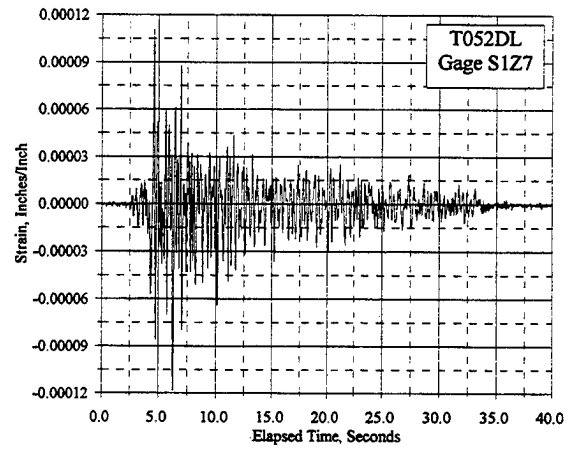
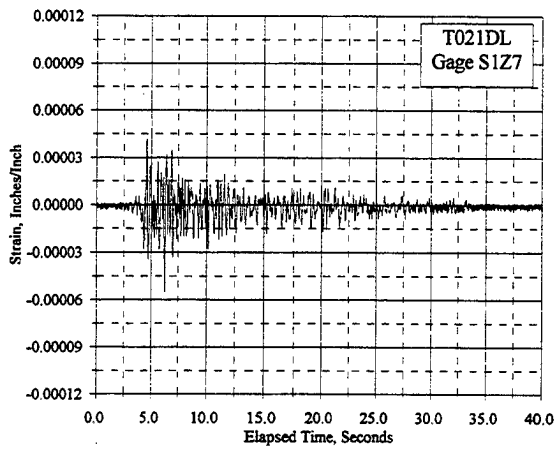
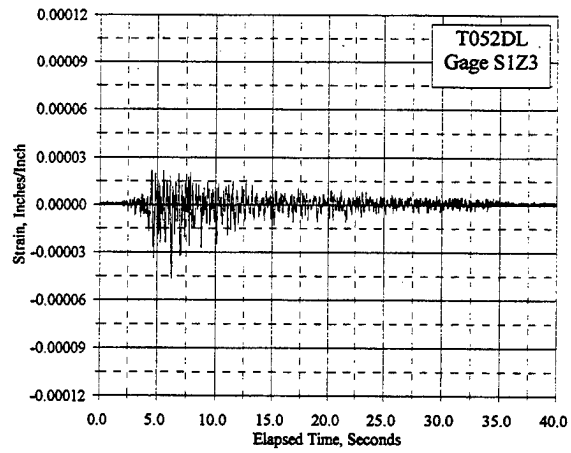
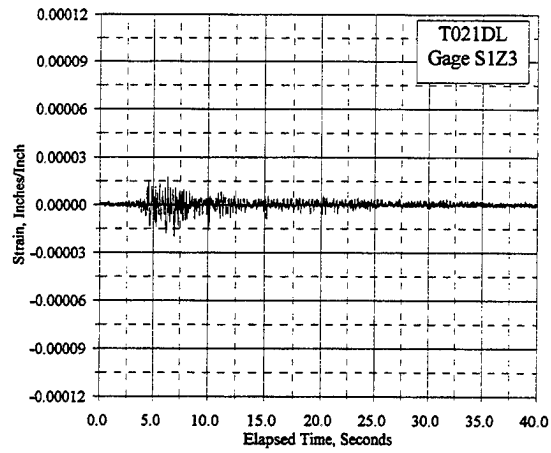


Figure C.20.5 Reinforcement Strain Vs. Elapsed Time, Gages S1Z3, S1Z7, S1Z8: T021DL, T052DL

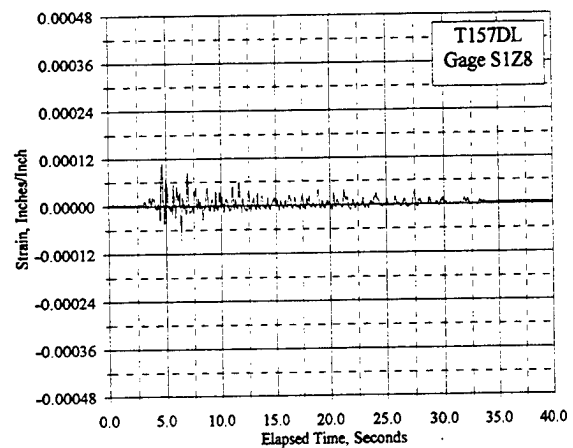
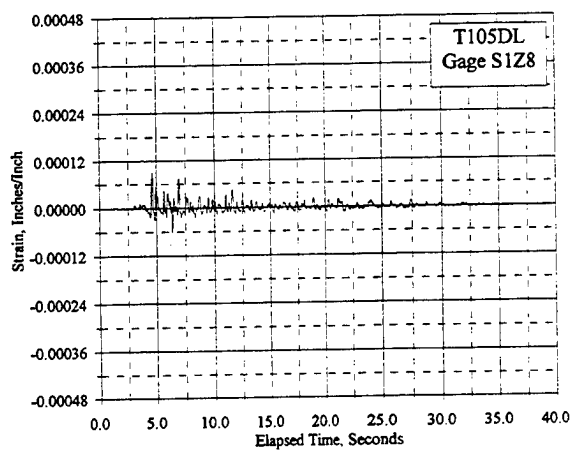
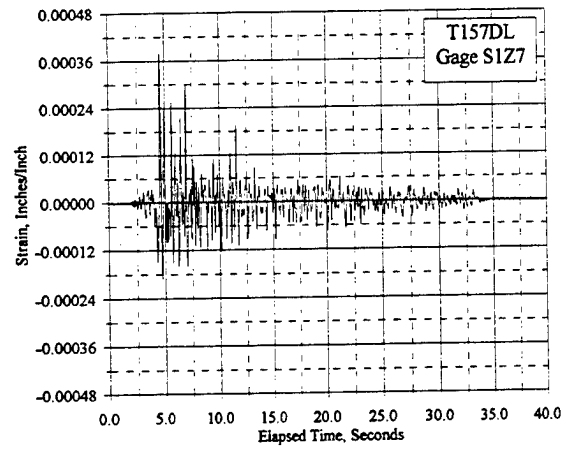
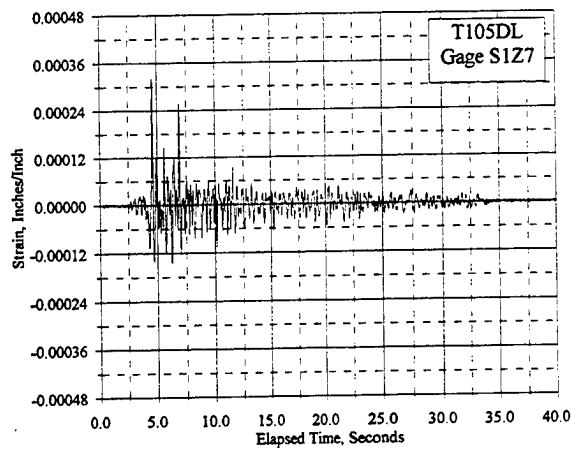
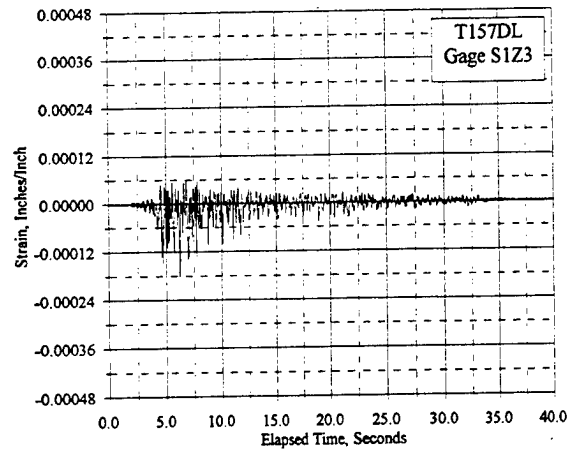
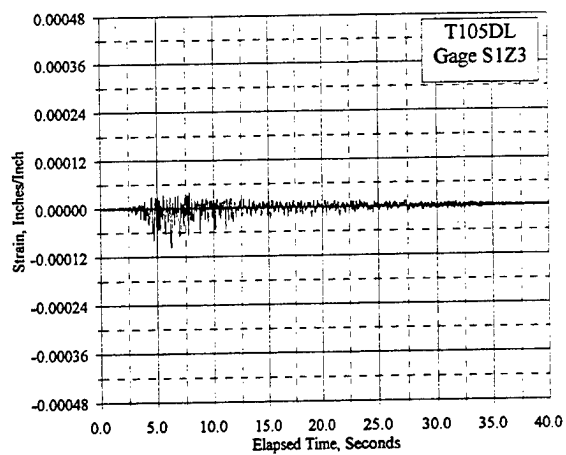


Figure C.20.6 Reinforcement Strain Vs. Elapsed Time, Gages S1Z3, S1Z7, S1Z8: T105DL, T157DL

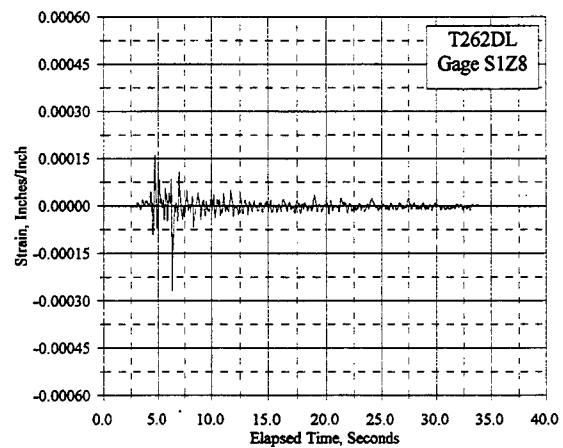
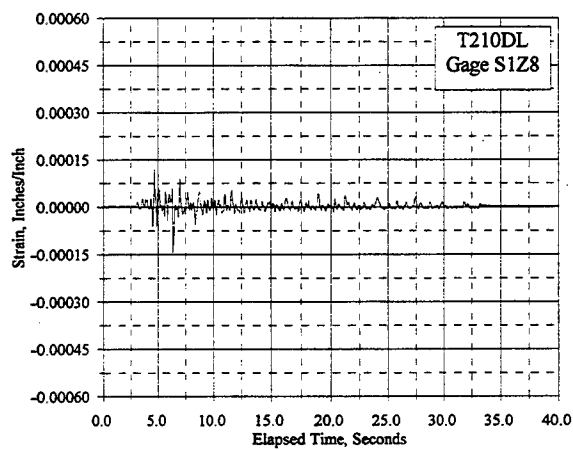
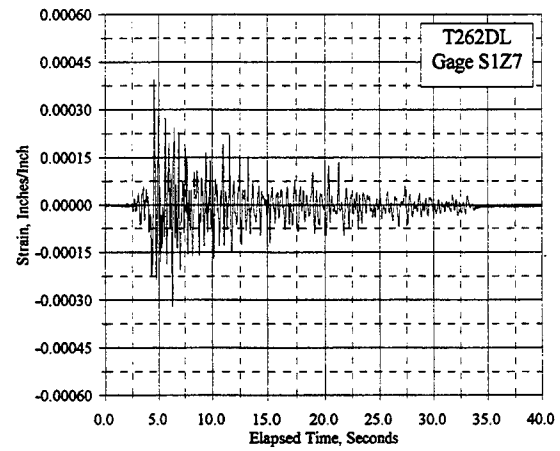
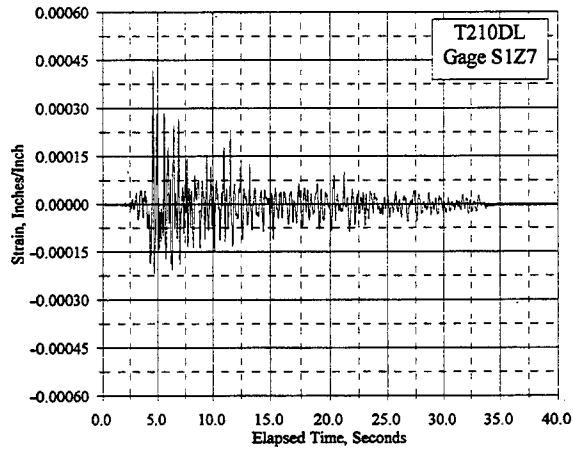
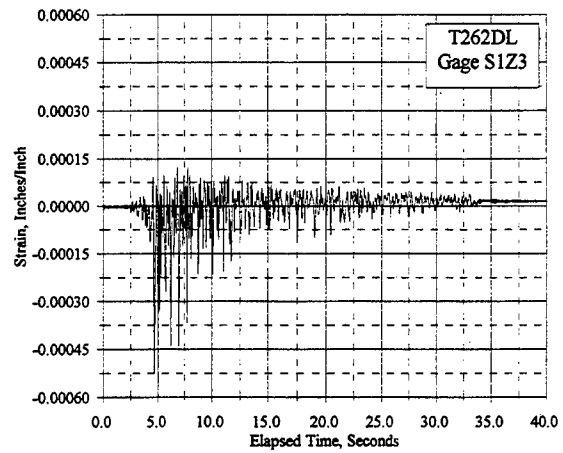
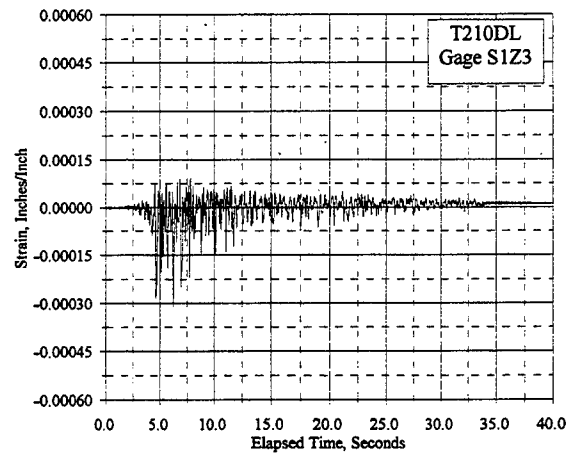


Figure C.20.7 Reinforcement Strain Vs. Elapsed Time, Gages S1Z3, S1Z7, S1Z8: T210DL, T262DL

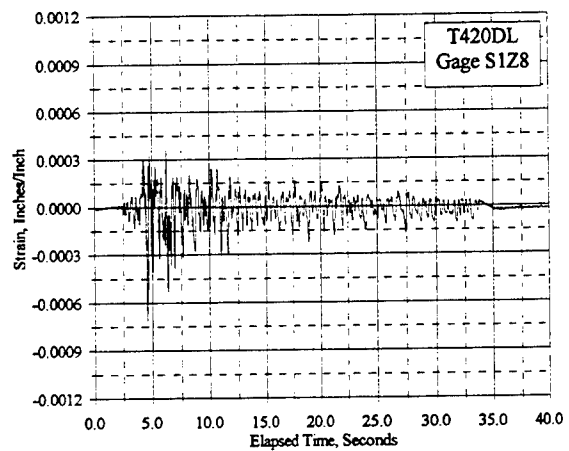
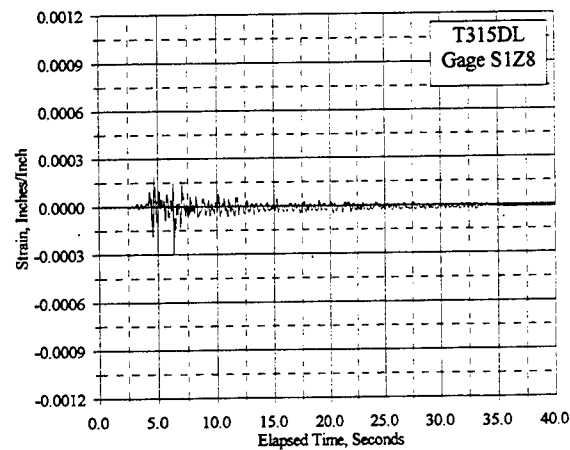
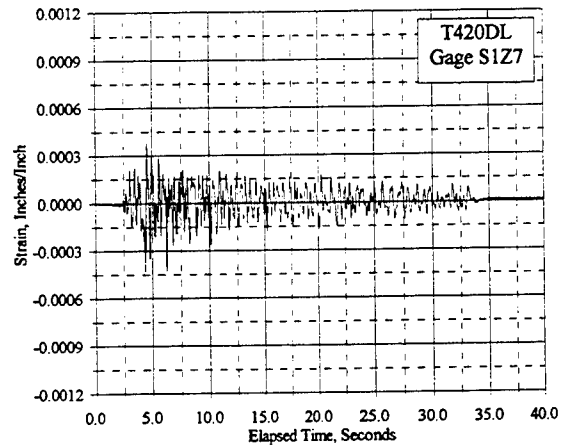
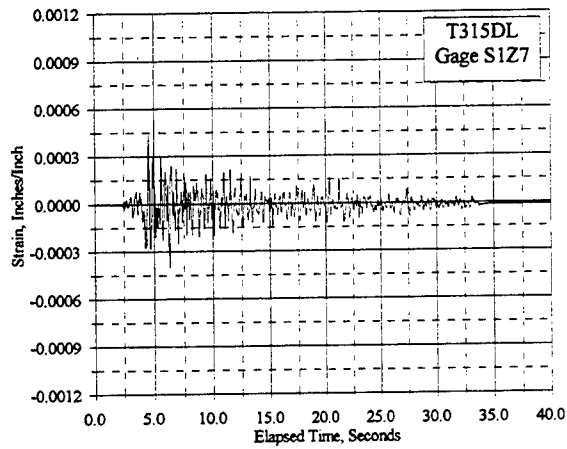
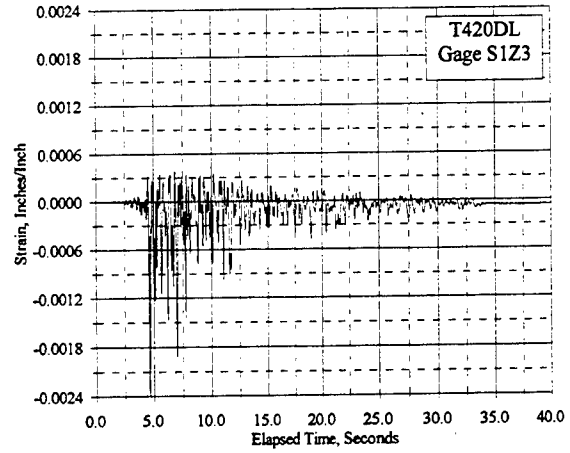
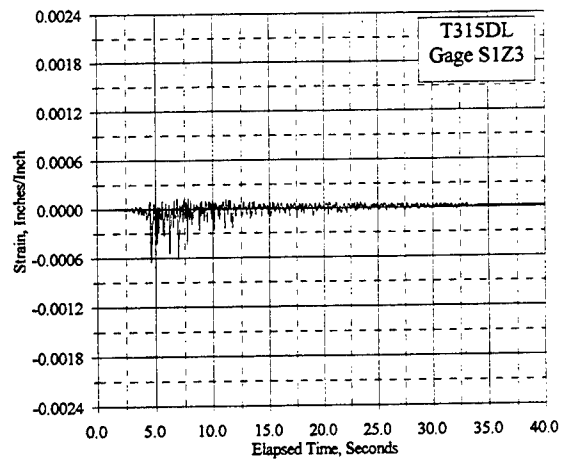


Figure C.20.8 Reinforcement Strain Vs. Elapsed Time, Gages S1Z3, S1Z7, S1Z8: T315DL, T420DL

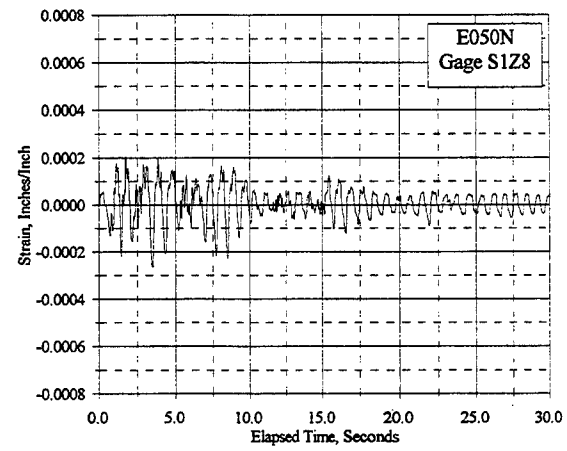
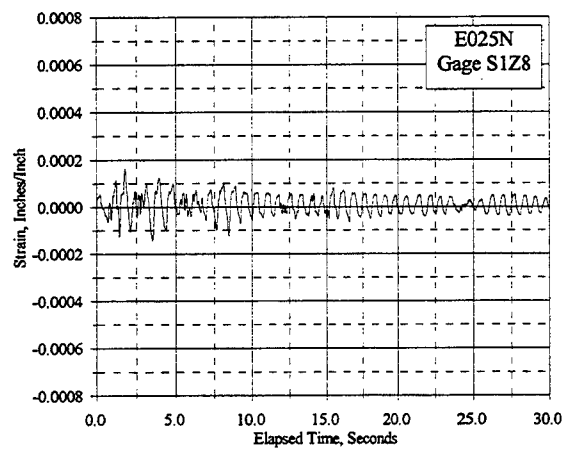
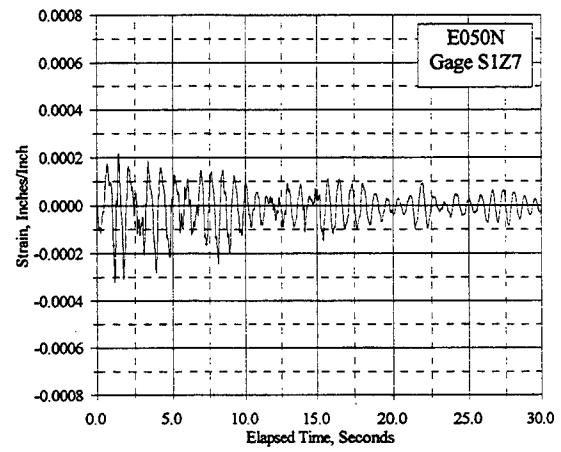
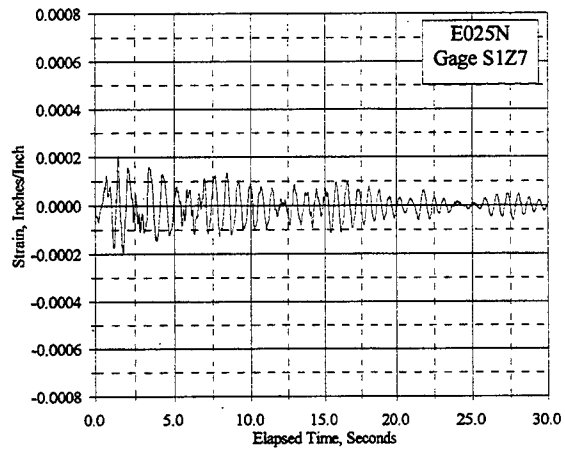
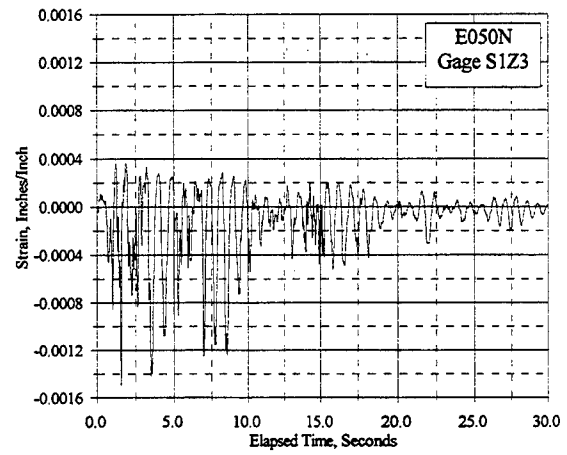
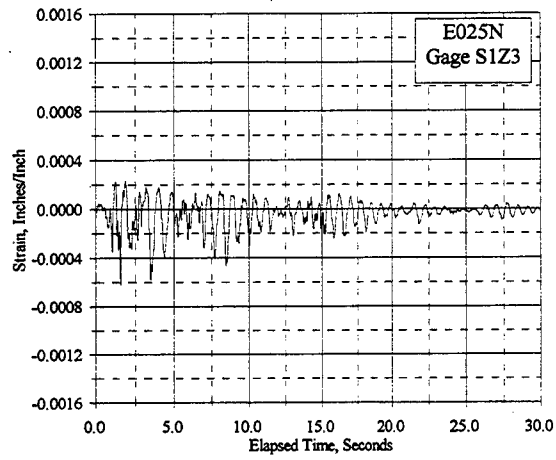


Figure C.20.9 Reinforcement Strain Vs. Elapsed Time, Gages S1Z3, S1Z7, S1Z8: E025N, E050N

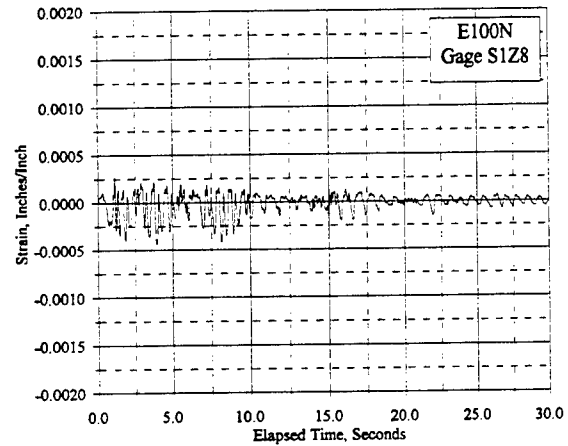
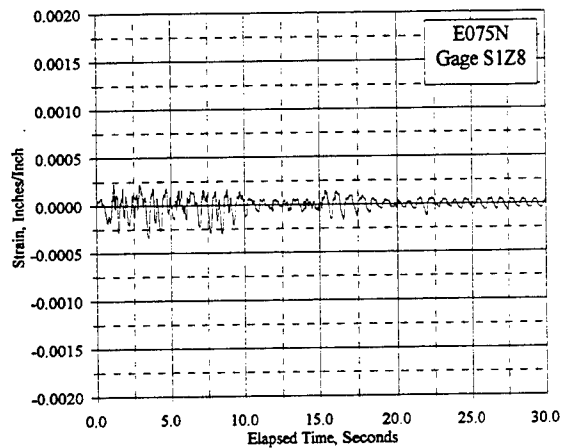
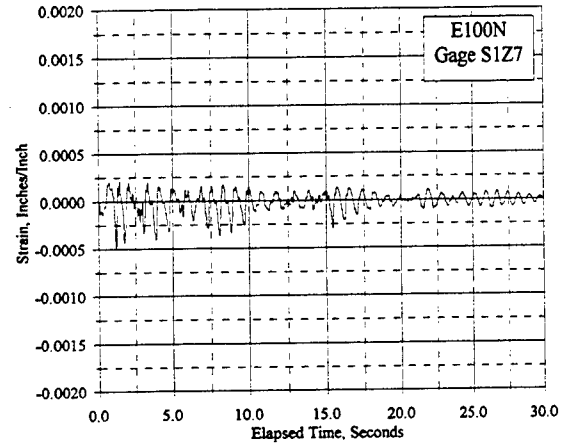
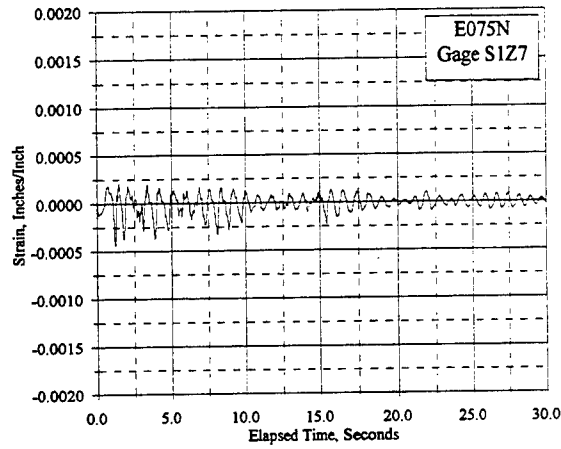
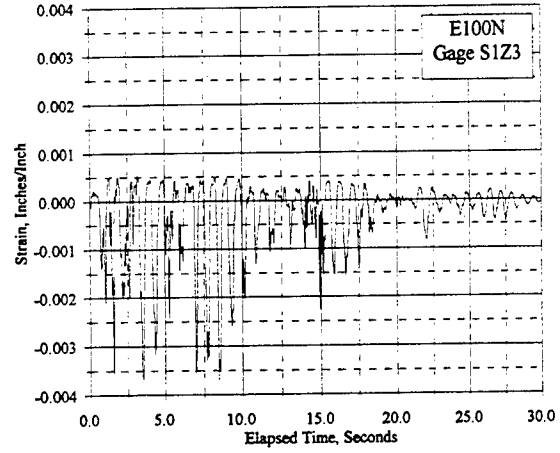
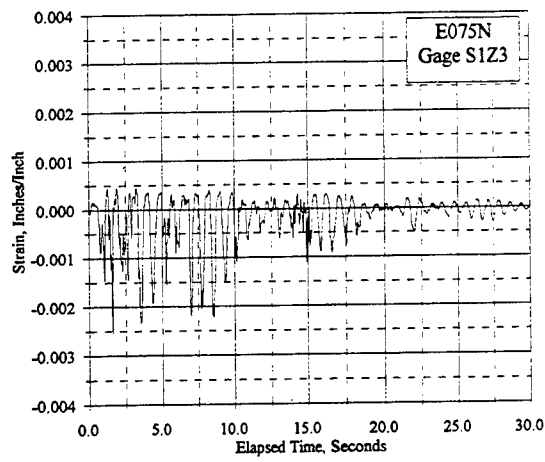


Figure C.20.10 Reinforcement Strain Vs. Elapsed Time, Gages S1Z3, S1Z7, S1Z8: E075N, E100N

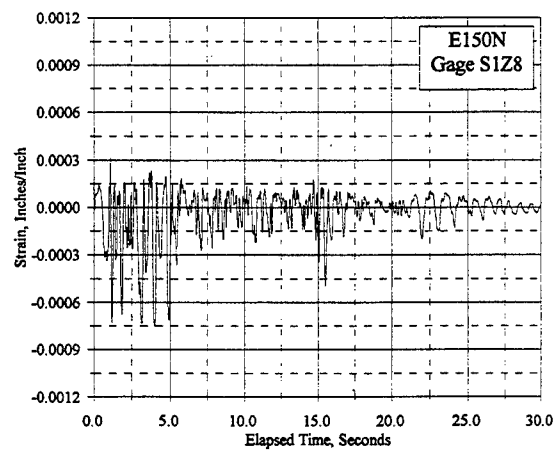
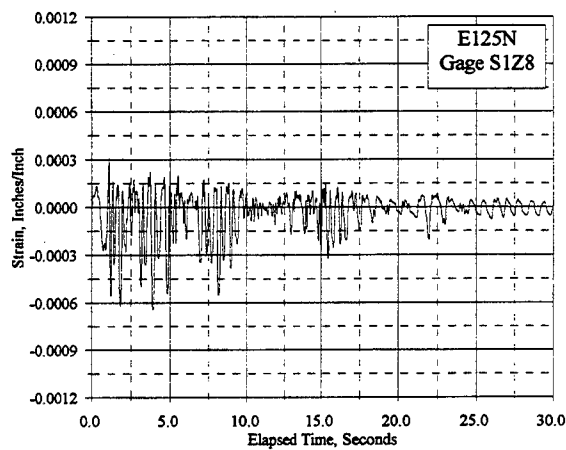
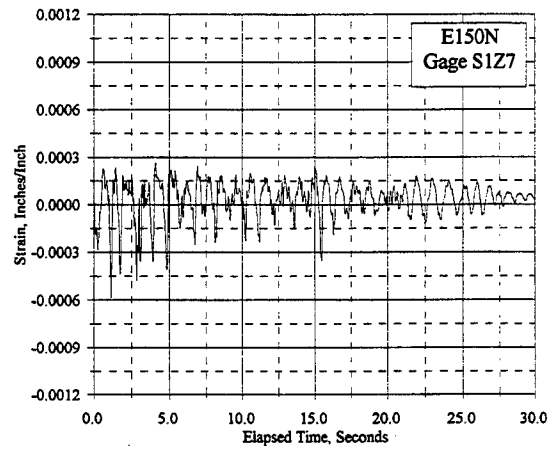
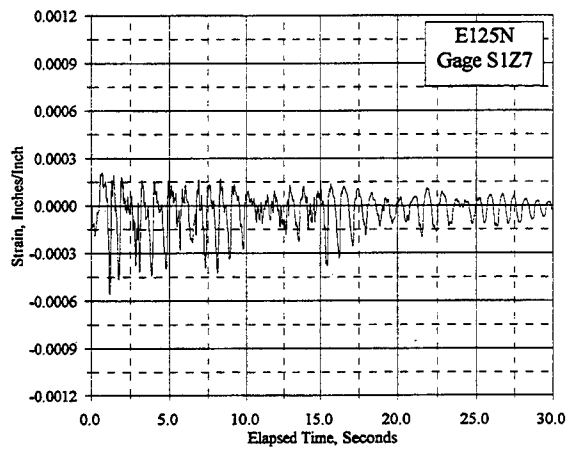
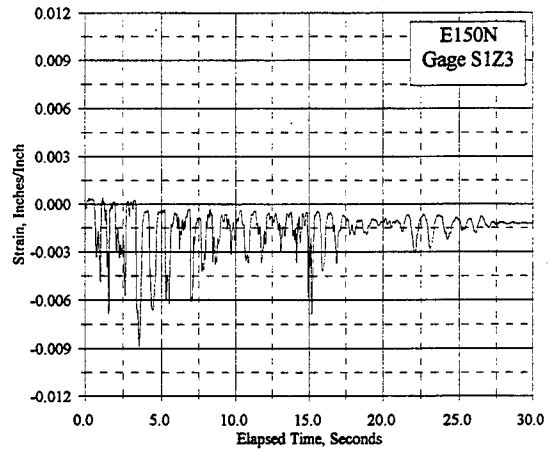
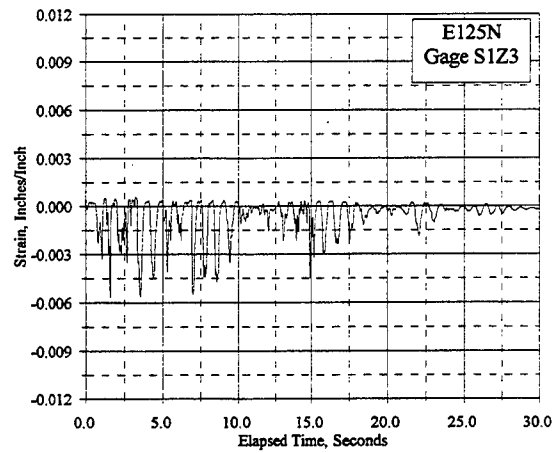


Figure C.20.11 Reinforcement Strain Vs. Elapsed Time, Gages S1Z3, S1Z7, S1Z8: E125N, E150N

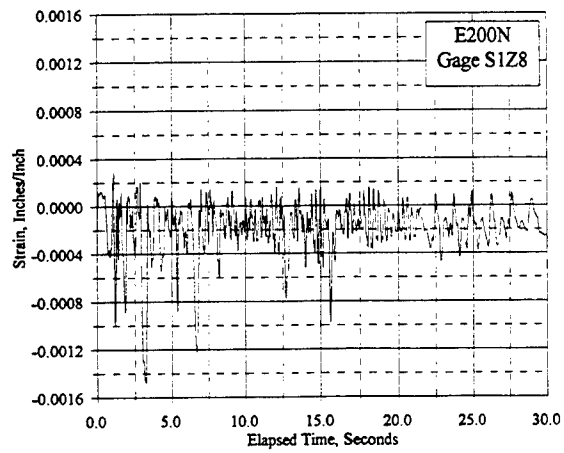
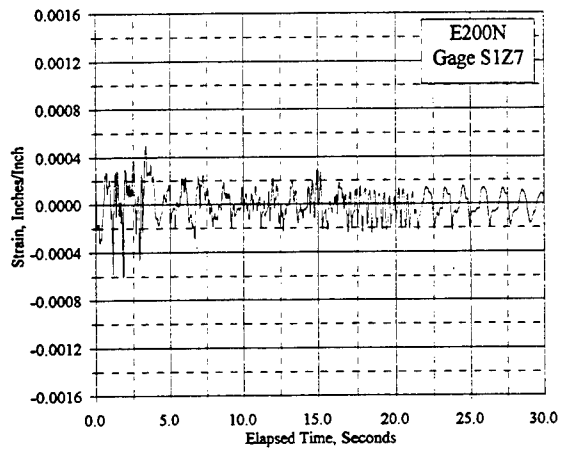
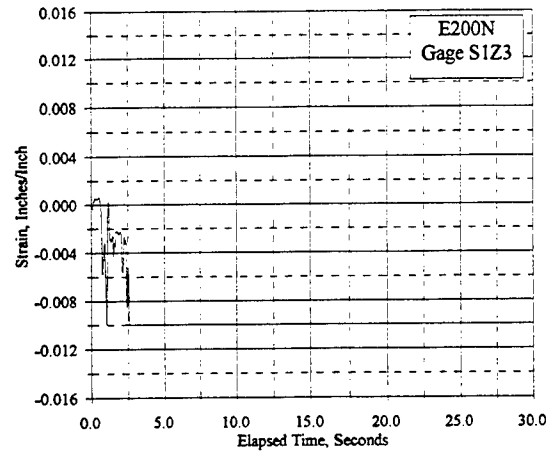


Figure C.20.12 Reinforcement Strain Vs. Elapsed Time, Gages S1Z3, S1Z7, S1Z8: E200N

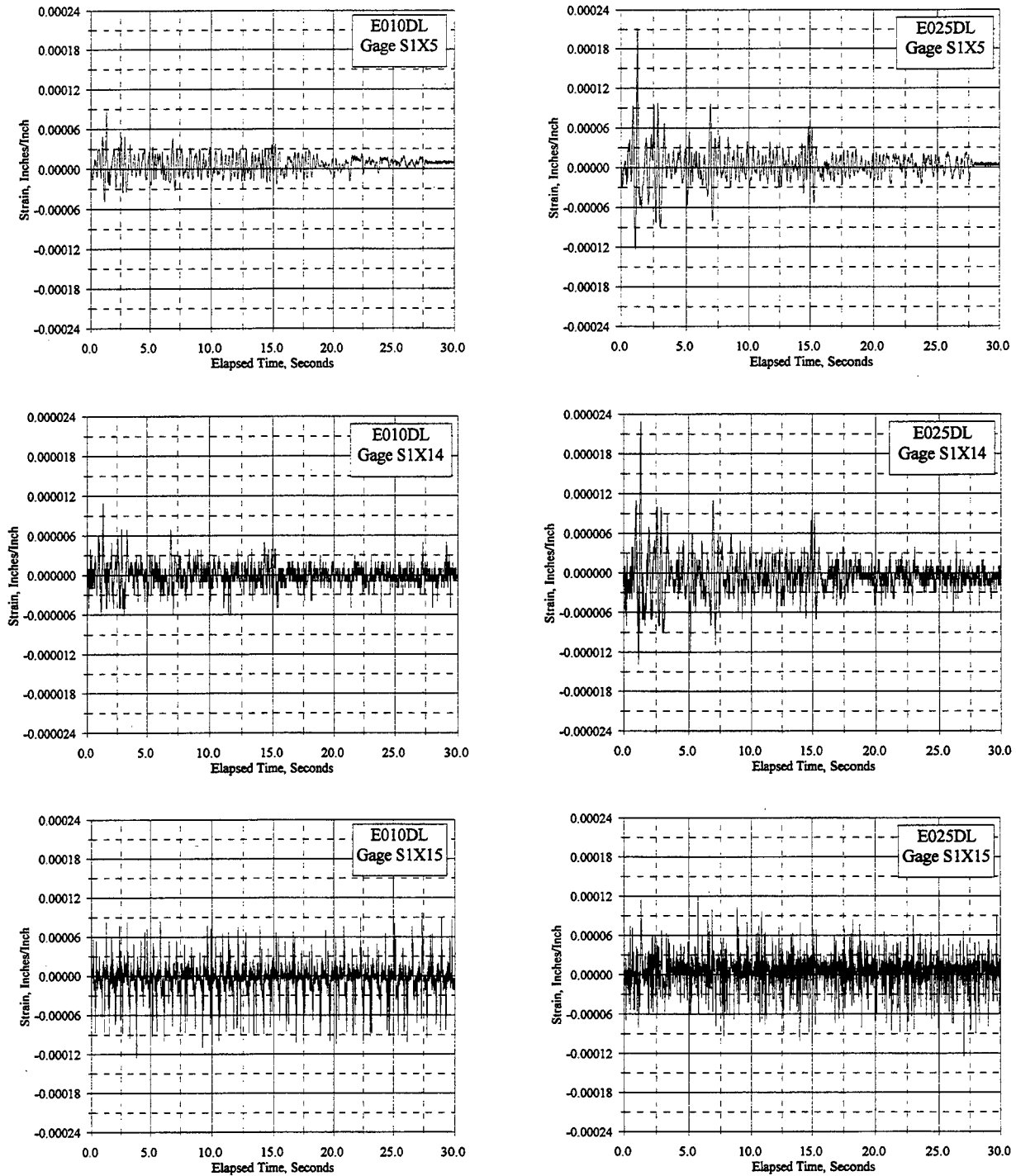


Figure C.21.1 Reinforcement Strain Vs. Elapsed Time, Gages S1X5, S1X14, S1X15: E010DL, E025DL

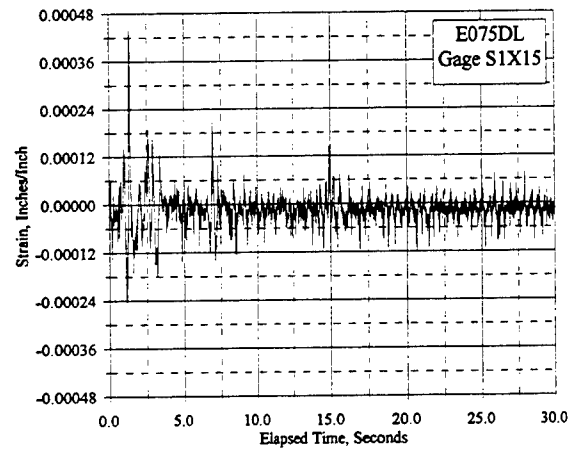
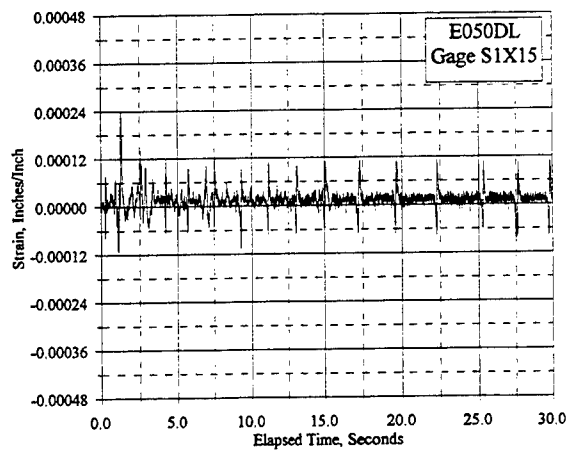
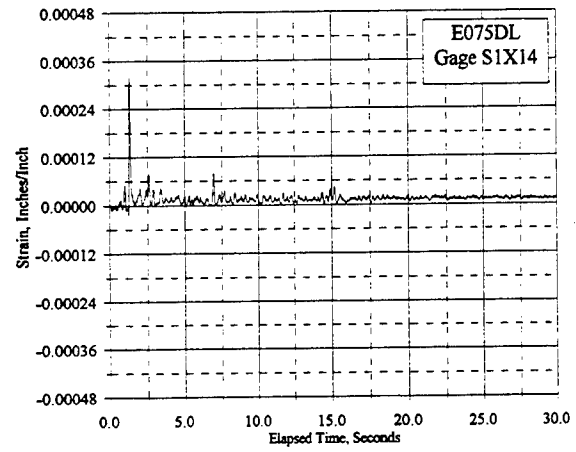
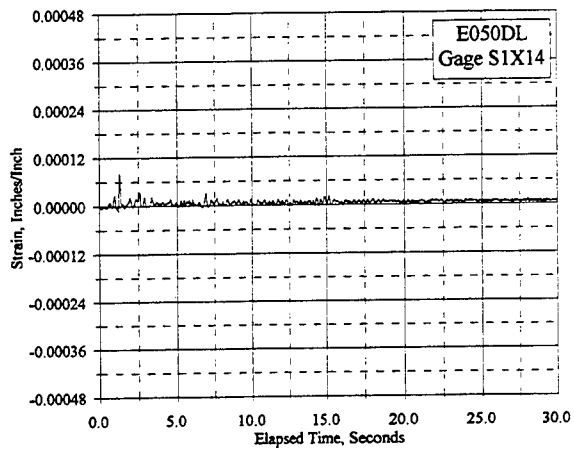
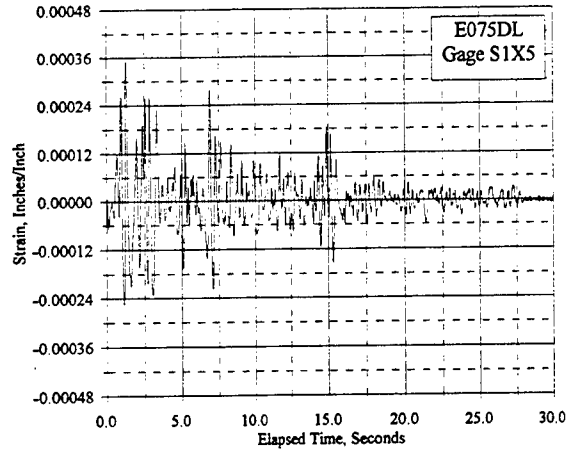
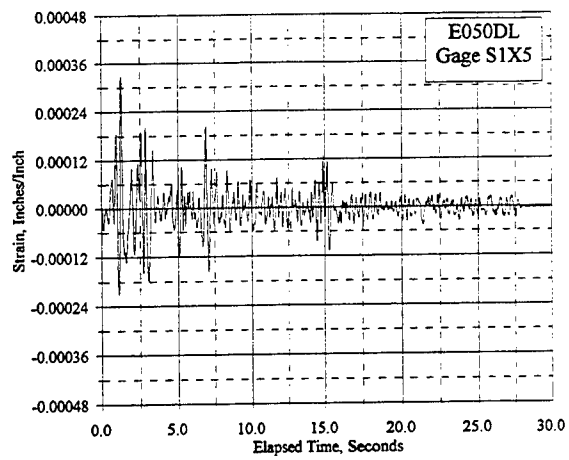


Figure C.21.2 Reinforcement Strain Vs. Elapsed Time, Gages S1X5, S1X14, S1X15: E050DL, E075DL

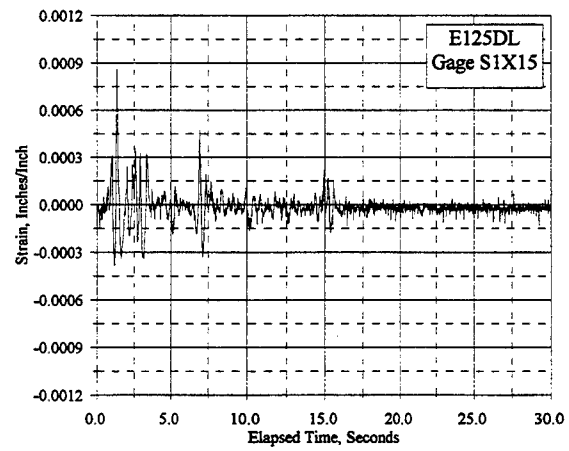
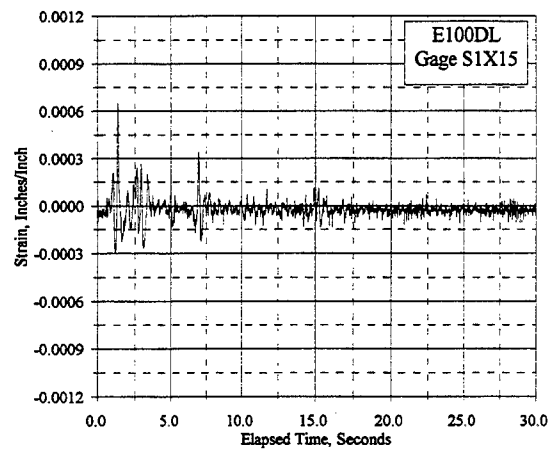
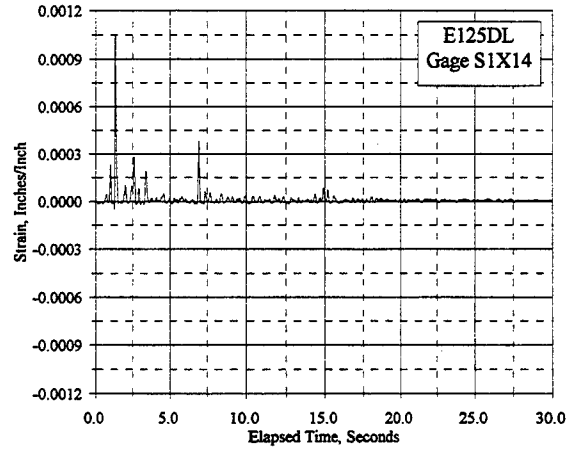
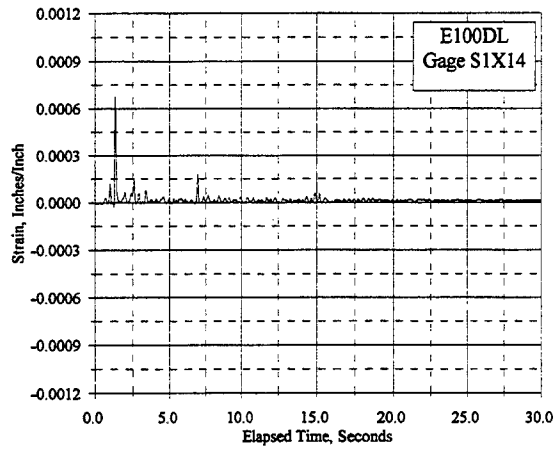
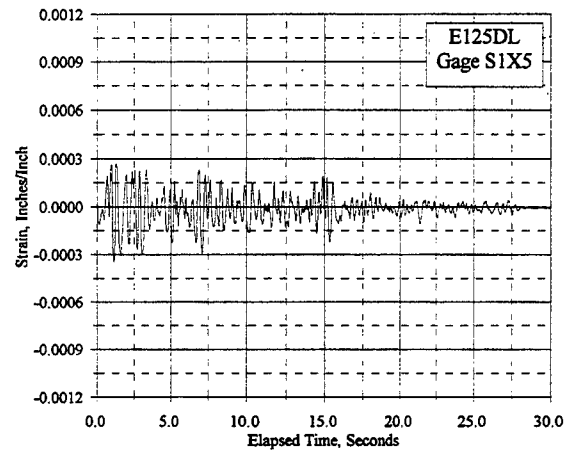
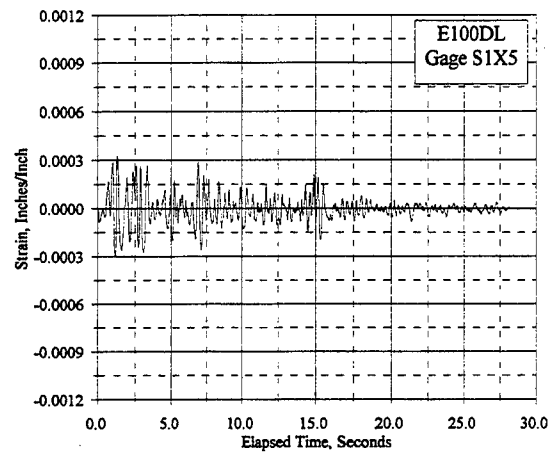


Figure C.21.3 Reinforcement Strain Vs. Elapsed Time, Gages S1X5, S1X14, S1X15: E100DL, E125DL

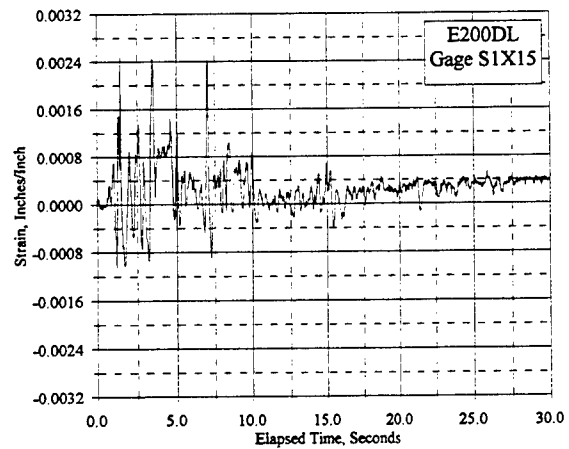
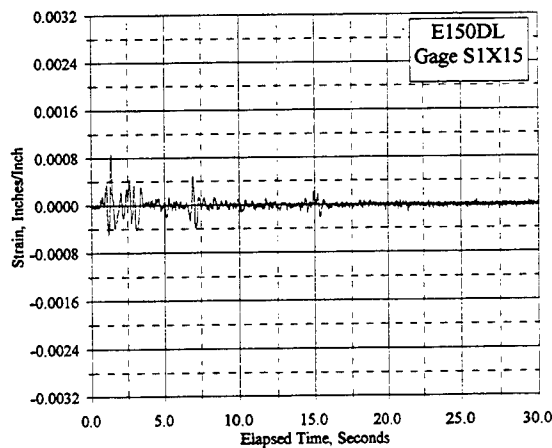
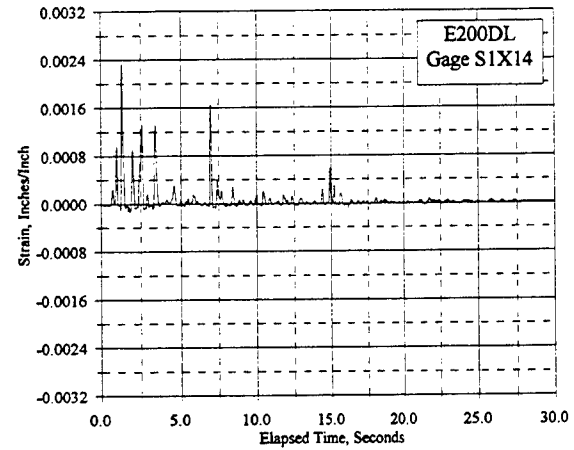
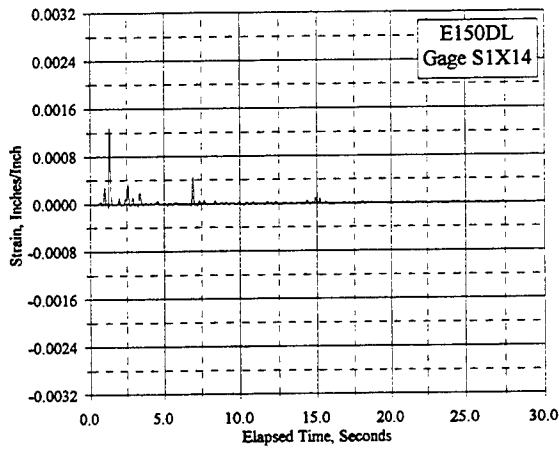
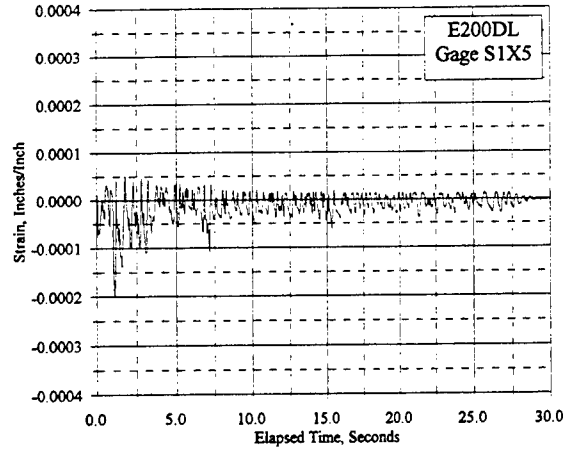
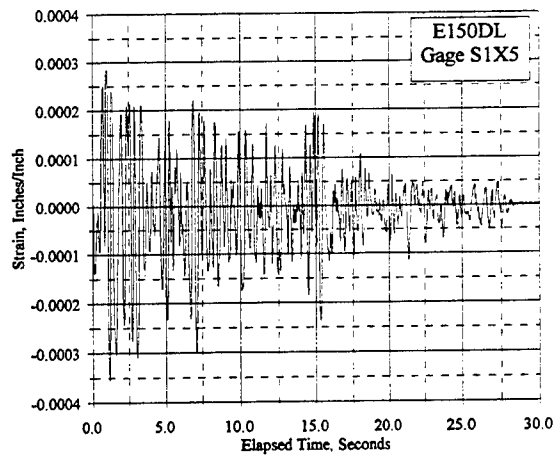


Figure C.21.4 Reinforcement Strain Vs. Elapsed Time, Gages S1X5, S1X14, S1X15: E150DL, E200DL

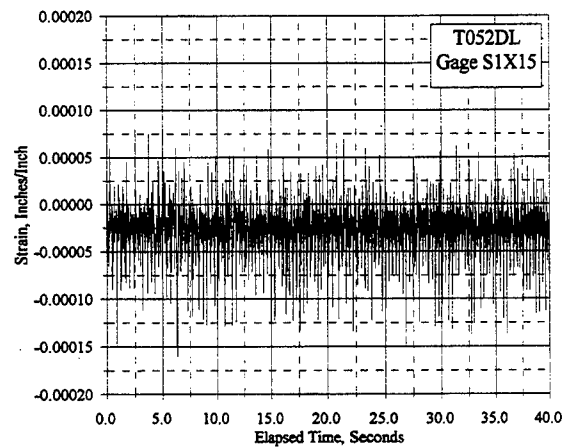
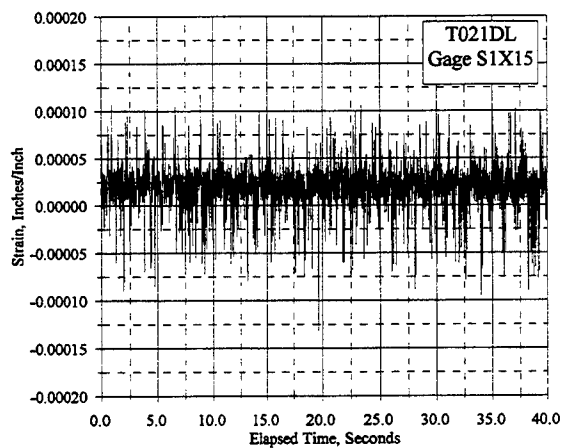
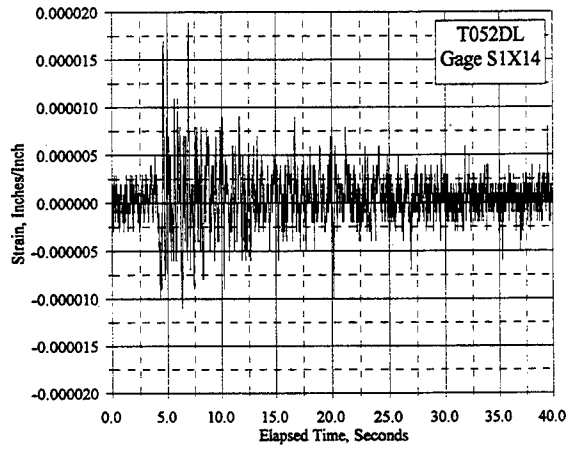
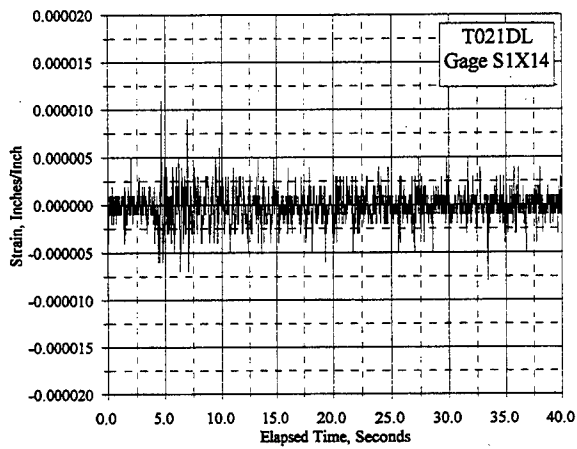
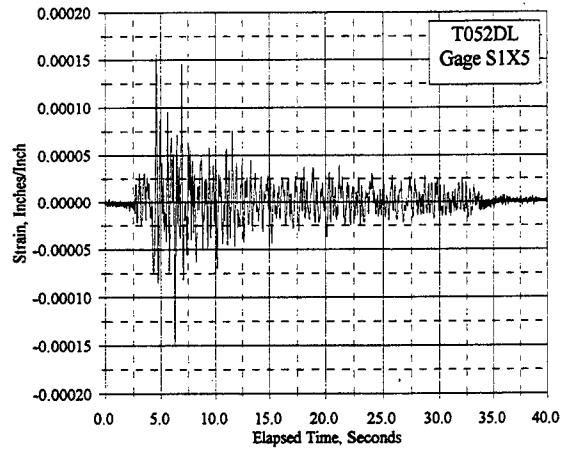
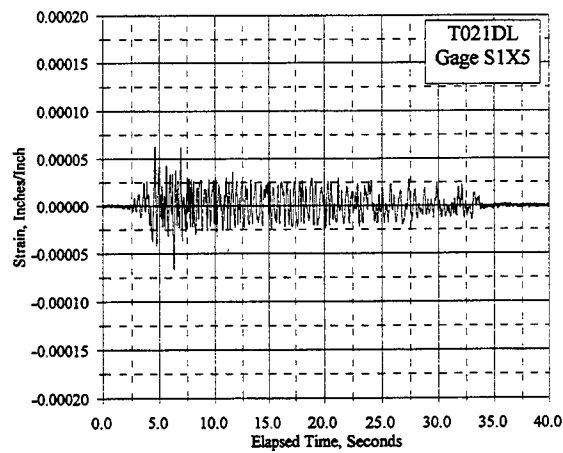


Figure C.21.5 Reinforcement Strain Vs. Elapsed Time, Gages S1X5, S1X14, S1X15: T021DL, T052DL

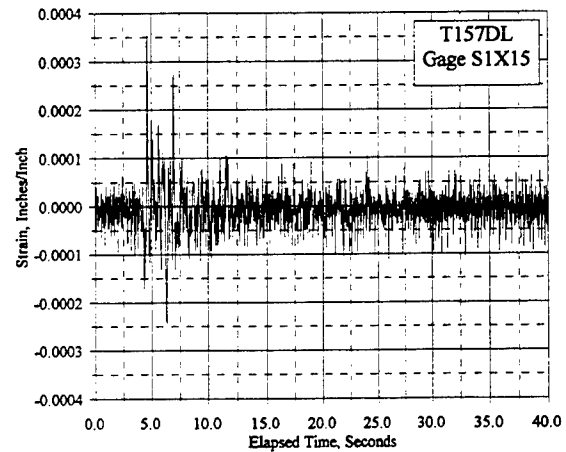
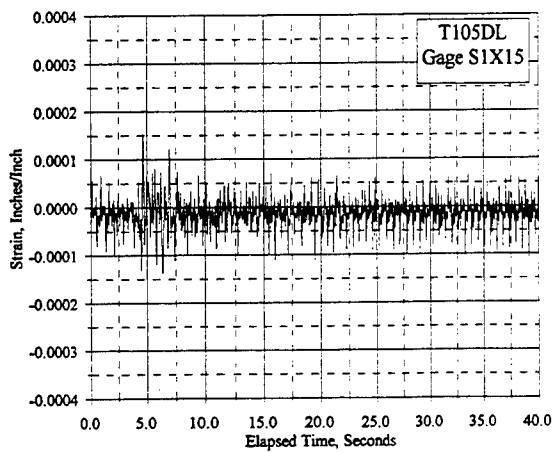
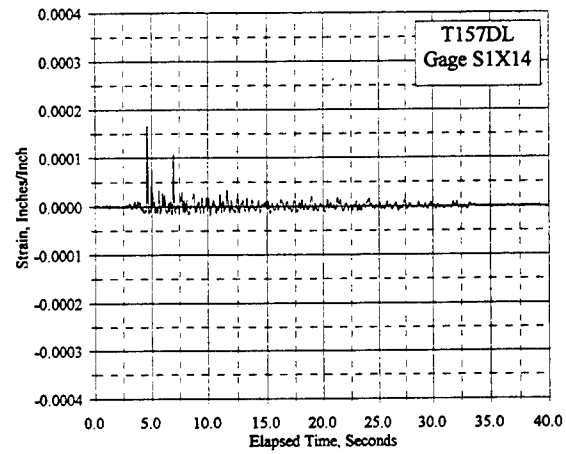
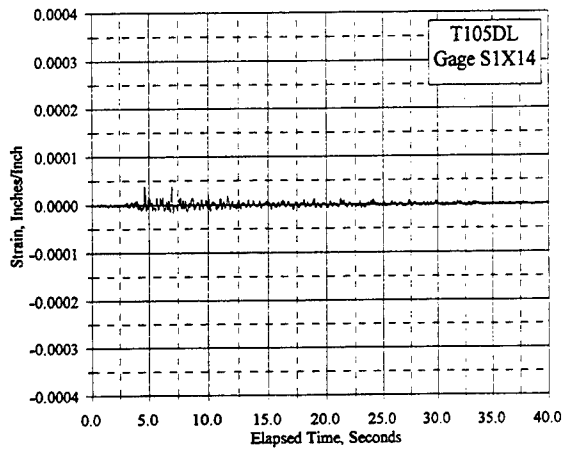
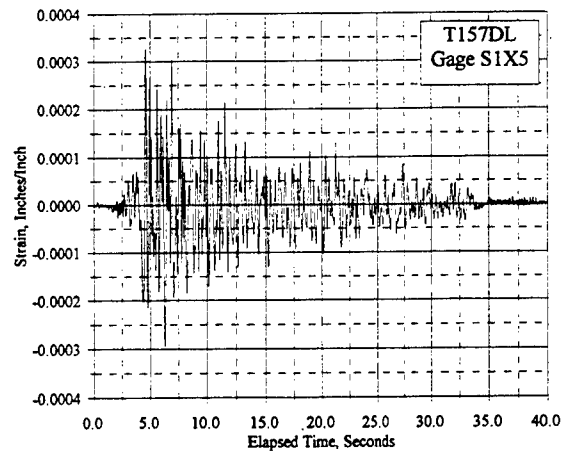
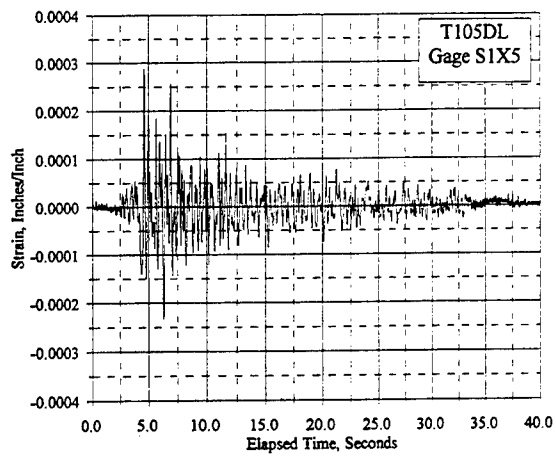


Figure C.21.6 Reinforcement Strain Vs. Elapsed Time, Gages S1X5, S1X14, S1X15: T105DL, T157DL

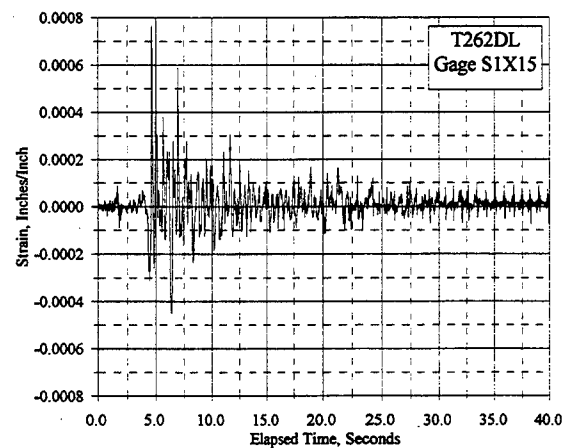
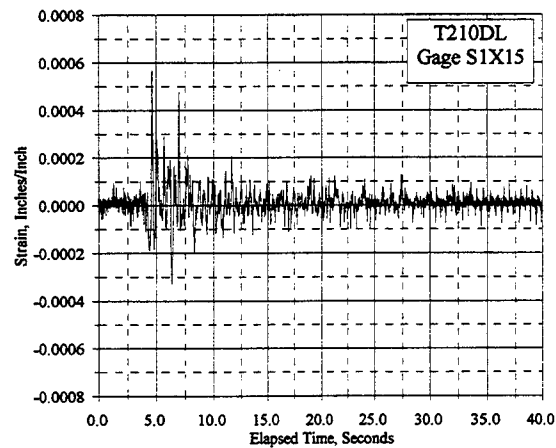
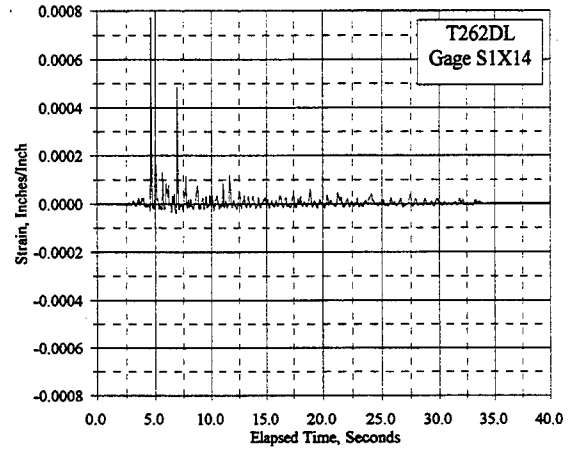
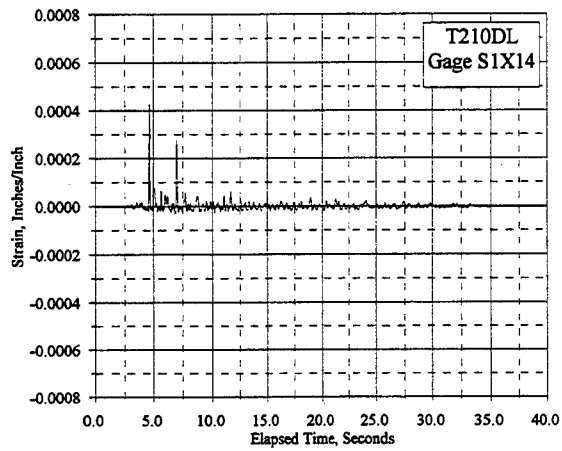
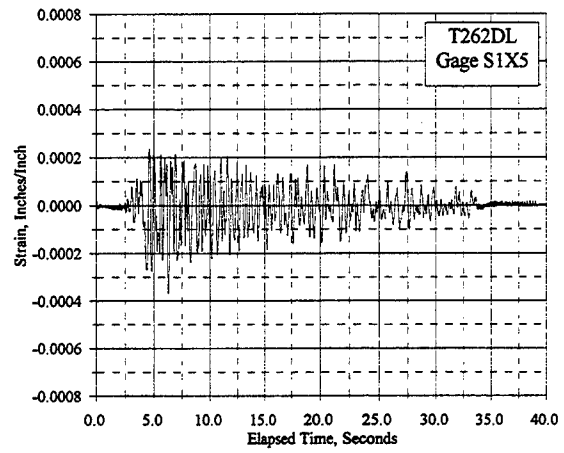
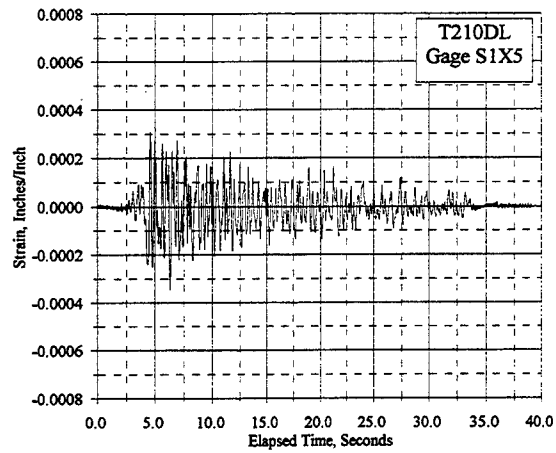


Figure C.21.7 Reinforcement Strain Vs. Elapsed Time, Gages S1X5, S1X14, S1X15: T210DL, T262DL

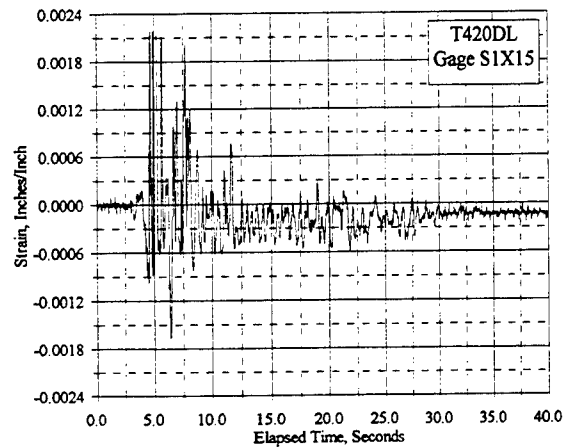
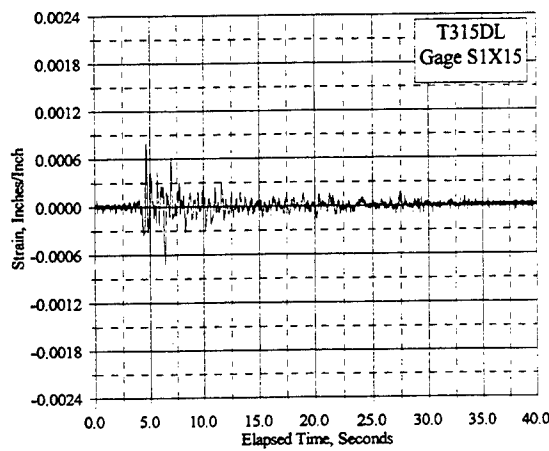
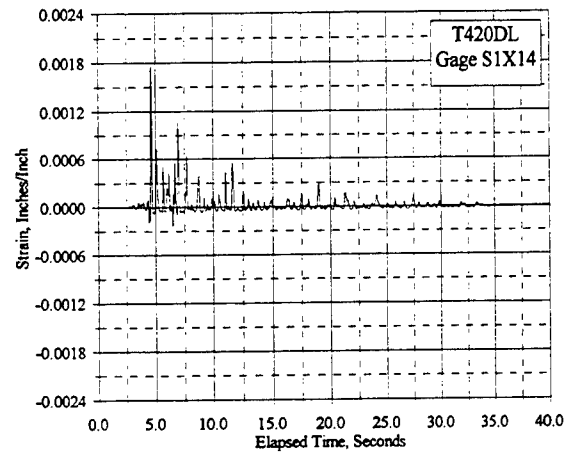
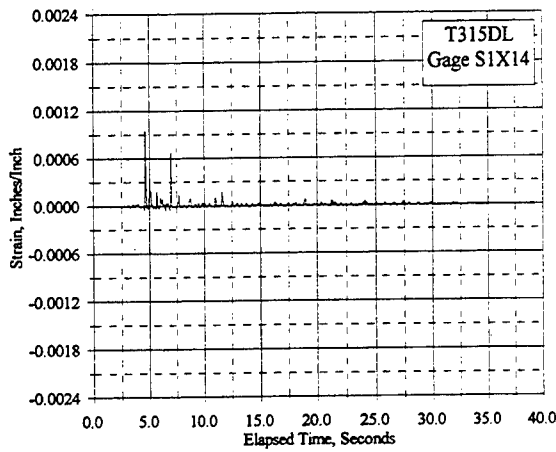
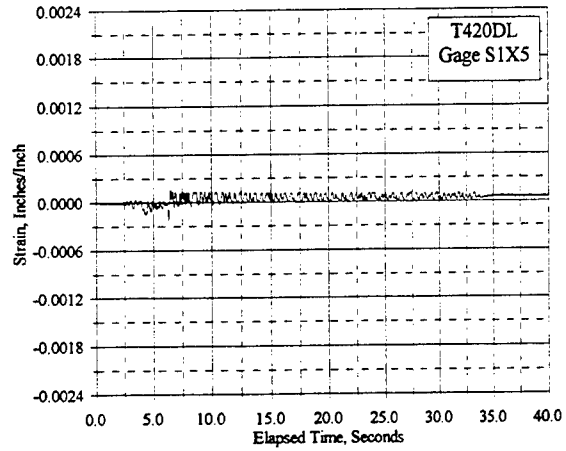
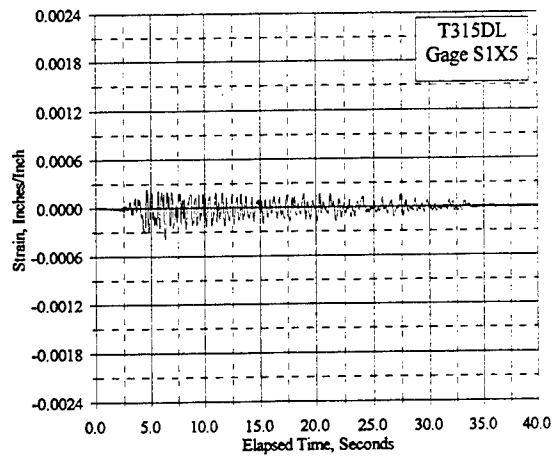


Figure C.21.8 Reinforcement Strain Vs. Elapsed Time, Gages S1X5, S1X14, S1X15: T315DL, T420DL

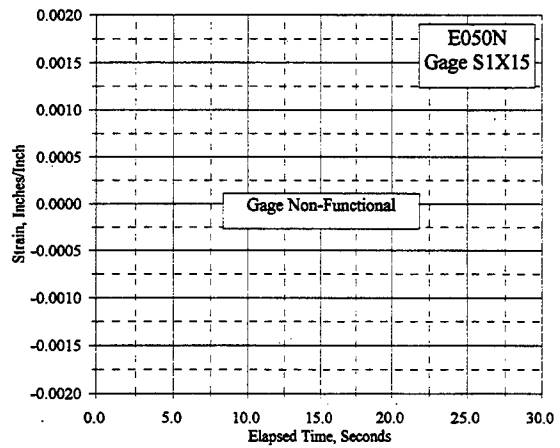
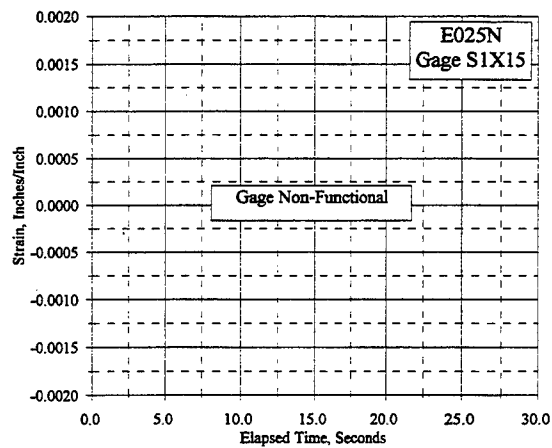
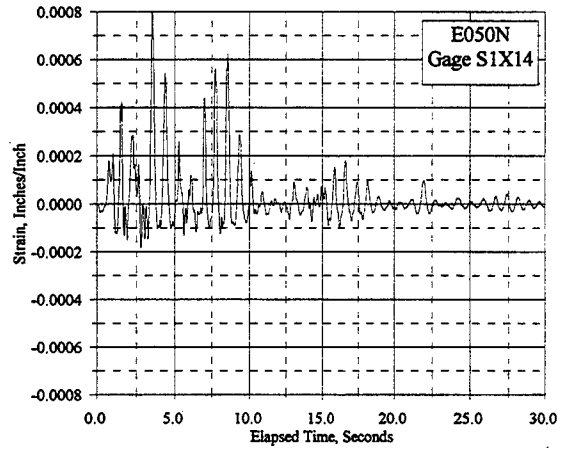
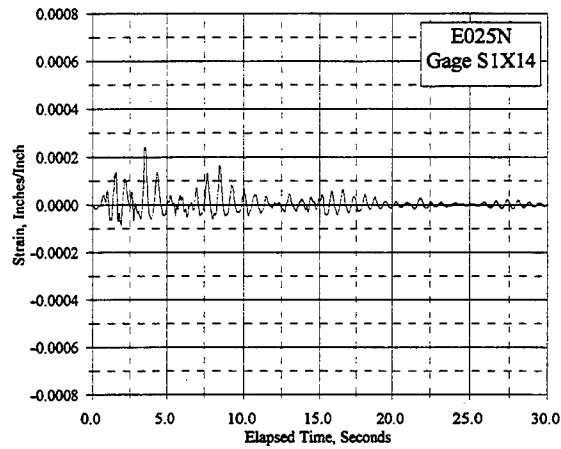
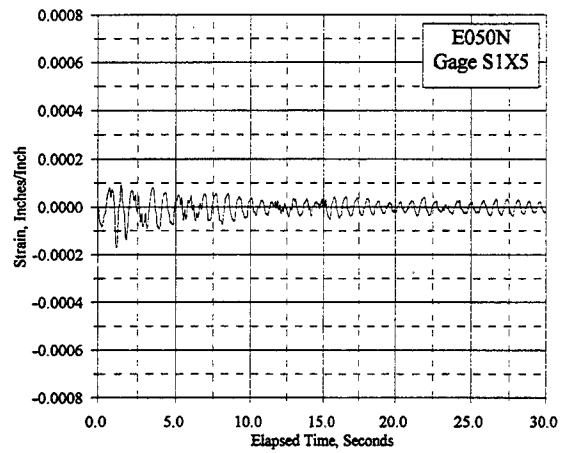
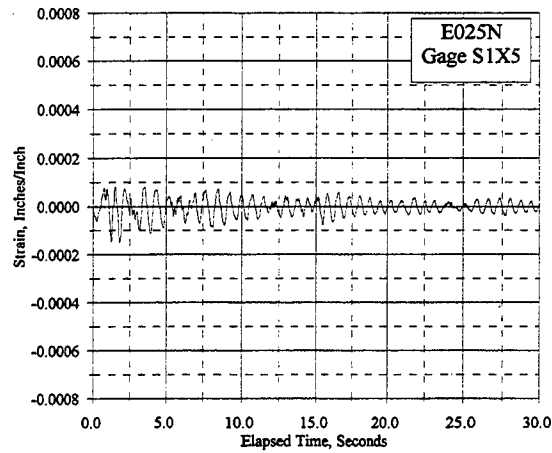


Figure C.21.9 Reinforcement Strain Vs. Elapsed Time, Gages S1X5, S1X14, S1X15: E025N, E050N

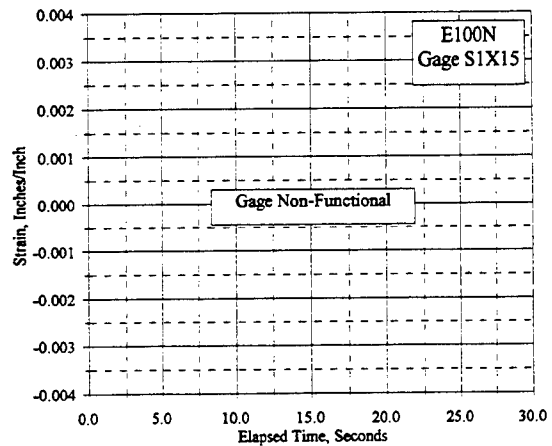
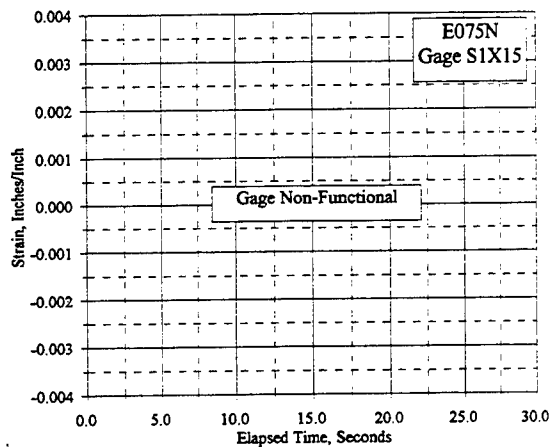
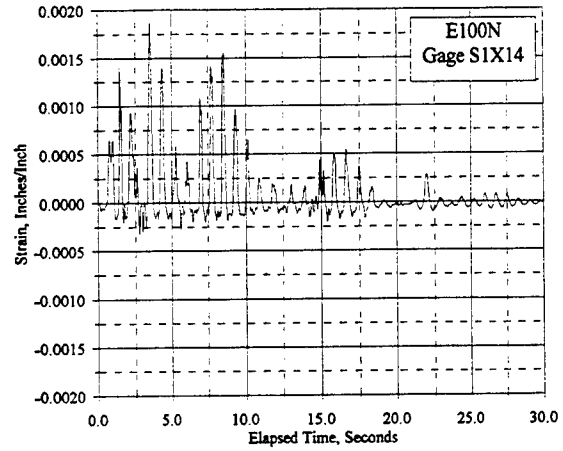
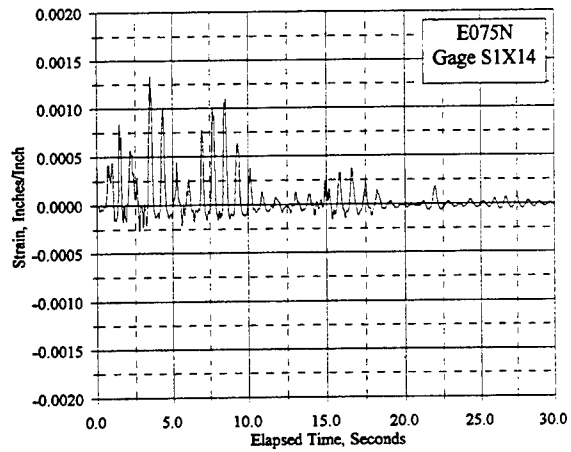
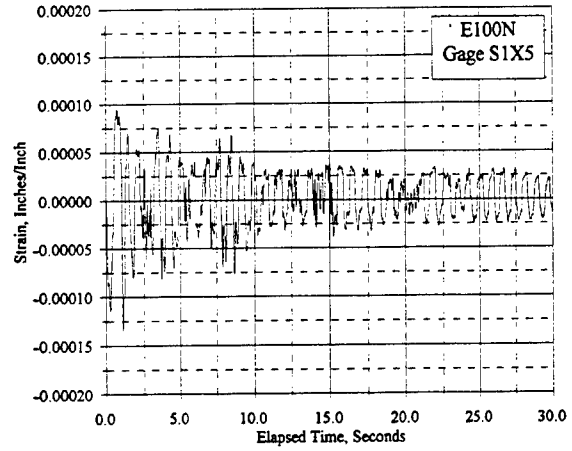
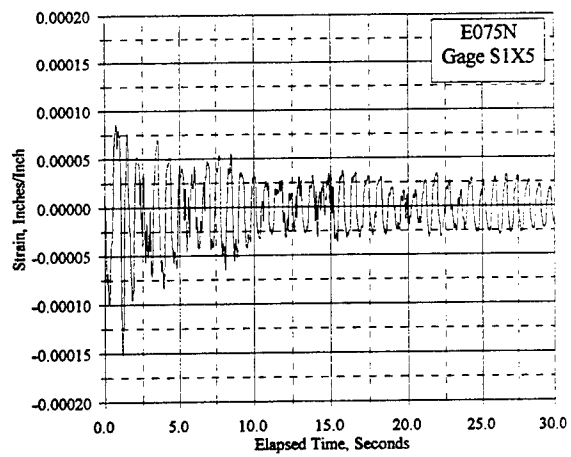


Figure C.21.10 Reinforcement Strain Vs. Elapsed Time, Gages S1X5, S1X14, S1X15: E075N, E100N

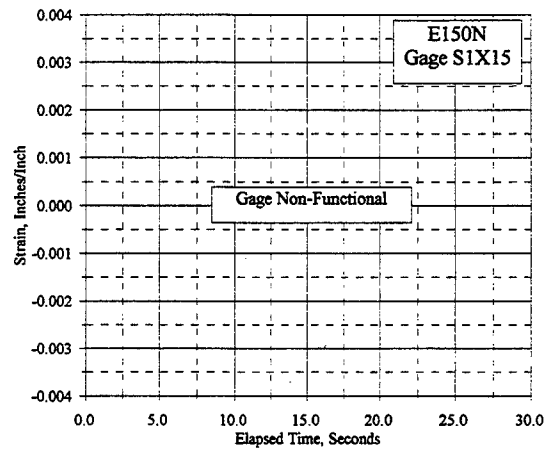
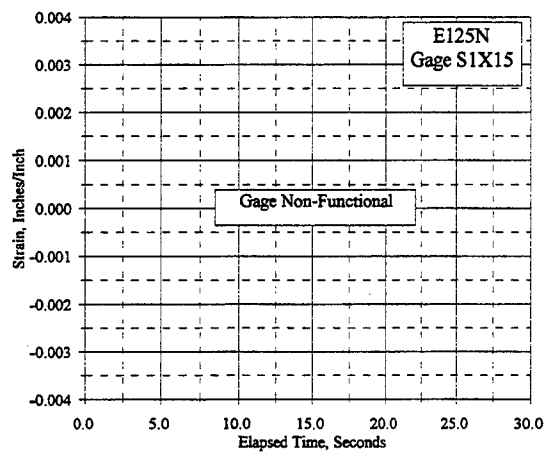
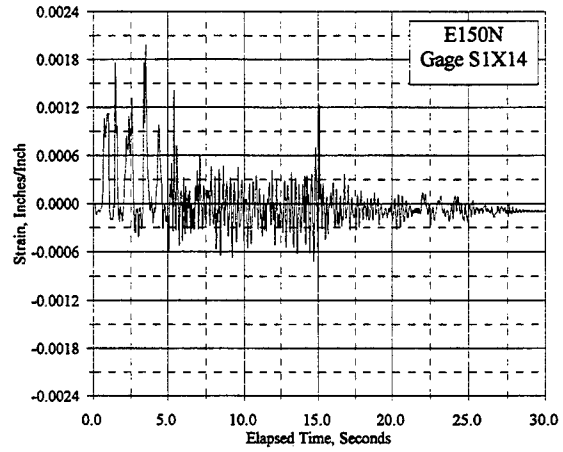
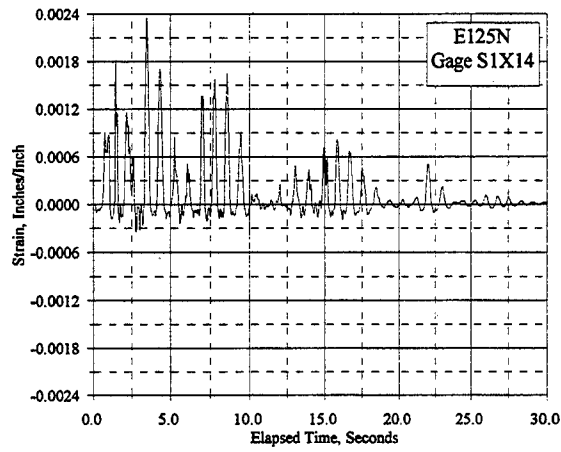
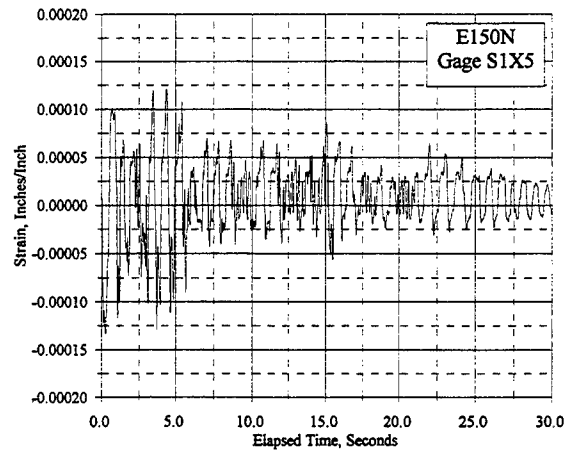
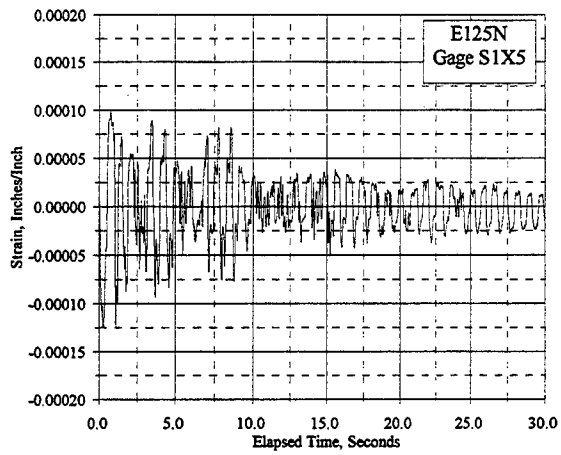


Figure C.21.11 Reinforcement Strain Vs. Elapsed Time, Gages S1X5, S1X14, S1X15: E125N, E150N

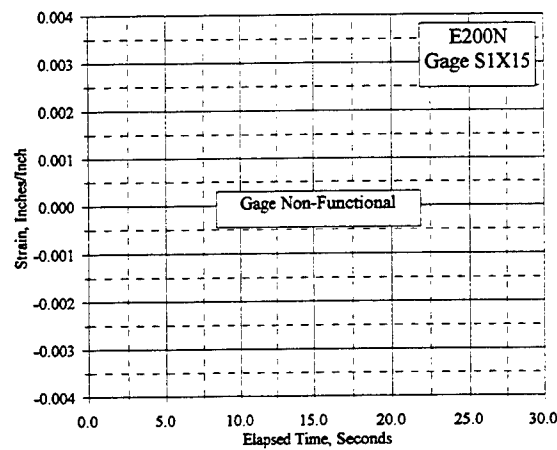
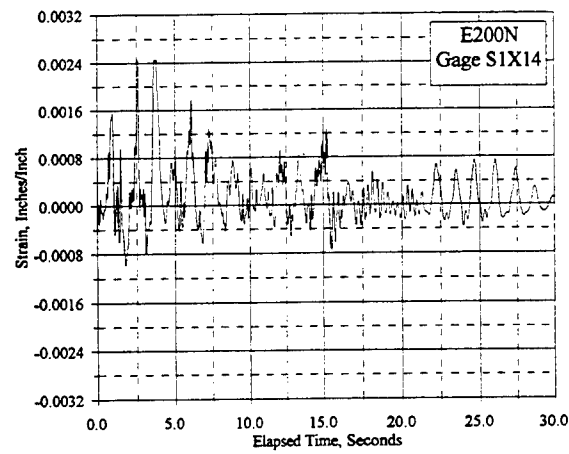
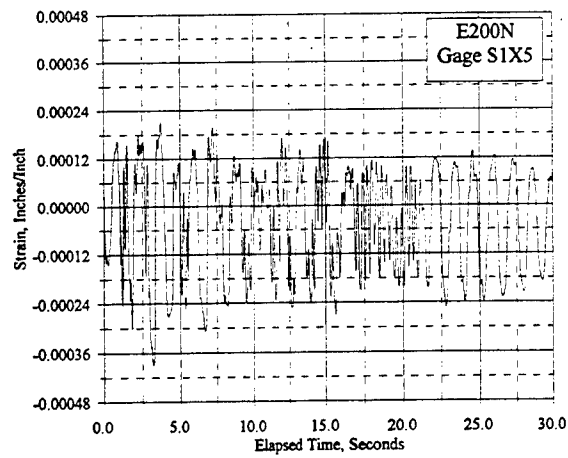


Figure C.21.12 Reinforcement Strain Vs. Elapsed Time, Gages S1X5, S1X14, S1X15: E200N

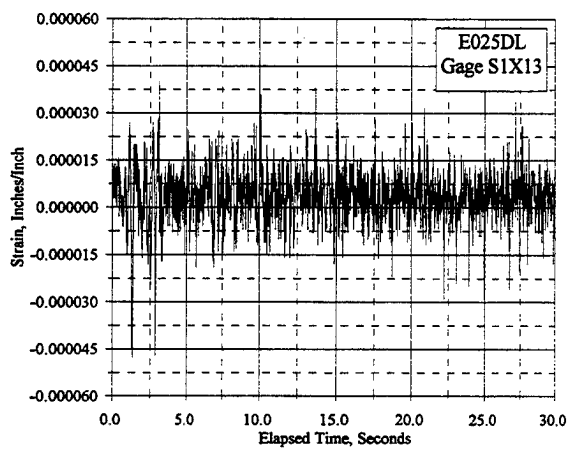
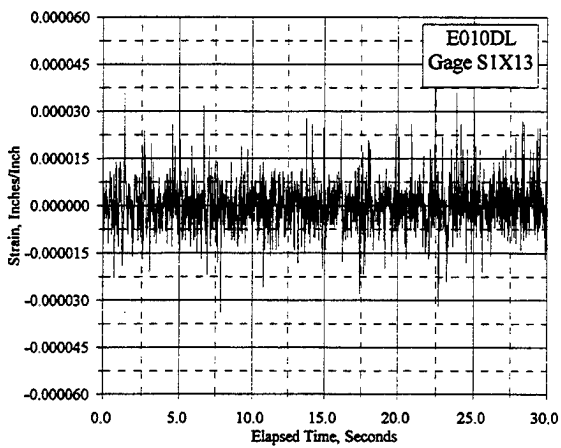
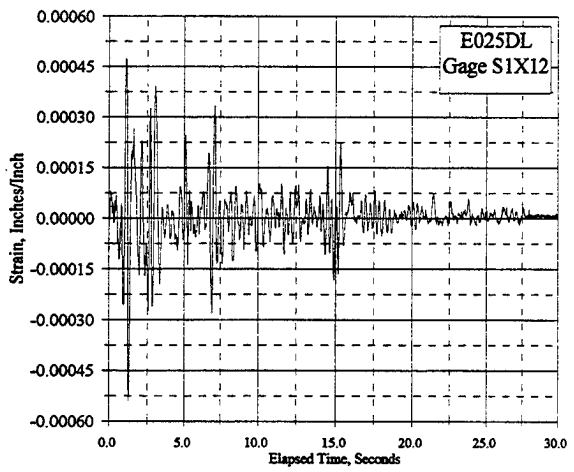
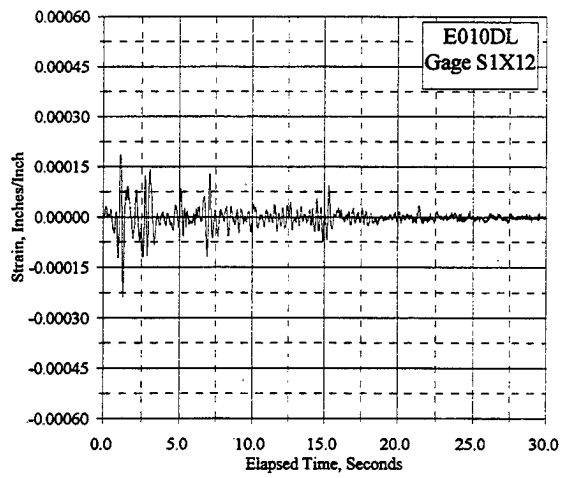
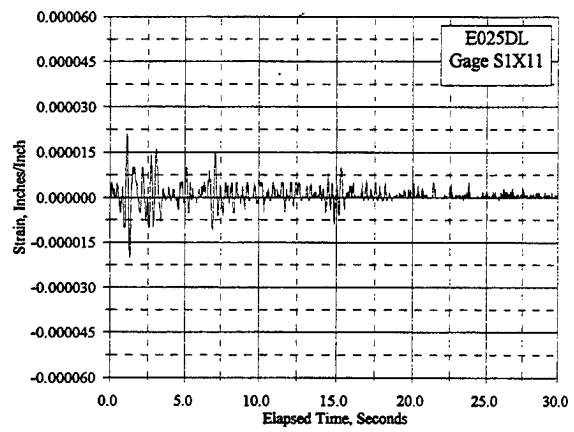
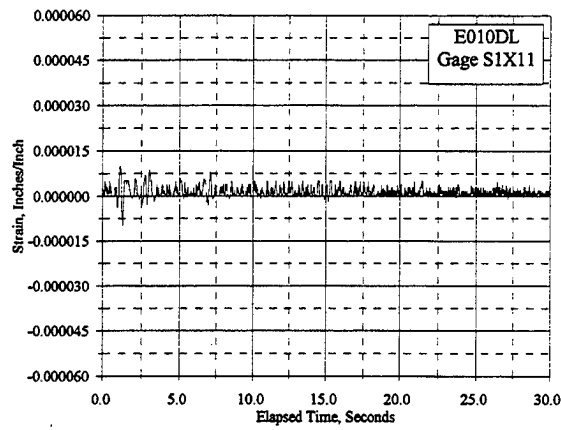


Figure C.22.1 Reinforcement Strain Vs. Elapsed Time, Gages S1X11, S1X12, S1X13: E010DL, E025DL

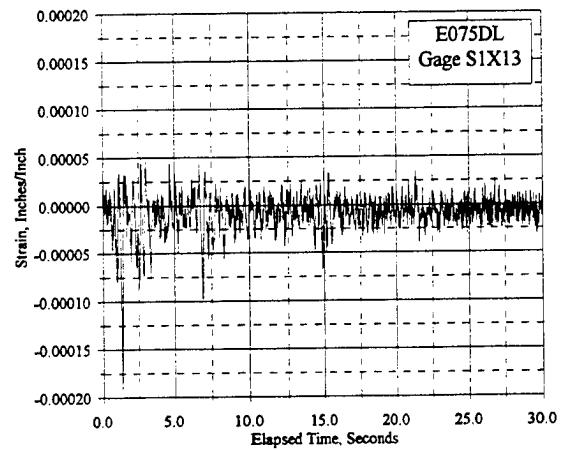
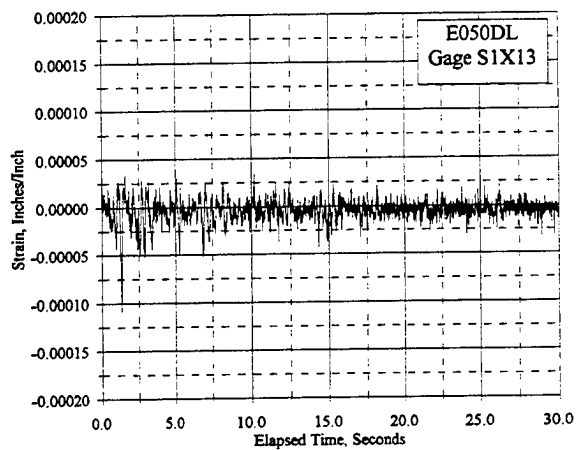
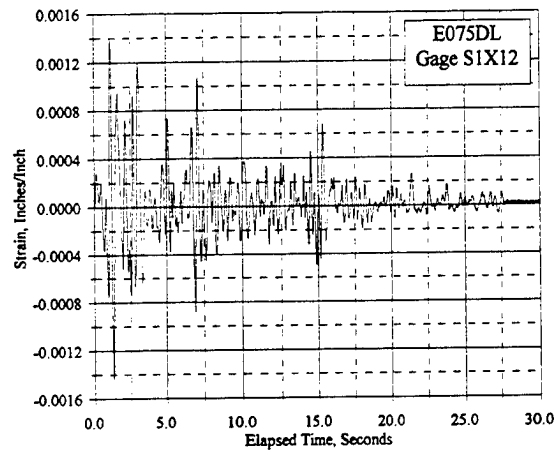
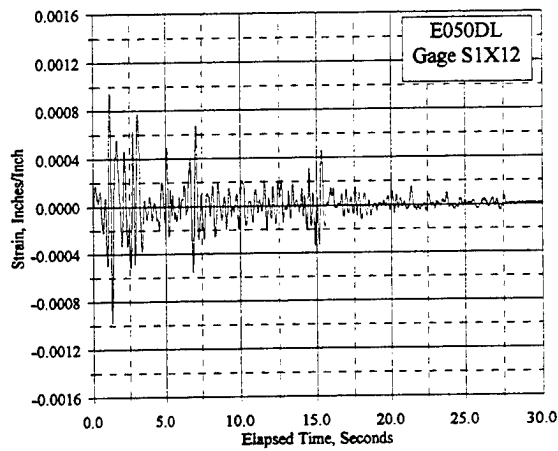
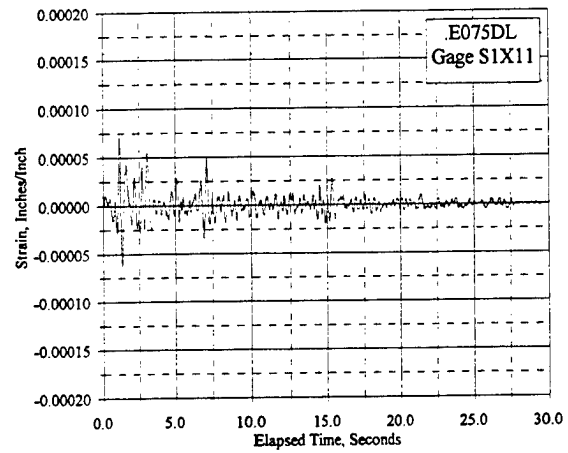
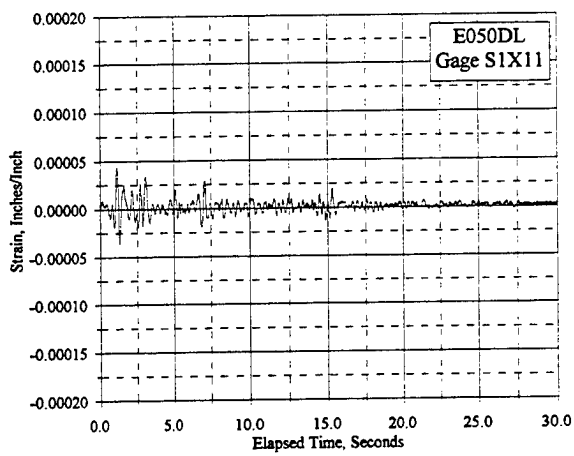


Figure C.22.2 Reinforcement Strain Vs. Elapsed Time, Gages S1X11, S1X12, S1X13: E050DL, E075DL

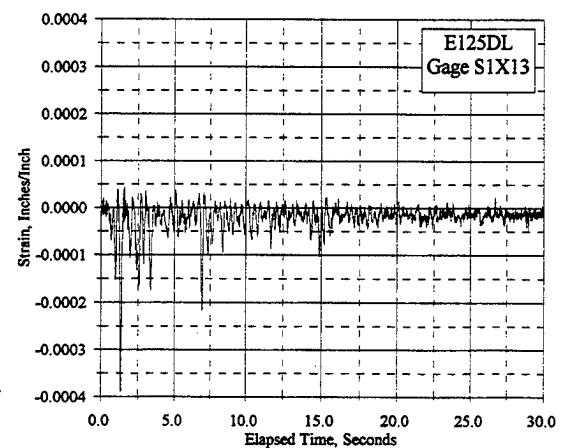
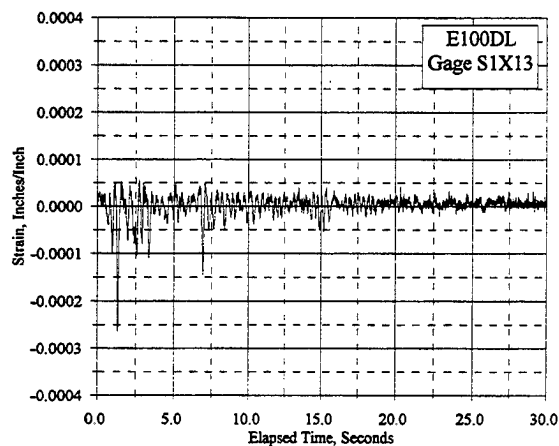
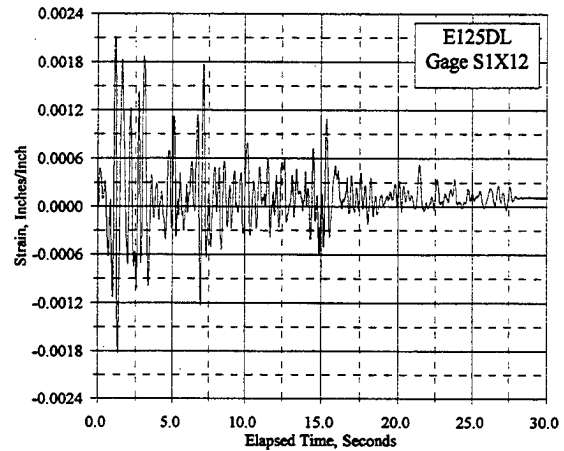
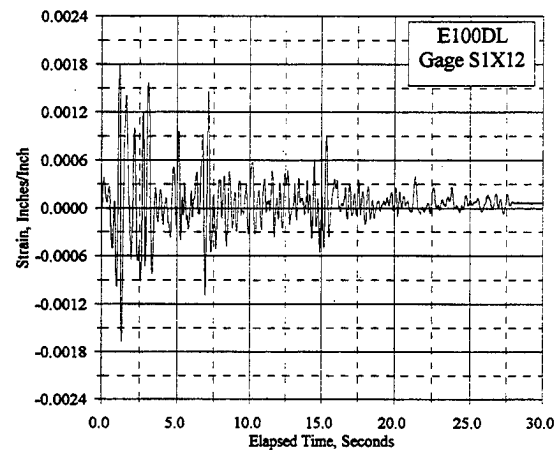
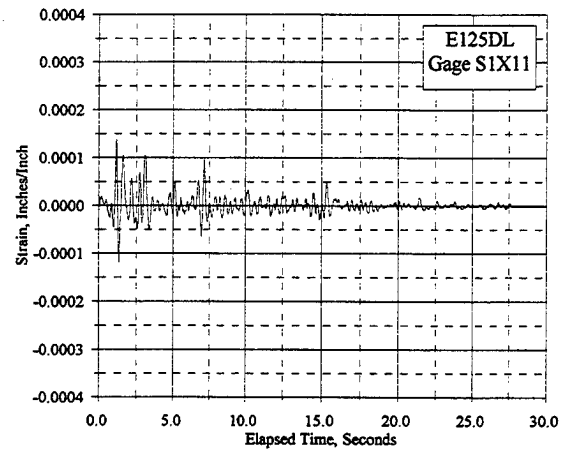
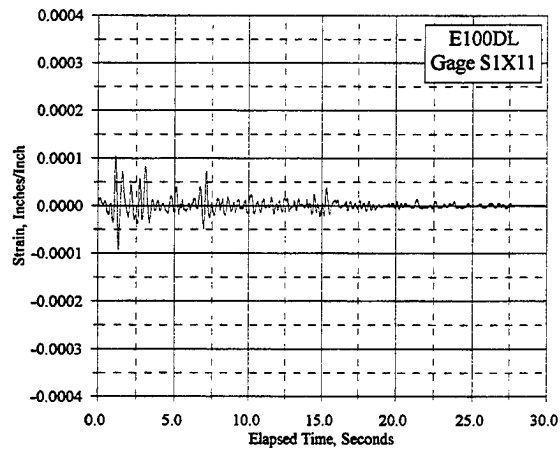


Figure C.22.3 Reinforcement Strain Vs. Elapsed Time, Gages S1X11, S1X12, S1X13: E100DL, E125DL

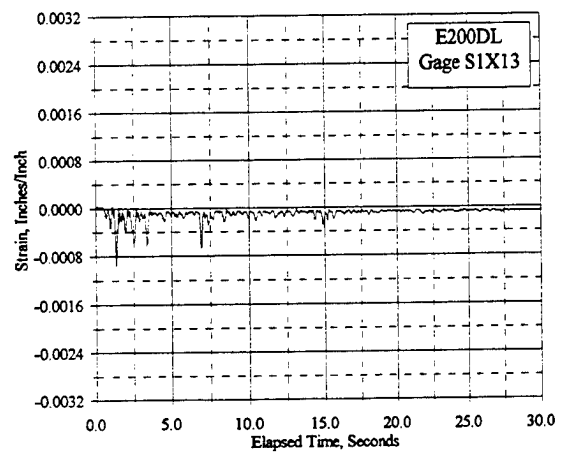
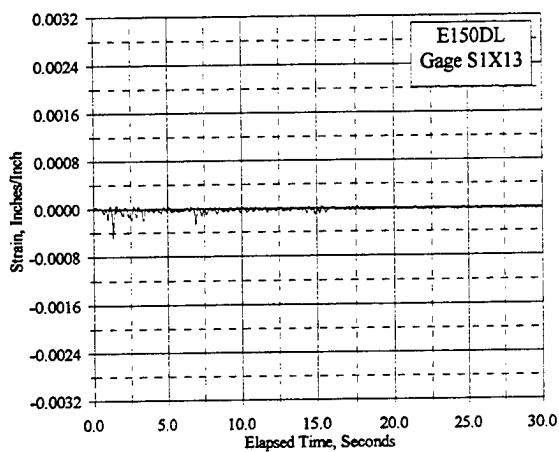
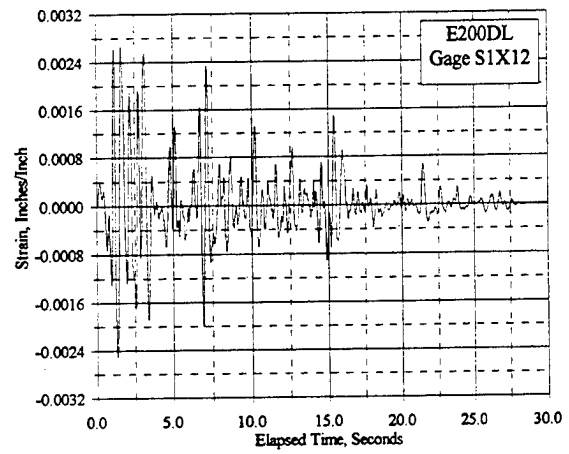
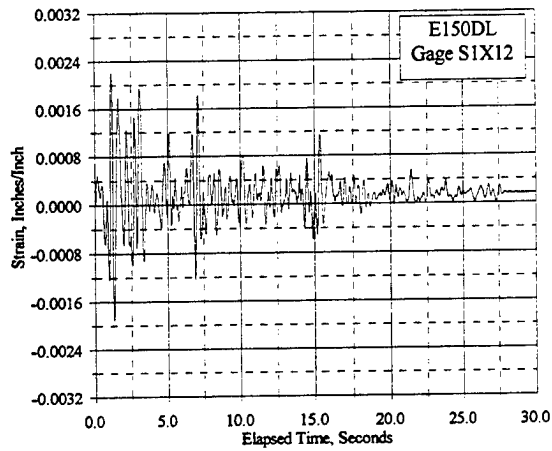
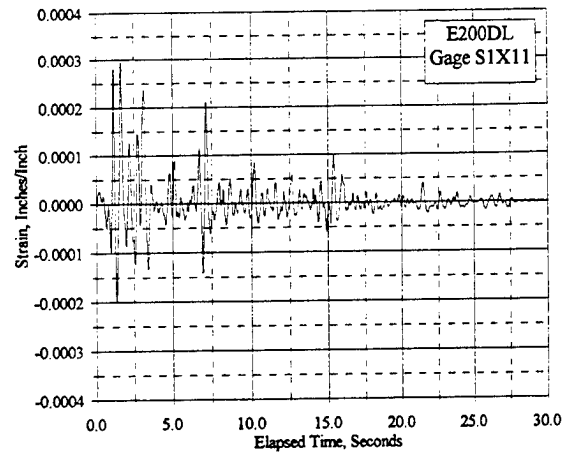
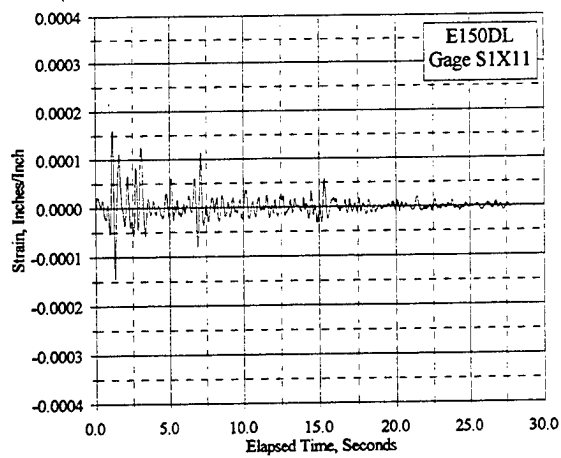


Figure C.22.4 Reinforcement Strain Vs. Elapsed Time, Gages S1X11, S1X12, S1X13: E150DL, E200DL

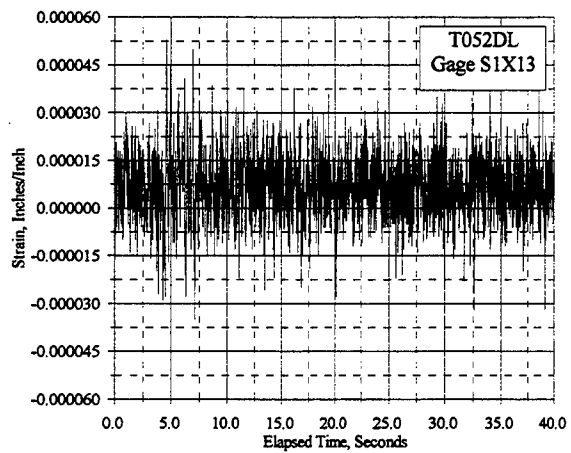
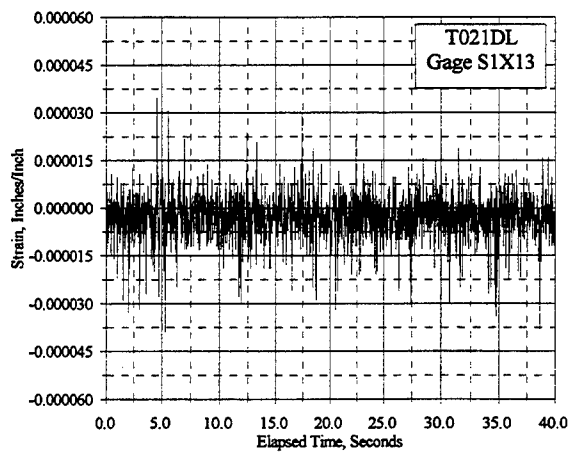
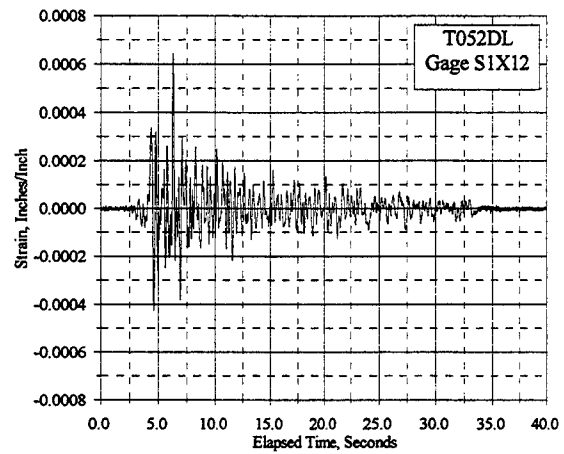
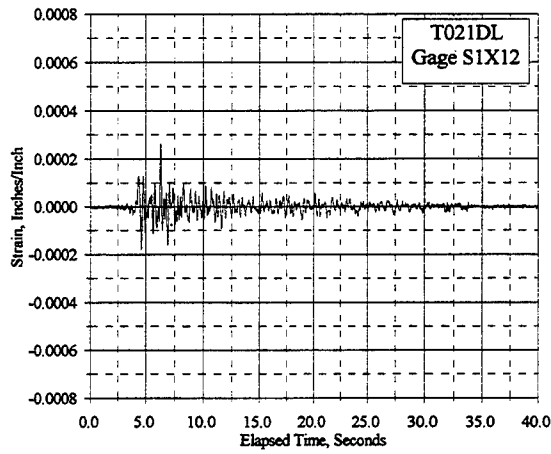
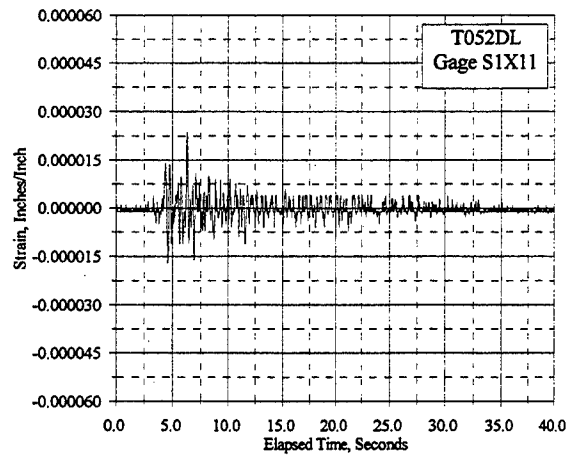
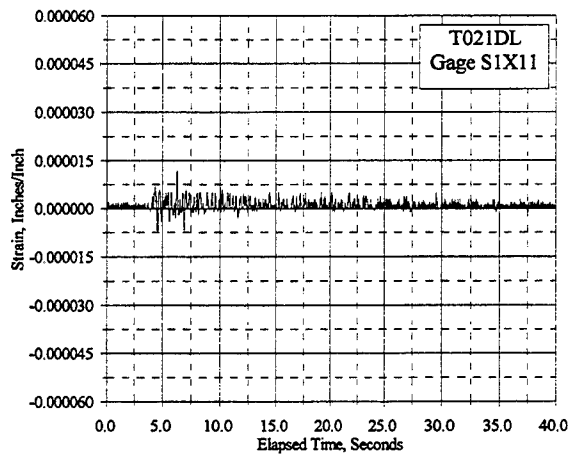


Figure C.22.5 Reinforcement Strain Vs. Elapsed Time, Gages S1X11, S1X12, S1X13: T021DL, T052DL

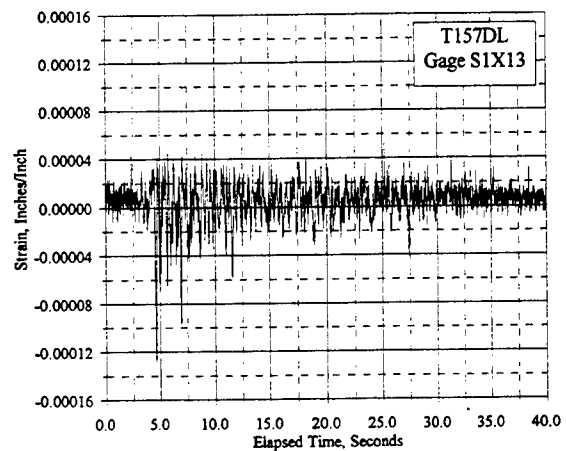
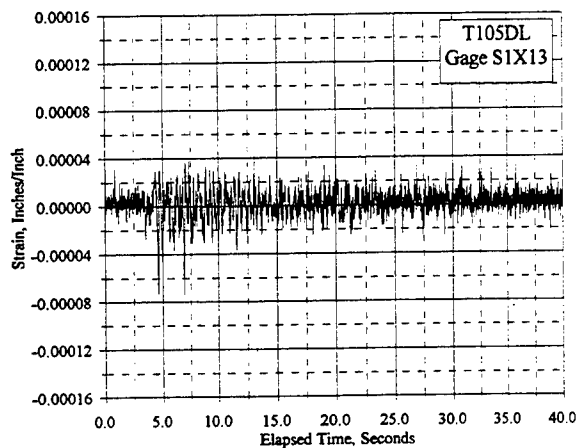
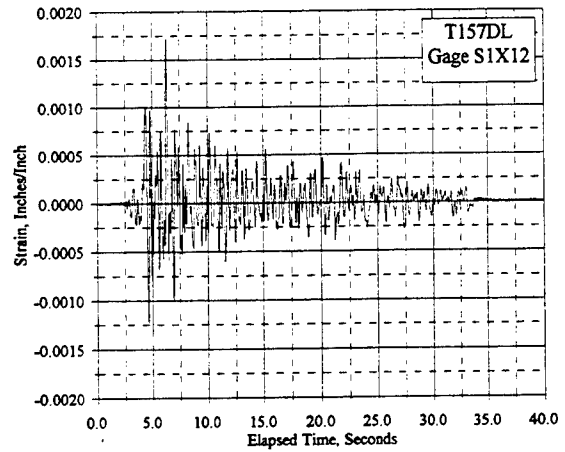
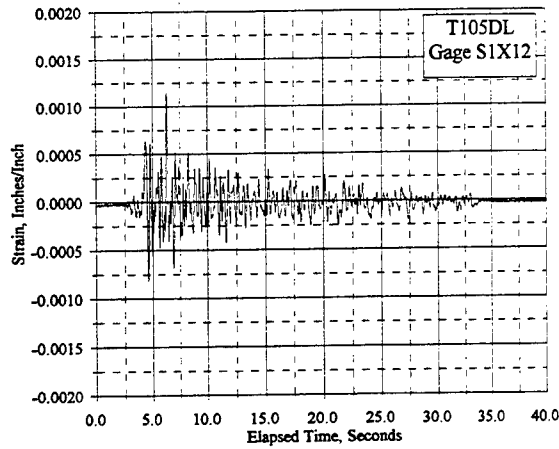
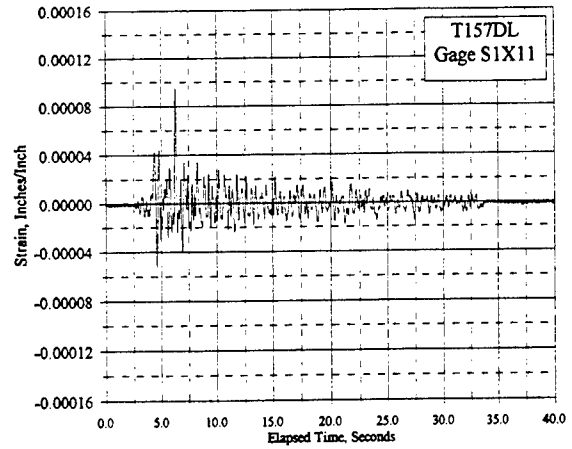
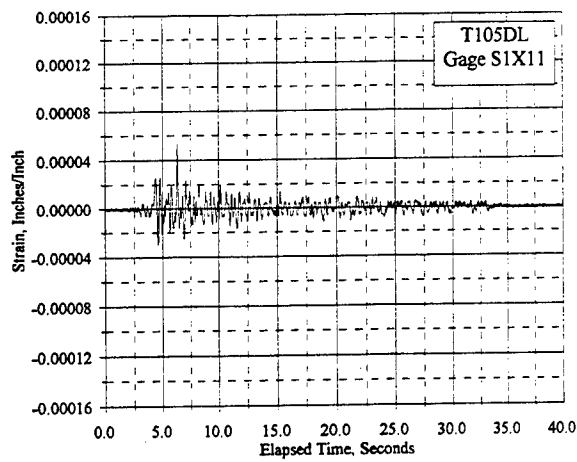


Figure C.22.6 Reinforcement Strain Vs. Elapsed Time, Gages S1X11, S1X12, S1X13: T105DL, T157DL

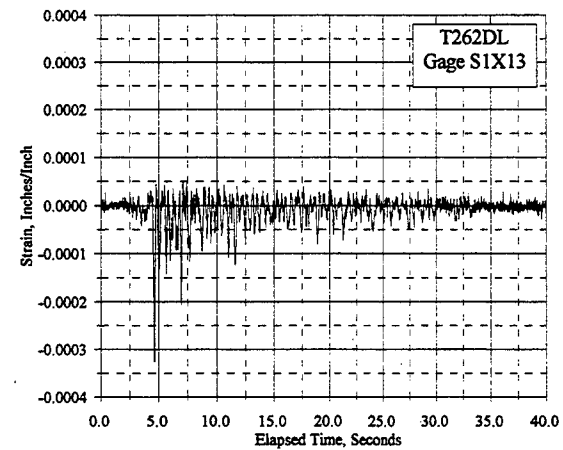
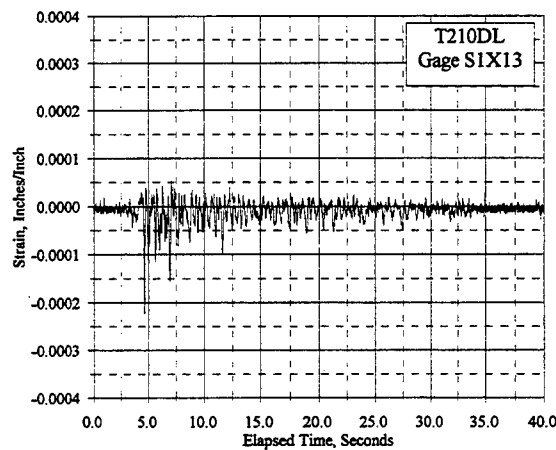
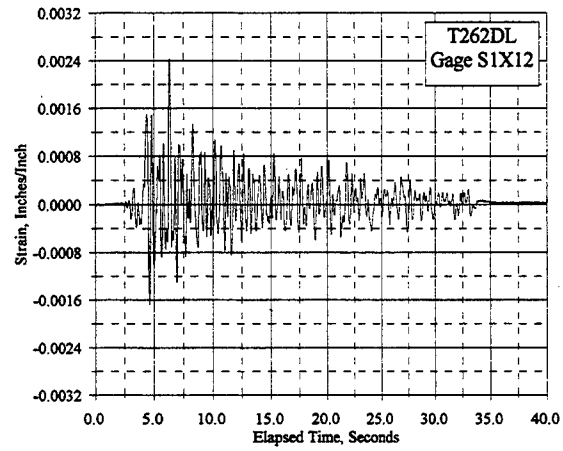
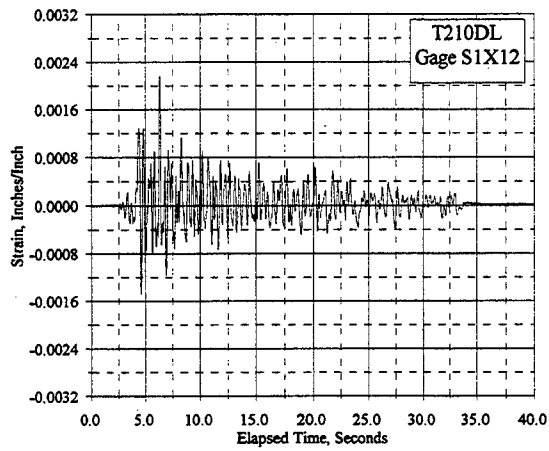
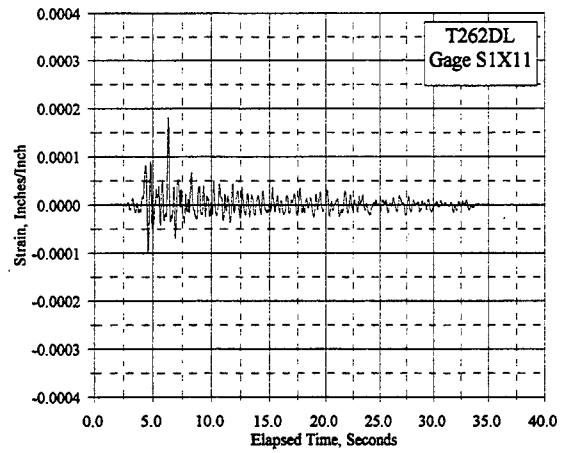
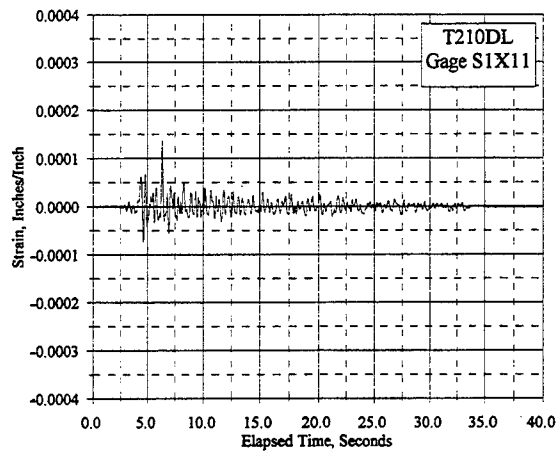


Figure C.22.7 Reinforcement Strain Vs. Elapsed Time, Gages S1X11, S1X12, S1X13: T210DL, T262DL

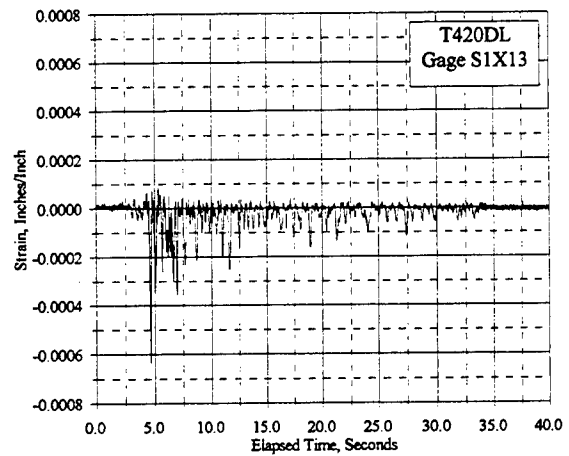
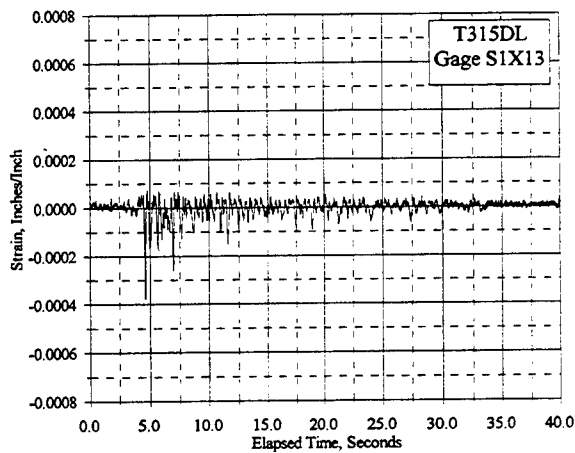
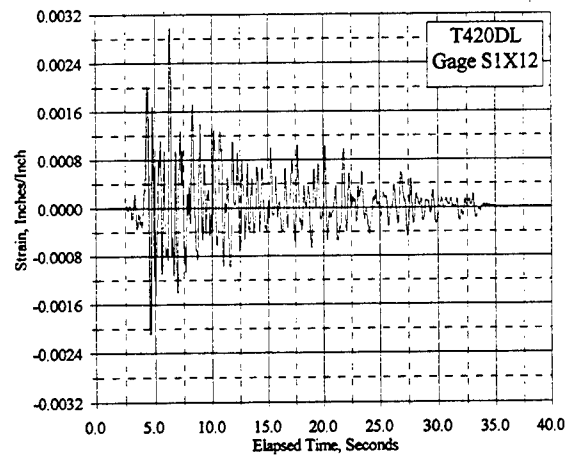
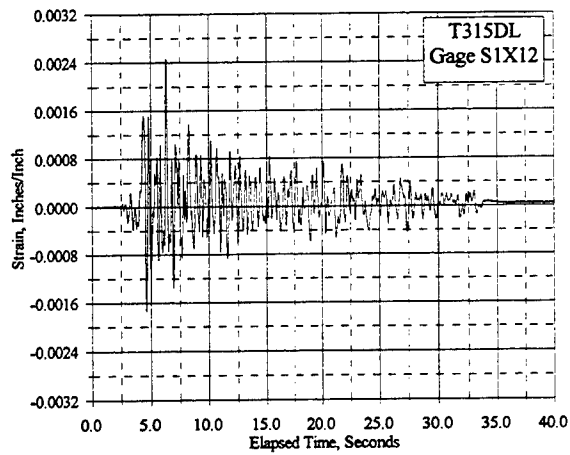
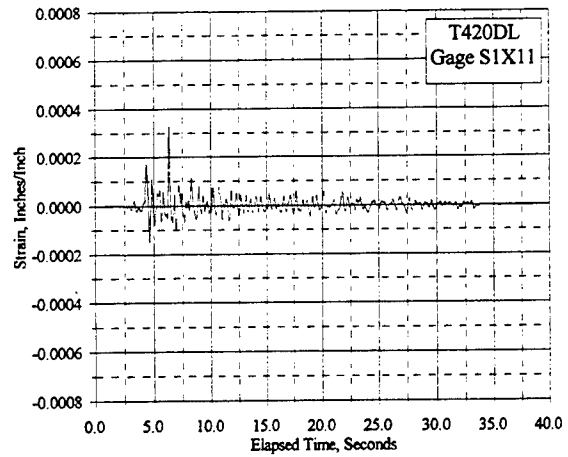
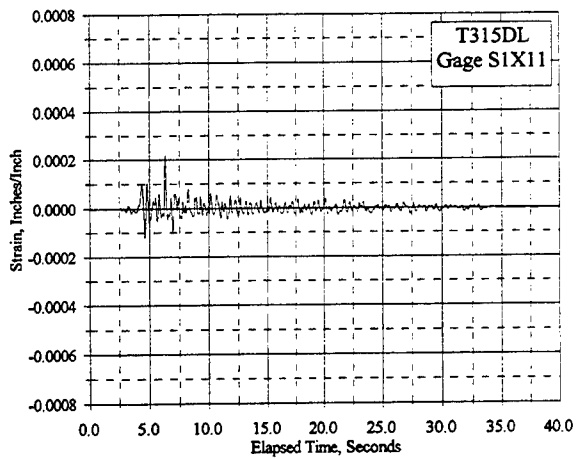


Figure C.22.8 Reinforcement Strain Vs. Elapsed Time, Gages S1X11, S1X12, S1X13: T315DL, T420DL

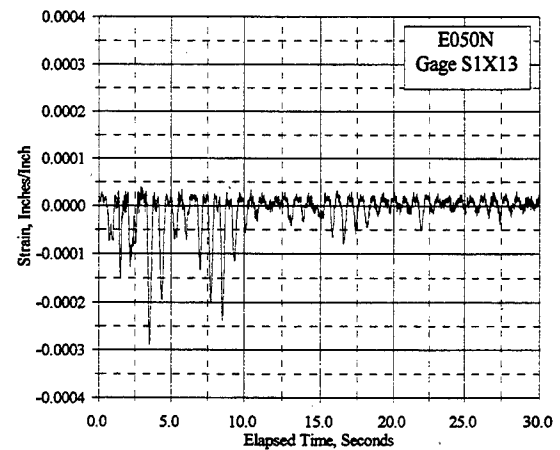
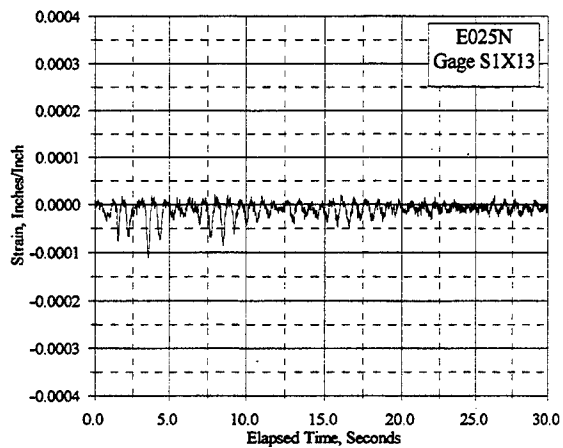
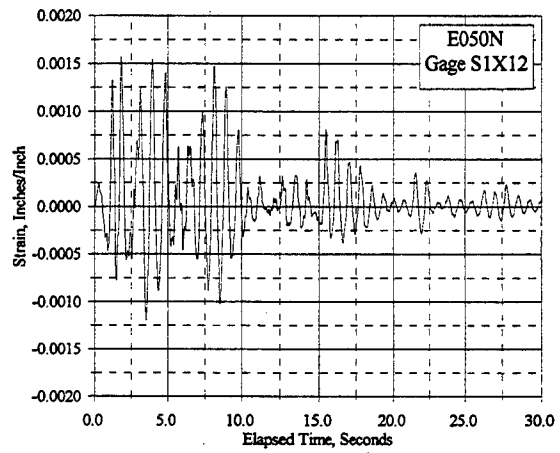
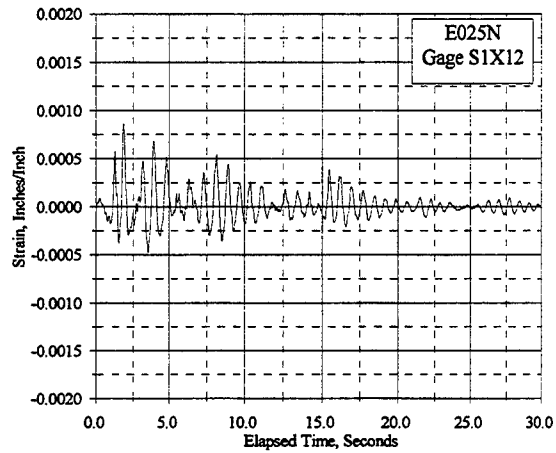
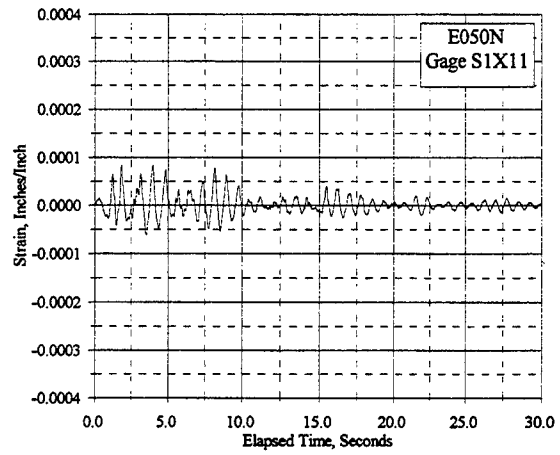
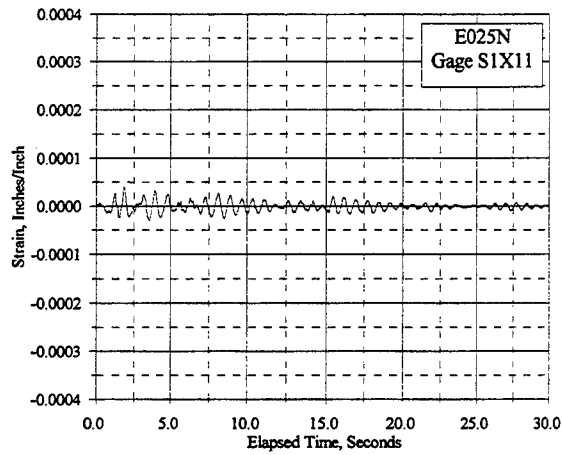


Figure C.22.9 Reinforcement Strain Vs. Elapsed Time, Gages S1X11, S1X12, S1X13: E025N, E050N

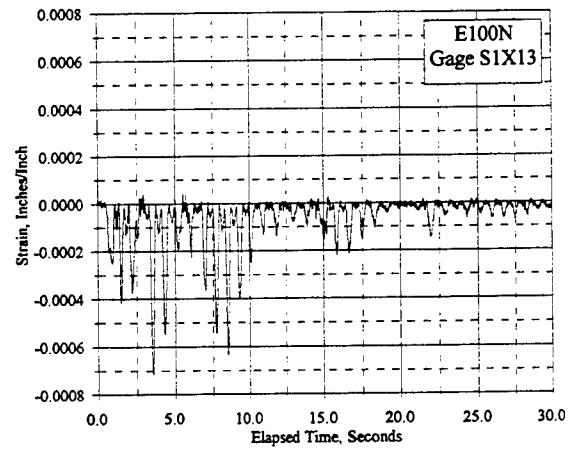
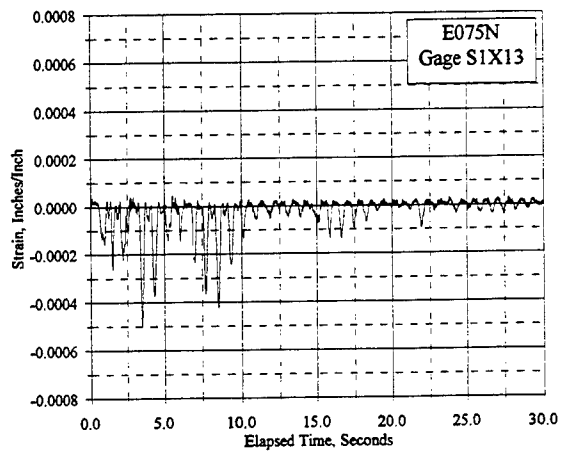
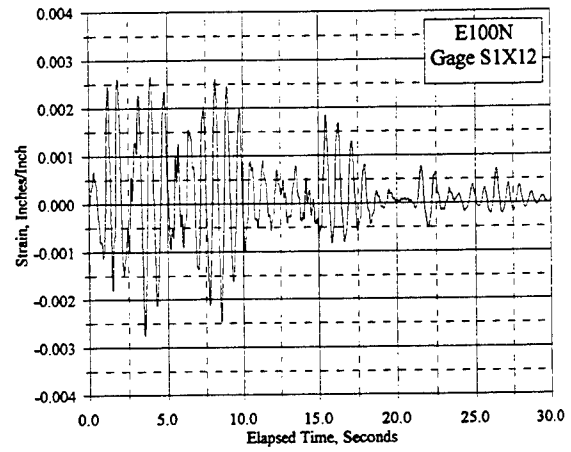
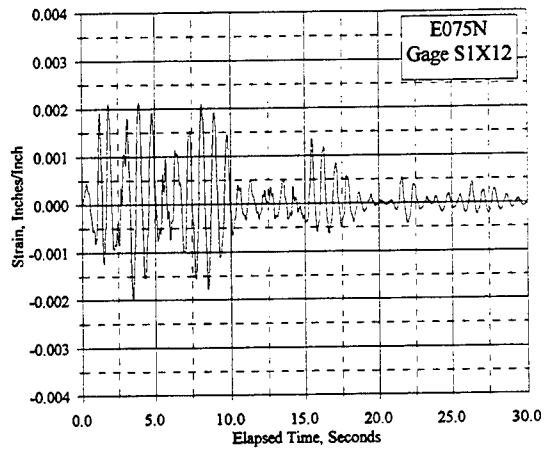
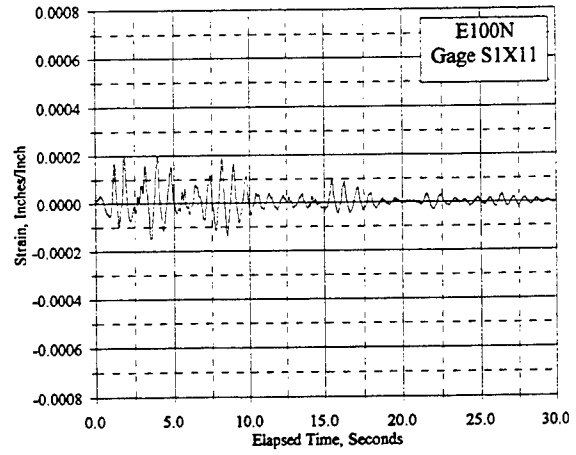
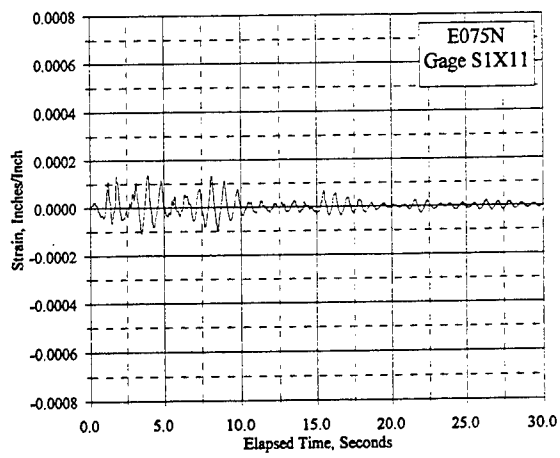


Figure C.22.10 Reinforcement Strain Vs. Elapsed Time, Gages S1X11, S1X12, S1X13: E075N, E100N

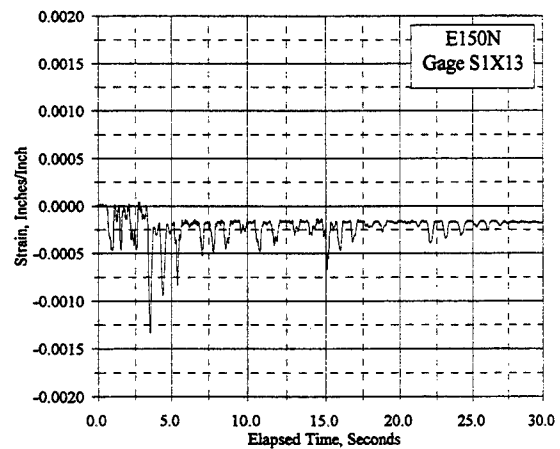
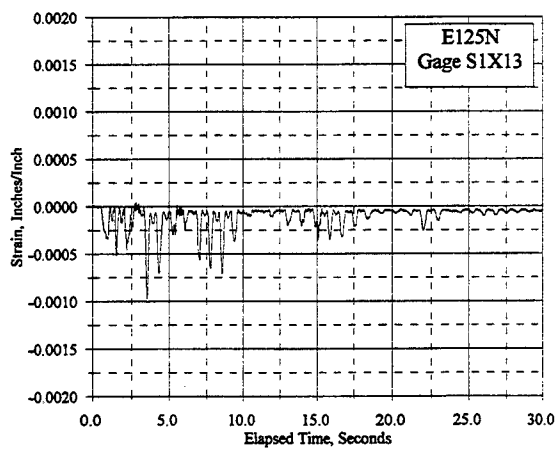
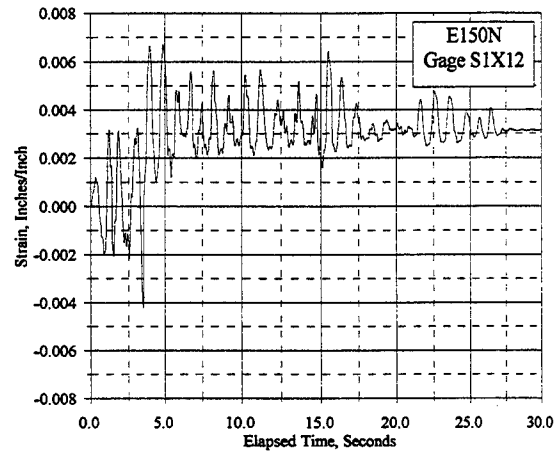
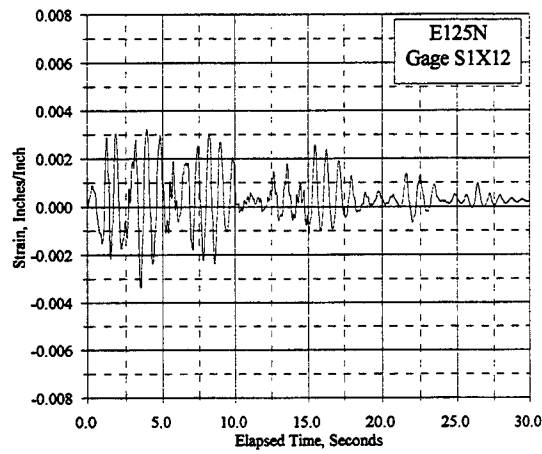
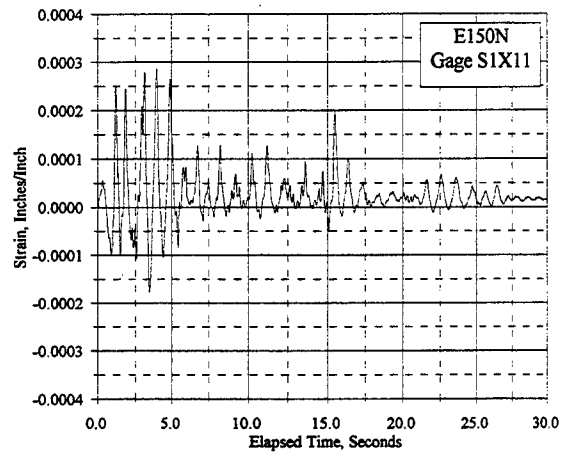
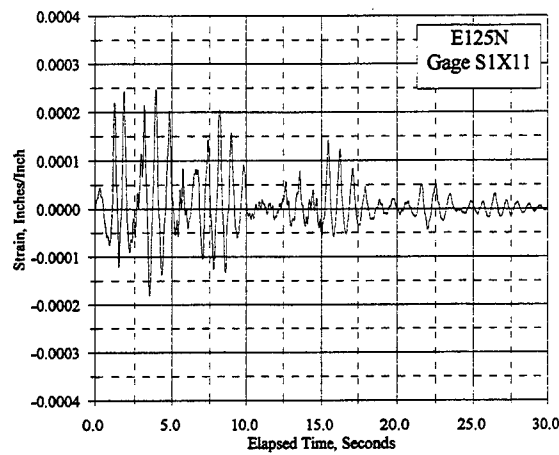


Figure C.22.11 Reinforcement Strain Vs. Elapsed Time, Gages S1X11, S1X12, S1X13: E125N, E150N

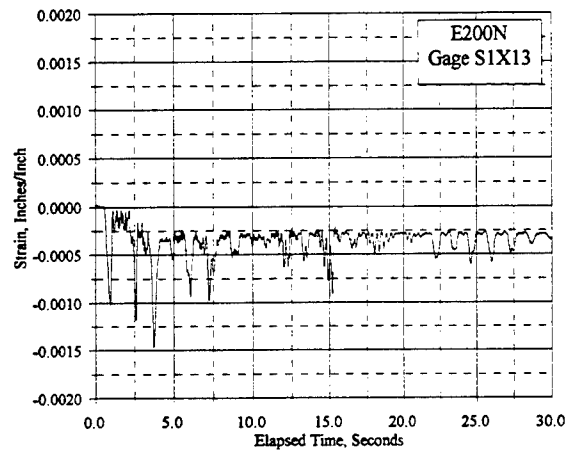
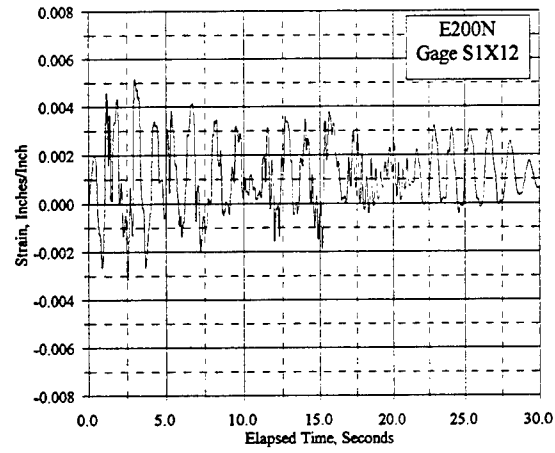
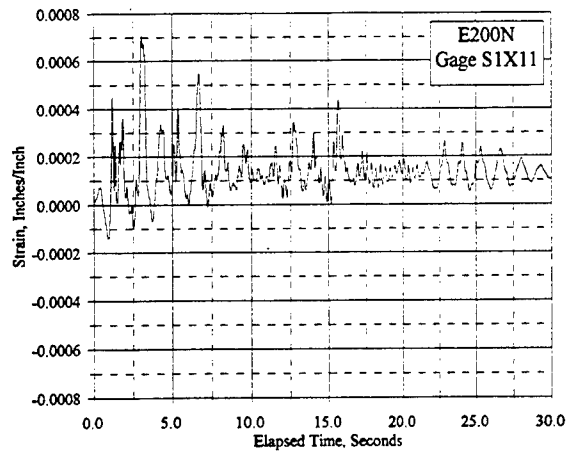


Figure C.22.12 Reinforcement Strain Vs. Elapsed Time, Gages S1X11, S1X12, S1X13: E200N

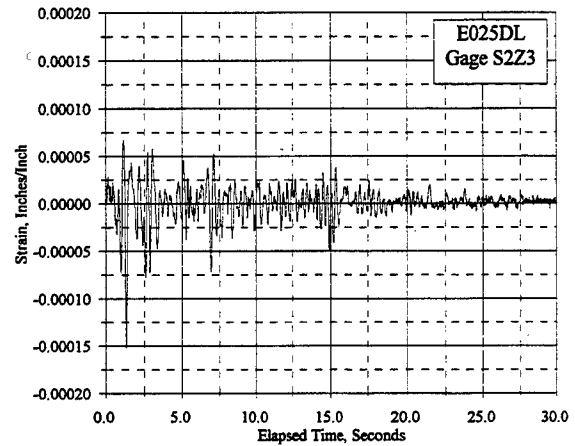
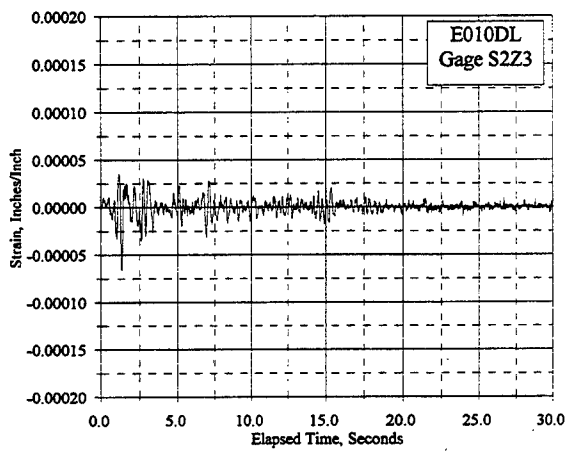
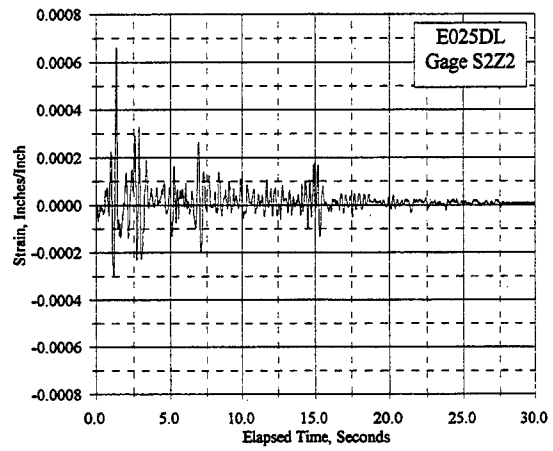
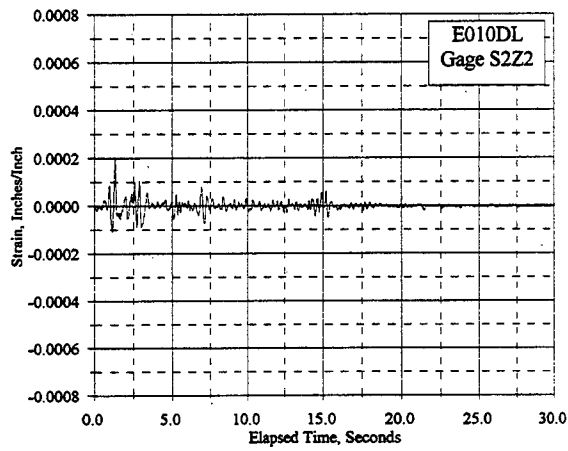
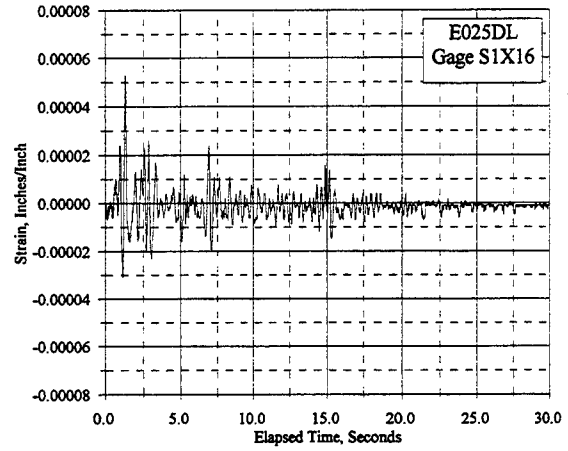
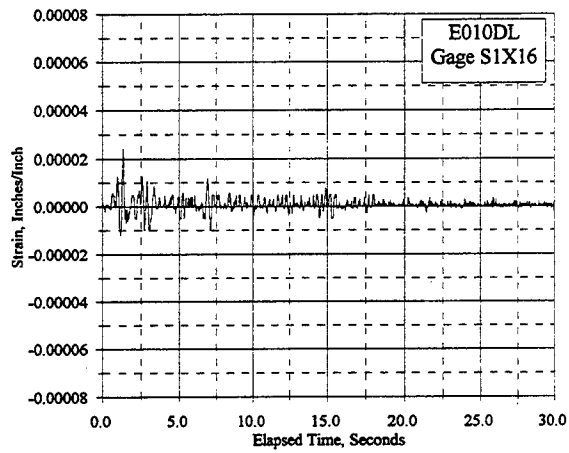


Figure C.23.1 Reinforcement Strain Vs. Elapsed Time, Gages S1X16, S2Z2, S2Z3: E010DL, E025DL

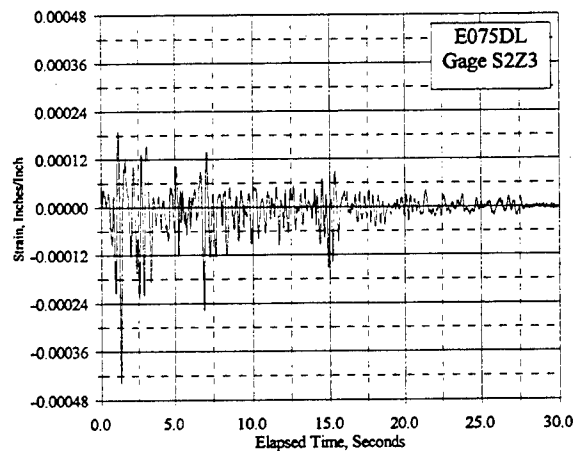
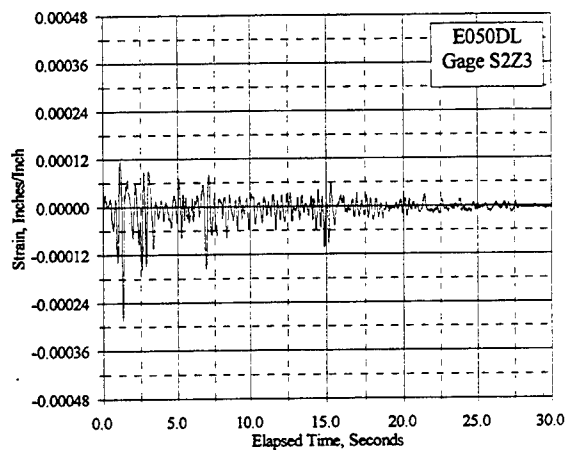
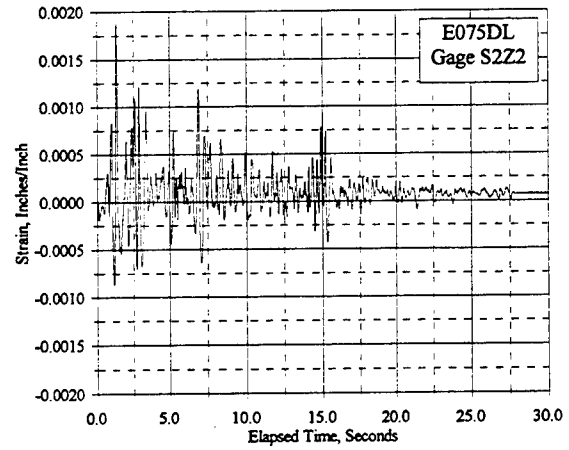
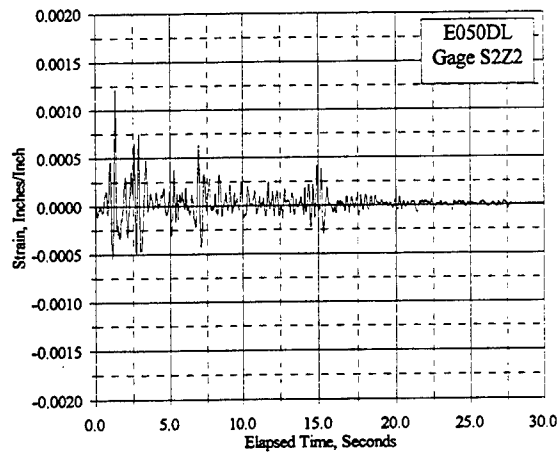
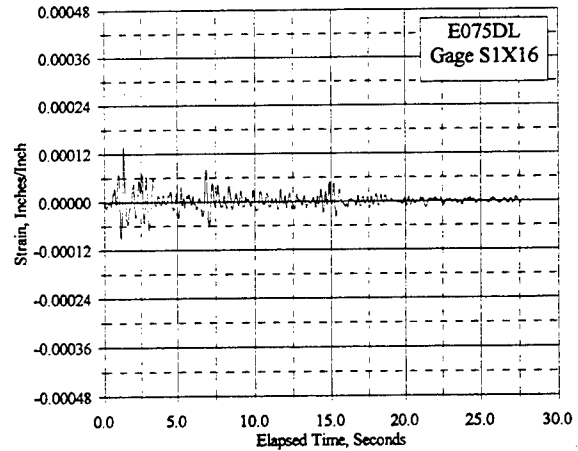
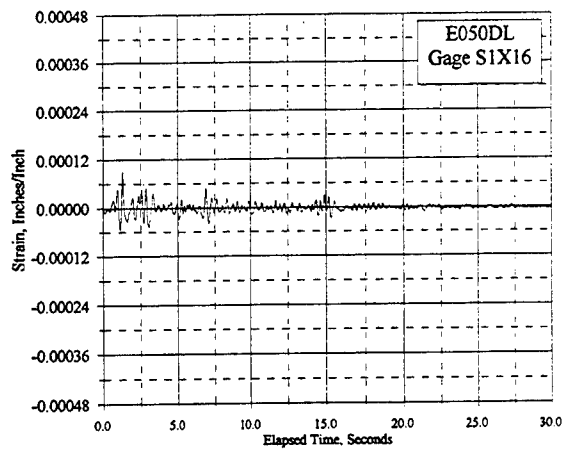


Figure C.23.2 Reinforcement Strain Vs. Elapsed Time, Gages S1X16, S2Z2, S2Z3: E050DL, E075DL

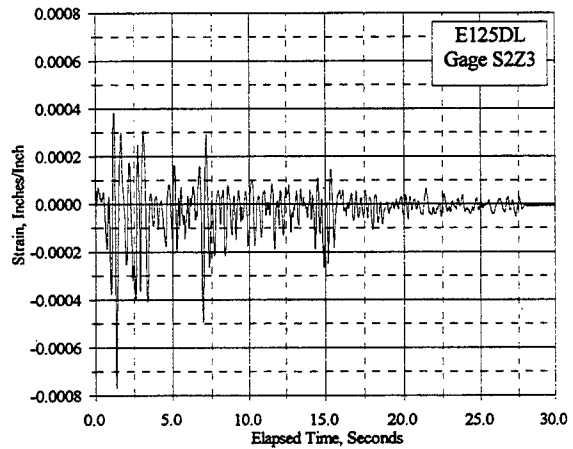
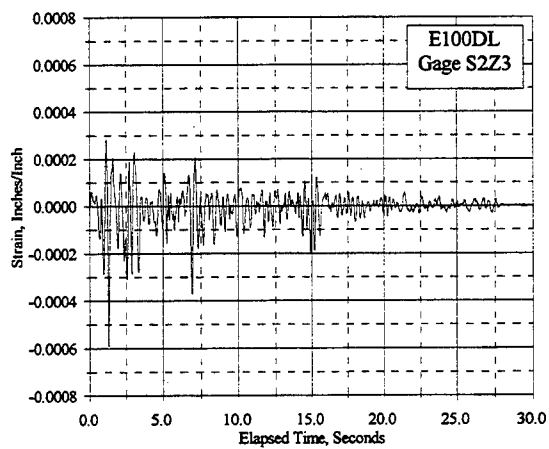
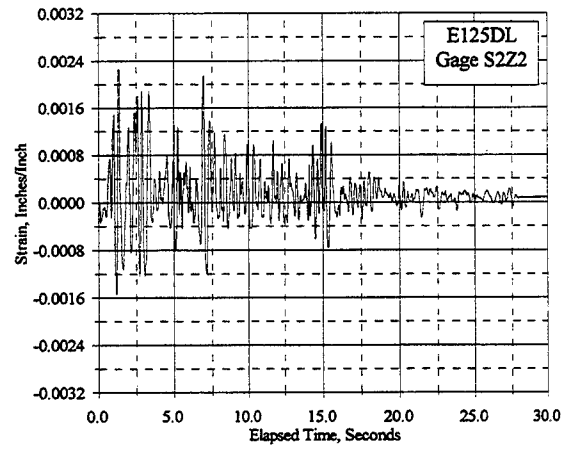
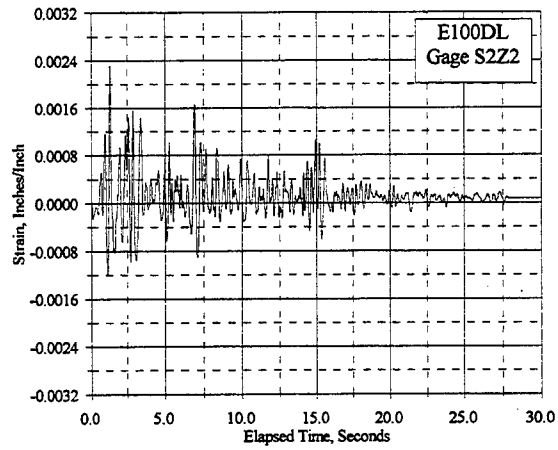
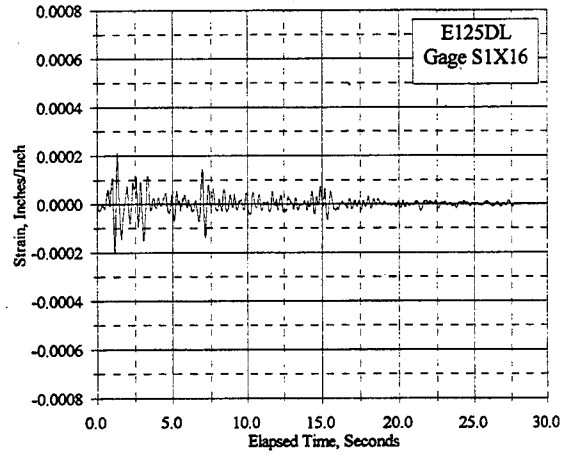
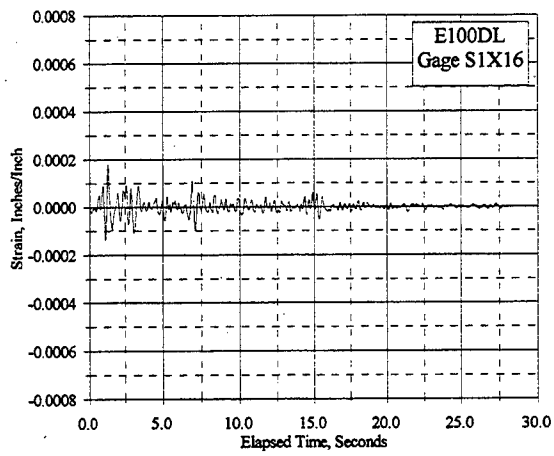


Figure C.23.3 Reinforcement Strain Vs. Elapsed Time, Gages S1X16, S2Z2, S2Z3: E100DL, E125DL

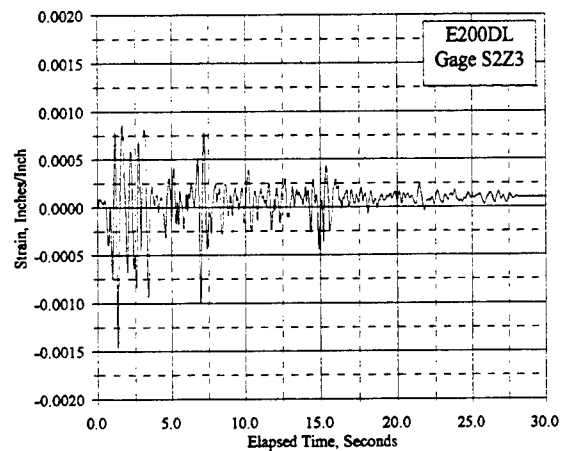
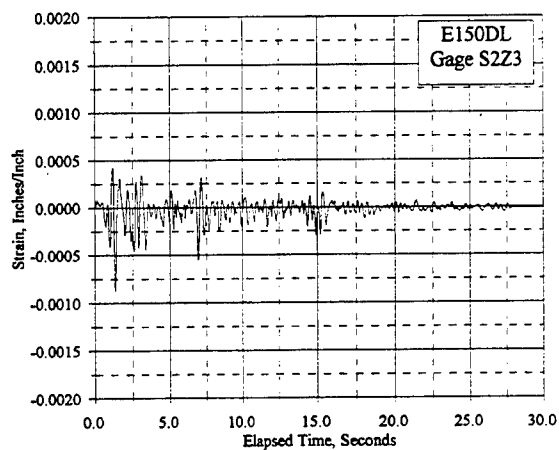
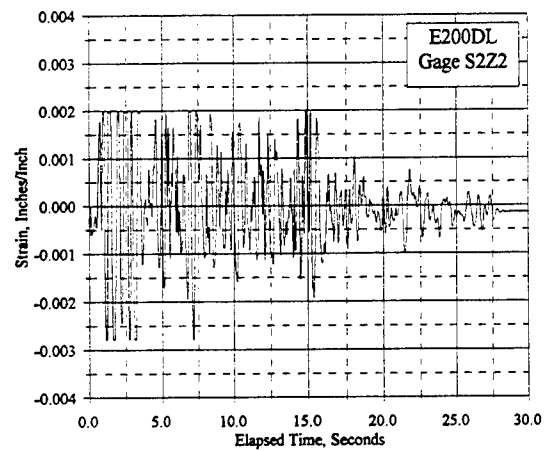
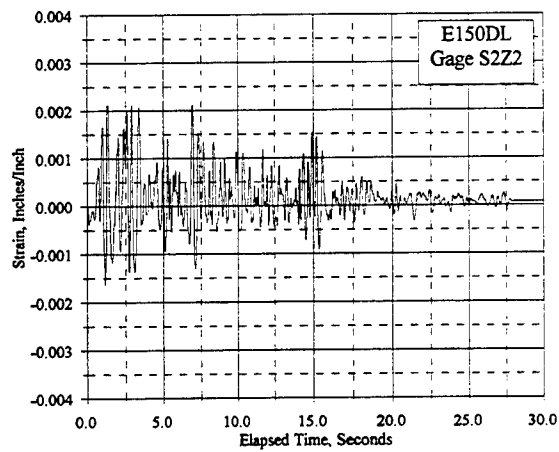
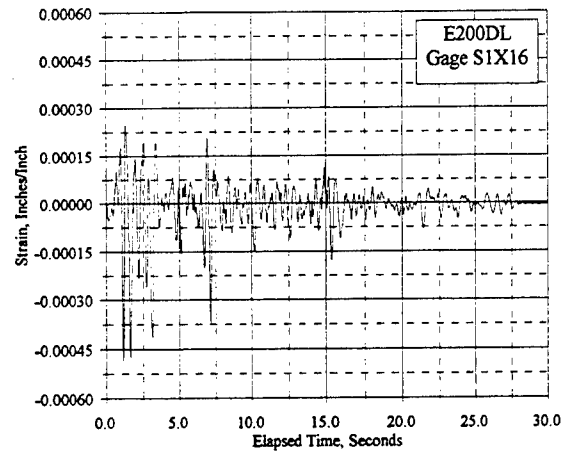
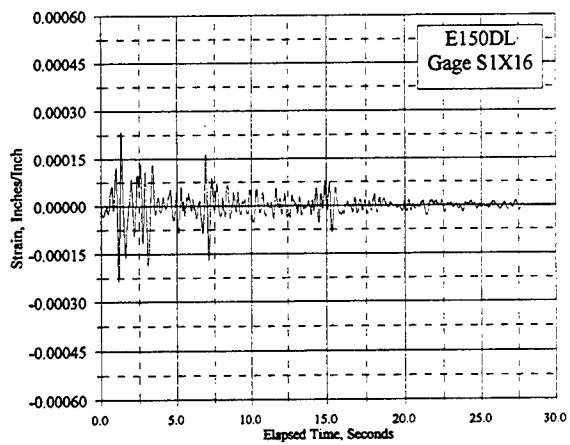


Figure C.23.4 Reinforcement Strain Vs. Elapsed Time, Gages S1X16, S2Z2, S2Z3: E150DL, E200DL

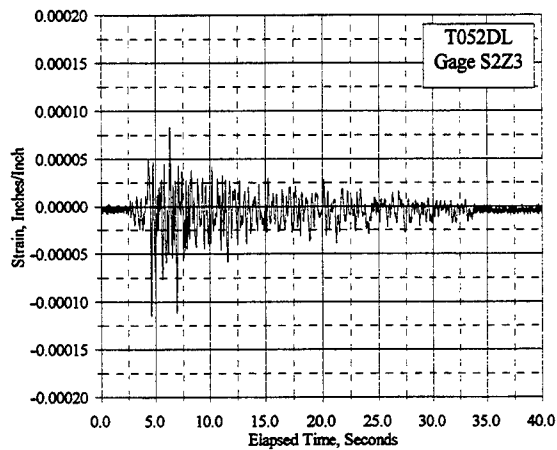
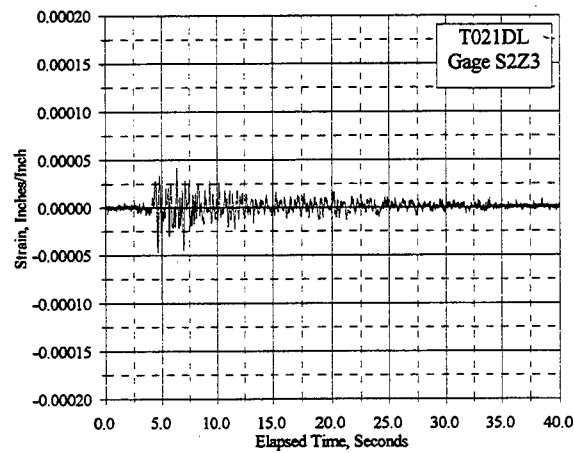
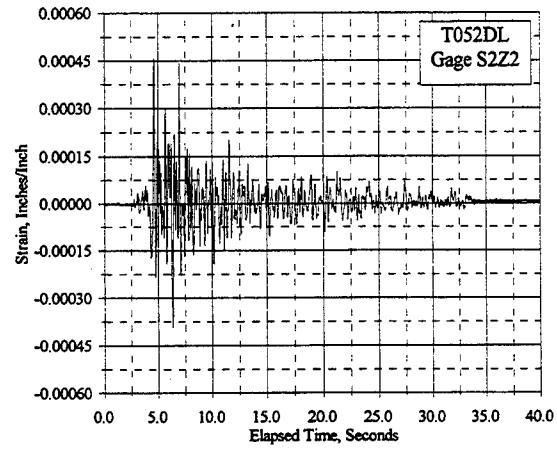
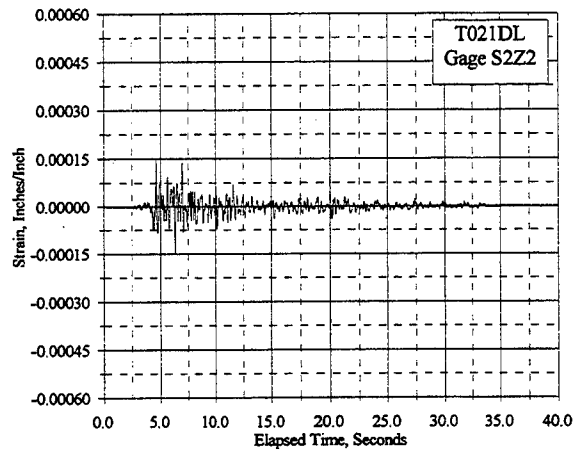
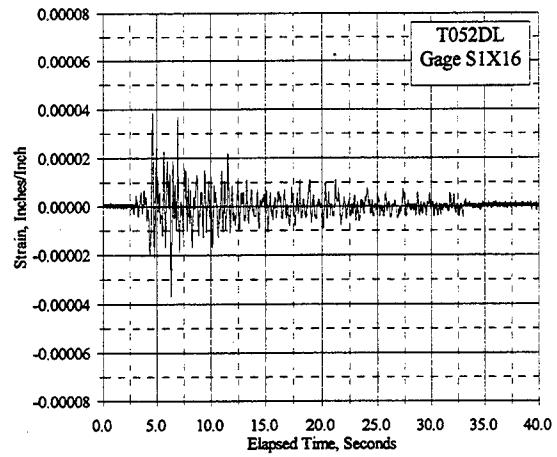
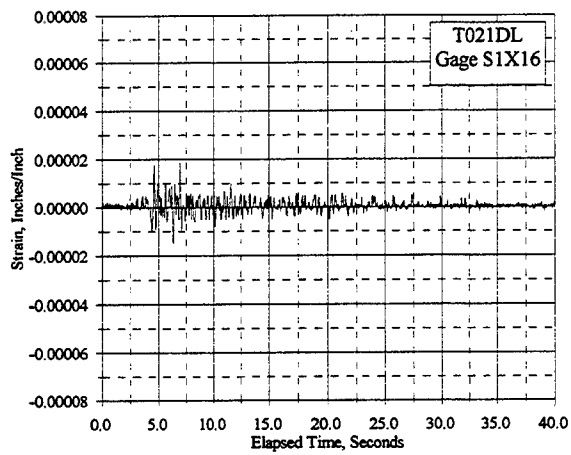


Figure C.23.5 Reinforcement Strain Vs. Elapsed Time, Gages S1X16, S2Z2, S2Z3: T021DL, T052DL

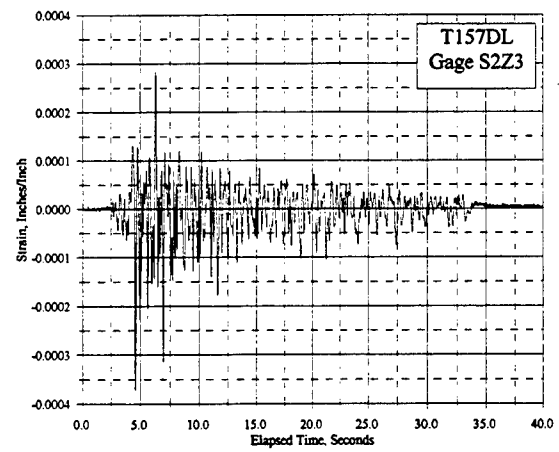
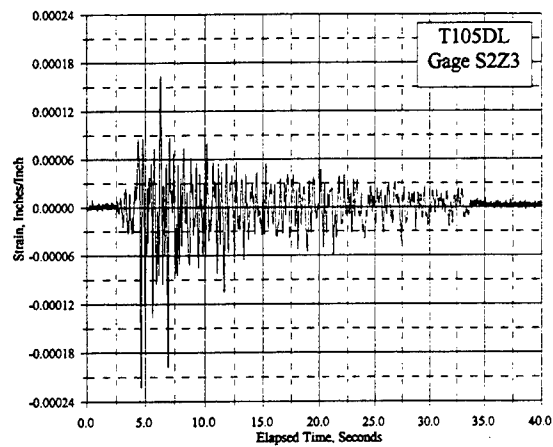
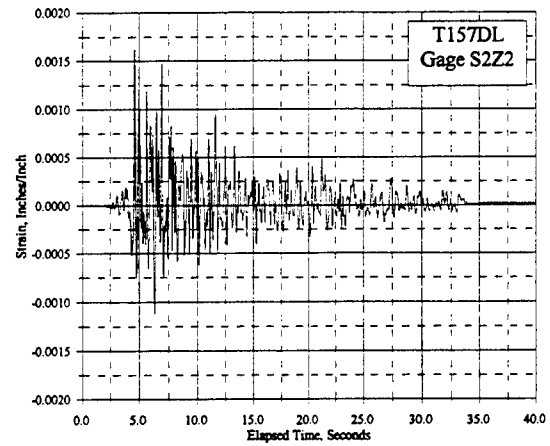
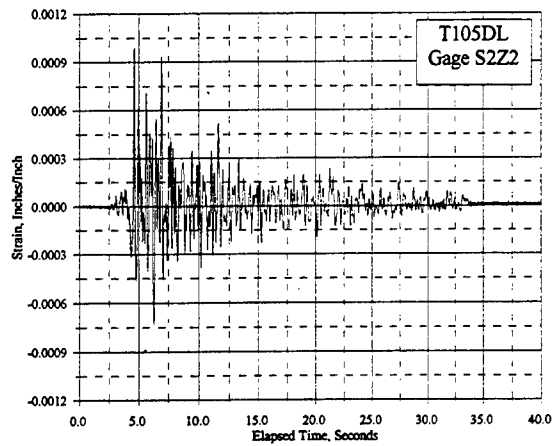
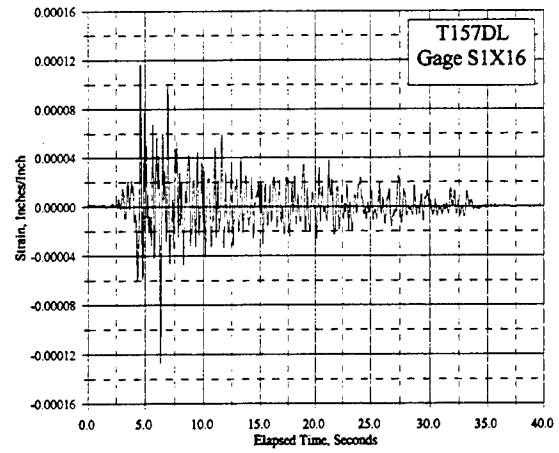
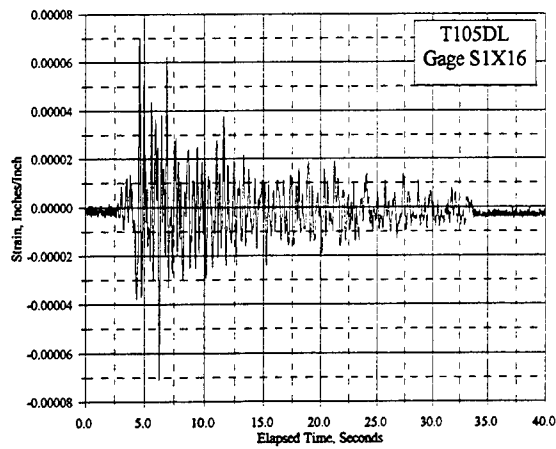


Figure C.23.6 Reinforcement Strain Vs. Elapsed Time, Gages S1X16, S2Z2, S2Z3: T105DL, T157DL

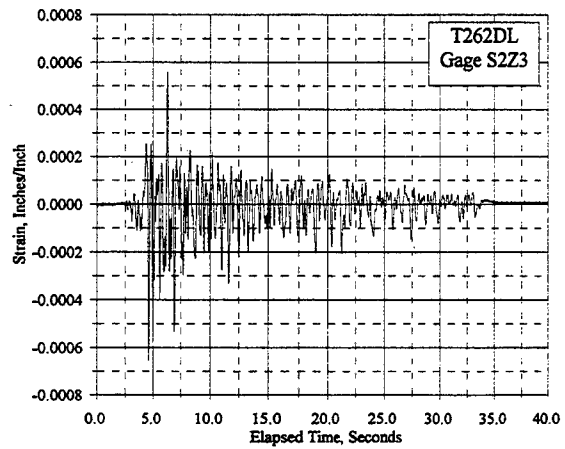
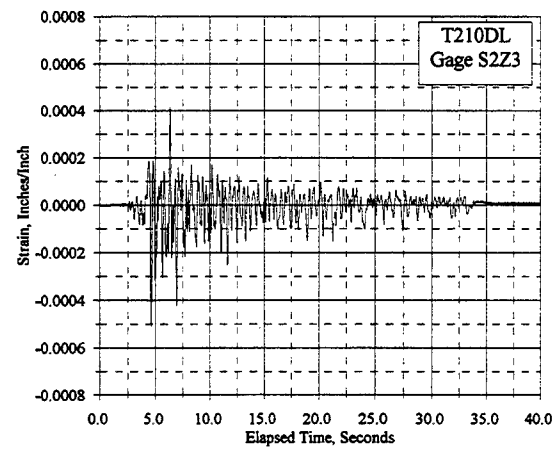
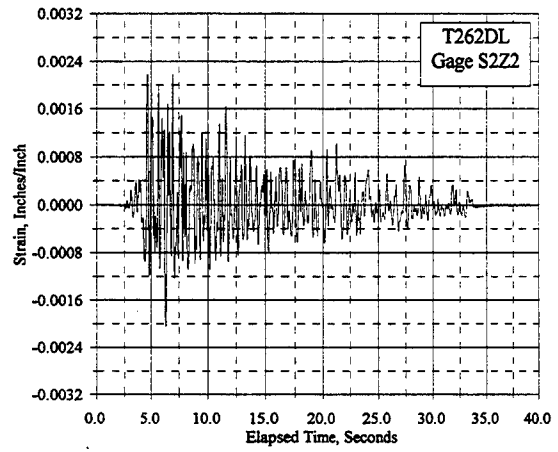
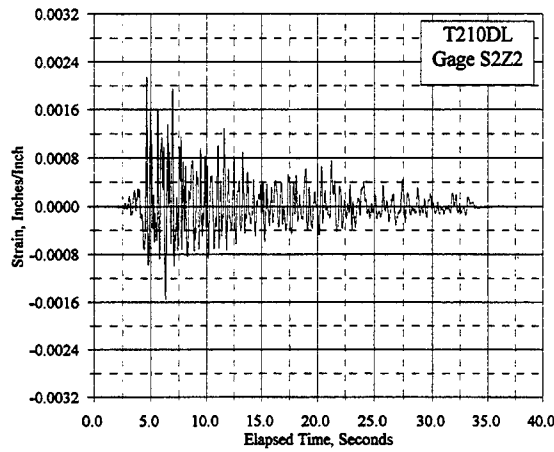
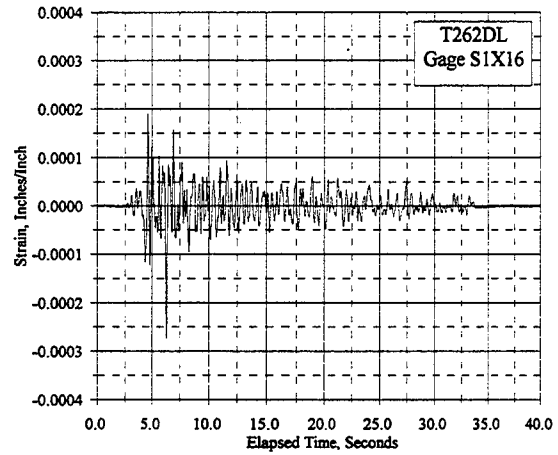
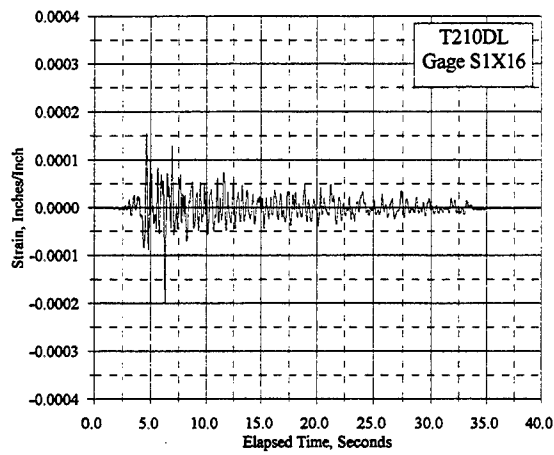


Figure C.23.7 Reinforcement Strain Vs. Elapsed Time, Gages S1X16, S2Z2, S2Z3: T210DL, T262DL

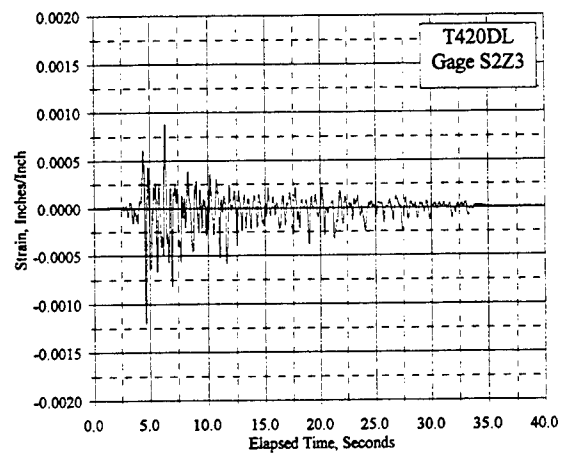
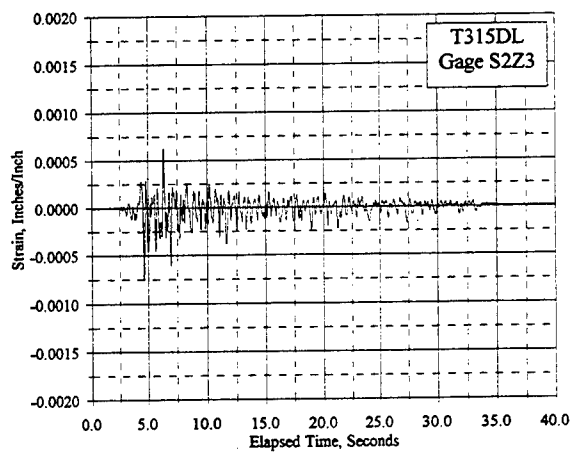
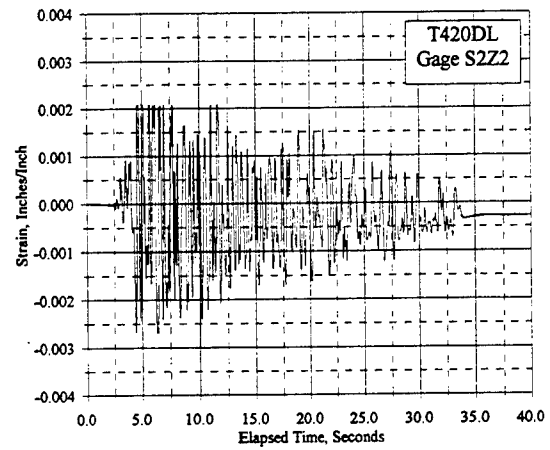
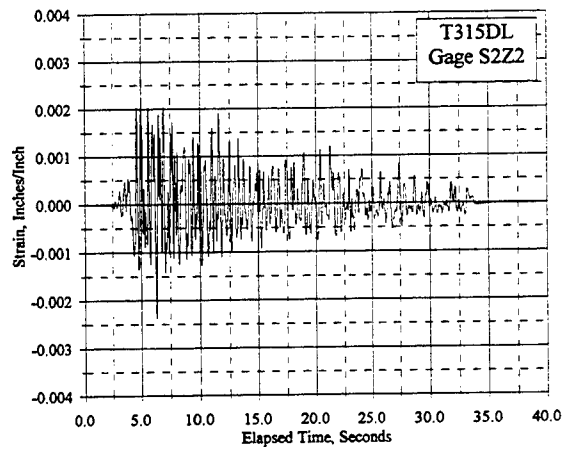
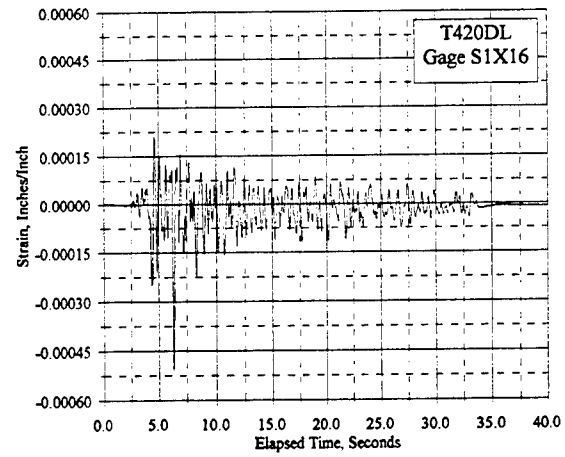
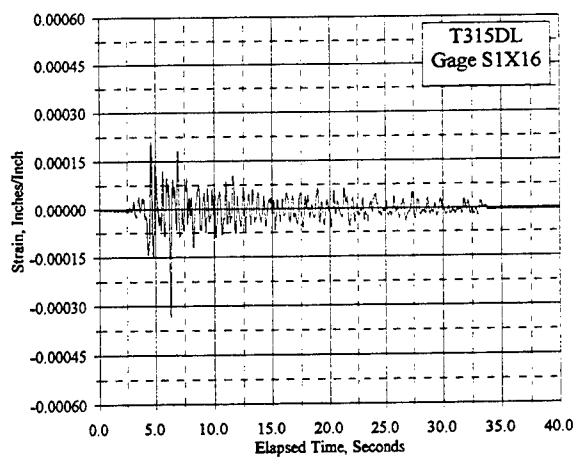


Figure C.23.8 Reinforcement Strain Vs. Elapsed Time, Gages S1X16, S2Z2, S2Z3: T315DL, T420DL

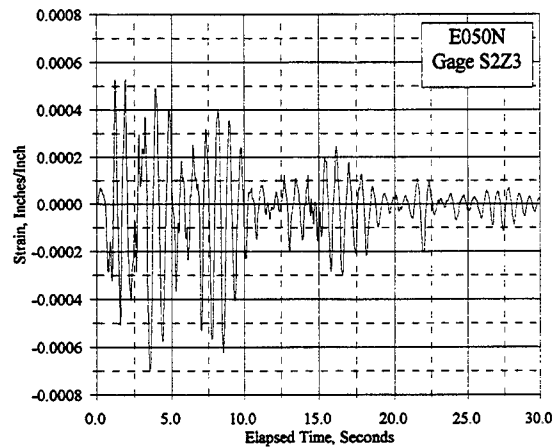
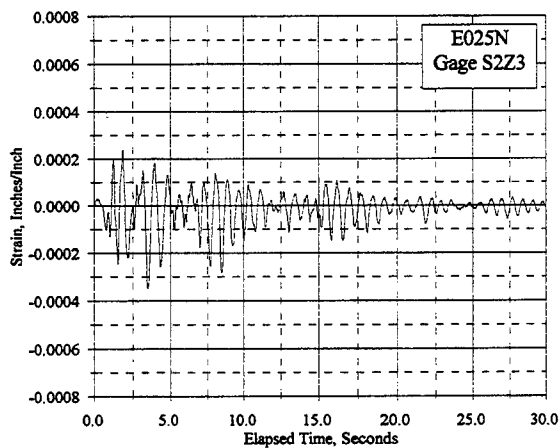
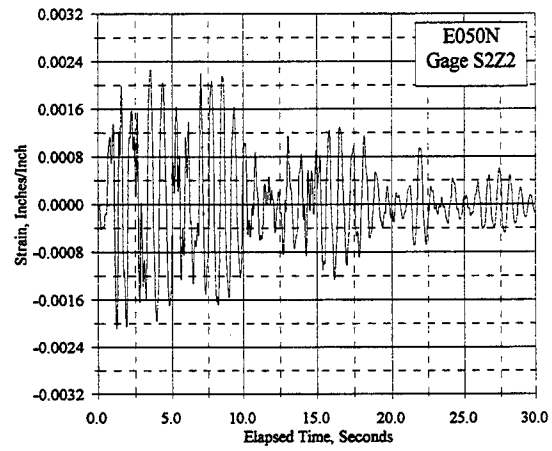
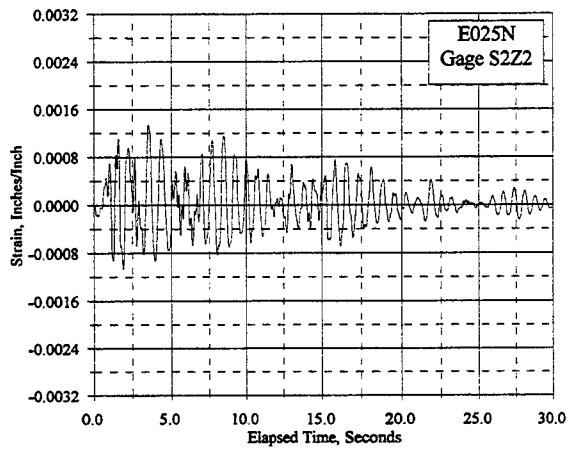
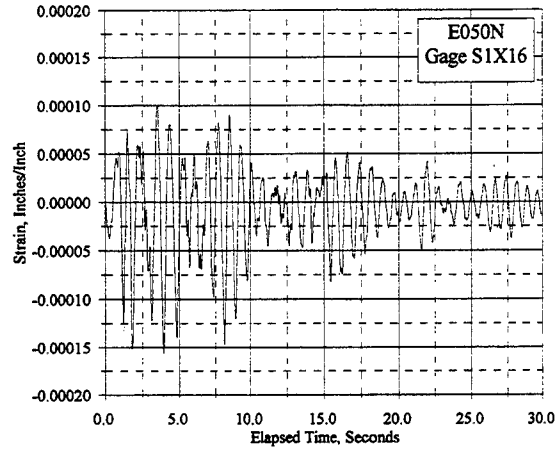
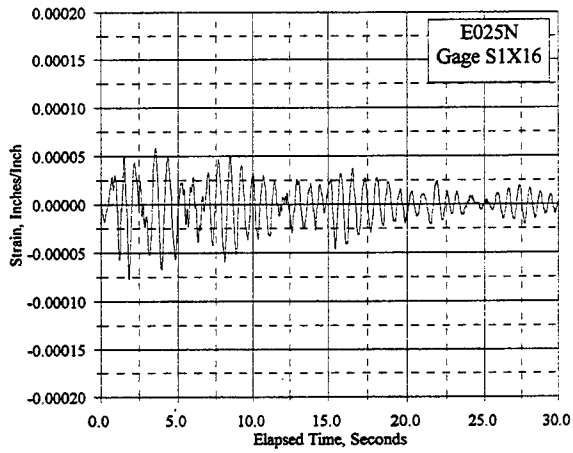


Figure C.23.9 Reinforcement Strain Vs. Elapsed Time, Gages S1X16, S2Z2, S2Z3: E025N, E050N

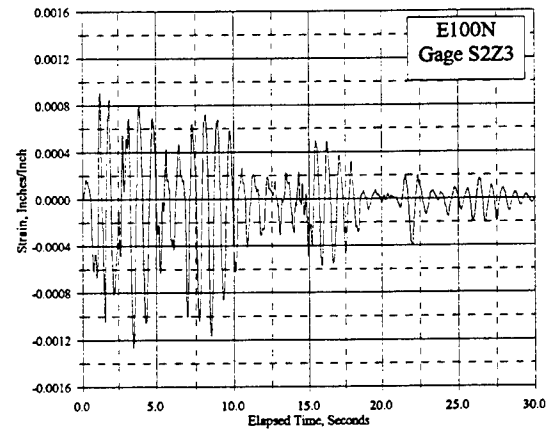
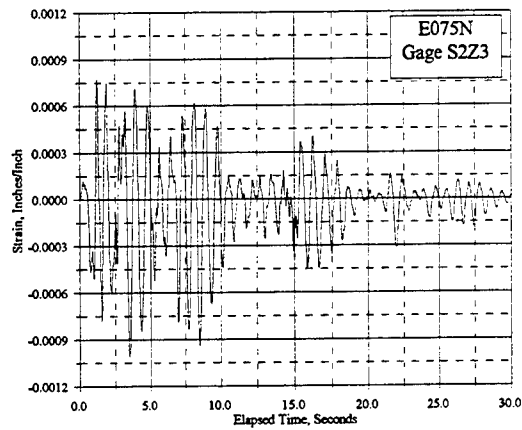
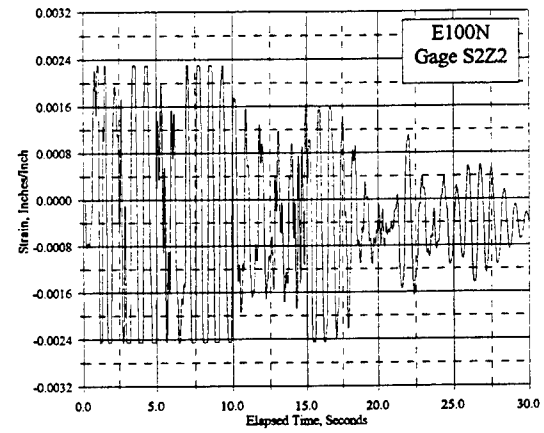
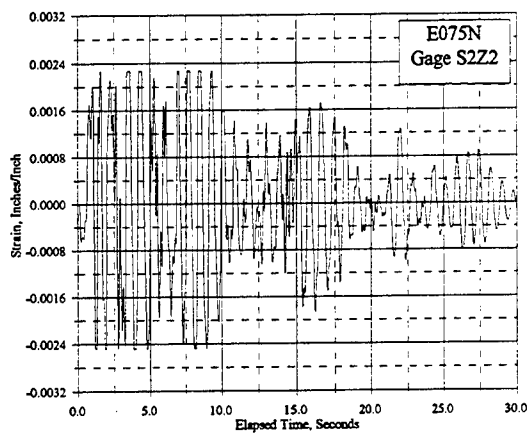
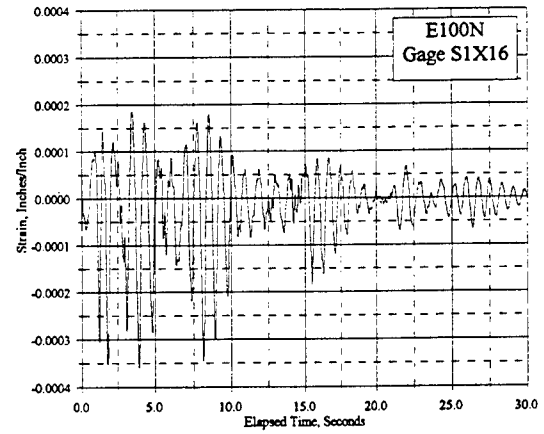
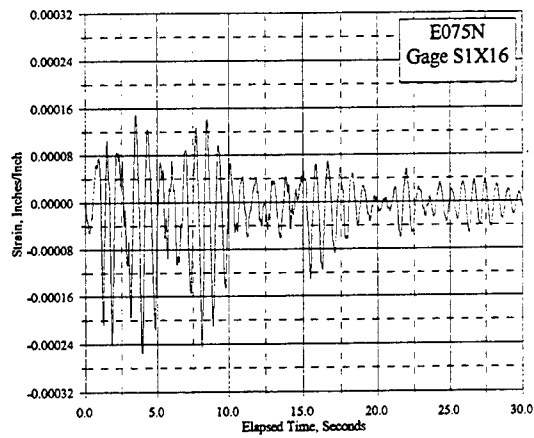


Figure C.23.10 Reinforcement Strain Vs. Elapsed Time, Gages S1X16, S2Z2, S2Z3: E075N, E100N

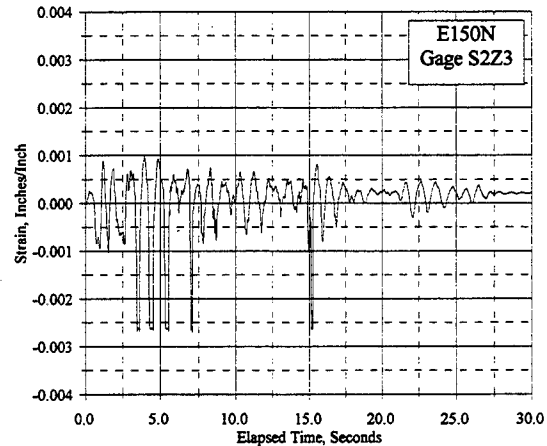
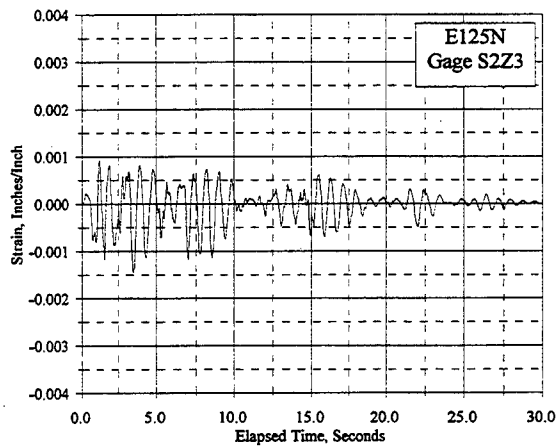
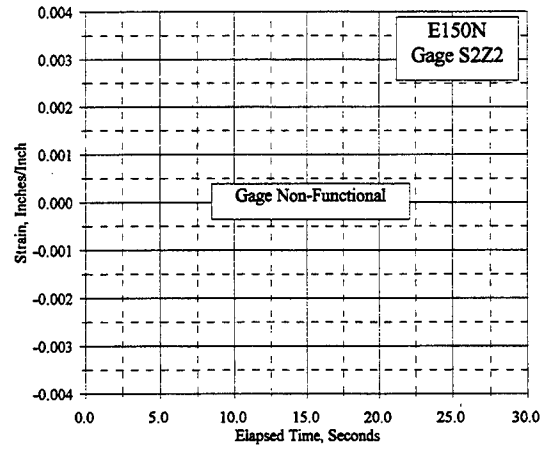
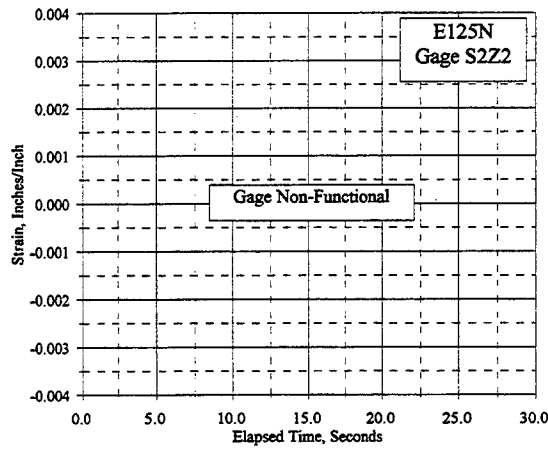
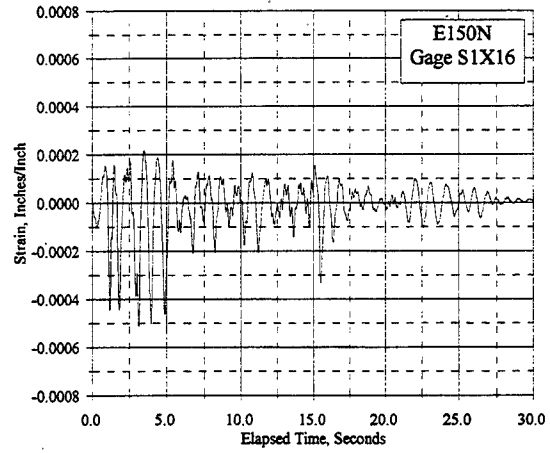
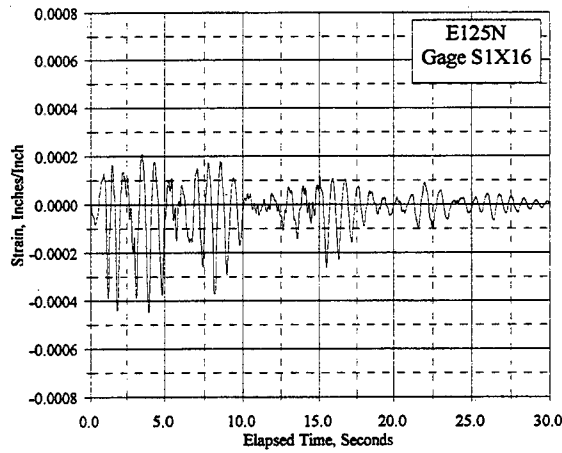


Figure C.23.11 Reinforcement Strain Vs. Elapsed Time, Gages S1X16, S2Z2, S2Z3: E125N, E150N

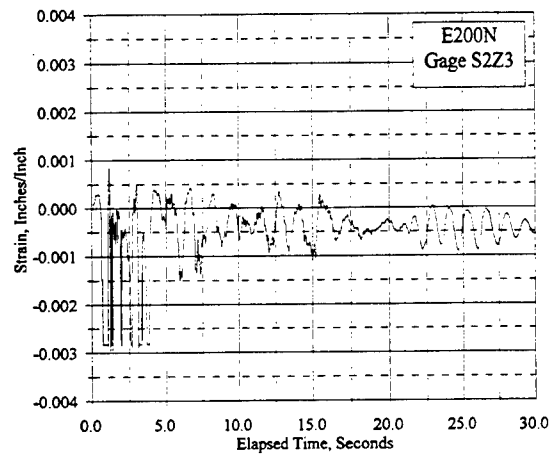
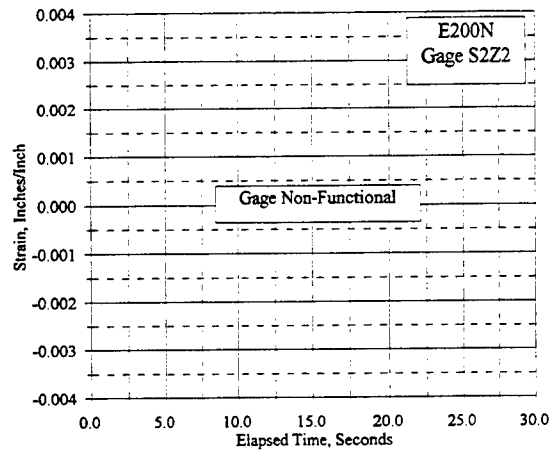
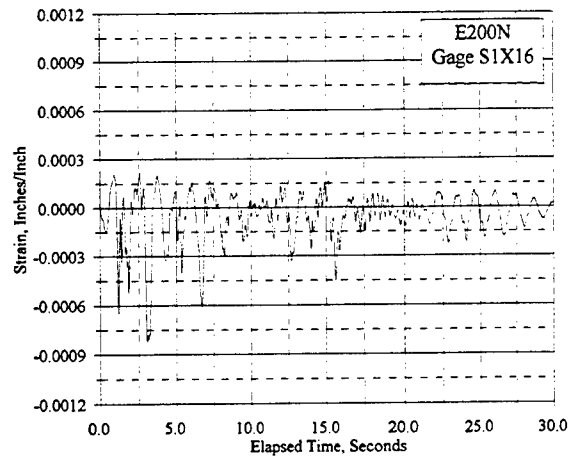


Figure C.23.12 Reinforcement Strain Vs. Elapsed Time, Gages S1X16, S2Z2, S2Z3: E200N

APPENDIX D

VISCOELASTIC DAMPER CHARACTERIZATION

This appendix summarizes viscoelastic material and damper properties, presents data that were recorded in damper characterization tests, and introduces a technique that may be used to model a viscoelastic damper (VED). Section D.1 provides a summary of the stress-strain characteristics of viscoelastic materials in general and the force-deformation characteristics of the VED's studied herein. This summary is a compilation of highlights of discussions by other authors, with common notation used, that serves as background for modeling structural behavior when VED's are used. Section D.2 describes sinusoidal testing of the VED's used in this study and presents the load-deformation properties that were determined from the test results. Finally, Section D.3 briefly describes a simplified procedure that may be used to model VED characteristics in structural models. More complete discussions of this procedure are provided in the main body of the report.

D.1 Viscoelastic Material Properties

Numerous references [E.G., 1, 4, 9, 10, 22, 23] present detailed viscoelastic material property descriptions. Those properties that directly relate to viscoelastic damper (VED) characterization and design are presented here. This overview adopts the nomenclature used in Reference 1.

"Viscoelastic" properties are exhibited by many polymeric materials. The term "viscoelastic" arises from the materials' exhibiting properties of both *viscous* liquids and *elastic* solids when they are deformed [1] in shear. A viscoelastic material that is placed in a sinusoidal shear loading exhibits hysteretic behavior like that shown in Figure D.1. The steady state response of the material can be described using a linear viscoelastic law [1] with the following relationships:

$$\begin{aligned}\gamma(t) &= \gamma_o \sin(\omega t) \\ \tau(t) &= \tau_o \sin(\omega t + \delta)\end{aligned}\tag{D.1}$$

In these equations, $\gamma(t)$ and $\tau(t)$ are the time-varying magnitudes of shear strain and shear stress, respectively, while γ_o and τ_o are the maximum shear strain and maximum shear stress, respectively. The symbol ω represents the circular frequency of the loading, and “ t ” represents elapsed time. The symbol δ represents the phase angle between stress and strain that is a characteristic of viscoelastic behavior; in these materials, stress precedes strain. The linear viscoelastic law further states that constant stress applied to a viscoelastic material results in a strain that increases with time, and that a constant strain applied to a viscoelastic material results in a stress that decreases with time. Figure D.16 illustrates this property. In a quasi-static load test on a VED, run under displacement control, the load required to sustain a constant strain decreased over time.

The relationship between shear stress and shear strain is characterized as [9]:

$$\begin{aligned}\tau(t) &= G^* \gamma_o \sin(\omega t + \delta) \\ \tau(t) &= \gamma_o [G' \sin(\omega t) + G'' \cos(\omega t)]\end{aligned}\tag{D.3}$$

In these relationships, G^* is known as the “complex shear modulus;” G' is known as the “shear storage modulus;” and G'' is known as the “shear loss modulus.” These moduli are defined as follows [1]:

$$G' = \left(\frac{\tau_o}{\gamma_o} \right) \cos \delta \tag{D.4}$$

$$G'' = \left(\frac{\tau_o}{\gamma_o} \right) \sin \delta \tag{D.5}$$

$$G^* = \sqrt{(G')^2 + (G'')^2} = \frac{\tau_o}{\gamma_o} \tag{D.6}$$

One additional relationship is defined by the “loss factor,” or η :

$$\eta = \frac{G''}{G'} = \tan \delta \tag{D.7}$$

References 4 and 22 describe these moduli: The shear storage modulus (G') is in phase with the strain and represents the stiffness capacity (or recoverable energy) of the material. Higher values of G' indicate

higher stiffness properties for the material. The shear loss modulus (G'') leads the strain and represents the "damping" capacity (or dissipated energy) of the material. Higher values of G'' indicate higher energy dissipation, or damping, capacities for the material. The complex modulus, G^* , arises from a restatement of the material properties using complex variables, in which G^* can be expressed in terms of a real constant, G' , and an imaginary constant, iG'' . The loss factor (η) characterizes the relative damping capacity of the material. A small loss factor indicates that the hysteresis loops that describe the material behavior will be small, with corresponding low damping characteristics; a large loss factor indicates that the hysteresis loops that describe the material behavior will be large, with corresponding high damping characteristics.

These properties depend significantly on temperature, excitation frequency, and peak shear strain. At low temperatures or high frequencies, the storage modulus is large compared to the loss modulus; the material behaves stiffly and with less energy dissipation. At high temperatures or low frequencies, both the storage and loss moduli are small, yielding both low stiffness and low energy dissipation. At intermediate temperatures and frequencies, the loss modulus, and loss factor are relatively larger, with corresponding higher energy dissipation capacity. The energy dissipation mechanism results in heating the material, which lowers both the storage and loss moduli, so that its efficiency lowers with continuing loading. Stiffness properties are reported [E.G., 1] to decrease with increasing peak shear strain. Reference 1 indicates that the storage modulus drops sharply in the range of 0 - 50% peak shear strain but remains relatively unchanged in the range of 50 - 200% peak shear strain.

Several researchers have developed data bases of viscoelastic material properties and performed regression analyses using temperature, excitation frequency, and peak shear strain as independent variables, and G' and G'' as dependent variables [1, 9]. In general, these studies show that G' and G'' are approximately proportional to the square root of the frequency and approximately inversely proportional to the fifth root of the maximum shear strain. The moduli are related to the ambient temperature as approximate functions of $e^{(73/T)}$, where T is the ambient temperature ($^{\circ}\text{C}$).

The direct relationship between shear stress and shear strain may be rewritten in a form that clearly delineates the linear and viscous components of the material behavior [1]:

$$\tau(t) = G' \gamma(t) \pm G'' \sqrt{(\gamma_0)^2 - [\gamma(t)]^2} \quad (\text{D.8})$$

The first term in Equation D.8 represents the linear, or elastic, component of the behavior, while the second

term represents the elliptical, or energy dissipation, component of the behavior.

It is also possible to define the equivalent viscous damping ratio (ξ_d) for the material in terms of the storage and loss moduli [1]:

$$\xi_d = \frac{E_d}{4\pi E_s} = \frac{\pi G''(\gamma_o)^2}{4\pi(0.5G'(\gamma_o)^2)} = \frac{G''}{2G'} = 0.5\eta \quad (\text{D.9})$$

In Equation D.9, E_d is the energy dissipated in one loading cycle, while E_s is the elastic strain energy stored in the structure at maximum deformation, for the same loading cycle.

With the provision that a VED consists of a layer of viscoelastic material placed in pure shear (see Figure 2.26), the above material relationships may be used to characterize a VED [1]:

$$k_d = \frac{G'A}{t} \quad (\text{D.10})$$

$$c_d = \frac{G''A}{\omega t} = \frac{\eta k_d}{\omega} = \frac{\eta k_d}{2\pi f} \quad (\text{D.11})$$

In these equations, k_d represents the damper stiffness and c_d represents the VED viscous damping coefficient. The thickness of the viscoelastic layer is “ t ,” while the area of the viscoelastic layer placed in shear is “ A .” Equations D.10 and D.11 repeat Equations 2.21 and 2.22 for the convenience of the reader.

With these material and VED properties, it is possible to develop a set of three equations that enable the shear and loss to moduli to be calculated from sinusoidal tests of VEDs [4]:

$$G^* = \left(\frac{\tau_o}{\gamma_o} \right) = \frac{\left(\frac{F_{\max}}{A} \right)}{\left(\frac{D_{\max}}{t} \right)} = \frac{F_{\max} t}{D_{\max} A} \quad (\text{D.12})$$

$$G'' = \frac{E_d}{\pi V(\gamma_o)^2} \quad (\text{D.13})$$

$$G' = \sqrt{(G^*)^2 - (G'')^2}$$

In Equation D.12, F_{\max} and D_{\max} refer to the maximum shear force and maximum shear displacement for the VED, respectively. The energy dissipated, E_d , is calculated as the area of the hysteresis loop (one

cycle). The term V represents the volume of viscoelastic material that is placed in shear. In computing V and A , one must be aware of the number of layers of material, and their thicknesses, that are subjected to the same shear strain. For example, the VED shown in Figure 2.26 has two layers of material in shear, each of which is 1" (2 x ½") thick.

D.2 Viscoelastic Damper Testing

Considerable testing of various viscoelastic materials has been conducted and reported [1, 4, 9, 10, 23]. The 3M *ISD 110* polymer used for the VED in this project has been tested extensively. For example, Table C.2 of reference 1 presents the results of testing this material at various ambient temperatures, peak shear strains, and excitation frequencies. 3M Corporation supplied additional unpublished data that were very similar, for use on the project.

Two VEDs of each size used in this project were tested in Newmark Civil Engineering Laboratory, to validate the applicability of the data base for this project. The testing consisted of deforming the VEDs sinusoidally at several different combinations of excitation frequency and peak displacement in a standard load frame (Figure D.2), with the load frame operated in the displacement control mode. 3M engineers recommended that each test consist of 4 - 5 full sinusoidal displacement cycles. The load frame extensometer and load cell were used for displacement and force measurements. The validation testing was conducted at approximately the same ambient temperature that was expected for the seismic simulations.

Excitation frequencies of 1, 2, and 3 Hz were used in the tests, to bracket the anticipated structural response frequencies that had been determined in pretest calculations. Peak displacements corresponding to 25%, 50%, and 62.5% shear strains were used in the tests. 3M engineers expressed a desire not to strain the dampers much beyond a peak shear strain of 50%, so the upper bound of 62.5% was chosen for the tests that were conducted, with the assumption that such strain would be an upper bound for the seismic simulations that were to follow. A waiting period of approximately 30 minutes followed each test, to permit the polymer to cool down before retesting.

In the test data reported here, VED with a "65" designation had 3" x 6" x ½" polymer pads, and VED with a "66" designation had 3" x 3" x ½" polymer pads. All tests were conducted at an ambient temperature of 73° F. Figures D.3 - D.16 present plots of the results of these tests. Tables D.1 - D.4 summarize the test results and present the calculated values for the quantities discussed above for each cycle, as well as for the average of four cycles. Table D.5 compares test data averages with published 3M

data [1] that were interpolated to match the test data; the interpolations were made linearly between the nearest two adjacent ambient temperature conditions.

In observing the test data plots and the resulting derived quantities for each damper, the reader will note that each subsequent displacement cycle in each test series resulted in lower measured shear force, hence lower energy dissipation. The material softened with each cycle, indicating that the heating that occurs in the energy dissipation process causes material property changes. This is most noticeable in the shear storage moduli and in the damper stiffness quantities. The data show decreasing quantities for these properties. For the four complete cycles that are reported for each test, the energy dissipated in the first complete cycle ranges from 12% to 37% higher than the energy dissipated in the fourth cycle. The data are consistent with the previously published data. Figure D.17 graphically portrays the effects of excitation frequency and maximum shear strain on the material properties.

In Table D.5, the comparison with 3M data shows consistently lower stiffness-related quantities for the VEDs tested in this project than for the 3M data. Discussions with 3M engineers indicate that the 3M data reports the properties observed on the first cycle, rather than a multi-cycle average. There is considerable discussion in the literature concerning appropriate material properties to use in design. The sinusoidal testing that is commonly performed to establish material properties should be more demanding than actual seismic excitation, since the peak structural displacements in a seismic event usually are repeated for only a cycle or two.

Two concluding notes on the tests relate to events that occurred during the tests. First, one of the "66" series VED failed during testing, when one of the viscoelastic pads partially delaminated from the steel plate to which it was attached. The pads were attached with an epoxy adhesive that began failing at one corner of the pad. The VED was replaced. Second, the testing on VED 66M, at 2 Hz, ± 0.50 ", was prematurely halted. This error was not discovered until after the conclusion of the testing; a repeat of the test to gain additional shear cycles was not deemed to be worth the cost of a new test setup.

D.3 Viscoelastic Damper Modeling

The above discussions on VED properties and testing lead to a procedure that can assist with modeling the responses of VED-equipped structures to either static or dynamic lateral loads, using Equations D.10 and D.11. The individual VED can be modeled by using a linear spring element and a viscous damper dashpot element in parallel. The linear spring stiffness is represented by Equation D.10,

while the damping properties are represented by Equation D.11. In a dynamic analysis, both elements are used, while, in a static analysis, only the linear spring is used. Dashpot elements are becoming more common in commercial structural analysis software; for example, the program ETABS [17], used in this study, has such a dashpot element.

There are several shortcomings to this procedure. First, the frequency, temperature, and strain-dependent characteristics cannot be modeled for an entire response time-history; all three characteristics will change. One has to select the material properties that best represent the conditions to which the VED will be subjected. Second, modeling in this manner will not accurately depict the phase angle that exists between stress and strain [1], which leads to some unavoidable inaccuracy. Finally, this simplified approach is predicated on the assumption that the braces containing the VEDs are much stiffer than the VEDs. Reference 1 describes this as a "rigid brace model" and contrasts its performance with a "flexible brace model," in which the brace stiffness is much closer to being the same as the stiffness of the VEDs.

These shortcomings are not large and can be accommodated within the range of accuracy that is generally possible in engineering analysis. The authors of Reference 1 performed a number of comparisons of VED tests like those described here with single-degree-of-freedom analytical models and concluded that the likely error using these models does not exceed 10%. As mentioned earlier, the sinusoidal testing upon which material characterization is based is a more severe environment than is likely to be seen in the field, for a given peak displacement condition. The peak displacement will not occur for a large number of cycles. Even though the VED energy dissipation capacity may be lessened following the ground motion that induces peak VED strain, it is unlikely that repeated displacements to this strain level will occur. The rate-dependency of the material is controllable, in that the response frequency of a VED-equipped structure can be reasonably well defined in terms of the structure's first mode; the variations in response frequency that occur about the first mode are fairly narrowly banded. Since the rate-dependency is approximately a function of the square root of the frequency, minor variations from the frequency used to define the material parameters will not result in significant changes in them. Most studies [E.G. 1] report that the temperature rise that occurs with energy dissipation tends to reach an equilibrium level after the large strain excursions have subsided. A suggested "rule of thumb" [1] is to use the ambient temperature + 10° F for the design temperature for the VED. A practical application problem here is the need to control the ambient temperature of the VED. Temperature extremes, either high or low, result in significant loss of efficiency. A large temperature change from the design temperature would result in performance that is significantly different from the anticipated design performance.

| Damper | Frequency Hz | Displacement Inches | Cycle | Energy In-Kips | Fmax Kips | Dmax Inches | G* | G'' | G' | η | K' K/In | Ceq K-Sec/In |
|------------|-----------------|------------------------|------------|-------------------|--------------|----------------|--------------|--------------|--------------|-------------|-------------|-----------------|
| 65I | 1 | 0.25 | 1 | 1.77 | 2.93 | 0.258 | 0.315 | 0.235 | 0.210 | 1.12 | 7.57 | 1.35 |
| 65I | 1 | 0.25 | 2 | 1.68 | 2.76 | 0.257 | 0.298 | 0.225 | 0.196 | 1.14 | 7.07 | 1.29 |
| 65I | 1 | 0.25 | 3 | 1.64 | 2.68 | 0.258 | 0.289 | 0.217 | 0.191 | 1.14 | 6.86 | 1.24 |
| 65I | 1 | 0.25 | 4 | 1.58 | 2.63 | 0.257 | 0.284 | 0.211 | 0.190 | 1.11 | 6.82 | 1.21 |
| 65I | 1 | 0.25 | AVG | 1.66 | 2.75 | 0.26 | 0.297 | 0.222 | 0.197 | 1.13 | 7.08 | 1.27 |
| 65L | 1 | 0.25 | 1 | 1.79 | 2.86 | 0.257 | 0.309 | 0.239 | 0.196 | 1.22 | 7.07 | 1.37 |
| 65L | 1 | 0.25 | 2 | 1.69 | 2.75 | 0.256 | 0.298 | 0.227 | 0.192 | 1.18 | 6.93 | 1.30 |
| 65L | 1 | 0.25 | 3 | 1.65 | 2.67 | 0.255 | 0.291 | 0.224 | 0.186 | 1.20 | 6.69 | 1.28 |
| 65L | 1 | 0.25 | 4 | 1.59 | 2.61 | 0.256 | 0.283 | 0.214 | 0.185 | 1.16 | 6.66 | 1.23 |
| 65L | 1 | 0.25 | AVG | 1.68 | 2.72 | 0.26 | 0.295 | 0.226 | 0.190 | 1.19 | 6.84 | 1.30 |
| 65 | 1 | 0.25 | AVG | 1.67 | 2.74 | 0.26 | 0.296 | 0.224 | 0.193 | 1.16 | 6.96 | 1.28 |
| 65I | 1 | 0.50 | 1 | 6.63 | 5.66 | 0.501 | 0.314 | 0.234 | 0.209 | 1.12 | 7.54 | 1.34 |
| 65I | 1 | 0.50 | 2 | 6.00 | 5.01 | 0.499 | 0.279 | 0.213 | 0.180 | 1.19 | 6.47 | 1.22 |
| 65I | 1 | 0.50 | 3 | 5.60 | 4.59 | 0.500 | 0.255 | 0.198 | 0.160 | 1.23 | 5.77 | 1.13 |
| 65I | 1 | 0.50 | 4 | 5.27 | 4.44 | 0.499 | 0.247 | 0.187 | 0.161 | 1.16 | 5.80 | 1.07 |
| 65I | 1 | 0.50 | AVG | 5.87 | 4.92 | 0.50 | 0.274 | 0.208 | 0.178 | 1.17 | 6.40 | 1.19 |
| 65L | 1 | 0.50 | 1 | 7.00 | 5.93 | 0.494 | 0.333 | 0.254 | 0.216 | 1.17 | 7.78 | 1.45 |
| 65L | 1 | 0.50 | 2 | 6.25 | 5.25 | 0.494 | 0.295 | 0.227 | 0.189 | 1.20 | 6.81 | 1.30 |
| 65L | 1 | 0.50 | 3 | 5.83 | 4.84 | 0.493 | 0.272 | 0.212 | 0.171 | 1.24 | 6.16 | 1.22 |
| 65L | 1 | 0.50 | 4 | 5.42 | 4.40 | 0.493 | 0.248 | 0.197 | 0.150 | 1.31 | 5.40 | 1.13 |
| 65L | 1 | 0.50 | AVG | 6.13 | 5.10 | 0.49 | 0.287 | 0.222 | 0.182 | 1.22 | 6.54 | 1.27 |
| 65 | 1 | 0.50 | AVG | 6.00 | 5.01 | 0.50 | 0.280 | 0.215 | 0.180 | 1.20 | 6.47 | 1.23 |
| 65I | 1 | 0.625 | 1 | 9.33 | 6.28 | 0.627 | 0.278 | 0.210 | 0.183 | 1.15 | 6.59 | 1.20 |
| 65I | 1 | 0.625 | 2 | 8.16 | 5.44 | 0.627 | 0.241 | 0.183 | 0.157 | 1.17 | 5.64 | 1.05 |
| 65I | 1 | 0.625 | 3 | 7.47 | 4.94 | 0.626 | 0.219 | 0.168 | 0.141 | 1.20 | 5.06 | 0.97 |
| 65I | 1 | 0.625 | 4 | 6.82 | 4.57 | 0.625 | 0.203 | 0.154 | 0.132 | 1.17 | 4.76 | 0.88 |
| 65I | 1 | 0.625 | AVG | 7.94 | 5.31 | 0.63 | 0.236 | 0.179 | 0.153 | 1.17 | 5.51 | 1.03 |
| 65L | 1 | 0.625 | 1 | 9.82 | 6.62 | 0.628 | 0.293 | 0.220 | 0.193 | 1.14 | 6.95 | 1.26 |
| 65L | 1 | 0.625 | 2 | 8.49 | 5.71 | 0.628 | 0.252 | 0.190 | 0.166 | 1.15 | 5.96 | 1.09 |
| 65L | 1 | 0.625 | 3 | 7.75 | 5.16 | 0.628 | 0.228 | 0.174 | 0.148 | 1.17 | 5.33 | 1.00 |
| 65L | 1 | 0.625 | 4 | 7.04 | 4.76 | 0.627 | 0.211 | 0.158 | 0.139 | 1.14 | 5.01 | 0.91 |
| 65L | 1 | 0.625 | AVG | 8.27 | 5.56 | 0.63 | 0.246 | 0.186 | 0.161 | 1.15 | 5.81 | 1.06 |
| 65 | 1 | 0.625 | AVG | 8.11 | 5.44 | 0.63 | 0.241 | 0.182 | 0.157 | 1.16 | 5.66 | 1.04 |

Table D.1 Damper Characterization Test Results, Dampers 65I and 65L @ 1 Hz

| Damper | Frequency Hz | Displacement Inches | Cycle | Energy In-Kips | Fmax Kips | Dmax Inches | G* KSI | G'' KSI | G' KSI | η | K' K/In | Ceq K-Sec/In |
|------------|-----------------|------------------------|------------|-------------------|--------------|----------------|--------------|--------------|--------------|-------------|--------------|-----------------|
| 65I | 2 | 0.25 | 1 | 2.41 | 3.77 | 0.260 | 0.403 | 0.315 | 0.251 | 1.26 | 9.02 | 0.90 |
| 65I | 2 | 0.25 | 2 | 2.34 | 3.64 | 0.259 | 0.390 | 0.309 | 0.239 | 1.29 | 8.59 | 0.88 |
| 65I | 2 | 0.25 | 3 | 2.29 | 3.53 | 0.260 | 0.377 | 0.299 | 0.230 | 1.30 | 8.27 | 0.86 |
| 65I | 2 | 0.25 | 4 | 2.03 | 3.44 | 0.259 | 0.368 | 0.268 | 0.253 | 1.06 | 9.11 | 0.77 |
| 65I | 2 | 0.25 | AVG | 2.27 | 3.59 | 0.26 | 0.385 | 0.298 | 0.243 | 1.22 | 8.76 | 0.85 |
| 65L | 2 | 0.25 | 1 | 3.09 | 6.09 | 0.278 | 0.609 | 0.354 | 0.495 | 0.71 | 17.83 | 1.01 |
| 65L | 2 | 0.25 | 2 | 3.61 | 5.47 | 0.276 | 0.550 | 0.419 | 0.356 | 1.18 | 12.83 | 1.20 |
| 65L | 2 | 0.25 | 3 | 3.48 | 5.20 | 0.276 | 0.523 | 0.404 | 0.332 | 1.22 | 11.94 | 1.16 |
| 65L | 2 | 0.25 | 4 | 3.37 | 4.97 | 0.275 | 0.502 | 0.394 | 0.311 | 1.27 | 11.19 | 1.13 |
| 65L | 2 | 0.25 | AVG | 3.39 | 5.43 | 0.28 | 0.546 | 0.393 | 0.380 | 1.03 | 13.66 | 1.12 |
| 65 | 2 | 0.25 | AVG | 2.83 | 4.51 | 0.27 | 0.468 | 0.348 | 0.312 | 1.12 | 11.24 | 1.00 |
| 65I | 2 | 0.50 | 1 | 9.84 | 8.55 | 0.505 | 0.470 | 0.341 | 0.324 | 1.05 | 11.66 | 0.98 |
| 65I | 2 | 0.50 | 2 | 8.66 | 7.33 | 0.505 | 0.403 | 0.300 | 0.269 | 1.12 | 9.69 | 0.86 |
| 65I | 2 | 0.50 | 3 | 8.07 | 6.66 | 0.504 | 0.367 | 0.281 | 0.236 | 1.19 | 8.49 | 0.80 |
| 65I | 2 | 0.50 | 4 | 7.60 | 6.20 | 0.507 | 0.340 | 0.261 | 0.217 | 1.21 | 7.81 | 0.75 |
| 65I | 2 | 0.50 | AVG | 8.54 | 7.18 | 0.51 | 0.395 | 0.296 | 0.262 | 1.13 | 9.42 | 0.85 |
| 65L | 2 | 0.50 | 1 | 9.92 | 8.74 | 0.502 | 0.483 | 0.348 | 0.335 | 1.04 | 12.08 | 1.00 |
| 65L | 2 | 0.50 | 2 | 8.60 | 7.52 | 0.502 | 0.416 | 0.302 | 0.286 | 1.05 | 10.31 | 0.86 |
| 65L | 2 | 0.50 | 3 | 7.98 | 6.80 | 0.502 | 0.376 | 0.280 | 0.251 | 1.12 | 9.04 | 0.80 |
| 65L | 2 | 0.50 | 4 | 7.46 | 6.24 | 0.502 | 0.345 | 0.262 | 0.225 | 1.16 | 8.11 | 0.75 |
| 65L | 2 | 0.50 | AVG | 8.49 | 7.32 | 0.50 | 0.405 | 0.298 | 0.275 | 1.08 | 9.89 | 0.85 |
| 65 | 2 | 0.50 | AVG | 8.52 | 7.25 | 0.50 | 0.400 | 0.297 | 0.268 | 1.11 | 9.66 | 0.85 |
| 65I | 3 | 0.25 | 1 | 3.91 | 6.22 | 0.264 | 0.654 | 0.496 | 0.426 | 1.16 | 15.35 | 0.95 |
| 65I | 3 | 0.25 | 2 | 3.50 | 5.53 | 0.261 | 0.588 | 0.455 | 0.373 | 1.22 | 13.44 | 0.87 |
| 65I | 3 | 0.25 | 3 | 3.35 | 5.27 | 0.259 | 0.566 | 0.442 | 0.353 | 1.25 | 12.71 | 0.84 |
| 65I | 3 | 0.25 | 4 | 3.26 | 5.06 | 0.261 | 0.539 | 0.424 | 0.333 | 1.27 | 11.97 | 0.81 |
| 65I | 3 | 0.25 | AVG | 3.51 | 5.52 | 0.26 | 0.587 | 0.454 | 0.371 | 1.22 | 13.37 | 0.87 |
| 65L | 3 | 0.25 | 1 | 3.87 | 6.26 | 0.262 | 0.664 | 0.499 | 0.438 | 1.14 | 15.78 | 0.95 |
| 65L | 3 | 0.25 | 2 | 3.55 | 5.50 | 0.261 | 0.586 | 0.461 | 0.362 | 1.27 | 13.03 | 0.88 |
| 65L | 3 | 0.25 | 3 | 3.42 | 5.25 | 0.263 | 0.555 | 0.437 | 0.342 | 1.28 | 12.32 | 0.83 |
| 65L | 3 | 0.25 | 4 | 3.27 | 5.08 | 0.262 | 0.539 | 0.421 | 0.336 | 1.25 | 12.10 | 0.80 |
| 65L | 3 | 0.25 | AVG | 3.53 | 5.52 | 0.26 | 0.586 | 0.454 | 0.370 | 1.23 | 13.31 | 0.87 |
| 65 | 3 | 0.25 | AVG | 3.52 | 5.52 | 0.26 | 0.586 | 0.454 | 0.371 | 1.23 | 13.34 | 0.87 |
| 65I | 3 | 0.50 | 1 | 8.93 | 8.23 | 0.491 | 0.466 | 0.327 | 0.331 | 0.99 | 11.92 | 0.63 |
| 65I | 3 | 0.50 | 2 | 8.25 | 7.31 | 0.465 | 0.437 | 0.337 | 0.277 | 1.22 | 9.98 | 0.64 |
| 65I | 3 | 0.50 | 3 | 7.78 | 6.76 | 0.470 | 0.399 | 0.312 | 0.250 | 1.25 | 9.00 | 0.59 |
| 65I | 3 | 0.50 | 4 | 7.31 | 6.34 | 0.472 | 0.373 | 0.290 | 0.235 | 1.24 | 8.44 | 0.55 |
| 65I | 3 | 0.50 | AVG | 8.07 | 7.16 | 0.47 | 0.419 | 0.317 | 0.274 | 1.15 | 9.88 | 0.61 |
| 65L | 3 | 0.50 | 1 | 9.21 | 8.49 | 0.503 | 0.469 | 0.322 | 0.341 | 0.94 | 12.27 | 0.61 |
| 65L | 3 | 0.50 | 2 | 8.48 | 7.65 | 0.469 | 0.453 | 0.341 | 0.298 | 1.14 | 10.74 | 0.65 |
| 65L | 3 | 0.50 | 3 | 8.04 | 7.05 | 0.474 | 0.413 | 0.316 | 0.266 | 1.19 | 9.56 | 0.60 |
| 65L | 3 | 0.50 | 4 | 7.47 | 6.45 | 0.476 | 0.376 | 0.291 | 0.238 | 1.22 | 8.58 | 0.56 |
| 65L | 3 | 0.50 | AVG | 8.30 | 7.41 | 0.48 | 0.428 | 0.318 | 0.287 | 1.11 | 10.34 | 0.61 |
| 65 | 3 | 0.50 | AVG | 8.18 | 7.28 | 0.48 | 0.424 | 0.317 | 0.281 | 1.13 | 10.11 | 0.61 |

Table D.2 Damper Characterization Test Results, Dampers 65I and 65L @ 2 and 3 Hz

| Damper | Frequency Hz | Displacement Inches | Cycle | Energy In-Kips | Fmax Kips | Dmax Inches | G* KSI | G'' KSI | G' KSI | η | K' K/In | Ceq K-Sec/In |
|------------|-----------------|------------------------|------------|-------------------|--------------|----------------|--------------|--------------|--------------|-------------|-------------|-----------------|
| 66D | 1 | 0.50 | 1 | 3.45 | 2.84 | 0.495 | 0.318 | 0.249 | 0.198 | 1.26 | 3.57 | 0.71 |
| 66D | 1 | 0.50 | 2 | 3.00 | 2.51 | 0.494 | 0.283 | 0.218 | 0.180 | 1.21 | 3.24 | 0.62 |
| 66D | 1 | 0.50 | 3 | 2.76 | 2.30 | 0.494 | 0.258 | 0.200 | 0.164 | 1.22 | 2.95 | 0.57 |
| 66D | 1 | 0.50 | 4 | 2.52 | 2.14 | 0.494 | 0.240 | 0.183 | 0.156 | 1.17 | 2.81 | 0.52 |
| 66D | 1 | 0.50 | AVG | 2.93 | 2.45 | 0.49 | 0.275 | 0.212 | 0.174 | 1.22 | 3.14 | 0.61 |
| 66M | 1 | 0.50 | 1 | 3.25 | 2.72 | 0.494 | 0.305 | 0.236 | 0.194 | 1.21 | 3.50 | 0.68 |
| 66M | 1 | 0.50 | 2 | 2.90 | 2.39 | 0.494 | 0.269 | 0.210 | 0.168 | 1.25 | 3.02 | 0.60 |
| 66M | 1 | 0.50 | 3 | 2.68 | 2.19 | 0.493 | 0.247 | 0.195 | 0.152 | 1.28 | 2.73 | 0.56 |
| 66M | 1 | 0.50 | 4 | 2.48 | 2.06 | 0.493 | 0.232 | 0.180 | 0.146 | 1.24 | 2.62 | 0.52 |
| 66M | 1 | 0.50 | AVG | 2.83 | 2.34 | 0.49 | 0.263 | 0.205 | 0.165 | 1.24 | 2.97 | 0.59 |
| <i>66</i> | <i>1</i> | <i>0.50</i> | <i>AVG</i> | <i>2.88</i> | <i>2.39</i> | <i>0.49</i> | <i>0.269</i> | <i>0.209</i> | <i>0.170</i> | <i>1.23</i> | <i>3.06</i> | <i>0.60</i> |
| 66D | 1 | 0.625 | 1 | 5.80 | 3.84 | 0.628 | 0.340 | 0.260 | 0.219 | 1.19 | 3.94 | 0.74 |
| 66D | 1 | 0.625 | 2 | 4.79 | 3.17 | 0.626 | 0.281 | 0.216 | 0.180 | 1.20 | 3.24 | 0.62 |
| 66D | 1 | 0.625 | 3 | 4.21 | 2.78 | 0.627 | 0.246 | 0.189 | 0.157 | 1.21 | 2.82 | 0.54 |
| 66D | 1 | 0.625 | 4 | 3.72 | 2.50 | 0.627 | 0.222 | 0.167 | 0.146 | 1.15 | 2.62 | 0.48 |
| 66D | 1 | 0.625 | AVG | 4.63 | 3.07 | 0.63 | 0.272 | 0.208 | 0.175 | 1.19 | 3.16 | 0.60 |
| 66M | 1 | 0.625 | 1 | 5.45 | 3.62 | 0.627 | 0.321 | 0.245 | 0.207 | 1.19 | 3.72 | 0.70 |
| 66M | 1 | 0.625 | 2 | 4.62 | 3.00 | 0.626 | 0.266 | 0.208 | 0.165 | 1.26 | 2.97 | 0.60 |
| 66M | 1 | 0.625 | 3 | 4.13 | 2.66 | 0.626 | 0.236 | 0.186 | 0.146 | 1.28 | 2.62 | 0.53 |
| 66M | 1 | 0.625 | 4 | 3.68 | 2.42 | 0.626 | 0.214 | 0.166 | 0.136 | 1.22 | 2.44 | 0.48 |
| 66M | 1 | 0.625 | AVG | 4.47 | 2.92 | 0.63 | 0.259 | 0.201 | 0.163 | 1.23 | 2.94 | 0.58 |
| <i>66</i> | <i>1</i> | <i>0.625</i> | <i>AVG</i> | <i>4.55</i> | <i>3.00</i> | <i>0.63</i> | <i>0.266</i> | <i>0.205</i> | <i>0.169</i> | <i>1.21</i> | <i>3.05</i> | <i>0.59</i> |

Table D.3 Damper Characterization Test Results, Dampers 66D and 66M @ 1 Hz

| Damper | Frequency Hz | Displacement Inches | Cycle | Energy In-Kips | Fmax Kips | Dmax Inches | G* KSI | G'' KSI | G' KSI | η | K' K/In | Ceq K-Sec/In |
|------------|-----------------|------------------------|------------|-------------------|--------------|----------------|--------------|--------------|--------------|-------------|-------------|-----------------|
| 66D | 2 | 0.25 | 1 | 1.82 | 2.67 | 0.287 | 0.517 | 0.390 | 0.340 | 1.15 | 6.11 | 0.56 |
| 66D | 2 | 0.25 | 2 | 1.64 | 2.37 | 0.285 | 0.462 | 0.356 | 0.294 | 1.21 | 5.30 | 0.51 |
| 66D | 2 | 0.25 | 3 | 1.56 | 2.24 | 0.285 | 0.437 | 0.339 | 0.276 | 1.23 | 4.97 | 0.49 |
| 66D | 2 | 0.25 | 4 | 1.49 | 2.13 | 0.285 | 0.415 | 0.324 | 0.259 | 1.25 | 4.67 | 0.46 |
| 66D | 2 | 0.25 | AVG | 1.63 | 2.35 | 0.29 | 0.458 | 0.353 | 0.292 | 1.21 | 5.26 | 0.51 |
| 66M | 2 | 0.25 | 1 | 1.62 | 2.43 | 0.274 | 0.492 | 0.382 | 0.310 | 1.23 | 5.59 | 0.55 |
| 66M | 2 | 0.25 | 2 | 1.48 | 2.18 | 0.271 | 0.447 | 0.355 | 0.271 | 1.31 | 4.88 | 0.51 |
| 66M | 2 | 0.25 | 3 | 1.41 | 2.08 | 0.271 | 0.427 | 0.340 | 0.257 | 1.32 | 4.63 | 0.49 |
| 66M | 2 | 0.25 | 4 | 1.36 | 2.00 | 0.271 | 0.410 | 0.327 | 0.247 | 1.32 | 4.45 | 0.47 |
| 66M | 2 | 0.25 | AVG | 1.47 | 2.17 | 0.27 | 0.444 | 0.352 | 0.272 | 1.29 | 4.89 | 0.50 |
| 66 | 2 | 0.25 | AVG | 1.55 | 2.26 | 0.28 | 0.451 | 0.352 | 0.282 | 1.25 | 5.08 | 0.50 |
| 66D | 2 | 0.50 | 1 | 5.91 | 5.00 | 0.492 | 0.564 | 0.431 | 0.364 | 1.19 | 6.54 | 0.62 |
| 66D | 2 | 0.50 | 2 | 4.87 | 4.05 | 0.490 | 0.459 | 0.358 | 0.287 | 1.25 | 5.16 | 0.51 |
| 66D | 2 | 0.50 | 3 | 4.29 | 3.56 | 0.489 | 0.405 | 0.317 | 0.251 | 1.26 | 4.52 | 0.45 |
| 66D | 2 | 0.50 | 4 | 3.84 | 3.18 | 0.489 | 0.361 | 0.284 | 0.223 | 1.27 | 4.02 | 0.41 |
| 66D | 2 | 0.50 | AVG | 4.73 | 3.95 | 0.49 | 0.447 | 0.348 | 0.281 | 1.24 | 5.06 | 0.50 |
| 66M | 2 | 0.50 | 1 | 4.87 | 4.12 | 0.509 | 0.449 | 0.333 | 0.302 | 1.10 | 5.44 | 0.48 |
| 66M | 2 | 0.50 | 2 | 4.30 | 3.52 | 0.509 | 0.384 | 0.293 | 0.247 | 1.19 | 4.45 | 0.42 |
| 66M | 2 | 0.50 | AVG | 4.59 | 3.82 | 0.51 | 0.417 | 0.313 | 0.275 | 1.14 | 4.95 | 0.45 |
| 66 | 2 | 0.50 | AVG | 4.66 | 3.88 | 0.50 | 0.432 | 0.331 | 0.278 | 1.19 | 5.01 | 0.47 |
| 66D | 3 | 0.25 | 1 | 2.54 | 3.68 | 0.296 | 0.691 | 0.512 | 0.463 | 1.11 | 8.34 | 0.49 |
| 66D | 3 | 0.25 | 2 | 2.19 | 3.17 | 0.290 | 0.608 | 0.461 | 0.396 | 1.17 | 7.12 | 0.44 |
| 66D | 3 | 0.25 | 3 | 2.10 | 2.98 | 0.291 | 0.569 | 0.438 | 0.364 | 1.20 | 6.55 | 0.42 |
| 66D | 3 | 0.25 | 4 | 1.98 | 2.80 | 0.293 | 0.531 | 0.407 | 0.341 | 1.19 | 6.15 | 0.39 |
| 66D | 3 | 0.25 | AVG | 2.20 | 3.16 | 0.29 | 0.600 | 0.455 | 0.391 | 1.16 | 7.04 | 0.43 |
| 66M | 3 | 0.25 | 1 | 2.12 | 3.39 | 0.267 | 0.706 | 0.525 | 0.472 | 1.11 | 8.49 | 0.50 |
| 66M | 3 | 0.25 | 2 | 1.93 | 3.01 | 0.259 | 0.646 | 0.510 | 0.397 | 1.28 | 7.15 | 0.49 |
| 66M | 3 | 0.25 | 3 | 1.83 | 2.83 | 0.260 | 0.606 | 0.478 | 0.372 | 1.28 | 6.70 | 0.46 |
| 66M | 3 | 0.25 | 4 | 1.73 | 2.69 | 0.258 | 0.579 | 0.458 | 0.353 | 1.30 | 6.36 | 0.44 |
| 66M | 3 | 0.25 | AVG | 1.90 | 2.98 | 0.26 | 0.635 | 0.493 | 0.399 | 1.24 | 7.19 | 0.47 |
| 66 | 3 | 0.25 | AVG | 2.05 | 3.07 | 0.28 | 0.616 | 0.474 | 0.395 | 1.20 | 7.10 | 0.45 |
| 66D | 3 | 0.50 | 1 | 5.60 | 5.10 | 0.462 | 0.613 | 0.464 | 0.401 | 1.16 | 7.22 | 0.44 |
| 66D | 3 | 0.50 | 2 | 4.80 | 4.21 | 0.458 | 0.511 | 0.404 | 0.312 | 1.30 | 5.62 | 0.39 |
| 66D | 3 | 0.50 | 3 | 4.27 | 3.71 | 0.461 | 0.447 | 0.355 | 0.272 | 1.31 | 4.89 | 0.34 |
| 66D | 3 | 0.50 | 4 | 3.84 | 3.32 | 0.460 | 0.401 | 0.320 | 0.241 | 1.33 | 4.34 | 0.31 |
| 66D | 3 | 0.50 | AVG | 4.63 | 4.09 | 0.46 | 0.493 | 0.386 | 0.307 | 1.26 | 5.52 | 0.37 |
| 66M | 3 | 0.50 | 1 | 5.53 | 4.77 | 0.500 | 0.530 | 0.391 | 0.358 | 1.09 | 6.45 | 0.37 |
| 66M | 3 | 0.50 | 2 | 4.80 | 4.01 | 0.484 | 0.461 | 0.363 | 0.284 | 1.28 | 5.11 | 0.35 |
| 66M | 3 | 0.50 | 3 | 4.35 | 3.59 | 0.488 | 0.408 | 0.323 | 0.250 | 1.29 | 4.50 | 0.31 |
| 66M | 3 | 0.50 | 4 | 3.95 | 3.24 | 0.487 | 0.370 | 0.294 | 0.223 | 1.32 | 4.02 | 0.28 |
| 66M | 3 | 0.50 | AVG | 4.66 | 3.90 | 0.49 | 0.443 | 0.343 | 0.280 | 1.23 | 5.03 | 0.33 |
| 66 | 3 | 0.50 | AVG | 4.64 | 3.99 | 0.48 | 0.467 | 0.364 | 0.293 | 1.24 | 5.28 | 0.35 |

Table D.4 Damper Characterization Test Results, Dampers 66D and 66M @ 2 and 3 Hz

| Damper Series | Frequency Hz | Shear Strain % | G' (KSI) | | G'' (KSI) | | η | | Damping (%) | | Phase Angle (Degrees) | |
|---------------|--------------|----------------|----------|--------|-----------|--------|--------|--------|-------------|--------|-----------------------|--------|
| | | | (3M) | (Data) | (3M) | (Data) | (3M) | (Data) | (3M) | (Data) | (3M) | (Data) |
| 65 | 1 | 25 | 0.228 | 0.193 | 0.316 | 0.224 | 1.39 | 1.16 | 69% | 58% | 54 | 49 |
| 65 | 1 | 50 | 0.184 | 0.180 | 0.263 | 0.215 | 1.43 | 1.19 | 71% | 60% | 55 | 50 |
| 65 | 1 | 62.5 | 0.170 | 0.157 | 0.243 | 0.182 | 1.43 | 1.16 | 71% | 58% | 55 | 49 |
| 66 | 1 | 50 | 0.184 | 0.170 | 0.263 | 0.209 | 1.43 | 1.23 | 71% | 61% | 55 | 51 |
| 66 | 1 | 62.5 | 0.170 | 0.169 | 0.243 | 0.205 | 1.43 | 1.21 | 71% | 61% | 55 | 50 |
| 65 | 2 | 25 | 0.331 | 0.312 | 0.453 | 0.348 | 1.37 | 1.12 | 68% | 56% | 54 | 48 |
| 65 | 2 | 50 | 0.249 | 0.268 | 0.364 | 0.297 | 1.46 | 1.11 | 73% | 55% | 56 | 48 |
| 66 | 2 | 25 | 0.331 | 0.282 | 0.453 | 0.352 | 1.37 | 1.25 | 68% | 62% | 54 | 51 |
| 66 | 2 | 50 | 0.249 | 0.278 | 0.364 | 0.331 | 1.46 | 1.19 | 73% | 60% | 56 | 50 |
| 65 | 3 | 25 | 0.409 | 0.371 | 0.547 | 0.454 | 1.34 | 1.22 | 67% | 61% | 53 | 51 |
| 65 | 3 | 50 | 0.293 | 0.281 | 0.421 | 0.317 | 1.44 | 1.13 | 72% | 56% | 55 | 48 |
| 66 | 3 | 25 | 0.409 | 0.395 | 0.547 | 0.474 | 1.34 | 1.20 | 67% | 60% | 53 | 50 |
| 66 | 3 | 50 | 0.293 | 0.293 | 0.421 | 0.364 | 1.44 | 1.24 | 72% | 62% | 55 | 51 |

Test data recorded at 73 degrees F. 3M data quoted here were interpolated from 21 & 24 degrees C.

Table D.5 Comparison of Damper Properties from Tests with Published Data

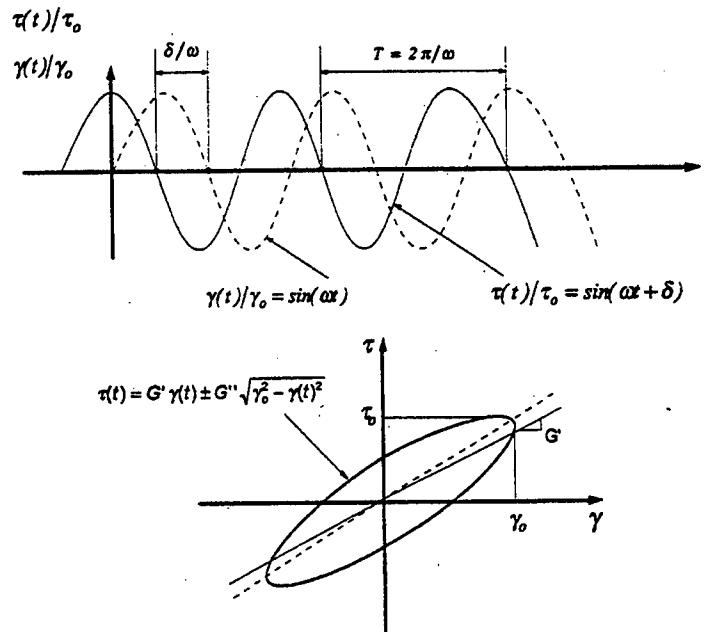


Figure D.1 Viscoelastic Damper Response to Sinusoidal Loading (1)

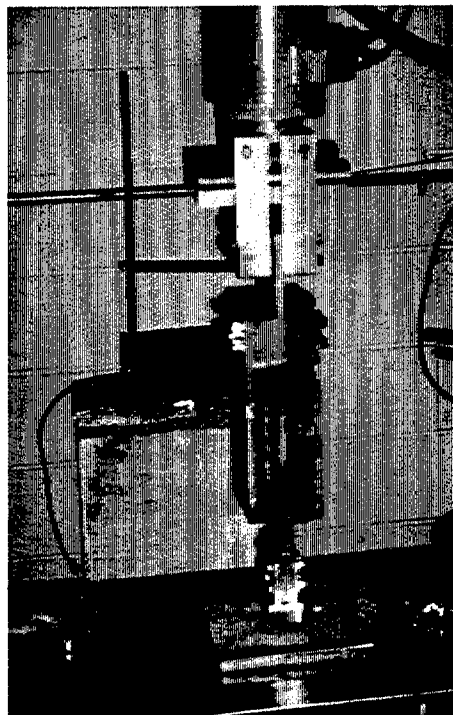


Figure D.2 Damper Characterization Testing

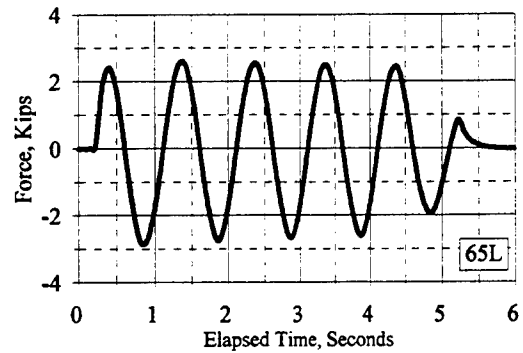
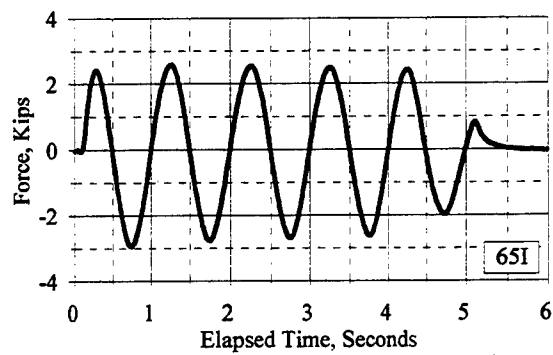
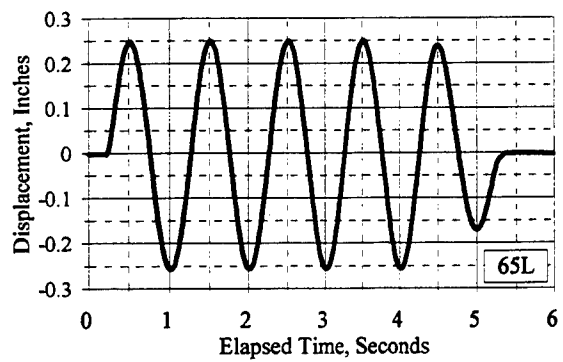
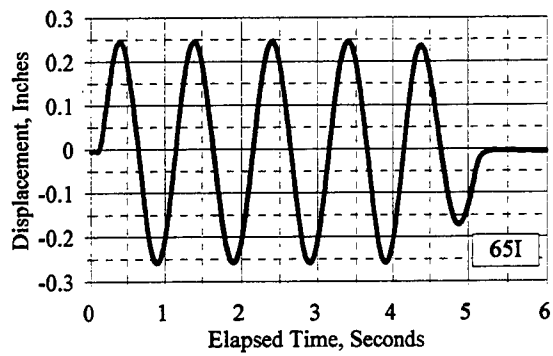
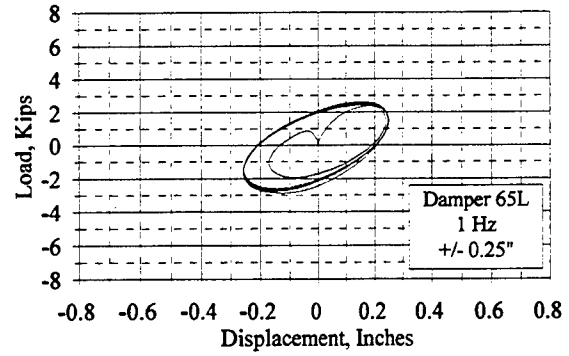
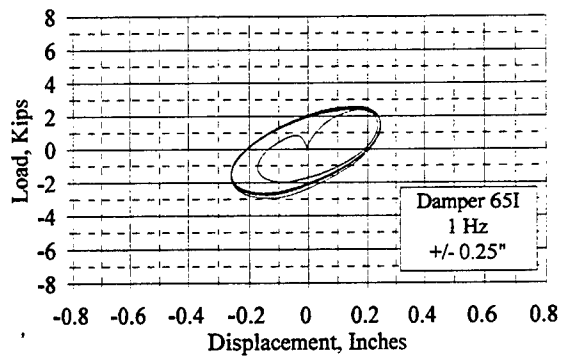


Figure D.3 Damper Test Results, Dampers 65I and 65L, 1 Hz, 0.250"

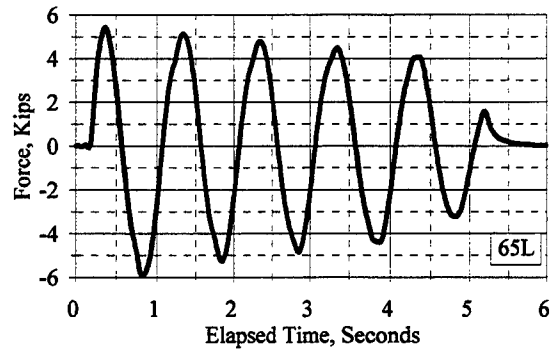
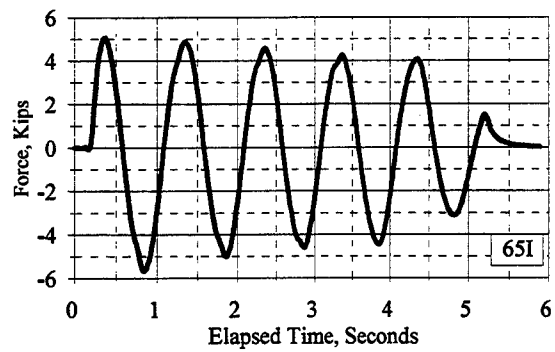
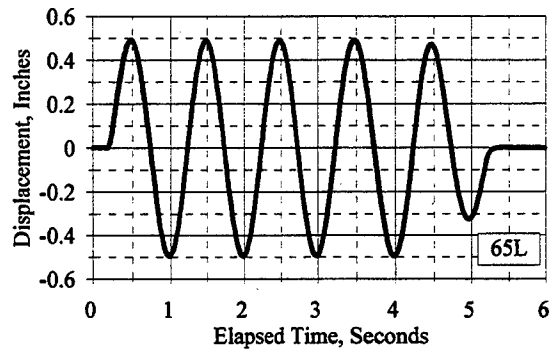
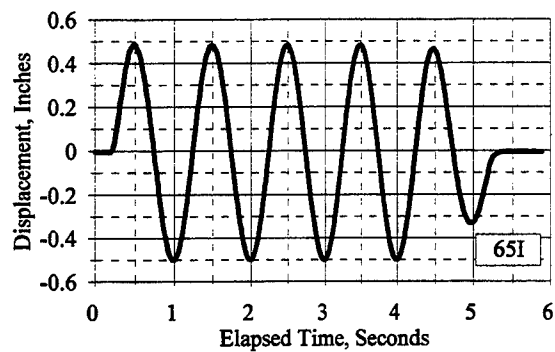
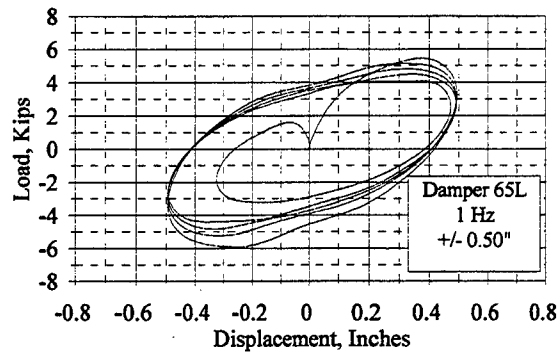
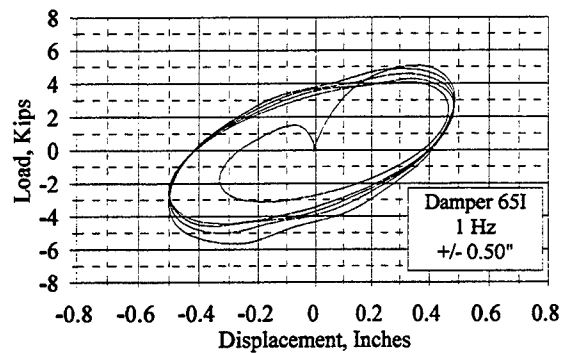


Figure D.4 Damper Test Results, Dampers 65I and 65L, 1 Hz, 0.500"

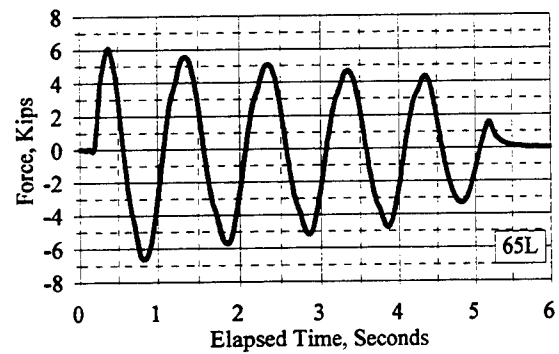
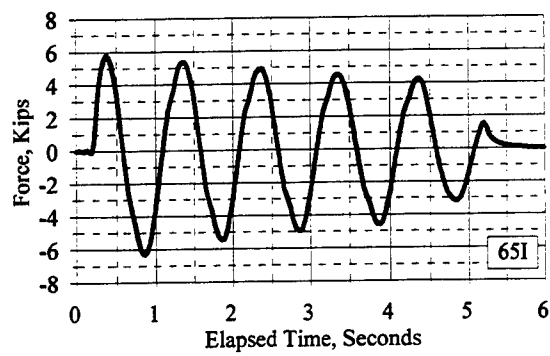
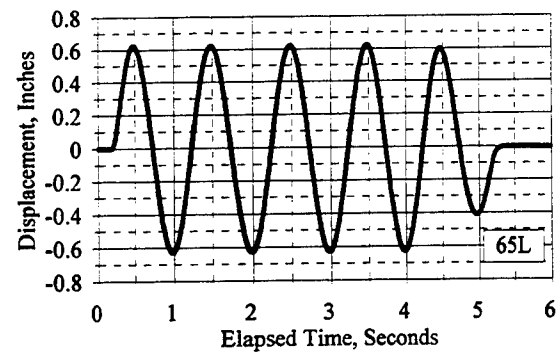
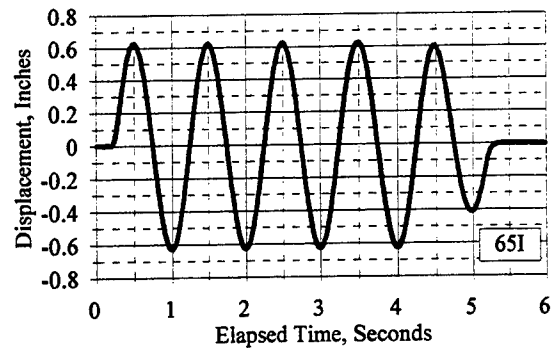
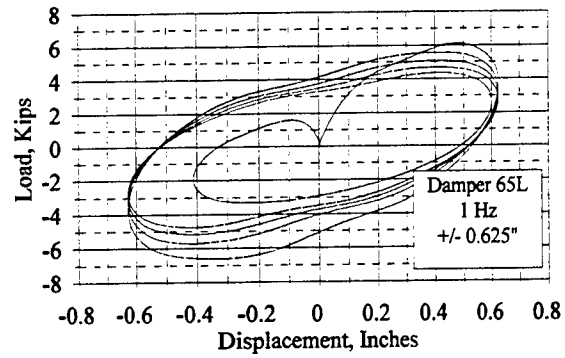
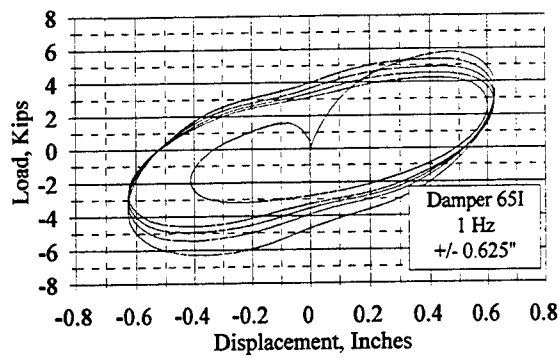


Figure D.5 Damper Test Results, Dampers 65I and 65L, 1 Hz, 0.625"

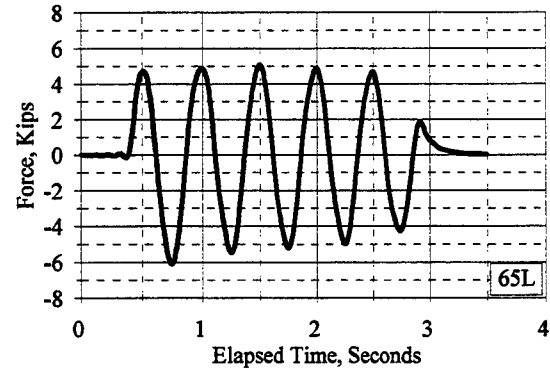
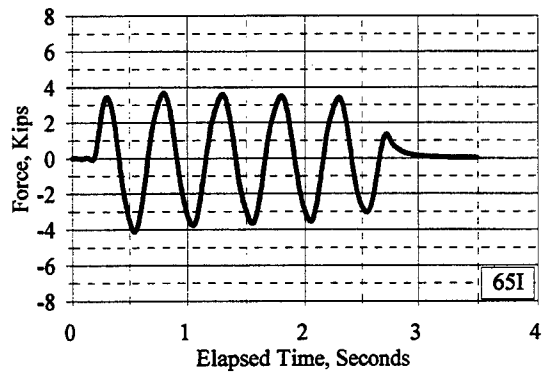
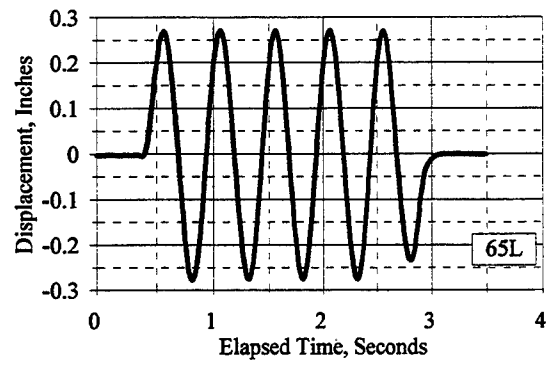
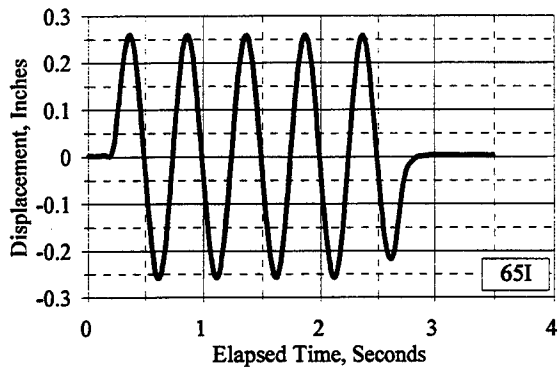
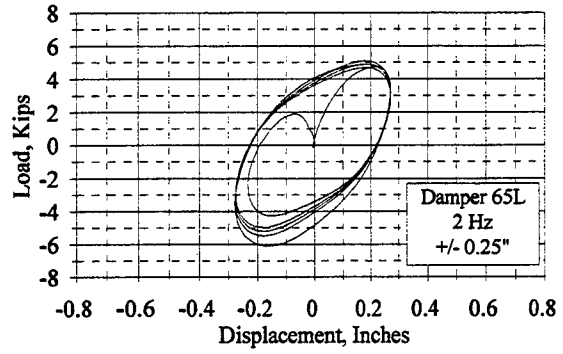
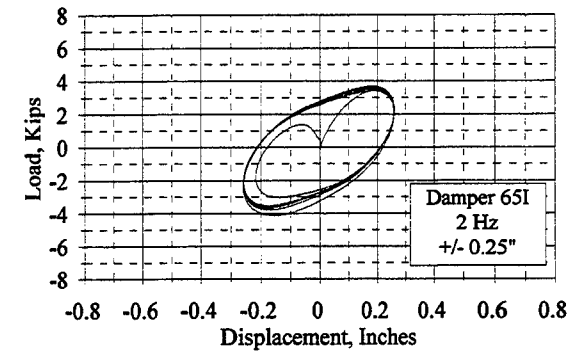


Figure D.6 Damper Test Results, Dampers 65I and 65L, 2 Hz, 0.250"

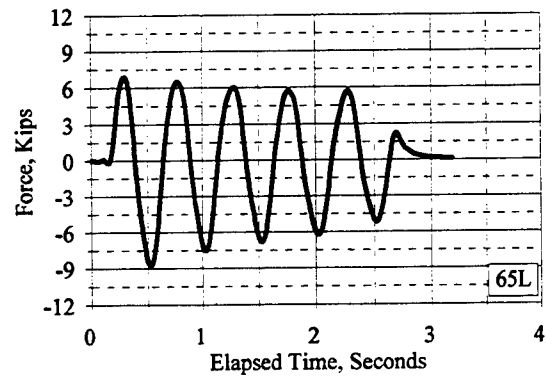
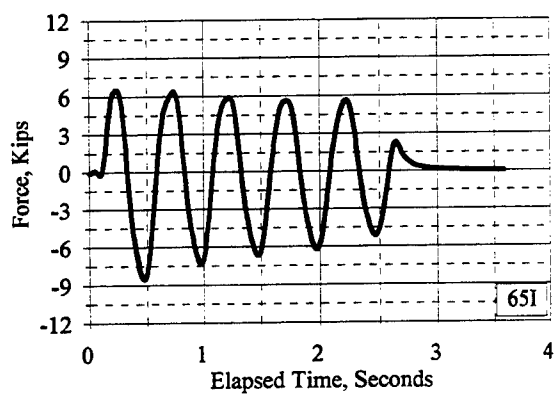
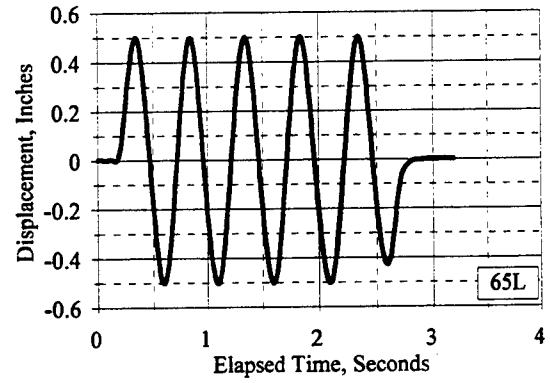
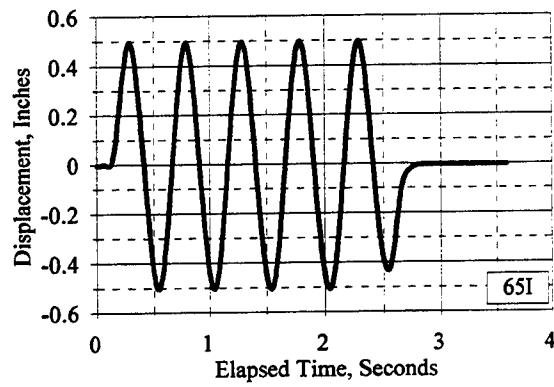
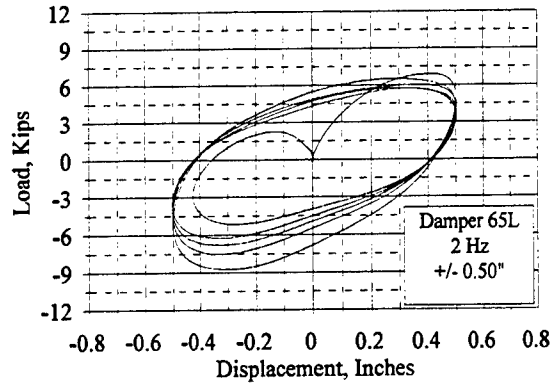
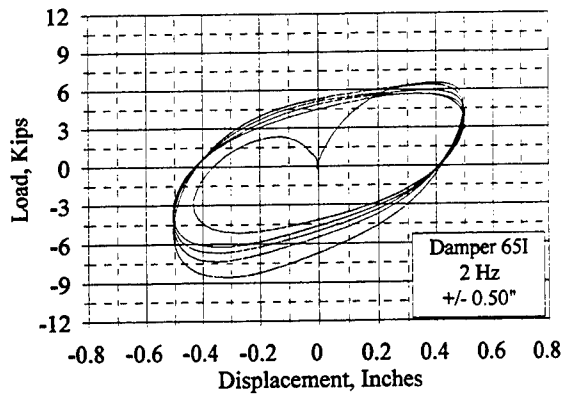


Figure D.7 Damper Test Results, Dampers 65I and 65L, 2 Hz, 0.500"

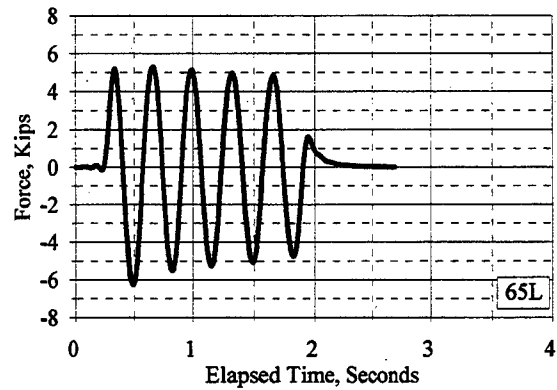
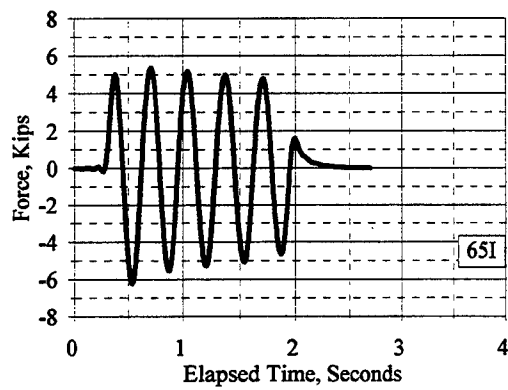
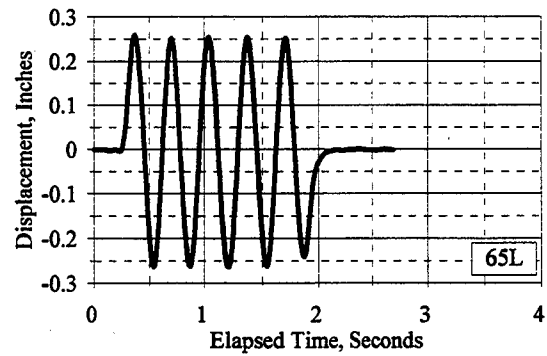
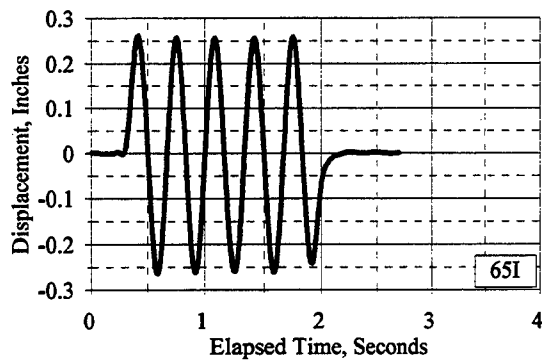
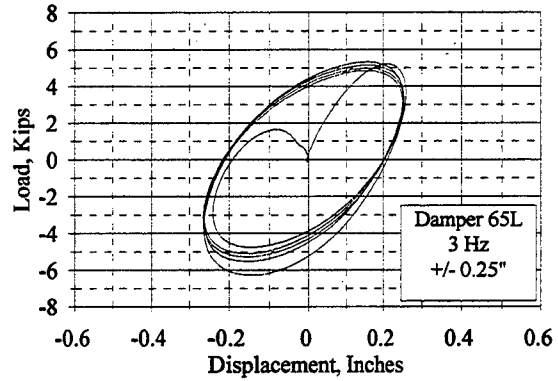
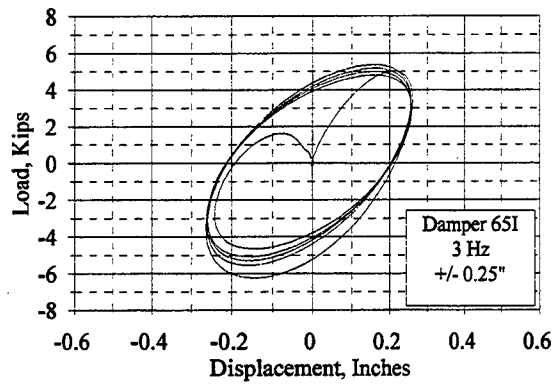


Figure D.8 Damper Test Results, Dampers 65I and 65L, 3 Hz, 0.250"

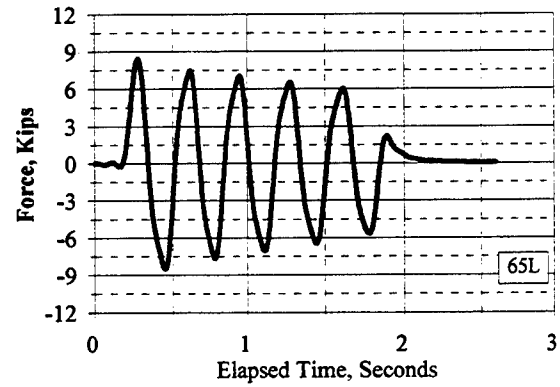
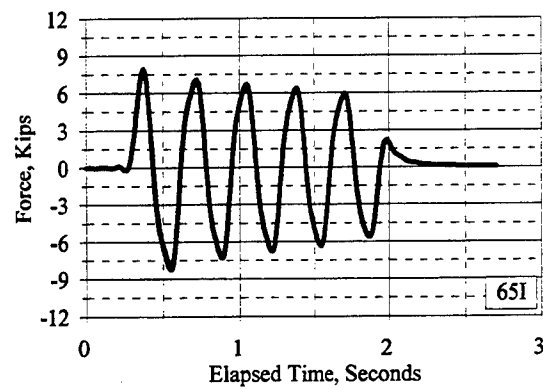
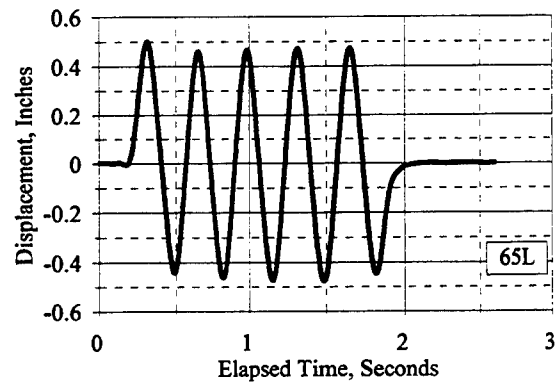
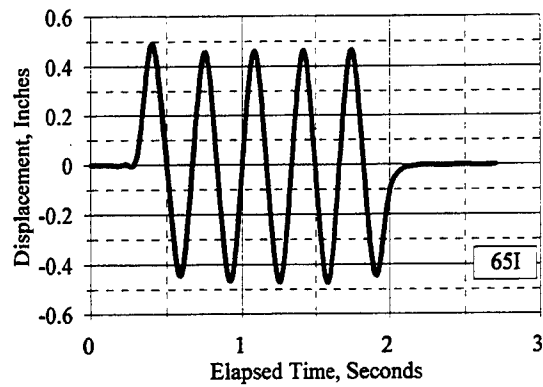
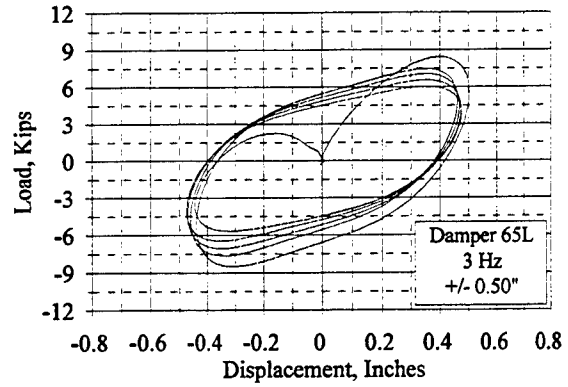
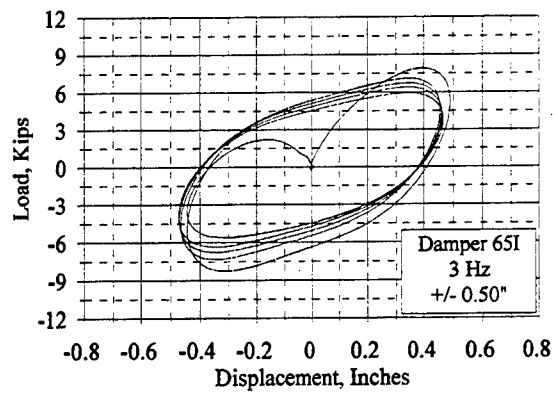


Figure D.9 Damper Test Results, Dampers 65I and 65L, 3 Hz, 0.500"

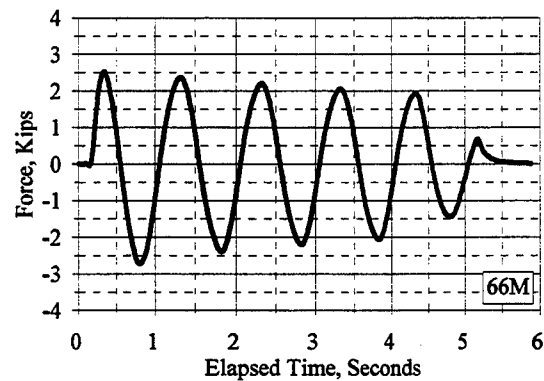
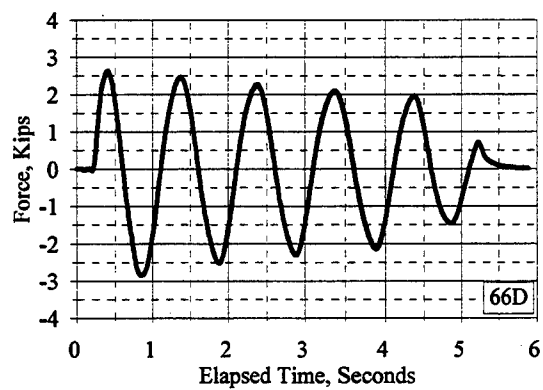
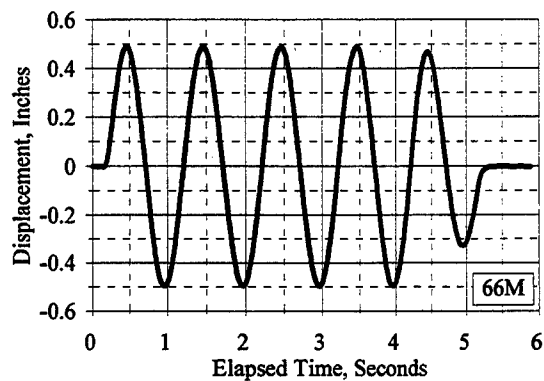
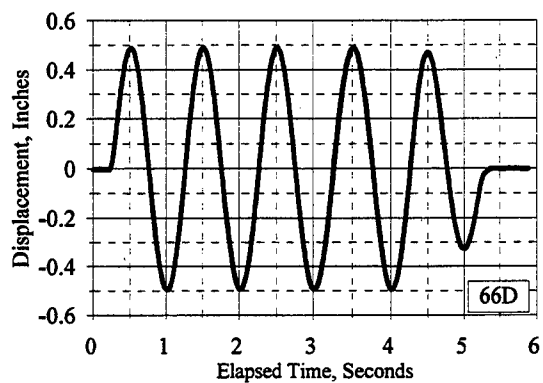
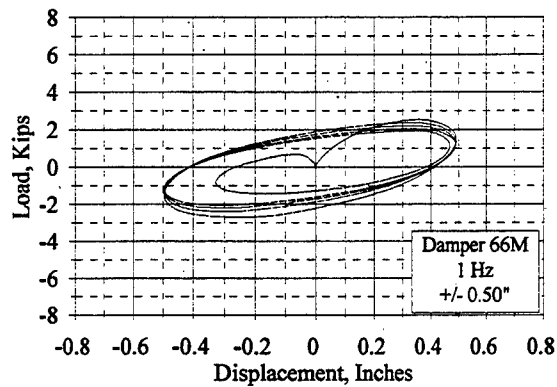
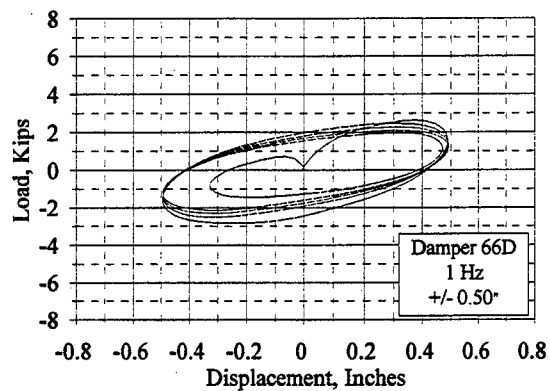


Figure D.10 Damper Test Results, Dampers 66D and 66M, 1 Hz, 0.500"

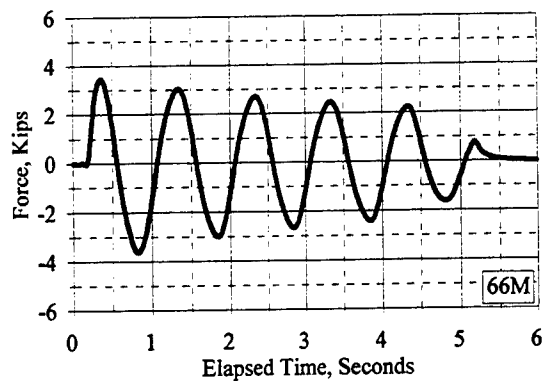
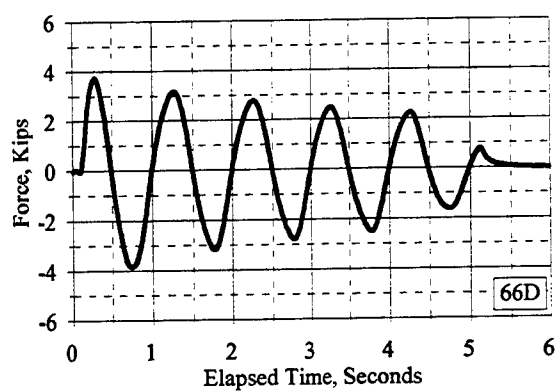
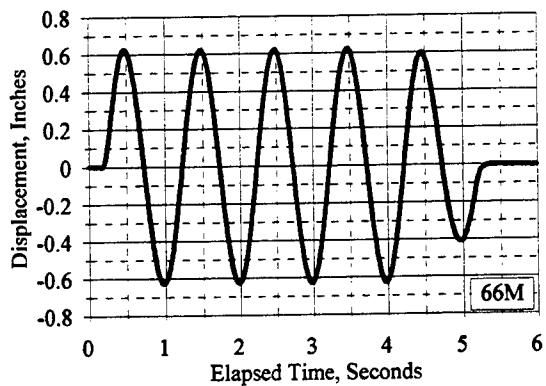
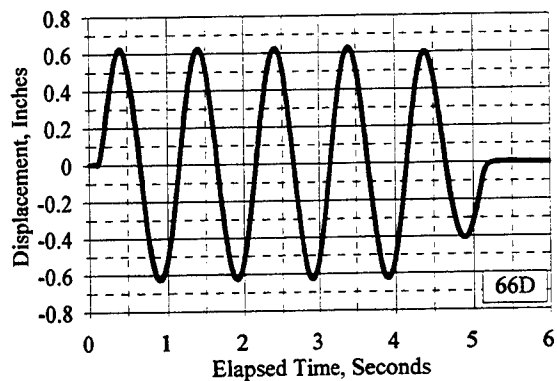
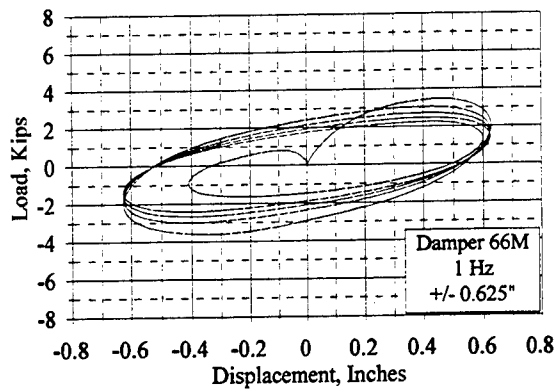
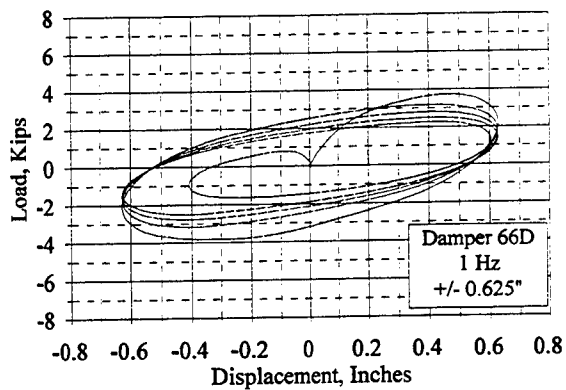


Figure D.11 Damper Test Results, Dampers 66D and 66M, 1 Hz, 0.625"

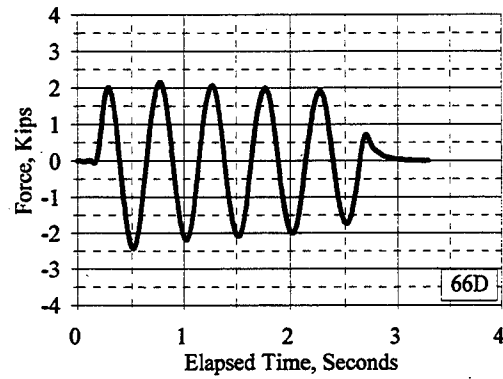
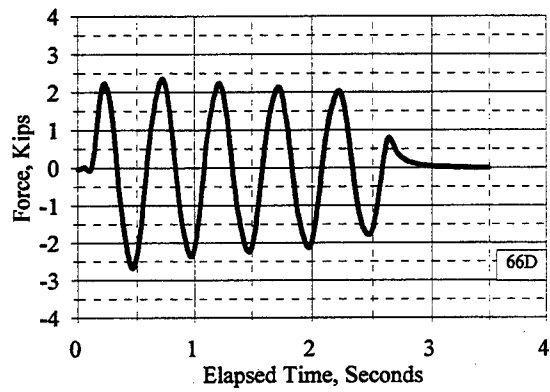
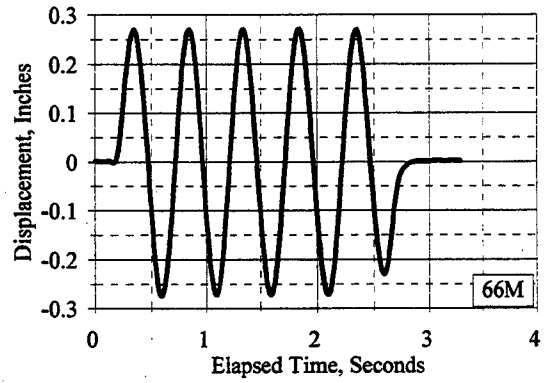
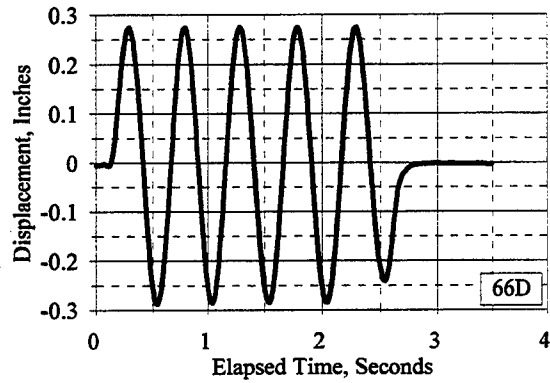
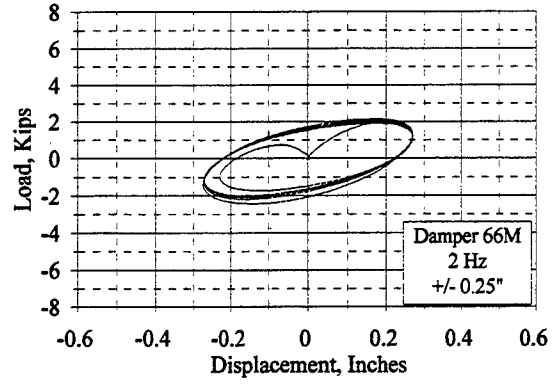
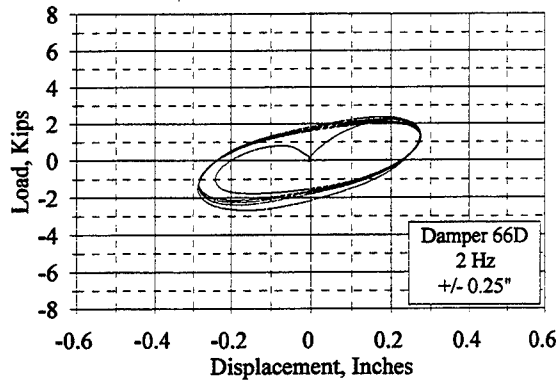


Figure D.12 Damper Test Results, Dampers 66D and 66M, 2 Hz, 0.25"

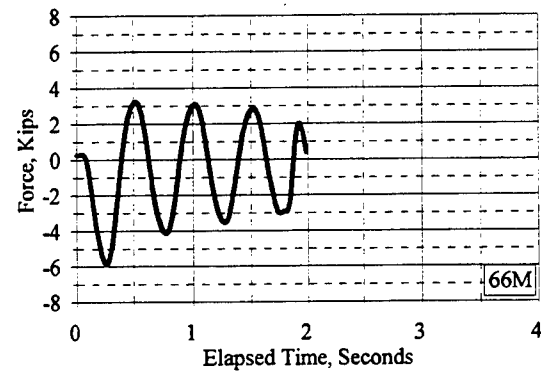
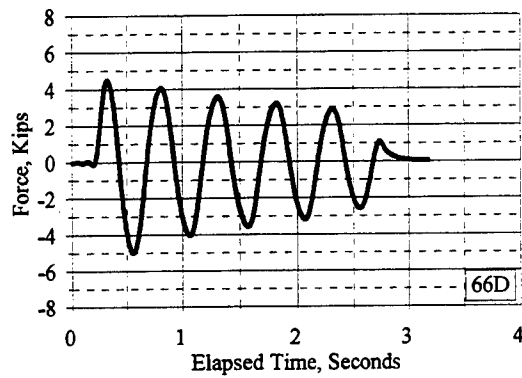
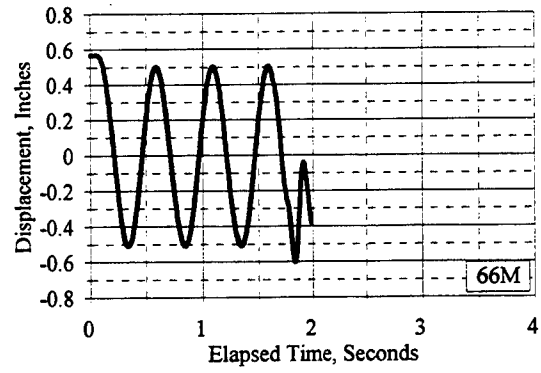
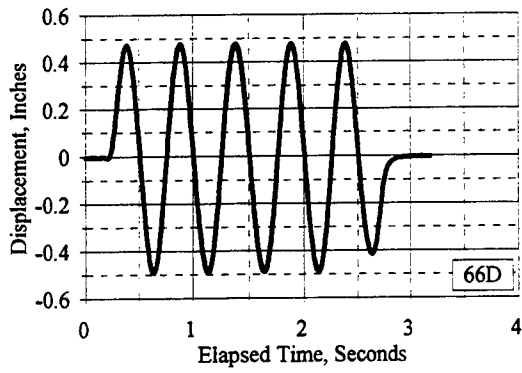
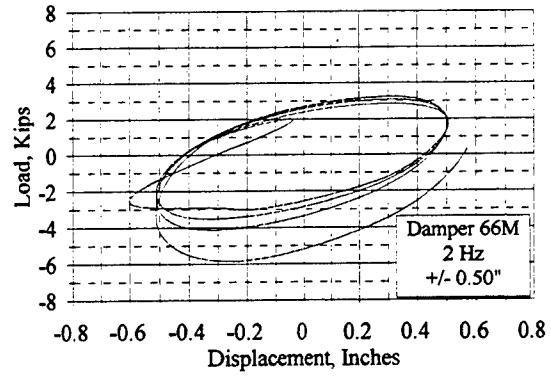
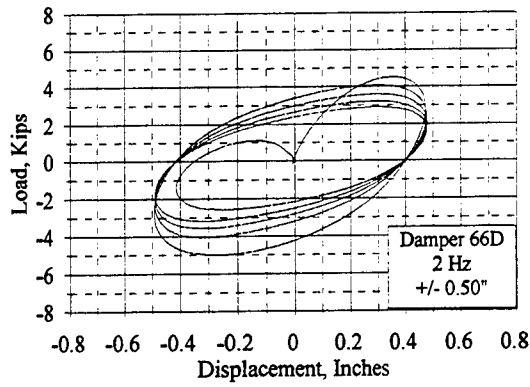


Figure D.13 Damper Test Results, Dampers 66D and 66M, 2 Hz, 0.500"

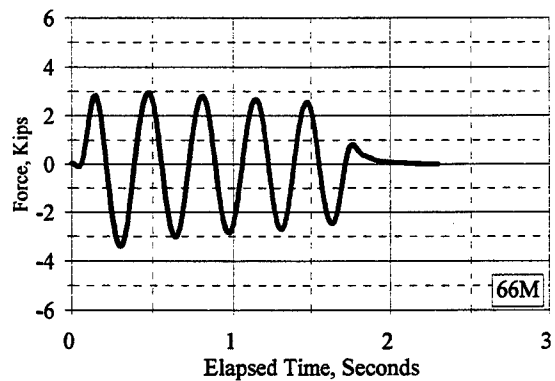
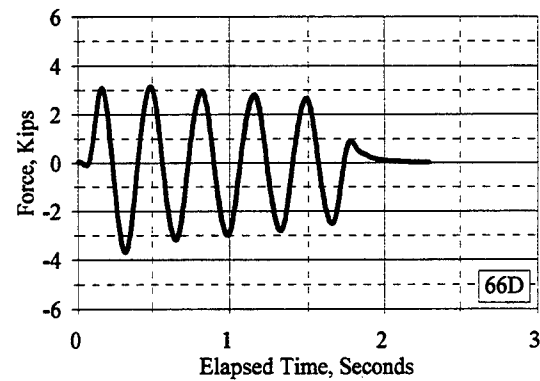
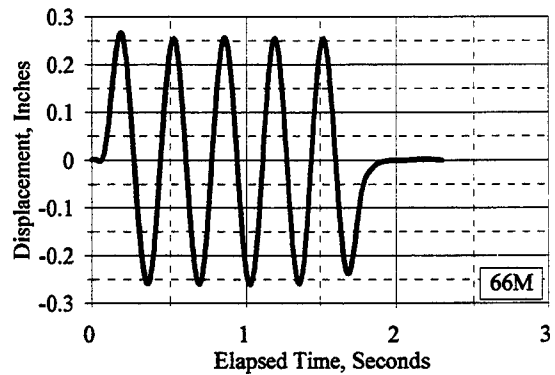
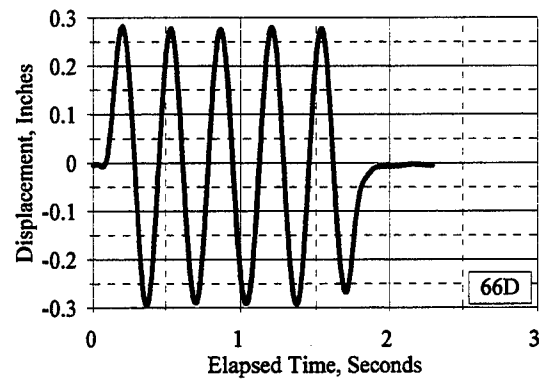
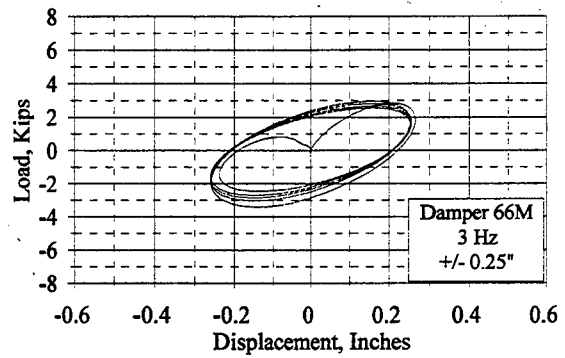
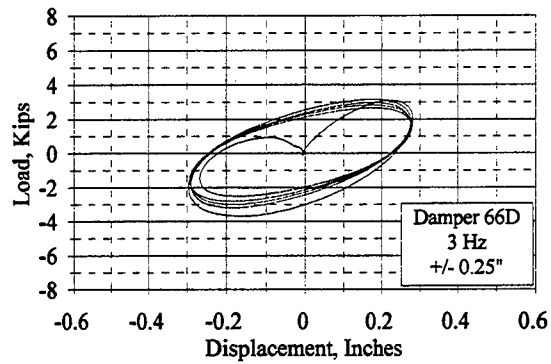


Figure D.14 Damper Test Results, Dampers 66D and 66M, 3 Hz, 0.250"

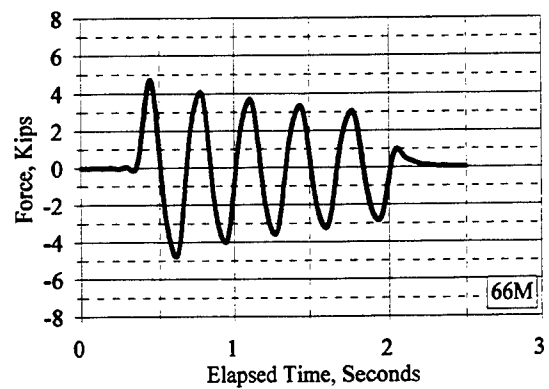
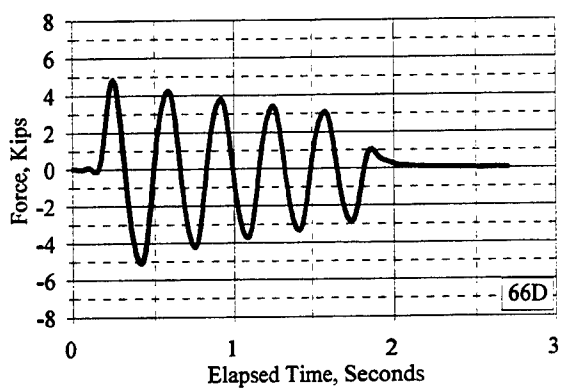
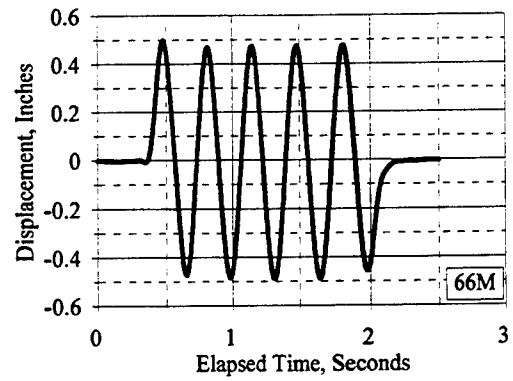
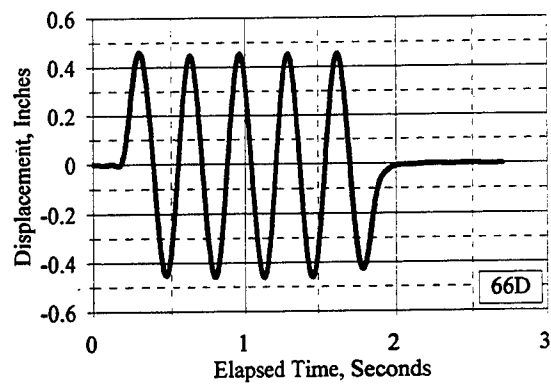
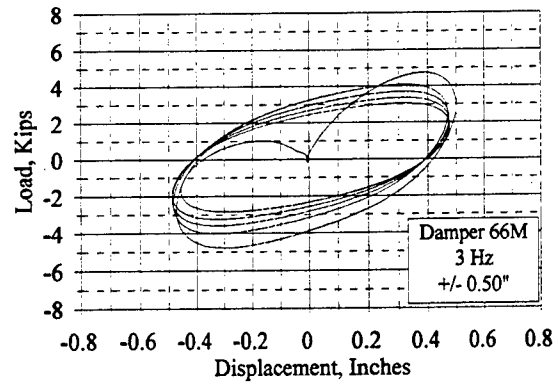
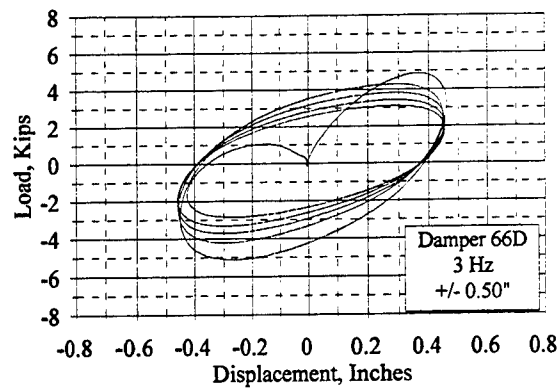


Figure D.15 Damper Test Results, Dampers 66D and 66M, 3 Hz, 0.500"

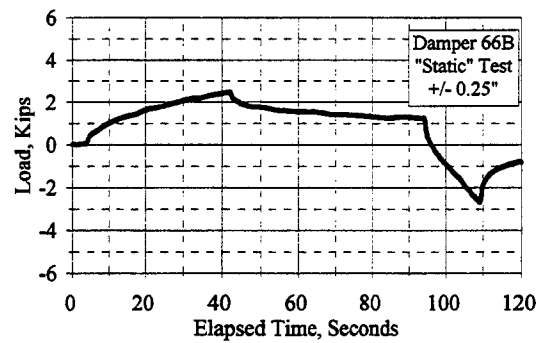
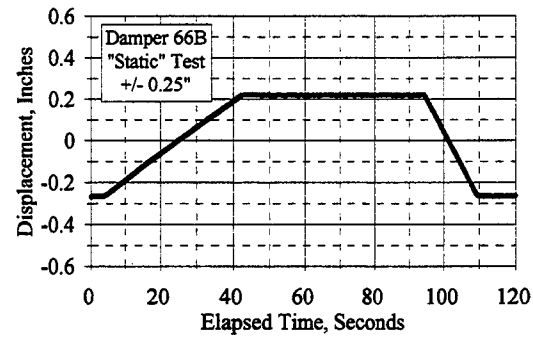
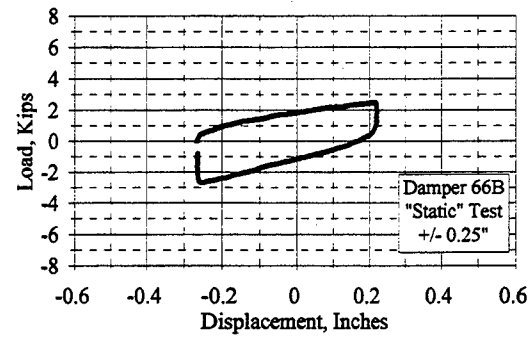


Figure D.16 Damper Test Results, Damper 66B, Quasi-Static Loading, 0.250"

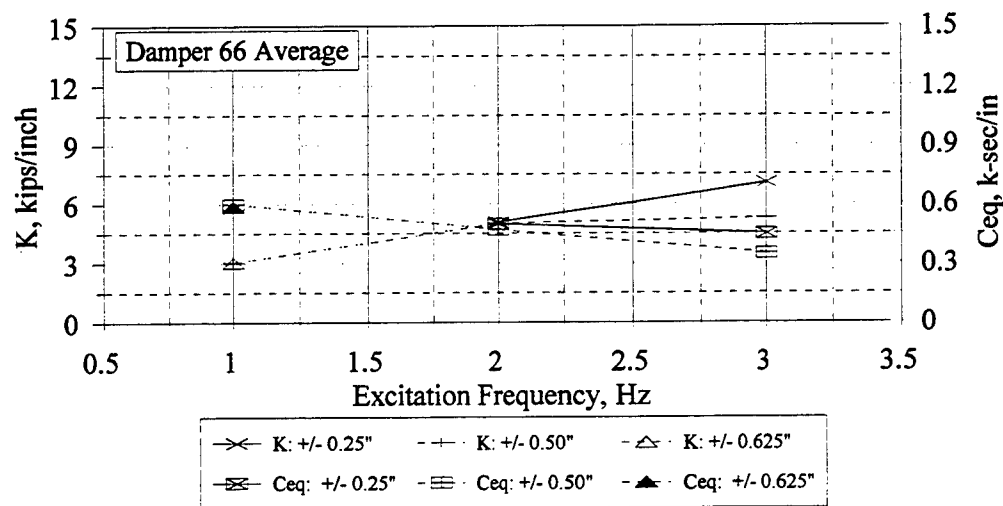
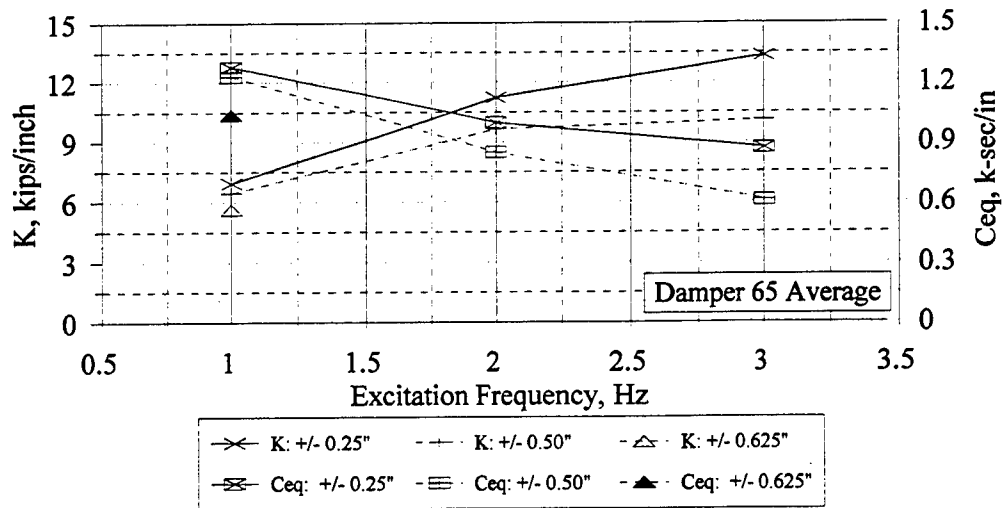


Figure D.17 Average Damper Properties from Tests

VITA

John R. Hayes, Jr. ("Jack"), was born in Richmond, Virginia, on May 12, 1951. He attended Virginia Military Institute (VMI) from 1969 to 1973, where he received a Bachelor of Science degree in Civil Engineering. He was graduated from VMI as both an academically Distinguished Graduate and a Distinguished Military Graduate. He attended the University of Virginia from 1973 to 1975, where he received a Master of Engineering degree in Civil Engineering. During his time at the University of Virginia, Mr. Hayes was inducted into the Tau Beta Pi national engineering honor society.

From 1975 to 1980, Mr. Hayes served as a Civil Engineer Officer in the United States Air Force (USAF), first in Oklahoma (1975-1977) and then in Germany (1977-1980). During his tenure in Germany, Mr. Hayes was instrumental in developing structural design criteria for military protective structures for the USAF and for allied agencies in the North Atlantic Treaty Organization. From 1980 to 1982, Mr. Hayes served as an Assistant Professor of Civil Engineering at VMI, where he taught structural engineering courses. From 1982 to 1988, Mr. Hayes performed structural engineering research as a civilian employee of the USAF at Eglin and Tyndall Air Force Bases in Florida. At the end of that tenure, Mr. Hayes was the Senior Scientist of the Engineering Division of the Air Force Engineering and Services Laboratory. Since 1988, Mr. Hayes has been a civilian employee of the U.S. Army Corps of Engineers at the U.S. Army Construction Engineering Research Laboratories (USACERL), Champaign, Illinois, where he serves as the leader of the USACERL Seismic and Structural Engineering Group.

Following his active duty military career, Mr. Hayes was a member of the USAF Reserves (USAFR) from 1980 until 1995, serving in various civil engineering capacities. He retired from the USAFR at the rank of Lieutenant Colonel.

Mr. Hayes is a registered Professional Engineer in Florida and Virginia.

Mr. Hayes has been married since 1977 to the former Sally Elizabeth Troop of Enid, Oklahoma. Mr. and Mrs. Hayes are the parents of one son, Thomas, who was born in 1987.